

THE JOURNAL

of the

Acoustical Society of America

Vol. 101, No. 2

February 1997

ACOUSTICAL NEWS—USA		631
USA Meetings Calendar		632
DIRECTORY OF GRADUATE EDUCATION IN ACOUSTICS	Wayne W. Wright	637
ACOUSTICAL NEWS—INTERNATIONAL		657
International Meetings Calendar		657
REVIEWS OF ACOUSTICAL PATENTS		659
SELECTED RESEARCH ARTICLE [10]		
Temporal integration of loudness, loudness discrimination, and the form of the loudness function	Søren Buus, Mary Florentine, Torben Poulsen	669
GENERAL LINEAR ACOUSTICS [20]		
Resonant scattering of acoustic waves by ellipsoid air bubbles in liquids	Zhen Ye	681
Determination of grain-size distribution from ultrasonic attenuation: Transformation and inversion	Denise Nicoletti, Aran Anderson	686
Partial coherence of transient ultrasonic fields in anisotropic random media: Application to coherent echo detection	Arnaud Derode, Mathias Fink	690
Singular points of intensity streamlines in two-dimensional sound fields	C. F. Chien, R. V. Waterhouse	705
NONLINEAR ACOUSTICS, MACROSONICS [25]		
Acoustic radiation force on a spherical particle in a viscous heat-conducting fluid. I. General formula	Alexander A. Doinikov	713
Acoustic radiation force on a spherical particle in a viscous heat-conducting fluid. II. Force on a rigid sphere	Alexander A. Doinikov	722
Acoustic radiation force on a spherical particle in a viscous heat-conducting fluid. III. Force on a liquid drop	Alexander A. Doinikov	731
UNDERWATER SOUND [30]		
Computing effective reflection coefficients in layered media	David H. Berman	741
Robust wideband matched-field processing with a short vertical array	Stephen P. Czenszak, Jeffrey L. Krolik	749
Rational square-root approximations for parabolic equation algorithms	Fausto A. Milinazzo, Cedric A. Zala, Gary H. Brooke	760
Scattering from an elastic shell and a rough fluid-elastic interface: Theory	Garner C. Bishop, Judy Smith	767
Acoustic propagation through an internal wave field in a shallow water waveguide	Dirk Tielbürger, Steven Finette, Stephen Wolf	789

(Continued)

CONTENTS—Continued from preceding page

A note on nonlinear radiation from a gas bubble in liquids	Zhen Ye	809
ULTRASONICS, QUANTUM ACOUSTICS, AND PHYSICAL EFFECTS OF SOUND [35]		
Optimal recovery of the elasticity tensor of general anisotropic materials from ultrasonic velocity data	Christophe Aristégui, Stéphane Baste	813
Modal analysis of Lamb wave generation in elastic plates by liquid wedge transducers	X. Jia	834
Laser ultrasonic studies of solid–liquid interfaces	Douglas T. Queheillalt, Yichi Lu, Haydn N. G. Wadley	843
TRANSDUCTION [38]		
A study on beam optimizing of wideband stagger-tuned array	Qimin Chen, Shanhui Bao, Xiaofei Zang, Wei Wei, Jianzhong Guo	854
STRUCTURAL ACOUSTICS AND VIBRATION [40]		
Transient waves in a periodic stack: Experiments and comparison with analysis	Michael El-Raheb, Reinhard Tham	860
Structural and acoustical wave interaction at a wedge-shaped junction of fluid-loaded plates	A. N. Norris, A. V. Osipov	867
Wave-number space response of a near periodically ribbed shell	Douglas M. Photiadis, Earl G. Williams, Brian H. Houston	877
Extension of the tip excitation technique to the rotational compliance measurement of curved structures	L. Cheng, Y. C. Qu	887
The effect of internal oscillators on the acoustic response of a submerged shell	Douglas M. Photiadis, J. A. Bucaro, Brian H. Houston	895
Structural wave reflection coefficients of cylindrical shell terminations: Numerical extraction and reciprocity constraints	P. W. Smith, Jr., J. Gregory McDaniel, Kevin D. LePage, Robert Barile	900
Free vibration of a partially fluid-filled cross-ply laminated composite circular cylindrical shell	Z. C. Xi, L. H. Yam, T. P. Leung	909
Sensitivity analysis of coupled structural-acoustic problems using perturbation techniques	Steven R. Hahn, Aldo A. Ferri	918
The application of analytical/numerical matching to structural discontinuities in structural/acoustic problems	Rickard C. Loftman, Donald B. Bliss	925
NOISE: ITS EFFECTS AND CONTROL [50]		
Wave propagation and attenuation in Herschel–Venturi tubes	A. Selamet, V. Easwaran	936
Status of road traffic noise in Calcutta metropolis, India	Debashis Chakrabarty, Subhas Chandra Santra, Abirlal Mukherjee, Biva Roy, Prasun Das	943
A re-examination of risk estimates from the NIOSH Occupational Noise and Hearing Survey (ONHS)	Mary M. Prince, Leslie T. Stayner, Randall J. Smith, Stephen J. Gilbert	950
ARCHITECTURAL ACOUSTICS [55]		
Sound transmission through a double leaf partition with edge flanking	R. J. M. Craik, T. R. T. Nightingale, J. A. Steel	964
ACOUSTICAL MEASUREMENTS AND INSTRUMENTATION [58]		
A study of the transmission of ultrasound across solid–rubber interfaces	Bruce Drinkwater, Rob Dwyer-Joyce, Peter Cawley	970
PHYSIOLOGICAL ACOUSTICS [64]		
Optimal binaural processing based on point process models of preprocessed cues	Lin Yue, Don H. Johnson	982

CONTENTS—Continued from preceding page

Auditory-nerve fiber responses to clicks in guinea pigs with a damaged cochlea	Huib Versnel, Vera F. Prijs, Ruurd Schoonhoven	993
PSYCHOLOGICAL ACOUSTICS [66]		
Masking of a brief probe by sinusoidal frequency modulation	Brent W. Edwards, Neal F. Viemeister	1010
A new way to account for binaural detection as a function of interaural noise correlation	Marcel van der Heijden, Constantine Trahiotis	1019
Asymmetry of masking revisited: Generalization of masker and probe bandwidth	Joseph L. Hall	1023
On the Duifhuis pitch effect	Jian-Yu Lin, William M. Hartmann	1034
The relation between gap detection, loudness, and loudness growth in noise-masked normal-hearing listeners	Joseph W. Hall III and, John H. Grose	1044
Monastral sound localization revisited	Frederic L. Wightman, Doris J. Kistler	1050
SPEECH PRODUCTION [70]		
Toward articulatory-acoustic models for liquid approximants based on MRI and EPG data. Part I. The laterals	Shrikanth S. Narayanan, Abeer A. Alwan, Katherine Haker	1064
Toward articulatory-acoustic models for liquid approximants based on MRI and EPG data. Part II. The rhotics	Abeer Alwan, Shrikanth Narayanan, Katherine Haker	1078
SPEECH PERCEPTION [71]		
Perceptual magnet effect in the light of behavioral and psychophysiological data	Olli Aaltonen, Osmo Eerola, Åke Hellström, Esa Uusipaikka, A. Heikki Lang	1090
SPEECH PROCESSING AND COMMUNICATION SYSTEMS [72]		
Improving discrimination of confusable words using the divergence measure	Philipos Loizou, Andreas Spanias	1106
MUSIC AND MUSICAL INSTRUMENTS [75]		
Materials for guitar back plates made from sustainable forest resources	Hiroyuki Yano, Yuuzoh Furuta, Hiroyuki Nakagawa	1112
A passive nonlinear digital filter design which facilitates physics-based sound synthesis of highly nonlinear musical instruments	John R. Pierce, Scott A. Van Duyne	1120
BIOACOUSTICS [80]		
Can acoustic multipath explain finback (<i>B. physalus</i>) 20-Hz doublets in shallow water?	V. Premus, J. L. Spiesberger	1127
Error analysis in acoustic elastography. I. Displacement estimation	Mehmet Bilgen, Michael F. Insana	1139
Error analysis in acoustic elastography. II. Strain estimation and SNR analysis	Mehmet Bilgen, Michael F. Insana	1147
Broadband through-transmission signal loss measurements of Albunex[®] suspensions at concentrations approaching <i>in vivo</i> doses	Jon N. Marsh, Christopher S. Hall, Michael S. Hughes, Joel Mobley, James G. Miller, Gary H. Brandenburger	1155
Broadband measurements of the attenuation coefficient and backscatter coefficient for suspensions: A potential calibration tool	Christopher S. Hall, Jon N. Marsh, Michael S. Hughes, Joel Mobley, Kirk D. Wallace, James G. Miller, Gary H. Brandenburger	1162
Harmonic amplitude distribution in a wideband ultrasonic wavefront after propagation through human abdominal wall and breast specimens	Dong-Lai Liu, Robert C. Waag	1172

(Continued)

CONTENTS—Continued from preceding page

LETTERS TO THE EDITOR

On the Mie potential, the acoustic nonlinear parameter B/A [25]	B. Frank, J. D. N. Cheeke	1184
Understanding the periodic driving pressure in the Rayleigh–Plesset equation [25]	William C. Moss	1187
An empirical relation to predict ultrasonic velocity in electrolytic solutions [35]	S. Sivaramakrishna Iyer, M. Abdulkhadar	1191
The frequency response of the ER-2 speaker at the eardrum [64]	M. L. Whitehead, I. Simons, B. B. Stagner, G. K. Martin	1195

TECHNICAL NOTES AND RESEARCH BRIEFS

A demonstration apparatus of the cochlea	Robert M. Keolian	1199
--	-------------------	------

CUMULATIVE AUTHOR INDEX

1203

NOTES CONCERNING ARTICLE ABSTRACTS

1. The number following the abstract copyright notice is a Publisher Item Identifier (PII) code that provides a unique and concise identification of each individual published document. This PII number should be included in all document delivery requests for copies of the article.
2. PACS numbers are for subject classification and indexing. See June and December issues for detailed listing of acoustical classes and subclasses.
3. The initials in brackets following the PACS numbers are the initials of the JASA Associate Editor who accepted the paper for publication.

Document Delivery: Copies of articles can be ordered for \$15 per copy from the AIP/Member Society document delivery service “Articles in Physics,” 75 Varick Street, New York, NY 10013; Fax: 212-301-4060; Telephone: 800-480-PHYS (800-480-7497) (in U.S. and Canada), or 212-301-4000; E-mail: articles@aip.org; URL: <http://www.aip.org/articles.html>

ACOUSTICAL NEWS—USA

Elaine Moran

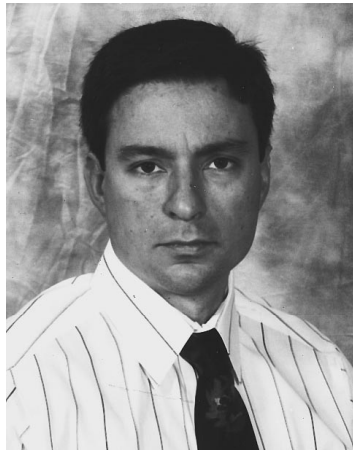
Acoustical Society of America, 500 Sunnyside Boulevard, Woodbury, New York 11797

Editor's Note: Deadline dates for news items and notices are 2 months prior to publication.

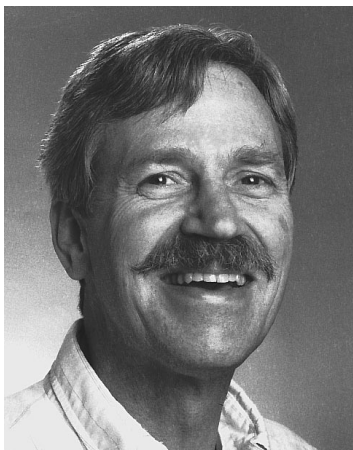
New Fellows of the Acoustical Society of America



Ching-Sang Chiu—For research and leadership in acoustical oceanography.



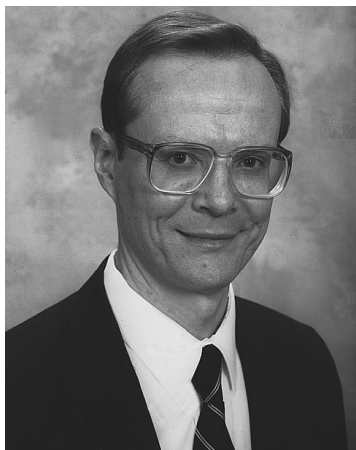
D. Felipe Gaitan—For the first observation of single bubble sonoluminescence.



D. Wesley Grantham—For contributions to the understanding of the auditory perception of motion.



Seiichiro Namba—For contributions and international leadership in the understanding of loudness and noisiness.



Victor Nedzelnitsky—For contributions to microphone calibration and international standards.

Ronald Bannister receives ASME Medal

Ronald L. Bannister, manager, Gasification and Advanced Cycles at Westinghouse Electric Corporation, Orlando, Florida, received the Performance Test Codes Medal of the ASME International (The American Society of Mechanical Engineers) at its International Mechanical Engineering Congress and Exposition in November 1996. The medal was established in 1981 to recognize the first voluntary codes and standards activity in the Society and in the United States. It is awarded to an individual who has made outstanding contribution to the development and promotion of ASME Performance Test Codes.

Mr. Bannister received the award for "his outstanding contribution to the performance test codes (PTC) activity while serving as a member of the PTC Board, chair of PTC 47 on Gasification Combined Cycles, member of PTC 36 on Measurement of Industrial Sound, and Board liaison to PTC 45 on stack testing of municipal waste combustors."

Ronald Bannister received his B.S. in mechanical engineering from the Georgia Institute of Technology, Atlanta, his master's degree in mechanical engineering from Villanova University, and his M.B.A. from Florida Institute of Technology. He is a Member of the Acoustical Society of America and a Fellow of the American Society of Mechanical Engineers.

Harold L. Saxton • 1901–1996



Harold Lavern Saxton, a Fellow of the Society and the 1970 recipient of the Society's "Pioneers of Underwater Acoustics" Medal, died on 24 January 1996 at age 94. He attended Union College in Schenectady and received a BS in physics in 1924. In 1925 he married Elizabeth Bliss. Harold joined the technical staff of the General Electric Company as a research physicist, developing radio transmitters and receivers, studying electromagnetic propagation, and developing thyratrons. He continued study at Union College, receiving an MS degree in 1930.

Then Saxton went to Pennsylvania State College to study ultrasonics under Professor W. H. Pielemeier. For his Ph.D. in physics in 1934 his thesis concerned the propagation of ultrasound in gases. While at Penn State he became an Assistant Professor in 1939. In 1940 Dr. Saxton joined the Sound Division of the Naval Research Laboratory (NRL) to apply his knowledge of acoustics to underwater problems. As the wartime staff of the Sound Division grew rapidly, Dr. Saxton was soon promoted to the position of Section Head.

At NRL he developed transducer shading to reduce the sidelobes of directional response patterns, an automatic attack plotter to help the conning officer track his target, and an attack teacher used for training sonar men and officers; and also carried on research on multipath propagation of sound in the ocean. Outstanding among his early contributions was the sector scan indicator (SSI). In recognition of his invention of the sector scan indicator and other outstanding contributions to antisubmarine warfare, he received the Meritorious Civilian Service Award of the U.S. Navy in 1945.

In 1947 Dr. Saxton became Superintendent of the Sound Division, leading the Laboratory in improving the Navy's sonar capability. Active sonars were operated at lower frequencies and at higher powers, despite penalties in cost and size; and at 1 kHz NRL received the first convergence-zone echoes from a surface ship, making an order of magnitude increase in the range of active sonar. Dr. Saxton established the East Coast transducer test facility on Seneca Lake to calibrate transducers and arrays, without limit of size.

As Superintendent, Dr. Saxton recommended vigorous research in signal processing, with attention to the complicated phenomena of sound propagation in the sea. He not only directed the research but personally contributed many ideas and became an early expert in signal processing. Dr. Saxton wisely considered sonar to involve the physiology and psychology of the listener, and the chemistry, physics, and biology of the ocean medium.

Many of the systems developed by the Sound Division were used for research on the Laboratory's ships.

From 1949 to 1963 Dr. Saxton was the Chairman of the Underwater Sound Advisory Group (USAG), the Navy's top-level council responsible for coordinating the scientific work of all the various laboratories concerned with underwater sound. USAG organizes symposia where classified papers are presented to a restricted audience, and it publishes periodically the classified *U.S. Navy Journal of Underwater Acoustics*.

When Dr. Saxton retired in 1967 he was employed by TRACOR Incorporated, who furnished his services to the Navy. There he served for 2 years as Editor of the *U.S. Navy Journal of Underwater Acoustics*, and updated the chapter on "Ambient Noise" in *A Summary of Underwater Acoustic Data*.

In the Acoustical Society of America, Saxton was a member of the Executive Council from 1953 to 1956, and vice-president in 1965–1966. He was also a member of the Washington Philosophical Society and a member of St. Wilfred's Episcopal Church in Sarasota.

His hobbies included contract bridge, dancing, and flying an airplane (after the age of 60).

Survivors include a son, John, of Rockland, MA, and two grandchildren.

BURTON G. HURDLE

Naval Research Laboratory, Code 7103
Washington, DC 20375

USA Meetings Calendar

Listed below is a summary of meetings related to acoustics to be held in the U.S. in the near future. The month/year notation refers to the issue in which a complete meeting announcement appeared.

- 1997**
- 27–28 Feb. Penn State Ultrasonic Transducer Engineering Workshop, Newport Beach, CA [Donna Rode, SPIE, P.O. Box 10, Bellingham, WA 98227-0010, Tel.: 360-676-3290; E-mail: donnar@mom.spie.org or K. Kirk Shung, 231 Hallowell Bldg., Penn State Univ., University Park, PA 16802, Tel.: 814-865-1407; E-mail: kksbio@engr.psu.edu].
- 13–16 April 23rd International Symposium on Acoustical Imaging, Boston, MA [Sidney Lees, Bioengineering Dept., Forsyth Dental Ctr., 140 Fenway, Boston, MA 02115; FAX: 617-262-4021; E-mail: sleeves@forsyth.org].
- 12–14 May Third AIAA/CEAS Aeroacoustic Conference, Atlanta, GA [Dr. Stephen Engelstad, Lockheed Martin Aeronautical Systems, D/73-47, Z/O-685, Marietta, GA 30063, Tel.: 770-494-9178; FAX: 770-494-3055; E-mail: sengelstad@fs2.mar.lmco.com].
- 15–20 June Eighth International Symposium on Nondestructive Characterization of Materials, Boulder, CO [Debbie Harris, The Johns Hopkins University, Ctr. for Nondestructive Evaluation, 102 Maryland Hall, 3400 N. Charles St., Baltimore, MD 21218, Tel.: 410-516-5397; FAX: 410-516-72249, E-mail: cnde@jhvmshcf.jhu.edu].
- 15–17 June NOISE-CON 97, State College, PA [Institute of Noise Control Engineering, P.O. Box 320, Arlington Branch, Poughkeepsie, NY 12603, Tel.: 914-891-1407; FAX: 914-463-0201].
- 16–20 June 133rd meeting of the Acoustical Society of America, State College, PA [ASA, 500 Sunnyside Blvd., Woodbury, NY 11797, Tel.: 516-576-2360; FAX: 516-576-2377; E-mail: asa@aip.org, WWW: http://asa.aip.org].
- 9–13 July International Clarinet Association, Texas Tech Univ., Lubbock, TX [Keith Koons, Music Department, Univ. of Central Florida, P.O. Box 161354, Orlando, FL 23816-1354, Tel.: 407-823-5116; E-mail: kkoons@pegasus.cc.ucf.edu].
- 7–11 Sept. American Academy of Otolaryngology—Head and Neck Surgery, San Francisco, CA [American Academy

- of Otolaryngology—Head and Neck Surgery, One Prince St., Alexandria, VA 22314, Tel.: 703-836-4444; FAX: 703-683-5100].
- 22–24 Sept. Second Biennial Hearing Aid Research and Development Conference, Bethesda, MA [National Institute of Deafness and Other Communication Disorders, 301-970-3844; FAX: 301-907-9666; E-mail: hearingaid@tascon.com]. Deadline for abstracts is 15 March.
- 1–5 Dec. 134th meeting of the Acoustical Society of America, San Diego, CA [ASA, 500 Sunnyside Blvd., Woodbury, NY 11797, Tel.: 516-576-2360; FAX: 516-576-2377; E-mail: asa@aip.org, WWW: <http://asa.aip.org>].
- 22–26 June 135th meeting of the Acoustical Society of America/ 16th International Congress on Acoustics, Seattle, WA [ASA, 500 Sunnyside Blvd., Woodbury, NY 11797, Tel.: 516-576-2360; FAX: 516-576-2377; E-mail: asa@aip.org, WWW: <http://asa.aip.org>].
- 13–17 Sept. American Academy of Otolaryngology—Head and Neck Surgery, San Francisco, CA [American Academy of Otolaryngology—Head and Neck Surgery, One Prince St., Alexandria, VA 22314, Tel.: 703-836-4444; FAX: 703-683-5100].
- 12–16 Oct. 136th meeting of the Acoustical Society of America, Norfolk, VA [ASA, 500 Sunnyside Blvd., Woodbury, NY 11797, Tel.: 516-576-2360; FAX: 516-576-2377; E-mail: asa@aip.org, WWW: <http://asa.aip.org>].

1998

ACOUSTICAL NEWS—INTERNATIONAL

Walter G. Mayer

Physics Department, Georgetown University, Washington, DC 20057

The International Commission on Acoustics— A change in status

In September 1996 a letter was sent by the chairman of ICA to national acoustical societies worldwide informing them of a change in status of the commission within IUPAP. Below is an abbreviated abstract of this letter.

The International Commission on Acoustics, ICA, was established in 1951 as a subcommittee of the International Union for Pure and Applied Physics, IUPAP. In a letter, dated 10 May 1996, the Commission informed the National Societies about the initiative to change the status of the International Commission on Acoustics from an ordinary commission to an affiliated commission.

The reason for the change is the desire by the commission to have its mandate directly from the national acoustical societies of the world with the objective of improving the commission's service to the acoustics community.

The new commission is an international non-governmental organization. Its mission is to promote international development and collaboration in all fields of acoustics including research, development, education, and standardization.

This change of status as well as new statutes were approved at the IUPAP General Assembly in September 1996. The new commission will be based on the membership of the national acoustical societies (or corresponding organizations). The member societies will appoint official delegates who will form a General Assembly that elects members of a Board of the commission. The General Assembly will meet for the first time in connection with the International Congress on Acoustics in Seattle, Washington, in June 1998. Further relevant information can be obtained from <http://www.nrc.ca/ims/ica>

Marine Electromagnetics Conference—Topics related to underwater acoustics?

The First International Conference on Marine Electromagnetics will be held at Imperial College, London, 23–25 June 1997. This meeting may well be of interest to scientists working in underwater acoustics, judging from the announcement released by the organizers which reads:

“Interest is growing in a relatively new, and virtually unexplored, area of magnetism concerned with the magnetic, electric and electromagnetic fields which occur in an ocean/marine environment. These might arise due to a number of effects, some widely known, some less so. To investigate the underlying phenomena, expertise from many disciplines may well be required. It is the object of this conference to bring together workers from a wide range of fields to examine the collective current state of the art. This is believed to be the first conference of its kind anywhere and is being organized jointly by the Defence Evaluation and Research Agency and Imperial College. The emphasis will be on fundamental mechanisms and coupled effects, and papers are invited on any topic which relates to electromagnetic, magnetic, and associated fields in a marine environment.”

Further information is available from Secretariat “Marelec97,” Electronic and Electrical Engineering, Imperial College, Exhibition Road, London SW7 2BT, UK; Fax: +44 171 823 8125; E-mail: marelec@ic.ac.uk

Institute of Acoustics honors W. W. Lang

The Institute of Acoustics (UK) has honored Bill Lang by awarding him an Honorary Fellow in recognition of his outstanding contributions and international leadership in the field of noise control engineering. Having received the award, he joins a very small group of acousticians who are presently Honorary Fellows. Their number is indeed very small because the Institute has a rule which says that “...the total number of Honorary Fellows for the time being shall not exceed 2 per centum of the number of persons elected as Corporate Members...” The first American acoustician who received an Honorary Fellowship was Warren P. Mason.

Silver Jubilee—Swiss Acoustical Society

The 25th General Assembly of the Swiss Acoustical Society was held in Lucerne in early November 1996. The festive program which was dedicated to the 25th birthday of the society included three main sections: technical sessions and workshops, discussions of new bylaws and election of officers, and status of the society within FASE (Federation of Acoustical Societies of Europe) or within EAA (European Acoustics Association); at this writing it is not clear whether or not the Swiss Acoustical Society will continue its membership in FASE. A number of social events contributed to the success of the Silver Jubilee meeting.

Homepages

Several acoustical societies have established homepages containing information about various aspects of the organization, membership, meetings, and other items of interest. Below are the most recent announcements of homepages:

Canadian Acoustical Association	http://www.uwo.ca/hhcr/caa
French Acoustical Society	http://ww.loa.espci.fr
German Acoustical Society	http://www.itap.physik.uni-oldenburg.de/dega.htm
International Commission on Acoustics	http://www.nrc.ca/ims/ica

International Meetings Calendar

Below are announcements of meetings to be held abroad. Entries preceded by an * are new or updated listings with contact addresses given in parentheses. Month/year listings following other entries refer to issues of the *Journal* which contain full calendar listings or meeting announcements.

March 1997

- 2–7 ***16th World Congress of Otorhinolaryngology, Head and Neck Surgery**, Sydney, Australia. (Congress Secretariat, GPO Box 128, Sydney NSW 2001, Australia; Fax: +61 2 262 2323; E-mail: tourhosts@tourhosts.com.au; WEB: <http://www.eventscamp.com.au/conferences/oto.html>)
- 3–7 **DATA 97** (German Acoustical Society Meeting), Kiel. 8/96
- 17–19 **Spring Meeting ASJ**, Kyoto. 6/96

April 1997

- 2–4 **International Symposium on Simulation, Visualization, and Auralization for Acoustic Research and Education**, Tokyo. 2/96
- 7–9 ***Acoustics 97**, Windermere, UK. (Institute of Acoustics, Agriculture House, 5 Holywell Hill, St. Albans, Herts AL1 1EU, UK; Fax: +44 1727 850 533; E-mail: acousites@clus1.ulcc.ac.uk)
- 14–18 **Fourth French Congress on Acoustics**, Marseille. 6/96
- 16–19 ***2nd European Conference on Protection Against Noise**, London, United Kingdom. (D. Prasher, Institute of Laryngology and Otology, University College London, 330 Gray's Inn Road, London WC1X 8EE; Fax: +44 171 278 8041)
- 21–24 **International Conference on Acoustics, Speech, and Signal Processing—ICASSP 97**, Munich. 10/95
- 21–25 **International Conference on Shallow-Water Acoustics**, Beijing. 10/96

- May 1997**
 12–16 **FASE Symposium on Hydroacoustics and Ultrasonics**, Jurata/Gdańsk. 4/96
 21–23 **Italian Acoustical Association Annual Meeting**, Perugia. 8/96
- June 1997**
 3–5 ***8th International Meeting on Low Frequency Noise & Vibration**, Gothenburg, Sweden. (W. Tempest, Multi-Science Publishing Co. Ltd., 107 High Street, Brentwood, Essex CM14 4RX, UK; Fax: +44 1277 223453)
 5–7 **Conference on ICP and Inner Ear Pressure**, Bath. 4/96
 18–21 **3rd European Conference on Audiology**, Prague. 12/96
 23–25 ***1st International Conference on Marine Electromagnetics**, London. 2/97
 24–27 **1st European Conference on Signal Analysis and Prediction**, Prague. 8/96
 25–27 **12th Echocardiology Symposium and 9th Meeting of the International Cardia Doppler Society**, Rotterdam. 6/96
 25–27 **5th International Congress of the International Society of Applied Psycholinguistics (ISAPL '97)**, Porto. 10/96
- July 1997**
 2–4 **Ultrasonics International '97**, Delft. 4/96
 14–17 ***6th International Conference on Recent Advances in Structural Dynamics**, Southampton, UK. (N. S. Ferguson, ISVR, University of Southampton, Southampton SO17 IJ, UK; Fax: +44 1703 593033; E-mail: mzs@isvr.soton.ac.uk)
- August 1997**
 14–27 **1997 World Congress on Ultrasonics**, Yokohama. 4/96
 18–22 **3rd EUROMECH Solid Mechanics Conference**, Stockholm. 10/96
 19–22 **International Symposium on Musical Acoustics**, Edinburgh. 8/96
 21–23 **ACTIVE 97 Inter-Noise Satellite Symposium**, Budapest. 6/96
 25–27 **Inter-Noise 97**, Budapest. 2/96
- September 1997**
 1–4 **Modal Analysis Conference (IMAC-XV Japan)**, Tokyo. 10/96
 10–12 **Biennial Conference New Zealand Acoustical Society**, Christchurch. 4/96, 12/96
- 9–12 **31st International Acoustical Conference "Acoustics—High Tatra 97,"** High Tatra. 10/96
 10–12 **Biomechanics of Hearing**, Stuttgart. 10/96
 15–18 **3rd EUROMECH Fluid Mechanics Conference**, Göttingen. 10/96
 18–20 ***Intonation: Theory, Models and Applications**, Athens, Greece. (ESCA Workshop, Department of Informatics, University of Athens, Panepistimioupolis, Ilisia, 15784 Athens, Greece; Fax: +30 1 722 8981; E-mail: tonesca@di.uoa.gr)
 22–25 **5th European Conference on Speech Communication and Technology**, Patras. 2/96
 23–26 **Fluid–Structure Interaction in Acoustics**, Delft. 10/96
- October 1997**
 7–10 **1997 IEEE Ultrasonics Symposium**, Toronto. 2/96
 8–10 **Acoustics Week in Canada 1997**, Windsor. 12/96
 23–26 ***Reproduced Sound 13**, Windermere, UK. (Institute of Acoustics, Agriculture House, 5 Holywell Hill, St. Albans, Herts AL1 1EU, UK; Fax: +44 1727 850 533; E-mail: acoustics@clus1.ulcc.ac.uk)
- November 1997**
 19–21 **WESTPRAC'97**, Hong Kong. 10/96
 20–23 ***IOA Autumn Conference: Environmental Noise**, Windermere, UK. (Institute of Acoustics, Agriculture House, 5 Holywell Hill, St. Albans, Herts AL1 1EU, UK; Fax: +44 1727 850 533; E-mail: acoustics@clus1.ulcc.ac.uk)
- December 1997**
 15–18 **5th International Congress on Sound and Vibration**, Adelaide. 10/96
- March 1998**
 23–27 **DAGA 98 (German Acoustical Society Meeting)**, Zürich. 8/96
- May 1998**
 25–27 ***Noise and Planning 98**, Naples, Italy. (Noise & Planning, via Bragadino 2, 20144 Milano, Italy; Fax: +39 248018839; E-mail: md1467@cmlink.it)
- June 1998**
 8–10 **EAA/EEAA Symposium "Transport Noise and Vibration,"** Tallinn. 10/96
- November 1998**
 16–18 **Inter-Noise 98**, Christchurch. 4/96
 23–27 **ICBEN 98: Biological Effects of Noise**, Sydney. 12/96

REVIEWS OF ACOUSTICAL PATENTS

Daniel W. Martin

7349 Clough Pike, Cincinnati, Ohio 45244

The purpose of these acoustical patent reviews is to provide enough information for a Journal reader to decide whether to seek more information from the patent itself. Any opinions expressed here are those of reviewers as individuals and are not legal opinions. Printed copies of United States Patents may be ordered at \$3.00 each from the Commissioner of Patents and Trademarks, Washington, DC 20231. [S0001-4966(97)04602-X]

Reviewers for this issue:

HARVEY H. HUBBARD, 23 Elm Avenue, Newport News, Virginia 23601

SAMUEL F. LYBARGER, 101 Oakwood Road, McMurray, Pennsylvania 15317

D. LLOYD RICE, 11222 Flatiron Drive, Lafayette, Colorado 80026

ROBERT C. WAAG, University of Rochester Medical Center, 601 Elmwood Avenue, Rochester, New York 14642

ROBERT W. YOUNG, 1696 Los Altos Road, San Diego, California 92109

5,540,079

43.35.Ud MICROWAVE EXCITED PHOTOACOUSTIC EFFECT CARBON MONITOR

Robert C. Brown and Jeffrey R. Dykstra, assignors to Iowa State University Research Foundation, Incorporated
30 July 1996 (Class 73/23.33); filed 30 August 1994

This patent describes "a method and apparatus for directing modulated microwave radiation at fly ash which absorbs the microwave energy and, in turn, emits minute acoustical waves. These acoustic waves are measured by a microphone to determine the carbon content of the fly ash."—DWM

5,535,627

43.35.Yb ROLL STRUCTURE ACOUSTIC GAGE AND METHOD

R. P. Swanson et al., assignors to Oklahoma State University
16 July 1996 (Class 73/597); filed 11 May 1995

This is a device and method for determining the radial pressure profile of a wound roll of material. Internal and external sensors measure the time of flight of an acoustic wave induced in the roll by sharp impacts on the surface, or by sharp impacts on a member in contact with the surface. "The wave measurements are fed to a computer which uses a modification of Hakiel's model to compute the radial pressure profile."—RWY

5,525,854

43.35.Zc IN-PLANE ULTRASONIC VELOCITY MEASUREMENT

Maclin S. Hall et al., assignors to Institute of Paper Science and Technology, Incorporated
11 June 1996 (Class 310/334); filed 6 March 1995

"An improved system for measuring the velocity of ultrasonic signals within the plane of moving web-like materials, such as paper, paperboard and the like...the system is also adapted to provide on-line indication of the polar specific stiffness of the moving web...the velocity of ultrasonic signals in the plane of the web are measured by way of a plurality of ultrasonic transducers carried by synchronously driven wheels or cylinders, thus eliminating undue transducer wear due to any speed differences between the transducers and the web. In order to provide relatively constant contact force between the transducers and the webs, the transducers are mounted in sensor housings which include a spring for biasing the transducer radially outwardly. The sensor housings are adapted to be easily and conveniently mounted to the carrier to provide a relatively constant contact force between the transducers and the moving web."—RWY

5,546,792

43.35.Zc COMPUTERIZED SONIC PORTABLE TESTING LABORATORY

Harold L. Becker, assignor to Harold L. Becker
20 August 1996 (Class 73/64.53); filed 22 December 1994

"A portable sonic testing device for the testing of waxy and emulsified fluids, utilizing variations in soundwave propagation, light propagation, and changes in electrical resistance in the liquid, all over a range of temperatures and chemical treatment conditions." Empirical equations are included in the patent to relate observed cooling rate to melting point of carbon chain length of normal paraffin, and "to transform frequencies, voltage, resistance, velocity, and probe dimensions to units of viscosity."—RWY

5,511,095

43.38.Md AUDIO SIGNAL CODING AND DECODING DEVICE

Takeo Inoue et al., assignors to Sanyo Electric Company
23 April 1996 (Class 375/244); filed in Japan 15 April 1992

This audio compression technique is intended for use in a CD player, to fill in for real time samples from the disk surface in case the playback rate gets ahead of reads from the disk. In that case, buffer memory is required and the patented scheme may be used to reduce the required memory size. The input signal passes through an integration to reduce intersample differences before being coded with a typical ADPCM circuit. The decoded output is correspondingly differentiated to restore the original spectral balance.—DLR

5,519,774

43.38.Si METHOD AND SYSTEM FOR DETECTING AT A SELECTED STATION AN ALERTING SIGNAL IN THE PRESENCE OF SPEECH

Ralph N. Battista et al., assignors to Bell Communications Research, Incorporated
21 May 1996 (Class 379/386); filed 8 December 1992

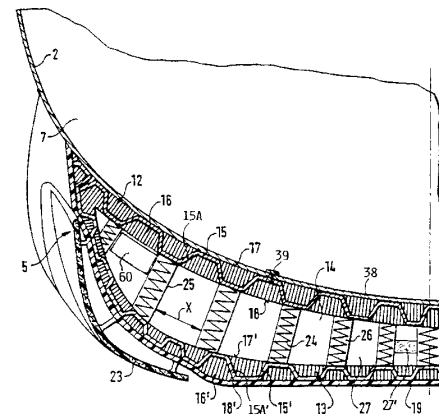
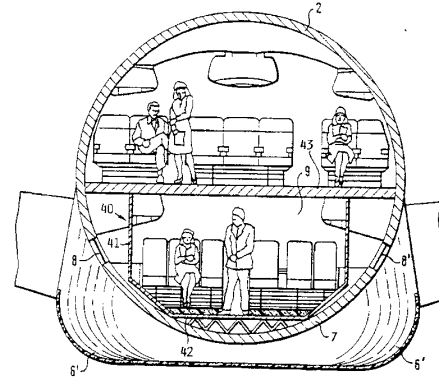
New telephone services, such as call-waiting alert, impose greater demands on the proper detection of in-band signalling tones than has been the case for DTMF (touch tone) usage. This patent covers an improved system of detection, which relies on the fact that the tone will be computer generated, allowing the use of duration as a distinguishing parameter. A new alerting tone is defined using

43.40.Kd MULTI-DECK PASSENGER AIRCRAFT HAVING IMPACT ENERGY ABSORBING STRUCTURES

Guenter Beuck *et al.*, assignors to Deutsche Aerospace Airbus GmbH

6 August 1996 (Class 244/107); filed in Germany 26 April 1993

The impact energy absorbing structure of this patent is intended to be attached to the fuselage belly of an aircraft that is large enough to allow its lower half to be used as passenger space instead of cargo space. The added



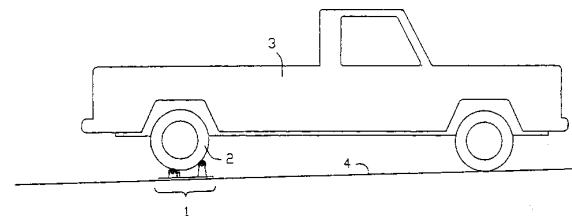
structure is intended to absorb impact energy arising in an emergency landing. Obviously it will also increase the passenger capacity of the aircraft.—DWM

43.40.Ph LAND SEISMIC ACOUSTIC SOURCE

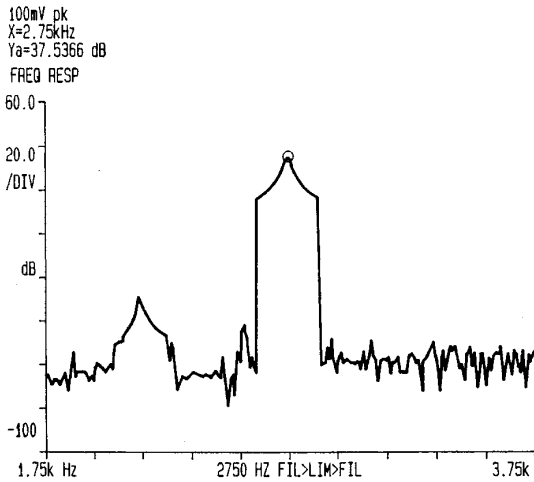
Bill L. Jaworski, Burley, WA

10 September 1996 (Class 181/114); filed 14 February 1995

This patent describes a simple, readily available apparatus for generating a seismic signal in the earth. It combines "force-modulating means" 1, resting on the ground 4 and in contact with the tire surface on drivewheel



2 of vehicle 3 at two idler rollers of different elevation. The difference in position and elevation of the two rollers causes the rotating tire surface to modulate the force transmitted to the earth surface. This is intended to facilitate seismic surveys.—DWM



new dual tone frequency assignments which better avoid speech interference. A more elaborate logic of energy detection in tone-present and tone-absent bands improves the rate of both false and missed detections.—DLR

43.38.Si EARPHONE ASSEMBLY

Atsushi Nagayoshi and Kazunori Kono, assignors to Matsushita Electric Industrial Company

6 August 1996 (Class 381/187); filed in Japan 6 August 1993

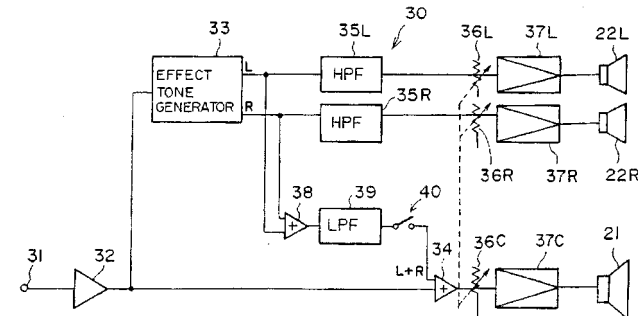
The earphone shown is relatively small and fits into the auricle cavity. An outer part of the earphone housing extends downward and carries the cord. A rotatable part outside the back of the earphone mechanism can be adjusted to suit the size of the auricle cavity to provide better fit and retention.—SFL

43.38.Vk EFFECTOR

Masazumi Moringa and Kousuke Takata, assignors to Roland Corporation

6 August 1996 (Class 84/701); filed in Japan 22 July 1994

The term "effector" as used in this patent refers to circuitry that modifies musical tone input signals by adding an effect such as time delay, reverberation, or chorus effect. Previously, according to the patent, the original tone signals and the effect tone signals have been radiated through



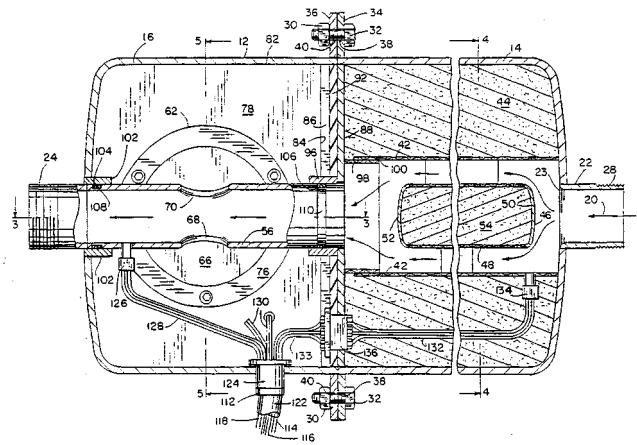
separate loudspeakers. In the present patent the effect tone generator 33 creates two separate output signals L and R having different tonal effects. These outputs are combined through lowpass filter 39 and recombined with direct (unmodified) signal, then radiated by loudspeaker 21, but the high-frequency portions of the separate effect outputs from highpass filters 35L and 35R are separately amplified and radiated from loudspeakers 22L and 22R to provide "a feeling of expanse effective in a sound field," intended to simulate stereophonic reproduction.—DWM

5,552,562

43.40.Yq INERTIAL ACOUSTIC PICKUP

Allen D. Hertz *et al.*, assignors to Motorola, Incorporated
3 September 1996 (Class 84/726); filed 29 August 1994

This is an inertial vibration pickup of the electromagnetic type in which the pickup chassis is fastened to or is in contact with a vibrating surface. The internal mass is coupled to the chassis through planar circular non-linear spring members. The relative motion of coils and magnets generates the pickup output when the chassis is vibrated. The example given is picking up vibrations from the soundboard or body of a stringed musical instrument. The basic principle and, to some extent, the design reminds the reviewer of his inertia-operated throat microphone design [Figs. 8 and 9, *J. Acoust. Soc. Am.* **19**, 43-50 (1947)], but design details are different.—DWM



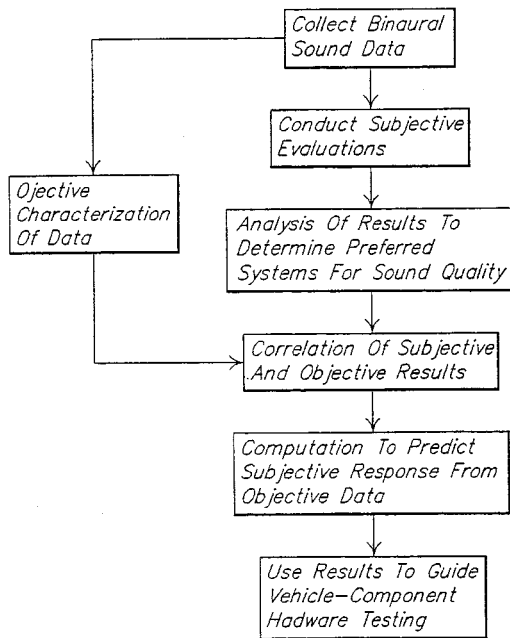
made for passive components to reduce the high-frequency noise and for active components to reduce the lower-frequency noise. Advantages cited are ease of installation, ease of maintenance, minimization of flow restrictions and the reduced size resulting from the use of a ported tuning chamber to improve loudspeaker efficiencies.—HHH

5,540,590

43.50.Ba METHOD FOR PREDICTING HUMAN EVALUATION OF LATCHING AND UNLATCHING SOUNDS

Jerome Avery *et al.*, assignors to Ford Motor Company
30 July 1996 (Class 434/236); filed 6 April 1995

This patent describes an analytical method "for predicting human evaluation response to the quality of sounds" by correlation of subjective



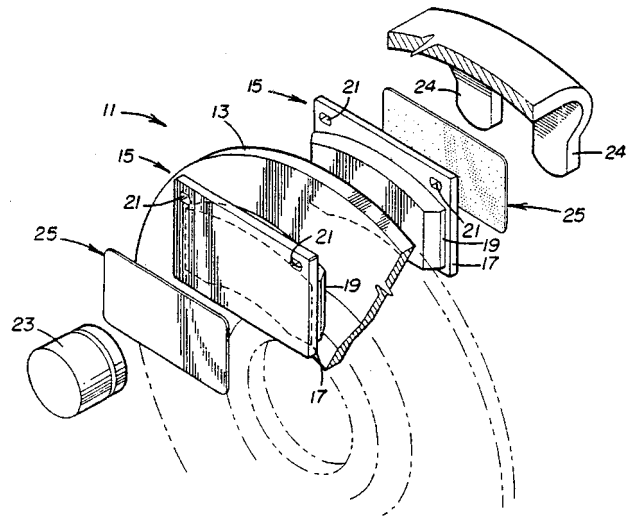
results with objective measurement data. The specific application of the method applies to sounds produced by the operation of a power door lock actuator in an automobile.—DWM

5,518,088

43.50.Gf SHIM STRUCTURE FOR SOUND DAMPENING BRAKE SQUEAL NOISE

Jerry L. Brosilow, San Francisco, CA
21 May 1996 (Class 188/73.37); filed 7 February 1992

The patent discloses the reduction of brake squeal noise caused by vibrations in a disk brake apparatus. It features a sheet of aluminum shim structure and a continuous membrane of high-temperature acrylic adhesive



on one surface only of the aluminum, which in turn is bonded to the back side of the friction pad. The aluminum shim is partially cut through in certain locations to permit material to be popped out, and thus facilitate the fitting of many different friction pad configurations.—HHH

5,513,266

43.50.Gf INTEGRAL ACTIVE AND PASSIVE SILENCER

Michael T. Zuroski, assignor to Digisonix, Incorporated
30 April 1996 (Class 381/71); filed 29 April 1994

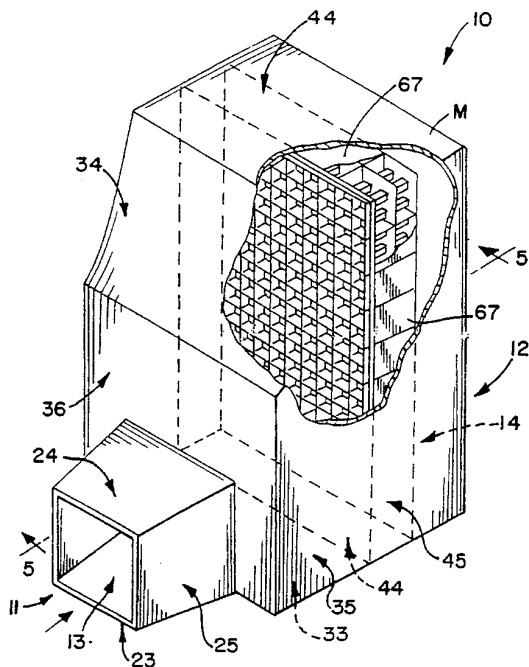
This silencer is for control of broadband noise propagating through pipes or ducts which carry air or gases in industrial applications. Provision is

5,532,439

43.50.Gf SILENCER ASSEMBLY WITH ACOUSTICAL MODULES THEREIN

Yuriy Minkin, assignor to Transco Products, Incorporated
2 July 1996 (Class 181/224); filed 23 June 1994

This is apparatus for the muffling of gas turbine power units and auxiliary fan equipment used in large stationary power plants. Key elements are box-like rectangular acoustical modules which are self-contained and self-



supporting, and which eliminate the need for turning vanes, flow distribution grids, and conventional baffles. These passive acoustical modules are easily stackable to occupy existing or new structures.—HHH

5,526,805

43.50.Gf IN-LINE SILENCER FOR CLEAN ROOM BREATHING APPARATUS

Donald G. Lutz *et al.*, assignors to Dryden Engineering Company
18 June 1996 (Class 128/204.18); filed 3 November 1993

The patent describes the control of internal noise in breathing room apparatus for clean room environments. Communication between workers can be reduced by noise generated by the air blowers. Noise is controlled by means of an in-line silencer, consisting of cylindrically shaped sound absorbing material with an axial airflow passage.—HHH

5,531,196

43.50.Gf OIL PAN NOISE ENCLOSURE AND ATTACHMENT FOR SAME

Kent H. Clark, assignor to the Cummins Engine Company
2 July 1996 (Class 123/195C); filed 1 September 1995

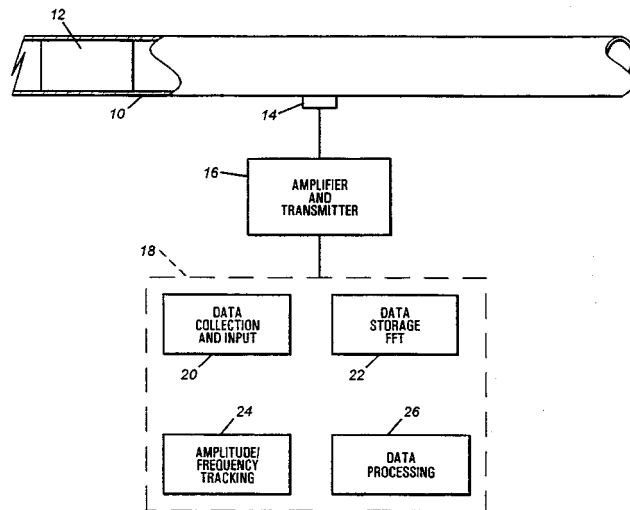
This patent relates particularly to the radiation of noise radiation from the oil pan of a large diesel engine. This is achieved by the attachment of a sound-deadening enclosure to the exterior of the oil pan. The resulting enclosure is attached by means of spring clips in such a manner as to clamp its outer skin and a foam isolation layer against the exterior sidewall of the oil pan. When the oil pan is removed for servicing, the enclosure can remain attached.—HHH

5,549,000

43.50.Yw PASSIVE ACOUSTIC DETECTION OF PIPELINE PIGS

Winthrop K. Brown *et al.*, assignors to Texaco, Incorporated
27 August 1996 (Class 73/587); filed 9 June 1995

Devices propelled through pipelines by fluid flow (called "pigs") are used to clean or inspect the pipe or to separate different batches of fluid



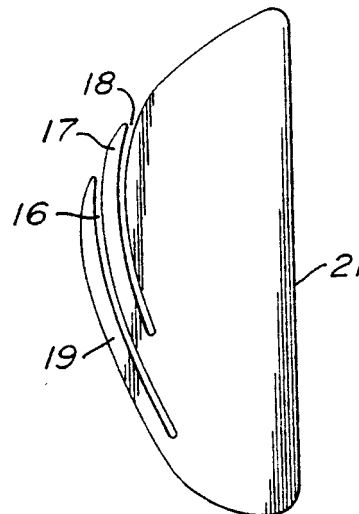
during flow. Their presence and position may be determined by conventional acoustical reflection methods. This patent introduces the additional use of passive acoustical detection of the internal condition of the pipe from analysis of the noise generated by "pig" contact with the pipe during motion.—DWM

5,551,694

43.58.Hp SOUNDING GOLF PUTTER

J. Lawrence Grim, Jr., Perkasio, PA and Jacob H. Malta, New Britain, PA
3 September 1996 (Class 473/234); filed 16 June 1995

The club head of this golf putter has two tines 17 and 19 created by machining slots 16 and 18 on the back side away from the ball-striking surface 21. An alternative, symmetrical design positions the slots on either side of the shaft of the putter creating a tine on both sides. In this design the



ball is actually struck by one of the tines, either left or right, depending upon whether the user is left-handed or right-handed. The primary object is "to provide a sounding golf putter which produces accurate golf putting."—DWM

43.66.Sr TESTING HEARING

Arthur R. D. Thornton, assignor to Medical Research Council, London, U.K.

20 August 1996 (Class 128/746); filed under Patent Cooperation Treaty 29 March 1993

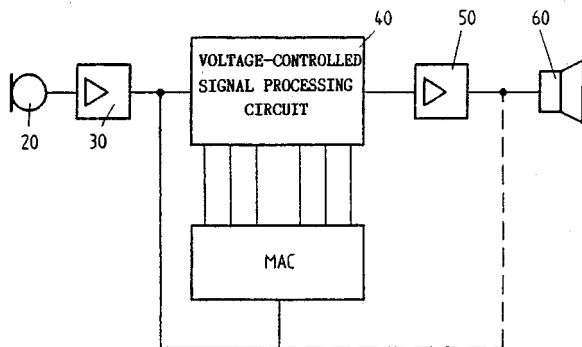
An apparatus for testing hearing has a sound source for applying a sound to the subject's ear and a sound detector for measuring the sound returned from the subject's inner ear. The sound source, which is driven by stimulus generation equipment connected to an analyzer, produces a sequence of sounds and records evoked otoacoustic emissions. Details of the method are given.—SFL

43.66.Ts HEARING AID

Zlatan Ribic, assignor to Viennatone GmbH

18 June 1996 (Class 381/68.2); filed in Austria 27 September 1993

A hearing aid is described in which information obtained from the input to the signal processing circuit is modified to adapt the output signal to the hearing loss characteristics of the user. The signal analyzing circuit is



formed by a Hilbert circuit, the two outputs of which are fed to the voltage-controlled signal processing circuits.—SFL

43.66.Ts IMPLANTABLE AUDITORY SYSTEM WITH MICROMACHINED MICROSENSOR AND MICROACTUATOR

S. George Lesinski and H. Thurman Henderson, both of Cincinnati, OH

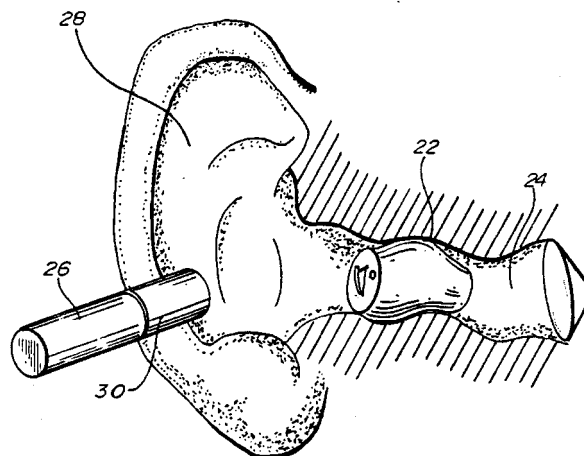
2 July 1996 (Class 623/10); filed 25 January 1993

An implanted hearing aid system includes a microsensor, a processor, and a microactuator. The sensor may be a piezoresistive vibration pickup that is clamped to one of the ossicles. The output of the sensor goes to the processor, which is implanted subcutaneously in the mastoid region of the skull and that contains the electronic system and battery. The output of the processor drives the microactuator, which may be an electrostatic transducer that vibrates the cochlear fluid. Details of a number of possible constructions are given. The specification does not seem to describe how the nonremovable battery can be recharged. However, Fig. 2 shows an rf receiver in series with the battery that could make recharging possible.—SFL

43.66.Ts APPARATUS AND METHOD FOR MAGNETICALLY CONTROLLING A HEARING AID

James R. Newton, assignor to Argosy Electronics, Incorporated
3 September 1996 (Class 381/68.6); filed 31 August 1994

The patent describes an apparatus and method for controlling a plurality of adjustable operational parameters of a hearing aid by the movement of an external magnetic actuator into and out of proximity with a magnetically operated switch in the hearing aid. The hearing aid has processing circuitry



for controlling adjustable operational parameters. The desired adjustment is obtained by moving the magnetic actuator into and out of proximity with the hearing aid a selected number of times. Details of the required circuitry are given.—SFL

43.72.Gy SELECTIVE APPLICATION OF SPEECH CODING TECHNIQUES TO INPUT SIGNAL SEGMENTS

Willem B. Kleijn and Peter Kroon, assignors to AT&T Corporation

30 April 1996 (Class 395/2.32); filed 10 July 1992

The performance of a speech coder may be improved, according to this patent, by combining more than one type of coder along with a decision element able to choose the best type of coding for each short speech segment. The key to the strategy lies in choosing a coding type based on segment characteristics and possibly on the outcomes of previous attempts to code the segment. In general, a preferred coding is first applied to all segments. Code excited linear prediction of pitch-period segments is suggested for this first pass.—DLR

43.72.Gy DIGITAL TRANSMISSION OF ACOUSTIC SIGNALS OVER A NOISY COMMUNICATION CHANNEL

John C. Hardwick and Jae S. Lim, assignors to Digital Voice Systems, Incorporated

14 May 1996 (Class 371/37.4); filed 30 November 1992

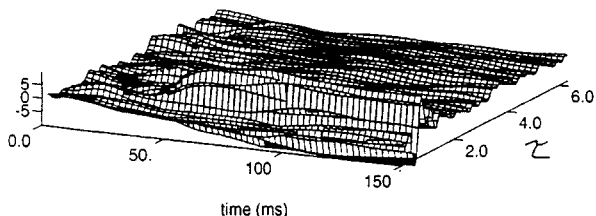
This patent combines several strategies for the allocation of signal and error correction bits in a coded speech channel. Bits are prioritized according to their perceptual importance in the decoded signal, using more redundancy to transmit the more important bits. Blocks of bits are "modulated" by binary addition of a constrained random pattern after error correction coding in a way that increases the number of correctable errors. Finally, the reconstructed speech synthesis parameters are smoothed depending on the detected bit error rate.—DLR

5,517,595

43.72.Gy DECOMPOSITION IN NOISE AND PERIODIC SIGNAL WAVEFORMS IN WAVEFORM INTERPOLATION

Willem B. Kleijn, assignor to AT&T Corporation
14 May 1996 (Class 395/2.14); filed 8 February 1994

In this speech coding system the input signal is first analyzed using linear prediction methods to extract a pitch-period-length residual excitation segment. A Fourier transform of the excitation is partitioned into low- and high-frequency bands. A type of clustering is then applied to each band,



averaging similar occurrences within each band to produce prototype excitation waveforms known as the slowly evolving and rapidly evolving waveforms. Inputs are generally coded using the slowly evolving components as shown in the figure, optionally using the rapid components as required.—DLR

5,519,806

43.72.Gy SYSTEM FOR SEARCH OF A CODEBOOK IN A SPEECH ENCODER

Makio Nakamura, assignor to NEC Corporation
21 May 1996 (Class 395/2.27); filed in Japan 15 December 1992

This is a strategy for speeding up the codebook search in a code-excited linear predictive vocoder. The explanation given is far from lucid. If understood correctly, a set of basis vectors is used to index the excitation waveforms. By correlating the input speech with the relatively small set of basis vectors, a good excitation can be located quickly. Gray codes and something called "ordination" (sorting?) are somehow involved.—DLR

5,519,807

43.72.Gy METHOD OF AND DEVICE FOR QUANTIZING EXCITATION GAINS IN SPEECH CODERS BASED ON ANALYSIS-SYNTHESIS TECHNIQUES

Luca Cellario and Daniele Sereno, assignors to SIP—Societa Italiana per l'Esercizio delle Telecomunicazioni p. a.
21 May 1996 (Class 395/2.33); filed in Italy 4 December 1992

In this code-excited linear predictive vocoder, the signal gain within a frame is compactly coded by dividing the frame into subframes. The individual subframe gains are normalized with respect to the maximum of the subframe gains, reducing the bitrate while maintaining a high level of accuracy in coding a gain profile for the frame.—DLR

5,522,011

43.72.Gy SPEECH CODING APPARATUS AND METHOD USING CLASSIFICATION RULES

Mark E. Epstein *et al.*, assignors to International Business Machines Corporation
28 May 1996 (Class 395/2.31); filed 27 September 1993

This patent discloses a type of vector quantization applied to the coding of speech analysis vectors, such as amplitude and spectral data. Rather than code the entire analysis vector, as is often done, vector quantizations

are individually applied to subsets of the feature values. An indexing scheme relates entries between the various codebooks, capturing correlations and speeding up the codebook searches.—DLR

5,519,764

43.72.Kb CIRCUIT AND METHOD FOR DETECTING ERROR CAUSING TONES IN A VOICE MESSAGING SYSTEM

David A. Pierce and Barry S. Davies, assignors to AG Communication Systems Corporation
21 May 1996 (Class 379/67); filed 8 March 1993

A recurring problem in voice interaction systems which use DTMF (touch tone) signalling is the occasional false DTMF detection resulting from a voice or other sound. This method is intended to avoid the problem as caused by system-generated phrases by a priori screening the possible system-generated utterances. Any false DTMF detections during the screening process are noted along with the synthesis controls for that utterance. During system operation, the controlling processor is then forewarned of the time and duration of possible DTMF triggers.—DLR

5,513,298

43.72.Ne INSTANTANEOUS CONTEXT SWITCHING FOR SPEECH RECOGNITION SYSTEMS

Vince M. Stanford *et al.*, assignors to International Business Machines Corporation
30 April 1996 (Class 395/2.52); filed 21 September 1992

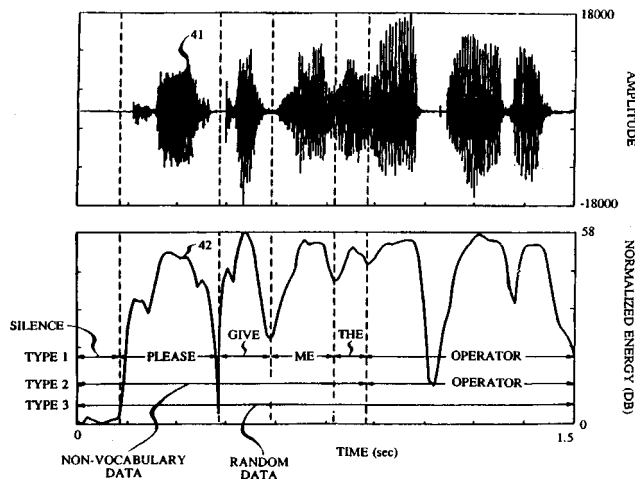
Current large-vocabulary, continuous-speech recognizers remain hobbled by the dependency on a grammar matching the recognition task. The difficulty is that as the tasks grow in complexity, growing grammars may need to be switched frequently. Keeping many large grammars in memory consumes valuable resources. This patent deals with the challenge by a dynamic interconnection strategy in which large numbers of HMM word models remain in memory, referenced by a changeable pointer mechanism which can be set to reflect the current recognition context.—DLR

5,509,104

43.72.Ne SPEECH RECOGNITION EMPLOYING KEYWORD MODELING AND NON-KEYWORD MODELING

Chin H. Lee *et al.*, assignors to AT&T Corporation
16 April 1996 (Class 395/2.65); filed 17 May 1989

Full recognition of unconstrained speech lies at some distance over the horizons of the future. This patent discloses a method which could be an approach toward that goal. In a long-distance telephone interface context, a simpler recognition strategy is possible by opting to recognize only a limited vocabulary. A hidden Markov model technique is used to build speaker-



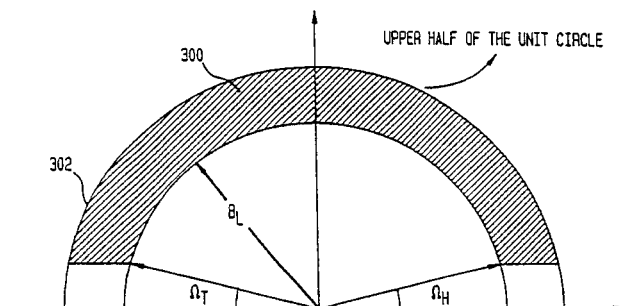
independent phonetic models for selected keywords and also for monkey-word sounds, including other words as well as background sounds. A grammar allows specific keyword sequences having each keyword, in general, surrounded by arbitrary nonkeyword sounds. This allows the entry of continuous unconstrained utterances containing the targeted keywords.—DLR

5,522,012

43.72.Ne SPEAKER IDENTIFICATION AND VERIFICATION SYSTEM

Richard J. Mammone and Khaled T. Assaleh, assignors to Rutgers University
28 May 1996 (Class 395/2.59); filed 28 February 1994

This is a method of increasing the separation between speaker-related and other components of a recognizer input signal. A linear prediction analysis is performed and the bandwidths of the spectral poles are obtained. The set of poles is then partitioned by bandwidth, based on the observation that formants will generally have narrower bandwidths than poles which



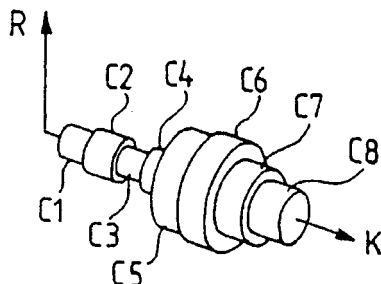
characterize the channel. Bandwidths below a certain threshold are further narrowed and those above are widened. The modified spectrum is then converted to cepstral features, which capture the vocal tract-related relationships among the formants.—DLR

5,522,013

43.72.Ne METHOD FOR SPEAKER RECOGNITION USING A LOSSLESS TUBE MODEL OF THE SPEAKER'S VOCAL TRACT

Marko Vaenskae, assignor to Nokia Telecommunications Oy
28 May 1996 (Class 395/2.64); filed in Finland 30 April 1991

This speech recognition system computes a vocal tract shape representation for each speech frame based on the lossless tube model. Reflection coefficients corresponding to the well-known PARCOR coefficients are con-



verted to area functions, which are then directly stored as templates to represent the trained reference database.—DLR

5,524,169

43.72.Ne METHOD AND SYSTEM FOR LOCATION-SPECIFIC SPEECH RECOGNITION

Paul S. Cohen *et al.*, assignors to International Business Machines, Incorporated
4 June 1996 (Class 395/2.4); filed 30 December 1993

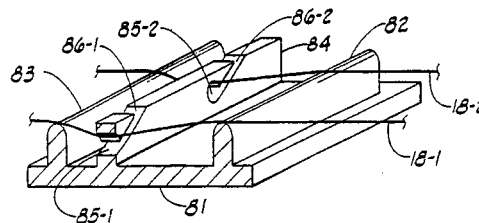
The novelty in the patented method will no doubt seem obvious once the supporting mechanisms are in place and the need arises for the services described here. An automotive speech recognition system recognizes spoken travel directions and destinations. The recognition task (grammar perplexity) is greatly simplified by using inputs from a global positioning system receiver to narrow the context of destinations to those in the immediate vicinity.—DLR

5,549,027

43.75.Gh STRINGED ACOUSTIC MUSICAL INSTRUMENT

Richard N. Steinberger, New Windsor, NY and Stephen H. Grimes, Kula, HI
27 August 1996 (Class 84/297R); filed 10 January 1994

This bridge for a guitar or other stringed instrument is designed to balance the vertical and lateral forces caused by the tension of strings to balance out so as to avoid stressing the top of the guitar on which the bridge



is mounted. Several such structures are described, one of which is shown here.—DWM

5,539,142

43.75.Mn COMBINED ACOUSTIC AND ELECTRONIC PIANO IN WHICH THE ACOUSTIC ACTION IS DISABLED WHEN PLAYED IN THE ELECTRONIC MODE

George F. Emerson and Thomas E. Kimble, assignors to Baldwin Piano and Organ Company
23 July 1996 (Class 84/171); filed 7 June 1995

“An improved combination acoustic-mode and electronic-mode piano is provided which includes a hammer shank stop rail that intercepts the hammer shank, when in the electronic mode, so that the hammer cannot complete its normal travel and cannot strike its corresponding string(s) when its piano key is actuated.” Five different designs for the hammer shank stop rail are shown, including a fluid-actuated version, all applicable to an upright piano. The reader’s attention is also called to patent 5,541,353 reviewed below.—DWM

5,541,353

43.75.Mn KEYBOARD INSTRUMENT FOR SELECTIVELY PRODUCING MECHANICAL SOUNDS AND SYNTHETIC SOUNDS WITHOUT ANY MECHANICAL VIBRATIONS ON MUSIC WIRES

Kiyoshi Kawamura *et al.*, assignors to Yamaha Corporation
30 July 1996 (Class 84/171); filed in Japan 9 June 1992

When an electronic musical synthesizer is combined with an upright piano, and the player uses the same keyboard for either piano or synthesizer, this patent describes a "stopper" that blocks the hammer shanks before the hammers strike the strings, in order to prevent the production of piano tones when only synthesizer music is to be heard.—DWM

5,545,839

43.75.Mn KEYBOARD MUSICAL INSTRUMENT WITH MOVABLE KEY BED FOR PERFORMING MUSIC WITHOUT ACOUSTIC SOUNDS

Kiyoshi Kawamura *et al.*, assignors to Yamaha Corporation
13 August 1996 (Class 84/171); filed in Japan 30 November 1993

The purpose of this patent is similar to that of patent 5,541,353 (reviewed above), but this piano is a grand piano, and the key action assembly is quite different, requiring a somewhat different means. Two of the inventors here are also among the four inventors of the other patent and the assignee is the same. Both patents assume that it is an advantage for the player to experience a piano-like key touch whether producing a piano tone or a synthesizer tone.—DWM

5,552,559

43.75.Mn KEYBOARD MUSICAL INSTRUMENT EQUIPPED WITH HAMMER SENSORS CHANGING POSITION BETWEEN RECORDING MODE AND SILENT MODE

Nobuo Sugiyama and Kiyoshi Kawamura, assignors to Yamaha Corporation
3 September 1996 (Class 84/171); filed in Japan 31 March 1994

In the combination of an upright piano with an electronic synthesizer, both operated from the same keyboard as in patent 5,541,353 reviewed above, piano hammer sensors are provided for measuring hammer velocities before hammer motion is stopped short of the piano strings. The sensor output signals are used to control the amplitude of the corresponding electronically generated tones when the instrument has been switched from piano mode to electronic mode. The co-inventors for this patent were also involved in patent 5,541,353 assigned to the same assignee.—DWM

5,557,052

43.75.Mn KEYBOARD MUSICAL INSTRUMENT HAVING VARIABLE CONTACT POINT BETWEEN JACK AND REGULATION BUTTON

Hajime Hayashida and Satoshi Inoue, assignors to Yamaha Corporation
17 September 1996 (Class 84/243); filed in Japan 31 March 1994

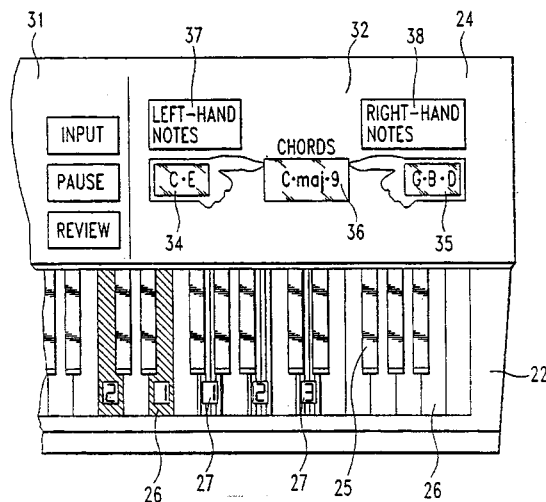
This grand piano action provides for each key "a first regulating button and a second regulating button with which the jack is selectively brought into contact; and the jack imparts a force variable in dependence on the regulating button to the hammer assembly so as to generate loud or soft tones."—DWM

5,557,055

43.75.St MUSICAL KEYBOARD HAVING AN ELECTRONICALLY CONTROLLED DISPLAY AND A METHOD OF KEYBOARD DISPLAY

Frederick W. Breitweiser, Jr., assignor to Breitweiser Music Technology, Incorporated
17 September 1996 (Class 84/478); filed 17 May 1994

Sequential illumination of keys to be played by a keyboard musician during the course of learning a piece to be played was demonstrated and patented over 20 years ago. This patent uses red-green illuminators that



project light into the hollow interior of the appropriate keys, and the key surfaces are translucent. A display board identifies the left-hand and right-hand notes to be played and also gives the name of the chord, all under the control of an external computer system.—DWM

5,544,562

43.75.St APPARATUS OF A PLAYING PRACTICE FOR ELECTRONIC MUSICAL INSTRUMENT AND CONTROL METHOD THEREOF

Ik B. Jeon, assignor to Goldstar Company
13 August 1996 (Class 84/470R); filed in Korea 8 July 1993

When in the music teacher mode, this digital electronic organ displays a musical score and a sequence of illuminated keys corresponding to the melody or chords to be played. If the person playing plays a wrong key when the keys are illuminated, no sound occurs. Correct playing of the keys gives a successful rendition of the music composition displayed.—DWM

5,541,354

43.75.Tv MICROMANIPULATION OF WAVEFORMS IN A SAMPLING MUSIC SYNTHESIZER

Peter W. Farrett and Daniel J. Moore, assignors to International Business Machines Corporation
30 July 1996 (Class 84/603); filed 30 June 1994

This computer music patent describes a technique for converting a digitized audio sample of an individual musical instrument to produce the

5,552,561

43.75.Tv PLAYING-STYLE DETECTING APPARATUS AND ELECTRONIC MUSICAL INSTRUMENT UTILIZING THE SAME

Akira Nakada *et al.*, assignors to Yamaha Corporation
3 September 1996 (Class 84/658); filed in Japan 30 March 1994

Previously some electronic musical instruments have used key switching systems in which the velocity of key motion has controlled the amplitude of electronically generated tones, and a "second-touch" pressure switch actuated at the end of the key stroke has effected additional tones or affected existing tones. In the present patent for a computerized electronic musical instrument, the depression speed of the key and the aftersensor are used in combination "to provide a playing-style detecting apparatus" for imparting to the musical output "a delicate expression according to the playing style."—DWM

5,522,392

43.80.Qf ENHANCING INTRAVASCULAR ULTRASONIC BLOOD VESSEL IMAGE

Veijo Suorsa and Axel Briskén, assignors to Cardiovascular Imaging System
4 June 1996 (Class 128/661.08); filed 15 November 1994

Ultrasonic depiction of blood vessel walls is enhanced by extracting parameters from the phase information of ultrasonic echoes, and using the parameters of the phase to suppress ultrasonic echoes from the blood. The parameters may be based on statistics of the phase, or the phase difference, or from the slope of the phase or the phase difference, either between neighboring scan lines in the same image frame or between images in successive frames.—RCW

5,524,626

43.80.Qf SYSTEM AND METHOD FOR DETERMINING LOCAL ATTENUATION FOR ULTRASONIC IMAGING

Dong-Chyuan Liu, assignor to Siemens Medical Systems, Incorporated
11 June 1996 (Class 128/660.06); filed 30 June 1995

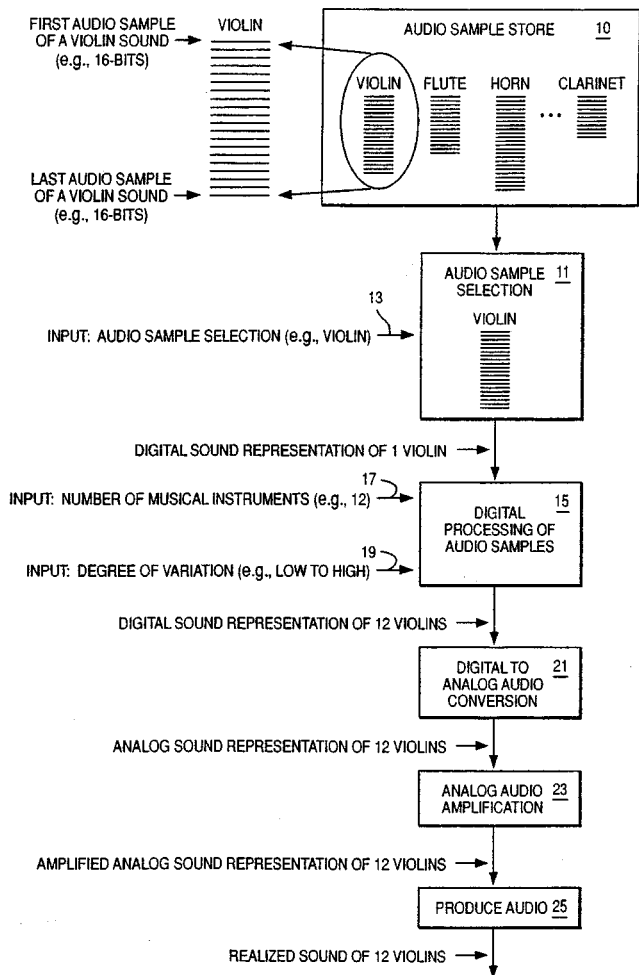
Ultrasonic backscattered power within an interrogated region is stored in a two-dimensional pattern of image elements that are grouped into processing windows. After row averaging the power values in each window, a window attenuation coefficient that corresponds to a decay parameter is found. The coefficients are used to compensate the power values for local attenuation before scan conversion and display. Tissue heterogeneity can also be tested by defining convergence and nonconvergence criteria. A gain control processor then iteratively estimates the window attenuation coefficients until either criterion is satisfied. Heterogeneity within the processing window is indicated when the nonconvergent criterion is met.—RCW

5,539,831

43.80.Qf ACTIVE NOISE CONTROL STETHOSCOPE

Thomas R. Harley, assignor to The University of Mississippi
23 July 1996 (Class 381/67); filed 16 August 1993

The patent describes an active noise control stethoscope that permits the checking of vital signs in the presence of high background noise levels. A digital processing technique is used to remove noise from the output of a main detection sensor. The detector uses a piezoceramic transflexural actuator mounted in a cylindrical piece of brass. An identical sensor is placed



tonal effect of a group of such instruments by micromanipulation in parallel of digital processors corresponding to the number of instruments selected for the group.—DWM

5,541,356

43.75.Tv ELECTRONIC MUSICAL TONE CONTROLLER WITH FUZZY PROCESSING

Satoshi Usa, assignor to Yamaha Corporation
30 July 1996 (Class 84/626); filed in Japan 9 April 1993

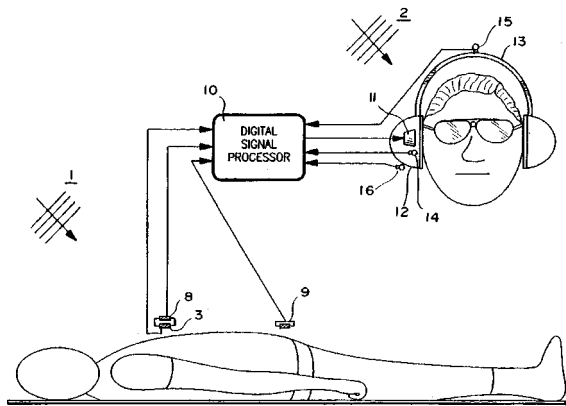
This electronic musical instrument includes a "logical calculation unit performing a fuzzy calculation" to control electronically a sensory related tone parameter, such as the tone spectrum, in a manner that is independent of control signals related to playing performance.—DWM

5,550,320

43.75.Tv ELECTRONIC SOUND GENERATING DEVICE FOR GENERATING MUSICAL SOUND BY ADDING VOLUME FLUCTUATION TO PREDETERMINED HARMONICS

Sayoko Hirano, assignor to Kabushiki Kaisha Kawai Gakki Seisakusho
27 August 1996 (Class 84/623); filed in Japan 27 May 1993

The temporal fluctuations in the spectrum of a musical tone are called sonance, and are present in the tone of many types of bowed and blown musical instruments. The present patent describes computerized means for creating such fluctuations in selected harmonics of tones generated in the computer system of electronic musical instruments.—DWM



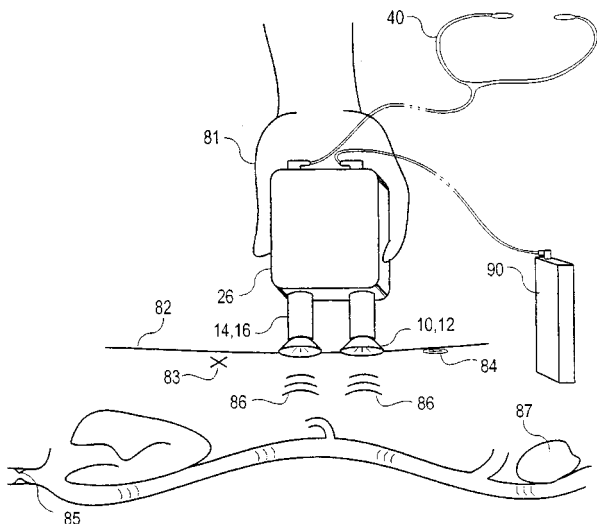
above the device to detect adjacent background noise and the signals are combined to obtain a noise-free signal. A third sensor is also provided to remove noise coupled through the patient's body. In addition, means are shown to provide noise cancellation in the earcups.—SFL

5,548,651

43.80.Qf STEREPHONIC STETHOSCOPE

Howard F. Long, Pleasanton, CA
20 August 1996 (Class 381/67); filed 28 March 1994

The patent shows an electronically amplified stethoscope that utilizes the binaural phase effect from two probes held in one chest-piece. An amplifier is located in the chest-piece. Skin contact of the probes is



small for good localization. It is stated that more sensitive detection and recognition of disease and functions by the physician can result from the use of the device.—SFL

5,524,625

43.80.Sh SHOCK WAVE GENERATING SYSTEM CAPABLE OF FORMING WIDE CONCRETION-DISINTEGRATING REGION BY ENERGIZING RING-SHAPED TRANSDUCERS AND HYPERTHERMIA CURING SYSTEM

Kiyoshi Okazaki *et al.*, assignors to Kabushiki Kaisha Toshiba
11 June 1996 (Class 128/660.03); filed in Japan 10 March 1992

This system forms multiple focal points from shock waves produced by a number of ring-shaped piezoelectric transducer elements excited with appropriate voltages. The dimension of the region synthesized from a num-

ber of focal points is varied according to the size of the concretion to be disintegrated.—RCW

5,522,391

43.80.Vj DELAY GENERATOR FOR PHASED ARRAY ULTRASOUND BEAMFORMER

Raymond A. Beaudin and Michael P. Anthony, assignors to Hewlett-Packard Company
4 June 1996 (Class 128/660.070); filed 9 August 1994

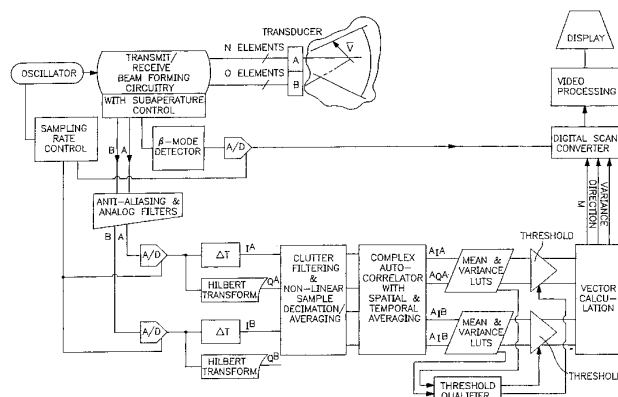
This delay generator includes a delay generator and a controller. The delay for each array element is varied by the delay controller at discrete times during reception. The delay is, within the quantization error of the delay unit, an exact solution of the equation for the delay at a given steering angle for the array element and focal depth. The delay controller generates a change delay signal that steers the received beam to a dynamically variable angle and focus during reception.—RCW

5,522,393

43.80.Vj MULTI-DIMENSIONAL REAL-TIME ULTRASONIC BLOOD FLOW IMAGING APPARATUS AND METHOD

Patrick J. Phillips and Olaf T. von Ramm, assignors to Duke University
4 June 1996 (Class 128/661.09); filed 24 May 1994

In this apparatus and method, the ultrasonic transducer is divided into two or more independently controlled subapertures, each used for transmitting ultrasonic beams and for receiving echoes. Signal processing includes



quadrature detection circuitry and use of the Hilbert transform to filter echo signals.—RCW

5,522,878

43.80.Vj SOLID MULTIPURPOSE ULTRASONIC BIOMEDICAL COUPLANT GEL IN SHEET FORM AND METHOD

David A. Montecalvo and David Rolf, assignors to LecTec Corporation
4 June 1996 (Class 607/152); filed 26 April 1993

This couplant sheet is placed on the skin of the patient to facilitate the transfer of ultrasonic energy between an ultrasonic transducer and the body. The sheet is flexible and holds its form when placed on the body. The sheet contains water and a humectant such as triethylene glycol or glycerin and a network of long hydrophilic polymer molecules that hold the liquid in place and give solidity.—RCW

Temporal integration of loudness, loudness discrimination, and the form of the loudness function^{a),b)}

Søren Buus

Communication and Digital Signal Processing Center, Department of Electrical and Computer Engineering (409DA), Northeastern University, Boston, Massachusetts 02115

Mary Florentine

Communication Research Laboratory, Department of Speech-Language Pathology and Audiology (133FR), Northeastern University, Boston, Massachusetts 02115

Torben Poulsen

Department of Acoustic Technology (Building 352), Technical University of Denmark, DK-2800 Lyngby, Denmark

(Received 7 May 1996; accepted for publication 25 July 1996)

Temporal integration for loudness of 5-kHz tones was measured as a function of level between 2 and 60 dB SL. Absolute thresholds and levels required to produce equal loudness were measured for 2-, 10-, 50-, and 250-ms tones using adaptive, two-interval, two-alternative forced-choice procedures. The procedure for loudness balances was new and employed ten interleaved tracks to obtain concurrent measurements for ten tone pairs. Each track converged at the level required to make the variable stimulus just louder than the fixed stimulus. Thus, the data yield estimates of the just-noticeable difference (jnd) for loudness level and temporal integration for loudness. Results for four listeners show that the amount of temporal integration, defined as the level difference between equally loud short and long tones, varies markedly with level and is largest at moderate levels. The effect of level increases as the duration of the short stimulus decreases and is largest for comparisons between the 2- and 250-ms tones. The loudness-level jnds are also largest at moderate levels and, contrary to traditional jnds for the level of two equal-duration tones, they do not appear to depend on duration. The latter finding indicates that loudness discrimination between stimuli that differ along multiple dimensions is not the same as level discrimination between stimuli that differ only in level. An equal-loudness-ratio model, which assumes that the ratio of loudnesses for a long and short tone at equal SPL is the same at all SPLs, can explain the level dependence of temporal integration and the loudness jnds. It indicates that the loudness function [$\log(\text{loudness})$ versus SPL] is flatter at moderate levels than at low and high levels in agreement with earlier findings for 1-kHz tones [M. Florentine *et al.*, *J. Acoust. Soc. Am.* **99**, 1633–1644 (1996)]. © 1997 Acoustical Society of America. [S0001-4966(97)02112-7]

PACS numbers: 43.66.Cb, 43.66.Mk, 43.66.Ba [WJ]

INTRODUCTION

The purpose of this paper is to examine the effect of level on the amount of temporal integration for loudness, defined as the level difference between equally loud short and long sounds. This information is important to understand the perception of natural sounds and may also provide insight into intensity coding in the auditory system.

Temporal integration of loudness for tones has been measured at more than one level in a number of studies (e.g., Munson, 1947; Ekman *et al.*, 1966; Stephens, 1973; Pederesen *et al.*, 1977; Poulsen, 1981; Florentine *et al.*, 1996).

However, it has been difficult to ascertain how the amount of temporal integration depends on level, because most studies examined only a limited range of levels and many did not use the very short durations that are likely to yield the largest effect of level. To our knowledge, only two studies measured temporal integration of loudness of tones over wide ranges of levels and durations (Munson, 1947; Florentine *et al.*, 1996). Unfortunately, Munson (1947) used a method in which a test tone (5, 10, 40, 100, or 200 ms) always preceded a 1-s tone and only the 1-s tone was varied in level. Both of these procedural features are known sources of bias. For example, the second of two identical tones tends to sound louder than the first (e.g., Stevens and Davis, 1938) and listeners tend to underestimate the loudness of the variable stimulus at low levels and overestimate it at high levels (e.g., Stevens, 1956; Stevens and Greenbaum, 1966; Florentine *et al.*, 1996). In addition, it was not possible to determine the internal consistency of Munson's loudness matches because no control conditions were included in the measurements. These shortcomings make the data difficult to interpret.

^{a)}Parts of this paper were presented at the 11th Meeting of the International Society of Psychophysics, October 1995, Cassis, France [S. Buus *et al.*, in *Fechner Day '95*, edited by C.-A. Possamai (Int. Soc. Psychophysics, Cassis, France), pp. 55–60 (1995)] and at the 131st meeting of the Acoustical Society of America, May 1996, Indianapolis, Indiana [S. Buus *et al.*, *J. Acoust. Soc. Am.* **99**, 2490 (A) (1996)].

^{b)}“Selected research articles” are ones chosen occasionally by the Editor-in-Chief, that are judged (a) to have a subject of wide acoustical interest, and (b) to be written for understanding by broad acoustical readership.

In contrast, Florentine *et al.* (1996) used a modern psychophysical procedure and included control conditions. These data indicated that the amount of temporal integration for loudness of 1-kHz tones varied nonmonotonically with level. The effect of level was greatest at short durations. Therefore, one purpose of the present study was to examine the effect of level on temporal integration of loudness with durations even shorter than those used in our previous study. To minimize confounding effects of spectral splatter that arise when the stimuli are brief, the present study used tones at 5 kHz where the critical band is wide enough to accommodate very brief tone bursts.

Another purpose of the present study was to investigate a new loudness-balance procedure that was designed to minimize biases and increase consistency. Although Florentine *et al.*'s (1996) data showed a high degree of internal consistency, they indicated a small bias that caused the variable stimulus to migrate towards a comfortable loudness. In addition, the judgments were not completely transitive, because the level difference between equally loud 5- and 200-ms stimuli tended to be larger than the sum of level differences between 5- and 30-ms stimuli and between 30- and 200-ms stimuli. Thus, our new procedure attempted to minimize biases by interleaving adaptive tracks for several conditions such that listeners would not know which stimulus was the variable in a particular trial. Control conditions were included to allow an evaluation of transitivity in the data.

Because the new procedure was designed to estimate the level at which the variable-level tone was just louder than the fixed-level tone, it also provided measurements of difference limens for loudness level as a function of level and duration of the variable tone (cf. Schlauch and Wier, 1987; Zeng, 1994). Thus, a third purpose of the present study was to compare difference limens for loudness level to DLs obtained in traditional level-discrimination experiments in which the listeners compare two tones that have the same duration and differ only in level (e.g., Florentine, 1986; Buus and Florentine, 1992). As discussed later, the comparison of difference limens obtained for tones that differ both in duration and level with those for equal-duration tones differing only in level may reveal important differences between loudness discrimination and level discrimination.¹

I. METHOD

A. Stimuli

The stimuli were 5-kHz tone bursts with nominal durations of 2, 10, 50, and 250 ms. These durations were measured between the half-amplitude points of the 2-ms linear rise and fall. The equivalent rectangular durations are 0.67 ms shorter than the nominal durations. The 2-ms stimulus consisted of only the rise and fall. The longer stimuli contained steady-state segments with a duration 2 ms less than the nominal duration. These envelope shapes ensured that almost all the energy of the tone bursts was contained within the 900-Hz-wide critical band centered at 5 kHz (cf. Zwicker, 1961; Scharf, 1970). Even for the 2-ms tone burst, the energy within the critical band was only 0.02 dB less than the overall energy. Nine test levels were used for each

duration of the fixed-level stimulus. They were 2, 5, 10, 15, 20, 30, 40, 50, and 60 dB SL. All SPLs reported are equivalent free-field SPLs as determined by threshold measurements in free field and with the Sony MDR-V6 earphone in a group of ten normal listeners (cf. Villchur, 1969).

B. Procedure

1. Absolute thresholds

In the first part of the experiment, absolute thresholds were measured for each of the four test durations using an adaptive procedure in a two-interval, two-alternative forced-choice (2I, 2AFC) paradigm. Each trial contained two observation intervals, marked by lights and separated by 500 ms. The signal was presented in either the first or the second observation interval with equal *a priori* probability. The listener's task was to indicate which interval contained the signal by pressing a key. One hundred milliseconds after the listener responded, the correct answer was indicated by a 200-ms light. Following the feedback, the next trial began after a 200-ms delay.

A single threshold measurement was based on three interleaved adaptive tracks, each of which ended after five reversals. Reversals occurred when the signal level changed from increasing to decreasing or *vice versa*. On each trial, the track was selected at random among the tracks that had not yet ended. For each track, the level of the signal initially was set approximately 15 dB above the listener's threshold. It decreased following three correct responses and increased following one incorrect response, such that the signal converged on the level yielding 79.4% correct responses (Levitt, 1971). The step size was 5 dB until the second reversal, after which it was 2 dB.

The threshold for one track was calculated as the average signal level at the fourth and fifth reversals, and one threshold measurement was taken as the average threshold across the three tracks. Three such threshold measurements (for a total of nine tracks) were obtained for each listener and condition. The average across all measurements was used as the reference to set the sensation level for each listener and condition in the second part of the experiment.

2. Loudness matches

In the second part of the experiment, stimuli of different durations were matched in loudness to one another using a new procedure, which combines features of Fletcher and Munson's (1933) forced-choice procedure and Jesteadt's (1980) adaptive procedure for loudness matching. The new procedure was intended to eliminate some biases that may have affected previous loudness-matching data obtained with adaptive procedures. For example, if all trials in a measurement use the same pair of sounds (except for small changes in level of the variable sound), listeners may start to ignore the fixed sound, which is always the same, and base their judgments on comparisons with previous trials. If the variable sound in a trial sounds louder than it did in the previous trial, the listener is likely to respond "variable louder." In addition, judgments that ignore the fixed sound are likely to be affected by a comparison to comfortable loudness such

that the variable is more likely to be judged “too soft” when the sounds are soft and “too loud” when they are loud (Florentine *et al.*, 1996).

To reduce such biases, the present experiment employed a procedure in which the loudnesses of both the long and the short tones vary from trial to trial. This is similar to the random selection of stimulus pairs for each trial used by Fletcher and Munson (1933) for loudness matching with the method of constant stimuli. The random variation of overall loudness level was intended to force the listeners to base their responses on loudness judgments of the two tones presented in the trial. Roving loudness and mixing trials with both the long and the short tone varied also help listeners focus on loudness and ignore other differences, which remain constant throughout a measurement.

Loudness matches were made at nine levels for each of five duration pairs (i.e., 2 vs 10 ms, 2 vs 250 ms, 10 vs 50 ms, 10 vs 250 ms, and 50 vs 250 ms). To keep the number of trials within a block of trials reasonable, the nine levels were divided into a low-SL set (i.e., 2, 5, 10, 15, and 20 dB SL) and a high-SL set (i.e., 20, 30, 40, 50, and 60 dB SL). Both sets included 20 dB SL, which allowed the possible effect of loudness range on listeners’ judgments to be examined. For each listener and duration pair, three low-SL and three high-SL sets were obtained in mixed order. Each set consisted of ten interleaved tracks for one duration pair: matches were made at five different levels with both the long and the short tones varied. A set was completed in about 250 trials.

The loudness matches were obtained in a 2I, 2AFC paradigm. On each trial, the listener heard two tones separated by 600 ms. The fixed-level tone followed the variable tone or the reverse with equal *a priori* probability. The listener’s task was to indicate which sound was louder by pressing a key. The response initiated the next trial after a 1-s delay. The level of the variable tone for each track was adjusted according to a one-up, two-down procedure. If the listener indicated that the variable tone was louder than the fixed tone on two successive trials for a particular track, its level was reduced, otherwise it was increased. The step size was 5 dB until the second reversal, after which it was 2 dB.

For each track, the variable stimulus was initially set approximately 15 dB below the expected equal-loudness level. (If that level was below threshold, the variable stimulus was set to its threshold.) The choice of starting levels ensured that the listener would hear trials in which both the short and the long tone was clearly the louder one, because both the long and short tones were varied within a block of trials. On each trial, the track was chosen at random among those that had not yet ended, which they did after nine reversals. The average level of the last four reversals of each track was used as an estimate of the level at which the variable tone was just louder than the fixed-level tone. This procedure made the variable tone converge towards the level at which it was judged louder than the fixed tone in 71% of the trials (Levitt, 1971). Thus, the procedure provides an estimate of the level at which the variable is just noticeably louder than the fixed-level tone (Schlauch and Wier, 1987). These “just-louder” levels are used in the subsequent data analysis.

C. Apparatus

An APR 486/33 PC-compatible computer controlled the stimulus generation, sampled the listeners’ responses, and executed the adaptive procedure. The tone bursts were produced by a programmable waveform generator (TDT WG1) whose output was attenuated (two TDT PA4s in series), and led to a headphone amplifier (TDT HB5), which fed one earpiece of a Sony MDR-V6 headset.

The earphone was calibrated daily on an acoustic test fixture (ISO, TR 4869-3, 1989). The microphone (Brüel & Kjør 4144) received its DC bias from a measuring amplifier (Brüel & Kjør 2607), which also measured the SPL produced by the earphone.

D. Listeners

Four listeners, three males and one female, were tested on all conditions. One relatively inexperienced listener, SP, was 25 years old and the other listeners, who are the authors, were between 41 and 49. The authors had extensive experience making loudness judgments; SP practiced loudness judgments for one 2-h session before data collection. The listeners had normal audiometric thresholds (ISO 389, 1991) at standard octave frequencies from 0.125–8 kHz, except for one author who had a mild cochlear hearing loss below 2 kHz. Because that listener’s data were similar to those of the others, data from all listeners were averaged.

E. Data analysis

For each listener and condition, the three “just-louder” levels were averaged. These averages were then used to calculate group averages and standard deviations across listeners. Because our primary interest was to investigate the effect of level on the amount of temporal integration, statistical analyses were performed on the level differences between the short and the long tone when the variable was judged “just louder.” To examine the statistical significance of the effects of stimulus variables and differences among listeners, a four-way ANOVA (stimulus level \times duration pair \times long or short variable \times listener) for repeated measures was performed (Data Desk 4.2, Data Description, Inc., Ithaca, NY, 1994). Scheffé *post hoc* tests for contrast (Data Desk 4.2, 1994) were performed as appropriate to explore the sources of significant effects and interactions. Unless otherwise stated, differences were considered significant when these tests indicated a probability less than 0.05.

II. RESULTS

A. Individual listeners

Figure 1 shows the levels at which each listener judged the variable to be just louder than the fixed stimulus. The unfilled symbols show the “just-louder” levels for the short tones; they show the level at which the short tone is judged louder in 71% of the trials, which corresponds to one just-noticeable difference above the equal-loudness level. The filled symbols show the “just-louder” levels for the long tones; they show the level at which the long tone is judged louder in 71% of the trials, which corresponds to one just-

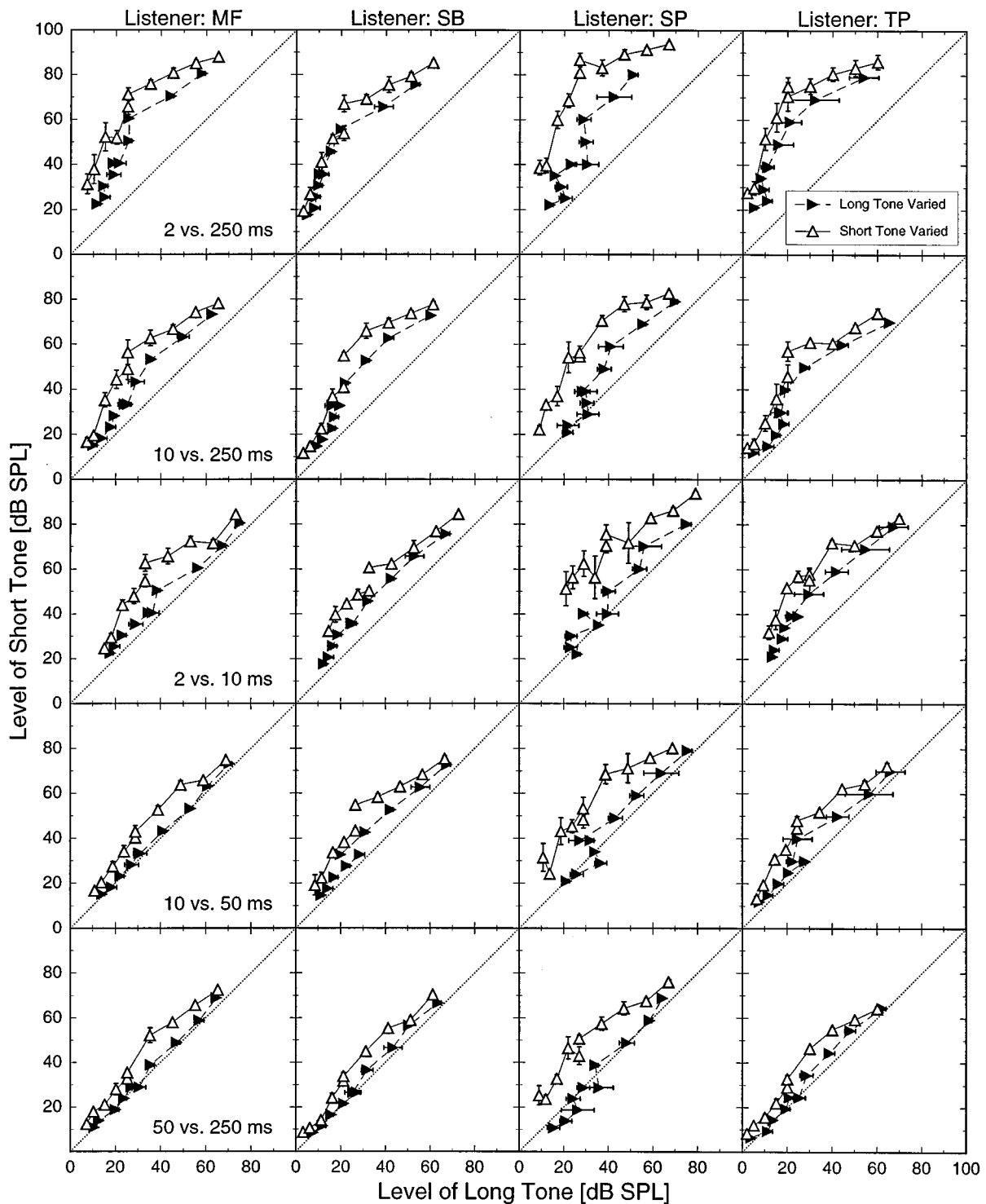


FIG. 1. Individual loudness judgments for four listeners. The level of the short tone is plotted as a function of the level of the long tone. The symbols show the levels of the variable stimuli at which they were judged "just louder" than the fixed stimuli. The unfilled symbols show data obtained when the short tones were varied; the filled symbols show data obtained when the long tones were varied. Each row of panels shows the data for a particular duration pair. Each column shows the data for an individual listener. The error bars show plus and minus one standard error calculated across the three repetitions for each listener and condition.

noticeable difference to the right of the equal-loudness level. As indicated by the error bars, the listeners' judgments are quite consistent. The average standard error is 2.3 dB. However, the data for the less experienced listener, SP, tend to be more irregular and have larger standard errors than those for the experienced listeners. Although the ANOVA, which is

discussed later, showed some highly significant interlistener differences, the data are reasonably consistent across listeners. The average across-listener standard deviations of the level differences required for the variable stimuli to be just louder is 4.1 dB.

The amount of temporal integration for the data in Fig. 1

is indicated by the distance from the centroid of the two functions to the dotted diagonal, which shows equal levels of the short and long tones. For all four listeners, the distance is larger at moderate levels than at low and high levels, which indicates that the amount of temporal integration is a non-monotonic function of level in agreement with the findings for 1-kHz tones and noises in our previous study (Florentine *et al.*, 1996). For the duration pairs differing by a factor of 5, the effect of level is relatively modest, but it clearly increases as the tones become briefer: the data for the 2- and 10-ms tones are considerably farther from the diagonal and show a larger effect of level than those for the 50- and 250-ms tones. As the duration ratio increases, both the amount of temporal integration and the effect of level increase. For the 2- and 250-ms tones, the amount of temporal integration is 15–20 dB at low levels, reaches a peak of about 40 dB when the 250-ms tone is around 20 dB SL, and decreases to about 20–25 dB at the highest levels. (Thresholds for the 250-ms tone were 5.3 dB SPL for MF, 1.2 dB SPL for SB, 7.0 dB SPL for SP, and 0.1 dB SPL for TP.)

The just-noticeable differences in loudness level are indicated by the separation between the data for the short tone varied and the long tone varied. This distance tends to be larger for SP than for the other listeners, indicating that SP's just-noticeable differences for loudness level are larger than those for the experienced listeners. For all four listeners, the jnd's appear to be larger at moderate levels than at levels below 25 dB SPL and above 65 dB SPL. This mid-level "hump" of the jnds for loudness level is qualitatively similar to the jnds obtained by Zeng (1994), when listeners compared the loudness of a forward-masked tone to that of a tone presented in isolation. Somewhat surprisingly, no consistent difference is apparent among the five duration pairs. Certainly, the filled and unfilled functions for the 50- and 250-ms tone pair are not markedly closer together than those for the 2- and 10-ms or even 2- and 250-ms tone pairs.

Each function contains two data points with the fixed stimulus set to 20 dB SL, because this level was included in both the low- and the high-SL set. The difference between the two points indicates the extent to which the listeners' judgments depended on the range of levels presented in a block of trials. Generally, the level at which the variable is just louder than the 20-dB SL fixed stimulus is higher for the high- than for the low-SL set. The average difference is 2.8 dB. Thus, the data show a context effect, which may be related to the range of loudnesses encompassed by the stimuli tested within the block. This effect is reminiscent of the context effects in Durlach and Braida's (1969) memory model for intensity perception. It should be noted that this context effect generally is much smaller than the amount of temporal integration.

B. Group data

The large symbols in Fig. 2 show the average data for the four listeners plotted in the same manner as Fig. 1. The small symbols and the solid lines show predictions by a model, which is discussed later. The average data reflect the trends in the individual data. The amount of temporal integration varies markedly with level and is largest at moderate

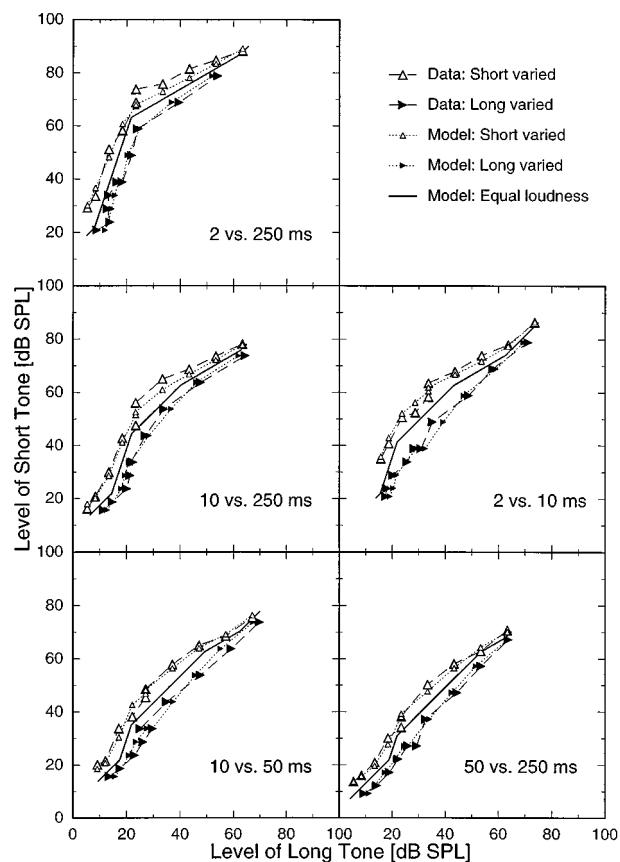


FIG. 2. Average of loudness judgments across four listeners. The level of the short tone is plotted as a function of the level of the long tone. As in Fig. 1, unfilled symbols show the "just louder" levels for the short tones and filled symbols show the "just-louder" levels for long tones. The large symbols show the data and the small symbols show predictions by a model (see text). The solid lines show equal-loudness functions predicted by the model. Each panel shows data for a different duration pair.

levels, especially for the short durations and large duration ratios. The just-noticeable difference in loudness level, indicated by the vertical distance to the solid line for the unfilled symbols and the horizontal distance for the filled symbols, also is largest at moderate levels. A comparison across panels shows no systematic effect of duration on the jnd. Finally, the data at 20 dB SL indicate that the jnd generally is larger for the high-SL set than for the low-SL set. This context effect varies somewhat across durations and tends to be largest when the short tone is varied.

These effects are supported by the ANOVA shown in Table I. Effects of stimulus variables that are consistent across listeners are shown in the top half of the table and individual differences (i.e., effect of and interactions with listener) in the bottom half. The top half of the table shows that all the experimental variables had highly significant effects on the level difference between the short and the long tone. The effect of SL shows that the amount of temporal integration varies with level. The Scheffé tests for contrast showed that, overall, the amount of temporal integration is larger at 20, 30, and 40 dB SL than at lower and higher levels. However, this effect depends both on the duration pair and whether the short or the long tone is varied as indicated by the interactions between SL and these other vari-

TABLE I. Four-way analysis of variance for repeated measures of loudness matching. The dependent variable is the level difference between the variable and the fixed stimulus, when the variable was judged “just louder” than the fixed stimulus. The stimulus variables Sensation Level (SL; 9 levels: 2,5,10,15,20,30,.....60 dB SL), Pair (Pr; 5 levels: 2 vs 250 ms, 10 vs 250 ms, 2 vs 10 ms, 10 vs 50 ms, and 50 vs 250 ms), and Variable (Vrb; 2 levels: Short or Long) are fixed factors. Listener (Lsr; 4 levels: MF, SB, SP, and TP) is a random factor.

Source	df	Error df	Sums of squares	Mean square	F ratio	Probability
Const	1	3	273 204	273 204	357.5	0.0003
SL	8	24	17 399	2175	88.70	≤0.0001
Pr	4	12	66 011	16 503	94.40	≤0.0001
SL*Pr	32	96	6649	207.8	8.948	≤0.0001
Vrb	1	3	35 688	35 688	19.01	0.0223
SL*Vrb	8	24	6867	858.4	16.70	≤0.0001
Pr*Vrb	4	12	473.7	118.4	7.958	0.0023
SL*Pr*Vrb	32	96	2750	85.95	3.321	≤0.0001
Lsr	3	840	2293	764.2	28.30	≤0.0001
SL*Lsr	24	840	588.5	24.52	0.908	0.5915
Pr*Lsr	12	840	2098	174.8	6.474	≤0.0001
SL*Pr*Lsr	96	840	2229	23.22	0.860	0.8239
Vrb*Lsr	3	840	5633	1878	69.53	≤0.0001
SL*Vrb*Lsr	24	840	1234	51.41	1.904	0.0057
Pr*Vrb*Lsr	12	840	178.6	14.88	0.551	0.8813
SL*Pr*Vrb*Lsr	96	840	2485	25.88	0.958	0.5935
Error	840		22 683.7	27.00		
Total	1199		189 234			

ables. The Scheffé tests showed no significant differences among the various levels for duration pairs that differed only by a factor of 5, but for the 10- and 250-ms and the 2- and 250-ms pairs, the amount of temporal integration was significantly larger between 20 and 50 dB SL than at lower or higher levels.

As expected, the effect of duration pair is highly significant. Although the magnitude of this effect depends on whether the long or the short tone is varied and on the SL, the significant differences were the same whether the long or the short tone was varied. When the tone durations differed by a factor of 5, the amount of temporal integration increased significantly as duration decreased. The Scheffé tests showed that, averaged across SLs, the amount of temporal integration is significantly larger for the 2- and 10-ms pair than for the 10- and 50-ms tones, which yielded more temporal integration than the 50- and 250-ms tones. As expected, the amount of temporal integration increased as the duration ratio increased. The 2- and 250-ms pair yielded more temporal integration than the 10 and 205 ms pair, which yielded more temporal integration than the 50- and 250-ms pair.

Although the effects in the average data generally are apparent in the individual data, the analysis also indicated some highly significant differences among listeners as evident in the lower half of Table I. The amount of temporal integration differs somewhat among listeners. The Scheffé tests show that, overall, the amount of temporal integration is larger for TP than for SB, and smaller for MF than for the other three listeners. The differences are small, however, about 1.6 dB between TP and SB and an average of 3 dB between MF and the other three listeners. These differences depend somewhat on condition as indicated by the significant interactions between listener and duration pair, between

listener and variable (long or short), and among listener, stimulus level, and variable.

III. DISCUSSION

A. Model of temporal integration and discrimination of loudness

The results indicate that the just-noticeable loudness-level difference and the amount of temporal integration show similar dependencies on level: both are larger at moderate levels than at low and high levels. This similarity may result from a common underlying factor. Florentine *et al.* (1996) argued that the ratio between the loudness of a long and a short tone at equal SPL was likely to be independent of the SPL. In fact, Stevens and Hall's (1996) data for burst of white noise agree with this contention, which was also a fundamental property of Zwislocki's (1969) analysis of temporal integration of loudness. Accordingly, the amount of temporal integration for a given duration pair should be inversely proportional to the slope of the function relating the logarithm of loudness to SPL. To account for the finding of a maximal amount of temporal integration at moderate levels, Florentine *et al.* (1996) assumed that the loudness function was shallower at moderate than at high and low levels. This idea appears applicable to the present data.

To account for the present measurements of “just louder” levels, the just-noticeable loudness-level difference also must be considered. For a given just-noticeable difference in loudness, the just-noticeable loudness-level difference is inversely proportional to the slope of the log(loudness)-vs-SPL function. Thus, a loudness function that accounts for the effect of level on the amount of temporal integration of loudness also is likely to account for the

present finding of larger just-noticeable loudness-level differences at moderate than at low and high levels. Indeed, the data in Figs. 1 and 2 indicate rather directly that the logarithm of loudness grows considerably more slowly at moderate levels than at low and high levels. Consider, for example, the comparison of 2- and 250-ms tones (top panel in Fig. 2). As the 250-ms tone increases from 5 to 23 dB SPL, the 2-ms tone must increase from about 19 to about 64 dB SPL to maintain equal loudness. An 18-dB change in level at low SPLs increases the loudness as much as a 45-dB change in level at moderate SPLs. On the other hand, as the 250-ms tone increases another 30 dB—from about 25 to 55 dB SPL—the equally loud 2-ms tone increases only 18 dB—from about 65 to about 83 dB SPL. The data for the other duration pairs show similar trends and all indicate that loudness grows more slowly at moderate than at low and high levels.

To investigate if a loudness function of the form described above can account for the present data, these ideas were incorporated into a model. For simplicity, the loudness, N , of a tone was modeled as three power-function segments. The form of such functions resembles the input–output functions of the basilar membrane described by Yates (1990). As in our previous paper (Florentine *et al.*, 1996), the ratio between the loudnesses of short and long tones of equal SPL was assumed to be independent of the SPL. Thus, the loudness of a tone was calculated as

$$N(I, \text{Dur}) = k(\text{Dur}) * \begin{cases} \left(\frac{I}{I_0}\right)^a, & I \leq I_1, \\ \left(\frac{I_1}{I_0}\right)^{(a-b)} \left(\frac{I}{I_0}\right)^b, & I_1 < I \leq I_2, \\ \left(\frac{I_1}{I_0}\right)^{(a-b)} \left(\frac{I_2}{I_0}\right)^{(b-c)} \left(\frac{I}{I_0}\right)^c, & I > I_2, \end{cases} \quad (1)$$

where I is the intensity of the tone, Dur is its duration, and I_0 is the reference intensity ($=10^{-12}$ W/m²). The exponents a , b , and c , the intensity limits (or break points) I_1 and I_2 , and $k(\text{Dur})$ are free parameters, which are used to fit the data and to make the fitted loudness function for the 250-ms tones similar to a “standard” 5-kHz loudness function. The standard loudness function was obtained by using Zwislocki’s (1965) modified power function to calculate the loudness in sones from the loudness level in phons. The loudness levels of the 5-kHz tones were determined from the ISO 226 (1987) equal-loudness-level contours.

The just-noticeable difference in loudness was assumed to be proportional to the square root of the loudness as suggested by Hellman and Hellman (1990).² To account for the effect of context seen in the data at 20 dB SL, discrimination was assumed to be corrupted by an additional internal noise, which was proportional to the range of loudnesses encompassed by the stimuli in the set of ten adaptive tracks. Thus, the just-noticeable difference in loudness, ΔN_{DL} , was modeled as

$$\Delta N_{\text{DL}} = \sqrt{\partial^2 N_{\text{fix}} + r^2 (N_{\text{max}} - N_{\text{min}})^2}, \quad (2)$$

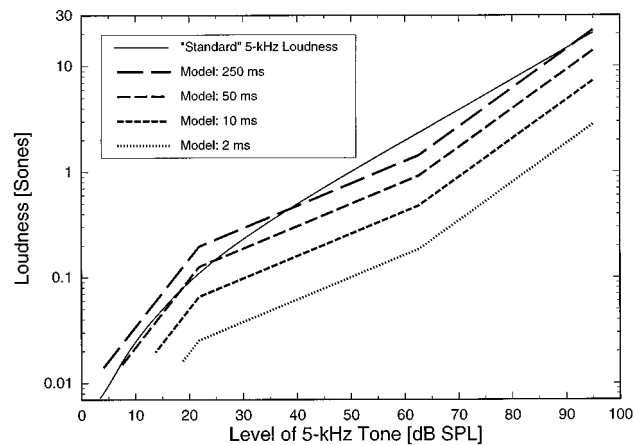


FIG. 3. The thick lines show loudness functions obtained by fitting a simple model to the present data for temporal integration of loudness and loudness-level jnd’s. The model loudness function for 250-ms tones is compared to a “standard” loudness function for 5-kHz tones (see text for details).

where N_{fix} is the loudness of the fixed stimulus of the pair, N_{max} and N_{min} are the maximum and minimum loudnesses of the stimuli in the set of tracks, ∂ is a free parameter that determines the just-noticeable difference for loudness in the absence of roving loudness, and r is a free parameter that determines the magnitude of the context effect.³

Accordingly, the intensity of the variable stimulus for a given comparison could be predicted as the intensity, I_{var} , for which

$$N(I_{\text{var}}, \text{Dur}_{\text{var}}) = N(I_{\text{fix}}, \text{Dur}_{\text{fix}}) + \Delta N_{\text{DL}}, \quad (3)$$

where I_{fix} is the intensity of the fixed stimulus, Dur_{fix} is its duration, and Dur_{var} is the duration of the variable stimulus. Optimizing the parameters to yield a loudness function that is similar to the “standard” loudness function for 5-kHz tones for the 250-ms duration, while providing a small rms error of the predictions, yielded $a=0.64$, $b=0.21$, $c=0.36$, $k(250 \text{ ms})=0.0077$, $k(50 \text{ ms})=0.0049$, $k(10 \text{ ms})=0.0026$, and $k(2 \text{ ms})=0.0010$. The break points, I_1 and I_2 , corresponded to 22 and 63 dB SPL, ∂^2 was 0.021 sones, and r was 0.029.

As shown in Fig. 2, the model predictions (small symbols) obtained with these parameters agree very well with the average data and the predicted equal-loudness functions describe the central tendencies of the data. In addition, no systematic errors are apparent, except that the context effect at 20 dB SPL generally is larger than predicted. Despite the underprediction of the context effect, the rms error is only 2.1 dB. This error is slightly smaller than the average standard error of the individual listeners’ data. The model also is able to predict the individual listeners’ data with rms errors that approach the rms values of the standard errors for the means across repetitions. The rms error of the model predictions is about 50% larger than the rms value of the standard error for MF and SB, whereas they are about equal for TP and SP. Thus, this simple model provides a satisfactory account of the data, as is also evident in Fig. 2.

The loudness functions obtained from the model are shown by the thick lines in Fig. 3. The model loudness func-

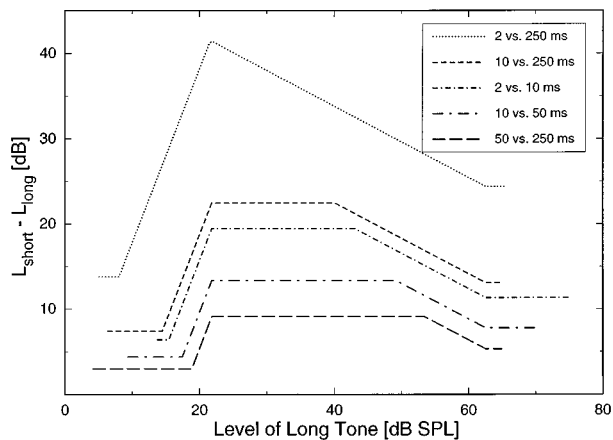


FIG. 4. The amount of temporal integration, defined as the level difference between equally loud short and long tones, is plotted as a function of level of the longer tone. The different lines show results for different duration pairs as indicated by the legend.

tions for the shorter tones are parallel to that for the 250-ms tone in accordance with Florentine *et al.*'s (1996) assumption that the ratio between the loudnesses of a long and a short tone at equal SPL is independent of the SPL. The loudness function for the 250-ms tones is compared to the loudness function obtained by combining Zwislocki's (1965) modified power function and the ISO 226 (1987) equal-loudness contours. The differences between the modified power function and the model loudness function are relatively minor, which indicates that the model loudness function for the 250-ms tones may be considered consistent with existing data. Although the ISO 226 (1987) equal-loudness contours indicate that the loudness of high-level tones grows faster at 5 than at 1 kHz, it should be noted that few data exist to support the relatively steep slope of 0.36 obtained at high levels.

The equal-loudness functions shown in Fig. 2 are derived from the loudness functions in Fig. 3. Because the loudness function was fixed for each stimulus duration, the predicted equal-loudness functions are perfectly transitive. The good agreement between the data and the model predictions indicate that the listeners' judgments also show nearly perfect transitivity. Thus, it appears that our new method for loudness-balance measurements was successful in reducing biases that interfered with transitivity in previous loudness-matching data obtained with adaptive procedures.

B. Effect of level on the amount of temporal integration

The amount of temporal integration clearly varies with level and is largest at moderate levels, as shown in Fig. 4. These functions are obtained from the equal-loudness functions predicted by the model. At low levels, the amount of temporal integration is close to the threshold difference between the stimuli in a pair. (Average thresholds were 3.4, 7.2, 13.7, and 18.8 dB SPL for durations of 250, 50, 10, and 2 ms, respectively.) At moderate levels, it reaches a plateau of three times that obtained at low levels, except for the 2- vs 250-ms comparison. For this pair, the amount of temporal

integration reaches a peak around 24 dB SPL; this maximum is also about three times that obtained at low levels. At levels above the plateau or peak, the amount of temporal integration decreases again to reach a lower plateau of about 1.8 times that obtained near threshold.

The amounts of temporal integration obtained in the present study are larger and show more variation with level than those obtained in our previous study for 1-kHz tones and broadband noises (Florentine *et al.*, 1996). This is particularly true for the largest duration ratio used. The amount of temporal integration between 2- and 250-ms tones varies from about 14 dB near threshold to over 40 dB around 20 dB SL; above this level it decreases to reach about 25 dB around 60 dB SL. Thus, the effect of level on temporal integration exceeds 25 dB when the brief tone lasts only 2 ms. This large effect of level clearly exceeds the 8-to-9-dB level effect obtained for 5- and 200-ms stimuli in our previous study. As expected, decreasing the duration of the briefest stimuli increased the effect of level as well as the amount of temporal integration.

The differences between the two studies may not be attributable entirely to the stimulus durations. Even when the duration ratios are roughly comparable, the amounts of temporal integration obtained in the present study exceed those obtained in our previous study. For example, Florentine *et al.* (1996) reported a maximal level difference of about 7 dB between equally loud 30- and 200-ms tones (ratio: 6.7), whereas the present data show a maximum of about 9 dB difference between 50- and 250-ms tones (ratio: 5). For 5- and 200-ms tones (ratio: 40), our previous study obtained a maximal amount of temporal integration of about 19 dB, whereas the present data show about 22 dB between 10- and 250-ms tones (ratio: 25). Although the differences are not large, they are surprising because their direction is opposite what might be expected. The amount of temporal integration increases as the duration ratio increases and the duration decreases. Because, in these comparisons, the duration ratios are smaller and the tones longer in the present study than in the previous study, one would expect the amounts of temporal integration to be smaller in the present study than in the previous study, not larger.

The discrepancy between the present study and our previous study may result from the different frequencies used. The larger amounts of temporal integration obtained in the present study may reflect that the auditory system shows more mid-level compression at high than at low frequencies. Cooper and Yates (1994) showed that input-output functions derived from comparisons between rate-intensity functions for below-CF tones and tones at CF are much more compressive for CFs above 4 kHz than below this frequency. Indeed, the flattest parts the loudness functions derived from our temporal-integration data have exponents of about 0.25 at 1 kHz and 0.21 at 5 kHz. If the loudness ratio between a short and a long tone of equal level is independent of level, a flattening of the loudness function increases the amount of temporal integration. Thus, part of the difference between our previous data for 1-kHz tones and the present data for 5-kHz tones may reflect that the loudness function is more compressive at 5 than at 1 kHz. It should be noted, however,

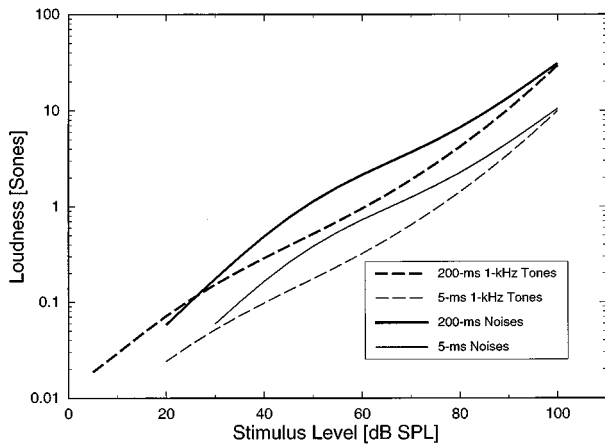


FIG. 5. Loudness functions for 1-kHz tones and white noises derived from Florentine *et al.*'s (1996) data for temporal integration. The dashed lines show loudness functions for 1-kHz tones and the solid lines show loudness functions for white noises. The thick lines are for 200-ms stimuli and the thin lines for 5-ms stimuli.

that the difference in the compressiveness of the loudness functions at 1 and 5 kHz is much smaller than the difference between the input-output functions reported by Cooper and Yates (1994).

C. Further support for the equal-loudness-ratio model

The hypothesis that the loudness ratio between a short and a long tone of equal level is independent of level may be tested further by using the loudness functions it produces to predict loudness data other than those used to derive them. For example, one may assume that the relative loudnesses of the brief noises in Florentine *et al.*'s (1996) experiment should be the same as those they obtained for the 1-kHz tone. This assumption permits deriving loudness functions for broadband noises based only on the amounts of temporal integration measured for noise bursts, except for a single multiplicative factor. The resulting loudness functions for 5- and 200-ms noise bursts are shown in Fig. 5 together with the loudness functions Florentine *et al.* (1996) derived from their data for 1-kHz tones.

These loudness functions may be used to predict loudness-balance functions between a 1-kHz tone and a wideband noise as shown in Fig. 6. The multiplicative factor allows the loudness functions for the noises in Fig. 5 to be shifted vertically, but their shapes and slopes are fixed by the temporal-integration data. Thus, the average amount of loudness summation, defined as level difference between equally loud tones and noises, may be adjusted to agree with the data, but the predicted level dependence of loudness summation is determined by the temporal-integration data. As shown in Fig. 6, the amount of loudness summation predicted from the loudness functions shown in Fig. 5 agrees closely with Pollack's (1951) data for loudness balance between white noise and 1-kHz tones. It is also in reasonable agreement with the amount of loudness summation derived from Scharf's (1978) loudness functions for 1-kHz tones and white noises. Considering that Florentine *et al.*'s (1996) listeners never heard tones together with the noises and that no

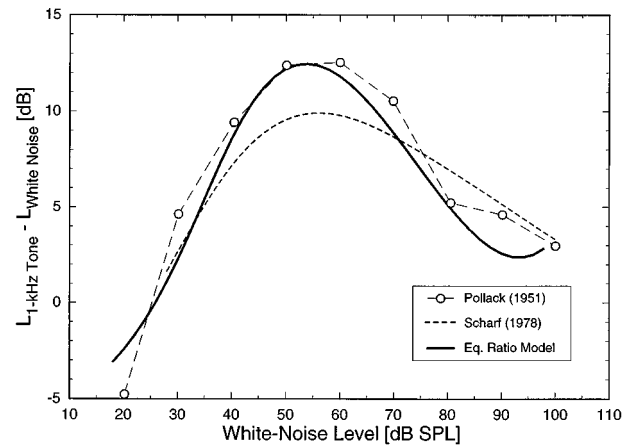


FIG. 6. Loudness summation as a function of level. The level difference between equally loud tones and white noises is plotted as a function of the level of the white noise. The circles show data from Pollack (1951), the dashed line shows data derived from Scharf's (1978) loudness functions for 1-kHz tones and white noises, and the thick solid line shows predictions from the loudness functions in Fig. 5.

attempt was made to have them relate loudness of one to the loudness of the other, we find this prediction of loudness summation quite remarkable. Moreover, because the loudness ratio between the 5- and the 200-ms stimuli is the same for tones and noises, the equal-loudness-ratio model also predicts that the amount of loudness summation should be independent of duration, which agrees with the data (Port, 1963; Zwicker, 1965). Altogether, these predictions offer strong support of the equal-loudness-ratio model. It should be noted, however, that little evidence is available to support the relatively large exponent of about 0.43 obtained for the 1-kHz tones at high levels on the basis of our temporal-integration data.

Finally, the equal-loudness-ratio model should also be able to predict Florentine *et al.*'s (1996) data for 30-ms stimuli. The loudness functions in Fig. 5 are determined only from the data for the 5- and 200-ms stimuli, but if the equal-loudness-ratio model is correct, the loudness functions for the 30-ms stimuli should be parallel to those for the other durations and the loudness ratios should be the same for tones and noises. Thus, only one free parameter is available to predict Florentine *et al.*'s (1996) data for the amount of temporal integration between 5- and 30-ms stimuli and between 30- and 200-ms stimuli for both tones and noises. In other words, with only one free parameter the model should predict four functions based on a total of 76 data points.

As shown in Fig. 7, the predicted functions are in good agreement with the polynomials used by Florentine *et al.* (1996) to summarize their data. The difference between the data and the predictions is always less than 2 dB, which is well within the variability of the data. The tendency for the predicted amounts of temporal integration to exceed that measured reflects the minor deviations from perfect transitivity observed in our previous data. The sum of level differences between 5- and 30-ms stimuli and between 30- and 200-ms stimuli tended to be a few dB less than that between 5- and 200-ms stimuli. In contrast, the predictions maintain

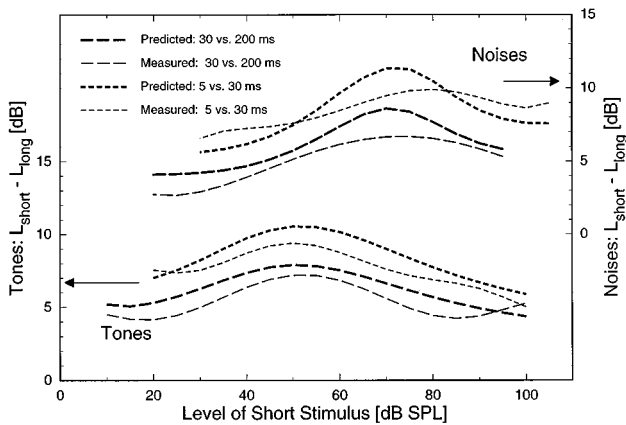


FIG. 7. Data and predictions for Florentine *et al.*'s (1996) 30-ms stimuli. The level difference between equally loud 5- and 30-ms stimuli (short-dashed lines) and between equally loud 30- and 200-ms stimuli (long-dashed lines) is plotted as a function of level of the shorter stimulus in the pair. The thick lines show predictions by the equal-loudness-ratio model and the thin lines show Florentine *et al.*'s (1996) summary of their data. The functions at the bottom are for tones and refer to the left ordinate; the functions at the top are for noises and refer to the right ordinate.

perfect transitivity. Because the level difference between 5- and 200-ms tones is fixed by the loudness functions shown in Fig. 5, the model was forced to exaggerate slightly the level differences between the 30-ms stimuli and the other stimuli. Overall, the forms of the predicted functions match those of the data very well. Thus, it appears that the loudness functions shown in Fig. 5 and the equal-loudness-ratio model can account for the effect of level on the amount of temporal integration observed between 5- and 30-ms stimuli and between 30- and 200-ms stimuli.

D. Loudness discrimination compared to level discrimination

It is often assumed that the just-noticeable difference in sound level, ΔL_{DL} , represents a difference limen for loudness (e.g., Harris, 1963; Hellman and Hellman, 1990; Neely and Allen, 1996). To examine this assumption, previous data for level discrimination as a function of duration may be compared with the present data for the just-noticeable loudness-level difference for variable stimuli of different durations. When listeners are asked to detect a small difference in level between two equal-duration tones, the ΔL_{DL} typically decreases by a factor of about 2 for each tenfold increase in duration (Florentine, 1986; Buus and Florentine, 1992). On the other hand, when listeners have to pick the louder of two tones with unequal duration, the jnds for loudness level appear to be independent of duration as indicated by the present data and the model. This result differs markedly from the expectation that the loudness-level jnds should be at least a factor of 4 smaller for 250-ms variable tones than for 2-ms variable tones, if level discrimination and loudness discrimination were governed by the same processes. This indicates that the ΔL_{DL} s measured in level-discrimination experiments in which the stimuli differ only in level are unlikely to correspond to a just-noticeable difference in loudness.⁴

The difference between level discrimination and loudness discrimination may be understood by considering the information available for each kind of discrimination. The Multiband Excitation-Pattern Model for Level Discrimination (Florentine and Buus, 1981) indicates that the excitation-level difference in each critical band provides highly reliable information for discrimination between two tones that differ only in level. The excitation-level difference in each critical band presumably can be observed for the duration of the stimuli, such that the number of observations increases in proportion to the stimulus duration. In fact, the increased number of observations accounts for the decrease in the jnds if the effects of auditory-nerve adaptation are taken into account (Buus and Florentine, 1992).

On the other hand, when the stimuli differ in several aspects, as in the present experiment, excitation-level differences in any one critical band are not reliable indicators of a change in level of the variable stimulus. Then, the listeners' judgments are likely to reflect an overall quality such as loudness. Indeed, our listeners were instructed to judge the loudness of the stimuli and probably their judgments were governed by loudness because the data indicate a close relation between the jnds and the loudness function. Difference limens based on judgments of loudness may be expected to be independent of the stimulus duration. Because the loudness is thought to represent the maximal output of an integrator (e.g., Zwicker, 1977; Zwicker and Fastl, 1990), the number of observations does not increase with stimulus durations—at least not when the stimuli are briefer than the relatively long time constant of the integrator [45 ms (Zwicker and Fastl, 1990) to 120 ms (Boone, 1973)]. Thus, the duration independence of the difference limens in the present experiment may reflect that loudness represents just one observation for both long and short stimuli. These considerations indicate that the difference between level jnds and loudness jnds is more than semantic.

IV. SUMMARY

The present study applied a new loudness-balance procedure to investigate temporal integration of loudness for 5-kHz tone bursts with durations ranging from 2 to 250 ms and levels ranging between 2 and 60 dB SL. The new procedure used ten interleaved adaptive tracks to obtain concurrent loudness balances at several levels with both the short and the long tone varied. It was designed to increase the consistency of the listeners' judgments by discouraging comparisons with previous trials. The data were interpreted in terms of an equal-loudness-ratio model, which assumes that the loudness ratio between two tones of different durations is independent of level and that the just-noticeable difference in loudness is proportional to the square root of loudness. The main conclusions are as follows:

- (1) The new procedure appears successful as indicated by a high degree of internal consistency in the data. The transitivity of the loudness judgments appears nearly perfect.
- (2) The amount of temporal integration, defined as the level difference between equally loud short and long tones, depends markedly on level. With the very brief tones

used in the present study, it varied more than 25 dB—from about 14 dB near threshold to over 40 dB when the 250-ms tone is about 22 dB SPL and the 2-ms tone is about 63 dB SPL. For all duration pairs, the amount of temporal integration is about three times larger at moderate levels than at low and high levels.

- (3) The just-noticeable difference in loudness level also varies with level and is largest at moderate levels.
- (4) Both effects of level can be explained by the equal-loudness-ratio model by assuming that the loudness function [$\log(\text{loudness})$ as a function of SPL] is flatter at moderate levels than at low and high levels.
- (5) The data and the model indicate that the just-noticeable difference for loudness level is independent of stimulus duration. This finding contrasts with previous data for level discrimination and indicates that level discrimination between stimuli that differ only in level is not the same as loudness discrimination between stimuli that differ along multiple dimensions.
- (6) The equal-loudness-ratio model can predict the effect of level on loudness summation from previous data for temporal integration of loudness for 1-kHz tones and white noises. This finding offers strong support for the model because the measurements did not attempt to relate the loudness of white noise to that for tones.
- (7) The equal-loudness-ratio model applied to data obtained with 5- and 200-ms stimuli also produces good predictions of the amount of temporal integration obtained with 30-ms stimuli.

ACKNOWLEDGMENTS

Part of this research was carried out at the Technical University of Denmark while the first and second authors were on sabbatical and leave of absence, respectively, from Northeastern University. It was supported by NIH-NIDCD R01 DC02241 and the Technical University of Denmark. The authors thank Rhona Hellman, Hannes Müsch, Bertram Scharf, Fan-Gang Zeng, and an anonymous reviewer for helpful comments on an earlier version of this paper.

¹The reader should note that the term “loudness discrimination” is used to describe measurements of difference limens in tasks requiring the listeners to judge the loudness of stimuli that differ in more than one dimension (e.g., duration and level). The term “level discrimination” is used to describe measurements of difference limens for stimuli that differ only in level. Likewise, jnds for loudness level are used to indicate the difference limens (in dB) obtained for loudness discrimination, whereas jnds for sound level, ΔL_{DLs} , are used to indicate the just-audible difference between two sounds that differ only in level, as measured in traditional level- (or intensity-) discrimination experiments.

²The just-noticeable difference in loudness, ΔN_{DL} , often has been suggested to follow Weber’s law such that $\Delta N_{\text{DL}}/N$ (where N is the loudness in sones) is constant (e.g., Zwicker and Feldtkeller, 1967). Using this assumption in the model results in a fit that is only marginally poorer than the fit obtained when the just-noticeable difference in loudness is assumed to be proportional to the square root of the loudness.

³The Weber fraction for loudness, $\Delta N_{\text{DL}}/N$, could conceivably depend on duration. However, the data show no clear effect of duration on the just-noticeable loudness-level differences. Moreover, models in which ∂ depended on duration showed no systematic effect of duration on ∂ and they provided only a marginally better fit to the data than the model in which ∂ is independent of duration. Therefore, ∂ was made independent of duration in the final model.

⁴It should be noted that Garner (1949) measured difference limens for loudness level by loudness balances between tones of different durations. Contrary to the present data, Garner’s data indicate that the difference limen, calculated from the variability of loudness matches by the method of adjustment, increased as the duration of the short tone decreased. However, Garner’s listeners varied only the long tone, which always was 500 ms in duration. Therefore, Garner’s effect of duration may be confounded by effects of the level of the variable tone, which makes his data difficult to interpret. Moreover, when the two tones being compared had the same duration and the pause between them was 500 ms, only a small effect of duration on the differences limens was obtained—contrary to the effect of duration obtained in modern measurements of level discrimination (Florentine, 1986; Buus and Florentine, 1992). Thus, it appears that Garner’s measurements with the method of adjustment are not comparable to measurements with modern forced-choice procedures.

Boone, M. M. (1973). “Loudness measurements on pure tone and broad band impulsive sounds,” *Acustica* **29**, 198–204.

Buus, S., and Florentine, M. (1992). “Possible relation of auditory-nerve adaptation to slow improvement in level discrimination with increasing duration,” in *Auditory Physiology and Perception*, edited by Y. Cazals, L. Démany, and K. Horner (Pergamon, New York), pp. 279–288.

Cooper, N. P., and Yates, G. K. (1994). “Nonlinear input-output functions derived from the responses of guinea-pig cochlear nerve fibers: Variations with characteristic frequency,” *Hear. Res.* **78**, 221–234.

Durlach, N. I., and Braida, L. D. (1969). “Intensity perception. I. Preliminary theory of intensity resolution,” *J. Acoust. Soc. Am.* **46**, 372–383.

Ekman, G., Berglund, B., and Berglund, U. (1966). “Loudness as a function of the duration of auditory stimulation,” *Scand. J. Psychol.* **7**, 201–208.

Fletcher, H., and Munson, W. A. (1933). “Loudness, its definition, measurement and calculation,” *J. Acoust. Soc. Am.* **5**, 82–108.

Florentine, M. (1986). “Level discrimination as a function of duration,” *J. Acoust. Soc. Am.* **79**, 792–798.

Florentine, M., and Buus, S. (1981). “An excitation-pattern model for intensity discrimination,” *J. Acoust. Soc. Am.* **70**, 1646–1654.

Florentine, M., Buus, S., and Poulsen, T. (1996). “Temporal integration of loudness as a function of level,” *J. Acoust. Soc. Am.* **99**, 1633–1644.

Garner, W. R. (1949). “The loudness and loudness matching of short tones,” *J. Acoust. Soc. Am.* **21**, 398–403.

Harris, J. D. (1963). “Loudness discrimination,” *J. Speech Hear. Dis. Monogr.* **11**.

Hellman, W., and Hellman, R. P. (1990). “Intensity discrimination as the driving force for loudness. Application to pure tones in quiet,” *J. Acoust. Soc. Am.* **87**, 1255–1271.

ISO 226 (1987). *Acoustics—Normal equal-loudness level contours* (International Organization for Standardization, Geneva).

ISO 389 (1991). *Acoustics—Standard reference zero for the calibration of pure-tone air conduction audiometers* (International Organization for Standardization, Geneva).

ISO TR 4869-3 (1989). *Acoustics—hearing protectors—part 3: Simplified method for the measurement of insertion loss of ear-muff type protectors for quality inspection purposes* (International Organization for Standardization, Geneva).

Jesteadt, W. (1980). “An adaptive procedure for subjective judgments,” *Percept. Psychophys.* **28**, 85–88.

Levitt, H. (1971). “Transformed up–down procedures in psychoacoustics,” *J. Acoust. Soc. Am.* **49**, 467–477.

Munson, W. A. (1947). “The growth of auditory sensation,” *J. Acoust. Soc. Am.* **19**, 584–591.

Neely, S. T., and Allen, J. B. (1996). “Relationship between the rate of growth of loudness and the intensity DL,” in *Modeling Sensorineural Hearing Loss*, edited by W. Jesteadt (Erlbaum, Hillsdale, NJ), in press.

Pedersen, O. J., Lyregaard, P. E., and Poulsen, T. (1977). “The round robin test on impulsive noise,” Report No. 22 (The Acoustics Laboratory, Technical University of Denmark, Lyngby).

Pollack, I. (1951). “On the measurement of the loudness of white noise,” *J. Acoust. Soc. Am.* **23**, 654–657.

Port, E. (1963). “Über die Lautstärke einzelner kurzer Schallimpulse,” *Acustica* **13**, 212–223.

Poulsen, T. (1981). “Loudness of tone pulses in a free field,” *J. Acoust. Soc. Am.* **69**, 1786–1790.

Scharf, B. (1970). “Critical bands,” in *Foundations of Modern Auditory Theory*, edited by J. V. Tobias (Academic, New York), Vol. I, pp. 157–202.

- Scharf, B. (1978). "Loudness," in *Handbook of Perception: Vol. 4. Hearing*, edited by E. C. Carterette and M. P. Friedman (Academic, New York), pp. 187–242.
- Schlauch, R. S., and Wier, C. C. (1987). "A method for relating loudness-matching and intensity-discrimination data," *J. Speech Hear. Res.* **30**, 13–20.
- Stephens, S. D. G. (1973). "Auditory temporal integration as a function of intensity," *J. Sound Vib.* **30**, 109–126.
- Stevens, J. C., and Hall, J. W. (1966). "Brightness and loudness as a function of stimulus duration," *Percept. Psychophys.* **1**, 319–327.
- Stevens, S. S. (1956). "Calculation of the loudness of complex noise," *J. Acoust. Soc. Am.* **28**, 807–832.
- Stevens, S. S., and Davis, H. (1938). *Hearing. Its Psychology and Physiology* (Wiley, New York; reprinted by AIP, New York, 1983).
- Stevens, S. S., and Greenbaum, H. B. (1966). "Regression effect in psychophysical judgment," *Percept. Psychophys.* **1**, 439–446.
- Villchur, E. (1969). "Free-field calibration of earphones," *J. Acoust. Soc. Am.* **46**, 1527–1534.
- Yates, G. K. (1990). "The basilar membrane input-output function," in *The Mechanics and Biophysics of Hearing*, edited by P. Dallos, C. D. Geisler, J. M. Matthews, M. A. Ruggero, and C. R. Steele (Springer-Verlag, New York), pp. 106–113.
- Zeng, F.-G. (1994). "Loudness growth in forward masking: Relation to intensity discrimination," *J. Acoust. Soc. Am.* **96**, 2127–2132.
- Zwicker, E. (1961). "Subdivision of the audible frequency range into critical bands (Frequenzgruppen)," *J. Acoust. Soc. Am.* **33**, 248.
- Zwicker, E. (1965). "Temporal effects in simultaneous masking and loudness," *J. Acoust. Soc. Am.* **38**, 132–141.
- Zwicker, E. (1977). "Procedure for calculating loudness of temporally variable sounds," *J. Acoust. Soc. Am.* **62**, 675–682.
- Zwicker, E., and Fastl, H. (1990). *Psychoacoustics: Facts and Models* (Springer-Verlag, New York).
- Zwicker, E., and Feldtkeller, R. (1967). *Das Ohr als Nachrichtenempfänger* (Hirzel, Stuttgart).
- Zwislocki, J. J. (1965). "Analysis of some auditory characteristics," in *Handbook of Mathematical Psychology*, edited by R. D. Luce, R. R. Bush, and E. Galanter (Wiley, New York), pp. 1–97.
- Zwislocki, J. J. (1969). "Temporal summation of loudness: An analysis," *J. Acoust. Soc. Am.* **46**, 431–441.

Resonant scattering of acoustic waves by ellipsoid air bubbles in liquids

Zhen Ye

Institute of Ocean Sciences, Sidney, British Columbia, Canada and Department of Physics, National Central University, Chungli, Taiwan, R.O.C.

(Received 15 March 1996; accepted for publication 26 September 1996)

This paper reports the first analytic study of resonant scattering of acoustic waves by ellipsoid air bubbles in liquids. Based on the Kirchhoff integral theorem, the function of sound scattering is derived in a simple closed form and is shown to bear analogy with the well-known expression for sound scattering from spherical air bubbles. The resonance frequency and the quality factor Q are also derived. For the special cases such as spherical and prolate spheroid bubbles, the results reduce to the previously known results. © 1997 Acoustical Society of America. [S0001-4966(97)01202-2]

PACS numbers: 43.20.Fn, 43.30.Ft, 43.20.Bi [JEG]

INTRODUCTION

Resonant scattering of acoustic waves by air bubbles has attracted considerable attention over the years as it plays a significant role in a variety of situations of interest, such as wave propagation in the upper ocean surfaces (Thorpe, 1982), generation of ambient noise in the ocean (Farmer and Lemon, 1984), and modeling sound scattering from fish swimbladders (Ye, 1996). One reason for this to continue to be interesting is that bubbles are a strong acoustic target, and therefore are useful tracers for studies of many upper ocean processes, including turbulence generated by breaking surface waves, Langmuir circulation, fronts, and internal waves (Thorpe, 1982, 1995).

In most previous studies, it had been assumed that bubbles are not deformed from interaction with the surrounding medium, and thus take the ideal spherical shape. This assumption is only valid for sufficiently small bubbles for which the tension at the air-medium interface can sustain deformation. When this condition is not satisfied, it would be necessary to investigate sound scattering from deformed bubbles. Indeed, the study of sound scattering from deformed bubbles has become an important area. This is not only because deformed bubbles can be used to model many actual targets such as fish swimbladders, large air bubbles in upper ocean surfaces, and air bubbles embedded in the sediments in ocean bottoms, but the problem of sound scattering by deformed bubbles itself is theoretically challenging.

The problem of sound scattering by deformed bubbles was first studied by Strasberg (1953), who derived an analytic expression for the resonance frequency using a modified equation of motion for deformed bubbles. In his study, no mention was made about how the scattering amplitude can be affected by the deformation. It is only recently that more detailed studies of sound scattering by deformed bubbles have been given by Feuillade and Werby (1994) and Ye (1996, 1997). The former authors studied the problem using the T -matrix method, while the latter presented analytic expressions for the sound scattering function. In these works, however, the study has been limited to prolate spheroid air bubbles or cylindrical bubbles with hemispherical endcaps. A more general class of scatterers, namely air-filled

ellipsoids, remains untackled. In fact, recent observations suggest that air bubbles in the sediments can neither be modeled as spheres nor prolate spheroids and a compromising model may be ellipsoids. Moreover, it is more appropriate to model actual fish swimbladders as ellipsoids rather than the other shapes considered. Therefore, a study of sound scattering by ellipsoidal bubbles is desirable.

The purpose of this work is to study the resonance sound scattering by air-filled ellipsoids, for which the maximum dimension is considerably small compared with the acoustic wavelength so that the monopole mode dominates. In principle, the problem may be exactly solved in terms of the ellipsoidal harmonics by variable separation (Morse and Feshbach, 1953.) However, the complication of the ellipsoidal harmonics handicaps actual computation. In this paper, the problem is investigated by means of a novel method (Ye, 1996b) which is based on the Kirchhoff integral theorem (Waterman, 1969) and the analogy between the scattering problem and the electrostatic problem (Strasberg, 1953). When the maximum dimension of the ellipsoid is small compared with the acoustic wavelength, an analytic expression can be derived for its resonant scattering. The resonance frequency and the quality factor (Q) characterizing the broadening of the resonance will also be shown in a simple closed form.

I. THEORY

Consider a plane wave incident on an ellipsoidal gas bubble (Fig. 1). The equation representing the surface of an ellipsoid is

$$\frac{x^2}{a^2} + \frac{y^2}{b^2} + \frac{z^2}{c^2} = 1. \quad (1)$$

For congruity of analysis, the three axes of the ellipsoid are arranged in the order $a \geq b \geq c$.

The unit incident plane wave can be expressed as $p_i = e^{i\mathbf{k}_i \cdot \mathbf{r}}$ with suppressed time dependence $e^{-i\omega t}$. The pressure wave equation in the surrounding liquid can be written as

$$(\nabla^2 + k^2)p = 0. \quad (2)$$

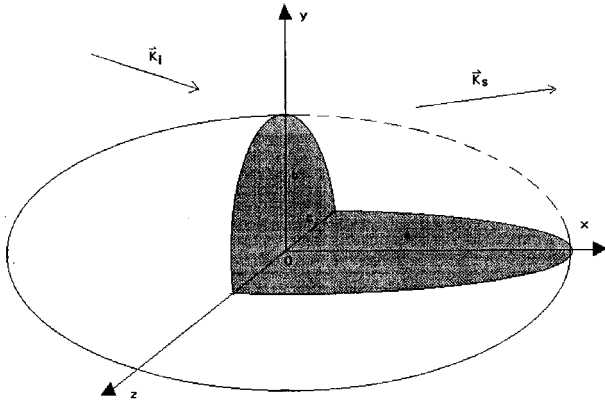


FIG. 1. A sketch of an ellipsoid scatterer in the rectangular coordinates.

The total wave field satisfying this equation is given by Kirchhoff integral theorem (e.g., Waterman, 1969):

$$p(\mathbf{r}) \Big|_0 = p_i(\mathbf{r}) + \frac{1}{4\pi} \int_S ds [p_+ \mathbf{n} \cdot \nabla G(k|\mathbf{r}-\mathbf{r}'|) - i\omega\rho_l u_n G(k|\mathbf{r}-\mathbf{r}'|)], \quad \text{for } \mathbf{r} \begin{cases} \text{outside } S \\ \text{inside } S, \end{cases} \quad (3)$$

where the integration is performed over the surface of the object, \mathbf{r}' is taken on s , \mathbf{n} is a unit outward normal vector to the surface, and G is the usual 3-D Green's function $G(r) = \exp(ikr)/r$. In this expression, p_+ and u_n are the total pressure field and the normal velocity on the surface, approached from outside, and ρ_l is the density of the surrounding liquid. It is clear that the scattered wave p_s represented by the integral in Eq. (3) is due to the response of the scatterer to the incident wave.

In the far-field region, where $r \gg r'$, p_s behaves as a spherically spreading wave (Sommerfeld radiation condition),

$$p_s(\mathbf{r}) \rightarrow f(\mathbf{k}_i, \mathbf{k}_s) \frac{e^{ikr}}{r}, \quad (4)$$

where \mathbf{k}_i , \mathbf{k}_s are the incident and scattering wave vectors, respectively. The function of scattering amplitude $f(\mathbf{k}_i, \mathbf{k}_s)$ can be derived from Eq. (3) as [refer to Eq. (9.125) in Jackson, 1975]

$$f(\mathbf{k}_i, \mathbf{k}_s) = -\frac{1}{4\pi} \int_S ds e^{-i\mathbf{k}_s \cdot \mathbf{r}} [i\mathbf{k}_s \cdot \mathbf{n} p_+ + i\omega\rho_l u_n]. \quad (5)$$

Thus, $f(\mathbf{k}_i, \mathbf{k}_s)$ can be determined once the surface values p_+ and u_n are known.

Using boundary conditions in Eq. (3), we can obtain an analytic expression for f at low frequencies, i.e., $ka \ll 1$. Here for brevity we write out the expression directly. The interested reader may refer to the Appendix for a detailed derivation. Ignoring heat conductance, viscosity effects, and surface tension, a simple expression is derived for the scattering function f of an ellipsoidal air bubble:

$$f = \frac{R_0}{\omega_0^2/\omega^2 - 1 - ikR_0}, \quad (6)$$

where f has been normalized by the amplitude of the incident wave, and the quantity R_0 and resonance frequency ω_0 are defined as

$$R_0 \equiv aE_c/F, \quad (7)$$

$$\omega_0^2 \equiv \frac{4\pi\gamma P_0}{\rho_l V_0} R_0, \quad (8)$$

with the volume of the ellipsoid $V_0 = 4\pi abc/3$. The term kR_0 in the denominator of Eq. (6) is identified as the radiation damping factor. Here we define $e_b = b/a$, $e_c = c/a$, and $E_b = \sqrt{1-e_b^2}$, $E_c = \sqrt{1-e_c^2}$. The function F in Eq. (7) is the elliptic function of the first kind (Gradshteyn and Ryzhik, 1980):

$$F(\phi, m) = \int_0^\phi \frac{d\alpha}{\sqrt{1-m^2 \sin^2 \alpha}}. \quad (9)$$

The two variables in the elliptic function F are given as $\phi = \sin^{-1} E_c$ and $m = E_b/E_c$, and the values for F may be obtained from mathematical tables or by numerical computation.

The scattering function and resonance frequency in Eqs. (6) and (8) can be regarded as general formulas for scattering by the family of ellipsoids, including spheres, oblate spheroids and prolate spheroids. Table I summarizes the results for the family. In the table, it can be seen that the results reduce to the previous solutions for the case of a sphere (Clay and Medwin, 1977) or a prolate spheroid (Ye, 1997). It is interesting to note that the scattering by air-filled ellipsoidal bubbles is omni-directional in the resonance region.

II. NUMERICAL ANALYSIS

The scattering function in Eq. (6) shows a resonant feature of an air-filled ellipsoid. We first consider a few special cases. When $\omega \ll \omega_0$

$$f \approx \frac{\rho_l V_0}{4\pi\gamma P_0} \omega^2. \quad (10)$$

The scattering function is independent of the shape of the ellipsoid at very low frequencies, following the Rayleigh volume scattering. When $\omega = \omega_0$, the scattering amplitude, the peak amplitude, is inversely proportional to the damping factor, and equals

$$f = \frac{ic_s}{\omega_0}, \quad (11)$$

where c_s is the sound speed in the medium. Equation (11) suggests that the higher the resonance frequency, the lower the resonant amplitude. When $\omega \gg \omega_0$ and $kR_0 \ll 1$, the scattering function becomes

$$f \approx R_0. \quad (12)$$

Figures 2, 3, and 4 are plotted to show some features of the resonance frequency ω_0 , the target strength $TS = 20 \log_{10}|f|$ and quality factor Q , defined as the inverse of

TABLE I. Scattering function and resonance frequency for ellipsoidal air bubbles.

	a, b, c	ϕ	m	$F(\phi, m)$	R_0	ω_0^2
Ellipsoid	$a > b > c$	$\sin^{-1} E_c$	E_b/E_c	$F(\phi, m)$	$\frac{aE_c}{F}$	$\frac{\gamma P_0}{\rho_l V_0} 4\pi R_0$
Oblate spheroid	$a = b > c$	$\sin^{-1} E_c$	0	$\sin^{-1} E_c$	$\frac{aE_c}{\sin^{-1} E_c}$	$\frac{3\gamma P_0}{\rho_l a c} \frac{E_c}{\sin^{-1} E_c}$
Prolate spheroid	$a > b = c$	$\sin^{-1} E_c$	1	$\ln\left(\frac{1+E_c}{e_b}\right)$	$\frac{aE_c}{\ln\left(\frac{1+E_c}{e_b}\right)}$	$\frac{3\gamma P_0}{\rho_l c^2} \frac{E_c}{\ln\left(\frac{1+E_c}{e_b}\right)}$
Sphere	$a = b = c$	0	1	0	a	$\frac{3\gamma P_0}{\rho_l a^2}$

the damping factor, for various ellipsoidal shape; in the present case, $Q = 1/kR_0$. The parameters used in the calculation are: $c_s = 1500$ m/s, $\rho_l = 1000$ kg/m³, $\gamma = 1.4$, and $P_0 = 10^5$ N/m². In addition, we assume that the volume V_0 remains constant, for which the equivalent sphere has the radius $a_e = (3V_0/4\pi)^{1/3} = 0.01$ m, and the resonant frequency $\omega_e = (1/a_e)\sqrt{3\gamma P_0/\rho_l}$. In Fig. 2, the curves for ω_0/ω_e as a function of e_b are different for two special shapes, (a) $c/b = 0.01$, corresponding to a nearly flat ellipsoid, and (b) $c/b = 0.99$, almost spheroidal shape. Here and in the following, the number 0.99 is chosen in order to avoid the indeterminacy in the integral of the elliptic function $F(\phi, m)$. Both curves indicate that resonance frequency increases with decreased e_b . When the shapes deform into a rod, the change of resonance frequency becomes rather steep, while the nearly flat ellipsoid always has a higher resonance frequency than the nearly spheroidal shape for the same e_b . Figure 3 shows that the quality factor of a nearly flat ellipsoid is much smaller than that of a spheroid, which implies a larger damping factor for the nearly flat ellipsoid.

Figure 4 depicts the target strength as a function of frequency for four different shapes of ellipsoids: (a) an approximate sphere, solid line; (b) disklike, dashed line; (c) rod,

dotted-dashed line; (d) sliver, dotted line. As we can see from this figure, at very low frequencies, the target strength is independent of shape, consistent with what has been shown in Eq. (10). At frequencies above the resonance while still within the low-frequency region $ka_e \ll 1$, the target strength appears to depend on R_0 only, in consistence with Eq. (12). The resonance frequency for these four shapes increases as the order sphere, rod, disk and sliver, while the amplitude at resonance and the quality factor Q decrease in this order.

III. SUMMARY

In this paper, we derived an analytic solution for acoustic scattering by an ellipsoid bubble at low frequencies. This solution, accommodating the previous results for spheres and prolate spheroids, may be used as a check for any numerical method to be developed to calculate acoustic scattering by gas ellipsoids. To our best knowledge, such a numerical computation is still lacking in the literature.

The analytic results have been used to investigate some features in acoustic scattering from an ellipsoid by a few numerical examples. It was shown that at constant volume, the resonance frequency, quality factor, and the scattering

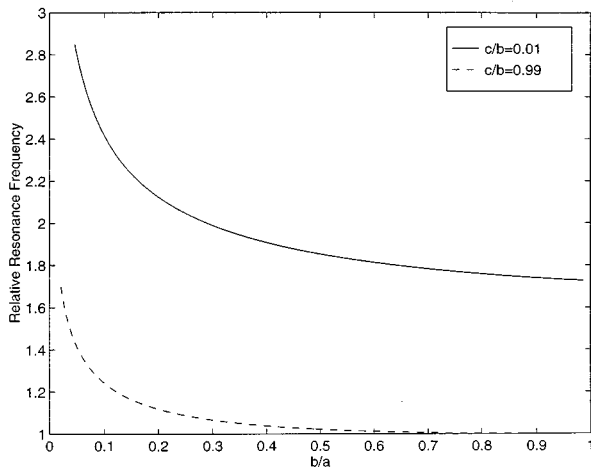


FIG. 2. The relative frequency ω_0/ω_e vs b/a for two values of c/b : 0.99 and 0.01.

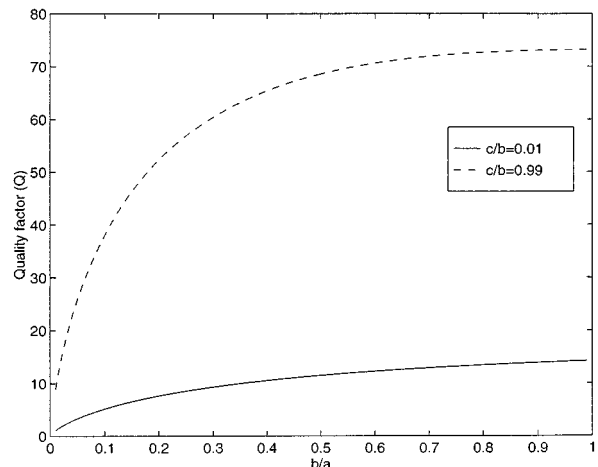


FIG. 3. The quality factor Q as a function of b/a for $c/b = 0.99$ and 0.01, respectively.

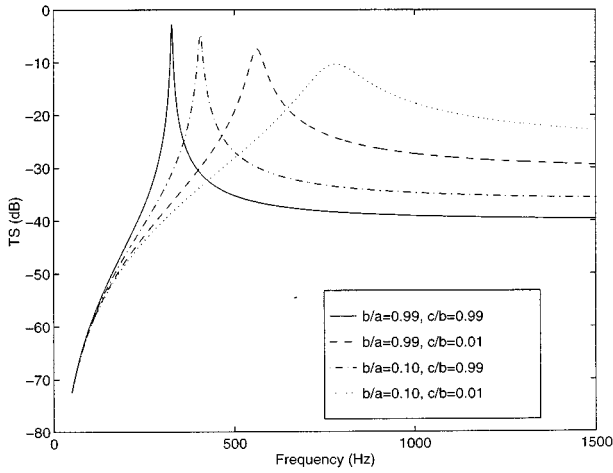


FIG. 4. Target strength as a function of frequency for four different shapes of ellipsoid: (a) approximated sphere (solid line); (b) disk (dashed line); (c) rod (dotted-dashed line); (d) sliver (dotted line).

function are affected significantly by the variation in axis ratios among the three axes. It was explicitly shown that a disklike ellipsoid has a higher resonance frequency and a larger damping factor than that of a rod at the same b/a .

Finally, we state that the present results are derived when the heat transfer and viscosity effects are ignored. When these effects are taken into account, the quality factor Q and the target strength at resonance are both expected to reduce. In addition, the assumed adiabatic behavior of the gas may not be appropriate for some extreme cases such as very flat or slender bubbles. The inclusion of thermal and viscosity effects remains to be the subject of a future work.

ACKNOWLEDGMENTS

E. Wang is thanked for preparing materials for this paper. The referee is sincerely thanked for many valuable comments and constructive suggestions. The work received support from a National Program for Fisheries Acoustics, Department of Fisheries and Oceans, Canada.

APPENDIX

Scattering function $f(\mathbf{k}_i, \mathbf{k}_s)$ is determined by the surface values of p_+ and u_n . To solve p_+ and u_n , we employ the following conditions: (1) Continuity across the boundary requires

$$p_g = p_+, \quad u_{g,n} = u_n. \quad (\text{A1})$$

The index “g” refers to the quantities inside the ellipsoid bubble. For low frequencies, p_g can be treated as a constant (Clay and Medwin, 1977). (2) Thermodynamics equation gives

$$PV^\gamma = \text{constant}, \quad (\text{A2})$$

for ideal gases in an adiabatic process, and the polytropic exponent γ may have the value of 1.4 for the air. When viscosity and heat conduction are considered, γ should be expressed as a complex number (Clay and Medwin, 1977). (3) Equation (A2) gives

$$\frac{dV}{dt} = \int_S u_n ds = \frac{i\omega V_0}{\gamma P_0} p_g, \quad (\text{A3})$$

where volume of the ellipsoid $V_0 = 4\pi abc/3$. (4) Using Eq. (3) for a point inside the bubble leads to

$$0 = p_i(\mathbf{r}) + \frac{1}{4\pi} \int_S ds [p_+ \mathbf{n} \cdot \nabla G(k|\mathbf{r}-\mathbf{r}'|) - i\omega \rho_l u_n G(k|\mathbf{r}-\mathbf{r}'|)]. \quad (\text{A4})$$

Setting $\mathbf{r}=0$ and using

$$G(kr') = \frac{1}{r'} e^{ikr'},$$

$$\nabla G(k|\mathbf{r}'|) = (-1 + ikr') \frac{\mathbf{r}'}{r'^3} e^{ikr'}.$$

Normalized by p_i , Eq. (A4) is reduced to

$$\frac{i\omega \rho_l}{4\pi} \int_S \frac{e^{ikr'}}{r'} u_n ds + \frac{p_g}{4\pi} \int_S \frac{\mathbf{r}' \cdot \mathbf{n}}{r'^3} (1 - ikr') e^{ikr'} ds = 1, \quad (\text{A5})$$

At low frequencies, $kr' \sim ka \ll 1$, making a Taylor expansion for $e^{ikr'}$; we get the following equation to the first order of kr' :

$$\frac{i\omega \rho_l}{4\pi} \int_S \frac{1 + ikr'}{r'} u_n ds + \frac{p_g}{4\pi} \int_S \frac{\mathbf{r}' \cdot \mathbf{n}}{r'^3} ds = 1. \quad (\text{A6})$$

(5) According to Strasberg (1953), u_n is mathematically equivalent to the charge density on a perfect conductor having the same shape and can be written in the following form for the ellipsoid (Stratton, 1941):

$$u_n = \frac{A}{\sqrt{x^2/a^4 + y^2/b^4 + z^2/c^4}}, \quad (\text{A7})$$

where A is a constant to be determined. Substituting u_n into Eqs. (A3) and (A6), we obtain analytical solutions for A , p_g :

$$A = \frac{i\omega}{3\gamma P_0 B - \omega^2 \rho_l a^2 [(e_b e_c / E_c) F + ika e_b e_c]}, \quad (\text{A8})$$

$$p_g = \frac{3\gamma P_0}{3\gamma P_0 B - \omega^2 \rho_l a^2 [(e_b e_c / E_c) F + ika e_b e_c]}. \quad (\text{A9})$$

In deriving Eqs. (A8) and (A9), we used the following integrals over the surface of the ellipsoid:

$$\int_S ds \frac{1}{\sqrt{x^2/a^4 + y^2/a^4 + z^2/b^4}} = 4\pi abc, \quad (\text{A10})$$

and

$$\int_S ds \frac{1}{\sqrt{x^2/a^4 + y^2/b^4 + z^2/c^4}} \frac{1}{\sqrt{x^2 + y^2 + z^2}} = \frac{8\pi a^2 e_b e_c}{E_c} F(\phi, m), \quad (\text{A11})$$

where the two ratio aspects are defined as $e_b \equiv b/a$, $e_c \equiv c/a$, and $E_b \equiv \sqrt{1 - e_b^2}$, $E_c \equiv \sqrt{1 - e_c^2}$. $F(\phi, m)$ is the first kind el-

liptic function, in which two parameters $\phi = \sin^{-1} E_c$, $m = E_b/E_c$ (Gradshteyn and Eyzhik, 1980).

Substituting the above solutions for u_n and p_g into Eq. (5), the scattering function can be solved as

$$f(\mathbf{k}_i, \mathbf{k}_s) = \frac{U_1 - U_2}{(\omega_0^2/\omega^2) - 1 - ika(E_c/F)}, \quad (\text{A12})$$

where

$$\omega_0^2 = \frac{3\gamma P_0}{a^2 \rho_l} \left[\frac{E_c}{e_b e_c F} \right], \quad (\text{A13})$$

$$U_1 = \frac{1}{4\pi a^2} \left[\frac{E_c}{e_b e_c F} \right] \int_S e^{-i\mathbf{k}_s \cdot \mathbf{r}} \frac{1}{\sqrt{x^2/a^4 + y^2/b^4 + z^2/c^4}} ds, \quad (\text{A14})$$

$$U_2 = \frac{\omega_0^2}{\omega^2} \frac{1}{4\pi} \int_S (i\mathbf{k}_s \cdot \mathbf{n}) e^{-i\mathbf{k}_s \cdot \mathbf{r}} ds. \quad (\text{A15})$$

At low frequencies, Eq. (A14) is reduced to $U_1 = aE_c/F$, and U_2 is in the order of $(ka_e)^2$ and can be ignored to the first order approximation. The scattering of the bubble is therefore almost omnidirectional. Finally the scattering function at low frequencies is simplified as

$$f = \frac{aE_c/F}{(\omega_0^2/\omega^2) - 1 - ikaE_c/F}. \quad (\text{A16})$$

- Clay, C. S., and Medwin, H. (1977). *Acoustic Oceanography* (Wiley, New York).
- Devin, Jr., C. (1959). "Survey of thermal, radiation, and viscous damping of pulsation air bubbles in water," J. Acoust. Soc. Am. **31**, 1654–1667.
- Feuillade, C., and Werby, M. F. (1994). "Resonances of deformed gas bubbles in liquids," J. Acoust. Soc. Am. **96**, 3684–3692.
- Farmer, D. M., and Lemon, D. D. (1984). "The influence of bubbles on ambient noise in the ocean at high wind speeds," J. Phys. Oceanogr. **14**, 855–863.
- Gradshteyn, I. S., and Ryzhik, I. M. (1980). *Table of Integrals, Series, and Products* (Academic, New York).
- Jackson, J. D. (1975). *Classical Electrodynamics* (Wiley, New York).
- Morse, P. M., and Feshbach, H. (1953). *Methods of Theoretical Physics* (McGraw-Hill, New York).
- Strasberg, M. (1953). "The pulsation frequency of nonspherical gas bubbles in liquids," J. Acoust. Soc. Am. **25**, 536–537.
- Stratton, J. A. (1941). *Electromagnetic Theory* (McGraw-Hill, New York).
- Thorpe, S. A. (1982). "On the clouds of bubbles formed by breaking wind waves in deep water, and their role in air–sea gas transfer," Phys. Rev. A **304**, 155–210.
- Thorpe, S. A. (1995). "Dynamical processes of transfer at the sea surface," Prog. Oceanogr. **35**, 315–352.
- Waterman, P. C. (1969). "New formulation for acoustic scattering," J. Acoust. Soc. Am. **45**, 1417–1429.
- Ye, Z. (1996). "Acoustic scattering from fish swimbladders," J. Acoust. Soc. Am. **99**, 785–792.
- Ye, Z. (1997). "On low-frequency acoustic scattering by gas-filled prolate spheroids in liquids," J. Acoust. Soc. Am. (to be published).

Determination of grain-size distribution from ultrasonic attenuation: Transformation and inversion

Denise Nicoletti and Aran Anderson

Electrical and Computer Engineering Department, Worcester Polytechnic Institute, 100 Institute Road, Worcester, Massachusetts 01609

(Received 7 February 1996; accepted for publication 26 September 1996)

Although researchers often describe a particular medium with only a single grain size or an average grain size, distributions of grain sizes can have significant effects on the physical characteristics of the material. Ultrasonic attenuation due to energy scattered at the grain boundaries depends on the ultrasonic wavelength, the grain size, and certain material properties such as elastic constants. This paper examines the relationship between the wavelength dependency of ultrasonic attenuation and grain-size distributions. A transformation is developed which solves a general class of Fredholm equations of the first kind. The equation relating attenuation to grain-size distributions belongs to this class of equations. The transformation allows attenuation to be calculated by discrete convolution, and provides a method for estimating the grain-size distribution directly from attenuation measurements. © 1997 Acoustical Society of America. [S0001-4966(97)01802-X]

PACS numbers: 43.20.Jr, 43.35.Cg [JEG]

INTRODUCTION

Ultrasonic attenuation depends on both the wavelengths of the ultrasonic pulse and the sizes of the grains in a polycrystalline material. The thrust of our work is the exploration of the relationship between the wavelength dependence of ultrasonic attenuation and grain-size distributions in polycrystalline materials. This paper provides a transformation of the equations relating grain-size distributions and attenuation, calculation of attenuation using discrete convolution and the transformed equations, and estimation of grain-size distribution from attenuation based on an inversion of the transformed system.

I. BACKGROUND

Polycrystalline materials are made of collections of tiny grains. The change in elastic constants between adjacent grains scatters energy from an incident ultrasonic wave. This grain-boundary scattering is the predominant cause for ultrasonic attenuation in polycrystalline materials. The effect of absorption loss is considered to be negligible.¹

A wealth of literature embraces the subject of ultrasonic wave propagation in polycrystalline materials.² Since the physical structure of these materials is so complex, a number of common assumptions have been used by researchers to simplify analysis. Four of these assumptions are discussed below.

The first two assumptions are closely related. Often, the crystalline structure of the grains is assumed to be only weakly anisotropic.² If the anisotropy is weak, then the orientation-dependent change in elastic constants is very small, which in turn means that the acoustic properties of adjacent grains are similar, and the scattered energy is small. Under the single-scattering assumption, once the energy has been scattered from a grain boundary, it is forever lost.³ In contrast, theories that consider multiple scattering account for the possibility that this energy is still present.

Third, the grains are often assumed to possess a regular geometry. Mostly, they are assumed to be spherical, or equivalently equiaxed, although other shapes have been used.^{3,4} These grain-shaped models, frequently used by material scientists, can be good approximations for certain materials. Agreement between theoretical and experimental results has validated their use.

The final assumption pertains to the sizes of the grains. Researchers often use only a single grain size or an average grain size.²⁻⁶ They are assuming that the first moment of the grain-size distribution is sufficient to describe the sizes of the grains. For narrow distributions, this may be valid, however, it may not be for wide distributions.

Ultrasonic attenuation, α , depends upon the wavelength of the ultrasonic pulse, λ , the grain diameters, D , and material properties. These dependencies vary with the relative sizes of λ and D , and three well-known regions emerge:

$$\text{Rayleigh region: } \alpha(D, \lambda) = C_r D^3 \lambda^{-4}, \quad \lambda \gg D,$$

$$\text{Stochastic region: } \alpha(D, \lambda) = C_s D \lambda^{-2}, \quad \lambda \cong D, \quad (1)$$

$$\text{Diffusion region: } \alpha(D, \lambda) = C_d / D, \quad \lambda \ll D,$$

where C_r , C_s , and C_d are constants of the material.

Two generalized theories, which are valid over all ranges of wavelengths and grain sizes, will now be reviewed. Roney developed an equation for the attenuation due to a single grain size and any wavelength.³ He did this by first assuming a rigid, spherical scatterer in a homogeneous medium, and calculating the scattered energy of an impinging ultrasonic plane wave. He then used the number of scatterers in a given length, which he assumed to be $1/D$, to determine the total scattered energy, and from that the attenuation. His work assumes weak anisotropy, and single scattering, and yields the following expression for attenuation when absorption effects are neglected:

$$\alpha(\lambda, D) = \frac{2}{D\mu^2} \left(\frac{\Delta\kappa}{\kappa} \right)^2 \sum_{m=0}^{\infty} (2m+1) \sin_m^2 \delta, \quad (2)$$

where $\mu = \pi D/\lambda$, $\tan_m \delta = [mj_{m-1}(\mu) - (m+1)j_{m+1}(\mu)] / [mn_{m-1}(\mu) - (m+1)n_{m+1}(\mu)]$, $j_m(\cdot)$ is the spherical Bessel function of order m , $n_m(\cdot)$ is the spherical Neumann function of order m , and $(\Delta\kappa/\kappa)^2$ is the average elastic mismatch parameter. Roney showed that the classical scattering regions in Eq. (1) hold.

More recently, Stanke developed a ‘‘unified’’ theory of wave propagation in polycrystalline media.² His approach, valid for all frequencies, is much more sophisticated than Roney’s, and can allow for high anisotropy, multiple scattering, and unusual or nonuniform grain shapes. It can also be applied to textured media, in which the grain sizes or crystal orientations are not independent of direction. Essential to his approach is a geometric correlation function, $W(r)$, which is the probability that two points separated by a distance r are in the same grain. Although his theory is more general, for his calculations he assumes untextured media and equiaxed grains. He also assumes a particular analytic model for $W(r)$. His attenuation calculations yield the same wavelength dependencies found in Eq. (1).

Some researchers have considered a distribution of grain sizes.⁷⁻⁹ This investigation is warranted by the fact that distributions of grain sizes have been shown to affect material properties.¹⁰ The following relationship between attenuation and grain-size distribution was used, which will be known as the attenuation equation:

$$\alpha(\lambda) = \int_0^{\infty} N(D) \alpha(\lambda, D) dD, \quad (3)$$

where $N(D)dD$ is the number of grains between size D and $D+dD$, and $\alpha(\lambda, D)$ is an expression for the attenuation due to a single grain size. The following was assumed: the size of each grain is sufficiently described by a single parameter, D , single scattering, and $\alpha(\lambda, D)$ is valid for all D/λ . With these restrictions, Eq. (3) is valid for any $N(D)$ and $\alpha(\lambda, D)$. Nicoletti⁹ concentrated first on power law distributions, which have the following form:

$$N(D) = KD^{-\gamma}, \quad 0 < D < \infty, \quad (4)$$

and then truncated power law distributions:

$$N(D) = KD^{-\gamma}, \quad D_{\min} < D < D_{\max}. \quad (5)$$

She showed that for $\lambda \ll D_{\min}$, $\alpha(\lambda)$ is independent of λ , and for $\lambda \gg D_{\max}$, $\alpha(\lambda)$ is proportional to λ^{-4} , which correspond respectively to the diffusion and Rayleigh attenuation regions. Also proven was that for a power law grain-size distribution with exponent γ , and $D_{\min} \ll \lambda \ll D_{\max}$, $\alpha(\lambda)$ follows a power law with exponent γ . Therefore, for some wavelengths, the grain-size distribution exponent determines the attenuation exponent. Estimates of the power law parameters, such as the exponent γ and maximum grain size, were then obtained from the attenuation.^{11,12} A number of reasons validate the use of a power law distribution model; however, the use of any distribution model potentially restricts application of this research.

II. TRANSFORMATIONS

The transformation developed in this section provides a foundation for the solution of the inverse problem, i.e., estimation of $N(D)$ directly from $\alpha(\lambda)$. The attenuation equation [Eq. (3)] belongs to a class of equations known as Fredholm equations of the first kind, whose members share the following structure:¹³

$$g(y) = \int f(x)K(y, x)dx, \quad (6)$$

where $K(y, x)$ is the kernel, $g(y)$ is known, and a solution for $f(x)$ is desired. A variety of methods exists to solve these equations, and often certain properties of the kernel function can be used advantageously. Examination of the relationships in Eq. (1) reveals that in each region

$$\alpha(\lambda, D) = \frac{1}{D} f\left(\frac{\lambda}{D}\right). \quad (7)$$

If this proportionality is assumed to be true for all values of wavelength and gain size [as is the case for Eq. (2)], then the attenuation can be rewritten as

$$\alpha(\lambda) = \int_0^{\infty} N(D) f\left(\frac{\lambda}{D}\right) \frac{1}{D} dD, \quad (8)$$

where $f(\lambda/D)(1/D)$ is the attenuation kernel.

Analytic solutions exist for equations in the form of Eq. (8). The solution relies on properties of the Mellin and inverse Mellin transform. Unfortunately, the complexity of these transformations renders this approach impractical. In general, the forward transformation is extremely difficult to perform, and the inverse transformation, requiring a complex contour integration, even more so. For the specific case of the attenuation equation, this approach is useless since $f(\lambda/D)$ must be evaluated for all λ/D . A practical solution to Eq. (8) is developed next.

The following technique yields practical, analytic, and numerical solutions for $N(D)$ in Eq. (8). First, let

$$N(D) = x(\ln D), \quad (9)$$

$$f(\lambda/D) = y(\ln(\lambda/D)), \quad (10)$$

where $\ln(\cdot)$ denotes the natural logarithm. Then,

$$\alpha(\lambda) = \int_0^{\infty} x(\ln D) y(\ln(\lambda/D)) \frac{1}{D} dD. \quad (11)$$

Further, let $t = \ln(\lambda)$ and $\tau = \ln(D)$. Therefore,

$$\alpha(e^t) = \int_{-\infty}^{\infty} x(\tau) y(t - \tau) d\tau. \quad (12)$$

Finally, let

$$z(t) = \alpha(e^t). \quad (13)$$

Then,

$$z(t) = \int_{-\infty}^{\infty} x(\tau) y(t - \tau) d\tau, \quad (14)$$

which is simply the convolution integral. This equation can now be solved with the Fourier and inverse Fourier trans-

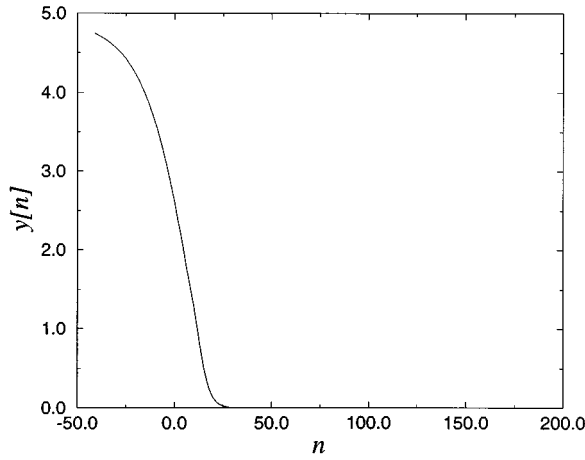


FIG. 1. $y[n]$ vs n .

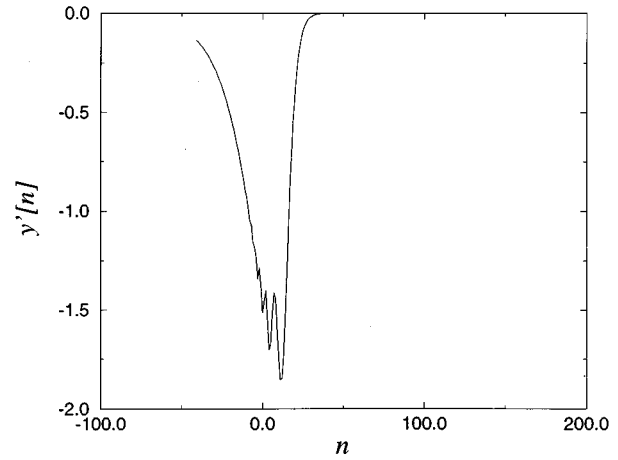


FIG. 2. $y'[n]$ vs n .

form, which are both practical calculations. It should be noted here that although this Fourier transform method provides a solution, it is not the only solution method.

The following approach is therefore used to analytically solve for $N(D)$ given $\alpha(\lambda)$ and $f(\lambda/D)$. First, create $z(t)$ and $y(t)$ from $\alpha(\lambda)$ and $f(\lambda/D)$, respectively, using Eqs. (10) and (13). Solve for $x(t)$ using the Fourier and inverse Fourier transforms. Finally, find $N(D)$ from $x(t)$ using Eq. (9),

$$x(t) = \mathcal{F}^{-1} \left\{ \frac{\mathcal{F}\{z(t)\}}{\mathcal{F}\{y(t)\}} \right\}, \quad (15)$$

where $\mathcal{F}\{\bullet\}$ and $\mathcal{F}^{-1}\{\bullet\}$ denote forward and inverse Fourier transforms, respectively. This technique provides an analytic solution for $N(D)$ when the Fourier transforms of $z(t)$ and $y(t)$ exist, and provided $\mathcal{F}\{y(t)\}$ is never 0.

Equation (15) can be evaluated numerically when $z[n]$ and $y[n]$ are finite sequences, windowing effects due to truncation of an infinite sequence are negligible, and a suitably small sampling period T_s is chosen. For illustration, $y[n]$ is shown in Fig. 1 using Roney's expression for the attenuation, Eq. (2).

III. INVERSION

The transformation dramatically changes the inverse problem of determining $N(D)$ directly from $\alpha(\lambda)$. Unfortunately, any attenuation kernel $\alpha(\lambda, D)$ does not satisfy the square-integrable condition necessary for the Fourier transform solution. A simple manipulation of the transformed equation overcomes this problem. The discrete versions of Equations (9), (10), (13), and (14) are used:

$$z[n] = T_s \sum_{m=-\infty}^{\infty} x[m]y[n-m], \quad (16)$$

$$x[n] = N(e^{nT_s}), \quad y[n] = f(e^{nT_s}), \quad z[n] = z(nT_s).$$

Based on Eq. (1), $\alpha(\lambda, D)$ is assumed to approach a constant, nonzero value for $\lambda \ll D$. Therefore, the fast Fourier transform (FFT) of $y[n]$ cannot be computed. The problem of determining $N(D)$ from $\alpha(\lambda)$ using the transformed equation

is a deconvolution problem, for which many alternative techniques have been tried.

Matrix deconvolution¹⁴ fails because $y[n]$ extremely small values that adversely effects matrix inversion. Two closely related methods, Van Cittert's method and the "point simultaneous" method, solve for $x[n]$ iteratively.¹⁴ Unfortunately, both of these methods assume that the filter kernel is short. Since the attenuation filter kernel has infinite duration, these methods will not work. Nonlinear deconvolution techniques surveyed for this work (Gold's ratio, Schell's method, Jansson's method, Biraud's method, Frieden's method, and Burg's method) also work only for short filter kernels.

The seemingly bleak outlook for development of a working inversion technique is dismal in appearance only. The problem that must be overcome is the infinite length of the attenuation filter kernel, $y[n]$. A characteristic of $y[n]$ is that it converges to 0 for large positive n and to a constant value for large negative n , as shown in Fig. (1). If $n \ll 0$, then $D/\lambda \gg 1$, which corresponds to the diffusive region of attenuation where the attenuation is independent of λ . Although $y[n]$ does not converge to 0 on both the right and left tails, its derivative does, as shown in Fig. 2. This can be fully appreciated by taking the derivative of both sides of the transformed attenuation equation in its discrete form:

$$z'[n] = T_s \sum_{m=-\infty}^{\infty} x[m]y'[n-m]. \quad (17)$$

Since $y'[n]$ is finite, Fourier transform deconvolution techniques can be used to solve for $x[n]$.

IV. NUMERICAL RESULTS

In this section, the inversion process is verified with two examples using the Fourier transform method. Throughout this section, $x[n]$ will denote the known signal computed from $N(D)$; $\hat{x}[n]$ will denote the signal estimated from the attenuation. Here $y[n]$ was constructed using Eq. (2) and sampling with a period $T_s = 0.087518417846$. Here, $y[n]$ was extended to the left using a fourth-order polynomial curve fit on $y[n]$ for $-59 < n < -39$.

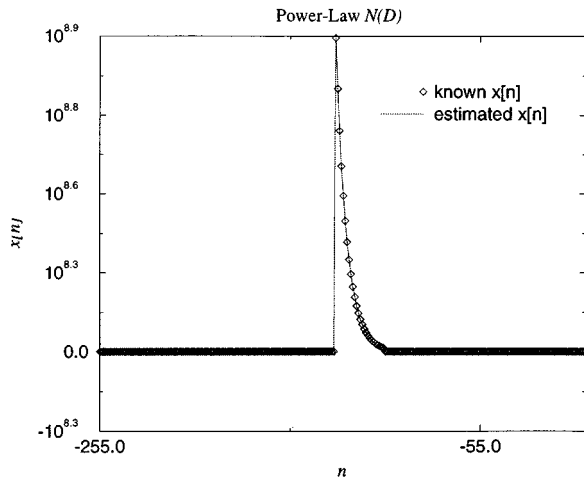


FIG. 3. Comparison of $x[n]$ and $\hat{x}[n]$ for power-law $N(D)$.

First, $x[n]$ was constructed for a given $N(D)$, and $z[n]$ computed by convolving $x[n]$ with the extended $y[n]$. Second, $z'[n]$ and $y'[n]$ were approximated with

$$z'[n] = \frac{z[n+1] - z[n]}{T_s}, \quad y'[n] = \frac{y[n+1] - y[n]}{T_s},$$

then $z'[n]$ and $y'[n]$ were appropriately zero-padded to 512 points to ensure linear convolution. The inversion was then performed to yield $\hat{x}[n]$ using Eqs. (15) and (17).

Two trials were performed using the procedure outlined above. The results are shown in Figs. 3 and 4. In the first trial, $N(D)$ is a power law distribution with $\gamma=2.0$, $D_{\min}=10 \mu\text{m}$, and $D_{\max}=100 \mu\text{m}$. The second trial uses a log normal distribution:

$$N(D) = \begin{cases} \frac{1}{D \ln \sigma_g \sqrt{2\pi}} \exp\left[-\frac{(\ln D - \ln \mu_g)^2}{2 \ln^2 \sigma_g}\right], & D_{\min} \leq D \leq D_{\max}, \\ 0, & \text{elsewhere} \end{cases} \quad (18)$$

where $\mu_g = -9.210$, $\ln \sigma_g = 0.766$, $D_{\min} = 10 \mu\text{m}$, and $D_{\max} = 100 \mu\text{m}$. These examples show that the inversion process works.

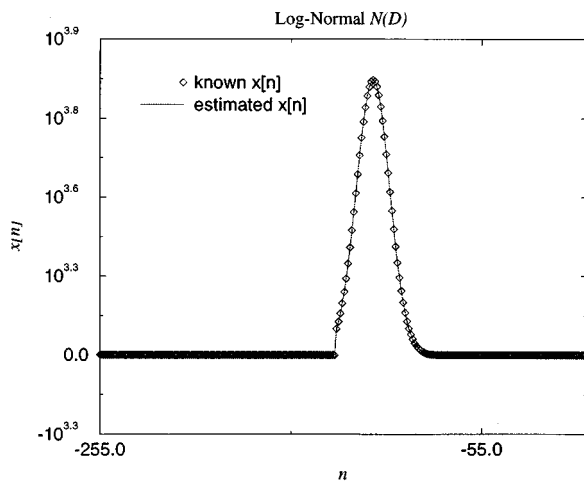


FIG. 4. Comparison of $x[n]$ and $\hat{x}[n]$ for log-normal $N(D)$.

V. CONCLUSIONS

The theoretical and numerical analysis of the attenuation equation presented in this paper helps broaden our understanding of the relationship between the wavelength dependency of ultrasonic attenuation and grain-size distributions in polycrystalline materials. The accomplishments documented here are the transformations that allow the estimation of $N(D)$ from $\alpha(\lambda)$ using the transformed equations with no *a priori* grain-size distribution model. This is essentially a deconvolution problem, and a number of techniques can be applied to its solution. One method that takes advantage of the characteristics of the attenuation kernel is presented and demonstrated numerically. The transformations also allow for an alternative method for calculating $\alpha(\lambda)$ from a known $N(D)$. Instead of using Eq. (3), a convolution approach can be used as in Eq. (14). A comparison of these two methods was analyzed previously.¹⁵

Three immediate goals suggest themselves as directions for future continuation of this research. First, $y[n]$ for the Roney attenuation kernel should be extended until it becomes constant. Since the summation in Roney's expression converges so slowly for these low ratios of λ/D , accelerated convergence techniques should be attempted.¹⁶ Different deconvolution techniques should be compared, and the effect of noise should be considered in this development. Second, some experiments should be performed to validate the theory. Either actual metal samples, or appropriate phantoms, or both, could be used in these experiments. It should be noted that in order for $N(D)$ to be determined, a range of wavelengths must extend from the Rayleigh region into the diffusion region. Care should be taken so that $\alpha(\lambda)$ is precisely measured (i.e., no diffraction, absorption, or surface scattering effects). Third, other generalized theories such as the one proposed by Stanke should be considered, and the results compared with those obtained using Roney's theory.

¹R. L. Wegel and H. Walther, *Physics* **6**, 141–157 (1935).

²F. E. Stanke and G. S. Kino, *J. Acoust. Soc. Am.* **75**, 665–681 (1984).

³R. K. Roney, "The Influence of Metal Grain Size on the Attenuation of an Ultrasonic Wave," Ph.D. thesis, California Institute of Technology, 1950.

⁴L. L. Rokhlin, *Sov. Phys. Acoust.* **18**, 71–75 (1972).

⁵E. P. Papadakis, *J. Acoust. Soc. Am.* **44**, 1437–1441 (1968).

⁶W. P. Mason and H. J. McSkimin, *J. Acoust. Soc. Am.* **19**, 464–473 (1947).

⁷H. A. Kesler and I. Shraifel'd, *Sov. J. Non-Destruct. Test.* **11**, 76–80 (1975).

⁸R. L. Smith, *Ultrasonics* **20**, 211–214 (1982).

⁹D. W. Nicoletti, "Scaling Properties of Ultrasonic Attenuation and Grain Size in Metals," Ph.D. thesis, Drexel University, 1991.

¹⁰F. N. Rhines and B. R. Patterson, *Metall. Trans. A* **13**, 985–993 (1982).

¹¹D. W. Nicoletti and D. Kasper, *IEEE Trans. Ultrason. Ferroelec. Freq. Control* **41**, 144–149 (1994).

¹²D. Nicoletti and A. Anderson, *IEEE Trans. Ultrason. Ferroelec. Freq. Control* **2**, 701–704 (1993).

¹³A. J. Jerri, *Introduction to Integral Equations with Applications* (Marcel Dekker, New York, 1985).

¹⁴P. A. Jansson, *Deconvolution with Applications in Spectroscopy* (Academic, New York, 1984).

¹⁵A. Anderson, "A Study of the Relationships Between Ultrasonic Attenuation and Grain-Size Distributions in Polycrystalline Materials, Master's thesis, Worcester Polytechnic Institute, 1995.

¹⁶T. Fessler, W. Ford, and D. Smith, *ACM Trans. Math. Softw.* **9**, 347–354 (1983).

Partial coherence of transient ultrasonic fields in anisotropic random media: Application to coherent echo detection

Arnaud Derode and Mathias Fink

Laboratoire Ondes et Acoustique, Université Paris 7-ESPCI, URA CNRS 1503, 10 rue Vauquelin, 75005 Paris, France

(Received 15 January 1994; revised 25 September 1996; accepted 26 September 1996)

In this paper the spatial coherence properties of the speckle noise backscattered from random media insonified by a broadband pulse are studied. The approach presented is an adaptation of the optical notion of coherence introduced by Zernike. How the statistical parameters (particularly the second-order moment) of the medium determine those of the speckle noise is studied. This is applied to fully or partially incoherent media, and media with anisotropic scatterer distribution such as unidirectional and cross-ply composites; also investigated is the possibility of detecting a coherent reflector among speckle noise through measurements of coherence length. Experimental as well as theoretical results are presented. Measurements were carried out with a linear array of 128 programmable transmitters/receivers. © 1997 Acoustical Society of America.

[S0001-4966(97)01402-1]

PACS numbers: 43.20.Px, 43.20.Fn, 43.20.Bi, 43.30.Nb [JEG]

LIST OF SYMBOLS

ω	angular frequency
k	angular wave number
λ	wavelength
x, y	coordinates in the plane of the array
X, Y	coordinates in the z plane
z	axial coordinate
F	focal length
$\text{rect}(x)$	$\begin{cases} = 1, & \text{if } x < 1/2 \\ = 0, & \text{elsewhere} \end{cases}$
$\text{tri}(x)$	$\begin{cases} = 1 - x , & \text{if } x < 1 \\ = 0, & \text{elsewhere} \end{cases}$

R_{PP}	autocorrelation function of a random process $P(x)$: $R_{PP}(x_1, x_2) = E\{P(x_1)P^*(x_2)\}$
$*$ _{x}	convolution $f(x) *_x g(x) = \int f(\xi)g(x - \xi)d\xi$
$\text{FT}\{f(x)\}_{X/\lambda z}$	Fourier transform $= \int_{-\infty}^{+\infty} f(x)e^{-2\pi xX/\lambda z} dx$
$O(x, y)$	aperture function
$\tilde{O}(x, y)$	modified aperture function
$\tilde{\Omega}(X, Y)$	$\text{FT}\{\tilde{O}(x, y)\}_{X/\lambda z, Y/\lambda z}$
$\chi(X, Y)$	random reflectivity function
$\phi(x, y)$	$\text{FT}\{R_{\chi\chi}(\Delta X, \Delta Y)\}_{x/\lambda z, y/\lambda z}$
$\psi_\omega(x, y)$	backscattered field

INTRODUCTION

This paper is devoted to the study of spatial coherence of the backscattered field in ultrasonic pulse-echo measurements. We will investigate the interest of studying the spatial coherence of the backscattered field in terms of medium characterization and detection of a deterministic reflector among random speckle noise. We will show that speckle noise carries information about the medium structure, and how this information can be extracted from a measurement of spatial coherence. This approach will be applied to composite materials, theoretically as well as experimentally; in such media, the scatterer distribution is anisotropic since the composite consists in a stacking of very thin and long fibers, and we will see that due to this anisotropy, the backscattered field is more or less coherent according to the orientation of the fibers relatively to the acoustic beam.

To make this more concrete, the general principle of the experiments is drawn in Fig. 1: a linear array sends a short ultrasonic signal into a scattering medium. The same array acts as a receiver, and records a backscattered noise (ultrasonic speckle) that consists in the addition of all echoes re-

flected from the scatterers. Each element on the array receives a different waveform, and the data we study are this set of time signals. The question we try to answer is: to what degree do these signals look alike? How far apart must be two elements on the array to receive different informations? What is the influence of the transmitting aperture size, focal distance, depth of interest, and of the statistical parameters of the medium? For instance, in the case of a unidirectional composite, we can expect different results according to whether the fibers are parallel or perpendicular to the array (Fig. 2). As we will see, resemblance between signals recorded at different points is important in several respects: first, it can give information about the medium structure and the possible presence of a small defect; second, because according to whether the signals look alike or not, the summation of all these signals will yield constructive or destructive interference and therefore influence the speckle noise level.

Resemblance between two signals can easily be assessed by calculating a correlation coefficient. And it can be shown that this degree of resemblance is simply related to the classical definition of coherence for monochromatic wave fields,¹ so measuring resemblance between backscattered sig-

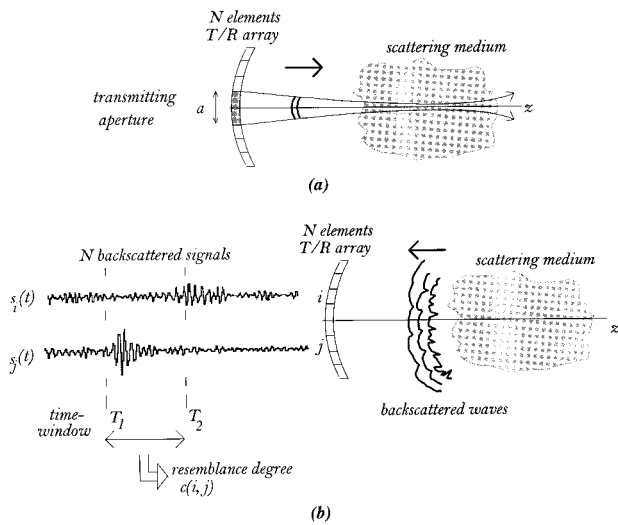


FIG. 1. In a first step (a) a group of transducers on the array send a short pulse. Then (b) all the elements record the backscattered field. A time window is selected, and we calculate the degree of correlation between signals received on two elements i and j .

nals is equivalent to assessing the spatial coherence of the ultrasonic field. The notion of spatial coherence was first introduced in optics by Frederik Zernike.^{2,3}

The approach we develop in this paper is linked with the notion of coherence such as Zernike had defined it for monochromatic stationary fields; yet we generalize his approach to the backscattering of short pulses as those employed in pulse-echo ultrasound. Propagation of coherence from a fully incoherent source is mathematically described by the Van Cittert–Zernike theorem, a well-known theorem in statistical optics that has been recently applied to pulse-echo ultrasound⁴ for the case of a fully incoherent medium. We will use a similar formalism, but we will deal with partial coherence and obtain a more general result.

The paper is organized in four sections. Section I presents a theoretical analysis of backscattering by a random mirror in terms of spatial coherence. The results are applied in Sec. II to different cases: coherent, incoherent, partially coherent, and anisotropic media. Section III presents the experimental results we obtained on unidirectional and crossply composites. Eventually, Sec. IV deals with detection of a

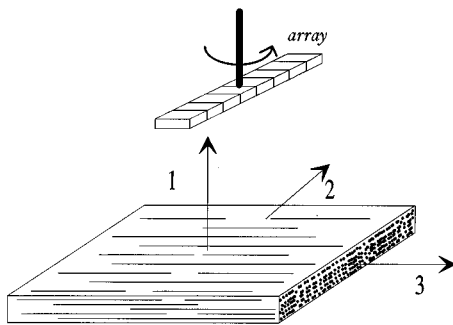


FIG. 2. The unidirectional composite is made of thin and long fibers embedded in a resin matrix, all fibers are aligned along the same axis (#3). The array is fixed on a rotating device and can turn around the vertical axis (#1).

small defect in speckle noise through coherence measurements. The main symbols we use in the theoretical part are given in the nomenclature; some mathematical calculations are presented in the Appendices.

As words such as coherence, incoherence, and correlation will often be mentioned, we first recall the definition of the statistical autocorrelation function $R_{AA}(x_1, x_2)$ of a random process $A(x)$:

$$R_{AA}(x_1, x_2) = E\{A(x_1)A^*(x_2)\}. \quad (1)$$

In this expression, E denotes an ensemble average and the asterisk denotes complex conjugation. If A is a stationary process with respect to x , then $R_{AA}(x_1, x_2)$ only depends on the distance $\Delta x = x_1 - x_2$, and we will call *coherence length* the characteristic width of $R_{AA}(\Delta x)$. In the same way, we will say that any process is “coherent” or “incoherent” according to whether $R_{AA}(\Delta x)$ is wide or narrow. Some mathematic properties regarding correlation functions and Fourier transforms are presented in Appendix A.

I. THE RANDOM MIRROR APPROACH

As they use very short signals, ultrasonic pulse-echo techniques permit us to relate time and depth. So when we have a set of time signals received on an array and select a segment in each backscattered signal, we know that it comes from a given region of interest, the so-called isochronous volume,⁵ located at a given depth z inside the medium. When this segment is short enough, the isochronous volume can be reduced to a simple slice: hence, for a given time window $[T_1, T_2]$, everything happens as if the backscattered signal was coming only from an “isochronous slice” with width $c(T_2 - T_1)/2$; if this slice is thin enough, it can be considered as a mirror with random reflectivity located at a distance $z \approx c(T_1 + T_2)/2$ from the array.

So the problem can be divided into three steps: propagation of a signal from the array to the mirror, reflection of the signal on the mirror (here appears the randomness of the mirror), then propagation of the reflected signal back to the array. Then we study the degree of coherence of the wave as it is received on the array.

The transmitted signal is short (typically one or two cycles), and hence has a wide frequency band; in the following theoretical analysis, we will consider distinctly the propagation of each frequency component ω . The three steps mentioned above can then be treated in terms of Fourier optics.⁶

Let us consider a transmitting aperture $O(x, y)$ in the $z=0$ plane; for instance, the typical case that we will deal with is a rectangular array with dimensions $a \times b$, its aperture function is then:

$$O(x, y) = \text{rect}\left(\frac{x}{a}\right) \text{rect}\left(\frac{y}{b}\right). \quad (2)$$

It is a well-known result of Fourier optics that in the focal plane of a focused aperture, the field $U(X, Y)$ writes as the Fourier transform of the aperture function:

$$U_{z=F}(X, Y) = \frac{1}{\lambda z} e^{j(\pi/\lambda z)(X^2 + Y^2)} \times \text{FT}_{2D}\{O(x, y)\}_{(X/\lambda z, Y/\lambda z)}. \quad (3)$$

A similar expression exists when the depth of interest z is different from the focal distance F . As is shown in Appendix B₂, in such a case we can define a *modified aperture function* $\tilde{O}(x, y)$ that takes into account both the depth of interest z and the focus F :

$$\tilde{O}(x, y) = O(x, y) \exp\left[j \frac{\pi(x^2 + y^2)}{\lambda} \left(\frac{1}{z} - \frac{1}{F}\right)\right]. \quad (4)$$

And the diffracted field at depth z simply writes

$$U_z(X, Y) = \frac{1}{\lambda z} e^{j(\pi/\lambda z)(X^2 + Y^2)} \tilde{\Omega}(X, Y), \quad (5)$$

where

$$\tilde{\Omega}(X, Y) = \text{FT}_{2D}\{\tilde{O}(x, y)\}_{(X/\lambda z, Y/\lambda z)}. \quad (6)$$

Introducing the modified aperture function is a simple way to describe any case, a plane as well as a focused transducer, the depth of interest z being at the focus or out of focus. Equation (5) gives the expression of the field amplitude at depth z , just in front of the random mirror. Let $\chi(X, Y)$ be the reflectivity function of the mirror. χ is a random variable, and right after the reflection of the wave, the reflected field writes

$$U_z^{\text{refl}}(X, Y) = \chi(X, Y) U_z(X, Y). \quad (7)$$

Then this field backpropagates toward the array, so eventually the received field $\psi(x, y)$ results from the propagation of $U_z^{\text{refl}}(X, Y)$ from z to 0. As is shown in Appendix B, this involves another Fourier transform and leads to a simple approximate expression for the backscattered field:

$$\psi(x, y) \approx \frac{1}{\lambda^2 z^2} \tilde{O}(x, y) \text{FT}_{2D}\{\chi(X, Y) \tilde{\Omega}(X, Y)\}_{(x/\lambda z, y/\lambda z)}. \quad (8)$$

Equation (8) gives the amplitude of the field backscattered on the transducer by the slice located at depth z , for a given frequency ω , from now on, we will denote it $\psi_\omega(x, y)$ in order to recall that it only represents the amplitude of one of the spectral components. Equation (8) contains deterministic terms (related to propagation distance and transducer geometry) and a random contribution (due to the medium reflectivity χ). So $\psi_\omega(x, y)$ is a random variable and we want to calculate its autocorrelation function:

$$R_{\psi\psi}^\omega(x_1, x_2, y_1, y_2) = E\{\psi_\omega(x_1, y_1) \psi_\omega^*(x_2, y_2)\}. \quad (9)$$

Using the properties stated in Appendix A and assuming that \tilde{O} is an even function, we have:

$$R_{\psi\psi}^\omega(x_1, x_2, y_1, y_2) = \frac{1}{\lambda^2 z^2} \tilde{O}(x_1, y_1) \tilde{O}^*(x_2, y_2) \times [\tilde{O}(x_1, y_1) \tilde{O}^*(x_2, y_2) \text{****}]_{x_1 x_2 y_1 y_2}$$

$$\times \text{FT}_{4D}\{R_{\chi\chi}(x_1, x_2, y_1, y_2)\}_{(x_1/\lambda z, y_1/\lambda z, x_2/\lambda z, y_2/\lambda z)}. \quad (10)$$

This expression is a generalization of the Van Cittert–Zernike theorem to all kinds of media (fully or partially incoherent) and depths of interest.

If we consider the case of a *stationary* reflectivity, then $R_{\chi\chi}$ only depends on two variables, $\Delta X = X_1 - X_2$ and $\Delta Y = Y_1 - Y_2$. This assumption means that the statistical parameters of the medium do not change in all the region of interest. Let ϕ be the 2D Fourier transform of $R_{\chi\chi}(\Delta X, \Delta Y)$:

$$\phi(x, y) = \int \int R_{\chi\chi}(\Delta X, \Delta Y) e^{(-2\pi j/\lambda z)(x\Delta X + y\Delta Y)} \times d\Delta X d\Delta Y. \quad (11)$$

Then the spatial coherence function for frequency ω reduces to

$$R_{\psi\psi}^\omega(x_1, x_2, y_1, y_2) = \frac{1}{\lambda^2 z^2} \tilde{O}(x_1, y_1) \tilde{O}^*(x_2, y_2) \times [\tilde{O}(x_1, y_1) \tilde{O}^*(x_2, y_2) \text{****}]_{x_1 x_2 y_1 y_2} \phi(x_1, y_1). \quad (12)$$

In this expression, ϕ characterizes the medium (is it incoherent, partially coherent...) and \tilde{O} the experimental conditions (focus, depth of interest, apodization, aperture shape...). Equation (12) can be applied as long as approximation (B12) in Appendix B is valid, which implies that the beam section in the region of interest must be small compared to λz . This is true when the region of interest is at the focus or near the focus of the transducer. Situations in which (B12) does not apply are briefly discussed in Appendix B.

Remember that each frequency has its own spatial coherence function, given by (12). Now, in order to measure the degree of spatial coherence of wavefront received by a transducer array, we study the resemblance between signals $s(x_1, t)$ and $s(x_2, t)$ received at two points x_1 and x_2 on the receiving surface:

$$c(x_1, x_2) = \int s(x_1, t) s(x_2, t) dt. \quad (13)$$

This can be normalized in order to obtain a dimensionless resemblance coefficient:

$$C(x_1, x_2) = \frac{c(x_1, x_2)}{\sqrt{c(x_1, x_1) c(x_2, x_2)}}. \quad (14)$$

Since they are time limited, each of the time signals $s(x, t)$ can be written as a continuous sum of monochromatic signals, and it has been shown¹ that the degree of resemblance $c(x_1, x_2)$ calculated in the time domain is simply related to the spatial coherence function by

$$E\{c(x_1, x_2)\} = \int_{\text{bandwidth}} R_{\psi\psi}^\omega(x_1, x_2) d\omega. \quad (15)$$

This means that, on average, the degree of resemblance equals the sum of all spectral coherence functions. So the coherence function $R_{\psi\psi}^\omega$ that we defined for each frequency can be linked to a more intuitive notion, i.e., resemblance between time signals, provided that we integrate all the spectral contributions that exist in the transmitted signal.

In the previous discussion, the reflectivity function χ was studied as a function of the space coordinate X ; we ignored a possible dependence of χ with respect to frequency ω . In fact, this simplification does not affect the validity of our reasoning as long as the autocorrelation function $R_{\chi\chi}$ can be written as a separable function of space and frequency such as

$$E\{\chi(X_1, \omega)\chi^*(X_2, \omega)\} = \zeta(\omega)R_{\chi\chi}(X_1, X_2). \quad (16)$$

Ueda and Ichikawa⁷ showed that this assumption of separability is justified as long as $z > a$. Then, the frequency dependence appears as a mere multiplicative term that vanishes when we integrate along ω and normalize the result. As long as the scatterers can be modeled as a distribution of points with random reflectivity, this simplification is valid, provided that no multiple scattering takes place. This condition is also crucial in the random mirror approach, because time and depth can no longer be simply linked if multiple scattering takes place.

II. EXAMPLES

In the following examples, we will consider the case of a focused rectangular (dimensions $a \times b$) transducer with focal length F , and the region of interest will be located in the focal plane, i.e., at depth $z = F$. In that case, the modified aperture function is real valued and simply equal to the aperture function:

$$\begin{aligned} \tilde{O}(x, y) &= O(x, y)e^{-j(\pi/\lambda F)(x^2+y^2)}e^{j(\pi/\lambda z)(x^2+y^2)} \\ &= O(x, y) = \text{rect}\left(\frac{x}{a}\right)\text{rect}\left(\frac{y}{b}\right). \end{aligned} \quad (17)$$

And in order to simplify the mathematical expressions we will first consider one space dimension x , the results can be easily generalized to two dimensions.

A. Fully incoherent medium

What we call a fully incoherent medium is a medium in which each point reflects the wave totally independently, even from its closest neighbor. For that case, the reflectivity function χ is such that $R_{\chi\chi}(\Delta x) \propto \delta(\Delta x)$. Inserting this into (12) leads to the simple expression:

$$R_{\psi\psi}^\omega(\Delta x) \propto \frac{1}{\lambda^2 z^2} \text{rect}\left(\frac{x}{a}\right)_{\Delta x} * \text{rect}\left(\frac{x}{a}\right) \propto \frac{1}{\lambda^2 z^2} \text{tri}\left(\frac{\Delta x}{a}\right). \quad (18)$$

This means that for each frequency, the spatial coherence function decreases linearly, as a triangle whose base is twice the transmitting aperture length a . Moreover, frequency only appears in the multiplicative factor $1/\lambda^2 z^2$, so when integrating the spatial coherence function over the frequency domain, the result we obtain is also a triangle-like function:

$$\begin{aligned} C(\Delta x) &= \int R_{\psi\psi}^\omega(\Delta x) d\omega \\ \text{hence } c(\Delta x) &= \frac{C(\Delta x)}{C(0)} = \text{tri}\left(\frac{\Delta x}{a}\right). \end{aligned} \quad (19)$$

So, around the focal time, the signals received at two points should bear less and less resemblance to each other, until they utterly differ when they are apart by a distance larger than the transmitting aperture a . Note that *all frequencies have the same coherence length*.

B. Perfectly coherent medium

The opposite of a fully incoherent medium is a perfectly coherent medium, which acts as a perfect mirror. The reflectivity function is the same for each point on the mirror, $R_{\chi\chi}(\Delta X) = \text{constant}$, so its FT is $\phi(x) \propto \delta(x)$. From (12) the spatial coherence function for frequency ω is then:

$$R_{\psi\psi}^\omega(x_1, x_2) \propto \frac{1}{\lambda^2 z^2} \text{rect}\left(\frac{x_1}{a}\right)\text{rect}\left(\frac{x_2}{a}\right). \quad (20)$$

Once again, the shape of this function does not depend on frequency. Moreover, it is a constant over the transducer surface, and it equals 0 outside, which can be justified by a simple argument of geometrical optics: indeed a perfect mirror located at the focus of a converging lens reflects the light beams exactly on the lens surface, and nothing outside. For that case, it leads to

$$c(x_1, x_2) = \text{rect}\left(\frac{x_1}{a}\right)\text{rect}\left(\frac{x_2}{a}\right). \quad (21)$$

So in the time domain, the signals received around the focal time should be identical over all the transmitting aperture.

C. Partially coherent medium

Between these two extremes, one can consider the case of partial coherence: the medium now has a given coherence length ϵ that is neither 0 nor ∞ ; ϵ is a distance that characterizes the fluctuations of $\chi(X)$: if ϵ is large, then the reflectivity function is rather smooth; on the contrary if ϵ is small then χ varies very abruptly. Let us examine what this changes in the coherence of the backscattered waves. If ϵ is the effective width of $R_{\chi\chi}$, then the characteristic width of its Fourier transform ϕ is $\lambda F/\epsilon$. Developing the convolution product in (12) yields

$$R_{\psi\psi}^\omega(x_1, x_2) \propto \frac{1}{\lambda^2 z^2} \int \text{rect}\left(\frac{x_1 - \xi}{a}\right)\text{rect}\left(\frac{x_2 - \xi}{a}\right)\phi(\xi) d\xi. \quad (22)$$

This is a convolution between two functions: one with characteristic width a , the other one $\lambda F/\epsilon$. If ϕ varies very slowly compared to rect , i.e., if $\lambda F/\epsilon \gg a$, then integral (22) is proportional to $\text{tri}(|x_1 - x_2|/a)$, as in the incoherent case. On the contrary, if ϕ is very narrow compared to the aperture function ($\lambda F/\epsilon \ll a$), it only differs from 0 in the vicinity of $\xi \approx 0$, and we find the same result as in the coherent case, $c(x_1, x_2) = \text{rect}(x_1/a)\text{rect}(x_2/a)$.

So, according to whether $\lambda F/a\epsilon \ll 1$ or $\lambda F/a\epsilon \gg 1$, the same medium can behave either coherently or incoherently. This can be easily accounted for. As a matter of fact, $\lambda F/a$ is the beamwidth in the focal plane, so $\lambda F/a\epsilon$ is the “number of coherence lengths inside the beam.” If the beam is very thin compared to ϵ , it means that we observe the medium at much too small a scale to feel its incoherence; the incoherence of the medium can only be effective at scales larger than ϵ . If, on the contrary, the beam is wide compared to ϵ , then the wave can be affected by the medium incoherent nature. On the whole, in a short temporal signal each frequency will be affected differently (in terms of spatial coherence) by the medium; if we observe this phenomenon in the time domain, by measuring the degree of resemblance, there will be an averaging effect between low frequencies (that can feel the incoherence) and high frequencies (that can only see a coherent aspect of a medium). Note that the coefficient $1/\lambda^2$ tends to give more weight to high frequencies, but in reality this effect should be balanced by frequency-dependent attenuation.

We can also note that the backscattered acoustic field ψ as a function of x is no longer a stationary process. Indeed, from (22), $R_{\psi\psi}^\omega$ depends both on x_1 and x_2 and no longer on only one variable $\Delta x = x_1 - x_2$. This can be understood in terms of wave propagation and Fourier optics. Indeed, the reflectivity χ of a fully incoherent mirror shows rapid variations, so such a mirror has a poor directivity and reflects waves uniformly in all directions. In other words, $\chi(X)$ contains high spatial frequencies and its angular spectrum is very wide. On the contrary, if the mirror is very smooth, then it sends the wave back on the transmitting aperture, and nothing outside the aperture. Between these two extremes, the mirror reflects waves with an intermediate directivity. This is the reason why the backscattered field, as a function of space, is not stationary: when the medium is not fully incoherent, the field is not uniformly reflected. However, this nonstationarity can only be effective if the observing points x_1 and x_2 are apart by a distance much larger than the transmitting aperture. If such is not the case (for instance, if the transmitting and receiving apertures have the same size), we can reasonably consider that the field is *locally* stationary. A theoretical set of curves showing the transition from incoherence to coherence, according to the value of the parameter $\lambda F/a\epsilon$, is plotted in Fig. 3 (see Appendix C for the corresponding calculations).

D. Slightly outside the focal plane

Equation (12) gives us the degree of coherence of the backscattered field, for whatever focal distance F and depth of interest z —under the assumption that the condition stated in (B12) is valid—so we can examine what happens if the region of interest is located slightly out of focus ($z \neq F$) but still within the depth of focus. In that case, the modified aperture function \tilde{O} is no longer real valued; it contains a phase term:

$$\tilde{O}(x) = T(x) e^{j(\pi/\lambda z)x^2} = \text{rect}\left(\frac{x}{a}\right) \exp\left[-j \frac{\pi}{\lambda} \left(\frac{1}{F} - \frac{1}{z}\right) x^2\right]. \quad (23)$$

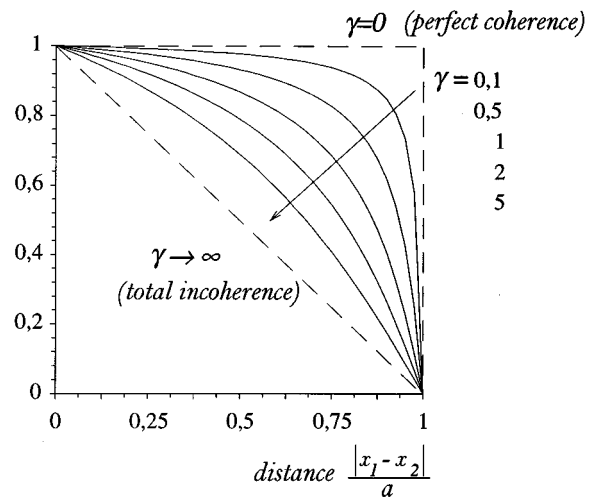


FIG. 3. Coherence degree of the field backscattered by a random mirror with coherence length ϵ (theoretical result). In abscissa, the distance $|x_1 - x_2|$ is expressed in fractions of the transmitting aperture size a . The transition from coherence (rect function) to incoherence (triangle function) depends on the parameter $\gamma = \lambda F/a\epsilon$.

Let $\beta = (\pi/\lambda)(1/F - 1/z)$. β depends on how far the region of interest is from the focal plane, if $z \neq F$ then $\beta \neq 0$. In the case of a fully incoherent medium, (12) yields:

$$\begin{aligned} R_{\psi\psi}^\omega(x_1, x_2) &\propto \text{rect}\left(\frac{x_1}{a}\right) e^{-j\beta x_1^2} \text{rect}\left(\frac{x_2}{a}\right) e^{j\beta x_2^2} \\ &\quad \times \left[\text{rect}\left(\frac{x}{a}\right) e^{-j\beta x^2} *_{\Delta x} \text{rect}\left(\frac{x}{a}\right) e^{j\beta x^2} \right] \\ &\propto \text{rect}\left(\frac{x_1}{a}\right) \text{rect}\left(\frac{x_2}{a}\right) e^{-j\beta(x_1^2 - x_2^2)} \\ &\quad \times \text{tri}\left(\frac{\Delta x}{a}\right) \text{sinc}[\beta \Delta x (a - |\Delta x|)]. \quad (24) \end{aligned}$$

If $\beta = 0$, then logically we find the triangular function once again. But if $\beta \neq 0$, different frequency components do not have the same coherence length any more: low frequencies are less affected (in terms of spatial coherence) by defocussing than high frequencies [since for lower frequencies, the sinc in (24) is closer to 1, so the spatial coherence function $R_{\psi\psi}^\omega$ is broader]; as a matter of fact, it is well known in optics that the depth of focus varies proportionally to λ , so high frequencies are more sensitive to defocussing. Moreover, the final result given in (24) is always inferior to the triangle function $\text{tri}(\Delta x/a)$, which means the focal plane is the region that generates the most coherent backscatter. If the region of interest is not exactly in the focal plane, then the correlation function $R_{\psi\psi}^\omega$ will be narrower.

In addition to this, there is a quadratic phase term in (24), which means that the backscattered waves have a curvature that is different from the transducer's. In the time domain, this implies a difference in the arrival times: if the mirror is placed in front of the focal plane ($z < F$), the array

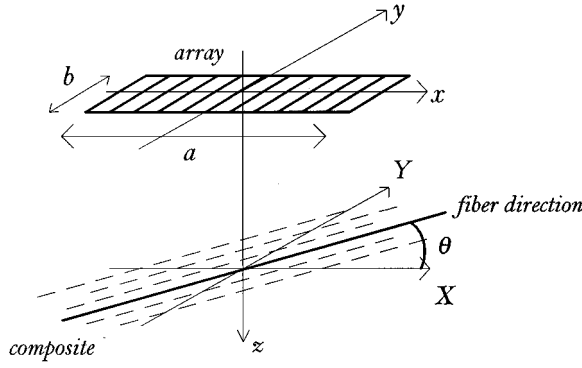


FIG. 4. (x, y) : coordinates in the plane of the array aperture. (X, Y) : coordinates in the plane of the fibers. The direction of alignment makes an angle θ with the X axis.

sees convex wavefronts ($\beta < 0$); their curvature reverses at $z = F$, and they become concave if the mirror is behind the focus ($\beta > 0$).

In the case of a perfectly coherent medium, (12) yields

$$R_{\psi\psi}^{\omega}(\Delta x) \propto \text{rect}\left(\frac{x_1}{a}\right) \text{rect}\left(\frac{x_2}{a}\right) e^{-2j\beta(x_1^2 - x_2^2)}. \quad (25)$$

This time, the modulus of $R_{\psi\psi}^{\omega}$ remains the same whatever the frequency, and has the same value as when $z = F$ (perfect coherence). As to the phase term, it is twice what it was in the case of an incoherent medium, so the reversing of the curvature around the focal plane is more apparent. In the time domain, this means that the backscattered signals received on two elements of the array are still identical, but arrive at different times.

E. The unidirectional composite

In the light of these remarks, an anisotropic material,⁸ such as a unidirectional composite, seems particularly interesting. Indeed, we will see that because of its structure, it can behave either coherently or incoherently, depending on how it is explored. A unidirectional composite is made of long fibers drowned in a resin matrix.⁹ The fibers are supposed to be infinitely long, thin, perfectly aligned along the same direction (axis 3 in Fig. 2), but randomly distributed in the perpendicular directions (axes 1 and 2).

Consider the case of a rectangular array with length a and width b , aligned along the x axis (Fig. 4); the plane of the fibers is parallel to the array, and the fiber direction makes an angle θ with the X axis. The array is focused in both directions and the region of interest we consider is located around the focal time. Given the fiber alignment, the autocorrelation of the reflectivity function can be written $R_{\chi\chi}(\Delta X, \Delta Y) \propto \delta(\Delta X - \Delta Y \tan \theta)$: this means two points (X_1, Y_1) and (X_2, Y_2) will have the same reflectivity if they are located on a line parallel to the fiber direction, and will reflect the wave independently otherwise.

From Eq. (12), the coherence function of the ω component in the backscattered signal is

$$R_{\psi\psi}^{\omega}(x_1, x_2, y_1, y_2) \propto \frac{1}{\lambda z} \text{rect}\left(\frac{x_1}{a}\right) \text{rect}\left(\frac{y_1}{b}\right) \text{rect}\left(\frac{x_2}{a}\right) \text{rect}\left(\frac{y_2}{b}\right) \delta(x_1 - x_2) \delta(y_1 - y_2) \delta(x_1 + y_1 \tan \theta). \quad (26)$$

Once more, frequency only appears in the multiplicative factor $1/\lambda z$, so for a given orientation θ , all frequencies have the same coherence length. In the two simple cases of parallel ($\theta = 0^\circ$) and perpendicular ($\theta = 90^\circ$) orientation, $R_{\psi\psi}^{\omega}$ can be easily calculated: parallel orientation: $\theta = 0^\circ$

$$R_{\psi\psi}^{\omega}(x_1, x_2, y_1, y_2) \propto \frac{b}{\lambda z} \text{rect}\left(\frac{x_1}{a}\right) \text{rect}\left(\frac{x_2}{a}\right) \text{tri}\left(\frac{y_1 - y_2}{b}\right); \quad (27)$$

perpendicular orientation: $\theta = 90^\circ$

$$R_{\psi\psi}^{\omega}(x_1, x_2, y_1, y_2) \propto \frac{a}{\lambda z} \text{rect}\left(\frac{y_1}{b}\right) \text{rect}\left(\frac{y_2}{b}\right) \text{tri}\left(\frac{x_1 - x_2}{a}\right). \quad (28)$$

So when the fibers oriented along X ($\theta = 0^\circ$), the backscattered field is perfectly coherent along x and incoherent along y , and vice versa when the fibers are oriented along Y ($\theta = 90^\circ$); in other words, the field is always coherent along the axis parallel to the fiber direction (\rightarrow rect function) and incoherent (\rightarrow tri function) along the perpendicular direction.

It would require a rectangular 2D array to verify this experimentally. But as a linear array can only sample the backscattered field along the x axis, the acoustic signal measured by such an array, $\psi(x)$, is in fact an average of the real signal $\psi(x)$ along the y axis:

$$\tilde{\psi}(x) = \frac{1}{b} \int_{-b/2}^{b/2} \psi(x, y) dy. \quad (29)$$

Straightforwardly the spatial correlation function of this signal, $R_{\tilde{\psi}\tilde{\psi}}^{\omega}$ is

$$R_{\tilde{\psi}\tilde{\psi}}^{\omega}(x_1, x_2) = E\{\tilde{\psi}(x_1) \tilde{\psi}^*(x_2)\} = \frac{1}{b^2} \int_{-b/2}^{b/2} \int_{-b/2}^{b/2} R_{\psi\psi}^{\omega}(x_1, x_2, y_1, y_2) dy_1 dy_2, \quad (30)$$

which yields:

parallel orientation ($\theta = 0^\circ$)

$$R_{\tilde{\psi}\tilde{\psi}}^{\omega}(x_1, x_2) \propto \frac{b}{\lambda z} \frac{2}{3} \text{rect}\left(\frac{x_1}{a}\right) \text{rect}\left(\frac{x_2}{b}\right); \quad (31)$$

perpendicular orientation ($\theta = 90^\circ$)

$$R_{\tilde{\psi}\tilde{\psi}}^{\omega}(x_1, x_2) \propto \frac{a}{\lambda z} \text{tri}\left(\frac{x_1 - x_2}{a}\right). \quad (32)$$

So, when observed with a linear array, the same composite seems to behave either as a fully incoherent medium (perpendicular case) or as a fully coherent medium (parallel case).

The intermediate case ($0^\circ < \theta < 90^\circ$) is a little more complicated, a detailed analysis is given in Ref. 10; to sum up, for intermediate angles, there is a progressive transition from incoherence to coherence (i.e., from the triangle to the rect-

angle), this transition is governed by the parameter $\gamma=(b/a)\tan\theta$: precisely, if $\gamma\gg 1$, the composite is in incoherent regime and the backscattered coherence function is a triangle, in the opposite case $\gamma\ll 1$, the composite is in its coherent regime and the backscattered coherence function is a rectangle. For given dimensions a and b , there is a transition angle that separate the incoherent and coherent regimes. This transition angle is important in the study of cross-ply composites as we will see.

The transition is analogous to what happens for a partially incoherent medium (Fig. 3), but here there is no frequency dependence: each frequency has the same spatial coherence function, except for an amplitude factor. So the degree of resemblance between time signals, which is calculated by integrating $R_{\psi\psi}^{\omega}$ over ω , keeps the same shape (triangle with base a if $\theta=90^\circ$, rectangle if $\theta=0^\circ$, intermediate form for $0^\circ<\theta<90^\circ$).

Thus, it is not quite exact to say that a composite behaves as a partially coherent medium whose coherence length would be a function of θ , because unlike a partially coherent medium, the composite such as we modelled it behaves, in terms of coherence, *identically* for each frequency. Yet a finer model that would take into account the finite fiber width and length would certainly imply a frequency dependence, because the fibers would show a characteristic size that would affect each wavelength differently.

III. CHARACTERISTICS OF THE UNIDIRECTIONAL COMPOSITE

A real composite is in fact more complex than our simple model, but our approach can be justified under some approximations. First of all, the composite is anisotropic, so the ultrasound velocity varies according to the propagation and polarization directions. But at small incidence angles, and neglecting the possibility of mode conversion at the water/composite interface, we can consider that inside the medium, only longitudinal waves propagate along direction 1 (Fig. 2). Their speed has been experimentally measured and a value of 2920 m/s was obtained.¹¹

This velocity is quite different from that of sound in water, which can deteriorate the quality of focusing inside the material. As a matter of fact, for too large apertures, there is no focusing so to speak, because rays perpendicular to the transducer do not intersect at a unique point (Fig. 5). The water/composite interface is located at distance d from the transducer center. Consider two rays emanating from O and A . These rays intersect inside the medium in F' :

$$OF' = OI_0 + I_0F' = d + (F-d) \frac{\tan \alpha}{\tan \beta}, \quad (33)$$

and Snell's law writes $c_2 \sin \alpha = c_1 \sin \beta$, so F' is on the horizontal axis at abscissa:

$$OF' = d + (F-d) \frac{c_1}{c_2} \sqrt{\frac{1 - (c_2/c_1)^2 \sin^2 \alpha}{1 - \sin^2 \alpha}}. \quad (34)$$

All rays coming from the transducer intersect in the same point if OF' is independent from α , i.e., if

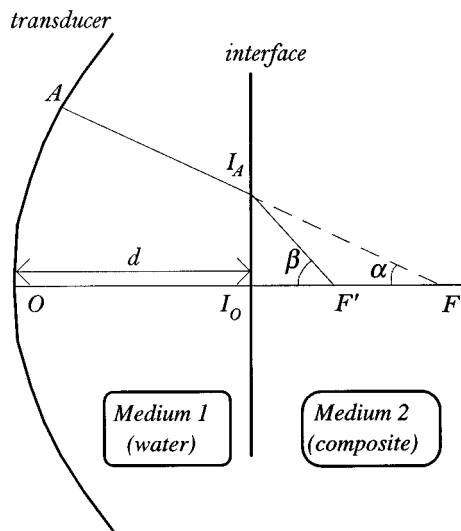


FIG. 5. Refraction at the water/composite interface.

$$\sqrt{\frac{1 - (c_2/c_1)^2 \sin^2 \alpha}{1 - \sin^2 \alpha}} \approx 1.$$

With $c_2/c_1 \approx 2$, this condition is satisfied for incidence angles $\alpha \leq 10^\circ$. In addition to this, even if the converging point is unique, the travel time of the rays are slightly different. In the transmit mode, it means that the pulses transmitted at the same time by each point on the array do not arrive simultaneously at F' , so the signal must spread a little in F' . Precisely, the time delay between AF' and OF' is

$$\delta\tau = -\frac{F-d}{c_1} \left[1 - \left(\frac{c_1}{c_2}\right)^2 \right] \left(\frac{1}{\cos \alpha} - 1 \right). \quad (35)$$

In order to avoid destructive interferences, the maximum value of $\delta\tau$ must be inferior to half a period.

A. Experimental procedure

The transducer we used is a wideband 128-element spherically focused array (pitch 0.426 mm, height $b=10$ mm) with radius of curvature $F=90$ mm and center frequency $f_0=3.5$ MHz. Since the array is naturally focused, there is no need to apply different time shifts to the transmitted/received signals. We used three different transmitting apertures sizes: 16, 32, and 64 elements (i.e., $a=6.8, 13.6,$ and 27.3 mm) which correspond to maximal incidences of $2.2^\circ, 4.3^\circ,$ and 8.7° respectively, so the focusing criterion $\alpha \leq 10^\circ$ is satisfied. The sample is immersed in water, its front face is at a typical distance $d \approx 70$ mm in order to focus inside the medium. For such distances, the maximum time delay $\delta\tau$ is $0.12 \mu\text{s}$, which satisfies the condition $\delta\tau < 1/2f_0$.

The sample is a piece of carbon-epoxy unidirectional composite, its dimensions are $20 \times 14.5 \times 2.1$ cm and the fiber width is approximately 7 μm .

The transmitted signal is made of two periods of a 3.5-MHz sine function. During the experiment, only the central elements (16, 32, or 64 according to the required aperture size) are transmitting a signal, then all 128 elements receive the backscattered waves. The signals are 10 bit digitized and sampled at a 40-MHz rate. Then in each time signal, we

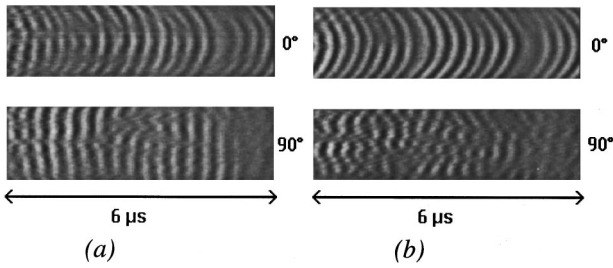


FIG. 6. Experimental results on the unidirectional composite: backscattered signals around the focal time for the parallel ($\theta=0^\circ$) and perpendicular ($\theta=90^\circ$) cases. Transmitting aperture size: $a=64$ elements (a) and $a=16$ elements (b). Time is in abscissa, and each line corresponds to one array element.

select a segment $[T_1, T_2]$ (see Fig. 1) centred around the focal time (typically $|T_1 - T_2| \approx 2-3 \mu\text{s}$). This time window must be wide enough to allow a proper estimation of the resemblance between signals, but short enough to be consistent with the approximations of our model. This implies that the time window must correspond to a region of interest that remains within the depth of focus.

The depth of focus is $\approx \lambda(F/a)^2$; in our experiments its minimum value is 11.4λ , and the largest time window we used contained 10 cycles.

Once the time window is selected, we calculate the correlation coefficient $C(i, j)$ between array elements $\#i$ and $\#j$:

$$C(i, j) = \frac{1}{\sqrt{\sum_{t=T_1}^{t=T_2} [s_i(t) - \bar{s}_i][s_j(t) - \bar{s}_j]}} \sum_{t=T_1}^{t=T_2} [s_i(t) - \bar{s}_i][s_j(t) - \bar{s}_j],$$

$$\bar{s}_i = \frac{1}{T_2 - T_1} \sum_{t=T_1}^{t=T_2} s_i(t), \quad i, j = 1, \dots, N. \quad (36)$$

Then $C(i, j)$ is averaged for all couples (i, j) apart by the same distance $m = |i - j|$, and normalized in order to obtain a dimensionless correlation coefficient $c(m)$:

$$c(m) = \frac{\sum_{i=1}^{N-m} C(i, i+m)}{\sum_{i=1}^N C(i, i)}. \quad (37)$$

Here N is the number of elements that are active in reception. When the field is only *locally* stationary, N equals the number of elements active in transmission; if the field is stationary then $N=128$.

Then c can be plotted as a function of m ; these curves measure the degree of correlation between signals received on two points apart by a distance $m \times \text{pitch}$. We also present the received signals on 2D *B-scan*-like diagrams: time is in abscissa, and each line corresponds to an element active in reception. The signal is represented in a gray level scale; this enables to visualize more directly the degree of coherence and the possible curvature of the wavefronts.

B. Experimental results

Figure 6 represents the backscattered signals around the focal time, for two different aperture sizes, 64 and 16 elements. We see that when the transmitting aperture gets

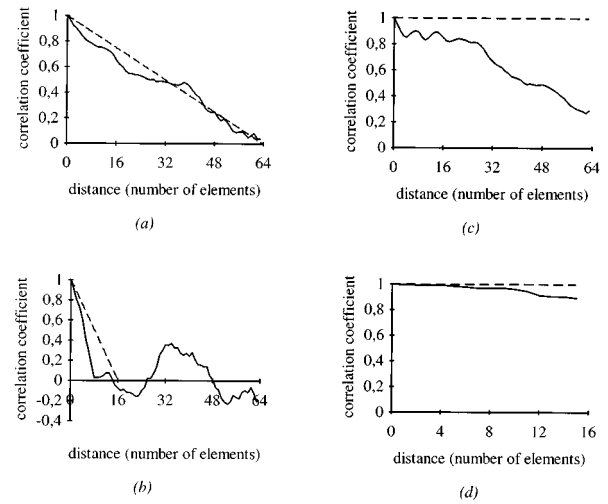


FIG. 7. Experimental results on the unidirectional composite: correlation curves $c(m)$ for orientation θ and transmitting aperture size a : (a) $a=64$ elements, $\theta=90^\circ$; (b) $a=16$ elements, $\theta=90^\circ$; (c) $a=64$ elements, $\theta=0^\circ$; (d) $a=16$ elements, $\theta=0^\circ$. m denotes the distance between two elements on the array, in number of elements.

smaller, the backscattered wavefronts remain very coherent in the parallel case; on the contrary, in the perpendicular case the coherence is degraded.

Note that in the parallel case, the outer elements of the array receive the signal slightly before the center elements, which gives an additional curvature to the wavefronts. This could be an effect of the large aperture. Indeed, in the parallel case, the composite behaves as a coherent medium; as we said before, if a coherent pointlike source is located at F' , the wave front received at the transducer edges arrive with a delay $\delta\tau$ [Eq. (35)]. In other terms, a spherical wave front does not remain exactly spherical as it traverses a plane interface.¹² At small angles (if the transmitting aperture size is 64 elements, the maximum angle is 8.7°), the theoretical time delay between the center and the outer elements is $\delta\tau = 0.12 \mu\text{s}$; the experimental value is $0.15 \mu\text{s}$.

From these data, we can plot the correlation curves $c(m)$ for each case. They are displayed in Fig. 7. Note that in the parallel case when the transmitting aperture size is 64 elements, we compensated the abovementioned time delay $\delta\tau$ on the outer elements before calculating the correlation coefficient. $c(m)$ is calculated as described above: we select a time window around the focal time, we correlate all signals pairs to obtain $C(i, j)$, then we average $C(i, j)$ for all couples apart by the same distance m . When correlating the signals, we add a possible delay of ± 1 sample and we keep the highest value for $C(i, j)$ in order to compensate possible aberrations.

The results show a good agreement with theoretical studies; that is to say, a high degree of correlation for the parallel case, whatever the transmitting aperture size, and for the perpendicular case, a linear decreasing of c as a function of m , this decreasing being steeper as the transmitting aperture gets smaller. On the whole, the experimental correlations are rather inferior to the theoretical predictions, but our random mirror approach did not take into account the deteriorating effects of the water/composite interface, and the

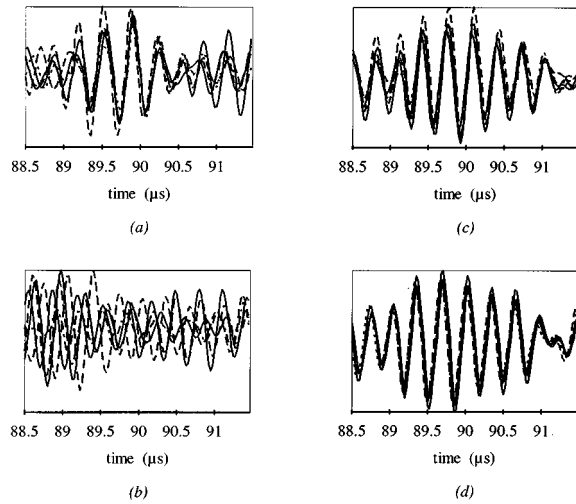


FIG. 8. Experimental results on the unidirectional composite: signals received on elements #56, 60, 64, 68, and 72, around the focal time. (a) $a = 64$ elements, $\theta = 90^\circ$; (b) $a = 16$ elements, $\theta = 90^\circ$; (c) $a = 64$ elements, $\theta = 0^\circ$; (d) $a = 16$ elements, $\theta = 0^\circ$.

resulting defocusing effects, even though they are minor, result in a spreading of the beam in the focal zone. In classical monochromatic optics, the Van Cittert–Zernike³ theorem states that the coherence length of the field radiated by a fully incoherent source is inversely proportional to the source size. In our case, the random mirror acts as an incoherent source and the size of this “source” is the beam width in the focal plane, so it is logical that the distortions that contribute to spreading the beam tend to shorten the coherence length of the backscattered field.

The influence of the aperture size is even more striking in Fig. 8: It represents the signals received on elements #56, 60, 64, 68, 72. For the parallel case, these 5 signals are very much alike, whatever the transmitting aperture size (64 or 16 elements). For the perpendicular orientation, the resemblance is still quite strong when the transmitting aperture is large, but the signals are utterly different for a smaller aperture.

As it will be useful in the study of cross-ply composites, Fig. 9 displays the signals received for the intermediate angle $\theta = 45^\circ$, and the corresponding correlation curve. Note that even if the array is no longer parallel to the fibers, the level of correlation is still quite high, so the unidirectional composite behaves almost coherently for $\theta = 45^\circ$.

C. Bidirectional composite

The same approach can be extended to the case of a bidirectional composite. Like the unidirectional composite, it is made by stacking elementary layers of unidirectional fibers, each new layer being rotated by 90° around the vertical axis (Fig. 10). The overall thickness of two successive layers is $2 \times 130 \mu$, which roughly corresponds to a quarter of a wavelength; so the distance between two successive layers is not resolved at our frequencies, and everything happens as if the array saw a mirror with a global reflectivity:

$$R_{XX}(\Delta X, \Delta Y) \propto 1_{\Delta X} \delta(\Delta Y) + 1_{\Delta Y} \delta(\Delta X). \quad (38)$$

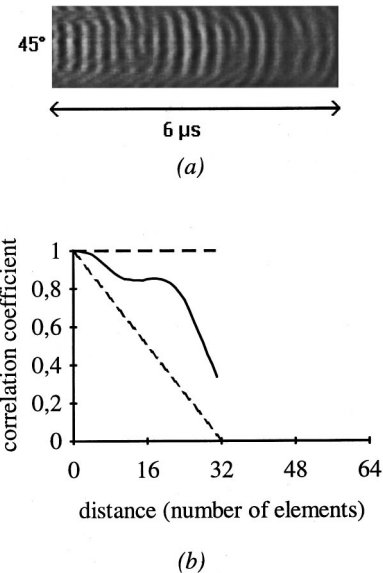


FIG. 9. Experimental results on the unidirectional composite. Transmitting aperture: $a = 32$ elements, angle $\theta = 45^\circ$. (a) Backscattered signals around the focal time. Time is in abscissa, and each line corresponds to one array element. (b) Corresponding correlation curve $c(m)$. Dashed lines: theoretical results for $\theta = 0^\circ$ and $\theta = 90^\circ$.

If the array is parallel to one of the two fiber directions, the backscattered signal contains a coherent and an incoherent component; and the correlation function is the sum of a rectangle and a triangle. However, in this combination, the rectangle and the triangle do not have the same weight. Indeed, from (31) and (32), the correlation function is a sum of two terms:

$$R_{\psi\psi}^{\omega}(x_1, x_2) \propto \underbrace{\frac{2}{3} \frac{b}{\lambda z} \text{rect}\left(\frac{x_1}{a}\right) \text{rect}\left(\frac{x_2}{a}\right)}_{\text{coherent component}} + \underbrace{\frac{a}{\lambda z} \text{tri}\left(\frac{x_1 - x_2}{a}\right)}_{\text{incoherent component}}. \quad (39)$$

So the weight of the incoherent component relatively to the coherent component equals $3a/2b$.

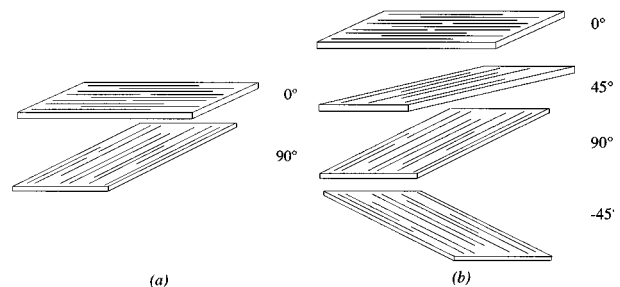


FIG. 10. Regular stacking of layers for bidirectional (a) and quadridirectional (b) cross-ply composites.

TABLE I. σ_θ^2 =variance of the signal backscattered by a unidirectional composite around the focal time for orientation θ .

	16 elements	64 elements
Theoretical ratio $\sigma_{90^\circ}/\sigma_{0^\circ}$	1.01	2.02
Experimental ratio $\sigma_{90^\circ}/\sigma_{0^\circ}$	1.2	2.1

Besides, this effect can also be observed on an unidirectional composite, because the coefficients $2b/3\lambda z$ and $a/\lambda z$ are simply proportional to the variance of the backscattered signals, in the perpendicular and parallel cases, respectively. And experimentally we observe that the variance of the signal differs in the perpendicular and the parallel case, by a factor that depends on the aperture size a : with the dimensions $a \times b$ of our linear array, we observed that when $\theta=0^\circ$, the signals fluctuated around their mean value with a bigger amplitude than in the parallel case (experimental and theoretical results are presented in Table I). So, depending on the ratio $3a/2b$, it is either the coherent or the incoherent component that predominates in the field backscattered by a bidirectional composite. Given the dimensions of the array and the aperture sizes we used, we seem to always be in the case where the incoherent part wins over the coherent component. And indeed, the correlation curve agrees with this diagnosis: Fig. 11 shows $c(m)$ for a 16-element aperture; the correlation curve is much closer to the triangle than to the rectangle, which witnesses the importance of the incoherent component. Given the symmetry of the medium, the results are equivalent for $\theta=0^\circ$ and $\theta=90^\circ$. For the intermediate case $\theta=45^\circ$, there is no longer a coherent and an incoherent component, but two partially coherent contributions with equivalent weights. As it is shown in Fig. 11, it results a larger coherence length than when $\theta=0^\circ$; indeed, as we have seen in Fig. 9 for the unidirectional composite, $\theta=45^\circ$ is rather in the coherent regime of the composite. So on the whole, the combination of layers is more coherent at 45° than at 0° or 90° , where the incoherent part wins over the coherent one.

D. The quadridirectional composite

The same principle can be applied to a quadridirectional composite, which is constituted by a regular stacking of el-

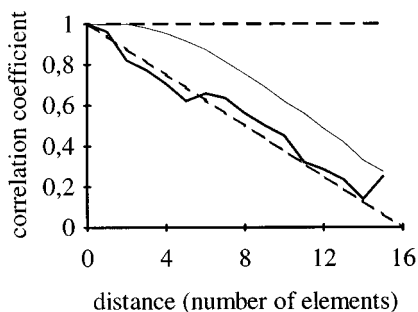
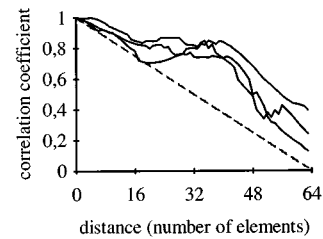
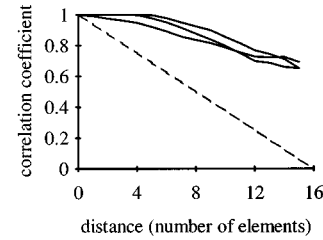


FIG. 11. Experimental results on the bidirectional composite: correlations curves $c(m)$. Transmitting aperture size: $a = 16$ elements. Thick line: $\theta=0^\circ$, thin line: $\theta=45^\circ$. Dashed lines: theoretical results expected for a coherent (\rightarrow rect) and an incoherent (\rightarrow triangle) medium.



(a)



(b)

FIG. 12. Experimental results on the quadridirectional composite: correlations curves $c(m)$. Transmitting aperture size: $a = 64$ elements (a) and $a = 16$ elements (b). Thick lines: experimental results for $\theta=0^\circ$, 22.5° and 45° . Dashed lines: theoretical results expected for a coherent (\rightarrow rect) and an incoherent (\rightarrow triangle) medium.

ementary layers with an helicoidal step of 45° (Fig. 10). The overall thickness of a “superlayer” is $4 \times 130 \mu$; this distance is still unresolved at our frequencies. So if the array is parallel to one of the four directions of alignment, the backscattered signal contains four contributions: a coherent component (due to the 0° layer), an incoherent component (due to the 90° layer) and two partially coherent components (45° and -45°). The question is, which one is going to win? Figure 12 shows correlation curves $c(m)$ calculated for 64- and 16-element aperture, and it is quite clear at a simple glance that the coherent component is more important than the incoherent one, whatever θ : the experimental curves are closer to the rectangle, and quite comparable to the parallel case of the unidirectional composite.

Compared to a bidirectional composite, each “superlayer” of the quadridirectional composite contains two more layers (45° and -45°); these are responsible for the victory of coherence. Indeed, we have seen in the study of the uni- and bidirectional composites that given the dimensions of the array, 45° is rather a coherent angle so the global backscattered signal contains one incoherent component, one coherent component and two nearly coherent components. It would be interesting to check the validity of this explanation with another array, with dimensions b and a such as 45° is an incoherent angle; in such conditions, the quadridirectional composite should behave incoherently. This experiment would require a transmitting aperture with b much bigger than a , so that $\gamma \gg 1$.

If we change the orientation of the array, with an intermediate angle ($\theta=22.5^\circ$), we observe very similar results (Fig. 12); this time, the backscattered signal contains four partially coherent contributions. Note that it is no longer possible to point out an anisotropic behavior in terms of coherence: although the fiber distribution is still anisotropic, in such a medium the array can no longer detect a particular

direction in terms of correlation, it receives a quasi-coherent signal whatever the angle θ .

IV. DETECTION OF A DEFECT INSIDE A MEDIUM

So far, we have considered media in which the reflectivity function was modeled as a stationary random process, i.e., the statistical properties of the equivalent random mirror are invariant under translation. This model is no longer adequate if there is a defect, or a small lesion, inside the region of interest. In such a case, the total signal contains the echo of the defect, surrounded by the speckle noise generated by the scatterers. Classical techniques try to detect the defect by its amplitude inside the total backscattered signal. We investigate here, on a simple example, the ability of the Zernike method to identify the defect by its coherent nature rather than by its amplitude. The basic idea is that a small defect behaves as a pointlike source and reflects a spherical coherent wave that should be detectable among the speckle noise.

For the case of a defect inside an incoherent medium, the global reflectivity writes

$$\chi(X, Y) = \chi_{\text{defect}}(X, Y) + \chi_{\text{medium}}(X, Y). \quad (40)$$

So the coherence function of the backscattered signal will contain two components: one due to the defect, the second one due to the scattering medium. Consider a simple case, a rectangular flat defect of size d , such that

$$\chi_{\text{defect}}(X, Y) = A_{\text{def}} \text{rect}\left(\frac{X}{d}\right) \text{rect}\left(\frac{Y}{d}\right). \quad (41)$$

Of course, this rectangular profile is not realistic, but what we try here is not to perform a precise calculation, but rather to understand the role of each parameter (defect size d , wavelength λ ...).

The autocorrelation of the defect reflectivity is therefore

$$R_{\chi\chi}^{\text{defect}}(X_1, X_2, Y_1, Y_2) = A_{\text{def}}^2 \text{rect}\left(\frac{X_1}{d}\right) \text{rect}\left(\frac{X_2}{d}\right) \times \text{rect}\left(\frac{Y_1}{d}\right) \text{rect}\left(\frac{Y_2}{d}\right). \quad (42)$$

If the defect is small compared to the beamwidth (i.e., $d < \lambda F/a$), then the field backscattered by the defect may be approximated by

$$\psi_{\omega}^{\text{defect}}(x, y) \approx \frac{d^2 \Sigma}{\lambda^2 F^2} A_{\text{def}} O(x, y), \quad (43)$$

where Σ is the transducer surface (see Appendix D for a detailed demonstration). So the coherence function of the field backscattered by the defect is

$$R_{\psi\psi}^{\text{defect}}(x_1, x_2, y_1, y_2) = \frac{d^4 \Sigma^2}{\lambda^4 F^4} A_{\text{def}}^2 O(x_1, y_1) O(x_2, y_2). \quad (44)$$

Now, let us calculate the coherence function of the field backscattered by the random medium alone. Consider a stationary partially incoherent medium with coherence length ϵ , such that, for instance,

$$R_{\chi\chi}^{\text{medium}}(\Delta X, \Delta Y) = A_{\text{med}}^2 \text{rect}\left(\frac{\Delta X}{\epsilon}\right) \text{rect}\left(\frac{\Delta Y}{\epsilon}\right). \quad (45)$$

Its Fourier transform is

$$\phi(x, y) = A_{\text{med}}^2 \epsilon^2 \text{sinc}\left(2\pi \frac{x\epsilon}{\lambda F}\right) \text{sinc}\left(2\pi \frac{y\epsilon}{\lambda F}\right). \quad (46)$$

Suppose the coherence length is smaller than the beamwidth in the focal plane (i.e., $\epsilon < \lambda F/a$), then the main lobe of the sinc in (46) is larger than the aperture size a , so from (22), the coherence function of the backscattered speckle noise can be approximated by

$$R_{\psi\psi}^{\text{medium}}(\Delta x, \Delta y) \approx \frac{\Sigma \epsilon^2}{\lambda^2 F^2} A_{\text{med}}^2 \text{tri}\left(\frac{\Delta x}{a}\right) \text{tri}\left(\frac{\Delta y}{b}\right). \quad (47)$$

On the whole, the coherence function of the total signal results from the summation of a rectangle (coherent component due to the defect) and a triangle (incoherent component due to the speckle noise) with respective weights

$$\sigma_{\text{coh}}^2 = \frac{d^4 \Sigma^2}{\lambda^4 F^4} A_{\text{def}}^2 \quad \text{and} \quad \sigma_{\text{inc}}^2 = \frac{\Sigma \epsilon^2}{\lambda^2 F^2} A_{\text{med}}^2. \quad (48)$$

In terms of coherence, the defect can be detected if its contribution is stronger than that of the speckle noise, in such a way that the total field exhibits a larger coherence length than the medium without defect. Precisely, the ratio of the coherent part to the incoherent contribution equals

$$\frac{\sigma_{\text{coh}}}{\sigma_{\text{inc}}} = \frac{A_d d^2 \sqrt{\Sigma}}{A_m \epsilon \lambda F} = \eta \frac{n_{\epsilon}}{n_{d^2}}, \quad (49)$$

where $\eta = A_d/A_m$ characterizes the defect contrast inside the medium, $n_{\epsilon} = \lambda F/\epsilon\sqrt{\Sigma}$ is the ‘‘number of coherence lengths in the beam,’’ and $n_{d^2} = \lambda^2 F^2/\Sigma d^2$ is the ratio of the focal spot surface to the defect surface. For a given contrast η , we see that $\sigma_{\text{coh}}/\sigma_{\text{inc}}$ gets smaller when ϵ increases; indeed, as we have seen, the speckle noise becomes more and more coherent as ϵ increases, so it is more difficult to identify the coherent component due to the defect among the speckle noise. On the contrary, when the medium is fully incoherent, one might detect a small coherent reflector in the speckle noise more easily.

To illustrate this, we put a thin (diameter=0.11 mm) metallic wire inside a piece of foam, and we used the same experimental setup. The foam was immersed and contained no air; the wire was a few centimeters long, and perpendicular to the (x, z) plane. First, the coherence length of the acoustic field backscattered by foam alone is measured. Then the foam+wire sample is placed in the focal zone [Fig. 13(a)]; the array records the received field and we calculate its coherence degree.

The experiment was carried out with a 16 elements transmitting aperture size. The results are displayed in Fig. 13(b); they show that foam alone acts as an incoherent medium [$c(m)$ decreases linearly as a triangle]. On the contrary, when the wire is placed inside the foam, we observe an increase in the coherence degree, that remains very high for distances much larger than the transmitting aperture size. The wire is thin enough to be hardly detectable by a single

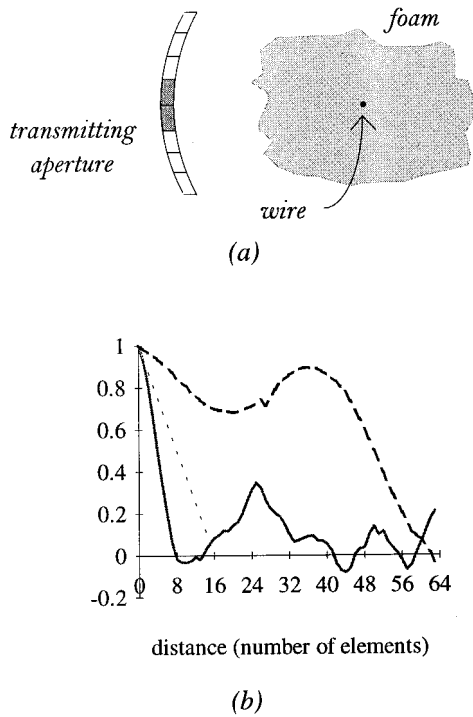


FIG. 13. (a) Experimental setup. (b) Correlation curves in foam. Transmitting aperture size: $a=16$ elements. Thick line: foam alone. Thick dashed line: foam+wire. Fine dashed line: theoretical results for a fully incoherent medium.

classical transducer: Figure 14 shows the signal obtained by coherent summation of all signals received on the transmitting aperture (16 central elements on the array), which corresponds to the echographic A-scan that a single transducer with the same dimensions would have received. We observe that the echo due to the wire is not contrasted enough to detect it unmistakably among the ambient speckle noise. So it may be useful to consider an echo not only in terms of its amplitude, but to consider its coherent or incoherent nature as well.

If the defect is larger than the focal spot, the approximation we made to obtain (43) is no longer valid, but can be

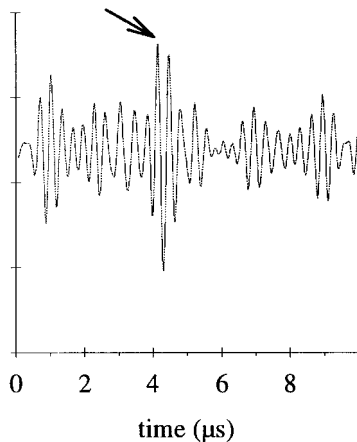


FIG. 14. Coherent summation of the acoustic signals received on the 16 elements that were active in transmission. The arrow shows the echo of the wire.

replaced by another one: indeed, as is shown in Appendix D, if $d > \lambda F/a$ then the contribution of the defect to the total backscattered field writes

$$\psi_{\psi}^{\text{defect}}(x,y) \approx A_{\text{def}} O(x,y). \quad (50)$$

In this case, $\sigma_{\text{coh}}^2 = A_{\text{def}}^2$ and the ratio of the coherent component to the incoherent component becomes

$$\frac{\sigma_{\text{coh}}}{\sigma_{\text{inc}}} = \frac{A_{\text{def}}}{A_{\text{med}}} \frac{\lambda F}{\sqrt{\Sigma} \epsilon} = \eta n \epsilon. \quad (51)$$

Apart from the relative contrast of the defect η , this ratio is proportional to $\lambda F/\sqrt{\Sigma} \epsilon$ which indicates the “number of coherence lengths inside the beam.” The size of the defect d does not appear in this expression, since the defect has been considered larger (and in fact, infinitely larger) than the beam. We see once again that it is more and more difficult to detect the defect as ϵ increases: indeed, total incoherence of the surrounding medium is the easiest situation to detect a coherent reflector inside the speckle noise.

V. CONCLUSION

We have studied a technique for measuring the degree of coherence of the backscattered acoustic field, theoretically as well as experimentally. This approach enables to understand how the echographic signal forms on a single transducer: indeed, on such a transducer, the echographic signal is the summation of signals received all over its surface; and according to whether the field is coherent or incoherent, this summation will yield constructive or destructive interferences, hence a higher or lower speckle noise level. Knowing the coherence length of the acoustic field is crucial if one wants to:

- (1) characterize the material, for instance its anisotropy as we did for the composite, or reveal its coherent, incoherent, or partially coherent nature from the statistical characteristics of its speckle noise;
- (2) reduce the speckle noise level with adaptive techniques;¹³
- (3) identify a coherent component among an incoherent speckle, in order to detect a small defect by its coherent nature rather than by its amplitude.

We named this method after Zernike because it is an adaptation of Frederik Zernike’s works on the coherence of optical monochromatic vibrations. He studied, as we did, the degree of correlation between waves received at two observing points, but we adapted his optical formalism to wide-band backscattered acoustic signals. Experimentally, this Zernike technique requires a transducer array that performs a spatial sampling of the acoustic field. One could use another method, which only one transducer scanning the medium; this technique is known as *spatial compound*, and will be discussed and compared to the Zernike method in a future paper.

APPENDIX A: FOURIER TRANSFORMS AND RANDOM PROCESSES

The definition of the Fourier transform:

$$F(X) = \text{FT}\{f(x)\}_{X/\lambda z} = \int f(x) e^{-2\pi j(xX/\lambda z)} dx \quad (\text{A1})$$

yields the following properties:

$$\begin{aligned} \text{FT}\{f * g\} &= \text{FT}\{f\} \text{FT}\{g\}, \\ \text{FT}\{\text{FT}\{f\}\} &= \lambda z f(-x). \end{aligned} \quad (\text{A2})$$

If $A(x)$ is a random process with autocorrelation function $R_{AA}(x_1, x_2)$, its FT $B(X)$ is also a random process and its autocorrelation is

$$\begin{aligned} R_{BB}(X_1, X_2) &= E\{B(X_1)B^*(X_2)\} \\ &= E\left\{ \int_{-\infty}^{\infty} A(x_1) e^{-2\pi j(x_1 X_1/\lambda z)} dx_1 \right. \\ &\quad \left. \times \int_{-\infty}^{\infty} A^*(x_2) e^{2\pi j(x_2 X_2/\lambda z)} dx_2 \right\}. \end{aligned} \quad (\text{A3})$$

Since the expected value E is a linear operation, we can deduce

$$R_{BB}(X_1, X_2) = \text{FT}_{2D}[R_{AA}(x_1, x_2)]_{(X_1/\lambda z, -X_2/\lambda z)}. \quad (\text{A4})$$

The autocorrelation of the FT of a 1D random process equals the 2D FT of the autocorrelation of the original process, with a reversal in the sign of the second variable. This can be generalized easily to the case of multidimensional random processes.

Moreover, if $A(x)$ is a stationary process, then its autocorrelation depends only on one variable $\Delta x = x_1 - x_2$, so R_{BB} simplifies into a 1D Fourier transform:

$$R_{BB}(X_1, X_2) = \delta(X_1 - X_2) \text{FT}_{1D}[R_{AA}(\Delta x)]_{(X_1/\lambda z)}. \quad (\text{A5})$$

Consider the case where a random process $A(x)$ is multiplied by a deterministic function $D(x)$: a new random process $M(x) = A(x)D(x)$ is created and its autocorrelation is

$$\begin{aligned} R_{MM}(x_1, x_2) &= E\{D(x_1)A(x_1)D^*(x_2)A^*(x_2)\} \\ &= D(x_1)D^*(x_2)R_{AA}(x_1, x_2). \end{aligned} \quad (\text{A6})$$

APPENDIX B: APPROXIMATE EXPRESSION FOR ψ AND $R_{\psi\psi}$

Let us consider a transmitting aperture $O(x, y)$ in the $z=0$ plane, such as a rectangular array with dimensions $a \times b$:

$$O(x, y) = \text{rect}\left(\frac{x}{a}\right) \text{rect}\left(\frac{y}{b}\right); \quad (\text{B1})$$

denoting F its radius of curvature, the transmittance function of this aperture is

$$T(x, y) = O(x, y) e^{-j(\pi/\lambda F)(x^2 + y^2)}. \quad (\text{B2})$$

In optics, $T(x, y)$ would be the transmittance of a thin lens with focal distance F : if the lens is illuminated by a plane wave $e^{j(\omega t - kz)}$, the outgoing wave $T(x, y) e^{j(\omega t - kz)}$ is spheri-

cal and converges to the point $z=F$. The quadratic phase term in (B2) corresponds to a focusing effect within Fresnel's approximation.⁶ In acoustics, such a transmittance can be realized either with a naturally focused transducer with radius of curvature F , or with a transducers array by applying the appropriate time shifts on each channel in order to simulate the curvature. If F has a finite value, then the aperture behaves as a converging lens focusing the wave at depth $z=F$; the limit case $F \rightarrow \infty$ corresponds to a plane transducer.

In the following, we will have to consider the propagation of a wave field from one plane to another. We know that within Fresnel's approximation,⁶ propagation from 0 to z can be described by a spatial impulse response:

$$h_z(x, y) = e^{jkz}/j\lambda z \times e^{j(\pi/\lambda z)(x^2 + y^2)}. \quad (\text{B3})$$

Indeed, a point source $\delta(x, y)$ in the $z=0$ plane would generate a spherical wavelet e^{jkr}/kr , where r is the distance from the point source to the observer, and (B3) is simply an approximation of the spherical wavelet when $z \gg x, y$. So the propagation of a wave field $U(x, y)$ over a distance z is simply described by a convolution of $U(x, y)$ by $h_z(x, y)$.

First step: propagation from 0 to z:

In the plane of the array ($z=0$), the amplitude of the transmitted field is

$$U_0(x, y) = T(x, y) e^{-j\omega t}. \quad (\text{B4})$$

This field propagates along z , so the amplitude of the diffracted field at depth z can be written as

$$U_z(X, Y) = U_0(X, Y) \underset{XY}{**} h_z(X, Y). \quad (\text{B5})$$

Developing the convolution product in (B5) and dropping the propagation term $e^{j(kz - \omega t)}$, the field can be expressed as a Fourier transform of the transmittance function:

$$\begin{aligned} U_z(X, Y) &= \frac{1}{\lambda z} e^{j(\pi/\lambda z)(X^2 + Y^2)} \\ &\quad \times \int \int T(x, y) e^{j(\pi/\lambda z)(x^2 + y^2)} \\ &\quad \times e^{-2\pi j[(xX + yY)/\lambda z]} dx dy. \end{aligned} \quad (\text{B6})$$

We introduce the *modified aperture function* $\tilde{O}(x, y)$ that takes into account the depth of interest z and the focus F :

$$\begin{aligned} \tilde{O}(x, y) &= T(x, y) e^{j(\pi/\lambda z)(x^2 + y^2)} \\ &= O(x, y) \exp\left[j \frac{\pi(x^2 + y^2)}{\lambda} \left(\frac{1}{z} - \frac{1}{F} \right) \right]; \end{aligned} \quad (\text{B7})$$

thus appears the Fourier transform of $\tilde{O}(x, y)$ taken at spatial frequencies $X/\lambda z$ and $Y/\lambda z$:

$$U_z(X, Y) = \frac{1}{\lambda z} e^{j\pi/\lambda z(X^2 + Y^2)} \text{FT}_{2D}\{\tilde{O}(x, y)\}_{(X/\lambda z, Y/\lambda z)}. \quad (\text{B8})$$

We define

$$\tilde{\Omega}_z(X, Y) = \text{FT}_{2D}\{\tilde{O}(x, y)\}_{(X/\lambda z, Y/\lambda z)}. \quad (\text{B9})$$

$|\tilde{\Omega}_z(X, Y)|^2$ is simply the beam intensity profile at depth z .

Second step: reflection on the random mirror:

Equation (B8) gives the expression of the field amplitude at depth z , just in front of the random mirror. Let $\chi(X, Y)$ be the reflectivity function of the mirror. χ is a random variable, and right after the reflection of the wave, the reflected field writes

$$U_z^{\text{refl}}(X, Y) = \chi(X, Y) U_z(X, Y) \\ = \frac{1}{\lambda z} e^{j(\pi/\lambda z)(X^2 + Y^2)} \chi(X, Y) \tilde{\Omega}_z(X, Y). \quad (\text{B10})$$

Third step: back propagation from z to 0:

Then this field propagates toward the array. So in order to calculate the received field $\psi_\omega(x, y)$, we have to convolve once again $U_z^{\text{refl}}(X, Y)$ by the propagation impulse response and to multiply the result by the transmittance of the array:

$$\psi_\omega(x, y) = T(x, y) \left(U_z^{\text{refl}} *_{x, y} h_z \right) \\ = \frac{1}{\lambda^2 z^2} T(x, y) e^{j(\pi/\lambda z)(x^2 + y^2)} \\ \times \int \int e^{j(\pi/\lambda z)(X^2 + Y^2)} e^{-j(2\pi/\lambda z)(xX + yY)} \\ \times \tilde{\Omega}(X, Y) \chi(X, Y) dX dY. \quad (\text{B11})$$

Under some conditions, the first term under the integral, can be neglected. In fact, $\tilde{\Omega}(X, Y)$ represents the beam profile in the z plane; let l be the beamwidth, then

$$e^{j(2\pi/\lambda z)(X^2 + Y^2)} \tilde{\Omega}(X, Y) \approx \tilde{\Omega}(X, Y) \quad \text{if } l^2 \ll \lambda z. \quad (\text{B12})$$

This condition is usually satisfied if the region of interest is in the focal zone of a focused transducer: since the beamwidth in the focal plane is roughly $l = \lambda F/a$, then the condition $l^2 \ll \lambda z$ implies $l \ll a$; that is to say, the beamwidth has to be much smaller than the aperture size, which is true in the focal zone.

Under this assumption the backscattered field writes

$$\psi_\omega(x, y) = \frac{1}{\lambda^2 z^2} \tilde{O}(x, y) \text{FT}_{2D} \{ \chi(X, Y) \tilde{\Omega}(X, Y) \}_{(x/\lambda z, y/\lambda z)}. \quad (\text{B13})$$

If we consider the case of a focused transducer and the region of interest is located around the focal plane, then this approximate expression may be used.

As to the autocorrelation of the backscattered field, from the mathematical properties presented in Appendix A, it writes

$$R_{\psi\psi}^\omega(x_1, x_2, y_1, y_2) \\ = E \{ \psi_\omega(x_1, y_1) \psi_\omega^*(x_2, y_2) \} \\ = \frac{1}{\lambda^4 z^4} \tilde{O}(x_1, y_1) \tilde{O}^*(x_2, y_2) \text{FT}_{4D} \{ \tilde{\Omega}(X_1, Y_1) \tilde{\Omega}^*(X_2, Y_2) \\ \times R_{\chi\chi}(X_1, Y_1, X_2, Y_2) \}_{(x_1/\lambda z, y_1/\lambda z, x_2/\lambda z, y_2/\lambda z)}. \quad (\text{B14})$$

Noting that

$$\text{FT}_{2D} \{ \tilde{\Omega}(X, Y) \}_{(x/\lambda z, y/\lambda z)} = \lambda^2 z^2 \tilde{O}(-x, -y) \\ = \lambda^2 z^2 \tilde{O}(x, y), \quad (\text{B15})$$

and applying the convolution theorem (A2), we derive (10) from (B14).

In the case where the approximation (B12) is not valid, as would be the case for a plane transducer for instance, a similar expression exists: indeed, as (B12) consisted in writing $e^{j(2\pi/\lambda z)(X^2 + Y^2)} \tilde{\Omega}(X, Y) \approx \tilde{\Omega}(X, Y)$, then we have to replace $\lambda^2 z^2 \tilde{O}(-x, -y)$ by

$$\tilde{O}(-x, -y) * * \text{FT}_{2D} \{ e^{j(\pi/2\lambda z)(X^2 + Y^2)} \}_{(x/\lambda z, y/\lambda z)} \\ \propto \lambda z \tilde{O}(-x, -y) * * e^{j(\pi/2\lambda z)(x^2 + y^2)}$$

in (B15) in order to obtain the correct expression. However, since (B12) holds for the cases we investigated here, we always used the approximate relation (10).

APPENDIX C: PARTIAL COHERENCE

Consider a mirror with random reflectivity $\chi(X)$ such that

$$R_{\chi\chi}(X_1, X_2) = R_{\chi\chi}(\Delta X) \propto e^{-\Delta X/\epsilon}. \quad (\text{C1})$$

The spatial Fourier transform of this function is

$$\phi(\xi) \propto \frac{1}{1 + ((2\pi\epsilon/\lambda F)\xi)^2}. \quad (\text{C2})$$

From (22), we derive the autocorrelation of the backscattered field:

$$R_{\psi\psi}^\omega(x_1, x_2) \propto \int_{x_2 - a/2}^{x_1 + a/2} \phi(\xi) d\xi \\ \propto \left[\arctan \left(2\pi \frac{\epsilon\xi}{\lambda F} \right) \right]_{\xi=x_2 - a/2}^{\xi=x_1 + a/2}. \quad (\text{C3})$$

This expression depends on both x_1 and x_2 , and not on $\Delta x = x_2 - x_1$ only, because the field is a nonstationary random process. However, if we are interested in the degree of resemblance between signals received in x_1 and in x_2 as a function of the distance Δx , we have to average for all pairs (x_1, x_2) apart by the same distance:

$$\bar{R}_{\psi\psi}^\omega(\Delta x) = \langle R_{\psi\psi}^\omega(x_1, x_1 + \Delta x) \rangle_{\text{array}} \\ = \frac{1}{a - \Delta x} \int_{-a/2}^{a/2 - \Delta x} R_{\psi\psi}^\omega(x_1, x_1 + \Delta x) dx_1 \\ \text{with } 0 < \Delta x < a, \quad (\text{C4})$$

and (C3) yields

$$\bar{R}_{\psi\psi}^\omega(\Delta n) = \arctan \left\{ 2\pi \left(\frac{1 - \Delta n}{\gamma} \right) \right\} - \frac{1}{2} \frac{\gamma}{(1 - \Delta n)} \\ \times \ln \left\{ 1 + \left(\frac{1 - \Delta n}{\gamma} \right)^2 \right\}. \quad (\text{C5})$$

Here we introduced the dimensionless variable $\Delta n = \Delta x/a$ and the dimensionless parameter $\gamma = \lambda F/a\epsilon$ which represents the ‘‘number of coherence lengths within the beam.’’

The dimensionless correlation coefficient $\bar{R}_{\psi\psi}^{\omega}(\Delta n)/\bar{R}_{\psi\psi}^{\omega}(0)$ is plotted in Fig. 3, which shows the progressive transition from coherence to incoherence as γ increases.

A Gaussian correlation model could have been employed instead of an exponential correlation, but the choice of the medium correlation function does not affect the physical meaning of the result plotted in Fig. 3; besides, unlike a Gaussian model, an exponential model requires no numerical integration to derive $\bar{R}_{\psi\psi}^{\omega}(\Delta n)$.

APPENDIX D: DEFECT DETECTION

From (8), the backscattered signal is

$$\psi_{\omega}(x, y) = \frac{1}{\lambda^2 F^2} \tilde{O}(x, y) \text{FT}_{2\text{D}}\{\chi(X, Y) \times \tilde{\Omega}(X, Y)\}_{(x/\lambda F, y/\lambda F)}. \quad (\text{D1})$$

If the defect is small compared to the beamwidth (i.e., $d < \lambda F/a$), then

$$\begin{aligned} & \text{FT}_{2\text{D}}\{\chi(X, Y) \tilde{\Omega}(X, Y)\}_{(x/\lambda F, y/\lambda F)} \\ & \approx \tilde{\Omega}(0, 0) \text{FT}_{2\text{D}}\{\chi(X, Y)\}_{(x/\lambda F, y/\lambda F)} \\ & = \Sigma A_{\text{def}} d^2 \text{sinc}\left(2\pi \frac{xd}{\lambda F}\right) \text{sinc}\left(2\pi \frac{yd}{\lambda F}\right), \end{aligned} \quad (\text{D2})$$

and the sinc function is wider than $O(x, y)$, so finally:

$$\psi_{\omega}^{\text{def}}(x, y) \approx \frac{d^2 \Sigma}{\lambda^2 F^2} A_{\text{def}} O(x, y). \quad (\text{D3})$$

If, on the contrary, the defect is larger than the beamwidth (i.e., $d > \lambda F/a$) then

$$\begin{aligned} & \text{FT}_{2\text{D}}\{\{\chi(X, Y) \tilde{\Omega}(X, Y)\}\}_{(x/\lambda F, y/\lambda F)} \\ & \approx \chi(0, 0) \text{FT}_{2\text{D}}\{\tilde{\Omega}(X, Y)\}_{(x/\lambda F, y/\lambda F)} \\ & = A_{\text{def}} \lambda^2 F^2 O(x, y), \end{aligned} \quad (\text{D4})$$

and the approximate expression becomes

$$\psi_{\omega}^{\text{defect}}(x, y) \approx A_{\text{def}} O(x, y). \quad (\text{D5})$$

- ¹A. Derode and M. Fink, "The notion of coherence in optics and its application to acoustics," *Eur. J. Phys.* **15**, 81–96 (1994).
- ²F. Zernike, "The concept of degree of coherence and its application to optical problems," *Physica* **V**, 785–795 (1938).
- ³J. W. Goodman, *Statistical Optics* (Wiley, New York, 1985), Chap. 5.
- ⁴R. Mallart and M. Fink, "The Van Cittert–Zernike theorem in pulse-echo measurements," *J. Acoust. Soc. Am.* **90**, 2718–2727 (1991).
- ⁵M. Fink and J.-F. Cardoso, "Diffraction effects in pulse-echo measurement," *IEEE Trans. Sonics Ultrason.* **SU-31(4)**, 313–318 (1984).
- ⁶J. W. Goodman, *Introduction to Fourier Optics* (McGraw-Hill, New York, 1968), Chap. 4.
- ⁷M. Ueda and H. Ichikawa, "Analysis of an echo signal reflected from a weakly scattering volume by a discrete model of the medium," *J. Acoust. Soc. Am.* **70**, 1768–1788 (1981).
- ⁸J. G. Mottley and J. G. Miller, "Anisotropy of the ultrasonic backscatter of myocardial tissue: Theory and measurements *in vitro*," *J. Acoust. Soc. Am.* **83**, 755–767 (1988).
- ⁹T. D. Lhermitte, S. M. Handley, M. R. Holland, and J. G. Miller, "Anisotropy of the frequency-dependent ultrasonic attenuation in unidirectional graphite/epoxy composite material," 1991 IEEE Ultrasonics Symposium, p. 819.
- ¹⁰A. Derode and M. Fink, "Spatial coherence of ultrasonic speckle noise in composites," *IEEE Trans. Ultrason. Ferroelectr. Freq. Control* **40(6)**, 666–676 (1993).
- ¹¹T. Lhermitte, Thèse de 3e cycle, Université Paris 6, January 1991.
- ¹²D. Cassereau and D. Guyomar, "Reflection of an impulse spherical wave at a plane interface separating two fluids," *J. Acoust. Soc. Am.* **92**, 1706–1720 (1992).
- ¹³J. J. Giesey, P. L. Carson, D. W. Fitting, and C. R. Meyer, "Speckle reduction in pulse-echo ultrasonic imaging using a two dimensional receiving transducer array," *IEEE Trans. Ultrason. Ferroelectr. Freq. Control* **39(2)**, 167–179 (1992).

Singular points of intensity streamlines in two-dimensional sound fields

C. F. Chien

P. O. Box 30646, Causeway Bay Post Office, Hong Kong

R. V. Waterhouse

2190 Washington Street, Apt. 906, San Francisco, California 94109

(Received 18 April 1994; revised 1 August 1996; accepted 26 September 1996)

Continuing earlier work on this subject, a more rigorous discussion is given of the singular points of streamlines and the critical points of the stream function. The results for vortex and saddle points obtained earlier in piecemeal fashion and by way of examples are obtained systematically and by generally utilizing the applicable theory of differential equations and calculus. New results are also obtained. For example, a saddle point can occur when the phase of pressure and velocity differ by $\pi/2$, and in certain parts of the sound field, specifically inside a closed streamline, the number of vortex points and saddle points are related. Finally, the streamlines and singular point are considered for a discrete source: the line source. © 1997 Acoustical Society of America.

[S0001-4966(97)01302-7]

PACS numbers: 43.20.Tb, 43.20.Rz, 43.40.Rj [JEG]

INTRODUCTION

This paper is concerned with some of the properties of the isolated singular points of acoustic intensity streamlines in two-dimensional sound fields. Streamline plots have been introduced, making it easy to follow the flow of energy in the sound field.¹ For two-dimensional sound fields, equally spaced streamlines are given by evenly spaced level curves of the stream function.² Examples have been given for a number of two-dimensional sound fields: the sound fields generated by a force-excited plate,³ the sound field in a duct of square cross section,⁴ and tangential vortex modes in a rectangular room.⁵

Interesting features of the intensity streamline plots include (1) two kinds of isolated singular points: the vortex and the saddle points, (2) the behavior of the streamlines near the singular points: closed streamlines around a vortex and the two branches of a streamline crossing at a saddle point, and (3) that the streamlines through the saddle points separate the plane into regions in which the streamlines behave in different ways.

Other results have also been obtained. From examples, it has been inferred that the sound pressure goes to zero at a vortex point, and the particle velocity goes to zero at a saddle point.⁶ Using a geometric argument, it was concluded that the necessary and sufficient condition for a vortex to exist at a point is that it is an isolated extremum of the stream function.⁴

The character of the isolated singularities is important in determining the qualitative nature of the streamlines. It seems useful to study such singularities in a more systematic and unifying manner. Further, the previous papers have concentrated on specific examples. It is desirable to obtain the properties of the isolated singular points in a general manner, rather than by way of examples. This is accomplished here by describing the intensity streamline by a differential equation, an approach not previously taken. Then the relation

between the types of singular points of the differential equation of the streamline and the types of critical points of the stream function and the criteria for each type are obtained directly from elementary differential equation theory and calculus.

The criteria for each type of singular point or critical point are then used to determine the nature of singular points at isolated zeroes of pressure and velocity, and at isolated points where the phases of pressure and velocity differ by odd multiples of $\pi/2$.

With this background, some previous results can be more easily understood, and some previous omissions and minor errors are rectified. For example, it explains why only two kinds of singular points, a vortex and a saddle point, are found in the examples of streamlines plotted for two-dimensional sound fields. The conclusion that the velocity vanishes at a saddle point⁶ was a wrong generalization from examples since a saddle point can occur other than at an isolated zero of velocity. An example is used for illustration. Finally, the nature of the singular point at a discrete source, a line source, is considered.

I. INTENSITY STREAMLINES AND THE STREAM FUNCTION

For a steady two-dimensional sound field, averaging over the period $2\pi/\omega$, the x and y components of the acoustic intensity vector are given by¹

$$\begin{aligned} I_x(x,y) &= \frac{1}{2} \operatorname{Re}[p^*(x,y)v_x(x,y)], \\ I_y(x,y) &= \frac{1}{2} \operatorname{Re}[p^*(x,y)v_y(x,y)]. \end{aligned} \quad (1)$$

An energy streamline is a line which is at all points tangential to the intensity vectors. The streamline passing through the point (x,y) is tangential to the intensity vector \mathbf{I} at (x,y) and is given by

$$\frac{dy}{dx} = \frac{\mathbf{I}_y(x,y)}{\mathbf{I}_x(x,y)}. \quad (2)$$

By considering x and y as functions of a parameter t , Eq. (2) can be replaced by an equivalent autonomous system of first-order differential equations (to be abbreviated by DE),

$$\dot{x} = \mathbf{I}_x(x,y), \quad \dot{y} = \mathbf{I}_y(x,y), \quad (3)$$

where \mathbf{I}_x and \mathbf{I}_y are assumed to be smooth functions of x and y , and the $(\dot{\quad})$ indicates differentiation with respect to t . The singular points of the DE of the streamline are those points (x_0, y_0) at which the slope of the streamline is not defined, i.e., the intensity vector is the null vector,⁷

$$\mathbf{I}_{x0} = \mathbf{I}_{y0} = 0. \quad (4)$$

In a two-dimensional steady sound field, a scalar energy stream function $\psi(x,y)$ exists and is related to the intensity by²

$$\mathbf{I}_x = \frac{\partial \psi}{\partial y}, \quad \mathbf{I}_y = -\frac{\partial \psi}{\partial x}. \quad (5)$$

This follows from the fact that in the fluid, sound energy is conserved, and there are no sources or sinks, so²

$$\text{div } \mathbf{I} = 0 \quad \text{or} \quad \frac{\partial \mathbf{I}_x}{\partial x} + \frac{\partial \mathbf{I}_y}{\partial y} = 0. \quad (6)$$

The level curves of $\psi(x,y)$ represent intensity streamlines, and the amount of energy flow between streamlines is proportional to the differences in the values of the stream function.² These can easily be shown following the procedure for velocity streamlines in fluid mechanics. Note that the level curves of ψ have no directions associated with them. The directions are provided by the intensity vectors. If the level curves have constant values in arithmetic progression, the amounts of energy flowing between these level curves are equal. Evenly spaced level curves provide equally spaced streamlines.

An interior point (x_0, y_0) of the domain of the stream function is a critical point of ψ if

$$\left(\frac{\partial \psi}{\partial x}\right)_0 = 0, \quad \left(\frac{\partial \psi}{\partial y}\right)_0 = 0, \quad (7)$$

where $(\quad)_0$ denotes the value of (\quad) at (x_0, y_0) . A nondegenerate critical point can be a relative maximum, a relative minimum or a saddle point. The criteria for each type can be found in calculus texts, for example, Taylor and Mann.⁸

II. RELATION OF THE SINGULAR POINTS TO THE CRITICAL POINTS OF $\Psi(x,y)$ AND THEIR CRITERIA

Substitution of Eq. (5) in Eq. (3) gives

$$\dot{x} = \frac{\partial \psi}{\partial y}, \quad \dot{y} = -\frac{\partial \psi}{\partial x}. \quad (8)$$

It is clear that a singular point of the DE of the streamline is also a critical point of the stream function $\psi(x,y)$. Now Eq. (8) is a plane Hamiltonian system with ψ the Hamiltonian function. More can be said by the results given in Sever⁹ or

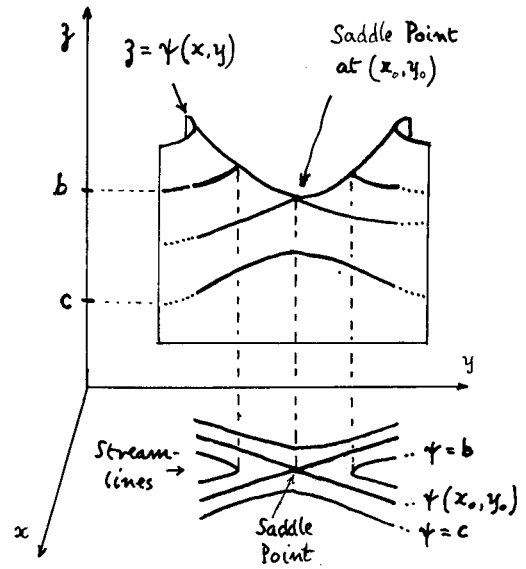


FIG. 1. Saddle point: this stationary value of the stream function is neither a maximum nor a minimum.

by a theorem in Birkhoff and Rota.¹⁰ Let J_0 be the Jacobian matrix evaluated at (x_0, y_0) ,

$$J_0 = \begin{bmatrix} \left(\frac{\partial \mathbf{I}_x}{\partial x}\right)_0 & \left(\frac{\partial \mathbf{I}_x}{\partial y}\right)_0 \\ \left(\frac{\partial \mathbf{I}_y}{\partial x}\right)_0 & \left(\frac{\partial \mathbf{I}_y}{\partial y}\right)_0 \end{bmatrix}. \quad (9)$$

Then

$$\begin{aligned} \det J_0 &= \left(\frac{\partial \mathbf{I}_x}{\partial x}\right)_0 \left(\frac{\partial \mathbf{I}_y}{\partial y}\right)_0 - \left(\frac{\partial \mathbf{I}_x}{\partial y}\right)_0 \left(\frac{\partial \mathbf{I}_y}{\partial x}\right)_0 \\ &= \left(\frac{\partial^2 \psi}{\partial x^2}\right)_0 \left(\frac{\partial^2 \psi}{\partial y^2}\right)_0 - \left(\frac{\partial^2 \psi}{\partial x \partial y}\right)_0^2. \end{aligned} \quad (10)$$

If $\det J_0 \neq 0$, the singular point is nondegenerate and a singular point of Eq. (8) can be only one of two kinds. When $\det J_0 < 0$, the singular point at (x_0, y_0) is a saddle point where $\Psi(x,y)$ has neither a maximum nor a minimum. Figure 1 shows the situation. When $\det J_0 > 0$, the singular point at (x_0, y_0) is a vortex point, where $\Psi(x,y)$ has a maximum or a minimum. Figure 2 shows the case when Ψ has a relative minimum.

The vortex and the relative extreme of $\Psi(x,y)$ occur at (x_0, y_0) simultaneously. This gives the earlier result obtained by Waterhouse *et al.* using a geometrical argument: the necessary and sufficient condition for a vortex to exist at a point is that it is an isolated extremum of the stream function.⁴ How the vortices differ at a maximum or minimum of Ψ can be easily determined from the sign of the z component of the curl of $\bar{\mathbf{I}}$ at (x_0, y_0) :

$$(\text{curl } \bar{\mathbf{I}})_{z0} = \left(\frac{\partial \mathbf{I}_y}{\partial x}\right)_0 - \left(\frac{\partial \mathbf{I}_x}{\partial y}\right)_0 = -\left[\left(\frac{\partial^2 \psi}{\partial x^2}\right)_0 + \left(\frac{\partial^2 \psi}{\partial y^2}\right)_0\right].$$

Since $\det J_0 > 0$, $(\partial^2 \psi / \partial x^2)_0$ and $(\partial^2 \psi / \partial y^2)_0$ are of the same sign and different from zero. If $(\partial^2 \psi / \partial x^2)_0 < 0$, ψ has a

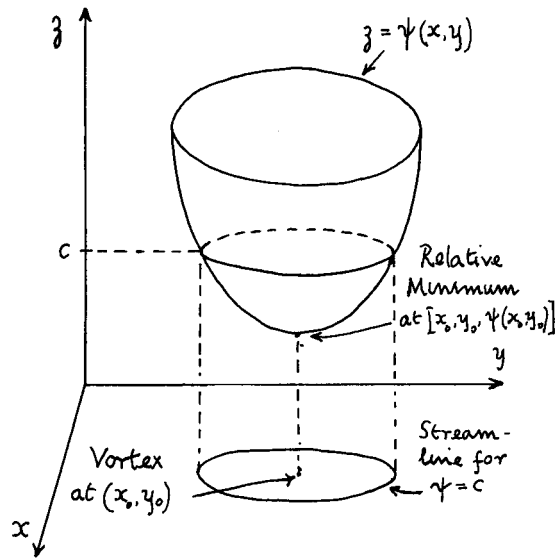


FIG. 2. Vortex and relative extremum of the stream function.

relative maximum at (x_0, y_0) ,⁸ $(\text{curl } \mathbf{I})_{z_0} > 0$, and (x_0, y_0) is a vortex with \mathbf{I} circulating counterclockwise around it. If $(\partial^2 \psi / \partial x^2)_0 > 0$, ψ has a relative minimum,⁸ $(\text{curl } \mathbf{I})_{z_0} < 0$ and (x_0, y_0) is a vortex with \mathbf{I} circulating clockwise around it.

The streamline is given by $dy/dx = \mathbf{I}_y / \mathbf{I}_x$. This is similar to that in fluid mechanics with velocity instead of intensity. A singular point is a stagnation point ($v_{x0} = v_{y0} = 0$), and in general it can be a node, a saddle, a spiral, or a vortex.¹¹ However, \mathbf{I}_x and \mathbf{I}_y are connected by $\nabla \cdot \mathbf{I} = 0$. This DE ensures the existence of a stream function, and limits the type of singular points the streamlines can have to correspond to the critical points of $\psi(x, y)$ as described above. This explains why only a vortex or a saddle are found in streamline plots.

III. RELATION OF PRESSURE AND VELOCITY TO THE CRITICAL POINTS OF ψ

It is convenient to relate the critical point of ψ and hence the singular point of the DE of the streamline directly to the acoustic variables. From Eqs. (1) and (5)

$$\begin{aligned} \frac{\partial \psi}{\partial y} &= \frac{1}{2} p |v_x| \cos(\arg p - \arg v_x) \\ &= \frac{1}{2} (p' v'_x + p'' v''_x) \\ -\frac{\partial \psi}{\partial x} &= \frac{1}{2} p |v_y| \cos(\arg p - \arg v_y) \\ &= \frac{1}{2} (p' v'_y + p'' v''_y), \end{aligned} \quad (11)$$

where $()'$ and $()''$ represent real and imaginary parts of $()$, and $| () |$ and $\arg ()$ represents the absolute value and argument of $()$. It follows that a critical point of $\psi(x, y)$ can occur at (x_0, y_0) in any one of the following situations:

- (1) $p'_0 = p''_0 = 0$;
- (2) $v'_{x0} = v''_{x0} = 0, v'_{y0} = v''_{y0} = 0$;

- (3) arguments of pressure and velocity at (x_0, y_0) differ by an odd multiple of $\pi/2$;
- (4) a combination of (2) and (3). For example, $\arg p_0 - \arg v_{x0} = \pm \pi/2$ and $v'_{y0} = v''_{y0} = 0$.

To determine the nature of the critical point in these situations, it is necessary to calculate the second partial derivatives of $\psi(z, y)$ in terms of pressure and velocity at (x_0, y_0) . For a steady two-dimensional sound field with a time factor $e^{i\omega t}$, since $\rho_0(\partial \bar{v} / \partial t) = -\text{grad } p$,

$$\omega \rho_0 v'_x = -\frac{\partial p''}{\partial x}, \quad \omega \rho_0 v''_x = \frac{\partial p'}{\partial x}$$

and

$$\omega \rho_0 v'_y = -\frac{\partial p''}{\partial y}, \quad \omega \rho_0 v''_y = \frac{\partial p'}{\partial y}.$$

Also, since the acoustic field is irrotational,

$$\frac{\partial v'_x}{\partial y} = \frac{\partial v'_y}{\partial x}, \quad \frac{\partial v''_x}{\partial y} = \frac{\partial v''_y}{\partial x}.$$

Using these and Eq. (11) gives

$$\left(\frac{\partial^2 \psi}{\partial x^2} \right) = \frac{1}{2} \rho_0 \omega (v'_x v''_y - v''_x v'_y) - \frac{1}{2} \left(p' \frac{\partial v'_y}{\partial x} + p'' \frac{\partial v''_y}{\partial x} \right), \quad (12)$$

$$\left(\frac{\partial^2 \psi}{\partial y^2} \right) = \frac{1}{2} \rho_0 \omega (v'_x v''_y - v''_x v'_y) + \frac{1}{2} \left(p' \frac{\partial v'_y}{\partial x} + p'' \frac{\partial v''_y}{\partial x} \right), \quad (13)$$

$$\left(\frac{\partial^2 \psi}{\partial x \partial y} \right) = -\frac{1}{2} \left(p' \frac{\partial v'_y}{\partial y} + p'' \frac{\partial v''_y}{\partial y} \right), \quad (14)$$

$$\begin{aligned} \left(\frac{\partial^2 \psi}{\partial x^2} \right) \left(\frac{\partial^2 \psi}{\partial y^2} \right) - \left(\frac{\partial^2 \psi}{\partial x \partial y} \right)^2 &= \frac{1}{4} \rho_0^2 \omega^2 (v'_x v''_y - v''_x v'_y)^2 \\ &\quad - \frac{1}{4} \left(p' \frac{\partial v'_x}{\partial y} + p'' \frac{\partial v''_x}{\partial y} \right)^2 \\ &\quad - \frac{1}{4} \left(p' \frac{\partial v'_y}{\partial y} + p'' \frac{\partial v''_y}{\partial y} \right)^2. \end{aligned} \quad (15)$$

The z component of $\text{curl } \bar{\mathbf{I}}$ is given by

$$\begin{aligned} (\text{curl } \mathbf{I})_z &= \frac{\partial \mathbf{I}_y}{\partial x} - \frac{\partial \mathbf{I}_x}{\partial y} \\ &= -\left(\frac{\partial^2 \psi}{\partial x^2} + \frac{\partial^2 \psi}{\partial y^2} \right) \\ &= -\rho_0 \omega (v'_x v''_y - v''_x v'_y). \end{aligned} \quad (16)$$

The values of these expressions at (x_0, y_0) will be evaluated for the different situations. It is assumed that

$$\left(\frac{\partial^2 \psi}{\partial x^2} \right)_0 \left(\frac{\partial^2 \psi}{\partial y^2} \right)_0 - \left(\frac{\partial^2 \psi}{\partial x \partial y} \right)_0^2 \neq 0.$$

A. Isolated zero of pressure

Suppose an isolated zero of pressure occurs at (x_0, y_0) . Then by the assumption above, Eq. (15) gives

$$\begin{aligned} & \left(\frac{\partial^2 \psi}{\partial x^2} \right)_0 \left(\frac{\partial^2 \psi}{\partial y^2} \right)_0 - \left(\frac{\partial^2 \psi}{\partial x \partial y} \right)_0^2 \\ & = \frac{1}{4} \omega^2 \rho_0^2 (\nu'_{x0} \nu''_{y0} - \nu''_{x0} \nu'_{y0})^2 > 0. \end{aligned}$$

If at (x_0, y_0) , by Eq. (12),

$$\left(\frac{\partial^2 \psi}{\partial x^2} \right)_0 = \frac{1}{2} \omega \rho_0 (\nu'_{x0} \nu''_{y0} - \nu''_{x0} \nu'_{y0}) < 0, \quad (17)$$

then by the criteria in Sec. II, ψ has a relative maximum, and an energy vortex exists with $\bar{\mathbf{I}}$ circulating counterclockwise. If

$$\left(\frac{\partial^2 \psi}{\partial x^2} \right)_0 = \frac{1}{2} \omega \rho_0 (\nu'_{x0} \nu''_{y0} - \nu''_{x0} \nu'_{y0}) > 0, \quad (18)$$

then ψ has a relative minimum, and an energy vortex exists with $\bar{\mathbf{I}}$ circulating clockwise. At this critical point, by Eq. (16)

$$(\text{curl } \bar{\mathbf{I}})_{z0} = -\omega \rho_0 (\nu'_{x0} \nu''_{y0} - \nu''_{x0} \nu'_{y0}) \neq 0. \quad (19)$$

The converse, that the pressure vanishes at a vortex can also be shown to be true. The fact that a vortex is a singular point round which the intensity vector circulates, gives for a vortex at (x_0, y_0) ,

$$\mathbf{I}_{x0} = \left(\frac{\partial \psi}{\partial y} \right)_0 = 0, \quad \mathbf{I}_{y0} = -\left(\frac{\partial \psi}{\partial x} \right)_0 = 0, \quad (20)$$

and

$$(\text{curl } \bar{\mathbf{I}})_{z0} \neq 0. \quad (21)$$

Substituting Eq. (16) in Eq. (21) gives

$$\omega \rho_0 (\nu'_{x0} \nu''_{y0} - \nu''_{x0} \nu'_{y0}) \neq 0$$

or

$$\left| \begin{array}{l} \nu'_{x0} \nu''_{x0} \\ \nu'_{y0} \nu''_{y0} \end{array} \right| \neq 0.$$

Substituting Eq. (11) in Eq. (20) gives

$$\nu'_{x0} p'_0 + \nu''_{x0} p''_0 = 0, \quad \nu'_{y0} p'_0 + \nu''_{y0} p''_0 = 0.$$

Since the matrix of coefficients of this homogeneous set of linear algebraic equations for p'_0 and p''_0 is nonsingular, the unique solution is $p'_0 = p''_0 = 0$.

B. Isolated zero of velocity

Suppose an isolated zero of velocity occurs at (x_0, y_0) . Then Eq. (15) gives

$$\begin{aligned} & \left(\frac{\partial^2 \psi}{\partial x^2} \right)_0 \left(\frac{\partial^2 \psi}{\partial y^2} \right)_0 - \left(\frac{\partial^2 \psi}{\partial x \partial y} \right)_0^2 \\ & = -\frac{1}{4} \left\{ \left[p'_0 \left(\frac{\partial \nu'_y}{\partial x} \right)_0 + p''_0 \left(\frac{\partial \nu''_y}{\partial x} \right)_0 \right]^2 \right. \\ & \quad \left. + \left[p'_0 \left(\frac{\partial \nu'_y}{\partial y} \right)_0 + p''_0 \left(\frac{\partial \nu''_y}{\partial y} \right)_0 \right]^2 \right\} < 0. \end{aligned}$$

Hence there is a saddle point at (x_0, y_0) . At this critical point, Eq. (16) gives

$$(\text{curl } \bar{\mathbf{I}})_{z0} = -\left[\left(\frac{\partial^2 \psi}{\partial x^2} \right)_0 + \left(\frac{\partial^2 \psi}{\partial y^2} \right)_0 \right] = 0. \quad (22)$$

C. Isolated point at which the arguments of pressure and velocity differ by an odd multiple of $\pi/2$

Several different situations can be considered. (1) p_0 is real and ν_{x0}, ν_{y0} are imaginary. (2) p_0 is imaginary and ν_{x0}, ν_{y0} are real. (3) Real and imaginary parts of p_0 and ν_{x0}, ν_{y0} are nonzero. Since

$$\begin{aligned} \arg p_0 - \arg \nu_0 &= \tan^{-1} \frac{p''_0}{p'_0} - \tan^{-1} \frac{\nu''_0}{\nu'_0} \\ &= \tan^{-1} \frac{p''_0 \nu'_0 - p'_0 \nu''_0}{p''_0 \nu''_0 + p'_0 \nu'_0}. \end{aligned}$$

$\arg p_0 - \arg \nu_0 = \pm \text{odd multiple of } \pi/2$ would just mean

$$p'_0 \nu'_{x0} + p''_0 \nu''_{x0} = 0, \quad p'_0 \nu'_{y0} + p''_0 \nu''_{y0} = 0,$$

or

$$\frac{\nu''_{x0}}{\nu'_{x0}} = \frac{\nu''_{y0}}{\nu'_{y0}} = -\frac{p'_0}{p''_0}.$$

Hence in any of the three situations

$$\nu'_{x0} \nu''_{y0} - \nu''_{x0} \nu'_{y0} = 0,$$

and Eq. (15) gives

$$\begin{aligned} & \left(\frac{\partial^2 \psi}{\partial x^2} \right)_0 \left(\frac{\partial^2 \psi}{\partial y^2} \right)_0 - \left(\frac{\partial^2 \psi}{\partial x \partial y} \right)_0^2 \\ & = -\frac{1}{4} \left\{ \left[p'_0 \left(\frac{\partial \nu'_x}{\partial y} \right)_0 + p''_0 \left(\frac{\partial \nu''_x}{\partial y} \right)_0 \right]^2 \right. \\ & \quad \left. + \left[p'_0 \left(\frac{\partial \nu'_y}{\partial y} \right)_0 + p''_0 \left(\frac{\partial \nu''_y}{\partial y} \right)_0 \right]^2 \right\} < 0. \end{aligned}$$

Here, (x_0, y_0) is a saddle point. At this critical point, Eq. (16) gives

$$(\text{curl } \bar{\mathbf{I}})_{z0} = - \left[\left(\frac{\partial^2 \psi}{\partial x^2} \right)_0 + \left(\frac{\partial^2 \psi}{\partial y^2} \right)_0 \right] = 0. \quad (23)$$

D. A combination of the two previous cases

For example, $v'_{y0} = v''_{y0} = 0$, $[(\partial\psi/\partial x)_0 = 0]$ and $p''_0 = v'_{x0} = 0$ while $p'_0 \neq 0$, $v''_{x0} \neq 0$, so that $\arg p_0 - \arg v_{x0} = \pm \pi/2$ $[(\partial\psi/\partial y)_0 = 0]$. At such a critical point, by Eq. (15),

$$\begin{aligned} & \left(\frac{\partial^2 \psi}{\partial x^2} \right)_0 \left(\frac{\partial^2 \psi}{\partial y^2} \right)_0 - \left(\frac{\partial^2 \psi}{\partial x \partial y} \right)_0^2 \\ &= -\frac{1}{4} p'_0 \left[\left(\frac{\partial v'_x}{\partial y} \right)_0^2 + \left(\frac{\partial v'_y}{\partial y} \right)_0^2 \right] < 0. \end{aligned}$$

Hence, there is a saddle point at (x_0, y_0) . Equation (16) gives

$$(\text{curl } \bar{\mathbf{I}})_{z0} = - \left[\left(\frac{\partial^2 \psi}{\partial x^2} \right)_0 + \left(\frac{\partial^2 \psi}{\partial y^2} \right)_0 \right] = 0. \quad (24)$$

E. Streamlines at a saddle point

The procedure for velocity streamlines in hydrodynamics¹² can be followed and specialized to the present case. Since $(\partial\psi/\partial x)_0 = (\partial\psi/\partial y)_0 = 0$ near (x_0, y_0) , by Taylor series expansion,

$$\begin{aligned} \psi = \psi_0 + \frac{1}{2} & \left[\left(\frac{\partial^2 \psi}{\partial x^2} \right)_0 (x-x_0)^2 + 2 \left(\frac{\partial^2 \psi}{\partial x \partial y} \right)_0 (x-x_0) \right. \\ & \left. \times (y-y_0) + \left(\frac{\partial^2 \psi}{\partial y^2} \right)_0 (y-y_0)^2 \right]. \end{aligned}$$

Then $\psi = \psi_0$ is given by

$$a(x-x_0)^2 + 2b(x-x_0)(y-y_0) + c(y-y_0)^2 = 0, \quad (25)$$

where

$$a = \left(\frac{\partial^2 \psi}{\partial x^2} \right)_0, \quad b = \left(\frac{\partial^2 \psi}{\partial x \partial y} \right)_0, \quad c = \left(\frac{\partial^2 \psi}{\partial y^2} \right)_0.$$

In all situations where a saddle point can occur, as described in Secs. B, C, and D, $c = -a$ by Eqs. (22), (23), and (24). The cross term can be eliminated by transforming to x' , y' coordinate: translating the origin to (x_0, y_0) and rotating an angle α from the positive x axis,

$$x - x_0 = x' \cos \alpha - y' \sin \alpha, \quad (26)$$

$$y - y_0 = x' \sin \alpha + y' \cos \alpha,$$

where α is given by

$$\tan 2\alpha = \frac{2b}{a-c} = \frac{b}{a}. \quad (27)$$

Substituting Eq. (26) in Eq. (25) gives

$$x'^2 - y'^2 = 0.$$

So $x' - y' = 0$ or $x' + y' = 0$. This shows that the two branches of the streamline at the saddle point cross at right angles.

F. Summary of results

A singular point is a vortex if and only if it is an isolated zero of pressure. The vorticity is nonzero. A singular point is a saddle point if it is an isolated zero of velocity, an isolated point at which the phases of velocity and pressure differ by odd multiples of $\pi/2$ or a combination of the previous two situations. The vorticity is zero. For these cases, at the saddle point, two branches of the streamline cross at right angles. It is clear that the previous generalization from examples that the velocity vanishes at a saddle point⁶ is not necessarily true.

IV. THE INDEX OF A CLOSED CURVE

The notion of the index of a singular point and the index of a closed curve with respect to the intensity field can be useful. Relevant material is summarized from Stoker.⁷ Similar material can be found in texts on differential equation.¹⁰

Let C be a simple closed curve not necessarily a streamline in the x, y plane, and assume that C does not pass through any singular point of the system in Eq. (3). At each intersection of C with a streamline, then $\bar{\mathbf{I}}(x, y) = \mathbf{I}_x(x, y)\bar{i} + \mathbf{I}_y(x, y)\bar{j}$ is a nonzero vector and has a definite direction. The angle made by the field vector with the horizontal is $\theta = \arctan(\mathbf{I}_y(x, y)/\mathbf{I}_x(x, y))$. On making one complete circuit around C in the counterclockwise direction the angle θ changes by an amount $2\pi j$, j being a positive or negative integer (or zero) since the field vector returns to its original position after completing the circuit. For example, $j = -1$ means that $\bar{\mathbf{I}}$ makes one complete revolution in the clockwise sense when C is traversed once counterclockwise.

If C is small, only one singular point is enclosed by it, and j is the index of the singular point. The index has the same value for every curve C enclosing a given singular point and no others. A regular point has the index 0, a vortex has the index +1, and a saddle point has the index -1.

If C encloses more than one singular point, j is the index of the closed curve. The index of a closed curve containing a finite number of singular points is equal to the algebraic sum of their indices. The sum of indices of all singularities inside any closed streamline free of singularities is +1. It follows that there must be at least one vortex inside such a closed streamline. Furthermore the number of saddle points must be one less than the number of vortices.

How some of these can be applied will be illustrated by an example in a following section.

V. EXAMPLE

An example is taken from Ref. 5 for a pair of tangential modes with the same frequency in phase quadrature. The results of Sec. II can be applied using intensity or the stream function. It is more convenient to apply the results of Sec. III to obtain information directly from pressure and velocity as

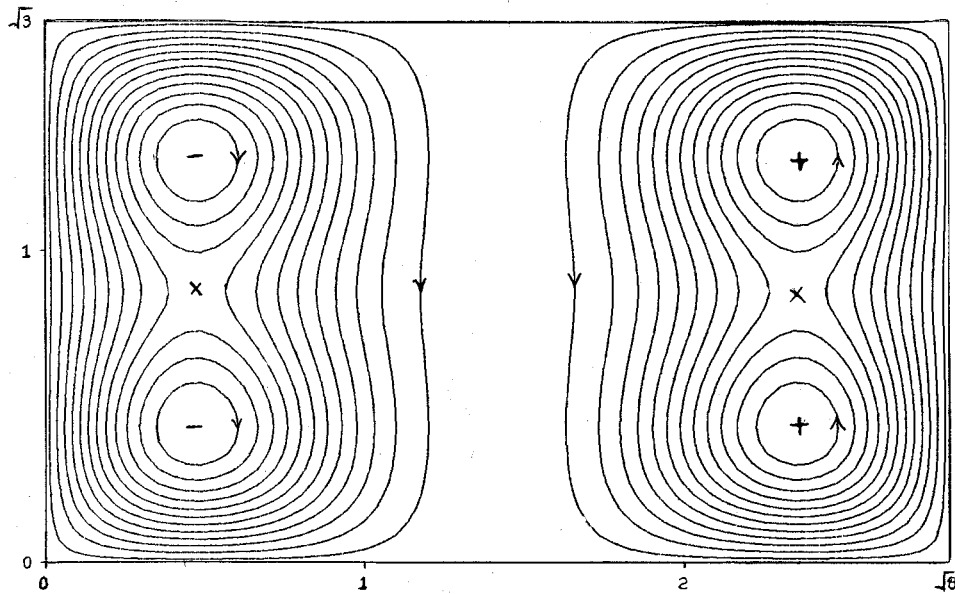


FIG. 3. Energy streamlines for the (3,1), (1,2) tangential modes across a rectangular duct. There are four vortex points and two saddle points. The + and - signs show maxima and minima of the stream function.

this example will show. Equal energy streamlines are shown in Fig. 3 which corrects the figure in Ref. 5. By I_x and I_y given below, it is easy to see the directions on the streamlines should be reversed and the relative maxima and minima of ψ interchanged.

The velocity potential is given by

$$\phi = \cos \frac{3\pi x}{\sqrt{8}} \cos \frac{\pi y}{\sqrt{3}} + i \cos \frac{\pi x}{\sqrt{8}} \cos \frac{2\pi y}{\sqrt{3}}.$$

Then it follows that

$$p = \omega \rho_0 \left(\cos \frac{\pi x}{\sqrt{8}} \cos \frac{2\pi y}{\sqrt{3}} - i \cos \frac{3\pi x}{\sqrt{8}} \cos \frac{\pi y}{\sqrt{3}} \right),$$

$$v_x = -\frac{3\pi}{\sqrt{8}} \sin \frac{3\pi x}{\sqrt{8}} \cos \frac{\pi y}{\sqrt{3}} - i \frac{\pi}{\sqrt{8}} \sin \frac{\pi x}{\sqrt{8}} \cos \frac{2\pi y}{\sqrt{3}},$$

$$v_y = -\frac{\pi}{\sqrt{3}} \cos \frac{3\pi x}{\sqrt{8}} \sin \frac{\pi y}{\sqrt{3}} - i \frac{2\pi}{\sqrt{3}} \cos \frac{\pi x}{\sqrt{8}} \sin \frac{2\pi y}{\sqrt{3}}.$$

Further,

$$\frac{2I_x}{\omega \rho_0} = -\frac{3\pi}{\sqrt{8}} \sin \frac{3\pi x}{\sqrt{8}} \cos \frac{\pi y}{\sqrt{3}} \cos \frac{2\pi y}{\sqrt{3}}$$

$$+ \frac{\pi}{\sqrt{8}} \sin \frac{\pi x}{\sqrt{8}} \cos \frac{3\pi x}{\sqrt{8}} \cos \frac{\pi y}{\sqrt{3}} \cos \frac{2\pi y}{\sqrt{3}}$$

$$= -\frac{\pi}{2\sqrt{8}} \left(\cos \frac{3\pi y}{\sqrt{3}} + \cos \frac{\pi y}{\sqrt{3}} \right)$$

$$\times \left(\sin \frac{4\pi x}{\sqrt{8}} + 2 \sin \frac{2\pi x}{\sqrt{8}} \right),$$

$$\frac{2I_y}{\omega \rho_0} = \frac{-\pi}{\sqrt{3}} \cos \frac{3\pi x}{\sqrt{8}} \cos \frac{\pi x}{\sqrt{8}} \sin \frac{\pi y}{\sqrt{3}} \cos \frac{2\pi y}{\sqrt{3}}$$

$$+ \frac{2\pi}{\sqrt{3}} \cos \frac{\pi x}{\sqrt{8}} \cos \frac{3\pi x}{\sqrt{8}} \cos \frac{\pi y}{\sqrt{3}} \sin \frac{2\pi y}{\sqrt{3}}$$

$$= \frac{\pi}{4\sqrt{3}} \left(\cos \frac{4\pi x}{\sqrt{8}} + \cos \frac{2\pi x}{\sqrt{8}} \right)$$

$$\times \left(\sin \frac{3\pi y}{\sqrt{3}} + 3 \sin \frac{\pi y}{\sqrt{3}} \right)$$

and

$$\psi = -\frac{\rho_0 \omega}{4\sqrt{24}} \left(\sin \frac{3\pi y}{\sqrt{3}} + 3 \sin \frac{\pi y}{\sqrt{3}} \right)$$

$$\times \left(\sin \frac{4\pi x}{\sqrt{8}} + 2 \sin \frac{2\pi x}{\sqrt{8}} \right).$$

By taking derivatives it is easy to show that ψ gives the correct I_x and I_y .

Isolated zeros of pressure occur at $(\sqrt{8}/6, \sqrt{3}/4)$ $(\sqrt{8}/6, 3\sqrt{3}/4)$ $(5\sqrt{8}/6, \sqrt{3}/4)$, and $(5\sqrt{8}/6, 3\sqrt{3}/4)$. At each of the first two points, $\frac{1}{2}\rho_0\omega(v'_{x0}v''_{y0} - v''_{x0}v'_{y0}) = (3\pi^2/8)\rho_0\omega > 0$ and there is a vortex with \mathbf{I} circulating clockwise. At each of the last two points, $\frac{1}{2}\rho_0\omega(v'_{x0}v''_{y0} - v''_{x0}v'_{y0}) = -(3\pi^2/8)\rho_0\omega < 0$ and there is a vortex with \mathbf{I} circulating counterclockwise.

$(\sqrt{8}/6, \sqrt{3}/2)$ and $(5\sqrt{8}/6, \sqrt{3}/2)$ are indicated by x in Fig. 3. At each of these two points, $v'_{y0} = v''_{y0} = 0$, $v'_{x0} = 0$, $v''_{x0} = \pi/2\sqrt{8}$, and $p'_0 = 0$. At the first, $p'_0 = -(\sqrt{3}/2)\rho_0\omega$ while at the second, $p'_0 = (\sqrt{3}/2)\rho_0\omega$. $I_{y0} = -(\partial\psi/\partial x)_0 = 0$ as a result of $v'_{y0} = v''_{y0} = 0$ while $I_{x0} = (\partial\psi/\partial y)_0 = 0$ because the phases of pressure and velocity differ by $\pi/2$. These are saddle points as discussed in part D of Sec. III. They are not

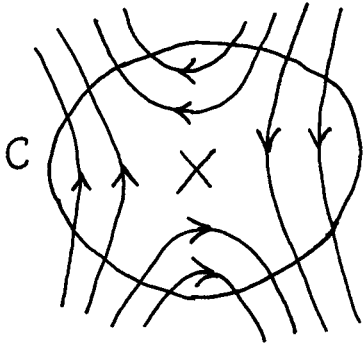


FIG. 4. Index of singular point shown by cross.

zeros of velocity and have not been noted before. At each of these saddle points, the development in part E of Sec. III can be specialized with $\tan 2\alpha=0$ and $\alpha=0$. The two branches of the streamline through (x_0, y_0) near (x_0, y_0) are given by $y - y_0 = x - x_0$ and $y - y_0 = -(x - x_0)$, and hence cross at right angle near the saddle point, making angles of $\pi/4$ and $3\pi/4$ with the x axis. The streamlines at the two saddle points were not plotted in Fig. 3, but the nearby streamlines clearly indicate the correctness of the above description.

Alternatively, critical points of ψ occur at $(\sqrt{8}/6, \sqrt{3}/4)$, $(\sqrt{8}/6, 3\sqrt{3}/4)$, $(5\sqrt{8}/6, \sqrt{3}/4)$, and $(5\sqrt{8}/6, 3\sqrt{3}/4)$. At each of the first two points,

$$\left(\frac{\partial^2 \psi}{\partial x^2}\right)_0 \left(\frac{\partial^2 \psi}{\partial y^2}\right)_0 - \left(\frac{\partial^2 \psi}{\partial x \partial y}\right)_0^2 = \left(\frac{3\pi^2}{8} \rho_0 \omega\right)^2 > 0,$$

$$\left(\frac{\partial^2 \psi}{\partial x^2}\right)_0 = \frac{3\pi^2}{8} \rho_0 \omega > 0,$$

and ψ has a relative minimum. At each of the last two points,

$$\left(\frac{\partial^2 \psi}{\partial x^2}\right)_0 \left(\frac{\partial^2 \psi}{\partial y^2}\right)_0 - \left(\frac{\partial^2 \psi}{\partial x \partial y}\right)_0^2 = \left(-\frac{3\pi^2}{8} \rho_0 \omega\right)^2 > 0,$$

$$\left(\frac{\partial^2 \psi}{\partial x^2}\right)_0 = -\frac{3\pi^2}{8} \rho_0 \omega < 0,$$

and ψ has a relative maximum. Critical points of ψ occur also at $(\sqrt{8}/6, \sqrt{3}/2)$ and $(5\sqrt{8}/6, \sqrt{3}/2)$. At each of these two points,

$$\left(\frac{\partial^2 \psi}{\partial x^2}\right)_0 \left(\frac{\partial^2 \psi}{\partial y^2}\right)_0 - \left(\frac{\partial^2 \psi}{\partial x \partial y}\right)_0^2 = -\left(\frac{3\pi^2}{8\sqrt{2}} \rho_0 \omega\right)^2 < 0$$

and ψ has neither a maximum nor a minimum. By applying the results from Sec. II, the same conclusion on the type of singular points can be reached as before.

It is also easy to show the points indicated by X in Fig. 3 are saddle points by the index of a singular point or the index of a closed curve. Figure 4 shows a simple closed curve C surrounding the point indicated by X. When C is traversed once counterclockwise, the field vector makes one complete revolution in the clockwise sense, $j = -1$. The singular point is a saddle point. Alternatively, inside a closed streamline such as the outermost one on the

left side in Fig. 3, the number of saddle points must be one less than the number of vortices. Since there are two vortices indicated by the minus signs, the singularity indicated by the cross is a saddle point.

VI. SINGULAR POINT FOR A LINE SOURCE

The previous sections considered the singular point at which the slope of the intensity streamline is not defined in a sound field where \mathbf{I} is continuous and $\nabla \cdot \bar{\mathbf{I}} = 0$. Such a singular point occurs at a point of zero intensity. This section considers the nature of the singular point of the streamlines at the position of a simple discrete source, a line source of cylindrical waves. The results are obvious but show how the singular point of the streamlines can occur as a node at the position of a discrete source at which the direction $\bar{\mathbf{I}}$ is indeterminate. It is convenient to use the plane polar coordinates, r and θ , which are related to the rectangular coordinates, x and y , by

$$x = r \cos \theta, \quad y = r \sin \theta$$

and

$$r = (x^2 + y^2)^{1/2}, \quad \theta = \tan^{-1} \frac{y}{x}.$$

For a line source at the origin, the acoustic pressure with a time factor $e^{i\omega t}$ is given by (p. 58, Ref. 13)

$$p = AH_0^{(2)}(kr),$$

where $H_n^{(2)}(\)$ is an n th order Hankel function of the second kind. It follows that

$$v_r = -\frac{iA}{\rho c} H_1^{(2)}(kr), \quad v_\theta = 0$$

and

$$\mathbf{I}_r = \frac{1A^2}{\pi \rho c k r}, \quad \mathbf{I}_\theta = 0.$$

Except at $r=0$, the intensity vectors at all positions are in the r direction. The intensity streamlines are straight lines directed away from the line source. If it had been a sink at the origin, the directions on the streamlines would be reversed and directed toward the origin. \mathbf{I}_r is singular at the origin, $\nabla \cdot \bar{\mathbf{I}} = 0$ is satisfied except at the origin.

The relation between ψ and $\bar{\mathbf{I}}$ is

$$\mathbf{I}_r = \frac{1}{r} \frac{\partial \psi}{\partial \theta}, \quad \mathbf{I}_\theta = -\frac{\partial \psi}{\partial r}.$$

For a line source at the origin, the solution is

$$\psi = \frac{1A^2}{\pi \rho c k} \theta.$$

If ψ is to be a properly defined function on the plane, ψ must have a single value at each point, and θ is restricted, for example, by $-\pi < \theta \leq \pi$. Each stream function can easily be checked to give the correct intensity components by differentiation. The level curves of ψ for either kind of source are given by $\theta = \text{constant}$. Since streamlines with different values of ψ meet at the origin, it is a singularity of the energy flow.

It is clear that the streamline at any point not the origin, is described by the DE

$$\frac{dy}{dx} = \frac{y}{x}$$

or by its integral curve

$$y = cx,$$

where c is any arbitrary constant. At the origin, the field of directions is no longer uniquely defined. This is connected with the fact that the origin is a singular point of the DE and there are an infinite number of streamlines from the source. The singular point of the DE at the origin is a node (p. 38, Ref. 7). The index of this singular point can be found easily following the discussion in Sec. IV. By considering a closed curve C surrounding the origin, it is easy to see that the intensity vector makes one complete revolution in the counterclockwise sense when C is traversed once counterclockwise. The index is $j=1$ (p. 46, Ref. 7).

¹R. V. Waterhouse, T. W. Yates, D. Feit, and Y. N. Lin, "Energy streamlines of a sound source," J. Acoust. Soc. Am. **78**, 758–762 (1985).

²R. V. Waterhouse and D. Feit, "Equal energy streamlines," J. Acoust. Soc. Am. **80**, 681–684 (1986).

³"Proceedings of the 2nd International Congress on Acoustic Intensity," held at Senlis, France, 1985, pp. 79–84.

⁴R. V. Waterhouse, D. G. Crighton, and J. E. Ffowcs-Williams, "A criterion for an energy vortex in a sound field," J. Acoust. Soc. Am. **81**, 1323–1326 (1987).

⁵R. V. Waterhouse, "Vortex modes in rooms," J. Acoust. Soc. Am. **82**, 1782–1791 (1987).

⁶E. A. Skelton and R. V. Waterhouse, "Energy streamlines for a spherical shell scattering plane waves," J. Acoust. Soc. Am. **80**, 1473–1478 (1986).

⁷J. J. Stoker, *Nonlinear Vibrations* (Interscience–Wiley, New York, 1950), Chap. 3.

⁸A. E. Taylor and W. R. Mann, *Advanced Calculus* (Wiley, New York, 1983).

⁹M. Sever, *Ordinary Differential Equations* (Boole, Dublin, Ireland, 1987), pp. 103–109.

¹⁰G. Birkhoff and G. Rota, *Ordinary Differential Equations* (Wiley, New York, 1989), 4th ed., pp. 385–386.

¹¹K. Karamcheti, *Principles of Ideal—Fluid Aerodynamics* (Krieger, Huntington, NY, 1980), pp. 172–174.

¹²L. M. Milne-Thompson, *Theoretical Hydrodynamics* (MacMillan, New York, 1965), 4th ed., pp. 115–116.

¹³A. P. Dowling and J. E. Ffowcs Williams, *Sound and Sources of Sound* (Ellis Horwood, London, 1983).

Acoustic radiation force on a spherical particle in a viscous heat-conducting fluid. I. General formula

Alexander A. Doinikov

Institute of Nuclear Problems, Bobruiskaya 11, 220050 Minsk, Byelorussia

(Received 26 January 1996; accepted for publication 20 September 1996)

The acoustic radiation force exerted by an axisymmetric sound field on a spherical particle is calculated assuming that the surrounding fluid is viscous and heat conducting. The incident sound field pressure amplitude is supposed to be small enough such that nonlinear effects like generation of subharmonics do not occur. No restrictions are imposed on the particle size, which means that the particle can be of an arbitrary radius with respect to the sound, viscous, and thermal wavelengths in the surrounding fluid. The obtained formula for the radiation force is general in that it is applicable to first, any axisymmetric sound field, such as a plane, traveling or standing wave and a spherical wave, and, second, any of the following types of dispersed particles: a gas bubble, a liquid drop, a rigid or elastic sphere, a spherical shell, etc. The force is expressed in terms of the linear scattering coefficients to be determined by the particle type. Thus, to obtain the force on a specific particle the problem of linear scattering for that particle must be solved. Problems of this sort are known not to be mathematically difficult, but can be laborious enough if a particle at issue has a complicated internal structure. The radiation forces on particles of most interest are examined in papers that follow [J. Acoust. Soc. Am. **101**, 722–740 (1997)]. © 1997 Acoustical Society of America.

[S0001-4966(97)00602-4]

PACS numbers: 43.25.Qp [MAB]

INTRODUCTION

The time-averaged force exerted by a sound field on a spherical inclusion suspended in a fluid has been the subject of a great deal of theoretical, numerical, and experimental investigations,^{1–13} detailed reviews of which and also discussion of practical applications of the acoustic radiation forces can be found, for example, in Refs. 14–18. In most of the theoretical works the viscosity and heat conduction of the surrounding fluid are assumed to be negligible. Results obtained in those few works in which attempts have been made to examine effects of dissipative mechanisms on radiation forces (for review, see Refs. 19–21) cannot be considered to be satisfactory from the standpoint of their generality, rigor, and completeness, but they predict new interesting phenomena. This fact prompted the present author to undertake a study of his own, the strategic aim of which is to obtain an analytical expression for the acoustic radiation force on a spherical particle in a viscous heat-conducting fluid under minimum restrictions imposed on parameters of this task. In previous papers the present author^{19,20} derived an expression for the radiation force exerted by an axisymmetric sound field on a spherical, rigid or compressible, particle immersed in a viscous, but not heat-conducting, fluid (liquid or gas). It has been shown that in many cases of interest viscous effects can drastically change the radiation force, so that the classic theory developed for perfect fluids becomes quite inapplicable.

The present paper is the first part of a study that aims to take into account both the viscosity of the surrounding fluid and its heat conduction. In this paper, by extending an approach applied in the previous papers by the present author,^{19,20} a general formula is deduced for the acoustic radiation force exerted by an axisymmetric sound field on a

spherical particle suspended in a viscous heat-conducting fluid. It is supposed that the particle radius is arbitrary with respect to the sound, viscous, and thermal wavelengths in the surrounding fluid which are, in turn, arbitrary relative to one another. The fluid outside the particle is considered to be either a liquid or a gas. As regards the medium inside the particle, it is assumed that the particle may be a gas bubble, a liquid drop, a rigid or elastic sphere, a spherical shell, etc. In other words, the internal structure of the particle is assumed to be arbitrary as well. The general formula for the radiation force is expressed in terms of linear scattering coefficients to be determined by the type of a dispersed particle. Thus, to apply this formula to a given particle it is necessary to solve the problem of linear scattering for that particle and then substitute explicit expressions for the linear scattering coefficients into the general formula. Problems of this sort are not difficult mathematically yet can be laborious if the internal structure of a particle under consideration is complicated as is the case with a spherical shell or a gas bubble coated by a thin liquid layer immiscible in the outer liquid. The radiation forces on dispersed particles of most interest (rigid spheres, gas bubbles, and liquid drops) will be dealt with in detail in papers that follow.

I. PROBLEM FORMULATION

The motion of a viscous heat-conducting fluid is known to be described by the following tensor equations:²²

$$\frac{\partial}{\partial t} (\rho v_i) = \frac{\partial}{\partial x_k} (\sigma_{ik} - \rho v_i v_k), \quad (1)$$

$$\frac{\partial \rho}{\partial t} + \frac{\partial}{\partial x_i} (\rho v_i) = 0, \quad (2)$$

$$\rho T \left(\frac{\partial s}{\partial t} + v_i \frac{\partial s}{\partial x_i} \right) = (\sigma_{ik} + p \delta_{ik}) \frac{\partial v_i}{\partial x_k} + \frac{\partial}{\partial x_i} \left(\kappa \frac{\partial T}{\partial x_i} \right), \quad (3)$$

in which σ_{ik} is the stress tensor, given by

$$\sigma_{ik} = -p \delta_{ik} + \eta \left(\frac{\partial v_i}{\partial x_k} + \frac{\partial v_k}{\partial x_i} - \frac{2}{3} \frac{\partial v_j}{\partial x_j} \delta_{ik} \right) + \xi \frac{\partial v_j}{\partial x_j} \delta_{ik}, \quad (4)$$

\mathbf{v} is the fluid velocity, ρ is the fluid density, T is the absolute temperature, s is the specific entropy, p is the fluid pressure, κ is the thermal conductivity, η is the shear viscosity, ξ is the bulk viscosity, δ_{ik} is the Kronecker delta, and as usual summation over repeated indices is implied.

The set of tensor equations (1)–(3) contains five scalar equations in seven unknowns. Therefore it is supplemented with two thermodynamic relations:

$$d\rho = (\gamma/c^2) dp - \alpha \rho dT, \quad (5)$$

$$ds = (c_p/T) dT - (\alpha/\rho) dp, \quad (6)$$

where γ is the ratio of specific heats, c is the sound speed, c_p is the specific heat at constant pressure, and α is the volume thermal expansion coefficient of the fluid defined as $\alpha = -(1/\rho)(\partial\rho/\partial T)_p$.

Let us consider a spherical particle immersed in a fluid whose motion is governed by Eqs. (1)–(6). Suppose that the particle is subject to an axisymmetric acoustic field, the pressure amplitude of this field being so small that nonlinear effects such as the erratic dancing of pulsating gas bubbles, generation of subharmonics, etc.,^{23–25} do not occur. Then, as shown in Refs. 19 and 20, the acoustic radiation force on the particle can be represented as follows:

$$F_i = \int_{S_0} \langle \sigma_{ik}^{(2)} - \rho_0 v_i^{(1)} v_k^{(1)} \rangle n_k dS_0, \quad (7)$$

where S_0 is the particle surface at rest, ρ_0 is the equilibrium fluid density, \mathbf{n} is the outward normal to S_0 , the superscript (j) ($j=1,2$) is used to denote quantities of j th order in the incident wave amplitude, and $\langle \rangle$ means an average over the incident wave period.

In a perfect fluid, the tensor $\langle \sigma_{ik}^{(2)} \rangle$ is known to be expressed in terms of quantities of first order only, which considerably expedites calculating the radiation force. In order to find this tensor in an imperfect fluid, one must solve the time-averaged equations of the fluid motion with accuracy up to the second-order terms in the incident wave amplitude. Thus, to calculate the acoustic radiation force in a viscous heat-conducting fluid, we must first solve Eqs. (1)–(6) in the linear approximation and then, after having averaged them over time, find their solutions in the second approximation. That is what we are going to do in the following two sections.

II. SOLUTION OF THE LINEARIZED EQUATIONS

After linearizing and eliminating $\rho^{(1)}$ and $s^{(1)}$ by use of Eqs. (5) and (6), Eqs. (1)–(3) become

$$\rho_0 \frac{\partial \mathbf{v}^{(1)}}{\partial t} = -\nabla p^{(1)} + \eta_0 \nabla \nabla \cdot \mathbf{v}^{(1)} + (\xi_0 + \eta_0/3) \nabla (\nabla \cdot \mathbf{v}^{(1)}), \quad (8)$$

$$\frac{\partial p^{(1)}}{\partial t} = \frac{c_0^2 \rho_0}{\gamma_0} \left(\alpha_0 \frac{\partial T^{(1)}}{\partial t} - \nabla \cdot \mathbf{v}^{(1)} \right), \quad (9)$$

$$\Delta T^{(1)} - \frac{1}{\chi_0} \frac{\partial T^{(1)}}{\partial t} = -\frac{\alpha_0 T_0}{\kappa_0} \frac{\partial p^{(1)}}{\partial t}, \quad (10)$$

where χ_0 is the thermal diffusivity defined as $\chi_0 = \kappa_0 / (\rho_0 c_p)$, and the subscript 0 denotes the equilibrium conditions.

Both the incident sound field and the sound field scattered by the particle must satisfy Eqs. (8)–(10). Therefore, to specify both the fields, it is necessary to find a general form of solutions of the above equations. Suppose that the incident sound field depends on time as $\exp(-i\omega t)$, where ω is the angular frequency. It follows that all the first-order quantities must vary with time along similar lines. After taking this into account and excluding $p^{(1)}$ by use of Eq. (9), Eqs. (8) and (10) take the form

$$\begin{aligned} \Delta \mathbf{v}^{(1)} + \left(\frac{1}{3} + \frac{\xi_0}{\eta_0} + \frac{ic_0^2}{\gamma_0 \omega \nu_0} \right) \nabla (\nabla \cdot \mathbf{v}^{(1)}) + \frac{i\omega}{\nu_0} \mathbf{v}^{(1)} \\ = \frac{\alpha_0 c_0^2}{\gamma_0 \nu_0} \nabla T^{(1)}, \end{aligned} \quad (11)$$

$$\Delta T^{(1)} + \frac{i\omega}{\gamma_0 \chi_0} T^{(1)} = \frac{\gamma_0 - 1}{\alpha_0 \chi_0 \gamma_0} \nabla \cdot \mathbf{v}^{(1)}, \quad (12)$$

where $\nu_0 = \eta_0 / \rho_0$ is the kinematic viscosity.

The velocity $\mathbf{v}^{(1)}$ can be represented as²⁶

$$\mathbf{v}^{(1)} = \nabla \varphi^{(1)} + \nabla \times \boldsymbol{\psi}^{(1)}, \quad (13)$$

where $\varphi^{(1)}$ and $\boldsymbol{\psi}^{(1)}$ are the scalar and vorticity velocity potentials of first order, respectively. Substituting Eq. (13) into Eqs. (11) and (12), one obtains two combined equations for $\varphi^{(1)}$ and $T^{(1)}$:

$$(\Delta + \beta_1) \varphi^{(1)} = -\frac{i\omega \alpha_0}{\beta_3} T^{(1)}, \quad (14)$$

$$(\Delta + \beta_2) T^{(1)} = \frac{(1 - \gamma_0) \beta_1}{\alpha_0 \chi_0 \gamma_0} \varphi^{(1)}, \quad (15)$$

in which

$$\beta_1 = \gamma_0 \omega^2 / (c_0^2 \beta_3), \quad (16)$$

$$\beta_2 = i\omega (\gamma_0 + \beta_3 - 1) / (\chi_0 \beta_3 \gamma_0), \quad (17)$$

$$\beta_3 = 1 - i\omega \gamma_0 (\xi_0 + 4\eta_0/3) / (\rho_0 c_0^2), \quad (18)$$

and an equation for $\psi^{(1)}$:

$$(\Delta + k_3^2)\psi^{(1)} = 0, \quad (19)$$

where $k_3 = (1+i)/\delta_v$ is the viscous wave number, and $\delta_v = \sqrt{2\nu_0/\omega}$ is the depth of penetration of the viscous wave. Note also that the quantity $\lambda_v = 2\pi/\text{Re}(k_3) = 2\pi\delta_v$ (where Re denotes the real part) is called the viscous wavelength.

Let us start with solving Eqs. (14) and (15). We seek their solutions in the form

$$\varphi^{(1)} = A \exp(-i\omega t)f_\tau, \quad T^{(1)} = B \exp(-i\omega t)f_\tau, \quad (20)$$

where f_τ is the Laplacian eigenfunction corresponding to the eigenvalue τ , so that

$$\Delta f_\tau = \tau f_\tau. \quad (21)$$

Substitution of Eq. (20) into Eqs. (14) and (15) yields

$$\begin{aligned} \beta_3(\tau + \beta_1)A + i\omega\alpha_0 B &= 0, \\ (\gamma_0 - 1)\beta_1 A + \alpha_0\chi_0\gamma_0(\tau + \beta_2)B &= 0. \end{aligned} \quad (22)$$

This system has nonzero solutions only if its determinant is equal to zero. By imposing such conditions, one finds an equation for the eigenvalues

$$\tau^2 + (\beta_1 + \beta_2)\tau + i\omega\beta_1/(\chi_0\gamma_0) = 0, \quad (23)$$

which yields

$$\tau_{1,2} = -\frac{1}{2}(\beta_1 + \beta_2) \left[1 \mp \sqrt{1 - \frac{4i\omega\beta_1}{\chi_0\gamma_0(\beta_1 + \beta_2)^2}} \right], \quad (24)$$

where τ_1 relates to the negative root, and τ_2 to the positive one.

Using the first of equations (22) so as to express B in terms of A , one obtains

$$\varphi^{(1)} = \exp(-i\omega t)(A_1 f_{\tau_1} + A_2 f_{\tau_2}), \quad (25)$$

$$T^{(1)} = \frac{i\beta_3}{\omega\alpha_0} \exp(-i\omega t)[(\tau_1 + \beta_1)A_1 f_{\tau_1} + (\tau_2 + \beta_1)A_2 f_{\tau_2}], \quad (26)$$

where A_1 and A_2 are arbitrary constants.

Now one must choose a specific form of the eigenfunctions f_τ . Recall that in accordance with our assumption the problem involved is axisymmetric about the direction of the incident wave propagation. Therefore, for f_τ we take only the axisymmetric Laplacian eigenfunctions which are known to be written as follows:

$$f_m = z_n(i\sqrt{\tau r})P_n(\cos \theta), \quad n = 0, 1, \dots, \quad (27)$$

where z_n is a spherical cylindrical function of order n , P_n is the Legendre polynomial of degree n , and r and θ are the coordinates of the spherical coordinate system (r, θ, ε) whose origin is at the equilibrium center of the particle and the z axis (the zero direction of θ) lies in the direction of the incident wave propagation. It is seen from Eq. (27) that there is an infinite number of the eigenfunctions corresponding to the

same eigenvalue. It follows that solutions of Eqs. (14) and (15) in the general case are written as

$$\varphi^{(1)} = e^{-i\omega t} \sum_{n=0}^{\infty} [A_{1n} z_n(k_1 r) + A_{2n} z_n(k_2 r)] P_n(\cos \theta), \quad (28)$$

$$\begin{aligned} T^{(1)} = \frac{i\beta_3}{\omega\alpha_0} e^{-i\omega t} \sum_{n=0}^{\infty} [(\beta_1 - k_1^2)A_{1n} z_n(k_1 r) \\ + (\beta_1 - k_2^2)A_{2n} z_n(k_2 r)] P_n(\cos \theta), \end{aligned} \quad (29)$$

where $k_{1,2}^2 = -\tau_{1,2}$.

The axisymmetric solution of Eq. (19) is well known.²⁶

$$\psi^{(1)} = \mathbf{e}_\varepsilon e^{-i\omega t} \sum_{n=1}^{\infty} B_n z_n(k_3 r) P_n^1(\cos \theta), \quad (30)$$

where \mathbf{e}_ε is the unit vector of the spherical coordinate system introduced above, P_n^1 is the associated Legendre polynomial of the first order and degree n , and B_n are arbitrary constants.

So, the general solutions of Eqs. (14), (15), and (19) have been obtained, and now we must specialize them to the incident field and the scattered field. Let us begin with the former, denoting quantities that concern it by the subscript I . We assume the incident field to be irrotational, so that $\psi_I^{(1)} = 0$. Further, the incident field should be finite at $r=0$, therefore we must substitute the spherical Bessel functions j_n for the functions z_n into Eqs. (28) and (29). This results in

$$\varphi_I^{(1)} = e^{-i\omega t} \sum_{n=0}^{\infty} [A_{1n} j_n(k_1 r) + A_{2n} j_n(k_2 r)] P_n(\cos \theta), \quad (31)$$

$$\begin{aligned} T_I^{(1)} = \frac{i\beta_3}{\omega\alpha_0} e^{-i\omega t} \sum_{n=0}^{\infty} [(\beta_1 - k_1^2)A_{1n} j_n(k_1 r) \\ + (\beta_1 - k_2^2)A_{2n} j_n(k_2 r)] P_n(\cos \theta). \end{aligned} \quad (32)$$

These equations describe the propagation of an axisymmetric acoustic wave through a viscous heat-conducting fluid when inclusions are absent. The constants A_{1n} and A_{2n} are determined by the conditions of sound generation and are assumed to be the given quantities in the present study. When the heat conduction of the surrounding fluid is small it follows from Eqs. (16)–(18) and (24) that k_1 turns into $k_c = \omega/(c_0\sqrt{\beta_3})$ and k_2 into $k_t = (1+i)/\delta_t$, where $\delta_t = \sqrt{2\chi_0/\omega}$. The former is the wave number of sound waves in a barotropic fluid. Sound waves of this kind are called elastic or compressional since they arise due to the compressibility of the fluid. Their phase speed is equal to about c_0 . The quantity k_t is the wave number of the so-called thermal sound waves, and δ_t is referred to as the depth of penetration of these waves. The thermal sound waves occur through nonzero heat conduction of the fluid. Their speed equals about $\omega\delta_t$ and is much less than c_0 in cases of interest. Thus, we conclude that the first term between the brackets in Eq. (31) defines the elastic sound waves while the second one defines the thermal sound waves. It is known that the

thermal sound waves die down on passage through a fluid much more than the elastic ones. Therefore, they can play a distinct role only within a thin layer with the thickness of the order of δ_t near the sound transducer. For simplicity, we shall assume that the particle is placed at such a distance from the sound transducer that the thermal component of the incident sound field is negligible. Then, setting A_{2n} equal to zero and writing A_n for A_{1n} , instead of Eqs. (31) and (32) one obtains

$$\varphi_I^{(1)} = e^{-i\omega t} \sum_{n=0}^{\infty} A_n j_n(k_1 r) P_n(\cos \theta), \quad (33)$$

$$T_I^{(1)} = \frac{i\beta_3(\beta_1 - k_1^2)}{\omega\alpha_0} \varphi_I^{(1)}. \quad (34)$$

These expressions are what will be considered as a general form of the incident sound field in this paper.

Quantities that concern the scattered field will be denoted by the subscript S . Since the scattered field is a diverging wave the functions z_n in Eqs. (28)–(30) should be replaced by the spherical Hankel functions of the first kind $h_n^{(1)}$, which gives

$$\begin{aligned} \varphi_S^{(1)} = e^{-i\omega t} \sum_{n=0}^{\infty} A_n [\alpha_{1n} h_n^{(1)}(k_1 r) \\ + \alpha_{2n} h_n^{(1)}(k_2 r)] P_n(\cos \theta), \end{aligned} \quad (35)$$

$$\begin{aligned} T_S^{(1)} = \frac{i\beta_3}{\omega\alpha_0} e^{-i\omega t} \sum_{n=0}^{\infty} A_n [(\beta_1 - k_1^2) \alpha_{1n} h_n^{(1)}(k_1 r) \\ + (\beta_1 - k_2^2) \alpha_{2n} h_n^{(1)}(k_2 r)] P_n(\cos \theta), \end{aligned} \quad (36)$$

$$\psi_S^{(1)} = \mathbf{e}_e e^{-i\omega t} \sum_{n=1}^{\infty} \alpha_{3n} A_n h_n^{(1)}(k_3 r) P_n^1(\cos \theta), \quad (37)$$

where α_{1n} , α_{2n} , and α_{3n} are dimensionless constants, which are usually referred to as the linear scattering coefficients, to be determined by the boundary conditions at the particle surface, namely, the conditions of continuity of the velocity, stress, temperature, and heat flux. However, to apply these conditions one must point out precisely which medium is inside the particle: fluid or solid. Each of these cases will be examined in detail in the following papers. As already mentioned, the purpose of the present paper is to derive a general expression for the radiation force applicable to any type of dispersed particles. Therefore we now consider the linear scattering coefficients to be known and proceed to solving the equations of second order.

III. SOLUTION OF THE TIME-AVERAGED EQUATIONS OF SECOND ORDER

Such material parameters as viscosity, thermal conductivity, volume thermal expansion coefficient, etc. are temperature dependent. However, they show generally a weak dependence unless temperature varies over a very wide range. Therefore we consider them here to be independent of

temperature. Note, however, that the technique developed in Refs. 19 and 20 for solving the time-averaged equations of the fluid motion and applied here allows the above dependence to be taken into account if necessary.

By time averaging Eqs. (1)–(3) and keeping up to the second order, we obtain

$$\begin{aligned} \eta_0 \Delta \langle \mathbf{v}^{(2)} \rangle + (\xi_0 + \eta_0/3) \nabla (\nabla \cdot \langle \mathbf{v}^{(2)} \rangle) - \nabla \langle p^{(2)} \rangle \\ = \rho_0 \langle \mathbf{v}^{(1)} (\nabla \cdot \mathbf{v}^{(1)}) + (\mathbf{v}^{(1)} \cdot \nabla) \mathbf{v}^{(1)} \rangle, \end{aligned} \quad (38)$$

$$\nabla \cdot \langle \mathbf{v}^{(2)} \rangle = -\frac{1}{\rho_0} \nabla \cdot \langle \rho^{(1)} \mathbf{v}^{(1)} \rangle, \quad (39)$$

$$\begin{aligned} \kappa_0 \Delta \langle T^{(2)} \rangle = \left\langle (\rho_0 T^{(1)} + T_0 \rho^{(1)}) \frac{\partial s^{(1)}}{\partial t} \right\rangle \\ + \rho_0 T_0 \langle \mathbf{v}^{(1)} \cdot \nabla s^{(1)} \rangle - (\xi_0 - 2\eta_0/3) \\ \times \langle (\nabla \cdot \mathbf{v}^{(1)})^2 \rangle - \frac{\eta_0}{2} \left\langle \left(\frac{\partial v_i^{(1)}}{\partial x_k} + \frac{\partial v_k^{(1)}}{\partial x_i} \right)^2 \right\rangle, \end{aligned} \quad (40)$$

where $\rho^{(1)}$ and $s^{(1)}$ are defined by Eqs. (5) and (6).

One can see that Eq. (40), which describes a stationary temperature distribution in the fluid, is not related to Eqs. (38) and (39), which govern acoustic streaming. As the quantity $\langle T^{(2)} \rangle$ in itself does not appear in the expression for the radiation force there is no necessity to solve Eq. (40).

The velocity $\langle \mathbf{v}^{(2)} \rangle$ can be represented as follows:

$$\langle \mathbf{v}^{(2)} \rangle = \langle \mathbf{v}_I^{(2)} \rangle + \langle \mathbf{v}_S^{(2)} \rangle, \quad (41)$$

where $\langle \mathbf{v}_I^{(2)} \rangle$ is the fluid velocity as if the particle were absent, and $\langle \mathbf{v}_S^{(2)} \rangle$ is the velocity of the acoustic streaming arising around the particle.

The velocity $\langle \mathbf{v}_I^{(2)} \rangle$ satisfies Eqs. (38) and (39) when their right-hand sides only involve the incident field. The fluid flow defined by this velocity gives rise to a steady force on the particle that is an analogue of Stokes' drag force. This force, generally speaking, does not concern the acoustic radiation force, but it should be taken into consideration when the total force acting on the particle in a sound field is calculated. We shall return to this point below.

The velocity $\langle \mathbf{v}_S^{(2)} \rangle$, like $\mathbf{v}^{(1)}$, can be written as

$$\langle \mathbf{v}_S^{(2)} \rangle = \nabla \Phi + \nabla \times \Psi, \quad (42)$$

where Φ and Ψ are the scalar and vorticity velocity potentials of the acoustic streaming, respectively. Note that in view of the axial symmetry of the problem involved Ψ must be of the following form: $\Psi = \mathbf{e}_f f(r, \theta)$, where $f(r, \theta)$ is a certain function. It follows that $\nabla \cdot \Psi = 0$. Taking this fact into account and substituting Eq. (42) into Eqs. (38) and (39), we obtain, after some manipulation, equations for Φ and Ψ as

$$\Delta \Phi = -\frac{1}{\rho_0} \nabla \cdot \langle \rho^{(1)} \mathbf{v}^{(1)} \rangle_{IS+SS}, \quad (43)$$

$$\Delta\Delta\Psi = -\frac{1}{\nu_0} \nabla \times \langle \mathbf{v}^{(1)}(\nabla \cdot \mathbf{v}^{(1)}) + (\mathbf{v}^{(1)} \cdot \nabla) \mathbf{v}^{(1)} \rangle_{IS+SS}, \quad (44)$$

where the subscript *IS+SS* indicates that on the right-hand sides of these equations the cross terms dependent on the incident and scattered fields (the *IS* terms) and the terms dependent only on the scattered field (the *SS* terms) are retained while the terms that are expressed only through the incident field (the *II* terms) are omitted.

Since a procedure of solving Eqs. (43) and (44) is described in detail in Refs. 19 and 20, we only present here the final results:

$$\Phi = \sum_{n=0}^{\infty} \Phi_n(r/R_0) P_n(\cos \theta), \quad (45)$$

$$\Psi = \mathbf{e}_\epsilon \sum_{n=1}^{\infty} \Psi_n(r/R_0) P_n^1(\cos \theta), \quad (46)$$

where R_0 is the particle radius (if the particle is compressible R_0 means its equilibrium radius),

$$\Phi_n(x) = x^{-(n+1)} [K_n(x, n+2) - C_{\varphi n}] - x^n [K_n(x, 1-n) - K_n(\infty, 1-n)], \quad (47)$$

$$\Psi_n(x) = \frac{1}{2(2n+3)} \{x^{-(n+1)} N_n(x, n+3) - x^{n+2} [N_n(x, -n) - N_n(\infty, -n)]\} + \frac{1}{2(2n-1)} \{x^n [N_n(x, 2-n) - N_n(\infty, 2-n)] - x^{1-n} [N_n(x, n+1) - C_{\psi n}]\}, \quad (48)$$

$$K_n(x, j) = \int_1^x y^j \mu_n(y) dy, \quad (49)$$

$$N_n(x, j) = \int_1^x y^j [\chi_{rn}(y) + j \chi_{\theta n}(y)] dy, \quad (50)$$

$$\mu_n(r/R_0) = \frac{R_0^2}{2\rho_0} \int_0^\pi \nabla \cdot \langle \rho^{(1)} \mathbf{v}^{(1)} \rangle_{IS+SS} \times P_n(\cos \theta) \sin \theta d\theta, \quad (51)$$

$$\chi_{rn}(r/R_0) = \int_0^\pi W_r(r/R, \theta) P_n(\cos \theta) \sin \theta d\theta, \quad (52)$$

$$\chi_{\theta n}(r/R_0) = -\frac{1}{n(n+1)} \times \int_0^\pi W_\theta(r/R_0, \theta) P_n^1(\cos \theta) \sin \theta d\theta, \quad (53)$$

$$\mathbf{W}(r/R_0, \theta) = \frac{R_0^3}{2\nu_0} \langle \mathbf{v}^{(1)}(\nabla \cdot \mathbf{v}^{(1)}) + (\mathbf{v}^{(1)} \cdot \nabla) \mathbf{v}^{(1)} \rangle_{IS+SS}, \quad (54)$$

$$C_{\varphi n} = \frac{n(2n-1)}{2(n+1)} K_n(\infty, 1-n) + \frac{n(2n+1)}{4(2n+3)} N_n(\infty, -n) - \frac{n}{4} N_n(\infty, 2-n) + \frac{(2n+1)(n-2)}{2(n+1)} a_n + \frac{n(2n+1)}{2} b_n, \quad (55)$$

$$C_{\psi n} = (4n^2 - 1) \left[\frac{N_n(\infty, 2-n)}{2(2n-1)} - \frac{N_n(\infty, -n)}{2(2n+1)} - \frac{K_n(\infty, 1-n) + a_n - b_n}{n+1} \right], \quad (56)$$

$$a_n = \int_0^\pi U_r(R_0, \theta) P_n(\cos \theta) \sin \theta d\theta, \quad (57)$$

$$b_n = -\frac{1}{n(n+1)} \int_0^\pi U_\theta(R_0, \theta) P_n^1(\cos \theta) \sin \theta d\theta, \quad (58)$$

$$\mathbf{U}(r, \theta) = \frac{R_0}{2} \left\langle \mathbf{v}_I^{(2)} - \frac{1}{\omega^2} \frac{\partial v_r^{(1)}}{\partial t} \frac{\partial \mathbf{v}^{(1)}}{\partial r} \right\rangle. \quad (59)$$

When Eqs. (45) and (46) are substituted into Eq. (42) and then into Eq. (38), one obtains an expression for the acoustic streaming pressure $\langle p_S^{(2)} \rangle$ which is also required for calculating the radiation force:

$$\langle p_S^{(2)} \rangle = -\eta_0 Q - (\xi_0 / \rho_0 + 4\nu_0/3) \nabla \cdot \langle \rho^{(1)} \mathbf{v}^{(1)} \rangle_{IS+SS}, \quad (60)$$

where

$$Q(r/R_0, \theta) = \frac{1}{R_0^2} \sum_{n=0}^{\infty} Q_n(r/R_0) P_n(\cos \theta), \quad (61)$$

$$Q_n(x) = nx^{-(n+1)} [N_n(x, n+1) - C_{\psi n}] + (n+1)x^n [N_n(x, -n) - N_n(\infty, -n)]. \quad (62)$$

In this paper, the solutions of Eqs. (43) and (44) are represented in more compact form than in Refs. 19 and 20. Therefore, to guard the readers against confusion, we draw their attention to the fact that some of the designations used here are other than in the above-mentioned papers. It should also be noted that the expressions for the constants $C_{\varphi n}$ and $C_{\psi n}$ given by Eqs. (55)–(59) have been obtained assuming that the particle is not moving in the second approximation.

IV. CALCULATION OF THE RADIATION FORCE

Now we have all that is needed for calculating the radiation force. Substituting Eqs. (42) and (45)–(62) into Eq. (7), after laborious but straightforward calculations one obtains

$$\begin{aligned} \mathbf{F} = & 6\pi\eta_0\mathbf{e}_z(a_1+2b_1)+3\pi R_0\mathbf{e}_z\int_{R_0}^{\infty}dr\int_0^{\pi}\sin\theta d\theta \\ & \times\{v_0\nabla\cdot\langle\rho^{(1)}\mathbf{v}^{(1)}\rangle\cos\theta-\rho_0(1-R_0^2/r^2) \\ & \times[\langle v_r^{(1)}(\mathbf{e}_z\cdot\mathbf{v}^{(1)})\rangle+(r/2)\sin\theta\mathbf{e}_\theta\cdot\langle\mathbf{v}^{(1)}(\nabla\cdot\mathbf{v}^{(1)}) \\ & +(\mathbf{v}^{(1)}\cdot\nabla)\mathbf{v}^{(1)}]\}_{IS+SS} \end{aligned} \quad (63)$$

where \mathbf{e}_z is the unit vector in the direction of wave propagation. To complete the calculations, it only remains to substitute the linear solutions from Sec. II into Eq. (63). After carrying out this operation, one finally obtains

$$F = F_r + F_d, \quad (64)$$

where $F = \mathbf{F} \cdot \mathbf{e}_z$ is the total force (its magnitude including sign to be exact) exerted by a sound field on a spherical particle, and F_r is just what is called the acoustic radiation force, or the acoustic radiation pressure. It is defined by

$$\begin{aligned} F_r = & \frac{3}{2}\pi\rho_0\sum_{n=0}^{\infty}\frac{n+1}{(2n+1)(2n+3)} \\ & \times(Z_n A_n A_{n+1}^* + Z_n^* A_n^* A_{n+1}), \end{aligned} \quad (65)$$

where

$$Z_n = \sum_{j=1}^3 \left(F_n^{(0j)} \alpha_{jn+1}^* + F_n^{(j0)} \alpha_{jn} + \sum_{k=1}^3 F_n^{(jk)} \alpha_{jn} \alpha_{kn+1}^* \right), \quad (66)$$

and the functions $F_n^{(jk)}$ are given in the Appendix.

As regards F_d , it is the drag force brought about by the stationary fluid flow that is generated by the incident sound field in the absence of the particle. This force is given by

$$\begin{aligned} F_d = & 3\pi\eta_0 R_0 \int_0^{\pi} \left\langle v_{Iz}^{(2)} - \frac{1}{\omega^2} \frac{\partial v_{Ir}^{(1)}}{\partial t} \frac{\partial v_{Iz}^{(1)}}{\partial r} \right\rangle \Big|_{r=R_0} \sin\theta d\theta \\ = & 3\pi\eta_0 R_0 \int_0^{\pi} \langle v_{Iz}^{(2)} \rangle \Big|_{r=R_0} \sin\theta d\theta - 3\pi\rho_0 |x_1|^2 \\ & \times \sum_{n=0}^{\infty} \frac{n+1}{(2n+1)(2n+3)} \\ & \times \operatorname{Re} \left\{ \frac{A_n A_{n+1}^*}{x_3^2} [x_1^* |j'_n(x_1)|^2 + x_1 |j'_{n+1}(x_1)|^2] \right\}, \end{aligned} \quad (67)$$

where the subscript z denotes the projection on the z axis, $x_1 = k_1 R_0$, $x_3 = k_3 R_0$, the prime denotes differentiation, and Re signifies the real part of the expression which follows it.

In the previous papers by the present author,^{19–21} the second term on the right-hand side of Eq. (67) was mistakenly attributed to the acoustic radiation force [see the term S_9 in Eq. (5.6) of Refs. 19 and 20 and in Eq. (5) of Ref. 21]. It is seen from Eq. (67) that the above term depends on the incident field only: it does not contain the coefficients α_{jn} which describe the scattered field. Therefore it should be

included as a component of the drag force but not the radiation one. Note, however, that the total force F is not changed by such a movement.

V. RADIATION FORCE IN SOME SOUND FIELDS

In this section, we apply the general equations obtained above to three sound fields of most interest, namely a plane traveling wave, a plane standing wave, and a diverging spherical wave, the thermal component of an incident wave being supposed to be negligible as before.

A. Plane traveling wave

The plane traveling wave is specified by

$$\varphi_{\text{tr}}^{(1)} = A \exp(i\mathbf{k}_1 \cdot \mathbf{r} - i\omega t), \quad (68)$$

where $\mathbf{k}_1 = k_1 \mathbf{e}_z$, and \mathbf{r} is the position vector. By expanding Eq. (68) in the Legendre polynomials²⁷ and comparing the series obtained with Eq. (33), one finds

$$A_n = A(2n+1)i^n. \quad (69)$$

Substitution of Eq. (69) into Eq. (65) yields

$$F_r^{(\text{tr})} = 3\pi\rho_0 |A|^2 \sum_{n=0}^{\infty} (n+1) \operatorname{Im}(Z_n), \quad (70)$$

where Im denotes the imaginary part.

The part of the drag force that is given by the first term on the right-hand side of Eq. (67) has been calculated in Ref. 19 [see Eq. (5.12) of that paper]. Using that result and substituting Eq. (69) into the second term on the right-hand side of Eq. (67), one obtains

$$\begin{aligned} F_d^{(\text{tr})} = & -\frac{3}{2}\pi\rho_0 |A|^2 |x_1|^2 (x_1 + x_1^*) i x_3^{-2} \left[\frac{\sin(x_1 - x_1^*)}{x_1 - x_1^*} \right. \\ & \left. - \sum_{n=0}^{\infty} (n+1) (|j'_n(x_1)|^2 + |j'_{n+1}(x_1)|^2) \right]. \end{aligned} \quad (71)$$

B. Plane standing wave

The plane standing wave is given by

$$\varphi_{\text{st}}^{(1)} = A \cos(\mathbf{k}_1 \cdot \mathbf{r} + k_1 d) \exp(-i\omega t), \quad (72)$$

where d is the distance between the equilibrium center of the particle and the nearest plane of the velocity nodes. By expanding Eq. (72) in the Legendre polynomials²⁷ and comparing the series obtained with Eq. (33), one finds

$$A_n = \frac{1}{2} A (2n+1) i^n [e^{ik_1 d} + (-1)^n e^{-ik_1 d}]. \quad (73)$$

Substitution of Eq. (73) into Eq. (65) results in

$$F_r^{(\text{st})} = \frac{3}{2}\pi\rho_0 |A|^2 \sum_{n=0}^{\infty} (-1)^{n+1} (n+1) \operatorname{Re}\{Z_n \sin(2k_1 d)\}. \quad (74)$$

The first part of the drag force is given by Eq. (5.17) of Ref. 19. Taking this into account and substituting Eq. (73) into Eq. (67), one obtains

$$F_d^{(st)} = \frac{3}{4} \pi \rho_0 |A|^2 |x_1|^2 x_3^{-2} \left\{ (x_1 + x_1^*) \sin(k_1 d - k_1^* d) \times \left[\frac{\sin(x_1 - x_1^*)}{x_1 - x_1^*} - \sum_{n=0}^{\infty} (n+1) (|j'_n(x_1)|^2 + |j'_{n+1}(x_1)|^2) \right] - (x_1 - x_1^*) \sin(k_1 d + k_1^* d) \times \left[\frac{\sin(x_1 + x_1^*)}{x_1 + x_1^*} + \sum_{n=0}^{\infty} (-1)^n (n+1) \times (|j'_n(x_1)|^2 - |j'_{n+1}(x_1)|^2) \right] \right\}. \quad (75)$$

C. Diverging spherical wave

The diverging spherical wave is represented as

$$\varphi_{l\text{sph}}^{(1)} = \frac{A}{k_1 r_s} \exp(ik_1 r_s - i\omega t), \quad (76)$$

where $r_s = |\mathbf{r}_s|$, and \mathbf{r}_s is the position vector whose origin coincides with the point sound source. Expansion of Eq. (76) at the particle surface into a series of the Legendre polynomials yields²⁷

$$\varphi_{l\text{sph}}^{(1)} = iA e^{-i\omega t} \sum_{n=0}^{\infty} (-1)^n (2n+1) h_n^{(1)} \times (k_1 l) j_n(k_1 r) P_n(\cos \theta), \quad (77)$$

where $l = |\mathbf{l}|$, and \mathbf{l} is the vector drawn from the sound source to the equilibrium center of the particle. By comparing Eq. (77) with Eq. (33), one finds

$$A_n = iA (-1)^n (2n+1) h_n^{(1)}(k_1 l). \quad (78)$$

Substitution of Eq. (78) into Eq. (65) results in

$$F_r^{(\text{sph})} = -3 \pi \rho_0 |A|^2 \sum_{n=0}^{\infty} (n+1) \text{Re}\{Z_n h_n^{(1)}(k_1 l) \times [h_{n+1}^{(1)}(k_1 l)]^*\}. \quad (79)$$

Making use of the expression for the first term on the right-hand side of Eq. (67), which has been derived in Ref. 21 [see Eqs. (16)–(20) of that paper], and substituting Eq. (78) into the second term, we have

$$F_d^{(\text{sph})} = -3 \pi \rho_0 |A|^2 |x_1|^2 i x_3^{-2} \times \text{Re} \left\{ (1/8) (k_1 l)^{-2} e^{i(k_1 - k_1^*)l} (L_1 + iL_2 + iL_3 L_4 + 4x_1 \sin(x_1 - x_1^*) / (x_1 - x_1^*)) + i \sum_{n=0}^{\infty} (n+1) h_n^{(1)} \times (k_1 l) [h_{n+1}^{(1)}(k_1 l)]^* (x_1^* |j'_n(x_1)|^2 + x_1 |j'_{n+1}(x_1)|^2) \right\}, \quad (80)$$

where

$$L_1 = (k_1 + k_1^*) [(l + R_0) e^{i(x_1^* - x_1)} - (l - R_0) e^{i(x_1 - x_1^*)}], \quad (81)$$

$$L_2 = \frac{l + R_0}{l - R_0} e^{i(x_1^* - x_1)} - \frac{l - R_0}{l + R_0} e^{i(x_1 - x_1^*)}, \quad (82)$$

$$L_3 = (R_0/l) [2 + (k_1^2 - k_1^{2*})(l^2 - R_0^2)], \quad (83)$$

$$L_4 = \int_{-1}^1 (1 + R_0 y/l)^{-1} e^{i(x_1 - x_1^*)y} dy. \quad (84)$$

VI. CONCLUSIONS

In this paper, a general expression has been derived for the acoustic radiation force exerted by a sound field on a spherical particle suspended in a viscous heat-conducting fluid. Assumptions made in deriving this expression are as follows:

- (1) the incident sound field is axisymmetric;
- (2) the sound pressure amplitude does not exceed a threshold above which nonlinear effects like dancing motions of pulsating gas bubbles start developing;
- (3) the particle is at such a distance from the sound transducer that the thermal component of the incident field is negligible;
- (4) the viscosity, thermal conductivity, volume thermal expansion coefficient, etc., are temperature independent;
- (5) the particle is immovable in the second approximation.

No restrictions have been imposed on the size and the internal structure of the particle. In other words, it has been assumed that the particle can have an arbitrary radius with respect to the sound, viscous, and thermal wavelengths and be of one of the following types: a gas bubble, a liquid drop, a rigid or elastic sphere, a spherical shell, etc. The general formula obtained is expressed in terms of the linear scattering coefficients. Therefore, in order to apply it to a specific dispersed particle, one must solve the problem of linear scattering for that particle. Solution of such problems is known not to present great mathematical difficulties, yet can be laborious enough in some cases such as a gas bubble coated by a thin liquid layer immiscible in the outer liquid. The acoustic radiation forces on dispersed particles of most interest will be examined in detail in papers that follow.^{28,29}

ACKNOWLEDGMENTS

This work was supported by the Ministry of Education and Science of the Republic of Belarus and the International Science Foundation.

APPENDIX: EXPRESSIONS FOR THE FUNCTIONS $F_n^{(jk)}$

Below are given exact expressions for the functions $F_n^{(jk)}$, which hold for any values of x_1, x_2 , and x_3 :

$$\begin{aligned}
 F_n^{(01)} &= \frac{1}{2}[X_n^{(11)}(x_1, x_1) + X_n^{(21)}(x_1, x_1)], \\
 F_n^{(02)} &= \frac{1}{2}[X_n^{(11)}(x_1, x_2) + X_n^{(21)}(x_1, x_2)], \\
 F_n^{(03)} &= \frac{1}{2}[Y_n^{(110)}(x_1) + Y_n^{(210)}(x_1)]^*, \\
 F_n^{(10)} &= \frac{1}{2}[X_n^{(11)}(x_1, x_1) + X_n^{(12)}(x_1, x_1)], \\
 F_n^{(20)} &= \frac{1}{2}[X_n^{(11)}(x_2, x_1) + X_n^{(12)}(x_2, x_1)], \\
 F_n^{(30)} &= \frac{1}{2}[Y_n^{(101)}(x_1) + Y_n^{(201)}(x_1)], \\
 F_n^{(11)} &= X_n^{(11)}(x_1, x_1), \quad F_n^{(21)} = X_n^{(11)}(x_2, x_1), \\
 F_n^{(12)} &= X_n^{(11)}(x_1, x_2), \quad F_n^{(22)} = X_n^{(11)}(x_2, x_2),
 \end{aligned}$$

$$F_n^{(13)} = [Y_n^{(110)}(x_1)]^*, \quad F_n^{(23)} = [Y_n^{(110)}(x_2)]^*,$$

$$F_n^{(31)} = Y_n^{(101)}(x_1), \quad F_n^{(32)} = Y_n^{(101)}(x_2),$$

$$\begin{aligned}
 F_n^{(33)} &= n(n+2)\{(n+1)x_3^2[H_{n+1}^{(011)}(x_3, x_3) - H_{n+1}^{(211)} \\
 &\quad \times (x_3, x_3)] + ix_3^2[H_{n+1}^{(011)}(x_3, x_3) - H_{n+1}^{(211)} \\
 &\quad \times (x_3, x_3)] + (n+1)[h_n^{(1)}(x_3)(h_n^{(1)'})^* \\
 &\quad + (h_{n+1}^{(1)}(x_3))^* h_{n+1}^{(1)'}(x_3)]\}.
 \end{aligned}$$

Here $x_j = k_j R_0$ ($j = 1, 2, 3$),

$$\begin{aligned}
 X_n^{(kl)}(x, y) &= \frac{1}{2}(ny^{2*} - (n+2)x^2)[H_{n+1}^{(0kl)}(x, y) - H_{n+1}^{(2kl)} \\
 &\quad \times (x, y)] + xy^*[H_{n+1}^{(0kl)}(x, y) - H_{n+1}^{(2kl)}(x, y)] \\
 &\quad + \frac{y^{2*} - x^2}{x_3^2} [ny^* H_{nn}^{(1kl)}(x, y) - xy^* H_{n+1}^{(0kl)} \\
 &\quad \times (x, y) + (n+2)x H_{n+1}^{(1kl)}(x, y)] \\
 &\quad - \frac{xy^*}{x_3^2} [y^* h_n^{(k)'}(x)(h_n^{(l)'})^* + x h_{n+1}^{(k)'}(x) \\
 &\quad \times (h_{n+1}^{(l)'})^*], \quad k, l = 1, 2,
 \end{aligned}$$

and

$$\begin{aligned}
 Y_n^{(jkl)}(x) &= \frac{n+2k}{2} \{ [(n+1)x^{2*} - (n+2l)x^2][H_{n+kn+l}^{(01j)}(x_3, x) - H_{n+kn+l}^{(21j)} \\
 &\quad \times (x_3, x)] - x^{2*}x_3[H_{n+ln+l}^{(-11j)}(x_3, x) - H_{n+ln+l}^{(11j)}(x_3, x)] + 2x^*h_{n+l}^{(1)'}(x_3)(h_{n+l}^{(j)'})^* \} + (n+2k)(-1)^l \\
 &\quad \times \left\{ x^*x_3[H_{n+ln+k}^{(01j)}(x_3, x) - H_{n+ln+k}^{(21j)}(x_3, x)] + \frac{(n+1)x^{2*}}{x_3^2} h_{n+k}^{(1)}(x_3)(h_{n+k}^{(j)'})^* - \frac{x^{2*}}{x_3^2} [(n+1)x^* H_{n+kn+k}^{(11j)} \right. \\
 &\quad \left. \times (x_3, x) - (n+2l)x_3 H_{n+ln+l}^{(11j)}(x_3, x)] \right\}, \quad j = 1, 2, \quad k, l = 0, 1,
 \end{aligned}$$

in which

$$\begin{aligned}
 H_{nm}^{(jkl)}(x, y) &= \int_1^\infty z^{-j} h_n^{(k)}(xz)[h_m^{(l)}(yz)]^* dz \\
 &= \sum_{p=0}^n \sum_{q=0}^m D_{pq}^{(nm)} x^{-(p+1)} \\
 &\quad \times (y^*)^{-(q+1)} E_{p+q+j+2}[i(-1)^k x \\
 &\quad - i(-1)^l y^*] \delta_{pq}^{(nm)}(k, l), \\
 j &= -1, 0, 1, 2, \quad k, l = 1, 2,
 \end{aligned}$$

$$D_{pq}^{(nm)} = \frac{-i^{n+m}(n+p)!(m+q)!}{(2i)^{p+q} p!(n-p)! q!(m-q)!},$$

$$\delta_{pq}^{(nm)}(1, 1) = (-1)^{n+p+1},$$

$$\delta_{pq}^{(nm)}(1, 2) = (-1)^{n+m+p+q},$$

$$\delta_{pq}^{(nm)}(2, 1) = 1, \quad \delta_{pq}^{(nm)}(2, 2) = (-1)^{m+q+1},$$

$h_n^{(k)}$ is the spherical Hankel function of the k th kind, $E_n(z)$ is the integral exponent of order n ,²⁷ and the prime denotes differentiation.

For information, we present relations connecting the functions S_{jn} , $H_{nm}^{(j)}(x, y)$, and $J_{nm}^{(j)}(x, y)$ introduced in the previous papers by the author¹⁹⁻²¹ to the functions $F_n^{(jk)}$ and $H_{nm}^{(jkl)}(x, y)$ used in this paper:

$$S_{1n} = -F_n^{(11)}, \quad S_{2n} = -F_n^{(33)}, \quad S_{3n} = -F_n^{(13)},$$

$$S_{4n} = -F_n^{(31)},$$

$$S_{5n} = -F_n^{(10)}, \quad S_{6n} = -F_n^{(01)}, \quad S_{7n} = -F_n^{(30)},$$

$$S_{8n} = -F_n^{(03)},$$

$$H_{nm}^{(j)}(x, y) = H_{nm}^{(j11)}(x, y),$$

$$J_{nm}^{(j)}(x, y) = \frac{1}{2}[H_{nm}^{(j11)}(x, y) + H_{nm}^{(j12)}(x, y)].$$

- ¹L. V. King, "On the acoustic radiation pressure on spheres," Proc. R. Soc. Lond., Ser. A **147**, 212–240 (1934).
- ²T. F. W. Embleton, "Mean force on a sphere in a spherical sound field. I. (Theoretical)," J. Acoust. Soc. Am. **26**, 40–45 (1954).
- ³T. F. W. Embleton, "The radiation force on a spherical obstacle in a cylindrical sound field," Can. J. Phys. **34**, 276–287 (1956).
- ⁴K. Yosioka and Y. Kawasima, "Acoustic radiation pressure on a compressible sphere," Acustica **5**, 167–173 (1955).
- ⁵L. P. Gor'kov, "On the forces acting on a small particle in an acoustic field in an ideal fluid," Sov. Phys. Dokl. **6**, 773–775 (1962).
- ⁶W. L. Nyborg, "Radiation pressure on a small rigid sphere," J. Acoust. Soc. Am. **42**, 947–952 (1967).
- ⁷A. I. Eller, "Force on a bubble in a standing acoustic wave," J. Acoust. Soc. Am. **43**, 170–171 (1968).
- ⁸T. Hasegawa and K. Yosioka, "Acoustic radiation force on a solid elastic sphere," J. Acoust. Soc. Am. **46**, 1139–1143 (1969).
- ⁹T. Hasegawa, "Comparison of two solutions for acoustic radiation pressure on a sphere," J. Acoust. Soc. Am. **61**, 1445–1448 (1977).
- ¹⁰T. Hasegawa and Y. Watanabe, "Acoustic radiation pressure on an absorbing sphere," J. Acoust. Soc. Am. **63**, 1733–1737 (1978).
- ¹¹T. Hasegawa, "Acoustic radiation force on a sphere in a quasistationary wave field-theory," J. Acoust. Soc. Am. **65**, 32–40 (1979).
- ¹²T. Hasegawa, M. Ochi, and K. Matsuzawa, "Acoustic radiation pressure on a rigid sphere in a spherical wave field," J. Acoust. Soc. Am. **67**, 770–773 (1980).
- ¹³T. Hasegawa, M. Ochi, and K. Matsuzawa, "Acoustic radiation force on a solid elastic sphere in a spherical wave field," J. Acoust. Soc. Am. **69**, 937–942 (1981).
- ¹⁴L. A. Crum, "Acoustic force on a liquid droplet in an acoustic stationary wave," J. Acoust. Soc. Am. **50**, 157–163 (1971).
- ¹⁵M. Barmatz and P. Collas, "Acoustic radiation potential on a sphere in plane, cylindrical, and spherical standing wave fields," J. Acoust. Soc. Am. **77**, 928–945 (1985).
- ¹⁶J. Wu and G. Du, "Acoustic radiation force on a small compressible sphere in a focused beam," J. Acoust. Soc. Am. **87**, 997–1003 (1990).
- ¹⁷R. Löfstedt and S. Putterman, "Theory of long wavelength acoustic radiation pressure," J. Acoust. Soc. Am. **90**, 2027–2033 (1991).
- ¹⁸T. Watanabe and Y. Kukita, "Translational and radial motions of a bubble in an acoustic standing wave field," Phys. Fluids A **5**, 2682–2688 (1993).
- ¹⁹A. A. Doinikov, "Acoustic radiation pressure on a compressible sphere in a viscous fluid," J. Fluid Mech. **267**, 1–21 (1994).
- ²⁰A. A. Doinikov, "Acoustic radiation pressure on a rigid sphere in a viscous fluid," Proc. R. Soc. London, Ser. A **447**, 447–466 (1994).
- ²¹A. A. Doinikov, "Radiation force due to a spherical sound field on a rigid sphere in a viscous fluid," J. Acoust. Soc. Am. **96**, 3100–3105 (1994).
- ²²L. D. Landau and E. M. Lifshitz, *Fluid Mechanics* (Pergamon, New York, 1959).
- ²³A. I. Eller and H. G. Flynn, "Generation of subharmonics of order one-half by bubbles in a sound field," J. Acoust. Soc. Am. **46**, 722–727 (1969).
- ²⁴A. I. Eller and L. A. Crum, "Instability of the motion of a pulsating bubble in a sound field," J. Acoust. Soc. Am. **47**, 762–767 (1970).
- ²⁵L. A. Crum and A. I. Eller, "Motion of bubbles in a stationary sound field," J. Acoust. Soc. Am. **48**, 181–189 (1970).
- ²⁶H. Lamb, *Hydrodynamics* (Cambridge U.P., Cambridge, 1932).
- ²⁷M. Abramowitz and I. A. Stegun, *Handbook of Mathematical Functions* (Dover, New York, 1965).
- ²⁸A. A. Doinikov, "Acoustic radiation force on a spherical particle in a viscous heat-conducting fluid. II. Force on a rigid sphere," J. Acoust. Soc. Am. **101**, 722–730 (1997).
- ²⁹A. A. Doinikov, "Acoustic radiation force on a spherical particle in a viscous heat-conducting fluid. III. Force on a liquid drop," J. Acoust. Soc. Am. **101**, 731–740 (1997).

Acoustic radiation force on a spherical particle in a viscous heat-conducting fluid. II. Force on a rigid sphere

Alexander A. Doinikov

Institute of Nuclear Problems, Bobruiskaya 11, 220050 Minsk, Byelorussia

(Received 26 January 1996; accepted for publication 20 September 1996)

The general expression derived in Part I of this study [J. Acoust. Soc. Am. **101**, 713–721 (1997)] for the acoustic radiation force on a spherical particle immersed in a viscous heat-conducting fluid is applied here to the case of a rigid sphere. Three types of incident sound field are considered: a plane traveling wave, a plane standing wave, and a diverging spherical wave. To demonstrate dissipative effects on the force clearly, for each of these fields two limiting cases of interest are investigated. In the first of these, the sphere radius is assumed to be large compared with the viscous and thermal wavelengths in the surrounding fluid and the thermal wavelength inside the sphere. In the second case, the sphere radius is assumed to be small compared with the above wavelengths. In addition, in both cases, it is assumed that the sound wavelength is much larger than the above parameters. Since viscous effects have been examined in earlier papers by the present author, in this paper, the main attention is given to thermal effects. It is shown that these can drastically change the radiation force, resulting in, for example, the movement of light spheres both from the sound source and to it in a plane traveling wave and levitation in a diverging spherical wave. © 1997 Acoustical Society of America. [S0001-4966(97)00702-9]

PACS numbers: 43.25.Qp [MAB]

INTRODUCTION

When the compressibility of a dispersed particle is much smaller than that of the surrounding fluid the particle can be assumed to be rigid. As a result, one need not solve the equations of motion for the medium inside the particle and calculation of the radiation force is substantially simplified. In spite of its explicit abstraction, the model of a rigid body is quite sufficient for many applications since, as shown by Hasegawa and Yosioka,^{1–3} the elasticity of dispersed particles of solid material such as steel, brass, silica, etc., manifests itself only when the particle size is of the order of, or more than, the sound wavelength, which is not often met with in practice, except perhaps in determining the absolute acoustic intensity by the radiation force method.

The acoustic radiation force on a rigid sphere was first calculated by King⁴ who considered the surrounding fluid to be ideal. Later various aspects of the problem were theoretically investigated by Embleton,^{5,6} Maidanik and Westervelt,⁷ Olsen *et al.*,⁸ Nyborg,⁹ and Hasegawa and collaborators.^{1,10–14} Like King, all these authors considered the surrounding fluid to be perfect and neglected the heat conduction of the sphere. There are a number of experimental investigations which showed that the theory developed for perfect fluids is in good agreement with experimental measurements of the radiation forces on solid spheres (see, for example, Refs. 1–3 and 15–19). It is, however, only natural that the imperfect behavior of the surrounding fluid did not manifest itself in the above-mentioned experiments. It will be shown in this paper that in a plane standing wave field, which was used in Rudnick¹⁶ and Leung *et al.*'s¹⁹ experiments, and in a diverging spherical wave field, which was used by Embleton,¹⁵ the imperfect behavior of the surrounding fluid begins to play an important role only when the sphere radius R_0 is small compared with the depth of

penetration of the viscous wave δ_v . This was not the case in the experiments listed above, in which the magnitude of R_0/δ_v exceeded 9, 98, and 19, respectively. In a plane traveling wave field, the imperfect behavior of the surrounding fluid can manifest itself even when the ratio of R_0 to δ_v or/and to the depth of penetration of the thermal wave δ_t exceeds unity provided that the excess is not too large. But in the experiments of Hasegawa and collaborators^{1–3,17,18} who studied sound fields of this sort, the magnitudes of R_0/δ_v and R_0/δ_t exceeded 2000 and 5000, respectively.

Judging by the existing literature, there are no special experiments on studying viscous and thermal effects on the acoustic radiation forces. We are only aware of one experiment²⁰ in which an anomalous behavior of dispersed particles in a plane standing wave field was observed: heavy particles, i.e., those denser than the surrounding fluid, moved to the nodes of the fluid velocity but not to the antinodes as expected in accordance with the theory of the acoustic radiation forces in perfect fluids. It is of interest to note that the magnitude of R_0/δ_v was about within a range of 0.08–8.6 in that experiment.

Attempts to evaluate the radiation force experienced by a rigid sphere in an imperfect fluid were made by several researchers.^{21–26} The detailed analysis of their work is given in Ref. 27 and therefore will not be repeated here. Note only that, the common and most important demerit of all those papers is the absence of generality and rigor similar to those of the theory for perfect fluids.

In previous papers the present author^{27,28} examined the radiation force on a rigid sphere assuming the surrounding fluid to be viscous but not heat conducting. For example, it has been shown that taking the viscosity into account allows one to explain the anomalous behavior of heavy particles observed by Avetisyan *et al.*²⁰ in the case when they used

glycerin as the host fluid. In the present paper, on the basis of the general theory developed in Part I,²⁹ the radiation force on a rigid sphere is investigated assuming that the surrounding fluid is both viscous and heat conducting. Since the general formula for the radiation force derived in Part I is expressed in terms of the linear scattering coefficients, which depend on the internal structure of a particle considered, Sec. I of the present paper is devoted to calculating these coefficients for the case of a rigid sphere. In Sec. II, the radiation force is calculated for three types of incident sound field: a plane traveling wave, a plane standing wave, and a diverging spherical wave. To demonstrate dissipative effects clearly, for each of these sound fields two limiting cases are examined that allow the expressions for the radiation forces to be considerably simplified. In Sec. III, for completeness of exposition, expressions for the radiation forces on a fixed sphere are presented, calculations being performed for the same sound fields and limiting cases as in Sec. II. Finally, in Sec. IV a summary of the results obtained in this paper is given.

I. CALCULATION OF THE LINEAR SCATTERING COEFFICIENTS

As already mentioned, the general formula derived in Part I for the radiation force on a spherical object is expressed in terms of the linear scattering coefficients α_{1n} , α_{2n} , and α_{3n} which identify the linear scattered field from the object. In the case of a rigid sphere, these coefficients are calculated by making use of the following boundary conditions:

$$\mathbf{v}_I^{(1)} + \mathbf{v}_S^{(1)} = \mathbf{u}^{(1)} \quad \text{at } r = R_0, \quad (1)$$

$$T_I^{(1)} + T_S^{(1)} = \tilde{T}^{(1)} \quad \text{at } r = R_0, \quad (2)$$

$$\kappa_0 \frac{\partial}{\partial r} (T_I^{(1)} + T_S^{(1)}) = \tilde{\kappa}_0 \frac{\partial \tilde{T}^{(1)}}{\partial r} \quad \text{at } r = R_0, \quad (3)$$

where $\mathbf{u}^{(1)}$ is the first-order translational velocity of the sphere, the tilde denotes quantities that concern the medium inside the sphere, and the other symbols are the same as in Part I. Note also that the equilibrium temperature of the sphere \tilde{T}_0 is assumed to be equal to that of the surrounding fluid T_0 . The boundary conditions are supplemented with the equation of the translational motion of the sphere which in linear approximation is written as

$$\frac{4}{3} \pi R_0^3 \tilde{\rho}_0 \frac{d\mathbf{u}_i^{(1)}}{dt} = \int_{S_0} \sigma_{ik}^{(1)} n_k dS, \quad (4)$$

and an equation describing heat propagation inside the sphere for which we take the well-known Fourier equation:

$$\frac{\partial \tilde{T}^{(1)}}{\partial t} = \tilde{\chi}_0 \Delta \tilde{T}^{(1)}. \quad (5)$$

Substituting Eqs. (33)–(37) from Part I into Eq. (4), one obtains for $\mathbf{u}^{(1)}$

$$\begin{aligned} \mathbf{u}^{(1)} = & (A_1 \lambda_\rho / R_0) \mathbf{e}_z e^{-i\omega t} [j_1(x_1) + \alpha_{11} h_1^{(1)}(x_1) \\ & + \alpha_{21} h_1^{(1)}(x_2) + 2\alpha_{31} h_1^{(1)}(x_3)], \end{aligned} \quad (6)$$

where $\lambda_\rho = \rho_0 / \tilde{\rho}_0$, $x_j = k_j R_0$, and k_1 , k_2 , and k_3 are defined in Part I.

Axisymmetric solution of Eq. (5), which is also required to be finite at $r=0$ and to oscillate at the driving frequency, is given by

$$\tilde{T}^{(1)} = e^{-i\omega t} \sum_{n=0}^{\infty} \tilde{\alpha}_n A_n j_n(\tilde{k}_2 r) P_n(\cos \theta), \quad (7)$$

where $\tilde{k}_2 = (1+i)/\tilde{\delta}_t$, $\tilde{\delta}_t = \sqrt{2\tilde{\chi}_0/\omega}$, and $\tilde{\alpha}_n$ are dimensionless constants to be determined by the boundary conditions.

Substituting Eqs. (6) and (7) and also Eqs. (33)–(37) of Part I into Eqs. (1)–(3) and eliminating $\tilde{\alpha}_n$, one obtains a set of three simultaneous equations in α_{1n} , α_{2n} , and α_{3n} :

$$a_{ij} \alpha_{jn} = b_i, \quad i, j = 1, 2, 3, \quad (8)$$

where

$$\begin{aligned} a_{11} = & (1 - \lambda_\rho \delta_{1n}) n h_n^{(1)}(x_1) - x_1 h_{n+1}^{(1)}(x_1), \\ a_{12} = & (1 - \lambda_\rho \delta_{1n}) n h_n^{(1)}(x_2) - x_2 h_{n+1}^{(1)}(x_2), \\ a_{13} = & n(n+1)(1 - \lambda_\rho \delta_{1n}) h_n^{(1)}(x_3), \\ a_{21} = & (1 - \lambda_\rho \delta_{1n}) h_n^{(1)}(x_1), \\ a_{22} = & (1 - \lambda_\rho \delta_{1n}) h_n^{(1)}(x_2), \\ a_{23} = & (1 - \lambda_\rho \delta_{1n})(n+1) h_n^{(1)}(x_3) - x_3 h_{n+1}^{(1)}(x_3), \\ a_{31} = & (1 - nq_n) h_n^{(1)}(x_1) + q_n x_1 h_{n+1}^{(1)}(x_1), \end{aligned} \quad (9)$$

$$a_{32} = \frac{\beta_1 - k_2^2}{\beta_1 - k_1^2} [(1 - nq_n) h_n^{(1)}(x_2) + q_n x_2 h_{n+1}^{(1)}(x_2)],$$

$$a_{33} = 0,$$

$$b_1 = x_1 j_{n+1}(x_1) - (1 - \lambda_\rho \delta_{1n}) n j_n(x_1),$$

$$b_2 = (\lambda_\rho \delta_{1n} - 1) j_n(x_1),$$

$$b_3 = (nq_n - 1) j_n(x_1) - q_n x_1 j_{n+1}(x_1),$$

$$q_n = \lambda_\kappa j_n(\tilde{x}_2) / [n j_n(\tilde{x}_2) - \tilde{x}_2 j_{n+1}(\tilde{x}_2)],$$

$\lambda_\kappa = \kappa_0 / \tilde{\kappa}_0$, $\tilde{x}_2 = \tilde{k}_2 R_0$, β_1 is given by Eq. (16) of Part I, and as usual summation over repeated indices is implied.

Solutions of Eq. (8) are written as

$$\alpha_{1n} = [a_{13}(b_2 a_{32} - b_3 a_{22}) - a_{23}(b_1 a_{32} - b_3 a_{12})] / D, \quad (10)$$

$$\alpha_{2n} = [a_{13}(b_3 a_{21} - b_2 a_{31}) - a_{23}(b_3 a_{11} - b_1 a_{31})] / D, \quad (11)$$

$$\alpha_{3n} = [b_1(a_{21}a_{32} - a_{31}a_{22}) - b_2(a_{11}a_{32} - a_{31}a_{12}) + b_3(a_{11}a_{22} - a_{21}a_{12})]/D, \quad (12)$$

in which

$$D = a_{13}(a_{21}a_{32} - a_{31}a_{22}) - a_{23}(a_{11}a_{32} - a_{12}a_{31}). \quad (13)$$

The explicit expressions for α_{jn} are extremely cumbersome and therefore are not presented here.

II. RADIATION FORCE IN THE LIMIT OF LONG SOUND WAVELENGTH

The expression for the radiation force in the general case is too complicated and does not allow us to see clearly effects due to the imperfect behavior of the fluid and the material inside the sphere. For this reason, we consider in this section the limit of long sound wavelength by which one

means the limiting case where the sound wavelength is much larger than the sphere radius and also the viscous and thermal wavelengths. The expression for the radiation force is substantially simplified under such conditions. Besides, the above limit is of most interest for applications.

In the limit of long sound wavelength, the main contribution to the radiation force, given by Eq. (65) of Part I, comes from terms for which $n=0, 1$. Calculation of these terms requires the linear scattering coefficients α_{jn} for which $n=0,1,2$ and the functions $F_n^{(jk)}$ (see the Appendix of Part I) for which $n=0,1$. The expressions for α_{jn} in the limit involved are given in Appendix A and for $F_n^{(jk)}$ in Appendix B. When these expressions are substituted into Eq. (66) of Part I and only the leading terms in x_1 are retained, we obtain for Z_0 and Z_1

$$\begin{aligned} Z_0 = & -2x_1^3(1+x_3^2)/(9x_3^2) + 2ix_1^3g_1/(3x_2) + 2x_1^3g_2(3-6x_3-x_3^2)/9 + \frac{x_1^3x_3g_2}{3x_2^2} [x_2^2 + 3g_1(1-ix_2)] \\ & \times [x_3(f_2(x_3) - f_4(x_3)) + 3(f_3(x_3) - f_5(x_3))] + \frac{x_1^3g_1g_2}{3x_2^2} \{2x_2^2 - ix_2x_3^{-2}(3+3x_3+x_3^2) \\ & \times [x_3^2f_3(-ix_2) - 2ix_2f_4(-ix_2) + (2-x_3^2)f_5(-ix_2)] + [3x_3^{-2}/(x_3-ix_2)][ix_2x_3^4(x_3-ix_2)f_1(x_3-ix_2) - x_3^3(x_3^2-x_2^2) \\ & - 3ix_2x_3)f_2(x_3-ix_2) - x_3(3x_3^3+2ix_2^3-x_2^2x_3+x_2^2x_3^3+ix_2x_3^4)f_3(x_3-ix_2) - (2ix_2^3-2x_2^2x_3+3ix_2x_3^4+x_2^2x_3^3-x_3^5) \\ & \times f_4(x_3-ix_2) + (2x_2^2-x_2^2x_3^2+3x_3^4)f_5(x_3-ix_2)\}, \end{aligned} \quad (14)$$

$$\begin{aligned} Z_1 = & -\frac{2x_1^3}{9x_3^2} - \frac{x_1^3g_2^*}{45(1+x_3)} \{30 + (30+24i)x_3 + (20+24i)x_3^2 + 10x_3^3 + (15-15ix_3-5x_3^2)[x_3f_3(x_3) + 6f_4(x_3) \\ & - (x_3-6/x_3)f_5(x_3) - 6f_6(x_3) - 6f_7(x_3)/x_3] + 3(15+15x_3+6x_3^2+x_3^3)[f_4(x_3^*) + if_5(x_3^*)/x_3 - f_6(x_3^*) - if_7(x_3^*)/x_3] \\ & + 7.5[(3i-1)x_3f_2(x_3+x_3^*) + (8i-10)f_3(x_3+x_3^*) - (18+(3i-1)x_3)f_4(x_3+x_3^*) \\ & - (9(1+i)/x_3 + (8i-10)x_3)f_5(x_3+x_3^*) + 18f_6(x_3+x_3^*) + 9(1+i)f_7(x_3+x_3^*)/x_3]\}, \end{aligned} \quad (15)$$

where

$$g_1 = (\gamma_0 - 1)/(1 + q_0 - iq_0x_2), \quad (16)$$

$$g_2 = (1 - \lambda_\rho)/[9\lambda_\rho(1 + x_3) + (2 + \lambda_\rho)x_3^2], \quad (17)$$

$$f_n(z) = z \exp(z)E_n(z), \quad n = 1, 2, \dots, 7, \quad (18)$$

and $E_n(z)$ is the integral exponent of order n .³⁰

We consider below three types of incident sound field which are of most interest for acoustic applications: a plane traveling wave, a plane standing wave, and a diverging spherical wave.

A. Plane traveling wave

In the limit of long sound wavelength, from Eqs. (70) and (71) of Part I one has, respectively,

$$F_r^{(tr)} = 3\pi\rho_0|A|^2 \operatorname{Im}\{Z_0 + 2Z_1\}, \quad (19)$$

$$F_d^{(tr)} = -\pi\rho_0|A|^2(\omega R_0/c_0)^3(\delta_v/R_0)^2. \quad (20)$$

One can see that the expression for $F_r^{(tr)}$ still is too complicated. Therefore we consider below two limiting cases that allow further simplifications.

1. $|x_1| \ll |x_2|^{-1}, |x_3|^{-1}, |\tilde{x}_2|^{-1} \ll 1$

This condition describes the case where the sound wavelength is much larger than the sphere radius which is, in turn,

large compared with the viscous and thermal wavelengths in the surrounding fluid and the thermal wavelength inside the sphere yet not so large as to consider the latter wavelengths to be negligible. Passing to this limit in Eqs. (14)–(18), one finds

$$Z_0 = -\frac{2(\omega R_0/c_0)^3}{3(2+\lambda_\rho)} \left[1 + \frac{(1-i)(1-\lambda_\rho)^2}{2+\lambda_\rho} \frac{\delta_v}{R_0} - \frac{(1+i)(\gamma_0-1)(2+\lambda_\rho)}{2(1+\lambda_\kappa \widetilde{\delta}_t/\delta_t)} \frac{\delta_t}{R_0} \right], \quad (21)$$

$$Z_1 = \frac{2(1-\lambda_\rho)(\omega R_0/c_0)^3}{9(2+\lambda_\rho)} \left[1 + \frac{3(1+i)(1-\lambda_\rho)}{2+\lambda_\rho} \frac{\delta_v}{R_0} \right]. \quad (22)$$

Substitution of Eqs. (21) and (22) into Eq. (19) yields

$$F_r^{(tr)} = 2\pi\rho_0|A|^2 \left(\frac{\omega R_0}{c_0} \right)^3 \left[3 \left(\frac{1-\lambda_\rho}{2+\lambda_\rho} \right)^2 \frac{\delta_v}{R_0} + \frac{\gamma_0-1}{2(1+\lambda_\kappa \widetilde{\delta}_t/\delta_t)} \frac{\delta_t}{R_0} \right]. \quad (23)$$

Comparison of Eq. (20) with Eq. (23) shows that the drag force can be neglected in this limiting case.

King,⁴ who considered the surrounding fluid to be perfect, derived the following formula for the radiation force exerted by a plane traveling wave on a rigid sphere in the long sound wavelength limit:

$$F_K^{(tr)} = 2\pi\rho_0|A|^2 \left(\frac{\omega R_0}{c_0} \right)^6 \frac{9+2(1-\lambda_\rho)^2}{9(2+\lambda_\rho)^2}. \quad (24)$$

Note that the assumption of the ideality of the fluid and the sphere material has the same effect as the condition $|x_2|^{-1}, |x_3|^{-1}, |\widetilde{x}_2|^{-1} \ll |x_1| \ll 1$. By comparing Eq. (24) with Eq. (23), one can see that the imperfect behavior of the system involved, when it is no longer negligible (or, more exactly, when the condition entitling this subsection is valid), results in a substantial increase of the radiation force.

2. $|x_1| \ll |x_2|, |x_3|, |\widetilde{x}_2| \ll 1$

This condition corresponds to the case where the sphere radius is small compared with the viscous and thermal wavelengths in the fluid and the thermal wavelength inside the sphere which, as before, remain small compared with the sound wavelength. In this limit, from Eqs. (14)–(18) one obtains

$$Z_0 = \frac{2}{9} \left(\frac{\omega R_0}{c_0} \right)^3 \left[\frac{i\delta_v^2}{2R_0^2} + \frac{1-4\lambda_\rho}{3\lambda_\rho} - \frac{(1+i)(1-\lambda_\rho)}{\lambda_\rho} \frac{R_0}{\delta_v} + \frac{(1-i)(\gamma_0-1)\delta_t}{\lambda_\kappa \widetilde{\delta}_t} \frac{R_0}{\delta_t} \right], \quad (25)$$

$$Z_1 = \frac{2}{9} \left(\frac{\omega R_0}{c_0} \right)^3 \left[\frac{i\delta_v^2}{2R_0^2} - \frac{1-\lambda_\rho}{3\lambda_\rho} + \frac{3(1-i)(1-\lambda_\rho)}{5\lambda_\rho} \frac{R_0}{\delta_v} \right]. \quad (26)$$

Substitution of Eqs. (25) and (26) into Eq. (19) results in

$$F_r^{(tr)} = \pi\rho_0|A|^2 \left(\frac{\omega R_0}{c_0} \right)^3 \left[\left(\frac{\delta_v}{R_0} \right)^2 - \frac{22(1-\lambda_\rho)}{15\lambda_\rho} \frac{R_0}{\delta_v} - \frac{2(\gamma_0-1)\delta_t}{3\lambda_\kappa \widetilde{\delta}_t} \frac{R_0}{\delta_t} \right]. \quad (27)$$

It can be seen that the drag force is now equal and opposite to the leading term of the radiation force. As a result, the total force on the sphere becomes

$$F_{tr} = -\frac{2}{3} \pi\rho_0|A|^2 \left(\frac{\omega R_0}{c_0} \right)^3 \left[\frac{11(1-\lambda_\rho)}{5\lambda_\rho} \frac{R_0}{\delta_v} + \frac{(\gamma_0-1)\delta_t}{\lambda_\kappa \widetilde{\delta}_t} \frac{R_0}{\delta_t} \right]. \quad (28)$$

Equation (28) shows that heavy spheres for which $\lambda_\rho < 1$ are urged away toward the sound transducer while light ones for which $\lambda_\rho > 1$ can be forced away both from the sound transducer and toward it depending on whether the first or the second of the two terms between the square brackets of Eq. (28) is dominant. It should be emphasized that this distinguishing feature of light spheres is brought out as a result of the heat conduction being taken into account.

B. Plane standing wave

From Eq. (74) of Part I, one has

$$F_r^{(st)} = \frac{3}{2} \pi\rho_0|A|^2 \sin(2\omega d/c_0) \operatorname{Re}\{2Z_1 - Z_0\}. \quad (29)$$

From Eq. (75) of Part I it follows that the magnitude of the drag force $F_d^{(st)}$ is of the higher order in x_1 than that of $F_r^{(st)}$, and hence the drag force can be neglected.

Let us consider the same limiting cases as before.

1. $|x_1| \ll |x_2|^{-1}, |x_3|^{-1}, |\widetilde{x}_2|^{-1} \ll 1$

Upon substitution of Eqs. (21) and (22) into Eq. (29), one finds

$$F_r^{(st)} = \pi\rho_0|A|^2 \sin\left(\frac{2\omega d}{c_0}\right) \left(\frac{\omega R_0}{c_0} \right)^3 \left[\frac{5-2\lambda_\rho}{3(2+\lambda_\rho)} + 3 \left(\frac{1-\lambda_\rho}{2+\lambda_\rho} \right)^2 \frac{\delta_v}{R_0} - \frac{\gamma_0-1}{2(1+\lambda_\kappa \widetilde{\delta}_t/\delta_t)} \frac{\delta_t}{R_0} \right]. \quad (30)$$

The first term in the square brackets of Eq. (30) corresponds to the expression obtained by King⁴ for the radiation force in a perfect fluid. We see that accounting for viscosity and heat conduction only gives rise to small corrections to King's formula, these corrections being opposite in sign.

2. $|\mathbf{x}_1| \ll |\mathbf{x}_2|, |\mathbf{x}_3|, |\tilde{\mathbf{x}}_2| \ll 1$

Substitution of Eqs. (25) and (26) into Eq. (29) yields

$$F_r^{(st)} = \pi \rho_0 |A|^2 \sin\left(\frac{2\omega d}{c_0}\right) \left(\frac{\omega R_0}{c_0}\right)^3 \left[\frac{2\lambda_\rho - 1}{3\lambda_\rho} + \frac{11(1 - \lambda_\rho)}{15\lambda_\rho} \frac{R_0}{\delta_v} - \frac{(\gamma_0 - 1)\delta_t}{3\lambda_\kappa \tilde{\delta}_t} \frac{R_0}{\tilde{\delta}_t} \right]. \quad (31)$$

The first term in the square brackets of Eq. (31) has been derived in Ref. 27 where the surrounding fluid was considered to be viscous but not heat conducting. It can be seen from Eq. (31) that accounting for heat conduction only gives a small correction to the leading term caused by viscosity.

C. Diverging spherical wave

From Eqs. (79) and (80) of Part I, one finds, respectively,

$$F_r^{(sph)} = -3\pi\rho_0|A|^2\tau^{-5} \operatorname{Re}\{Z_0\tau^2(1+i\tau) + 2Z_1(3+2\tau^2+i\tau^3)\}, \quad (32)$$

$$F_d^{(sph)} = -\pi\rho_0|A|^2(\omega R_0/c_0)^3\tau^{-2}(\delta_v/R_0)^2. \quad (33)$$

It will be recalled that $\tau = \omega l/c_0$ in which l is the distance between the equilibrium center of the sphere and the point source of sound.

1. $|\mathbf{x}_1| \ll |\mathbf{x}_2|^{-1}, |\mathbf{x}_3|^{-1}, |\tilde{\mathbf{x}}_2|^{-1} \ll 1$

Upon substitution of Eqs. (21) and (22) into Eq. (32), one obtains

$$F_r^{(sph)} = \frac{2}{3}\pi\rho_0|A|^2(\omega R_0/c_0)^3[M_1\tau^{-5} + M_2\tau^{-3} + M_3\tau^{-2}], \quad (34)$$

where

$$M_1 = -2B(1 + B\delta_v/R_0), \quad (35)$$

$$M_2 = 1 - B - B^2 \frac{\delta_v}{R_0} - \frac{3(\gamma_0 - 1)}{2(1 + \lambda_\kappa \tilde{\delta}_t/\delta_t)} \frac{\delta_t}{R_0}, \quad (36)$$

$$M_3 = B^2 \frac{\delta_v}{R_0} + \frac{3(\gamma_0 - 1)}{2(1 + \lambda_\kappa \tilde{\delta}_t/\delta_t)} \frac{\delta_t}{R_0}, \quad (37)$$

$$B = 3(1 - \lambda_\rho)/(2 + \lambda_\rho). \quad (38)$$

First of all, note that comparison of Eq. (33) with Eq. (34) shows that the drag force can be neglected in this limiting case. By comparing Eqs. (34)–(38) with the corresponding equations obtained in Ref. 28 for a viscous but not heat-conducting fluid [see Eqs. (31)–(35) of that paper], we conclude that in the limit involved the heat conduction most appreciably manifests itself in the case of spheres for which $\lambda_\rho < \frac{1}{4}$. As shown in Ref. 28, spheres of this sort experience a force of attraction (i.e., the radiation force directed to the sound source) in the vicinity of the sound source and a force

of repulsion (i.e., the radiation force directed away from the sound source) when l is so large that the third term in the square brackets of Eq. (34) becomes dominant. From Eq. (37) it follows that accounting for heat conduction leads to an enhancement of the magnitude of the aforementioned term and hence to the reduction of the extent of the attraction region as compared with the case of a nonheatconducting fluid.

2. $|\mathbf{x}_1| \ll |\mathbf{x}_2|, |\mathbf{x}_3|, |\tilde{\mathbf{x}}_2| \ll 1$

Substitution of Eqs. (25) and (26) into Eq. (32) results in

$$F_r^{(sph)} = \frac{2}{3}\pi\rho_0|A|^2\left(\frac{\omega R_0}{c_0}\right)^3 \left\{ G_1\tau^{-5} + G_2\tau^{-3} + \left[G_3 + \frac{3}{2}\left(\frac{\delta_v}{R_0}\right)^2 \right] \tau^{-2} \right\}, \quad (39)$$

where

$$G_1 = 2(1 - \lambda_\rho)[1 - 9R_0/(5\delta_v)]/\lambda_\rho, \quad (40)$$

$$G_2 = \frac{1}{\lambda_\rho} - \frac{7(1 - \lambda_\rho)}{5\lambda_\rho} \frac{R_0}{\delta_v} - \frac{(\gamma_0 - 1)\delta_t}{\lambda_\kappa \tilde{\delta}_t} \frac{R_0}{\tilde{\delta}_t}, \quad (41)$$

$$G_3 = -\frac{11(1 - \lambda_\rho)}{5\lambda_\rho} \frac{R_0}{\delta_v} - \frac{(\gamma_0 - 1)\delta_t}{\lambda_\kappa \tilde{\delta}_t} \frac{R_0}{\tilde{\delta}_t}. \quad (42)$$

One can see from comparison of Eq. (39) with Eq. (33) that, in this case, the drag force is no longer negligible so that the total force on the sphere is written as

$$F_{sph} = (2/3)\pi\rho_0|A|^2(\omega R_0/c_0)^3[G_1\tau^{-5} + G_2\tau^{-3} + G_3\tau^{-2}]. \quad (43)$$

From Eqs. (40)–(42) it follows that for $\lambda_\rho < 1$, $G_1, G_2 > 0$ while $G_3 < 0$. Hence, according to Eq. (43), heavy spheres for which $\lambda_\rho < 1$ are acted on by a repulsive force when placed in the vicinity of the sound source. While at large distances from the sound source such that the third term in the square brackets of Eq. (43) is dominant, these spheres are subjected to an attractive force. Since repulsion changes to attraction but not vice versa, the heavy spheres can be levitated by a diverging spherical wave as is the case with a plane standing wave. This curious result was first obtained in Ref. 28. From Eq. (42) it follows that the heat conduction reduces the distance between a levitated sphere and the sound source since it increases the magnitude of the third term in the square brackets of Eq. (43).

In the case of light spheres for which $\lambda_\rho > 1$, $G_1 < 0$ and $G_2 > 0$. As regards G_3 , its value can be both positive and negative according to whether the first or the second of the two terms in Eq. (42) is larger in magnitude. If the first term is larger than the second one, then $G_3 > 0$ and, as follows from Eq. (43), near the sound source there is a region of attraction while far from it there is a region of repulsion. Thus, there are no stable states and levitation is impossible. If, however, the second term predominates over the first one,

then $G_3 < 0$ and as the distance from the sound source increases the attraction first changes to repulsion [when the second term in the square brackets of Eq. (43) becomes dominant] and then the repulsion again turns into attraction [when the third term in the square brackets of Eq. (43) begins to predominate]. Thus, in this case, there are states of stable equilibrium and hence the light spheres, like the heavy ones, can be levitated by a diverging spherical wave. It should be emphasized that this effect comes to light only because the heat conduction of the system is taken into account.

III. RADIATION FORCE ON A FIXED SPHERE

Up to here, we assumed a sphere to be free to move. In this section, for completeness of exposition, we present expressions for the radiation force on a fixed rigid sphere; we consider the same sound fields and the same limiting cases as in Sec. II.

A. Limiting case $|x_1| \ll |x_2|^{-1}, |x_3|^{-1}, |\tilde{x}_2|^{-1} \ll 1$

In this limit, the radiation force on a fixed sphere is readily found from appropriate formulas for a mobile sphere by setting $\lambda_p = 0$.

For a *plane traveling wave*, from Eq. (23) one has

$$F_r^{(tr)} = \pi \rho_0 |A|^2 \left(\frac{\omega R_0}{c_0} \right)^3 \left(\frac{3 \delta_v}{2 R_0} + \frac{\gamma_0 - 1}{1 + \lambda_\kappa \tilde{\delta}_t / \delta_t} \frac{\delta_t}{R_0} \right). \quad (44)$$

For a *plane standing wave*, from Eq. (30) one obtains

$$F_r^{(st)} = \frac{\pi}{2} \rho_0 |A|^2 \sin \left(\frac{2 \omega d}{c_0} \right) \left(\frac{\omega R_0}{c_0} \right)^3 \times \left(\frac{5}{3} + \frac{3 \delta_v}{2 R_0} - \frac{\gamma_0 - 1}{1 + \lambda_\kappa \tilde{\delta}_t / \delta_t} \frac{\delta_t}{R_0} \right). \quad (45)$$

Finally, for a *diverging spherical wave*, from Eq. (34) one finds

$$F_r^{(sph)} = \frac{2}{3} \pi \rho_0 |A|^2 (\omega R_0 / c_0)^3 \times (M_{1f} \tau^{-5} + M_{2f} \tau^{-3} + M_{3f} \tau^{-2}), \quad (46)$$

where

$$M_{1f} = -3 [1 + 3 \delta_v / (2 R_0)], \quad (47)$$

$$M_{2f} = -\frac{1}{2} - \frac{9 \delta_v}{4 R_0} - \frac{3(\gamma_0 - 1)}{2(1 + \lambda_\kappa \tilde{\delta}_t / \delta_t)} \frac{\delta_t}{R_0}, \quad (48)$$

$$M_{3f} = \frac{9 \delta_v}{4 R_0} + \frac{3(\gamma_0 - 1)}{2(1 + \lambda_\kappa \tilde{\delta}_t / \delta_t)} \frac{\delta_t}{R_0}. \quad (49)$$

The drag force is negligible in all these cases.

B. Limiting case $|x_1| \ll |x_2|, |x_3|, |\tilde{x}_2| \ll 1$

Setting $\lambda_p = 0$ in Eqs. (14)–(18) and then passing to the limit $|x_2|, |x_3|, |\tilde{x}_2| \ll 1$, one obtains

$$Z_0 = (\omega R_0 / c_0)^3 (1 - 6x_3) / (9x_3^2), \quad (50)$$

$$Z_1 = (\omega R_0 / c_0)^3 (1 + 12ix_3/5) / (9x_3^2). \quad (51)$$

Substituting Eqs. (50) and (51) into Eq. (19) and using Eq. (20), for the radiation and total forces in a *plane traveling wave* one obtains

$$F_r^{(tr)} = -\pi \rho_0 |A|^2 \left(\frac{\omega R_0}{c_0} \right)^3 \left(\frac{\delta_v^2}{2 R_0^2} - \frac{9 \delta_v}{5 R_0} \right), \quad (52)$$

$$F_{tr} = -\pi \rho_0 |A|^2 \left(\frac{\omega R_0}{c_0} \right)^3 \left(\frac{3 \delta_v^2}{2 R_0^2} - \frac{9 \delta_v}{5 R_0} \right). \quad (53)$$

For a *plane standing wave*, from Eq. (29) one has

$$F_r^{(st)} = F_{st} = 0.9 \pi \rho_0 |A|^2 (\omega R_0 / c_0)^3 (\delta_v / R_0) \sin(2 \omega d / c_0). \quad (54)$$

Finally, substituting Eqs. (50) and (51) into Eq. (32) and using Eq. (33), for a *diverging spherical wave* one finds

$$F_r^{(sph)} = -\pi \rho_0 |A|^2 \left(\frac{\omega R_0}{c_0} \right)^3 \left[\frac{12 \delta_v}{5 R_0} \tau^{-5} + \frac{3 \delta_v}{5 R_0} \tau^{-3} + \left(\frac{\delta_v^2}{2 R_0^2} - \frac{9 \delta_v}{5 R_0} \right) \tau^{-2} \right], \quad (55)$$

$$F_{sph} = -\pi \rho_0 |A|^2 \left(\frac{\omega R_0}{c_0} \right)^3 \left[\frac{12 \delta_v}{5 R_0} \tau^{-5} + \frac{3 \delta_v}{5 R_0} \tau^{-3} + \left(\frac{3 \delta_v^2}{2 R_0^2} - \frac{9 \delta_v}{5 R_0} \right) \tau^{-2} \right]. \quad (56)$$

Comparison of Eqs. (53), (54), and (56) with Eqs. (28), (31), and (43) shows that for all the three sound fields the total force on a fixed sphere is much larger than that on a mobile sphere. It is also of interest to note that in this limiting case thermal effects do not contribute to the leading terms of the radiation forces.

IV. CONCLUSIONS

In this paper, by use of the general theory developed in Part I of our study, we have examined the acoustic radiation force exerted by a sound field on a rigid sphere immersed in a viscous heat-conducting fluid. We have considered three types of incident sound field: a plane traveling wave, a plane standing wave, and a diverging spherical wave. To demonstrate clearly effects due to the imperfect behavior of the surrounding fluid and the material inside the sphere for each of these sound fields two limiting cases of interest have been investigated. In both cases, the sound wavelength was assumed to be much larger than the sphere radius, the viscous and thermal wavelengths in the surrounding fluid, and the thermal wavelength inside the sphere. In addition, in the first case, the sphere radius was assumed to be large compared with the three latter wavelengths, and in the second case, it

was assumed to be small compared with them. Since the influence of viscosity on the radiation force was studied in detail in earlier papers by the present author,^{27,28} in this paper, emphasis was on effects caused by heat conduction. It was found that for a plane standing wave the thermal effects only give rise to small corrections while in two other sound fields they result in a substantial refinement of the expression for the radiation force, especially in the second of the considered limiting cases. Taking the thermal mechanisms into account allowed one to ascertain that light spheres subject to

a plane traveling wave can be urged away by the radiation force both from the sound source and toward it and levitated by a diverging spherical wave. This latter result is likely to be of special interest for applications.

ACKNOWLEDGMENTS

This work was supported by the Ministry of Education and Science of the Republic of Belarus and the International Science Foundation.

APPENDIX A: EXPRESSIONS FOR THE LINEAR SCATTERING COEFFICIENTS $\alpha_{jn}(j=1,2,3;n=0,1,2)$ IN THE LIMIT OF LONG SOUND WAVELENGTH

$$\begin{aligned}\alpha_{10} &= -\frac{ix_1^3}{3} \left[1 + \frac{3(\gamma_0 - 1)(1 - ix_2)}{x_2^2(1 + q_0 - iq_0x_2)} \right], & \alpha_{20} &= \frac{ix_1^2(\gamma_0 - 1)\exp(-ix_2)}{x_2(1 + q_0 - iq_0x_2)}, & \alpha_{30} &= -\exp(-ix_3), \\ \alpha_{11} &= \frac{ix_1^3(1 - \lambda_\rho)(1 - ix_3 - x_3^2/3)}{9\lambda_\rho(1 - ix_3) - (2 + \lambda_\rho)x_3^2}, & \alpha_{21} &= \frac{ix_1^3(\gamma_0 - 1)\exp(-ix_2)\{[1 + 2\lambda_\rho + q_1(2 - 5\lambda_\rho)](1 - ix_3) + (\lambda_\rho q_1 - 1)x_3^2\}}{[(1 + 2q_1)(1 - ix_2) - q_1x_2^2][9\lambda_\rho(1 - ix_3) - (2 + \lambda_\rho)x_3^2]}, \\ \alpha_{31} &= \frac{ix_1x_3^2(1 - \lambda_\rho)\exp(-ix_3)}{9\lambda_\rho(1 - ix_3) - (2 + \lambda_\rho)x_3^2}, & \alpha_{12} &= \frac{2ix_1^5(15 - 15ix_3 - 6x_3^2 + ix_3^3)}{135x_3^2(ix_3 - 1)}, \\ \alpha_{22} &= \frac{ix_1^4x_2(\gamma_0 - 1)\exp(-ix_2)[6 - 6ix_3 - 3x_3^2 + ix_3^3 + 6q_2(3 - 3ix_3 - x_3^2)]}{9x_3^2(ix_3 - 1)[3 - 3ix_2 - x_2^2 + q_2(9 - 9ix_2 - 4x_2^2 + ix_2^3)]}, & \alpha_{32} &= \frac{ix_1^2x_3}{9(ix_3 - 1)} \exp(-ix_3).\end{aligned}$$

Note that in the long sound wavelength limit $x_1 \approx \omega R_0/c_0$ and $x_2 \approx (1 + i)R_0/\delta_t$.

APPENDIX B: EXPRESSIONS FOR THE FUNCTIONS $F_n^{(jk)}$ ($n=0,1$) IN THE LIMIT OF LONG SOUND WAVELENGTH

$$F_0^{(01)} = 2i(1 - x_3^2)/(3x_3^2), \quad F_1^{(01)} = 2i(14 - 5x_3^2)/(15x_3^2),$$

$$F_0^{(02)} = -\frac{2ix_1^2(1 + x_2 - x_3^2)}{3x_2^2x_3^2} \exp(-x_2),$$

$$F_1^{(02)} = -\frac{x_1(2 + 2x_2 + x_3^2)}{3x_2x_3^2} \exp(-x_2),$$

$$F_0^{(03)} = \frac{2ix_1^2(1 + x_3 - 2x_3^2)}{3x_3^4} \exp(-x_3),$$

$$F_1^{(03)} = -\frac{2x_1(1 + x_3)}{x_3^3} \exp(-x_3),$$

$$F_0^{(10)} = -2i(1 + x_3^2)/(3x_3^2),$$

$$F_1^{(10)} = -2i(14 + 5x_3^2)/(15x_3^2),$$

$$F_0^{(11)} = -4/(x_1^3x_3^2), \quad F_1^{(11)} = -81/(x_1^5x_3^2),$$

$$\begin{aligned}F_0^{(12)} &= \frac{1}{x_1} [(1 + x_2^2/x_3^2)E_3(x_2) + (2x_2/x_3^2)E_4(x_2) \\ &\quad - (1 - 2/x_3^2)E_5(x_2)] + (4 + 4x_2 + x_2^2 - x_3^2) \\ &\quad \times \exp(-x_2)/(x_1x_2^2x_3^2),\end{aligned}$$

$$\begin{aligned}F_1^{(12)} &= \frac{i}{2x_1^2x_2} [x_2^2E_3(x_2) + x_2(9 + 4x_2^2/x_3^2)E_4(x_2) + (9 \\ &\quad + 22x_2^2/x_3^2 - x_2^2)E_5(x_2) - 9(1 - 6/x_3^2)[x_2E_6(x_2) \\ &\quad + E_7(x_2)]] - \frac{i \exp(-x_2)}{x_1^2x_2^2x_3^2} (81 - 81ix_2 - 32x_2^2 \\ &\quad + 5ix_2^3 - 2x_2^4),\end{aligned}$$

$$\begin{aligned}F_0^{(13)} &= \frac{1}{x_1} [x_3E_2(x_3) + 3E_3(x_3) - x_3E_4(x_3) - 3E_5(x_3)] \\ &\quad - 2 \exp(-x_3)(2 + 2x_3 + x_3^2 + x_3^3)/(x_1x_3^4),\end{aligned}$$

$$\begin{aligned}F_1^{(13)} &= \frac{3i}{x_1^2x_3} [x_3^2E_3(x_3) + 6x_3E_4(x_3) + (6 - x_3^2)E_5(x_3) \\ &\quad - 6x_3E_6(x_3) - 6E_7(x_3)] - 6i \exp(-x_3) \\ &\quad \times (27 + 27x_3 + 11x_3^2 + 2x_3^3 + x_3^4)/(x_1^2x_3^5),\end{aligned}$$

$$F_0^{(20)} = -2ix_1(1 - ix_2 + x_3^2)\exp(ix_2)/(3x_2x_3^2),$$

$$\begin{aligned}F_1^{(20)} &= -x_1^2(28i + 28x_2 - 12ix_2^2 + 10ix_2^3 \\ &\quad + 3x_2x_3^2)\exp(ix_2)/(15x_2^2x_3^2),\end{aligned}$$

$$\begin{aligned}F_0^{(21)} &= -(x_2/x_1^2)[E_3(-ix_2) - (2ix_2/x_3^2)E_4(-ix_2) \\ &\quad - (1 - 2/x_3^2)E_5(-ix_2)] - 2(2 - 2ix_2 - x_2^2) \\ &\quad \times \exp(ix_2)/(x_1^2x_2x_3^2),\end{aligned}$$

$$\begin{aligned}
F_1^{(21)} &= \frac{9}{2x_1^3} [ix_2E_4(-ix_2) - (1 - 2x_2^2/x_3^2)E_5(-ix_2) + (1 - 6/x_3^2)[E_7(-ix_2) - ix_2E_6(-ix_2)]] \\
&\quad - \frac{9 \exp(ix_2)}{x_1^3x_2^2x_3^2} (9 - 9ix_2 - 4x_2^2 + ix_2^3), \\
F_0^{(22)} &= X_0^{(11)}(x_2, x_2), \quad F_1^{(22)} = X_1^{(11)}(x_2, x_2), \\
F_1^{(23)} &= [Y_1^{(110)}(x_2)]^*, \\
F_0^{(23)} &= -(x_2 + ix_3)E_1(x_3 - ix_2) + (x_3^2 - x_2^2 - 3ix_2x_3)E_2(x_3 - ix_2)/(x_2x_3) + (3x_3^3 + 2ix_2^3 - x_2^2x_3 + x_2^2x_3^3 + ix_2x_3^4) \\
&\quad \times E_3(x_3 - ix_2)/(x_2x_3^3) + (2ix_2^3 - 2x_2^2x_3 + 3ix_2x_3^4 + x_2^2x_3^3 - x_3^5)E_4(x_3 - ix_2)/(x_2x_3^4) + (2x_2^2 + x_2^2x_3^2 - 3x_3^4) \\
&\quad \times E_5(x_3 - ix_2)/(x_2x_3^4) + 2i(1 + x_3)(2i + 2x_2 - ix_2^2 + ix_3^2 + x_2x_3^2)\exp(ix_2 - x_3)/(x_2x_3^4), \\
F_0^{(30)} &= 0, \quad F_1^{(30)} = 2x_1^2(14i + 14x_3 + ix_3^2)\exp(ix_3)/(15x_3^4), \\
F_1^{(31)} &= \frac{9}{2x_1^3} [ix_3E_4(x_3^*) - E_5(x_3^*) - ix_3E_6(x_3^*) + E_7(x_3^*)] - 9i(9i + 9x_3 - 4ix_3^2 - x_3^3)\exp(ix_3)/(x_1^3x_3^4), \\
F_0^{(31)} &= 0, \quad F_0^{(32)} = 0, \quad F_1^{(32)} = Y_1^{(101)}(x_2), \quad F_0^{(33)} = 0, \\
F_1^{(33)} &= 3ix_3^{-3}[(1 + 2i)x_3^3E_2(x_3 + x_3^*) + (9i - 1)x_3^2E_3(x_3 + x_3^*) + (9(i - 1)x_3 - (1 + 2i)x_3^3)E_4(x_3 + x_3^*) - (9 + (9i - 1)x_3^2) \\
&\quad \times E_5(x_3 + x_3^*) - 9(i - 1)x_3E_6(x_3 + x_3^*) + 9E_7(x_3 + x_3^*)] + 6x_3^{-7} \exp(ix_3 - x_3)[27i + 27(1 + i)x_3 + (27 - i)x_3^2 \\
&\quad + (8 - 10i)x_3^3 - (1 + 3i)x_3^4].
\end{aligned}$$

Explicit expressions for the functions $F_0^{(22)}$, $F_1^{(22)}$, $F_1^{(23)}$, and $F_1^{(32)}$, which are extremely cumbersome, are not given here for the following reason. These functions are independent of x_1 , therefore the order of the contribution that they give to the radiation force is completely determined by the order in x_1 of the linear scattering coefficients α_{jn} corresponding to the above functions. The analysis of these coefficients shows that the contribution from the above functions is negligible in comparison with that from other terms. Thus, the functions listed above are not required for calculating the radiation force in the limit of long sound wavelength.

¹T. Hasegawa and K. Yosioka, "Acoustic-radiation force on a solid elastic sphere," *J. Acoust. Soc. Am.* **46**, 1139–1143 (1969).

²T. Hasegawa and K. Yosioka, "Acoustic radiation force on super duralumin sphere as an intensity standard in water," *J. Acoust. Soc. Jpn.* **30**, 443–447 (1974).

³T. Hasegawa and K. Yosioka, "Acoustic radiation force on fused silica spheres and intensity determination," *J. Acoust. Soc. Am.* **58**, 581–585 (1975).

⁴L. V. King, "On the acoustic radiation pressure on spheres," *Proc. R. Soc. London, Ser. A* **147**, 212–240 (1934).

⁵T. F. W. Embleton, "Mean force on a sphere in a spherical sound field. I. (Theoretical)," *J. Acoust. Soc. Am.* **26**, 40–45 (1954).

⁶T. F. W. Embleton, "The radiation force on a spherical obstacle in a cylindrical sound field," *Can. J. Phys.* **34**, 276–287 (1956).

⁷G. Maidanik and P. J. Westervelt, "Acoustic radiation pressure due to incident plane progressive waves on spherical objects," *J. Acoust. Soc. Am.* **29**, 936–940 (1957).

⁸H. Olsen, W. Romberg, and H. Wergeland, "Radiation force on bodies in a sound field," *J. Acoust. Soc. Am.* **30**, 69–76 (1958).

⁹W. L. Nyborg, "Radiation pressure on a small rigid sphere," *J. Acoust. Soc. Am.* **42**, 947–952 (1967).

¹⁰T. Hasegawa, "Comparison of two solutions for acoustic radiation pressure on a sphere," *J. Acoust. Soc. Am.* **61**, 1445–1448 (1977).

¹¹T. Hasegawa, "Acoustic radiation force on a sphere in a quasistationary wave field-theory," *J. Acoust. Soc. Am.* **65**, 32–40 (1979).

¹²T. Hasegawa, M. Ochi, and K. Matsuzawa, "Acoustic radiation pressure on a rigid sphere in a spherical wave field," *J. Acoust. Soc. Am.* **67**, 770–773 (1980).

¹³T. Hasegawa, M. Ochi, and K. Matsuzawa, "Acoustic radiation force on a solid elastic sphere in a spherical wave field," *J. Acoust. Soc. Am.* **69**, 937–942 (1981).

¹⁴T. Hasegawa, T. Kido, S. Takeda, N. Inoue, and K. Matsuzawa, "Acoustic radiation force on a rigid sphere in the near field of a circular piston vibrator," *J. Acoust. Soc. Am.* **88**, 1578–1583 (1990).

¹⁵T. F. W. Embleton, "Mean force on a sphere in a spherical sound field. II. (Experimental)," *J. Acoust. Soc. Am.* **26**, 46–50 (1954).

¹⁶I. Rudnick, "Measurements of the acoustic radiation pressure on a sphere in a standing wave field," *J. Acoust. Soc. Am.* **62**, 20–22 (1977).

¹⁷T. Hasegawa, "Acoustic radiation force on a sphere in a quasistationary wave field-experiment," *J. Acoust. Soc. Am.* **65**, 41–44 (1979).

¹⁸T. Hasegawa, M. Ochi, and K. Matsuzawa, "Acoustic radiation force on a fused silica sphere of large ka," *J. Acoust. Soc. Am.* **70**, 242–244 (1981).

¹⁹E. Leung, N. Jacobi, and T. Wang, "Acoustic radiation force on a rigid sphere in a resonance chamber," *J. Acoust. Soc. Am.* **70**, 1762–1767 (1981).

²⁰A. G. Avetisyan, V. S. Arakelyan, O. V. Bagdasaryan, and A. K. Dudyoyan, "On heavy particle behaviour in a viscous liquid in a standing ultrasonic wave field," *Akust. Zh.* **31**, 385–386 (1985) (in Russian).

²¹P. J. Westervelt, "The theory of steady forces caused by sound waves," *J. Acoust. Soc. Am.* **23**, 312–315 (1951).

²²A. P. Zhuk, "Interaction between a solid particle and a sound wave in a viscous fluid," *Prikl. Mekh. (Kiev)* **19**, 92–99 (1983) (in Russian).

²³A. N. Guz and A. P. Zhuk, "On the hydrodynamic forces acting in an acoustic field in a viscous liquid," *Dokl. Akad. Nauk SSSR* **266**, 32–35 (1982) (in Russian).

²⁴A. N. Guz and A. P. Zhuk, "On the forces acting on a spherical particle in a sound field in a viscous fluid," *Dokl. Akad. Nauk SSSR* **274**, 1313–1316 (1984) (in Russian).

²⁵S. D. Danilov, "Average force acting on a small sphere in a traveling wave field in a viscous fluid," *Akust. Zh.* **31**, 45–49 (1985) (in Russian).

- ²⁶S. D. Danilov, "Mean force acting on a small body in an axisymmetric sound field in actual medium," *Izv. Akad. Nauk SSSR, Mekh. zhid. gaza* **5**, 161–169 (1986) (in Russian).
- ²⁷A. A. Doinikov, "Acoustic radiation pressure on a rigid sphere in a viscous fluid," *Proc. R. Soc. London, Ser. A* **447**, 447–466 (1994).
- ²⁸A. A. Doinikov, "Radiation force due to a spherical sound field on a rigid sphere in a viscous fluid," *J. Acoust. Soc. Am.* **96**, 3100–3105 (1994).
- ²⁹A. A. Doinikov, "Acoustic radiation force on a spherical particle in a viscous heat-conducting fluid. I. General formula," *J. Acoust. Soc. Am.* **101**, 713–721 (1997).
- ³⁰M. Abramowitz and I. A. Stegun, *Handbook of Mathematical Functions* (Dover, New York, 1965).

Acoustic radiation force on a spherical particle in a viscous heat-conducting fluid. III. Force on a liquid drop

Alexander A. Doinikov

Institute of Nuclear Problems, Bobruiskaya 11, 220050 Minsk, Byelorussia

(Received 26 January 1996; accepted for publication 20 September 1996)

The general expression derived in Part I of this work [J. Acoust. Soc. Am. **101**, 713–721 (1997)] for the acoustic radiation force exerted by a sound field on a spherical particle in a viscous heat-conducting fluid is applied here to a liquid drop. To demonstrate dissipative effects clearly, two limiting cases are studied. In both cases, the sound wavelength is taken to be much larger than other characteristic parameters of the system, such as the drop radius and the viscous, and thermal wavelengths both outside and inside the drop. Within this assumption, two reverse situations are considered, in the first of which the dissipative effects are assumed to be weak, and in the second, to be strong. For each of these two cases, three types of incident wave are dealt with: a plane traveling wave, a plane standing wave, and a diverging spherical wave. Emphasis is given to the thermal effects on the radiation force. These are found to be greatest in the traveling and spherical waves, while in the standing wave, for both limiting cases, the thermal effects only give rise to small corrections to the leading terms due to compressibility and viscosity. © 1997 Acoustical Society of America. [S0001-4966(97)00802-3]

PACS numbers: 43.25.Qp [MAB]

INTRODUCTION

This paper is an extension of an earlier work by the present author¹ in which heat conduction has been neglected. In addition, the present paper considers three types of incident field, a plane traveling wave, a plane standing wave, and a diverging spherical wave, whereas in the previous paper only the first two waves have been dealt with.

There are a number of papers containing detailed reviews of the acoustic radiation forces on various objects, liquid drops included (see, for example, Refs. 2–5). Therefore only the most important, “classical,” works will be mentioned here, primarily for the purpose of comparing their predictions with ours. One such work is by Yosioka and Kawasima,⁶ who first calculated the acoustic radiation force on a compressible sphere of arbitrary radius containing an ideal fluid and surrounded by an ideal fluid. Their results, for the limiting case of a sphere much smaller than the wavelength of an incident sound field, were repeated by Gor’kov⁷ who applied a different, rather elegant, approach and also considered spherical waves in addition to plane traveling and standing waves, which Yosioka and Kawasima’s analysis is restricted to. For the same limiting case of a small sphere, Crum² obtained theoretically and then investigated experimentally the radiation force exerted on a liquid droplet by a stationary sound wave. In deriving the theoretical formula for the force, he used a very simple method that is the assimilation of two independent approaches, namely, of Nyborg’s approach,⁸ who considered rigid spheres, and Eller’s approach,⁹ who dealt with air bubbles. It is very interesting that despite such a purely mechanical integration of these two different approaches the resulting expression obtained by Crum is in complete agreement with the previous much more rigorous approaches of Yosioka and Kawasima⁶ and Gor’kov.⁷

Although the neglect of viscosity and heat conduction is

a rather strong abstraction, Yosioka and Kawasima’s theory,⁶ as well as the less general results of the other authors,^{2,7} is in good agreement with experimental observations, especially those related to acoustic levitation of liquid drops in a standing sound wave field (see, for example, Refs. 2 and 10–15). It is, however, not surprising if it is taken into consideration that in these experiments driving frequencies and drop sizes are such that viscosity and heat effects are negligible as far as the radiation pressure is concerned. The imperfect behavior of the outer and inner media of a drop involved is known and can be ignored when the wavelengths of viscous and thermal waves both outside and inside the drop are much smaller than the radius of the drop. It is such a situation that takes place in the above-mentioned experiments. However, a situation where one or both of these wavelengths are comparable with, or even much larger than, the drop radius is a quite realistic one, even in low-viscosity cases like a water drop in air. This can be easily illustrated by specific examples, taking a driving frequency of a few kilohertz and a drop radius of a few microns. In such a situation, the main contribution to the radiation force is shown by the present calculations to come from viscosity and heat conduction but not from terms obtained by Yosioka and Kawasima⁶ and Gor’kov,⁷ which result from compressibility alone. In the case of a plane traveling wave, this can occur even when the viscous and thermal wavelengths are small compared with the drop radius.

I. CALCULATION OF THE LINEAR SCATTERING COEFFICIENTS

Recall that the general formula obtained in Part I of this work¹⁶ for the radiation force is expressed in terms of the linear scattering coefficients which specify the linear scattered field from a particle under consideration. Thus, in the present paper these coefficients must be calculated to fit the

case of a liquid drop. Assume that the medium inside the drop is a viscous heat-conducting liquid. Then its linear motion is bound to be governed by equations similar in form to Eqs. (35)–(37) of Part I. We should only replace the spherical Hankel functions $h_n^{(1)}$ by the spherical Bessel functions j_n (since the sound and heat fields inside the drop must be finite at $r=0$) and the quantities associated with the host fluid by those associated with the drop liquid. This results in

$$\tilde{\mathbf{v}}^{(1)} = \nabla \tilde{\varphi}^{(1)} + \nabla \cdot \tilde{\boldsymbol{\psi}}^{(1)}, \quad (1)$$

where

$$\tilde{\varphi}^{(1)} = e^{-i\omega t} \sum_{n=0}^{\infty} A_n [\tilde{\alpha}_{1n} j_n(\tilde{k}_1 r) + \tilde{\alpha}_{2n} j_n(\tilde{k}_2 r)] P_n(\cos \theta), \quad (2)$$

$$\tilde{\boldsymbol{\psi}}^{(1)} = \mathbf{e}_e e^{-i\omega t} \sum_{n=1}^{\infty} \tilde{\alpha}_{3n} A_n j_n(\tilde{k}_3 r) P_n^1(\cos \theta), \quad (3)$$

and

$$\tilde{T}^{(1)} = \frac{i\tilde{\beta}_3}{\omega\tilde{\alpha}_0} e^{-i\omega t} \sum_{n=0}^{\infty} A_n [(\tilde{\beta}_1 - \tilde{k}_1^2) \tilde{\alpha}_{1n} j_n(\tilde{k}_1 r) + (\tilde{\beta}_1 - \tilde{k}_2^2) \tilde{\alpha}_{2n} j_n(\tilde{k}_2 r)] P_n(\cos \theta). \quad (4)$$

The tilde denotes quantities that concern the drop liquid. The dimensionless coefficients $\tilde{\alpha}_{jn}$, like the linear scattering coefficients α_{jn} , shall be determined from the boundary conditions at the drop surface. These are given by

$$v_r^{(1)} = \tilde{v}_r^{(1)}, \quad (5)$$

$$v_\theta^{(1)} = \tilde{v}_\theta^{(1)}, \quad (6)$$

$$\sigma_{rr}^{(1)} - p_{st} - p_0 = \tilde{\sigma}_{rr}^{(1)} - \tilde{p}_0, \quad (7)$$

$$\sigma_{r\theta}^{(1)} = \tilde{\sigma}_{r\theta}^{(1)}, \quad (8)$$

$$T^{(1)} = \tilde{T}^{(1)}, \quad (9)$$

$$\kappa_0 \frac{\partial T^{(1)}}{\partial r} = \tilde{\kappa}_0 \frac{\partial \tilde{T}^{(1)}}{\partial r}, \quad (10)$$

putting r equal to the mean drop radius R_0 . Here, $v_r^{(1)}$ and $v_\theta^{(1)}$ are the r - and θ -components of the total velocity of the host fluid defined as $\mathbf{v}^{(1)} = \mathbf{v}_l^{(1)} + \mathbf{v}_s^{(1)}$, $\sigma_{rr}^{(1)}$ and $\sigma_{r\theta}^{(1)}$ are the spherical components of the stress tensor given by Eq. (4) of Part I, p_0 is the equilibrium pressure in the host fluid, p_{st} is the pressure of surface tension, $T^{(1)}$ is the total change in the temperature of the host fluid, given by $T^{(1)} = T_l^{(1)} + T_s^{(1)}$ (the equilibrium temperature T_0 of the host fluid is assumed to be equal to that of the drop liquid \tilde{T}_0), and the other symbols are the same as in Part I. As before, quantities associated with the drop are denoted by the tilde. Equations (5) and (6) are the boundary condition of continuity of the fluid velocity across the drop surface, Eqs. (7) and (8) are that of stress, and Eqs. (9) and (10) are those of temperature and heat flux, respectively. Before applying Eqs. (5)–(10), some preliminaries should be fulfilled. First of all, an equation for p_{st} is wanted. Writing the perturbed surface of the drop as

$$R(\theta, t) = R_0 + X(\theta, t), \quad (11)$$

where

$$X(\theta, t) = e^{-i\omega t} \sum_{n=0}^{\infty} X_n P_n(\cos \theta), \quad (12)$$

one has for p_{st} ⁴

$$p_{st} = \sigma R_0^{-2} \left(2R_0 + e^{-i\omega t} \sum_{n=0}^{\infty} (n-1)(n+2) X_n P_n(\cos \theta) \right), \quad (13)$$

where σ is the surface tension, and the X_n can be found by using the following obvious equality:

$$\tilde{v}_r^{(1)}|_{r=R_0} = \frac{\partial R(\theta, t)}{\partial t} = \frac{\partial X(\theta, t)}{\partial t}. \quad (14)$$

Substituting Eqs. (1)–(3) and (12) into Eq. (14), one obtains

$$X_n = \frac{iA_n}{\omega R_0} [\tilde{x}_1 j_n'(\tilde{x}_1) \tilde{\alpha}_{1n} + \tilde{x}_2 j_n'(\tilde{x}_2) \tilde{\alpha}_{2n} + n(n+1) j_n(\tilde{x}_3) \tilde{\alpha}_{3n}], \quad (15)$$

where $\tilde{x}_j = \tilde{k}_j R_0$ ($j=1,2,3$), and $j_n'(\tilde{x}_j) = dj_n(\tilde{x}_j)/d\tilde{x}_j$.

This form of Eqs. (7) and (8) is not a convenient form, and we now recast these equations for the benefit of subsequent calculations. We begin with Eq. (7). By using the well-known formulas for the spherical components of the stress tensor in a viscous fluid,¹⁷ one obtains

$$\sigma_{rr}^{(1)} = -p^{(1)} + 2\eta_0 \frac{\partial v_r^{(1)}}{\partial r} + (\xi_0 - 2\eta_0/3) \nabla \cdot \mathbf{v}^{(1)}, \quad (16)$$

where $p^{(1)}$ is the perturbed pressure in the host fluid, which is determined by Eq. (9) of Part I, and the subscript 0 denotes the equilibrium conditions as before. Taking into consideration that quantities of first order varies with time as $\exp(-i\omega t)$, one finds from Eq. (9) of Part I

$$p^{(1)} = -ic_0^2 \rho_0 (i\omega \alpha_0 T^{(1)} + \nabla \cdot \mathbf{v}^{(1)}) / (\omega \gamma_0). \quad (17)$$

Furthermore, by using the formula for the divergence of a vector in spherical coordinates,¹⁸ $\partial v_r^{(1)}/\partial r$ can be written as

$$\frac{\partial v_r^{(1)}}{\partial r} = \nabla \cdot \mathbf{v}^{(1)} - \frac{2}{r} v_r^{(1)} - \frac{1}{r \sin \theta} \frac{\partial}{\partial \theta} (v_\theta^{(1)} \sin \theta). \quad (18)$$

Substituting Eqs. (17) and (18) into Eq. (16) and using Eqs. (13), (14), (16), and (18) of Part I, one has

$$\sigma_{rr}^{(1)} = -i\omega \rho_0 \varphi^{(1)} - 2\eta_0 \left[\frac{2}{r} v_r^{(1)} + \frac{1}{r \sin \theta} \frac{\partial}{\partial \theta} (v_\theta^{(1)} \sin \theta) \right]. \quad (19)$$

A similar expression holds for $\tilde{\sigma}_{rr}^{(1)}$. Upon substitution of the latter along with Eq. (19) into Eq. (7) and the use of Eq. (5) and the fact that, in view of Eq. (6),

$$\frac{\partial}{\partial \theta} (v_\theta^{(1)} \sin \theta) = \frac{\partial}{\partial \theta} (\tilde{v}_\theta^{(1)} \sin \theta) \quad \text{at } r=R_0, \quad (20)$$

one obtains the following result:

$$\begin{aligned} \tilde{\varphi}^{(1)} - \frac{\rho_0}{\tilde{\rho}_0} \varphi^{(1)} + \frac{2R_0(\tilde{\eta}_0 - \eta_0)}{\tilde{\eta}_0 \tilde{x}_3^2} \\ \times \left[2v_r^{(1)} + \frac{1}{\sin \theta} \frac{\partial}{\partial \theta} (v_\theta^{(1)} \sin \theta) \right] \\ = (p_0 - \tilde{p}_0 + p_{st}) / (i\omega \tilde{\rho}_0) \quad \text{at } r = R_0. \end{aligned} \quad (21)$$

We now rearrange Eq. (8). The component $\sigma_{r\theta}^{(1)}$ is given by¹⁷

$$\sigma_{r\theta}^{(1)} = \eta_0 \left(\frac{1}{r} \frac{\partial v_r^{(1)}}{\partial \theta} + \frac{\partial v_\theta^{(1)}}{\partial r} - \frac{v_\theta^{(1)}}{r} \right). \quad (22)$$

With the aid of the formula for the curl of $\mathbf{v}^{(1)}$ in spherical coordinates,¹⁸ one obtains

$$\frac{\partial v_\theta^{(1)}}{\partial r} = (\nabla \times \mathbf{v}^{(1)})_\varepsilon - \frac{v_\theta^{(1)}}{r} + \frac{1}{r} \frac{\partial v_r^{(1)}}{\partial \theta}. \quad (23)$$

Using Eqs. (13) and (19) of Part I and the fact that $\nabla \cdot \boldsymbol{\psi}^{(1)} = 0$, one has

$$\nabla \times \mathbf{v}^{(1)} = \nabla \times (\nabla \times \boldsymbol{\psi}^{(1)}) = -\Delta \boldsymbol{\psi}^{(1)} = k_3^2 \boldsymbol{\psi}^{(1)}. \quad (24)$$

Substituting Eq. (24) into Eq. (23) and then Eq. (23) into Eq. (22), one finds

$$\sigma_{r\theta}^{(1)} = \eta_0 \left[k_3^2 \boldsymbol{\psi}^{(1)} + \left(\frac{2}{r} \right) \frac{\partial v_r^{(1)}}{\partial \theta} - \frac{2v_\theta^{(1)}}{r} \right], \quad (25)$$

where $\boldsymbol{\psi}^{(1)} = \boldsymbol{\psi}^{(1)} \cdot \mathbf{e}_\varepsilon$. Upon substitution of Eq. (25) along with a similar expression for $\tilde{\sigma}_{r\theta}^{(1)}$ into Eq. (8) and the use of Eq. (6) and the equality

$$\frac{\partial v_r^{(1)}}{\partial \theta} = \frac{\partial \tilde{v}_r^{(1)}}{\partial \theta} \quad \text{at } r = R_0, \quad (26)$$

which results from Eq. (5), one finally obtains

$$\begin{aligned} \tilde{\psi}^{(1)} - \frac{\rho_0}{\tilde{\rho}_0} \boldsymbol{\psi}^{(1)} + \frac{2R_0(\tilde{\eta}_0 - \eta_0)}{\tilde{\eta}_0 \tilde{x}_3^2} \left(\frac{\partial v_r^{(1)}}{\partial \theta} - v_\theta^{(1)} \right) = 0 \\ \text{at } r = R_0. \end{aligned} \quad (27)$$

Although they appear much more cumbersome, Eqs. (21) and (27) are more convenient in practical calculations than Eqs. (7) and (8).

Now we can employ the boundary conditions. Substituting Eqs. (1)–(4), (13), (15), and Eqs. (33)–(37) from Part I into Eqs. (5), (6), (9), (10), (21), and (27) and eliminating the $\tilde{\alpha}_{jn}$, which are not required for calculating the radiation force, we obtain three combined equations in the unknowns α_{jn} :

$$a_{i1}^{(n)} \alpha_{1n} + a_{i2}^{(n)} \alpha_{2n} + a_{i3}^{(n)} \alpha_{3n} = b_i^{(n)}, \quad i = 1, 2, 3. \quad (28)$$

Inasmuch as the quantities $a_{ij}^{(n)}$ and $b_i^{(n)}$ are rather cumbersome, they are given in Appendix A. Note that for $n=0$ only the first two equations should be retained in Eq. (28) since $\alpha_{30} \equiv 0$. Except for extremely unwieldy expressions for α_{jn} , solving Eq. (28) presents no problems, and hence our goal can be regarded to be achieved. By substituting α_{jn} from Eq.

(28) into appropriate equations of Part I, the radiation force on a liquid drop can be calculated for any parameters of the system involved. We would like, however, to show effects of viscosity and heat conduction on the radiation force more dramatically, for which purpose we consider in the next section some limiting cases. These allow considerable simplifications and are of immediate interest for applications.

II. RADIATION FORCE IN SOME LIMITING CASES

In this section, the wavelength of the incident sound field is assumed to be much larger than the drop radius, the viscous wavelength, and the thermal wavelength both outside and inside the drop ($|x_1|, |\tilde{x}_1| \ll 1, |x_2|, |\tilde{x}_2|, |x_3|, |\tilde{x}_3|$). In this limit, the main contribution to the radiation force, which is given by Eq. (65) of Part I, comes from the first two terms of that formula, so that the radiation force is represented as follows:

$$F_r = \pi \rho_0 \operatorname{Re}(Z_0 A_0 A_1^* + \frac{2}{3} Z_1 A_1 A_2^*), \quad (29)$$

where Z_0 and Z_1 are given by Eq. (66) of Part I to be

$$Z_n = \sum_{j=1}^3 \left(F_n^{(0j)} \alpha_{jn+1}^* + F_n^{(j0)} \alpha_{jn} + \sum_{k=1}^3 F_n^{(jk)} \alpha_{jn} \alpha_{kn+1}^* \right). \quad (30)$$

The quantities $F_n^{(jk)}$ are presented in the Appendix of Part I. It is seen that for calculating Z_0 and Z_1 we need α_{jn} for which $n=0, 1, 2$ and $F_n^{(jk)}$ for which $n=0, 1$. Expressions for the first quantities in the limit of long sound wavelength are given in Appendix B of this paper, and those for the second quantities have been obtained in Part II and are presented in Appendix B of that paper.¹⁹ Under close examination of the above expressions it is seen that Z_0 and Z_1 can be reduced to

$$\begin{aligned} Z_0 = \alpha_{10}(F_0^{(10)} + \alpha_{11}^* F_0^{(11)} + \alpha_{31}^* F_0^{(13)}) \\ + \alpha_{20}(F_0^{(20)} + \alpha_{11}^* F_0^{(21)} + \alpha_{31}^* F_0^{(23)}) \\ + \alpha_{11}^* F_0^{(01)} + \alpha_{31}^* F_0^{(03)} + O(x_1^5), \end{aligned} \quad (31)$$

$$\begin{aligned} Z_1 = \alpha_{11}(F_1^{(10)} + \alpha_{12}^* F_1^{(11)} + \alpha_{32}^* F_1^{(13)}) + \alpha_{31}(F_1^{(30)} \\ + \alpha_{12}^* F_1^{(31)} + \alpha_{32}^* F_1^{(33)}) + \alpha_{32}^* F_1^{(03)} + O(x_1^5), \end{aligned} \quad (32)$$

where only leading terms in x_1 , which are proportional to x_1^3 , are retained. However, if we calculate Z_0 and Z_1 by Eqs. (31) and (32) and substitute them into Eq. (29), the resulting expression for the radiation force still will be too complicated. Therefore, remaining within the limit of long sound wavelength, we consider below two limiting cases that allow further simplifications. In the first of these, the drop radius is assumed to be large compared with the viscous and thermal wavelengths both outside and inside the drop, so that the following inequality holds: $|x_1|, |\tilde{x}_1| \ll 1 \ll |x_2|, |\tilde{x}_2|, |x_3|, |\tilde{x}_3|$. In other words, viscous and heat effects are treated as weak in this case. In the second case, on the contrary, these effects are assumed to be strong, such that the drop radius is small compared with the above wavelengths both outside and in-

side the drop: $|x_1|, |\tilde{x}_1| \ll 1 \ll |x_2|, |\tilde{x}_2|, |x_3|, |\tilde{x}_3|$. For each of these limiting cases, three types of incident wave are studied: a plane traveling wave, a plane standing wave, and a diverging spherical wave.

A. Weak dissipative effects:

$$|x_1|, |\tilde{x}_1| \ll 1 \ll |x_2|, |\tilde{x}_2|, |x_3|, |\tilde{x}_3|$$

Expressions for α_{jn} and $F_n^{(jk)}$ required for calculating Z_0 and Z_1 in this limit are given with necessary accuracy in Appendix C. Substituting them into Eqs. (31) and (32), one has

$$Z_0 = \frac{2}{9} \left(\frac{\omega R_0}{c_0} \right)^3 \left(\frac{\rho_0 c_0^2}{\tilde{\rho}_0 \tilde{c}_0^2} - \frac{3}{2 + \lambda_\rho} - \frac{\delta_v}{R_0} Z_v^* + \frac{\delta_t}{R_0} Z_t \right), \quad (33)$$

$$Z_1 = \frac{2}{9} \left(\frac{\omega R_0}{c_0} \right)^3 \left(\frac{1 - \lambda_\rho}{2 + \lambda_\rho} + \frac{\delta_v}{R_0} Z_v \right), \quad (34)$$

where

$$Z_v = 3 \left(\frac{1 - \lambda_\rho}{2 + \lambda_\rho} \right)^2 \frac{(1 + i) [1 + \lambda_\rho \delta_v / \tilde{\delta}_v + 2 \lambda_\eta \tilde{\delta}_v / R_0 + 2 (\lambda_\eta \tilde{\delta}_v / R_0)^2] + 2 i \lambda_\rho \lambda_\eta \delta_v / R_0}{(1 + \lambda_\rho \delta_v / \tilde{\delta}_v + \lambda_\eta \tilde{\delta}_v / R_0)^2 + (\lambda_\eta \tilde{\delta}_v / R_0)^2}, \quad (35)$$

$$Z_t = \frac{3(1 + i) [(\gamma_0 - 1) \tilde{\rho}_0 \tilde{c}_0^2 - \lambda_\alpha (\tilde{\gamma}_0 - 1) \rho_0 c_0^2] (\lambda_\alpha \delta_t^2 - \lambda_\kappa \tilde{\delta}_t^2)}{2 \tilde{\rho}_0 \tilde{c}_0^2 \lambda_\alpha \delta_t (\delta_t + \lambda_\kappa \tilde{\delta}_t)}, \quad (36)$$

$\lambda_\rho = \rho_0 / \tilde{\rho}_0$, $\lambda_\eta = \eta_0 / \tilde{\eta}_0$, $\lambda_\alpha = \alpha_0 / \tilde{\alpha}_0$, $\lambda_\kappa = \kappa_0 / \tilde{\kappa}_0$, $\delta_v = \sqrt{2 \eta_0 / (\rho_0 \omega)}$ is the depth of penetration of the viscous wave in the host fluid, $\delta_t = \sqrt{2 \chi_0 / \omega}$ is that of the thermal wave, and $\tilde{\delta}_v, \tilde{\delta}_t$ are similar quantities in the drop liquid. It follows from the inequality heading this subsection that $\delta_v, \tilde{\delta}_v, \delta_t, \tilde{\delta}_t \ll R_0$. Thus, Eqs. (33) and (34) are accurate up to the first order of smallness. Furthermore, we have remained in Eq. (35) terms containing the product $\lambda_\eta (\tilde{\delta}_v / R_0)$ because these can be essential when $\eta_0 \gg \tilde{\eta}_0$. Let us consider how the liquid drop behaves in various sound fields.

1. Plane traveling wave

The radiation force exerted by a plane traveling wave is given by Eq. (70) of Part I. Substitution of Eqs. (33) and (34) into that formula yields

$$F_r^{(tr)} = 2 \pi \rho_0 |A|^2 \left(\frac{\omega R_0}{c_0} \right)^3 \left[\frac{\delta_v}{R_0} \text{Im}(Z_v) + \frac{\delta_t}{3 R_0} \text{Im}(Z_t) \right]. \quad (37)$$

First of all, let us compare Eq. (37) with the corresponding formula of Yosioka and Kawasima [see Eq. (58) of Ref. 6]:

$$F_{Y\&K}^{(tr)} = 2 \pi \rho_0 |A|^2 \frac{(\omega R_0 / c_0)^6}{(2 + \lambda_\rho)^2} \left[\left(1 - \frac{\lambda_\rho c_0^2 (2 + \lambda_\rho)}{3 \tilde{c}_0^2} \right)^2 + \frac{2}{9} (1 - \lambda_\rho)^2 \right]. \quad (38)$$

Recall that this latter formula has been derived on the assumption that media both outside and inside the drop are ideal. It should be understood that both these expressions, Eqs. (37) and (38), are terms of a unified one that is the expansion of the radiation force in x_1 . Equation (38) is the leading term when viscosity and heat conduction are zero, while Eq. (37) is that when viscosity and heat conduction are small but still finite. By comparing Eq. (37) with Eq. (38), we can evaluate when Eq. (37) begins to predominate. This occurs when $(\omega R_0 / c_0)^3 \ll \delta_v / R_0 \ll 1$ and/or $(\omega R_0 / c_0)^3$

$\ll \delta_t / R_0 \ll 1$. As a result of these conditions, an interesting problem arises. Consider a typical case, such as a drop of immiscible liquid in water. For water one has $\rho_0 = 1000 \text{ kg/m}^3$, $c_0 = 1485 \text{ m/s}$, $\eta_0 = 10^{-3} \text{ Pa s}$, $\chi_0 = 1.4 \times 10^{-7} \text{ m}^2/\text{s}$. Let us take characteristic values for R_0 and the driving frequency f , say, $R_0 = 50 \text{ }\mu\text{m}$ and $f = 25 \text{ kHz}$. Then one obtains $(\omega R_0 / c_0) \approx 5.3 \times 10^{-3}$ [accordingly, $(\omega R_0 / c_0)^3 \approx 1.5 \times 10^{-7}$], $\delta_v / R_0 \approx 0.07$, and $\delta_t / R_0 \approx 0.03$. It is seen that the above conditions are satisfied. Even though we increase R_0 by a factor of 10, they will still hold. It follows that in the majority of cases the radiation force exerted by plane traveling waves on liquid drops must be determined by Eq. (37) but not Eq. (38). If this is the case, then the magnitude of the radiation force should be much larger than that is predicted by Yosioka and Kawasima's theory.⁶ To verify this conclusion, experimental measurements of the radiation force on liquid drops in plane traveling waves are required. As far as we are aware there are no such measurements.

Let us now consider Eq. (37) itself. This is seen to consist of two parts. The first is due to viscosity. It was first obtained in Ref. 1, except for the corrections like $\lambda_\eta \tilde{\delta}_v / R_0$. The second is caused by heat conduction. Unlike the viscous term which is always positive, the thermal one can be, in principle, of any sign. As for the magnitudes of these terms, specific examples show those are of the same order. To illustrate this, consider, for instance, a benzene drop in water. The data for water, which were given above, should be supplemented with $\alpha_0 = 2.1 \times 10^{-4} \text{ K}^{-1}$, $\kappa_0 = 0.58 \text{ J/(smK)}$, and $\gamma_0 = 1.007$. For benzene similar physical parameters are $\tilde{\rho}_0 = 880 \text{ kg/m}^3$, $\tilde{c}_0 = 1321 \text{ m/s}$, $\tilde{\eta}_0 = 6.5 \times 10^{-4} \text{ Pa s}$, $\tilde{\chi}_0 = 1.18 \times 10^{-7} \text{ m}^2/\text{s}$, $\tilde{\alpha}_0 = 1.24 \times 10^{-3} \text{ K}^{-1}$, $\tilde{\kappa}_0 = 0.14 \text{ J/(smK)}$, $\tilde{\gamma}_0 = 1.1$. Putting $R_0 = 50 \text{ }\mu\text{m}$ and $f = 25 \text{ kHz}$ as before, one obtains for the interior of the drop: $\omega R_0 / \tilde{c}_0 \approx 5.9 \times 10^{-3}$ [$(\omega R_0 / \tilde{c}_0)^3 \approx 2.1 \times 10^{-7}$], $\tilde{\delta}_v / R_0 \approx 0.06$, $\tilde{\delta}_t / R_0 \approx 0.024$. Considering also related quantities for the exterior

of the drop evaluated before, one can see that all the required conditions are satisfied. The ratio of the thermal term to the viscous term is equal to about 5, and the ratio of $F_r^{(tr)}$ to $F_{Y\&K}^{(tr)}$ is of the order of 10^5 .

For a liquid drop suspended in a gas $\lambda_\rho \ll 1$, $\lambda_\eta \ll 1$, $\rho_0 c_0^2 \ll \tilde{\rho}_0 \tilde{c}_0^2$, $\lambda_\kappa \tilde{\delta}_t \ll \lambda_\alpha \delta_t^2$, and $\lambda_\kappa \tilde{\delta}_t \ll \delta_t$. As a result, Eq. (37) reduces to

$$F_r^{(tr)} = \pi \rho_0 |A|^2 (\omega R_0 / c_0)^3 (3 \delta_v / 2 R_0 + (\gamma_0 - 1) \delta_t / R_0). \quad (39)$$

As an illustration let us consider a drop with $R_0 = 100 \mu\text{m}$, suspended in air and subjected to a sound wave with $f = 30 \text{ kHz}$. Taking for air $\rho_0 = 1.2 \text{ kg/m}^3$, $c_0 = 330 \text{ m/s}$, $\eta_0 = 1.8 \times 10^{-5} \text{ Pa s}$, $\chi_0 = 2.8 \times 10^{-5} \text{ m}^2/\text{s}$, and $\gamma_0 = 1.4$, one finds $\omega R_0 / c_0 \approx 0.057$ [$(\omega R_0 / c_0)^3 \approx 1.86 \times 10^{-4}$], $\delta_v / R_0 \approx 0.12$, and $\delta_t / R_0 \approx 0.17$. Thus, the required conditions are satisfied. The ratio of the thermal term to the viscous one is about 0.38, that is the main contribution comes now from viscosity. The ratio of $F_r^{(tr)}$ to $F_{Y\&K}^{(tr)}$ is of the order of 10^3 .

2. Plane standing wave

To obtain the radiation force due to this wave, substitute Eqs. (33) and (34) into Eq. (74) of Part I. The result is

$$F_r^{(st)} = \pi \rho_0 |A|^2 \sin\left(\frac{2\omega d}{c_0}\right) \left(\frac{\omega R_0}{c_0}\right)^3 \left[\frac{1}{3} \left(\frac{5 - 2\lambda_\rho}{2 + \lambda_\rho} - \frac{\lambda_\rho c_0^2}{\tilde{c}_0^2} \right) + \frac{\delta_v}{R_0} \text{Re}(Z_v) - \frac{\delta_t}{3R_0} \text{Re}(Z_t) \right], \quad (40)$$

where d is the distance between the equilibrium center of the drop and the nearest plane of the velocity nodes. The first term within square brackets in Eq. (40) is Yosioka and Kawasima's result [see Eq. (61) of Ref. 6]. Taking into account viscosity and heat conduction is seen to only give rise to small corrections. This explains why Yosioka and Kawasima's theory is in such a good agreement with experiments for plane standing waves.

3. Diverging spherical wave

Substituting Eqs. (33) and (34) into Eq. (79) of Part I, one finds

$$F_r^{(sph)} = \frac{2}{3} \pi \rho_0 |A|^2 (\omega R_0 / c_0)^3 [M_1 \tau^{-5} + M_2 \tau^{-3} + M_3 \tau^{-2}], \quad (41)$$

where

$$M_1 = 6 \left(\frac{\lambda_\rho - 1}{2 + \lambda_\rho} - \frac{\delta_v}{R_0} \text{Re}(Z_v) \right), \quad (42)$$

$$M_2 = \frac{4\lambda_\rho - 1}{2 + \lambda_\rho} - \frac{\lambda_\rho c_0^2}{\tilde{c}_0^2} - \frac{3\delta_v}{R_0} \text{Re}(Z_v) - \frac{\delta_t}{R_0} \text{Re}(Z_t), \quad (43)$$

$$M_3 = \frac{3\delta_v}{R_0} \text{Im}(Z_v) + \frac{\delta_t}{R_0} \text{Im}(Z_t), \quad (44)$$

and $\tau = \omega l / c_0$ in which l is the distance between the equilibrium center of the drop and the spherical wave source. When $\delta_v, \delta_t \rightarrow 0$, Eq. (41) reduces to Gor'kov's formula.⁷ Accounting for the dissipative effects gives rise to small corrections to M_1 and M_2 and the third term, $M_3 \tau^{-2}$, within the square

brackets in Eq. (41). This term predominates at large distances (i.e., when $\tau \gg 1$) from the sound source. Its effect upon the drop behavior becomes particularly pronounced when it is opposite in sign to the second term, $M_2 \tau^{-3}$. This occurs, for example, for a liquid drop in gas. In this case, $M_1, M_2 < 0$, which means that in the vicinity of the sound source the drop is attracted to it. Since $M_3 = 3(3\delta_v + 2(\gamma_0 - 1)\delta_t)/(4R_0) > 0$, the presence of the third term results in changing the attraction to repulsion when the drop is at a large distance from the sound source. It should be noted that when the dissipative effects are neglected, the reversal of the radiation force occurs, too, but this happens at much larger distances from the sound source because stems from a term of much higher order in $\omega R_0 / c_0$ [see Eq. (31a) of Ref. 8]. Thus, the dissipative effects considerably reduce the extent of the attraction region.

In closing Sec. II A, it will be recalled that the total time-averaged force exerted on a particle by a sound wave, apart from the acoustic radiation force F_r considered here, involves the drag force F_d , which is given for an arbitrary axisymmetric field by Eq. (67) of Part I, and for the three sound fields covered here by Eqs. (71), (75), and (80) of Part I. This latter force has not been mentioned in this subsection because it is negligible when compared with the radiation force in all the three sound fields in the limiting case studied above. This is not always the case in the next subsection, and the drag force will be dealt with there when necessary.

B. Strong dissipative effects: $|\mathbf{x}_1|, |\tilde{\mathbf{x}}_1| \ll |\mathbf{x}_2|, |\tilde{\mathbf{x}}_2|, |\mathbf{x}_3|, |\tilde{\mathbf{x}}_3| \ll 1$

Expressions for the quantities α_{jn} and $F_n^{(jk)}$, which are required for calculating Z_0 and Z_1 in this limiting case, are given in Appendix D. Substituting these into Eqs. (31) and (32), one obtains

$$Z_0 = \frac{2}{9} \left(\frac{\omega R_0}{c_0} \right)^3 \left[\left(\frac{\tilde{\gamma}_0 \lambda_\rho c_0^2}{\tilde{c}_0^2} - \frac{\gamma_0 - 1}{\lambda_\alpha} - 1 \right) \times \left(\frac{1}{x_3^2} + \frac{1 + 8\lambda_\rho + 6\lambda_\rho \lambda_\eta}{3\lambda_\rho(3 + 2\lambda_\eta)} \right) + \frac{(1 - \lambda_\rho)(4 + 3\lambda_\eta)}{3\lambda_\rho(3 + 2\lambda_\eta)} - \left(\frac{\lambda_\rho - 1}{2\lambda_\rho} + \frac{5 + \lambda_\kappa}{5\lambda_\alpha} \right) \frac{\gamma_0 - 1 - \lambda_\alpha \lambda_\rho (\tilde{\gamma}_0 - 1) c_0^2 / \tilde{c}_0^2}{3\rho_0 \lambda_\kappa \tilde{\chi}_0 / \eta_0} \right], \quad (45)$$

$$Z_1 = \frac{4}{9} \left(\frac{\omega R_0}{c_0} \right)^3 \frac{\Lambda}{x_3^2}, \quad (46)$$

where

$$\Lambda = \frac{3 + 16\lambda_\eta - 19/\lambda_\eta + 4\sigma x_3^2(5 + 2\lambda_\eta)/(\rho_0 \omega^2 R_0^3)}{89 + 48\lambda_\eta + 38/\lambda_\eta - 40\sigma x_3^2(1 + \lambda_\eta)/(\rho_0 \omega^2 R_0^3)}. \quad (47)$$

It should be noted that in calculating the quantities α_{jn} , which were used for derivation of Eqs. (45) and (46), we had to make some assumptions in addition to the condition heading this subsection. These assumptions and justifications for their introduction are expounded in Appendix D.

Let us now apply Eqs. (45) and (46) to the same sound fields as in Sec. II A.

1. Plane traveling wave

Recall that the radiation force $F_r^{(tr)}$ exerted by the plane traveling wave is defined by Eq. (70) of Part I. One should also take account of the drag $F_d^{(tr)}$ which is given by Eq. (71) of Part I, since the latter is of the same order as $F_r^{(tr)}$ in the case under consideration. Thus, substituting Eqs. (45) and (46) into Eq. (70) of Part I, going to the appropriate limit in Eq. (71) of Part I, and adding together the results, one finds the total force to be

$$F_{tr} = \frac{\pi}{3} \rho_0 |A|^2 \left(\frac{\omega R_0}{c_0} \right)^3 \left(\frac{\delta_v}{R_0} \right)^2 \left[\frac{\gamma_0 - 1}{\lambda_\alpha} - (\tilde{\gamma}_0 - 1) \frac{\lambda_\rho c_0^2}{\tilde{c}_0^2} - 2 - \frac{\lambda_\rho c_0^2}{\tilde{c}_0^2} - 4 \operatorname{Re}(\Lambda) \right]. \quad (48)$$

Comparison of Eq. (48) with Eq. (7.7) of Ref. 1 (the latter was obtained neglecting heat conduction under other conditions being equal) shows that the heat conduction gives rise to the first two terms within square brackets in Eq. (48). These become particularly important for liquid drops in a gas. As an example let us consider an ethyl alcohol drop in air. The data for air, presented in Sec. II A 1, should be supplemented with $\alpha_0 = 3.665 \times 10^{-3} \text{ K}^{-1}$ and $\kappa_0 = 0.034 \text{ J/(smK)}$, and the appropriate parameters for ethyl alcohol are $\tilde{\rho}_0 = 790 \text{ kg/m}^3$, $\tilde{c}_0 = 1165 \text{ m/s}$, $\tilde{\eta}_0 = 1.2 \times 10^{-3} \text{ Pas}$, $\tilde{\chi}_0 = 1.3 \times 10^{-7} \text{ m}^2/\text{s}$, $\tilde{\kappa}_0 = 0.24 \text{ J/(smK)}$, $\tilde{\alpha}_0 = 1.12 \times 10^{-3} \text{ K}^{-1}$, $\tilde{\gamma}_0 = 1.16$, $\sigma = 0.0223 \text{ N/m}$. To satisfy all the necessary conditions (see the title of Sec. II B and Appendix D), we set $R_0 = 0.1 \text{ }\mu\text{m}$ and $f = 1 \text{ kHz}$. Then the contribution from the terms due to heat conduction will be about seven times as great as that from the purely viscous terms [the last three terms between square brackets in Eq. (48)].

2. Plane standing wave

Substituting Eqs. (45) and (46) into Eq. (74) of Part I and retaining only the leading term, one obtains

$$F_r^{(st)} = \frac{2}{3} \pi \rho_0 |A|^2 \left(\frac{\omega R_0}{c_0} \right)^3 \left(\frac{\delta_v}{R_0} \right)^2 \sin(2\omega d/c_0) \operatorname{Im}(\Lambda). \quad (49)$$

The drag force, defined by Eq. (75) of Part I, is negligible in this case. It follows from Eq. (49) that in the limit involved the heat conduction does not contribute to the leading term of the radiation force exerted by the plane standing wave. Equation (49) is adequate to Eq. (7.8) of Ref. 1 when it is considered that the latter is an excessive expression as compared with Eq. (49). This means that Eq. (7.8), apart from terms making the main contribution, contains a large number of secondary terms which give only negligible corrections, whereas Eq. (49) involves only the leading terms. If the secondary terms are dropped, then Eq. (7.8) will be exactly equivalent to Eq. (49). The presence of the secondary terms resulted in a regrettable error: the present author has overestimated their contribution to the radiation force in the limit $\lambda_\eta \ll 1$ (the case of a liquid drop in a gas or a high-viscosity

liquid drop in a low-viscosity liquid). He has dropped terms due to surface tension assuming those to be small compared with the above secondary terms and only recently found that it is the surface-tension terms that are dominant in the situation in question. As a result, Eq. (7.13) of Ref. 1 and its discussion are wrong. The correct result for $F_r^{(st)}$ at $\lambda_\eta \ll 1$ is

$$F_r^{(st)}(\lambda_\eta \ll 1) = \frac{\pi |A|^2 (\omega R_0/c_0)^3 \sin(2\omega d/c_0) \sigma (38\eta_0)^2}{3R_0[(20\sigma)^2 + (19\omega R_0 \tilde{\eta}_0)^2]}. \quad (50)$$

It is seen that drops of this sort will be gathered at the standing wave pressure nodes.

For $\lambda_\eta \gg 1$, a low-viscosity liquid drop in a high-viscosity liquid, Eq. (49) reduces to

$$F_r^{(st)}(\lambda_\eta \gg 1) = \frac{16\pi |A|^2 (\omega R_0/c_0)^3 \sigma \sin(2\omega d/c_0)}{27\omega^2 R_0^3 [1 + 25\sigma^2/(6\omega R_0 \eta_0)^2]}. \quad (51)$$

This formula is adequate to Eq. (7.18) of Ref. 1 with the provision that the secondary terms in the latter are dropped. The condition $\lambda_\eta \gg 1$ occurs, for instance, for a water drop in glycerin. According to Eq. (51), the drop must move toward the pressure node. It is of interest to note that in the limit of weak dissipative effects such a drop is urged away toward the pressure antinode [cf. Eq. (40)].

3. Diverging spherical wave

Substituting Eqs. (45) and (46) into Eq. (79) of Part I and taking into account the drag force given by Eq. (80) of Part I, one finds the total force to be

$$F_{sph} = -\frac{\pi}{3} \rho_0 |A|^2 \left(\frac{\omega R_0}{c_0} \right)^3 \left(\frac{\delta_v}{R_0} \right)^2 \left[4(3\tau^{-5} + 2\tau^{-3}) \times \operatorname{Im}(\Lambda) + \tau^{-2} \left(2 + 4 \operatorname{Re}(\Lambda) + \frac{\tilde{\gamma}_0 \lambda_\rho c_0^2}{\tilde{c}_0^2} - \frac{\gamma_0 - 1}{\lambda_\alpha} \right) \right]. \quad (52)$$

From Eq. (47) it follows that $\operatorname{Im}(\Lambda)$ is always positive. Consequently, in the vicinity of the spherical wave source the drop will undergo an attractive force regardless of its physical properties. Recall that in the limit of weak dissipative effects only heavy drops, i.e., those for which $\lambda_\rho < 1$, are attracted to the sound source [cf. Eq. (41)]. At a large distance from the sound source, such that the second term within square brackets in Eq. (52) becomes dominant, the behavior of the drop begins to depend on its parameters. For example, an ethyl alcohol drop in air will be repelled from the sound source, while when placed in glycerin, it will be attracted to the sound source, this change in behavior being due to the thermal effects.

III. CONCLUSIONS

In this paper, the acoustic radiation force has been examined due to a sound wave on a liquid drop when viscous and heat effects are no longer negligible. Basic calculations, using the general theory developed in Part I of this work as a background, have been performed for arbitrary relationships between characteristic parameters of the system such as the

drop radius and the sound, viscous, and thermal wavelengths. Since, however, the thus obtained general expressions are very complicated and do not allow us to dramatically see how the radiation force is affected by viscosity and heat conduction, some limiting cases of interest have then been considered. First we have gone to the limit of long sound wavelength, which is to say that the wavelength of an incident sound field has been taken to be much larger than the other parameters listed above both outside and inside the drop. Within this assumption, two reverse cases have been dealt with. In the first of these, the drop radius is assumed to be large compared with the viscous and thermal wavelengths both outside and inside the drop, which occurs when the dissipative effects are weak. In the second case, on the contrary, these effects are treated to be strong, so that the drop radius is small compared with the above wavelengths. For each of these two cases, three types of incident wave have been considered: a plane traveling wave, a plane standing wave, and a diverging spherical wave. Emphasis has been given to the thermal effects on the radiation force since the viscous effects have been investigated in a previous paper by the present author.¹ It has been found that in the standing wave field the heat conduction only gives rise to small corrections to the previously obtained expressions for both limiting cases. For the spherical wave, the thermal effects have been found to manifest themselves at large distances from the sound source, sometimes resulting in change not only in magnitude of the radiation force but also in its sign. The thermal effects on the radiation force have turned out to be greatest for the traveling wave. It has been shown that in both limiting cases the heat conduction can make a main contribution to the radiation force exerted by the traveling wave. In connection with this type of incident wave, an interesting question has been posed: Which expression, obtained in this paper or Yosioka and Kawasima's,⁶ yields the radiation force exerted by the plane traveling wave on a liquid drop in the limit of weak dissipative effects? It has been shown that theoretically, in most cases of interest, the radiation force should be determined by the expression obtained here and thus be much larger than that predicted by Yosioka and Kawasima's theory. The final answer, however, can only be achieved by comparison with experimental measurements which are presently absent.

ACKNOWLEDGMENTS

This work was supported by the Ministry of Education and Science of the Republic of Belarus and the International Science Foundation.

APPENDIX A: EXPRESSIONS FOR $a_{ij}^{(n)}$ AND $b_i^{(n)}$ ($i, j=1,2,3$)

Expressions given here hold for any values of the drop radius and the sound, viscous, and thermal wavelengths.

$$a_{ij}^{(n)} = \mu_{ij}^{(n)} h_n^{(1)}(x_j) + \nu_{ij}^{(n)} x_j h_n^{(1)'}(x_j),$$

$$b_i^{(n)} = -\mu_{i1}^{(n)} j_n(x_1) - \nu_{i1}^{(n)} x_1 j_n'(x_1).$$

Here, the prime denotes differentiation, summation over repeated indices is absent, and

$$\mu_{11}^{(n)} = f_1^{(n)}(k_1), \quad \mu_{12}^{(n)} = f_1^{(n)}(k_2),$$

$$\mu_{13}^{(n)} = n(n+1)(g - g_{1n}),$$

$$\mu_{21}^{(n)} = f_2^{(n)}(k_1), \quad \mu_{22}^{(n)} = f_2^{(n)}(k_2),$$

$$\mu_{23}^{(n)} = n(n+1)[1 - \lambda_\rho - (n^2 + n - 1)g],$$

$$\mu_{31}^{(n)} = \mu_{32}^{(n)} = 1 - \lambda_\rho + g(g_{2n} + 1 - n - n^2),$$

$$\mu_{33}^{(n)} = 1 + n(n+1)(g - g_{1n}) - (1 + g_{2n})$$

$$\times [\lambda_\rho + g(n^2 + n - 1)],$$

$$\nu_{11}^{(n)} = f_3^{(n)}(k_1), \quad \nu_{12}^{(n)} = f_3^{(n)}(k_2), \quad \nu_{13}^{(n)} = -n(n+1)g,$$

$$\nu_{21}^{(n)} = f_4^{(n)}(k_1), \quad \nu_{22}^{(n)} = f_4^{(n)}(k_2), \quad \nu_{23}^{(n)} = n(n+1)g,$$

$$\nu_{31}^{(n)} = \nu_{32}^{(n)} = g(1 - g_{2n}) - g_{1n},$$

$$\nu_{33}^{(n)} = 1 + g(g_{2n} + 1 - n - n^2),$$

in which

$$f_1^{(n)}(k_l) = (\beta_1 - k_l^2) g_{3n} [(\tilde{\beta}_1 - \tilde{k}_l^2) \tilde{x}_{1j_n}'(\tilde{x}_1) j_n(\tilde{x}_2) - (\tilde{\beta}_1 - \tilde{k}_l^2) \tilde{x}_{2j_n}'(\tilde{x}_2) j_n(\tilde{x}_1)] - n(n+1)g - \lambda_\rho,$$

$$f_2^{(n)}(k_l) = n(n+1)g + (\beta_1 - k_l^2) g_{3n} (\tilde{k}_1^2 - \tilde{k}_2^2) \times \tilde{x}_{1j_n}'(\tilde{x}_1) \tilde{x}_{2j_n}'(\tilde{x}_2),$$

$$f_3^{(n)}(k_l) = (\beta_1 - k_l^2) g_{3n} \lambda_\kappa (\tilde{k}_1^2 - \tilde{k}_2^2) j_n(\tilde{x}_1) j_n(\tilde{x}_2) + 2g - g_{1n},$$

$$f_4^{(n)}(k_l) = 1 - n(n+1)g - (\beta_1 - k_l^2) g_{3n} \times \lambda_\kappa [(\tilde{\beta}_1 - \tilde{k}_2^2) \tilde{x}_{1j_n}'(\tilde{x}_1) j_n(\tilde{x}_2) - (\tilde{\beta}_1 - \tilde{k}_1^2) \times \tilde{x}_{2j_n}'(\tilde{x}_2) j_n(\tilde{x}_1)], \quad l=1,2,$$

$$g = 2(\tilde{\eta}_0 - \eta_0) / (\tilde{\eta}_0 \tilde{x}_3^2),$$

$$g_{1n} = \sigma(n-1)(n+2) / (\tilde{\rho}_0 \omega^2 R_0^3),$$

$$g_{2n} = \tilde{x}_3 j_n'(\tilde{x}_3) / j_n(\tilde{x}_3),$$

$$g_{3n} = \tilde{\alpha}_0 \beta_3 \{ \alpha_0 \tilde{\beta}_3 (\tilde{\beta}_1 - \tilde{k}_1^2) (\tilde{\beta}_1 - \tilde{k}_2^2) [\tilde{x}_{1j_n}'(\tilde{x}_1) j_n(\tilde{x}_2) - \tilde{x}_{2j_n}'(\tilde{x}_2) j_n(\tilde{x}_1)] \}^{-1},$$

$$\lambda_\rho = \rho_0 / \tilde{\rho}_0, \quad \lambda_\kappa = \kappa_0 / \tilde{\kappa}_0,$$

and β_1 and β_3 (and, accordingly, $\tilde{\beta}_1$ and $\tilde{\beta}_3$) are defined by Eqs. (16) and (18) of Part I, respectively.

APPENDIX B: EXPRESSIONS FOR α_{jn} ($n=0,1,2$) IN THE LIMIT OF LONG SOUND WAVELENGTH

$$\alpha_{10} = -\frac{i}{3} \left(\frac{\omega R_0}{c_0} \right)^3 \left(1 - \frac{Q \lambda_\rho c_0^2}{\tilde{c}_0^2} + \frac{(Q-1)(\gamma_0-1)}{\lambda_\alpha (\tilde{\gamma}_0-1)} \right),$$

$$\alpha_{20} = \frac{(\omega R_0 / c_0)^2}{x_2 D_0} (\gamma_0 - 1 - (\tilde{\gamma}_0 - 1) \lambda_\alpha \lambda_\rho c_0^2 / \tilde{c}_0^2),$$

where

$$Q = (q + 3(\tilde{\gamma}_0 - 1)(\lambda_\alpha - \lambda_\kappa / \lambda_\chi) h_1^{(1)}(x_2)) / D_0,$$

$$q = x_2 h_0^{(1)}(x_2) - \lambda_\kappa x_2^2 j_0(\tilde{x}_2) h_1^{(1)}(x_2) / (\tilde{x}_2 j_1(\tilde{x}_2)),$$

$$D_0 = q + 2\sigma\lambda_\alpha(\tilde{\gamma}_0 - 1)h_1^{(1)}(x_2)/(\tilde{\rho}_0\tilde{c}_0^2R_0),$$

$$\lambda_\alpha = \alpha_0/\tilde{\alpha}_0, \quad \lambda_\kappa = \kappa_0/\tilde{\kappa}_0, \quad \lambda_\chi = \chi_0/\tilde{\chi}_0,$$

$$\alpha_{11} = \frac{i(1-\lambda_\rho)}{3D_1} \left(\frac{\omega R_0}{c_0} \right)^3 (q_1 x_3 h_2^{(1)}(x_3) + \lambda_\rho(1-g_{21})h_1^{(1)}(x_3)),$$

$$\alpha_{21} = \frac{(\gamma_0 - 1)(\omega R_0/c_0)^3}{x_2^2 D_1 (q_2 x_2 h_1^{(1)'}(x_2) - q_3 h_1^{(1)}(x_2))} \times [(\lambda_\rho q_2 - \lambda_\rho - q_3)(q_1 x_3 h_2^{(1)}(x_3) + \lambda_\rho(1-g_{21}) \times h_1^{(1)}(x_3)) + 2(\lambda_\rho - 1)(q_2 - q_3)q_1 h_1^{(1)}(x_3)],$$

$$\alpha_{31} = (\omega R_0/c_0)(1-\lambda_\rho)q_1/D_1,$$

where

$$q_1 = g(1-g_{21}) - 1, \quad q_2 = \frac{(\gamma_0 - 1)\tilde{c}_0^2 \lambda_\kappa j_1(\tilde{x}_2)}{(\tilde{\gamma}_0 - 1)c_0^2 \lambda_\alpha \tilde{x}_2 j_2(\tilde{x}_2)},$$

$$q_3 = \frac{(\gamma_0 - 1)\tilde{c}_0^2 j_1'(\tilde{x}_2)}{(\tilde{\gamma}_0 - 1)c_0^2 \lambda_\alpha j_2(\tilde{x}_2)},$$

$$D_1 = q_1(6(\lambda_\rho - 1)h_1^{(1)}(x_3) + (2 + \lambda_\rho)x_3 h_2^{(1)}(x_3)) + \lambda_\rho(2 + \lambda_\rho)(1 - g_{21})h_1^{(1)}(x_3)$$

$$\alpha_{12} = \frac{2i}{45D_2} \left(\frac{\omega R_0}{c_0} \right)^5 [\lambda_\rho(g_{22} - 2)s_1 h_2^{(1)}(x_3) + [s_1 s_2 - 3g^2(g_{22} - 2)]x_3 h_3^{(1)}(x_3)],$$

$$\alpha_{22} = \frac{(\gamma_0 - 1)(\omega R_0/c_0)^4}{3x_2^2 D_2 [(s_4 - 2s_3)h_2^{(1)}(x_2) + s_3 x_2 h_3^{(1)}(x_2)]} \times \{ [3(s_4 - 2s_3)(\lambda_\rho - 3g + s_2(8g + 2g_{12} - 1)) - 3\lambda_\rho s_1 + \lambda_\rho(g_{22} - 2)(\lambda_\rho + 3g + s_4 - 2\lambda_\rho s_3 - 2g_{12}s_4 - 18gs_3 + 4gs_4)]h_2^{(1)}(x_3) - [3g(\lambda_\rho - s_4) + s_2(s_4(8g + 2g_{12} - 1) + \lambda_\rho(2s_3 - 1))]x_3 h_3^{(1)}(x_3) \} \times (x_3),$$

$$\alpha_{32} = \frac{(\omega R_0/c_0)^2}{3D_2} [g(2 - g_{22})(\lambda_\rho + 3g) + s_1 s_2],$$

where

$$s_1 = 1 - \lambda_\rho - 5g - 2g_{12}, \quad s_2 = 1 + g(g_{22} - 2),$$

$$s_3 = \frac{(\gamma_0 - 1)\lambda_\kappa \tilde{c}_0^2 j_2(\tilde{x}_2)}{(\tilde{\gamma}_0 - 1)\lambda_\alpha c_0^2 \tilde{x}_2 j_3(\tilde{x}_2)}, \quad s_4 = \frac{(\gamma_0 - 1)\tilde{c}_0^2 j_2'(\tilde{x}_2)}{(\tilde{\gamma}_0 - 1)\lambda_\alpha c_0^2 j_3(\tilde{x}_2)},$$

$$D_2 = (3 + 2\lambda_\rho - 6g_{12})[(g_{22} - 2)(\lambda_\rho + 3g)h_2^{(1)}(x_3) + s_2 x_3 h_3^{(1)}(x_3)] - 3(5 - 16g + 8gg_{22}) \times [s_1 h_2^{(1)}(x_3) + gx_3 h_3^{(1)}(x_3)].$$

The quantities g , g_{21} , g_{22} , and g_{12} are defined in Appendix A.

APPENDIX C: EXPRESSIONS FOR $F_n^{(jk)}$ ($n=0,1$) AND α_{jn} ($n=0,1,2$) IN THE LIMIT $|\mathbf{x}_1|, |\tilde{\mathbf{x}}_1| \ll 1 \ll |\mathbf{x}_2|, |\tilde{\mathbf{x}}_2|, |\mathbf{x}_3|, |\tilde{\mathbf{x}}_3|$

The required expressions for $F_n^{(jk)}$ are obtained by going to the appropriate limit from more general ones which are presented in Appendix B of Part II:

$$F_0^{(01)} = 2i(1 - x_3^2)/(3x_3^2),$$

$$F_0^{(20)} = 2ix_1(ix_2 - x_3^2)\exp(ix_2)/(3x_2x_3^2),$$

$$F_0^{(03)} = 2ix_1^2(1 - 2x_3)\exp(-x_3)/(3x_3^3),$$

$$F_1^{(03)} = -2x_1(1 + x_3)\exp(-x_3)/x_3^3,$$

$$F_0^{(10)} = -2i(1 + x_3^2)/(3x_3^2),$$

$$F_1^{(10)} = -2i(14 + 5x_3^2)/(15x_3^2),$$

$$F_0^{(11)} = -4/(x_1^3 x_3^2), \quad F_1^{(11)} = -81/(x_1^5 x_3^2),$$

$$F_0^{(13)} = 2(21 - 5x_3)\exp(-x_3)/(x_1 x_3^3),$$

$$F_1^{(13)} = 6i(4 - 5x_3)\exp(-x_3)/(x_1^2 x_3^3),$$

$$F_0^{(21)} = 2(x_3^2 + 5ix_2 - 9ix_3^2/x_2)\exp(ix_2)/(x_1^2 x_2 x_3^2),$$

$$F_0^{(23)} = 2x_2 \exp(ix_2 - x_3)/(x_3^2 - ix_2 x_3),$$

$$F_1^{(30)} = 2x_1^2(14 + ix_3)\exp(ix_3)/(15x_3^3),$$

$$F_1^{(31)} = 18i(7ix_3 - 65)\exp(ix_3)/(x_1^3 x_3^3),$$

$$F_1^{(33)} = -3(1 + 2i)\exp(ix_3 - x_3)/x_3^2.$$

The required expressions for α_{jn} are obtained from the preceding Appendix:

$$\alpha_{10} = \frac{i}{3} \left(\frac{\omega R_0}{c_0} \right)^3 \left(\frac{\lambda_\rho c_0^2}{\tilde{c}_0^2} - 1 + \frac{3i(1 - \lambda_\kappa/\lambda_\chi/\lambda_\alpha)[\gamma_0 - 1 - (\tilde{\gamma}_0 - 1)\lambda_\alpha \lambda_\rho c_0^2/\tilde{c}_0^2]}{x_2(1 + \lambda_\kappa \tilde{\delta}_t/\delta_t)} \right),$$

$$\alpha_{20} = \frac{i}{x_2} \left(\frac{\omega R_0}{c_0} \right)^2 \frac{\gamma_0 - 1 - (\tilde{\gamma}_0 - 1)\lambda_\alpha \lambda_\rho c_0^2/\tilde{c}_0^2}{1 + \lambda_\kappa \tilde{\delta}_t/\delta_t} \times \exp(-ix_2),$$

$$\alpha_{11} = \frac{i(1 - \lambda_\rho)}{3(2 + \lambda_\rho)} \left(\frac{\omega R_0}{c_0} \right)^3 \left[1 + \frac{6i(1 - \lambda_\rho)}{x_3(2 + \lambda_\rho)} \times \left(1 + \frac{\lambda_\rho \delta_v/\tilde{\delta}_v}{1 + (1 + i)\lambda_\eta \tilde{\delta}_v/R_0} \right)^{-1} \right],$$

$$\alpha_{31} = \frac{i(\lambda_\rho - 1)}{2 + \lambda_\rho} \frac{\omega R_0}{c_0} \exp(-ix_3)$$

$$\times \left[1 + \frac{\lambda_\rho \delta_v/\tilde{\delta}_v}{1 + (1 + i)\lambda_\eta \tilde{\delta}_v/R_0} \right]^{-1},$$

$$\alpha_{12} = \frac{2i}{45} \left(\frac{\omega R_0}{c_0} \right)^5 \times \frac{(1 - \lambda_\rho - 2g_{12})(1 + \lambda_\rho \delta_v / \tilde{\delta}_v - i\tilde{x}_3 g) + 8i\tilde{x}_3 g^2}{(3 + 2\lambda_\rho - 6g_{12})(1 + \lambda_\rho \delta_v / \tilde{\delta}_v - i\tilde{x}_3 g) + 24i\tilde{x}_3 g^2},$$

$$\alpha_{32} = \frac{\exp(-ix_3)}{3} \left(\frac{\omega R_0}{c_0} \right)^2 \times \frac{1 - \lambda_\rho - 2g_{12} - i\tilde{x}_3 g(1 - 2\lambda_\rho - 2g_{12}) + 8i\tilde{x}_3 g^2}{(3 + 2\lambda_\rho - 6g_{12})(1 + \lambda_\rho \delta_v / \tilde{\delta}_v - i\tilde{x}_3 g) + 24i\tilde{x}_3 g^2}.$$

In the expressions for α_{12} and α_{32} , we retain terms containing g (recall that g and g_{12} are specified in Appendix A) since $|g|$, while inversely proportional to $|\tilde{x}_3|^2$, can be large when $\eta_0 \gg \tilde{\eta}_0$. It can be seen, however, that the third factors in α_{12} and α_{32} are of the order of unity at any values of g and other parameters because their numerators and denominators are of the same type. In view of this, it is revealed in calculating Z_1 that α_{12} and α_{32} do not contribute to the leading terms.

APPENDIX D: EXPRESSIONS FOR $F_n^{(jk)}$ ($n=0,1$) AND α_{jn} ($n=0,1,2$) IN THE LIMIT $|\mathbf{x}_1|, |\tilde{\mathbf{x}}_1| \ll |\mathbf{x}_2|, |\tilde{\mathbf{x}}_2|, |\mathbf{x}_3|, |\tilde{\mathbf{x}}_3| \ll 1$

The required expressions for $F_n^{(jk)}$ are obtained by going to the appropriate limit from ones presented in Appendix B of Part II:

$$F_0^{(01)} = 2i(1 - x_3^2)/(3x_3^2),$$

$$F_0^{(20)} = -ix_1(2 + 2x_3^2 + x_2^2)/(3x_2x_3^2),$$

$$F_0^{(03)} = ix_1^2(2 - 5x_3^2)/(3x_3^4), \quad F_1^{(03)} = x_1(x_3^2 - 2)/x_3^3,$$

$$F_0^{(10)} = -2i(1 + x_3^2)/(3x_3^2),$$

$$F_1^{(10)} = -2i(14 + 5x_3^2)/(15x_3^2),$$

$$F_0^{(11)} = -4/(x_1^3x_3^2), \quad F_1^{(11)} = -81/(x_1^5x_3^2),$$

$$F_0^{(13)} = -4(3 + x_3^3)/(3x_1x_3^4),$$

$$F_1^{(13)} = 3i(5x_3^2 - 54)/(x_1^2x_3^5),$$

$$F_0^{(21)} = -(8 + x_2^2)/(2x_1^2x_2x_3^2),$$

$$F_0^{(23)} = (x_2^2 - 8)/(2x_2x_3^4),$$

$$F_1^{(30)} = 4ix_1^2(7 + 4x_3^2)/(15x_3^4),$$

$$F_1^{(31)} = 9(18 + x_3^2)/(2x_1^3x_3^4), \quad F_1^{(33)} = 6i(27 - x_3^2)/x_3^7.$$

The required expressions for α_{jn} are obtained from Appendix B of the present paper:

$$\alpha_{10} = \frac{i}{3} \left(\frac{\omega R_0}{c_0} \right)^3 \left[\frac{\lambda_\rho c_0^2}{\tilde{c}_0^2} - 1 - \frac{[\gamma_0 - 1 - \lambda_\rho \lambda_\alpha (\tilde{\gamma}_0 - 1) c_0^2 / \tilde{c}_0^2] (\lambda_\kappa - \lambda_\alpha \lambda_\chi)}{\lambda_\alpha \lambda_\kappa} \right. \\ \left. \times \left(1 + \frac{5 + \lambda_\kappa}{15\lambda_\kappa} \tilde{x}_2^2 \right) \right],$$

$$\alpha_{20} = -ix_2 \left(\frac{\omega R_0}{c_0} \right)^2 \frac{\gamma_0 - 1 - \lambda_\rho \lambda_\alpha (\tilde{\gamma}_0 - 1) c_0^2 / \tilde{c}_0^2}{3\lambda_\kappa / \lambda_\chi} \\ \times \left[1 - \left(\frac{1}{2} - \frac{\lambda_\chi (5 + \lambda_\kappa)}{15\lambda_\kappa} \right) x_2^2 \right].$$

In deriving these expressions, it has been additionally assumed that

$$\frac{2\sigma\lambda_\alpha\lambda_\chi(\tilde{\gamma}_0 - 1)}{3\lambda_\kappa\tilde{\rho}_0\tilde{c}_0^2R_0} \ll 1,$$

which can be verified by specific examples to be well satisfied, in the limit considered, in most cases of interest.

$$\alpha_{11} = \frac{i(1 - \lambda_\rho)}{9\lambda_\rho} \left(\frac{\omega R_0}{c_0} \right)^3 \left(1 + \frac{2(1 - \lambda_\rho)(1 + \lambda_\eta)}{3\lambda_\rho(3 + 2\lambda_\eta)} x_3^2 \right),$$

$$\alpha_{31} = \frac{ix_3^2(1 - \lambda_\rho)}{9\lambda_\rho} \frac{\omega R_0}{c_0} \\ \times \left(1 + \frac{4 - 7\lambda_\rho + 4\lambda_\eta(1 - \lambda_\rho)}{6\lambda_\rho(3 + 2\lambda_\eta)} x_3^2 \right).$$

In deriving these expressions, no additional restrictions have been imposed.

Derivation of the needed expressions for α_{12} and α_{32} merits more detailed description. Keeping up in the numerators and denominators of α_{12} and α_{32} from Appendix B terms up to the order of x_3^4 , one obtains

$$\alpha_{12} = \frac{4i}{9x_3^2} \left(\frac{\omega R_0}{c_0} \right)^5 \frac{a + x_3^2 a_2 + x_3^4 a_4}{b + x_3^2 b_2 - 2iax_3^3/3 + x_3^4 b_4},$$

$$\alpha_{32} = \frac{2ix_3}{9} \left(\frac{\omega R_0}{c_0} \right)^2 \frac{a + x_3^2 c_2 + x_3^4 c_4}{b + x_3^2 b_2 - 2iax_3^3/3 + x_3^4 b_4},$$

where

$$a = 3 + 16\lambda_\eta - 19/\lambda_\eta, \quad b = 89 + 48\lambda_\eta + 38/\lambda_\eta,$$

$$a_2 = -1.2 - 0.4\lambda_\eta - 1.9/\lambda_\eta + (347 + 62\lambda_\eta + 32\lambda_\eta^2)/ \\ (126\lambda_\rho) - g_{12}(5 + 2\lambda_\eta)/\lambda_\rho,$$

$$a_4 = -7/120 - \lambda_\eta/30 - 19/(120\lambda_\eta) + (347 - 24\lambda_\eta - 8\lambda_\eta^2)/ \\ (1260\lambda_\rho) - \lambda_\eta(45 - 13\lambda_\eta - 32\lambda_\eta^2)/ \\ (4851\lambda_\rho^2) - g_{12}[3 - 4\lambda_\eta/(21\lambda_\rho) \\ + 4\lambda_\eta^2/(21\lambda_\rho)]/(6\lambda_\rho),$$

$$\begin{aligned}
b_2 &= 9.5 - 6\lambda_\eta + 19/\lambda_\eta - (347 + 331\lambda_\eta - 48\lambda_\eta^2)/(63\lambda_\rho) \\
&\quad + 10g_{12}(1 + \lambda_\eta)/\lambda_\rho, \\
b_4 &= 73/24 + 19\lambda_\eta/3 - 19/(4\lambda_\eta) - (347 + 149\lambda_\eta + 12\lambda_\eta^2)/ \\
&\quad (126\lambda_\rho) + \lambda_\eta(30 - 139\lambda_\eta + 32\lambda_\eta^2)/ \\
&\quad (1617\lambda_\rho^2) + g_{12}[5 + 3\lambda_\eta - 4\lambda_\eta/(63\lambda_\rho) \\
&\quad + 10\lambda_\eta^2/(63\lambda_\rho)]/\lambda_\rho, \\
c_2 &= -1.5 - 2\lambda_\eta + (347 + 62\lambda_\eta + 32\lambda_\eta^2)/ \\
&\quad (126\lambda_\rho) - g_{12}(5 + 2\lambda_\eta)/\lambda_\rho, \\
c_4 &= \lambda_\eta(1 - \lambda_\eta)[2 - 32\lambda_\eta/(77\lambda_\rho) - 45/(77\lambda_\rho)]/ \\
&\quad (63\lambda_\rho) + 2\lambda_\eta(1 - \lambda_\eta)g_{12}/(63\lambda_\rho).
\end{aligned}$$

Let us now take into consideration that for typical media such as water, air, alcohol, glycerin, etc. the condition $|x_1|, |\tilde{x}_1| \ll |x_2|, |\tilde{x}_2|, |x_3|, |\tilde{x}_3| \ll 1$ is satisfied only when the drop radius R_0 and the driving frequency f are the order of a few microns and kilohertz, respectively. It is easy to verify by specific examples that for such values of R_0 and f the terms containing g_{12} are much larger than the other in the above expressions. Hence, we can neglect all the other terms in comparison with the terms containing g_{12} . These are so great that the magnitudes of $x_3^2 a_2$, $x_3^2 b_2$, and $x_3^2 c_2$, as a rule, far exceed those of a and b . However, to warrant the expansion in x_3 , we have to require

$$|x_3^4 a_4/a| \ll 1, \quad |x_3^4 b_4/b| \ll 1, \quad |x_3^4 c_4/a| \ll 1$$

Again, it can be verified by specific examples that these limitations are quite realized in many cases of interest. On this basis, α_{12} and α_{32} can be rewritten as follows:

$$\begin{aligned}
\alpha_{12} &= \frac{4i}{9x_3^2} \left(\frac{\omega R_0}{c_0} \right)^5 \frac{a + x_3^2 \bar{a}_2}{b + x_3^2 \bar{b}_2} \\
&\quad \times \left(1 + \frac{x_3^4 \bar{a}_4}{a + x_3^2 \bar{a}_2} + \frac{2iax_3^3/3 - x_3^4 \bar{b}_4}{b + x_3^2 \bar{b}_2} \right), \\
\alpha_{32} &= \frac{2ix_3}{9} \left(\frac{\omega R_0}{c_0} \right)^2 \frac{a + x_3^2 \bar{a}_2}{b + x_3^2 \bar{b}_2} \\
&\quad \times \left(1 + \frac{x_3^4 [\bar{a}_4 + g_{12}/(2\lambda_\rho)]}{a + x_3^2 \bar{a}_2} + \frac{2iax_3^3/3 - x_3^4 \bar{b}_4}{b + x_3^2 \bar{b}_2} \right),
\end{aligned}$$

where

$$\begin{aligned}
\bar{a}_2 &= -(5 + 2\lambda_\eta)g_{12}/\lambda_\rho, \quad \bar{b}_2 = 10(1 + \lambda_\eta)g_{12}/\lambda_\rho, \\
\bar{a}_4 &= [4\lambda_\eta(1 - \lambda_\eta)/(63\lambda_\rho) - 1]g_{12}/(2\lambda_\rho), \\
\bar{b}_4 &= [5 + 3\lambda_\eta - 2\lambda_\eta(2 - 5\lambda_\eta)/(63\lambda_\rho)]g_{12}/\lambda_\rho.
\end{aligned}$$

- ¹A. A. Doinikov, "Acoustic radiation pressure on a compressible sphere in a viscous fluid," *J. Fluid Mech.* **267**, 1–21 (1994).
- ²L. A. Crum, "Acoustic force on a liquid droplet in an acoustic stationary wave," *J. Acoust. Soc. Am.* **50**, 157–163 (1971).
- ³M. Barmatz and P. Collas, "Acoustic radiation potential on a sphere in plane, cylindrical, and spherical standing wave fields," *J. Acoust. Soc. Am.* **77**, 928–945 (1985).
- ⁴H. W. Jackson, M. Barmatz, and C. Shipley, "Equilibrium shape and location of a liquid drop acoustically positioned in a resonant rectangular chamber," *J. Acoust. Soc. Am.* **84**, 1845–1862 (1988).
- ⁵R. Löfstedt and S. Putterman, "Theory of long wavelength acoustic radiation pressure," *J. Acoust. Soc. Am.* **90**, 2027–2033 (1991).
- ⁶K. Yosioka and Y. Kawasima, "Acoustic radiation pressure on a compressible sphere," *Acustica* **5**, 167–173 (1955).
- ⁷L. P. Gor'kov, "On the forces acting on a small particle in an acoustic field in an ideal fluid," *Sov. Phys. Dokl.* **6**, 773–775 (1962).
- ⁸W. L. Nyborg, "Radiation pressure on a small rigid sphere," *J. Acoust. Soc. Am.* **42**, 947–952 (1967).
- ⁹A. L. Eller, "Force on a bubble in a standing acoustic wave," *J. Acoust. Soc. Am.* **43**, 170–171 (1968).
- ¹⁰R. E. Apfel, "Technique for measuring the adiabatic compressibility, density, and sound speed of submicroliter liquid samples," *J. Acoust. Soc. Am.* **59**, 339–343 (1976).
- ¹¹E. H. Trinh, A. Zwern, and T. G. Wang, "An experimental study of small-amplitude drop oscillations in immiscible liquid systems," *J. Fluid Mech.* **115**, 453–474 (1982).
- ¹²P. L. Marston and S. G. Goosby, "Ultrasonically stimulated low-frequency oscillation and breakup of immiscible liquid drops: photographs," *Phys. Fluids* **28**, 1233–1242 (1985).
- ¹³E. H. Trinh, P. L. Marston, and J. L. Robey, "Acoustic measurement of the surface tension of levitated drops," *J. Colloid Interface Sci.* **124**, 95–103 (1988).
- ¹⁴C. P. Lee, A. V. Anilkumar, and T. G. Wang, "Static shape and instability of an acoustically levitated liquid drop," *Phys. Fluids A* **3**, 2497–2515 (1991).
- ¹⁵A. V. Anilkumar, C. P. Lee, and T. G. Wang, "Stability of an acoustically levitated and flattened drop: an experimental study," *Phys. Fluids A* **5**, 2763–2774 (1993).
- ¹⁶A. A. Doinikov, "Acoustic radiation force on a spherical particle in a viscous heat-conducting fluid. I. General formula," *J. Acoust. Soc. Am.* **101**, 713–721 (1997).
- ¹⁷L. D. Landau and E. M. Lifshitz, *Fluid Mechanics* (Pergamon, New York, 1959).
- ¹⁸G. A. Korn and T. M. Korn, *Mathematical Handbook* (McGraw-Hill, New York, 1968).
- ¹⁹A. A. Doinikov, "Acoustic radiation force on a spherical particle in a viscous heat-conducting fluid. II. Force on a rigid sphere," *J. Acoust. Soc. Am.* **101**, 722–730 (1997).

Computing effective reflection coefficients in layered media

David H. Berman

Department of Physics and Astronomy, University of Iowa, Iowa City, Iowa 52242

(Received 22 March 1996; accepted for publication 22 August 1996)

Computations are presented which show that the effective reflection and transmission coefficients for a rough interface embedded in a layered medium can differ significantly from the mean reflection and transmission coefficients computed for the same rough interface when it separates two homogeneous half-spaces. These differences are large when the correlation length of the roughness is long compared to the skip distance of rays associated with normal modes in the layered medium. Otherwise, these differences may be generally neglected. However, increasing the rms roughness decreases the ratio of correlation length to skip distance at which the effect of the layering is important. The case of a Pekeris waveguide with a rough fluid–fluid interface and the case of a rough Dirichlet surface bounding an upwardly refracting medium are considered. © 1997 Acoustical Society of America. [S0001-4966(97)05102-3]

PACS numbers: 43.30.-k [JHM]

INTRODUCTION

In a layered medium with rough interfaces the mean field can be computed by replacing the rough interfaces with flat interfaces, and using effective reflection and transmission coefficients at each interface instead of the reflection and transmission coefficients appropriate to the flat interface. In Ref. 1 it was shown that the effective coefficients at a particular interface not only differ from the flat surface coefficients, but that they also differ from the mean coefficients when the interface separates two homogeneous half-spaces. This difference results from there being more ways to scatter into the forward direction when the interface is embedded in a layered medium than when it is isolated: Sound can scatter back and forth between several interfaces before emerging in the forward direction. The present paper examines the size of this effect for Pekeris-like waveguides using perturbation theory and using mean half-space reflection and transmission coefficients to describe propagation between scattering events (the Bourret approximation).

This paper is arranged as follows. Section II reviews the formalism of Ref. 1 and specializes that formalism to the case when one side of the rough interface is a homogeneous half-space. In Sec. III the computation is specialized still further by using an algebraically decaying spectrum. The advantage of this spectrum is that it allows integrals to be closed in the complex plane so that Cauchy's theorem can be used. Section IV gives the results of these computations both for a Pekeris waveguide and an n^2 -linear waveguide bounded by a rough pressure release surface.

Bass and Fuks² discuss a computation similar to what is presented here. However, since the present formalism is cast in terms of the mean isolated surface reflection coefficient, and since penetrable interfaces are considered here, there are no divergences at cutoff frequencies as in Bass and Fuks. Furthermore, the computation by residues shows that the residue from the poles of the spectrum dominates the residues associated with the normal modes. This last fact could not have been anticipated from the discussion by Bass and Fuks. The use of an effective impedance has also been dis-

cussed by Voronovich³ and Furutsu.⁴ The present work fleshes out their work with computations.

I. THE NET REFLECTION MATRIX

In this section a review of the main points of Ref. 1 is presented.

Consider a rough interface S between two fluids within a stratified medium of many layers. Imagine (with the help of Fig. 1) fictitious flat boundaries S_2 and S_1 just above and below S . These are sufficiently close to S that the sound speed between S and S_1 can be assumed constant. Similarly, the sound speed between S_2 and S can be assumed constant. Because of the structure of the remainder of the medium, plane waves which impinge upward on S_2 and downward on S_1 are reflected back toward S according to reflection coefficients $R_{0,2}$ and $R_{0,1}$. Plane waves ϕ_1 and ϕ_2 impinging on S are reflected and transmitted, becoming scattered waves ϕ_1^{scatt} and ϕ_2^{scatt} in the absence of the remaining medium according to

$$\begin{pmatrix} \phi_1^{\text{scatt}}(\mathbf{Q}) \\ \phi_2^{\text{scatt}}(\mathbf{Q}) \end{pmatrix} = \int \begin{pmatrix} R_{1,1}(\mathbf{Q}, \mathbf{K}) & T_{1,2}(\mathbf{Q}, \mathbf{K}) \\ T_{2,1}(\mathbf{Q}, \mathbf{K}) & R_{2,2}(\mathbf{Q}, \mathbf{K}) \end{pmatrix} \times \begin{pmatrix} \phi_1^{\text{inc}}(\mathbf{K}) \\ \phi_2^{\text{inc}}(\mathbf{K}) \end{pmatrix} d\mathbf{K}, \quad (1)$$

or more succinctly,

$$\phi^{\text{scatt}} = R \phi^{\text{inc}}. \quad (2)$$

[To be precise, $\phi_1(\mathbf{Q})$ is the complex amplitude of the plane-wave $\exp(i\mathbf{Q} \cdot \mathbf{R} + iq_z z)$ impinging on S from below, etc.] These waves are subsequently returned toward S with amplitudes given by

$$\begin{pmatrix} \phi_1^{\text{scatt}}(\mathbf{Q}) \\ \phi_2^{\text{scatt}}(\mathbf{Q}) \end{pmatrix} = \begin{pmatrix} R_{0,1}(\mathbf{Q}) & 0 \\ 0 & R_{0,2}(\mathbf{Q}) \end{pmatrix} \begin{pmatrix} \phi_1^{\text{scatt}}(\mathbf{Q}) \\ \phi_2^{\text{scatt}}(\mathbf{Q}) \end{pmatrix}, \quad (3)$$

or

$$\phi'^{\text{scatt}} = R_0 \phi^{\text{scatt}}. \quad (4)$$

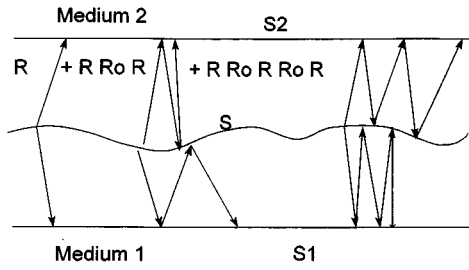


FIG. 1. The geometry of multiple scattering at a rough interface S within a waveguide. The remainder of the waveguide is described by the reflections at S_2 and S_1 . The sum of repeated reflections and transmissions through S is given by Eq. (5) in the text. Transmission through S is included in Eq. (5) but not indicated in this cartoon for reasons of clarity.

These in turn are scattered by S and returned again, etc. The result of all this rattling around is described by a net reflection/transmission matrix operator

$$R^{\text{net}} = R + RR_0R + RR_0RR_0R \dots = R \frac{1}{1 - R_0R}. \quad (5)$$

Note that only R is off-diagonal in horizontal wave vector; R_0 is diagonal in wave vector. Equation (5) can also be written

$$R^{\text{net}} = \frac{1}{R_0} \left[-1 + \frac{1}{R_0^{-1} - R} \frac{1}{R_0} \right]. \quad (6)$$

The random part of this expression is the part containing R because R_0 is assumed “sure” for the purposes of this work. For that reason, focus on the quantity

$$G = \frac{1}{R_0^{-1} - R} = \frac{1}{1 - R_0R} R_0. \quad (7)$$

Noting this form of G for any one realization of the rough interface, write the mean of G , $\langle G \rangle$, in terms of an effective reflection operator, R^{eff} , as

$$\langle G \rangle = \frac{1}{R_0^{-1} - R^{\text{eff}}}. \quad (8)$$

The problem now is to find the effective reflection operator, R^{eff} . The mean field at points far from the interface can be treated as if it were a deterministic field controlled by a flat interface with reflection coefficients R^{eff} . Statistical homogeneity requires R^{eff} to be diagonal in horizontal wave numbers. Write the effective reflection operator as the sum of the mean reflection and transmission operator in the absence of layering plus a correction, Σ .

$$R^{\text{eff}} = \langle R \rangle + \Sigma. \quad (9)$$

In quantum field theory Σ would be called the “self-energy,” and this terminology will be used here as well.

One can try to find $\langle G \rangle$ by expanding in powers of the fluctuations of R , ΔR . However, it is desirable to have propagation between scattering events described by $\langle G \rangle$ rather than

$$G_0 = \frac{1}{R_0^{-1} - \langle R \rangle}.$$

For this reason the following procedure for finding $\langle G \rangle$ described by Brown *et al.*⁵ will be used. Write G as

$$G = \frac{1}{R_0^{-1} - \langle R \rangle - \Sigma - (R - \langle R \rangle - \Sigma)} = \frac{1}{1 - \langle G \rangle v} \langle G \rangle, \quad (10)$$

where

$$v \equiv R - \langle R \rangle - \Sigma = \Delta R - \Sigma. \quad (11)$$

Adding and subtracting 1 gives

$$G = \langle G \rangle + \left[\frac{1}{1 - \langle G \rangle v} - 1 \right] \langle G \rangle = \langle G \rangle + \langle G \rangle T \langle G \rangle, \quad (12)$$

where

$$T = v \frac{1}{1 - \langle G \rangle v}. \quad (13)$$

In this arrangement of operators scattering occurs via the operator $v = R - R^{\text{eff}}$ and propagation between scattering events is described by $\langle G \rangle$. Averaging Eq. (12) shows that $\langle T \rangle = 0$. This fact provides an expression for Σ which leads to an expansion in powers of v . From the definition of T , Eq. (13), it follows that

$$T = v + T \langle G \rangle v. \quad (14)$$

Averaging and using

$$\langle v \rangle = \langle R - \langle R \rangle \rangle - \Sigma = -\Sigma$$

gives

$$\Sigma = \langle T \langle G \rangle \Delta R \rangle. \quad (15)$$

To lowest order in v ,

$$T = v = \Delta R - \Sigma$$

so that the self-energy Σ is approximated by what in field theory would be called a Dyson equation

$$\Sigma \approx \langle \Delta R \langle G \rangle \Delta R \rangle. \quad (16)$$

Since $\langle G \rangle$ depends on Σ , this is an integral equation for Σ . Here we are content to replace $\langle G \rangle$ by its isolated surface form obtained by setting $\Sigma = 0$ in $\langle G \rangle$ of Eq. (16):

$$\langle G \rangle \approx G_0 = \frac{1}{R_0^{-1} - \langle R \rangle} \quad (17)$$

to obtain the approximation,

$$\Sigma_B \approx \langle \Delta R G_0 \Delta R \rangle. \quad (18)$$

In the context of scattering by volume inhomogeneities this approximation is called the Bourret approximation.^{6,7} Note that G_0 contains the mean isolated rough surface reflection/transmission matrix so that poles that might occur on the real axis are pushed into the complex plane; even $\langle R \rangle$ causes modal damping.

Finally, a word is necessary concerning the averaging procedure, indicated here by angular brackets. It is assumed here that the averaging takes place over a statistical ensemble of rough interfaces. Whether or not this is appropriate for surfaces which are in fact physically stationary is not entirely clear. One might argue that in a single experiment involving

long-range propagation (more specifically, many correlation lengths of the roughness) that what is received represents an ensemble average of many independent samplings of the interface and therefore that ensemble averaging is appropriate. Alternatively, an experiment might be performed repeatedly on moving platforms and the results averaged. If the motion takes the experiment over many correlation lengths, again the ensemble average should be relevant to the experimental result. In any event, the relevance of ensemble averaging is an issue not only in the case of propagation in a waveguide, but is even more problematic in the case of isolated interfaces.

II. COMPUTATION OF Σ_B

Consider the computation of Σ_B when medium 1 is a homogeneous half-space. This restriction makes the computation considerably easier because it means that matrix computations can be replaced by scalar computations. To see this, let

$$R_{0,2}(\mathbf{Q}) = r(\mathbf{Q})$$

and let P be the projection matrix

$$P = \begin{pmatrix} 0 & 0 \\ 0 & 1 \end{pmatrix}. \quad (19)$$

Obviously, P is a projection matrix since $P^2 = P$. If medium 1 is a homogeneous half-space, then $R_{0,1} = 0$ because no energy is reflected back from this half space. The reflection matrix R_0 given in Eqs. (3) and (4) now becomes

$$R_0 = rP = Pr.$$

The ‘‘propagator’’ G_0 becomes

$$G_0 = \frac{1}{1 - rP\langle R \rangle} Pr = P \frac{1}{1 - rP\langle R \rangle P} Pr. \quad (20)$$

Only $\langle R_{2,2} \rangle$ enters the computations and the matrix inverse can be replaced by the diagonal-in-wave number scalar operator $1/(1 - r\langle R_{2,2} \rangle)$. The self-energy in the Bourret approximation becomes

$$\Sigma_{Bi,j} = \left\langle \Delta R_{i,2} \frac{1}{1 - r\langle R_{2,2} \rangle} r \Delta R_{2,j} \right\rangle. \quad (21)$$

Even more explicitly

$$\Sigma_{Bi,j}(\mathbf{K}, \mathbf{K}') = \int \left\langle \Delta R_{i,2}(\mathbf{K}, \mathbf{Q}) \frac{1}{1 - r(\mathbf{Q})\langle R_{2,2}(\mathbf{Q}) \rangle} \times r(\mathbf{Q}) \Delta R_{2,j}(\mathbf{Q}, \mathbf{K}') \right\rangle d\mathbf{Q}. \quad (22)$$

If the scattering interface is statistically homogeneous, the self-energy is diagonal in wave vector since then

$$\langle \Delta R_{i,2}(\mathbf{K}, \mathbf{Q}) \Delta R_{2,j}(\mathbf{Q}, \mathbf{K}') \rangle = \delta(\mathbf{K} - \mathbf{K}') W_{i,j}(\mathbf{K}, \mathbf{Q}). \quad (23)$$

From here on Σ_B will refer only to the wave number diagonal part of Σ_B :

$$\Sigma_{Bi,j}(\mathbf{K}) = \int W_{i,j}(\mathbf{K}, \mathbf{Q}) \frac{1}{1 - r(\mathbf{Q})\langle R_{2,2}(\mathbf{Q}) \rangle} r(\mathbf{Q}) d\mathbf{Q}. \quad (24)$$

With this result a number of cases could be investigated:

(a) $i = j = 2$ when medium 1 is a half-space of constant sound speed c_1 and constant density ρ_1 and medium 2 is a finite layer of constant sound speed c_2 and density ρ_2 bounded by a pressure release (Dirichlet) flat surface a distance H from the rough interface between media 1 and 2. This means that $r = -\exp[2i\beta_2(\mathbf{Q})H]$. In this case $R^{\text{eff}} = \langle R_{2,2} \rangle + \Sigma_{2,2}$ is the effective reflection coefficient internal to a Pekeris waveguide with a rough interface between the two fluids.

(b) $i = j = 1$ with the same media as above. $R_{1,1}^{\text{eff}}$ describes the reflection external to a Pekeris layer.

(c) r is the reflection coefficient from an n -square-linear half-space beginning at $z = h$. Let the rough fluid–fluid interface be located at $z = 0$. This rough interface can then describe scattering from the air–water interface in an upward refracting profile.

(d) $i, j = 1$ but with there being a second penetrable interface at $z = H$.

In each case, however, the importance of the self-energy is determined by the dispersion relation, $1 - r(\mathbf{Q})\langle R_{2,2} \rangle$. In this paper only cases (a) and (c) are presented.

The aim here is simply to determine if and when the self-energy is a significant correction to the isolated surface mean reflection $\langle R \rangle$. For simplicity’s sake ΔR will be computed only to first order in perturbation theory while the coherent reflection coefficient $\langle R_{2,2} \rangle$ will be computed to second order. Computations will be done in two dimensions only, in effect assuming corrugated roughness.

In perturbation theory $W_{i,j}(\mathbf{K}, \mathbf{Q})$ depends on the surface shape only through the spectrum of surface heights $S(\mathbf{K} - \mathbf{Q})$:

$$W_{i,j}(\mathbf{K}, \mathbf{Q}) = f_{i,j}(\mathbf{K}, \mathbf{Q}) S(\mathbf{K} - \mathbf{Q}). \quad (25)$$

Sometimes for the purposes of making estimates of rough surface scattering a Gaussian spectrum is used.² Here, in contrast, a spectrum of the form

$$S(\mathbf{K}) = (2\sigma^2 L / \pi) / (1 + K^2 L^2)^2 \quad (26)$$

will be used, not only because it is a somewhat more realistic model of naturally occurring rough surfaces,^{8,9} but primarily because when the surface is one dimensional, it allows the integral in Eq. (24) giving Σ_B to be closed in the complex- \mathbf{Q} plane. [Goff and Jordan⁸ actually suggest a one-dimensional spectrum of the form $(1 + K^2 L^2)^{-\nu}$ with $0 < \nu < 1$. I use $\nu = 2$ because this gives a finite rms slope. For noninteger ν there will be branch points rather than poles at $Q = K \pm i/L$ and evaluation of Σ_B will require a numerical integration along branch cuts rather than a simple function evaluation. One might hope that the qualitative features of the present computations would be present also for more realistic spectra.] Here σ is the rms surface height and L is the correlation length of the surface. A Gaussian spectrum does not allow closure on a semicircle at infinity. If the contour can be closed, then Σ_B as given by Eq. (24) can be written as a sum of residues resulting from a pole of $S(K - Q)$ and the poles

of $1/(1-r\langle R_{2,2} \rangle)$. The last correspond to the normal modes in the waveguide bounded by our two surfaces or by the rough surface and the n^2 -linear medium. In addition to these poles, there are branch cuts resulting from the dependence of $f_{i,j}$ on vertical wave numbers

$$\beta_i(\mathbf{Q}) = \sqrt{k_i^2 - \mathbf{Q}^2}. \quad (27)$$

As it happens, the branch cut contributions are usually very small, so that evaluation of Σ_B becomes simply a matter of function evaluation.

To find $W_{i,j}$ we need the first-order expression for $\Delta R_{i,2}$. This is proportional to the Fourier transform of the surface height

$$\hat{h}(\mathbf{K}-\mathbf{Q}) = \frac{1}{(2\pi)^d} \int \exp(-i(\mathbf{K}-\mathbf{Q})\cdot\mathbf{R})h(\mathbf{R})d\mathbf{R}. \quad (28)$$

(d is 1 or 2 according to whether the surface is one or two dimensional.) This Fourier transform is related to the spectrum of surface heights by

$$\langle \hat{h}(\mathbf{K}-\mathbf{Q})\hat{h}(\mathbf{Q}-\mathbf{P}) \rangle = \delta(\mathbf{K}-\mathbf{P})S(\mathbf{K}-\mathbf{Q}). \quad (29)$$

Write the first-order fluctuations of the components of the reflection matrix as

$$\Delta R_{i,j}(\mathbf{K}, \mathbf{Q}) = g_{i,j}^{(1)}(\mathbf{K}, \mathbf{Q})\hat{h}(\mathbf{K}-\mathbf{Q}), \quad (30)$$

so that

$$f_{i,j}(\mathbf{K}, \mathbf{Q}) = g_{i,2}(\mathbf{K}, \mathbf{Q})g_{2,j}(\mathbf{Q}, \mathbf{K}). \quad (31)$$

The coefficients $g_{i,j}^{(1)}(\mathbf{K}, \mathbf{Q})$ can be found either using the Rayleigh hypothesis or the extinction theorem. The procedure is straightforward and can be done using a computer based symbolic manipulation program to ease the tedium. For a fluid–fluid interface these coefficients have been worked out in very elegant form by Voronovich (Ref. 3, pp. 95–100).

The first nonvanishing contribution to $\langle R_{i,j} \rangle$ beyond the flat interface result is second order in the surface roughness h so that $\langle R_{i,j} \rangle$ is of the form

$$\langle R_{i,j}(\mathbf{K}) \rangle = R_{i,j}^{\text{flat}}(\mathbf{K}) + \int g_{i,j}^{(2)}(\mathbf{K}, \mathbf{Q})S(\mathbf{K}-\mathbf{Q})d\mathbf{Q}. \quad (32)$$

The function $g_{i,j}^{(2)}(\mathbf{K}, \mathbf{Q})$ can also be found using the Rayleigh method and the result is again presented in Ref. 3. These coefficients agree with those inferred from the effective boundary conditions at a rough fluid–fluid interface given by Kuperman and Ingenito.¹⁰ (Note that it makes a difference whether one uses boundary conditions for the pressure or for the velocity potential. Here we use pressure boundary conditions, $[p]=0$ and $[n\cdot\nabla p/\rho]=0$.)

The self-energy is now given by

$$\Sigma_{B,i,j}(\mathbf{K}, \mathbf{K}') = \int \frac{f_{i,j}(\mathbf{K}, \mathbf{Q})S(\mathbf{K}-\mathbf{Q})r(\mathbf{Q})}{1-r(\mathbf{Q})\langle R_{2,2}(\mathbf{Q}) \rangle} d\mathbf{Q}. \quad (33)$$

When the upper interface is flat and pressure release and located at $z=H$, then the reflection coefficient, r , is given by

$$r(\mathbf{Q}) = -\exp(+2i\beta(\mathbf{Q})H). \quad (34)$$

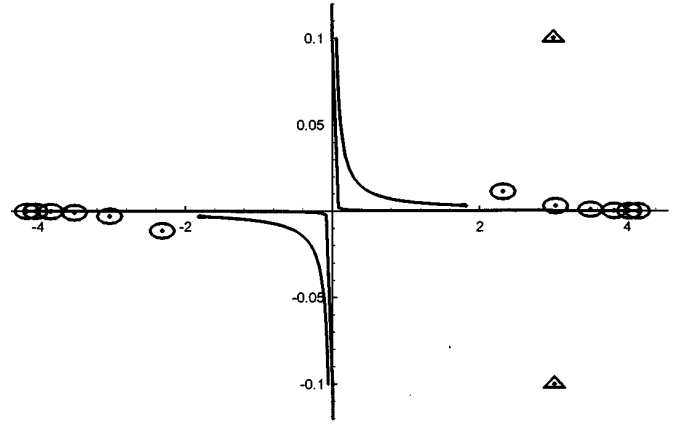


FIG. 2. The arrangement of branch cuts and zeros of the dispersion relation (circles) in a Pekeris waveguide. The figure shows the complex Q plane with the imaginary axis corresponding to the vertical axis of the figure. The branch cuts (one of which is so close to the axes as to be nearly invisible) arise from the presence of two sound speeds and the associated vertical wave numbers, β_i . The triangles here indicate the location of the two singularities of the spectrum, $S(K-Q)$, at $Q=K\pm i/L$.

In order that the imaginary part of the vertical wave numbers be non-negative we write

$$\beta_i(\mathbf{Q}) = i\sqrt{\mathbf{Q}^2 - k_i^2}$$

with the understanding that the square root has a cut along the negative real axis and that it will be evaluated on the sheet with non-negative real part. The branch cuts associated with $\beta_i(\mathbf{Q})$ lie in the first and third quadrants of the complex Q beginning at branch points $z = \pm k_i = \pm(1+i\alpha_i)\omega/c_i$ where α_i and c_i are the dissipation and sound speed in medium i . These branch cuts can be parametrized by

$$Q = \pm\sqrt{k_i^2 - t^2}$$

for

$$0 \leq t < \infty$$

in the first and third quadrants of the complex Q plane.

The zeros of $[1-r(Q)\langle R_{2,2}(Q) \rangle]$ also lie in the first and third quadrants, but near the real axis. These zeros are the modal eigenvalues.¹¹ Figure 2 illustrates the configuration of poles and branch cuts.

The spectrum we have chosen, $S(K-Q)$, has two second-order poles at $Q=K\pm i/L$. Thus, in two dimensions (one surface dimension) for $K>0$ the self-energy Σ_B given in Eq. (32) could be found by closing the original contour of integration along the real axis with a semicircle at infinity either in the lower or upper half-complex Q plane. Closure in the lower half-plane is chosen because then for $K>0$ the contributions of the poles and branch cuts in the third quadrant are minimized by the presence of the spectrum, $S(K-Q)$ in the integrand. The chosen contour must follow along both sides of the two branch cuts in the third quadrant. The contribution from the semicircle vanishes. The contour now encloses the (first-order) modal poles and the second-order pole from the spectrum, both of which contribute residues to the integral. In addition there is a contribution from integrat-

ing along each side of the branch cuts. Letting Q_n be the zeros of the dispersion relation *in the third quadrant*,

$$1 - r(Q_n) \langle R_{2,2}(Q_n) \rangle = 0, \quad (35)$$

and $D(Q_n)$ be the derivative of the left-hand side of this equation evaluated at these zeros, i.e., at the modal eigenvalues, the self-energy in the Bourret approximation can be written

$$\begin{aligned} \Sigma_{B_{i,j}}(K) &= 2\pi i \sum_n \frac{f_{i,j}(K, Q) S(K - Q_n) r(Q_n)}{D(Q_n)} + 2\pi i \left(\frac{2\sigma^2}{\pi L^3} \right) \\ &\times \frac{d}{dQ} \frac{f_{i,j}(K, Q) r(Q)}{(K - Q + i/L)^2 (1 - r(Q) \langle R_{2,2}(Q) \rangle)} \Big|_{Q=K-i/L} \\ &+ \text{branch cut contributions.} \end{aligned} \quad (36)$$

The derivative in this expression comes about from evaluating the residue of the second-order spectral pole. Because we assume $\text{Re}(K) > 0$ and because the modal poles in the lower half-plane lie in the third quadrant, $S(K - Q_n)$ will generally be small. [It is sufficient to consider only $\text{Re}(K) > 0$ because $\Sigma_B(-K) = \Sigma_B(K)$.] Thus, the modal contributions to Σ_B will generally be small. The branch cut contributions can be computed, and in practice these are smaller still. The approximation obtained by neglecting the branch cuts and/or the modal poles can be assessed by direct evaluation of the integral in Eq. (33). In general, the poles near the real axis make this a difficult computation. However, deforming the contour of integration so that it passes from $-\infty$ to $-K + i/(2L)$ to 0 to $K - i/(2L)$ to $+\infty$ makes the effects of the poles less pronounced and thereby makes it feasible, but still time consuming, to evaluate the integral numerically. This deformation assumes that $\text{Im}[K] < i/(2L)$.

Similarly, the integrand in Eq. (32) for the mean isolated surface reflection coefficient has four branch cuts associated with β_1 and β_2 , and the two poles of the spectrum. Again, it proves to be a good approximation to neglect the branch cut contributions, and to approximate $\langle R_{2,2} \rangle$ by the residue from the pole of S found in the lower half-complex Q plane. Incidentally, this method of evaluation provides an analytic continuation of $\langle R_{2,2}(K) \rangle$ into the first quadrant. That this continuation can be a problem can be seen in the case of Dirichlet boundary conditions for which $g_{2,2}^{(2)}(K, Q) = 2\beta_2(K)\beta_2(Q)$. If the spectrum $S(K - Q)$ were approximated by a delta function in the limit of large correlation lengths, L , the integral in Eq. (32) would give a result proportional to $\beta_2(K)^2 \sigma^2$. Although this may be an excellent approximation for *real* K , it clearly has a different analytic structure than the original integral when continued into the complex plane. It misses the branch cut of β_2 . Note too that original integral will be discontinuous as $\text{Im}[K]$ crosses $1/L$. Evaluation using the residue from the pole found originally in the lower half- Q plane will give a smooth (analytic) continuation.

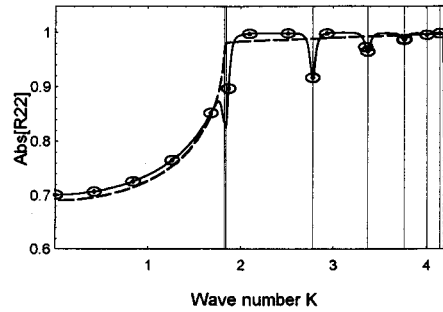


FIG. 3. The absolute value of the effective reflection coefficient, $|R^{\text{eff}}(K)|$ for a Pekeris waveguide. The solid line is computed using Eq. (36) without the branch cut contributions. In fact the modal pole contributions are also negligible. This is indicated by the circles which were computed using the integral in Eq. (33) since these circles fall on curve computed by residues. The dashed curve is $\langle R_{2,2}(K) \rangle$ computed using Eq. (32). For these computations $c_1=3450$, $c_2=1500$, where “2” refers to the finite part of the waveguide and “1” to the bounding half-space. Attenuations were chosen so that $k_i = (\omega/c_i)(1 + i\alpha_i)$. For all these computations $\omega=2\pi 1000$, $\alpha_1=0.001739$, and $\alpha_2=10^{-5}$. The density in the upper medium is 1 and in the lower medium it is 2.5. The width of the waveguide is $H=4.59726$. For this figure the correlation length is $L=18.3891$ so that $H/L=0.25$. The rms roughness is $\sigma=0.0225$. The vertical grid lines in all the following figures are drawn at the real part of the zeros of the dispersion relation $1 - r(Q) \langle R_{2,2}(Q) \rangle$ and at $\text{Re}(k_1)$ and $\text{Re}(k_2)$.

III. RESULTS

As indicated by Voronovich,³ one might expect that the self-energy correction to the isolated surface reflection coefficient will be small when the skip distance associated with a given wave number is large compared to the correlation length of the surface roughness. The computations below confirm this. If the width of the Pekeris waveguide is H , the skip distance between successive encounters with an interface is

$$L_{\text{skip}} = 2QH/\beta_2(Q)$$

when the sound speed in layer 2 is constant as in the computations here. Figures 3 and 4 show the effective reflection coefficient at the rough interface between two fluids in a Pekeris waveguide. Parameters of the two media were chosen to correspond roughly to those of sea water (medium 2) and sedimentary rock (medium 1). Shear effects, however, have been completely neglected. The width of the waveguide has been adjusted so that there are six propagating modes in the absence of roughness and attenuation. One of the modes

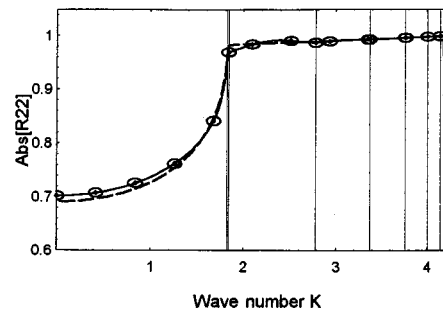


FIG. 4. Same parameters as Fig. 3 except that now $L=2.29863$ so that $H/L=2$. For small correlation lengths there is virtually no difference between the computations using R^{eff} and $\langle R_{2,2} \rangle$.

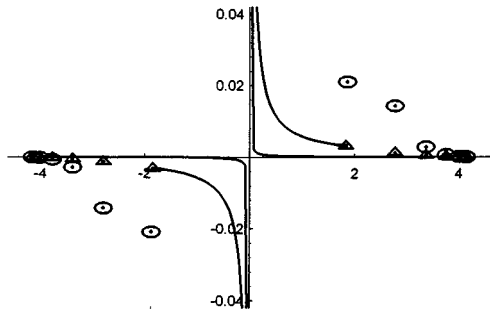


FIG. 5. The zeros of the dispersion relations $1 - r(Q)\langle R_{2,2}(Q) \rangle$ (triangles) $1 - r(Q)R^{\text{eff}}(Q)$ (circles) for the Pekeris waveguide described in Fig. 3.

is very near to cutoff. The only difference between these computations is the correlation length. In Fig. 3 the correlation length has been chosen so that the ratio of skip distance to correlation length is $L_{\text{skip}}/L = 0.24$ for $Q = k_{\text{min}} = 1.82 \text{ m}^{-1}$. In Fig. 4 the correlation length of the roughness has been chosen to be 1/8 as large so that $L_{\text{skip}}(k_2)/L = 1.96$. The deep structures in the effective reflection coefficient have nearly disappeared in the case of shorter correlation length. In these figures note that the isolated surface reflection coefficient with roughness, Eq. (32), $\langle R_{2,2} \rangle$ represented by the dashed curves, and describing the waveguide side of the interface, is nearly featureless except for the slope discontinuity at the cutoff wave number. The solid curves are computed using Eq. (36). Branch cuts have been neglected. Furthermore, the spectral residue has been computed using the approximation

$$\langle R_{2,2}(Q) \rangle \approx R_{2,2}^{\text{flat}}(Q)(1 - 2\beta_2(Q)^2\sigma^2) \quad (37)$$

in the second term of Eq. (36). Kuperman has called this the Kirchhoff approximation.¹² That this approximation is valid for computing Σ , and neglect of the branch cuts justified, is shown by the circles in Figs. 3 and 4 which are computed directly from the integral in Eq. (33) with the contour of integration deformed into the second and fourth quadrants. This computation giving the circles is essentially an exact evaluation of the integral in Eq. (33); it does not use the Kirchhoff (or infinite L) approximation, nor are branch cuts or poles neglected. In both Fig. 3 and Fig. 4 it can be seen that neglect of the branch cuts and use of the Kirchhoff approximation to compute the self-energy give excellent results

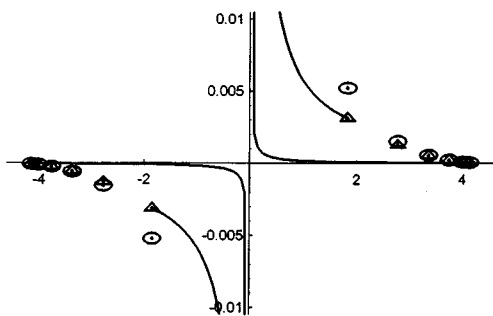


FIG. 6. The zeros of the dispersion relations for the case shown in Fig. 4. Note the change in vertical scale relative to Fig. 5. These zeros correspond to modal amplitudes with much smaller attenuations.

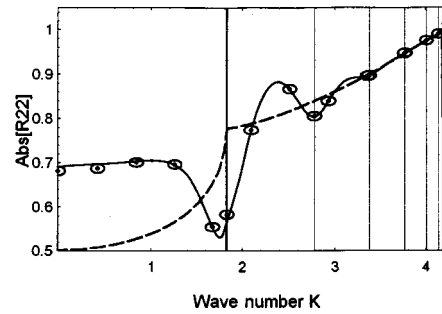


FIG. 7. The effective reflection coefficient as in Fig. 4. Now however the rms roughness is four times larger. Even though the correlation length is longer than the skip distance by about a factor of 2 there are large differences between R^{eff} and $\langle R_{2,2} \rangle$. The circles again are the results of direct evaluation of the integral in Eq. (33).

for far less computer time. (Note, however, that the Kirchhoff approximation would give poor results if used in a contour integral that strayed across the branch cuts of the β 's.) Figures 5 and 6 show the zeros of the dispersion relations $1 - r(Q)\langle R_{2,2}(Q) \rangle$ (triangles) and $1 - r(Q)R^{\text{eff}}(Q)$ (circles). These zeros are the modal wave numbers and their distance from the real axis determines the modal attenuations. Use of the self energy in R^{eff} has the effect of increasing modal attenuation, especially for modes with smaller horizontal wave numbers. This is so because the smaller the horizontal wave number, the smaller is the skip distance, thus making successive reflections/transmission more correlated.

Comparing Fig. 7 with Fig. 4 shows that increasing the root mean square roughness σ increases the deviation of R^{eff} from $\langle R \rangle$, the mean reflection coefficient for the surface considered in isolation from the waveguide. However, the σ dependence of this difference is due almost entirely to the spectrum S being proportional to σ^2 . Although the self-energy depends on the rms roughness though $\langle R \rangle$ as well as through the spectrum, this dependence is very weak; in fact Σ/σ^2 is nearly independent of σ . In Fig. 7, σ has been increased by a factor of 4 over the value used in Fig. 4. However, the Rayleigh parameter, $k_2\sigma = 0.38$, is still small enough that the perturbation results should have some validity. The difference between Fig. 7 and Fig. 4 shows that the importance of the self-energy scales with the difference between the isolated mean reflection coefficient and the flat interface reflection coefficient.

The case of an n^2 -linear sound-speed profile gives qualitatively similar results. The geometry is shown in Fig. 8. With z positive downward assume that at $z=0$ there is rough

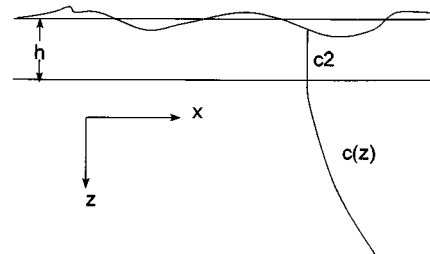


FIG. 8. Geometry for the treatment of the n^2 -linear sound-speed profile. Sound is returned to the scattering surface by refraction rather than reflection from an interface.

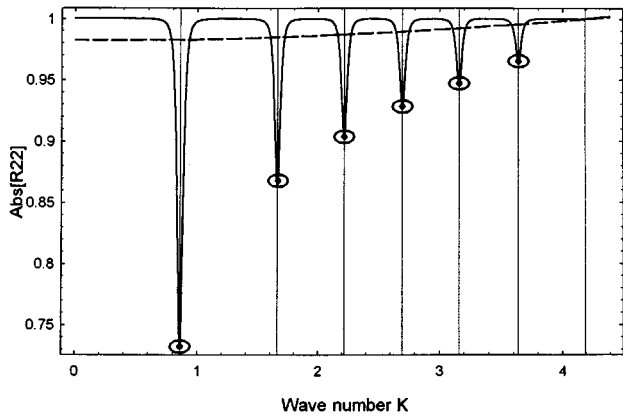


FIG. 9. $|R^{\text{eff}}(K)|$ for the case of the n^2 -linear sound-speed profile. The scattering surface is Dirichlet with a roughness $\sigma=0.0225$. The frequency is again 1000, $c_2=1500$, and there is a small attenuation, $\alpha_2=3.\times 10^{-6}$. The thin layer of constant sound speed is of thickness $h=0.02475$. The correlation length L is twice the skip distance at $Q=\text{Re}(k_2)/2$. The ratio of the skip distance to L for the lowest mode 0.2318. $\rho_2=1$. There is no cutoff wave number as in the Pekeris case. Since L is longer than the skip distance, deep spikes are observed in R^{eff} which are not present in $\langle R_{2,2} \rangle$. The parameter a in Eq. (38) is chosen to be 0.145719 so that $H_0=0.73131$.

Dirichlet (pressure release) surface. Between $z=0$ and $z=h \approx \sigma$ there is a thin layer fluid with constant sound-speed c_2 . Below $z=h$ the sound speed increases according to

$$c^2(z) = c_2^2 / (1 - az). \quad (38)$$

Decaying solutions of the Helmholtz equation in this region can be expressed in terms of Airy functions:¹¹

$$\psi(R, z) = B \exp(iQR) \text{Ai}(t_0 + (z-h)/H_0), \quad (39)$$

where

$$H_0 = 1/(k_2^2 a)^{1/3}$$

and

$$t_0 = H_0^2(Q^2 - k_2^2).$$

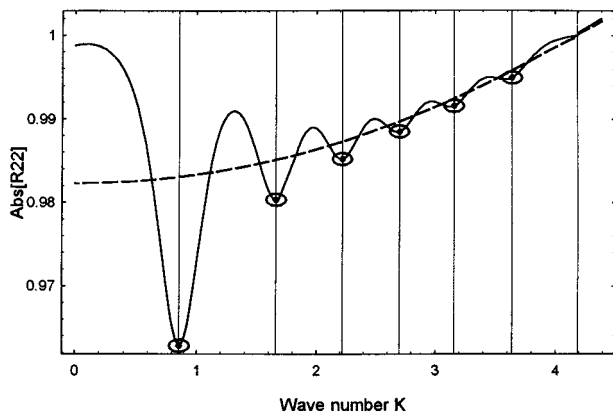


FIG. 10. Same as Fig. 9, now with a correlation length one eighth as large. Note the change in vertical scale. The spikes in $|R^{\text{eff}}|$ are much less pronounced and the differences between R^{eff} and $\langle R_{2,2} \rangle$ are comparable to those in Fig. 4 where the ratio of skip distances to the correlation lengths are comparable.

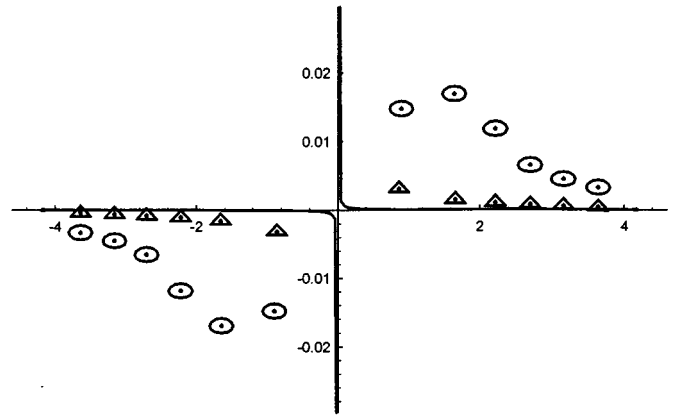


FIG. 11. The zeros of the dispersion relations for the case of Fig. 9. Note that the imaginary parts of the zeros are not monotonically decreasing with wave number.

The reflection coefficient of a plane wave in the constant sound-speed region by the n^2 -linear region beginning at $z=h$ is given by

$$r(Q) = \exp(2ik_2h) \frac{(ik_2H_0)\text{Ai}(t_0) - \text{Ai}'(t_0)}{(ik_2H_0)\text{Ai}(t_0) + \text{Ai}'(t_0)}. \quad (40)$$

The exponential in $r(Q)$ accounts for the interface between the two media not being at $z=0$ but rather at $z=h$. The n^2 -linear medium is also characterized by a skip distance. A ray entering the region with an angle θ corresponding to a horizontal wave number Q

$$\theta = \tan^{-1}(\beta_2(Q)/Q),$$

will re-emerge from this region at a distance

$$L_{\text{skip}}(Q) = 4Q\beta_2(Q)\text{Re}(H_0^3)$$

from where it entered.³

The thin layer of constant sound speed is used simply so that plane-wave computations can be used for the rough Dirichlet surface. For such a surface it is easy to show using the notation of the previous section that

$$g_{2,2}^{(1)}(K, Q) = i\beta_2(Q), \quad (41)$$

and

$$g_{2,2}^{(2)}(K, Q) = 2\beta_2(K)\beta_2(Q). \quad (42)$$

The mean reflection coefficient of the isolated rough surface at $z=0$ is therefore given by

$$\langle R_{2,2}(K) \rangle = -1 + 2\beta_2(K) \int S(K-Q)\beta_2(Q)dQ. \quad (43)$$

Using these results, the self-energy can be computed using either Eq. (33) (slow) or Eq. (36) (faster). Results of such computations are shown in Figs. 9 and 10 for two correlation lengths. Again, the effective reflection coefficient shows substantial deviations from the isolated surface mean reflection coefficient, Eq. (43), shown by the dashed curves. These deviations become less pronounced when the skip distances are larger than the correlation length of the surface roughness. This point was made by Voronovich³ and is confirmed by the present computations.

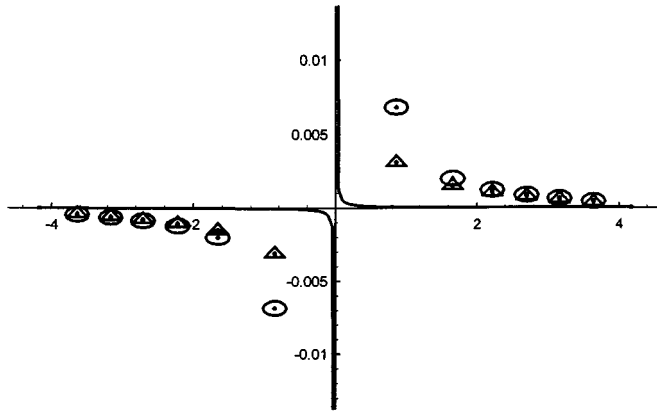


FIG. 12. The zeros of the dispersion relations for the case of Fig. 10. Note the scale of the vertical (imaginary Q) axis compared to that of Fig. 11.

In Figs. 11 and 12 the zeros Q_n of the dispersion relation

$$1 - r(Q)\langle R^{\text{eff}}(Q) \rangle = 0 \quad (44)$$

are displayed along with the zeros Q_n^{iso} of the dispersion relation obtained by using the isolated surface reflection coefficient:

$$1 - r(Q)\langle R_{2,2}(Q) \rangle = 0 \quad (45)$$

for the case of the n^2 -linear profile. These zeros are in fact the modal wave numbers of the mean Green's functions computed first with R^{eff} , then with $\langle R_{2,2} \rangle$. The distance from the real axis is a direct measure of the modal attenuations. As expected, use of R^{eff} predicts substantially more modal attenuation than predicted by use of $\langle R_{2,2} \rangle$. Of course these zeros merge when the skip distance is long compared to the correlation length, L , as in Fig. 12. As expected, also, the larger the horizontal wave number, the less a mode will be attenuated.

In summary, the computations carried out here show that self-energy corrections to the isolated surface reflection coefficient in a waveguide can be substantial if the skip dis-

tances are comparable to or shorter than the correlation length of surface roughness. Even when the skip distance is nearly twice the correlation length, as in Fig. 7, if the roughness is large enough, the self-energy correction can be large. In other words, the skip distance/correlation length ratio is not the only parameter determining the importance of the self-energy. In addition it has been shown that R^{eff} is well approximated by evaluating only the residue associated with the poles of the spectrum. Modal poles and branch cuts can be safely neglected.

ACKNOWLEDGMENT

This work was carried out with the support of a grant from the Office of Naval Research.

- ¹D. H. Berman, "The mean acoustic field in layered media with rough interfaces," *J. Acoust. Soc. Am.* **98**, 542–551 (1995).
- ²F. G. Bass and I. M. Fuks, *Wave Scattering from Statistically Rough Surfaces* (Pergamon, Oxford, 1979), pp. 451–82.
- ³A. G. Voronovich, *Wave Scattering from Rough Surfaces* (Springer-Verlag, Berlin, 1994), pp. 207–208.
- ⁴K. Furutsu, *Random Media and Boundaries* (Springer-Verlag, Berlin, 1993), p. 43 ff.
- ⁵G. Brown, V. Celli, M. Haller, A. A. Maradudin, and A. Marvin, "Resonant light scattering from a randomly rough surface," *Phys. Rev. B* **31**, 4993–5005 (1985).
- ⁶U. Frisch, "Wave propagation in random media," in *Probabilistic Methods in Applied Mathematics*, Vol. 1, edited by A. T. Bharucha-Reid (Academic, New York, 1968), pp. 77–197. See particularly p. 113.
- ⁷R. C. Bourret, "Propagation of randomly perturbed fields," *Can. J. Phys.* **40**, 782–790 (1962).
- ⁸J. A. Goff and T. H. Jordan, "Stochastic modeling of seafloor morphology: Inversion of sea beam data for second-order statistics," *J. Geophys. Res.* **95**, 13 589–13 608 (1988).
- ⁹J. A. Goff, "Monostatic shadowing of homogeneous fractal profiles," *J. Acoust. Soc. Am.* **92**, 1008–1016 (1992).
- ¹⁰W. A. Kuperman and F. Ingenito, "Attenuation of the coherent component of sound propagating in shallow water with rough boundaries," *J. Acoust. Soc. Am.* **61**, 1178–1187 (1977).
- ¹¹L. M. Brekhovskikh, *Waves in Layered Media* (Academic, San Diego, 1980), p. 306 (also pp. 243–244 for discussion of contours and p. 415 for n square linear profiles).
- ¹²W. A. Kuperman, "Coherent component of specular reflection and transmission at a randomly rough two-fluid interface," *J. Acoust. Soc. Am.* **58**, 365–370 (1975).

Robust wideband matched-field processing with a short vertical array

Stephen P. Czenszak and Jeffrey L. Krolik

Department of Electrical and Computer Engineering, Duke University, Durham, North Carolina 27708

(Received 13 March 1996; accepted for publication 13 September 1996)

This paper addresses the problem of matched-field passive localization of broadband underwater acoustic sources with a short vertical array. In previous work, incoherent averaging of narrow-band Bartlett ambiguity surfaces has been proposed to improve the robustness of matched-field processing (MFP) to environmental uncertainties. While computationally efficient, the effectiveness of this approach is dependent on the type of environmental mismatch present. In this paper, to provide robust source localization performance for short arrays, an alternative wideband MFP method is proposed which utilizes the fourth-order statistics of the data. The method is "coherent" in that it exploits cross-frequency dependencies in the random acoustic channel response. The proposed coherent wideband minimum variance method with environmental perturbation constraints (MV-EPC) consists of minimizing the *squared* output power of a beamformer subject to constraints defined across the signal band. The constraints are designed to provide robustness over an ensemble of random environmental realizations. Monte Carlo simulation results using a canonical shallow-water scenario indicate that the coherent wideband MV-EPC method yields improved probability of correct localization performance versus incoherent averaging of narrow-band Bartlett ambiguity functions with a short array above a threshold signal-to-noise ratio.
© 1997 Acoustical Society of America. [S0001-4966(97)03401-2]

PACS numbers: 43.30.Wi, 43.60.Gk [MBP]

INTRODUCTION

Matched-field processing (MFP) consists of using a full-wave model of multipath propagation to facilitate localization of underwater acoustic sources.¹ Bartlett MFP involves correlating measured narrow-band array outputs with versions of the field, predicted by a computational acoustic propagation model, for a set of hypothesized source positions. As demonstrated in several articles,²⁻⁴ two major difficulties facing this approach are that the localization process is both ambiguity prone and sensitive to errors in the assumed propagation conditions. Narrow-band MFP methods which have been proposed to address these issues include: (1) simultaneously estimating the source location and the environmental parameters using techniques such as simulated annealing,⁵ genetic algorithms,⁶ or maximum *a posteriori* estimation,⁷ and (2) using a minimum variance beamformer with environmental perturbation constraints (MV-EPC) designed to maximize the average output signal-to-noise ratio over an ensemble of random environmental variations.^{7,8} The joint source location and environmental fitting methods suffer from the computational burden of having to compute a large number of replica fields for each hypothesized source location and data snapshot. The MV-EPC beamformer is much more computationally efficient but its use has thus far been restricted to narrow-band signals received by vertical arrays which span nearly the entire water column. This paper concerns the extension of the MV-EPC method to the localization of wideband sources with a short vertical array.

Several previous approaches have been proposed for wideband matched-field source localization. In Ref. 9, a time-domain Bartlett matched-field processor was used to

localize an impulsive source in a channel of moderate depth. The time-domain replica vectors were obtained by Fourier synthesis of narrow-band solutions to the wave equation computed at frequencies across the signal band. Because the frequency domain must be densely sampled in order to avoid temporally aliasing the channel dispersion characteristics, the computational requirements of time-domain methods are high. A frequency-domain correlation-based broadband MFP method is presented in Ref. 10, where the sensor data cross spectra are correlated with cross-spectra predicted for a broadband source at different hypothesized locations. Probably the most common approach to the wideband MFP problem, however, has been to incoherently average narrow-band ambiguity surfaces obtained at widely spaced frequencies across the signal band.¹¹⁻¹³ This was first proposed in Ref. 11, where geometric averaging was used to suppress ambiguous Bartlett and minimum variance (MV) MFP sidelobes in a shallow-water simulation study. More recently, results from the SWELL-EX experiments performed off the southern California coast indicate that incoherent arithmetic averaging of narrow-band Bartlett surfaces can provide robust wideband source localization in the presence of bathymetric mismatch.¹³ A simulation discussed in this paper compares the source localization performance of incoherent wideband averaging in the SWELL-EX scenario versus a benchmark shallow-water channel used in the 1993 NRL MFP workshop.¹⁴ The simulation results indicate that incoherent averaging of Bartlett ambiguity surfaces provides improved source localization performance in the SWELL-EX scenario but fails in the NRL workshop case. In contrast, the MV-EPC yields improved source localization performance and good sidelobe suppression in both scenarios provided a suf-

ficiently large vertical array is used.^{7,15} For short arrays, however, the narrow-band MV-EPC beamformer becomes overconstrained, leaving insufficient adaptive degrees of freedom to suppress ambiguous sidelobes. This precludes use of the narrow-band or incoherently averaged wideband MV-EPC beamformer with short arrays.

In this paper, a wideband MV-EPC matched-field method is proposed for use with short vertical arrays which exploits cross-frequency dependencies in the random acoustic channel response. The processor uses the magnitude-squared Frobenius matrix inner product as a distance measure between the estimated cross-spectral density matrices of the received data and a weight matrix. The generalization of the beamformer weight vector to a weight matrix means that a much larger number of adaptive degrees of freedom are available to suppress ambiguous sidelobes. The proposed wideband MV-EPC method is “coherent” in that it uses environmental constraints defined across the signal frequency band in order to provide robustness over an ensemble of random environmental realizations. The proposed approach differs from previous coherent MFP techniques¹⁶ in that it is applicable to the localization of broadband random sources with uncorrelated temporal frequency components. In contrast, the coherent broadband MFP technique of Ref. 16 assumes a source signal composed of discrete tonals whose phase differences remain constant over time. An example of a broadband random source is the acoustic signal resulting from cavitation due to bubbles produced by the propeller of a ship. Discrete tonal acoustic signals, on the other hand, may be generated as a result of the vibration of shipboard rotating machinery.

The remainder of this paper is organized as follows. In Sec. I, the acoustic propagation model is presented. A discussion of wideband incoherent averaging of narrowband ambiguity surfaces and motivation for the coherent wideband approach is given in Sec. II. Derivation of the coherent wideband MV-EPC method appears in Sec. III and simulation results are discussed in Sec. IV.

I. WIDEBAND ACOUSTIC PROPAGATION IN AN OCEAN WAVEGUIDE

Consider the measurement of a wideband acoustic source in a shallow-water ocean channel. A T second snapshot of the acoustic field may be represented approximately by its Fourier series coefficients across the signal band at frequencies $\omega_l = \omega_0 + 2\pi l/T$ for $l=0, \dots, L-1$. Using an adiabatic normal mode solution to the wave equation, the complex Fourier series coefficient at frequency ω_l of the field measured at depth z from a distant source at range r_s and depth z_s can be expressed as^{8,17}

$$p(z; r_s, z_s, \omega_l) = a(\omega_l) \sqrt{2\pi} \sum_{n=1}^{N(\omega_l)} \frac{\varphi_n^{(0)}(z) \varphi_n(z_s)}{\sqrt{k_n r_s}} e^{-jk_n r_s}, \quad (1)$$

where $k_n = (1/r_s) \int_0^{r_s} k_n(r) dr$, for $n=1, \dots, N(\omega_l)$ are the range-averaged modal horizontal wave numbers, while $\varphi_n(z_s)$ and $\varphi_n^{(0)}(z)$ are the modal depth eigenfunctions at the source and receiver, respectively. Note that both the modal

horizontal wave numbers and eigenfunctions depend on the source frequency and various parameters of the acoustic channel, such as the bathymetry, the water-column sound-speed profile, and the bottom properties. The parameter $N(\omega_l)$ is the number of modes and the complex-valued scalar, $a(\omega_l)$, represents the source amplitude and phase at frequency ω_l .

For a vertical array of M sensors, an $M \times 1$ frequency-domain snapshot of the complex-valued pressure field, denoted \mathbf{x}_l , at frequency ω_l can be expressed by evaluating Eq. (1) at the sensor depths, z_1, \dots, z_M . Writing the result in matrix notation gives

$$\mathbf{x}_l = a(\omega_l) \mathbf{U}_l \mathbf{s}_l(r_s, z_s) + \boldsymbol{\eta}_l, \quad (2)$$

where the m th element of the $M \times N(\omega_l)$ matrix \mathbf{U}_l is $\varphi_n^{(0)}(z_m)$ and the n th element of the vector $\mathbf{s}_l(r_s, z_s)$ is $\sqrt{2\pi} [\varphi_n(z_s) / \sqrt{k_n r_s}] e^{-jk_n r_s}$. The vector $\boldsymbol{\eta}_l$ represents the diffuse additive background noise at frequency ω_l . Since both the source and noise considered here are broadband zero-mean random processes, the $a(\omega_l)$ and the elements of $\boldsymbol{\eta}_l$ are uncorrelated across frequency [i.e., $E\{a(\omega_i) a(\omega_j)^*\} = 0$ and $E\{\eta_i \eta_j^+\} = 0$ for $i \neq j$] provided T is much larger than the signal and noise correlation lengths. Note that the superscripts $*$ and $+$ denote the complex conjugate and Hermetian transpose, respectively. A complete observation of the data consists of the set of N_s uncorrelated snapshots of sensor output vectors at each of the L frequency bins, $\mathbf{x}_l(n)$, for $n=1, \dots, N_s$ and $l=1, \dots, L$. The problem of concern here is to estimate the source location in the presence of background noise and random uncertainties in the environmental parameters.

For a particular realization of the environmental parameters, the signal and noise are modeled as being zero-mean complex Gaussian distributed. Thus, their statistics are completely determined by the cross-spectral density matrix (CSDM) at each frequency ω_l , denoted $\mathbf{R}_l = E\{\mathbf{x}_l \mathbf{x}_l^+\}$ for $l=0, \dots, L-1$. For the model of Eq. (2), the CSDM can be expressed as:

$$\mathbf{R}_l = \mathbf{P}_l + \mathbf{Q}_l = \sigma_s^2 \mathbf{U}_l \mathbf{s}_l \mathbf{s}_l^+ \mathbf{U}_l^+ + \sigma_n^2 \mathbf{I}, \quad (3)$$

where the signal and noise components of the CSDM are denoted \mathbf{P}_l and \mathbf{Q}_l , respectively. For the coherent wideband method developed in this paper, the shape of the signal power spectrum, $\sigma_s^2(\omega_l) = E\{|a(\omega_l)|^2\}$, is assumed known. Further, in the cases examined here, the noise is assumed to be spatially uncorrelated with a flat power spectrum of σ_n^2 in the signal band.

In principle, matched-field processing in the temporal correlation domain could be performed by using a Fourier synthesis of the CSDMs in Eq. (3). However, to avoid temporal aliasing in the presence of channel dispersion, T must be chosen larger than twice the maximum relative group delay between the modes. As an example, for a source range of 10 km, the channel dispersion time can be on the order of 0.5 s. Even for modest signal bandwidths of a few hundred Hertz this would require the computationally intensive calculation of replica fields at several hundred frequencies for each hypothesized source location. This paper therefore considers

only frequency-domain methods which can be used when computational limitations permit only a small subset of the data CSDMs of Eq. (3) to be processed.

II. INCOHERENT WIDEBAND MATCHED-FIELD PROCESSING

The term ‘‘incoherent’’ wideband matched-field processing refers to the process of averaging narrow-band matched-field ambiguity surfaces computed at different frequencies. At each frequency, the ambiguity surface for a hypothesized source range, r , and depth, z , can be expressed as the output power of a beamformer with weight vector $\mathbf{w}_l(r, z)$, i.e.,

$$Z_l(r, z) = E\{|\mathbf{w}_l(r, z)^+ \mathbf{x}_l|^2\} = \mathbf{w}_l(r, z)^+ \mathbf{R}_l \mathbf{w}_l(r, z), \quad (4)$$

where the choice of $\mathbf{w}_l(r, z)$ depends on the specific MFP method. For the Bartlett, MV, and MV-EPC methods, the weight vectors at frequency ω_l are given by, respectively,^{1,8}

$$\text{Bartlett: } \mathbf{w}_l(r, z) = \tilde{\mathbf{d}}_l(r, z), \quad (5)$$

$$\text{MV: } \mathbf{w}_l(r, z) = \frac{\mathbf{R}_l^{-1} \tilde{\mathbf{d}}_l(r, z)}{\tilde{\mathbf{d}}_l(r, z)^+ \mathbf{R}_l^{-1} \tilde{\mathbf{d}}_l(r, z)}, \quad (6)$$

$$\text{MV-EPC: } \mathbf{w}_l(r, z) = \mathbf{R}_l^{-1} \mathbf{H}_l(r, z) \times (\mathbf{H}_l(r, z)^+ \mathbf{R}_l^{-1} \mathbf{H}_l(r, z)) \mathbf{e}_1, \quad (7)$$

where $\mathbf{d}_l(r, z) = \mathbf{U}_l \mathbf{s}_l(r, z)$, $\tilde{\mathbf{d}}_l(r, z) = \mathbf{d}_l(r, z) / \|\mathbf{d}_l(r, z)\|$ is the normalized replica field vector computed using the hypothesized environmental conditions, and $\mathbf{e}_1 = [1 \ 0 \ \dots \ 0]^T$. The superscript ‘‘ T ’’ represents the transpose operation. Normalization of the replica field vector is performed to ensure the ambiguity surface is flat when the field consists of only spatially uncorrelated noise. In the MV-EPC method, the columns of the matrix $\mathbf{H}_l(r, z)$ are the dominant eigenvectors of the signal field correlation matrix, defined as $E\{\mathbf{d}_l(r, z) \mathbf{d}_l(r, z)^+\}$, where the expectation is taken over a set of random environmental parameters. The MV-EPC method corresponds to using multiple linear MV beamformer constraints designed to maintain the array response for the hypothesized range and depth over an ensemble of environmental perturbations.

Incoherent wideband matched-field processing corresponds to summing the narrow-band beamformer output powers across frequency:

$$\begin{aligned} Z_{\text{inc}}(r, z) &= E\left\{\sum_{l=1}^L |\mathbf{w}_l(r, z)^+ \mathbf{x}_l|^2\right\} \\ &= \sum_{l=1}^L \mathbf{w}_l(r, z)^+ \mathbf{R}_l \mathbf{w}_l(r, z). \end{aligned} \quad (8)$$

Estimates of the source locations are obtained by finding the ranges and depths which correspond to the peaks of $Z_{\text{inc}}(r, z)$. Since the data CSDMs are not known *a priori*, a finite-time estimate

$$\hat{\mathbf{R}}_l = \frac{1}{N} \sum_{n=1}^{N_s} \mathbf{x}_l(n) \mathbf{x}_l(n)^+,$$

made using N_s uncorrelated snapshots of data, is typically used in place of \mathbf{R}_l in Eqs. (4), (6), (7), and (8) to obtain an estimate, $\hat{Z}_{\text{inc}}(r, z)$, of $Z_{\text{inc}}(r, z)$.

The primary motivation for averaging across frequency has been to suppress ambiguous peaks in $\hat{Z}_{\text{inc}}(r, z)$ which often result in large localization errors. These anomalous peaks are caused by background additive noise and/or sidelobes in the array response which are exacerbated by environmental mismatch. Since in principle the ambient noise components of the narrow-band ambiguity surfaces are uncorrelated, incoherent averaging over frequency should reduce the variance of $Z_{\text{inc}}(r, z)$ by a factor of $5 \log L$ over the individual $\mathbf{w}_l(r, z)^+ \mathbf{R}_l \mathbf{w}_l(r, z)$.¹² However, the extent to which incoherent averaging improves the robustness of MFP methods to environmental mismatch is scenario dependent, as demonstrated by the simulation studies in Sec. IV.

To achieve robustness to environmental mismatch, the MV-EPC method models the uncertain environmental perturbations as random variables with known distribution. Because uncertain environmental characteristics, such as the sound-speed profile and bathymetry, are not frequency dependent, the signal field vectors at different frequencies are not statistically independent. However, because the incoherent MV-EPC constraints are computed independently at each frequency, the method cannot exploit cross-frequency dependencies. Further, since $E\{a(\omega_i) a(\omega_j)^*\} = 0$ and $E\{\eta_i \eta_j^+\} = 0$ for $i \neq j$, the truly coherent sum given by $|\sum_{l=1}^L \mathbf{w}_l(r, z)^+ \mathbf{x}_l|^2$ collapses to the incoherent sum, i.e.,

$$E\left\{\left|\sum_{l=1}^L \mathbf{w}_l(r, z)^+ \mathbf{x}_l\right|^2\right\} = Z_{\text{inc}}(r, z), \quad (9)$$

which means that MV-EPC weight designs based on the metric of Eq. (9) simply yields the same incoherent MV-EPC processor. The desire to incorporate cross-frequency dependencies in the signal replica field is an important motivation for the use of higher-order statistics in formulating a coherent wideband matched-field processing method.

For large vertical arrays, the number of MV-EPC constraints at each frequency is small relative to the total number of degrees of freedom and so the beamformer can adaptively suppress ambiguous sidelobes. For short vertical arrays, however, the number of constraints required at a single frequency can easily become larger than the number of sensors which means that the beamformer is overconstrained and is unable to provide any adaptive sidelobe suppression. A means of increasing the number of adaptive degrees of freedom available with short arrays can be obtained by rewriting

$$|\mathbf{w}_l(r, z)^+ \mathbf{x}_l|^2 = \text{trace}(\mathbf{W}_l^+ \mathbf{x}_l \mathbf{x}_l^+) = \text{vec}(\mathbf{W}_l)^+ \text{vec}(\mathbf{x}_l \mathbf{x}_l^+), \quad (10)$$

where

$$\text{vec}(\mathbf{A}) = [a_{11} \ a_{21} \ a_{31} \ \dots \ a_{n1} \ a_{12} \ a_{22} \ \dots \ a_{nm}]^T$$

is an $nm \times 1$ column vector for a general $n \times m$ matrix \mathbf{A} and $\mathbf{W}_l = \mathbf{w}_l \mathbf{w}_l^+$ is an $M \times M$ rank-one Hermitian weight matrix. Note that there are at most M degrees of freedom when adaptively choosing the elements of \mathbf{w}_l such that $\mathbf{W}_l = \mathbf{w}_l \mathbf{w}_l^+$. Observe that Eq. (10) is of the form, $\text{trace}(\mathbf{A}^+ \mathbf{B})$, which is a

Frobenius inner product measuring the ‘‘angle’’ between two matrices \mathbf{A} and \mathbf{B} . By removing the restriction that \mathbf{W}_l must be a rank-one Hermetian matrix, a total of M^2 degrees of freedom now become available when adaptively choosing the elements of \mathbf{W}_l . The expression $\text{trace}(\mathbf{W}_l^+ \mathbf{x}_l \mathbf{x}_l^+)$ is now a complex-valued Frobenius inner product. The squared magnitude of $\text{trace}(\mathbf{W}_l^+ \mathbf{x}_l \mathbf{x}_l^+)$ is the norm used in the next section as the basis for a coherent wideband MV-EPC method. Because of the additional degrees of freedom available in the choice of \mathbf{W}_l , this proposed extension of the MV-EPC method does not become overconstrained for short arrays.

III. COHERENT WIDEBAND MATCHED-FIELD PROCESSING

In this section, the Frobenius inner product introduced in the previous section is used to obtain an MV-EPC MFP technique which can exploit cross-frequency dependencies in the signal field variability. In particular, the squared magnitude of a ‘‘coherent’’ sum of terms given by Eq. (10) across the signal band can be written as

$$\begin{aligned} Z_{\text{coh}}(r, z) &= E \left\{ \left| \sum_{l=1}^L \text{trace}(\mathbf{W}_l^+ \mathbf{x}_l \mathbf{x}_l^+) \right|^2 \right\} \\ &= E \left\{ \left| \sum_{l=1}^L \text{vec}(\mathbf{W}_l)^+ \text{vec}(\mathbf{x}_l \mathbf{x}_l^+) \right|^2 \right\}. \end{aligned} \quad (11)$$

Note that in contrast to the sum in Eq. (9), the cross terms, i.e., $E\{\text{vec}(\mathbf{x}_k \mathbf{x}_k^+) \text{vec}(\mathbf{x}_j \mathbf{x}_j^+)^+\}$, are not zero. This facilitates weight vector design incorporating cross-frequency dependencies in an uncertain environment. Note that Eq. (11) involves the fourth-order moments of the data. Letting $\mathbf{W} = [\mathbf{W}_1 \ \mathbf{W}_2 \ \cdots \ \mathbf{W}_L]$ and $\mathbf{X} = [\mathbf{x}_1 \mathbf{x}_1^+ \ \mathbf{x}_2 \mathbf{x}_2^+ \ \cdots \ \mathbf{x}_L \mathbf{x}_L^+]$, Eq. (11) can be compactly expressed as

$$Z_{\text{coh}}(r, z) = E\{|\text{trace}(\mathbf{W}^+ \mathbf{X})|^2\} = E\{|\bar{\mathbf{w}}^+ \bar{\mathbf{x}}|^2\} = \bar{\mathbf{w}}^+ \mathfrak{R} \bar{\mathbf{w}}, \quad (12)$$

where $\bar{\mathbf{w}} = \text{vec}(\mathbf{W})$ is the generalized weight vector, $\bar{\mathbf{x}} = \text{vec}(\mathbf{X})$, and $\mathfrak{R} = E\{\bar{\mathbf{x}} \bar{\mathbf{x}}^+\}$. Comparison of Eq. (12) with Eq. (4) indicates that the coherent wideband processor is a quadratic form which is very similar to that which defines narrow-band MFP methods. In Eq. (12), however, it is the cross spectra of the field that is being matched rather than the field itself.

Consider a wideband Bartlett-style weight vector defined by

$$\begin{aligned} \bar{\mathbf{w}}_{\text{Bart}} &= \text{vec}([\mathbf{P}_1(r, z) \ \mathbf{P}_2(r, z) \ \cdots \ \mathbf{P}_L(r, z)]) \\ &= \text{vec}(\mathbf{P}(r, z)), \end{aligned} \quad (13)$$

where $\mathbf{P}_l(r, z) = \sigma_s^2(\omega_l) \tilde{\mathbf{d}}_l(r, z) \tilde{\mathbf{d}}_l(r, z)^+$ is the signal-only cross-spectral density matrix at frequency ω_l . The wideband MFP ambiguity surface which would be obtained by substituting (13) into (12) is, in fact, just the same as the expectation of the squared sum of narrow-band Bartlett beamformer outputs weighted by the signal spectrum, i.e.,

$$E \left\{ \left| \sum_{l=1}^L \sigma_s^2(\omega_l) \tilde{\mathbf{d}}_l(r, z)^+ \mathbf{x}_l \right|^2 \right\}.$$

Note that it is the position of the expectation and the presence of cross-frequency terms in \mathfrak{R} due to the fourth-order moment which make $Z_{\text{coh}}(r, z)$ in (12) different from $|Z_{\text{inc}}(r, z)|^2$ in (9). A similar type of approach has been previously proposed in Ref. 10 where broadband matched-field processing was performed by correlating elements of the estimated data cross-spectral density matrices with those of the hypothesized CSDMs at multiple frequencies across the bandwidth of interest.

Application of a minimum variance approach to the quadratic function given in Eq. (12) could be achieved, for example, by adaptively selecting $\bar{\mathbf{w}}$ to

$$\text{minimize } \bar{\mathbf{w}}^+ \mathfrak{R} \bar{\mathbf{w}} \text{ subject to } \text{vec}(\mathbf{P}(r, z))^+ \bar{\mathbf{w}} = 1. \quad (14)$$

The resulting coherent wideband MV ambiguity surface is given by

$$Z_{\text{coh-mv}}(r, z) = (\text{vec}(\mathbf{P}(r, z))^+ \mathfrak{R}^{-1} \text{vec}(\mathbf{P}(r, z)))^{-1}, \quad (15)$$

which, because of the inverse of the fourth-order moment matrix, \mathfrak{R} , cannot be expressed simply as a function of the incoherent wideband MV MFP. However, because of the single constraint involved, one would expect a coherent wideband MV method to be very sensitive to environmental mismatch in the generalized field vector, $\text{vec}(\mathbf{P}(r, z))$.

The desirability of incorporating environmental uncertainty into the adaptive design of the weight vectors in (14) suggests the use of a coherent wideband MV-EPC approach.⁸ A coherent wideband MV-EPC MFP is obtained by minimizing the quadratic norm of (12) subject to a set of linear constraints designed to enhance the robustness of the processor to perturbations of the environmental parameters. These constraints consist of the dominant eigenvectors, \mathbf{H} , of the matrix $\mathbf{C}(r, z)$ as obtained via singular value decomposition. The columns of the matrix $\mathbf{C}(r, z)$ are defined by a set of generalized signal field vectors corresponding to different random realizations, ζ_k , of the environmental parameter vector ζ , i.e.,

$$\begin{aligned} \mathbf{C}(r, z) &= [\text{vec}(\mathbf{P}(r, z; \zeta_1)) \ \text{vec}(\mathbf{P}(r, z; \zeta_2)) \ \cdots \\ &\quad \text{vec}(\mathbf{P}(r, z; \zeta_K))]. \end{aligned} \quad (16)$$

Note that each column of $\mathbf{C}(r, z)$ describes the signal field over a set of L frequencies and thus the column space of $\mathbf{C}(r, z)$ characterizes cross-frequency field dependencies. The columns of $\mathbf{C}(r, z)$ are generated from a set of K Monte Carlo realizations of the environment based on the assumed environmental uncertainties, as was done in Ref. 7. The dominant eigenvectors of $\mathbf{C}(r, z)$ can be found by performing a singular value decomposition and retaining those singular vectors that correspond to singular values greater than some small fraction of the maximum singular value. For moderate environmental uncertainty, the column space of $\mathbf{C}(r, z)$ is low rank. Following the narrow-band MV-EPC approach,⁸ the coherent wideband MV-EPC method is then obtained by selecting $\bar{\mathbf{w}}$ to

$$\text{minimize } \bar{\mathbf{w}}^+ \mathfrak{R} \bar{\mathbf{w}} \text{ subject to } \mathbf{H}^+ \bar{\mathbf{w}} = \mathbf{H}^+ \bar{\mathbf{w}}_q. \quad (17)$$

The weight vector, $\bar{\mathbf{w}}_q$, which defines the desired response, is chosen to maximize the output signal-to-noise ratio aver-

aged over the ensemble of environmental realizations. The average output signal-to-noise ratio for a weight vector, $\bar{\mathbf{w}}$, is given by

$$\text{SNR}_0(r, z) = \frac{\bar{\mathbf{w}}^+ \mathfrak{R}_p \bar{\mathbf{w}}}{\bar{\mathbf{w}}^+ \mathfrak{R}_Q \bar{\mathbf{w}}}, \quad (18)$$

where $\mathfrak{R}_p = E\{\overline{\mathbf{x}\mathbf{x}^+} | \text{signal only}\}$ and $\mathfrak{R}_Q = E\{\overline{\mathbf{x}\mathbf{x}^+} | \text{noise only}\}$ are the fourth-order expectations of the data in the presence of signal only and noise only, respectively. These expectations are taken over the ensemble of signal, noise, and environmental realizations. The generalized weight vector which maximizes Eq. (18) is given by

$$\bar{\mathbf{w}}_q = \mathfrak{R}_G^{-1} \tilde{\mathbf{h}}_1, \quad (19)$$

where $\mathfrak{R}_Q = \mathfrak{R}_G^+ \mathfrak{R}_G$ is obtained via the Cholesky decomposition and $\tilde{\mathbf{h}}_1$ is the eigenvector corresponding to the largest eigenvalue of $(\mathfrak{R}_G^+)^{-1} \mathfrak{R}_p \mathfrak{R}_G^{-1}$. Substituting (19) into (17) and solving gives the generalized weight vector for the coherent wideband MV-EPC method:

$$\bar{\mathbf{w}}_0 = \mathfrak{R}^{-1} \mathbf{H} (\mathbf{H}^+ \mathfrak{R}^{-1} \mathbf{H})^{-1} \mathbf{H}^+ \mathfrak{R}_G^{-1} \tilde{\mathbf{h}}_1. \quad (20)$$

Substituting (20) into (12) and normalizing by the noise-only response of the processor gives the final expression for the coherent wideband MV-EPC ambiguity surface:

$$Z_{\text{epc}}(r, z) = \frac{\tilde{\mathbf{h}}_1 (\mathfrak{R}_G^+)^{-1} \mathbf{H} (\mathbf{H}^+ \mathfrak{R}^{-1} \mathbf{H})^{-1} \mathbf{H}^+ \mathfrak{R}_G^{-1} \tilde{\mathbf{h}}_1}{\tilde{\mathbf{h}}_1 (\mathfrak{R}_G^+)^{-1} \mathbf{H} (\mathbf{H}^+ \mathfrak{R}_Q^{-1} \mathbf{H})^{-1} \mathbf{H}^+ \mathfrak{R}_G^{-1} \tilde{\mathbf{h}}_1}. \quad (21)$$

Note that in order for the coherent wideband MV-EPC method to exploit cross-frequency dependencies in the generalized field vector perturbations, the method implicitly requires *a priori* knowledge of the power spectrum of the signal. This information is used in forming $\mathbf{C}(r, z)$, from which the constraints, \mathbf{H} , are derived. Evaluation of the processor with moderately mismatched hypothesized source spectra for the scenarios described in Sec. IV indicated, at least qualitatively, that the processor is not very sensitive to the known source spectrum assumption.

Since the fourth-order statistics of the data are not known *a priori*, a finite-time observation must be used to obtain an estimate of \mathfrak{R} , denoted by $\hat{\mathfrak{R}}$, for use in Eq. (21). Without any prior knowledge of the data distribution, estimation of the required fourth-order moments would require an excessively long observation time in order to achieve reasonable accuracy. In the complex zero-mean Gaussian case assumed here, however, the fourth-order moments can be expressed in terms of second-order moments. Thus, \mathfrak{R} can be computed from second-order statistics of the data which can be accurately computed using a much shorter observation of the data. In particular, for the Gaussian case, \mathfrak{R} can be expressed in terms of the data cross-spectral density matrices at each frequency, \mathbf{R}_l , by

$$\mathfrak{R} = \text{vec}(\mathbf{R}) \text{vec}(\mathbf{R})^+ + \text{diag}(\mathbf{R}_1^* \otimes \mathbf{R}_1, \mathbf{R}_2^* \otimes \mathbf{R}_2, \dots, \mathbf{R}_L^* \otimes \mathbf{R}_L), \quad (22)$$

where $\mathbf{R} = [\mathbf{R}_1 \ \mathbf{R}_2 \ \dots \ \mathbf{R}_L]$ and $\text{diag}(\mathbf{X}_1, \dots, \mathbf{X}_L)$ is a block-diagonal matrix whose l th diagonal block is \mathbf{X}_l . The derivation of Eq. (22) is given in the Appendix. A statistically stable estimate, $\hat{\mathfrak{R}}$, of the required fourth-order mo-

ments can be obtained by replacing the \mathbf{R}_l in Eq. (22) by $\hat{\mathbf{R}}_l$. Note that an accurate estimate of \mathbf{R}_l can be obtained by using N_s uncorrelated snapshots where $N_s \gg M$ in contrast to the $N_s \gg M^2 L$ snapshots which would be required without the Gaussian assumption. Note that Eq. (22) can also be used to obtain the matrix \mathfrak{R}_Q in Eq. (21) for uncorrelated noise by substituting $\sigma_n \mathbf{I}$ for \mathbf{R}_l . Although spatially and temporally uncorrelated noise has been assumed here, evaluation of \mathfrak{R}_Q suggests that it is only weakly dependent on smooth variations of the diffuse noise spectrum.

Note that the noise component of the fourth-order moment matrix, \mathfrak{R}_Q , is not simply an identity matrix, as is the case for the noise component of \mathbf{R}_l but is obtained by letting $\mathbf{R}_l = \mathbf{I}$ for $l = 1, \dots, L$ in Eq. (22). Rather, the noise cross-spectral density matrix appears in both terms of Eq. (22). In particular, the noise contributes to the rank-one component $\text{vec}(\mathbf{R}) \text{vec}(\mathbf{R})^+$ and at low signal-to-noise ratio (SNR) has an effect similar to a signal field mismatch which is not due to environmental uncertainty. In long observation time settings, the coherent MV-EPC performance at lower SNRs can be improved by using

$$\tilde{\mathbf{R}}_l = \hat{\mathbf{R}}_l - \alpha \lambda_{\min} \mathbf{I} \quad (23)$$

in place of $\hat{\mathbf{R}}_l$ in Eq. (22), where λ_{\min} is the minimum eigenvalue of $\hat{\mathbf{R}}_l$ and $0 < \alpha < 1$ is close to unity. The performance of the resulting ‘‘modified’’ coherent wideband MV-EPC processor is better at low SNRs, as shown in Sec. IV. Subtracting $\alpha \lambda_{\min} \mathbf{I}$ in Eq. (23) has the effect of reducing the mean noise contribution to the data CSDMs used in Eq. (22) which in turn reduces the noise component of $\text{vec}(\mathbf{R}) \text{vec}(\mathbf{R})^+$. Note that although the mean noise contribution to \mathfrak{R} is reduced by using $\tilde{\mathbf{R}}_l$, the variance of the fourth-order moment estimate increases which will degrade the performance of the modified coherent MV-EPC in short observation time scenarios. Indeed, the low SNR, limited observation time, short array case can be expected to pose difficulties for all source localization methods.

The coherent wideband processor presented here is to some extent a generalization of the ‘‘matched processor’’ proposed by Vural in Ref. 18 for dealing with random signal fields described by a non-rank-one covariance matrix, \mathbf{S} . Vural’s approach considers a Hermitian quadratic product of the form $\mathbf{x}^+ \mathbf{K} \mathbf{x}$ with the vector, \mathbf{x} , representing the input data operated on by the Hermitian weight matrix, \mathbf{K} . The ‘‘spectral-spatial’’ minimum variance matched-field processor developed in Ref. 18 minimizes the variance of $\mathbf{x}^+ \mathbf{K} \mathbf{x}$ subject to $\text{trace}(\mathbf{K} \mathbf{S}) = 1$. In conventional minimum variance adaptive beamforming, the weight vector, \mathbf{w} , is chosen to minimize the variance of $\mathbf{w}^+ \mathbf{x}$ subject to constraints. Since \mathbf{x} is zero mean, the MV beamformer equivalently minimizes beamformer output power. However, $\mathbf{x}^+ \mathbf{K} \mathbf{x}$ is typically not zero mean and so it makes sense to minimize the fourth-order moment corresponding to the beamformer output power squared, $|\mathbf{x}^+ \mathbf{K} \mathbf{x}|^2$, rather than the variance of $\mathbf{x}^+ \mathbf{K} \mathbf{x}$. The squared sum of beamformer output powers is the quantity minimized by the coherent wideband MV-EPC MFP.

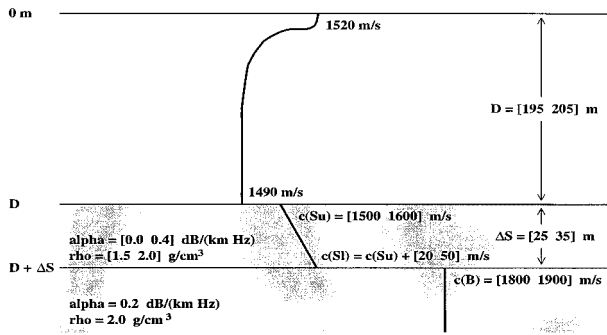


FIG. 1. SWELL-EX ocean environment.

IV. SIMULATION RESULTS

In this section, the probability of correct source localization and typical ambiguity surfaces are evaluated for the incoherent Bartlett and coherent MV-EPC wideband matched-field processing methods. In order to demonstrate that the impact of environmental mismatch on wideband matched-field processing performance is scenario dependent, two different environments are considered. The first environment, shown in Fig. 1, models a set of matched-field experiments conducted by NRAd/NCCOSC off the coast near San Diego, CA. These experiments are known as the SWELL-EX trials.¹³ The uncertain environmental parameters are assumed to be uniformly distributed between the minimum and maximum values given in the brackets within Fig. 1. Note that the sound-speed profile in the water column is assumed known and is isovelocity over most of the approximately 200-m-deep channel. Environmental mismatch is limited to the bottom parameters. The environmental parameters assumed by the Bartlett MFP were $D = 198.5$ m, $c(Su) = 1554$ m/s, $c(Sl) = 1576$ m/s, $\alpha = 0.20$ dB/(km Hz), $\rho = 1.78$ g/cm³, $\Delta S = 30$ m, and $c(B) = 1861$ m/s. The second environment considered here is modeled after the “general mismatch” benchmark scenario used in the 1993 NRL/ONR matched-field Workshop.¹⁴ This model is referred to below as the “NRL environment” and is illustrated in Fig. 2. The uncertain parameters for this case are again assumed to be uniformly distributed between the minimum and maximum values shown in Fig. 2. Note that the NRL environment includes an uncertain downward refracting sound-speed profile as well as uncertain geoacoustic parameters in the approximately 100-m-deep ocean. For this scenario the expected values of the

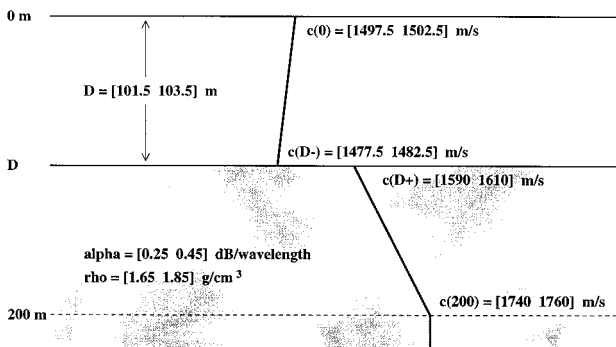


FIG. 2. Modified NRL workshop general mismatch ocean environment.

seven uncertain parameters shown in Fig. 2 were used as the assumed environmental parameters for the Bartlett MFP. For both scenarios, the source spectrum and the noise spectrum were assumed to be flat from 100 to 600 Hz. Because of the multipath nature of the propagation, the signal power varies with depth along the receiving array as well as with frequency. Therefore, in these simulations, the SNR is defined by averaging across both depth and frequency, i.e.,

$$\text{SNR} = \frac{1}{L} \sum_{l=0}^{L-1} \frac{\text{trace}(\sigma_s^2 \mathbf{P}_l)}{\text{trace}(\sigma_n^2 \mathbf{I})}. \quad (24)$$

A short, nonuniformly spaced, five-sensor array was considered in both scenarios. In the SWELL-EX case, the sensor depths were 76, 88, 104, 114, and 122 m. In the NRL case, the sensors were at depths of 38, 44, 52, 57, and 61 m, corresponding to roughly the same fractional depths in the water column. Eleven narrow-band frequencies were chosen for processing at a spacing of roughly 45.5 Hz. These frequencies were: 106.6, 151.5, 197.0, 242.4, 287.9, 333.3, 378.8, 424.2, 469.7, 515.2, and 560.6 Hz. At each frequency, the data cross-spectral density matrices were estimated using $N_s = 200$ uncorrelated snapshots. This corresponds to a total integration time which depends on the length of each snapshot, T . As noted in Sec. I, for a typical choice of T of between 0.5 and 1 s and 50% overlap of the snapshots, 200 snapshots would correspond to an integration time of between 50 and 100 s. Note that over 65 s, a 3-knot target could move 100 m which may result in some degradation in the ambiguity surface peak. In practice, the conflicting requirements of a long observation in order to detect low SNR sources and a short observation time to track moving targets poses a fundamental limit on localization performance. Note that the choice of only 11 distinct frequencies was for computational convenience only and should not be misconstrued as implying that this is a multi-frequency rather than a broadband approach. Additional frequencies could also be used or this processor could likewise be formulated in the time domain, as discussed briefly in Sec. I, although this necessitates the generation of an extensive number of narrow-band replica vectors to be able to synthesize the hypothesized time-domain waveforms without aliasing.

The main performance measure used here is the probability of correct localization (PCL) computed using $K_p = 50$ Monte Carlo realizations for each of the two environments. The source was placed at a range of 8900 m and a depth of 55 m. For each trial, the source location estimate was taken as the position of the ambiguity surface peak between 5000 m and 12 000 m in range and between the surface and the bottom in depth. Ambiguity surfaces were computed using a 100-m step size in range and 2-m step size in depth. For the SWELL-EX case, the probability of correct localization was then the proportion of trials that gave location estimates within ± 600 m in range and ± 10 m in depth of the true source position. For the modified NRL scenario, correct location estimates were defined as being within ± 300 m in range and ± 5 m in depth of the true source position. Note that the size of the search regions used scales with channel depth for the two environments.

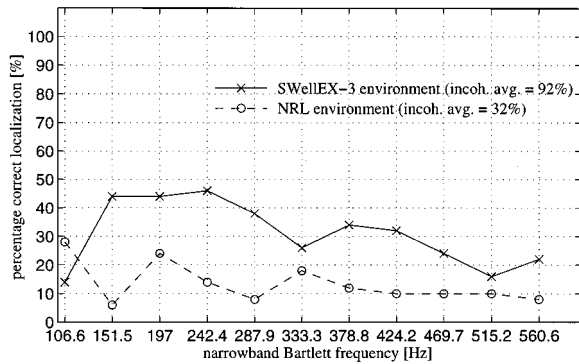


FIG. 3. Probability of correct localization versus frequency for narrow-band Bartlett processor.

The performance of the narrow-band Bartlett MFP with a short array as a function of frequency for the two environmental scenarios at an SNR of 0 dB is shown in Fig. 3. While the performance of the narrow-band Bartlett MFP differed both as a function of frequency and environmental scenario, it was consistently less than 50% for both environments. Three significant effects influence the PCL performance of the narrow-band Bartlett MFP. First, undersampling of the modal depth eigenfunctions increases both the number and the heights of range and depth sidelobes in the narrow-band ambiguity surfaces. Undersampling occurs when the number of sensors in the array (in this case, 5) is less than the number of propagating modes supported by the water column (e.g., at 333 Hz there were 35 modes in the NRL scenario and 60 modes in the SWELL-EX case). Second, mismatch of the environmental parameters can cause either a shift and/or a reduction in the ambiguity surface peak, depending on the scenario. The effect of environmental mismatch on shallow-water matched-field processors has been extensively studied previously.^{3,4,19} Mismatch in the SWELL-EX scenario most closely approximates a Pekeris waveguide where it has been shown that channel depth or the sediment parameter errors result in a frequency-independent shift of the ambiguity surface peak position.^{4,19} In contrast, the NRL scenario includes both water-column sound-speed profile and bottom mismatch which has been shown to result in a serious reduction and distortion of the ambiguity surface peak.^{3,4} Third, finite observation time introduces variance to the ambiguity surface. Statistical variability in the ambiguity surface can cause secondary peaks to exceed the peak near the true source position, therefore further degrading PCL performance. Statistical variability can be reduced both by increasing the observation time and by incoherently averaging across frequency.¹²

Incoherent wideband averaging will improve robustness to environmental mismatch when the effect of mismatch is a frequency-independent shift in the location of the ambiguity surface peak at the true source location. This occurs because the sidelobe pattern, relative to the mainlobe position, is a function of source frequency. As a result, when narrow-band surfaces are incoherently averaged, the mainlobe peaks add constructively while the sidelobes average out for sufficiently large frequency separations, thus reducing the number of localization errors due to exceedingly high sidelobes.

As noted above, of the two scenarios considered here, only mismatch in the SWELL-EX case results in a frequency-independent shift of the mainlobe peak. This explains why incoherent averaging significantly increased the PCL performance to 92% in the SWELL-EX case, while the PCL performance in the NRL scenario increased only to 32%, as indicated in Fig. 3. For these results, $N_s=200$ snapshots were used to generate statistically stable estimates of the narrow-band CSDMs with the result that the narrow-band PCL performance of the Bartlett processor closely tracked the performance obtained when the CSDMs were assumed to be known exactly. This indicates that in these simulations, the effect of incoherent wideband averaging on PCL performance was due to its effectiveness (or ineffectiveness) in mitigating environmental mismatch rather than reducing statistical variability in the ambiguity surface.

Incoherently averaged broadband Bartlett ambiguity surfaces for the SWELL-EX scenario at 0 dB and the NRL scenario at 10 dB are shown in Figs. 4 and 5, respectively, for a typical random realization of the environment. The true source position is 8900 m in range and 55 m in depth. Note that for the SWELL-EX scenario a slightly biased estimate of the source position is obtained, the source being estimated at 9200 m in range and 55 m in depth. The smooth sidelobes are the result of averaging out the frequency-dependent range and depth ambiguities of the individual surfaces. For the NRL scenario, however, the source is incorrectly estimated at 10 900 m in range and 95 m in depth and significant sidelobes persist even after incoherent broadband averaging.

It is worth noting that when a long 50-sensor array which fully spanned the water column was used in the SWELL-EX and NRL scenarios, narrow-band PCL performance was over 90% for all 11 frequencies in the SWELL-EX scenario but was between 30% and 50% for the NRL scenario. For the fully spanning array case, incoherent averaging resulted in a PCL of close to 100% for the SWELL-EX scenario but only a PCL of 52% for the NRL scenario. This again illustrates the inability of incoherent broadband averaging to compensate for environmental mismatch in the NRL scenario. The fact that the narrow-band PCL performance was over 90% for the SWELL-EX scenario was due to the fact that there were significantly fewer large sidelobes present in the narrow-band ambiguity surfaces as a result of using a densely sampled array which fully spans the water column. Despite the difficulty of the NRL scenario, incoherent averaging of narrow-band MV-EPC surfaces for a fully spanning array yielded near 100% correct localization. The performance of the MV-EPC method with a long array is more fully discussed in Ref. 7 for the NRL scenario and in Ref. 20 using real Mediterranean vertical array data. Unfortunately, however, for short arrays the number of constraints required to provide robustness to environmental mismatch can quickly exceed the number of sensors in the array, leading to an overconstrained beamformer which is no longer able to adaptively suppress ambiguous sidelobes. This is illustrated in Fig. 6 by the ambiguity surface for the incoherently averaged wideband MV-EPC beamformer using the short array in the NRL scenario. The inability of the incoherent MV-EPC to adaptively suppress

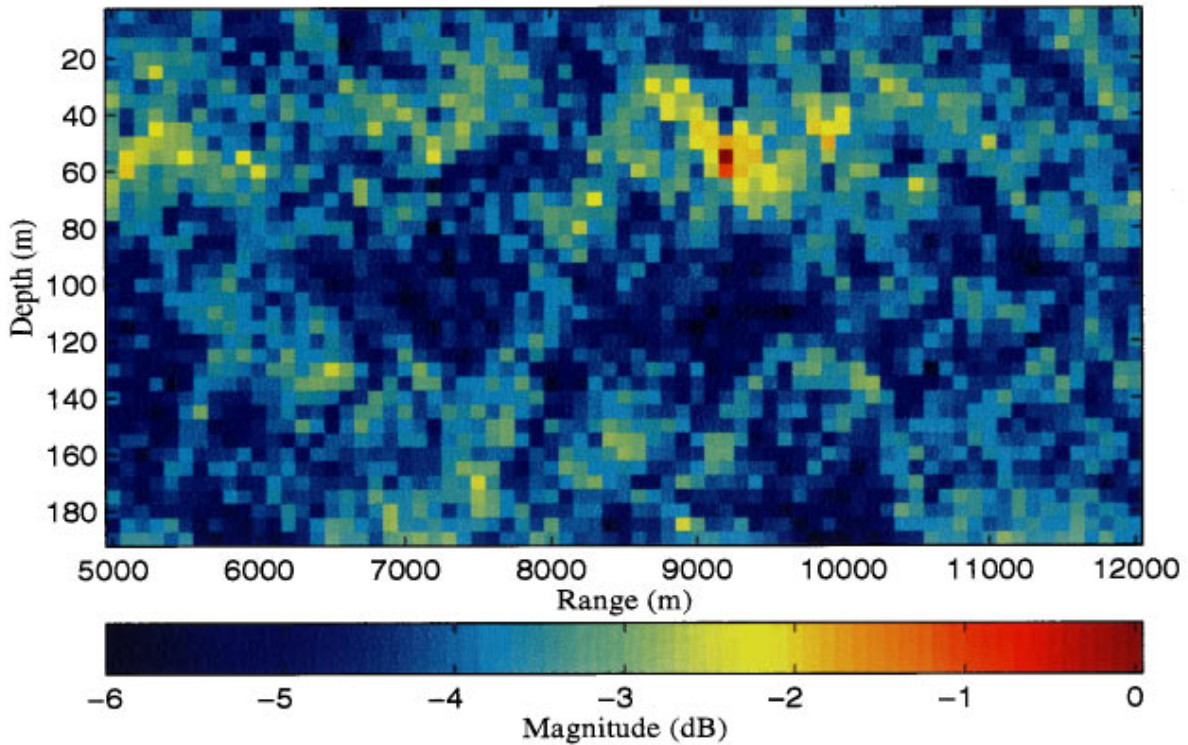


FIG. 4. Incoherent wideband Bartlett ambiguity surface for SWELL-EX scenario of Fig. 1.

sidelobes necessitates the use of an alternative MFP method when short arrays are involved, as is the case of interest here. This motivates the use of the coherent wideband MV-EPC method derived in the previous section.

A typical ambiguity function of the coherent wideband MV-EPC method applied to the short array in the NRL sce-

nario at 10 dB SNR is shown in Fig. 7. The dominant eigenvectors used in Eq. (17) were computed using $K=50$ independent realizations, performing a singular value decomposition on $\mathbf{C}(\mathbf{r}, \mathbf{z})$, and retaining all singular vectors whose eigenvalues were greater than 10% of the largest singular value. Note that the dimension of $\mathbf{C}(\mathbf{r}, \mathbf{z})$ is $M^2L \times K$

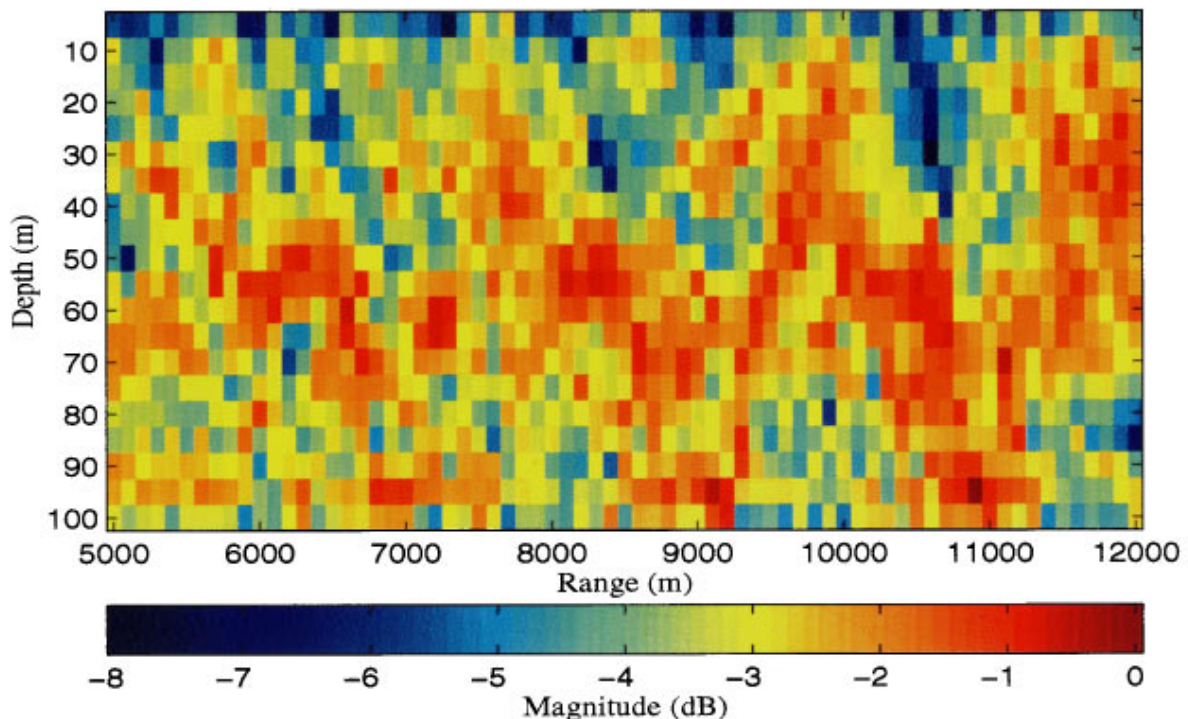


FIG. 5. Incoherent wideband Bartlett ambiguity surface for NRL scenario of Fig. 2.

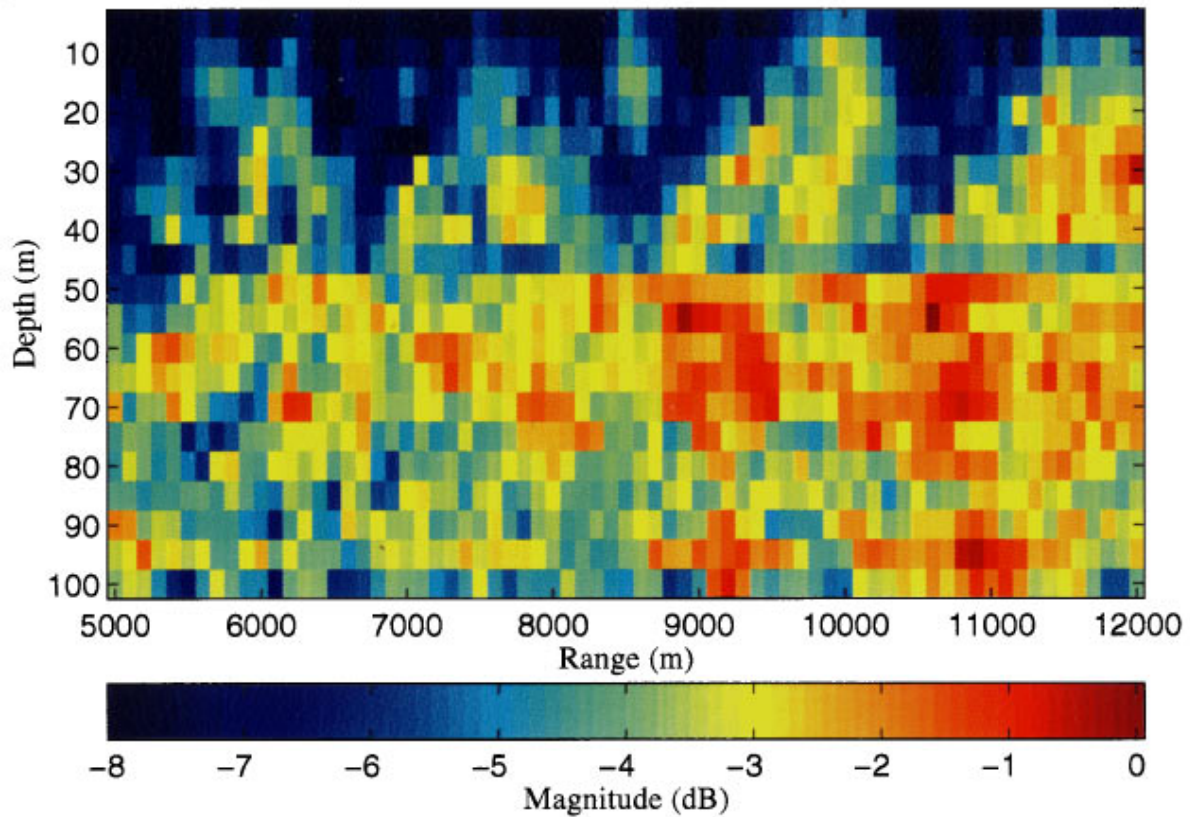


FIG. 6. Incoherent wideband MV-EPC ambiguity surface for NRL scenario of Fig. 2.

which in this example corresponds to 275×50 . This resulted in between 12 and 20 constraints being used in the coherent MV-EPC method, depending on hypothesized source position. Thus, \mathfrak{R} is 275×275 and a typical dimension for

$\mathbf{H}(r, z)$ is 275×15 . Note that although the singular value decompositions required to compute $\mathbf{H}(r, z)$ for each hypothesized range and depth may be performed before the data are processed, the storage requirements and computation time

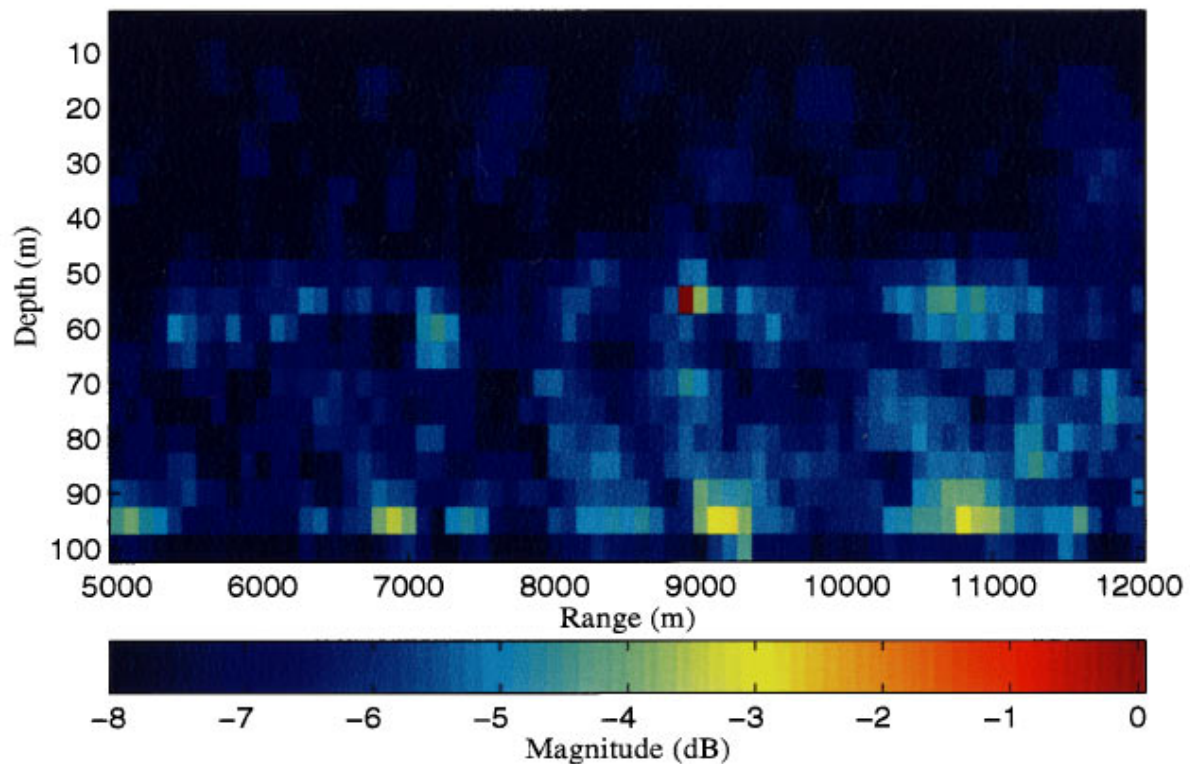


FIG. 7. Coherent wideband MV-EPC ambiguity surface for NRL scenario of Fig. 2.

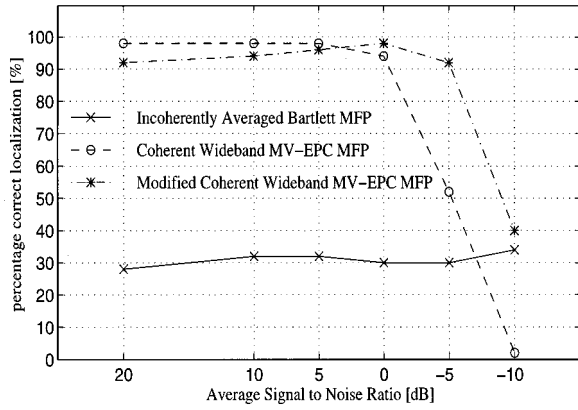


FIG. 8. PCL versus SNR for coherent and incoherent wideband MFP methods.

are significantly greater for the coherent MV-EPC than incoherent MFP methods. In these simulations, for example, coherent MV-EPC processing took about six times longer than any of the incoherent methods [not including the precomputation of $\mathbf{H}(r, z)$]. Note that since the coherent methods involve the squared power output, to permit comparison with incoherent Bartlett, $5 \log(Z_{\text{epc}})$ is the dB scale plotted in Fig. 7. Observe that the coherent wideband MV-EPC ambiguity surface exhibits a peak at the correct source location of 8900 m in range and 55 m in depth with sidelobes which are at least 3 dB down. It is because the coherent wideband MV-EPC processor adapts a larger number of degrees of freedom over the signal band that it is able to achieve better sidelobe suppression. The probability of correct localization performance of the coherent MV-EPC and incoherent Bartlett processor for the short array is plotted versus SNR in Fig. 8. Note that the coherent MV-EPC method exhibited superior PCL performance at SNRs above -5 dB. However, below -5 dB SNR the coherent wideband MV-EPC processor performance falls off very significantly. The reason the coherent wideband MV-EPC exhibits poor performance at low SNR is that the noise component of the fourth-order moment matrix, \mathfrak{R} , is not simply an identity matrix, as is the case for the noise component of \mathbf{R}_l . As shown in Fig. 8, the modified coherent MV-EPC method which uses $\tilde{\mathbf{R}}_l$ of (23) in place of $\hat{\mathbf{R}}_l$ in Eq. (22) gives better performance at lower SNRs provided sufficient observation time is available.

V. CONCLUSION

In this paper, the problem of matched-field passive localization of broadband underwater acoustic sources with a short vertical sensor array has been addressed. A new coherent wideband MFP method has been proposed to improve the robustness of matched-field processing to environmental uncertainties. This method has been compared with incoherent averaging of narrow-band Bartlett ambiguity surfaces across the signal band. The results indicate that the effectiveness of the incoherent wideband Bartlett processor is dependent on the type of environmental mismatch. In particular, incoherent averaging works well when the environmental mismatch results in a frequency-independent shift in source position. For more difficult environments, the incoherently averaged mini-

um variance beamformer with environmental perturbation constraints (MV-EPC) provides better performance when used with large vertical arrays. For short arrays, however, the MV-EPC beamformer becomes overconstrained, which precludes the adaptive suppression of beamformer sidelobes. The coherent wideband MV-EPC processor makes available a much larger number of adaptive degrees of freedom for suppressing ambiguous sidelobes and also exploits cross-frequency dependencies in the random acoustic channel response. The method uses environmental constraints defined across the signal frequency band in order to provide robustness over an ensemble of random environmental realizations. In particular, the method consists of minimizing the squared output power of the beamformer subject to these constraints. Monte Carlo simulation results for a canonical shallow-water scenario indicate that the coherent wideband MV-EPC method yields improved probability of correct localization performance versus incoherent averaging of narrow-band Bartlett ambiguity functions with a short array above a threshold SNR.

ACKNOWLEDGMENTS

The authors would like to thank the reviewers for their useful suggestions. This work was supported by the NUWC under Contract No. N70024-4054-0708 and by NRaD/NCCOSC under Contract No. N66001-95-C-6032.

APPENDIX: DERIVATION OF \mathfrak{R}

From Eq. (12), the fourth-order moment of the data is defined as

$$\mathfrak{R} = E\{\text{vec}(\mathbf{X})\text{vec}(\mathbf{X})^+\}, \quad (\text{A1})$$

where we also define $\mathbf{X} = [\mathbf{X}_1 \ \mathbf{X}_2 \ \cdots \ \mathbf{X}_L]$, $\mathbf{X}_l = \mathbf{x}_l \mathbf{x}_l^+$, $\bar{\mathbf{x}} = \text{vec}(\mathbf{X})$, $\bar{\mathbf{x}}_l = \text{vec}(\mathbf{X}_l)$, and let $^+$ represent the Hermetian transpose, $*$ represent the complex conjugate, and T represent the transpose. For zero-mean, Gaussian random variables it is known that

$$E\{v_1 v_2^* v_3 v_4^*\} = E\{v_1 v_2^*\} E\{v_3 v_4^*\} + E\{v_1 v_4^*\} E\{v_3 v_2^*\}. \quad (\text{A2})$$

The expectation $E\{X_k^{ij} X_l^{mn*}\} = E\{x_k^i x_k^{j*} x_l^m x_l^{n*}\}$, conditioned on the environmental parameters ζ , where x_l^i corresponds to the value of \mathbf{x}_l at the i th sensor, can be evaluated as

$$E\{X_k^{ij} X_l^{mn*}\} = R_k^{ij} R_l^{mn*} + R_k^{im} R_l^{jn*} \delta^{kl}, \quad (\text{A3})$$

where $R_k^{ij} = E\{x_k^i x_k^{j*}\}$ represents the ij th element of the data cross-spectral density matrix, \mathbf{R}_k . Defining $\mathbf{X}_l = [\mathbf{X}_l^1 \ \mathbf{X}_l^2 \ \cdots \ \mathbf{X}_l^M]$ and $\mathbf{X}_l^i = [\mathbf{X}_l^{1i} \ \mathbf{X}_l^{2i} \ \cdots \ \mathbf{X}_l^{Mi}]^T$, it is possible to write

$$E\{\mathbf{X}_k^i \ \mathbf{X}_l^{j+}\} = \begin{bmatrix} E\{X_k^{1i} X_l^{1j*}\} & \cdots & E\{X_k^{1i} X_l^{Mj*}\} \\ \vdots & \ddots & \vdots \\ E\{X_k^{Mi} X_l^{1j*}\} & \cdots & E\{X_k^{Mi} X_l^{Mj*}\} \end{bmatrix}, \quad (\text{A4})$$

$$E\{\mathbf{X}_k^i \mathbf{X}_l^{j+}\} = \begin{bmatrix} \mathbf{R}_k^{1i} \mathbf{R}_l^{1j*} & \cdots & \mathbf{R}_k^{1i} \mathbf{R}_l^{Mj*} \\ \vdots & \ddots & \vdots \\ \mathbf{R}_k^{Mi} \mathbf{R}_l^{1j*} & \cdots & \mathbf{R}_k^{Mi} \mathbf{R}_l^{Mj*} \end{bmatrix} + \begin{bmatrix} \mathbf{R}_k^{11} \mathbf{R}_l^{ij*} & \cdots & \mathbf{R}_k^{1M} \mathbf{R}_l^{ij*} \\ \vdots & \ddots & \vdots \\ \mathbf{R}_k^{M1} \mathbf{R}_l^{ij*} & \cdots & \mathbf{R}_k^{MM} \mathbf{R}_l^{ij*} \end{bmatrix} \delta_{kl}, \quad (\text{A5})$$

$$E\{\mathbf{X}_k^i \mathbf{X}_l^{j+}\} = \mathbf{R}_k^i \mathbf{R}_l^{j+} + \mathbf{R}_l^{ij*} \mathbf{R}_k \delta_{kl}, \quad (\text{A6})$$

where \mathbf{R}_k^i represents the i th column of the data cross-spectral density matrix \mathbf{R}_k .

Noting that $\bar{\mathbf{x}}_l = \text{vec}(\mathbf{X}_l) = [\mathbf{X}_l^{1T} \mathbf{X}_l^{2T} \cdots \mathbf{X}_l^{MT}]^T$, it follows that

$$E\{\bar{\mathbf{x}}_k \bar{\mathbf{x}}_l^+\} = \begin{bmatrix} \mathbf{R}_k^1 \mathbf{R}_l^{1+} & \cdots & \mathbf{R}_k^1 \mathbf{R}_l^{M+} \\ \vdots & \ddots & \vdots \\ \mathbf{R}_k^M \mathbf{R}_l^{1+} & \cdots & \mathbf{R}_k^M \mathbf{R}_l^{M+} \end{bmatrix} + \begin{bmatrix} \mathbf{R}_l^{11*} \mathbf{R}_k & \cdots & \mathbf{R}_l^{1M*} & \mathbf{R}_k \\ \vdots & \ddots & \vdots & \\ \mathbf{R}_l^{M1*} \mathbf{R}_k & \cdots & \mathbf{R}_l^{MM*} & \mathbf{R}_k \end{bmatrix} \delta_{kl}, \quad (\text{A7})$$

$$E\{\bar{\mathbf{x}}_k \bar{\mathbf{x}}_l^+\} = \bar{\mathbf{r}}_k \bar{\mathbf{r}}_l^+ + [\mathbf{R}_l^* \otimes \mathbf{R}_k] \delta_{kl}, \quad (\text{A8})$$

where $\bar{\mathbf{r}}_l = \text{vec}(\mathbf{R}_l)$ and \otimes represents the Kronecker product.

Defining $\mathbf{R} = [\mathbf{R}_1 \mathbf{R}_2 \cdots \mathbf{R}_L]$, $\bar{\mathbf{r}} = \text{vec}(\mathbf{R})$, and making note that $\bar{\mathbf{x}} = [\bar{\mathbf{x}}_1^T \bar{\mathbf{x}}_2^T \cdots \bar{\mathbf{x}}_L^T]^T$ it follows that

$$E\{\bar{\mathbf{x}} \bar{\mathbf{x}}^+\} = \begin{bmatrix} \bar{\mathbf{r}}_1 \bar{\mathbf{r}}_1^+ & \bar{\mathbf{r}}_1 \bar{\mathbf{r}}_2^+ & \cdots & \bar{\mathbf{r}}_1 \bar{\mathbf{r}}_L^+ \\ \bar{\mathbf{r}}_2 \bar{\mathbf{r}}_1^+ & \bar{\mathbf{r}}_2 \bar{\mathbf{r}}_2^+ & \cdots & \bar{\mathbf{r}}_2 \bar{\mathbf{r}}_L^+ \\ \vdots & \vdots & \ddots & \vdots \\ \bar{\mathbf{r}}_L \bar{\mathbf{r}}_1^+ & \bar{\mathbf{r}}_L \bar{\mathbf{r}}_2^+ & \cdots & \bar{\mathbf{r}}_L \bar{\mathbf{r}}_L^+ \end{bmatrix} + \begin{bmatrix} \mathbf{R}_1^* \otimes \mathbf{R}_1 & 0 & \cdots & 0 \\ 0 & \mathbf{R}_2^* \otimes \mathbf{R}_2 & \cdots & 0 \\ \vdots & \vdots & \ddots & \vdots \\ 0 & 0 & \cdots & \mathbf{R}_L^* \otimes \mathbf{R}_L \end{bmatrix}, \quad (\text{A9})$$

$$\mathfrak{R} = \bar{\mathbf{r}} \bar{\mathbf{r}}^+ + \text{diag}\{\mathbf{R}_1^* \otimes \mathbf{R}_1, \mathbf{R}_2^* \otimes \mathbf{R}_2, \cdots, \mathbf{R}_L^* \otimes \mathbf{R}_L\}. \quad (\text{A10})$$

- ¹A. B. Baggeroer, W. A. Kuperman, and P. N. Mikhalevsky, "An overview of matched field methods in ocean acoustics," *IEEE J. Ocean. Eng.* **18**, 401–424 (1993).
- ²D. F. Gingras, "Methods for predicting the sensitivity of matched-field processors to mismatch," *J. Acoust. Soc. Am.* **86**, 1940–1949 (1989).
- ³C. Feuillade, D. R. DelBalzo, and M. M. Rowe, "Environmental mismatch in shallow-water matched-field processing: Geoacoustic parameter variability," *J. Acoust. Soc. Am.* **85**, 2354–2364 (1989).
- ⁴E. C. Shang, and Y. Y. Wang, "Environmental mismatching effects on source localization processing in mode space," *J. Acoust. Soc. Am.* **89**, 2285–2290 (1991).
- ⁵M. D. Collins and W. A. Kuperman, "Focalization: Environmental focusing and source localization," *J. Acoust. Soc. Am.* **90**, 1410–1422 (1991).
- ⁶D. F. Gingras and P. Gerstoft, "Inversion for geometric and geoacoustic parameters in shallow water: experimental results," *J. Acoust. Soc. Am.* **97**, 3589–3589 (1995).
- ⁷J. Shorey, L. W. Nolte, and J. L. Krolik, "Computationally-efficient Monte Carlo estimation algorithms for matched-field processing in uncertain ocean environments," *Computat. Acoust.* **2**, 285–314 (1994).
- ⁸J. L. Krolik, "Matched-field minimum variance beamforming in a random ocean channel," *J. Acoust. Soc. Am.* **92**, 1408–1419 (1992).
- ⁹R. K. Brienzo and W. S. Hodgkiss, "Broadband matched-field processing," *J. Acoust. Soc. Am.* **94**, 2821–2831 (1993).
- ¹⁰E. K. Westwood, "Broadband matched-field source localization," *J. Acoust. Soc. Am.* **91**, 2777–2789 (1992).
- ¹¹A. B. Baggeroer, W. A. Kuperman, and H. Schmidt, "Matched field processing: Source localization in correlated noise as an optimum parameter estimation problem," *J. Acoust. Soc. Am.* **83**, 571–587 (1988).
- ¹²G. B. Smith, C. Feuillade, and D. R. DelBalzo, "Matched-field processing enhancement in a shallow-water environment by incoherent broadband averaging," *J. Acoust. Soc. Am.* **91**, 1447–1455 (1992).
- ¹³N. Booth and P. Schey, "Broadband matched-field processing of low level signals in shallow water," *J. Acoust. Soc. Am.* **97**, 3291(A) (1995).
- ¹⁴M. B. Porter and A. Tolstoy, "The matched field processing benchmark problems," *J. Computat. Acoust.* **2**, 161–185 (1994).
- ¹⁵W. S. Hodgkiss, K. H. Kim, J. J. Murray, and J. L. Krolik, "Robust MFP Processor Performance with SWellEx Data," presentation at the *8th International Workshop on MFP and Model-Based Signal Processing*, Esquimalt Defence Research Detachment, Victoria, BC, 12–14 June 1996.
- ¹⁶M. B. Porter and Z. H. Michalopoulou, "A coherent approach to broadband matched-field processing: Application in the Hudson Canyon," *Proc. of the IEEE ICASSP-96*, pp. 1189–1192, 1996.
- ¹⁷L. Brekhovskikh and Y. Lysanov, *Fundamentals of Ocean Acoustics* (Springer-Verlag, Berlin, 1982).
- ¹⁸A. M. Vural, "Effects of perturbations on the performance of optimum/adaptive arrays," *IEEE Trans. Aerospace Electron. Syst.* **AES-15**, 76–87 (1979).
- ¹⁹G. L. D'Spain, W. S. Hodgkiss, and W. A. Kuperman, "Broadband matched-field processing in shallow-water" *Proc. 15th Intl. Congress on Acoustics*, Trondheim, Norway, pp. 231–234, June 1995.
- ²⁰J. Krolik, "The performance of matched-field beamformers with Mediterranean vertical array data," *IEEE Trans. Signal Process.* **44**(10), 2605–2611 (1996).
- ²¹C. W. Therrien, *Discrete Random Signals and Statistical Signal Processing* (Prentice-Hall, Englewood Cliffs, NJ, 1992).

Rational square-root approximations for parabolic equation algorithms

Fausto A. Milinazzo

Victoria Applied Analysis, 1483 Thames Place, Victoria, British Columbia V8N 5G9, Canada

Cedric A. Zala

Barrodale Computing Services Ltd., P.O. Box 3075, Victoria, British Columbia V8P 2H1, Canada

Gary H. Brooke

Numerical Decisions Group, Suite 8A, 947 Fort Street, Victoria, British Columbia V8V 3K3, Canada

(Received 11 August 1995; accepted for publication 22 August 1996)

In this article, stable Padé approximations to the function $\sqrt{1+z}$ are derived by choosing a branch cut in the negative half-plane. The Padé coefficients are complex and may be derived analytically to arbitrary order from the corresponding real coefficients associated with the principal branch defined by $z < -1$, $\Im(z) = 0$ [$\Im(z)$ denotes the imaginary part of z]. The characteristics of the corresponding square-root approximation are illustrated for various segments of the complex plane. In particular, for waveguide problems it is shown that an increasingly accurate representation may be obtained of both the evanescent part of the mode spectrum for the acoustic case and the complex mode spectrum for the elastic case. An elastic parabolic equation algorithm is used to illustrate the application of the new Padé approximations to a realistic ocean environment, including elasticity in the ocean bottom. © 1997 Acoustical Society of America. [S0001-4966(97)01601-9]

PACS numbers: 43.30.Bp, 43.20.Bi [MBP]

INTRODUCTION

Parabolic equation (PE) approximations to the wave equation are widely used in propagation algorithms for underwater acoustic applications. Over the years, these algorithms have progressed from a narrow-angle split-step formulation¹ to a wide-angle finite-element approach.² Motivation for the advancement in the capability of the algorithms stems from the requirement for acoustic predictions in environments involving high-angle propagation with significant ocean-bottom interaction, range dependence, and acousto-elastic coupling. Because the PE methodology depends critically upon a square-root approximation to a pseudo-differential operator, it is not surprising that recent advances can be linked directly to improvements in the square-root approximations. The Thomson-Chapman wide-angle approximation³ and Collins' sum and product Padé expansions^{4,5} are but two examples.

Rational square-root approximations with complex coefficients have been particularly important because they have extended the range of applicability of the PE to elastic media. Propagation in elastic media involves interaction of compressional and shear components and raises important stability issues for the square-root approximations. Wetton and Brooke,⁶ using a first-order rational-linear approximation, showed that stable elastic wave propagation with the PE was possible, provided complex square-root coefficients were employed. Collins⁴ improved upon the analysis by presenting a method for computing higher-order Padé approximations with complex coefficients.

In this paper, we examine an alternative procedure for obtaining high-order rational linear square-root approximations with complex coefficients. We show that a more natural branch of the square-root function can be defined for PE

algorithms by rotating the principal branch (i.e., the negative real line) into the lower complex plane. The resulting complex square-root coefficients can be found directly from the corresponding real-valued Padé coefficients, eliminating the previous requirement for a nonlinear search procedure.⁴ Since the number of coefficients with this new procedure is not limited in any theoretical or numerical sense, extremely high-order approximations are possible. In principle, within the context of the PE approximation,⁷ redefining the branch of the square root allows both real and complex eigenvalues (i.e., all spectral components) of the corresponding waveguide problem to be treated in a stable and accurate manner. Of course, precise accounting for the entire evanescent part of the spectrum would require an infinite number of coefficients. As demonstrated herein, a restricted portion of the evanescent spectrum can be represented with a reasonable number of terms. Finally, it is worth noting that finite-difference acoustic PE algorithms can also benefit from using complex Padé coefficients. That is, the use of appropriate complex coefficients can result in a natural attenuation of extremely high-angle energy, including the evanescent part of the mode spectrum. Generally speaking, this energy is propagated improperly in algorithms utilizing real coefficients. Normally, such algorithms would have to eliminate high-angle energy through a judicious choice of absorbing layer or boundary condition.

This article is organized in the following manner: first, we give a brief overview of the square-root approximation within the context of the PE algorithm. Second, we derive the complex coefficients for the rotated branch cut of the square root and demonstrate the behavior of this approximation in the complex plane. Third, we use numerical examples to illustrate the spectral properties of the new approximation.

Finally, we use this approximation in an elastic PE prediction for the ASA benchmark wedge-shaped waveguide (including elasticity) and examine its application to acousto-elastic waveguide propagation problems.

I. BACKGROUND

The formulation of PE methods begins with the reduced wave equation, or Helmholtz equation,

$$p_{rr} + \frac{1}{r}p_r + p_{zz} + [k_0n(z)]^2p = 0, \quad (1)$$

written in cylindrical coordinates. In Eq. (1), $p(r, z)$ is the acoustic pressure due to a point source with time dependence $\exp(-i\omega t)$. A reference sound speed, c_0 , is used to define a reference wave number, $k_0 = \omega/c_0$, and an index of refraction, $n(z) = c_0/c(z)$. The sound speed, $c(z)$, is assumed to depend only on depth. Assuming that the pressure is of the form $p = \psi(r, z)\exp(ik_0r)/\sqrt{r}$, where the envelope function, ψ , varies slowly with r , we can obtain the following equation for $k_0r \gg 1$:

$$\psi_{rr} + 2ik_0\psi_r + \psi_{zz} + k_0^2[n^2 - 1]\psi = 0. \quad (2)$$

Equation (2) can be written as the product of two factors

$$\left[\frac{\partial}{\partial r} + ik_0[1 - Q] \right] \left[\frac{\partial}{\partial r} + ik_0[1 + Q] \right] \psi = 0, \quad (3)$$

where we have introduced the pseudo-differential operator $Q = \sqrt{n^2 + (1/k_0^2)(\partial^2/\partial z^2)}$. The first factor of Eq. (3) governs the evolution of the outgoing component of ψ , while the second governs the evolution of the incoming component of ψ . PE methods are based on approximations of the pseudo-differential operators $1 \pm Q$.

For the purpose of the presentation of this analysis, we neglect backscattering and concentrate on the outgoing component of ψ by writing

$$\frac{\partial \psi}{\partial r} = ik_0[Q - 1]\psi = ik_0[\sqrt{1 + Q} - 1]\psi, \quad (4)$$

where $Q = n^2 - 1 + (1/k_0^2)(\partial^2/\partial z^2)$. A number of approximations of $\sqrt{1 + Q}$ which are based on Taylor or rational approximations of the function $\sqrt{1 + z}$ appear in the literature (i.e., Refs. 1, 8, 9). In particular, rational approximations of the form

$$R_N(z) = 1 + \sum_{n=1}^N \frac{a_n z}{1 + b_n z} \quad (5)$$

to $S(z) = \sqrt{1 + z}$ are of interest for PE algorithms since they can provide good estimates for use in Eq. (4) and allow efficient numerical implementations. As shown in Ref. 10, the real-valued coefficients

$$a_n = \frac{2}{2N+1} \sin^2 \frac{n\pi}{2N+1} \quad \text{and} \quad b_n = \cos^2 \frac{n\pi}{2N+1} \quad (6)$$

correspond to Padé approximations of the square root with branch cut along the negative real line from $z = -1$. In Refs. 4 and 5, these approximations are used to implement numeri-

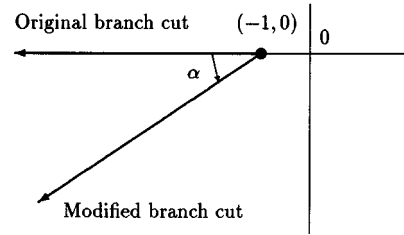


FIG. 1. A schematic of the z plane and the position of the branch cut of $S_\alpha(z)$.

cal marching schemes which are applied to acoustic propagation.

The real-valued coefficients given in Eq. (6), while useful for certain problems, result in a square-root approximation which maps the real axis onto itself. In the context of waveguide propagation, this leads to inappropriate treatment of eigenvalues corresponding to evanescent modes in acoustic media (which, in the context of this analysis, should be mapped onto the positive imaginary axis) and to computational instability in elastic media (where eigenvalues in the lower half-plane are mapped into the same half-plane, resulting in an exponentially growing solution⁶). Both these difficulties can be overcome by using complex coefficients, provided suitable stability conditions are met. Collins^{4,11} presented a technique to enhance stability whereby one or more of the derivative constraints used to determine the coefficients given by Eq. (6) are replaced by stability constraints. Computations indicate that convergence of Collins' procedure becomes increasingly difficult as the order of the approximation increases, and above a certain order no solution can be reasonably obtained.¹²

In view of the above comments, it is therefore desirable to define a more direct method for computing complex rational coefficients which provide accurate and stable approximations to the square-root function. In the next section we show how the coefficients of Eq. (6) can be used to generate such approximations for $\sqrt{1 + z}$, for which the corresponding branch cut is chosen to lie in the negative half-plane.

II. THE ROTATED BRANCH CUT RATIONAL APPROXIMATION

A. Derivation

We have noted that $R_N(z)$ approximates the branch of $\sqrt{1 + z}$ with a branch cut along the negative real line. To obtain an approximation with branch cut along the ray $z = -1 + re^{i(\pi + \alpha)}$ with $r > 0$, we consider the function

$$S_\alpha(z) = e^{i\alpha/2} \sqrt{(1 + z)e^{-i\alpha}}. \quad (7)$$

If we take the square root in Eq. (7) to be that branch of the square-root function with branch cut along the negative real line, then it is easy to see that $S_\alpha(z)$ is the branch of the square-root function with branch cut along the desired ray. Figure 1 gives a schematic showing a position of the branch cut in the z plane. From Eq. (7), we have

$$S_\alpha(z) = e^{i\alpha/2} \sqrt{1 + [(1 + z)e^{-i\alpha} - 1]}. \quad (8)$$

Using Eq. (5) to approximate the square root in Eq. (8), we obtain

$$S_\alpha(z) \approx R_{\alpha,N}(z) = e^{i\alpha/2} \left[1 + \sum_{n=1}^N \frac{a_n [(1+z)e^{-i\alpha} - 1]}{1 + b_n [(1+z)e^{-i\alpha} - 1]} \right]. \quad (9)$$

Equation (9) can be put into the form

$$R_{\alpha,N}(z) = C_0 + \sum_{n=1}^N \frac{A_n z}{1 + B_n z}. \quad (10)$$

From Eq. (9) and Eq. (10), we obtain

$$C_0 = e^{i\alpha/2} \left(1 + \sum_{n=1}^N \frac{a_n [e^{-i\alpha} - 1]}{1 + b_n (e^{-i\alpha} - 1)} \right)$$

and

$$B_n = \frac{b_n e^{-i\alpha}}{1 + b_n (e^{-i\alpha} - 1)}. \quad (11)$$

The coefficient, A_n , is determined by noting that the pole at $z = -1/B_n$ must have the same strength in both Eq. (9) and Eq. (10). This is accomplished by considering the expression

$$\begin{aligned} & \lim_{z \rightarrow -1/B_n} \left[[B_n z + 1] \left[C_0 + \sum_{k=1}^N \frac{A_k z}{1 + B_k z} - e^{i\alpha/2} \left(1 + \sum_{k=1}^N \frac{a_k [(1+z)e^{-i\alpha} - 1]}{1 + b_k [(1+z)e^{-i\alpha} - 1]} \right) \right] \right] \\ & = \lim_{z \rightarrow -1/B_n} \left[A_n z - \frac{e^{i\alpha/2} a_n [(1+z)e^{-i\alpha} - 1]}{[1 + b_n (e^{-i\alpha} - 1)]} \right] = 0 \end{aligned} \quad (12)$$

and evaluating the limit to obtain

$$A_n = \frac{e^{-i\alpha/2} a_n}{[1 + b_n (e^{-i\alpha} - 1)]^2}. \quad (13)$$

The coefficients A_n , B_n , and C_0 with a_n and b_n given by Eq. (6) are used in the simulations below.

B. Characteristics of the rotated branch cut approximation in the complex plane

In this and the following sections, we shall define $z = x + iy$ and denote the real and imaginary parts of z by $\Re(z)$ and $\Im(z)$, respectively. The accuracy of the approximation $R_{\alpha,N}(z)$ applied to the real line is illustrated in Figs. 2 and 3, which show the difference $\sqrt{1+x} - R_{\alpha,N}(x)$ for $N=2,4,8$ and $\alpha=10^\circ, 45^\circ$. The absolute values of the difference of the real parts and the difference of the imaginary parts are plotted separately. These differences are taken along the segment $[-1, +0.6]$ of the real line. It is clear from the plots that, for fixed α and sufficiently large N , $R_{\alpha,N}(x)$ is an excellent approximation to the $S_\alpha(x)$ in a large region corresponding to the real wave-number spectrum for waveguide problems. Conversely, for fixed N , the accuracy of the approximation decreases as α increases.

Figure 4 shows the images of the real line segment $[-4,4]$ when $\alpha=10^\circ, 45^\circ$ and $N=4,7$. For comparison the images obtained using Collins' coefficients given in Ref. 4

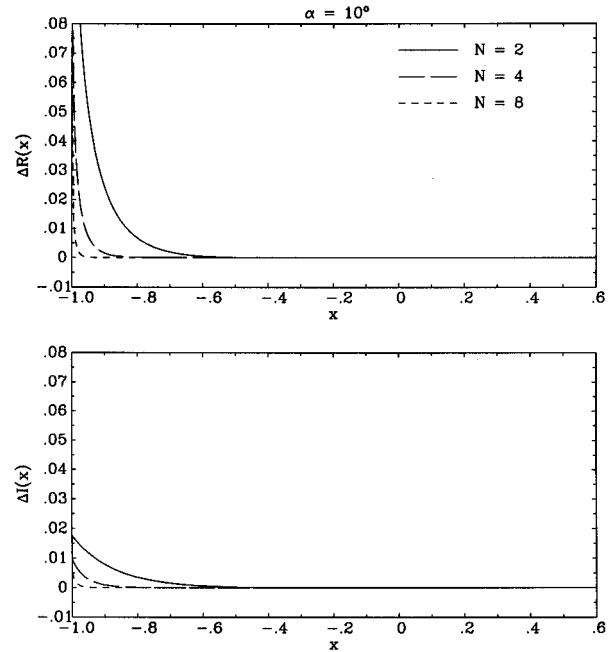


FIG. 2. The difference $\sqrt{1+x} - R_{\alpha,N}(x)$ for $\alpha=10^\circ$ and $x \in [-1.0, +0.6]$. The functions $\Delta R(x) = |\Re(\sqrt{1+x} - R_{\alpha,N}(x))|$ and $\Delta I(x) = |\Im(\sqrt{1+x} - R_{\alpha,N}(x))|$ are plotted for $N=2,4,8$.

are also presented. Note that in all cases (including those from Ref. 4) the mapping is stable; the image of the real line segment lies totally within the upper half-plane. Furthermore, Fig. 5 shows images of the real line segment $[-100,100]$ for $\alpha=45^\circ$ and $N=8,12,16$. It is evident that increasing N improves the representation of the correspond-

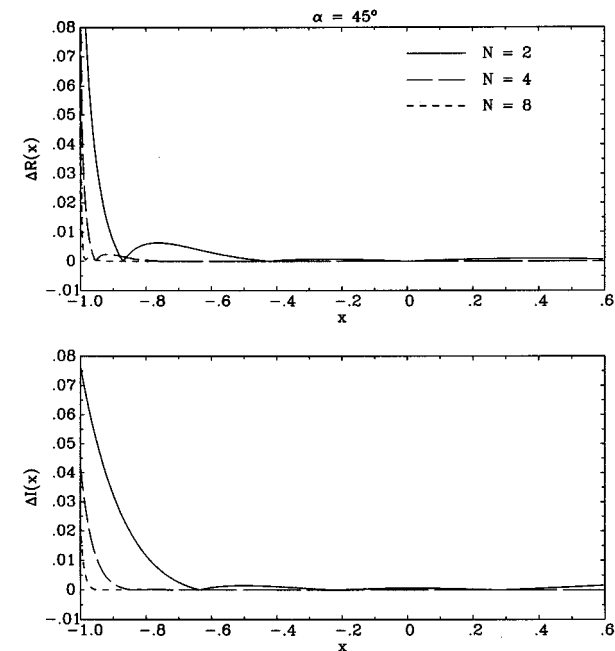


FIG. 3. The difference $\sqrt{1+x} - R_{\alpha,N}(x)$ for $\alpha=45^\circ$ and $x \in [-1.0, +0.6]$. The functions $\Delta R(x) = |\Re(\sqrt{1+x} - R_{\alpha,N}(x))|$ and $\Delta I(x) = |\Im(\sqrt{1+x} - R_{\alpha,N}(x))|$ are plotted for $N=2,4,8$.

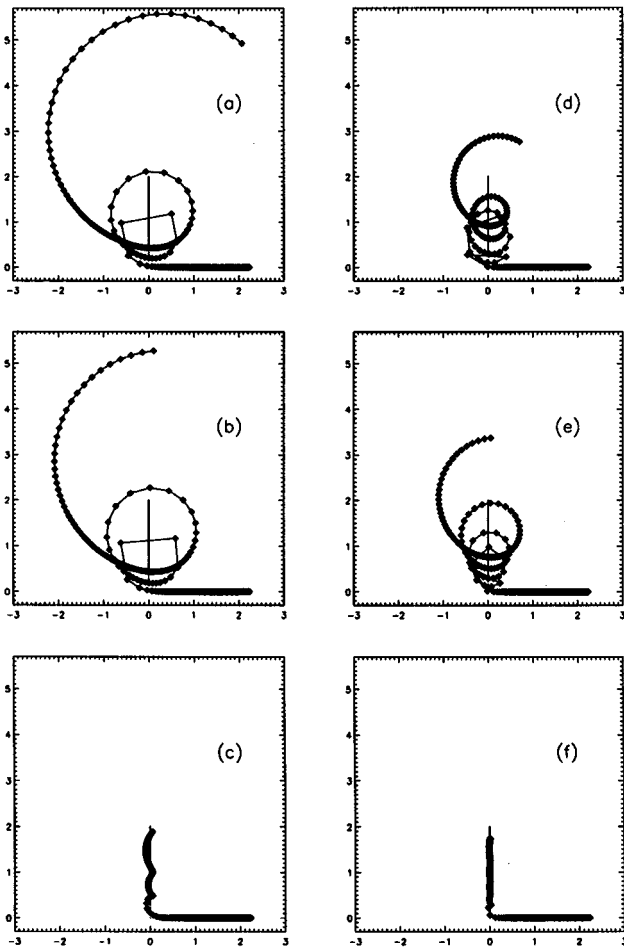


FIG. 4. Images of the real line segment $[-4,4]$ computed using Collins' complex coefficients⁴ and the rotated Padé coefficients: (a) Collins, $N=4$; (b) rotated, $N=4, \alpha=10^\circ$; (c) rotated, $N=4, \alpha=45^\circ$; (d) Collins, $N=7$; (e) rotated, $N=7, \alpha=10^\circ$; (f) rotated, $N=7, \alpha=45^\circ$.

ing branch of the square root and, correspondingly, the treatment of the evanescent part of the spectrum.

Finally, Fig. 6 shows the contour of zero imaginary part of $R_{\alpha,N}(z)$ with $\alpha=0^\circ, 10^\circ, 45^\circ$, and 90° for different values of N . For fixed α , it can be seen (as expected) that $R_{\alpha,N}(z)$ approaches the appropriate branch of the square-root function as N increases.

III. RESULTS

A. Stability

Acousto-elastic waveguides place stringent stability constraints on the square-root approximations involved in parabolic equation propagation models. This is due to complicated spectral behavior which allows modes to have complex horizontal wave numbers.

Such a case is provided by the following layered waveguide example consisting of a fluid layer (100 m thick) overlaying an elastic layer of thickness 900 m. The waveguide structure is bounded above and below by free and rigid surfaces, respectively. The physical parameters of the liquid are chosen as $1500-1.00i$ m/s for the compressional wave speed and 1.00 g/cm^3 for the density. In the elastic layer the com-

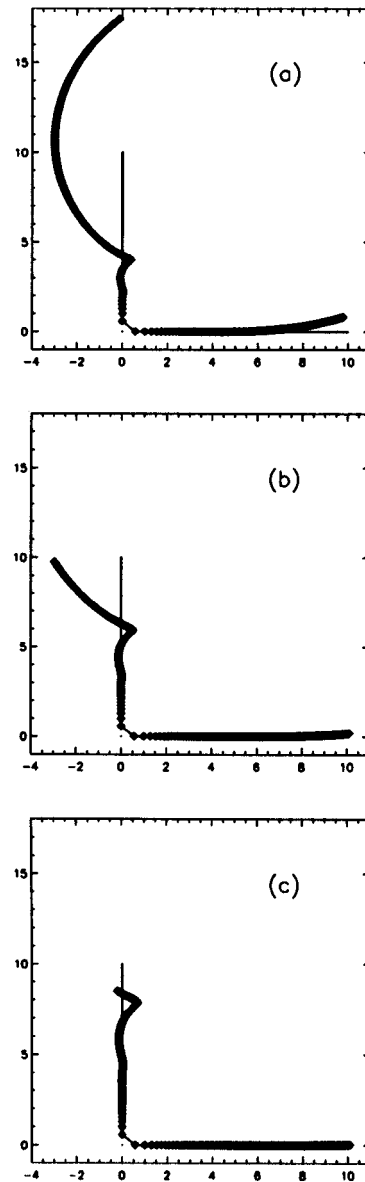


FIG. 5. Images of the real line segment $[-100,100]$ computed using the rotated Padé coefficients, with $\alpha=45^\circ$: (a) $N=8$, (b) $N=12$, (c) $N=16$.

pressional and shear wave speeds are taken as $5500.00-55.43i$ m/s and $2400.00-6.33i$ m/s, respectively, and the density is assumed to be 2.6 g/cm^3 . Note that complex wave speeds are used to model lossy media. Also, as demonstrated below, this particular choice of material parameters, though unrealistic from an underwater acoustics point of view, leads to complex eigenvalues and allows the application of the rotated Padé approximation to be tested thoroughly.

The spectral components of this waveguide can be represented as an infinite set of modes with corresponding complex values of horizontal wave numbers. With reference to Sec. I, the eigenvalues associated with these modes lie clustered about the real line in the complex z plane. Those eigenvalues with positive real parts correspond to propagating modes in the waveguide and thus also have a positive imaginary part (i.e., satisfy the radiation condition). Conversely those modes with negative real parts correspond to evanes-

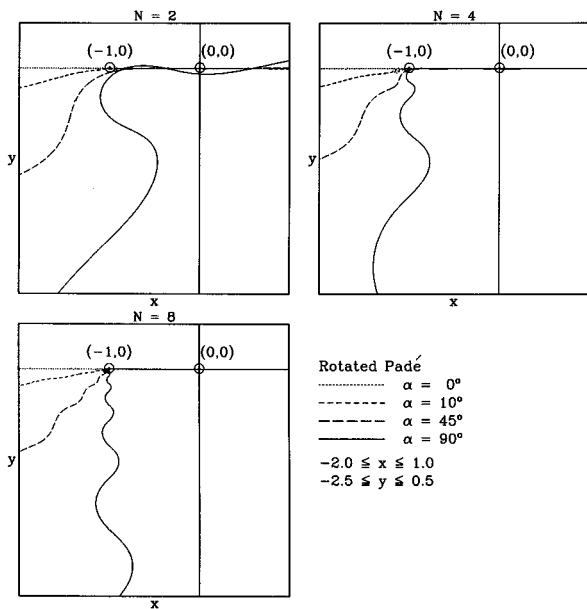


FIG. 6. Contours of $\Im(R_{\alpha,N}(z))=0$. The contours of $\Im(R_{\alpha,N}(z))=0$, $z=x+iy$, are plotted for $\alpha=0^\circ, 10^\circ, 45^\circ, 90^\circ$ and $N=2, 4, 8$.

cent or nonpropagating modes and can have either positive or negative imaginary parts.

It is the evanescent modes which pose problems for the square-root approximation. That is, propagation is cast in terms of horizontal wave numbers which are defined by the relationship $\sqrt{1+z_k}$, where $k=1, \dots, \infty$ is the mode index and z_k is the k th eigenvalue. In order for stable propagation to occur, all the horizontal wave numbers must lie in the upper half-plane. Of course, integral transform solutions to the propagation problem allow one to choose exactly the proper behavior for the square root, whereas numerical solution techniques like the PE are only approximate. Nonetheless, it is possible to choose rotated complex Padé square-root coefficients to closely represent the exact square-root behavior.

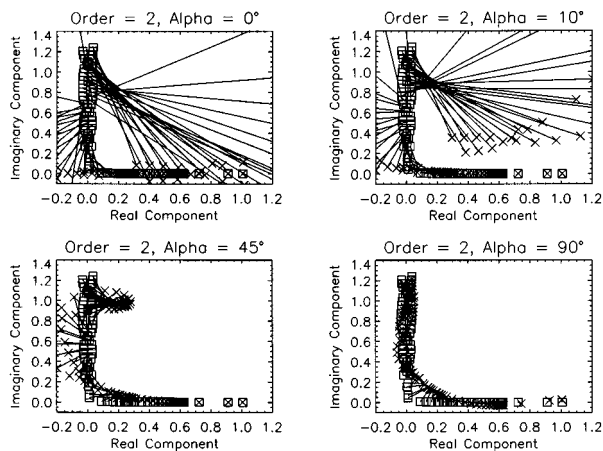


FIG. 7. A comparison of the exact modal wave-number locations with those locations obtained using a rotated two term square-root approximation. Results are given for $\alpha=0^\circ, 10^\circ, 45^\circ, 90^\circ$. The exact locations are marked by boxes and the approximate locations are marked by crosses. To show the displacement, each pair of corresponding points is connected by a straight line.

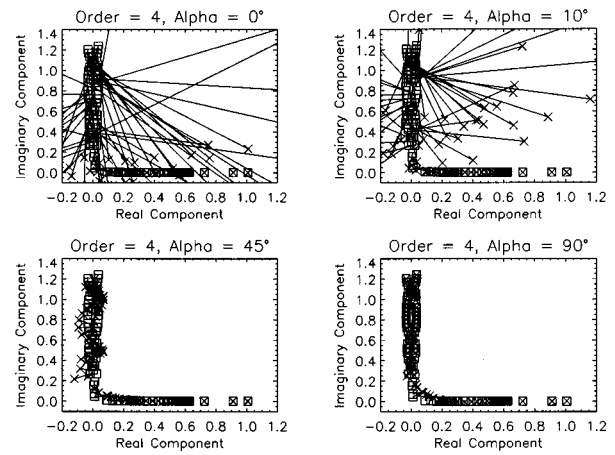


FIG. 8. A comparison of the exact modal wave-number locations with those locations obtained using a rotated four term square-root approximation. Results are given for $\alpha=0^\circ, 10^\circ, 45^\circ, 90^\circ$. The exact locations are marked by boxes and the approximate locations are marked by crosses. To show the displacement, each pair of corresponding points is connected by a straight line.

Figures 7, 8, and 9 demonstrate the performance of the rotated Padé square-root approximation, as a function of rotation angle when applied to the waveguide problem described above. Here, the square root maps the eigenvalues in z space to horizontal wave numbers in k space; thus the eigenvalues clustered about the negative z axis under the mapping will lie clustered about the positive imaginary axis in k space. In each figure, the positions of the exact modal wave-number locations (boxes) and the approximate locations obtained with the corresponding rotated square-root approximation (crosses) are joined together by straight lines. Clearly, as the angle of the rotated square-root approximation is increased, the ability of the Padé approximation to accurately represent the nonpropagating mode wave numbers is much improved. Indeed, for a rotation angle equal to 90° , an eighth-order Padé approximation appears to be nearly perfect except for a few modes close to the origin. This example demonstrates that the rotated Padé square-root approximation should extend the applicability of PE modeling to those cases such as higher-order rough surface scattering for which near-field (evanescent mode) effects are important.

B. Performance of PE using the rotated branch cut approximation

In the previous section, we discussed the rotated branch cut rational square-root approximation in the context of stable representations of the complex eigenvalues in a waveguide. In this section, the properties of the rotated branch cut rational approximation with respect to PE propagation modeling are established. The aim is to verify that suitable values of N and α can be defined for which the propagation is reliably modeled. For this purpose, numerical experiments were conducted using the model environment defined by the ASA wedge-shaped waveguide benchmark for range-dependent propagation problems¹³ modified to include elasticity in the ocean bottom. The main features of this environ-

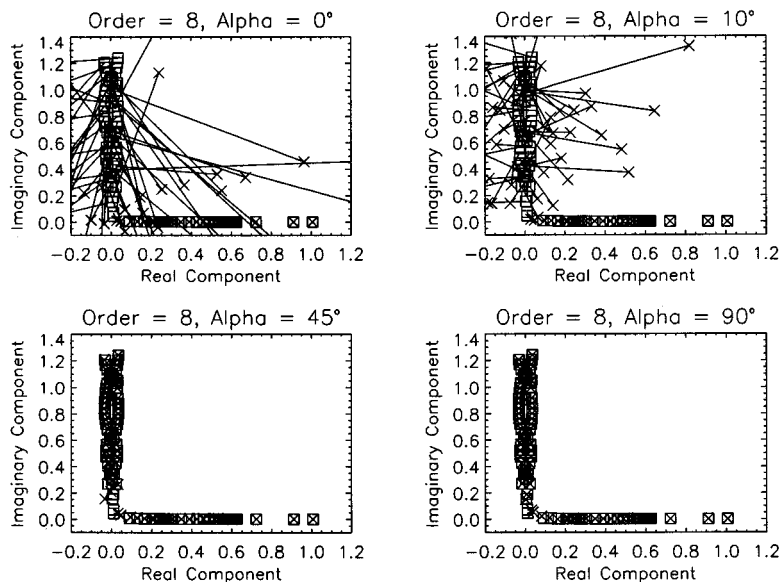


FIG. 9. A comparison of the exact modal wave-number locations with those locations obtained using a rotated eight term square-root approximation. Results are given for $\alpha=0^\circ, 10^\circ, 45^\circ, 90^\circ$. The exact locations are marked by boxes and the approximate locations are marked by crosses. To show the displacement, each pair of corresponding points is connected by a straight line.

ment are: (i) an initial channel depth of 200.0 m, sloping to zero depth at 4.0-km range, (ii) a homogeneous water layer with sound speed 1500.0 m/s and density 1.0 g/cm^3 , and (iii) a bottom with constant compressional and shear speeds of 1700.0 and 300.0 m/s, respectively. We have also assumed that both compressional and shear attenuations in the ocean bottom are given by $0.5 \text{ dB}/\lambda$. An elastic PE algorithm^{14,15} was used to compute the acoustic field at a receiver depth of 30.0 m due to a 25.0-Hz source at 100.0-m depth for ranges from 0.0 to 4.0 km. Step sizes of 0.5 m for depth and 5.0 m for range were employed in the PE calculations.

Propagation loss curves were computed using the rotated branch cut rational approximation coefficients for orders $N=2, 4, 8$, and for angles of $\alpha=0.0^\circ, 10.0^\circ, 45.0^\circ, 90.0^\circ$. The results are shown in Figs. 10–12. In Fig. 10, we show

four curves all obtained using $N=2$ but with different sets of square-root coefficients. The solid curve was obtained using Collins' complex coefficients⁴ and is used as the reference solution. The dotted curve was obtained with $\alpha=0.0^\circ$ (equivalent to real Padé coefficients) and clearly demonstrates the numerical instability⁶ that can occur in elastic PE calculations when the coefficients are chosen inappropriately. The dashed curve was obtained with $\alpha=10.0^\circ$ and essentially overlays the reference solution. Thus the rotated coefficients allow for stable propagation. The dot-dash curve was obtained with $\alpha=45^\circ$ and indicates a substantial difference from the reference solution. The reason for this discrepancy is that rotation of the branch cut to higher angles implies higher-order coefficients are necessary for accurate representations of the square root. This behavior, first dem-

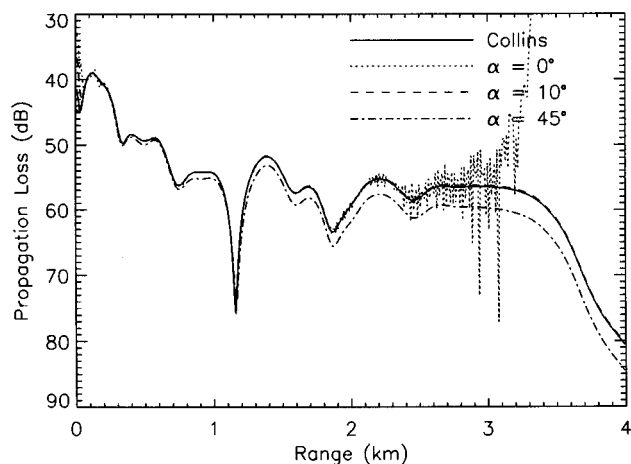


FIG. 10. Propagation loss curves computed for the ASA benchmark problem by an elastic PE algorithm using the order $N=2$ rotated branch cut rational approximation, for various angles of rotation α .

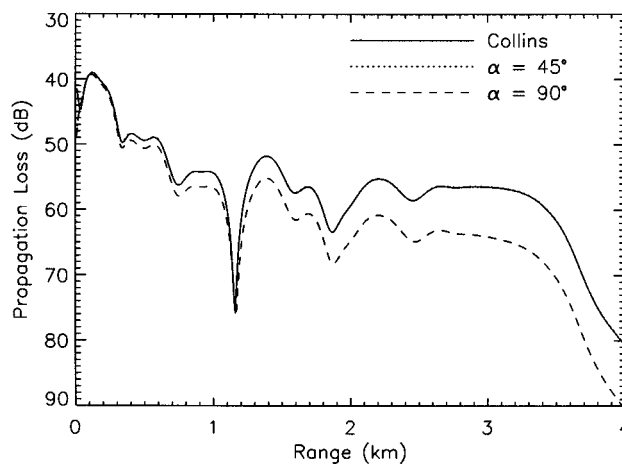


FIG. 11. Propagation loss curves computed for the ASA benchmark problem by an elastic PE algorithm using the order $N=4$ rotated branch cut rational approximation, for various angles of rotation α .

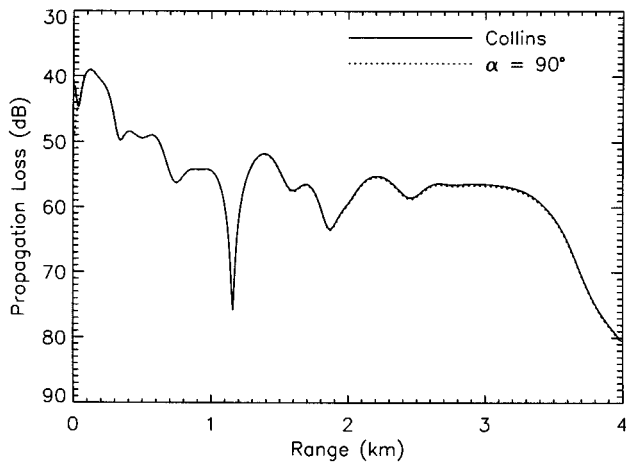


FIG. 12. Propagation loss curves computed for the ASA benchmark problem by an elastic PE algorithm using the order $N=8$ rotated branch cut rational approximation, for angle of rotation $\alpha=90^\circ$.

onstrated in Figs. 2 and 3, is confirmed by the results shown in Figs. 11 and 12. In Fig. 11 we compare the results for $N=4$ and $\alpha=45^\circ$ (dotted curve) and $\alpha=90.0^\circ$ (dashed curve) with the reference solution (solid curve). Here we see that increasing the order of the approximation has brought the results for $\alpha=45.0^\circ$ into line with the reference but those for $\alpha=90.0^\circ$ are still in error. As shown in Fig. 12, by increasing the order to $N=8$ we can bring the results for $\alpha=90.0^\circ$ into line with the reference as well. Implicit to the results shown in Fig. 12 is the fact that for $N=8$, all branch rotation angles to 90.0° produce accurate results for this problem.

The results shown in this section demonstrate that for small angles of rotation α , low-order rotated branch cut rational approximations are accurate for elastic PE propagation modeling. For many acousto-elastic applications involving thick elastic layers for which the modal complex eigenvalues lie below but close to the negative real axis, such low-order approximations will likely be sufficient to provide the required accuracy and stability during the computations. Conversely, applications which involve a thin elastic layer (e.g., an ice cover) can have modal eigenvalues that are located farther from the negative real axis¹⁶ and, hence, require larger angles of rotation (i.e., in order to place these eigenvalues in the upper half-plane in horizontal wave-number space). Consequently, higher-order coefficients will likely be required in such cases to maintain accuracy and stability.

IV. CONCLUSIONS

In this article, we have derived rational approximations to $\sqrt{1+z}$ which have branch cuts in the lower half-plane. Exact expressions are given for the coefficients, in contrast to the approximations given in Ref. 4 where the computation of the coefficients becomes more ill-conditioned as the order of

the approximation increases. For waveguide problems, it is demonstrated that increasing the order of the approximation results in a better representation of the evanescent part of the mode spectrum. Propagation loss curves for the ASA wedge waveguide, modified to include elasticity in the ocean bottom, were computed using various angles of branch cut rotation and orders of coefficients. The results demonstrate that accurate and stable elastic PE propagation modeling is achieved using appropriate sets of rotated coefficients. Clearly, the complex Padé coefficients based on the procedures outlined in this article not only provide a simple and straightforward alternative to the coefficients obtained previously by solving of a set of nonlinear equations, but also potentially extend the applicability of the PE method to problems involving near-field calculations.

- ¹F. D. Tappert, "The parabolic approximation method," in *Wave Propagation and Underwater Acoustics*, edited by J. Keller and J. Papadakis (Springer-Verlag, New York, 1977), Vol. 70, pp. 224–287.
- ²M. D. Collins and E. K. Westwood, "A higher-order energy-conserving parabolic equation for range-dependent ocean depth, sound speed, and density," *J. Acoust. Soc. Am.* **89**, 1068–1075 (1991).
- ³D. J. Thomson and N. R. Chapman, "A wide-angle split-step algorithm for the parabolic equation," *J. Acoust. Soc. Am.* **74**, 1848–1854 (1983).
- ⁴M. D. Collins, "Higher-order Padé approximations for accurate and stable elastic parabolic equations with application to interface wave propagation," *J. Acoust. Soc. Am.* **89**, 1050–1057 (1991).
- ⁵M. D. Collins and R. B. Evans, "A two-way parabolic equation for acoustic backscattering in the ocean," *J. Acoust. Soc. Am.* **91**, 1357–1368 (1992).
- ⁶B. T. R. Wetton and G. H. Brooke, "One-way wave equation for seismo-acoustic propagation in elastic waveguides," *J. Acoust. Soc. Am.* **87**, 624–632 (1990).
- ⁷C. A. Zala, "Complex square root coefficients for DREP PE software," DREP Contractors Report Series **94-125** (1994).
- ⁸F. B. Jensen, W. A. Kuperman, M. B. Porter, and H. Schmidt, *Computational Ocean Acoustics* (American Institute of Physics, Woodbury, NY, 1993).
- ⁹R. R. Greene, "The rational approximation to the wave equation with bottom interaction," *J. Acoust. Soc. Am.* **76**, 1764–1773 (1984).
- ¹⁰A. Bamberger, B. Engquist, L. Halpern, and P. Joly, "Higher order paraxial wave equation approximations in heterogeneous media," *SIAM (Soc. Ind. Appl. Math.) J. Appl. Math.* **48**, 129–154 (1988).
- ¹¹M. D. Collins, "A two-way parabolic equation for elastic media," *J. Acoust. Soc. Am.* **93**, 1815–1825 (1993).
- ¹²F. A. Milinazzo (unpublished observations, 1994).
- ¹³F. B. Jensen and C. M. Ferla, "Numerical solutions of range-dependent bench-mark problems in ocean acoustics," *J. Acoust. Soc. Am.* **87**, 1499–1510 (1990).
- ¹⁴G. H. Brooke, "Elastic PE: A parabolic approximation for propagation modelling of shear wave effects in sediment layers," in *Shear Waves in Marine Sediments*, edited by J. M. Hovem, M. D. Richardson, and R. D. Stoll (Kluwer, Dordrecht, The Netherlands, 1991), pp. 487–494.
- ¹⁵G. H. Brooke and D. J. Thomson, "A single-scatter formalism for improving PE calculations in range-dependent media," in *Proceedings of the Second Parabolic Equations Workshop*, edited by S. Chin-Bing, D. King, J. Davis, and R. Evans (Naval Res. Lab, Washington, DC, 1993), pp. 126–144.
- ¹⁶B. T. R. Wetton and G. H. Brooke, "One-way seismo-acoustic propagation in elastic waveguides with range-dependent material parameters," in *Computational Acoustics*, edited by D. Lee, A. Cakmak, and R. Vichnevetsky (Elsevier Science, North-Holland, Amsterdam, 1990), Vol. 3.

Scattering from an elastic shell and a rough fluid–elastic interface: Theory

Garner C. Bishop and Judy Smith

Naval Undersea Warfare Center Division Newport, Newport, Rhode Island 02840

(Received 13 November 1995; accepted for publication 13 April 1996)

A null-field T -matrix formalism is developed for scattering a pressure wave from a stationary elastic shell immersed in a homogeneous and isotropic fluid half-space and in proximity to a rough fluid–elastic interface. Helmholtz–Kirchhoff integral representations of the various scattered pressure and displacement fields are constructed. The surface fields are required to satisfy the elastic tensor boundary conditions and the scattered fields are required to satisfy the extended boundary condition. Spherical basis functions are used to construct a free-field T -matrix for the elastic shell and rectangular vector basis functions are used to construct a representation of the free-field T -matrix for the rough fluid–elastic interface. The free-field T -matrices are introduced into the Helmholtz–Kirchhoff and the null-field equations for the shell-interface system and a general system of equations for the spectral amplitudes of the various fields is obtained. The general system of equations is specialized to scattering from periodic surface roughness and an exact solution for the scattered pressure field in the fluid is obtained. Then the general system of equations is specialized to scattering from small-amplitude arbitrary roughness profiles and a perturbative solution is obtained. It is shown that the formalism contains multiple scattering effects on the rough surface and between the rough surface and the shell. [S0001-4966(97)02602-7]

PACS numbers: 43.30.Hw [JHM]

INTRODUCTION

This is the first of two papers in which scattering from an elastic shell in proximity to a rough fluid–elastic interface is investigated. In this paper, a null-field T -matrix formalism is developed and in the second paper a variety of numerical results are shown. The formalism is similar to that used by Kristensson and Strom^{1,2} to calculate acoustic scattering from a buried inhomogeneity and to that developed by Hackmann and Sammelmann^{3–6} to calculate acoustic scattering from an elastic shell in a waveguide. In the former work, the elastic properties of the inhomogeneity and of the infinite solid were not considered, the elastic tensor boundary conditions were not applied, and although the formalism was applicable for a rough interface, numerical results for a rough interface were not presented. In the latter work, it was demonstrated that multiple scattering between an elastic shell and a planar waveguide boundary may result in super-resonant phenomena and that symmetry breaking produced by the waveguide boundaries partially splits degenerate free-field resonances of the shell. However, the effects of surface roughness were not considered. The formalism developed in this paper is an extension of this previous work and includes mode conversion at fluid-solid interfaces and multiple scattering on the rough surface and between the rough surface and the shell.

The problem admits two points of view: It may be viewed as scattering from a rough surface in the presence of a spherical shell, i.e., an inhomogeneity, in which case the free-field T -matrix of the spherical shell modifies the free-field T -matrix of the rough surface. From this point of view, it is more convenient to consider Weyl rectangular spectral amplitudes of the scattered field than spherical spectral am-

plitudes. Alternatively, it may be viewed as scattering from a spherical shell in the presence of a rough surface, in which case, the free-field T -matrix of the rough surface modifies the free-field T -matrix of spherical shell and it is more convenient to consider the spherical spectral amplitudes of the scattered field than the Weyl rectangular spectral amplitudes. The former point of view is similar to that of Kristensson and Strom while the latter is similar to that of Hackmann and Sammelmann. Since the free-field T -matrix for the shell relates the spherical components of the scattered field to the spherical components of the incident field, while the free-field T -matrix for the rough surface relates the rectangular components of the scattered field to the rectangular components of the incident field, depending on the point of view, it is necessary to project the free-field T -matrix of the shell onto a rectangular basis or to project the free-field T -matrix for the rough surface onto a spherical basis. These transformations complicate both the analytical and numerical solution to the scattering problem: If the second point of view is adopted for the problem being considered in this paper, it is necessary to solve an integral equation for the spectral amplitudes of the fields on the rough surface even in zeroth order perturbation theory, while if the first point of view is adopted, it is necessary to solve an infinite system of linear equations to determine the coupling of the free-field T -matrix of the spherical shell at each order of perturbation theory. In this paper, the first point of view is adopted and the construction of the T -matrix for the scattered pressure field in the fluid is described. A general system of equations is developed for arbitrary surface roughness. Then two special cases are considered: First the equations are specialized to scattering from periodic surface roughness and an exact

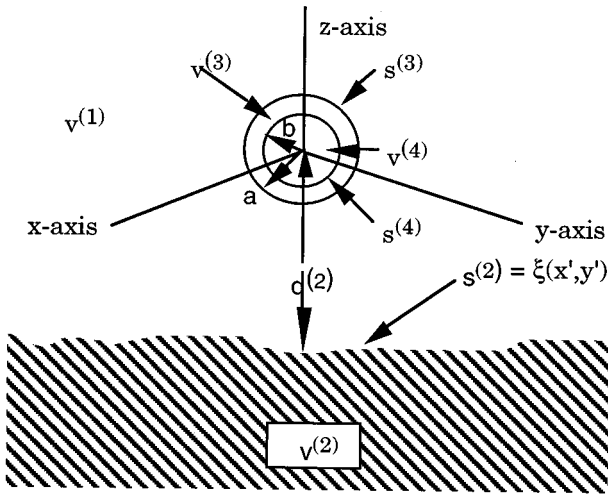


FIG. 1. Shell-rough interface geometry.

solution is obtained for the scattered pressure field in the fluid. Then it is assumed that the maximum height of the surface roughness is small and a perturbative solution is developed for an arbitrary roughness profile.

The various volumes and surfaces are denoted in the following manner: The volume $v^{(1)}$ is exterior to the shell and above the rough surface; $v^{(2)}$ is the volume within the elastic solid; $v^{(3)}$ is the volume in the annular region bounded by the inner and outer surfaces of the shell; and $v^{(4)}$ is the volume bounded by the inner surface of the shell. The rough surface is $s^{(2)}$ and $s^{(3)}$ and $s^{(4)}$ are, respectively, the outer and inner surfaces of the shell. These volumes and surfaces are shown in Fig. 1. The origin of coordinates is at the center of the shell with the z axis directed upward. The outer and inner radii of the shell are, respectively, a and b . The mean plane of the rough surface is located a distance $d^{(2)}$ below the center of the shell so that the surface of the elastic solid is given by $z' = -d^{(2)} + \xi^{(2)}(x', y')$ where $\xi^{(2)}(x', y')$ is the roughness profile function. It is assumed that $\xi^{(2)}(x', y')$ is homogeneous, nonisotropic, and has zero mean, and that the maximum amplitudes of the roughness in the x and y directions are, respectively, h_x and h_y . It is assumed that all fluid and solid media are homogeneous and isotropic. The Lamé parameters in the n th volume are $\lambda^{(n)}$ and $\mu^{(n)}$ (for elastic media), the mass density is $\rho^{(n)}$, and the wave speeds for p and s waves are, respectively, $c_p^{(n)2} = (\lambda^{(n)} + 2\mu^{(n)})/\rho^{(n)}$ and $c_s^{(n)2} = \mu^{(n)}/\rho^{(n)}$. It is assumed that a stationary time harmonic source $p^{(i)}(\mathbf{r})e^{-i\omega t}$ is present in the volume $v^{(1)}$ and all fields are time harmonic. The wave vectors for p and s waves in the n th medium are, respectively, $\mathbf{k}_p^{(n)}$ with $k_p^{(n)} = \omega/c_p^{(n)}$ and $\mathbf{k}_s^{(n)}$ with $k_s^{(n)} = \omega/c_s^{(n)}$. In the following the factor $e^{-i\omega t}$ and explicit dependence on time are omitted.

The unknown fields are the scattered pressure fields $p^{(1,s)}(\mathbf{r})$ exterior to the shell and above the rough fluid-elastic surface and $p^{(4,s)}(\mathbf{r})$ interior to the shell and the displacement fields $\mathbf{u}^{(2,s)}(\mathbf{r})$ within the elastic solid and $\mathbf{u}^{(3,s)}(\mathbf{r})$ within the elastic shell. The unknown surface fields are the pressure field $p_+^{(2)}(\mathbf{r}')$ and the displacement field $\mathbf{u}^{(2)}(\mathbf{r}')$ on the surface of the rough elastic solid, and the pressure fields

$p_+^{(3)}(\mathbf{r}')$ and $p_-^{(4)}(\mathbf{r}')$ and displacement fields $\mathbf{u}^{(3)}(\mathbf{r}')$ and $\mathbf{u}^{(4)}(\mathbf{r}')$ on, respectively, the outer and inner surfaces of the elastic shell. The subscripts “plus” and “minus” are used, respectively, to indicate that a surface field is evaluated in the limit in which \mathbf{r}' approaches the surface from the volume above and below the surface.

On fluid-elastic interfaces, the normal component of the particle displacement and traction are continuous and the tangential component of the traction vanishes: The equations that follow from these boundary conditions are given by

$$\hat{n}^{(n)}(\mathbf{r}') \cdot \mathbf{u}^{(n)}(\mathbf{r}') = \hat{n}^{(n)}(\mathbf{r}') \cdot \nabla' p^{(n)}(\mathbf{r}') / \lambda^{(m)} k_p^{(m)2}, \quad (1)$$

$$\hat{n}^{(n)}(\mathbf{r}') \cdot [\hat{n}^{(n)}(\mathbf{r}') \cdot \boldsymbol{\tau}^{(n)}(\mathbf{r}')] = -p_+^{(n)}(\mathbf{r}'), \quad (2)$$

and

$$\hat{n}^{(n)}(\mathbf{r}') \times [\hat{n}^{(n)}(\mathbf{r}') \cdot \boldsymbol{\tau}^{(n)}(\mathbf{r}')] = 0. \quad (3)$$

In Eqs. (1)–(3), $(m, n) \in [(1, 2), (1, 3), (4, 4)]$, $\mathbf{u}^{(n)}(\mathbf{r}') \in [\mathbf{u}^{(2)}(\mathbf{r}'), \mathbf{u}^{(3)}(\mathbf{r}'), \mathbf{u}^{(4)}(\mathbf{r}')]$, $p^{(n)}(\mathbf{r}') \in [p_+^{(2)}(\mathbf{r}'), p_+^{(3)}(\mathbf{r}'), p_-^{(4)}(\mathbf{r}')]$, and $\lambda^{(m)}$ and $k_p^{(m)}$ are, respectively, the Lamé parameter and wave number of the fluid medium bounding the interface. The quantity $\boldsymbol{\tau}^{(n)}(\mathbf{r}') \in [\boldsymbol{\tau}^{(2)}(\mathbf{r}'), \boldsymbol{\tau}^{(3)}(\mathbf{r}'), \boldsymbol{\tau}^{(4)}(\mathbf{r}')]$, where $\boldsymbol{\tau}^{(2)}(\mathbf{r}')$ is the stress tensor on the surface of the elastic solid and $\boldsymbol{\tau}^{(3)}(\mathbf{r}')$ and $\boldsymbol{\tau}^{(4)}(\mathbf{r}')$ are, respectively, the stress tensors on outer and inner surfaces of the elastic shell. The subscripts “plus” and “minus” are used to denote the same limiting process used to evaluate the surface pressure and displacement fields. The unit vector $\hat{n}^{(2)}(\mathbf{r}')$ is normal to the rough surface, has its z component directed in the positive z direction, and is given by

$$\hat{n}^{(2)}(\mathbf{r}') = \frac{\hat{z}' - \partial_{x'} \xi^{(2)}(x', y') \hat{x}' - \partial_{y'} \xi^{(2)}(x', y') \hat{y}'}{\sqrt{1 + [\partial_{x'} \xi^{(2)}(x', y')]^2 + [\partial_{y'} \xi^{(2)}(x', y')]^2}}. \quad (4)$$

The unit vectors $\hat{n}^{(3)}(\mathbf{r}')$ and $\hat{n}^{(4)}(\mathbf{r}')$ are normal, respectively, to the outer and inner surfaces of the shell and are directed radially outward.

The scattered fields are forced to satisfy the extended boundary condition or null-field hypothesis: In regions exterior to $v^{(1)}$, the total pressure field $p^{(1)}(\mathbf{r})$ exactly cancels the incident field and since there are no other sources, the fields $p^{(4,s)}(\mathbf{r})$, $\mathbf{u}^{(2,s)}(\mathbf{r})$, and $\mathbf{u}^{(3,s)}(\mathbf{r})$ vanish in volumes exterior to those in which these fields are defined.

I. HELMHOLTZ-KIRCHHOFF INTEGRAL REPRESENTATION OF FIELDS

The Helmholtz-Kirchhoff integral equation representation of the scattered fields and the equations that follow from the null-field hypothesis are given by

$$\begin{aligned}
& \int_{s^{(2)}} ds'{}^{(2)} [p_+^{(2)}(\mathbf{r}') \hat{n}^{(2)}(\mathbf{r}') \cdot \nabla' g_0(\mathbf{r}', \mathbf{r}; \mathbf{k}_p^{(1)}) \\
& - \lambda^{(1)} k_p^{(1)2} g_0(\mathbf{r}', \mathbf{r}; \mathbf{k}_p^{(1)}) \hat{n}^{(2)}(\mathbf{r}') \cdot \mathbf{u}_-^{(2)}(\mathbf{r}')] \\
& + \int_{s^{(3)}} ds'{}^{(3)} [p_+^{(3)}(\mathbf{r}') \hat{n}^{(3)}(\mathbf{r}') \cdot \nabla' g_0(\mathbf{r}', \mathbf{r}; \mathbf{k}_p^{(1)}) \\
& - \lambda^{(1)} k_p^{(1)2} g_0(\mathbf{r}', \mathbf{r}; \mathbf{k}_p^{(1)}) \hat{n}^{(3)}(\mathbf{r}') \cdot \mathbf{u}_-^{(3)}(\mathbf{r}')] \\
& = \begin{cases} p^{(1s)}(\mathbf{r}) = p^{(1)}(\mathbf{r}) - p^{(i)}(\mathbf{r}) & (r \in v^{(1)}) \\ -p^{(i)}(\mathbf{r}) & (r \notin v^{(1)}) \end{cases}, \quad (5)
\end{aligned}$$

$$\begin{aligned}
& \int_{s^{(2)}} ds'{}^{(2)} \{-p_+^{(2)}(\mathbf{r}') \hat{n}^{(2)}(\mathbf{r}') \cdot \mathbf{G}_0(\mathbf{r}', \mathbf{r}; \mathbf{k}_p^{(2)}, \mathbf{k}_s^{(2)}) \\
& - \mathbf{u}_-^{(2)}(\mathbf{r}') \cdot [\hat{n}^{(2)}(\mathbf{r}') \cdot \Sigma_0(\mathbf{r}', \mathbf{r}; \mathbf{k}_p^{(2)}, \mathbf{k}_s^{(2)})]\} \\
& = \begin{cases} \mathbf{u}^{(2s)}(\mathbf{r}) & (r \in v^{(2)}) \\ 0 & (r \notin v^{(2)}) \end{cases}, \quad (6)
\end{aligned}$$

$$\begin{aligned}
& \int_{s^{(3)}} ds'{}^{(3)} \{-p_+^{(3)}(\mathbf{r}') \hat{n}^{(3)}(\mathbf{r}') \cdot \mathbf{G}_0(\mathbf{r}', \mathbf{r}; \mathbf{k}_p^{(3)}, \mathbf{k}_s^{(3)}) \\
& - \mathbf{u}_-^{(3)}(\mathbf{r}') \cdot [\hat{n}^{(3)}(\mathbf{r}') \cdot \Sigma_0(\mathbf{r}', \mathbf{r}; \mathbf{k}_p^{(3)}, \mathbf{k}_s^{(3)})]\} \\
& + \int_{s^{(4)}} ds'{}^{(4)} \{p_-^{(4)}(\mathbf{r}') \hat{n}^{(4)}(\mathbf{r}') \cdot \mathbf{G}_0(\mathbf{r}', \mathbf{r}; \mathbf{k}_p^{(3)}, \mathbf{k}_s^{(3)}) \\
& + \mathbf{u}_+^{(4)}(\mathbf{r}') \cdot [\hat{n}^{(4)}(\mathbf{r}') \cdot \Sigma_0(\mathbf{r}', \mathbf{r}; \mathbf{k}_p^{(3)}, \mathbf{k}_s^{(3)})]\} \\
& = \begin{cases} \mathbf{u}^{(3s)}(\mathbf{r}) & (r \in v^{(3)}) \\ 0 & (r \notin v^{(3)}) \end{cases}, \quad (7)
\end{aligned}$$

and

$$\begin{aligned}
& \int_{s^{(4)}} ds'{}^{(4)} [-p_-^{(4)}(\mathbf{r}') \hat{n}^{(4)}(\mathbf{r}') \cdot \nabla' g_0(\mathbf{r}', \mathbf{r}; \mathbf{k}_p^{(4)}) \\
& + \lambda^{(4)} k_p^{(4)2} g_0(\mathbf{r}', \mathbf{r}; \mathbf{k}_p^{(4)}) \hat{n}^{(4)}(\mathbf{r}') \cdot \mathbf{u}_+^{(4)}(\mathbf{r}')] \\
& = \begin{cases} p^{(4s)}(\mathbf{r}) & (r \in v^{(4)}) \\ 0 & (r \notin v^{(4)}) \end{cases}. \quad (8)
\end{aligned}$$

When the Helmholtz–Kirchhoff integral is used to represent a field, the unit vector normal to the surface that bounds the scattering volume is directed outward. Since the unit vectors defined here are directed into the scattering volume, minus signs are included in Eq. (5) in the integrals over the surfaces of the elastic solid and the shell. The pressure field $p^{(1s)}(\mathbf{r}) = p^{(1)}(\mathbf{r}) - p^{(i)}(\mathbf{r})$ is the scattered pressure field in the fluid volume and the vectors $\mathbf{r} = x\hat{x} + y\hat{y} + z\hat{z}$ and $\mathbf{r}' = x'\hat{x}' + y'\hat{y}' + z'\hat{z}'$ are, respectively, radius vectors to a field point and to a point on a scattering surface. The quantities $ds'{}^{(3)}$ and $ds'{}^{(4)}$ are, respectively, area elements on the outer and inner surfaces of the shell and $ds'{}^{(2)}$ is an area element on the rough surface and is given by

$$\begin{aligned}
ds'{}^{(2)} &= dx'{}^{(2)} dy'{}^{(2)} \\
&\times \sqrt{1 + [\partial_{x'} \xi^{(2)}(x', y')]^2 + [\partial_{y'} \xi^{(2)}(x', y')]^2}. \quad (9)
\end{aligned}$$

The quantity $g_0(\mathbf{r}', \mathbf{r}; \mathbf{k}_p^{(n)})$ is the scalar Green function for a point source in an unbounded region and the quantities

$\mathbf{G}_0(\mathbf{r}', \mathbf{r}; \mathbf{k}_p^{(n)}, \mathbf{k}_s^{(n)})$ and $\Sigma_0(\mathbf{r}', \mathbf{r}; \mathbf{k}_p^{(n)}, \mathbf{k}_s^{(n)})$ are, respectively, the Green displacement dyadic and Green stress triadic for an unbounded region. Representations of these functions as well as the surface and scattered fields that appear in Eqs. (5)–(8) are given in Sec. III.

Since the solution for the scattered pressure field in the fluid is the quantity of interest, and since the scattered displacement fields in the infinite elastic solid and in the annular region of the shell, and the pressure field interior to the shell are not necessary for the solution, these fields are not considered further. However, when these fields are required to satisfy the null-field condition, equations for fields on the surface of the rough elastic solid and on the surfaces of the elastic shell are obtained. These equations are necessary for a solution to the system of surface fields and need to be considered.

II. BASIS FUNCTIONS

Fundamental to the T -matrix formalism is the representation of the unknown scattered and surface fields, and scalar and tensor Green functions in terms of appropriate scalar and vector basis functions. When scattering from an elastic shell, the most appropriate basis functions are spherical basis functions. However, when scattering from nonisotropic surface roughness, rectangular basis functions are appropriate. The properties of spherical scalar and vector basis functions are well known.^{1,2,3,5,7–12} However, a variety of definitions and normalizations are used for these functions and the properties of rectangular scalar and vector basis functions are less well known. Therefore, in the following these basis functions are defined and their properties as well as some useful transformations between the two basis functions are described.

A. Spherical basis functions

The spherical scalar basis functions are given by

$$\psi_{\lambda\sigma}(\mathbf{r}; k) = Y_\lambda(\theta, \phi) z_\nu^{(\sigma)}(kr), \quad (10a)$$

where

$$z_\nu^{(\sigma)}(kr) = \begin{cases} j_\nu(kr), & \sigma = 1, \\ h_\nu^{(1)}(kr), & \sigma = 2. \end{cases} \quad (10b)$$

The functions $j_\nu(kr)$ and $h_\nu^{(1)}(kr)$ are, respectively, the spherical Bessel and Hankel functions of the first kind. The functions $Y_\lambda(\theta, \phi)$ are orthonormal real scalar spherical harmonics and are given by¹³

$$\begin{aligned}
Y_\lambda(\theta, \phi) &= \sqrt{\epsilon_\mu \frac{2\nu+1}{4\pi} \frac{(\nu-\mu)!}{(\nu+\mu)!}} P_\nu^\mu(\cos \theta) \\
&\times \begin{cases} \cos \mu\phi, & \lambda = 2, \\ \sin \mu\phi, & \lambda = 1; \mu \neq 0, \end{cases} \quad (11)
\end{aligned}$$

where $P_\nu^\mu(\cos \theta)$ is an associated Legendre polynomial and ϵ_μ is the Neumann factor. The angles θ and ϕ are, respectively, the polar and azimuthal angles of the radius vector and the index $\lambda = (\lambda, \mu, \nu)$ is used to simplify notation with $\lambda = 1, 2, 0 \leq \nu < \infty$, and $0 \leq \mu \leq \nu$. The inner products of scalar spherical harmonics and basis functions are given by

$$\begin{aligned}\langle Y_{\lambda'}(\theta, \phi) | Y_{\lambda}(\theta, \phi) \rangle &= \int d\Omega Y_{\lambda'}(\theta, \phi) Y_{\lambda}(\theta, \phi) \\ &= \delta_{\lambda, \lambda'}\end{aligned}\quad (12a)$$

and

$$\begin{aligned}\langle \psi_{\lambda' \sigma'}(\mathbf{r}; k') | \psi_{\lambda \sigma}(\mathbf{r}; k) \rangle &= \int d\Omega \psi_{\lambda' \sigma'}^*(\mathbf{r}; k') \psi_{\lambda \sigma}(\mathbf{r}; k) \\ &= z_{\nu'}^{(\sigma')*}(k' r) z_{\nu}^{(\sigma)}(k r) \delta_{\lambda, \lambda'},\end{aligned}\quad (12b)$$

where $\int d\Omega = \int_0^{2\pi} d\phi \int_0^{\pi} d\theta \sin \theta$ and an asterisk denotes the complex conjugate.

Preliminary to constructing spherical vector basis functions, it is convenient to define the following vector spherical harmonics:¹⁴

$$\begin{aligned}\mathbf{Y}_{1\lambda}(\theta, \phi) &= \frac{1}{\sqrt{\nu(\nu+1)}} \nabla \times [\mathbf{r} Y_{\lambda}(\theta, \phi)] \\ &= -\hat{r} \times \mathbf{Y}_{2\lambda}(\theta, \phi),\end{aligned}\quad (13a)$$

$$\begin{aligned}\mathbf{Y}_{2\lambda}(\theta, \phi) &= \frac{1}{\sqrt{\nu(\nu+1)}} r \nabla Y_{\lambda}(\theta, \phi) \\ &= \frac{1}{\sqrt{\nu(\nu+1)}} \hat{r} \times \nabla \times [\mathbf{r} Y_{\lambda}(\theta, \phi)] \\ &= \hat{r} \times \mathbf{Y}_{1\lambda}(\theta, \phi),\end{aligned}\quad (13b)$$

and

$$\mathbf{Y}_{3\lambda}(\theta, \phi) = \hat{r} Y_{\lambda}(\theta, \phi). \quad (13c)$$

The normalization of the vector spherical harmonics is chosen so that their inner product is given by

$$\begin{aligned}\langle \mathbf{Y}_{\kappa' \lambda'}(\theta, \phi) | \mathbf{Y}_{\kappa \lambda}(\theta, \phi) \rangle &= \int d\Omega \mathbf{Y}_{\kappa' \lambda'}(\theta, \phi) \cdot \mathbf{Y}_{\kappa \lambda}(\theta, \phi) = \delta_{\kappa, \kappa'} \delta_{\lambda, \lambda'},\end{aligned}\quad (14)$$

where $\kappa, \kappa' = 1, 2, 3$.

Vector spherical basis functions are constructed from the scalar spherical basis functions $\psi_{\lambda \sigma}(\mathbf{r}; k)$ and are given by¹⁵

$$\begin{aligned}\Psi_{1\lambda \sigma}(\mathbf{r}; k_s) &= \frac{1}{\sqrt{\nu(\nu+1)}} \nabla \times [\mathbf{r} \psi_{\lambda \sigma}(\mathbf{r}; k_s)] \\ &= z_{\nu}^{(\sigma)}(k_s r) \mathbf{Y}_{1\lambda}(\theta, \phi),\end{aligned}\quad (15a)$$

$$\Psi_{2\lambda \sigma}(\mathbf{r}; k_s) = \frac{1}{k_s} \nabla \times \Psi_{1\lambda \sigma}(\mathbf{r}; k_s), \quad (15b)$$

and

$$\Psi_{3\lambda \sigma}(\mathbf{r}; k_p) = \left(\frac{k_p}{k_s}\right)^{3/2} \frac{1}{k_p} \nabla \psi_{\lambda \sigma}(\mathbf{r}; k_p). \quad (15c)$$

The inner product of vector spherical basis functions is defined by

$$\begin{aligned}\langle \Psi_{\kappa' \lambda' \sigma'}(\mathbf{r}; k') | \Psi_{\kappa \lambda \sigma}(\mathbf{r}; k) \rangle &= \int d\Omega \Psi_{\kappa' \lambda' \sigma'}^*(\mathbf{r}; k') \cdot \Psi_{\kappa \lambda \sigma}(\mathbf{r}; k).\end{aligned}\quad (16)$$

The inner products of all pairs of vector spherical basis functions are given by

$$\langle \Psi_{1\lambda' \sigma'}(\mathbf{r}; k_s) | \Psi_{1\lambda \sigma}(\mathbf{r}; k_s) \rangle = |z_{\nu}^{(\sigma)}(k_s r)|^2 \delta_{\lambda, \lambda'}, \quad (17a)$$

$$\begin{aligned}\langle \Psi_{2\lambda' \sigma'}(\mathbf{r}; k_s) | \Psi_{2\lambda \sigma}(\mathbf{r}; k_s) \rangle &= \frac{1}{(k_s r)^2} \left\{ \left| \frac{d}{dr} [r z_{\nu}^{(\sigma)}(k_s r)] \right|^2 \right. \\ &\quad \left. + \nu(\nu+1) |z_{\nu}^{(\sigma)}(k_s r)|^2 \right\} \delta_{\lambda, \lambda'},\end{aligned}\quad (17b)$$

$$\begin{aligned}\langle \Psi_{3\lambda' \sigma'}(\mathbf{r}; k_p) | \Psi_{3\lambda \sigma}(\mathbf{r}; k_p) \rangle &= \frac{k_p}{k_s^3} \left\{ \left| \frac{d}{dr} [z_{\nu}^{(\sigma)}(k_p r)] \right|^2 \right. \\ &\quad \left. + \nu(\nu+1) \left| \frac{z_{\nu}^{(\sigma)}(k_p r)}{r} \right|^2 \right\} \delta_{\lambda, \lambda'},\end{aligned}\quad (17c)$$

$$\langle \Psi_{1\lambda' \sigma'}(\mathbf{r}; k_s) | \Psi_{2\lambda \sigma}(\mathbf{r}; k_s) \rangle = \langle \Psi_{1\lambda' \sigma'}(\mathbf{r}; k_s) | \Psi_{3\lambda \sigma}(\mathbf{r}; k_p) \rangle = 0, \quad (17d)$$

and

$$\begin{aligned}\langle \Psi_{2\lambda' \sigma'}(\mathbf{r}; k_s) | \Psi_{3\lambda \sigma}(\mathbf{r}; k_p) \rangle &= \left(\frac{k_p}{k_s}\right)^{3/2} \frac{\sqrt{\nu(\nu+1)}}{k_p k_s} \left\{ \frac{z_{\nu}^{(\sigma)}(k_p r)}{r^2} \frac{d}{dr} [r z_{\nu}^{(\sigma)*}(k_s r)] \right. \\ &\quad \left. + \frac{z_{\nu}^{(\sigma)*}(k_s r)}{r} \frac{d}{dr} [z_{\nu}^{(\sigma)}(k_p r)] \right\} \delta_{\lambda, \lambda'}.\end{aligned}\quad (17e)$$

B. Nonperiodic rectangular basis functions

To calculate scattering from a surface with arbitrary roughness, the most convenient and appropriate scalar basis functions are Weyl plane waves. A Weyl plane wave is a solution to the scalar wave equation in rectangular coordinates and is given by

$$\chi(\mathbf{r}; \mathbf{K}^{(\pm)}) = e^{i\mathbf{K}^{(\pm)} \cdot \mathbf{r}} \quad (18)$$

with

$$\mathbf{K}^{(\pm)} = \mathbf{K}_{\perp} \pm K_z \hat{z}, \quad (19a)$$

$$\mathbf{K}_{\perp} = K_x \hat{x} + K_y \hat{y}, \quad (19b)$$

$$K_z = \sqrt{k^2 - K_{\perp}^2} \Theta(k^2 - K_{\perp}^2) + i \sqrt{K_{\perp}^2 - k^2} \Theta(K_{\perp}^2 - k^2), \quad (19c)$$

and

$$K_{\perp}^2 = K_x^2 + K_y^2, \quad (19d)$$

where $\Theta(K)$ is the Heaviside step function. The inner product of Weyl plane waves is given by

$$\begin{aligned}
& \langle \chi(\mathbf{r}; \mathbf{K}'^{(\pm)}) | \chi(\mathbf{r}; \mathbf{K}^{(\pm)}) \rangle \\
&= \frac{1}{(2\pi)^2} \int_{-\infty}^{\infty} d\mathbf{r}_{\perp} \chi^*(\mathbf{r}; \mathbf{K}'^{(\pm)}) \chi(\mathbf{r}; \mathbf{K}^{(\pm)}) \\
&= \delta(\mathbf{K}_{\perp} - \mathbf{K}'_{\perp}) \begin{cases} 1, & K'_z \text{ real,} \\ \exp(\mp 2|K'_z|z), & K'_z \text{ imag.} \end{cases} \quad (20)
\end{aligned}$$

In Eq. (20), the symbol $\int_{-\infty}^{\infty} d\mathbf{r}_{\perp} = \int_{-\infty}^{\infty} dx \int_{-\infty}^{\infty} dy$. Equations (18)–(20) show that Weyl plane waves include both propagating and evanescent waves and that the propagating waves are orthonormal but the evanescent waves are not.

Rectangular vector basis functions are constructed from the scalar plane waves and are given by

$$\begin{aligned}
\hat{X}_1(\pm \mathbf{r}; \mathbf{K}_s^{(\pm)}) &= \frac{1}{K_t} \nabla \times \hat{z} \chi(\pm \mathbf{r}; \mathbf{K}_s^{(\pm)}) \\
&= \pm i \hat{K}_t \chi(\pm \mathbf{r}; \mathbf{K}_s^{(\pm)}), \quad (21a)
\end{aligned}$$

$$\begin{aligned}
\hat{X}_2(\pm \mathbf{r}; \mathbf{K}_s^{(\pm)}) &= \frac{1}{k_s K_t} \nabla \times \nabla \times \hat{z} \chi(\pm \mathbf{r}; \mathbf{K}_s^{(\pm)}) \\
&= -\hat{K}_s^{(\pm)} \times \hat{K}_t \chi(\pm \mathbf{r}; \mathbf{K}_s^{(\pm)}), \quad (21b)
\end{aligned}$$

and

$$\begin{aligned}
\hat{X}_3(\pm \mathbf{r}; \mathbf{K}_p^{(\pm)}) &= \left(\frac{k_p}{k_s}\right)^{3/2} \frac{1}{k_p} \nabla \chi(\pm \mathbf{r}; \mathbf{K}_p^{(\pm)}) \\
&= \pm i \left(\frac{k_p}{k_s}\right)^{3/2} \hat{K}_p^{(\pm)} \chi(\pm \mathbf{r}; \mathbf{K}_p^{(\pm)}). \quad (21c)
\end{aligned}$$

On the right-hand side of Eqs. (21a)–(21c), the \pm sign in front of the expressions refers to the sign of \mathbf{r} . The vector $\hat{K}_t = \mathbf{K}_s \times \hat{z} / K_t$ with $K_t = |\mathbf{K}_s \times \hat{z}|$ and is the transverse wave vector so that $\mathbf{K}_s \cdot \hat{K}_t = \hat{z} \cdot \mathbf{K}_t = 0$. The normalization is chosen to be consistent with the normalization of the spherical vector basis functions and to provide a simple representation of the Green dyadic when expressed in terms of rectangular vector basis functions. The inner product of rectangular vector basis functions is defined by

$$\begin{aligned}
& \langle \hat{X}_{\kappa'}(\mathbf{r}; \mathbf{K}'^{(\pm)}) | \hat{X}_{\kappa}(\mathbf{r}; \mathbf{K}^{(\pm)}) \rangle \\
&= \frac{1}{(2\pi)^2} \int_{-\infty}^{\infty} d\mathbf{r}_{\perp} \hat{X}_{\kappa'}^*(\mathbf{r}; \mathbf{K}'^{(\pm)}) \cdot \hat{X}_{\kappa}(\mathbf{r}; \mathbf{K}^{(\pm)}) \\
&(\kappa, \kappa' = 1-3). \quad (22)
\end{aligned}$$

The inner products of the rectangular vector basis functions are given by

$$\begin{aligned}
& \langle \hat{X}_1(\mathbf{r}; \mathbf{K}_s'^{(\pm)}) | \hat{X}_1(\mathbf{r}; \mathbf{K}_s^{(\pm)}) \rangle \\
&= \langle \hat{X}_2(\mathbf{r}; \mathbf{K}_s'^{(\pm)}) | \hat{X}_2(\mathbf{r}; \mathbf{K}_s^{(\pm)}) \rangle \\
&= \delta(\mathbf{K}_{\perp} - \mathbf{K}'_{\perp}) \begin{cases} 1, & K'_{sz} \text{ real,} \\ \exp(\mp 2|K'_{sz}|z), & K'_{sz} \text{ imag.,} \end{cases} \quad (23a)
\end{aligned}$$

$$\begin{aligned}
& \langle \hat{X}_3(\mathbf{r}; \mathbf{K}_p'^{(\pm)}) | \hat{X}_3(\mathbf{r}; \mathbf{K}_p^{(\pm)}) \rangle \\
&= \delta(\mathbf{K}_{\perp} - \mathbf{K}'_{\perp}) \left(\frac{k_p}{k_s}\right)^3 \begin{cases} 1, & K'_{pz} \text{ real,} \\ \exp(\mp 2|K'_{pz}|z), & K'_{pz} \text{ imag.,} \end{cases} \quad (23b)
\end{aligned}$$

$$\begin{aligned}
& \langle \hat{X}_1(\mathbf{r}; \mathbf{K}_s'^{(\pm)}) | \hat{X}_2(\mathbf{r}; \mathbf{K}_s^{(\pm)}) \rangle = \langle \hat{X}_1(\mathbf{r}; \mathbf{K}_s'^{(\pm)}) | \hat{X}_3(\mathbf{r}; \mathbf{K}_p^{(\pm)}) \rangle \\
&= 0, \quad (23c)
\end{aligned}$$

and

$$\begin{aligned}
& \langle \hat{X}_2(\mathbf{r}; \mathbf{K}_s'^{(\pm)}) | \hat{X}_3(\mathbf{r}; \mathbf{K}_p^{(\pm)}) \rangle \\
&= -i \delta(\mathbf{K}_{\perp} - \mathbf{K}'_{\perp}) \left(\frac{k_p}{k_s}\right)^{3/2} (\hat{K}_s^{(\pm)} \times \hat{K}_t)^* \\
&\cdot \hat{K}_p^{(\pm)} \exp[\pm i(K_{pz} - K_{sz}^*)]. \quad (23d)
\end{aligned}$$

C. Periodic rectangular basis functions

When scattering from periodic surface roughness, it is more convenient to use periodic basis functions constructed from Floquet plane waves. The m th order Floquet plane-wave mode is denoted $\chi(\mathbf{r}; \mathbf{k}_m^{(\pm)})$ and is obtained from Eq. (18) by replacing $\mathbf{K}^{(\pm)}$ by $\mathbf{k}_m^{(\pm)}$ where

$$\mathbf{k}_m^{(\pm)} = k_{xm} \hat{x} + k_{ym} \hat{y} \pm k_{zm} \hat{z}, \quad (24a)$$

$$\begin{aligned}
k_{xm} &= k \sin \theta_{m_x} \cos \phi_{m_x} = k \left(\sin \theta^{(i)} \cos \phi^{(i)} + \frac{m_x K_x}{k} \right) \\
&= k \alpha_{m_x}, \quad (24b)
\end{aligned}$$

$$\begin{aligned}
k_{ym} &= k \sin \theta_{m_y} \sin \phi_{m_y} = k \left(\sin \theta^{(i)} \sin \phi^{(i)} + \frac{m_y K_y}{k} \right) \\
&= k \beta_{m_y}, \quad (24c)
\end{aligned}$$

and

$$k_{zm} = \sqrt{k^2 - k_{xm}^2 - k_{ym}^2} = k \gamma_m. \quad (24d)$$

The symbol \mathbf{m} is used to denote the ordered pair of indices (m_x, m_y) where m_x and m_y are positive or negative integers that specify the order of the mode. The quantity $K_x = 2\pi/\Lambda_x$ and $K_y = 2\pi/\Lambda_y$, where Λ_x and Λ_y are, respectively, the periods of the roughness in the x and y directions. Equation (24d) shows that k_{zm} is double valued and may be real or imaginary so that the spectrum of Floquet modes includes both upwardly and downwardly propagating modes as well as evanescent modes. The branch cut is chosen so that the evanescent waves obey the radiation boundary condition.

D. Transformations between spherical and rectangular basis functions

In the development of the shell-rough surface T -matrix, both spherical and rectangular basis functions appear. These functions appear not only in different equations that result from the application of the Helmholtz–Kirchhoff integral to different scatterers, but also within the same equation. Therefore, it is necessary to transform from one basis to the other. The expansion of a plane wave in terms of scalar spherical harmonics is given by¹⁶

$$\chi(\mathbf{r}; \mathbf{K}) = e^{i\mathbf{K} \cdot \mathbf{r}} = \sum_{\lambda} a_{\lambda}(\hat{K}) \psi_{\lambda 1}(\mathbf{r}; k) \quad (25a)$$

with

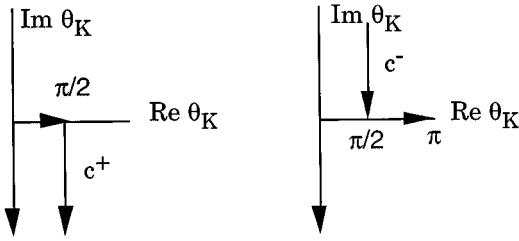


FIG. 2. Curves c^\pm for the evaluation of $\psi_{\lambda 2}(\mathbf{r}; k)$.

$$a_\lambda(\hat{K}) = 4\pi i^\nu Y_\lambda(\hat{K}). \quad (25b)$$

The symbol $\Sigma_\lambda = \sum_{\lambda=1}^{\infty} \sum_{\nu=0}^{\infty} \sum_{\mu=0}^{\nu}$ and \hat{K} is used to denote the polar angle $\theta_K = \sin^{-1}[\sqrt{K_x^2 + K_y^2}/k]$ and the azimuthal angle $\phi_K = \tan^{-1}[K_y/K_x]$ of the wave vector \mathbf{K} . Similarly, the symbol \hat{r} is used to denote the polar angle θ_r and azimuthal angle ϕ_r of the field point. This expansion is valid not only for propagating waves, but also for evanescent waves when the analytic continuation of the Legendre functions for complex arguments is evaluated on the physical Riemann sheet. In the problems considered in this paper, the argument of the Legendre functions is purely real for propagating waves or purely imaginary for evanescent waves. The proper analytic continuation of the Legendre function onto the physical Riemann sheet for an imaginary argument $i|z|$ with $|z| > 1$ is $P_\nu^\mu(i|z|)$. Equation (25) can be used to evaluate the inner products of a Weyl plane wave with a $\psi_{\lambda 1}(\mathbf{r}; k)$ spherical basis function and with a spherical harmonic:

$$\langle \psi_{\lambda 1}(\mathbf{r}; k) | \chi(\mathbf{r}; \mathbf{K}) \rangle = a_\lambda(\hat{K}) \quad (26a)$$

and

$$\langle Y_\lambda(\hat{r}) | \chi(\mathbf{r}; \mathbf{K}) \rangle = a_\lambda(\hat{K}) j_\nu(kr). \quad (26b)$$

A integral representation of $\Psi_{\lambda 2}(\mathbf{r}; k)$ in terms of the rectangular scalar basis functions is given by¹

$$\begin{aligned} \psi_{\lambda 2}(\mathbf{r}; k) &= \frac{1}{2\pi i^\nu} \int_0^{2\pi} d\phi_K \\ &\times \int_{c^\pm} \sin \theta_K d\theta_K Y_\lambda(\hat{K}) e^{i\mathbf{K} \cdot \mathbf{r}} \quad (z \geq 0) \end{aligned} \quad (27)$$

with $K_x = k \sin \theta_K \cos \phi_K$, $K_y = k \sin \theta_K \sin \phi_K$, and $K_z = k \cos \theta_K$ and $x = r \sin \theta_r \cos \phi_r$, $y = r \sin \theta_r \sin \phi_r$, and $z = r \cos \theta_r$. The curves c^\pm are shown in Fig. 2. Equation (27) provides the transformation from a $\psi_{\lambda 2}(\mathbf{r}; k)$ spherical scalar basis function to rectangular scalar basis functions. Another representation for $\psi_{\lambda 2}(\mathbf{r}; k)$ may be obtained from the representation given by Eq. (27) by transforming the integration over polar angles to an integration over the rectangular components of the transverse wave vector. The Jacobian of the transformation is $J(K_x, K_y) = (K_z \sqrt{K_x^2 + K_y^2})^{-1}$ and a representation of $\Psi_{\lambda 2}(\mathbf{r}; k)$ is given by

$$\psi_{\lambda 2}(\mathbf{r}; k) = \int_{-\infty}^{\infty} d\mathbf{K}_\perp b_\lambda(\hat{K}) \chi(\mathbf{r}; \mathbf{K}^\pm) \quad (z \geq 0). \quad (28a)$$

with

$$b_\lambda(\hat{K}) = \frac{1}{2\pi i^\nu} \frac{1}{k K_z} Y_\lambda(\hat{K}). \quad (28b)$$

Equation (28) can be used to evaluate the inner product of a $\Psi_{\lambda 2}(\mathbf{r}; k)$ spherical basis function and a Weyl plane wave:

$$\langle \chi(\mathbf{r}_\perp; \mathbf{K}_\perp) | \psi_{\lambda 2}(\mathbf{r}; k) \rangle = b_\lambda(\hat{K}) e^{\pm i K_z z} \quad (z \leq 0). \quad (29)$$

III. FIELD REPRESENTATIONS

In the following, scalar and vector spherical and rectangular basis functions are used to construct representations of scalar and tensor-fields that are convenient for the construction of the T matrix for the shell-interface system for arbitrary surface roughness. It is convenient to construct representations of the incident field in terms of both spherical and rectangular basis functions and these representations are given by

$$p^{(i)}(\mathbf{r}) = \lambda^{(1)} k_p^{(1)} \sum_\lambda p_\lambda^{(i)} \psi_{\lambda \sigma}(\mathbf{r}; k_p^{(1)}) \quad (30a)$$

and

$$p^{(i)}(\mathbf{r}) = \frac{\lambda^{(1)}}{k_p^{(1)}} \frac{1}{(2\pi)^2} \int_{-\infty}^{\infty} d\mathbf{K}_\perp p^{(i)}(\mathbf{K}_\perp) \chi(\mathbf{r}; \mathbf{K}_\perp^{(1-)}). \quad (30b)$$

The factors $\lambda^{(1)}/k_p^{(1)}$ and $\lambda^{(1)} k_p^{(1)}$ are introduced so that the spectral amplitudes $p_\lambda^{(i)}$ and $p^{(i)}(\mathbf{K}_\perp)$ have the same physical dimension as the spectral amplitudes for the displacement fields. For plane-wave incidence $\sigma=1$ and for a point source $\sigma=2$.

The representation of the scattered pressure field in the fluid and the surface pressure and displacement fields are given by

$$p^{(1s)}(\mathbf{r}) = \frac{\lambda^{(1)}}{k_p^{(1)}} \frac{1}{(2\pi)^2} \int_{-\infty}^{\infty} d\mathbf{K}_\perp p^{(1s)}(\mathbf{K}_\perp) \chi(\mathbf{r}; \mathbf{K}_\perp^{(1+)}), \quad (31)$$

$$\begin{aligned} p_+^{(2)}(\mathbf{r}') &= \frac{\lambda^{(1)}}{k_p^{(1)}} \frac{1}{(2\pi)^2} \int_{-\infty}^{\infty} d\mathbf{K}'_\perp \\ &\times p^{(2)}(\mathbf{K}'_\perp) \chi(\mathbf{r}'_\perp; \mathbf{K}'_\perp), \end{aligned} \quad (32)$$

$$p_+^{(3)}(\mathbf{r}') = \lambda^{(1)} k_p^{(1)} \sum_{\lambda'} p_{\lambda'}^{(3)} Y_{\lambda'}(\hat{r}'), \quad (33)$$

$$p_-^{(4)}(\mathbf{r}') = \lambda^{(4)} k_p^{(4)} \sum_{\lambda'} p_{\lambda'}^{(4)} Y_{\lambda'}(\hat{r}'), \quad (34)$$

$$\begin{aligned} \mathbf{u}_-^{(2)}(\mathbf{r}') &= \frac{1}{(2\pi)^2} \int_{-\infty}^{\infty} d\mathbf{K}'_\perp \\ &\times \sum_{\kappa'=1}^3 \frac{1}{k_{\kappa'}^{(2)}} u_{\kappa'}^{(2)}(\mathbf{K}'_\perp) \hat{X}_{\kappa'}(\mathbf{r}'_\perp; \mathbf{K}'_\perp), \end{aligned} \quad (35)$$

$$\mathbf{u}_-^{(3)}(\mathbf{r}') = \sum_{\kappa'=1}^3 \sum_{\lambda'} u_{\kappa'\lambda'}^{(3)} \mathbf{Y}_{\kappa'\lambda'}(\hat{r}'), \quad (36)$$

and

$$\mathbf{u}_+^{(4)}(\mathbf{r}') = \sum_{\kappa'=1}^3 \sum_{\lambda'} u_{\kappa'\lambda'}^{(4)} \mathbf{Y}_{\kappa'\lambda'}(\hat{r}'). \quad (37)$$

where

$$k_{\kappa}^{(n)} = k_s^{(n)}(\delta_{\kappa 1} + \delta_{\kappa 2}) + k_p^{(n)}\delta_{\kappa 3} \quad (38a)$$

and

$$\mathbf{K}_{\kappa}^{(n\pm)} = \mathbf{K}_s^{(n\pm)}(\delta_{\kappa 1} + \delta_{\kappa 2}) + \mathbf{K}_p^{(n\pm)}\delta_{\kappa 3}. \quad (38b)$$

The factor of $1/k_{\kappa}^{(n)2}$ in the representation of $\mathbf{u}_{\pm}^{(2)}(\mathbf{r}')$ is introduced so that spectral amplitudes in the spherical and rectangular representations have the same dimension. It is important to note that the fields $p_{\pm}^{(3)}(\mathbf{r}')$, $p_{\pm}^{(4)}(\mathbf{r}')$, $\mathbf{u}_{\pm}^{(3)}(\mathbf{r}')$, and $\mathbf{u}_{\pm}^{(4)}(\mathbf{r}')$ are represented in terms of spherical harmonics instead of the spherical vector basis functions as is sometimes done in null-field T -matrix formalisms.⁴ Representations of this type have been used previously^{5,7,17} and it has been shown that they improve the numerical properties of the T matrix. Similarly, the representations of the fields $p_{\pm}^{(2)}(\mathbf{r}')$ and $\mathbf{u}_{\pm}^{(2)}(\mathbf{r}')$ are in the form of a two-dimensional Fourier transform in the horizontal wave number and do not include explicit dependence on z' so that a representation that appears to invoke the Rayleigh hypothesis is not used.

In the following, representations for scalar and tensor Green functions are given for arbitrary media and specific reference to the various media in the present problem is temporarily suppressed. The scalar Green function in terms of spherical scalar basis functions is given by¹⁶

$$g_0(\mathbf{r}', \mathbf{r}; \mathbf{k}) = \begin{cases} ik \sum_{\lambda} \psi_{\lambda 1}(\mathbf{r}'; k) \psi_{\lambda 2}(\mathbf{r}; k) & (r > r') \\ ik \sum_{\lambda} \psi_{\lambda 2}(\mathbf{r}'; k) \psi_{\lambda 1}(\mathbf{r}; k) & (r < r') \end{cases} \quad (39)$$

and in terms of rectangular scalar basis functions is given by

$$g_0(\mathbf{r}', \mathbf{r}; \mathbf{k}) = \frac{i}{8\pi^2} \times \int_{-\infty}^{\infty} d\mathbf{K}_{\perp} \frac{\chi(-\mathbf{r}'; \mathbf{K}^{(\pm)}) \chi(\mathbf{r}; \mathbf{K}^{(\pm)})}{K_z} \quad (z \geq z'). \quad (40)$$

The Green dyadic represented in terms of spherical vector basis functions is given by¹⁸

$$\mathbf{G}_0(\mathbf{r}', \mathbf{r}; \mathbf{k}_p, \mathbf{k}_s) = \begin{cases} \frac{ik_s}{\mu} \sum_{\kappa=1}^3 \sum_{\lambda} \Psi_{\kappa \lambda 1}(\mathbf{r}'; k_{\kappa}) \Psi_{\kappa \lambda 2}(\mathbf{r}; k_{\kappa}) & (r > r') \\ \frac{ik_s}{\mu} \sum_{\kappa=1}^3 \sum_{\lambda} \Psi_{\kappa \lambda 2}(\mathbf{r}'; k_{\kappa}) \Psi_{\kappa \lambda 1}(\mathbf{r}; k_{\kappa}) & (r < r') \end{cases} \quad (41)$$

and in terms of rectangular vector basis functions is given by

$$\mathbf{G}_0(\mathbf{r}', \mathbf{r}; \mathbf{k}_p, \mathbf{k}_s) = \frac{i}{8\pi^2} \frac{k_s}{\mu} \int_{-\infty}^{\infty} d\mathbf{K}_{\perp} \sum_{\kappa=1}^3 \frac{1}{k_{\kappa}} \frac{1}{K_{\kappa z}} \times \hat{X}_{\kappa}(-\mathbf{r}'; \mathbf{K}_{\kappa}^{(\pm)}) \hat{X}_{\kappa}(\mathbf{r}; \mathbf{K}_{\kappa}^{(\pm)}) \quad (z \geq z'). \quad (42)$$

Similarly, the Green stress triadic is represented in terms of both spherical and rectangular vector basis functions:

$$\begin{aligned} \Sigma_0(\mathbf{r}', \mathbf{r}; \mathbf{k}_p, \mathbf{k}_s) &= \frac{ik_s}{\mu} \sum_{\kappa=1}^3 \sum_{\lambda} \{ \lambda |\nabla \cdot \Psi_{3\lambda 1}(\mathbf{r}'; k_{\kappa}) \delta_{\delta 3} + \mu [\nabla' \Psi_{\kappa \lambda 1}(\mathbf{r}'; k_{\kappa}) + \Psi_{\kappa \lambda 1}(\mathbf{r}'; k_{\kappa}) \nabla'] \} \Psi_{\kappa \lambda 2}(\mathbf{r}; k_{\kappa}) \quad (r > r') \\ &= \frac{ik_s}{\mu} \sum_{\kappa=1}^3 \sum_{\lambda} \{ \lambda |\nabla' \cdot \Psi_{3\lambda 2}(\mathbf{r}'; k_{\kappa}) \delta_{\kappa 3} + \mu [\nabla' \Psi_{\kappa \lambda 2}(\mathbf{r}'; k_{\kappa}) + \Psi_{\kappa \lambda 2}(\mathbf{r}'; k_{\kappa}) \nabla'] \} \Psi_{\kappa \lambda 1}(\mathbf{r}; k_{\kappa}) \quad (r < r') \end{aligned} \quad (43)$$

and

$$\begin{aligned} \Sigma_0(\mathbf{r}', \mathbf{r}; \mathbf{k}_p, \mathbf{k}_s) &= \frac{i}{8\pi^2} \frac{k_s}{\mu} \int_{-\infty}^{\infty} d\mathbf{K}_{\perp} \sum_{\kappa=1}^3 \left\{ \frac{\lambda}{k_p} \frac{1}{K_{p z}} |\nabla' \cdot \hat{X}_3(-\mathbf{r}'; \mathbf{K}_p^{(\pm)}) \delta_{\kappa 3} + \frac{\mu}{k_{\kappa}} \frac{1}{K_{\kappa z}} [\nabla' \hat{X}_{\kappa}(-\mathbf{r}; \mathbf{K}_{\kappa}^{(\pm)}) \right. \\ &\quad \left. + \hat{X}_{\kappa}(-\mathbf{r}'; \mathbf{K}_{\kappa}^{(\pm)}) \nabla'] \hat{X}_{\kappa}(\mathbf{r}; \mathbf{K}_{\kappa}^{(\pm)}) \right\} \quad (z \geq z'). \end{aligned} \quad (44)$$

To obtain equations for the spectral amplitudes of the various fields, the representations of the various fields are used in the Helmholtz–Kirchhoff equations, Eqs. (5)–(8). Then Eq. (5) is used to evaluate the inner products $\langle \chi(\mathbf{r}_{\perp}; \mathbf{K}_{\perp}^{(1s)}) | p^{(1s)}(\mathbf{r}) \rangle$ in $v^{(1)}$ with $z > -d^{(2)} + \max(h_x, h_y)$, $\langle \chi(\mathbf{r}_{\perp}; \mathbf{K}_{\perp}^{(1)}) | -p^{(i)}(\mathbf{r}) \rangle$ in $v^{(2)}$ with $z < -d^{(2)} - \max(h_x, h_y)$, and $\langle \psi_{\lambda 1}(\mathbf{r}; k_p^{(1)}) | p^{(1s)}(\mathbf{r}) \rangle$ in $v^{(3)}$. To simplify notation, the inner products are evaluated and then a notational change is made from \mathbf{K}_{\perp}'' to \mathbf{K}_{\perp} and from λ' to λ . The results of these calculations are given by

$$p^{(1s)}(\mathbf{K}_\perp) = \frac{1}{(2\pi)^2} \int_{-\infty}^{\infty} d\mathbf{K}'_\perp \left[\sum_{\kappa'=1}^3 V_{4\kappa}^{(2-)}(\mathbf{K}_\perp, \mathbf{K}'_\perp) u_{\kappa'}^{(2)}(\mathbf{K}'_\perp) + V_{44}^{(2-)}(\mathbf{K}_\perp, \mathbf{K}'_\perp) p^{(2)}(\mathbf{K}'_\perp) \right] e^{iK'_p z} d^{(2)} \\ + (2\pi)^2 k_p^{(1)2} \sum_{\lambda} \sum_{\lambda'} \left[Q_{\lambda 1; \lambda'}^{(3)} p_{\lambda'}^{(3)} - \sum_{\kappa'=1}^3 B_{\lambda 1; \kappa' \lambda'}^{(3)} u_{\kappa' \lambda'}^{(3)} \right] b_{\lambda}(\hat{K}_p^{(1+)}) \quad (r \in v^{(1)}), \quad (45a)$$

$$-p^{(i)}(\mathbf{K}_\perp) = \frac{1}{(2\pi)^2} \int_{-\infty}^{\infty} d\mathbf{K}'_\perp \left[\sum_{\kappa'=1}^3 V_{4\kappa'}^{(2+)}(\mathbf{K}_\perp, \mathbf{K}'_\perp) u_{\kappa'}^{(2)}(\mathbf{K}'_\perp) + V_{44}^{(2+)}(\mathbf{K}_\perp, \mathbf{K}'_\perp) p^{(2)}(\mathbf{K}'_\perp) \right] e^{-iK'_p z} d^{(2)} \\ + (2\pi)^2 k_p^{(1)2} \sum_{\lambda} \sum_{\lambda'} \left[Q_{\lambda 1; \lambda'}^{(3)} p_{\lambda'}^{(3)} - \sum_{\kappa'=1}^3 B_{\lambda 1; \kappa' \lambda'}^{(3)} u_{\kappa' \lambda'}^{(3)} \right] b_{\lambda}(\hat{K}_p^{(1-)}) \quad (r \in v^{(2)}), \quad (45b)$$

and

$$-p_{\lambda}^{(i)} = \frac{1}{k_p^{(1)2}} \frac{1}{(2\pi)^4} \int_{-\infty}^{\infty} d\mathbf{K}'_\perp \int_{-\infty}^{\infty} d\mathbf{K}''_\perp \left[\sum_{\kappa'=1}^3 V_{4\kappa'}^{(2-)}(\mathbf{K}'_\perp, \mathbf{K}''_\perp) u_{\kappa'}^{(2)}(\mathbf{K}''_\perp) + V_{44}^{(2-)}(\mathbf{K}'_\perp, \mathbf{K}''_\perp) p^{(2)}(\mathbf{K}''_\perp) \right] \\ \times a_{\lambda}(\hat{K}'_p^{(1+)}) e^{iK'_p z} d^{(2)} + \sum_{\lambda'} \left[Q_{\lambda 2; \lambda'}^{(3)} p_{\lambda'}^{(3)} - \sum_{\kappa'=1}^3 B_{\lambda 2; \kappa' \lambda'}^{(3)} u_{\kappa' \lambda'}^{(3)} \right] \quad (r \in v^{(3)}). \quad (45c)$$

In Eqs. (45a)–(45c), the volume in which an equation is obtained is indicated in parentheses. The matrix elements $B_{\lambda\sigma; \kappa' \lambda'}^{(3)}$ and $Q_{\lambda\sigma; \lambda'}^{(3)}$ are those for the elastic shell and these and all subsequent matrix elements related to the shell are given in Appendix A. The matrix elements $V_{4\kappa'}^{(2\pm)}(\mathbf{K}'_\perp, \mathbf{K}''_\perp)$ and $V_{44}^{(2\pm)}(\mathbf{K}'_\perp, \mathbf{K}''_\perp)$ are those for the rough elastic solid and these all subsequent matrix elements related to the elastic solid are given in Appendix B. The sign convention for these matrix elements is chosen so that the matrix of coefficients of the null-field equations is $V^{(2+)}(\mathbf{K}'_\perp, \mathbf{K}''_\perp)$ and the matrix of coefficients for the scattered field equations is $V^{(2-)}(\mathbf{K}'_\perp, \mathbf{K}''_\perp)$. The matrix $V^{(2-)}(\mathbf{K}'_\perp, \mathbf{K}''_\perp)$ arises when the solution for the scattered displacement field in the elastic solid is obtained in addition to that for the scattered pressure field in fluid. In this paper, however, only the solution for the scattered pressure field is being considered and only the matrix elements $V_{4\gamma}^{(2-)}(\mathbf{K}'_\perp, \mathbf{K}''_\perp)$ arise explicitly. It is important to note that the displacement field in the solid and the pressure field scattered from its surface propagate in opposite directions so that the scattered displacement field depends on the wave vector $\mathbf{K}_\kappa^{(2-)}$ while the scattered pressure field depends on the wave vector $\mathbf{K}_p^{(1+)}$, and $V^{(2-)}(\mathbf{K}'_\perp, \mathbf{K}''_\perp)$ depends on $\mathbf{K}_\kappa^{(2-)}$ and $\mathbf{K}_p^{(1+)}$. The superscript on these matrix elements refers to the surface from which scattering occurs.

Equations for the displacement field on the surface of the infinite elastic solid are obtained by enforcing the null-field condition on the scattered displacement field in the elastic solid and are obtained by using Eq. (6) to evaluate the inner products $\langle \mathbf{X}_1(\mathbf{r}_\perp; \mathbf{K}''_\perp) | \nabla \times \mathbf{u}^{(2s)}(\mathbf{r}) \rangle$, $\langle \mathbf{X}_2(\mathbf{r}_\perp; \mathbf{K}''_\perp) | \nabla \times \mathbf{u}^{(2s)}(\mathbf{r}) \rangle$, and $\langle \chi(\mathbf{r}_\perp; \mathbf{K}''_\perp) | \nabla \cdot \mathbf{u}^{(2s)}(\mathbf{r}) \rangle$ in $v^{(1)}$ with $z > -d^{(2)} + \max(h_x, h_y)$ and are given by

$$0 = \frac{1}{(2\pi)^2} \int_{-\infty}^{\infty} d\mathbf{K}'_\perp \left[\sum_{\kappa'=1}^3 V_{\kappa\kappa'}^{(2+)}(\mathbf{K}_\perp, \mathbf{K}'_\perp) u_{\kappa'}^{(2)}(\mathbf{K}'_\perp) + V_{\kappa 4}^{(2+)}(\mathbf{K}_\perp, \mathbf{K}'_\perp) p^{(2)}(\mathbf{K}'_\perp) \right] e^{iK'_p z} d^{(2)} \quad (r \notin v^{(2)}). \quad (46)$$

Equations for the fields on the surfaces of the shell are obtained when the displacement field in the annular region of the shell is forced to satisfy the null-field hypothesis in $v^{(4)}$ with $r < b$ and in $v^{(1)}$ with $r > a$ and when the pressure field in the interior of the shell is forced to satisfy the null-field hypothesis in the region $r > b$:

$$0 = \sum_{\lambda'} \left[-P_{\kappa\lambda 2; \lambda'}^{(3)} p_{\lambda'}^{(3)} - \sum_{\kappa'=1}^3 R_{\kappa\lambda 2; \kappa' \lambda'}^{(3)} u_{\kappa' \lambda'}^{(3)} + P_{\kappa\lambda 2; \lambda'}^{(4)} p_{\lambda'}^{(4)} + \sum_{\kappa'=1}^3 R_{\kappa\lambda 2; \kappa' \lambda'}^{(4)} u_{\kappa' \lambda'}^{(4)} \right] \quad (r < b), \quad (47a)$$

$$0 = \sum_{\lambda'} \left[-P_{\kappa\lambda 1; \lambda'}^{(3)} p_{\lambda'}^{(3)} - \sum_{\kappa'=1}^3 R_{\kappa\lambda 1; \kappa' \lambda'}^{(3)} u_{\kappa' \lambda'}^{(3)} + P_{\kappa\lambda 1; \lambda'}^{(4)} p_{\lambda'}^{(4)} + \sum_{\kappa'=1}^3 R_{\kappa\lambda 1; \kappa' \lambda'}^{(4)} u_{\kappa' \lambda'}^{(4)} \right] \quad (r > a), \quad (47b)$$

and

$$0 = \sum_{\lambda'} \left[-Q_{\lambda 1; \lambda'}^{(4)} p_{\lambda'}^{(4)} + \sum_{\kappa'=1}^3 B_{\lambda 1; \kappa' \lambda'}^{(4)} u_{\kappa' \lambda'}^{(4)} \right] \quad (r > b). \quad (48)$$

In Appendix C, the equations that follow from Eqs. (45a) and (45c) when the terms that depend on the surface $s^{(2)}$ are omitted and Eqs. (47) and (48) are used to construct a representation of the free-field T -matrix for the shell. These results may be used to introduce the free-field T -matrix of the shell in the remaining field equations and to eliminate explicit dependence on the surface fields of the shell. This is the same procedure used by Hackman and Sammelmann.⁵ To introduce the free-field T -matrix for the elastic shell, the coefficient $c_\lambda^{(3)}$ is defined in the following manner:

$$c_\lambda^{(3)} = \sum_{\lambda'} \left[Q_{\lambda 2; \lambda'}^{(3)} p_{\lambda'}^{(3)} - \sum_{\kappa'=1}^3 B_{\lambda 2; \kappa' \lambda'}^{(3)} u_{\kappa' \lambda'}^{(3)} \right]. \quad (49)$$

Then, when Eq. (C9) and the definition of $U_{\lambda 2; \lambda'}^{(3)}$ given by Eq. (C12b) is used in Eq. (49), $c_\lambda^{(3)}$ is given by

$$c_\lambda^{(3)} = \sum_{\lambda'} U_{\lambda 2; \lambda'}^{(3)} p_{\lambda'}^{(3)}. \quad (50)$$

When the result of inverting this equation and the matrices $U_{\lambda 1; \lambda'}^{(3)}$ and $U_{\lambda 2; \lambda'}^{(3)}$ given by Eq. (C12) and the free-field T -matrix for the shell $T_{\lambda' \lambda}^{(3)}$ are used in Eqs. (45a)–(45c), the results are given by

$$p^{(1s)}(\mathbf{K}_\perp) = \frac{1}{(2\pi)^2} \int_{-\infty}^{\infty} d\mathbf{K}'_\perp \times \left[\sum_{\kappa'=1}^3 V_{4\kappa'}^{(2-)}(\mathbf{K}_\perp, \mathbf{K}'_\perp) u_{\kappa'}^{(2)}(\mathbf{K}'_\perp) + V_{44}^{(2-)}(\mathbf{K}_\perp, \mathbf{K}'_\perp) p^{(2)}(\mathbf{K}'_\perp) \right] e^{iK_{pz}^{(1)} d^{(2)}} - (2\pi)^2 k_p^{(1)2} \sum_{\lambda} \sum_{\lambda'} T_{\lambda; \lambda'}^{(3)} c_{\lambda'}^{(3)} b_\lambda(\hat{K}_p^{(1+)}) \quad (51)$$

$$-p^{(i)}(\mathbf{K}_\perp) = \frac{1}{(2\pi)^2} \int_{-\infty}^{\infty} d\mathbf{K}'_\perp \times \left[\sum_{\kappa'=1}^3 V_{4\kappa'}^{(2+)}(\mathbf{K}_\perp, \mathbf{K}'_\perp) u_{\kappa'}^{(2)}(\mathbf{K}'_\perp) + V_{44}^{(2+)}(\mathbf{K}_\perp, \mathbf{K}'_\perp) p^{(2)}(\mathbf{K}'_\perp) \right] e^{-iK_{pz}^{(1)} d^{(2)}} - (2\pi)^2 k_p^{(1)2} \sum_{\lambda} \sum_{\lambda'} T_{\lambda; \lambda'}^{(3)} c_{\lambda'}^{(3)} b_\lambda(\hat{K}_p^{(1-)}), \quad (52)$$

and

$$-p_\lambda^{(i)} = c_\lambda^{(3)} + \frac{1}{k_p^{(1)2}} \frac{1}{(2\pi)^4} \int_{-\infty}^{\infty} d\mathbf{K}'_\perp \int_{-\infty}^{\infty} d\mathbf{K}''_\perp \times \left[\sum_{\kappa'=1}^3 V_{4\kappa'}^{(2-)}(\mathbf{K}'_\perp, \mathbf{K}''_\perp) u_{\kappa'}^{(2)}(\mathbf{K}''_\perp) + V_{44}^{(2-)}(\mathbf{K}'_\perp, \mathbf{K}''_\perp) p^{(2)}(\mathbf{K}''_\perp) \right] \times a_\lambda(\hat{K}'_p^{(1+)}) e^{iK_{pz}^{(1)} d^{(2)}}. \quad (53)$$

These equations are regarded as the free-field equations for scattering from a rough fluid–elastic interface of an incident field that consists of the field produced by the source and that scattered from the shell and whose spectral amplitude $s_4(\mathbf{K}_\perp)$ is given by

$$s_4(\mathbf{K}_\perp) = \left[p^{(i)}(\mathbf{K}_\perp) - (2\pi)^2 k_p^{(1)2} \times \sum_{\lambda} \sum_{\lambda'} T_{\lambda; \lambda'}^{(3)} c_{\lambda'}^{(3)} b_\lambda(\hat{K}_p^{(1-)}) \right] e^{iK_{pz}^{(1)} d^{(2)}}. \quad (54)$$

The solution to the rough surface problem is obtained and then used in Eq. (53) to determine $c_\lambda^{(3)}$. This procedure allows the free-field T -matrix for the fluid–elastic interface to be introduced in a relatively simple manner.

Although Eqs. (47) and (51)–(53) are valid for arbitrary surface roughness, they are a complicated system of integral equations for the surface and scattered fields and as a practical matter, they are very difficult to solve in general. Therefore in the following, two special cases of these general equations are considered: First, the system of equations is specialized to scattering from periodic surface roughness and an “exact” solution is obtained. Then, it is specialized to scattering from small amplitude arbitrary surface roughness and a perturbative solution is obtained. It is shown that the analytic form of the solution for scattering from periodic surface roughness is considerably simpler than that of the perturbative solution and the details of the scattering process are considerably more transparent than in the perturbative solution.

IV. AN “EXACT” SOLUTION FOR SCATTERING FROM PERIODIC SURFACE ROUGHNESS

To begin, it is assumed that the roughness on the interface is periodic with periods Λ_x and Λ_y in the x and y directions, respectively, so that the surface-field spectral amplitudes become

$$p^{(2)}(\mathbf{K}'_\perp) = (2\pi)^2 k_p^{(1)2} \sum_{\mathbf{n}=-\infty}^{\infty} p_{\mathbf{n}}^{(2)} \delta(\mathbf{K}'_\perp - \mathbf{k}_{\perp \mathbf{n}}) \quad (55a)$$

and

$$u_{\kappa'}^{(2)}(\mathbf{K}'_\perp) = (2\pi)^2 k_{\kappa'}^{(2)2} \sum_{\mathbf{n}=-\infty}^{\infty} u_{\kappa' \mathbf{n}}^{(2)} \delta(\mathbf{K}'_\perp - \mathbf{k}_{\perp \mathbf{n}}). \quad (55b)$$

The amplitudes $p_{\mathbf{n}}^{(2)}$ and $u_{\kappa' \mathbf{n}}^{(2)}$ are the Floquet spectral amplitudes for the pressure and displacement fields on the rough surface. These equations transform the representations of the surface fields from infinite integrals over Weyl plane waves into discrete sums of Floquet plane-wave modes and when they are introduced into the field equations, the infinite integrations over the transverse wave numbers that occur in these equations are also transformed into infinite sums of Floquet plane-wave modes. In addition, in Appendix B, it is shown that for periodic surface roughness, the Fourier transform of the rough surface phase $C(\mathbf{K}_\perp - \mathbf{k}_{\perp \mathbf{n}}, \pm K_z)$ that occurs in the matrix elements can be written in the following manner:

$$C(\mathbf{K}_\perp - \mathbf{k}_\perp, \pm K_z) = \sum_{\mathbf{m}'=-\infty}^{\infty} C_{\mathbf{m}'-\mathbf{n}}(\pm k_{z\mathbf{m}'}) \times \delta(-\mathbf{K}_\perp + \mathbf{k}_\perp, \mathbf{m}'), \quad (56)$$

where $C_{\mathbf{m}'-\mathbf{n}}(\pm k_{z\mathbf{m}'})$ is the spectral amplitude in a Fourier series representation of the rough surface phase $\exp[\pm iK_z \xi(\mathbf{r}'_\perp)]$.⁷ When Eq. (56) is introduced into the system of field equations, $C_{\mathbf{m}'-\mathbf{n}}(\pm k_{z\mathbf{m}'})$ replaces $C(\mathbf{K}_\perp - \mathbf{k}_\perp, \pm K_z)$ in the rough surface matrix elements and the Dirac delta function and the infinite sum over \mathbf{m}' are retained in the field equations. However, this process produces only four null-field equations for the surface-field Floquet spectral amplitudes, i.e., the equations that follow from Eqs. (46) and (52). An infinite system of linear equations for the Floquet spectral amplitudes of the fields on the rough interface is obtained by projecting the rough surface null-field equations onto a Floquet basis by operating on these equations with the projection operator $P_{\mathbf{m}}$ defined in the following manner:¹⁹

$$P_{\mathbf{m}}\Psi(\mathbf{K}_\perp) \equiv \frac{\Lambda_x \Lambda_y}{\pi^2} \int_{-\infty}^{\infty} d\mathbf{K}_\perp \exp[iK'_z/k_p^{(1)}] \times j_0[(k_{xm_x} - K_x)\Lambda_x/2] \times j_0[(k_{ym_y} - K_y)\Lambda_y/2]\Psi(\mathbf{K}_\perp). \quad (57)$$

The resulting equation for the scattered pressure field spectral amplitude and the rough surface and shell null-field equations for scattering from periodic surface roughness are given by

$$p^{(1s)}(\mathbf{K}_\perp) = k_p^{(1)2} \sum_{\mathbf{m}'=-\infty}^{\infty} \sum_{\mathbf{n}=-\infty}^{\infty} \left[\sum_{\kappa'=1}^3 V_{4\kappa'\mathbf{m}'\mathbf{n}}^{(2-)} u_{\kappa'\mathbf{n}}^{(2)} + V_{44\mathbf{m}'\mathbf{n}}^{(2-)} p_{\mathbf{n}}^{(2)} \right] e^{ik_{pz\mathbf{m}'}d^{(2)}} \delta(-\mathbf{K}_\perp + \mathbf{k}_\perp, \mathbf{m}') - (2\pi)^2 k_p^{(1)2} \sum_{\lambda} \sum_{\lambda'} T_{\lambda;\lambda'}^{(3)} c_{\lambda'}^{(3)} b_{\lambda}(\hat{K}_p^{(1+)}) , \quad (58)$$

$$0 = \sum_{\mathbf{n}=-\infty}^{\infty} \left[\sum_{\kappa'=1}^3 V_{\kappa\kappa'\mathbf{m}\mathbf{n}}^{(2+)} u_{\kappa'\mathbf{n}}^{(2)} + V_{\kappa4\mathbf{m}\mathbf{n}}^{(2+)} p_{\mathbf{n}}^{(2)} \right], \quad (59)$$

$$s_{\mathbf{m}}^{(i)} = \sum_{\mathbf{n}=-\infty}^{\infty} \left[\sum_{\kappa'=1}^3 V_{4\kappa'\mathbf{m}\mathbf{n}}^{(2+)} u_{\kappa'\mathbf{n}}^{(2)} + V_{44\mathbf{m}\mathbf{n}}^{(2+)} p_{\mathbf{n}}^{(2)} \right], \quad (60)$$

and

$$-p_{\lambda}^{(i)} = c_{\lambda}^{(3)} + \frac{1}{(2\pi)^2} \sum_{\mathbf{m}'=-\infty}^{\infty} \sum_{\mathbf{n}=-\infty}^{\infty} \left[\sum_{\kappa'=1}^3 V_{4\kappa'\mathbf{m}'\mathbf{n}}^{(2-)} u_{\kappa'\mathbf{n}}^{(2)} + V_{44\mathbf{m}'\mathbf{n}}^{(2-)} p_{\mathbf{n}}^{(2)} \right] a_{\lambda}(\hat{k}_{p\mathbf{m}'}^{(1+)}) e^{ik_{pz\mathbf{m}'}d^{(2)}}, \quad (61)$$

where the source term in Eq. (60) is

$$s_{\mathbf{m}}^{(i)} \equiv (2\pi)^2 \left[p_{\mathbf{m}}^{(i)} - \sum_{\lambda} \sum_{\lambda'} b_{\mathbf{m}\lambda'} T_{\lambda;\lambda'}^{(3)} c_{\lambda'}^{(3)} \right] e^{ik_{pz\mathbf{m}}d^{(2)}} \quad (62)$$

and $p_{\mathbf{m}}^{(i)} = \delta_{m_x,0} \delta_{m_y,0}$ and $b_{\mathbf{m}\lambda} = (\pi^2/\Lambda_x \Lambda_y) \exp[-ik_{pz\mathbf{m}}^{(1)}/k_p^{(1)}] P_{\mathbf{m}} b_{\lambda}(\hat{K}_p^{(1-)})$. It is important to note that the sum in Eq. (62) is convergent for $k_p^{(1)} d^{(2)} > 1$. The quantities $V_{\gamma\gamma'\mathbf{m}\mathbf{n}}^{(2\pm)}$ are the matrix elements for scattering from periodic roughness and their derivation from the general matrix elements $V_{\gamma\gamma'}^{(2\pm)}(\mathbf{K}'_\perp, \mathbf{K}''_\perp)$ is described in Appendix B.

The system of null-field equations (58)–(60) is identical to that for scattering from a fluid-elastic interface with periodic surface roughness of a source field with a spectral amplitude $s_{\mathbf{m}}^{(i)}$. When the matrix $[V_{\mathbf{m}\mathbf{n}}^{(2+)}]^{-1}$ is nonsingular, these equations may be solved and the results used in Eq. (61) to obtain a solution for $c_{\lambda}^{(3)}$. Then both results can be used to obtain an ‘‘exact’’ expression for $p^{(1s)}(\mathbf{K}_\perp)$ and then $p^{(1s)}(\mathbf{r})$:

$$p^{(1s)}(\mathbf{r}) = \lambda^{(1)} k_p^{(1)} \left[\sum_{\mathbf{m}=-\infty}^{\infty} \sum_{\mathbf{n}=-\infty}^{\infty} T_{\mathbf{m}\mathbf{n}}^{(2)}(d^{(2)}) p_{\mathbf{n}}^{(i)} \chi(\mathbf{r}; \mathbf{k}_{p\mathbf{m}}^{(1+)}) + \sum_{\mathbf{m}=-\infty}^{\infty} \sum_{\mathbf{n}=-\infty}^{\infty} T_{\mathbf{m}\mathbf{n}}^{(22)} p_{\mathbf{n}}^{(i)} \chi(\mathbf{r}; \mathbf{k}_{p\mathbf{m}}^{(1+)}) + \sum_{\mathbf{m}=-\infty}^{\infty} \sum_{\lambda} T_{\mathbf{m}\lambda}^{(23)} p_{\lambda}^{(i)} \chi(\mathbf{r}; \mathbf{k}_{p\mathbf{m}}^{(1+)}) + \sum_{\lambda} \sum_{\mathbf{n}=-\infty}^{\infty} T_{\lambda\mathbf{n}}^{(32)} p_{\mathbf{n}}^{(i)} \psi_{\lambda 2}(\mathbf{r}; k_p^{(1)}) + \sum_{\lambda} \sum_{\lambda'} T_{\lambda\lambda'}^{(33)} p_{\lambda'}^{(i)} \psi_{\lambda 2}(\mathbf{r}; k_p^{(1)}) \right] \quad (63a)$$

with the T matrices

$$T_{\mathbf{m}\mathbf{n}}^{(2)}(d^{(2)}) = e^{ik_{pz\mathbf{m}}d^{(2)}} T_{\mathbf{m}\mathbf{n}}^{(2)} e^{ik_{pz\mathbf{n}}d^{(2)}}, \quad (63b)$$

$$T_{\mathbf{m}\mathbf{n}}^{(22)} = \sum_{\mathbf{n}'=-\infty}^{\infty} T_{\mathbf{m}\mathbf{n}'}^{(2)}(d^{(2)}) T_{\mathbf{n}'\mathbf{n}}^{(32)}, \quad (63c)$$

$$T_{\mathbf{m}\lambda}^{(23)} = \sum_{\mathbf{n}=-\infty}^{\infty} T_{\mathbf{m}\mathbf{n}}^{(2)}(d^{(2)}) T_{\mathbf{n}\lambda}^{(33)}, \quad (63d)$$

$$T_{\lambda\mathbf{n}}^{(32)} = \sum_{\lambda'} T_{\lambda\lambda'}^{(33)} T_{\lambda'\mathbf{n}}^{(2)}(d^{(2)}), \quad (63e)$$

and

$$T_{\lambda\lambda'}^{(33)} = \sum_{\lambda''} T_{\lambda;\lambda''}^{(3)} v_{\lambda''\lambda'}, \quad (63f)$$

the projections




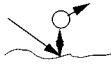

$$T_{\lambda\mathbf{n}}^{(2)}(d^{(2)}) = \sum_{\mathbf{m}=-\infty}^{\infty} a_{\lambda}(\hat{k}_{p\mathbf{m}}^{(1+)}) T_{\mathbf{m}\mathbf{n}}^{(2)}(d^{(2)}), \quad (63g)$$

$$T_{\mathbf{m}\lambda}^{(3)} = \sum_{\lambda'} b_{\mathbf{m}\lambda'} T_{\lambda'\lambda}, \quad (63h)$$

$$T_{\mathbf{m}\lambda}^{(33)} = \sum_{\lambda'} T_{\mathbf{m}\lambda'}^{(3)} v_{\lambda'\lambda}, \quad (63i)$$

and

TABLE I. Schematic representation of scattering from an elastic target in proximity to a fluid elastic interface with periodic roughness.

Expression	Schematic representation
1. $\sum_{m=-\infty}^{\infty} \sum_{n=-\infty}^{\infty} T_{mn}^{(2)}(d^{(2)}) p_n^{(i)} \chi(\mathbf{r}; \mathbf{k}_{\rho m}^{(1+)})$	
2. $\sum_{m=-\infty}^{\infty} \sum_{n=-\infty}^{\infty} T_{mn}^{(22)} p_n^{(i)} \chi(\mathbf{r}; \mathbf{k}_{\rho m}^{(1+)})$	
3. $\sum_{m=-\infty}^{\infty} \sum_{\lambda} T_{m\lambda}^{(23)} p_{\lambda}^{(i)} \chi(\mathbf{r}; \mathbf{k}_{\rho m}^{(1+)})$	
4. $\sum_{m=-\infty}^{\infty} \sum_{\lambda} T_{m\lambda}^{(32)} p_{\lambda}^{(i)} \chi(\mathbf{r}; \mathbf{k}_{\rho m}^{(1+)})$	
5. $\sum_{\lambda} \sum_{\lambda'} T_{\lambda\lambda'}^{(33)} p_{\lambda'}^{(i)} \psi_{\lambda 2}(\mathbf{r}; \mathbf{k}_{\rho m}^{(1+)})$	

$$T_{mn}^{(32)} = \sum_{\lambda} b_{m\lambda} T_{\lambda n}^{(32)}, \quad (63j)$$

and the shell-interface multiple scattering vertex

$$v_{\lambda\lambda'}^{(3)} = [I + A]_{\lambda\lambda'}^{-1} \quad (63k)$$

with

$$A_{\lambda\lambda'} = - \sum_{n=-\infty}^{\infty} T_{\lambda n}^{(2)}(d^{(2)}) T_{n\lambda'}^{(3)}. \quad (63l)$$

For plane-wave incidence considered in this paper, $p_{\lambda}^{(i)} = a_{\lambda}(\hat{k}_{\rho}^{(i)})$.

In Eqs. (63a)–(63e), the first superscript denotes the surface from which the wave is scattered and the second denotes the surface on which the plane wave is incident. The quantity $T_{mn}^{(2)} = V_{4\gamma mn}^{(2-)} V_{\gamma 4mn}^{(2+)-1}$ and is the free-field T -matrix for the periodic surface and $T_{mn}^{(2)}(d^{(2)})$ simply includes the phase produced by the displacement of the interface below the origin a distance $d^{(2)}$. The quantities $T_{\lambda n}^{(2)}(d^{(2)})$ and $T_{mn}^{(3)}$ are, respectively, the projection of the free-field T -matrix for the periodic surface onto spherical basis functions and the free-field T -matrix for the shell onto Floquet basis functions. Since the formal infinite series expansion of $v_{\lambda\lambda'}^{(3)}$, in terms of powers of $A_{\lambda\lambda'}$, may be understood as describing a multiple-scattering process between the rough interface and the shell, $v_{\lambda\lambda'}^{(3)}$ is called the shell-interface multiple-scattering vertex.

The expression for $p^{(1s)}(\mathbf{r})$ given by Eq. (63) shows that $p^{(1s)}(\mathbf{r})$ is a superposition of both Floquet and spherical waves and is given by a sum of five scattering processes: These five scattering processes are shown schematically in Table I. The first term describes free-field scattering of the incident plane wave from surface roughness and the second describes rough surface scattering accompanied by shell-interface multiple scattering. The third term describes scattering from surface roughness of the field produced by plane-wave scattering from an elastic shell accompanied by shell-interface multiple scattering. The fourth process is essentially the inverse of the third and describes scattering from the shell of the field produced by the shell-interface

multiple scatter of the plane-wave scatter from the rough interface. The last term describes plane-wave scattering from the shell accompanied by shell-interface multiple scattering. In the absence of the interface, this term describes free-field scattering from the shell.

The expression for $p^{(1s)}(\mathbf{r})$ shows that it does not exhibit the periodic translational symmetry of the surface roughness nor the spherical symmetry of the shell: The symmetry breaking is complete. Some of the consequences of symmetry breaking may be made apparent by comparing the present problem with a problem considered by Sammelmann and Hackman.⁴ They developed a T -matrix formalism for scattering from a spherical target in a homogeneous waveguide with planar boundaries. They showed that the spherical symmetry is partially broken by the planar boundaries and that the degeneracy of the free-field resonance spectrum of the target is partially removed and exhibits what might be called “fine structure” that depends on the shell-interface separation. In this problem, the symmetry breaking is not complete since there is a residual cylindrical symmetry. In addition, they showed that super-resonant phenomena, i.e., the enhancement of a free-field resonance due to coherent target-interface scattering, are present, and that the monostatic and bistatic scattering strengths of the target are changed relative to their free-field values and depend on incidence angle and shell-interface separation. In the problem being considered here, the surface roughness breaks the residual cylindrical symmetry and it appears that the free-field resonance spectrum of the target may exhibit “hyperfine structure” that depends on the surface roughness. However, scattering from periodic surface roughness causes energy to be scattered out of the specular mode and into higher-order Floquet modes and it is not clear to what extent the scattering strength of the target is changed relative to its free-field value or to the values noted by Sammelmann and Hackman or whether super-resonant phenomena are excited. It is anticipated that the effects of surface roughness and elastic-wave excitation on these phenomena can be shown by numerical calculation and some of these phenomena will be discussed in a subsequent paper devoted to numerical results.

Equation (63) could be used to obtain an approximate expression for $p^{(1s)}(\mathbf{r})$ by replacing the exact form of the roughness profile by the leading terms in its perturbative or small-slope representation. Although such a representation might provide satisfactory numerical results with considerably less computational effort for some special cases, in general, such a procedure would not provide a consistent perturbative or small-slope representation for the entire shell-interface problem since scattering from the rough surface is included in the shell-interface multiple scattering vertex. In the following, the general equations for the shell-interface system are specialized to scattering from arbitrary small-amplitude surface roughness and a perturbative representation for the scattered pressure field is obtained.

V. A PERTURBATIVE SOLUTION FOR SCATTERING FROM ARBITRARY SURFACE ROUGHNESS

In this section, it is assumed that the roughness on the fluid-elastic interface has arbitrary geometry and that

$k_p^{(1)}h < 1$, $k_s^{(2)}h < 1$, and $k_p^{(2)}h < 1$, where $h = \max[h_x, h_y]$, then techniques similar to those used previously^{20–22} are used to obtain a perturbative solution for the scattered pressure field in the fluid. To begin, it is assumed that the scattered-field spectral amplitudes, the surface-field spectral amplitudes, the matrix elements $V_{\gamma\gamma'}^{(2\pm)}(\mathbf{K}_\perp, \mathbf{K}'_\perp)$, and the coupling coefficient $c_{\lambda'}^{(3)}$ may be expanded as power series in hk_γ :

$$p^{(1s)}(\mathbf{K}_\perp) = \sum_{n=0}^{\infty} \frac{(hk_p^{(1)})^n}{n!} p^{(1s,n)}(\mathbf{K}_\perp) \\ = \sum_{n=0}^{\infty} \frac{(hk_p^{(1)})^n}{n!} \frac{1}{(2\pi)^2} \int_{-\infty}^{\infty} d\mathbf{K}'_\perp \\ \times t^{(n)}(\mathbf{K}_\perp, \mathbf{K}'_\perp) p^{(i)}(\mathbf{K}'_\perp), \quad (64)$$

$$u_{\kappa'}^{(2)}(\mathbf{K}'_\perp) = \sum_{m'=0}^{\infty} \frac{(hk_{\kappa'}^{(2)})^{m'}}{m'!} u_{\kappa'}^{(2,m')}(\mathbf{K}'_\perp), \quad (65)$$

$$p^{(2)}(\mathbf{K}'_\perp) = \sum_{m'=0}^{\infty} \frac{(hk_p^{(2)})^{m'}}{m'!} p^{(2,m')}(\mathbf{K}'_\perp), \quad (66)$$

$$V_{\gamma\gamma'}^{(2\pm)}(\mathbf{K}_\perp, \mathbf{K}'_\perp) = v_{\gamma\gamma'}^{(2\pm)}(\mathbf{K}_\perp, \mathbf{K}'_\perp) \\ \times \sum_{m=0}^{\infty} (hk_\gamma)^m v^{(g,m)}(\mathbf{K}_\gamma^{(\pm)}, \mathbf{K}'_\perp), \quad (67a)$$

with

$$k_p^{(1)n} p^{(1s,n)}(\mathbf{K}_\perp) = \frac{1}{(2\pi)^2} \int_{-\infty}^{\infty} d\mathbf{K}'_\perp \sum_{m=0}^n \frac{n!}{m!} k_p^{(1)n-m} v^{[g,(n-m)]}(\mathbf{K}_p^{(1+)}, \mathbf{K}'_\perp) [v_{4\kappa'}^{(2-)}(\mathbf{K}_\perp, \mathbf{K}'_\perp) k_{\kappa'}^{(2)m} u_{\kappa'}^{(2,m)}(\mathbf{K}'_\perp) \\ + v_{44}^{(2-)}(\mathbf{K}_\perp, \mathbf{K}'_\perp) k_p^{(1)m} p^{(1,m)}(\mathbf{K}'_\perp)] e^{iK_{pz}^{(1)}d^{(2)}} - (2\pi)^2 k_p^{(1)2} \sum_{\lambda} \sum_{\lambda'} T_{\lambda:\lambda}^{(3)} k_p^{(1)n} c_{\lambda'}^{(3,n)} b_{\lambda}(\hat{K}_p^{(1+)})], \quad (69)$$

$$-s_{\kappa}^{(n)}(\mathbf{K}_\perp) = \sum_{\kappa'=1}^3 v_{\kappa\kappa'}^{(2+)}(\mathbf{K}_\perp, \mathbf{K}_\perp) k_{\kappa'}^{(2)n} u_{\kappa'}^{(2,n)}(\mathbf{K}_\perp) + v_{\kappa 4}^{(2+)}(\mathbf{K}_\perp, \mathbf{K}_\perp) k_p^{(1)n} p^{(2,n)}(\mathbf{K}_\perp), \quad (70)$$

$$-s_4^{(n)}(\mathbf{K}_\perp) = \sum_{\kappa'=1}^3 v_{4\kappa'}^{(2+)}(\mathbf{K}_\perp, \mathbf{K}_\perp) k_{\kappa'}^{(2)n} u_{\kappa'}^{(2,n)}(\mathbf{K}_\perp) + v_{44}^{(2+)}(\mathbf{K}_\perp, \mathbf{K}_\perp) k_p^{(1)n} p^{(2,n)}(\mathbf{K}_\perp), \quad (71)$$

and

$$-p_{\lambda}^{(i)} \delta_{n,0} = k_p^{(1)n} c_{\lambda}^{(3,n)} + \frac{1}{k_p^{(1)2}} \frac{1}{(2\pi)^2} \int_{-\infty}^{\infty} d\mathbf{K}'_\perp \frac{1}{(2\pi)^2} \int_{-\infty}^{\infty} d\mathbf{K}''_\perp \sum_{m=0}^n \frac{n!}{m!} k_p^{(1)n-m} v^{[g,(n-m)]}(\mathbf{K}'_p^{(1-)}, \mathbf{K}''_\perp) \\ \times [k_{\kappa'}^{(2)m} v_{4\kappa'}^{(2-)}(\mathbf{K}'_\perp, \mathbf{K}''_\perp) u_{\kappa'}^{(2,m)}(\mathbf{K}''_\perp) + k_p^{(1)m} v_{44}^{(2-)}(\mathbf{K}'_\perp, \mathbf{K}''_\perp) p^{(2,m)}(\mathbf{K}''_\perp)] a_{\lambda}(\hat{K}'_p^{(1+)}) e^{iK'_{pz} d^{(2)}}. \quad (72)$$

with the source term $s_{\gamma}^{(n)}(\mathbf{K}_\perp)$ given by

$$v^{(g,m)}(\mathbf{K}^{(\pm)}, \mathbf{K}'_\perp) = \frac{[-i\hat{K}^{(\pm)} \cdot \hat{z}]^m}{m!} \\ \times \tilde{\xi}^{(m)}(\mathbf{K}_\perp - \mathbf{K}'_\perp) \quad (K_z \neq 0) \quad (67b)$$

and

$$c_{\lambda}^{(3)} = \sum_{n=0}^{\infty} \frac{(hk_p^{(1)})^n}{n!} c_{\lambda}^{(3,n)}. \quad (68)$$

In Appendix B, the matrix elements $v_{\gamma\gamma'}^{(2\pm)}(\mathbf{K}_\perp, \mathbf{K}'_\perp)$ are given as well as a description of their derivation from the matrix elements $V_{\gamma\gamma'}^{(2\pm)}(\mathbf{K}_\perp, \mathbf{K}'_\perp)$. The vector $\mathbf{K}_\gamma^{(\pm)} = \mathbf{K}_\perp + [\pm K_{sz}^{(2)}(\delta_{\gamma,1} + \delta_{\gamma,2}) \pm K_{pz}^{(2)}\delta_{\gamma,3} \mp K_{pz}^{(1)}\delta_{\gamma,4}]\hat{z}$ and $k_\gamma = k_s^{(2)}(\delta_{\gamma,1} + \delta_{\gamma,2}) + k_p^{(2)}\delta_{\gamma,3} + k_p^{(1)}\delta_{\gamma,4}$. The term $h\tilde{\xi}^{(m)}(\mathbf{K}'_\perp)$ is the Fourier transform of the m th power of the roughness profile function and $v^{(g,m)}(\mathbf{K}^{(\pm)}, \mathbf{K}'_\perp)$ is the geometric or rough surface vertex function. A representation of $v^{(g,m)}(\mathbf{K}^{(\pm)}, \mathbf{K}'_\perp)$ that is convenient for perturbation theory is given in Appendix B. It is important to note that $v^{(g,0)}(\mathbf{K}^{(\pm)}, \mathbf{K}'_\perp) = (2\pi)^2 \delta(\mathbf{K}_\perp - \mathbf{K}'_\perp)$ and that $v_{1\gamma'}^{(2\pm)}(\mathbf{K}_\perp, \mathbf{K}_\perp) = v_{\gamma 1}^{(2\pm)}(\mathbf{K}_\perp, \mathbf{K}_\perp) = 0$ for $\gamma, \gamma' \neq 1$ so that the SH component of the displacement field is not excited in zeroth order perturbation theory and is decoupled from the other field components for all nonzero orders, i.e., a pressure-wave incident on a planar fluid–elastic interface cannot excite an SH polarized shear wave.

To obtain a representation for $p^{1s,n}(\mathbf{K}_\perp)$, Eqs. (64)–(68) are used in Eqs. (46), (51)–(53) and the resulting equations are evaluated for each order of $(hk)^n$. The equation for the n th-order scattered pressure field spectral amplitude, and rough surface and shell null-field equations are given by

$$\begin{aligned}
s_{\gamma}^{(n)}(\mathbf{K}_{\perp}) &= \left[p^{(i)}(\mathbf{K}_{\perp}) - (2\pi)^2 k_p^{(1)2} \sum_{\lambda} \sum_{\lambda'} T_{\lambda;\lambda'}^{(3)} c_{\lambda'}^{(3,0)} b_{\lambda}(\hat{K}_p^{(1-)}) e^{iK_{pz}^{(1)} d^{(2)}} \right] \delta_{\gamma,4} \quad (n=0), \\
&= \frac{1}{(2\pi)^2} \int_{-\infty}^{\infty} d\mathbf{K}'_{\perp} \sum_{m=0}^{n-1} \frac{n!}{m!} k_{\gamma}^{n-m} v^{[g(n-m)]}(\mathbf{K}_{\gamma}, \mathbf{K}'_{\perp}) [v_{\gamma\kappa}^{(2+)}(\mathbf{K}_{\perp}, \mathbf{K}'_{\perp}) k_{\kappa}^{(2)m} u_{\kappa}^{(2,m)}(\mathbf{K}'_{\perp}) \\
&\quad + v_{\gamma 4}^{(2+)}(\mathbf{K}_{\perp}, \mathbf{K}'_{\perp}) k_p^{(1)m} p^{(1,m)}(\mathbf{K}'_{\perp})] - (2\pi)^2 k_p^{(1)2} \sum_{\lambda} \sum_{\lambda'} T_{\lambda;\lambda'}^{(3)} k_p^{(1)n} c_{\lambda'}^{(3,n)} b_{\lambda}(\hat{K}_p^{(1-)}) e^{iK_{pz}^{(1)} d^{(2)}} \delta_{\gamma,4} \quad (n \neq 0). \quad (73)
\end{aligned}$$

These equations form the basis for the perturbative formalism and are analogous to Eqs. (58)–(62) for scattering from periodic surface roughness. However, since none of the source terms for the n th surface-field spectral amplitudes vanish and since the n th-order source term depends on all the $n-1$ lower-order source terms, the solution to this system of equations is considerably more complicated and tedious than that for the system of equations for periodic roughness.

Since quantities that appear in zeroth-order perturbation theory are fundamental to the perturbative formalism, and since the method used to obtain the zeroth-order solution is similar to that used to obtain the solution for arbitrary order, zeroth-order perturbation theory is considered in detail. At zeroth order, the system of null-field integral equations is a system of linear equations for the unknown surface-field spectral amplitudes. This system of equations is solved and the result used to obtain a solution for $c_{\lambda}^{(3,0)}$ then both results are used to obtain the solution for the zeroth-order T -matrix:

$$\begin{aligned}
t^{(0)}(\mathbf{K}_{\perp}, \mathbf{K}'_{\perp}) &= t^{(2,0)}(\mathbf{K}_{\perp}, \mathbf{K}'_{\perp}; d^{(2)}) + t^{(22,0)}(\mathbf{K}_{\perp}, \mathbf{K}'_{\perp}) \\
&\quad + \sum_{\lambda} t_{\lambda}^{(23,0)}(\mathbf{K}_{\perp}) a_{\lambda}(\hat{K}'_p^{(1-)}) \\
&\quad + (2\pi)^2 \sum_{\lambda} b_{\lambda}(\hat{K}_p^{(1+)}) t_{\lambda}^{(32,0)}(\mathbf{K}'_{\perp}) \\
&\quad + (2\pi)^2 \sum_{\lambda} \sum_{\lambda'} b_{\lambda}(\hat{K}_p^{(1+)}) t_{\lambda\lambda'}^{(33,0)} a_{\lambda'}(\hat{K}'_p^{(1-)}) \quad (74a)
\end{aligned}$$

with the zeroth-order T -matrices

$$t^{(2,0)}(\mathbf{K}_{\perp}, \mathbf{K}'_{\perp}; d^{(2)}) = e^{iK_{pz} d^{(2)}} t^{(2,0)}(\mathbf{K}_{\perp}, \mathbf{K}'_{\perp}) e^{iK'_{pz} d^{(2)}}, \quad (74b)$$

$$\begin{aligned}
t^{(22,0)}(\mathbf{K}_{\perp}, \mathbf{K}'_{\perp}) &= \frac{1}{(2\pi)^2} \int_{-\infty}^{\infty} d\mathbf{K}''_{\perp} \\
&\quad \times t^{(2,0)}(\mathbf{K}_{\perp}, \mathbf{K}''_{\perp}; d^{(2)}) t^{(32,0)}(\mathbf{K}''_{\perp}, \mathbf{K}'_{\perp}), \quad (74c)
\end{aligned}$$

$$\begin{aligned}
t_{\lambda}^{(23,0)}(\mathbf{K}_{\perp}) &= \frac{1}{(2\pi)^2} \int_{-\infty}^{\infty} d\mathbf{K}'_{\perp} t^{(2,0)}(\mathbf{K}_{\perp}, \mathbf{K}'_{\perp}; d^{(2)}) \\
&\quad \times t_{\lambda'}^{(33,0)}(\mathbf{K}_{\perp}), \quad (74d)
\end{aligned}$$

$$t_{\lambda}^{(32,0)}(\mathbf{K}'_{\perp}) = \sum_{\lambda'} t_{\lambda\lambda'}^{(33,0)} t_{\lambda'}^{(2,0)}(\mathbf{K}'_{\perp}; d^{(2)}), \quad (74e)$$

and

$$t_{\lambda\lambda'}^{(33,0)} = \sum_{\lambda''} T_{\lambda;\lambda''}^{(3)} v_{\lambda''\lambda'}^{(3,0)}, \quad (74f)$$

and their projections

$$\begin{aligned}
t_{\lambda}^{(2,0)}(\mathbf{K}'_{\perp}; d^{(2)}) &= \frac{1}{(2\pi)^2} \int_{-\infty}^{\infty} d\mathbf{K}_{\perp} a_{\lambda}(\hat{K}_p^{(1-)}) \\
&\quad \times t^{(2,0)}(\mathbf{K}_{\perp}, \mathbf{K}'_{\perp}; d^{(2)}), \quad (74g)
\end{aligned}$$

$$T_{\lambda}^{(3)}(\mathbf{K}_{\perp}) = \sum_{\lambda'} b_{\lambda'}(\hat{K}_p^{(1-)}) T_{\lambda'\lambda}^{(3)}, \quad (74h)$$

$$t_{\lambda'}^{(33,0)}(\mathbf{K}_{\perp}) = (2\pi)^2 \sum_{\lambda} b_{\lambda'}(\hat{K}_p^{(1-)}) T_{\lambda'\lambda}^{(33)}, \quad (74i)$$

$$t^{(32,0)}(\mathbf{K}_{\perp}, \mathbf{K}'_{\perp}) = \sum_{\lambda} b_{\lambda}(\hat{K}_p^{(1-)}) t_{\lambda}^{(32,0)}(\mathbf{K}'_{\perp}), \quad (74j)$$

and the zeroth-order shell-interface multiple scattering vertex

$$v_{\lambda\lambda'}^{(3,0)} = [\mathbf{I} + \mathbf{A}^{(0)}]_{\lambda\lambda'}^{-1} \quad (74k)$$

with

$$A_{\lambda\lambda'}^{(0)} = - \int_{-\infty}^{\infty} d\mathbf{K}'_{\perp} t_{\lambda}^{(2,0)}(\mathbf{K}'_{\perp}; d^{(2)}) T_{\lambda'\lambda}^{(3)}(\hat{K}'). \quad (74l)$$

To obtain this result, the spherical-wave spectral amplitude of the incident field was projected onto the rectangular basis functions. The quantities defined in Eq. (74) are analogous to the quantities defined in Eq. (63) for periodic roughness: The quantity $T_{\lambda}^{(3)}(\hat{K})$ is the projection of the free-field T -matrix of the shell onto Weyl basis functions; $t^{(2,0)}(\mathbf{K}_{\perp}, \mathbf{K}'_{\perp})$ is the zeroth-order free-field T -matrix for the rough fluid-elastic interface; $t^{(2,0)}(\mathbf{K}_{\perp}, \mathbf{K}'_{\perp}; d^{(2)})$ includes the phase produced by the displacement of the interface below the origin; and $t_{\lambda}^{(2,0)}(\mathbf{K}_{\perp}; d^2)$ is the projection of $t^{(2,0)}(\mathbf{K}_{\perp}, \mathbf{K}'_{\perp}; d^{(2)})$ onto spherical basis functions.

In zeroth-order perturbation theory

$$t^{(2,0)}(\mathbf{K}_{\perp}, \mathbf{K}'_{\perp}) = (2\pi)^2 \delta(\mathbf{K}_{\perp} - \mathbf{K}'_{\perp}) t_{44}^{(2-)}(\mathbf{K}_{\perp}, \mathbf{K}'_{\perp})$$

and $t_{44}^{(2-)}(\mathbf{K}_{\perp}, \mathbf{K}'_{\perp})$ is the 44-element of the matrix

$$\begin{aligned}
t^{(2\pm)}(\mathbf{K}_{\perp}, \mathbf{K}'_{\perp}) &= -[\mathbf{v}^{(2\pm)}(\mathbf{K}_{\perp}, \mathbf{K}'_{\perp}) \\
&\quad \times \mathbf{v}^{(2\pm)}(\mathbf{K}'_{\perp}, \mathbf{K}_{\perp})^{-1}].
\end{aligned}$$

The T -matrix $t_{44}^{(2-)}(\mathbf{K}_{\perp}, \mathbf{K}'_{\perp})$ is given by

$$t_{44}^{(2-)}(\mathbf{K}_{\perp}, \mathbf{K}'_{\perp}) = \frac{A - B}{A + B}, \quad (75a)$$

where

$$A = K_{pz}^{(1)} [(K_{sz}^{(2)} - K_{\perp}^2)^2 + 4K_{\perp}^2 K_{sz}^{(2)} K_{pz}^{(2)}] \quad (75b)$$

and

$$B = \frac{\rho^{(1)}}{\rho^{(2)}} k_s^{(2)4} K_{pz}^{(2)}. \quad (75c)$$

This result agrees with that given by Brekhovskikh²³ for the plane-wave reflection coefficient for a planar fluid–elastic interface. Although at zeroth-order, only $t_{44}^{(2-)}(\mathbf{K}_{\perp}, \mathbf{K}_{\perp})$ occurs, beyond zeroth order, all the elements of the matrix $t^{(2\pm)}(\mathbf{K}_{\perp}, \mathbf{K}'_{\perp})$ occur. The elements of $t^{(2\pm)}(\mathbf{K}_{\perp}, \mathbf{K}'_{\perp})$ and the rough surface vertex function are the fundamental quantities of the perturbative formalism and the n th-order free-field T -matrix for the rough fluid–elastic interface $t^{(2,n)}(\mathbf{K}_{\perp}, \mathbf{K}'_{\perp})$ is expressed entirely in terms of these quantities.

Although Eq. (74) describes the same five scattering process that occurred in the exact solution, the details of the scattering process differ significantly. In particular, in zeroth-order perturbation theory, the interface is planar and the symmetry breaking produced by the interface is not complete: The shell-interface system retains cylindrical symmetry and phenomena similar to those noted by Sammelmann and Hackman should be excited.

To begin the calculation of n th-order scattering, it is necessary to obtain a solution for the n th-order surface-field spectral amplitudes. However, Eq. (73) shows that the source terms for the n th-order surface-field spectral amplitudes depend on all the $n-1$ lower-order surface-field spectral amplitudes. Therefore, it is necessary to solve these equations iteratively. The result of this process is used in the equations for the spectral amplitude of the scattered pressure field and the equation for the coefficient $c_{\lambda}^{(3,n)}$. After a very lengthy calculation, $p^{(1s,n)}(\mathbf{K}_{\perp})$ and $c^{(3,n)}$ are given by

$$\begin{aligned} p^{(1s,n)}(\mathbf{K}_{\perp}) &= \frac{1}{(2\pi)^2} \int_{-\infty}^{\infty} d\mathbf{K}'_{\perp} t^{(2,n)}(\mathbf{K}_{\perp}, \mathbf{K}'_{\perp}; d^{(2)}) \\ &\quad \times p^{(i)}(\mathbf{K}'_{\perp}) - (2\pi)^2 k_p^{(1)2} \\ &\quad \times \sum_{\lambda} \sum_{\lambda'} T_{\lambda;\lambda'}^{(3)} c_{\lambda'}^{(3,n)} b_{\lambda}(\hat{K}_p^{(1+)}) \\ &\quad - k_p^{(1)2} \int_{-\infty}^{\infty} d\mathbf{K}'_{\perp} \sum_{m=0}^n \frac{n!}{(n-m)!} \frac{1}{m!} \\ &\quad \times t^{(2,n-m)}(\mathbf{K}_{\perp}, \mathbf{K}'_{\perp}; d^{(2)}) \sum_{\lambda} T_{\lambda}^{(3)}(\hat{K}') c_{\lambda}^{(3,m)} \end{aligned} \quad (76)$$

and

$$\begin{aligned} k_p^{(1)2} c_{\lambda}^{(3,n)} &= -k_p^{(1)2} p_{\lambda}^{(i)} \delta_{n,0} - \frac{1}{(2\pi)^2} \int_{-\infty}^{\infty} d\mathbf{K}'_{\perp} \sum_{\lambda'} v_{\lambda\lambda'}^{(3,0)} \\ &\quad \times t_{\lambda'}^{(2,n)}(\mathbf{K}'_{\perp}; d^{(2)}) p^{(i)}(\mathbf{K}'_{\perp}) \\ &\quad + k_p^{(1)2} \int_{-\infty}^{\infty} d\mathbf{K}'_{\perp} \sum_{\lambda'} \sum_{m=0}^{n-1} \frac{n!}{m!(n-m)!} \\ &\quad \times v_{\lambda\lambda'}^{(3,0)} t_{\lambda'}^{(2,n-m)}(\mathbf{K}'_{\perp}) T_{\lambda'}^{(3)}(\hat{K}') c_{\lambda'}^{(3,m)}. \end{aligned} \quad (77)$$

To complete the solution, Eq. (77) is iterated so that $c_{\lambda}^{(3,n)}$ is expressed in terms of the spectral amplitudes of the incident field. This calculation is simplified somewhat by noting that the equations for $c_{\lambda}^{(3,n)}$ and $s_{\gamma}^{(2,n)}(\mathbf{K}_{\perp})$ have similar functional forms, so that the solution for $s_{\gamma}^{(2,n)}(\mathbf{K}_{\perp})$ may be used to construct the solution for $c_{\lambda}^{(3,n)}$. After a very lengthy calculation, the n th-order T -matrix for the scattered pressure field spectral amplitudes is given by

$$\begin{aligned} \frac{1}{n!} t^{(n)}(\mathbf{K}_{\perp}, \mathbf{K}'_{\perp}) &= \frac{1}{n!} t^{(2,n)}(\mathbf{K}_{\perp}, \mathbf{K}'_{\perp}; d^{(2)}) \\ &\quad + t^{(22,n)}(\mathbf{K}_{\perp}, \mathbf{K}'_{\perp}) \\ &\quad + \sum_{\lambda} t_{\lambda}^{(23,n)}(\mathbf{K}_{\perp}) a_{\lambda}(\hat{K}'_p^{(1-)}) \\ &\quad + (2\pi)^2 \sum_{\lambda} b_{\lambda}(\hat{K}'_p^{(1+)}) t_{\lambda}^{(32,n)}(\mathbf{K}'_{\perp}) \\ &\quad + (2\pi)^2 \sum_{\lambda} \sum_{\lambda'} b_{\lambda}(\hat{K}'_p^{(1+)}) \\ &\quad \times t_{\lambda\lambda'}^{(33,n)} a_{\lambda'}(\hat{K}'_p^{(1-)}) \end{aligned} \quad (78a)$$

with the n th-order T -matrices

$$t^{(2,n)}(\mathbf{K}_{\perp}, \mathbf{K}'_{\perp}; d^{(2)}) = e^{iK_{pz}d^{(2)}} t^{(2,n)}(\mathbf{K}_{\perp}, \mathbf{K}'_{\perp}) e^{iK'_{pz}d^{(2)}}, \quad (78b)$$

$$\begin{aligned} t^{(22,n)}(\mathbf{K}_{\perp}, \mathbf{K}'_{\perp}) &= \frac{1}{(2\pi)^2} \int_{-\infty}^{\infty} d\mathbf{K}''_{\perp} \sum_{m=0}^n \frac{1}{(n-m)!} \\ &\quad \times t^{(2,n-m)}(\mathbf{K}_{\perp}, \mathbf{K}''_{\perp}; d^{(2)}) \\ &\quad \times t^{(32,m)}(\mathbf{K}''_{\perp}, \mathbf{K}'_{\perp}), \end{aligned} \quad (78c)$$

$$\begin{aligned} t_{\lambda}^{(23,n)}(\mathbf{K}_{\perp}) &= \frac{1}{(2\pi)^2} \int_{-\infty}^{\infty} d\mathbf{K}'_{\perp} \sum_{m=0}^n \frac{1}{(n-m)!} \\ &\quad \times t^{(2,n-m)}(\mathbf{K}_{\perp}, \mathbf{K}'_{\perp}; d^{(2)}) t_{\lambda}^{(33,m)}(\mathbf{K}_{\perp}) \end{aligned} \quad (78d)$$

$$\begin{aligned} t_{\lambda}^{(32,n)}(\mathbf{K}'_{\perp}) &= \sum_{\lambda'} t_{\lambda\lambda'}^{(33,n)} V_{\lambda'}^{(3,0)}(\mathbf{K}'_{\perp}) + \sum_{\lambda'} t_{\lambda\lambda'}^{(33,0)} V_{\lambda'}^{(3,n)}(\mathbf{K}'_{\perp}) \\ &= \sum_{\lambda'} [t_{\lambda\lambda'}^{(33,n)} t_{\lambda'}^{(2,0)}(\mathbf{K}'_{\perp}; d^{(2)}) \\ &\quad + t_{\lambda\lambda'}^{(33,0)} V_{\lambda'}^{(3,n)}(\mathbf{K}'_{\perp})], \end{aligned} \quad (78e)$$

and

$$t_{\lambda\lambda'}^{(33,n)} = \frac{1}{(2\pi)^2} \int_{-\infty}^{\infty} d\mathbf{Q}_{\perp} \sum_{\lambda''} t_{\lambda\lambda''}^{(33,0)} V_{\lambda''}^{(3,n)}(\mathbf{Q}_{\perp}) t_{\lambda'}^{(33,0)}(\mathbf{Q}_{\perp}; d^{(2)}), \quad (78f)$$

and their projections

$$t_{\lambda}^{(2,n)}(\mathbf{K}'_{\perp}; d^{(2)}) = \frac{1}{(2\pi)^2} \int_{-\infty}^{\infty} d\mathbf{K}_{\perp} a_{\lambda}(\hat{K}_p^{(1-)}) \times t^{(2,n)}(\mathbf{K}_{\perp}, \mathbf{K}'_{\perp}; d^{(2)}), \quad (78g)$$

$$t_{\lambda'}^{(33,n)}(\mathbf{K}_{\perp}) = (2\pi)^2 \sum_{\lambda} b_{\lambda'}(\hat{K}_p^{(1-)}) t_{\lambda'\lambda}^{(33,n)}, \quad (78h)$$

$$t^{(32,n)}(\mathbf{K}_{\perp}, \mathbf{K}'_{\perp}) = \sum_{\lambda} b_{\lambda}(\hat{K}_p^{(1-)}) t_{\lambda}^{(32,n)}(\mathbf{K}'_{\perp}), \quad (78i)$$

and the vertex $V_{\lambda''}^{(3,n)}(\mathbf{Q}_{\perp})$ is given by

$$\begin{aligned} V_{\lambda''}^{(3,n)}(\mathbf{Q}_{\perp}) = & \frac{1}{n!} \left[t_{\lambda''}^{(2,n)}(\mathbf{Q}_{\perp}; d^{(2)}) (1 - \delta_{n,1}) + \sum_{\lambda_1} \sum_{m_1=1}^{n-1} \mathscr{W}_{\lambda''\lambda_1}^{(n-m_1)} \frac{1}{(2\pi)^2} \int_{-\infty}^{\infty} d\mathbf{Q}_{\perp} t_{\lambda_1}^{(2,m_1)}(\mathbf{Q}_{\perp}; d^{(2)}) (1 - \delta_{n,1} - \delta_{n,2}) \right. \\ & + \sum_{\lambda_1} \sum_{\lambda_2} \sum_{m_2=2}^{n-1} \sum_{m_1=m_2}^{n-1} \mathscr{W}_{\lambda''\lambda_1}^{(n-m_1)} \mathscr{W}_{\lambda_1\lambda_2}^{(m_1-m_2+1)} t_{\lambda_2}^{(2,m_2-1)}(\mathbf{Q}_{\perp}; d^{(2)}) (1 - \delta_{n,1} - \delta_{n,2} - \delta_{n,3}) + \dots \\ & + \sum_{\lambda_1} \sum_{\lambda_2} \dots \sum_{\lambda_{n-2}} \sum_{m_{n-2}=n-2}^{n-1} \sum_{m_{n-3}=m_{n-2}}^{n-1} \dots \sum_{m_1=m_2}^{n-1} \mathscr{W}_{\lambda''\lambda_1}^{(n-m_1)} \mathscr{W}_{\lambda_1\lambda_2}^{(m_1-m_2+1)} \dots \mathscr{W}_{\lambda_{n-3}\lambda_{n-2}}^{(m_{n-3}-m_{n-2}+1)} \\ & \times t_{\lambda_{n-2}}^{(2,m_{n-2}-n+3)}(\mathbf{Q}_{\perp}; d^{(2)}) (1 - \delta_{n,1} - \delta_{n,2} - \dots) \\ & \left. + \sum_{\lambda_1} \sum_{\lambda_2} \dots \sum_{\lambda_{n-1}} \mathscr{W}_{\lambda''\lambda_1}^{(1)} \mathscr{W}_{\lambda_1\lambda_2}^{(1)} \dots \mathscr{W}_{\lambda_{n-2}\lambda_{n-1}}^{(1)} t_{\lambda_{n-1}}^{(2,1)}(\mathbf{Q}_{\perp}; d^{(2)}) \right], \quad (78j) \end{aligned}$$

with

$$\mathscr{W}_{\lambda\lambda'}^{(n)} = \frac{1}{n!} \frac{1}{(2\pi)^2} \int_{-\infty}^{\infty} d\mathbf{Q}_{\perp} t_{\lambda}^{(2,n)}(\mathbf{Q}_{\perp}; d^{(2)}) t_{\lambda'}^{(33,0)}(\mathbf{Q}_{\perp}). \quad (78k)$$

Although the expression for $t^{(n)}(\mathbf{K}_{\perp}, \mathbf{K}'_{\perp})$ is qualitatively similar to $t^{(0)}(\mathbf{K}_{\perp}, \mathbf{K}'_{\perp})$ and describes the same five scattering processes, the fields that are involved are considerably more complicated since, among other factors, they are expressed in terms of products of the vertex function $\mathscr{W}_{\lambda\lambda'}^{(m)}$ in much the same way that $t^{(2,n)}(\mathbf{K}_{\perp}, \mathbf{K}'_{\perp})$ is expressed in terms of products of the vertex function $\mathscr{V}_{\gamma\sigma}^{(2,n)}(\mathbf{Q}_{\gamma}, \mathbf{Q}'_{\sigma})$ [see Eq. (B11)].

Although the general expression for $t^{(n)}(\mathbf{K}_{\perp}, \mathbf{K}'_{\perp})$ is formidable, the scattering processes described by $t^{(n)}(\mathbf{K}_{\perp}, \mathbf{K}'_{\perp})$ can be made transparent by constructing its diagrammatic representation. Examination of $t^{(n)}(\mathbf{K}_{\perp}, \mathbf{K}'_{\perp})$ shows that there are two fundamental scattering elements; the shell-interface multiple-scattering vertex function $T_{\lambda}^{(3)}(\mathbf{Q}_{\perp}) v_{\lambda\lambda'}^{(3,0)}$ and the rough surface vertex function $\mathscr{V}_{\gamma\gamma'}^{(2,n)}(\mathbf{Q}_{\gamma}, \mathbf{Q}'_{\gamma'})$: The shell-interface vertex function describes the multiple scattering that occurs between the shell and a planar fluid-elastic interface even in n th order. The rough surface vertex functions describe three processes: $\mathscr{V}_{44}^{(2,n)}(\mathbf{Q}_4, \mathbf{Q}'_4)$ describes a scalar scattering process in which the incident pressure field scatters without mode conversion; $\mathscr{V}_{4\kappa'}^{(2,n)}(\mathbf{Q}_4, \mathbf{Q}'_{\kappa'})$ and $\mathscr{V}_{\kappa\kappa'}^{(2,n)}(\mathbf{Q}_{\kappa}, \mathbf{Q}'_{\kappa'})$ describe vector scattering process in which the incident pressure field scatters and mode converts to a displacement field and vice versa; and $\mathscr{V}_{\kappa\kappa'}^{(2,n)}(\mathbf{Q}_{\kappa}, \mathbf{Q}'_{\kappa'})$ describes a tensor scattering process in which a displacement field scatters and mode converts. Table II shows the correspondence between the mathematical expression and graphical representation for each type of scattering process. To

simplify the diagrammatics, the shell-interface multiple-scattering vertex is represented by a single graphical element in which the double-pointed arrow indicates the infinite shell-interface multiple-scattering series and a single sawtooth line is used to represent any of the three polarization states of the displacement field. However, when scattering from a zeroth-order geometric vertex, $t_{\gamma}^{(2,0)}(\mathbf{K}_{\perp}, \mathbf{K}'_{\perp}) = t_{1\gamma}^{(2,0)}(\mathbf{K}_{\perp}, \mathbf{K}'_{\perp}) = 0$ for $\gamma \neq 1$ so that the SH polarization state is decoupled completely from all other states and diagrams that include these processes should be neglected. Wavy lines are used to indicate scattering from the rough surface and the number of lines indicates the number of times scattering from the rough surface occurs. The open circle is used to indicate that the wave numbers of the incident and scattered states and the transverse wave numbers of the surface interaction are constrained by the delta function that appears in Eq. (B10). The rules that determine the manner in which these fundamental vertices are iterated are determined by $t^{(n)}(\mathbf{K}_{\perp}, \mathbf{K}'_{\perp})$ and are given in Table III. These rules determine the diagrammatic representation of $t^{(n)}(\mathbf{K}_{\perp}, \mathbf{K}'_{\perp})$ and, conversely, may be used to construct the analytic expression for any scattering diagram.

The diagrammatic representation of $T(\mathbf{K}_{\perp}, \mathbf{K}'_{\perp})$ through first order is shown in Fig. 3. To simplify the diagrammatics, all first-order rough surface vertices are shown enclosed in a box. The complete diagrammatic representation of the scattering process is obtained by connecting all rough surface vertices within each box to the shell-interface multiple-scattering vertices exterior to the box. The first four diagrams in the series represent free-field scattering from the rough interface: The first diagram of this series is a zeroth-order diagram and represents coherent scattering from a planar fluid-elastic interface. The next three diagrams are first-order diagrams and represent scattering from the surface

TABLE II. Fundamental vertices for scattering a pressure wave from an elastic shell in proximity to a rough fluid-elastic interface.

Mathematical representation	Graphical representation
1. $t_{44}^{(\pm)}(\mathbf{K}_\perp, \mathbf{K}'_\perp) v^{(gm)}(\mathbf{K}_p^{(1\pm)}, \mathbf{K}'_\perp)$	
2. $t_{\kappa\kappa'}^{(\pm)}(\mathbf{K}_\perp, \mathbf{K}'_\perp) v^{(gm)}(\mathbf{K}_\kappa^{(2+)}, \mathbf{K}'_\perp)$	
3. $t_{\kappa\kappa'}^{(\pm)}(\mathbf{K}'_\perp, \mathbf{K}'_\perp) v^{(gm)}(\mathbf{K}_p^{(1\pm)}, \mathbf{K}'_\perp)$	
4. $t_{\kappa\kappa'}^{(\pm)}(\mathbf{K}_\perp, \mathbf{K}'_\perp) v^{(gm)}(\mathbf{K}_\kappa^{(2+)}, \mathbf{K}'_\perp)$	
5. $T_{\lambda\lambda'}^{(3)}(\mathbf{Q}_\perp) v_{\lambda\lambda'}^{(3)}$	

—→ fluid pressure field
 ~~~→ surface displacement field  
 ~~~→ surface field

without excitation of intermediate surface-field states and scattering in which intermediate surface pressure and displacement field states are excited, propagated, and then scattered from a planar fluid-elastic interface. So that even in first-order perturbation theory multiple scattering on the rough surface occurs. Although it is not apparent in the first-order diagrams, in general, there are two types of multiple scattering on the rough surface; (1) multiple scattering between vertices with a single-surface interactions that occurs with excitation and propagation of intermediate surface-field states and (2) multiple scattering from a single vertex with multiple-surface interactions that occurs without excitation and propagation of intermediate surface pressure and displacement field states. These latter multiple-scattering diagrams represent scattering from the rough surface at points that are displaced vertically from the same location in the horizontal plane.

These figures show that the total field consists of a sum of spherical-wave modes scattered from the shell and the Weyl wave modes scattered from the rough interface and that each of these fields is produced in two ways: Scattering from the shell is produced by the scatter of the incident field and the field scattered from the rough surface and, similarly,

scattering from the rough interface is produced by the scatter of the incident field and the field produced by shell-planar interface multiple scattering. In addition, it is shown that the multiple-scattering processes on the rough interface and be-

TABLE III. Diagrammatic rules for scattering from an elastic shell in proximity to a fluid-elastic interface.

1. Construct all topologically distinct diagrams consistent with the fundamental vertices.
2. Include a factor $a_{\lambda'}(\mathbf{K}'_p^{(1-)})$ for each external line incident on the shell.
3. Include a factor $T_{\lambda\lambda'}^{(3)}(\mathbf{Q}'_\perp) v_{\lambda\lambda'}^{(3)}$, for each multiple-scattering vertex. (The index λ' denotes the spectrum of spherical waves incident on the multiple-scattering vertex; λ'' denotes the spectrum of spherical waves incident on the shell; and the wave vector \mathbf{Q}'_\perp is the wave vector of the field scattered from the shell.)
4. Include a factor $t_{\lambda\lambda'}^{(2,n)}(\mathbf{Q}'_\perp; d^{(2)})$ for each internal n -th order rough surface vertex. (The wave vector \mathbf{Q}'_\perp is the incident wave vector and λ'' denotes the spectrum of spherical waves scattered from the rough surface.)
5. Include a factor $1/m!$ for each m th-order rough surface vertex. (The order of a vertex is determined by the number of surface interactions.)
6. Integrate over all internal wave numbers.
7. Sum over all spherical wave modes.

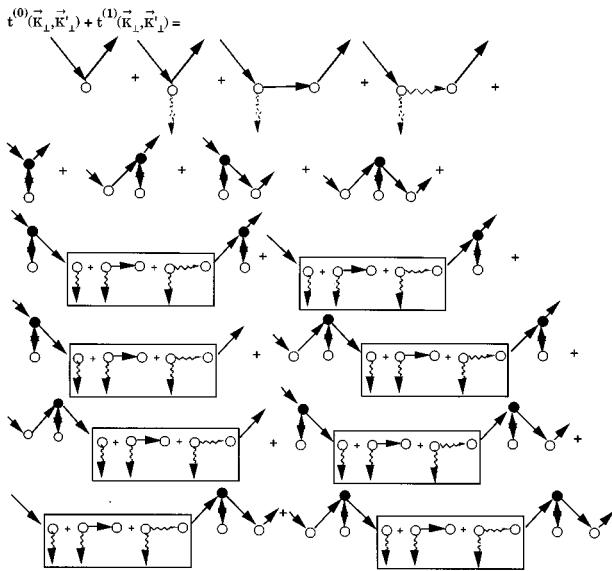


FIG. 3. Diagrammatic representation of the first-order T -matrix for scattering from an elastic shell in proximity to a rough fluid-elastic interface.

tween the shell and the planar interface are independent and that the total scattering amplitude is obtained by inserting rough surface multiple-scattering vertices into shell-interface multiple-scattering vertices and vice versa.

The same shell-interface multiple-scattering vertex that occurs in n th-order is the same vertex that occurs in zeroth order. Therefore, rough surface symmetry breaking phenomena do not occur as a result of shell-interface multiple-scattering, but occur when the field produced by the shell-interface multiple scatter, is scattered from the rough surface. In general, however, the successive scattering of the shell-interface multiple scatter from the rough surface may significantly change phenomena that arise due to shell-interface coherent scattering. The extent to which surface roughness and mode conversion effect super-resonant and similar phenomena needs to be determined numerically.

In general, perturbative formalisms of scattering from a rough fluid-elastic interface are subject to divergent phenomena when the transverse wave number approaches a Stoneley wave pole and in the formalism described in this paper, a Stoneley wave occurs when the determinant $|\mathbf{v}^{(2)}(\mathbf{Q}'_\perp; \mathbf{Q}'_\perp)|=0$. Since $\mathbf{v}^{(2)}(\mathbf{Q}'_\perp; \mathbf{Q}'_\perp)$ is the matrix of coefficients of the zeroth-order surface-field spectral amplitudes, the equations that determine the phase speed of the Stoneley wave do not depend on the order of perturbation and the SH component of the displacement field is not a component of the Stoneley wave. It has been shown that it is always possible to excite a Stoneley wave with a phase speed $c \leq \min(c_p^{(1)}, c_s^{(2)})$ (Ref. 24) so that ω/c is greater than $k_p^{(1)}$, $k_p^{(2)}$, and $k_s^{(2)}$ and the z component of the wave vectors in the fluid and solid are imaginary and the Stoneley wave is constrained to the interface region. Since the perturbative representation of the rough surface T -matrix contains doubly infinite integrals over transverse wave numbers, in general, Stoneley waves are excited and the transverse wave number integrations need to be treated carefully.

Dacol and Berman²⁰ calculated scattering from a ran-

domly rough surface that depended on a single horizontal coordinate so that the horizontal wave number integration was one dimensional. They showed that when a Stoneley wave is excited, it is necessary to evaluate the residue at the pole of the Stoneley wave and to evaluate a principal value integral, and that the contribution from the Stoneley wave to the coherent field reflection coefficient for a randomly rough fluid-elastic interface is strongest when the compressional and shear waves are evanescent. If the formalism described in this paper is applied to scattering from a fluid-elastic interface with random roughness, the integrals over horizontal wave numbers that occur in the perturbative representation of the rough surface T -matrix would have to be evaluated in a similar manner. In the shell-interface scattering problem described in this paper, Stoneley wave contributions may be particularly important in the shell-interface multiple-scattering process, especially when the shell is close to the interface.

VI. CONCLUSIONS

It was shown that when scattering from an elastic target in proximity to a rough fluid-elastic interface, the scattered field is produced by five separate scattering process: The first process is simply free-field scattering from the rough surface. The second two processes involve scattering from the shell in the presence of a rough interface and include scattering from the shell of the incident field and the field scattered from the rough interface. The last two processes involve scattering from the rough surface in the presence of the shell and include scattering from the rough surface of the incident field and the field scattered from the shell. Therefore the scattered field is a superposition of spherical wave modes scattered from the shell and Floquet (Weyl) wave modes scattered from a fluid-elastic interface with periodic (random) roughness. The form of the T -matrix suggests that surface roughness and elastic effects, i.e., Stoneley wave excitations, may effect excitation of super-resonant phenomena and that the symmetry breaking produced by nonisotropic surface roughness may split the free-field resonances of the shell by an amount that depends on the surface roughness.

When considering the effects of surface roughness on phenomena that depend on coherent shell-interface scattering, it may be more appropriate to consider a multiple-scattering representation of the rough surface T -matrix or the small-slope approximation of Voronovich²⁵ in which the exact form of the rough surface phase appears. The small-slope approximation for a rough fluid-elastic interface was derived by Berman²⁶ and used by himself and more recently by Yang and Borschat²⁷ to calculate scattering from such a surface. The application of this formalism to the present problem is very interesting and may be considered following numerical calculations.

Although the perturbative representation of the shell-interface T -matrix appears formidable, when the fundamental components are understood, it provides a very intuitive description of shell-interface scattering. From a computational point of view, perturbation theory is usually limited to a few low orders, so that considerable simplification occurs. The free-field perturbative formalism described here has

been applied to free-field scattering from periodic roughness through fourth order and Dacol and Berman have applied a similar formalism to scattering from arbitrary surface roughness through second order and, as already noted, they included Stoneley wave contributions. T -matrices for elastic shells and spheres are well known and do not present any computational problems that would prevent numerical evaluation of the shell-interface scattering problem as described here. Therefore, aside from constructing the rescattering terms in the perturbative representation of the T -matrix, the most difficult computational problem is to determine the Stoneley wave poles and to evaluate the corresponding residues.

Although the ‘‘exact’’ form of the T -matrix appears simpler than the perturbative form, to obtain an ‘‘exact’’ solution it is necessary to solve the system of coupled linear equations for the surface pressure and displacement fields on the rough interface. Therefore, although the formalism is not limited physically to rough surfaces with small amplitudes or slopes, the maximum order of the system of linear equations that can be solved imposes numerical constraints on the physical parameters that can be considered. Since Stoneley wave excitation can be avoided when scattering from periodic surface roughness, the most formidable computational problem is the evaluation of the rough surface T -matrix. Both forms of the shell-interface T -matrix are being coded and will be used to generate extensive numerical results which will be reported in a subsequent paper.

ACKNOWLEDGMENT

This work was funded by the Naval Undersea Warfare Center Division Newport Independent Research program managed by Dr. K. M Lima.

APPENDIX A: EVALUATION OF MATRIX ELEMENTS FOR A SPHERICAL SHELL

In the following, the matrix elements for a spherical shell are cataloged:

$$\begin{aligned} B_{\lambda\sigma;\kappa'\lambda'}^{(n)} &= i(\xi_p^{(n)}/\rho^{(n)})^2 \int_{s^{(n)}} dS'^{(n)} \psi_{\lambda\sigma}(\mathbf{r}'; \xi_p^{(n)}/\rho^{(n)}) \\ &\quad \times \hat{n}^{(n)}(\mathbf{r}') \cdot \mathbf{Y}_{\kappa'\lambda'}(\theta', \phi') \\ &= i \xi_p^{(n)2} z_\nu^{(\sigma)}(\xi_p^{(n)}) \delta_{\kappa'3} \delta_{\lambda,\lambda'}, \end{aligned} \quad (A1)$$

$$\begin{aligned} P_{\kappa\lambda\sigma;\lambda'}^{(n)} &= \frac{i\Lambda^{(n)} \xi_p^{(n)} \zeta_s^{(3)}}{\mu^{(3)} \rho^{(n)2}} \int_{s^{(n)}} dS'^{(n)} \hat{n}^{(n)}(\mathbf{r}') \\ &\quad \cdot \Psi_{\kappa\lambda\sigma}(\mathbf{r}'; k_\kappa^{(3)}) Y_{\lambda'}(\theta', \phi') \\ &= \frac{i\Lambda^{(n)} \xi_p^{(n)} \zeta_s^{(n)}}{\mu^{(3)}} \left\{ \sqrt{\nu(\nu+1)} \frac{z_\nu^{(\sigma)}(\zeta_s^{(n)})}{\zeta_s^{(3)}} \delta_{\kappa,2} \right. \\ &\quad \left. + \left(\frac{\zeta_p^{(n)}}{\zeta_s^{(n)}} \right)^{3/2} \frac{d}{d\zeta_p^{(n)}} z_\nu^{(\sigma)}(\zeta_p^{(n)}) \delta_{\kappa,3} \right\} \delta_{\lambda,\lambda'}, \end{aligned} \quad (A2)$$

$$\begin{aligned} Q_{\lambda\sigma;\lambda'}^{(n)} &= i(\xi_p^{(n)}/\rho^{(n)}) \int_{s^{(n)}} dS'^{(n)} \hat{n}^{(n)}(\mathbf{r}') \\ &\quad \cdot \nabla' \psi_{\lambda\sigma}(\mathbf{r}'; \xi_p^{(n)}/\rho^{(n)}) Y_{\lambda'}(\theta', \phi') \\ &= i \xi_p^{(n)2} \frac{\partial}{\partial \xi_p^{(n)}} z_\nu^{(\sigma)}(\xi_p^{(n)}) \delta_{\lambda,\lambda'}, \end{aligned} \quad (A3)$$

and

$$\begin{aligned} R_{\kappa\lambda\sigma;\kappa'\lambda'}^{(n)} &= \frac{ik_s^{(3)}}{\mu^{(3)}} \int_{s^{(n)}} dS'^{(n)} \{ \lambda^{(3)} \nabla' \cdot \Psi_{3\lambda\sigma}(\mathbf{r}'; k_\kappa^{(3)}) \hat{n}^{(n)}(\mathbf{r}') \cdot \mathbf{Y}_{\kappa'\lambda'}(\theta', \phi') \delta_{\kappa,3} + \mu^{(3)} \mathbf{Y}_{\kappa'\lambda'}(\theta', \phi') \\ &\quad \cdot \hat{n}^{(n)}(\mathbf{r}') \cdot [\nabla' \Psi_{\kappa\lambda\sigma}(\mathbf{r}'; k_\kappa^{(3)}) + \Psi_{\kappa\lambda\sigma}(\mathbf{r}'; k_\kappa^{(3)}) \nabla'] \} \\ &= i \xi_s^{(n)2} \delta_{\lambda,\lambda'} \left\{ \zeta_s^{(n)} \frac{d}{d\zeta_s^{(n)}} \left(\frac{z_\nu^{(\sigma)}(\zeta_s^{(n)})}{\zeta_s^{(n)}} \right) \delta_{\kappa,1} \delta_{\kappa',1} + \delta_{\kappa,2} \delta_{\kappa',2} \left[\frac{d^2}{d\zeta_s^{(n)2}} z_\nu^{(\sigma)}(\zeta_s^{(n)}) + \frac{\nu(\nu+1)-2}{\zeta_s^{(n)2}} z_\nu^{(\sigma)}(\zeta_s^{(n)}) \right] \right. \\ &\quad + \delta_{\kappa,2} \delta_{\kappa',3} 2\sqrt{\nu(\nu+1)} \frac{d}{d\zeta_s^{(n)}} \left(\frac{z_\nu^{(\sigma)}(\zeta_s^{(n)})}{\zeta_s^{(n)}} \right) + \delta_{\kappa,3} \delta_{\kappa',2} 2\sqrt{\nu(\nu+1)} \left(\frac{\zeta_p^{(n)}}{\zeta_s^{(n)}} \right)^{5/2} \frac{d}{d\zeta_p^{(n)}} \left(\frac{z_\nu^{(\sigma)}(\zeta_p^{(n)})}{\zeta_p^{(n)}} \right) \\ &\quad \left. + \delta_{\kappa,3} \delta_{\kappa',3} \left(\frac{\zeta_p^{(n)}}{\zeta_s^{(n)}} \right)^{5/2} \left[2 \frac{d^2 z_\nu^{(\sigma)}(\zeta_p^{(n)})}{d\zeta_p^{(n)2}} - \frac{\lambda^{(3)}}{\mu^{(3)}} z_\nu^{(\sigma)}(\zeta_p^{(n)}) \right] \right\} \quad (n=3,4) \end{aligned} \quad (A4)$$

with $\rho^{(3)}=b$, $\rho^{(4)}=a$, $\xi_p^{(3)}=k_p^{(1)}\rho^{(3)}$, $\xi_p^{(4)}=k_p^{(4)}\rho^{(4)}$, $\zeta_s^{(3)}=k_s^{(3)}\rho^{(3)}$, $\zeta_s^{(4)}=k_s^{(3)}\rho^{(4)}$, $\zeta_p^{(3)}=k_p^{(3)}\rho^{(3)}$, $\zeta_p^{(4)}=k_p^{(3)}\rho^{(4)}$, $\Lambda^{(3)}=\lambda^{(1)}$, and $\Lambda^{(4)}=\lambda^{(4)}$. The expression for $R_{\kappa\lambda\sigma;\kappa'\lambda'}^{(3)}$ was obtained by using the representation for the dyadic $\nabla\mathbf{A}+\mathbf{A}\nabla$ in spherical coordinates given by Morse and Feshbach.²⁸

APPENDIX B: MATRIX ELEMENTS FOR A ROUGH FLUID-ELASTIC INTERFACE

For arbitrary surface roughness, the matrix elements for the elastic solid in terms of nonperiodic rectangular basis functions are given by

$$V_{\kappa\kappa'}^{(2\pm)}(\mathbf{K}_\perp, \mathbf{K}'_\perp) = -\frac{i}{2} \frac{k_\kappa^{(2)^2}}{k_{\kappa'}^{(2)^2}} \frac{1}{K_{\kappa z}^{(2)}} \int_{-\infty}^{\infty} d\mathbf{r}'_\perp \{ \mathbf{n}^{(2)}(\mathbf{r}') \cdot [\nabla' \hat{X}_\kappa(-\mathbf{r}'; \mathbf{K}_\kappa^{(2\pm)}) + \hat{X}_\kappa(-\mathbf{r}'; \mathbf{K}_\kappa^{(2\pm)}) \nabla'] \} \cdot \hat{X}_{\kappa'}(\mathbf{r}'_\perp; \mathbf{K}'_\perp) \quad (\kappa=1,2; \kappa'=1-3), \quad (\text{B1a})$$

$$V_{3\kappa'}^{(2\pm)}(\mathbf{K}_\perp, \mathbf{K}'_\perp) = -\frac{i}{2} \frac{k_p^{(2)} k_s^{(2)}}{k_{\kappa'}^{(2)^2} K_{pz}^{(2)}} \int_{-\infty}^{\infty} d\mathbf{r}'_\perp \times \left\{ \mathbf{n}^{(2)}(\mathbf{r}') \cdot [\nabla' \hat{X}_3(-\mathbf{r}'; \mathbf{K}_p^{(2\pm)}) + \hat{X}_3(-\mathbf{r}'; \mathbf{K}_p^{(2\pm)}) \nabla'] + \frac{\lambda^{(2)}}{\mu^{(2)}} \mathbf{n}^{(2)}(\mathbf{r}') \nabla' \cdot \hat{X}_3(-\mathbf{r}'; \mathbf{K}_p^{(2\pm)}) \right\} \cdot \hat{X}_{\kappa'}(\mathbf{r}'_\perp; \mathbf{K}'_\perp) \quad (\kappa'=1-3), \quad (\text{B1b})$$

$$V_{\kappa 4}^{(2\pm)}(\mathbf{K}_\perp, \mathbf{K}'_\perp) = -\frac{i}{2} \frac{\lambda^{(1)} k_s^{(2)} k_\kappa^{(2)}}{\mu^{(2)} k_p^{(1)} K_{\kappa z}^{(2)}} \int_{-\infty}^{\infty} d\mathbf{r}'_\perp \times \mathbf{n}^{(2)}(\mathbf{r}') \cdot \hat{X}_\kappa(-\mathbf{r}'; \mathbf{K}_\kappa^{(2\pm)}) \times \chi(\mathbf{r}'_\perp; \mathbf{K}'_\perp) \quad (\kappa=1-3), \quad (\text{B1c})$$

$$V_{4\kappa}^{(2\pm)}(\mathbf{K}_\perp, \mathbf{K}'_\perp) = -\frac{i}{2} \frac{k_p^{(1)}}{K_{pz}^{(1)}} \left(\frac{k_p^{(1)}}{k_{\kappa'}^{(2)}} \right)^2 \int_{-\infty}^{\infty} d\mathbf{r}'_\perp \times \chi(-\mathbf{r}'; \mathbf{K}_p^{(1\mp)}) \mathbf{n}^{(2)}(\mathbf{r}') \cdot \hat{X}_{\kappa'}(\mathbf{r}'_\perp; \mathbf{K}'_\perp) \quad (\kappa'=1-3), \quad (\text{B1d})$$

and

$$V_{44}^{(2\pm)}(\mathbf{K}_\perp, \mathbf{K}'_\perp) = \frac{i}{2} \frac{1}{K_{pz}^{(1)}} \int_{-\infty}^{\infty} d\mathbf{r}'_\perp \mathbf{n}^{(2)}(\mathbf{r}') \cdot \nabla' \chi(-\mathbf{r}'; \mathbf{K}_p^{(1\mp)}) \chi(\mathbf{r}'_\perp; \mathbf{K}'_\perp). \quad (\text{B1e})$$

The matrix elements can be expressed in terms of the Fourier transform of the rough surface phase $C(\mathbf{K}_\perp, K_z)$ in the following manner:

$$V_{\gamma\gamma'}^{(2\pm)}(\mathbf{K}_\perp, \mathbf{K}'_\perp) = v_{\gamma\gamma'}^{(2\pm)}(\mathbf{K}_\perp, \mathbf{K}'_\perp) C(\mathbf{K}_\perp - \mathbf{K}'_\perp, K_z) \quad (\text{B2})$$

with

$$v_{\gamma\gamma'}^{(2\pm)}(\mathbf{K}_\perp, \mathbf{K}'_\perp) = \frac{1}{2} \frac{k_\gamma}{K_{\gamma z}} \mathbf{v}_{\gamma\gamma'}^{(\pm)}(\mathbf{K}_\perp, \mathbf{K}'_\perp) \cdot \mathbf{v}^{(gk)}(\mathbf{K}_\gamma^{(\pm)}, \mathbf{K}'_\perp) \quad (\gamma=1-3) \quad (\text{B3a})$$

and

$$v_{4\gamma'}^{(2\pm)}(\mathbf{K}_\perp, \mathbf{K}'_\perp) = \frac{1}{2} \frac{k_p^{(1)}}{K_{pz}^{(1)}} \mathbf{v}_{4\gamma'}^{(\pm)}(\mathbf{K}_\perp, \mathbf{K}'_\perp) \cdot \mathbf{v}^{(gk)}(\mathbf{K}_p^{(1\mp)}, \mathbf{K}'_\perp) \quad (\text{B3b})$$

with

$$\mathbf{v}^{(gk)}(\mathbf{K}^{(\pm)}, \mathbf{K}'_\perp) = \pm \frac{(K_x - K'_x) \hat{x}' + (K_y - K'_y) \hat{y}' \pm K_z \hat{z}'}{K_z} \quad (\text{B3c})$$

and

$$\mathbf{v}_{11}^{(2\pm)}(\mathbf{K}_\perp, \mathbf{K}'_\perp) = -[\hat{K}'_t \cdot \hat{K}_t \hat{K}_s^{(2\pm)} + \hat{K}'_t \cdot \hat{K}_s^{(2\pm)} \hat{K}_t], \quad (\text{B4a})$$

$$\mathbf{v}_{12}^{(2\pm)}(\mathbf{K}_\perp, \mathbf{K}'_\perp) = -i[(\hat{K}'_s^{(2+)} \times \hat{K}'_t) \cdot \hat{K}_t \hat{K}_s^{(2\pm)} + (\hat{K}'_s^{(2+)} \times \hat{K}'_t) \cdot \mathbf{K}_s^{(2\pm)} \hat{K}_t], \quad (\text{B4b})$$

$$\mathbf{v}_{13}^{(2\pm)}(\mathbf{K}_\perp, \mathbf{K}'_\perp) = -\left(\frac{k_s^{(2)}}{k_p^{(2)}} \right)^{1/2} [\hat{K}'_p^{(2+)} \cdot \hat{K}_t \hat{K}_s^{(2\pm)} + \hat{K}'_p^{(2+)} \cdot \hat{K}_s^{(2\pm)} \hat{K}_t], \quad (\text{B4c})$$

$$\mathbf{v}_{14}^{(2\pm)}(\mathbf{K}_\perp, \mathbf{K}'_\perp) = -\frac{\lambda^{(1)} k_s^{(2)}}{\mu^{(2)} k_p^{(1)}} \hat{K}_t, \quad (\text{B4d})$$

$$\mathbf{v}_{21}^{(2\pm)}(\mathbf{K}_\perp, \mathbf{K}'_\perp) = i[\hat{K}'_t \cdot (\hat{K}_s^{(2\pm)} \times \hat{K}_t) \hat{K}_s^{(2\pm)} + \hat{K}'_t \cdot \hat{K}_s^{(2\pm)} (\hat{K}_s^{(2\pm)} \times \hat{K}_t)], \quad (\text{B4e})$$

$$\mathbf{v}_{22}^{(2\pm)}(\mathbf{K}_\perp, \mathbf{K}'_\perp) = -[(\hat{K}'_s^{(2+)} \times \hat{K}'_t) \cdot (\hat{K}_s^{(2\pm)} \times \hat{K}_t) \hat{K}_s^{(2\pm)} + (\hat{K}'_s^{(2+)} \times \hat{K}'_t) \cdot \hat{K}_s^{(2\pm)} (\hat{K}_s^{(2\pm)} \times \hat{K}_t)], \quad (\text{B4f})$$

$$\mathbf{v}_{23}^{(2\pm)}(\mathbf{K}_\perp, \mathbf{K}'_\perp) = i \left(\frac{k_s^{(2)}}{k_p^{(2)}} \right)^{1/2} [\hat{K}'_p^{(2+)} \cdot (\hat{K}_s^{(2\pm)} \times \hat{K}_t) \hat{K}_s^{(2\pm)} + \hat{K}'_p^{(2+)} \cdot \hat{K}_s^{(2\pm)} (\hat{K}_s^{(2\pm)} \times \hat{K}_t)], \quad (\text{B4g})$$

$$\mathbf{v}_{24}^{(2\pm)}(\mathbf{K}_\perp, \mathbf{K}'_\perp) = i \frac{\lambda^{(1)} k_s^{(2)}}{\mu^{(2)} k_p^{(1)}} \hat{K}_s^{(2\pm)} \times \hat{K}_t, \quad (\text{B4h})$$

$$\mathbf{v}_{31}^{(2\pm)}(\mathbf{K}_\perp, \mathbf{K}'_\perp) = -\frac{k_p^{(2)}}{k_s^{(2)}} \left(\frac{k_p^{(2)}}{k_s^{(2)}} \right)^{3/2} [2\hat{K}'_t \cdot \hat{K}_p^{(2\pm)} \hat{K}_p^{(2\pm)} + \frac{\lambda^{(2)}}{\mu^{(2)}} \hat{K}'_t], \quad (\text{B4i})$$

$$\mathbf{v}_{32}^{(2\pm)}(\mathbf{K}_\perp, \mathbf{K}'_\perp) = -i \frac{k_p^{(2)}}{k_s^{(2)}} \left(\frac{k_p^{(2)}}{k_s^{(2)}} \right)^{3/2} \left[2(\hat{K}'_s^{(2+)} \times \hat{K}'_t) \cdot \hat{K}'_p^{(2\pm)} \hat{K}'_p^{(2\pm)} + \frac{\lambda^{(2)}}{\mu^{(2)}} (\hat{K}'_s^{(2+)} \times \hat{K}'_t) \right], \quad (\text{B4j})$$

$$\mathbf{v}_{33}^{(2\pm)}(\mathbf{K}_\perp, \mathbf{K}'_\perp) = - \left(\frac{k_p^{(2)}}{k_s^{(2)}} \right)^2 \left[2\hat{K}'_p^{(2+)} \cdot \hat{K}'_p^{(2\pm)} \hat{K}'_p^{(2\pm)} + \frac{\lambda^{(2)}}{\mu^{(2)}} \hat{K}'_p^{(2+)} \right], \quad (\text{B4k})$$

$$\mathbf{v}_{34}^{(2\pm)}(\mathbf{K}_\perp, \mathbf{K}'_\perp) = - \frac{\lambda^{(1)}}{\mu^{(2)}} \frac{k_s^{(2)}}{k_p^{(1)}} \left(\frac{k_p^{(2)}}{k_s^{(2)}} \right)^{3/2} \hat{K}'_p^{(2\pm)}, \quad (\text{B4l})$$

$$\mathbf{v}_{41}^{(2\pm)}(\mathbf{K}_\perp, \mathbf{K}'_\perp) = \left(\frac{k_p^{(1)}}{k_s^{(2)}} \right)^2 \hat{K}'_t, \quad (\text{B4m})$$

$$\mathbf{v}_{42}^{(2\pm)}(\mathbf{K}_\perp, \mathbf{K}'_\perp) = i \left(\frac{k_p^{(1)}}{k_s^{(2)}} \right)^2 \hat{K}'_s^{(2+)} \times \hat{K}'_t, \quad (\text{B4n})$$

$$\mathbf{v}_{43}^{(2\pm)}(\mathbf{K}_\perp, \mathbf{K}'_\perp) = \left(\frac{k_p^{(1)}}{k_s^{(2)}} \right)^2 \left(\frac{k_p^{(2)}}{k_s^{(2)}} \right)^{3/2} \hat{K}'_p^{(2+)}, \quad (\text{B4o})$$

and

$$\mathbf{v}_{44}^{(2\pm)}(\mathbf{K}_\perp, \mathbf{K}'_\perp) = \hat{K}'_p^{(1\mp)}. \quad (\text{B4p})$$

The quantity $C(\mathbf{K}_\perp - \mathbf{K}'_\perp, \pm K_z)$ is the Fourier transform of the rough surface phase:

$$C(\mathbf{K}_\perp - \mathbf{K}'_\perp, \pm K_z) = \int_{-\infty}^{\infty} d\mathbf{r}'_\perp e^{-i[(\mathbf{K}_\perp - \mathbf{K}'_\perp) \cdot \mathbf{r}'_\perp \pm K_z \xi(\mathbf{r}'_\perp)]}. \quad (\text{B5})$$

When the surface roughness is periodic, integration over the Dirac delta functions that occur in the surface-field spectral amplitudes given by Eq. (60) introduces $C(\mathbf{K}_\perp - \mathbf{k}_{\perp n}, K_z)$ into the matrix elements. In addition, the rough surface phase may be represented by a Fourier series:⁷

$$\tilde{\xi}^{(m)}(\mathbf{K}'_\perp) = \begin{cases} (2\pi)^2 \delta^2(\mathbf{K}'_\perp) & (m=0) \\ \frac{1}{(2\pi)^{2m-2}} \int_{-\infty}^{\infty} d\mathbf{Q}_\perp^{[1]} \int_{-\infty}^{\infty} d\mathbf{Q}_\perp^{[2]} \dots \int_{-\infty}^{\infty} d\mathbf{Q}_\perp^{[m]} \\ \quad \times \xi(\mathbf{Q}_\perp^{[1]}) \xi(\mathbf{Q}_\perp^{[2]}) \dots \xi(\mathbf{Q}_\perp^{[m]}) \delta^2(-\mathbf{K}'_\perp + \mathbf{Q}_\perp^{[1]} + \mathbf{Q}_\perp^{[2]} + \dots + \mathbf{Q}_\perp^{[m]}) & (m \neq 0). \end{cases} \quad (\text{B10})$$

The perturbative representation of the matrix elements is obtained by using the series expansion of the rough surface phase given by Eq. (B6a) in Eq. (B2).

The perturbative representation of the free-field T -matrix for the rough fluid-elastic interface is given by

$$e^{\pm iK_z \xi(\mathbf{r}'_\perp)} = \sum_{\mathbf{m}=-\infty}^{\infty} C_{\mathbf{m}}(\pm K_z) \exp[i(m_x K_x x' + m_y K_y y')] \quad (\text{B6a})$$

with

$$C_{\mathbf{m}}(\pm K_z) = \int_0^{\Lambda_x} \frac{dx'}{\Lambda_x} \int_0^{\Lambda_y} \frac{dy'}{\Lambda_y} \exp[-i(m_x K_x x' + m_y K_y y' \pm K_z \xi(\mathbf{r}'_\perp))]. \quad (\text{B6b})$$

When Eq. (B6a) is used to evaluate $C(\mathbf{K}_\perp - \mathbf{k}_{\perp n}, K_z)$ using Eq. (B5), it can be expressed in terms of $C_{\mathbf{m}}(\pm K_z)$ in the following manner:

$$C(\mathbf{K}_\perp - \mathbf{k}_{\perp n}, \pm K_z) = \sum_{\mathbf{m}'=-\infty}^{\infty} C_{\mathbf{m}'-\mathbf{n}}(\pm k_{z\mathbf{m}'}) \times \delta(-\mathbf{K}_\perp + \mathbf{k}_{\perp \mathbf{m}'}). \quad (\text{B7})$$

The matrix elements for periodic surface roughness are $V_{\gamma\gamma'\mathbf{m}\mathbf{m}}^{(2+)}$ with $V_{\gamma\gamma'\mathbf{m}\mathbf{m}}^{(2+)} = k_{\gamma'}^2 / k_\gamma^2 V_{\gamma\gamma'}^{(2\pm)}(\mathbf{k}_{\perp \mathbf{m}}, \mathbf{k}_{\perp \mathbf{n}})$ with $C(\mathbf{K}_\perp - \mathbf{k}_{\perp \mathbf{n}}, \pm K_z)$ replaced by $C_{\mathbf{m}'-\mathbf{n}}(\pm k_{z\mathbf{m}'})$ and $k_\gamma = k_s^{(2)} \times [\delta_{\gamma,1} + \delta_{\gamma,2}] + k_p^{(2)} \delta_{\gamma,3} + k_p^{(1)} \delta_{\gamma,4}$.

To construct a perturbative representation of the matrix elements, the exponential that contains the roughness profile function in Eq. (B5) is expanded in a series so that

$$C(\mathbf{K}'_t, \pm K_z) = \sum_{m=0}^{\infty} \frac{(kh)^m}{m!} [\mp iK_z/k]^m \tilde{\xi}^{(m)}(\mathbf{K}'_t) \quad (\text{B8a})$$

with

$$\tilde{\xi}^{(m)}(\mathbf{K}'_\perp) = \int_{-\infty}^{\infty} d\mathbf{r}'_\perp [\tilde{\xi}(\mathbf{r}'_\perp)]^m e^{-i\mathbf{K}'_\perp \cdot \mathbf{r}'_\perp} \quad (\text{B8b})$$

and $\tilde{\xi}(\mathbf{r}'_\perp) = \xi(\mathbf{r}'_\perp)/h$. A convenient expression for $\tilde{\xi}^{(m)}(\mathbf{K}'_\perp)$ is obtained by using the Fourier transform of $\tilde{\xi}(\mathbf{r}'_\perp)$ given by

$$\tilde{\xi}(\mathbf{r}'_\perp) = \frac{1}{(2\pi)^2} \int_{-\infty}^{\infty} d\mathbf{K}'_\perp \tilde{\xi}(\mathbf{K}'_\perp) e^{i\mathbf{K}'_\perp \cdot \mathbf{r}'_\perp} \quad (\text{B9})$$

in Eq. (B8b) so that

$$\begin{aligned}
\frac{1}{n!} k_p^{(1)^n} t^{(2,n)}(\mathbf{K}_\perp, \mathbf{K}'_\perp) &= \mathcal{F}_{44}^{(2,n)}(\mathbf{K}_p^{(1+)}, \mathbf{K}'_\perp) + \sum_{m_1=1}^n \frac{1}{(2\pi)^2} \int_{-\infty}^{\infty} d\mathbf{Q}_\perp^{[1]} \mathcal{F}_{4\gamma_1}^{(2,n-m_1)}(\mathbf{K}_p^{(1+)}, \mathbf{Q}_\perp^{[1]}) \mathcal{F}_{\gamma_1 4}^{(2,m_1)}(\mathbf{Q}_{\gamma_1}^{[1]}, \mathbf{K}'_\perp) \\
&\times (1 - \delta_{n,1}) + \sum_{m_2=2}^n \sum_{m_1=m_2}^n \frac{1}{(2\pi)^2} \int_{-\infty}^{\infty} d\mathbf{Q}_\perp^{[1]} \frac{1}{(2\pi)^2} \int_{-\infty}^{\infty} d\mathbf{Q}_\perp^{[2]} \\
&\times \mathcal{F}_{4\gamma_1}^{(2,n-m_1)}(\mathbf{K}_p^{(1+)}, \mathbf{Q}_\perp^{[1]}) \mathcal{F}_{\gamma_1 \gamma_2}^{(2,m_1-m_2+1)}(\mathbf{Q}_{\gamma_1}^{[1]}, \mathbf{Q}_\perp^{[2]}) \mathcal{F}_{\gamma_2 4}^{(2,m_2-1)}(\mathbf{Q}_{\gamma_2}^{[2]}, \mathbf{K}'_\perp) (1 - \delta_{n,1} \delta_{n,2}) + \dots \\
&+ \sum_{m_{n-1}=n-1}^n \sum_{m_{n-2}=m_{n-1}}^n \dots \sum_{m_1=m_2}^n \frac{1}{(2\pi)^2} \int_{-\infty}^{\infty} d\mathbf{Q}_\perp^{[1]} \frac{1}{(2\pi)^2} \int_{-\infty}^{\infty} d\mathbf{Q}_\perp^{[2]} \dots \frac{1}{(2\pi)^2} \\
&\int_{-\infty}^{\infty} d\mathbf{Q}_\perp^{[n-1]} \mathcal{F}_{4\gamma_1}^{(2,n-m_1)}(\mathbf{K}_p^{(1+)}, \mathbf{Q}_\perp^{[1]}) \mathcal{F}_{\gamma_1 \gamma_2}^{(2,m_1-m_2+1)}(\mathbf{Q}_{\gamma_1}^{[1]}, \mathbf{Q}_\perp^{[2]}) \times \dots \times \\
&\times \mathcal{F}_{\gamma_{n-1} 4}^{(2,m_{n-1}-n+2)}(\mathbf{Q}_{\gamma_{n-1}}^{[n-1]}, \mathbf{K}'_\perp) (1 - \delta_{n,1}) \\
&+ \frac{1}{(2\pi)^2} \int_{-\infty}^{\infty} d\mathbf{Q}_\perp^{[1]} \frac{1}{(2\pi)^2} \int_{-\infty}^{\infty} d\mathbf{Q}_\perp^{[2]} \dots \frac{1}{(2\pi)^2} \int_{-\infty}^{\infty} d\mathbf{Q}_\perp^{[n]} \\
&\times \mathcal{F}_{4\gamma_1}^{(2,0)}(\mathbf{K}_p^{(1+)}, \mathbf{Q}_\perp^{[1]}) \mathcal{F}_{\gamma_1 \gamma_2}^{(2,1)}(\mathbf{Q}_{\gamma_1}^{[1]}, \mathbf{Q}_\perp^{[2]}) \times \dots \times \mathcal{F}_{\gamma_n 4}^{(2,1)}(\mathbf{Q}_{\gamma_n}^{[n]}, \mathbf{K}'_\perp) \quad (n \neq 0)
\end{aligned} \tag{B11a}$$

with

$$\mathcal{F}_{\gamma\sigma}^{(2,n)}(\mathbf{Q}_\gamma, \mathbf{Q}'_\perp) = q^n \nu^{(g,n)}(\mathbf{Q}_\gamma, \mathbf{Q}'_\perp) t_{\gamma\sigma}^{(2)}(\mathbf{Q}_\perp, \mathbf{Q}'_\perp). \tag{B11b}$$

In Eq. (B11a), the implicit summation rule is used to indicate a summation over repeated lower-case Greek indices, a square bracket denotes wave numbers over which an integration is to be performed, and $\mathbf{Q}_\gamma = \mathbf{Q}_s^{(2+)}(\delta_{\gamma,1} + \delta_{\gamma,2}) + \mathbf{Q}_p^{(2+)}\delta_{\gamma,3} + \mathbf{Q}_p^{(1-)}\delta_{\gamma,4}$. The Kronecker delta functions are included to exclude m -sums in which the upper and lower summation limits are equal.

APPENDIX C: A T-MATRIX FOR FREE-FIELD SCATTERING FROM AN ELASTIC SHELL

In the absence of the rough interface, the spectral amplitude of the pressure field scattered from the shell is $p_\lambda^{(3s)}$. An equation for $p_\lambda^{(3s)}$ is obtained from Eq. (5) by neglecting the terms that relate to the rough surface and projecting the resulting equation onto a spherical basis so that

$$p_\lambda^{(3s)} = \sum_{\lambda'} \left[Q_{\lambda 1; \lambda'}^{(3)} p_{\lambda'}^{(3)} - \sum_{\kappa'=1}^{(3)} B_{\lambda 1; \kappa' \lambda'}^{(3)} u_{\kappa' \lambda'}^{(3)} \right]. \tag{C1}$$

The null-field equation that follows when $p^{(3s)}(\mathbf{r})$ is forced to satisfy the null-field hypothesis is given by

$$-p_\lambda^{(i)} = \sum_{\lambda'} \left[Q_{\lambda 2; \lambda'}^{(3)} p_{\lambda'}^{(3)} - \sum_{\kappa'=1}^{(3)} B_{\lambda 2; \kappa' \lambda'}^{(3)} u_{\kappa' \lambda'}^{(3)} \right]. \tag{C2}$$

The remaining null-field equations for the displacement field in the annular region of the shell and for the pressure-field interior to the shell are given by

$$0 = \sum_{\lambda'} \left[-P_{\kappa \lambda 2; \lambda'}^{(3)} p_{\lambda'}^{(3)} - \sum_{\kappa'=1}^3 R_{\kappa \lambda 2; \kappa' \lambda'}^{(3)} u_{\kappa' \lambda'}^{(3)} + P_{\kappa \lambda 2; \lambda'}^{(4)} p_{\lambda'}^{(4)} + \sum_{\kappa'=1}^3 R_{\kappa \lambda 2; \kappa' \lambda'}^{(4)} u_{\kappa' \lambda'}^{(4)} \right], \tag{C3}$$

$$0 = \sum_{\lambda'} \left[-P_{\kappa \lambda 1; \lambda'}^{(3)} p_{\lambda'}^{(3)} - \sum_{\kappa'=1}^3 R_{\kappa \lambda 1; \kappa' \lambda'}^{(3)} u_{\kappa' \lambda'}^{(3)} + P_{\kappa \lambda 1; \lambda'}^{(4)} p_{\lambda'}^{(4)} + \sum_{\kappa'=1}^3 R_{\kappa \lambda 1; \kappa' \lambda'}^{(4)} u_{\kappa' \lambda'}^{(4)} \right], \tag{C4}$$

and

$$0 = \sum_{\lambda'} \left[-Q_{\lambda 1; \lambda'}^{(4)} p_{\lambda'}^{(4)} + \sum_{\kappa'=1}^3 B_{\lambda 1; \kappa' \lambda'}^{(4)} u_{\kappa' \lambda'}^{(4)} \right]. \tag{C5}$$

In the following, boldface italic characters are used to indicate matrices. An expression for the column matrix $p_\lambda^{(4)}$ may be obtained from Eq. (C5) and used in Eqs. (C4) and (C3) to obtain the following:

$$0 = -\mathbf{P}_{\kappa \lambda 2; \lambda'}^{(3)} p_{\lambda'}^{(3)} - \mathbf{R}_{\kappa \lambda 2; \kappa' \lambda'}^{(3)} u_{\kappa' \lambda'}^{(3)} + \mathbf{U}_{\kappa \lambda 2; \kappa' \lambda'}^{(4)} u_{\kappa' \lambda'}^{(4)} \tag{C6}$$

and

$$0 = -\mathbf{P}_{\kappa \lambda 1; \lambda'}^{(3)} p_{\lambda'}^{(3)} - \mathbf{R}_{\kappa \lambda 1; \kappa' \lambda'}^{(3)} u_{\kappa' \lambda'}^{(3)} + \mathbf{U}_{\kappa \lambda 1; \kappa' \lambda'}^{(4)} u_{\kappa' \lambda'}^{(4)}, \tag{C7}$$

where

$$\mathbf{U}_{\kappa \lambda \sigma; \kappa' \lambda'}^{(4)} = \{ \mathbf{R}_{\kappa \lambda \sigma; \kappa' \lambda'}^{(4)} + \mathbf{P}_{\kappa \lambda \sigma; \lambda'}^{(4)} [\mathbf{Q}_{\lambda 1; \lambda'}^{(4)}]^{-1} \mathbf{B}_{\lambda 1; \kappa' \lambda'}^{(4)} \}. \tag{C8}$$

Equation (C6) may be solved for $\mathbf{u}_{\kappa'\lambda'}^{(4)}$ and the result used in Eq. (C7). The resulting equation may be solved for the displacement field $\mathbf{u}_{\kappa'\lambda'}^{(3)}$ on the exterior surface:

$$\mathbf{u}_{\kappa'\lambda'}^{(3)} = -[\mathbf{R}_{\kappa\lambda 1; \kappa'\lambda'}^{(3)} + \mathbf{T}_{\kappa\lambda; \kappa'\lambda'}^{(4)} \mathbf{R}_{\kappa\lambda 2; \kappa'\lambda'}^{(3)}]^{-1} \times [\mathbf{P}_{\kappa\lambda 1; \lambda'}^{(3)} + \mathbf{T}_{\kappa\lambda; \kappa'\lambda'}^{(4)} \mathbf{P}_{\kappa\lambda 2; \lambda'}^{(3)}] p_{\lambda'}^{(3)} \quad (\text{C9})$$

with

$$\mathbf{T}_{\kappa\lambda; \kappa'\lambda'}^{(4)} = -\mathbf{U}_{\kappa\lambda 1; \kappa'\lambda'}^{(4)} [\mathbf{U}_{\kappa\lambda 2; \kappa'\lambda'}^{(4)}]^{-1}. \quad (\text{C10})$$

The quantity $\mathbf{T}_{\kappa\lambda; \kappa'\lambda'}^{(4)}$ is the T -matrix for the inner surface. To develop the T -matrix for the shell, Eq. (C9) is used in Eqs. (C1) and (C2). These equations are used to eliminate the dependence of the spectral amplitude of the scattered field on the spectral amplitude of the surface field. Then $p_{\lambda}^{(3s)}$ is given by

$$p_{\lambda}^{(3s)} = \mathbf{T}_{\lambda; \lambda'}^{(3)} p_{\lambda'}^{(i)}, \quad (\text{C11})$$

where

$$\mathbf{T}_{\lambda; \lambda'}^{(3)} = -\mathbf{U}_{\lambda 1; \lambda'}^{(3)} [\mathbf{U}_{\lambda 2; \lambda'}^{(3)}]^{-1} \quad (\text{C12a})$$

and the matrix $\mathbf{U}_{\lambda\sigma; \lambda'}^{(3)}$ is given by

$$\mathbf{U}_{\lambda\sigma; \lambda'}^{(3)} = \mathbf{Q}_{\lambda\sigma; \lambda'}^{(3)} + \mathbf{B}_{\lambda\sigma; \kappa'\lambda'}^{(3)} [\mathbf{R}_{\kappa\lambda 1; \kappa'\lambda'}^{(3)} + \mathbf{T}_{\kappa\lambda; \kappa'\lambda'}^{(4)} \mathbf{R}_{\kappa\lambda 2; \kappa'\lambda'}^{(3)}]^{-1} \times [\mathbf{P}_{\kappa\lambda 1; \lambda'}^{(3)} + \mathbf{T}_{\kappa\lambda; \kappa'\lambda'}^{(4)} \mathbf{P}_{\kappa\lambda 2; \lambda'}^{(3)}] \quad (\text{C12b})$$

and $\mathbf{T}_{\lambda; \lambda'}^{(3)}$ is the free-field T -matrix for the elastic shell. When the shell is spherical, the matrix elements are diagonal, and a closed form expression for the T -matrix can be obtained by using the diagonal form of the matrix elements in Eqs. (C1)–(C5).

¹G. Kristensson and S. Strom, "Scattering from buried inhomogeneities—a general three-dimensional formalism," *J. Acoust. Soc. Am.* **64**, 917–936 (1978).

²G. Kristensson and S. Strom, "The T -matrix approach to scattering from buried inhomogeneities," in *Acoustic, Electromagnetic and Elastic Wave Scattering-Focus on the T -matrix Approach*, edited by V. K. Varadan and V. V. Varadan (Pergamon, New York, 1980), pp. 135–167.

³R. H. Hackman and G. S. Sammelmann, "Acoustic scattering in an inhomogeneous waveguide: Theory," *J. Acoust. Soc. Am.* **80**, 1447–1458 (1986).

⁴G. S. Sammelmann and R. H. Hackman, "Acoustic scattering in a homogeneous waveguide," *J. Acoust. Soc. Am.* **82**, 324–336 (1987).

⁵R. H. Hackman and G. S. Sammelmann, "Long-range scattering in a deep oceanic waveguide," *J. Acoust. Soc. Am.* **83**, 1776–1793 (1988).

⁶R. H. Hackman and G. S. Sammelmann, "Multiple scattering analysis for a target in an oceanic waveguide," *J. Acoust. Soc. Am.* **84**, 1813–1825 (1988).

⁷G. C. Bishop and J. Smith, "A T -matrix for scattering from a doubly infinite fluid-solid interface with doubly periodic surface roughness," *J. Acoust. Soc. Am.* **94**, 1560–1583 (1993).

⁸J. A. Stratton, *Electromagnetic Theory* (McGraw-Hill, New York, 1941), Chap. 7.

⁹P. M. Morse and H. Feshbach, *Methods of Theoretical Physics* (McGraw-Hill, New York, 1953), Chap. 13.

¹⁰Y. Pao and V. Varatharajulu, "Huygens' principle, radiation conditions, and integral formulas for the scattering of elastic waves," *J. Acoust. Soc. Am.* **59**, 1361–1371 (1976).

¹¹P. C. Waterman, "Matrix theory of elastic wave scattering," *J. Acoust. Soc. Am.* **60**, 567–580 (1976).

¹²A. Bostrom, "Scattering of stationary acoustic waves by an elastic obstacle immersed in a fluid," *J. Acoust. Soc. Am.* **67**, 390–398 (1980).

¹³The spherical scalar basis functions defined in Eq. (10) are identical to those defined by Hackmann and Sammelmann in Ref. 3, however, they differ from those defined by Morse and Feshbach in Ref. 9 who do not define orthonormal scalar spherical harmonics.

¹⁴The spherical vector harmonics defined in Eq. (13) are identical to those defined by Hackmann and Sammelmann in Ref. 5 and Bostrom in Ref. 12, but differ from those defined by Morse and Feshbach in Ref. 9 and Waterman in Ref. 11 who obtain the vector spherical harmonics from spherical scalar harmonics in the same manner given in Eq. (13), but who do not use orthonormal spherical scalar harmonics.

¹⁵The vector spherical basis functions defined here, are a generalization of those defined by Bostrom in Ref. 12 in that both regular and irregular vector spherical basis functions are defined, and are normalized differently than the vector spherical basis functions defined by Morse and Feshbach in Ref. 9, Waterman in Ref. 11, and Pao and Varatharajulu in Ref. 10 all of whom use different normalizations.

¹⁶Reference 9, p. 1466, Eq. 11.3.4; the scalar Green function defined by Morse and Feshbach satisfies the equation $(\nabla^2 + k^2)g_0(\mathbf{r}, \mathbf{r}'; \mathbf{k}) = -4\pi\delta(\mathbf{r} - \mathbf{r}')$. Therefore the expression for $g_0(\mathbf{r}, \mathbf{r}'; \mathbf{k})$ used in this paper includes an additional factor of $1/4\pi$. The Green function defined by Bostrom in Ref. 12 satisfies the equation $(\nabla^2 + k^2)g_0(\mathbf{r}, \mathbf{r}'; \mathbf{k}) = -(1/k)\delta(\mathbf{r} - \mathbf{r}')$.

¹⁷A. Bostrom, "Scattering of acoustic waves by a layered elastic object in a fluid—An improved null field approach," *J. Acoust. Soc. Am.* **76**, 588–593 (1984).

¹⁸The Green dyadic $\mathbf{G}_0(\mathbf{r}, \mathbf{r}')$ defined by Hackmann and Sammelmann in Ref. 5 satisfies the equation $(1/k_p^2)\nabla\nabla\cdot\mathbf{G}_0(\mathbf{r}, \mathbf{r}') - (1/k_s^2)\nabla\times\nabla\times\mathbf{G}_0(\mathbf{r}, \mathbf{r}') + \mathbf{G}_0(\mathbf{r}, \mathbf{r}') = -(1/k_s^3)\delta(\mathbf{r} - \mathbf{r}')\mathbf{I}$. This form of the Green dyadic is also used by Bostrom in Ref. 12.

¹⁹E. Mertzbacher, *Quantum Mechanics* (Wiley, New York, 1970), 2nd ed., pp. 299–301.

²⁰D. K. Dacol and D. H. Berman, "Sound scattering from a randomly rough fluid–solid interface," *J. Acoust. Soc. Am.* **84**, 292–302 (1988).

²¹M. Nieto-Vesperinas and N. Garcia, "A detailed study of the scattering of scalar waves from random rough surfaces," *Opt. Acta* **28**, 1651–1672 (1981).

²²D. R. Jackson, D. P. Winebrenner, and A. Ishimaru, "Comparison of perturbation theories for rough-surface scattering," *J. Acoust. Soc. Am.* **83**, 961–969 (1988).

²³L. M. Brekhovskikh, *Waves in Layered Media* (Academic, New York, 1980), 2nd ed., p. 43.

²⁴J. A. Hudson, *The Excitation and Propagation of Elastic Waves* (Cambridge U.P., Cambridge, England, 1987), pp. 67–71.

²⁵A. G. Voronovich, "Small slope approximation in wave scattering by rough surfaces," *Sov. Phys. JETP* **62**, 65–70 (1985).

²⁶D. H. Berman, "Simulations of rough surface scattering," *J. Acoust. Soc. Am.* **89**, 623–636 (1991).

²⁷T. Yang and S. L. Broschat, "Acoustic scattering from a fluid-elastic-solid interface using the small slope approximation," *J. Acoust. Soc. Am.* **96**, 1796–1804 (1994).

²⁸Reference 9, p. 117.

Acoustic propagation through an internal wave field in a shallow water waveguide

Dirk Tielburger,^{a)} Steven Finette, and Stephen Wolf
Acoustics Division, Naval Research Laboratory, Washington, DC 20375

(Received 19 March 1996; accepted for publication 8 August 1996)

This paper addresses the problem of predicting and interpreting acoustic wave field properties in a stochastic ocean waveguide, for which the sound-speed variability within the water column is treated explicitly as a random process. It is assumed that the sound-speed distribution is composed of three components: a deterministic, time-independent profile and two stochastic components induced by internal wave activity. One random contribution represents a spatially diffuse Garrett–Munk field whose spectrum is constrained by the shallow water waveguide, while the second corresponds to spatially localized soliton packets. A high-angle elastic parabolic equation method is applied to compute single frequency realizations of the pressure field using this three-component representation of the sound-speed distribution. Ensemble-averaged transmission loss and scintillation index measures for the full pressure field and its modal components are estimated for different source depths and for both flat and sloping bottoms. Probability distributions of the mode amplitudes for different ranges are also presented. These statistical measures are incorporated into the analysis of range-dependent mode coupling between the internal wave and acoustic fields, and evidence is presented which supports a recent prediction that the scintillation index grows exponentially with range due to the competition between mode coupling and mode stripping found in shallow water waveguides. Full-field estimates of the scintillation index are also presented for a shallow water region on the continental slope off the New Jersey coast. © 1997 Acoustical Society of America. [S0001-4966(97)00102-1]

PACS numbers: 43.30.Bp, 43.30.Re, 43.25.Rq [JHM]

INTRODUCTION

The environmental complexity associated with shallow water waveguides makes them a challenging medium in which to study acoustic wave propagation. In deep water waveguides, propagation via the sound channel axis often allows one to ignore boundary interactions, a simplification not justified in shallow water waveguides. For propagation in shallow water, wave–boundary interactions coupled with a range-dependent sound-speed distribution makes the prediction of acoustic field quantities a difficult problem. The problem becomes even more complex when the stochastic nature of the environment is included, and several stochastic components can be identified in shallow water propagation. Examples include volume, surface and bottom effects such as internal gravity waves, bubble clouds due to breaking surface waves, dynamically changing surface roughness and subbottom inhomogeneities. For these realistic environments, the field computation is amenable only through computer simulation.

In this paper, some acoustic field properties for a stochastic waveguide are examined through numerical experiments in which the sources of randomness are internal waves. We ignore the random effects associated with the ocean surface and bottom, assuming that these boundaries can be treated deterministically. The stochastic nature of the waveguide is represented here by volume fluctuations of the

sound-speed distribution, induced by the internal wave field. This description implies that the pressure field propagating through the waveguide, as well as the sound-speed distribution, should be treated as random processes with moments of the field describing the propagation characteristics. The emphasis is placed on the second and fourth moments of the pressure field, corresponding to field intensity and intensity fluctuations, respectively. Insight into the full-field results is obtained by a modal decomposition of the field and an analysis of modal statistics. Numerical experiments are performed to study the spatial and asymptotic (long-range) properties of the ensemble-averaged intensity and intensity fluctuations for realistic environmental parameters.

While many researchers have considered the problem of modeling propagation in the presence of an internal wave field for deep water environments^{1–10} there have been several recent studies devoted to stochastic propagation in shallow water.^{11–18} Moments of the acoustic field have been extensively studied for deep water environments and results are summarized in Ref. 19. Roughly speaking, two limiting acoustic environments can be distinguished: (a) a medium with a weakly fluctuating sound speed profile or one characterized by short range propagation and (b) a strongly fluctuating medium or one characterized by long range propagation. The former is called the weak scattering or unsaturated regime while the latter is known as the strong scattering or fully saturated regime. Physically, they correspond to situations where the propagated wave is weakly or strongly distorted, respectively. Due to the spatial and temporal decorrelation of the field in the saturated case, the scintillation index

^{a)}Permanent address: Forschungsanstalt der Bundeswehr fur Wasserschall- und Geophysik, Klausdorfer Weg 2-24, 24148 Kiel, Germany.

(variance of the intensity normalized by the squared average intensity) approaches unity at long range from the source. This result can be understood by considering the pressure field as a sum of phasors whose phases are uniformly distributed, i.e., decorrelated by wave propagation through a fully saturated environment. The amplitudes of such a field are Rayleigh distributed and therefore the intensity variance is equal to the squared average intensity, giving the result that the scintillation index approaches unity for large ranges. In addition, the saturated regime in a deep ocean waveguide (no boundary interactions or bottom loss) is characterized by an equipartitioning of the modal energy.^{5,6}

Theoretical work on deep water random waveguides is simplified, relative to the shallow water case, because the energy is typically confined to a region around the sound channel axis so that boundary interactions can be ignored. However, boundary interactions cannot be ignored in shallow water propagation and may introduce additional complications which lead to statistical behavior not predicted by deep water theories. An example of such a complication is the different modal attenuation decay rates (mode stripping) caused by sediment penetration of the acoustic field. A recent extension of stochastic coupled mode theory to shallow water waveguides¹⁶ predicts that both modal and full-field scintillation indices grow exponentially in range, rather than saturating as predicted for deep water propagation. This behavior is due to the competition between differential mode stripping and the tendency for equipartitioning of mode energy induced by sound-speed fluctuations. According to Ref. 16 this asymptotic growth in the scintillation index is attributed to the mismatch of the range-dependent decay rates between the average intensity and second moment of the intensity. The prediction of exponential growth in the scintillation index at large range is investigated here through simulations of intensity fluctuations and interpreted in the context of stochastic coupled mode theory, where it is shown that the results of the simulations are consistent with the theory.

The organization of the paper is as follows. In Sec. I we introduce the oceanographic relationships that relate the internal wave-field variables to fluctuations of the sound speed distribution. Examples of the internal wave modal structure, modal group speed, and sound-speed fluctuations are presented. In Sec. II we discuss the acoustic parameters, computation of the acoustic field, and statistics estimated from the ensemble of field realizations. In Sec. III we describe numerical simulations for both single-mode and full-field statistics. An outline of the theory predicting an exponentially increasing asymptotic behavior of the scintillation index in shallow water is discussed, and the results of numerical experiments that support and clarify this prediction are presented. Full-field scintillation index computations are illustrated using acoustic and oceanographic environments chosen to simulate a site on the continental shelf off the New Jersey coast. The environment and location were chosen because results presented here were used in the planning stages of the SWARM (shallow water random media) acoustic-internal wave experiment²⁰ performed in that area during July 1995. The numerical results are interpreted in terms of

the modal coupling discussion of Sec. III. A summary and conclusions are presented in Sec. IV.

I. INTERNAL WAVE FIELDS AND SOUND-SPEED FLUCTUATIONS

The volume sound-speed profile in shallow water is primarily dependent on temperature and salinity gradients and these gradients are perturbed in the presence of internal waves. Assuming that the only source of randomness is due to internal wave fluctuations in the water column, we represent the sound-speed field as a random process composed of three components. These components include (1) a dominant, deterministic sound-speed distribution, (2) a spatially diffuse background component due to an internal wave-field comprising a Garrett–Munk statistical mixture of plane wave components, and (3) a spatially localized contribution from internal wave soliton packets. The sound-speed field, along with appropriate boundary conditions, serve as input to a high-angle elastic parabolic equation solver which computes realizations of the acoustic field as functions of range, depth, and frequency. The ensemble of field realizations are then used to estimate transmission loss, scintillation index, and modal statistics.

This section considers the relationship between the oceanographic variables describing the internal wave fields and the random sound-speed variations induced by these fields. The analysis is confined to two dimensions, where r denotes the range variable and z corresponds to the depth variable, with $z=0$ at the surface and increasing in depth. The sound-speed distribution is composed of a deterministic spatial component $\bar{c}(r,z)$ and a stochastic space–time component $\delta c(r,z,t)$ representing the effects of internal waves: $c(r,z,t) = \bar{c}(r,z) + \delta c(r,z,t)$. In Sec. I A we discuss the general relationship between the sound-speed perturbations $\delta c(r,z,t)$ and internal wave displacements. These water particle displacements associated with internal wave motion are then related to a specific model of the internal wave field in Sec. I B.

A. Relationship between sound-speed fluctuations and internal wave variables

As mentioned above, the internal wave contributions to each sound-speed realization are assumed to be a superposition of a spectral mixture of plane waves weighted with a Garrett–Munk spectrum and spatially localized soliton packets. We now briefly address the problem of relating the sound-speed fluctuations δc to the internal wave variations in the temperature and salinity gradients, since these latter quantities are directly related to the internal wave model. Both the gradients and the resulting sound-speed fluctuations are generally functions of time. It is assumed below that the time dependencies of these gradients are caused by (internal wave induced) perturbations on the mean background temperature and salinity fields T and S .

The stability of a parcel of water displaced from its equilibrium position depends on the potential density gradient,²¹ $\partial \rho_p / \partial z$, where the potential density, ρ_p , is defined as the density that a parcel of fixed composition would acquire if moved adiabatically to a pressure reference level p_r . Analo-

gous definitions can be made for the potential temperature, T_p , and potential sound speed, c_p , since the latter is a function of the potential temperature. Measured gradients of these variables are sums of their potential and adiabatic gradients, e.g., $\partial c/\partial z = \partial c_p/\partial z + \partial c_a/\partial z$. The advantage of using potential variables is that a stability analysis shows that only the potential gradient in sound speed contributes to the fluctuations δc associated with internal waves. These fluctuations, in conjunction with the deterministic component \bar{c} , determine the acoustic properties of the sound channel.⁴

From thermodynamic arguments,^{1,2} the fractional depth gradient of the potential sound-speed field can be related to the mean potential temperature and salinity gradients through the buoyancy (Brunt–Väisälä) frequency $N(r, z)$:

$$\frac{1}{\bar{c}(r, z)} \frac{\partial}{\partial z} c_p(r, z) = G(r, z) N^2(r, z), \quad (1)$$

$$N^2(r, z) = -\frac{g}{\rho} \frac{\partial}{\partial z} \rho_p(r, z) = g \left(h \frac{\partial T_p}{\partial z} - s \frac{\partial S}{\partial z} \right). \quad (2)$$

The quantities h and s are the coefficients of thermal expansion and saline contraction, respectively, $G(r, z)$ is a function of these coefficients as well as the partial derivatives of sound speed relative to temperature and salinity, and the quantity g is the acceleration of gravity.

By defining $\eta(r, z, t)$ as a time-dependent displacement of an isopycnal (constant density) surface associated with the internal wave field, the oceanographic variables discussed above can be related to the sound-speed fluctuations which induce acoustic field variability. Multiplying Eq. (1) by $\bar{c}(r, z)$ and integrating from depth z through a displacement $z + \eta(r, z, t)$ of the isopycnal surface relates the fluctuations $\delta c(r, z, t)$ to both temperature and salinity gradients as well as the internal wave displacements:

$$\begin{aligned} \delta c(r, z, t) &\equiv \int_z^{z+\eta(r, z, t)} \frac{\partial}{\partial z'} c_p(r, z') dz' \\ &= \int_z^{z+\eta(r, z, t)} \bar{c}(r, z') G(r, z') N^2(r, z') dz', \end{aligned} \quad (3)$$

where $\delta c = c_p(r, z + \eta, t) - c_p(r, z, t)$. Since $\eta(r, z, t)$ is determined by contributions from a spatially diffuse Garrett–Munk field and spatially localized soliton packets, the next section gives explicit descriptions of these quantities so that the upper limit to the integral of Eq. (3) can be explicitly determined in terms of the internal wave-field parameters.

B. Description of the internal wave fields

It is assumed here that the internal wave displacement field $\eta(r, z, t)$ can be written in the form $\eta(r, z, t) = \eta_D(r, z, t) + \eta_S(r, z, t)$, where η_D represents the diffuse component and η_S describes the soliton contribution. These displacement fields are described in the following two subsections. The integral in Eq. (3) can then be computed to obtain the sound-speed fluctuations in terms of internal wave-field quantities.

1. Garrett–Munk diffuse background contribution

The diffuse component of the internal wave field in shallow water environments is currently a topic of active research. The simulations presented here were intended to provide guidance for the SWARM experiment and were performed using a modification of the Garrett–Munk spectrum. After this work was completed, measurements became available from the Barents Sea¹⁸ and the New Jersey Bight area²⁰ suggesting that a wave number exponent of $-\frac{3}{2}$ may be a better representation in shallow water than the Garrett–Munk exponent -2 . Furthermore, in contrast to the isotropy of the Garrett–Munk model, the background field in these shallow water data appear anisotropic; the directionality is distributed over a sector approximating a quadrant. Nevertheless, the use of the Garrett–Munk spectrum is not unreasonable since it provides a useful starting point for investigations of the type reported here, and the main points of this paper are unlikely to be sensitive to these differences.

Following an approach developed in Refs. 1 and 4, the diffuse field component is represented as a statistical mixture of plane waves weighted by the Garrett–Munk spectrum. This representation is obtained by expanding $\eta_D(r, z, t)$ in a complete orthonormal set of internal wave eigenfunctions W that are obtained from solving the linearized Navier–Stokes equation for an inviscid, incompressible, stratified fluid. In this manner, the diffuse field can then be expressed as a weighted double sum over mode number j and horizontal wave number $k_h = (k_x^2 + k_y^2)^{1/2}$:

$$\eta_D(r, z, t) = \sum_{k_h} \sum_j F(k_h, j) W(k_h, j, z) e^{i[k_h r - \omega(k_h, j)t]}, \quad (4)$$

where the weighting factors $F(k_h, j)$ are zero mean, complex Gaussian random variables with an associated power spectrum discussed below. The use of a scalar k_h assumes that the internal wave field is horizontally isotropic. When shear flow in the water column is negligible, the dispersion relation $\omega(k_h, j)$ and the depth-dependent eigenfunctions $W(k_h, j, z)$ satisfy the eigenvalue equation

$$\frac{d^2}{dz^2} W(z) + k_h^2 \left[\frac{N^2(z) - \omega^2}{\omega^2 - f_c^2} \right] W(z) = 0 \quad (5)$$

subject to the rigid boundary conditions $W(0) = W(H) = 0$, where H is the water depth. The Coriolis (inertial) frequency is $f_c = 2\Omega \sin(\text{latitude})$, where Ω represents the Earth's angular velocity.

Solutions to Eq. (5) are independent of range and therefore ignore *internal* wave mode coupling associated with a range-dependent buoyancy frequency. We do allow for *acoustic* mode coupling via the range-dependent solution of the parabolic equation; the range dependence caused by sound-speed fluctuations enters through the exponential term in Eq. (4), while bathymetric range dependence enters through the boundary conditions. The temporal coherence of the background internal wave field was not considered for this study; for convenience, the time t was set to $t=0$ in the computation of η_D . This choice implies that the acoustic field averages are computed from samples obtained at inter-

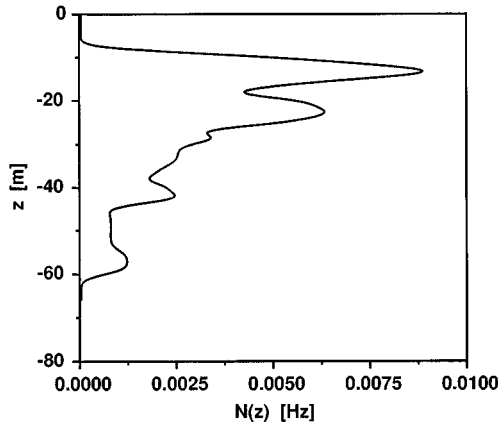


FIG. 1. Depth-dependent buoyancy frequency $N(z)$ used in the computation of the internal wave eigenfunctions.

vals greater than the correlation time for the evolution of the internal wave field (on the order of a few minutes).

Temperature and salinity profiles obtained from Fig. 5 in Ref. 22 for a site near the New Jersey coast were used to estimate the buoyancy frequency from Eq. (2). A mean (deterministic) sound-speed profile was computed from these profiles using an equation of state $\bar{c} = \bar{c}(T, S, z)$ given by the second equation of Table 5.2 in Ref. 23. The buoyancy frequency profile thus obtained is shown in Fig. 1 and shows a double ductlike structure between 10- and 25-m depth due to the competing nature of the temperature and salinity gradients in that part of the water column. The shortest period of internal wave variation, approximately 114 s, occurs at a depth of about 15 m.

A shooting method²⁴ was then applied to compute the eigenvalues $\omega(k_h, j)$ and eigenfunctions $W(k_h, j, z)$ from Eq. (5) over a range of $k_h \{0.0002, 0.25\} \text{ m}^{-1}$, corresponding to horizontal wavelengths from 25–31.4 km. This range of wave numbers amply covers the spatial scales important to the acoustic calculations in this paper. A water depth of $H = 66 \text{ m}$ was chosen and is an average value determined from the environment discussed in Sec. II. Latitude 40° was used to compute the Coriolis frequency. Representative normalized internal wave eigenfunctions are illustrated in Fig. 2 as a function of depth and horizontal wave number. The modal distribution varies smoothly with wave number, though there are mode-selective wave-number bands in which the energy is suppressed over a portion of the water column as seen for modes 10 and 15. This is due to the multiple peak structure of the buoyancy profile, shaped by the temperature and salinity gradients.

The power spectrum associated with $F(k_h, j)$ is assumed to be in the form of a Garrett–Munk spectrum:⁴

$$\langle |F(k_h, j)|^2 \rangle = E_0 M [j^2 + j_*^2]^{-p/2} \left(\frac{4}{\pi} \right) k_j k_h^2 (k_h^2 + k_j^2)^{-2}, \quad (6)$$

where the notation $\langle \rangle$ denotes ensemble average. The quantity k_j is given by $k_j = (\pi j f_c) / \int_0^H N(z) dz$ and corresponds to the spectral peak in the horizontal wave-number domain for each mode j , with the form of the integral in the denominator

of this expression chosen for consistency with the deep water case. A normalization factor M is specified by $1/M = \sum_{j=1}^{\infty} [j^2 + j_*^2]^{-p/2}$. The parameter E_0 represents the average energy density (J/m^2) and is associated with the strength of the internal wave fluctuations. The characteristic mode number, j_* , and spectral power law exponent, p , represent empirically determined parameters which control the relative contribution of the internal wave modes. A value $j_* = 3$, commonly used for deep water, was chosen to represent the mode number at which the energy begins to rapidly decrease as mode order increases. We used two constraints to bound the estimates of E_0 and p so that Eq. (6) is not underdetermined. The constraint on E_0 is that the isopycnal displacement at any depth z must be within the waveguide boundaries. Since the $F(k_h, j)$ are chosen for each realization by using a random number generator, the range-averaged variance $\chi_\eta(z) = \langle \eta^2(r, z) \rangle$ was computed for each depth using Eq. (4) and the first thirty eigenfunctions of Eq. (5). The constraint was chosen such that three standard deviations of the displacement at depth z should be within the waveguide boundaries. For a waveguide of depth H , this implies that $3\chi_\eta^{1/2} < z$ for negative displacements and $3\chi_\eta^{1/2} < H - z$ for positive displacements. In rare situations a displacement may still lie outside these bounds, and in these cases we simply truncate them to lie on the boundary. This argument represents only an upper limit to the displacements and it was found that a value of $E_0 \leq E_0^{\max} = 250 \text{ J/m}^2$ satisfied the displacement constraint. The value of E_0 chosen in most of the simulations was 25 J/m^2 , about 10% of E_0^{\max} and a more physically plausible value.²⁵ The mode weighting factor p was estimated by visual inspection of thermistor string data on the temperature fluctuations in a shallow water environment²⁶ and adjusting p to give visual consistency with those fluctuations. Based on this analysis we chose a value of $p = 4$.

Using these internal wave eigenfunctions and a pseudo-random number generator to provide the Gaussian distributed complex random variables, the double sum in Eq. (4) was evaluated by using the spectrum given by Eq. (6) and the constraint imposed on the particle displacements. Numerical integration of Eq. (3) using Eq. (4) to represent the diffuse internal wave field allows one to obtain realizations of the sound-speed fluctuations δc associated with the diffuse internal wave field η_D , together with an overlay of the deterministic sound-speed component, is shown in Fig. 3. These fluctuations depend on both range and depth, with the range dependence a function of k_h and the depth dependence a function of the modal structure determined by the buoyancy frequency [Eq. (2)] and spectrum parameters [Eq. (6)]. The range- and depth-averaged variance of the fluctuations relative to the mean sound speed is $\langle (\delta c / \bar{c})^2 \rangle \sim 0.5(10^{-6})$. The fluctuations are clearly confined to the region of the thermocline where temperature and/or salinity gradients make their maximum contribution to the buoyancy frequency. According to Ref. 1, while the higher-order modes make relatively small contributions to the overall spectra defined by Eq. (6), they are important in understanding acoustic propagation since the vertical structure of the high-order

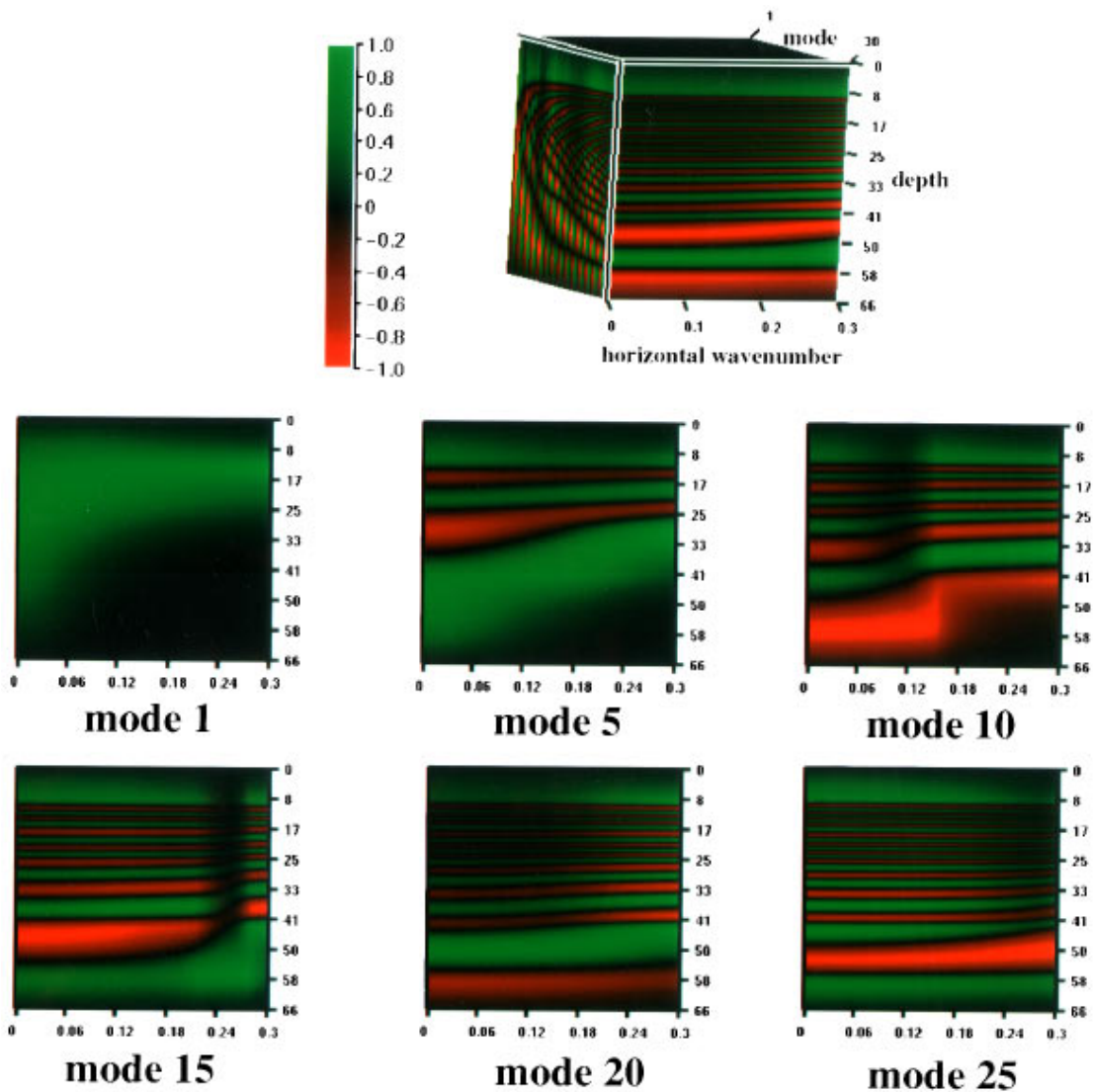


FIG. 2. Examples of several internal wave eigenmodes computed from Eq. (5).

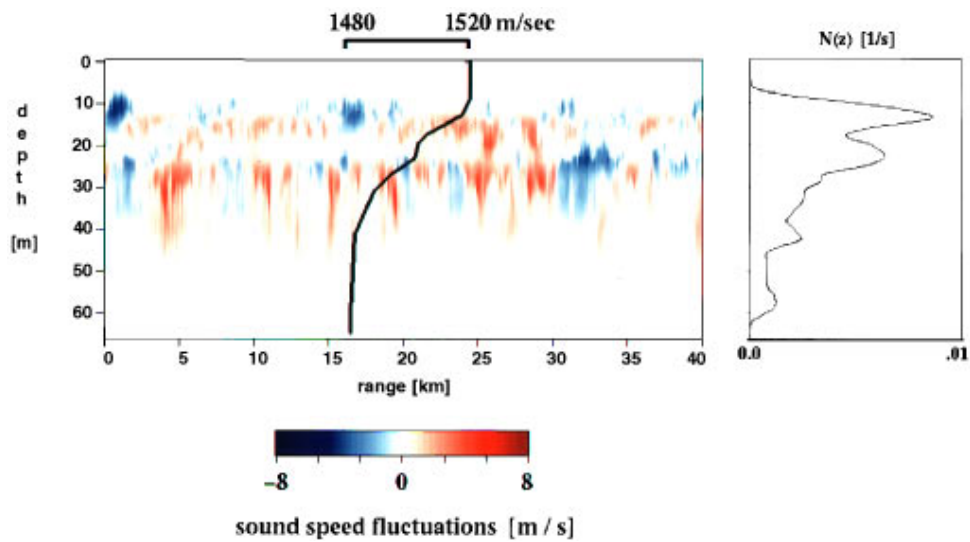


FIG. 3. Single realization of sound-speed fluctuations generated by a Garrett–Munk internal wavefield using the buoyancy frequency shown in Fig. 1. The deterministic background sound-speed distribution is superimposed on the figure, and was computed using the same temperature and salinity data used to determine the buoyancy frequency.

modes causes more acoustic scattering (i.e., mode coupling) than the relatively structureless low-order modes.

2. Soliton packet contribution

The second component of the internal wave field is a soliton displacement field, $\eta_S(r, z, t)$, representing an example of the nonlinear interaction of oceanic tides with bathymetric features such as the continental shelf edge. Solitons occur in many physical systems and have been studied both experimentally and theoretically in the oceanographic community.^{27,28} The isopycnal displacement for this component can be written in the form

$$\eta_S(r, z, t) = \sum_{j=1}^{\infty} (a_j(r, t) + b_j(r, t)) W(k_h, j, z), \quad (7)$$

where $W(k_h, j, z)$ is the j th depth-dependent eigenmode associated with the solution of Eq. (5) and a_j, b_j are coefficients corresponding to the left and right propagating modes originating in the source region.²⁹

It is sufficient for our purposes to consider only left propagating waves and limit the area of interest to be exterior to the source region. For the environment described here, the sum over eigenmodes in Eq. (7) can be approximated by the first term. This result can be inferred by computing the internal wave group speed, $c_g^{\text{IW}} = |\nabla_k \omega|$, from the dispersion relation $\omega = \omega(k_h, j)$ where ∇_k represents the 3-D k -space gradient operator. From Eq. (5) the square of the vertical wave number, k_v , can be identified with the term $k_h^2 [(N^2(z) - \omega^2) / (\omega^2 - f^2)]$. The gradient can be evaluated by letting $\vec{k} = l\hat{\sigma}_1 + m\hat{\sigma}_2 + n\hat{\sigma}_3$ with $\hat{\sigma}_i$ representing Cartesian unit vectors. The resulting c_g^{IW} for the first four modes are shown in Fig. 4 as a function of horizontal wave number and depth. This figure indicates that the group speed falls off quickly as a function of mode number and tends to be confined to depths where the buoyancy frequency is relatively large. Since the calculation shows that the first mode has a significantly larger group speed than the other modes, we make the approximation that the evolution of the isopycnal surface due to soliton propagation can be written as $\eta_S(r, z, t) \approx a_1(r, t) W(k_h, j = 1, z)$. Because we are confining ourselves to a region many kilometers from the source generation area, the higher-order modes will have negligible effect in the area of interest. The approximation is also consistent with the fact that the first mode dominates in the baroclinic response.²⁹

Keeping first order nonlinear terms in the Navier–Stokes equation for a nonrotating, stratified fluid²⁸ results in the Korteweg–de Vries (KdV) equation for the evolution of the amplitude $a_1(r, t)$:

$$\frac{\partial a_1}{\partial t} + \nu \frac{\partial a_1}{\partial r} + \alpha a_1 \frac{\partial a_1}{\partial r} + \beta \frac{\partial^3 a_1}{\partial r^3} = 0, \quad (8)$$

where α and β are the nonlinear and dispersion parameters, respectively. Solutions of this equation are well known.³⁰ A plane progressive wave solution to Eq. (8) can be written in the form

$$a_1(r, t) = \Lambda \operatorname{sech}^2 \left[\left(\frac{r - Vt}{\Delta} \right) \right], \quad (9)$$

where Λ is the amplitude factor and Δ , the characteristic width of the soliton, is given by $\Delta = \sqrt{12\beta/(\alpha\Lambda)}$. The amplitude-dependent wave speed V is related to the linear speed ν by $V = \nu + \alpha\Lambda/3$. The coefficients α and β , which are functionals of the depth-dependent eigenmodes and their derivatives, are given in Ref. 28.

While the KdV equation can be generalized to include the effects of variable depth topography, shoaling, dissipation, etc., the form given above is a surprisingly robust description for many environments.²⁸ The solution given by Eq. (9) represents a single progressive soliton, though what is commonly observed are soliton packets consisting of several solitons traveling as a group with different amplitudes, half widths and wave speeds. For the specific example of propagation in the continental shelf region off the New Jersey coast, we will assume that the displacements are given by soliton packets consisting of M solitons:

$$\eta_S(r, z, t) = W(k_h, j = 1, z) \sum_{m=1}^M \Lambda_m \operatorname{sech}^2 \left[\left(\frac{r_m - V_m t}{\Delta_m} \right) \right]. \quad (10)$$

This expression, combined with Eqs. (4)–(6), specify the displacement field $\eta(r, z, t)$ of the isopycnal surface associated with the total internal wave field. Substituting the equation for η in the upper limit of the integral in Eq. (3), numerical integration determines the sound speed fluctuations at depth z subject to the constraints on the displacements discussed above.

A uniform pseudo-random number generator was chosen to sample the time in Eq. (10); this determines the location of the soliton packet(s) and hence localizes the disturbance in space for each realization. Six solitons were used to form a packet. Individual soliton amplitudes, Λ_m , were represented by exponentially decaying functions with a maximum amplitude of 10 m for the first (leading) soliton in a packet: $\Lambda_m = 10e^{-0.3(m-1)}$, $m = 1, \dots, 6$. The horizontal wave number k_h was chosen for a typical soliton width of 100 m. The linear speed of a packet was $\nu = 0.6$ m/s, and α and β were chosen as 3.5×10^{-2} and 100, respectively. These data were chosen for consistency with data previously measured in the New York Bight area.²²

A single realization of the sound-speed distribution, including the deterministic, spatially diffuse, and spatially localized internal wave contributions, is illustrated in Fig. 5. Sound-speed variations associated with two soliton packets, each consisting of six solitons, are visible in the figure. They were assumed to be generated by tidal forcing with packets formed about 12.4 hours apart, corresponding to the period of the diurnal tide cycle. The initial source disturbance occurred about 25 km outside the region shown in the figure (i.e., about 65 km from the range origin). The solitons are moving to the left in the figure, with the packet on the left formed 12.4 hours earlier than the one on the right. The dispersion associated with the amplitude-dependent wave speed V is clearly visible in the figure.

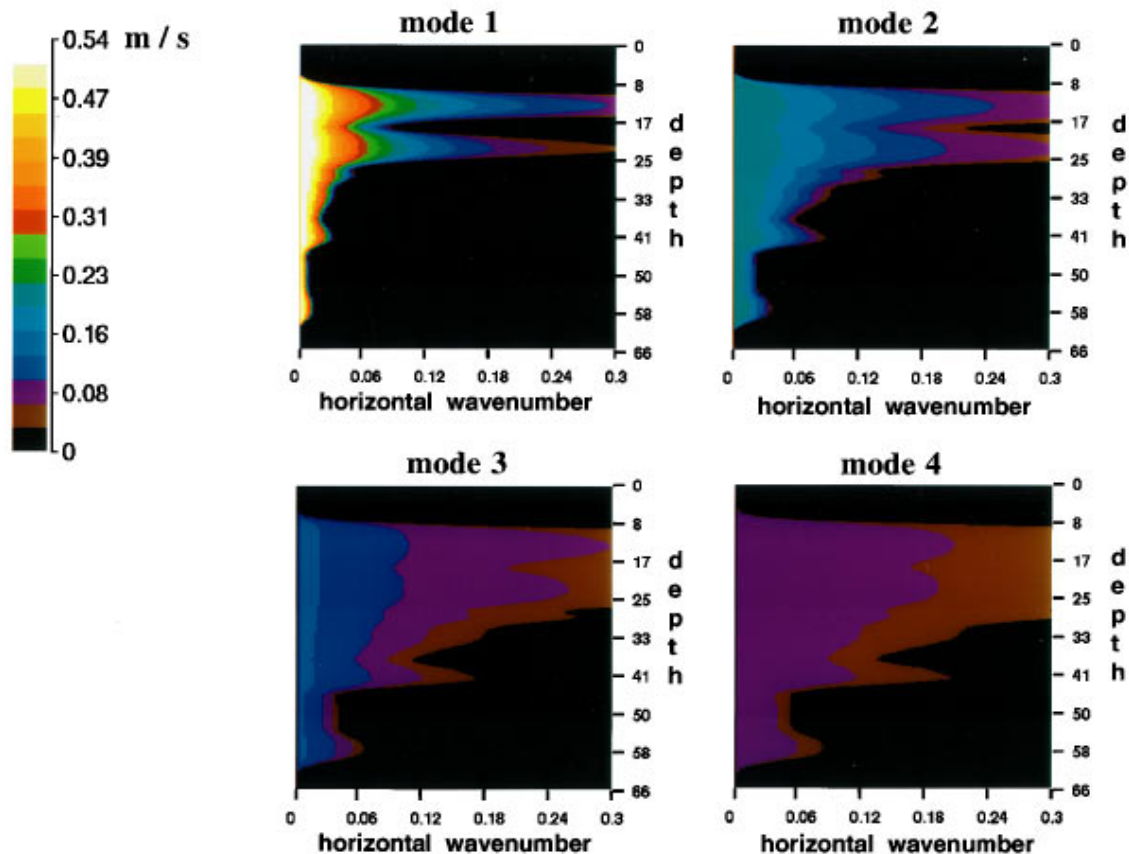


FIG. 4. Magnitude of the group velocity for the first four internal wave eigenmodes.

II. PRESSURE FIELD REALIZATIONS AND ENSEMBLE FIELD STATISTICS

The first subsection outlines the general method used to compute the pressure field realizations from the parabolic approximation to the elastic equations of motion. The sto-

chastic nature of the field in the water column is represented by treating the Lamé constant λ as a random variable. This variable, in turn, depends on the sound-speed profile. Statistically uncorrelated realizations of the internal wave field are computed, and each is written in the form

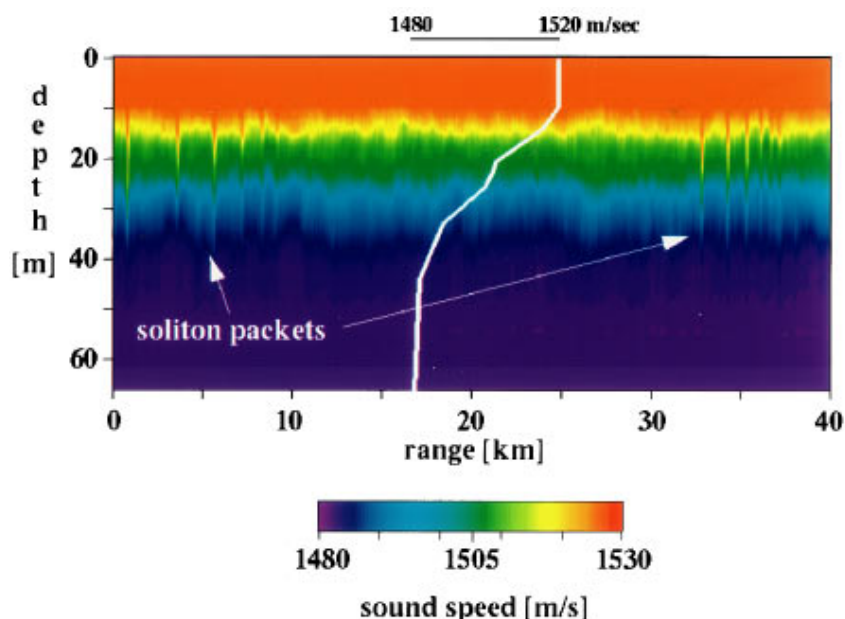


FIG. 5. Single realization of the sound-speed distribution consisting of a deterministic profile (superimposed in white), a Garrett–Munk contribution, and soliton packets. The solitons are generated about 25 km from the right edge of the figure and are traveling to the left.

$\delta c(r, z, t) \rightarrow \delta c_i(r, z)$, where the subscript i indicates the i th realization. This formulation corresponds to a ‘‘frozen ocean’’ approximation in which the fluctuations are frozen during passage of the acoustic signal. This is a reasonable assumption since Fig. 4 shows the highest group speed of the internal wave field is 0.54 m/s, compared to a speed of about 1500 m/s for the acoustic field. Statistical measures based on ensemble averages of the pressure field moments are discussed in the second subsection.

A. Computation of the pressure field realizations

We assume that the acoustic field propagates in a two-dimensional elastic waveguide with (r, z) representing the range and depth variables, respectively. For computational purposes, we employ the high-angle (Padé), elastic parabolic equation solver³¹ to compute the i th far-field realization of the pressure field $P_i(r, z, f)$ at frequency f . Each realization of the pressure field in the water column can be written in the form $P_i(r, z, f) = \lambda_i(r, z) \nabla \cdot \bar{u}(r, z, f)$, where \bar{u} represents the particle displacement and λ_i is a Lamé constant for the i th realization. Recalling the assumption that stochastic variations occur only in the water column sound-speed distribution, the Lamé constants are given by $\lambda_i(r, z, f) = \rho(C_i^2 - 2\hat{C}^2)$ and $\mu(r, z, f) = \rho\hat{C}^2$, where C_i and \hat{C} are the (complex) compressional and shear speeds, respectively. Note that in the water column C_i and, therefore, λ_i are random variables. In the bottom they are treated as deterministic variables. The Lamé constant μ is zero in the water column and deterministic in the bottom. Compressional and shear speeds are given by $C_i = (\bar{c}(r, z) + \delta c_i(r, z)) / (1 + i\sigma\beta)$ and $\hat{C} = \hat{c} / (1 + i\sigma\hat{\beta})$. The real shear speed is given by \hat{c} , with the compressional and shear attenuation coefficients $\beta, \hat{\beta}$ measured in decibels per wavelength. The constant σ is $(40\pi \log e)^{-1}$. Ensemble averages were estimated from 100 realizations of P_i , obtained at a frequency $f = 400$ Hz. Examination of the ensemble-averaged intensity and scintillation index for 50, 100, and 200 realizations indicated that quantitative differences in the averages obtained using 100 and 200 realizations was small enough to choose 100 realizations for computational efficiency.

The air–water interface is flat in these simulations. The compressional sound speed in the bottom has a dependency $\bar{c}(z) = 1700 + 0.737z - 165e^{-z/5}$ and the shear speed was represented by $\hat{c}(z) = 0.52(\bar{c}(z) - 1200)$, with all depths in meters. These profiles were estimated from data in Figs. 4, 7, and 12 from Ref. 32, and Fig. 2 in Ref. 33 and are values chosen to represent a terrigenous medium with silty-sandy layers near the water–sediment interface. The density in the substrate was chosen to be 1.8 g/cm³. A value of $\beta = 0.4$ dB/ λ for the compressional wave attenuation coefficient was estimated from Figs. 18 and 20 in Ref. 32. For the purposes of this paper, a high shear attenuation coefficient was picked ($\hat{\beta} = 20$ dB/ λ) so that any energy converted to shear waves is simply dissipated.

B. Field statistics

In this subsection we discuss full-field statistics and modal statistics of the pressure field. The deterministic full-

field transmission loss is defined by $-10 \log[P^*(r, z, f)P(r, z, f)]$ and is obtained using only the deterministic sound-speed profile $\bar{c}(r, z)$ for the pressure field calculations. Assuming independent realizations of the sound-speed fluctuations, a measure of the full-field transmission loss for the stochastic waveguide is given by the ensemble-averaged loss over realizations:

$$-10 \log\langle P_i^*(r, z, f)P_i(r, z, f) \rangle = -10 \log\langle I_i(r, z, f) \rangle, \quad (11)$$

where I_i is the i th realization of the intensity at a point in the waveguide. The brackets $\langle \rangle$ denote ensemble average. Another quantity of interest is the variance of the full-field intensity, normalized by the mean squared intensity. This is the field’s scintillation index $SI(r, z, f)$:

$$SI(r, z, f) = \frac{\langle I_i^2(r, z, f) \rangle - \langle I_i(r, z, f) \rangle^2}{\langle I_i(r, z, f) \rangle^2}. \quad (12)$$

The pressure computed from the parabolic equation gives the forward propagated field at location (r, z) within the waveguide. A modal decomposition can be performed on the realizations P_i in order to evaluate the contributions of individual modes. Expanding the field in terms of a complete set of eigenfunctions, ϕ , associated with the deterministic sound speed \bar{c} , a modal representation of the deterministic pressure field in the water column can be written in the far field as

$$P(r, z, f) = e^{i2\pi ft} \sum_n d(n, r, z_0, f) \phi(n, z, f), \quad (13)$$

with $d(n, r, z_0, f) = (2\pi/k_n r)^{1/2} e^{-i(k_n r + \pi/4)} \phi(n, z_0, f)$ for a harmonic point source located at $\{r=0, z_0\}$. For notational simplicity, the explicit dependence on source depth z_0 will be suppressed. Using the orthonormal property of the pressure eigenfunctions, $\int [\phi(m)\phi(n)/\rho(z)] dz = \delta_{mn}$, the modal amplitudes, d_i , are obtained by forming an inner product for each realization:

$$d_i(n, r, f) = \int_0^\infty \frac{\phi(n, z, f)P_i(r, z, f)}{\rho(z)} dz. \quad (14)$$

The second moment of the modal amplitude is then defined by $\langle I_i(n, r, f) \rangle = \langle d_i^*(n, r, f)d_i(n, r, f) \rangle$ with the ‘‘modal intensity’’ represented as

$$MI(n, r, f) = -10 \log\langle I_i(n, r, f) \rangle. \quad (15)$$

The modal scintillation index for mode n can be written in the form

$$SI(n, r, f) = \frac{\langle I_i^2(n, r, f) \rangle - \langle I_i(n, r, f) \rangle^2}{\langle I_i(n, r, f) \rangle^2}. \quad (16)$$

The full-field transmission loss and scintillation index are determined by both amplitude and phase contributions of the complex phasor sum represented by Eq. (13). For a deterministic waveguide, fluctuations of intensity caused by the interference of several modes has been studied using a random walk analogy.³⁴ For such a waveguide, the phases of the modes increase at different rates due to their distinct phase speeds while the modal amplitudes change at a much slower rate. An expression was obtained for the scintillation index

that was indistinguishable from the results obtained by regarding the mode phases to be uniformly distributed, uncorrelated random variables and computing an ensemble average instead of a range average.³⁴ In this paper, both the modal amplitudes and phases are random variables. The phase variations are not assumed to be sufficiently large that the modal field components are mutually incoherent over the ensemble; in fact, residual coherence was observed in the coherently averaged field (refer to discussion concerning Fig. 12, below). The mode representations in Eqs. (15) and (16) describe only the amplitude-dependent contributions of the pressure field. Neglecting phase correlations implies that $\langle d(n,r,f)d^*(m,r,f) \rangle = 0$ for $n \neq m$. By substituting Eq. (13) into Eq. (12) and using the fact that the variance of a sum of independent random variables is equal to the sum of the variances, one obtains an expression for the incoherently summed full-field scintillation index in terms of the modal amplitude contributions:

$$SI_{\text{amp}}(r,z,f) = \frac{\sum_n \langle |d(n,r,f)|^2 \rangle^2 \phi^4(n,z,f) SI(n,r,f)}{\sum_n \langle |d(n,r,f)|^2 \rangle^2 \phi^4(n,z,f)}. \quad (17)$$

It will be seen below that a number of features associated with the scintillation index are reproduced by considering only modal amplitude fluctuations, as expressed in Eq. (17).

III. NUMERICAL EXPERIMENTS

This section presents simulation results for the acoustic field statistics in several stochastic waveguides. The waveguides have either a flat or sloping bottom, and the sound speed fluctuations consist of either the diffuse Garrett–Munk component η_D or a combination of η_D and the soliton packet contribution η_S . To clarify some of the results, additional simulations were performed with only the spatially localized soliton packets, though these are not shown here. Results are illustrated for two source depths, one near the surface and one near the bottom. A comparison between deterministic and ensemble-averaged transmission loss in these waveguides is presented in Sec. III A. In order to illustrate the details of modal coupling and the asymptotic behavior of intensity fluctuations without the additional complication of variable bathymetry, these effects are investigated in Secs. III B and C for a shallow water (66 m) waveguide composed of plane, parallel boundaries at the surface and bottom. Following a brief summary of recent theoretical results concerning the long range behavior of the scintillation index,¹⁶ modal decomposition of the field is performed using Eq. (14), and the scintillation index is computed on a modal basis using Eq. (16). These numerical experiments are then related to the theoretical prediction of Ref. 16. The full-field scintillation index is estimated both directly from the pressure field calculations using Eq. (12) and indirectly from modal decomposition via Eq. (17), in order to provide an assessment of the relative importance of amplitude and phase contributions. In Sec. III D, the full-field scintillation indices are computed for both flat and sloping bottom environments. While modal decomposition is not performed in the sloping

bottom case, a physical interpretation of the modal behavior follows from the analysis of the simpler environment presented in Sec. III B.

A. Full-field deterministic and ensemble-averaged transmission loss

Plots of the full-field coherent transmission loss for deterministic cases (internal waves absent) and ensemble averages of 100 realizations with internal waves present are shown in Fig. 6. The acoustic source is located at depth 15 m at the range origin and denoted by a short white line in the figures. The figures show the adjusted transmission loss; the $1/r$ cylindrical spreading component of the loss has been removed in order to reduce the dynamic range of the loss values and thereby preserve resolution of the color scale. Figure 6(a)–(c) shows loss for a flat ocean bottom at depth $H=66$ m and Fig. 6(d)–(f) were calculated for the sloping bottom of the experimental site. The first figure in each set [Fig. 6(a) and (d)] represents the deterministic case. The second, Fig. 6(b) and (e), shows average coherent loss when only the diffuse background internal waves are present. For the third set, Fig. 6(c) and (f), loss is shown for the combined diffuse background and internal soliton fields.

Due to refraction of low-order modes toward the ocean bottom by the negative gradient profile, the acoustic field of the source at 15-m depth is initially propagated primarily in higher-order acoustic modes. It was found that the source coupling to mode orders 1–4 was 15 dB lower than to mode orders 5–7 and 9–10. If we consider the sequence Fig. 6(a)–(c) we note a progressive loss of detail in the coherent mode interference pattern as the diffuse background internal waves and the solitons are introduced. While this loss of coherence of the ensemble-averaged coherent field realizations may be due, in part, to random phase modulations of adiabatically propagated components, the influence of random coupling of energy between modes may also be responsible for some of this coherence loss. Evidence for the presence of coupling in these figures is seen in the increase in signal strength at depths greater than 20 m and reductions in signal strength at shallower depths, particularly at longer ranges. The higher-order modes, which produce the shallow-depth field, have lost energy to lower-order modes, which are confined to deeper depths by the negative-gradient profile and which propagate with less attenuation. Simulations not shown here, in which internal waves consisted only of the soliton components, indicate that the solitons do not dominate the coupling in Fig. 6(c); the diffuse background and soliton internal wave components used here produce similar coupling strengths. We note that the increase in signal strength at the deeper receiver depths accompanying the successive introduction of the background and soliton internal waves is equally visible in the calculations Fig. 6(d)–(f) for the sloping bottom waveguide.

In Fig. 7 we show a set of field calculations for the same environments as in Fig. 6, but for a deeper (45 m) sound source. Because this deeper source strongly couples to both the low- and high-order mode components, the deep receiver signal-strength evidence of mode coupling seen in Fig. 6 is now absent due to masking of energy coupled into low-order

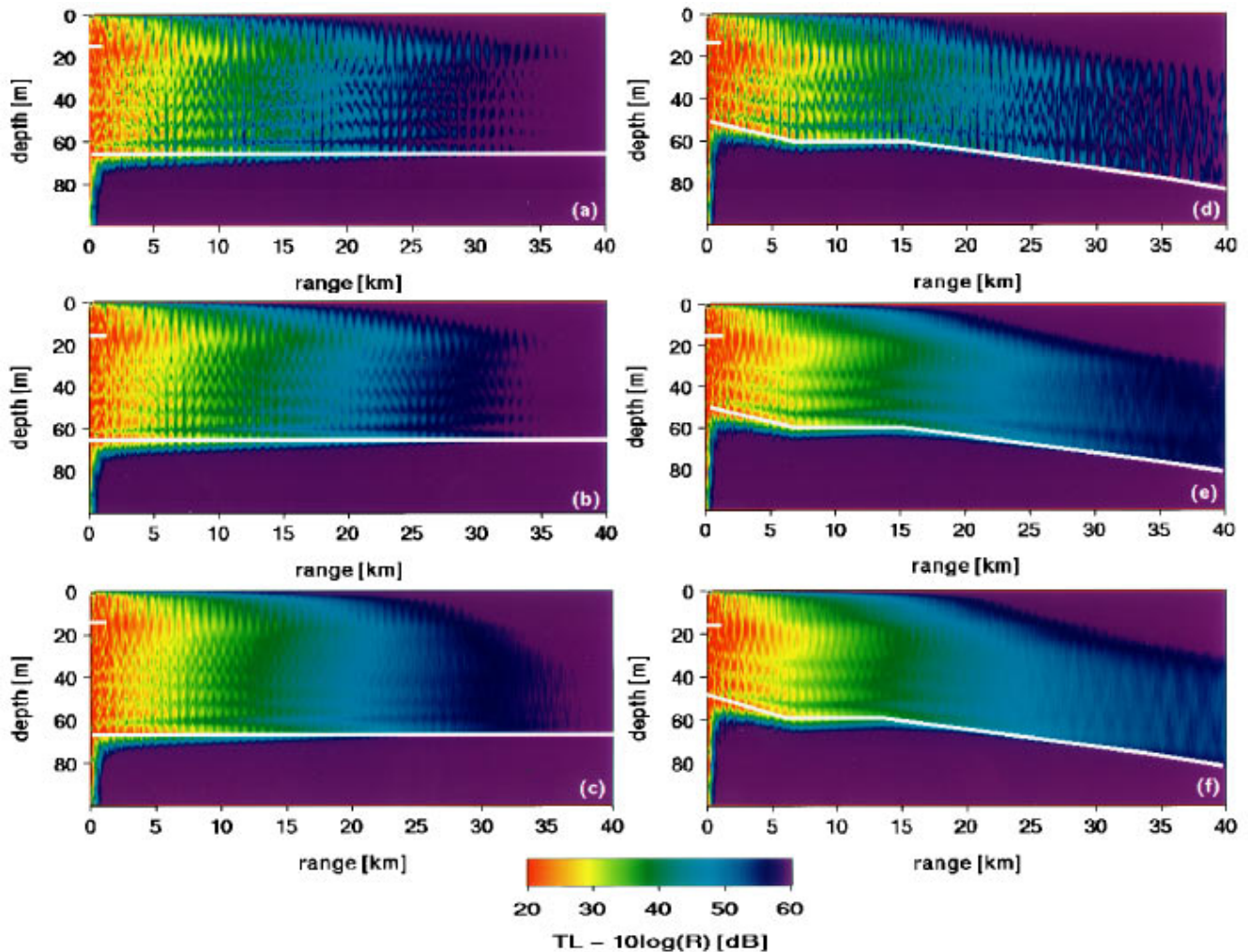


FIG. 6. Full-field deterministic and ensemble-averaged transmission loss plots for both flat [(a)–(c)] and sloping-bottom [(d)–(f)] waveguides. The acoustic source was a point source at ($r=0$, $z=15$ m) and is indicated by the short white line at the upper left corner of each figure. The cylindrical spreading component of the transmission loss has been suppressed. (a), (d) deterministic loss; (b), (e) ensemble-averaged loss with Garrett–Munk internal wavefield with $E_0=25$ J/m²; (c), (f) ensemble-averaged loss with both Garrett–Munk and soliton packet contributions to the internal wave field.

modes by strong adiabatically propagated low-order mode components. These adiabatic components increase the deep receiver field strength to values about 30 dB higher than those found with the shallow source. The loss of coherence (disappearance of the interference pattern in the ensemble averages) is of degree similar to that seen for the shallower source. This result suggests that the internal wave field can produce significant phase modulations of even the adiabatically propagated components. To gain additional insight into acoustic mode coupling induced by internal waves, we next consider the range dependence of intensity and scintillation index of single mode fields.

B. Asymptotic behavior of modal intensity and scintillation index in shallow water

A brief outline of a recent shallow water stochastic mode theory¹⁶ that accounts for both mode coupling and mode stripping is presented below, and is followed by simulations of modal coupling that give insight into the theoretical results on the asymptotic behavior of both modal intensity and modal intensity fluctuations. The notation used in

this section is the same as in Ref. 16. Assuming the quasi-static and narrow-angle forward scattering approximations, the modal amplitudes $A_n(r)$ in a range-dependent, stratified waveguide satisfy the first-order differential equation

$$\frac{\partial A_n}{\partial r} + (\alpha_n - ik_n)A_n = -i \sum_{m=1}^N \rho_{nm}(r,t)A_m, \quad (18)$$

where α_n and k_n are the modal attenuation coefficient and horizontal wave number for the n th mode, respectively. In this notation, $A_n(r)$ is related to $d(n,r,z_0,f)$ by $A_n(r) = (k_n r)^{1/2} d(n,r,z_0,f)$. The mode coupling coefficients ρ_{nm} are given by

$$\rho_{nm} = \frac{k^2}{\sqrt{k_n k_m}} \int dz \frac{\delta c(r,z,t)}{c(r,z)} \phi_n(z) \phi_m(z). \quad (19)$$

In this equation, k is the mean acoustic wave number and ϕ_n and ϕ_m are depth-dependent pressure eigenfunctions associated with the mean profile. Note that the coupling coefficients can be expressed in terms of the internal wave spectrum via Eqs. (3), (4), and (10). The coupling matrix represents the scattering of acoustic mode m into acoustic

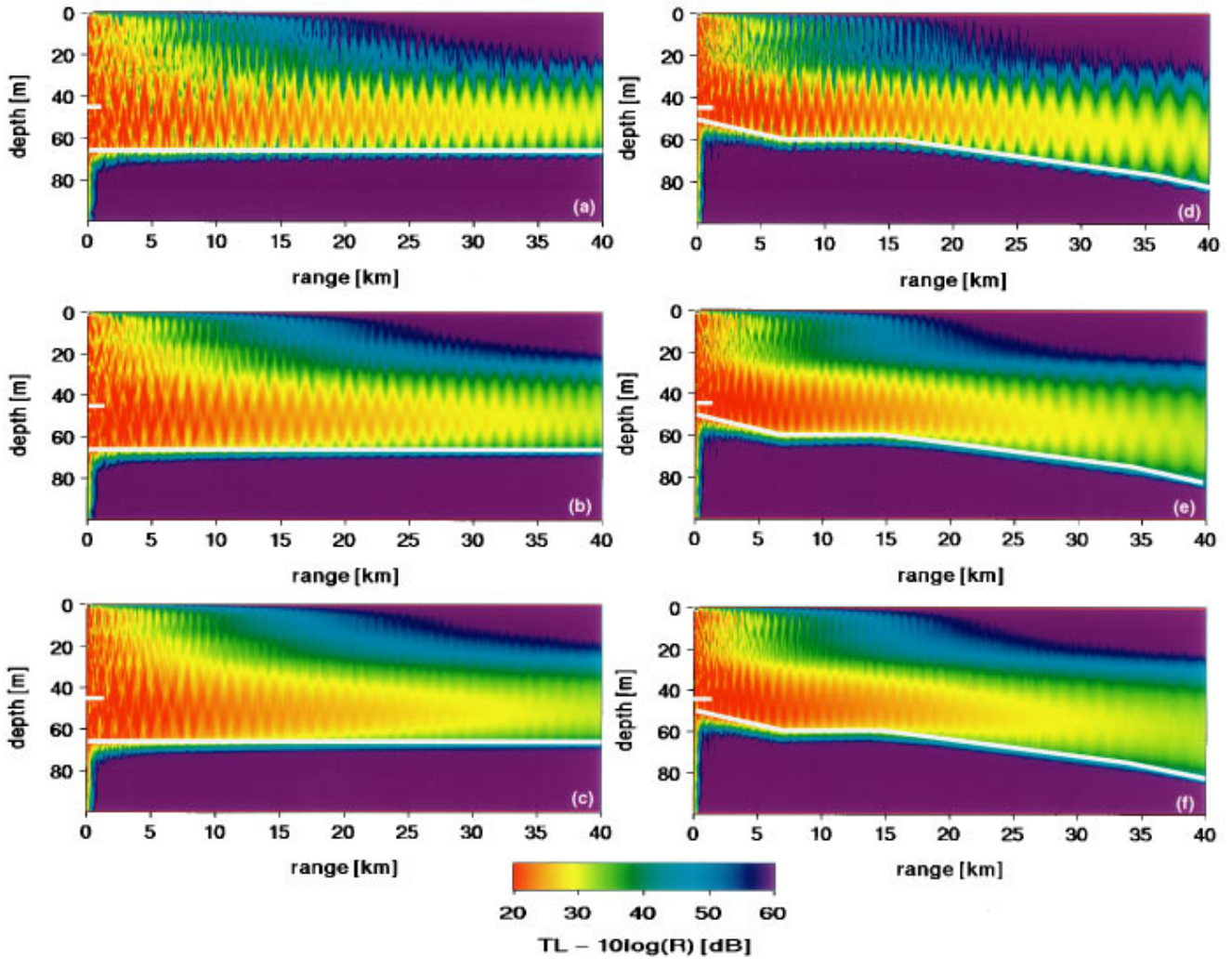


FIG. 7. Full-field deterministic and ensemble averaged transmission loss plots for both flat [(a)–(c)] and sloping bottom [(d)–(f)] waveguides. Same format as in Fig. 6 but with a source located at $(r=0, z=45 \text{ m})$.

mode n by internal wave modes that account for the sound-speed variability.

The range variation of both the modal intensities and intensity fluctuations are governed by master equations derived from Eq. (18) under the additional assumptions that the cross-modal coherence $\langle A_n^* A_m \rangle$ is negligible and the correlation range of the sound speed inhomogeneities in the direction of propagation is small.¹⁶ For large range R , one can derive an equation for the modal intensity vector Γ with components $\Gamma_n \equiv \langle |A_n|^2 \rangle$:

$$\frac{\partial \Gamma}{\partial R} = -\Xi \Gamma, \quad (20)$$

where the matrix Ξ is a function of the coupling and attenuation coefficients for the $n=1, \dots, N$ modes. The solution to Eq. (20) can be obtained by diagonalizing Ξ as $\Xi = U D_\Xi U^T$ where U is an orthogonal matrix containing eigenvectors of Ξ and D_Ξ is the diagonal matrix whose elements are the eigenvalues of Ξ , with the latter denoted by ξ_q . Using this decomposition, the asymptotic behavior of the solution to Eq. (20) can be shown to be dominated by the smallest eigenvalue, $\xi_{q=1}$, and can be written for the n th component (mode) in the form

$$\Gamma_n(R) \sim U_{n1} \left[\sum_m U_{m1} \Gamma_m(0) \right] e^{-\xi_1 R}, \quad R \rightarrow \infty. \quad (21)$$

The quantity $\Gamma_m(0)$ is the initial value of Γ at $r=0$ and represents the modal energy distribution excited by the source. The components of the first eigenvector U_{m1}, U_{n1} for modes m, n are associated with the smallest eigenvalue ξ_1 , where ξ_1 is a function of all modal coupling and attenuation coefficients. The first (smallest) eigenvalue controls the asymptotic decay rate for all modes, while the first eigenvector controls the asymptotic energy distribution among the modes. It is important to note that while Γ_n depends on the initial conditions, the (long range) ratio of the average modal intensities for any two modes n and l is a constant, $\Gamma_n/\Gamma_l = U_{n1}/U_{l1}$, independent of the initial conditions. The value of this ratio, however, is a function of the modal coupling and attenuation coefficients for all the modes. A master equation analysis of modal coupling caused by range-dependent fluctuations in sediment properties led to a similar conclusion for the asymptotic ratio of modal intensities.³⁵ In the deep water case with no bottom interacting energy, the components of the first eigenvector are equal at large range and the energy is equipartitioned among the modes.^{5,6}

A similar, though algebraically more complex, approach can be applied to derive an equation governing the second moment of the intensity whose elements are $\Psi_{ij} = \langle |A_i|^2 |A_j|^2 \rangle$. The result is an equation for Ψ with the form of Eq. (20) and Ξ replaced by the matrix Θ . Decomposition of Θ into $VD_\Theta V^T$ allows one to obtain the following asymptotic solution for the second moment of the intensity:

$$\Psi_{ij} \sim V_{ij,11} \left[\sum_n \sum_{m \leq n} V_{mn,11} \Psi_{mn}(0) \right] e^{-\theta_1 R}, \quad R \rightarrow \infty, \quad (22)$$

where θ_1 is the smallest eigenvalue of Θ . Using Eqs. (16), (21), and (22), the modal scintillation index $SI(i, r, f)$ behaves asymptotically as

$$SI(i, R, f) = \frac{\Psi_{ii}}{\Gamma_i^2} - 1 \sim \left\{ \frac{V_{ii,11} [\sum_n \sum_{m \leq n} V_{mn,11} \Psi_{mn}(0)]}{U_{i1}^2 [\sum_m U_{m1} \Gamma_m(0)]^2} \right\} \times e^{(2\xi_1 - \theta_1)R} - 1. \quad (23)$$

The growth rate factor $(2\xi_1 - \theta_1)$ depends on the difference in the smallest eigenvalues of the coupling matrices for the first and second moments of the intensity. This factor is always greater than or equal to zero since the variance is positive semi-definite; it is zero in the limit where there are no differences in attenuation between the modes. This statement, together with Eq. (23), form the main theoretical result of Ref. 16 and imply that the modal scintillation index increases exponentially with range. The coefficient multiplying the exponential term is a function of the modal coupling coefficients, modal attenuation, and the initial conditions associated with the distribution of modal energy at the acoustic source location. However, the asymptotic ratio $(SI(i, R, f) + 1)/(SI(l, R, f) + 1)$ for any two modes i and l is both independent of the initial conditions and range independent, though the value of the ratio still depends on the coupling between modes and the attenuation coefficients.

This unexpected result concerning the asymptotic behavior of the scintillation index arises from the interplay between mode stripping and mode coupling found in bottom-interacting waveguide propagation. Mode coupling is a mechanism for redistributing or equilibrating modal energy, while mode stripping acts like an irreversible loss mechanism. The predicted mismatch in decay rates between the second and fourth moments of field intensity is the cause of the asymptotic increase in scintillation index. By way of comparison, the deep water case with no mode stripping yields the result that the scintillation index asymptotically approaches $(N-1)/(N+1)$, where N is the number of modes.⁵ It is worth reiterating that these predictions are generally valid, i.e., are not dependent on the particular origin or form of the stochastic sound speed distribution, provided that (a) the forward scattering approximation is valid, (b) only short range correlations between sound-speed fluctuations (Markov assumption) occur, and (c) the cross-modal coherence can be neglected. While an experimental test is needed to verify the correctness of the theory discussed above, a

comparison with modal statistics derived from direct numerical solutions of the stochastic wave equation for realistic environments can be used as a consistency check. The results of several of these computations are presented below.

C. Range dependence of modal field statistics

In this subsection, implications of the theory outlined above are explored by computing the range dependence of the individual modal contributions to the field. The numerical experiments are illustrated for flat bottom waveguides with sources at depths of 15 and 45 m and include sound-speed fluctuations induced by diffuse component η_D . Mode filtering provides insight into modal coupling induced by the fluctuations in sound speed and presents a natural framework in which the predictions in Sec. III B can be evaluated. In addition, mode decomposition is useful in obtaining a qualitative interpretation of the full-field results. Simulations were performed to a range of 200 km using $E_0 = 25 \text{ J/m}^2$, though in the analysis of the asymptotic behavior of the scintillation index we present one calculation with a value of $E_0 = 100 \text{ J/m}^2$. The higher value of internal wave energy density induced larger sound-speed fluctuations in the waveguide which, in turn, led to strong mode coupling. This enhanced coupling allowed statistical trends to appear without extending the simulations over an unreasonably long range, a compromise necessary for studying the asymptotic behavior of the field quantities with reasonable computational efficiency. The modal decomposition of the field was obtained from the expressions in Sec. II B and the resulting curves were smoothed using a running Gaussian window with a standard deviation of 3.6 km. As before, cylindrical spreading has been removed.

We assessed the magnitude of numerically generated artifacts, which can be misinterpreted as mode coupling, by mode filtering the field calculated for a range-independent waveguide. These artifacts include errors due to numerical approximations in the parabolic equation implementation as well as errors associated with mode filter leakage. Results are presented in Fig. 8 for a source at $z = 45 \text{ m}$. Exponential intensity losses appear as straight lines on the logarithmic plot shown in this figure; in general, the decay rate of any particular mode depends on that mode's coupling to the other modes and on all the mode attenuation coefficients. No mode coupling should occur in this particular case since the sound-speed field is range invariant. However, Fig. 8 shows that the slopes of modes 2–10 are altered and become parallel to that of mode 1, the dominant mode, for ranges greater than 150 km. The dominance of this mode is also visible in the transmission loss plots of Fig. 7, where the contributions of the higher-order modes in the upper part of the water column become quite small at ranges greater than about 20 km from the source. We infer from Fig. 8 that mode 1 acts as the dominant energy source for the high-order mode filter outputs. This result is seen in the figure in the form of equal mode slopes after some transition range. We further note that this “numerical error coupling” is low; mode 2 is some 40 dB below mode 1 and the highest order modes are down by as much as 60 dB. These numerically driven coupling effects

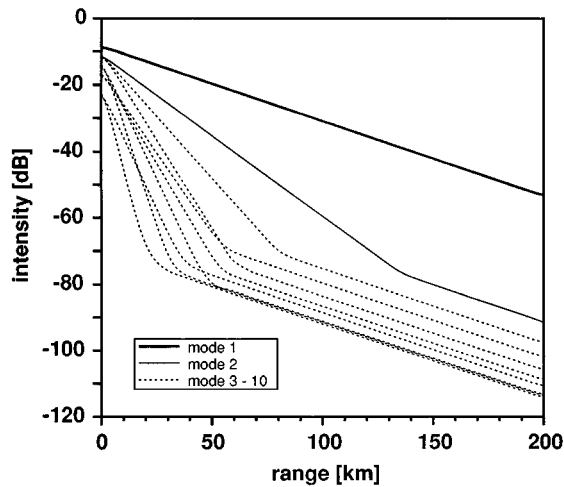


FIG. 8. Output level of spatial filters matched to the first ten mode orders as a function of range for a deterministic, range-independent environment. The relative strengths of the filter output at the longer ranges gauge the magnitude of the numerical noise, as inferred from the change in range-slope of the corresponding filter outputs to become parallel to that of the first-order mode. At these ranges the adiabatically propagated higher-order modes have been removed from the signal field by attenuation. The source was located at ($r=0, z=45$ m).

are small compared to the mode coupling results presented below for stochastic environments.

The ensemble-averaged modal intensities for the first ten modes, given by Eq. (15), are shown in Fig. 9(a) for a source depth of 45 m. It is apparent that the first two modes begin to dominate at ranges greater than about 15 km from the source, an observation also supported by examining the transmission loss plots in Fig. 7. The range dependence introduced by the presence of the diffuse internal wave component leads to increased modal coupling. This increase [Fig. 9(a), cf. Fig. 8] is seen in the higher intensity levels of higher-order modes relative to the first-order mode. The equality of the range rate of attenuation of the output of the higher-order mode filters to that of the first-order mode filter is interpreted as support of the prediction that in the asymptotic range limit all of the modal components of the field are attenuated at the same rate.¹⁶ A reasonable physical interpretation of this result is that virtually all of the energy appearing in a high-order mode at long range has been propagated over most of the track as a first mode field and has been coupled near the field point to a higher-order mode by the random environment. Higher-order mode decay rates at long range are thus dominated by the decay rate of the first mode, which acts as a local source of energy for the higher-order components.

The ensemble-averaged modal intensity for a source depth of 15 m is shown in Fig. 9(b) for the same ten modes. In this case, the higher-order modes initially contain more energy than the low-order modes, a result also seen in Fig. 6. This remains true up to a transition range of approximately 50 km, where the first mode becomes dominant due to mode stripping of the initial higher-order mode energy. Note that beyond range 100 km the modal losses of the higher-order modes are again proportional to that of mode 1.

A key assumption in the analysis is that the outputs of the higher-order mode filters represent signals propagating as

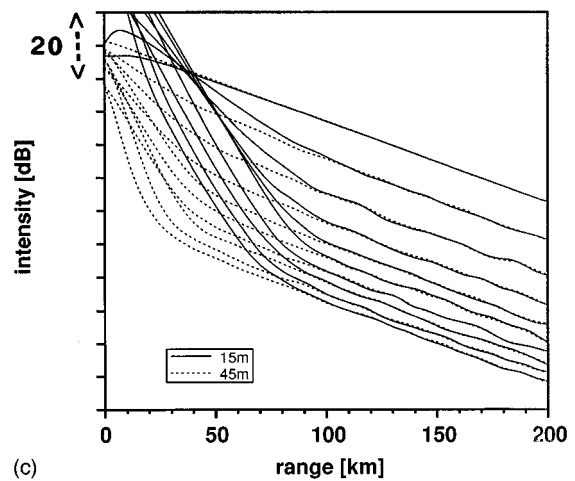
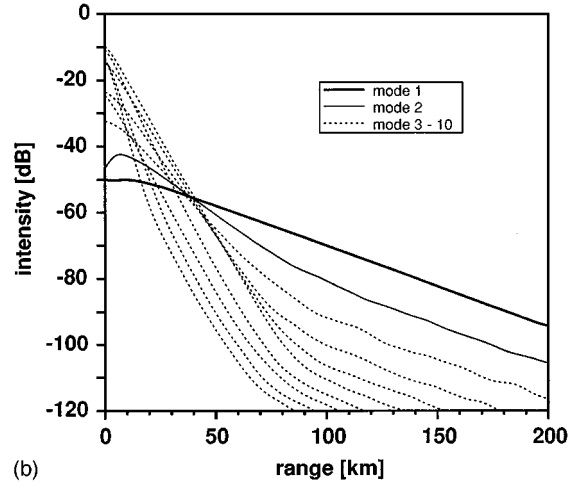
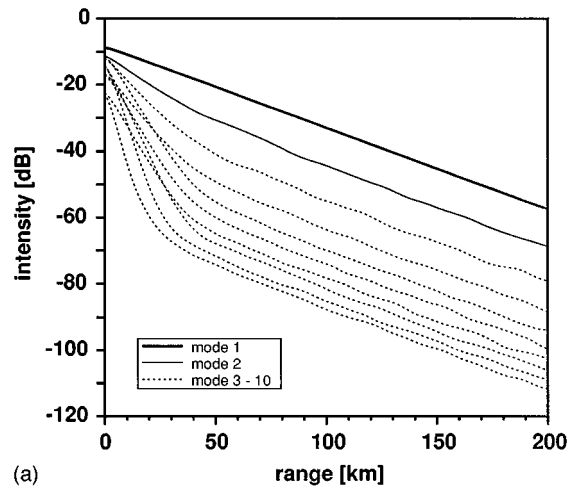


FIG. 9. Ensemble-averaged mode intensity plots as a function of range for the first ten modes for the stochastic waveguide case. (a) Results are for a source depth of 45 m and (b) results are for a source depth of 15 m. (c) An overlay of (a) and (b) with the 15-m source depth data (solid curves) translated up approximately 37 dB.

higher-order modes, rather than leakage of a low-order mode signal through the filter. In the absence of internal waves, we found that the leakage due to numerical artifacts was low, as discussed above in connection with Fig. 8. When the internal waves are present, the sound-speed profile, and therefore the shapes of the modes, become range dependent. Since the

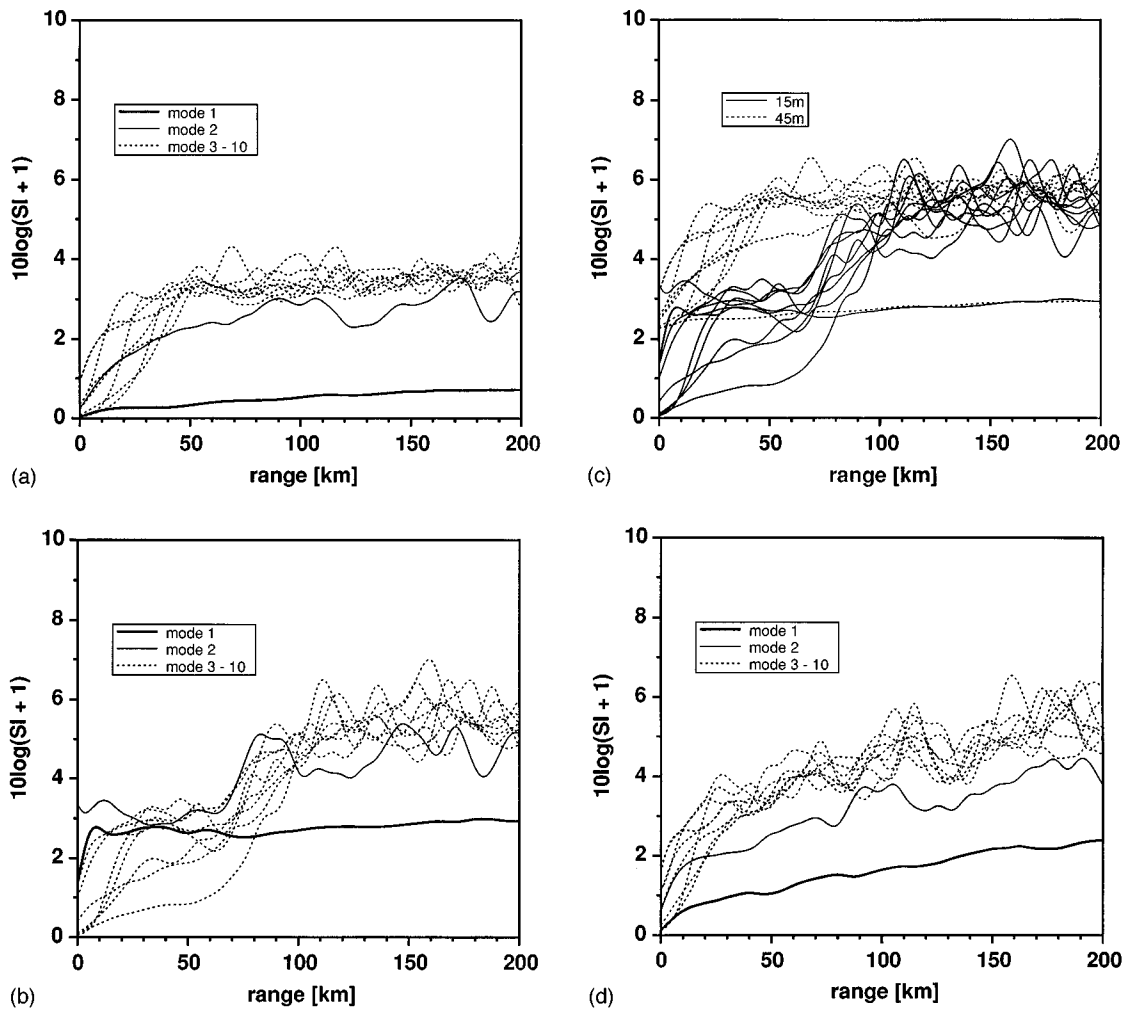


FIG. 10. Modal scintillation indices for the first ten modes as a function of range, plotted logarithmically in terms of $SI+1$. (a) Results are for a source depth of 45 m and (b) results are for a source depth of 15 m. In both (a) and (b) the Garrett–Munk component was used with an energy density of $E_0=25 \text{ J/m}^2$. (c) A superposition of the results in (a) and (b) with the individual mode data from (a) shifted up by about 2 dB. The modal scintillation indices for $E_0=100 \text{ J/m}^2$ and a source depth of 45 m are presented in (d).

spatial mode filters were calculated from the deterministic profile, alterations of the mode shapes in the field due to local changes in the sound speed profile can compromise the expected orthogonality upon which the performance of the filters depends. A specific concern focused on local changes in the shape of the first mode increasing the leakage of the first mode field component through the higher-order filters. The strength of this leakage would be expected to be proportional to the first mode energy and thus to be attenuated with range at the rate of the first-order mode attenuation. This leakage could potentially account for the results shown in Fig. 9(a) and (b). To distinguish between increased filter leakage and coupling into higher order modes as the source of the energy coming from the higher-order filters we repeated the calculations for Fig. 9(a) and (b) with the modification that the strength of the internal waves was set equal to zero for the range intervals 0–4 km and 196–200 km. In the intervals 4–5 km and 195–196 km the transition from zero to “full-strength” internal waves was given a “cosine-taper.” If the higher-order filter outputs had been due to increased leakage of a signal propagating adiabatically in the first mode, then we expected an abrupt drop in these outputs

to the levels shown in Fig. 8 beyond range 195 km, since beyond 196 km the shapes of the modes are identical to those in the calculation for Fig. 8. The results obtained (not shown here) showed a gradual decay of the filter outputs from the level at 195 km at rates associated with the attenuation of the respective adiabatically propagated modes which the filters were expected to pass. This result supports the interpretation of the filter outputs in Fig. 9(a) and (b) as being due to energy propagating near the receiver in the higher-order modes and argues against increased filter leakage of the first-order mode as the origin of the range dependence of the filter outputs.

The stochastic coupled mode theory outlined in Sec. III B predicts a constant *ratio* for the relative intensities of modes n and l at large R , independent of R and the initial conditions. The results presented in Fig. 9(a) and (b) are consistent with this prediction. In both cases the relative intensities of the modes are the same in the asymptotic region and independent of source depth. To see this more clearly, the modal intensity plots for the 15 m source depth from Fig. 9(b) are shifted upward by about 37 dB and overlaid with the modal intensity data for the source at 45 m. The result is

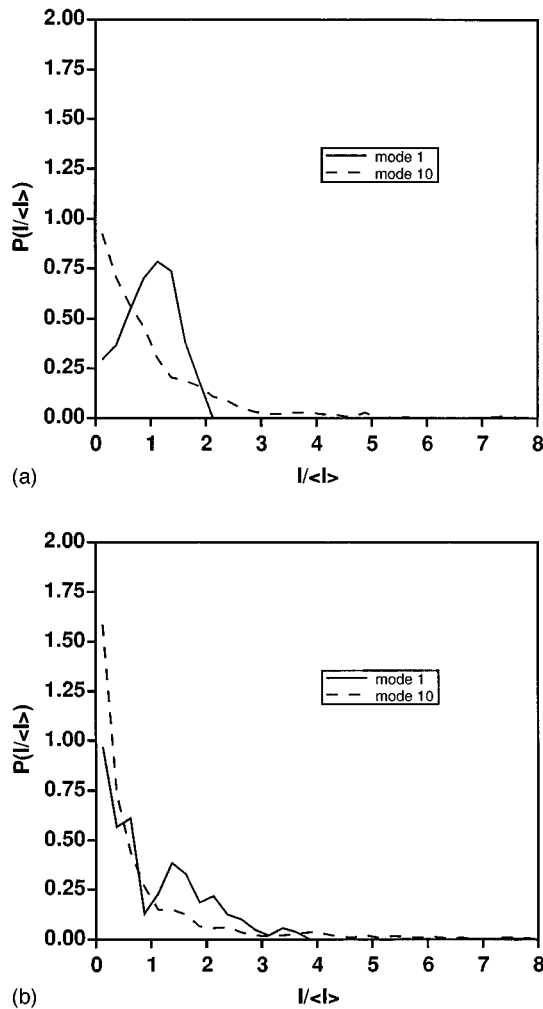


FIG. 11. Probability density functions $\varphi(I_i(n,r,f)/\langle I_i(n,r,f) \rangle)$ for modes 1 and 10 at a range $r=20$ km for (a) and $r=200$ km for (b). In both cases, the energy density was $E_0=100$ J/m² and the source depth was 45 m.

shown in Fig. 9(c), where the asymptotic region is clearly seen to begin around 100 km from the source; in this region the modal intensities are independent of the initial conditions (initial distribution of modal energy) as predicted in Ref. 16.

Energy pumped from relatively more energetic modes into those modes that initially contain little energy induce relatively large intensity fluctuations in the latter, and this energy transfer is revealed as a “high” modal scintillation index. Conversely, the transfer of energy induces relatively small intensity fluctuations in the dominant mode, resulting in a “low” scintillation index for that mode. These arguments are confirmed by results in Fig. 10(a) and (b) where modal scintillation indices are shown for the first ten modes using a point source located at depths of 45 and 15 m respectively. The curves are plotted as $10 \log [SI(n,r,f) + 1]$, where SI is given by Eq. (16). From Eq. (23), $10 \times \log [SI(n,r,f) + 1]$ should exhibit a linear dependence on range in the asymptotic region, and the range at which this occurs depends on the initial conditions, i.e., the initial distribution of energy among the modes. For the deep source case, Fig. 10(a) indicates a small, but exponentially increasing scintillation index for mode 1, while the higher-order

modes exhibit rapidly increasing scintillation indices until they have equilibrated with mode 1 at a range of roughly 70 km. For longer ranges, the scintillation indices of the higher-order modes are proportional to that of mode 1, consistent with the prediction discussed in Sec. III B. In addition, the other modes appear to have the same trend toward exponential increase with range. The first mode is the dominant energy source in this case, and its scintillation index is lower than that of the higher-order modes, as expected. In Fig. 10(b) the first mode is initially weakly excited due to the shallow source depth and energy is quickly transferred to it from the dominant high-order modes over the first few kilometers of propagation. The scintillation indices of the high-order modes are initially smaller than that of modes 1 and 2. After approximately 100 km the high-order modes suffer strong attenuation, and beyond that range an equilibrium is reached where energy pumped into the higher modes offsets the loss due to mode stripping. Unlike the result in Fig. 10(a), the scintillation index of mode 1 initially rises rapidly in this case and the fluctuations in the scintillation index are more pronounced for the higher-order modes in Fig. 10(b). Again, there is a small but noticeable exponential variation with range.

Note that, beyond the equilibrium (asymptotic) range of approximately 100 km, the ratios of SI+1 curves for modes 2–10 relative to that for mode 1 are approximately equal for the two different sets of initial conditions illustrated in Fig. 10(a) and (b). This result, predicted by Eq. (23) and discussed above, is better illustrated in Fig. 10(c) where the data in Fig. 10(a) were shifted up by about 2 dB and superimposed on Fig. 10(b). Beyond range 100 km, there is substantial agreement between the two sets of curves, even though the initial modal excitation was quite different in the two simulations. The asymptotic limit appears to be reached at shorter range for the 45-m source depth simulation. For each source depth, the *approach* to equilibrium depends on the initial conditions, though the *ratio* of modal scintillation indices for different source depths is independent of the initial distribution of energy among the modes once the asymptotic range has been reached for both sets of initial conditions.

The exponential increase in scintillation index is quite small over the range shown in Fig. 10(a) and (b). In order to more clearly view the trend, Fig. 10(d) shows the result obtained when the sound-speed fluctuations (and therefore the mode coupling) are enhanced by increasing the energy density to $E_0=100$ J/m². In this case the source depth was chosen to be 45 m. The asymptotic region is reached at a shorter range and the trend is clearly visible.

Additional insight into the character of the modal and full-field scintillation indices can be obtained by estimating the range-dependent probability density functions $\varphi(I_i(n,r,f)/\langle I_i(n,r,f) \rangle)$ for the modal intensities. Since the scintillation index is a normalized intensity variance, that variance is a rough indicator of the overall “spread” of the probability distribution φ and vice versa. Low scintillation indices should have peaked probability distributions, while higher indices imply broader distributions, with high probability associated with small values of the argument $I_i(n,r,f)/\langle I_i(n,r,f) \rangle$ and low, long tails for large values of

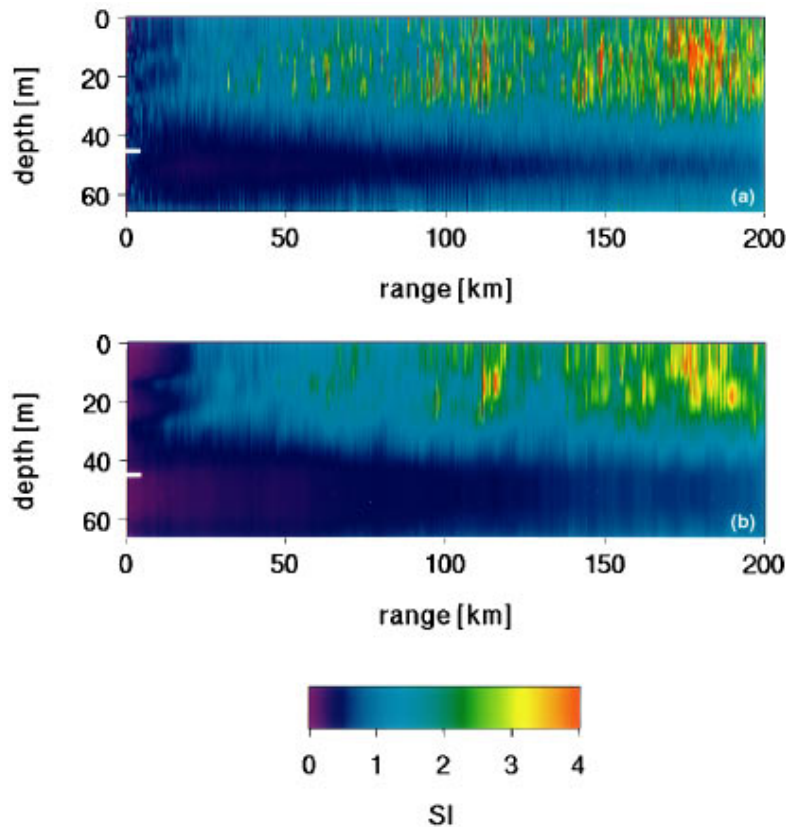


FIG. 12. Comparison between the full-field (coherent) scintillation index (a) with the mode amplitude scintillation index (b) for a source depth of 45 m and a diffuse background internal wave field with energy density $E_0=100 \text{ J/m}^2$.

the argument. For a source depth of 45 m and $E_0=100 \text{ J/m}^2$, Fig. 11 gives estimates of these distributions for modes 1 and 10 at ranges of 20 and 200 km [Fig. 11(a) and (b), respectively]. As expected, Fig. 11(a) indicates that the strong excitation of mode 1 for a source at 45 m will induce small intensity fluctuations (low variance) in mode 1. One can therefore infer a small scintillation index at short range for this mode. On the other hand, the initial excitation of mode 10 is weak and energy transferred to this mode from mode 1 will cause large fluctuations in mode 10 intensity. These results are evident from the structure of the distributions. At long range, Fig. 11(b) implies that modes 1 and 10 have higher scintillation indices than at 20 km. The mode 1 distribution has broadened considerably with range, and the mode 10 distribution has a more pronounced peak near the origin, as well as more outliers at larger values of $I_i(n,r,f)/\langle I_i(n,r,f) \rangle$. Some attempts have been made to fit the probability distribution of intensity with parametric distributions (e.g., Ref. 36), though theoretical justification is lacking.

In general, both modal amplitude and phase contribute to the pressure field, as seen from the phasor representation given by Eq. (13). On the other hand, the single mode intensity and scintillation index computations presented above ignore the phase contribution since we have that $I_i(n,r,f) = d_i^* C(n,r,f) d_i(n,r,f)$. A comparison between the scintillation index computed from the full (coherent) field by using Eq. (12), shown in Fig. 12(a), and the (mode amplitude) scintillation index computed from Eq. (17), pre-

sented in Fig. 12(b), indicates that the amplitude-only calculation with the first ten modes shows many of the qualitative features present in the full-field case for all but the shortest ranges. This result is consistent with the range-dependent decorrelation of modal phases as the acoustic field propagates through the stochastic sound speed environment, and was noted above in connection with Fig. 6. Qualitative agreement between Fig. 12(a) and (b) is seen in the growth to large values (>2) of the scintillation index at shallow depths and ranges beyond 100 km. While the inclusion of phase terms makes some difference, particularly at shorter range, the assumption of negligible cross-modal coherence does not greatly attenuate the phenomena of interest.

D. Full-field scintillation indices for different environments

The modal field statistics discussed in the previous section were obtained by computing depth integrals [Eq. (14)] of the full field and therefore only the range dependence was exhibited. Range and depth variability of the intensity fluctuations are determined by the full-field scintillation indices computed from Eq. (12), and some examples are displayed in Figs. 13 and 14. Results are shown in Fig. 13 for a source depth of 15 m and include the η_D component of sound-speed fluctuations in both flat and sloping bottom environments [Fig. 13(a) and (c)], and with both η_D and η_S contributions for flat and sloping environments in Fig. 13(b) and (d). The format of Fig. 14 (source depth 45 m) is identical to that of

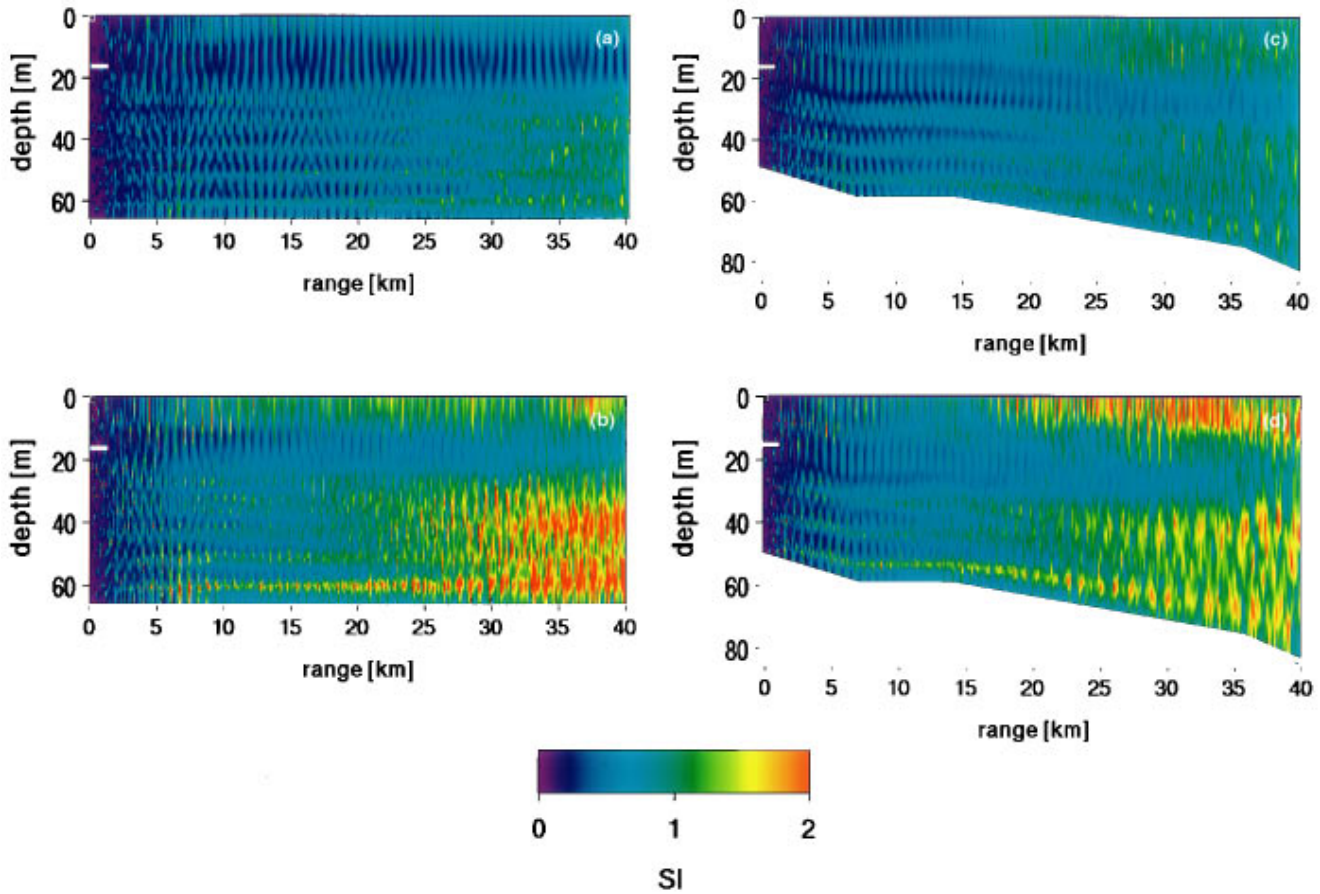


FIG. 13. Full-field scintillation indices for flat bottom [(a) and (b)] and sloping bottom [(c) and (d)] environments with source depth of 15 m. (a) and (c) include only the diffuse background internal wave field with energy density $E_0=25 \text{ J/m}^2$, while (b) and (d) include both the diffuse background and soliton packet contributions.

Fig. 13. The diffuse background internal wave energy density is $E_0=25 \text{ J/m}^2$ in both illustrations. Note that the scale does not cover the entire dynamic range of scintillation index; values greater than the scale's upper limit ($SI=2$) are observed.

The spatial dependence of the intensity fluctuations is nonuniform and rather complex for both figures. However, a qualitative understanding of the spatial structure of the intensity fluctuations can be obtained from the discussion of modal coupling in Sec. III C. According to the results presented in Fig. 9(b), the fields in Fig. 13 are associated with a transition region where the higher-order modes initially dominate and transfer energy into the low-order modes which are “energy poor” over this range. As the energy is deposited in the low-order modes, fluctuations in the intensity of those modes is relatively high, while fluctuations in the high-order modes is relatively low. Since the low-order modes dominate the mid and deep sections of the water column, the scintillation index tends to increase with range in that region, as depicted in Fig. 13. At increasing range, the energy balance begins to shift and the energy propagated adiabatically in high-order modes is attenuated, causing an increase in the scintillation index in the upper 10 m of the water column. Note that the asymptotic behavior can not be deduced from these figures since they cover only 40 km. The contribution of diffuse background and soliton components

of the internal wave field results in substantial increases in the scintillation indices in both the upper 10 m of the water column and below 25-m depth for both flat and sloping bottom cases, but does not qualitatively change the result obtained when only the diffuse component was present. Examination of the results obtained for the case where only the soliton packets were present (not shown here) indicates that the soliton component forms the dominant contribution to the increase in scintillation index. The opposite modal energy transfer conditions occur in Fig. 14. Referring to Fig. 9(a), the low-order modes dominate after approximately 15 km and pump energy to the higher order modes. For increasing range, this results in an elevation of the scintillation index in the upper part of the water column where low-order modes are evanescent and make little contribution. Since the low-order modes are the dominant energy source throughout the 40 km of propagation shown in Fig. 14 and reside primarily in the mid to deep sections of the waveguide, the scintillation index is low in that region. Again, the presence of the soliton contribution quantitatively enhances the effect but does not qualitatively change the result for either flat or sloping bottom environments.

IV. SUMMARY AND CONCLUSIONS

A model describing acoustic wave propagation in a stochastic, shallow water waveguide has been developed and

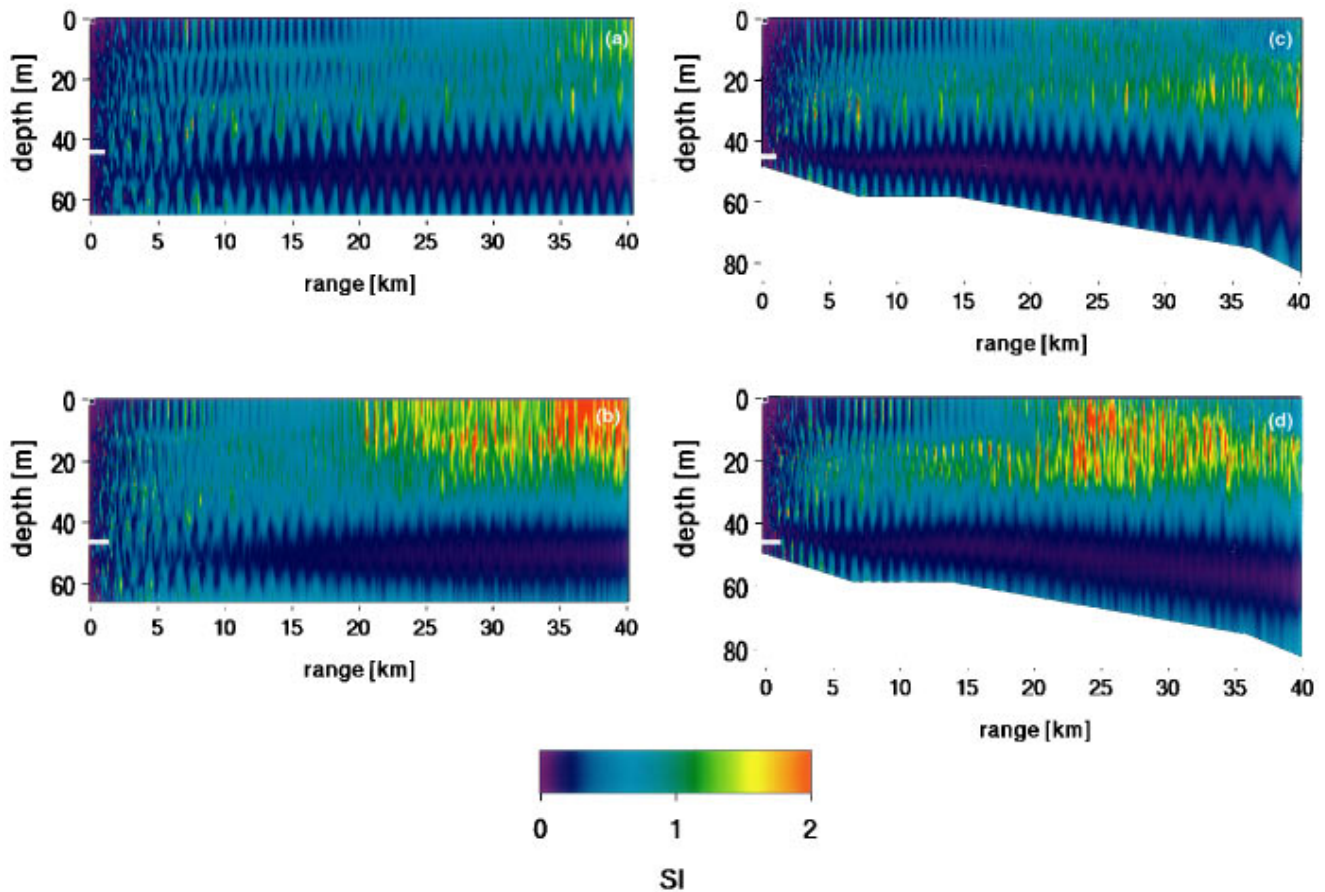


FIG. 14. Full-field scintillation indices for flat bottom [(a) and (b)] and sloping bottom [(c) and (d)] environments with source depth of 45 m. (a) and (c) include only the diffuse background internal wave field with energy density $E_0=25 \text{ J/m}^2$, while (b) and (d) include both the diffuse background and soliton packet contributions.

applied to compute both full-field and modal statistics. The statistical variability of the waveguide environment was characterized by internal wave-induced volume fluctuations in the sound speed distribution. Fluctuations were separated into spatially diffuse and localized contributions represented by a Garrett–Munk spectrum and tidally generated soliton packets, respectively. Physically reasonable oceanographic and acoustic parameters were incorporated into the simulations with data obtained from a site on the continental slope off the New Jersey coast. Using a wide-angle parabolic equation, the acoustic field was computed at a frequency of 400 Hz for each realization of the random process underlying the sound speed fluctuations. Statistical field measures such as second and fourth moments, scintillation indices, and modal probability densities were then estimated from the ensemble of realizations.

A comparison between the full-field deterministic and ensemble averaged intensity plots (Figs. 6 and 7) indicated a loss of spatial coherence with increasing range from the source. The loss of coherence occurred when either or both contributions to the internal wave-induced sound-speed fluctuations were present, and was found in both flat and sloping bottom environments. The full-field distribution of the intensity fluctuations in shallow water (Figs. 13 and 14) showed a complicated structure that was a function of both source depth and the spatial distribution of the sound speed fluctua-

tions (or, equivalently, the depth dependent buoyancy frequency and the internal wave spectrum). There was a trend toward increasing intensity fluctuations with range.

Performing a modal decomposition of the simulated pressure field as a function of range gave insight into the field characteristics through an analysis of modal statistics. For short ranges ($\leq 40 \text{ km}$), the modal decomposition results were used to qualitatively explain the spatial distribution of the scintillation index in terms of energy transfer among low- and high-order modes. While both mode amplitude and phase contribute to the pressure field, the qualitative features of the field were reasonably well represented by using only the amplitude contribution for the first ten modes, a result consistent with range-dependent decorrelation of modal phases in a stochastic sound speed environment. For large ranges, results were interpreted in the context of a stochastic mode coupling theory that incorporated the effects of both mode coupling and mode stripping due to bottom loss. The numerical experiments presented in Figs. 9 and 10 supported the theoretical predictions concerning the asymptotic range behavior of the modal intensity and mode scintillation index. Our results were consistent with the prediction that the ratio of the modal intensities is independent of the initial conditions in the asymptotic range limit. In addition, asymptotic results were presented in which the quantity $SI(i, R, f) + 1$ exponentially increased with range for mode i , and the ratio

$[SI(i,R,f)+1][SI(l,R,f)+1]$ for modes i,l was independent of both the initial conditions and range. These latter computations were also consistent with the predictions of Ref. 16. The asymptotic range-dependent structure of the field was caused by the competition between mode coupling and mode stripping found in shallow water waveguides, and is qualitatively different from that predicted for deep water problems where boundary interactions are small.

The stochastic mode theory predicting the asymptotic results gives sufficient conditions (Sec. III B) for its validity, and it would be interesting to determine criteria under which those conditions can be relaxed. For example, though the theory of Ref. 16 was developed under a narrow-angle parabolic approximation, we have used a wide-angle parabolic equation for the numerical experiments and found consistency between the asymptotic predictions and the results of these computations, implying the narrow-angle assumption is sufficient but not necessary. Strict adherence to the assumption that the cross-modal coherence should vanish may be relaxed somewhat, based on the discussion surrounding Eq. (17) and the results shown in Fig. 12. While the asymptotic range limit was reached around 100 km for the examples and the frequency (400 Hz) presented, consideration of other frequencies and other plausible oceanographic environments may lead to more rapid (or slower) approaches to the asymptotic regime. Such environments may include stronger internal wave fields that lead to higher mode coupling, bottom characteristics associated with range-dependent mode stripping different from that presented here, and/or other sources of volume variability such as microbubble layers that alter the acoustic field in a stochastic manner.³⁷

With the exception of propagation in the asymptotic range limit, it is difficult to draw general conclusions about the effects of volume fluctuations on acoustic fields. At shorter ranges, the variability of acoustic and oceanographic conditions, space-time scales, etc., makes the subject extremely complex and implies that a single theoretical approach to the problem may not be practical. A similar consensus appears to have been reached by researchers studying line of sight electromagnetic propagation in turbulent atmospheres.³⁸ It is worth noting that line of sight atmospheric propagation studies do not include the additional difficulties arising from multiple boundary interactions. Such interactions are commonplace in stochastic shallow water waveguides.

ACKNOWLEDGMENTS

The authors would like to thank Dr. Bradley Orchard, Dr. Dennis Creamer, Dr. Marshall Orr, Dr. John Apel, Dr. Jim Lynch, and Dr. Jeff Simmen for their comments on various aspects of this work. The research was supported by the Office of Naval Research.

- ¹S. M. Flatté and F. D. Tappert, "Calculation of the effect of internal waves on oceanic sound transmission," *J. Acoust. Soc. Am.* **58**, 1151–1159 (1975).
²W. Munk and F. Zachariasen, "Sound propagation through a fluctuating stratified ocean: Theory and observation," *J. Acoust. Soc. Am.* **59**, 818–838 (1976).

- ³G. R. Sutton and J. J. McCoy, "Spatial coherence of acoustic signals in randomly inhomogeneous waveguides—A multiple scatter theory," *J. Math. Phys. (N.Y.)* **18**, 1052–1057 (1977).
⁴S. Flatté, R. Dashen, W. Munk, K. Watson, and F. Zachariasen, *Sound Transmission Through a Fluctuating Ocean* (Cambridge U.P., Cambridge, 1979).
⁵L. B. Dozier and F. D. Tappert, "Statistics of normal mode amplitudes in a random ocean. I. Theory," *J. Acoust. Soc. Am.* **63**, 353–365 (1978).
⁶L. B. Dozier and F. D. Tappert, "Statistics of normal mode amplitudes in a random ocean. II. Computations," *J. Acoust. Soc. Am.* **64**, 533–547 (1978).
⁷B. J. Uscinski, C. Macaskill, and T. E. Ewart, "Intensity fluctuations, Part I. Theory," *J. Acoust. Soc. Am.* **74**, 1474–1483 (1983).
⁸T. E. Ewart, C. Macaskill, and B. J. Uscinski, "Intensity fluctuations, Part II. Comparison with the Cobb Experiment," *J. Acoust. Soc. Am.* **74**, 1484–1499 (1983).
⁹B. J. Uscinski and D. E. Reeve, "The effect of ocean inhomogeneities on array output," *J. Acoust. Soc. Am.* **87**, 2527–2534 (1990).
¹⁰J. A. Colosi, S. M. Flatté, and C. Bracher, "Internal-wave effects on 1000 km oceanic acoustic pulse propagation: Simulation and comparison with experiment," *J. Acoust. Soc. Am.* **96**, 452–468 (1994).
¹¹R. Thiele, "The application of coupled-mode theory to propagation in shallow water with randomly varying sound speed," Saclantcen Report SM-199 (1987).
¹²J. X. Zhou, X. Z. Zhang, and P. H. Rogers, "Resonant interaction of sound waves with internal solitons in the coastal zone," *J. Acoust. Soc. Am.* **90**, 2042–2054 (1991).
¹³M. J. Beran and S. Frankenthal, "Volume scattering in a shallow channel," *J. Acoust. Soc. Am.* **91**, 3203–3211 (1992).
¹⁴D. B. King, S. A. Chin-Bing, and R. W. McGirr, "Effects of shallow water internal waves on broadband acoustic wave propagation," in *Theoretical and Computational Acoustics*, edited by D. Lee and M. H. Schultz (World Scientific, Singapore, 1994), Vol. 2, pp. 793–807.
¹⁵R. Mazar and B. Katz, "Ray-mode analysis of a random medium waveguide," *J. Acoust. Soc. Am.* **95**, 2495–2504 (1994).
¹⁶D. B. Creamer, "Scintillating shallow-water waveguides," *J. Acoust. Soc. Am.* **99**, 2825–2838 (1996).
¹⁷M. K. Broadhead, "Dissipative shallow water internal waves and their acoustical properties," *IEEE Proceedings of Oceans 95* (IEEE, New York, 1995), Vol. 1, pp. 673–684.
¹⁸J. Lynch, G. Jin, R. Pawlowicz, D. Ray, A. J. Plueddemann, C. S. Chiu, J. H. Miller, R. H. Bourke, A. Rost Parsons, and R. Muench, "Acoustic travel-time perturbations due to shallow-water internal waves and internal tides in the Barents Sea Polar Front: Theory and experiment," *J. Acoust. Soc. Am.* **99**, 803–821 (1996).
¹⁹S. Flatté, "Wave propagation through random media: Contributions from Ocean Acoustics," *Proc. IEEE* **71**, 1267–1294 (1983).
²⁰J. Apel, M. Badiey, J. Berkson, K. P. Bongiovanni, J. Bouthellette, E. Carey, C. S. Chiu, T. Duda, C. Eck, S. Finette, R. Headrick, J. Irish, J. Kemp, J. Lynch, A. Newhall, M. Orr, B. Pasewark, J. Preisig, B. Racine, S. Rosenblad, S. A. Shaw, D. Taube, D. Tielburger, A. Turgut, K. von der Heydt, W. Witzell, and S. Wolf, "An overview of the 1995 SWARM shallow water internal wave acoustic scattering experiment," to appear in *IEEE J. Oceanic Eng.* (1997).
²¹A. E. Gill, *Atmosphere-Ocean Dynamics* (Academic, New York, 1982), Chap. 3.
²²A. K. Liu, "Analysis of nonlinear internal waves in the New York Bight," *J. Geophys. Res.* **93(C10)**, 12 317–12 329 (1988).
²³R. J. Urick, *Principles of Underwater Sound* (McGraw-Hill, New York, 1983), 3rd ed.
²⁴T. H. Bell, "Numerical calculation of dispersion relations for internal gravity waves," NRL Report 7294 Naval Research Laboratory (1971).
²⁵J. R. Apel (personal communication).
²⁶S. Wolf and B. Pasewark, unpublished data.
²⁷L. A. Ostrovsky and Yu. A. Stepanyants, "Do internal solitons exist in the ocean?" *Rev. Geophys.* **27**, 293–310 (1989).
²⁸J. R. Apel, L. A. Ostrovsky, and Yu. A. Stepanyants, "Internal solitons in the ocean," submitted to *Prog. Oceanogr.* (1996).
²⁹H. Sandstrom and N. S. Oakey, "Dissipation in internal tides and solitary waves," *J. Phys. Oceanogr.* **25**, 604–614 (1995).
³⁰G. B. Whitham, *Linear and Nonlinear Waves* (Wiley, New York, 1974).
³¹M. D. Collins, "A higher-order parabolic equation for wave propagation in an ocean overlying an elastic bottom," *J. Acoust. Soc. Am.* **86**, 1459–1464 (1989).

- ³²E. L. Hamilton, "Geoacoustic modeling of the sea floor," *J. Acoust. Soc. Am.* **68**, 1313–1340 (1980).
- ³³A. K. Rogers, T. Yamamoto, and W. Carey, "Experimental investigation of sediment effect on acoustic wave propagation in the shallow ocean," *J. Acoust. Soc. Am.* **93**, 1747–1761 (1993).
- ³⁴D. M. F. Chapman, "A simple estimate of propagation loss fluctuations due to modal interference," *J. Acoust. Soc. Am.* **85**, 1097–1106 (1988).
- ³⁵L. B. Dozier, "A coupled-mode model for spatial coherence of bottom-interacting energy," SAIC Report SAI-82-476-WA (1981).
- ³⁶T. E. Ewart and D. B. Percival, "Forward scattered waves in random media—The probability distribution of intensity," *J. Acoust. Soc. Am.* **80**, 1745–1753 (1986).
- ³⁷S. Finette and D. Tielbuerger, "Acoustic intensity fluctuations in a stochastic shallow water waveguide caused by scattering from near surface bubble clouds," *Proceedings at the 3rd European Conference on Underwater Acoustics*, edited by J. S. Papadakis (FORTH-IACM, Crete, Greece, 1996), Vol. 2, pp. 1167–1171.
- ³⁸Y. A. Kravtsov, "Propagation of electromagnetic waves through a turbulent atmosphere," *Rep. Prog. Phys.* **55**, 39–112 (1992).

A note on nonlinear radiation from a gas bubble in liquids

Zhen Ye

Institute of Ocean Sciences, Sidney, British Columbia V8L 4B2, Canada

(Received 25 March 1996; accepted for publication 20 September 1996)

This paper discusses nonlinear radiation from a gas bubble in liquids. The discrepant results from two previous approaches, the volume displacement approach and the radial displacement approach, were compared and discussed. By rederiving the governing equation used in the two approaches, it is shown that under the usual approximations the sound emission resulting from the volume displacement approach is correct, but the previous procedure which leads to the right answer is not rigorous; the lack of rigor has drawn considerable criticisms in the past. © 1997 Acoustical Society of America. [S0001-4966(97)05101-1]

PACS numbers: 43.30.Lz, 43.25.Jh, 43.25.Yw, 43.30.Pc [MAB]

INTRODUCTION

A few years ago, Du and Wu (1990) compared two approaches for solving nonlinear radiation from a bubble in a liquid. One approach takes the radial displacement as the variable, while the second approach assumes the volume displacement as the variable. Although the two approaches both start with the same well-known Rayleigh–Plesset equation for the radial displacement of the bubble, the radial displacement approach leads to the sound emission amplitude at a distance r from the center of the bubble

$$p(r) = \frac{\rho_0 R_0^2}{r} \frac{d^2 R(t-r/c_0)}{dt^2}, \quad (1)$$

while the second approach leads to

$$p(r) = \frac{\rho_0}{4\pi r} \frac{d^2 V(t-r/c_0)}{dt^2}. \quad (2)$$

Here, ρ_0 is the density of the fluid, R_0 is the equilibrium radius of the bubble, and c_0 is the sound speed in the liquid. Du and Wu further pointed out that the first approach is widely used in the literature of the USA (e.g., Miller, 1981), and the second one is more popular among Russian scientists (e.g., Zabolotskaya and Soluyan, 1973). It was found that in the linear acoustic region, the two approaches do not lead to different results. However, when nonlinear effects are included, although the two approaches still agree with each other in describing the motion of a pulsating bubble, there is significant disagreement between the two methods in describing sound emission when a bubble radiates as a monopole. Equation (1) from the radial displacement approach predicts that a bubble at pulsation can always radiate a second harmonic, while in Eq. (2) from the volume displacement approach a bubble at pulsation does not radiate a second harmonic at a certain frequency. The main conclusion of Du and Wu is that “there is no theoretical basis for the conclusion reached from the volume displacement approach that the second-harmonic amplitude of the sound emission is zero at a specific frequency.”

Later, Ilinskii and Zabolotskaya defended the volume displacement approach by taking into account near field effects due to hydrodynamic nonlinearity (Ilinskii and Zabolotskaya, 1992). They rederived Eq. (2) by assuming that the

velocity field takes the same form as in the incompressible liquids [Eq. (2) in Ilinskii and Zabolotskaya, 1992], and at the far field the pressure amplitude decreases as $1/r$, and time t is *ad hoc* replaced by the retarded $t-r/c_0$ in the end of computation. This work was further criticized by Wu and Du (1993) who pointed out that the incompressibility assumption is not appropriate as far as the radiation is concerned. They further argued that there will be no sound wave emitted from the bubble if the fluid is incompressible. In her reply, Zabolotskaya (1993) insisted that the second harmonic sound can only appear in the near field and there is no second harmonic at the far field when a bubble is pulsating at a specific frequency because at this frequency two types of nonlinearity compensate for each other. Zabolotskaya pointed out that it is not proper to assume that the pressure field behaves as $A(t-r/c_0)/r$ beginning at the bubble boundary, which led Wu and Du to Eq. (1).

Since the issue of the dispute still remains, the problem of nonlinear radiation from bubbles in liquids deserves further consideration. The main reasons why this problem is continuously of interest are because of many applications such as detection of resonant cavitation bubbles by their second harmonic emission (Miller, 1981) and bubble size measurements using nonlinear mixing of two frequencies (Newhouse and Shankar, 1984).

The primary purpose of this paper is to further investigate the nonlinear sound emission from bubbles and resolve the contradictory results from the aforementioned two approaches. For this purpose we will refresh the derivation of the Rayleigh–Plesset equation, following the line of Epstein and Keller (1971) and Prosperetti and Lezzi (1986). It will become clear that under certain conditions the sound emission result from the volume displacement approach is correct, so are the arguments by Wu and Du (1993) regarding the incompressibility of the fluid, but the procedure of Ilinskii and Zabolotskaya (1992) which leads to the right answer is not rigorous. In fact, their procedure may not be proper, as it is only valid for the near field, not for the concerned radiation field.

I. ANALYSIS

To resolve the disagreement between the sound emission results from the two approaches mentioned above, it is ap-

appropriate to get to the root of the problem, that is, one needs to find out how the governing Rayleigh–Plesset equation which was used by both approaches is derived. Although the derivation of this equation has been documented by many authors (refer to, for example, Epstein and Keller, 1971; and Prosperetti and Lezzi, 1986), in this section we purposely rederive the equation in detail so that the reader who may not be familiar with the literature can read through without difficulty. In addition, more importantly, through the derivation the question which of the equations in (1) and (2) correctly describes the sound emission pressure will have a clear answer. Following the derivation of the governing equation, we will show rigorously that the result from the volume displacement approach is correct under the usual assumptions.

Consider a fluid medium. The Newton second law states

$$\frac{D\mathbf{u}}{Dt} + \frac{1}{\rho} \nabla p = 0, \quad (3)$$

where $D/Dt = \partial/\partial t + \mathbf{u} \cdot \nabla$, \mathbf{u} is the velocity field, p is the pressure field, and ρ is the density of the fluid. The mass conservation gives the equation of continuity

$$\frac{D\rho}{Dt} + \rho \nabla \cdot \mathbf{u} = 0. \quad (4)$$

We define the enthalpy h as

$$h \equiv \int_{p_0}^p \frac{dp}{\rho}, \quad (5)$$

where p_0 is the ambient pressure. This equation leads to

$$\left(\frac{\partial h}{\partial p} \right)_s = \frac{1}{\rho}, \quad \frac{1}{c^2} \left(\frac{\partial h}{\partial p} \right)_s = \frac{1}{\rho}, \quad \text{and} \quad \nabla h = \frac{1}{\rho} \nabla p, \quad (6)$$

where the following adiabatic relation has been used

$$d\rho = \frac{1}{c^2} dp.$$

In the above equations, the partial derivatives are performed at constant entropy S . For an irrotational liquid, we can define a velocity potential ϕ such that

$$\mathbf{u} \equiv \nabla \phi. \quad (7)$$

Substituting \mathbf{u} and h into the equation of continuity, we obtain

$$\frac{1}{c^2} \frac{Dh}{Dt} + \nabla^2 \phi = 0. \quad (8)$$

Similarly the momentum equation (3) becomes

$$\frac{\partial \phi}{\partial t} + \frac{1}{2} u^2 + h = 0. \quad (9)$$

Write out the perturbation in density and sound speed in the medium explicitly

$$\rho = \rho_0 + d\rho \approx \rho_0 + \frac{p - p_0}{c^2} \quad (10)$$

and

$$c = c_0 + dc \approx c_0 + \frac{dc}{dp} (p - p_0). \quad (11)$$

These lead to

$$\frac{1}{c^2} \approx \frac{1}{c_0^2} \left(1 - A \frac{p - p_0}{\rho_0 c_0^2} + \dots \right). \quad (12)$$

Substituting Eq. (10) into Eq. (5), we get

$$h = \frac{p - p_0}{\rho_0} \left(1 - \frac{1}{2} \frac{p - p_0}{\rho_0 c_0^2} + \dots \right). \quad (13)$$

Then Eqs. (8) and (9) become

$$\nabla^2 \phi + \frac{1}{\rho_0 c_0^2} \frac{Dp}{Dt} \left(1 - (1 - A) \frac{p - p_0}{\rho_0 c_0^2} + \dots \right) \quad (14)$$

and

$$\frac{\partial \phi}{\partial t} + \frac{1}{2} u^2 + \frac{p - p_0}{\rho_0} \left(1 - \frac{p - p_0}{2\rho_0 c_0^2} + \dots \right) = 0. \quad (15)$$

When the higher-order terms represented by “...” are ignored, the two equations (14) and (15) reduce to

$$\nabla^2 \phi + \frac{1}{\rho_0 c_0^2} \frac{\partial p}{\partial t} = 0 \quad (16)$$

and

$$\frac{\partial \phi}{\partial t} + \frac{p - p_0}{\rho_0} + \frac{1}{2} u^2 = 0. \quad (17)$$

Combining these two equations, we obtain

$$\nabla^2 \phi - \frac{1}{c_0^2} \frac{\partial^2 \phi}{\partial t^2} - \frac{1}{c_0^2} \mathbf{u} \cdot \frac{\partial \mathbf{u}}{\partial t} = 0 \quad (18)$$

and

$$\frac{p - p_0}{\rho_0} = -\phi_t - \frac{(\nabla \phi)^2}{2}, \quad (19)$$

where $\phi_t = \partial \phi / \partial t$. Equation (19) is in fact the Bernoulli equation.

To proceed further, it is assumed that the nonlinear term in Eq. (18) can be ignored when the particle velocity is small compared to the sound speed c_0 . This results in a wave equation for the velocity potential:

$$\nabla^2 \phi - \frac{1}{c_0^2} \frac{\partial^2 \phi}{\partial t^2} = 0. \quad (20)$$

Now we consider a bubble at radial pulsation. The boundary condition requires that the velocity be continuous across the interface, i.e.,

$$\left. \frac{\partial \phi}{\partial r} \right|_{r=R} = R_t, \quad (21)$$

where $R_t = dR/dt$. At the boundary, Eq. (19) becomes

$$\frac{p(R) - p_0}{\rho_0} = -\phi_t - \frac{1}{2} \left(\frac{\partial \phi}{\partial r} \right)^2 \quad \text{at } r = R. \quad (22)$$

A general solution to Eq. (20) is

$$\phi(r,t) = \frac{f(t-r/c_0)}{r}. \quad (23)$$

Taking this solution into Eqs. (19) and (21), we arrive at

$$\frac{p(R)-p_0}{\rho_0} = -\frac{f'(t-R/c_0)}{R} - \frac{R_t^2}{2}, \quad (24)$$

and

$$R_t = -\frac{f(t-R/c_0)}{R^2} - \frac{f'(t-R/c_0)}{c_0 R}. \quad (25)$$

In the above, $f'(x) = df(x)/dx$. Eliminating $f'(\cdot)$ from Eqs. (24) and (25), we finally have

$$\left(1 - \frac{R_t}{c_0}\right) R R_{tt} + \frac{3}{2} \left(1 - \frac{R_t}{3c_0}\right) R_t^2 = \frac{1}{\rho_0} \left(1 + \frac{R_t}{c_0} + \frac{R}{c_0} \frac{d}{dt}\right) \times [p(R) - p_0], \quad (26)$$

where $R_{tt} = d^2R/dt^2$. In the above, $p(R)$ is the pressure field at the bubble boundary.

If the terms involving c_0 are ignored, Eq. (26) reduces to the well-known Rayleigh–Plesset equation (e.g., Epstein and Keller, 1971; Prosperetti, 1987):

$$R R_{tt} + \frac{3}{2} R_t^2 = \frac{1}{\rho_0} [p(R) - p_0]. \quad (27)$$

This equation has been used by Du and Wu (1990) and Ilinskii and Zabolotskaya (1992) to obtain the expressions for the sound emission by gas bubbles.

From the above derivation, it is clear that it is the velocity potential $\phi(r,t)$ which satisfies the linear wave equation, and the general solution to this equation is given in Eq. (23). Recognizing this, we can proceed to show that the result from the volume displacement approach is correct. The velocity field can be calculated as

$$u = -\frac{f(t-r/c_0)}{r^2} - \frac{f'(t-r/c_0)}{cr}. \quad (28)$$

In the far-field region, the first term may be ignored, then we would have

$$u = -\frac{f'(t-r/c_0)}{cr}, \quad \text{for } r \rightarrow \infty, \quad (29)$$

which decreases as $1/r$, in contrast to the relation in Eq. (2) of Ilinskii and Zabolotskaya (1992) which is essential in their derivation. However, at the near field, we may ignore the second term in Eq. (28) and then obtain

$$u = -\frac{f(t-r/c_0)}{r^2}, \quad \text{for } r \rightarrow 0. \quad (30)$$

In this limit, the function $f(t-r/c_0)$ can be determined by the boundary condition as

$$f\left(t - \frac{R}{c_0}\right) = -R^2 R_t = -\frac{1}{4\pi} \frac{dV(t)}{dt}, \quad (31)$$

with $V(t)$ being the volume given by $(4\pi/3)R^3(t)$.

Now we consider the radiation pressure field. At the far field, the radiation field behaves as a spherically spreading wave (Sommerfeld radiation condition),

$$p \approx \frac{A(t-r/c_0)}{r} \quad r \rightarrow \infty. \quad (32)$$

We note that this is only valid at far field. It would be incorrect *a priori* to assume this form for the pressure field near the bubble boundary. The function $A(t-r/c_0)$ can be determined by the momentum equation (3) or the Bernoulli equation as, ignoring the nonlinear terms,

$$A(t-r/c_0) = -\rho_0 f'(t-r/c_0). \quad (33)$$

Taking into account Eq. (31) and upon ignoring the terms of order c_0^{-1} as usual, we finally obtain the radiation field as

$$p = \frac{\rho_0}{4\pi r} \frac{d^2V(t-r/c_0)}{dt^2} \quad (34)$$

which is exactly the same as what has been obtained by Zabolotskaya and Soluyan (1973) and Ilinskii and Zabolotskaya (1992). This result is valid for pressure field in the far-field region, as correctly stated by these authors. This result is also consistent with what one would expect from the approach in Prosperetti (1987).

Now we return to the two previous approaches discussed by Du and Wu (1990). In the radial displacement approach of Du and Wu (1990), the radiation field is assumed to behave as $A(t-r/c_0)/r$ beginning at the bubble boundary [refer to Eq. (10) in Du and Wu, 1990]. From the above discussion, this is only correct at far field. On the other hand, in the volume displacement approach, Ilinskii and Zabolotskaya (1992) have assumed that the velocity field behaves as $u(r,t) = R^2 R_t / r^2$ [refer to their Eq. (2)]. According to what has been discussed above, this assumption is only valid for the near field, therefore it cannot be used for the far field radiation. However, we note that although the approach of Ilinskii and Zabolotskaya is in impropriety, as suggested by Wu and Du (1993), the sound radiation expression obtained by the volume displacement approach appears to be correct.

II. CONCLUSION

In this paper, we discussed the problem of sound radiation from bubbles. Two previous approaches, the volume displacement approach and the radial displacement approach, were compared and discussed. By rederiving the governing equation used in both approaches, we found that under the usual approximations the sound emission result from the volume displacement approach is correct, but the previous procedure which leads to the right answer is not rigorous, and has been criticized as inappropriate.

- Du, G., and Wu, J. (1990). "Comparison between two approaches for solving nonlinear radiations from a bubble in a liquid," *J. Acoust. Soc. Am.* **87**, 1965–1967.
- Epstein, D., and Keller, J. B. (1971). "Expansion and contraction of planar, cylindrical, and spherical underwater gas bubbles," *J. Acoust. Soc. Am.* **52**, 975–980.
- Ilinskii, Yu., and Zabolotskaya, A. (1992). "Cooperative radiation and scattering of acoustic waves by gas bubbles in liquids," *J. Acoust. Soc. Am.* **92**, 2837–2841.
- Miller, D. L. (1981). "Ultrasonic detection of resonant cavitation bubbles in a flow tube by their second-harmonic emission," *Ultrasonics* **19**, 214–217.
- Newhouse, V. L., and Shankar, P. M. (1984). "Bubble size measurements using the nonlinear mixing of two frequencies," *J. Acoust. Soc. Am.* **75**, 1473–1477.
- Prosperetti, A., and Lezzi, A. (1986). "Bubble dynamics in a compressible liquid. Part 1. First-order theory," *J. Fluid Mech.* **168**, 457–478.
- Prosperetti, A. (1987). "The equation of bubble dynamics in a compressible liquid," *Phys. Fluids* **30**, 3626–3628.
- Wu, J., and Du, G. (1993). "Comments on 'Cooperative radiation and scattering of acoustic waves by gas bubbles in liquids'," *J. Acoust. Soc. Am.* **94**, 2446–2447.
- Zabolotskaya, E. A., and Soluyan, S. I. (1973). "Emission of harmonic and combination-frequency waves by air bubbles," *Sov. Phys. Acoust.* **18**, 396–398.
- Zabolotskaya, E. A. (1993). "Response to Comments on 'Cooperative radiation and scattering of acoustic waves by gas bubbles in liquids'," *J. Acoust. Soc. Am.* **94**, 2448.

Optimal recovery of the elasticity tensor of general anisotropic materials from ultrasonic velocity data

Christophe Aristégui and Stéphane Baste

Université Bordeaux I, Laboratoire de Mécanique Physique, U.R.A. C.N.R.S. No. 867,
351, Cours de la Libération, 33405-TALENCE Cedex, France

(Received 13 February 1996; accepted for publication 13 September 1996)

An ultrasonic wave approach is presented for the optimal identification of the 21 independent elasticity constants of the most general linear homogeneous anisotropic elastic solid from wave speed measurements of obliquely incident ultrasonic bulk waves. Since the symmetry of acquisition planes is not taken into account, this inversion process is generalized to materials that do not possess three mutually orthogonal planes of symmetry. Minimization of an overdetermined system of nonlinear algebraic equations is solved by a constrained optimization method. Various classes of symmetry are considered. Several critical factors (initial guesses, scatter in experimental data) which can influence the accuracy of the elastic property reconstruction algorithm have been investigated by means of numerical examples that simulate in the best way a typical experiment. The sensitivity of the reconstruction algorithm to each identified elasticity constant is detected *a posteriori* by means of the estimation of a confidence interval associated with each identified constant. The generalized reconstruction method is applied to the experimental data for materials with various symmetry classes. © 1997 Acoustical Society of America. [S0001-4966(97)00502-X]

PACS numbers: 43.35.Cg, 43.35.Zc [HEB]

INTRODUCTION

Ultrasonic wave speed measurements appear to be the most widely used method for the determination of the elastic properties of anisotropic solids.¹⁻¹¹ By using mode conversion at a liquid–solid interface, quasilongitudinal and quasitransverse bulk waves can be generated and transmitted in numerous directions in the solid.¹ The phase velocities of bulk waves in the medium are related to the elasticity constants of an anisotropic medium through the well-known Christoffel equation.¹² By inverting this equation, the elasticity constants can be determined from a suitable set of experimental velocities for various directions. In this situation, there is more data than there are independent stiffnesses to be determined.¹³ That leads to the use of a nonlinear least-squares optimization procedure finding a set of elasticity constants that minimizes the squares of the Christoffel equation calculated for each experimental phase velocity.⁷ Another approach does not explicitly use the Christoffel equation, i.e., a relationship verified by the velocities, but minimizes the squares of the shift between the experimental velocities and the solutions of the Christoffel equation, solutions of a second-degree equation for a plane of symmetry¹⁴ or Cardan's solutions of a third-degree equation for any plane.¹⁵ This method requires the recognition of the character of the generated waves in order to assign each measured velocity to one of the two (or of the three) possible solutions. An erroneous recognition of polarizations induces a wrong identification of the stiffness tensor.¹⁶ For nonsymmetry planes, the separation of the two quasitransverse waves is sometimes difficult.

The maximum number of independent elasticity constants is 21 for any medium.¹² Usually this number is less because of additional restrictions imposed by the symmetry of the medium. According to the degree of material anisotropy,

the number of unknowns, that is, the number of independent elasticity constants, varies from 2 to 21 for the isotropic to the triclinic symmetry.

The main difficulty of the elastic property reconstruction is related to the convergence of the inversion algorithm. Clearly the difficulties of convergence decrease as the number of unknowns decreases. This explains that the orthorhombic symmetry is considered as general enough to describe the anisotropy of most of the natural (wood) or synthetic (composite materials) materials. This assumption requires the existence of three mutually orthogonal planes of symmetry and the knowledge of the material symmetry axes. In principle the coincidence between the symmetry axes and the geometric axes of the sample is assumed. However, difficulties of convergence remain when simultaneous determination of the nine independent stiffnesses is carried out. The problem of nine unknowns is then reduced to one direct calculation followed by two problems of three unknowns and then by a problem of two unknowns.¹⁷ These three minimizations do not pose any difficulty of convergence and classically identify the nine moduli of a material that presents a symmetry greater than orthorhombic symmetry, for example tetragonal or isotropic.

A priori choice of a given symmetry class and of the associated number of independent elasticity constants is sometimes hazardous. For unidirectional composites, the plane transverse to the fibers must be isotropic. But a possible weak anisotropy may occur in this plane during the manufacturing process due to uneven fiber distribution.^{14,17} The hexagonal symmetry is no longer sufficient to describe adequately such materials. Consequently, the number of independent stiffnesses increases. Instead of five elasticity constants characterizing hexagonal symmetry, one needs to find the nine moduli of the orthorhombic class. This allows one to

take into account the deviation from the hexagonal model. Such anisotropy may also remove the assumption of orthorhombic symmetry. For example, the strata's stacking defects in industrial composite material or the annular rings of a wood sample lead to the disappearance of the coincidence between the material symmetry coordinate system and the geometric coordinate system. Moreover, loading along an off-axis symmetry direction creates microcracks with a predominant orientation that does not coincide with the symmetry axes and that induces a fully anisotropic degradation.¹⁸ Because of these manufacturing defects, sample cutting or fully anisotropic degradation, a procedure must be developed to identify the 21 independent or nonindependent coefficients of the most general stiffness tensor.

To exceed limits of classical inversion methods (existence of three mutually orthogonal planes of symmetry, knowledge of the material symmetry axes, and coincidence between the symmetry axes and the geometric axes), the process used for reconstruction of the stiffness tensor must be generalized to the material symmetries that are lower than orthorhombic symmetry: monoclinic or triclinic. As for the characterization of orthorhombic media, this problem has been tackled first by using measurements of ultrasonic phase velocity along predetermined directions of high symmetry. Simple expressions relate particular elasticity constants, or combinations thereof, to individual velocities.^{19–23} However, these methods that require cutting the sample in specific directions are not usable when ultrasonic access is limited to one or two sides of the sample.

The main focus of this paper is to demonstrate that the stiffnesses of materials that possess any class of symmetry (including the most general anisotropy) can be extracted from the experimentally measured velocities of ultrasonic waves obliquely incident from water onto a plate. The proposed process for identifying the elasticity tensor takes no account of the symmetry of acquisition planes. This approach is applicable to materials that have a single (monoclinic symmetry) or even no (triclinic symmetry) plane of symmetry. The full stiffness tensor is reconstructed from a single minimization procedure. The main difficulty is to implement an efficient algorithm requiring a reasonable number of iterations to converge to a stable solution and, above all, to the right solution. The introduction of constraints that must be satisfied by the elasticity constants improves the convergence of the inversion. Therefore, the problem of 9 (orthorhombic medium), 13 (monoclinic medium), or 21 unknowns (triclinic medium) is solved by a constrained optimization method using the Lagrangian duality.²⁴

Questions still remain regarding the suitability of this numerical method for elastic property characterization. Of particular concern is the sensitivity of experimental measurements to all moduli and, since one is dealing with a system of nonlinear equations, error propagation in calculations. The accuracy of reconstruction has been investigated by several approaches. For example, the sensitivity coefficients, i.e., the dependence of phase velocity on elasticity constants, is estimated numerically,²⁵ analytically by a perturbation method,¹³ or pragmatically by analyzing²⁶ the effects of the initial guesses, experimental data random scatter, and the

range of the refraction angle. Another possibility is to recognize *a posteriori*, from variances and covariances delivered by the optimization procedure, which stiffnesses have been most accurately recovered and which less so. It amounts to estimating a confidence interval associated with each identified constant.²⁷ In fact, since the confidence intervals are sensitive to the level of scatter in the experimental data and to the angle range of velocity measurements,²⁷ they quantify the sensitivity of the inversion algorithm for identifying elasticity constants from wave speed data.

Various classes of symmetry are considered. Several critical factors (initial guesses, scatter in experimental data) which can influence the accuracy of elastic property reconstruction have been investigated by means of numerical examples that simulate in the best way a typical experiment. It is a way of proving that the inverse process has a unique and stable solution, that it converges on the same solution whatever the initial guesses, and that it is slightly sensitive to random scatter in experimental data.²⁶ Then the recovering method can be applied to experimental data for various symmetry class materials. In the case of orthorhombic media, the elasticity tensor is obviously recoverable if three waves are generated in a nonsymmetry plane and if all of them are experimentally measurable. However, the difficulty of identification increases as the anisotropy decreases. The isotropic symmetry is quite special. The recovering algorithm may converge to a fictive minimum due to an erroneous recognition of the polarization of experimental measurements. To remove this difficulty, it is necessary to link each experimental velocity to an effectively generated solution. The problem to be solved is well known.²⁶ For materials that possess a single or no plane of symmetry, identification of additional elasticity constants, four in the monoclinic case or twelve for triclinic symmetry, requires additional acquisition planes. To validate the experimental characterization of medium with monoclinic or triclinic symmetry, the generalized reconstruction method is applied to a material for which elasticity tensor is known but for which the acquisition coordinate system does not coincide with the principal material coordinate system.

I. ULTRASONIC DETERMINATION OF ELASTICITY CONSTANTS

A. General formulation of the problem

The propagation of bulk waves in an anisotropic medium is governed by the equations of motion:¹²

$$(\Gamma_{ij} - \rho V^2 \delta_{ij}) P_j = 0, \quad (1)$$

with $\Gamma_{ij} = C_{ijkl} n_k n_l$ ($i, j, k, l = 1$ to 3) and where (C_{ijkl}) is the stiffness tensor of the material. ρ is the density, \mathbf{P} is the polarization vector, V is the phase velocity of ultrasonic waves in the medium, δ_{ij} is the Kronecker symbol, and n_i are the components of the unit vector \mathbf{n} in the wave propagation direction. Three elastic waves, one quasilongitudinal (QL), a fast (QT1) and a slow (QT2) quasitransverse modes, can propagate along the direction \mathbf{n} with three different velocities and their associated polarization vectors. Their ve-

locities are the solution of the following third-degree equation in the unknown ρV^2 :

$$|\Gamma_{ij} - \rho V^2 \delta_{ij}| = 0. \quad (2)$$

If the phase velocities for a given propagation direction \mathbf{n} are known, the stiffnesses (C_{ijkl}) are obtained by inverting Eq. (2). Using the abbreviated subscripts notation, the elasticity tensor (C_{ijkl}) is expressed by the 21 components of a symmetric (6×6) matrix (C_{IJ}):

$$(C_{IJ}) = \begin{bmatrix} C_{11} & C_{12} & C_{13} & C_{14} & C_{15} & C_{16} \\ & C_{22} & C_{23} & C_{24} & C_{25} & C_{26} \\ & & C_{33} & C_{34} & C_{35} & C_{36} \\ & & & C_{44} & C_{45} & C_{46} \\ & \text{Sym.} & & & C_{55} & C_{56} \\ & & & & & C_{66} \end{bmatrix}. \quad (3)$$

Every measured wave speed V_p is approximately the solution of the nonlinear cubic equation, expanded form of the Christoffel equation (2). Due to the experimental errors, the following function is close to zero:

$$\begin{aligned} f_p(\lambda_p(\mathbf{n}), C_{IJ}) = & -\lambda_p^3 + \lambda_p^2(\Gamma_{11} + \Gamma_{22} + \Gamma_{33}) + \lambda_p(\Gamma_{12}^2 + \Gamma_{13}^2 \\ & + \Gamma_{23}^2 - \Gamma_{11}\Gamma_{22} - \Gamma_{11}\Gamma_{33} - \Gamma_{22}\Gamma_{33}) \\ & + \Gamma_{11}\Gamma_{22}\Gamma_{33} + 2\Gamma_{12}\Gamma_{23}\Gamma_{13} - \Gamma_{11}\Gamma_{23}^2 \\ & - \Gamma_{22}\Gamma_{13}^2 - \Gamma_{33}\Gamma_{12}^2 \approx 0, \end{aligned} \quad (4)$$

where $\lambda_p = \rho V_p^2$ and $p=1$ to N (N is the total number of measurements). Identification of the elasticity constants from wave speed measurements in various propagation directions is performed by minimizing the functional

$$F(C_{IJ}) = \sum_{p=1}^N \{f_p(\lambda_p(\mathbf{n}), C_{IJ})\}^2 \quad (5)$$

built from the overdetermined system of equations (4).

B. Phase velocity measurements

Wave speed measurements are performed by using ultrasonic pulses which are transmitted through a plate immersed in water (Fig. 1). Ultrasound was generated and sensed by a pair of piezoelectric transducers. They are supported by two goniometers^{28,29} which allow one to select any propagation direction \mathbf{n}_i of incident wave. The coordinate system $R=(\mathbf{x}_1, \mathbf{x}_2, \mathbf{x}_3)$ for ultrasonic measurements is chosen in such a way that axis \mathbf{x}_1 corresponds to the normal to the interface.

For an oblique incident angle, the longitudinal incident pulse is refracted at the liquid–solid interface and generates one, two, or three waves that propagate with different velocities along the directions $\mathbf{n}=\mathbf{n}_m$, $m=1, 2$ or 3 . So one, two, or three modes reach the receiver with time delay δt , depending on their respective velocities. Phase velocities V_p at incident angle θ_i , imposed by the goniometers, are calculated and collected in several incident planes (\mathbf{x}_1, Ψ) , where Ψ is the azimuthal angle (Fig. 1). The refraction angles $\theta_r=(\mathbf{x}_1, \mathbf{n}_m)$, $m=1, 2$ or 3 , of the phase velocities are directly related to the angle of incidence $\theta_i=(\mathbf{x}_1, \mathbf{n}_i)$ through Snell–Descartes'

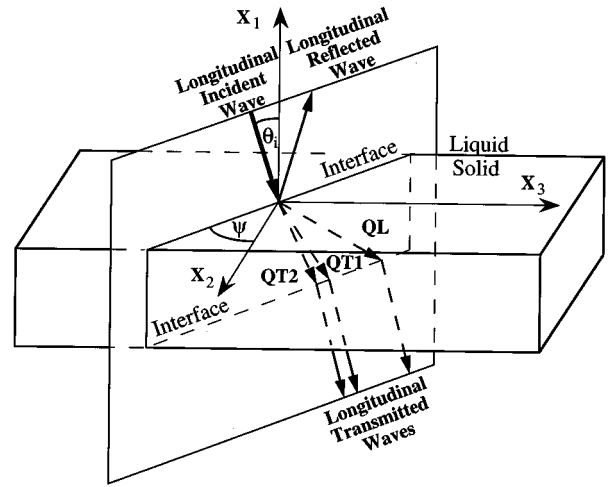


FIG. 1. Schematic diagram of the simple-transmission experiment. QL stands for a quasilongitudinal mode, and QT1 and QT2 stand for fast and slow quasitransverse modes, respectively. $R=(\mathbf{x}_1, \mathbf{x}_2, \mathbf{x}_3)$ is the observation coordinate system. The incident plane is defined by the azimuthal angle Ψ . The incident angle θ_i is reported for a positive value.

laws.¹² Continuity of displacements and constraints at the interface gives the number of waves effectively generated in the solid. If the incident plane coincides with a plane of symmetry, only two waves are generated¹² [one quasilongitudinal (QL) and one quasitransverse (QT)].

An appropriate signal processing of the received pulses is performed by using⁴ a reference signal propagating in water without the sample. Taking the transmitted signal at normal incidence as reference^{28–30} improves the accuracy of the time-of-flight difference δt measurement for a wave at arbitrary oblique incidence. The success of the (C_{IJ}) determination rests on the ability of the signal processing to improve the time resolution of overlapped waves when dispersive effects are present.^{31,32} Among the signal processings used for the time delay δt measurements, the Hilbert transform is from many points of view the most appropriate to the non-destructive evaluation of the elasticity constants.^{31,32} Contrary to the cross-correlation processing, this unambiguous measurement of phase velocity leads to the stiffnesses determination independently from the attenuation mechanisms.

C. Classical recovery

When the three planes $(\mathbf{x}_1, \mathbf{x}_2)$, $(\mathbf{x}_1, \mathbf{x}_3)$, and $(\mathbf{x}_2, \mathbf{x}_3)$ are planes of symmetry and are mutually orthogonal, the material presents at least an orthorhombic symmetry. Its elasticity tensor (C_{IJ}) has nine nonzero components:

$$(C_{IJ}) = \begin{bmatrix} C_{11} & C_{12} & C_{13} & & & \\ & C_{22} & C_{23} & & & \\ & & C_{33} & & & \\ & & & C_{44} & & \\ \text{Sym} & & & & C_{55} & \\ & & & & & C_{66} \end{bmatrix}. \quad (6)$$

When dealing with the propagation in one of these three

of the deviation between the slowness curves and the experimental data. The experimental data set covers the set of modes present in each of the three data planes: in the optimization process, information relative to the slow quasitransverse mode QT2^[45°], generated in the $(\mathbf{x}_1, 45^\circ)$ plane [respectively, the fast quasitransverse mode QT1^[45°], generated in the $(\mathbf{x}_1, 45^\circ)$ plane] associated with those related to the slow quasitransverse mode QT2^[13°], generated in the $(\mathbf{x}_1, \mathbf{x}_3)$ plane [respectively the fast quasitransverse mode QT1^[12°], generated in the $(\mathbf{x}_1, \mathbf{x}_2)$ plane], provide guidance on the slow quasitransverse mode QT2^[12°], nongenerated in the $(\mathbf{x}_1, \mathbf{x}_2)$ plane (respectively the fast quasitransverse mode QT1^[13°], nongenerated in the $(\mathbf{x}_1, \mathbf{x}_3)$ plane). So the slowness at the intersection of the QT2^[12°] mode (respectively the QT1^[13°] mode) and the axis \mathbf{x}_2 (respectively the axis \mathbf{x}_3) will converge naturally to the slowness $1/v(\mathbf{x}_2)$ [respectively $1/v(\mathbf{x}_3)$] associated directly with the elasticity constant C_{44} by

$$C_{44} = \rho v^2(\mathbf{x}_2) = \rho v^2(\mathbf{x}_3). \quad (12)$$

Therefore, for orthorhombic media, the minimization procedure does have the necessary data concerning each generated or nongenerated mode to determine simultaneously the nine independent elasticity constants from the three planes $\cup(3 \text{ Planes})$. Determination of additional elasticity constants, 4 and 12 for a medium with respectively monoclinic and triclinic symmetry, requires one to consider additional data planes in the set $\cup(\text{Planes})$ [Eq. (11)].

For a monoclinic medium, due to symmetry of the $(\mathbf{x}_2, \mathbf{x}_3)$ plane, in each data plane (\mathbf{x}_1, Ψ) (Fig. 1) the set of measured velocities at all positive incident angles θ_i is superimposed on the one collected for all negative incident angles. Therefore the data measurements are carried out for positive incident angles θ_i . Then (\mathbf{x}_1, Ψ) is identical to the $(\mathbf{x}_1, \Psi + \pi)$ data plane. The comparison of the measured velocities in the planes $(\mathbf{x}_1, -45^\circ)$ and $(\mathbf{x}_1, 45^\circ)$ [respectively $(\mathbf{x}_1, 45^\circ)$ and $(\mathbf{x}_1, 135^\circ)$] allows one to emphasize the symmetry of the geometric plane $(\mathbf{x}_1, \mathbf{x}_2)$ [respectively $(\mathbf{x}_1, \mathbf{x}_3)$]. The $(\mathbf{x}_1, -45^\circ)$ data plane is identical to the $(\mathbf{x}_1, 135^\circ)$ data plane. But, contrary to the orthorhombic case, the $(\mathbf{x}_1, 45^\circ)$ and $(\mathbf{x}_1, 135^\circ)$ data planes are different. Consequently, comparison of these planes allows one to differentiate the orthorhombic symmetry from the monoclinic symmetry. Introduction of the additional $(\mathbf{x}_1, 135^\circ)$ data plane in the set [Eq. (11)],

$$\begin{aligned} \cup(\text{Planes}) &= \cup(4\text{Planes}) \\ &= (\mathbf{x}_1, \mathbf{x}_2) \cup (\mathbf{x}_1, \mathbf{x}_3) \cup (\mathbf{x}_1, 45^\circ) \cup (\mathbf{x}_1, 135^\circ), \end{aligned} \quad (13)$$

is sufficient to the reconstruction of the stiffness tensor (10).

Ditri²³ has proved that wave speed and polarization data from two planes suffice to determine uniquely 20 of the 21 elasticity constants of a generally anisotropic medium. For example, the stiffness tensor (C_{IJ}) in the coordinate system $(\mathbf{x}_1, \mathbf{x}_2, \mathbf{x}_3)$ cannot be fully reconstructed from measurements collected in the planes $(\mathbf{x}_1, \mathbf{x}_2)$ and $(\mathbf{x}_1, \mathbf{x}_3)$: the constant C_{23} could not be obtained from the given acoustic data.²³ However, this stiffness can be determined with additional data planes. Let $(\mathbf{x}_1, \tilde{\mathbf{x}}_2, \tilde{\mathbf{x}}_3)$ be the coordinate system defined such that the planes $(\mathbf{x}_1, \tilde{\mathbf{x}}_2)$ and $(\mathbf{x}_1, \tilde{\mathbf{x}}_3)$ coincide respectively with

the planes $(\mathbf{x}_1, 45^\circ)$ and $(\mathbf{x}_1, 135^\circ)$. Identification of the stiffness tensor (C_{IJ}) in $(\mathbf{x}_1, \tilde{\mathbf{x}}_2, \tilde{\mathbf{x}}_3)$ from the velocities measured in the planes $(\mathbf{x}_1, \tilde{\mathbf{x}}_2)$ and $(\mathbf{x}_1, \tilde{\mathbf{x}}_3)$ is incomplete: the constant \tilde{C}_{23} cannot be reconstructed. Since $(\mathbf{x}_1, \tilde{\mathbf{x}}_2, \tilde{\mathbf{x}}_3)$ has been determined by a 45° rotation of $(\mathbf{x}_1, \mathbf{x}_2, \mathbf{x}_3)$ about \mathbf{x}_1 axis, (C_{IJ}) and (\tilde{C}_{IJ}) are related through the stiffness transformation laws.¹² With

$$C_{23} = \frac{1}{2}(C_{22} + C_{33}) - 2\tilde{C}_{44}, \quad (14)$$

the wave speed and polarization vector information from the four data planes $(\mathbf{x}_1, \mathbf{x}_2)$, $(\mathbf{x}_1, \mathbf{x}_3)$, $(\mathbf{x}_1, 45^\circ)$, and $(\mathbf{x}_1, 135^\circ)$ can supply information about the 21 independent elasticity constants (C_{IJ}) . As seen previously, the symmetry of the geometric planes $(\mathbf{x}_1, \mathbf{x}_2)$ and $(\mathbf{x}_1, \mathbf{x}_3)$ is emphasized by comparing the measured velocities in the planes $(\mathbf{x}_1, 45^\circ)$ and $(\mathbf{x}_1, 135^\circ)$. Use of positive and negative incident angles in each of these four planes allows recovery of the symmetry or nonsymmetry of the plane $(\mathbf{x}_2, \mathbf{x}_3)$. For the complete reconstruction of (C_{IJ}) , Eq. (3), these four data planes must be simultaneously introduced in the problem (8).

B. Determination of elasticity constants

Solving a problem with M unknowns, $M=9, 13$, or 21 , requires a robust optimization procedure. To improve the convergence of the simultaneous identification of the independent elasticity constants, one needs to introduce the constraints satisfied by the unknowns.

1. Constraints of the minimization problem

Due to the strict positivity of the material strain energy density $(1/2C_{ijkl}\epsilon_{ij}\epsilon_{kl})$, the stiffness tensor (C_{ijkl}) is positive definite, and then

$$C_{ijkl}a_{ij}a_{kl} > 0 \quad (15)$$

for arbitrary nonzero tensor (a_{ij}) . This induces³⁴ six constraints h_q ($q=1$ to 6) on the components of the stiffness tensor (C_{IJ}) :

$$\begin{aligned} h_1 &= C_{11} > 0, \quad h_2 = \begin{vmatrix} C_{11} & C_{12} \\ C_{12} & C_{22} \end{vmatrix} = |C_1^{(2)}, C_2^{(2)}| > 0, \\ h_3 &= \begin{vmatrix} C_{11} & C_{12} & C_{13} \\ C_{12} & C_{22} & C_{23} \\ C_{13} & C_{23} & C_{33} \end{vmatrix} = |C_1^{(3)}, C_2^{(3)}, C_3^{(3)}| > 0, \\ h_4 &= |C_1^{(4)}, C_2^{(4)}, C_3^{(4)}, C_4^{(4)}| > 0, \\ h_5 &= |C_1^{(5)}, C_2^{(5)}, C_3^{(5)}, C_4^{(5)}, C_5^{(5)}| > 0, \\ h_6 &= |C_1^{(6)}, C_2^{(6)}, C_3^{(6)}, C_4^{(6)}, C_5^{(6)}, C_6^{(6)}| > 0, \end{aligned} \quad (16)$$

denoting the m th column vector of the matrix (C_{IJ}) , with $I=1$ to n , as $(C_m^{(n)})$.

The condition of strong ellipticity³⁴ on the operator $(\Gamma_{ij} - \rho V^2 \delta_{ij})$ is less restrictive on the elasticity constants than those of positive definiteness, Eq. (15). Therefore only the six constraints h_q are considered.

2. Reconstruction algorithm

Minimization of the objective function $F(C_{IJ})$, problem (8), is solved by a constrained optimization method³⁵ using the Lagrangian duality and introducing the Lagrangian function $L(C_{IJ}, \mu)$, with $\mu \in \mathfrak{R}^{6+}$:

$$L(\tilde{C}_{IJ}, \mu) = L(C_{IJ}, \mu) = \sum_{\lambda_p \in \cup(\text{Planes})} \{f_p(\lambda_p(\mathbf{n}), C_{IJ})\}^2 + \sum_{q=1}^6 \{\mu_q(-h_q(C_{IJ}))\}, \quad (17)$$

where (\tilde{C}_{IJ}) is a $(1 \times M)$ vector that represents the M independent components of the symmetric (6×6) matrix (C_{IJ}) representative of the stiffness tensor:

$$\max_{\mu \in \mathfrak{R}^{6+}} 1(\mu) = \max_{\mu \in \mathfrak{R}^{6+}} \{ \min_{\tilde{C}_{IJ} \in \mathfrak{R}^M} L(\tilde{C}_{IJ}, \mu) \}. \quad (18)$$

The solving process of the dual problem (18) is composed of two stages that are repeated until the identification of the components of the stiffness tensor (C_{IJ}) , solution of the problem (8).

The minimization of $L(\tilde{C}_{IJ}, \mu)$, with μ fixed, is carried out by using successively the gradient method (steepest descent method³⁵) and the generalized Newton method.³⁵ The iterative schemes of these two successive approaches are identical and can be written as³⁵

$$(\tilde{C}_{IJ})_{k+1} = (\tilde{C}_{IJ})_k + \tau_k (\tilde{Z}_{IJ})_k, \quad (19)$$

with $(\tilde{C}_{IJ})_k$, $(\tilde{Z}_{IJ})_k \in \mathfrak{R}^M$, and $\tau_k \in \mathfrak{R}^+$. A symmetric (6×6) matrix (Z_{IJ}) defined as (C_{IJ}) is then associated with the $(1 \times M)$ vector (\tilde{Z}_{IJ}) . The descent directions $(\tilde{Z}_{IJ})_k$ vary according to the used method. They are defined from the $(1 \times M)$ gradient vector g_k and from the symmetric $(M \times M)$ Hessian matrix F_k . Here g_k and F_k contain respectively the first- and second-order partial derivatives of $L(\tilde{C}_{IJ}, \mu)$ with respect to the M elasticity unknowns. The steepest descent method is characterized by

$$(\tilde{Z}_{IJ})_k = -g_k / \|g_k\|, \quad (20)$$

whereas the generalized Newton method is built from

$$(\tilde{Z}_{IJ})_k = -F_k^{-1} g_k. \quad (21)$$

Contributions of the two constraints h_5 and h_6 to the g_k and F_k expressions are computed by finite differences. These related to the other constraint functions h_q are easily calculated. The step τ_k is introduced to minimize the function $L(C_{IJ}, \mu)$ along the direction $(\tilde{Z}_{IJ})_k$. This one-dimensional search corresponds to the minimization of the function $L^*(\tau)$:

$$\tau_k = \min_{\tau \in \mathfrak{R}^+} L^*(\tau) = \min_{\tau \in \mathfrak{R}^+} L((\tilde{C}_{IJ})_k + \tau (\tilde{Z}_{IJ})_k, \mu). \quad (22)$$

Introduction of τ in $f_p(\lambda_p(\mathbf{n}), C_{IJ})$ [Eq. (4)] defines a sixth-degree polynomial $f_p^*(\lambda_p(\mathbf{n}), \tau)$:

$$f_p^*(\lambda_p(\mathbf{n}), \tau) = f_p(\lambda_p(\mathbf{n}), \tilde{C}_{IJ} + \tau \tilde{Z}_{IJ}) = \sum_{m=0}^6 \{B_m(\lambda_p(\mathbf{n}), \tilde{C}_{IJ}, \tilde{Z}_{IJ}) \tau^m\}, \quad (23)$$

with $B_m(\lambda_p(\mathbf{n}), \tilde{C}_{IJ}, \tilde{Z}_{IJ}) \in \mathfrak{R}$. Therefore, $F^*(\tau)$ deduced directly from the objective function $F(C_{IJ})$ can be written as a sixth-degree polynomial:

$$F^*(\tau) = F(\tilde{C}_{IJ} + \tau \tilde{Z}_{IJ}) = \sum_{\lambda_p} \{f_p^*(\lambda_p(\mathbf{n}), \tau)\} = \sum_{m=0}^6 \left\{ \sum_{\lambda_p} B_m(\lambda_p(\mathbf{n}), \tilde{C}_{IJ}, \tilde{Z}_{IJ}) \right\} \tau^m, \quad (24)$$

with $\lambda_p \in \cup(\text{Planes})$. Denoting respectively the m th column vectors of the matrices (C_{IJ}) , (Z_{IJ}) , and (X_{IJ}) , with $I=1$ to n , as $(C_m^{(n)})$, $(Z_m^{(n)})$, and $(X_m^{(n)})$, and taking into account the properties of determinants, the functions $h_q^*(\tau)$ are deduced from the constraints h_q and then can be written as

$$h_1^*(\tau) = h_1((\tilde{C}_{IJ}) + \tau(\tilde{Z}_{IJ})) = C_{11} + \tau Z_{11},$$

$$h_2^*(\tau) = h_2((\tilde{C}_{IJ}) + \tau(\tilde{Z}_{IJ})) = |Z_1^{(2)}, Z_2^{(2)}| \tau^2 + (|C_1^{(2)}, Z_2^{(2)}| + |Z_1^{(2)}, C_2^{(2)}|) \tau + |C_1^{(2)}, C_2^{(2)}|,$$

$$h_3^*(\tau) = h_3((\tilde{C}_{IJ}) + \tau(\tilde{Z}_{IJ})) = |Z_1^{(3)}, Z_2^{(3)}, Z_3^{(3)}| \tau^3 + (|C_1^{(3)}, Z_2^{(3)}, Z_3^{(3)}| + |Z_1^{(3)}, C_2^{(3)}, Z_3^{(3)}| + |Z_1^{(3)}, Z_2^{(3)}, C_3^{(3)}|) \tau^2 + (|Z_1^{(3)}, C_2^{(3)}, C_3^{(3)}| + |C_1^{(3)}, Z_2^{(3)}, C_3^{(3)}| + |C_1^{(3)}, C_2^{(3)}, Z_3^{(3)}|) \tau + |C_1^{(3)}, C_2^{(3)}, C_3^{(3)}|, \dots,$$

or

$$h_q^*(\tau) = \sum_{m=0}^q \{ \text{Det}_{(m)}^{(q)} \} \tau^m \quad \text{for } q=1-6, \quad (25)$$

where $\text{Det}_{(m)}^{(q)}$ is the sum of $q!/(m!(q-m)!)$ $(q \times q)$ determinants $|X_1^{(q)}, \dots, X_m^{(q)}|$, exactly composed of m column vectors of the matrix (Z_{IJ}) , with $I=1$ to q , and such that $X_i^{(q)} = Z_i^{(q)}$ or $X_i^{(q)} = C_i^{(q)}$ for $i=1$ to q . So the function $L^*(\tau)$ may be written as a sixth-order polynomial in τ :

$$L^*(\tau) = L(C_{IJ} + \tau Z_{IJ}, \mu) = F^*(\tau) + \sum_{q=1}^6 \{ \mu_q(-h_q^*(\tau)) \}. \quad (26)$$

According to the polynomial form of $L^*(\tau)$, a usual search procedure of polynomial zero determines precisely the value of the optimal step τ_k [Eq. (22)].

The maximization of the function $1(\mu)$ is realized by the gradient method (steepest descent method). The iterative process can be written as

$$\mu_{k+1} = \mu_k + \tau_k \mathbf{Z}_k \quad (27)$$

with μ_k , $\mathbf{Z}_k \in \mathfrak{R}^6$, and $\tau_k \in \mathfrak{R}^+$. The descent direction \mathbf{Z}_k can be written as a (1×6) vector:

$$(Z_q)_k = \begin{cases} 0, & \text{if } (\mu_q)_k = 0 \text{ and} \\ & h_q(C_{IJ}) > 0, \\ \frac{d1(\mu)}{d(\mu_q)_k} = -h_q(C_{IJ}), & \text{if not,} \end{cases} \quad (28)$$

and the optimal step τ_k is such that

$$\tau_k = \max_{\tau} 1(\mu_k + \tau Z_k) \quad (29)$$

with

$$(\mu_q)_k + \tau(Z_q)_k > 0, \quad \text{for } q = 1-6.$$

3. Sensitivity for elastic property reconstruction

An estimation of the confidence interval $I(C_{IJ})$ associated with each identified constant can be calculated²⁷ by means of a statistical analysis of the velocity measurement set. The values $I(C_{IJ})$ are deduced from a linearization of Eq. (4) around the exact solution for each measured velocity with some assumptions on the angular distribution of the deviation between the measured and the recalculated velocities. The set of confidence intervals validates or not the choice of the data planes $\cup(\text{Planes})$. The intrinsic elasticity constants (C_{IJ}^{int}) will be such that

$$|C_{IJ}^{\text{int}} - C_{IJ}| < I(C_{IJ}) \quad (30)$$

with, for example, a 99% probability.

The confidence interval is the result of the $(M \times M)$ covariance matrix ($M = \text{number of unknowns}$). This matrix is built from the $(M \times N)$ gradient matrix ($N = \text{number of data}$) and the N error vector components. The gradient matrix contains the gradient of $f_p(\lambda_p(\mathbf{n}), C_{IJ})$ with respect to the M unknowns for any data. The error vector collects the final value of the function for any data. On assuming a Student's law, the confidence intervals are established by means of the variances associated with any elasticity constants.

III. DETERMINATION FOR MATERIALS POSSESSING THREE MUTUALLY ORTHOGONAL PLANES OF SYMMETRY

Due to the number of elasticity unknowns, the form of energy constraints is simplified. The relations h_q [Eq. (16)], are unchanged for $q \in \{1, 2, 3\}$, but they are written as

$$h_q = C_{qq} > 0 \quad \text{for } q = 4-6. \quad (31)$$

The expression of the $h_q^*(\tau)$ functions [Eq. (25)] vary also:

$$h_q^*(\tau) = C_{qq} + \tau Z_{qq}, \quad \text{for } q = 4-6. \quad (32)$$

First, we study the stability of the inversion procedure against random experimental error and the effect of initial guesses. Next, to demonstrate the method's applicability, we performed reconstruction by using experimental data. If three modes are generated in the $(\mathbf{x}_1, 45^\circ)$ plane and if they can be experimentally measured, then the stiffness tensor of the studied material can be easily identified. The higher the material symmetry is, or the closer to isotropic this symmetry is, the more important identification difficulties are: the $(\mathbf{x}_1, 45^\circ)$ plane is no longer a nonsymmetry plane.

A. Stability of reconstruction: Numerical simulation

To investigate the effect of initial guesses and possible experimental data random scatter, a set of elasticity constants is selected. From these "original data," a set of phase velocities was calculated for given propagation directions. This discrete set of refraction angles is selected to simulate a typical data set obtained by the ultrasonic bulk wave method (Sec. I B). Therefore we determine the range of refraction angles and the number of the simulated data for each of the data planes $\cup(3 \text{ Planes})$ from the experimental velocities measured in a 1-D SiC SiC composite material, taken as an example (Fig. 3). To approach the experimental conditions, it is useful to introduce random scatter that simulates possible experimental error. Therefore a random error ΔV is added to each computed velocity data V . The velocities are randomized within an interval $\Delta V/V$ of a fixed percentage. The random scatter applied to the velocity at normal incidence is identical for every plane of $\cup(3 \text{ Planes})$. The density for the 1-D SiC SiC composite is 2.5 g/cm^3 , the thickness of the sample is 3 mm, and the original elasticity constant set is given in Table I. The effect of the initial guesses of the iterative process is investigated by adding to each of the nine original data C_{IJ}^{or} an amount defined either arbitrarily or by a percentage Y of C_{IJ}^{or} with $Y \in \{-10\%, 10\%, -20\%, 20\%\}$ (Table I). Influence of the refraction angle ranges on determination of the stiffness tensor, and so sensitivity of the inversion algorithm for elastic property reconstruction from wave speed data is quantified by the confidence intervals.²⁷ Thus it is not necessary to discuss the ranges of the refraction angle to be taken.

The inversion algorithm is applied, for different initial guesses, to phase velocity sets simulated with different scatter levels. The reconstructed sets of elasticity constants are compared to the original set to discuss the accuracy of determination. Table I shows the results of the identifications from the simulated data with 0.5%, 1%, 1.5%, and 2% scatter. As in all the tables, the numbers in parentheses represent the confidence interval associated with each elasticity constant. For every scatter level, about ten sets of synthetic velocities are generated. So for each of these simulated sets, and whatever the sets of random errors $\Delta V/V$ associated with a fixed scatter level, the identified stiffness tensors are similar. These results have been checked for 0.5%, 1%, and 2% levels of scatter in the data. For the $\Delta V/V$ sets with 1.5% scatter, two typical identifications have been emphasized (Table I).

As can be seen from Table I, the identified stiffness tensor is independent of the initial guess selection for every level of scatter in the simulated data. For scatter levels less than or equal to 1% and for the first typical case of synthetic velocity data set with 1.5% scatter, the identified elasticity constants, with their respective confidence interval, coincide with the original constants. For the two other scatters, the minimum of the functional to be minimized is different from the exact solution: C_{44} is reconstructed less accurately. Thus the proposed method is sensitive to an important level of scatter in the velocity data. To discuss the applicability of this generalized reconstruction method, it is necessary to

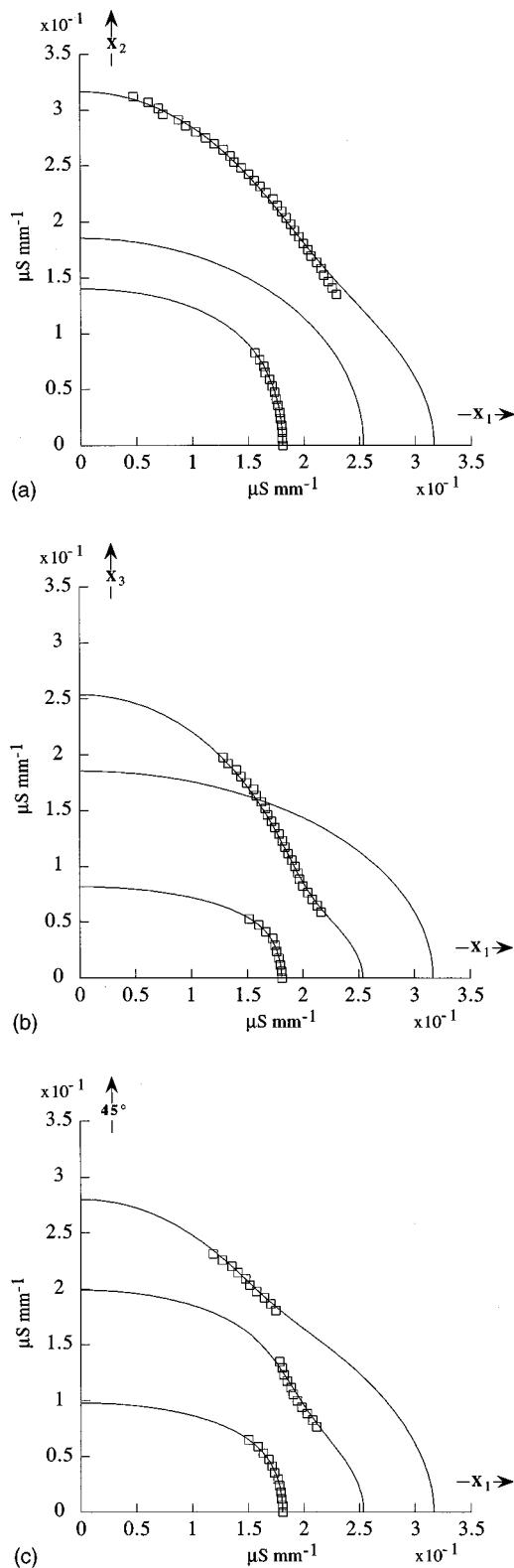


FIG. 3. Slownesses for a 1-D SiC SiC composite in the (a) (x_1, x_2) , (b) (x_1, x_3) , and (c) $(x_1, 45^\circ)$. The points are experimentally measured slownesses. The solid lines are slownesses calculated from the reconstructed elasticity constants.

quantify experimental errors on velocity measurements. Chu and Rokhlin^{26,30} have estimated the experimental error caused by ambient temperature fluctuation ($\Delta V/V$ is less than 0.5%). Analysis of the level of scatter in the experimen-

tal velocity set is realized in Sec. III B 1. The experimental random error is less than 1%. Satisfactory experimental results can therefore be achieved with the generalized reconstruction procedure.

Since confidence intervals are deduced from a linearization around the exact solution, the statistic parameters $I(C_{IJ})$ are meaningless when reconstruction is incorrect. Due to this remark, only the first three reconstruction results listed in Table I must be considered to discuss the confidence interval variation against random data scatter. Clearly the confidence interval set increases as the scatter level in the simulated data increases.

During given medium characterization, one can quantify the level of scatter in the experimental data by the velocities standard deviation³⁶ $\sigma(C_{IJ}, V_p)$, obtained from the experimental velocity set and velocities that are computed from the reconstructed stiffness tensor. We have noted that this standard deviation $\sigma(C_{IJ}, V_p)$ is proportional to the scatter level. So during an experimental characterization, if the computed value of $\sigma(C_{IJ}, V_p)$ is less than (1.5/2)%, the identified stiffness tensor must correspond to the elastic properties.

B. Application for various classes of symmetry: Experimental results

The choice of two, five, six, or nine independent stiffnesses according to the predicted material symmetry does not allow one to quantify the deviation of the medium symmetry from the chosen symmetry model. To do this, nine elasticity constants are determined independently for the media which have at least three mutually orthogonal planes of symmetry.

1. Orthorhombic symmetry

For this class of symmetry, the QL, QT1, and QT2 modes are experimentally accessible in the plane $(x_1, 45^\circ)$. The measurements were performed on a 1-D SiC SiC composite sample supplied by the Société Européenne de Propulsion. The physical properties of the sample are similar to the ones used for the previous numerical simulation. The stiffness tensors determined by the classical method (Sec. I C) or by the procedure which takes into account simultaneously the data planes, (Sec. II) coincide, to the nearest confidence intervals [Table II(a)]. Such a comparison validates reconstruction using the proposed approach. Figure 3 shows the measured data and the slowness curves calculated from the reconstructed elasticity constants using the generalized reconstruction method. The agreement between the experiment and the identified data is satisfactory. The value of the standard deviation $\sigma(C_{IJ}, V_p)$ is 0.6%. It points out the correct characterization of this 1-D SiC SiC sample. The (99%) confidence intervals associated with each of the elasticity constants identified using the proposed method are always less than the ones relative to the usual reconstruction. This is due to a surplus of experimental data resulting from the simultaneous data planes treatment.

For the generalized reconstruction, the confidence intervals associated with each determined constant [Table II(a)] are smaller than the ones that are associated with the elasticity moduli identified from simulated data with 1% scatter

TABLE I. Results (in GPa) of the elasticity constant reconstruction using simulated ultrasonic velocity data in $\cup(3$ Planes) with and without scatter for a medium with orthorhombic symmetry. The numbers in the parentheses indicate the confidence interval (in GPa) associated with each elasticity constant. The reconstructions performed for different initial guesses listed in the table have identical results.

| Data type | C_{11} | C_{12} | C_{13} | C_{22} | C_{23} | C_{33} | C_{44} | C_{55} | C_{66} |
|-----------------|----------|----------|----------|----------|----------|----------|----------|----------|----------|
| Original data | 76 | 29 | 35 | 134 | 98 | 396 | 81 | 37.4 | 24.6 |
| 0% | 76 | 29 | 35 | 134 | 98 | 396 | 81 | 37.4 | 24.6 |
| -10% | 68.4 | 26.1 | 31.5 | 120.6 | 88.2 | 356.4 | 72.9 | 33.7 | 22.1 |
| +10% | 83.6 | 31.9 | 38.5 | 147.4 | 107.8 | 435.6 | 89.1 | 41.1 | 27.1 |
| -20% | 60.8 | 23.2 | 28.0 | 107.2 | 78.4 | 316.8 | 64.8 | 29.9 | 19.7 |
| Initial guesses | 91.2 | 34.8 | 42.0 | 160.8 | 117.6 | 475.2 | 97.2 | 44.9 | 29.5 |
| <±20% | 84 | 32 | 30 | 110 | 100 | 433 | 88 | 34 | 26 |
| <±20% C_{33} | 96 | 43 | 78 | 153 | 39 | 450 | 62 | 19 | 6 |
| Fixed | 80 | 40 | 40 | 150 | 250 | 450 | 200 | 20 | 20 |
| Results | | | | | | | | | |
| 0% | 76 | 29 | 35 | 134 | 98 | 396 | 81 | 37.4 | 24.6 |
| scatter | (0) | (0) | (0) | (0) | (0) | (0) | (0) | (0) | (0) |
| 0.5% | 76.0 | 29.1 | 35.1 | 135 | 101 | 398 | 80 | 37.4 | 24.6 |
| scatter | (0.2) | (1.0) | (0.7) | (4) | (9) | (8) | (5) | (0.5) | (0.2) |
| 1% | 76.0 | 28.5 | 35.9 | 132 | 106 | 405 | 83 | 37.1 | 24.6 |
| scatter | (0.4) | (2.1) | (1.4) | (9) | (16) | (15) | (9) | (0.9) | (0.3) |
| 1.5% | 76.3 | 28.4 | 34.9 | 131 | 107 | 391 | 78 | 37.3 | 24.7 |
| scatter | one | | | | | | | | |
| typical run | (0.5) | (2.9) | (2.2) | (12) | (21) | (23) | (11) | (1.4) | (0.4) |
| second | 75.7 | 29.6 | 31.6 | 139 | 85 | 367 | 59 | 41.6 | 24.6 |
| typical run | (0.6) | (2.5) | (2.9) | (11) | (32) | (26) | (6) | (2.3) | (0.5) |
| 2% | 76.2 | 31.4 | 30.4 | 139 | 84 | 356 | 61 | 41.5 | 24.8 |
| scatter | (0.8) | (3.6) | (4.6) | (16) | (39) | (38) | (9) | (3.4) | (0.7) |

(Table I). However, as shown in Sec. III A, the statistic parameters $I(C_{IJ})$ are sensitive to the scatter in the velocity data. Since the synthetic velocity set has been generated from characterization of the 1-D SiC SiC studied in this section, clearly the random experimental error corresponds to a scatter level less than 1%.

Since all the components of the stiffness tensor (C_{IJ}) are identified by a single step, the associated compliance tensor ($S_{IJ}) = (C_{IJ})^{-1}$ is also the solution of the same minimization problem [Eq. (8)]. A confidence interval $I(S_{IJ})$ similar to the ones that are related to each elasticity constant is then associated with each compliance S_{IJ} [Table II(b)] and therefore with the engineering constant set. This allows the comparison of the ultrasonic characterization with the results obtained from more traditional mechanical measurements.

2. Tetragonal symmetry

The materials with this symmetry, as composites whose fibrous reinforcement has a balanced 2-D woven texture,

possess two equivalent directions: \mathbf{x}_2 and \mathbf{x}_3 . Two waves are excited in the symmetry plane ($\mathbf{x}_1, 45^\circ$). This causes some difficulties.

The material used in the experiment is a sample of 2-D carbon SiC composite supplied by the Société Européenne de Propulsion. The density is 2.1 g/cm^3 and the thickness is 3 mm. As one can see from Table III, the values of two stiffnesses C_{23} and C_{44} classically reconstructed from the single data plane ($\mathbf{x}_1, 45^\circ$) are wrong. Due to the condition (15), the value of the constraint $h_4 = C_{44} = -13 \text{ GPa}$ is unacceptable. In fact, the two constants C_{23} and C_{44} cannot be determined independently. The only stiffness³⁷ C^* ,

$$C^* = C_{23} + 2C_{44}, \quad (33)$$

can be measured from the ($\mathbf{x}_1, 45^\circ$) data plane. Supplementary information is needed. First, the contact measurement of the velocity V_c of a wave propagating in the direction \mathbf{x}_3 with particle displacements in the direction \mathbf{x}_2 allows the identification of C_{44} using Eq. (12):

TABLE II. Characterization of a 1-D SiC SiC composite. (a) Stiffness tensor components and associated confidence intervals (in GPa). (b) Compliance tensor components and associated confidence intervals (in 1/MPa).

| (a) Data type | C_{11} | C_{12} | C_{13} | C_{22} | C_{23} | C_{33} | C_{44} | C_{55} | C_{66} |
|--------------------------------|----------|----------|----------|----------|----------|----------|----------|----------|----------|
| Initial guesses | 76.0 | 30 | 35 | 135 | 92 | 397 | 81 | 37 | 25.0 |
| Classical method | (0.7) | (2) | (4) | (8) | (20) | (36) | (8) | (1) | (0.4) |
| Results | 76.0 | 28 | 33 | 127 | 81 | 375 | 73 | 39 | 25.0 |
| (GPa) | (0.3) | (2) | (2) | (6) | (16) | (12) | (6) | (1) | (0.3) |
| (b) $(S_{IJ}) = (C_{IJ})^{-1}$ | S_{11} | S_{12} | S_{13} | S_{22} | S_{23} | S_{33} | S_{44} | S_{55} | S_{66} |
| 1/(MPa) | 14.4 | -2.8 | -0.7 | 9.6 | -1.9 | 3.2 | 13.8 | 25.7 | 40.2 |
| | (0.2) | (0.2) | (0.2) | (0.7) | (0.6) | (0.2) | (0.4) | (0.5) | (0.5) |

TABLE III. Elasticity constants in GPa of a 2-D carbon SiC composite with quasi-tetragonal symmetry.

| Data type | C_{11} | C_{12} | C_{13} | C_{22} | C_{23} | C_{33} | C_{44} | C_{55} | C_{66} |
|------------------------|----------|----------|----------|----------|----------|----------|-----------|----------|----------|
| Classical method | | | | | | | | | |
| immersion measurements | 24.1 | 9.7 | 8.1 | 120 | 79 | 115 | -13 | 9.1 | 9.6 |
| | (0.3) | (0.9) | (0.5) | (8) | (24) | (5) | (12) | (0.3) | (0.2) |
| +contact measurement | 24.1 | 9.7 | 8.1 | 120 | 8.7 | 115 | 23.5 | 9.1 | 9.6 |
| | (0.3) | (0.9) | (0.5) | (8) | (1.8) | (5) | ± 1.2 | (0.3) | (0.2) |
| Generalized method | | | | | | | | | |
| immersion measurements | 24.1 | 9.5 | 7.7 | 119 | 11 | 110 | 19.5 | 9.2 | 9.9 |
| | (0.1) | (0.3) | (0.4) | (3) | (6) | (4) | (3) | (0.3) | (0.2) |
| +contact measurement | 24.1 | 9.6 | 7.7 | 118 | 3.8 | 111 | 23.52 | 9.1 | 9.9 |
| | (0.1) | (0.3) | (0.4) | (3) | (3.5) | (4) | ± 1.2 | (0.2) | (0.1) |

$$V_c = 3345 \text{ m/s} \Rightarrow C_{44} = 23.5 \text{ GPa} \quad \text{and} \quad \Delta C_{44} = 1.2 \text{ GPa}, \quad (34)$$

where ΔC_{44} represents the uncertainty of C_{44} . This uncertainty is related in a simple way to the experimental errors in the measurement. For our experimental system, the error $\Delta C_{44}/C_{44}$ has been estimated at 5%. Next, C_{23} is recovered from the data plane $(\mathbf{x}_1, 45^\circ)$.

The method of generalized reconstruction from the data measured by immersion ultrasonic technique also accurately determines seven of the nine components of the stiffness tensor: identification of C_{23} and C_{44} has failed. Figure 4 shows that the experimental velocity data set does not recover the set of modes present in each of the three $(\mathbf{x}_1, \mathbf{x}_2)$, $(\mathbf{x}_1, \mathbf{x}_3)$, and $(\mathbf{x}_1, 45^\circ)$ data planes. The optimization process has no information about the QT2^[12], QT1^[13], and QT1^[45°] modes. Consequently, the constant C_{44} reconstruction can only be performed from the $(\mathbf{x}_1, 45^\circ)$ data plane. In this classical case, sensitivity of these velocity data to the two stiffnesses C_{44} and C_{23} is known.³⁷ Since C_{44} is directly related

to the three modes QT2^[12], QT1^[13], and QT1^[45°], its identified value is completely random. So the C^* measurement is unacceptable and consequently, reconstruction of C_{23} also fails. From Fig. 4, it can be observed that the higher difference between the constants C_{55} and C_{66} to be reconstructed is, the stronger the sensitivity of the measured velocities in the planes $(\mathbf{x}_1, \mathbf{x}_2)$ and $(\mathbf{x}_1, \mathbf{x}_3)$ to the constant C_{44} is. The characterization is all the easier since the deviation of the material symmetry from the tetragonal model is important. Since the difficulties remain when the deviation is not sufficient, it is necessary to remove the indecisiveness on the determination of (C_{23}, C_{44}) . If the velocity measurement V_c is added to the $(\mathbf{x}_1, \mathbf{x}_3)$ data plane, one can see from Fig. 4 that the value of $1/V_c$ allows one to localize the slowness at the intersection of the QT1^[13] mode and the axis \mathbf{x}_3 . Due to the symmetry of the sample, V_c also fixes the slowness at the intersection of the QT2^[12] mode and the axis \mathbf{x}_2 . Consequently, the addition of this contact measurement in the two data planes $(\mathbf{x}_1, \mathbf{x}_2)$ and $(\mathbf{x}_1, \mathbf{x}_3)$ allows the localization of the modes QT2^[12], QT1^[13], and QT1^[45°]. An example of such a measurement set is shown for the $(\mathbf{x}_1, \mathbf{x}_2)$ plane in Fig. 5.

When the additional data V_c is not included, a fictive minimum is identified. The inversion result listed in the third row of Table III must therefore be taken cautiously. The confidence intervals, for example $I(C_{44}) = 3 \text{ GPa}$, have no meaning. Note that the value of C_{44} ($= 19.5 \text{ GPa}$) is close to the result using contact measurement but it is either a coincidence or due to deviation from the tetragonal symmetry. As shown by the difference between the reconstructed stiffnesses C_{55} and C_{66} and the one between C_{12} and C_{13} , the symmetry of the sample is indeed quasi-tetragonal. However, as it is not possible to know *a priori* the deviation from the tetragonal symmetry, the introduction of V_c is necessary.

By adding the contact measurement V_c , the estimation of the constants C_{23} and C_{44} of the 2-D carbon SiC composite material is correct. Evaluation of the C_{23} from the inversion process using separately the data planes, $C_{23} = 8.7 \text{ GPa}$, is performed without considering the uncertainties of the eight other constants already reconstructed. The identified value using the generalized method, $C_{23} = 3.8 \text{ GPa}$, coincides better with the experimental data set. This agreement be-

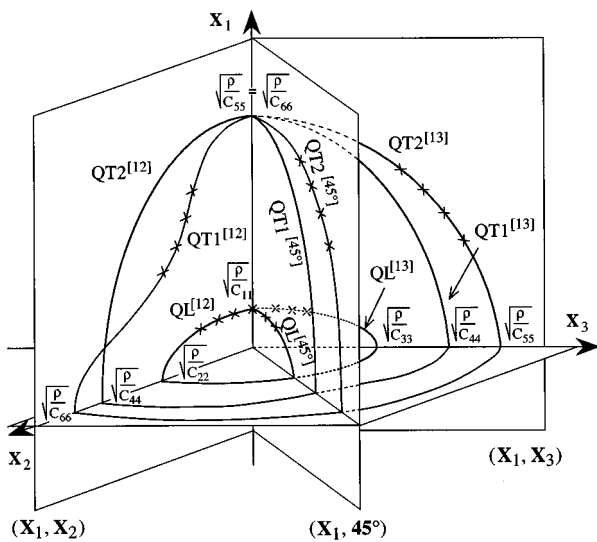


FIG. 4. Slownesses in the planes $(\mathbf{x}_1, \mathbf{x}_2)$, $(\mathbf{x}_1, \mathbf{x}_3)$, $(\mathbf{x}_1, 45^\circ)$ and $(\mathbf{x}_2, \mathbf{x}_3)$ for a medium with tetragonal symmetry. The crosses are experimentally accessible slownesses. The solid lines are slownesses calculated from the reconstructed elasticity constants.

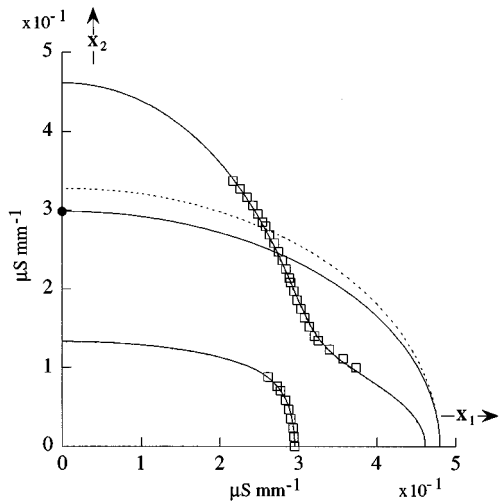


FIG. 5. Slownesses for a 2-D carbon SiC composite in the $(\mathbf{x}_1, \mathbf{x}_2)$ plane. The points are experimental slownesses: the squares and solid circles are respectively the slownesses measured by immersion and contact methods. The solid lines and dashed lines are slownesses calculated from the reconstructed elasticity constants taking into account or not the contact measurement.

tween the velocity measurements and all the nine determined elasticity constants (C_{IJ}) is pointed out by smaller associated confidence intervals $I(C_{IJ})$, except for the C_{23} . The value of $I(C_{23})$ is either naturally high due to the simultaneous treatment of data planes, $I(C_{23})=3.5$ GPa, or necessarily small, $I(C_{23})=1.8$ GPa, if the stiffness C_{44} is measured separately with a contact method. The value of $C_{23}=3.8$ GPa corresponds very probably to the elastic properties.

To avoid doing the contact measurement, one can replace in the problem (8) the incident plane $(\mathbf{x}_1, 45^\circ)$ with a nonsymmetry (\mathbf{x}_1, Ψ) data plane. The optimal choice of the azimuthal angle Ψ can be performed by studying beforehand the sensitivity of the solving algorithm to the moduli C_{23} and C_{44} . To do this, the stiffness tensor must already be known.

3. Hexagonal symmetry

A unidirectional composite is used for this class of symmetry. These composites are nearly isotropic in the plane transverse to the fiber direction: the plane $(\mathbf{x}_1, \mathbf{x}_2)$. In such a material, the three modes QL, QT1, and QT2 are experimentally accessible in the nonsymmetry plane $(\mathbf{x}_1, 45^\circ)$. So this

makes the characterization of the medium easier. The density of the studied sample of carbon epoxy is 1.56 g/cm^3 and the thickness is 3.45 mm .

Using the classical and generalized identification method, the study of this medium has been performed from the data measured in the planes $\cup(3 \text{ Planes})$ (Table IV). The reconstructed stiffness tensors coincide to the nearest confidence intervals. Since this last approach is independent of the symmetry of data planes, the study of this sample has also been carried out (Table IV) from the data measured in the four nonsymmetry planes $(\mathbf{x}_1, 30^\circ)$, $(\mathbf{x}_1, 120^\circ)$, $(\mathbf{x}_1, 75^\circ)$, and $(\mathbf{x}_1, 165^\circ)$. The confidence intervals associated with the elasticity constants identified by this last operation point out the fairly good determination of the elastic properties.

Let the anisotropy factor¹² be defined for example for the plane $(\mathbf{x}_1, \mathbf{x}_2)$ as $2C_{66}/(C_{11}-C_{12})$ or $2C_{66}/(C_{22}-C_{12})$. The calculation of the anisotropy factors from the identified elasticity constants C_{11} , C_{22} , C_{12} and C_{66} illustrate the isotropy of the plane $(\mathbf{x}_1, \mathbf{x}_2)$. For each of the three reconstructions, the computed anisotropy factors are close to 1. The deviation from hexagonal symmetry is therefore slight.

4. Isotropic symmetry

For isotropic media, every material plane is a plane of symmetry. A single quasitransverse mode QT is excited in every data plane. The result of the characterization of an aluminum sample whose density is 2.82 g/cm^3 and thickness is 4.1 mm is listed in Table V.

Due to the symmetry of the three data planes, the invariant C^* does not allow one to determine independently the nine moduli (C_{IJ}). This can also be seen by comparing the values of $I(C_{23})=90$ GPa and $I(C_{44})=45$ GPa with the other confidence intervals related to the constants reconstructed using the classical approach. Note that this sensitivity problem disappears when two independent moduli representative of the isotropic symmetry are searched for. However, this technique is no more applicable to media with quasi-isotropic symmetry. Reconstruction of C_{23} and C_{44} without taking into account the isotropic symmetry of the sample is impossible.

As it can be seen from the two first rows of Table V, the sets of elasticity constants C_{11} , C_{12} , C_{22} , C_{33} , and C_{66} identified, using the classical and the proposed reconstruction methods, coincide to the nearest confidence intervals. The anisotropy factors computed for each of the geometric planes

TABLE IV. Elasticity constants in GPa of a unidirectional carbon epoxy composite. Reconstruction performed from measured velocity data (a) in the three planes $(\mathbf{x}_1, \mathbf{x}_2)$, $(\mathbf{x}_1, \mathbf{x}_3)$ and $(\mathbf{x}_1, 45^\circ)$ and (b) in the four planes $(\mathbf{x}_1, 30^\circ)$, $(\mathbf{x}_1, 120^\circ)$, $(\mathbf{x}_1, 75^\circ)$ and $(\mathbf{x}_1, 165^\circ)$.

| Data type | | C_{11} | C_{12} | C_{13} | C_{22} | C_{23} | C_{33} | C_{44} | C_{55} | C_{66} |
|-----------------|------------------|-----------------|--------------|--------------|---------------|--------------|------------|--------------|----------------|----------------|
| Initial guesses | Classical method | 12.15
(0.03) | 5.5
(0.1) | 5.5
(0.4) | 12.5
(0.1) | 6.8
(0.3) | 136
(6) | 7.3
(0.4) | 5.9
(0.2) | 3.4
(0.1) |
| | (a) | 12.15
(0.01) | 5.5
(0.1) | 5.5
(0.1) | 12.5
(0.1) | 6.3
(0.7) | 134
(2) | 7.0
(0.5) | 6.0
(0.1) | 3.4
(0.1) |
| Results | | | | | | | | | | |
| | (b) | 12.15
(0.03) | 5.4
(0.1) | 5.5
(0.2) | 12.3
(0.2) | 5.7
(0.8) | 130
(3) | 6.8
(0.1) | 6.00
(0.04) | 3.48
(0.04) |

TABLE V. Aluminum elasticity constants (in GPa) reconstructed by using various methods.

| Data type | C_{11} | C_{12} | C_{13} | C_{22} | C_{23} | C_{33} | C_{44} | C_{55} | C_{66} |
|-----------------------------|---------------|-----------|------------|-----------|-----------|-----------|------------|------------|-----------|
| Classical method | 95
(1) | 37
(1) | 41
(3) | 93
(2) | 4
(90) | 90
(5) | 40
(45) | 25
(3) | 26
(1) |
| Generalized method | 94.7
(0.2) | 37
(2) | -7
(24) | 92
(2) | 35
(4) | 90
(3) | 25
(2) | 49
(12) | 26
(1) |
| Velocity generalized method | 94.7
(0.4) | 37
(1) | 40
(3) | 94
(3) | 39
(7) | 88
(5) | 24
(3) | 26
(2) | 25
(2) |

$(\mathbf{x}_1, \mathbf{x}_2)$, $(\mathbf{x}_1, \mathbf{x}_3)$, and $(\mathbf{x}_2, \mathbf{x}_3)$ are close to 1. Isotropy of these planes is recognized. However, although Fig. 6 illustrates the good agreement between the experimental data and the recalculated slowness curves, the reconstructed component C_{13} is very different from the elasticity constants C_{12} and C_{23} . The stiffness C_{55} is also distinct from the moduli C_{44} and C_{66} . This is due to the form of the objective function $F(C_{IJ})$. For the data collected in the plane $(\mathbf{x}_1, \mathbf{x}_3)$, the nonreduced Christoffel equation is minimum because the expression $(\Gamma_{22} - \lambda_p)$ is. Convergence of the generalized reconstruction algorithm to a fictive minimum can be illustrated by computing the polarization of each experimental measurement in the $(\mathbf{x}_1, \mathbf{x}_3)$ plane from the identified stiffness tensor. In every data plane, the polarization vectors are calculated for every mode using Eq. (1) and are jointly compared to the corresponding direction \mathbf{n} and to the normal \mathbf{n}_π to the incident plane:

$$\mathbf{n}_\pi = -\sin \Psi \mathbf{x}_2 + \cos \Psi \mathbf{x}_3, \quad (35)$$

where Ψ is the azimuthal angle. One sees in the plane $(\mathbf{x}_1, \mathbf{x}_3)$ that the QT1 mode [Fig. 7(b)], contrary to the QT2 mode [Fig. 7(a)], is excited and experimentally accessible. Figure 6(b) shows that the slowest experimental data set covers the nongenerated mode QT2 and illustrates therefore the wrong identification of the stiffnesses C_{13} and C_{55} . Comparison of the values $I(C_{13})=24$ GPa and $I(C_{55})=12$ GPa with the other confidence intervals confirm the inversion failure. Moreover, as mentioned previously, the moduli C_{23} and C_{44} cannot be determined separately. This is not shown by the confidence intervals $I(C_{23})=4$ GPa and $I(C_{44})=2$ GPa because the inversion result corresponds to a fictive minimum. Due to the incorrect mode assignment, it can be easily shown from Fig. 6(b) that the reconstructed values of C_{44} and C_{66} are an approximation of the stiffness C_{55} . Note that this fictive minimum appears only for this class of symmetry and that this superposition between the experimental data and the nongenerated quasitransverse mode is possible either in the $(\mathbf{x}_1, \mathbf{x}_2)$ plane or in the $(\mathbf{x}_1, \mathbf{x}_3)$ plane, but never simultaneously in both planes. Due to the isotropy or quasi-isotropy of the planes $(\mathbf{x}_1, \mathbf{x}_2)$ and $(\mathbf{x}_1, \mathbf{x}_3)$, introduction of the contact measurement V_c in the experimental data set does not improve the characterization of the aluminum sample. Although the polarization of V_c is collinear to \mathbf{n}_π of these two planes, V_c is consistently associated with the experimental data set corresponding to the generated quasitransverse mode. This is due to an erroneous recognition of mode.

C. Characterization from the solutions of the Christoffel equation: Velocity generalized method

The success of the quasi-isotropic media characterization is closely related to the recognition of the polarization vector \mathbf{P} of each velocity measurement V_p . To remove the difficulties raised in the previous section one needs to associate with each of the experimental data a predicted velocity $V_{\text{calculated}}$ that is effectively generated. Here $V_{\text{calculated}}$ is one of the solutions of the reduced or nonreduced Christoffel equation. Consequently, instead of minimizing the function $F(C_{IJ})$ [Eq. (9)] that is a relationship verified by the experimental velocities, let us minimize directly the deviation between each of the experimental data and their associated velocity $V_{\text{calculated}}$. This problem has been already posed.^{10,11} It becomes

$$(C_{IJ}) = \min_{(C_{IJ})} F_v(C_{IJ}), \quad (36)$$

with

$$F_v(C_{IJ}) = \frac{1}{2} \sum_{V_p \in \cup(\text{Planes})} \{f v_p(V_p(\mathbf{n}), C_{IJ})\}^2,$$

where

$$f v_p(V_p(\mathbf{n}), C_{IJ}) = V_{\text{calculated}}(C_{IJ}, \mathbf{n}) - V_p(\mathbf{n})$$

and $\cup(\text{Planes})$ is given in Eq. (11) or (13). To determine the elastic properties of any medium, the reconstruction algorithm must be independent of the symmetry of the data planes. Therefore $V_{\text{calculated}}$ is chosen as one of the solutions, in the phase velocity, of the nonreduced Christoffel equation [Eq. (4)]. Analytical expression of these three solutions is given¹⁰ by Cardan's solution of the third-degree equation. The step τ_k , minimizing the function $F_v(C_{IJ})$ along the direction $(\tilde{Z}_{IJ})_k$, is determined by solving

$$\tau_k = \min_{\tau \in R^+} F_v((\tilde{C}_{IJ})_k + \tau(\tilde{Z}_{IJ})_k). \quad (37)$$

Contrary to the solution of the halfway problem (22), the optimal τ_k [Eq. (37)] cannot be accurately determined because of the analytical form of $V_{\text{calculated}}$. Therefore the convergence domain of the inversion method (36) that treats directly the phase velocity is naturally narrower. On the other hand this optimization process is more robust against random scatter than the generalized reconstruction method.^{11,26,38} Confidence intervals $I(C_{IJ})$ are defined from the function $f v_p(V_p(\mathbf{n}), C_{IJ})$ [Eq. (36)]. Solving the problem (36) requires associating each experimental velocity of bulk

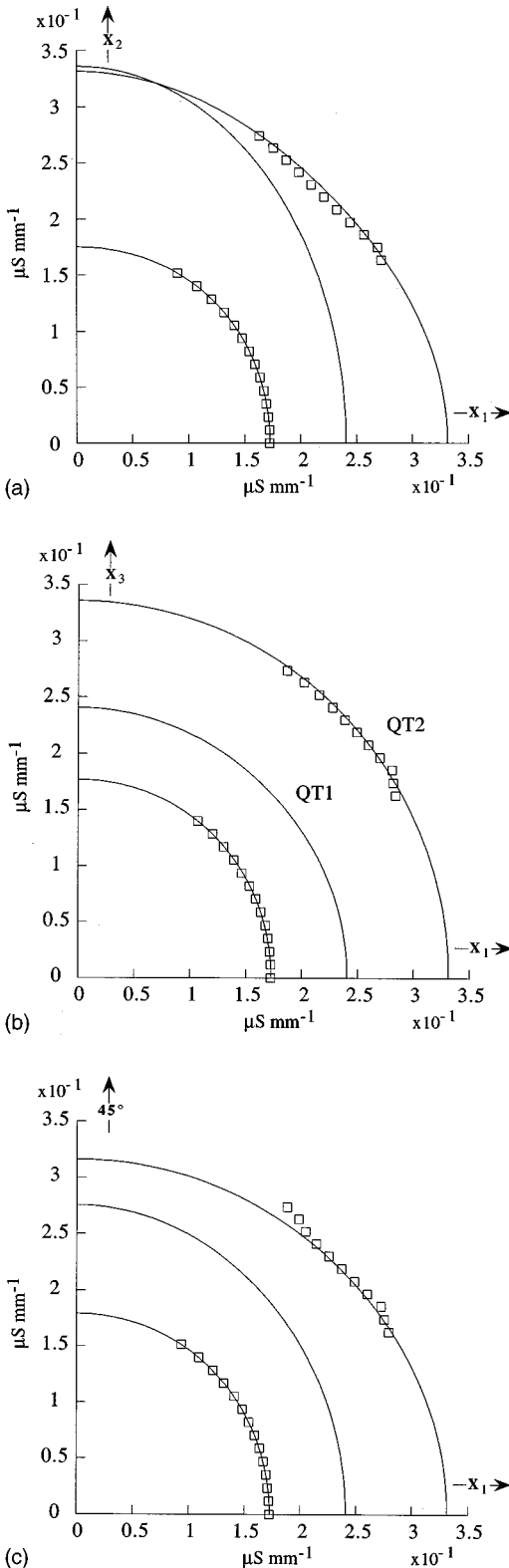


FIG. 6. Slownesses for an aluminum sample in the (a) (x_1, x_2) , (b) (x_1, x_3) , and (c) $(x_1, 45^\circ)$ planes. The points are experimentally measured slownesses. The solid lines are slownesses calculated from the wrong reconstructed elasticity constants due to an erroneous recognition of the polarization of experimental measurements.

wave propagating in the material along the direction \mathbf{n} with one of the three solutions $V_{\text{calculated}}$, calculated for the same propagation direction \mathbf{n} .

For a symmetry plane, the recognition of the QL or QT

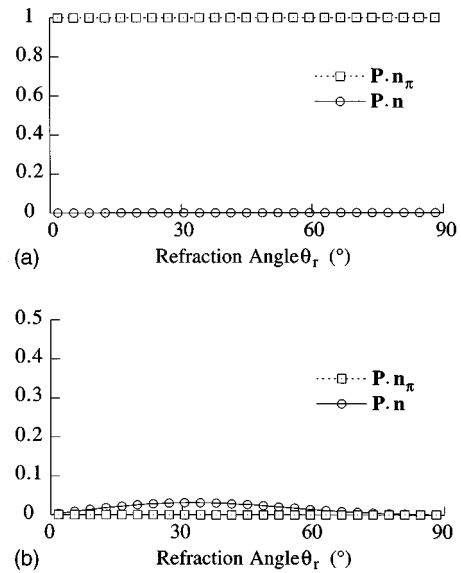


FIG. 7. Recognition of the character of the two quasitransverse modes present in the plane (x_1, x_3) of an aluminum material. The polarization vector \mathbf{P} is jointly compared with the propagation direction \mathbf{n} and the vector \mathbf{n}_π normal to the plane (x_1, x_3) . (a) The QT2 mode, (b) the QT1 mode.

character of the wave corresponding to each velocity measurement is immediate. The assignment of an experimental data to a solution $V_{\text{calculated}}$ is carried out by comparing the polarization vectors \mathbf{P} associated with each velocity $V_{\text{calculated}}$ with the propagation direction \mathbf{n} and with the normal \mathbf{n}_π to the incident plane.

If the incident plane is a nonsymmetry plane, each V_p assigned to the QL mode is associated with the highest solution $V_{\text{calculated}}$. The assignment of each remaining experimental data to one of the two slowest solutions $V_{\text{calculated}}$ is more difficult.

For characterization of an orthorhombic medium, only the velocities measured in the data plane $(x_1, 45^\circ)$ pose a problem. However, when the $QT1^{[45^\circ]}$ and $QT2^{[45^\circ]}$ modes are distinct, the simultaneous representation of the experimental data in the three planes (x_1, x_2) , (x_1, x_3) , and $(x_1, 45^\circ)$ (Fig. 2) allows one to determine unambiguously the QL, QT1, or QT2 character of the wave corresponding to each measured velocity. When three modes are experimentally accessible, the associations $(V_p, V_{\text{calculated}})$ are immediate.

1. Isotropic media: Experimental result

Due to the linear combination C^* emphasized for this symmetry, the contact measurement V_c is added to $\cup(3 \text{ Planes})$ [Eq. (11)]. The nine moduli of the aluminum sample studied in Sec. III B 4 are independently identified from this phase velocity set (Table V). The solution of the generalized reconstruction algorithm has been chosen as an initial guess.

The identified elasticity constants by the velocity generalized reconstruction method represent very well approximation (to the nearest confidence intervals) to the ones determined by the classical inversion. As discussed above, the value of $I(C_{23})$ is naturally high, $I(C_{23})=7 \text{ GPa}$. To their nearest confidence intervals, the (C_{11}, C_{22}, C_{33}) stiffnesses are identical. The (C_{12}, C_{13}, C_{23}) and (C_{44}, C_{55}, C_{66}) sets

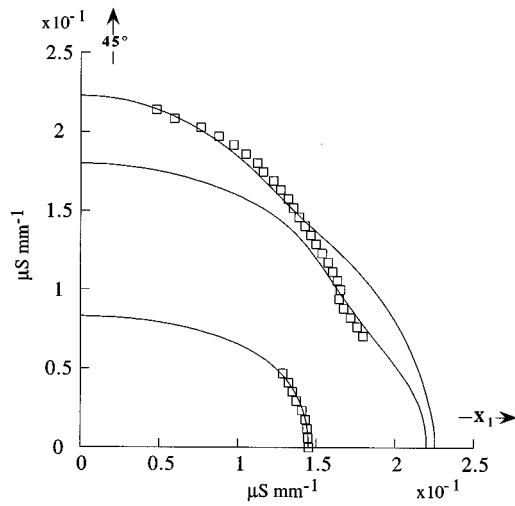


FIG. 8. Slownesses for a 2-D SiC SiC composite in the $(\mathbf{x}_1, 45^\circ)$ plane. The points are experimentally measured slownesses. The solid lines are slownesses calculated from the reconstructed elasticity constants.

have this specific feature. The anisotropy factors of each of the $(\mathbf{x}_1, \mathbf{x}_2)$, $(\mathbf{x}_1, \mathbf{x}_3)$, and $(\mathbf{x}_2, \mathbf{x}_3)$ geometric planes are also close to 1. The deviation from isotropic symmetry is therefore slight.

2. The main difficulty

As pointed out previously, when an ambiguity concerning the separation of two quasitransverse modes in the $(\mathbf{x}_1, 45^\circ)$ data plane exists, the velocity generalized reconstruction procedure cannot be used. To illustrate that, a 2-D SiC SiC composite is considered.²⁹ The density is 2.76 g/cm^3 and the thickness of the sample is 3.3 mm. Presence of porosity in the medium induces a slight degradation of the data measurement quality. The discrete points plotted in Fig. 8 show the measured phase velocities in the plane $(\mathbf{x}_1, 45^\circ)$. Introduction of the contact measurement or comparison of the experimental measurements in $\cup(3 \text{ Planes})$ does not improve the recognition of the QT1 or QT2 character of each of the experimental data measured in the plane $(\mathbf{x}_1, 45^\circ)$. The assignment of each of the experimental data to a phase velocity $V_{\text{calculated}}$ of a generated mode is difficult (Fig. 8). Is the experimental data set corresponding to the slowest velocities associated with the single excited quasitransverse mode QT or with the QT1 fast and QT2 slow quasitransverse modes? How feasible is it to relate two successive measurement data to two different quasitransverse modes? To illustrate this problem, first all the experimental data in the $(\mathbf{x}_1, 45^\circ)$ plane corresponding to the quasitransverse mode(s?) are associated with the slow quasitransverse mode QT2. Then the five measurements that have the smallest values of refraction angle are related to the fast quasitransverse mode QT1. This operation is then repeated by groups of 10, 15, and 20 measurements until the 26 slowest measured velocities in the plane $(\mathbf{x}_1, 45^\circ)$ are joined to the fast quasitransverse mode QT1. The velocity generalized reconstruction method is applied to these six cases. Figure 9 shows the reconstructed stiffness C_{23} as a function of the number of data assigned to QT1. An erroneous recognition of mode

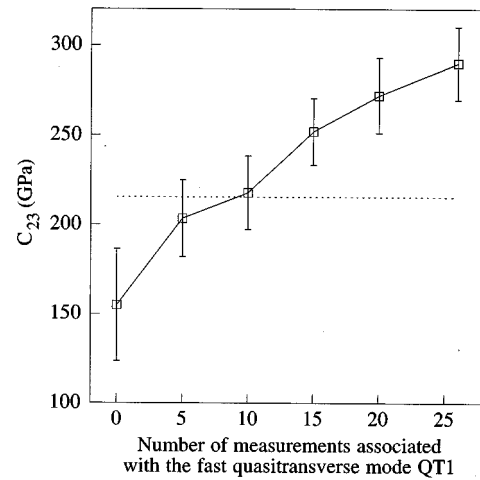


FIG. 9. The reconstructed elasticity constant C_{23} (using the velocity generalized procedure) as function of an arbitrary assignment of some slownesses measured in the $(\mathbf{x}_1, 45^\circ)$ plane to the QT1 mode. The error bars represent the confidence interval $I(C_{23})$ of the reconstructed C_{23} . The dashed line corresponds to the reconstructed elasticity constant C_{23} using the generalized reconstruction method.

induces a random identification of stiffness tensor. Nevertheless, note that the result of the generalized reconstruction is affected by the errors due to mode interference between both quasitransverse waves when their velocities are very close (Fig. 8).

IV. DETERMINATION FOR MATERIALS THAT DO NOT POSSESS THREE MUTUALLY ORTHOGONAL PLANES OF SYMMETRY

A. Monoclinic symmetry

The 13 components of the stiffness tensor (10) are simultaneously determined by solving the problem (8) from $\cup(4 \text{ Planes})$ [Eq. (13)]. The energy constraints h_q that have been established for $q=1$ to 5 in Eq. (16), and

$$h_6 = \begin{vmatrix} C_{55} & C_{56} \\ C_{56} & C_{66} \end{vmatrix} > 0 \quad (38)$$

are introduced in the generalized reconstruction procedure. Expression of the function $h_6^*(\tau)$ [Eq. (25)] varies also and can be written as

$$h_6^*(\tau) = \begin{vmatrix} Z_{55} & Z_{56} \\ Z_{56} & Z_{66} \end{vmatrix} \tau^2 + \left(\begin{vmatrix} C_{55} & Z_{56} \\ C_{56} & Z_{66} \end{vmatrix} + \begin{vmatrix} Z_{55} & C_{56} \\ Z_{56} & C_{66} \end{vmatrix} \right) \tau + \begin{vmatrix} C_{55} & C_{56} \\ C_{56} & C_{66} \end{vmatrix}. \quad (39)$$

The carbon epoxy sample that has been characterized in Sec. III B 3 is examined in a nonprincipal coordinate system. Figure 10 shows the coordinate system $R' = (\mathbf{x}'_1, \mathbf{x}'_2, \mathbf{x}'_3)$ obtained from a 30° rotation of the principal material coordinate system $R = (\mathbf{x}_1, \mathbf{x}_2, \mathbf{x}_3)$ about \mathbf{x}_1 axis. The \mathbf{x}_1 and \mathbf{x}'_1 axes are superimposed. The $(\mathbf{x}'_1, \mathbf{x}'_2)$ and $(\mathbf{x}'_1, \mathbf{x}'_3)$ planes are no longer planes of symmetry. The $(\mathbf{x}'_2, \mathbf{x}'_3) = (\mathbf{x}_2, \mathbf{x}_3)$ plane preserves its symmetric character.

To compare characterizations of the carbon epoxy sample in both R and R' frames, we consider the inversion

results obtained from the same set of velocity measured in the planes $(\mathbf{x}'_1, \mathbf{x}'_2) [=(\mathbf{x}_1, 30^\circ)]$, $(\mathbf{x}'_1, \mathbf{x}'_3) [=(\mathbf{x}_1, 120^\circ)]$, $(\mathbf{x}'_1, (45^\circ)') [=(\mathbf{x}_1, 75^\circ)]$, and $(\mathbf{x}'_1, (135^\circ)') [=(\mathbf{x}_1, 165^\circ)]$ (Figs. 10 and 11). The only QL and QT1 modes are experimentally accessible in the plane $(\mathbf{x}'_1, (45^\circ)')$. The third row

in Table IV lists the components of the (C_{IJ}) stiffness tensor that has been determined in R from this experimental data set. The elasticity constants in the rotated coordinate system R' are easily calculated using the stiffness transformation laws:¹²

$$(C'_{IJ})^{\text{computed}} = \begin{pmatrix} 12.15 & 5.4 & 5.5 & 0.0 & 0 & 0 \\ & 22.3 & 25.2 & 14.3 & 0 & 0 \\ & & 81 & 36.8 & 0 & 0 \\ & & & 26.3 & 0 & 0 \\ \text{Sym.} & & & & 5.4 & 1.1 \\ & & & & & 4.1 \end{pmatrix} \text{ (GPa)}. \quad (40)$$

$(C'_{IJ})^{\text{computed}}$ has 13 nonzero and dependent moduli [Eq. (10)]. The stiffness tensor (C'_{IJ}) reconstructed from the phase velocities measured in the nonprincipal coordinate system R' (Fig. 11) is

$$(C'_{IJ}) = \begin{pmatrix} 12.15 \pm 0.02 & 5.3 \pm 0.2 & 5.7 \pm 0.2 & -0.1 \pm 0.1 & 0 & 0 \\ & 21.4 \pm 1.0 & 24.4 \pm 1.0 & 13.6 \pm 0.5 & 0 & 0 \\ & & 83 \pm 2 & 36.9 \pm 0.7 & 0 & 0 \\ & & & 26.0 \pm 0.5 & 0 & 0 \\ \text{Sym.} & & & & 5.3 \pm 0.1 & 1.1 \pm 0.1 \\ & & & & & 4.2 \pm 0.1 \end{pmatrix} \text{ (GPa)}. \quad (41)$$

The 13 identified elasticity constants coincide, to the nearest confidence intervals, with the stiffnesses calculated from the nine moduli determined in R [Eq. (40)]. This validates the experimental characterization of a medium possessing at least one known symmetry plane. Note that (C_{IJ}) and (C'_{IJ}) are two components of the same stiffness tensor in two different coordinate systems. Here (C'_{IJ}) represents in R' the elastic properties of the sample. Identification of 13 elasticity constants does not imply a monoclinic symmetry. It can be higher in a principal coordinate system.

B. Triclinic symmetry

1. Triclinic media characterization: Numerical simulation

To conduct a numerical simulation of a typical experiment, the parameters of the experimental characterization performed from velocity measurements (in a nonprincipal coordinate system) on a carbon epoxy sample are selected. This composite material has previously been studied. The density is 1.56 g/cm^3 and the thickness is 3.45 mm . The original data listed in Table VI have been chosen closer to the stiffnesses reconstructed in Sec. IV B 2. Simulation has been carried out with the sound speed in water $V_0 = 1.483 \text{ mm}/\mu\text{s}$.

The $T(\theta_i)$ transmission coefficient of a signal propagating once through the sample is calculated for each of the three modes that could be generated in the plate. These quantities $T(\theta_i)$ represent the simple-transmission experiment described in Sec. I B. They quantify for an ultrasonic wave emitted at a fixed θ_i incident angle, the reception of the three modes on the receiver transducer. Figure 12 shows $T(\theta_i)$ as a function of incident angle in the four planes $\cup(4 \text{ Planes})$. To define accurately an angular range experimentally accessible, the critical angle θ_L of each mode is calculated in each plane $\cup(4 \text{ Planes})$. For anisotropic material, the critical angle³⁹ θ_L generally occurs at that incident angle for which the energy flux vector of the refracted mode is parallel to the surface and not necessarily when the value of the associated refraction angle is equal to 90° . For a homogeneous bulk wave propagating in an elastic medium, the energy flow vec-

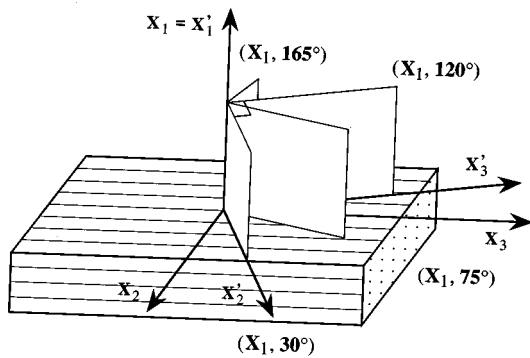


FIG. 10. Four data planes $(\mathbf{x}'_1, \mathbf{x}'_2) [=(\mathbf{x}_1, 30^\circ)]$, $(\mathbf{x}'_1, \mathbf{x}'_3) [=(\mathbf{x}_1, 120^\circ)]$, $(\mathbf{x}'_1, (45^\circ)') [=(\mathbf{x}_1, 75^\circ)]$, and $(\mathbf{x}'_1, (135^\circ)') [=(\mathbf{x}_1, 165^\circ)]$ for characterization of a unidirectional carbon epoxy composite in the nonprincipal coordinate system $(\mathbf{x}'_1, \mathbf{x}'_2, \mathbf{x}'_3)$.

TABLE VI. Results (in GPa) of the elasticity constant reconstruction using simulated velocity data in $\cup(4$ Planes) with and without scatter for a medium with triclinic symmetry. The reconstructions performed for different initial guesses listed in the table have identical results.

| Data type | C_{11} | C_{12} | C_{13} | C_{14} | C_{15} | C_{16} | C_{22} | C_{23} | C_{24} | C_{25} | C_{26} | C_{33} | C_{34} | C_{35} | C_{36} | C_{44} | C_{45} | C_{46} | C_{55} | C_{56} | C_{66} | |
|---|--------------|----------|----------|----------|----------|----------|----------|----------|----------|----------|----------|----------|----------|----------|----------|----------|----------|----------|----------|----------|----------|------|
| Original data | 12.25 | 5.48 | 6.25 | 0.31 | 0.44 | 0.29 | 20.91 | 23.95 | 13.14 | 1.94 | 1.31 | 83.89 | 36.66 | 6.49 | 3.26 | 25.51 | 3.57 | 2.14 | 5.94 | 1.43 | 4.34 | |
| Deviation from original data: 0%, $\pm 10\%$, $\pm 20\%$ | | | | | | | | | | | | | | | | | | | | | | |
| Initial guesses | $< \pm 20\%$ | C_{33} | 9.9 | 17 | 0.7 | -9.5 | 13.7 | 24.0 | 16.8 | 29.3 | 7.8 | -3.1 | 69.1 | 45.2 | 4.8 | -8.8 | 36.8 | 4.6 | -7.2 | 20.0 | 5.1 | -2.2 |
| Orthorhombic model + 20% | 14.7 | 6.6 | 7.5 | 0 | 0 | 0 | 25.1 | 28.7 | 0 | 0 | 0 | 100 | 0 | 0 | 0 | 30.6 | 0 | 0 | 7.1 | 0 | 5.2 | |
| Results | | | | | | | | | | | | | | | | | | | | | | |
| 0% scatter | 12.25 | 5.48 | 6.25 | 0.31 | 0.44 | 0.29 | 20.91 | 23.95 | 13.14 | 1.94 | 1.31 | 83.89 | 36.66 | 6.49 | 3.26 | 25.51 | 3.57 | 2.14 | 5.94 | 1.43 | 4.34 | |
| 0.5% scatter | (0) | (0) | (0) | (0) | (0) | (0) | (0) | (0) | (0) | (0) | (0) | (0) | (0) | (0) | (0) | (0) | (0) | (0) | (0) | (0) | (0) | |
| 1% scatter | 12.27 | 5.5 | 6.3 | 0.35 | 0.45 | 0.28 | 20.6 | 23.6 | 13 | 1.92 | 1.29 | 83.8 | 36.6 | 6.5 | 3.2 | 25.5 | 3.58 | 2.13 | 5.94 | 1.42 | 4.35 | |
| 1.5% scatter | (0.03) | (0.1) | (0.1) | (0.07) | (0.02) | (0.02) | (0.5) | (0.6) | (0.3) | (0.07) | (0.07) | (0.8) | (0.4) | (0.2) | (0.2) | (0.3) | (0.06) | (0.07) | (0.03) | (0.04) | (0.05) | |
| 2% scatter | 12.27 | 5.4 | 6.4 | 0.35 | 0.44 | 0.31 | 20.4 | 23.2 | 12.7 | 1.87 | 1.33 | 83.5 | 36.4 | 6.4 | 3.4 | 25.4 | 3.52 | 2.19 | 5.91 | 1.47 | 4.4 | |
| 0% scatter | (0.06) | (0.2) | (0.2) | (0.13) | (0.04) | (0.04) | (0.9) | (1.1) | (0.6) | (0.14) | (0.13) | (1.4) | (0.8) | (0.3) | (0.3) | (0.6) | (0.12) | (0.14) | (0.06) | (0.07) | (0.1) | |
| 0.5% scatter | 12.39 | 5.6 | 6.4 | 0.39 | 0.44 | 0.31 | 20.4 | 22.7 | 12.4 | 1.75 | 1.37 | 81.6 | 35.3 | 6.1 | 3.4 | 24.7 | 3.38 | 2.21 | 5.92 | 1.43 | 4.3 | |
| 1.5% scatter | (0.10) | (0.3) | (0.3) | (0.20) | (0.06) | (0.07) | (1.3) | (1.7) | (0.9) | (0.22) | (0.20) | (2.2) | (1.2) | (0.4) | (0.5) | (0.8) | (0.17) | (0.21) | (0.09) | (0.11) | (0.2) | |
| 2% scatter | 12.46 | 5.6 | 6.6 | 0.41 | 0.43 | 0.31 | 19.9 | 21.7 | 11.8 | 1.63 | 1.35 | 79.6 | 34.1 | 5.8 | 3.3 | 24.1 | 3.23 | 2.18 | 5.92 | 1.42 | 4.3 | |
| 0% scatter | (0.13) | (0.4) | (0.4) | (0.27) | (0.07) | (0.09) | (1.7) | (2.2) | (1.1) | (0.28) | (0.26) | (2.9) | (1.6) | (0.5) | (0.6) | (1.1) | (0.22) | (0.28) | (0.12) | (0.15) | (0.3) | |

tor is collinear to the (1×3) gradient vector that contains the derivative of the function $f_p(\lambda_p(\mathbf{n}), C_{IJ})$ [Eq. (4)] with respect to the three components of \mathbf{n} (see, for example, Ref. 12). The propagation directions \mathbf{n} corresponding to the critical angles satisfy

$$\frac{\partial f_p}{\partial n_1}(\lambda_p(\mathbf{n}), C_{IJ}) = 0, \quad (42)$$

where n_1 is the projection of \mathbf{n} upon the normal to the interface \mathbf{x}_1 . The solutions of Eq. (42) are shown in Fig. 12 for each data plane.

The previous considerations do not account for the difficulties in measuring the time delay of the overlapped modes. The signal processing using the Hilbert transform allows one to distinguish two modes when the temporal shift is greater than the quarter of the wavelength of the pseudo-period of the signal propagating in the water without the sample.^{31,32} Classically, two 5-MHz central frequency transducers are used. The associated wavelength is then equal to $0.2 \mu\text{s}$, i.e., the inverse of the central frequency. When the temporal shift between two modes is greater than $0.05 \mu\text{s}$, the correct temporal position of these modes can therefore be measured. From the original stiffnesses given in Table VI, the time delay δt is calculated using

$$\delta t = \frac{e}{V_0} \left[\cos \theta_i - \sqrt{\left(\frac{V_0}{V}\right)^2 - \sin^2 \theta_i} \right], \quad (43)$$

where V_0 is the sound speed in water and e is the thickness of the sample. Figure 13 shows the time-of-flight difference δt for the $(\mathbf{x}_1, \mathbf{x}_3)$ plane in which the temporal shift between the modes is the smallest. The θ_i belonging to the $[-\theta_L, \theta_L]$ angular range are considered. At a fixed incident angle, the temporal shifts between the time delay of the three modes are greater than $0.05 \mu\text{s}$ for the four data planes. The signal processing technique does not alter the angular range which is experimentally measurable. These ranges are established for each mode of each data plane from the transmission coefficients and critical angles. The angular ranges are expressed in refraction angle using the Snell-Descartes' laws and the Christoffel equation's solutions. The number of points taken in each domain corresponds to measurements performed at all degrees (in incident angle).

In the $(\mathbf{x}_1, \mathbf{x}_2)$ plane, the range of the refraction angle for the QL mode is $[-37^\circ; 19^\circ]$ and is respectively $[-77^\circ; -29^\circ] \cup [15^\circ; 73^\circ]$ and $[-55^\circ; -38^\circ] \cup [33^\circ; 56^\circ]$ for the QT1 and QT2 modes. The number of the simulated data is 27 for the QL mode, (18+27), 18 points in the first domain and 27 in the second for the QT1 mode, and (16+22) for the QT2 mode. In the plane $(\mathbf{x}_1, \mathbf{x}_3)$, the range of the refraction angle is respectively $[-24^\circ; 10^\circ]$, $[-85^\circ; -17^\circ] \cup [8^\circ; 71^\circ]$ and $[-76^\circ; -50^\circ] \cup [44^\circ; 73^\circ]$ for the QL, QT1, and QT2 modes [with 17, (32+35) and (11+16) synthetic data]. In the plane $(\mathbf{x}_1, \mathbf{x}_4)$, the ranges of the refraction angle for the QL, QT1, QT2 modes are respectively $[-21^\circ; 11^\circ]$, $[-78^\circ; -17^\circ] \cup [8^\circ; 71^\circ]$, and $[-74^\circ; -63^\circ] \cup [52^\circ; 69^\circ]$ [with 16,

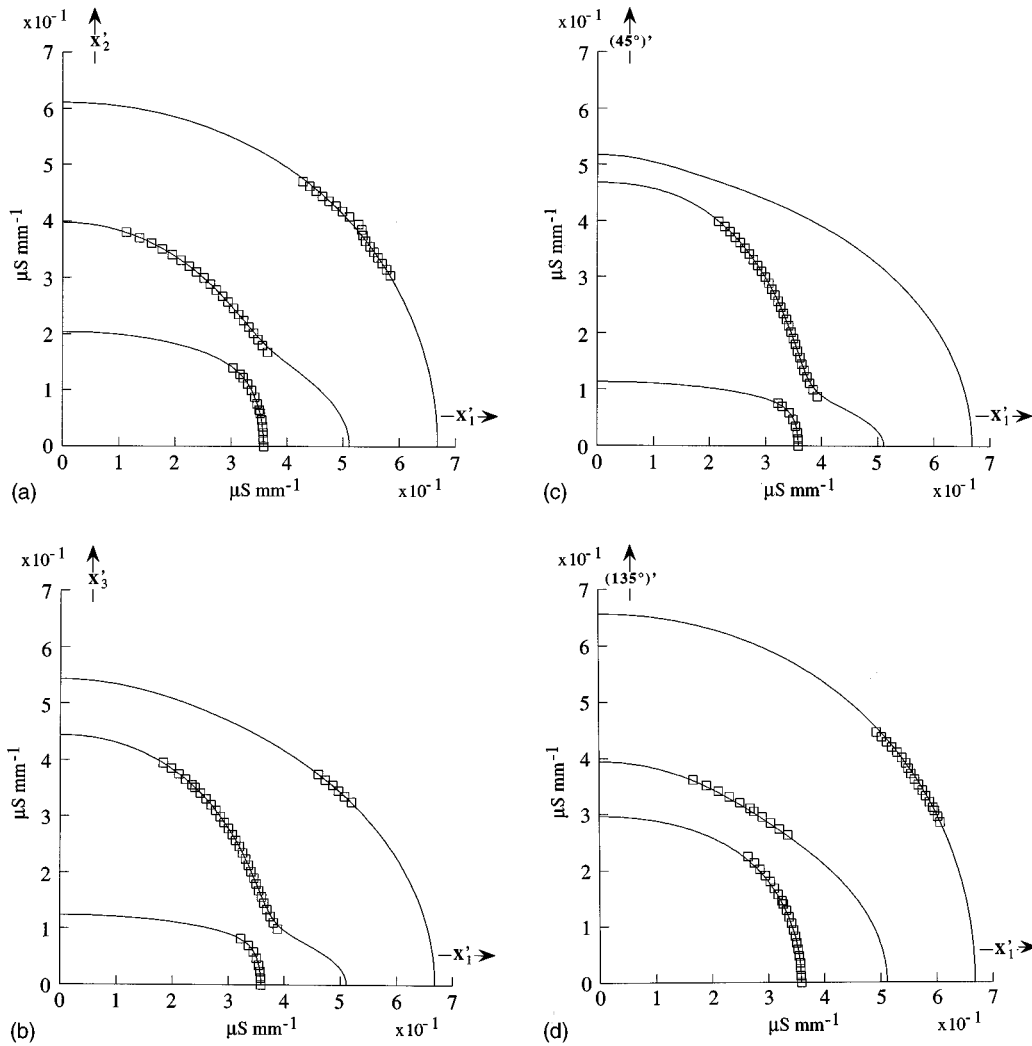


FIG. 11. Slownesses for a unidirectional carbon epoxy composite in the (a) (x'_1, x'_2) , (b) (x'_1, x'_3) , (c) $(x'_1, (45^\circ)')$, and (d) $(x'_1, (135^\circ)')$ planes. The points are experimentally measured slownesses. The solid lines are slownesses calculated from the reconstructed elasticity constants.

(34+37) and (4+9) simulated data]. The ranges of the refraction angle for the QL, QT1, and QT2 modes in the plane $(\mathbf{x}_1, \mathbf{135}^\circ)$ are respectively $[-58^\circ; 39^\circ]$, $[-77^\circ; -43^\circ] \cup [30^\circ; 73^\circ]$, and $[-52^\circ; -27^\circ] \cup [29^\circ; 52^\circ]$ [with 44, (10+18) and (26+23) simulated data]. The domains defined in this way simulate the angular ranges that can be measured on a carbon epoxy composite by the immersion bulk wave method. In Fig. 14, the synthetic velocity sets are shown by discrete points and the solid lines are calculated from the original elasticity constants given in Table VI. The slowness curves are plotted for every propagation direction \mathbf{n} with an associated energy flow vector pointing into the sample. These directions must satisfy the inequality:

$$\frac{\partial f_p}{\partial n_1}(\lambda_p(\mathbf{x}_1), C_{IJ}) \frac{\partial f_p}{\partial n_1}(\lambda_p(\mathbf{n}), C_{IJ}) > 0. \quad (44)$$

The asymmetry of the velocity data with respect to \mathbf{x}_1 axis justifies the search for 21 moduli. Note that the values of the refraction angles associated with the critical angles of inci-

dence $-\theta_L$ and θ_L are different. The angular ranges (in refraction angle) of the solid lines shown in Fig. 14(b) correspond to the ones (in incident angle) of the solid curves in Fig. 13.

To demonstrate the effectiveness of the proposed inversion algorithm, the initial guesses are either selected to be $\pm 10\%$ and $\pm 20\%$ off the original moduli or imposed as shown in Table VI. The optimization process is very stable for the given scatter levels. The initial guesses as nine non-zero stiffnesses or as a set of 21 values that do not satisfy the energy constraints ($h_3 < 0$) [Eq. (16)] show also the expanse of the convergence domain. Up to a 1.5% level the inversion results are closer to the exact solution. Since the experimental random error on the velocity measurements is typically less than 1% scatter in the velocity data set, the reconstruction algorithm is applicable to these experimental measurements. The value of each confidence interval with respect to the scatter level shows that the set of $I(C_{IJ})$ represents the sensitivity of the solving algorithm to the modulus set from the quality of velocity measurements.

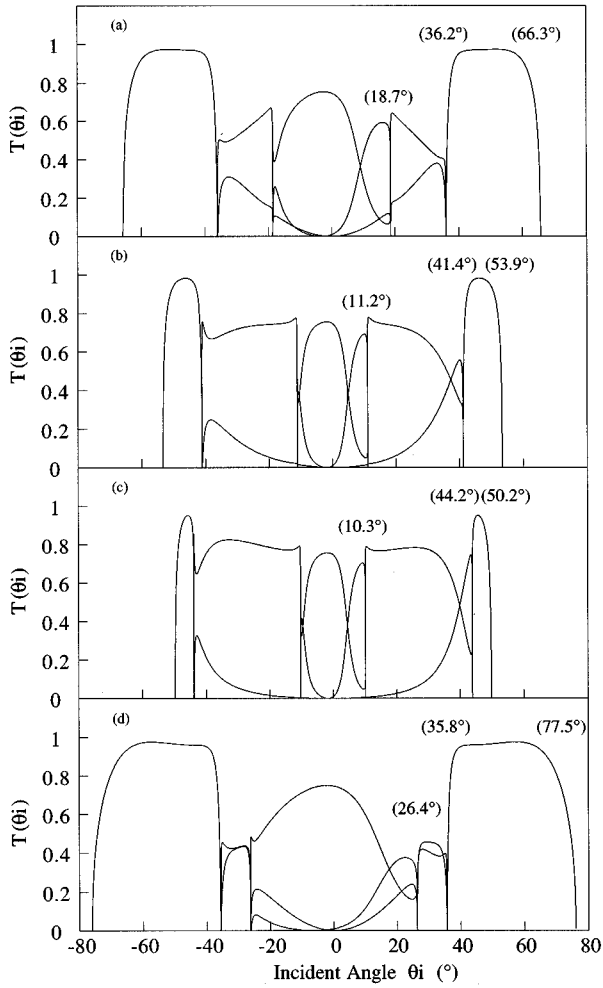


FIG. 12. The computed transmission coefficients $T(\theta_i)$ of acoustic waves propagating once through the sample from the 21 elasticity constants given in Table VI (original data). Calculations are performed for the four planes: (a) $(\mathbf{x}_1, \mathbf{x}_2)$, (b) $(\mathbf{x}_1, \mathbf{x}_3)$, (c) $(\mathbf{x}_1, 45^\circ)$, and (d) $(\mathbf{x}_1, 135^\circ)$. The numbers in the parentheses indicate the critical angle θ_L .

2. Triclinic media characterization: Experimental results

To validate the experimental characterization, the experiment must be done on a material whose stiffness tensor is known. From the stiffness transformation laws,¹² it is known that the stiffness tensor (C''_{IJ}) in a rotated coordinate system R'' , obtained from two rotations of the principal material coordinate system, can be equivalent in form to the tensor for a triclinic symmetry [Eq. (3)]. The approach consists of identifying the 21 components of (C''_{IJ}) from the velocity data measured in R'' .

The sample of the carbon epoxy composite studied in the previous sections is introduced again. Let $R' = (\mathbf{x}'_1, \mathbf{x}'_2, \mathbf{x}'_3)$ be the frame defined in Fig. 10. The chosen observation coordinate system $R'' = (\mathbf{x}''_1, \mathbf{x}''_2, \mathbf{x}''_3)$ is obtained from a 10° rotation of R' about \mathbf{x}'_3 axis. Therefore R'' is related to the principal coordinate system R by successive rotations. First R is rotated through an angle 30° about \mathbf{x}_1

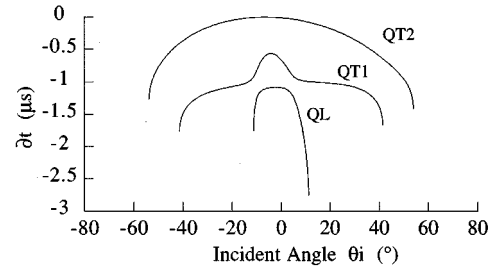


FIG. 13. The time delay (δt) between reference (through fluid) and through the sample (at angle θ_i) acoustic paths calculated from the 21 elasticity constants given in Table VI (original data). Calculations are performed for the $(\mathbf{x}_1, \mathbf{x}_3)$ plane.

axis, then through an angle 10° about the transformed \mathbf{x}'_3 axis. The planes $(\mathbf{x}'_1, \mathbf{x}'_2)$, $(\mathbf{x}'_1, \mathbf{x}'_3)$, and $(\mathbf{x}'_2, \mathbf{x}'_3)$ are no longer planes of symmetry.

The (C_{IJ}) stiffness tensor of this sample has been identified in R from the $(\mathbf{x}_1, 30^\circ)$, $(\mathbf{x}_1, 75^\circ)$, $(\mathbf{x}_1, 120^\circ)$, and $(\mathbf{x}_1, 165^\circ)$ data planes and is listed in the third row of Table IV. The 21 components of the (C''_{IJ}) stiffness tensor in R'' are calculated from (C_{IJ}) :

$$(C''_{IJ})^{\text{computed}} = \begin{pmatrix} 12.25 & 5.6 & 6.1 & 0.37 & 0.44 & 0.30 \\ & 21.8 & 24.6 & 13.7 & 2.0 & 1.4 \\ & & 81.3 & 36.2 & 6.49 & 3.4 \\ & & & 25.7 & 3.6 & 2.2 \\ \text{Sym.} & & & & 6.0 & 1.43 \\ & & & & & 4.3 \end{pmatrix} \text{ (GPa)}. \quad (45)$$

Here (C''_{IJ}) represents in R'' the elastic properties of the sample, but identification of 21 elasticity constants does not imply a triclinic symmetry. It can be higher in a principal coordinate system.

However, it is difficult to simulate such a frame R'' of propagation in the material from a rotation that is predetermined and applied to the apparatus emitting the ultrasonic waves. The base vector \mathbf{x}''_1 is indeed different from the normal to the sample \mathbf{x}_1 and according to Snell–Descartes' laws corresponds to several incident waves. These difficulties disappear as soon as the normal to a triclinic sample coincides with a base vector of the observation coordinate system R'' . The study is carried out from the experimental velocities measured for positive and negative incident angles in the $(\mathbf{x}_1, 30^\circ)$, $(\mathbf{x}_1, 120^\circ)$, $(\mathbf{x}_1, 75^\circ)$, and $(\mathbf{x}_1, 165^\circ)$ data planes. The 21 components of the equivalent stiffness tensor in R'' ,

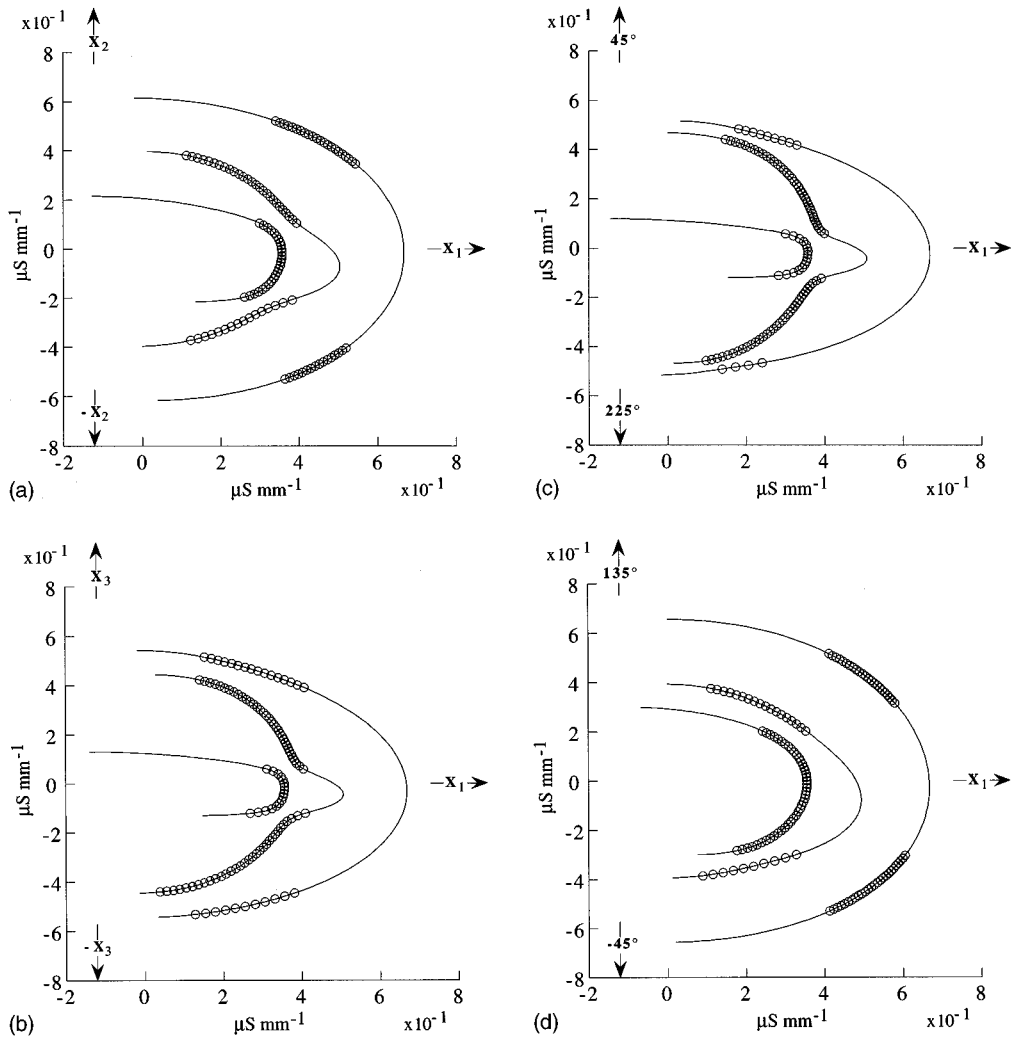


FIG. 14. Slownesses for a medium with triclinic symmetry in the planes (a) (x_1, x_2) , (b) (x_1, x_3) , (c) $(x_1, 45^\circ)$, and (d) $(x_1, 135^\circ)$. The points are synthetic slowness data without random scatter. The solid lines are slownesses calculated from the reconstructed elasticity constants.

$$(C''_{IJ}) = \begin{pmatrix} 12.24 \pm 0.02 & 5.4 \pm 0.2 & 6.2 \pm 0.2 & 0.27 \pm 0.07 & 0.43 \pm 0.02 & 0.28 \pm 0.02 \\ & 20.9 \pm 0.5 & 23.9 \pm 0.5 & 13.1 \pm 0.3 & 1.9 \pm 0.1 & 1.3 \pm 0.1 \\ & & 83.4 \pm 1.0 & 36.4 \pm 0.5 & 6.4 \pm 0.2 & 3.2 \pm 0.2 \\ & & & 25.4 \pm 0.3 & 3.5 \pm 0.1 & 2.2 \pm 0.1 \\ & \text{Sym.} & & & 5.9 \pm 0.1 & 1.43 \pm 0.03 \\ & & & & & 4.4 \pm 0.1 \end{pmatrix} \text{ (GPa)}, \quad (46)$$

are determined from these data collected in R and then related to R'' . The good agreement between the stiffness tensor, determined by the generalized reconstruction method [Eq. (46)] and the moduli [Eq. (45)], calculated from the nine elasticity constants determined in R , validates the experimental characterization of a general anisotropic medium. The smallest values of the confidence intervals validate *a posteriori* the choice of the data planes. Figure 15 shows the slowness surfaces calculated from the reconstructed moduli for each Christoffel equation's solution in velocity and the experimental measurements considered for characterization.

According to Fig. 11(c) where it can be seen that the slow quasitransverse mode has not been measured in the plane $(x_1, 75^\circ)$, note that only the data of the three other planes are represented on one of the calculated slowness surfaces [Fig. 15(c)]. The calculation of the $T(\theta_i)$ transmission coefficient from the 13 identified elasticity constants (C'_{IJ}) [Eq. (41)] shows that the range of the incident angle where the QT2 mode is generated in the plane $(x'_1, (45^\circ)')$ [$= (x_1, 75^\circ)$] is $[40^\circ, 50^\circ]$. This domain is not accessible with our experimental device.

V. SUMMARY

By using a constrained optimization method, the stiffnesses of materials that possess any class of symmetry (including the most general anisotropy) are extracted from the experimental velocities of ultrasonic waves obliquely incident from water onto a plate. Due to the accurate evaluation of the optimal descent direction, the inversion procedure is not affected by the selection of initial guesses and is very robust against scatter in the phase velocities. This approach does explicitly use the Christoffel equation and so does not require the recognition of polarization of all experimental data. The calculation of a confidence interval associated with each identified modulus allows one to recognize *a posteriori* which stiffnesses have been most accurately recovered and which less so.

The reconstruction algorithm is independent of the material anisotropy. Due to a possible weak anisotropy, *a priori* choice of a given symmetry class can sometimes be hazardous. Sensitivity of the stiffnesses determination for weak and strong anisotropies has been investigated using both numerical and experimental data in various materials with quasi-isotropic, quasi-hexagonal, quasi-tetragonal, orthorhombic, monoclinic, and triclinic symmetry. Clearly the difficulty of identification increases as the anisotropy decreases.

ACKNOWLEDGMENT

H. C. Aristégui is indebted to the Société Européenne de Propulsion for its partial financial support.

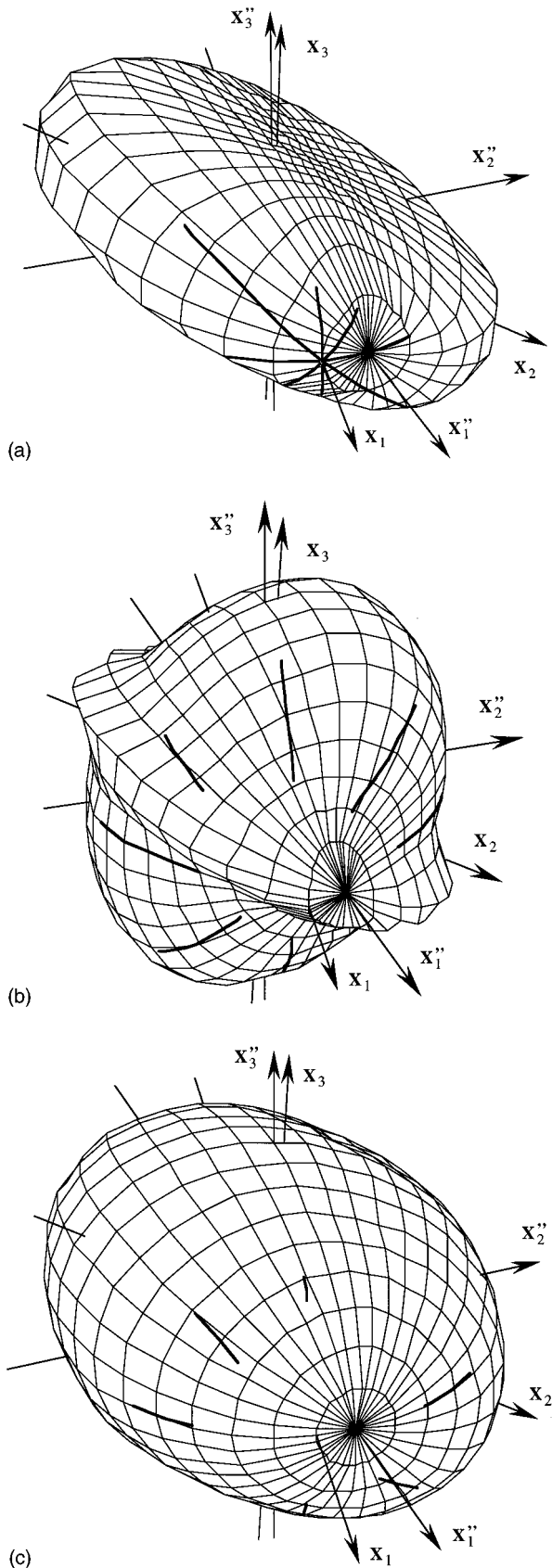


FIG. 15. Slowness surfaces for a unidirectional carbon epoxy composite in a nonprincipal coordinate system $R'' = (x_1'', x_2'', x_3'')$. The surfaces are calculated from the 21 reconstructed elasticity constants using Cardan's solutions: (a) $\alpha=1$, quasilongitudinal mode, (b) $\alpha=2$ and (c) $\alpha=3$ quasitransverse modes. The bold curves connect the experimental measurements collected in the principal coordinate system $R=(x_1, x_2, x_3)$ and reported in R'' .

¹M. F. Markham, "Measurement of the elastic constants of fibre composites by ultrasonics," *Composites* **1**, 145–149 (1970).

²R. E. Smith, "Ultrasonic elastic constants of carbon fibers and their composites," *J. Appl. Phys.* **43**, 2555–2561 (1972).

³B. Hosten, A. Barrot, and J. Roux, "Interférométrie numérique ultrasonore pour la détermination de la matrice de raideur des matériaux composites," *Acustica* **53**, 212–217 (1983).

⁴J. Roux, B. Hosten, B. Castagnède, and M. Deschamps, "Caractérisation mécanique des solides par spectro-interférométrie ultrasonore," *Rev. Phys. Appl.* **20**, 351–358 (1985).

⁵B. Hosten, M. Deschamps, and B. R. Tittmann, "Inhomogeneous wave generation and propagation in lossy anisotropic solids. Application to the characterization of viscoelastic composite materials," *J. Acoust. Soc. Am.* **82**, 1763–1770 (1987).

⁶B. Castagnède and W. Sachse, "Optimised determination of elastic constants of anisotropic solids from wavespeed measurements," in *Review of Progress in Quantitative Nondestructive Evaluation*, edited by D. O. Thompson and D. E. Chimenti (Plenum, New York, 1989), Vol. 8B, pp. 1855–1862.

⁷B. Castagnède, J. T. Jenkins, W. Sachse, and S. Baste, "Optimal determination of the elastic constants of composite materials from ultrasonic wavespeed measurements," *J. Appl. Phys.* **67**, 2753–2761 (1990).

⁸E. P. Papadakis, T. Patton, Y. M. Tsai, D. O. Thompson and R. B. Thompson, "The elastic moduli of a thick composite as measured by ultrasonic bulk wave pulse velocity," *J. Acoust. Soc. Am.* **89**, 2753–2757 (1991).

⁹S. C. Wood and I. M. Daniel, "Nondestructive determination of elastic constants of composite materials," in *Review of Progress in Quantitative Nondestructive Evaluation*, edited by D. O. Thompson and D. E. Chimenti (Plenum, New York, 1991), Vol. 10B, pp. 1445–1452.

¹⁰S. I. Rokhlin and W. Wang, "Ultrasonic evaluation of in-plane and out-of-plane elastic properties of composite materials," in *Review of Progress in Quantitative Nondestructive Evaluation*, edited by D. O. Thompson and D. E. Chimenti (Plenum, New York, 1989), Vol. 8B, pp. 1489–1496.

¹¹S. I. Rokhlin and W. Wang, "Double through-transmission bulk wave method for ultrasonic phase velocity measurement and determination of

- elastic constants of composite materials," J. Acoust. Soc. Am. **91**, 3303–3312 (1992).
- ¹² B. A. Auld, *Acoustic Fields and Waves in Solids* (Wiley–Interscience, New York, 1973).
- ¹³ A. G. Every and W. Sachse, "Sensitivity of inversion algorithms for recovering elastic constants of anisotropic solids from longitudinal wavespeed data," *Ultrasonics* **30**, 43–48 (1992).
- ¹⁴ Y. C. Chu and S. I. Rokhlin, "A method for determination of elastic constants of a unidirectional lamina from ultrasonic bulk velocity measurements on [0/90] cross-ply composites," J. Acoust. Soc. Am. **96**, 342–352 (1994).
- ¹⁵ S. I. Rokhlin and W. Wang, "Critical angle measurement of elastic constants in composite material," J. Acoust. Soc. Am. **86**, 1876–1882 (1989).
- ¹⁶ S. Baste and M. Deschamps, "Identification des constantes d'élasticité à partir des vitesses de propagation dans un plan principal de symétrie," C. R. Acad. Sci. Paris II **309**, 1521–1526 (1989).
- ¹⁷ S. Baste and B. Hosten, "Identification complète de la matrice de raideur par propagation hors plan principal," *Rev. Phys. Appl.* **25**, 161–168 (1990).
- ¹⁸ S. Baste and R. El Bouazzaoui, "Cracking orientation and induced anisotropy of a ceramic matrix composite under off-axis loading," J. Mater. Sci. **31**, 1575–1584 (1996).
- ¹⁹ J. R. Neighbours and G. E. Schacher, "Determination of elastic constants from sound-velocity measurements in crystals of general symmetry," J. Appl. Phys. **38**, 5366–5375 (1967).
- ²⁰ M. Hayes, "A simple statical approach to the measurement of the elastic constants in anisotropic media," J. Mater. Sci. **4**, 10–14 (1969).
- ²¹ W. C. Van Buskirk, S. C. Cowin, and R. Carter, Jr., "A theory of acoustic measurement of the elastic constants of a general anisotropic solid," J. Mater. Sci. **21**, 2749–2762 (1986).
- ²² A. N. Norris, "On the acoustic determination of the elastic moduli of anisotropic solids and acoustic conditions for the existence of symmetry planes," Q. J. Mech. Appl. Math. **42**, 412–426 (1989).
- ²³ J. J. Ditri, "On the determination of the elastic moduli of anisotropic media from limited acoustical data," J. Acoust. Soc. Am. **95**, 1761–1767 (1993).
- ²⁴ A. Gourdin and M. Boumahrat, *Méthodes numériques appliquées* (Lavoisier, Paris, 1983).
- ²⁵ R. A. Kline and S. K. Sahay, "Sensitivity analysis for elastic property reconstruction of anisotropic media," in *Review of Progress in Quantitative Nondestructive Evaluation*, edited by D. O. Thompson and D. E. Chimenti (Plenum, New York, 1992), Vol. 11B, pp. 1429–1435.
- ²⁶ Y. C. Chu and S. I. Rokhlin, "Stability of determination of composite moduli from velocity data in planes of symmetry for weak and strong anisotropies," J. Acoust. Soc. Am. **95**, 213–225 (1994).
- ²⁷ B. Audoin, S. Baste, and B. Castagnède, "Estimation de l'intervalle de confiance des constantes d'élasticité identifiées à partir des vitesses de propagation ultrasonores," C. R. Acad. Sci. Paris II **312**, 679–686 (1991).
- ²⁸ B. Audoin, "Evaluation ultrasonore de l'endommagement anisotrope d'un composite à matrice fragile," Ph.D. thesis, No. 620, Université Bordeaux I, 1991.
- ²⁹ B. Audoin and S. Baste, "Ultrasonic evaluation of stiffness tensor changes and associated anisotropic damage in a ceramic matrix composite," J. Appl. Mech. **61**, 309–316 (1994).
- ³⁰ Y. C. Chu and S. I. Rokhlin, "Comparative analysis of through-transmission ultrasonic bulk wave methods for phase velocity measurements in anisotropic materials," J. Acoust. Soc. Am. **95**, 3204–3212 (1994).
- ³¹ B. Audoin and J. Roux, "Traitement de signal ultrasonore adapté à l'évaluation non destructive de matériaux dispersifs," *Rev. Phys. Appl.* **25**, 1011–1017 (1990).
- ³² B. Audoin and J. Roux, "A innovative application of the Hilbert transform to time delay estimation of overlapped ultrasonic echoes," *Ultrasonics* **34**, 25–33 (1996).
- ³³ B. Hosten and B. Castagnède, "Optimisation du calcul des constantes élastiques à partir des mesures de vitesses d'une onde ultrasonore," C. R. Acad. Sci. Paris II **296**, 297–300 (1983).
- ³⁴ R. G. Payton, *Elastic wave propagation in transversely isotropic media* (Martinus Nijhoff, The Hague, 1983).
- ³⁵ M. Minoux, *Programmation mathématique Théorie et algorithmes* (Dunod, Paris, 1983).
- ³⁶ B. Hosten, "Elastic characterization of orthotropic composite materials from ultrasonic inspection through non-principal planes," in *Review of Progress in Quantitative Nondestructive Evaluation*, edited by D. O. Thompson and D. E. Chimenti (Plenum, New York, 1991), Vol. 10B, pp. 1437–1444.
- ³⁷ B. Hosten, "Stiffness matrix invariant to validate the characterization of composite materials with ultrasonic methods," *Ultrasonics* **30**, 365–371 (1992).
- ³⁸ Y. C. Chu and S. I. Rokhlin, "Determination of macro- and micromechanical and interfacial elastic properties of composites from ultrasonic data," J. Acoust. Soc. Am. **92**, 920–931 (1992).
- ³⁹ E. G. Henneke II, "Reflexion-refraction of a stress wave at a plane boundary between anisotropic media," J. Acoust. Soc. Am. **51**, 210–217 (1972).

Modal analysis of Lamb wave generation in elastic plates by liquid wedge transducers

X. Jia

Groupe de Physique des Solides, Universités Paris 7 et Paris 6, Tour 23, 2 place Jussieu, 75251 Paris Cedex 05, France

(Received 9 May 1996; accepted for publication 17 September 1996)

A modal analysis is presented to describe the excitation of Lamb waves in an elastic plate using a liquid wedge transducer. Analytical expression for the displacement of a given mode is derived for the excitation by a uniform bounded beam. In contrast to previous studies, the contribution of the reflected wave is included in the input exciting forces using a perturbation theory. The conversion efficiency, defined as the ratio of the guided mode power to the incident power, is related to a single parameter which depends on the rate of attenuation due to leakage from the guided wave into the liquid wedge. Numerical results relevant to the fundamental Lamb modes are obtained as a function of frequency for various incident beam widths and plate thickness. Using optical interferometric detection, direct measurements of the Lamb modes displacements have been carried out in aluminium plates to verify the theoretical analysis. © 1997 Acoustical Society of America. [S0001-4966(97)00402-5]

PACS numbers: 43.35.Pt, 43.35.Sx [HEB]

INTRODUCTION

Lamb waves propagating in an elastic plate have a great deal of interest for flaw detection and material characterization of layer structures.¹⁻⁶ Victorov¹ has reviewed in detail the use of Rayleigh and Lamb waves in nondestructive testing and monitoring applications. Also, in the past decade, there has been increasing interest in the fields of sensors that employ ultrasonic Lamb waves.⁷⁻⁹

Lamb waves can be excited and detected by a variety of methods. For signal processing applications, Lamb waves are generated by using interdigital electrodes on piezoelectric crystals or on piezoelectric films deposited on a nonpiezoelectric substrate.^{7,8} In nondestructive testing, the wedge method is probably the most well known in which a prism or wedge is employed to convert bulk waves into Lamb waves.¹ Other transduction techniques have also been reported in the literature, including optical methods,^{6,10,11} electromagnetic acoustic transducers (EMATs),¹² capacitance transducers, and air-coupled transducers.¹³ The major advantage of the noncontact techniques lies in the elimination of the coupling materials, which is undesirable or impossible in applications such as the testing of hot metals, or structures where the surface contamination produced by a coupling fluid cannot be tolerated. Recent work using lasers for both generation and detection is potentially very attractive.^{14,15} This laser ultrasonic technique has the advantage of being noncontact and scanned easily and rapidly over the surface of an object, though the required equipment is bulky and expensive and has mainly been used in the laboratory rather than in industrial testing applications. At present, in the majority of standard ultrasonic testing, piezoelectric transducers remain the most utilized for guided wave excitations, since the manufacture and use of these transducers are well understood and they are readily available.

Theoretical treatments of the excitation of Lamb and other guided waves have been reported extensively in the

literature by Victorov,¹ Miklowitz,¹⁶ Achenbach,¹⁷ and others.^{18,19} In most of these theoretical studies, the problem is generally resolved as a function of input force using integral transform techniques. For transient excitation problems, the solutions are derived by first applying the Laplace transform with respect to time and the exponential Fourier or Hankel transform with respect to space. The inverse transformation integrals are then carried out by the evaluation of residues via the method of stationary phase or by the method of generalized rays. As can be found in the literature (see Ref. 16; for example), the evaluation of these integrals in the first approach involves the understanding of the intricate behavior of the dispersion relations for real as well as complex wave numbers. The theory of generalized rays is an exact method involving dynamic Green's functions. It quickly becomes computationally intense as the number of ray paths from source to receiver becomes large. Furthermore, explicit expressions of the input forces are generally required in these formalisms for deriving displacement fields. However, this information is not always known *a priori* in practice. In the wedge method, for example, the input forces shall depend not only the incident wave but also the reflected one. This reflected wave is theoretically coupled to guided waves which are to be determined. Victorov¹ has calculated the displacement field of Lamb waves excited by a uniform bounded longitudinal beam, using the Fourier transform technique. In his analysis, the input force contributing to the wave reflection and radiation was neglected.

Normal-mode analysis offers an alternative approach for treating the problem of waveguide excitation. This approach, particularly practical and readily usable for descriptions in the far field, is widely used in electromagnetism²⁰ and acoustics.^{21,22} The principle of the mode theory is to express the excited field as the sum of normal modes obtained in a stress-free waveguide. The contribution of each mode to the resulted fields is determined in terms of the associated power

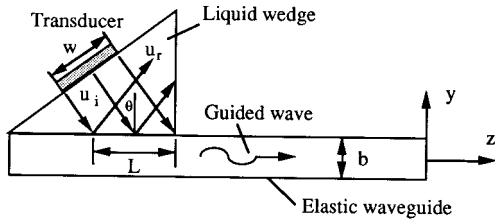


FIG. 1. Schematic diagram of Lamb wave excitation by the wedge method.

flow using the orthogonality condition of eigenmodes. Mode theory has been successfully applied to study the excitation by the wedge method of nondispersive surface waves such as Rayleigh^{23,24} and Stoneley modes.²⁵ Such an approach concerning the Lamb wave excitation was also reported recently, in which particular attention was focused on the angular dependence of the excitation amplitude of a given mode in the neighborhood of the Snell's law angle. Like Victorov's analysis, the influence of the wave reflection and radiation was again not considered in that work.²⁶

The purpose of this paper is to present a modal analysis of the Lamb wave excitation by a liquid wedge, which takes into account the effects of wave reflection and radiation. Special attention will be concentrated on the excited displacement and conversion efficiency of a given mode as a function of the parameters of the wedge transducer and the plate waveguide. Quantitative measurements of the displacement fields using optical interferometric detection will be used to verify the theoretical prediction.

I. THEORY

In this section, we shall first describe briefly the general treatment of waveguide excitation using the mode theory. Then we will examine the input force loading introduced by the wedge coupling before developing the numerical computation for the specific case of Lamb modes.

A. General formulation of the mode theory for waveguide excitation problem

Consider a waveguide in layered geometry as shown in Fig. 1, for example, where the field quantities such as particle displacement \mathbf{u} and stress \mathbf{T} are assumed to be independent of the x coordinate. The resulting fields in a perturbed waveguide can be expressed by the mode expansion:

$$\mathbf{u}(y, z) = \sum_n a_n(z) \mathbf{u}_n(y), \quad (1a)$$

$$\mathbf{T}(y, z) = \sum_n a_n(z) \mathbf{T}_n(y), \quad (1b)$$

where n denotes the n th eigenmode of a stress-free waveguide and a_n is the mode amplitude. For the observation at a distance far from the source only the propagating mode is significant. To determine the amplitude coefficient of each mode $a_n(z)$, we make use of the reciprocity relation and the orthogonality condition of eigenmodes, which leads to the equation governing a mode amplitude of the excited mode,^{21,22}

$$\left(\frac{d}{dz} + ik_n \right) a_n(z) = \frac{f_n(z)}{4P_n}, \quad (2)$$

where k_n is real representing the wave number of the n th propagating mode, P_n is the associated average power flow per unit width along the x direction,

$$P_n = \frac{i\omega}{4} \int_{-b/2}^{b/2} (-\mathbf{u}_n^* \cdot \mathbf{T}_n - \mathbf{u}_n \cdot \mathbf{T}_n^*) \cdot \mathbf{e}_z dy, \quad (3)$$

b being the thickness of the layer (e.g., elastic plate) and \mathbf{e}_z the unit vector along the z direction. Here f_n is the input loading applied across the layer,

$$f_n(z) = i\omega \int_{-b/2}^{b/2} \mathbf{u}_n^*(y) \cdot \mathbf{F}(y, z) dy. \quad (4)$$

B. Excitation of guided modes by a liquid wedge

The principle of the wedge method can be understood by a mode conversion process shown in Fig. 1. When a plane wave is incident on the guide at the angle defined by the Snell law $\sin \theta_n = c_0/v_n$, where c_0 is the sound velocity in the liquid wedge and v_n is the phase velocity of a guided mode, a part of the wave is reflected directly and the rest is to excite the given mode in the layer. In practice, the width of the incident beam is not infinite but several times larger than the acoustic wavelength. Generally speaking, the wider the wave beam is, the narrower the angular range allowed for exciting the given wave.^{1,26} The distribution of the exciting forces resulting from both the incident and reflected waves are located on the surface of the guide ($y=b/2$) within a length L under the wedge transducer along the z axis and with a width d along the x axis. As a result, the input force function of Eq. (4) takes the form

$$f_n(z) = i\omega [\mathbf{u}_n^*(y) \cdot \mathbf{T}(y, z) \cdot \mathbf{e}_y]_{y=b/2}. \quad (5)$$

In the case where the wedge is a nonviscous liquid, only normal stress T_{yy} is transferred onto the surface of the guide. Assuming the particle displacements u_i and u_r associated with incident and reflected waves, respectively, the boundary conditions to be satisfied at the surface, $y=b/2$, can be written as

$$(-u_i + u_r) \cos \theta_n = a_n u_{ny}(y=b/2) \quad (6a)$$

for the normal component of the particle displacement and

$$T_{yy}(y=b/2, z) = -i\omega Z_0(u_i + u_r) \quad (6b)$$

for the normal stress. Here Z_0 is the acoustic impedance of the liquid. The expression of the second member $u_y = a_n u_{ny}$ given in Eq. (6a) implies two assumptions. The first is that only the n th guided mode is excited by the incident wave. This situation is generally desirable in practice and can often be realized by choosing the incident angle according to the Snell's law and mode separation in the time domain (see also the discussion in the following section). Also the displacement associated with the excited mode given in Eq. (6a), when the liquid wedge is present, is assumed to be the same as that in the stress-free condition. This approximation is based on the approach of perturbation theory and is reasonable in most practical cases where the liquid density is much

smaller than that of the elastic waveguide.^{21,22}

By the use of the boundary conditions of Eqs. (6), the substitution of T_{yy} ($y=b/2, z$) into Eq. (2) leads to the mode amplitude equation written as

$$\left[\frac{d}{dz} + ik_n + \alpha_n \right] a_n(z) = - \frac{d\omega^2 Z_0 u_{ny}^*(b/2) u_i}{2P_n}, \quad (7)$$

where α_n is the attenuation per unit length of the guided wave in the presence of the liquid wedge and is given by

$$\alpha_n = d\omega^2 Z_0 |u_{ny}(b/2)|^2 / (4P_n \cos \theta_n). \quad (8)$$

This attenuation physically stems from the energy leakage of the guided mode into the surrounding liquid during its propagation along the interface liquid–solid. If the second member is zero corresponding to the case where the incident wave is absent, Eq. (7) becomes homogeneous and the amplitude of $a_n(z)$ is proportional to $\exp(-\alpha_n z)$, which represents clearly a leaky mode traveling along the waveguide. According to Eq. (8), the greater the normal component of the excited mode, the greater the energy radiation into the liquid. The second member in Eq. (7) can be considered as an input force term due to the excitation by the incident wave. Like the attenuation coefficient α , this input force provided by the incident wave is also proportional to the normal component of the mode to be excited. This is because of the mechanical coupling via the normal stress between the incident (and radiated) wave and the waveguide.

Let us now find out the solution of the amplitude equation (7) when the incident beam is uniform and parallel. As shown in Fig. 1, the incident wave u_i is assumed constant and bounded between $z=0$ and $L=w/\cos \theta_n$ along the waveguide. The incident angle is chosen to verify Snell's law $k_n = k_0 \sin \theta_n$, exciting the given mode cumulatively. The solution of the inhomogeneous equation (7) is the superposition of that of the homogeneous equation and a particular one. With the initial condition $a_n=0$ at $z=0$, the amplitude of the excited mode in the presence of the liquid wedge can be readily found as

$$a_n(z) = -a_i \exp(-ik_n z) [1 - \exp(-\alpha_n z)] (2/\alpha_n P_n)^{1/2}, \quad (9)$$

where $a_i = i\omega U_i (dZ_0 \cos \theta_n / 2)^{1/2}$ and U_i is the displacement amplitude of the incident wave. The amplitude of the excited mode leaving the liquid wedge is thus equal to the value of a_n taken at $z=L$. This amplitude will be constant during its propagation if lateral wave diffraction and material absorption are neglected. Substituting α_n of Eq. (8) into Eq. (9) yields the amplitude of the surface displacement of the excited mode $U_{ny} = a_n u_{ny}$ ($y=b/2$), when normalized to the particle displacement U_i of the incident wave, as

$$U_{ny}/U_i = -2 \cos \theta_n [1 - \exp(-\alpha_n L)]. \quad (10)$$

This relationship is practical and can be easily verified by the experiment (see the next section). Equation (10) shows that the amplitude of the excited mode strongly depends on the parameter $h_n = \alpha_n L$, related to the wave leakage into the liquid in a reverse process to the excitation by an incident wave. It is noted that the displacement of the excited mode increases rapidly with $(\alpha_n L)$ and then remains nearly con-

stant. Such ‘‘saturation’’ regions, already observed in the previous experiment (Fig. 41 of Ref. 1), confirm well this prediction. It implies that beyond certain values of L , the supplement of the incident power is totally utilized to balance the radiation into the liquid. To the contrary, without the inclusion of the reflected field ($u_r=0$) and consequently the leaky loss ($\alpha_n=0$), the surface displacement of the excited mode resolved from the mode amplitude equation, for $z=L$, is found as

$$U_{ny} = -U_i [d\omega^2 Z_0 |u_{ny}(b/2)|^2 / 4P_n] L, \quad (11)$$

which is, except for notation, identical to the results given by previous theories.^{1,26} Unlike Eq. (10), formula (11) predicts a linear dependence of the excited displacement on the width of the incident beam L . This divergent result, when increasing L , does not obviously agree with the experimental observation mentioned above. Moreover, the inclusion of the reflected field provides also the possibility to study²⁷ the nonspecular reflection phenomena, occurring when a bounded wave is incident on a layer at critical angles $\theta_n = \arcsin(c_0/v_n)$.²⁸

To determine the performance of the wedge transducer it is necessary to calculate the efficiency function η_n , defined as the ratio of excited mode power to incident power and given by^{23,24}

$$\eta_n = 2[1 - \exp(-\alpha_n L)]^{1/2} / (\alpha_n L). \quad (12)$$

Thus the conversion efficiency is expressed in terms of a single parameter $h_n = \alpha_n L$, attaining a maximum value of 82% at $h=1.3$. In this specific waveguide where the surface wave is nondispersive $v_n = v_R$ (constant),^{23,24} the efficiency η_R as a function of $h_R = \alpha_R L$ represents nothing else than efficiency vs frequency plot because the leak rate of the Rayleigh wave α_R is proportional to frequency.²¹ As will be seen in the following section, the situation becomes much more complicated in other waveguides such as an elastic plate where multiple and dispersive modes coexist. As a result, the efficiency depends not only on frequency but also on geometry parameters of the waveguide and the transducer. Numerical calculations are often necessary to determine these material and geometry parameters required for optimum efficiency.

C. Numerical computation of Lamb waves excited in a plate waveguide

Lamb waves are the eigenmodes propagating in an elastic plate with stress-free boundary conditions $T_{22} = T_{12} = 0$ at the two surfaces $y = \pm b/2$ (Fig. 1). Associated particle displacements are located in the sagittal plane formed by the direction of propagation and the axis normal to the plate plane. According to the symmetry of particle displacements with respect to the middle plane of the plate, the Lamb waves can be classified either as symmetric modes or as antisymmetric modes. Figure 2 displays the plots of phase velocity versus product fb (frequency \times plate thickness) for the first few Lamb modes in an aluminium plate. Since the phase velocities are generally frequency dependent, the Lamb modes are dispersive. Among multiple Lamb modes, the lowest symmetric S_0 and antisymmetric A_0 Lamb modes

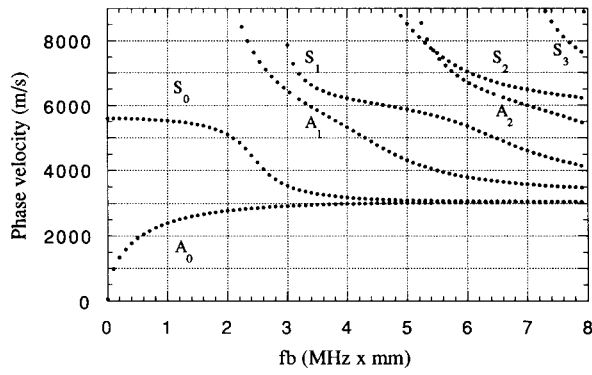


FIG. 2. Phase velocities of Lamb modes versus fb (product frequency-thickness) in an aluminium plate ($v_l=6290$ m/s and $v_s=3280$ m/s).

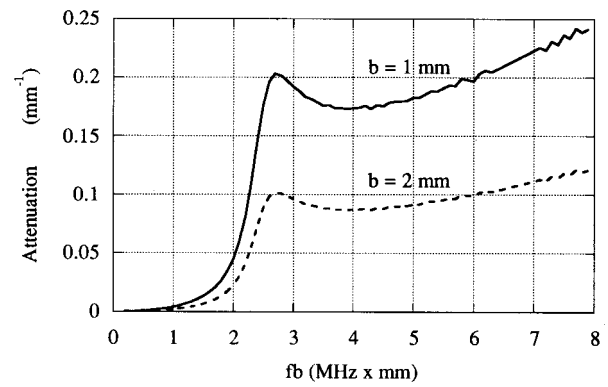
are of particular interest. They are qualitatively different from all other modes and can exist for any value of fb , whereas other high-order modes have cutoff frequencies. In the limit of $fb \gg 1$, both the S_0 and A_0 modes become asymptotic and approach to the velocity of Rayleigh wave.

Exciting a Lamb mode by the wedge method is to select the incident angle verifying the Snell law $\sin \theta_n = c_0/v_n$. The corresponding Lamb angles θ_n can be determined from the phase velocity shown in Fig. 2 as a function of the product fb . As mentioned in the preceding section, the mode amplitude as well as the efficiency function depend strongly on the leak rate of α_n into the liquid wedge [Eqs. (10) and (12)]. To determine α_n it is necessary, according to Eq. (8), to calculate the normal component of displacement at the plate surface normalized to $\sqrt{P_n}$. The power flow P_n defined by Eq. (3) is expressed in terms of stress and displacements, which can also be determined from the energy density and the group velocity V_g . For the n th guided mode, the average power flow takes the form^{17,21}

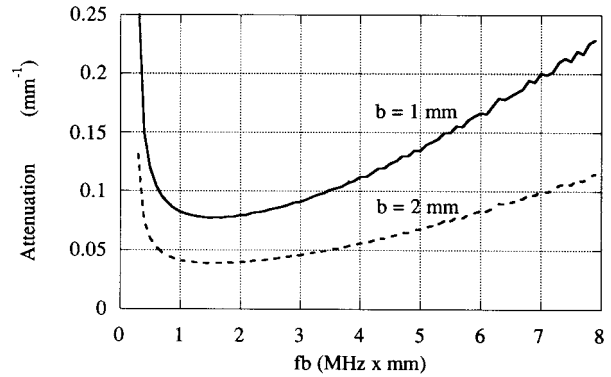
$$P_n = \frac{1}{2} \rho \omega^2 (V_g)_n \int_{-b/2}^{b/2} (|u_{ny}|^2 + |u_{nz}|^2) dy, \quad (13)$$

which avoids laborious calculations of the stress field required in Eq. (3). Using Eq. (13), it is possible to calculate α_n from the particle displacement of the given mode alone.

Figure 3(a) and (b) shows the attenuation curves α versus the product fb for the two fundamental S_0 and A_0 modes for two different thicknesses b . It is found that, for a given value of fb , the leak rate α is inversely proportional to the plate thickness. Similar curves were presented previously by Merkulov,²⁹ who has resolved mathematically the characteristic equation, in a first-order approximation, of a plate immersed in a surrounding liquid. In comparison with that work, the present analysis has the advantage of giving a physical feel to the phenomena and establishing explicitly the relationship between the attenuation due to the wave radiation and the normal component of the displacement normalized to the power flow. It is seen in Fig. 3(a) that α starts from zero with the frequency, reaches a maximum value at $fb \approx 2.6$ MHz \times mm, and increases asymptotically with f^2 when fb tends to infinity. In the limit as $fb \rightarrow 0$, the symmetrical mode S_0 behaves basically as a longitudinal wave with the displacement parallel to the plate surface, which



(a)

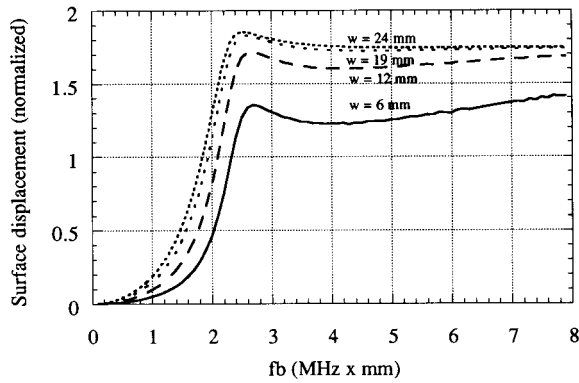


(b)

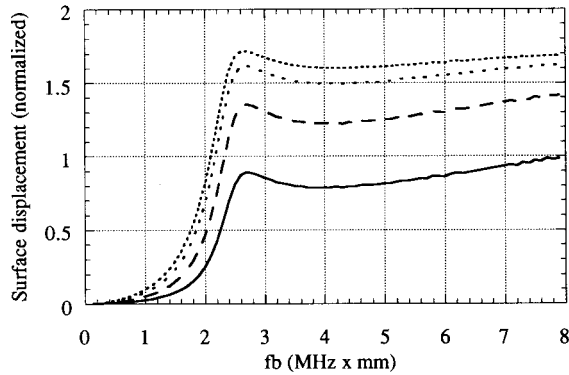
FIG. 3. Attenuation coefficients of Lamb modes S_0 (a) and A_0 (b) for two different thickness of plate $b=1$ and 2 mm, immersed in water.

explains the weak wave radiation (i.e., attenuation). When the frequency or the plate thickness becomes great ($fb \gg 1$), the S_0 mode is essentially concentrated at the surfaces of the plate. The radiation behavior into the surrounding liquid is thus the same as the Rayleigh wave which is proportional to f^2 .²¹ As shown in Fig. 3(b), the antisymmetrical A_0 mode behaves in the same way as the mode S_0 in the limit as $fb \rightarrow \infty$. To the contrary, the A_0 mode has an important radiation (and attenuation) in the low fb limit, caused by its flexural motion normal to the plate surface. The cutoff of the attenuation curves at $fb \approx 0.22$ MHz \times mm is because the phase velocities of the A_0 mode below this limit are smaller than the sound velocity in the wedge liquid. As a result, no radiation of guided waves is allowed by the Snell law.

Now we search for the amplitudes of Lamb modes excited by the wedge method. By making use of the dispersion and attenuation results illustrated in Figs. 2 and 3, we carried out the numerical calculations directly from Eq. (10). Figure 4(a) and (b) show the surface displacements versus the product fb for the symmetrical S_0 mode excited in plates of thickness $b=1$ and 2 mm, respectively, by the wedge transducers of different sizes. As expected, the S_0 mode is hardly excited at the low-frequency limit because of the lack of the normal component of displacement coupling with the incident wave. After undergoing a rapid increase with the frequency, the amplitude of the S_0 mode attains a maximum value and remains rather constant over a wide frequency range. The displacements excited by the same transducers of



(a)

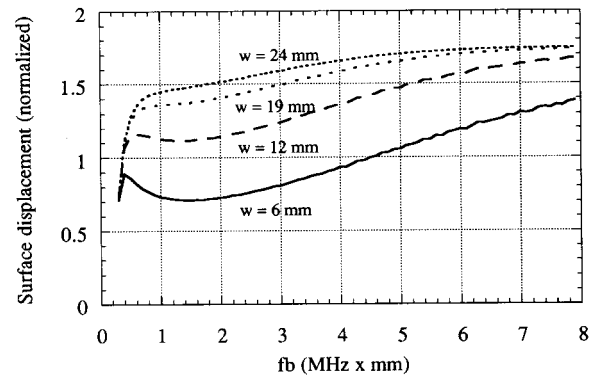


(b)

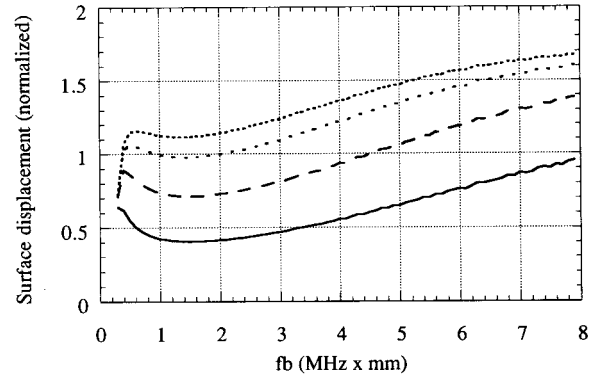
FIG. 4. Normalized surface displacement of S_0 mode in a 1-mm (a) and 2-mm (b) thick plates, excited by different sizes w of transducer.

the antisymmetrical A_0 mode are shown in Fig. 5. Compared to the S_0 mode, there is no abrupt variation although the amplitude of the A_0 mode increases a little with the frequency. For a given value of fb , the excited displacements of both the S_0 and A_0 modes are function of the plate thickness b . Besides, it is seen in Figs. 4 and 5 that the amplitude of the excited displacement increases, for a given frequency, with the size w of the transducer, i.e., the width of the incident beam. One possible explanation is that the Lamb waves are excited by an incident beam verifying the Snell's law. As the source is coherent, the larger the excitation zone, the greater the amplitude of the excited mode.

For a given amplitude of the incident wave U_i , increasing the beam width w implies an increase in the power supplied to the transducer. To appreciate the performance of a wedge transducer, it is useful to calculate its conversion efficiency η . Figures 6 and 7 present the efficiency functions obtained from Eq. (12) for the S_0 and A_0 modes, respectively. Maximum efficiencies of about 80% are attainable. In contrast to the Rayleigh wave where an ideal size of transducer $L = 1.3/\alpha_R(f)$ exists at a given frequency for a maximum efficiency, the conditions required for optimum efficiency of Lamb waves are not so simple to determine. Indeed, the efficiency functions depend not only on frequency and transducer size, but also on the plate thickness and type of the modes to be excited.



(a)

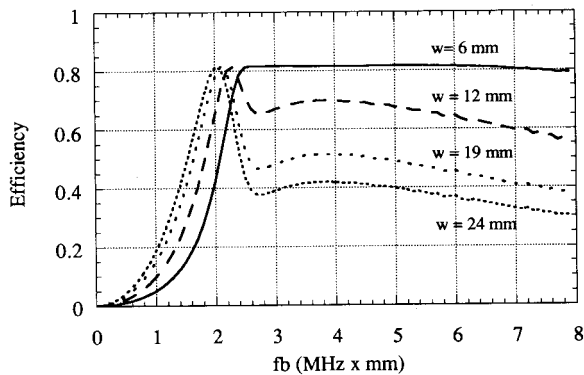


(b)

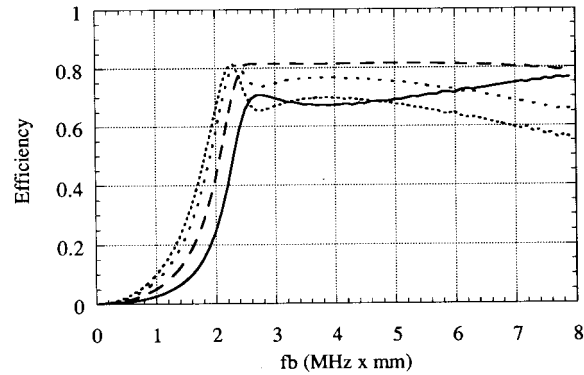
FIG. 5. Normalized surface displacement of A_0 mode in a 1-mm (a) and 2-mm (b) thick plates, excited by different sizes w of transducer.

II. EXPERIMENTS

To verify the above modal analysis of the Lamb excitation, we have made use of an experimental setup shown in Fig. 8. The wedge transducer is realized with a piezoelectric transducer immersed in a distilled water tank, which is in contact with an aluminum plate at the bottom across a thin plastic film ($\leq 10 \mu\text{m}$). The transducer is aligned so that the emitted beam strikes the boundary separating the water-loaded and the stress-free parts of the plate. The excited Lamb waves after leaving the liquid wedge propagate along a stress-free plate where the energy leakage into air is negligible. For a given incident beam, the normal displacement of the excited Lamb waves is detected at the polished plate surface using an optical heterodyne interferometer.³⁰ This displacement interferometer having a sensitivity of $10^{-4} \text{ \AA}/\sqrt{\text{Hz}}$ is calibrated to $10 \text{ mV}/\text{\AA}$. Detailed description of optical displacement or velocity interferometers operating at a reflecting or scattering surfaces can be found elsewhere.¹⁵ As described below, the amplitude of the incident beam is also determined optically using an original interferometric method. The ratio of the excited displacement amplitude to the incident one will then permit a direct comparison with the theoretical value computed from Eq. (12). In previous experiments, the efficiency function²⁴ and the excited mode amplitude³¹ were determined by measuring the round-trip insertion loss of the guided wave reflected from the edge of the waveguide. The present optical method presents an advan-



(a)



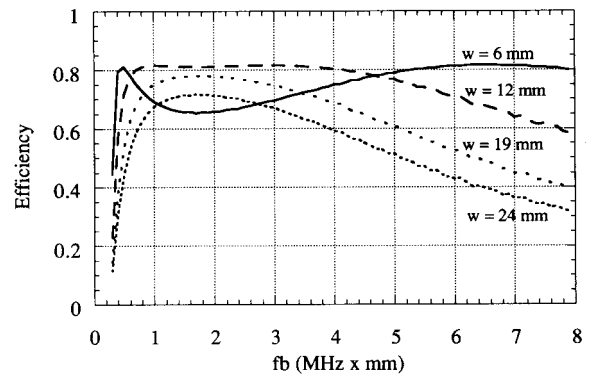
(b)

FIG. 6. Efficiencies for different sizes of transducer of generating the mode S_0 in 1-mm (a) and 2-mm (b) thick aluminium plates, respectively.

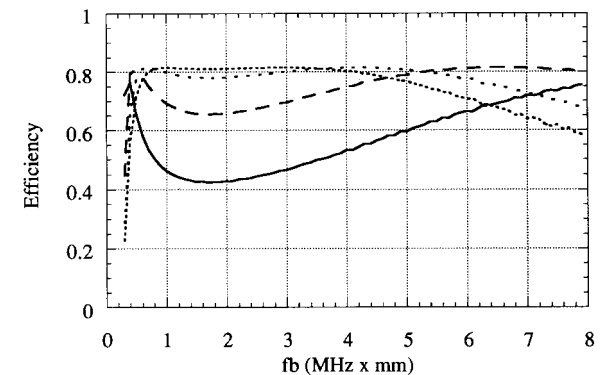
tage in being more direct and quantitative, avoiding the complicated process of mode conversion which may be encountered at the end of a plate waveguide.¹¹

A. Determination of the incident wave amplitude

In the preceding section, the displacement of the excited Lamb mode is calculated as function of the incident wave. To compare with the theory, we need to determine experimentally the displacement amplitude associated with the incident wave striking the plate via liquid wedge. For doing this, an acousto-optic method combined with heterodyning detection was employed. This method, recently developed by the authors,³²⁻³⁴ allows the acoustic pressure or dilatation to be measured inside a transparent medium. As shown by the schematic diagram in Fig. 9(a), a laser probe beam crossing normally an acoustic wave undergoes an optical phase shift due to the acousto-optic effect, $\Delta\phi(t) = (2\pi\mu/\lambda)p(t)d$. Here μ is the photoelastic constant of fluid media, $p(t)$ is the acoustic pressure, and d is the length of the acoustic beam. This probe beam is then mixed with a reference beam issuing from the same laser source. The signal resulting from the interference at the photodetector level will be $i(t) = (I_0/2) \cos[\omega_B t + \Delta\phi(t)]$, where I_0 is the laser intensity of the source and ω_B is the frequency shift of either the reference or probe beam produced by an acousto-optic modulator (heterodyning). This phase shift proportional to the acoustic pressure can be demodulated by a broadband electronic processing similar to that for displacement



(a)



(b)

FIG. 7. Efficiencies for different sizes of transducer of generating the mode A_0 in 1-mm (a) and 2-mm (b) thick aluminium plates, respectively.

measurement.³⁰ Figure 9(b) shows a typical pressure toneburst of an incident beam, emitted by a Panametrics transducer of nominal diameter of 12 mm. It is driven at 2 MHz by HP 8116A generator through an ENI A150 amplifier. The measured amplitude of pressure was 2.7 ± 0.15 atm. The corresponding particle displacement can be deduced readily by the relationship $u = p/(\omega Z_0)$, where Z_0 is the acoustic impedance of water and ω is the incident angular frequency. For example, the mean amplitude of the particle displacement deduced from the pressure shown in Fig. 9(b) is 14 nm.

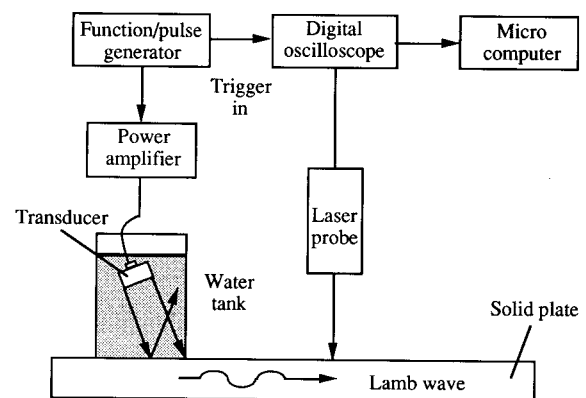


FIG. 8. Experimental arrangement for generating and detecting the Lamb waves in a plate.

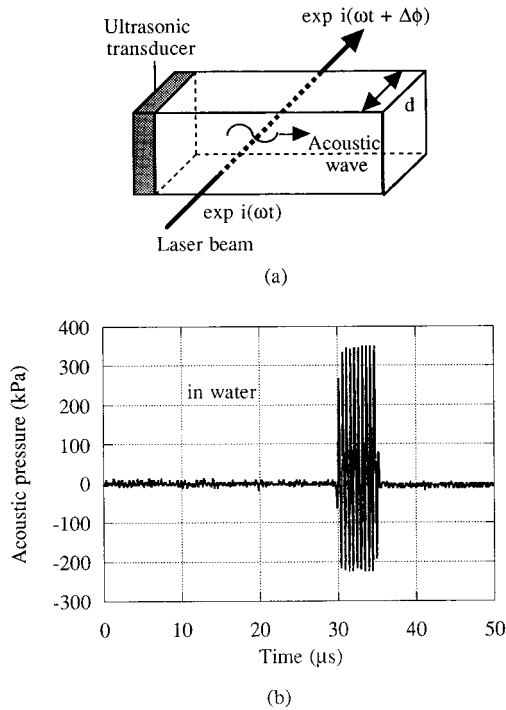


FIG. 9. (a) Schematic diagram of ultrasonic pressure detected by optical method; (b) longitudinal wave used to excite the Lamb modes through the water wedge is measured by an optical interferometric method.

B. Measurements of Lamb modes

A ten-cycle toneburst of longitudinal wave shown in Fig. 9(b) was used to excite Lamb modes in 1-mm-thick aluminum plate, placed in the far field of the transducer. In this work, our attention was focused on the observation of the two fundamental Lamb modes S_0 and A_0 . In order to ease the interpretation of the received signal, the frequency of the toneburst varied so as to give a product of fb (frequency thickness) from 1–3 MHz \times mm. In these regions of fb , only the fundamental S_0 and A_0 modes are dominant and propagate with different phase velocities. According to Snell's law $\sin \theta_n = c_0/v_n$, the two modes can be excited separately with different incident angles. When the frequency increases, the phase velocities of the S_0 and A_0 modes approach each other and the two modes can be excited at a given angle ($\theta \approx 30^\circ$) due to the beam spreading of incident wave. It was not a problem in our experiment to isolate the mode of interest from the rest of the received signal, since the corresponding group velocities are different, causing mode separation in the time domain. In the present case where the incident beam is large compared to the wavelength, the maximum amplitude of a given Lamb mode is achieved when the incident angle is chosen according to the Snell's law.^{1,26} Varying the incident angle θ as function of fb allows us to generate Lamb modes with different wavelength as shown in Fig. 2.

Typical displacement waveforms measured by optical interferometer of the Lamb modes S_0 and A_0 are displayed in Fig. 10. They were generated with a center frequency thickness of $fb = 2$ MHz \times mm at an incident angle of 19° and 34° , respectively. The phase velocities deduced from Snell's law, with sound velocity $c_0 = 1500$ m/s in water, were 4600 and

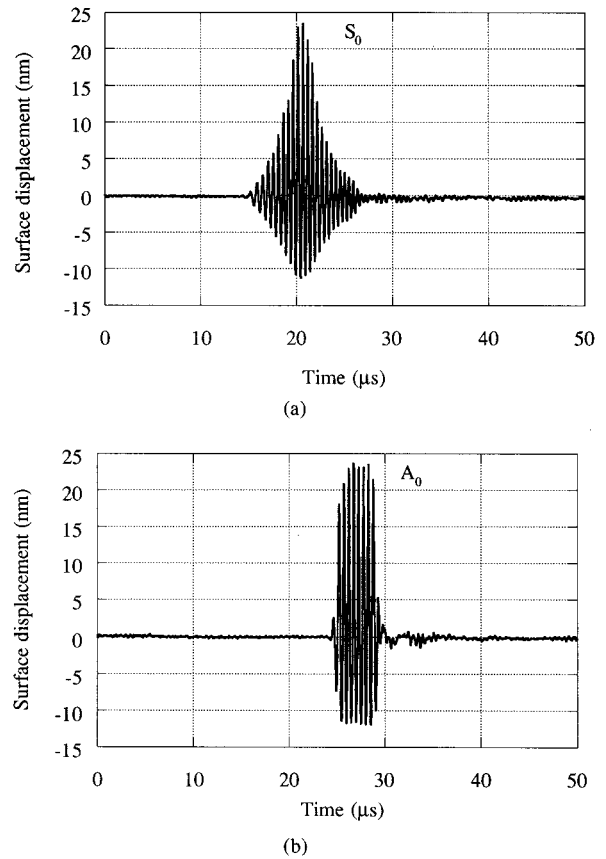


FIG. 10. Typical displacement waveforms of the excited Lamb modes S_0 (a) and A_0 (b) in a 1-mm-thick aluminium plate.

2680 m/s, corresponding well to those predicted by the theoretical dispersion curves (Fig. 2). Unlike mode A_0 , the waveform of mode S_0 was distorted in comparison with that of the incident wave. This distortion arose probably from the rapid variation of its displacement response at this frequency range [Fig. 4(a)]. The peak-to-peak amplitudes of the S_0 and A_0 modes were measured for different frequency of excitation. The frequency increment in each case was 0.1 MHz. Figure 11 shows the measured amplitudes normalized to the incident wave versus the product fb , along with the theoretical curves. Overall, there is a qualitative agreement between theory and experiment both for order and frequency dependence. Several observations can be made concerning the discrepancy between the theoretical and the experimental results. First, as in the previous studies,^{23,24,26} two-dimensional striplike sources were assumed in the present theory whereas the transducer used in the experiment was of circular nature. Second, the theoretical assumption of a uniform incident beam was different from the practical one generally in Gaussian form.³¹ Also the beam spreading effects neglected in the theory but present in the experiment can induce error for determining effective incident beam (transducer) size.

III. CONCLUSION

A modal analysis is developed for determining the amplitudes of Lamb waves generated by a parallel and uniform incident longitudinal wave. Using a perturbation theory, the reflected wave contribution as well as the Lamb wave leak-

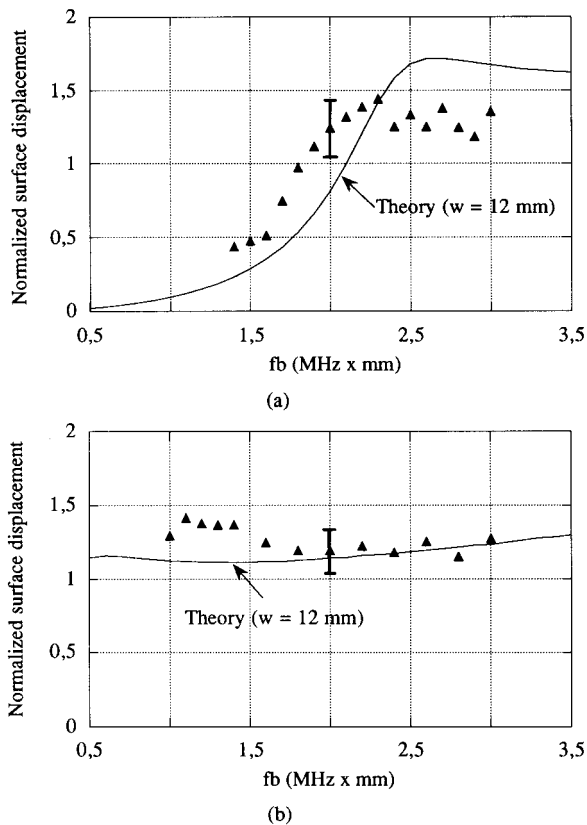


FIG. 11. Comparison between the theoretically predicted and experimental obtained (triangle dots) surface displacements for the modes S_0 (a) and A_0 (b). Experimental uncertainties are indicated by typical error bars.

age have been accounted for in the theory to give an analytical expression of the excited displacement. Numerical calculations have been performed for the two fundamental Lamb modes S_0 and A_0 propagating in 1- and 2-mm-thick aluminum plates, respectively. The theoretical results showed that, in addition to the thickness of the plate, the excited Lamb wave displacements and the efficiency function depend on the frequency and also the width of the incident beam. Owing to the optical interferometric method, the normalized surface displacement of excited S_0 and A_0 modes have been measured in a 1-mm-thick aluminum plate. These preliminary results confirmed quite well the theoretical prediction. In future work, we will improve the present theory by considering an inhomogeneous such as Gaussian incident beam and conduct the experiments with well-defined acoustic beams emitted by striplike (two-dimensional) transducers.

ACKNOWLEDGMENTS

The author is grateful to Professors B. Auld and G. Quentin for the helpful discussions and also thanks the reviewers for the critical reading of the manuscript.

- ¹I. A. Victorov, *Rayleigh and Lamb Waves* (Plenum, New York, 1967).
- ²S. I. Rokhlin, "Lamb wave interaction with lap-shear adhesive joint: Theory and experiment," *J. Acoust. Soc. Am.* **89**, 2758–2765 (1991).
- ³D. N. Alleyne and P. Cawley, "The interaction of Lamb waves with defects," *IEEE Trans. Ultrason. Ferroelectr. Freq. Control* **UFFC-39**, 381–397 (1992).
- ⁴A. H. Nayfeh and D. E. Chimenti, "Propagation of guided waves in

- fluid-coupled plates of fiber-reinforced composites," *J. Acoust. Soc. Am.* **83**, 1736–1743 (1988).
- ⁵V. Dayal and V. K. Kinra, "Leaky Lamb waves in an anisotropic plate. I: An exact solution and experiments," *J. Acoust. Soc. Am.* **85**, 2268–2276 (1989).
- ⁶D. A. Hutchins and K. Lundgren, "A laser study of transient Lamb waves in thin materials," *J. Acoust. Soc. Am.* **85**, 1441–1448 (1989).
- ⁷S. W. Wenzel and R. M. White, "A multisensor employing an ultrasonic Lamb wave oscillator," *IEEE Trans. Electron Devices* **ED-35**, 735–743 (1988).
- ⁸Y. Jin and S. G. Joshi, "Coupling of interdigital transducer to ultrasonic Lamb waves," *Appl. Phys. Lett.* **58**, 1830–1832 (1991).
- ⁹E. Dieulesaint, D. Royer, O. Legras, and A. Chaabi, "Acoustic plate mode touch screen," *Electron. Lett.* **27**, 49–51 (1991).
- ¹⁰R. J. Dewhurst, C. Edwards, A. D. W. McKie, and S. B. Plamer, "Estimation of the thickness of thin metal sheet using laser generated ultrasound," *Appl. Phys. Lett.* **51**, 1066–1068 (1987).
- ¹¹C. F. Ying, "Photoelastic visualization and theoretical analyses of scattering of ultrasonic pulses in solids," in *Physical Acoustics*, edited by R. N. Thurston (Academic, New York, 1990), Vol. 19, Chap. 7.
- ¹²R. B. Thompson, G. A. Alers, and M. A. Tennison, "Application of direct electromagnetic Lamb wave generation to gas pipeline inspection," in *Proceedings of IEEE Ultrasonics Symposium* (IEEE, New York, 1972), pp. 91–94.
- ¹³W. M. D. Wright, D. W. Schindel, and D. W. Hutchins, "Studies of laser-generated ultrasound using a micromachined silicon electrostatic transducer in air," *J. Acoust. Soc. Am.* **95**, 2567–2575 (1994).
- ¹⁴D. A. Hutchins, "Ultrasonic generation by pulsed lasers," in *Physical Acoustics*, edited by W. P. Mason and R. N. Thurston (Academic, New York, 1988), Vol. 18, Chap. 1.
- ¹⁵C. B. Scruby and L. E. Drain, *Laser Ultrasonics—Techniques and Applications* (Hilger, Bristol, 1990).
- ¹⁶J. Miklowitz, *The Theory of Elastic Waves and Waveguides* (North-Holland, Amsterdam, 1978).
- ¹⁷J. D. Achenbach, *Wave Propagation in Elastic Solids* (North-Holland, Amsterdam, 1973).
- ¹⁸R. L. Weaver and Y. H. Pao, "Axisymmetric elastic waves excited by a point source in a plate," *J. Appl. Mech.* **49**, 821–836 (1982).
- ¹⁹J. B. Spicer, A. D. W. McKie, and J. W. Wagner, "Quantitative theory for laser ultrasonic waves in a thin plate," *Appl. Phys. Lett.* **57**, 1882–1884 (1990).
- ²⁰V. V. Shevchenko, *Continuous Transmission in Open Waveguides* (Golem, Boulder, CO, 1971).
- ²¹B. A. Auld, *Acoustic Fields and Waves in Solids* (Wiley, New York, 1973), Vol. 2.
- ²²G. S. Kino, *Acoustic Waves: Devices, Imaging, and Analog Signal Processing* (Prentice-Hall, Englewood Cliffs, 1987).
- ²³H. L. Bertoni and T. Tamir, "Characteristics of wedge transducers for acoustic surface waves," *IEEE Trans. Sonics Ultrason.* **SU-22**, 415–420 (1975).
- ²⁴J. Fraser, B. T. Khuri-Yakub, and G. S. Kino, "The design of efficient broadband wedge transducers," *Appl. Phys. Lett.* **32**, 698–700 (1978).
- ²⁵R. Briens, O. Leroy, and G. N. Shkerdin, "Mode theory as a framework for the investigation of the generation of a Stoneley wave at liquid-solid interface," *J. Acoust. Soc. Am.* **95**, 1953–1966 (1994).
- ²⁶J. J. Ditri and J. L. Rose, "Excitation of guided waves in generally anisotropic layers using finite sources," *J. Appl. Mech.* **61**, 330–338 (1994).
- ²⁷X. Jia, "Normal-mode theory of nonspecular phenomena for a finite-aperture ultrasonic beam reflected from layered media," *Appl. Phys. Lett.* **70**(3), 309–311 (1997).
- ²⁸H. L. Bertoni and T. Tamir, "Unified theory of Rayleigh-angle phenomena for acoustic beams at liquid-solid interfaces," *Appl. Phys.* **2**, 157–172 (1973).
- ²⁹L. G. Merkulov, "Damping of Normal modes in a plate immersed in liquid," *Sov. Phys. Acoust.* **10**, 169–173 (1964).
- ³⁰D. Royer and E. Dieulesaint, "Optical detection of sub-ångström transient mechanical displacements," in *Proceedings of IEEE Ultrasonics Symposium* (IEEE, New York, 1986), pp. 527–530.

- ³¹K. M. Rajana, D. Hongerholt, J. L. Rose, and J. J. Ditri, "Analysis of the generation of guided waves using finite sources: an experimental approach," in *Review of Progress in Quantitative Nondestructive Evaluation, Vol. 14* (Plenum, New York, 1995), pp. 171–178.
- ³²X. Jia, G. Quentin, and M. Lassoued, "Optical heterodyne detection of pulsed ultrasonic pressures," *IEEE Trans. Ultrason. Ferroelectr. Freq. Control* **UFFC-40**, 67–69 (1993).
- ³³X. Jia, A. Boumiz, and G. Quentin, "Laser interferometric detection of ultrasonic waves propagating inside a transparent solid," *Appl. Phys. Lett.* **63**, 2192–2194 (1993).
- ³⁴X. Jia, Ch. Mattei, and G. Quentin, "Analysis of optical interferometric measurements of guided acoustic waves in transparent solid media," *J. Appl. Phys.* **77**, 5528–5537 (1995).

Laser ultrasonic studies of solid–liquid interfaces

Douglas T. Queheillalt, Yichi Lu, and Haydn N. G. Wadley

*Intelligent Processing of Materials Laboratory, School of Engineering and Applied Science,
University of Virginia, Charlottesville, Virginia 22903*

(Received 10 May 1996; accepted for publication 13 September 1996)

A laser ultrasonic approach has been developed and used to measure the time-of-flight (TOF) for rays penetrating model cylindrical solid–liquid interfaces. Since the longitudinal acoustic wave speed in the solid is 45% higher than the liquid, TOF measurements for ultrasonic rays that propagate through the interface are found to be sensitive to the instantaneous position and shape of the interface. A ray tracing code (incorporating both interface refracted and creeping rays) has predicted the ray paths and their time-of-flights as a function of axial position for opposingly aligned source/receiver points on the diametral plane. When used in conjunction with a nonlinear least-squares method, the ray propagation model enabled reconstruction of the interface position, its convexity, and the velocities of both the liquid and solid phases from a few parallel beam TOF measurements collected on the diametral plane. © 1997 Acoustical Society of America. [S0001-4966(97)00302-0]

PACS numbers: 43.35.Sx [HEB]

INTRODUCTION

Many semiconductors are grown by variants of the Bridgman technique in which an ampoule containing a molten semiconductor is translated through a thermal gradient, resulting in directional solidification and the growth of a single crystal. During crystal growth, factors such as the solidification velocity, the shape of the solid–liquid interface, the temperature gradient, and the position of the interface along the gradient control the mechanisms of solidification, the likelihood of secondary grain nucleation/twin formation, solute segregation, dislocation generation, etc., and thus the yield of premium quality single crystal material is a sensitive function of growth conditions.^{1–3} For crystals grown by the vertical Bridgman (VB) technique, the highest quality is obtained with a low (~1–5 mm/h) constant solidification velocity and a planar or near-planar (slightly convex towards liquid) interface shape maintained throughout growth.^{4–6} The solidification velocity and solid–liquid interface shape are functions of the temperature gradients (both axial and radial) imposed during solidification.^{7,8} Undesirable interface locations, interfacial velocity jumps, and interface shapes (i.e., concave) have been found to occur under some growth conditions, especially for semiconducting materials with low thermal conductivity (e.g., GaAs and CdTe).^{3,7–9} As a result, secondary grains are often observed during VB solidification of low stacking fault energy materials like CdTe and its related alloys. The presence of large interfacial curvatures is also associated with high thermal stresses and the formation of dislocations.^{10,11}

Although solidification modeling efforts are beginning to be used to explore and develop an understanding of the growth methodology,^{7,8} they are still not fully predictive, and the production of premium quality CdTe remains substantially an art. This has stimulated an interest in developing and applying noninvasive sensor technologies based on x-ray radiography,^{12,13} eddy-current techniques,^{14,15} and ultrasonics^{16–18} to monitor the single crystal growth process and

perhaps facilitate on-line feedback control of interface velocity, shape, and even the thermal gradients within the ampoule. Each of the potential sensor methodologies above is based on the change of one or more material properties at the melting point: density for x-ray radiography, electrical conductivity for eddy-current sensing and the density/elastic moduli for an ultrasonic approach.

One ultrasonic approach to sensing has sought to exploit the acoustic impedance difference across a solid–liquid interface by detecting ultrasonic reflections from the interface.^{16–18} The normal-incident plane wave amplitude reflection coefficient (R) at a planar interface is a function of the impedance difference across the interface:¹⁹

$$R = \frac{\nu_s \rho_s - \nu_l \rho_l}{\nu_s \rho_s + \nu_l \rho_l}, \quad (1)$$

where ν_s and ν_l are longitudinal wave velocities, ρ_s and ρ_l are densities of the solid and the liquid phase, and $\nu\rho$ is the mechanical impedance. Relatively strong reflections arise when ultrasound is normally incident upon a flat Si or Ge solid–liquid interface (Table I).^{20–24} This reflection approach has been investigated by Parker *et al.* for Si,¹⁶ Jen *et al.* for Ge,¹⁷ and Carter *et al.* also for Ge¹⁸ as a means for identifying the position of solid–liquid interfaces during vertical Bridgman solidification. In each of these investigations' ultrasound was generated piezoelectrically from the cold end of the already solidified cylindrical sample and they measured the time-of-flight (TOF) for signals *reflected* from the solid–liquid interface to determine the interface position. However, large poorly characterized axial temperature gradients introduced uncertainties in mapping TOF data into interface axial position and little information can be inferred about interfacial curvature by this method. In addition, as shown in Table I, some semiconductor materials (e.g., InSb) have quite small amplitude reflection coefficients, and are therefore poorly suited to this approach.

TABLE I. Longitudinal wave velocities and densities for solid (v_s, ρ_s) and liquid (v_l, ρ_l) phases and the amplitude reflection coefficient (R) of selected semiconductor materials at their melting point (T_m).^{20–24}

| Material | T_m
(°C) | v_s
(mm/ μ s) | v_l
(mm/ μ s) | $\frac{v_s - v_l}{v_s}$ | ρ_s
(g/cm ³) | ρ_l
(g/cm ³) | R |
|------------|---------------|------------------------|------------------------|-------------------------|----------------------------------|----------------------------------|--------|
| Ge [111] | 936 | 5.13 | 2.71 | 47.2% | 5.26 | 5.51 | 0.2875 |
| Ge [110] | 936 | 4.99 | 2.71 | 45.7% | 5.26 | 5.51 | 0.2748 |
| Ge [100] | 936 | 4.52 | 2.71 | 40.0% | 5.26 | 5.51 | 0.2285 |
| Si [111] | 1410 | 8.60 | 3.92 | 54.4% | 2.30 | 2.53 | 0.3321 |
| Si [110] | 1410 | 8.37 | 3.92 | 53.2% | 2.30 | 2.53 | 0.3200 |
| Si [100] | 1410 | 7.63 | 3.92 | 48.7% | 2.30 | 2.53 | 0.2778 |
| InSb [111] | 536 | 3.71 | 2.67 | 27.9% | 5.76 | 6.48 | 0.1052 |
| InSb [110] | 536 | 3.59 | 2.67 | 25.5% | 5.76 | 6.48 | 0.0889 |
| InSb [100] | 536 | 3.20 | 2.67 | 16.4% | 5.76 | 6.48 | 0.0316 |

An alternative approach exploits the ultrasonic delay when rays are partially transmitted through the liquid. Mauer *et al.*²⁵ and Norton *et al.*²⁶ have reported measurement of the TOF for rays *transmitted* through a solid–liquid interface during the controlled solidification of polycrystalline aluminum. In their experiments, the samples were stationary and their outer surface never exceeded 650 °C and so a combination of laser generation and waveguide coupled piezoelectric transduction was used to make the measurements. Because extensive *a priori* knowledge about the interface was available they were able to construct an interface model (with a small number of unknown coefficients) and could use a very simple ray tracing code to compute predicted TOF values for rays propagating between the known source and receiver points. In these studies, the rays were incident normal to the interface and ray refraction was negligible. A nonlinear least-squares method was able to reconstruct the interface shape from a small (10) ray path data set. When *a priori* information is less abundant, ultrasonic tomographic techniques using convolution backprojection algorithms have also successfully recovered velocity distributions from laser ultrasonic TOF projection data.^{27,28} In these situations, significantly more TOF values are needed, and the approach has not been extended to situations where ray bending is significant.

The recent emergence of laser ultrasonics (i.e., laser generation and laser interferometric detection)²⁹ now offers the possibility of noninvasively introducing ultrasonic sources and receivers into high-temperature crystal growth furnaces and thereby obtaining information from rays that have propagated through a region of solidification. Since the longitudinal acoustic wave speed in semiconductors exhibits an abrupt increase (of 15%–50%) upon solidification, TOF measurements for ultrasonic rays that propagate through a solidification interface are likely to be sensitive to the instantaneous position and shape of the interface. Simulations of wave propagation through a solidification interface indicate that ultrasonic TOF projection data collected on the diametral plane is particularly amenable for analysis because the incident and refracted rays remain in the diametral plane when the interface has axisymmetry.³⁰ In addition, when the source and receiver have the same axial coordinate, a rapid characterization of interface position and curvature might be possible from only a few rays. However, because the rays

make oblique contact with the interface, significant ray bending occurs.^{28,31,32} Thus, a key issue in the development of an ultrasonic approach to interface sensing is the design of a methodology for reliable reconstruction of interfacial geometry from refracted ray path data.

Here, we experimentally explore the use of laser ultrasonic sensor concepts for monitoring solid–liquid interface position and shape. A combination of ray path analysis and testing of a model system (where the interface geometries are precisely known) were used to evaluate sensing and interface reconstruction approaches. The model system used *isotropic* materials with ultrasonic velocities similar to those of solid and liquid semiconductors near their melting temperatures. While semiconductor crystals are elastically anisotropic, modeling has suggested that strategies that work on isotropic systems can be readily extrapolated to anisotropic ones, provided point sources and receivers are used, and an anisotropic generalization of Snell’s law is incorporated in the ray tracing.³⁰

I. MODEL SYSTEM

The bench-top model consisted of water and solid polymethylmethacrylate (PMMA) contained in a cylindrical aluminum (2024-T6) “ampoule.” This mimics the opaque pyrolytic boron nitride (PBN) ampoules that are often used during crystal growth (Fig. 1). The ampoule had an inner radius of 75.0 ± 0.1 mm and an outer radius of 77.0 ± 0.1 mm. Ultrasound was optically generated and laser interferometrically detected on the outer surface of this aluminum ampoule. To obtain good ultrasonic coupling between the ampoule and the solid, the PMMA was machined so that its diameter was slightly smaller (0.50 mm) than the inner diameter of the ampoule. This allowed a thin layer of liquid (0.25 mm) to exist between the inner wall of the ampoule and solid PMMA. By machining one end of the PMMA sample the interface curvature could be varied from convex through planar to concave. The interface convexities h (defined such that $h > 0$ corresponds to a convex interface when viewed from the liquid) were +15, ± 10 , ± 5 , ± 2 mm and planar (0 mm). The water and PMMA had a measured longitudinal wave velocity of 1.497 ± 0.01 mm/ μ s and 2.670 ± 0.01 mm/ μ s at 21 °C, respectively, while the 2024-T6 Al alloy had a measured longitudinal wave velocity of 6.35

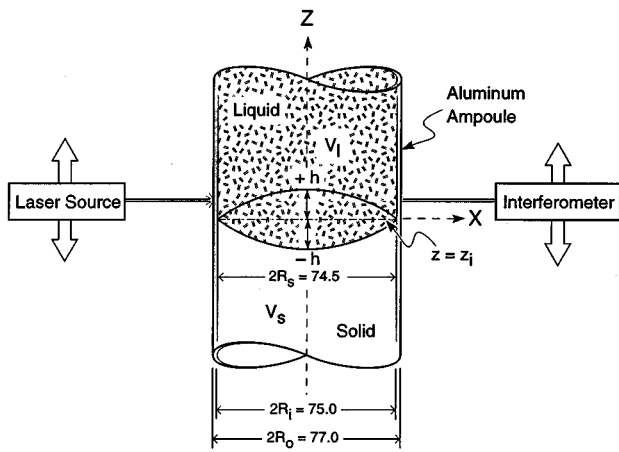


FIG. 1. A schematic of the H₂O/PMMA bench-top model showing the solid-liquid interface position (z_i), interfacial curvature (h), and the velocity fields of the liquid and solid phases (v_l, v_s) (all dimensions in mm).

± 0.01 mm/ μ s and a shear wave velocity of 3.01 ± 0.01 mm/ μ s at 21 °C. All experiments were conducted at 21 ± 2 °C.

II. LASER ULTRASONIC MEASUREMENTS

Ultrasonic time-of-flights between precisely positioned source and receiver points were measured using the laser ultrasonic system shown in Fig. 2. A ~ 10 -ns duration Q -switched Nd:YAG laser pulse of 1.064- μ m wavelength was used as the ultrasonic source. The energy per pulse was 50 mJ and the roughly Gaussian beam of the multimode pulse was focused to an approximate circular spot 1 mm in diameter. Thus, the source power density was ~ 600 MW/cm². Since the infrared absorption coefficient for the aluminum is low, a constraining layer consisting of a glass slide and a propylene glycol couplant was used to enhance the acoustic signal strength.²⁹

The ultrasonic receiver was a heterodyne laser interferometer. It responded to the sample's out-of-plane (normal)

surface displacement associated with wavefront arrivals at the receiver point.³³ It was powered by a 1-W single mode argon ion laser (operated at 0.25 W), which produced a continuous Gaussian beam of 514-nm wavelength focused to a circular spot ~ 100 μ m in diameter. The interferometer had a displacement sensitivity of 0.4 Å/mV and exhibited linear output for displacements up to about 300 Å. For the experiments reported here, maximum surface displacements were on the order of 150 Å. The signal from the interferometer was bandpass filtered between 10 kHz and 10 MHz and recorded with a (LeCroy 7200) precision digital oscilloscope at a 2-ns sampling interval using 8-bit analog-to-digital conversion. To improve the signal-to-noise ratio, each waveform used for TOF measurement was the average of ~ 100 pulses collected at a pulse repetition rate of 20 Hz. A fast photodiode identified the origination time for the ultrasonic signals.

The sensing configuration used opposingly aligned source/receiver points [i.e., the source and receiver had the same axial (z) coordinate] so that parallel beam TOF measurements could be collected on the diametral plane. A set of computer-controlled translation stages allowed the axial position of the sample to be translated so that the TOF as a function of position along the z axis was measured. The translational stages position accuracy was 1.175 μ m per 5.08 mm of linear motion. Errors in measured sample sizes, imprecision in the translation stage alignment, temperature fluctuations, etc., resulted in an estimated TOF error of about ± 100 ns.

III. RESULTS

A. Convex interfaces ($h > 0$)

Three typical ultrasonic waveforms corresponding to ray paths through the liquid, interface, and solid regions are shown in Fig. 3(a)–(c) for an interface with a positive convexity ($h = 5$ mm). In all three regions the first detectable signal arrived at ~ 22 μ s and corresponded to an encircling Lamb wave propagating in the aluminum ampoule.³⁴ When

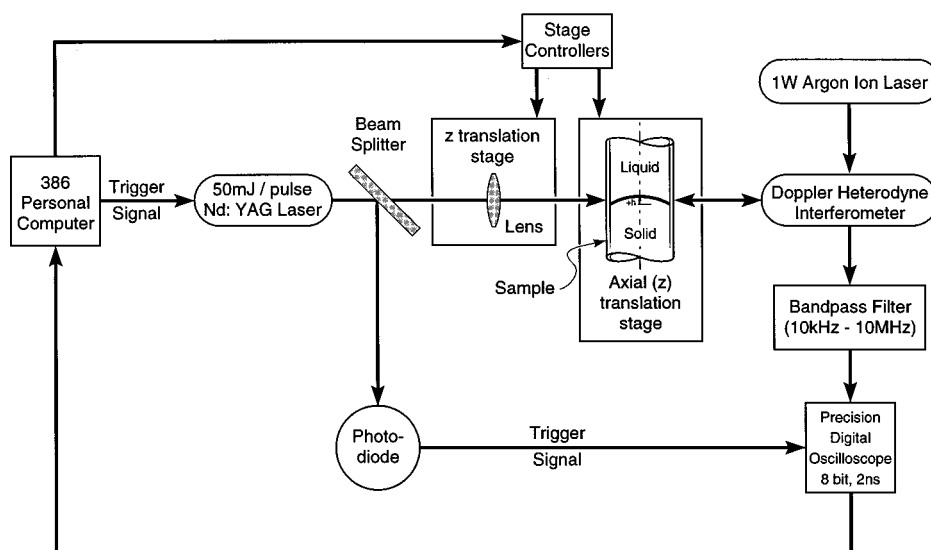


FIG. 2. A schematic of the laser ultrasonic test facility used to evaluate the sensor concepts.

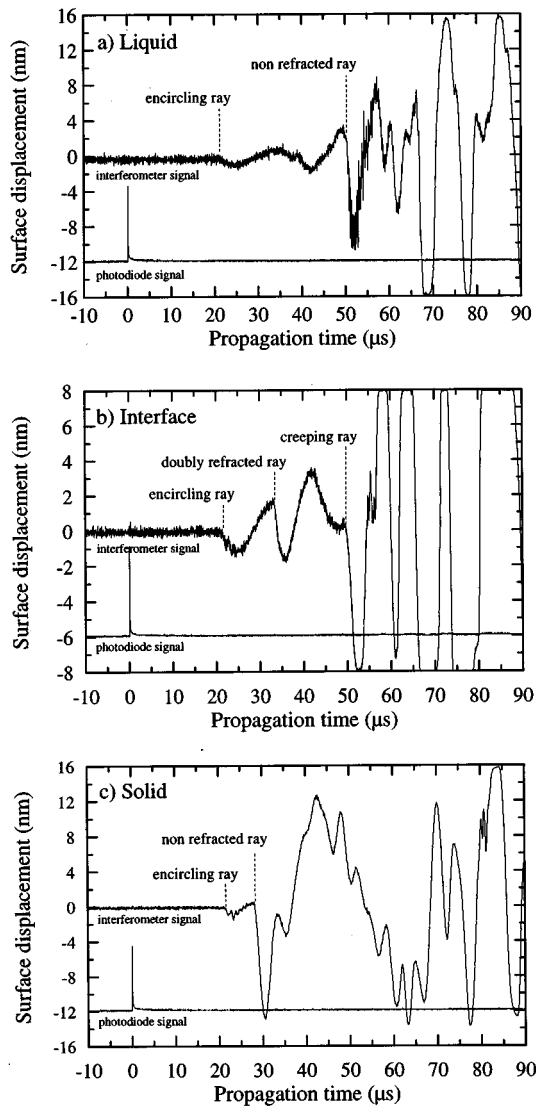


FIG. 3. Typical ultrasonic waveforms denoting the arrival time-of-flights (TOF) in the (a) liquid region, (b) interface region, and (c) solid region for a convex interface ($h=5$ mm).

$z_s = z_r > h$ the first arriving direct (nonrefracted) longitudinal wave propagated through the liquid [Fig. 3(a)] and arrived at $\sim 50 \mu\text{s}$. In the interface region, $0 < z_s < h$ [Fig. 3(b)], wave arrivals were seen at ~ 32 and $\sim 50 \mu\text{s}$. These are later shown to correspond to a doubly refracted ray and an interface critically refracted (creeping) ray. When $z_s = z_r < 0$, the first arriving direct (nonrefracted) longitudinal wave propagated through the solid [Fig. 3(c)] and arrived at $\sim 28 \mu\text{s}$.

Since the source (x_s, z_s) and the receiver (x_r, z_r) have the same axial coordinate ($z_s = z_r$), the data are most simply presented as a TOF projection for each interface as a function of axial (z axis) position. Figure 4 shows this ultrasonic TOF projection data for the nonrefracted ray arrivals for a planar interface ($h=0$ mm). It is clear that the position of the solid-liquid interface can be directly determined from the discontinuity in the time-of-flight (~ 28 to $\sim 50 \mu\text{s}$) for rays that propagate in the homogeneous solid and liquid regions.

Figure 5(a)–(c) shows the ultrasonic TOF projection data for either the non- or the doubly refracted rays for in-

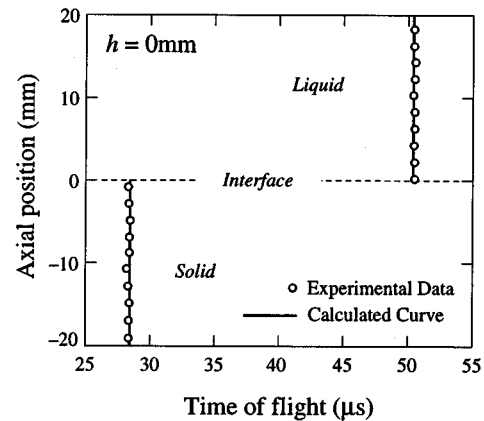


FIG. 4. Ultrasonic TOF projection data (nonrefracted rays) of the solid-liquid interface region for a planar interface ($h=0$ mm).

terface convexities $h=5, 10$, and 15 mm, respectively. When the source/receiver coordinate was below the interface region, $z_s = z_r < 0$, the TOF was a constant, and equal to that in the solid ($\sim 28 \mu\text{s}$). In the interface region, $0 < z_s < h$, the first arrival corresponded to a doubly refracted ray path. The TOF of the doubly refracted rays increased nonlinearly along the z -axis coordinate. The TOF became constant once again when the source/receiver was beyond the interface, $z_s = z_r > h$, and was then equal to that of a direct ray in the liquid ($\sim 50 \mu\text{s}$). The interface region can again be easily identified from TOF data and the convexity of a convex interface can be directly determined from either the TOF data of doubly refracted rays or from the TOF discontinuity of signals traveling directly to the receiver in only the homogeneous liquid or solid adjacent to the interface.

Figure 6(a)–(c) shows the ultrasonic TOF projection data again for either nonrefracted or interface creeping rays for convexities $h=2, 5$, and 10 mm. In the interface region, $0 < z_s < h$, the TOF for the interface creeping rays increased nonlinearly along the z -axis coordinate. The TOF for direct rays in either the solid or liquid were again constant when the source/receiver were beyond the interface region, $z_s = z_r < 0$ or $z_s = z_r > h$. The results above indicated that interface mapping with doubly refracted rays delineate the three regions (liquid, interface, solid) more clearly than using interface creeping rays. Also, the authors have found, due to the large difference in velocity ($v_l/v_s=0.561$), severe ray bending occurs and interface discrimination (using doubly refracted rays) for small interface convexities (i.e., $h=2$ mm) becomes difficult.

B. Concave interfaces ($h < 0$)

Figure 7(a)–(c) shows three typical ultrasonic waveforms corresponding to ray paths through the liquid, interface, and solid regions for a negative convexity ($h=-5$ mm). Again the first detectable signal arrived at $\sim 22 \mu\text{s}$ and corresponded to an encircling Lamb wave propagating in the ampoule. When $z_s = z_r > 0$, the first arriving direct (nonrefracted) longitudinal wave propagated through the liquid [Fig. 7(a)] and arrived at $\sim 50 \mu\text{s}$. In the interface region, $-h < z_s < 0$ [Fig. 7(b)], a wave arrival was seen at $\sim 30 \mu\text{s}$.

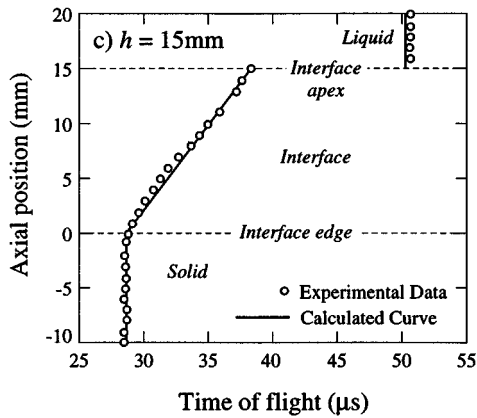
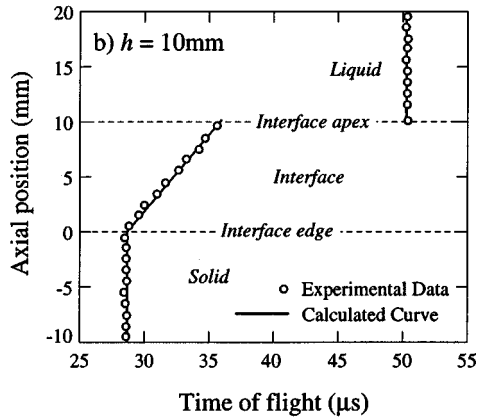
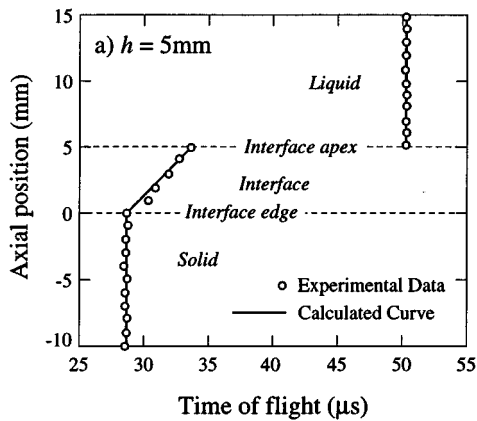


FIG. 5. Ultrasonic TOF projection data (non- and doubly refracted rays) of the solid-liquid interface region for interface convexities of (a) $h=5$ mm, (b) $h=10$ mm, and (c) $h=15$ mm.

This is shown below to correspond to an interface creeping ray. When $z_s = z_r < -h$ the first arriving direct (nonrefracted) longitudinal wave propagated through the solid [Fig. 7(c)] and arrived at $\sim 28 \mu\text{s}$.

Figure 8(a)–(c) shows the ultrasonic TOF projection data for either the nonrefracted or interface creeping rays for interface convexities $h = -2, -5,$ and -10 mm. Again when the source/receiver coordinate was below the interface region, $z_s = z_r < -h$, the TOF was a constant equal to that in the solid ($\sim 28 \mu\text{s}$). In the interface region, $-h < z_s < 0$, the TOF of the interface creeping rays increased nonlinearly along the z -axis coordinate. The TOF again became constant when the source/receiver was beyond the interface,

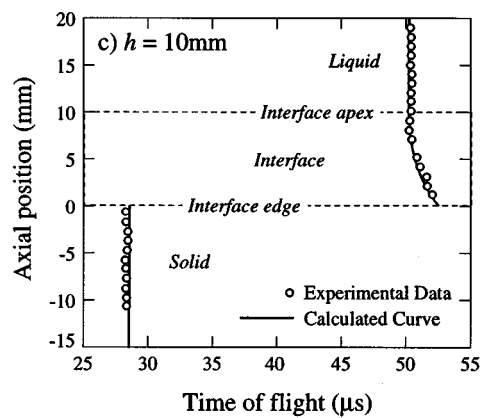
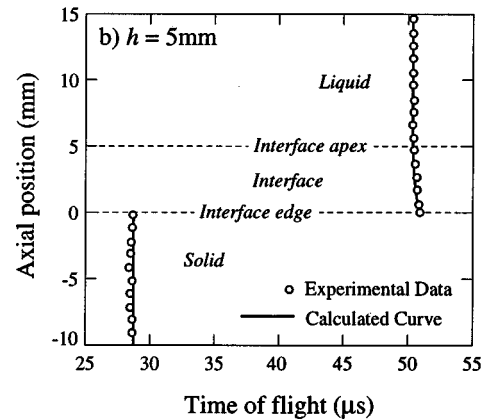
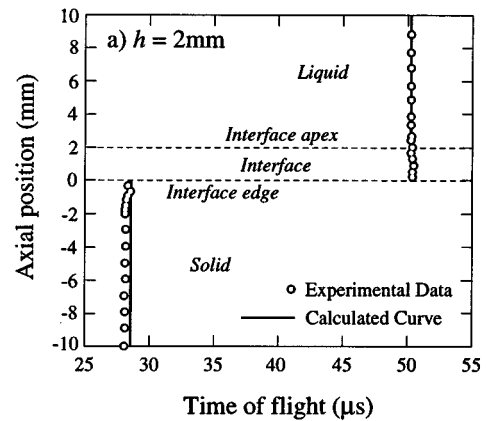


FIG. 6. Ultrasonic TOF projection data (nonrefracted and interface creeping rays) of the solid-liquid interface region for interface convexities of (a) $h=2$ mm, (b) $h=5$ mm, and (c) $h=10$ mm.

$z_s = z_r > 0$, and was equal to that of a direct ray in the liquid ($\sim 50 \mu\text{s}$).

Observation of the TOF data for direct/creeping rays through negative convexity interfaces does not provide a clear direct method for determining interfacial curvature of interfaces with small convexities (i.e., $h = -2$ and -5 mm). The interface critically refracted creeping ray TOFs are also an unreliable indicator of interface convexity due to the small TOF variations in the interface region. For direct observation of interfaces with small convexities (i.e., $h = \pm 2$ mm) other sensor methodologies such as offset source/receiver combinations on the diametral plane may be needed

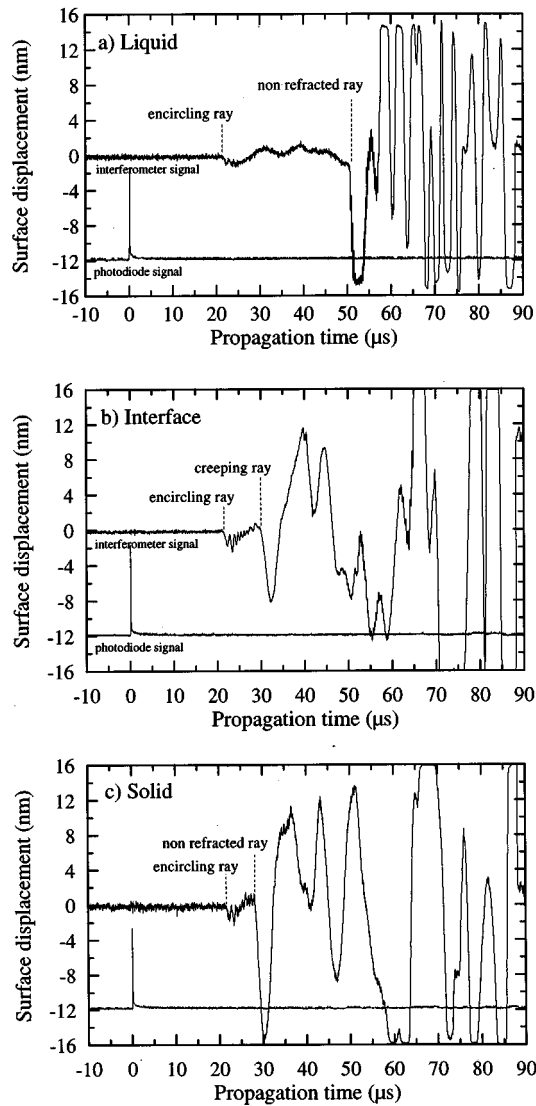


FIG. 7. Typical ultrasonic waveforms denoting the arrival time-of-flights (TOF) in the (a) liquid region, (b) interface region, and (c) solid region for a concave interface ($h = -5$ mm).

to more accurately determine the interface position and curvature by direct inspection.³⁵

IV. RAY PATH ANALYSIS

To gain a more detailed insight of the phenomena observed in the experiments, a ray tracing analysis has been applied to calculate the ray paths on the diametral plane of a cylindrical sample containing an axisymmetric liquid–solid interface. The measured time-of-flight, τ_m , for a ray that propagates along a path of length L_m is defined by

$$\tau_m = \int_{L_m} \frac{dl}{\nu}, \quad m = 1, 2, \dots, M, \quad (2)$$

where dl is an infinitesimal element of the path, ν is the ultrasonic velocity (l/ν is the local slowness) within the object, and M is the number of different rays. Fermat's least time principle can be used to find the TOF between defined source and receiver points.^{36,37} When an ultrasonic ray is incident upon an axisymmetric liquid–solid interface, both

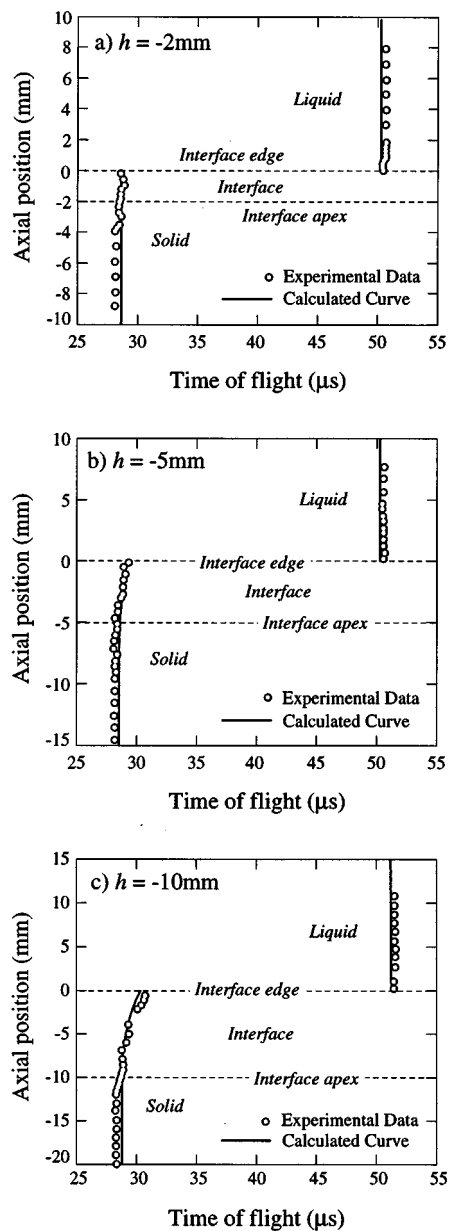


FIG. 8. Ultrasonic TOF projection data (nonrefracted and interface creeping rays) of the solid–liquid interface region for interface convexities of (a) $h = -2$ mm, (b) $h = -5$ mm, and (c) $h = -10$ mm.

reflected and refracted rays propagate on the diametral plane (defined by the incident propagation vector and the normal to the interface at the intersection of the incident ray with the interface).^{38,39} If it is assumed that during crystal growth the temperature gradients are small, the velocities are relatively uniform on either side of the interface, simplifying the computation of τ_m .

We arrange for the diametral cross-sectional plane on which ultrasonic rays propagate to coincide with the $x-z$ plane in a Cartesian coordinate system. Experiments have shown that during crystal growth the shape of the solid–liquid interface can be approximated by a spherical cap. On the diametral plane the interface is defined as a segment of a circle of radius R_c . If the solid cylinder radius is denoted by R_s , the interface convexity by h , the interface radius of curvature, R_c , is given by

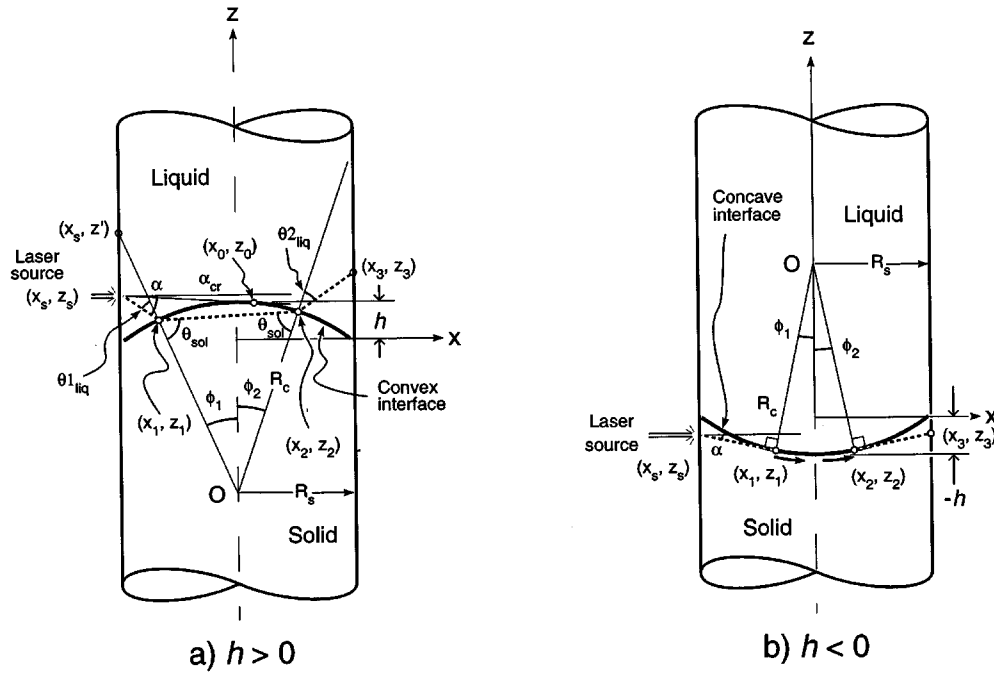


FIG. 9. Ray tracing on the diametral plane for a (a) convex solid-liquid interface and a (b) concave solid-liquid interface.

$$R_c = \frac{R_s^2 + h^2}{2h}. \quad (3)$$

The origin of the coordinate system is chosen so that when $h=0$ the interface is contained in the x - y plane.

A. Convex interfaces ($h>0$)

1. Direct and refracted rays

We first consider a convex interface shape [Fig. 9(a)] and investigate ray paths for prescribed source (x_s, z_s) coordinates with initial ray angles α . On the diametral plane, the interface is defined by the equation for a circle of radius R_c :

$$R_c = x^2 + [z + (R_c - h)]^2. \quad (4)$$

The equation for a ray path (with initial ray angle α) is

$$z = \tan \alpha (x - x_s) + z_s. \quad (5)$$

For $z_s > 0$ and the initial ray angle $\alpha > \alpha_c$, all the rays propagate in the liquid along straight ray paths, where $\alpha_c = \arctan(z - z_s / x - x_s)$ is the critical angle at which the ray path touches the interface tangentially. When $\alpha < \alpha_c$, rays intersect the liquid-solid interface at (x_1, z_1) . Since the intersection point (x_1, z_1) satisfies both Eqs. (4) and (5), it is obtained as one of two roots. Since the intersection point is to the left side of the tangential point (x_0, z_0) , we choose the root with $x_1 < x_0$.

The ray's incident angle to the interface, $\theta_{1\text{liq}}$, is defined as the angle between the normal to the interface at (x_1, z_1) and the ray path given by Eq. (5). The incident ray angle $\theta_{1\text{liq}}$ is

$$\theta_{1\text{liq}} = \arctan\left(\frac{x_1(x_1 - x_s) + z_1(z_1 - z_s)}{\sqrt{x_1^2 + z_1^2} \sqrt{(x_1 - x_s)^2 + (z_1 - z_s)^2}}\right). \quad (6)$$

The first refraction angle θ_{sol} at (x_1, z_1) is calculated next. Since the incident ray propagates in the liquid with a constant velocity v_l , the refraction angle θ_{sol} of the refracted ray in the solid can be determined simply using Snell's law:

$$\theta_{\text{sol}} = \arcsin\left(\frac{\sin \theta_{1\text{liq}}}{v_l} v_s\right), \quad (7)$$

where v_s is the longitudinal velocity in the solid.

After the first refraction has occurred, the equation for the refracted ray path in the solid is

$$z = \cot(\phi_1 + \theta_{\text{sol}})(x - x_1) + z_1, \quad (8)$$

where $(\theta_{\text{sol}} + \phi_1 - \pi/2)$ is the angle between the refracted ray path and the x axis and

$$\phi_1 = \arctan\left(\frac{x_1}{z_1 + (R_c - h)}\right). \quad (9)$$

A second refraction may sometimes occur at a point (x_2, z_2) on the solid-liquid interface. The point (x_2, z_2) is again obtained as one of the two roots of Eqs. (4) and (5). Since the second intersection point is on the right side of the tangential point (x_0, z_0) , the root with $x_2 > x_0$ is chosen.

The incident angle to the interface at (x_2, z_2) is also equal to θ_{sol} . Since the longitudinal velocity in the liquid is assumed to be a constant v_l , the second refraction angle $\theta_{2\text{liq}}$ at (x_2, z_2) can be determined again using Snell's law:

$$\theta_{2\text{liq}} = \arcsin\left(\frac{\sin \theta_{\text{sol}}}{v_s} v_l\right). \quad (10)$$

The doubly refracted ray path is now totally defined by the source point (x_s, z_s) , the first and second interface intersection points (x_1, z_1) and (x_2, z_2) , and the refraction angle $\theta_{2\text{liq}}$.

Assuming the source point and the receiver point are equal, $z_s = z_r$, we must now solve a two-point boundary-value problem.⁴⁰ For convex interfaces it is obvious that direct (nonrefracted) or doubly refracted ray paths can reach the receiver. To calculate the path of the latter, suppose the rays leave the source point (x_s, z_s) , intersect the interface at (x_1, z_1) , suffer refraction, intersect the interface again at (x_2, z_2) , suffer refraction again (i.e., are doubly refracted), and then reach the receiver point (x_r, z_r) . The shooting method⁴¹ obtains the ray path that connects the source point (x_s, z_s) and the receiver point (x_r, z_r) . We assume that the “doubly refracted” ray intersects the vertical line $x = x_r$, at z_3 where in general $z_3 \neq z_r$. The correct ray path is obtained when $|z_3 - z_r|$ is less than a prescribed allowable tolerance δ ($= 2.5 \times 10^{-3} R_s$ here). The ray path is then defined by (x_s, z_s) , (x_1, z_1) , (x_2, z_2) , and (x_r, z_3) .

If we assume that $z_s < 0$ (convex interface), then the ray path from the source point (x_s, z_s) to the receiver point (x_r, z_r) will not pass through the interface region. The TOF for such a ray path in the solid is given by

$$\tau_s = \frac{2(R_o - R_i)}{\nu_a} + \frac{2(R_i - R_s)}{\nu_l} + \frac{2R_s}{\nu_s}, \quad (11)$$

where R_o and R_i are the outside/inside radii of the ampoule and ν_a is the longitudinal wave velocity in the ampoule. For a convex interface [Fig. 9(a)] the doubly refracted rays that propagate through the solid carry information about the interface. In this case, each ray path is defined by four points: the source point (x_s, z_s) , the first intersection at the interface (x_1, z_1) , the second intersection (x_2, z_2) , and the receiver point (x_r, z_r) . The TOF is given by

$$\tau_i = \frac{2(R_o - R_i)}{\nu_a} + \frac{\sqrt{(x_s - x_1)^2 + (z_s - z_1)^2}}{\nu_l} + \frac{x_2 - x_1}{\nu_s} + \frac{\sqrt{(x_2 - x_r)^2 + (z_2 - z_3)^2}}{\nu_l}. \quad (12)$$

Now if $z_s > h$ for a convex interface, then once again a direct (nonrefracted) ray can propagate from the source point (x_s, z_s) to the receiver point (x_r, z_r) . The TOF for such a ray path in the liquid is given by

$$\tau_l = \frac{2(R_o - R_i)}{\nu_a} + \frac{x_r - x_s}{\nu_l}. \quad (13)$$

However, when the source/receiver points are just above the tip of the interface ($z_s = z_r > h$), two ray paths are available: one is directly via the (low velocity) liquid [Eq. (13)]; the second involves double refraction [Eq. (12)].

2. Creeping rays

According to Huygens' principle, each particle on an interface that is activated by a wavefront can be thought of as the source of a secondary disturbance.⁴² The secondary source emits rays in all directions, and the one tangential to the interface corresponds to the interface critically refracted (creeping) ray.⁴³ Thus as particles near the interface are activated by rays with a critical angle α_c , the interface creeping rays are generated in the liquid phase and travel in directions

tangential to the interface. These rays contact the interface tangentially, propagate along the interface, and then leave the interface tangentially to reach the receiver point.

The interface creeping ray paths are obtained by noting that the ray emitted from a source point (x_s, z_s) first touches the interface tangentially at (x_1, z_1) , where (x_1, z_1) are given by Eq. (5). Since the interface is symmetric with respect to the z axis, the surface creeping ray starts at (x_1, z_1) and leaves the interface at (x_2, z_2) where $x_2 = -x_1$ and $z_2 = -z_1$. The ray path now consists of the line linking (x_s, z_s) to (x_1, z_1) , the segment of the interface between (x_1, z_1) and (x_2, z_2) , and the line linking (x_2, z_2) to (x_r, z_r) . The TOF is given by

$$\tau_{cr} = \frac{2(R_o - R_i)}{\nu_a} + \frac{\sqrt{(x_s - x_1)^2 + (z_s - z_1)^2}}{\nu_l} + \frac{(\phi_1 + \phi_2)R_c}{\nu_l} + \frac{\sqrt{(x_2 - x_r)^2 + (z_2 - z_r)^2}}{\nu_l}, \quad (14)$$

where $(\phi_1 + \phi_2)$ (in radians) is the portion of the ray that “creeps” along the interface. The term $2(R_o - R_i)/\nu_a$ is the fraction of time the ray propagates in the ampoule.

3. Comparisons

Figure 4 shows a comparison between the predicted TOFs [Eqs. (11) and (13)] and the experimentally determined TOFs of nonrefracted rays for a planar interface. There is excellent agreement between experiment and model. Likewise, Fig. 5 shows a comparison between the predicted TOFs [Eqs. (11)–(13)] and the experimentally determined TOFs either non- or doubly refracted rays for convex interfaces ($h > 0$). Again there is good agreement between the experimental and predicted TOFs. Figure 6 shows reasonable agreement between the predicted TOFs [Eqs. (11), (13) and (14)] and the experimentally determined (interface creeping rays) TOFs for convex interfaces.

B. Concave interfaces ($h < 0$)

For a concave interface shape [Fig. 9(b)] with a source located in either the liquid ($z_s > 0$) or the solid ($z_s < -h$) the TOFs are equal to that of the homogeneous liquid [Eq. (13)] and solid [Eq. (11)]. In the interface region ($-h < z_s < 0$) the procedure for determination of the intersection coordinates with the interface for refracted ray paths and the calculation of the refraction angles is similar to that for the convex interfaces. However, due to the convergent nature of the concave interface, doubly refracted rays are not possible with this sensor arrangement and interface creeping rays are the first arriving signals.

From the analysis above, the ray path in the interface region ($-h < z_s < 0$) consists of the line linking (x_s, z_s) to (x_1, z_1) , the segment of the interface between (x_1, z_1) and (x_2, z_2) , and the line linking (x_2, z_2) to (x_r, z_r) . The TOF is therefore given by

$$\tau_{cr} = \frac{2(R_o - R_i)}{\nu_a} + \frac{\sqrt{(x_s - x_1)^2 + (z_s - z_1)^2}}{\nu_s} + \frac{(\phi_1 + \phi_2)R_c}{\nu_s} + \frac{\sqrt{(x_2 - x_r)^2 + (z_2 - z_r)^2}}{\nu_s}, \quad (15)$$

where $(\phi_1 + \phi_2)$ (in radians) is the portion of the ray that creeps along the interface.

Figure 8(a)–(c) shows a comparison between the predicted TOFs [Eqs. (11), (13), and (15)] and the experimentally determined (interface creeping ray) TOFs for concave interfaces. There is reasonable agreement between experiment and model. However, the interface convexity is clearly not determinable from direct inspection of the TOF projection data.

V. INTERFACE CURVATURE RECONSTRUCTIONS

In a crystal growth application, the location and curvature of the interface as well as the velocities of the solid/liquid regions are all unknown and must be determined from a set of TOF projection data. There are a variety of techniques available for reconstructing an object image from ultrasonic projection data.^{45,46} For crystal growth applications, approaches that can be used with scarce data and exploit the often significant *a priori* information available are preferable. For example, direct inspection of data reveals that an interface does exist, experiments have shown that its shape can be approximated as a segment of a circle, and, for most situations, the gradient in temperature is small so that the velocities are relatively uniform on either side of the interface. The crystal grower therefore requires only the axial position of the interface (its change with time gives the solidification velocity) and its approximate curvature. If the liquid and solid velocities could be also obtained, they might also be useful since they are related to the local temperature, composition, and to the crystals crystallographic orientation. The use of a simple model of the solidification geometry with a small number of unknown parameters combined with the ray tracing analysis above enables the application of a least-squares reconstruction approach.

We assume the model geometry is of the form shown in Fig. 1, where h , z_i , ν_l , and ν_s are all unknown. For the refracted ray path model, the TOF depends nonlinearly on the interface convexity (h), interface position (z_i), liquid (ν_l), and solid (ν_s) velocities and the mean-square error is given by

$$\chi^2 = \sum_{i=1}^M [\tau_i - \hat{\tau}_i(x_i; h, z_i, \nu_l, \nu_s)]^2, \quad (16)$$

where τ_i are the measured time-of-flights and $\hat{\tau}_i$ are the predicted time-of-flights for a model estimate of the interface. To reconstruct the model unknowns from the parallel beam TOF projection data a Levenberg–Marquardt nonlinear least-squares reconstruction method was used.⁴⁷ The nonlinear least-squares method determines the best-fit parameters (h, z_i, ν_l, ν_s) by minimizing χ^2 .

The reconstructed interfaces obtained using the nonlinear least-squares method and doubly refracted ray data are

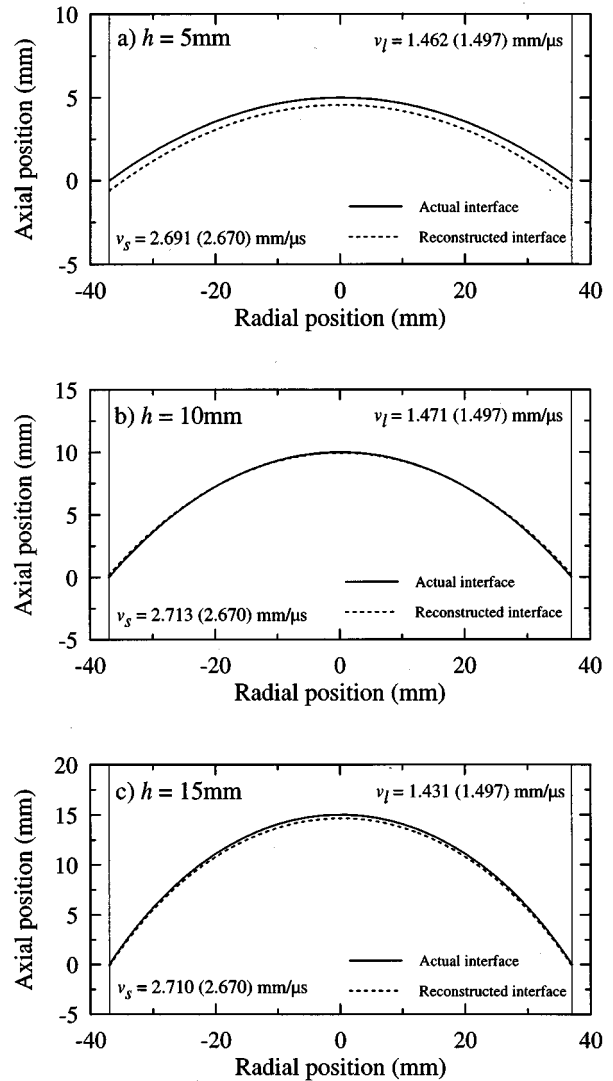


FIG. 10. Nonlinear least-squares interface reconstructions (doubly refracted rays) for convex interfaces with convexities of (a) $h=5$ mm, (b) $h=10$ mm, and (c) $h=15$ mm.

shown in Fig. 10(a)–(c) for convex interfaces with convexities of $h=5, 10$, and 15 mm, respectively. It is clear that the reconstructed interfaces coincide well with those of the model interfaces. Also shown in Fig. 10 are the deduced liquid and solid velocities, which were within 4.4% (for the liquid) and 1.5% (for the solid) of the model's velocities. The reconstructed interfaces obtained using the nonlinear least-squares method and interface creeping rays data are shown in Fig. 11(a)–(c) for convex interfaces with convexities of $h=2, 5$, and 10 mm, respectively. Again it is clear that the reconstructed interfaces coincided reasonably with the actual model's interfaces. Also shown in Fig. 11 are the deduced liquid and solid velocities, which were within 4.3% (for the liquid) and 2.1% (for the solid) of the model's velocities. The reconstructed interfaces obtained using the interface creeping rays are shown in Fig. 12(a)–(c) for concave interfaces with convexities of $h=-2, -5$, and -10 mm, respectively. The reconstructed interfaces coincide reasonably well with those of the model interfaces, and the deduced liquid and solid velocities were within 0.5% (for the liquid)

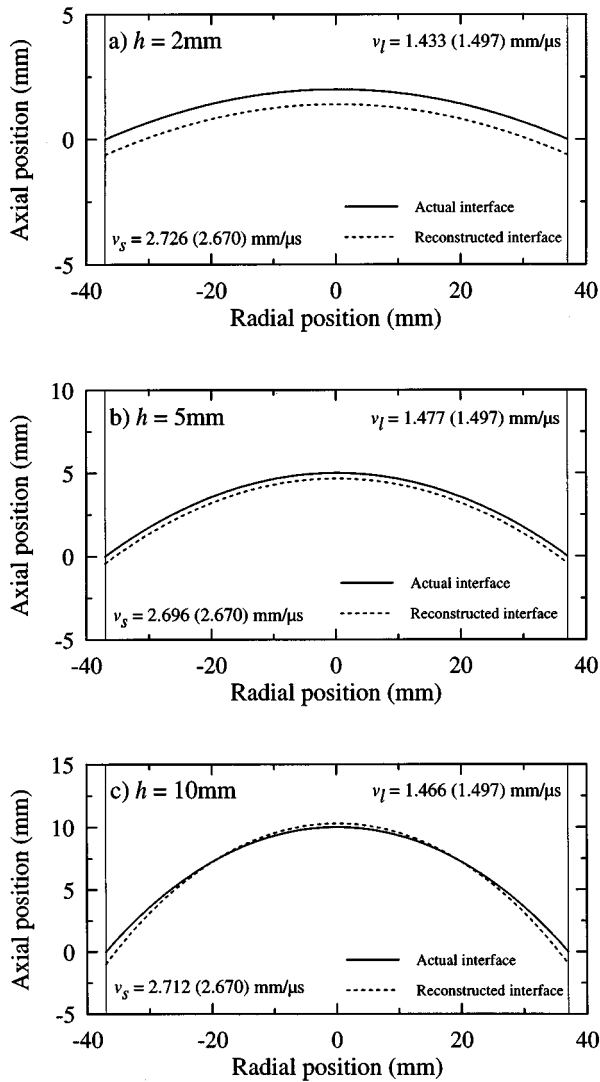


FIG. 11. Nonlinear least-squares interface reconstructions (creeping rays) for convex interfaces with convexities of (a) $h=2$ mm, (b) $h=5$ mm, and (c) $h=10$ mm.

and 3.7% (for the solid) of the model velocities.

Crystal growth models are now successfully able to predict the general form of the location–time behavior and the form of interfacial curvature, but they do not reliably give the exact values. Using the general form of these solutions with free parameters (h, z_i, v_l, v_s) together with the nonlinear least-squares reconstruction routine appears to represent a robust approach for converging upon the correct interface model, and thus recovery of the interface geometry (i.e., solid–liquid interface position, convexity, and velocity fields from sparse data). Although there was some loss of reconstruction precision in determining the location of z_i and the determination of h with the interface creeping ray model, the reconstruction results provide significant new information about the interface geometry to the crystal grower and promise a more detailed understanding of the growth process.

VI. CONCLUSIONS

An experimental study of laser ultrasonic sensor concepts for monitoring the solid–liquid interface position and

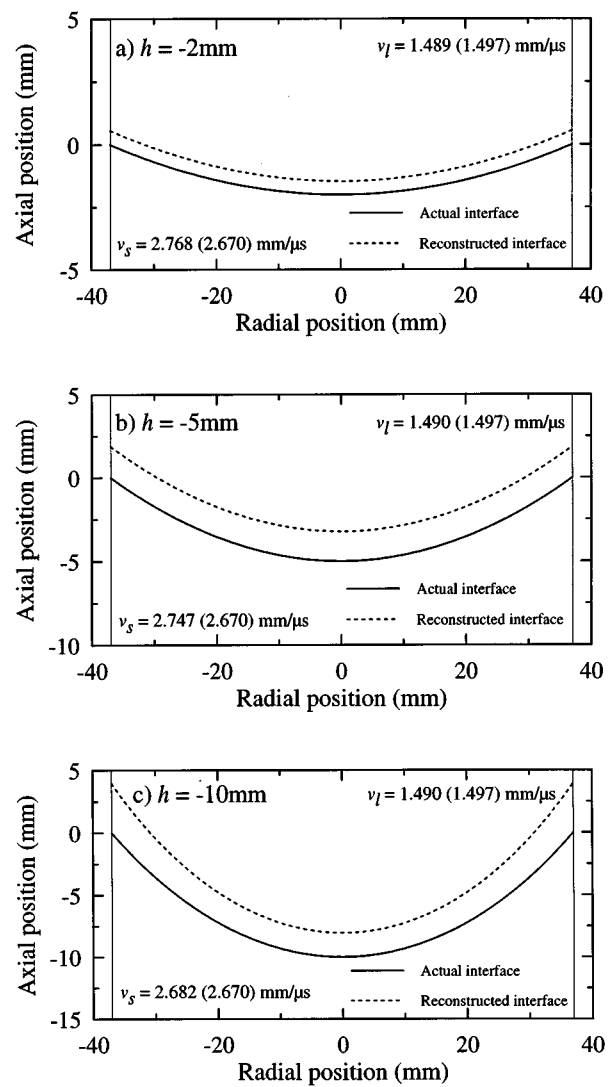


FIG. 12. Nonlinear least-squares interface reconstructions (creeping rays) for concave interfaces with convexities of (a) $h=-2$ mm, (b) $h=-5$ mm, and (c) $h=-10$ mm.

shape similar to those encountered in the vertical Bridgman growth of (Cd,Zn)Te and other semiconducting materials has been conducted. A combination of ray path analysis and bench-top testing on a model isotropic solid–liquid interface with a prototype laser ultrasonic system was used to explore various sensing concepts to determine the solid–liquid interface position and interfacial curvature from parallel beam ultrasonic TOF projection data on the diametral plane. From direct observation of the TOF projection data the interface region can be easily identified and the convexity of a convex interface directly determined from either the TOF data of doubly refracted rays or from the TOF discontinuity of signals traveling directly to the receiver in only the homogeneous liquid or solid adjacent to the interface. The interface region is not as clearly defined from the TOF data of interface creeping rays for either convex or concave interfaces. However, a nonlinear least-squares reconstruction routine robustly reconstructed the solid–liquid interface position, interface shape, and local velocity fields using either the doubly refracted or interface creeping ray data.

ACKNOWLEDGMENTS

We are grateful to Brent Bollong and Art Sochia of Johnson Matthey Electronics for helpful discussions concerning crystal growth. This work has been performed as part of the Infrared Materials Producibility Program (IRMP) managed by Duane Fletcher (JME) that includes Johnson Matthey Electronics, Texas Instruments, II-VI Inc., Loral, the University of Minnesota, and the University of Virginia. We are grateful for the many helpful discussions with our colleagues in these organizations. The IRMP consortium work, and our work within it, has been supported by ARPA/CMO under contract MD A972-91-C-0046 monitored by Raymond Balcerak.

- ¹T. Fu and W. R. Wilcox, "Influence of Insulation on Stability of Interface Shape and Position in the Vertical Bridgman-Stockbarger Technique," *J. Cryst. Growth* **48**, 416–424 (1980).
- ²M. Pfeiffer and M. Muhlberg, "Interface Shape Observation and Calculation in Crystal Growth of CdTe by the Vertical Bridgman Method," *J. Cryst. Growth* **118**, 269–276 (1992).
- ³P. Rudolf and M. Muhlberg, "Basic Problems of Vertical Bridgman Growth of CdTe," *Mater. Sci. Eng. B* **16**, 8–16 (1993).
- ⁴S. Sen, W. H. Konkell, S. J. Tighe, L. G. Bland, S. R. Sharma, and R. E. Taylor, "Crystal Growth of Large-Area Single-Crystal CdTe and CdZnTe by the Computer-Controlled Vertical Modified-Bridgman Process," *J. Cryst. Growth* **86**, 111–117 (1988).
- ⁵M. Azoulay, S. Rotter, G. Gafni, and M. Roth, "The Crystalline Quality Distribution in CdZnTe Single Crystal Correlated to the Interface Shape During Growth," *J. Cryst. Growth* **116**, 515–517 (1992).
- ⁶C. Parfeniuk, F. Weinberg, I. V. Samarasekera, C. Schvezov, and L. Li, "Measured Critical Resolved Shear Stress and Calculated Temperature and Stress Fields During Growth of CdZnTe," *J. Cryst. Growth* **119**, 261–270 (1992).
- ⁷S. Kuppuraio, S. Brandon, and J. J. Derby, "Modeling the Vertical Bridgman Growth of Cadmium Zinc Telluride, I Quasi-Steady Analysis of Heat-Transfer and Convection," *J. Cryst. Growth* **155**, 93–102 (1995).
- ⁸S. Kuppuraio, S. Brandon, and J. J. Derby, "Modeling the Vertical Bridgman Growth of Cadmium Zinc Telluride, II Transient Analysis of Zinc Segregation," *J. Cryst. Growth* **155**, 103–111 (1995).
- ⁹B. W. Choi and H. N. G. Wadley, submitted *J. Cryst. Growth*.
- ¹⁰M. Saitou and A. Hirata, "Ratio of Liquid to Solid Thermal Conductivity Calculated from the Solid-Liquid Interface Shape," *J. Cryst. Growth* **118**, 365–370 (1992).
- ¹¹W. R. Wilcox, F. M. Carlson, D. K. Aidun, V. White, W. Rosch, W. M. Chang, R. Shetty, A. Fritz, R. Balasubramanian, G. Rosen, J. Kweeder, and C. Wen, "Ground-Based Experiments and Theory in Preparation for Floating Zone Melting and Directional Solidification of Cadmium Telluride in Space," *Acta Astron.* **25**(8/9), 505–510 (1991).
- ¹²S. Ozawa and T. Fukunda, "In-Situ Observation of LEC GaAs Solid-Liquid Interface with Newly Developed X-Ray Image Processing System," *J. Cryst. Growth* **76**, 323–327 (1986).
- ¹³K. Kakimoto, M. Eguchi, H. Watanabe, and Hibiya, "In-Situ Observation of Solid-Liquid Interface Shape by X-Ray Radiography During Silicon Single Crystal Growth," *J. Cryst. Growth* **91**, 509–514 (1988).
- ¹⁴G. J. Rosen, F. M. Carlson, J. E. Thompson, W. R. Wilcox, and J. P. Wallace, "Monitoring Vertical Bridgman-Stockbarger Growth of Cadmium Telluride by an Eddy-Current Technique," *J. Electron. Mater.* **24**(5), 491–495 (1995).
- ¹⁵K. P. Dharmasena and H. N. G. Wadley, *J. Cryst. Growth* (in press).
- ¹⁶R. L. Parker and J. R. Manning, "Application of Pulse-Echo Ultrasonics to Locate the Solid/Liquid Interface During Solidification and Melting," *J. Cryst. Growth* **79**, 341–353 (1986).
- ¹⁷C. K. Jen, Ph. de Heering, P. Sutcliffe, and J. F. Bussiere, "Ultrasonic Monitoring of the Molten Zone of Single Crystal Germanium," *Mater. Eval.* **49**, 701–707 (1991).
- ¹⁸J. N. Carter, A. Lam, and D. M. Schleich, "Ultrasonic Time-of-Flight Monitoring of the Position of the Liquid-Solid Interface During the Bridgman Growth of Germanium," *Rev. Sci. Instrum.* **63**(6), 3472–3476 (1992).
- ¹⁹B. A. Auld, *Acoustic Fields and Waves in Solids* (Krieger, Malabar, FL, 1990).
- ²⁰Yu. A. Burenkov, S. P. Nikanorov, and A. V. Stepanov, "Elastic Properties of Germanium," *Sov. Phys. Solid State* **12**(8), 1940–1942 (1971).
- ²¹V. M. Glazov, A. A. Aivazov, and V. I. Timoshenko, "Temperature Dependence of the Velocity of Sound in Molten Germanium," *Sov. Phys. Solid State* **18**(4), 684–685 (1976).
- ²²Yu. A. Burenkov and S. P. Nikanorov, "Temperature Dependence of Elastic Constants of Silicon," *Sov. Phys. Solid State* **16**(5), 963–964 (1974).
- ²³N. M. Keita and S. Steinemann, "Sound Velocity in Liquid Silicon," *Phys. Lett. A* **72**(2), 153–154 (1979).
- ²⁴V. M. Glazov, S. N. Chizhevskaya, and N. N. Glagoleva, *Liquid Semiconductors* (Plenum, New York, 1969).
- ²⁵F. A. Mauer, S. J. Norton, Y. Grinberg, D. Pitchure, and H. N. G. Wadley, "An Ultrasonic Method for Reconstructing the Two Dimensional Liquid-Solid Interface During Solidifying Bodies," *Metall. Trans. B* **22**, 467–473 (1991).
- ²⁶S. J. Norton, A. H. Kahn, F. A. Mauer, and H. N. G. Wadley, "Inverse Problems in the Sensing of Materials Processing," in *Proceedings of the Symposium on Intelligent Processing of Materials*, edited by H. N. G. Wadley and W. E. Eckart (TMS, Warrendale, 1990), pp. 275–291.
- ²⁷D. A. Hutchins, J. K. Hu, R. P. Young, R. Stoner, D. Jansen, and Q. L. Zhang, "Ultrasonic Tomography of Metals Using Noncontact Transduction," *J. Acoust. Soc. Am.* **85**, 747–752 (1989).
- ²⁸Y. Lu, J. A. Goldman, and H. N. G. Wadley, "Quantitative Reconstruction of Internal Density Distributions from Laser Ultrasonic Data," *J. Acoust. Soc. Am.* **93**, 2678–2687 (1993).
- ²⁹C. B. Scruby and L. E. Drain, *Laser Ultrasonics: Techniques and Applications* (Hilger, New York, 1990).
- ³⁰Y. Lu and H. N. G. Wadley, "Two-Dimensional Wave Propagation in Cylindrical Single-Crystal Solid-Liquid Bodies," *J. Acoust. Soc. Am.* **98**, 2663–2680 (1995).
- ³¹S. J. Norton and M. Linzer, "Correcting for Ray Refraction in Velocity and Attenuation Tomography," *Ultrason. Imag.* **4**, 201–233 (1982).
- ³²A. H. Anderson and A. C. Kak, "Digital Ray Tracing in Two-Dimensional Refractive Fields," *J. Acoust. Soc. Am.* **72**, 1593–1606 (1982).
- ³³J. P. Monchalin, "Optical Detection of Ultrasound," *IEEE Trans. Ultrason. Ferroelectr. Freq. Control* **UFFC-33**(5), 485–499 (1986).
- ³⁴D. A. Hutchins, K. Lundgren, and S. B. Palmer, "A Laser Study of Transient Lamb Waves in Thin Materials," *J. Acoust. Soc. Am.* **85**, 1441–1448 (1989).
- ³⁵D. T. Queheillalt and H. N. G. Wadley (to be submitted to *J. Acoust. Soc. Am.*).
- ³⁶F. G. Friedlander, *Sound Pulses* (Cambridge U.P., New York, 1958).
- ³⁷M. Born and E. Wolf, *Principles of Optics* (Pergamon, New York, 1975).
- ³⁸F. I. Fedorov, *Theory of Elastic Waves* (Plenum, New York, 1968).
- ³⁹M. J. P. Musgrave, *Crystal Acoustics* (Holden-Day, San Francisco, 1970).
- ⁴⁰H. B. Keller, *Numerical Methods for Two-Point Boundary Value Problems* (Blaisdell, Waltham, MA, 1969).
- ⁴¹G. E. Forsythe, M. A. Malcolm, and C. B. Moler, *Computer Methods for Mathematical Computations* (Prentice-Hall, Englewood Cliffs, NJ, 1977).
- ⁴²C. Huygens, *Treatise on Light*, translated by S. P. Thompson (Macmillan, London, 1912).
- ⁴³Y. H. Pao and W. Sachse, "Interpretation of Time Records and Power Spectra of Scattered Ultrasonic Pulses in Solids," *J. Acoust. Soc. Am.* **56**, 1478–1486 (1974).
- ⁴⁴E. G. Henneke, "Reflection-Refraction of a Stress Wave at a Plane Boundary Between Anisotropic Media," *J. Acoust. Soc. Am.* **51**, 210–217 (1971).
- ⁴⁵Special Issue on Physical and Computational Aspects of 3-Dimensional Image Reconstruction, *IEEE Trans. Nucl. Sci.* **NS-21** (1974).
- ⁴⁶J. F. Greenleaf, S. A. Johnson, S. A. Samayoa, and F. A. Duck, "Algebraic Reconstruction of Spatial Distributions of Acoustic Absorption within Tissue from Their Two Dimensional Acoustic Projections," *Acoust. Hologr.* **5**, 591–603 (1974).
- ⁴⁷W. H. Press, B. P. Flannery, S. A. Teukolsky, and W. T. Vetterling, *Numerical Recipes: The Art of Scientific Computing (FORTRAN)* (Cambridge U.P., New York, 1990).

A study on beam optimizing of wideband stagger-tuned array

Qimin Chen, Shanhuai Bao, Xiaofei Zang, Wei Wei, and Jianzhong Guo

Applied Acoustics Institute, Shaanxi Teachers University, Xi'an, 710062, People's Republic of China

(Received 26 June 1995; revised 13 July 1996; accepted 24 August 1996)

A new method is presented for designing the wideband stagger-tuned array (WSTA) which was first put forward by Zhang *et al.* [Chin. J. Med. Instrum. **9**(3), 5–10 (1985)]. Based on the beam-equivalence principle and the sampling-composing law, this method is simple in calculation and good in precision. An optimized array scheme and expected beam pattern can be obtained by simulating a given beam pattern. Within $\pm 20^\circ$, the simulative error is below 1%. The experiment was conducted and the results showed excellent agreement with simulation and calculation for the major-lobe scope. © 1997 Acoustical Society of America.

PACS numbers: 43.38.Hz, 43.30.Yj [SLE]

INTRODUCTION

For an ultrasonic detecting transducer, two important specifications are the bandwidth and the spatial beam distribution of the array transducer. The so-called wideband stagger-tuned array (WSTA) transducer is a nonuniformly spaced line array in which each element has its own frequency, while the array has a fixed band as a whole. Both the frequency response and the spatial beam response of the array are affected by the elements' frequency and layout. A key problem in designing a WSTA is, according to the scanning system's requirements for bandwidth and beam distribution, to search out an optimized arrangement for the resonant elements. The traditional design method is complicated to calculate. Besides, it is limited by octave, frequency weighting, and the filter network and can hardly give a satisfactory result.^{2–4} A new method is presented where the WSTA's element frequency can be chosen separately in accordance with the array's bandwidth and response characteristic, and the elements' layout can be optimized to meet the scanning system's requirement for beam pattern. The essentials of this method are as follows: First, we introduce a set of amplitude weighting factors A_n , and derive the WSTA's sound pressure directivity function by using the superposition principle. Second, we apply the equivalence principle and the sampling-composing law to simulate a given beam pattern to collect necessary data for the array's layout. Active WSTA transducers were fabricated and tested to check the method's validity. The results have shown that, with such a simple beam-equivalent-simulation method, we can get an expected beam pattern which coincides with the given one exactly. Within the range of $\pm 20^\circ$, the simulation error was less than 1%. Within the major lobe ($\pm 5^\circ$), the experimental result agreed with the simulated one by and large. The error between the two was less than 10%.

I. THE FUNDAMENTS ON WSTA TRANSDUCER'S FREQUENCY ARRANGEMENT

An optimized scheme for the WSTA transducer's frequency arrangement has to fulfill two requirements:

(1) The array must have a satisfactory frequency response to an impulse voltage (or impulse force). In other words, it must have a required bandwidth.

(2) The array's beam spatial response must be optimized. According to the stagger-tuning principle, an ideal synthetic response can be obtained as long as the frequency interval Δf is rationally selected.¹ The element's number N is the least integer specified by inequality $N \geq (f_{\max} - f_{\min}) / \Delta f + 1$, where f_{\max} is the upper limit of the array's band and f_{\min} is the lower one. Each element's frequency f_n is then determined:

$$f_n = f_{\min} + n * \Delta f, \quad n = 0, 1, \dots, N-1.$$

When the elements are physically prepared, we can arrange them at will to see if the array's frequency response characteristic is satisfactory.

After the demand on frequency response has been met, the beam's spatial response is to be optimized. First, we rearrange the elements in frequency, leaving the spacings between the elements to be decided. Then we sample a given beam pattern and calculate for its directivity function. Make the being-designed array's directivity function equal to that of the given beam pattern to solve for the spacings. Upon the solved spacings, an optimized array scheme can be drawn up. This process is so called equivalent simulation. An expected beam pattern can be obtained with a so-constructed WSTA.

II. THE BEAM DIRECTIVITY FUNCTION OF THE WSTA

Assume that the stagger-tuned array is a nonuniformly spaced line one containing N elements, each with its respective frequency, as shown in Fig. 1. The elements will quasistably vibrate upon excitation by a voltage impulse. The n th element's contribution to the sound pressure at a far-field point, which is in θ direction and at distance r , is

$$P_n = \frac{A_{0n}}{r} \exp[-j(k_n + \Delta\Phi_n)],$$

where $n = 0, 1, 2, \dots, N-1$, k_n is the wave number corresponding to element n , A_{0n} is the response amplitude on element n 's radiating surface and is a real quantity, $\Delta\Phi_n$ is the phase difference between elements n and 0. According to the chart, $\Delta\Phi_n = k_n d_n \sin \theta$ and is positive, d_n is the element's abscissa (or its distance from element 0). We can rewrite above equation as

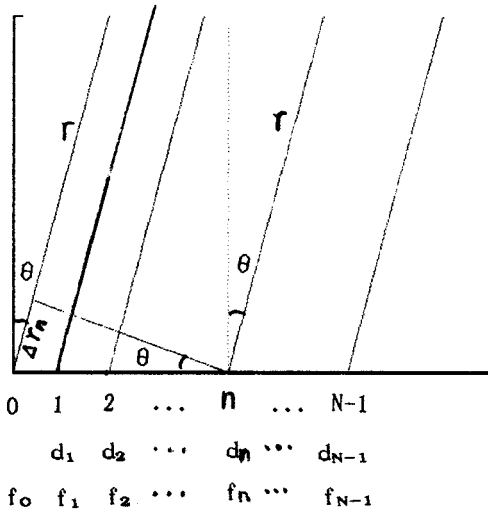


FIG. 1. The beam pattern of stagger-tuned array.

$$P_n = \frac{A_{0n}}{r} \exp(-jk_n r) \exp(-jk_n d_n \sin \theta). \quad (1)$$

The overall sound pressure produced by N elements at the reference field point is

$$P_T = \sum_{n=0}^{N-1} \frac{A_{0n}}{r} \exp(-jk_n r) \exp(-jk_n d_n \sin \theta). \quad (2)$$

If the array is stimulated by an impulse and the quasi-steady-state condition is met,⁵ we can introduce an amplitude-weighting factor A_n ($n = 0, 1, \dots, N-1$) to meet the following equation:

$$\begin{aligned} \frac{A_{00}A_0}{r} \exp(-jk_0 r) &= \frac{A_{01}A_1}{r} \exp(-jk_1 r) \\ &= \dots \\ &= \frac{A_{0N-1}A_{N-1}}{r} \exp(-jk_{N-1} r). \end{aligned} \quad (3)$$

It is clear that A_n has to be a complex. Now we can rewrite Eq. (2) for the weighted response amplitude. That is

$$P_T = \frac{A_{00}A_0}{r} \exp(-jk_0 r) \sum_{n=0}^{N-1} \exp(-jk_n d_n \sin \theta). \quad (4)$$

Normalize Eq. (4) and we get the normalized pressure produced by the array in direction θ :

$$D(\sin \theta) = \frac{1}{N} \sum_{n=0}^{N-1} \exp(-jk_n d_n \sin \theta). \quad (5)$$

For the far field, θ is small and we have $\sin \theta = r_n/d_n \approx \Delta s/r$. Here, Δs indicates the length of the arc against θ .

Assume that the sampling angle-interval is θ . Then, according to the sampling-composing law, the directivity pattern of a finite array can be reconstructed with a series of sampled values having taken in the arc direction and at an interval of $\sin \theta$.

Assume that the sampling number is M , the whole array's directivity function can be expressed as

$$D_1(\sin \theta_m) = \left| \frac{1}{N} \sum_{n=0}^{N-1} \exp(-jk_n d_n m \sin \theta) \right|, \quad (6)$$

where $m = 0, 1, 2, \dots, M-1$ is the sampling order.

III. THE PRINCIPLE AND METHOD FOR OPTIMIZING A WSTA BY SIMULATION

Once the element number N , element frequency f_n , and weighting factor A_n have been determined, the array's beam pattern depends only on the elements' layout. We can get an expected beam distribution by means of simulation. First, we write down the being-designed array's directivity function $D_1(\sin \theta_m)$ with the spacings Δd_n in the expression left unknown. Then we sample a given beam pattern to get its directivity function in concrete values. Let the two directivity functions be equal to each other and we get a set of equations about d_n 's. The last job is to solve those equations to get the values of d_n 's. An arrangement scheme based on those d_n 's will give a beam pattern exactly equal to the given one and therefore is an optimized pattern.

A. Equivalent to a uniform line array's beam pattern

Assume that a N -element uniform line array's frequency and element spacing are f_0 and d_0 , respectively. Its normalized pressure directivity function is

$$D_2(\sin \theta_m) = \left| \frac{1}{N} \sum_{n=0}^{N-1} \exp\left(-j \frac{2\pi}{c} f_0 d_0 m \sin \theta\right) \right|, \quad (7)$$

where $\sin \theta$ is the sampling radian, $m = 0, 1, 2, \dots, M-1$ is the sampling order at the sampling interval $\sin \theta$.

Let $D_1(\sin \theta_m) = D_2(\sin \theta_m)$. The corresponding terms on both sides of the equation should be equal to each other. Then we have

$$d_n = \frac{f_0}{f_n} n d_0. \quad (8)$$

If f_n is known, d_n can be calculated. A WSTA constructed on those d_n 's will have the same beam pattern as that of the given line array. The element spacings are

$$\Delta d_n = d_n - d_{n-1}. \quad (9)$$

B. Equivalent to an optimum beam pattern

Based on the scanning system's requirement and the principle on the array directivity characteristics,⁶ we can specify an optimum beam distribution $D_3(\sin \theta_m)$. Sample $D_3(\sin \theta_m)$ on the arc at interval $\sin \theta$ (in radian) to get a series of function values.

Let $D_1(\sin \theta_m) = D_3(\sin \theta_m)$. That is,

$$D_3(\sin \theta_m) = \left| \frac{1}{N} \sum_{n=0}^{N-1} \exp\left(-j \frac{2\pi}{c} f_n d_n m \sin \theta\right) \right|, \quad (10)$$

where $m = 0, 1, 2, \dots$ is the sampling order. When f_n 's ($n = 0, 1, 2, \dots, N-1$) are fixed, we can solve Eq. (10) by the descending method to get each element's abscissa d_n . Then

the array can be constructed to have a beam pattern exactly equivalent to the given beam distribution $D_3(\sin \theta_m)$. The details of the descending method are presented in the Appendix.

IV. ANALYSIS ON SIMULATION AND EXPERIMENT RESULTS

In order to make a WSTA transducer covering the band 2.5–5.0 MHz, we employ six elements whose frequencies (in MHz) and normalized response amplitudes are listed below:

$$f_0=5.0, \quad f_1=4.5, \quad f_2=4.0, \quad f_3=3.5,$$

$$f_4=3.0, \quad f_5=2.5,$$

$$A_{00}=0.6, \quad A_{01}=0.5, \quad A_{02}=1.0, \quad A_{03}=0.3,$$

$$A_{04}=0.75, \quad A_{05}=1.0.$$

Every element has the same radiation surface of $10 \times 0.25 \text{ mm}^2$ and a frequency-related thickness. The six-element array's dimension is about 3.5 mm. As the array is to be stimulated by pulses, according to the quasi-steady-state condition ($D/r \ll 1$ radian), the second-order phase factor can be ignored only when $r > 20$ cm. Equation (3) is then an accurate one. However, what we are concerned about is the module of the pressure amplitude $|A_{0n}A_n \cdot \exp(-jk_n r)/r|$ rather than the sound pressure at the observed point $A_{0n}A_n \cdot \exp(-jk_n r)/r$. Because A_n is a complex, we can replace it in Eq. (3) with its another form $|A_n| \cdot \exp(j\theta_n)$, where $|A_n|$ is A_n 's module and θ_n is its argument. To make Eq. (3) hole, we must ensure that the real part and the imaginary part are separately equal. For the real part we have

$$A_{00}|A_0|/r = A_{01}|A_1|/r = \dots = A_{0N-1}|A_{N-1}|/r,$$

or

$$|A_{00}A_0| = |A_{01}A_1| = \dots = |A_{0N-1}A_{N-1}|, \quad (11)$$

because A_{0n} 's are real.

Using Eq. (11), we can get each element's normalized amplitude-weighting coefficient:

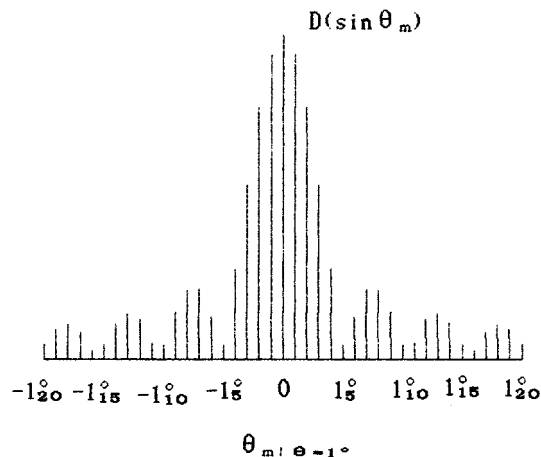


FIG. 2. The beam pattern of the uniform linear array. $f_0=5.0$ MHz, $\Delta d_0=0.3$ mm, $N=6$.

TABLE I. Normalized data of experiment results and equivalence simulation of stagger-tuned and uniform-linear array.

| $\theta_m _{\theta=1^\circ}$ | Calculated data of uniform liner array beam $D_2(\sin \theta_m)$ | Equivalence simulation data of stagger tuned array $D_1 \sin(\theta_m)$ | Measurement data | | | |
|-------------------------------|--|---|------------------|-------|--------------|-------|
| | | | Sample No. 1 | | Sample No. 2 | |
| | | | Left | Right | Left | Right |
| 0° | 1.0000 | 1.0000 | 1.0000 | 1.000 | 1.000 | 1.000 |
| 1° | 0.9409 | 0.9410 | 0.950 | 0.946 | 0.943 | 0.947 |
| 2° | 0.7761 | 0.7663 | 0.781 | 0.778 | 0.780 | 0.784 |
| 3° | 0.5394 | 0.5400 | 0.575 | 0.576 | 0.610 | 0.569 |
| 4° | 0.2784 | 0.2792 | 0.379 | 0.352 | 0.316 | 0.323 |
| 5° | 0.0422 | 0.0432 | 0.273 | 0.271 | 0.234 | 0.204 |
| 6° | 0.1292 | 0.1281 | 0.254 | 0.275 | 0.275 | 0.267 |
| 7° | 0.2141 | 0.2131 | 0.340 | 0.330 | 0.264 | 0.272 |
| 8° | 0.2127 | 0.2118 | 0.292 | 0.298 | 0.263 | 0.241 |
| 9° | 0.1448 | 0.1444 | 0.214 | 0.274 | 0.247 | 0.232 |
| 10° | 0.0435 | 0.0436 | 0.173 | 0.123 | 0.219 | 0.204 |
| 11° | 0.0512 | 0.0543 | 0.154 | 0.120 | 0.201 | 0.120 |
| 12° | 0.1213 | 0.1199 | 0.178 | 0.185 | 0.214 | 0.164 |
| 13° | 0.1390 | 0.1370 | 0.173 | 0.232 | 0.210 | 0.196 |
| 14° | 0.1088 | 0.1064 | 0.282 | 0.223 | 0.202 | 0.173 |
| 15° | 0.0458 | 0.0433 | 0.223 | 0.219 | 0.183 | 0.168 |
| 16° | 0.0264 | 0.0286 | 0.226 | 0.218 | 0.189 | 0.167 |
| 17° | 0.0834 | 0.0851 | 0.245 | 0.217 | 0.188 | 0.173 |
| 18° | 0.1079 | 0.1088 | 0.238 | 0.233 | 0.203 | 0.189 |
| 19° | 0.0942 | 0.0939 | 0.223 | 0.232 | 0.181 | 0.174 |
| 20° | 0.0454 | 0.0479 | 0.208 | 0.237 | 0.179 | 0.187 |

$$|A_0|=0.5, \quad |A_1|=0.6, \quad |A_2|=0.3, \quad |A_3|=1,$$

$$|A_4|=0.4, \quad |A_5|=0.3.$$

A. Simulating a uniform linear array's beam and the experiment

For a uniform line array, according to the array theory, the prerequisite for grating-lobe's absence within $\pm 90^\circ$ is $d_0/\lambda_0 \leq 1$, where d_0 is the element spacing and λ_0 is the wavelength. For medium of water and frequency $f_0 = 5.0$ MHz, we take the element spacing d_0 as 0.3 mm. When sampling the beam with a radian $\sin \theta$ corresponding to an

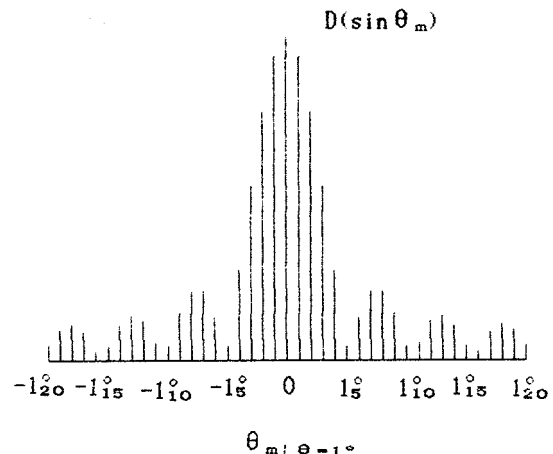


FIG. 3. The simulative beam pattern of the WSTA which is made equivalent to that of the uniform linear array.

TABLE II. Element abscissae d_n and element spacing Δd_n of WSTA.

| n : | 0 | 1 | 2 | 3 | 4 | 5 |
|--------------------|-------|-------|-------|-------|-------|-------|
| f_n (MHz): | 5.0 | 4.5 | 4.0 | 3.5 | 3.0 | 2.5 |
| d_n (mm): | 0.000 | 0.333 | 0.750 | 1.286 | 2.000 | 3.000 |
| Δd_n (mm): | | 0.333 | 0.417 | 0.536 | 0.714 | 1.000 |

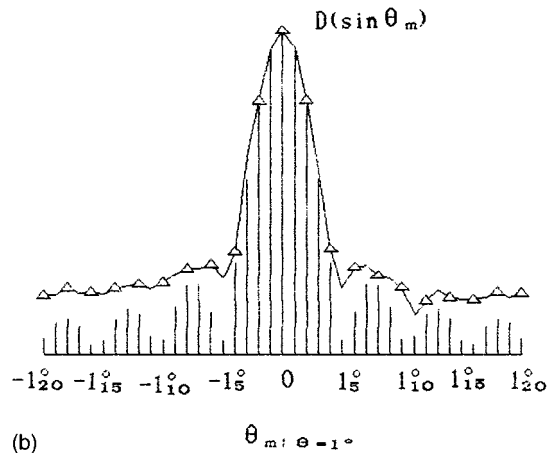
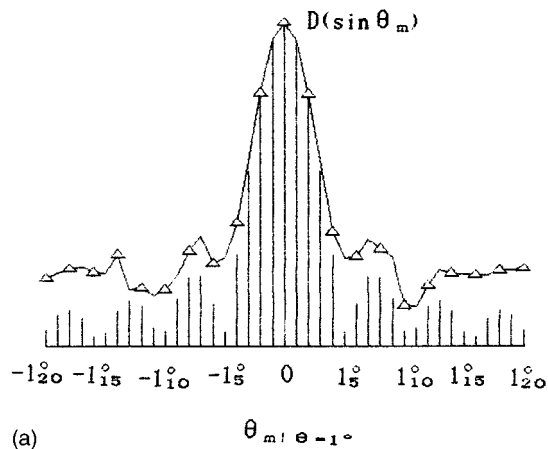


FIG. 4. The experimental beam pattern of the WSTA which is made equivalent to that of the uniform linear array. (a) and (b): sample 1 and sample 2, respectively. Δ : experimental results; $|$:simulative result.

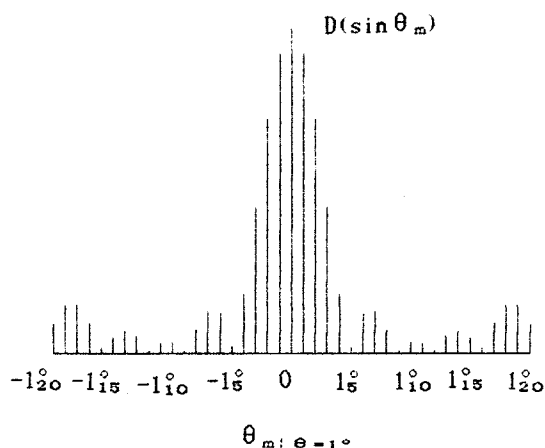


FIG. 5. The given beam pattern.

angle interval $\theta=1^\circ$, we can get calculated values on the beam pattern as shown in Table I and the beam pattern itself as shown in Fig. 2. When we employ the 5.0-MHz element as the reference element, the element's abscissae d_n and spacings Δd_n of the beam-equivalent WSTA, solved from Eq. (9), are listed in Table II.

With the calculated abscissae d_n , we can get the beam data on the simulated WSTA from Eq. (7), also listed in Table I, and the simulated beam pattern, as shown in Fig. 3.

It can be seen from Table I, Fig. 2, and Fig. 3 that the simulated beam pattern coincided with the given one well. In the range of $\pm 20^\circ$, the error is within 1%.

On the basis of simulation data, a group of WSTA transducers have been made. When stimulated by an pulse (with width 170 ns, amplitude 40 V, and repeat frequency 2 kHz), the normalized pressure directivity for quasi-steady-state far field ($r=20$ cm) was measured and the results are also shown in Table I. To make a comparison, the measured beam pattern is overdrawn in Fig. 4(a) and (b). It is clear that in the range of major lobe ($\pm 5^\circ$), the experiment result agreed with the simulated one by and large. The error was less than 10%. Outside the major lobe, however, the error raised and the minor lobes were dim.

B. Simulating an optimum beam pattern and the experiment

Shown in Fig. 5 is the expected beam pattern for a WSTA whose band is 2.5–5.0 MHz. Sample the pattern with the radian $\sin \theta$ of an angle interval $\theta=1$. The sampled data are listed in Table III.

We took the same element number N , element frequency f_n , and weighting coefficients A_n as above mentioned. Introduce f_n ($n=0,1,2,\dots,N-1$) and sampled data $D_3(\sin \theta_m)$ in Table III into Eq. (6), use the descending method for the computer-based simulation. A group of solution d_n is obtained and listed in Table IV.

Similarly, we applied Eq. (6) to derive a set of beam distribution data for the simulating array, whose beam pattern is exactly equivalent to the given optimum one. These data are shown in Table III and the simulating array's beam pattern is in Fig. 6.

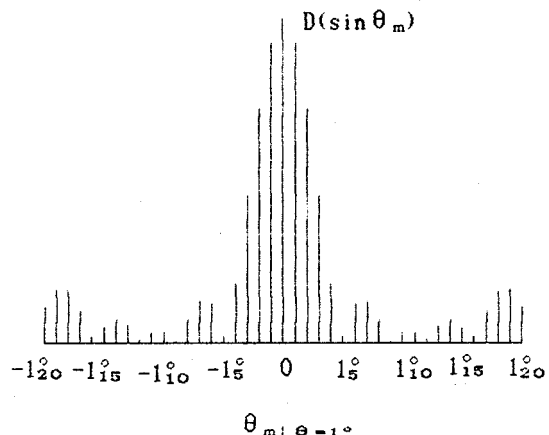


FIG. 6. The simulative beam pattern of the WSTA which is made equivalent to that of the given-beam pattern.

TABLE III. Normalized data of experiment results and equivalence simulation of stagger-tuned and optimum beam pattern.

| $\theta_m _{\theta=1^\circ}$ | Sampled data of the given beam pattern
$D_2(\sin \theta_m)$ | Equivalence simulation beam data of stagger tuned array
$D_1 \sin(\theta_m)$ | Measurement data | | | |
|-------------------------------|--|---|------------------|-------|--------------|-------|
| | | | Sample No. 3 | | Sample No. 4 | |
| | | | Left | Right | Left | Right |
| 0° | 1.0000 | 1.0000 | 1.000 | 1.000 | 1.000 | 1.000 |
| 1°_1 | 0.9254 | 0.9254 | 0.926 | 0.931 | 0.933 | 0.936 |
| 1°_2 | 0.7234 | 0.7235 | 0.725 | 0.727 | 0.737 | 0.741 |
| 1°_3 | 0.4513 | 0.4517 | 0.483 | 0.485 | 0.457 | 0.518 |
| 1°_4 | 0.1822 | 0.1827 | 0.253 | 0.271 | 0.285 | 0.285 |
| 1°_5 | 0.0205 | 0.0198 | 0.207 | 0.242 | 0.243 | 0.186 |
| 1°_6 | 0.1231 | 0.1223 | 0.214 | 0.228 | 0.271 | 0.171 |
| 1°_7 | 0.1294 | 0.1286 | 0.228 | 0.220 | 0.285 | 0.243 |
| 1°_8 | 0.0743 | 0.0735 | 0.186 | 0.193 | 0.250 | 0.214 |
| 1°_9 | 0.0059 | 0.0054 | 0.185 | 0.186 | 0.236 | 0.143 |
| 1°_{10} | 0.0351 | 0.0350 | 0.179 | 0.164 | 0.229 | 0.129 |
| 1°_{11} | 0.0312 | 0.0303 | 0.171 | 0.150 | 0.228 | 0.121 |
| 1°_{12} | 0.0078 | 0.0095 | 0.157 | 0.128 | 0.200 | 0.126 |
| 1°_{13} | 0.0528 | 0.0551 | 0.164 | 0.114 | 0.186 | 0.150 |
| 1°_{14} | 0.0716 | 0.0740 | 0.157 | 0.121 | 0.186 | 0.157 |
| 1°_{15} | 0.0461 | 0.0476 | 0.126 | 0.124 | 0.193 | 0.171 |
| 1°_{16} | 0.0187 | 0.0195 | 0.150 | 0.143 | 0.186 | 0.143 |
| 1°_{17} | 0.0958 | 0.1005 | 0.157 | 0.150 | 0.179 | 0.114 |
| 1°_{18} | 0.1489 | 0.1588 | 0.157 | 0.157 | 0.177 | 0.159 |
| 1°_{19} | 0.1493 | 0.1654 | 0.164 | 0.164 | 0.157 | 0.168 |
| 1°_{20} | 0.0904 | 0.1127 | 0.171 | 0.178 | 0.136 | 0.171 |

TABLE IV. The element spacings Δd_n and the element abscissae d_n obtained from computer-based simulation.

| n : | 0 | 1 | 2 | 3 | 4 | 5 |
|----------------------|--------|--------|--------|--------|--------|--------|
| f_n (MHz): | 5.0 | 4.5 | 4.0 | 3.5 | 3.0 | 2.5 |
| Δd_n^* (mm): | | 0.3371 | 0.4786 | 0.5260 | 0.7991 | 1.4654 |
| d_n^* (mm): | 0.0000 | 0.3371 | 0.8157 | 1.3417 | 2.1408 | 3.6062 |

From the sampled and simulated data in Table III as well as in Figs. 5 and 7, it can be seen that the equivalently simulative beam pattern coincides with the given one very well. In the range of $\pm 20^\circ$, the simulating error is within 1%.

In accordance with the result of optimized simulation, a group of WSTA transducers were fabricated. Under the effect of the same-as-above voltage impulse, the experiment results of normalized beam distribution for the quasi-steady-state far field ($r=20$ cm) are shown in Table III and Fig. 5. We can see that in the major-lobe scope (within $\pm 5^\circ$), the experimental results and the simulated ones are largely in keeping with each other. The error is within 10%. Similar to the above, outside the major lobe the error increases with the angle. The minor lobes are also dim.

C. Analysis on the simulation and the experiment results

From the two pairs of simulation and experiment results it is clear that the error inside the major lobe is relatively small. This is because that inside the major lobe the observation angles are small, the quasi-steady-state condition is more likely to hold, and the near-axis approximate condition ($r=2$) is tenable. While outside the major lobe, the influence of the frequency response's phase factor increases with the observation angle, causing the randomness of pressure composition to increase. As a result, the error increases and the minor lobes become dim. Besides, the array's finite dimension causes response's time deviation (or phase deviation) between the radiation of the center elements and that of the side elements at the observing point. Which will also make a contribution to the overall error.

No matter what happened to the minor lobes, it is of importance that the error inside the major lobe, which we are really interested in, is very small.

V. CONCLUSIONS

Conclusions drawn from the theoretical analysis, computer-based simulation, and experimental results are:

(1) It is feasible to make optimum simulation on the beam distribution and the arrangement scheme for a WSTA by using the beam equivalence principle and the sampling-composing law. This method is not limited by frequency weighting, octave, and filter network and therefore can bring about satisfactory precision.

(2) The WSTA's simulation to a uniform line array has indicated that through simple simulation calculation, we can get an arrangement scheme for constructing a WSTA whose beam distribution is excellently equivalent to that of a given uniform line array.

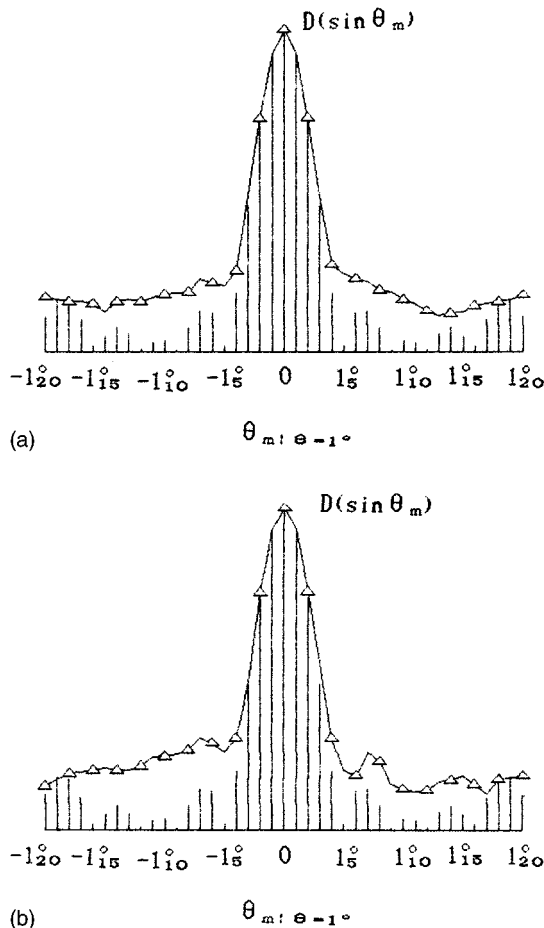


FIG. 7. The experimental beam pattern of the WSTA. (a) and (b): sample 3 and sample 4, respectively. |: simulative result; Δ : experimental results.

(3) Within the major lobe, there are little difference between the simulative result and the experiment one. While outside the major lobe, the error increases with the observing angle. The minor lobes are dim.

APPENDIX

The detail of the descending method:

First, we define a function $f_m(\Delta D_n)$

$$f_m(\Delta D_n) = \left| \sum_{n=0}^{N-1} \exp\left(-j \frac{2\pi}{c} f_n d_n \sin \theta\right) \right| - |ND_3(\sin \theta_m)|, \quad (\text{A1})$$

where $d_n = \sum_{i=1}^n \Delta d_i$, ($n=1, 2, \dots, N=1$), $\Delta D_n = (\Delta d_0, \Delta d_1, \dots, \Delta d_{N-1})$, $m=0, 1, \dots, M-1$.

Therefore Eq. (10) can be written as

$$f_m(\Delta D_n) = f_m(\Delta d_0, \Delta d_1, \dots, \Delta d_{N-1}) = 0. \quad (\text{A2})$$

Take the target function $F(\Delta D_n)$ as

$$F(\Delta D_n) = \sum_{n=0}^{N-1} f_m^2(\Delta D_n). \quad (\text{A3})$$

Predetermine an error ε and a group of initial values

$$\Delta D_n^{(0)} = (\Delta d_0^{(0)}, \Delta d_1^{(0)}, \dots, \Delta d_{N-1}^{(0)}).$$

Then we start iterative calculation.⁷ To improve the precision and to ensure a convergence result, we introduce a relaxation coefficient C_r . At the k th stage of iteration, the expression is

$$\Delta d_n^{(k+1)} = \Delta d_n^{(k)} - C_r \lambda_k \frac{\partial F(\Delta D_n)}{\partial \Delta d_n}, \quad (\text{A4})$$

where

$$\lambda_k = F(D_n^{(k)}) \left/ \left(\sum_{n=0}^{N-1} \frac{\partial F(\Delta D_n)}{\partial d_n} \right) \right. \quad (\text{A5})$$

C_r usually takes its value from 10^{-8} to 10^2 .

Once the inequality $F(\Delta D_n^*) < \varepsilon$ is met, $D_n^* = (\Delta d_0^*, \Delta d_1^*, \dots, \Delta d_{N-1}^*)$ is then a set of solutions which has reached the predetermined accuracy. The elements' abscissae d_n^* are therefore obtained.

¹Y. Zhang, Z. Hou, and Q. Chen, "The Development of A Wide-band Stagger-tuned Ultrasonic Transducer," *Chin. J. Med. Instrum.* **9**(3), 5–10 (1985).

²G. Luan, J. Zhang, and R. Wang, *Piezoelectric Transducer and Transducer Array* (Beijing U.P., Beijing, 1990), pp. 255–266.

³R. F. Smith, "Constant Beamwidth Receiving Array for Broadband Sounder System," *Acustica* **23**, 21–26 (1970).

⁴A. G. Requicha, Design of Wideband Constant Beamwidth Acoustical Array, Saclantcen Technical Report, No. 205, NATO, unclassified, 1972.

⁵A. Macovshi, "Ultrasonic Imaging Using Array," *Proc. IEEE* **67**(4), 485–495 (1979).

⁶F. Zhou, *Marine Acoustic Transducer and Array* (National Defence Industry Press, Beijing, 1984), pp. 248–251.

⁷L. Wang, X. Zhang, *Algorithm and Program on Microcomputer* (Science Technique Press, Shang Hai, 1985), pp. 90–91.

Transient waves in a periodic stack: Experiments and comparison with analysis

Michael El-Raheb

The Dow Chemical Company, Midland, Michigan 48674

Reinhard Tham

Ernst Mach Institut für Kurzezeitdynamik, Freiburg, Germany

(Received 15 December 1995; revised 22 August 1996; accepted 25 September 1996)

Transient waves were initiated by allowing a thick PMMA disk to strike a periodic stack of ceramic layers bonded by thin weak silicone rubber layers. Pressure at interfaces of ceramic and bond layers was measured by carbon gauges along the centerline of the stack. Comparison of experimental histories with those from a 1-D analysis [J. Acoust. Soc. Am. **94**, 172–184 (1993)] and a 2-D axisymmetric analysis [J. Acoust. Soc. Am. **99**, 3513–3527 (1996)] reveals that waves propagate two-dimensionally and that flexure of the ceramic layers controls attenuation and shape of compressive wave of first arrival. Viscoelasticity of the bond material sharply reduces tensile stresses. © 1997 Acoustical Society of America. [S0001-4966(97)01702-5]

PACS numbers: 43.40.At [PJR]

INTRODUCTION

Shock hardening of structures is receiving more interest due to increasing applications. One recent application is the protection of sensitive devices on board of space probes whose mission is to land on planets at velocities sufficient to penetrate the soil and perform subterranean measurements of soil properties. One method of shock attenuation is by crushing material of collapsible structures, transforming kinetic energy to plastic work irreversibly. This method is limited to velocities not exceeding 100 m/s as volume of crushable material rises with speed nonlinearly to reach impractical limits of space and weight. Weakly coupled periodic chains exhibit dispersive properties when subjected to impulse of short duration. When combined to the concept of collapsible structures, periodic chains add an advantage by raising the limiting speed. In weakly coupled chains, attenuation of a transient pulse along the chain can be tailored to specific requirements of force or acceleration by judicious choice of geometry and material properties.

Studies on wave propagation in periodic media are mostly limited to the frequency domain (see Refs. 1–10). Reference 11 treated transient waves in 1-D weakly coupled biperiodic stacks, concluding that the first propagation zone or pass band is paramount. In this zone, hard layers act as rigid masses and weak layers act as springs. Reference 12 extended the analysis to 2-D axisymmetric stacks including flexure of the hard layers and demonstrated that flexural phase velocity is essential in spreading the pulse radially.

In this paper we describe results of an experiment designed to verify the analysis in Refs. 11 and 12 and define the limitation of 1-D theory. In Sec. I we analyze the experimental stress histories. In Sec. II we compare experimental stress histories to 1-D and 2-D numerical results. We identify regimes of propagation, explain the difference between experimental and theoretical histories, and conclude with the limitation of 1-D and 2-D linear analyses.

I. EXPERIMENT

Transient stress waves were initiated in a weakly coupled periodic stack of square aluminum nitride (AlN) ceramic tiles 10.16 cm in side, bonded by a thin weak silicone rubber, ME625.¹³ Tile and bond thicknesses were 1.27 and 0.03 cm. Piezo resistive carbon gauges 0.008 cm thick of the type C300-50-EKRTE from Dynasen Inc. were inserted at the bottom face of the first four tiles along the center line of a stack with ten tiles [see Fig. 1(a)]. Each gauge served as the active resistor of a Wheatstone quarter-bridge circuit. Just before the passage of the wave, the bridge was supplied by a 45-V pulse with a 300- μ s duration. The initially balanced bridge was unbalanced by the change in resistance of the gauge from applied pressure. The output voltage was recorded by a 200-MHz transient recorder. Given the specific gauge calibration and nonlinearity of the bridge, pressure histories are valid up to 300 μ s from impact. The high electric current in the system produced an inevitable temperature drift of the gauges yielding a fictitious pressure rise of the order of 1.75 MPa per 100 μ s.

The stack was placed in a metal casing facing the muzzle of a 6-cm-diam compressed air gun at the Ernst Mach Institute, Freiburg, Germany. The stack was struck in its center by a PMMA disk 5.75 cm in diameter and 2 cm thick, launched by a compressed air accelerator. Velocity of the disk at impact ranged from 14–58 m/s. Velocities were kept low to avoid damaging the struck ceramic tile. A laser beam in the axis of the launch tube reflecting from the top surface of the first ceramic tile allowed the alignment of stack and disk axes. This procedure resulted in a tilt smaller than 2 mrad. The assembled experimental setup of the stack is shown in Fig. 1(b).

A typical digitized output of normal stress history σ_{zz} sensed by the carbon gauges in a stack of ten (10.16 \times 10.16 \times 1.27 cm) ceramic tiles is shown in Fig. 2. The broken horizontal line labeled p_{1D} defines the computed 1-D pres-

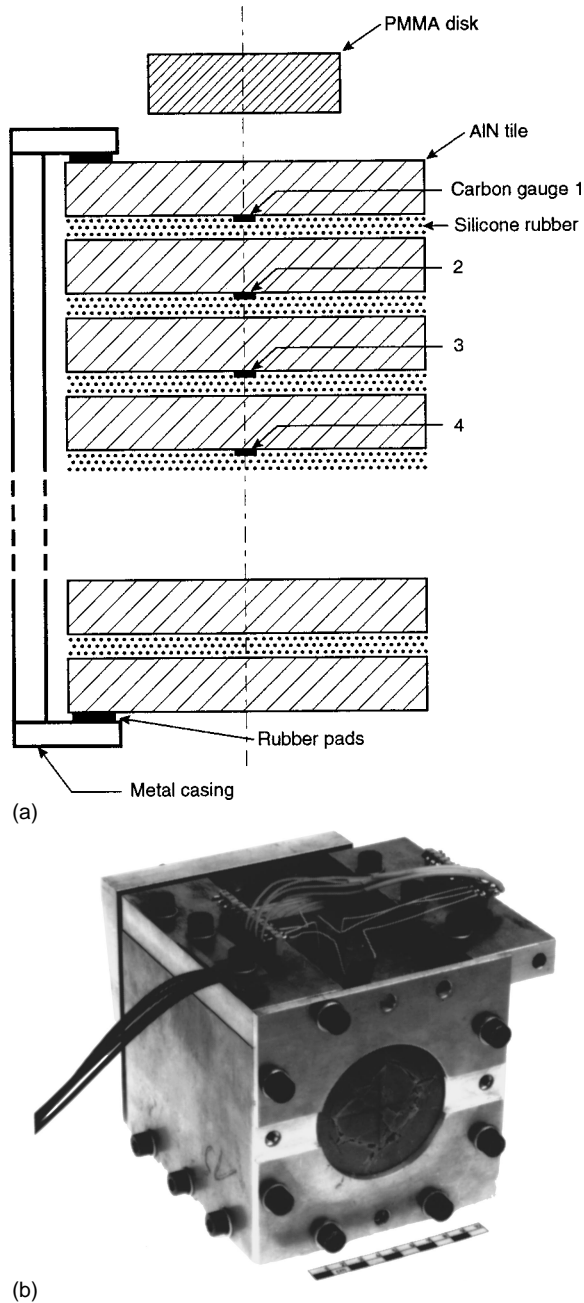


FIG. 1. (a) Schematic of experimental setup. (b) Assembled test configuration.

sure exerted by the PMMA disk upon the ceramic tile according to

$$p_{1D} = \rho_e c_e V_0, \quad (1)$$

$$\frac{1}{\rho_e c_e} = \frac{1}{\rho_c c_c} + \frac{1}{\rho_d c_d},$$

where $\rho_c c_c$ and $\rho_d c_d$ are longitudinal acoustic impedances of ceramic and disk materials, ρ and c are corresponding density and longitudinal speed of sound, $\rho_e c_e$ is the equivalent impedance for determining p_{1D} in a uniaxial strain condition, and V_0 is velocity of PMMA disk at impact in m/s. For PMMA striking AIN, substituting material properties from Table I in Eq. (1) yields $p_{1D} \approx 3.044 V_0$ MPa. Note that on the second tile the pulse is magnified, i.e., $(\sigma_{zz})_{\max} > p_{1D}$. On all

following tiles, $(\sigma_{zz})_{\max}$ attenuates typical of weakly coupled stacks.^{11,12}

At each tile, $(\sigma_{zz})_1$ of first arrival includes a double peak where the second peak is always weaker than the first. A second and third peak occur after $(\sigma_{zz})_1$. The second peak, weaker than the third and delayed by 20 μs after the first, is due to flexural reflection at the perimeter of the disk. The third peak is due to tensile reflection from the bottom tile. Those identifications are from considering flexural phase velocity in AIN ($c_{pf} = 2.3$ km/s), axial phase velocity along the stack ($c_{pz} = 3.7$ km/s), and geometry of disk and tile. The double peak in $(\sigma_{zz})_1$ is caused by axial oscillations of the tile. One final observation of the histories in Fig. 2 is that tensile stresses are very small, which may be caused by viscoelastic effects of the bond material.

II. ANALYSIS

The 1-D and 2-D axisymmetric analyses developed in Refs. 11 and 12 rely on a modal expansion solution of the coupled linear elastodynamic equations of the periodic stack. Both methods are adopted to reproduce the experimental stress histories at interfaces of layers. The effect of viscoelasticity of the bond material is then evaluated by including the standard linear viscoelastic solid in the 1-D simulation.

A. 1-D and 2-D axisymmetric analyses

Applying the 1-D analysis developed in Ref. 11 and 2-D axisymmetric analysis developed in Ref. 12 and comparing their results with the experiments yields further understanding of transient propagation in a periodic stack.

To gain an accurate pressure σ_{zz0} produced by the disk at impact, a finite volume algorithm developed in Ref. 14 was used. It assumes that PMMA and AIN materials are linear elastic for the range of velocities in the experiment. Figure 3 shows the time evolution of deformation of disk and struck tile in the first 16 μs after impact. Note the bulge along the perimeter of the disk from Poisson's effect, propagating toward the free face followed by the lifting of the edge which sets up a shear wave propagating back toward the axis. This lifting diminishes average stress at the interface as Fig. 4. shows by the attenuation of σ_{zz0} with time. Unlike the rectangular pressure profile used to compute p_{1D} , decaying oscillations about a downward sloping line ending 14 μs after impact is the 2-D normalized pressure pulse in Fig. 4. It was used to force both 1-D and 2-D analyses to follow.

The material properties of ceramic and bond are listed in

TABLE I. Properties of AIN ceramic and polymer bond materials.

| | AIN ceramic | Polymer bond |
|--|-------------------|-------------------|
| Modulus E (MPa) | 310×10^3 | 69 |
| Mass density ρ (kg/m ³) | 3200 | 1070 |
| Poisson ratio ν | 0.25 | 0.49 |
| Longitudinal speed c_L (km/s) | 9.8 | 1.05 ^a |
| Flexural phase velocity c_{pf} (km/s) | 2.3 ^b | not relevant |

^aUniaxial strain.

^bFor a 1.27-cm-thick plate.

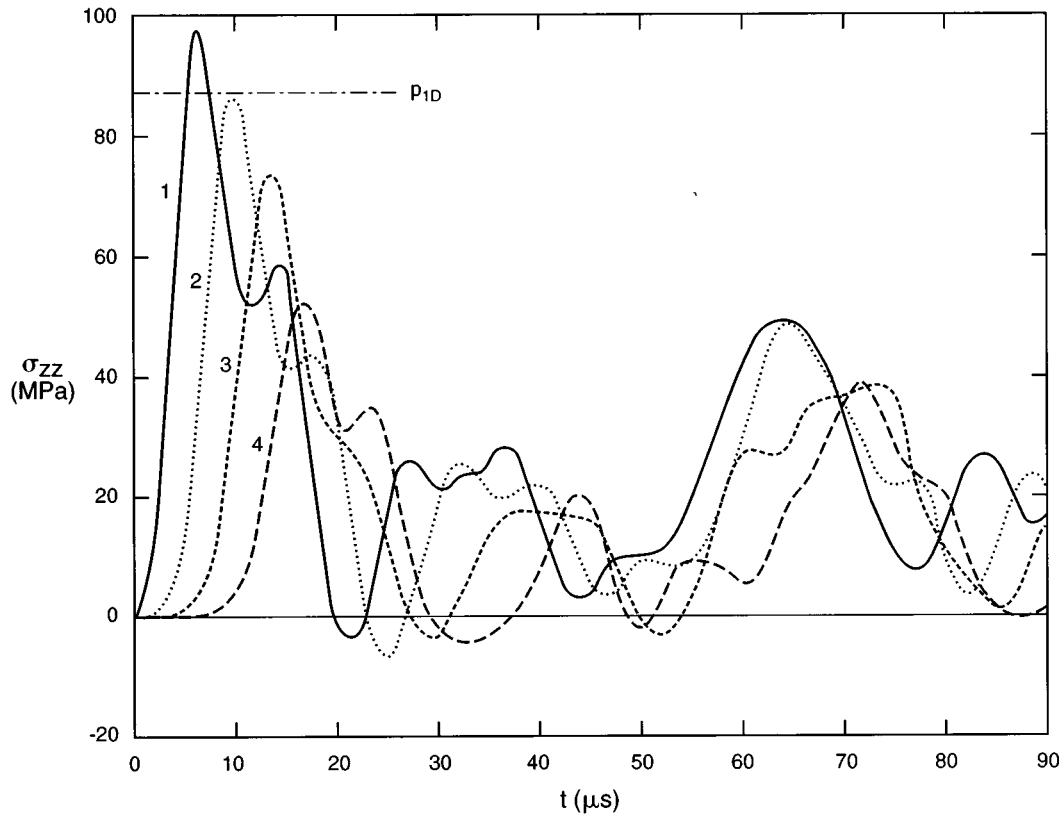


FIG. 2. Experimental histories at bottom of first to fourth tile $V_0 = 28.8$ m/s, $P_{1D} = 87.55$ MPa.

Table I. In one dimension, the equivalent bond modulus in uniaxial strain is

$$E_{be} = \frac{(1 - \nu_b)E_b}{(1 + \nu_b)(1 - 2\nu_b)}. \quad (2)$$

Histories of normalized axial stress $\bar{\sigma}_{zz}$ resulting from the 1-D simulation¹¹ with constant planform area are shown in Fig. 5. Note that, among other differences, $(\bar{\sigma}_{zz})_{\max}$ is not

attenuated along the stack. As the pressure pulse propagates through the layers, in the real stack flexural waves radially extend the footprint of pressure. Viewed in this way, the effective area of layers increases along a 1-D stack. Indeed, a 1-D simulation of a stack with sets varying in planform area along the direction of propagation produced the histories in Fig. 6(a) and (b) for two different planform area distributions. In Fig. 6(a), the distribution of tile area A_i along the stack follows an extension in radius of the n th ceramic layer r_n according to

$$r_n = r_d + (n-1)c_{pf}\Delta t_s, \quad (3)$$

$$\Delta t_s = c_{pz}/h_s,$$

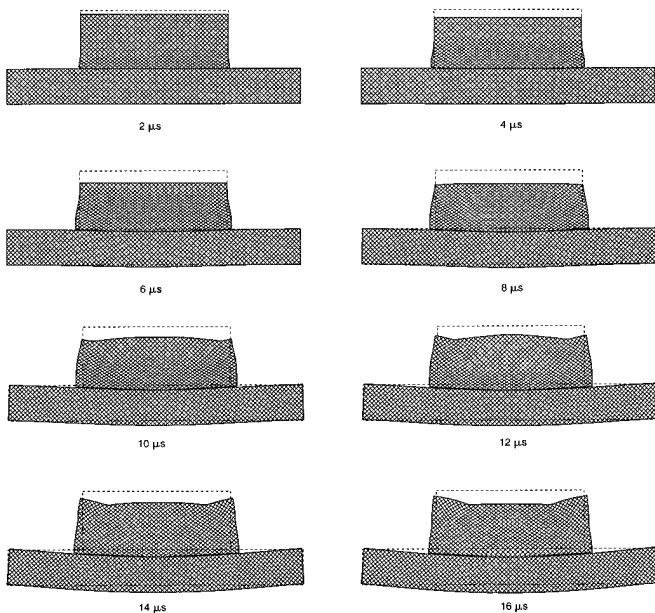


FIG. 3. Evolution of deformation pattern of PMMA disk striking AlN tile.

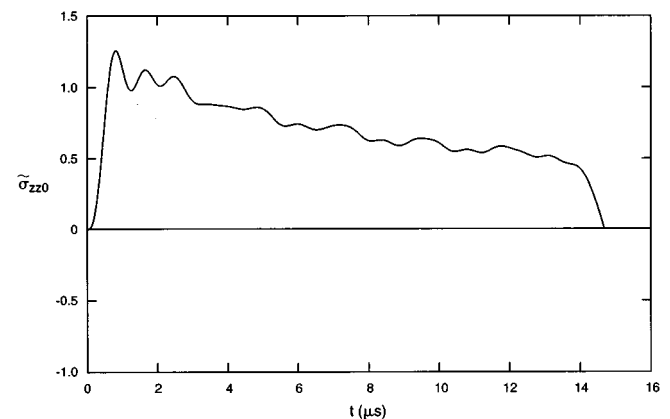


FIG. 4. History of normalized average pressure on struck tile.

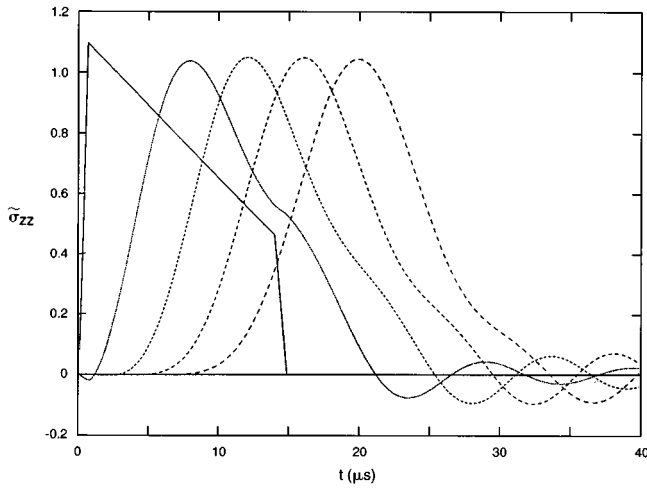


FIG. 5. Normalized $\tilde{\sigma}_{zz}$ histories from 1-D analysis with constant plan form area.

where r_d is radius of disk, $h_s = (h_c + h_b)$ is thickness of a periodic set, c_{pf} is flexural phase velocity in the ceramic tile, and c_{pz} is axial phase velocity along the stack measured experimentally. Note that in Fig. 6(a) $(\tilde{\sigma}_{zz})_{1 \max}$ attenuates along the stack and is lower than the corresponding experi-

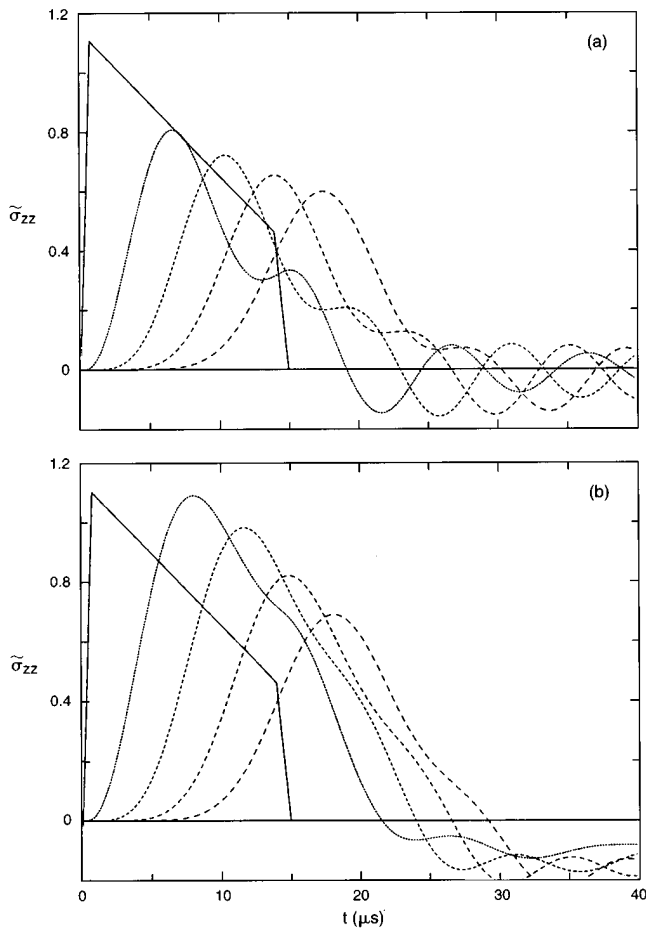


FIG. 6. Histories of $\tilde{\sigma}_{zz}$ in 1-D stack with 2 different plan form area distributions. (a) $A_i/A_1 \rightarrow 1.0, 1.5, 1.9, 2.2, 2.5, 2.8, 3.1, 3.4, 3.7, 4.0$; (b) $A_i/A_1 \rightarrow 1.0, 1.0, 1.3, 1.8, 2.4, 3.0, 3.6, 4.0, 4.0, 4.0$.

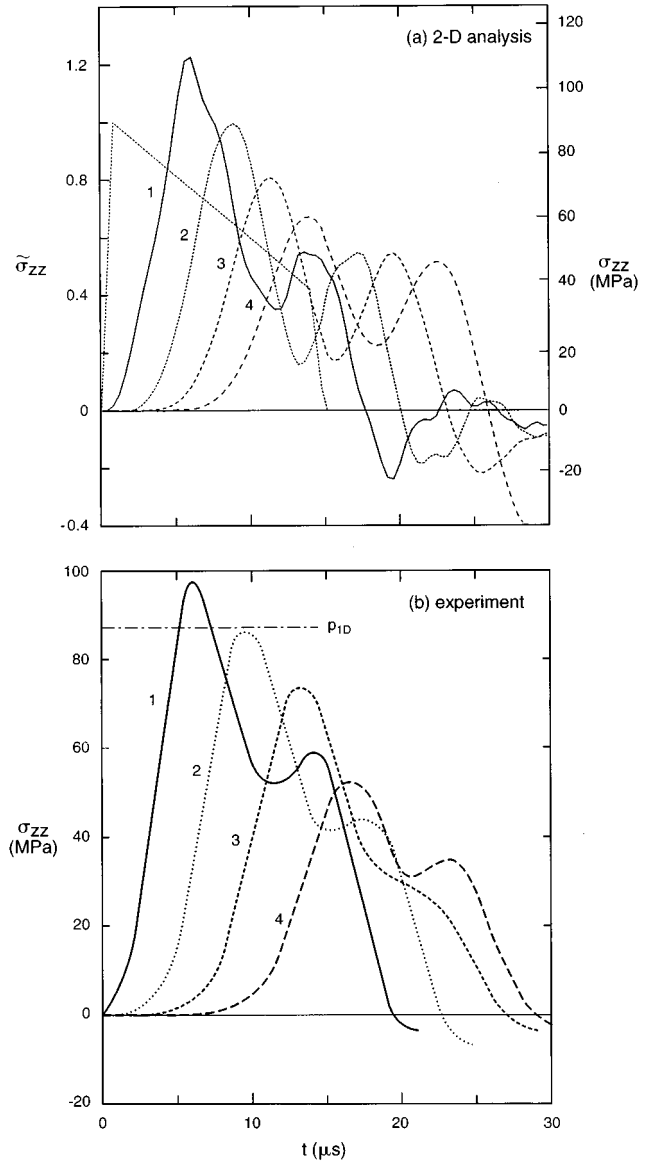


FIG. 7. Comparison of peaks of first arrival $(\sigma_{zz})_1$ from 2-D analysis and experiment.

mental values. An explanation is that in one dimension, tiles move as rigid bodies while, in two dimensions, tiles flex radially as they move axially. The radial deformation reduces contact area at the interface of consecutive tiles which in turn reduces effective planform area A_i . Considering this reduction, a second distribution of A_i produces the histories in Fig. 6(b) where now a better match with experiment of $(\tilde{\sigma}_{zz})_{1 \max}$ is achieved.

In Fig. 6(a), $(\tilde{\sigma}_{zz})_{1 \max}$ of all layers includes a double peak similar to that in the experiment. Clearly, this feature cannot be attributed to flexure but is caused from axial oscillations of the ceramic layers at the natural frequency of the set $\omega_{\text{set}} = (E_{be}/(\rho_c h_c h_b))^{1/2}$. When the set period $T_{\text{set}} = 2\pi/\omega_{\text{set}}$ is shorter than $2\Delta t_f$, where Δt_f is time interval of the forcing pulse, more than one peak will appear in $(\tilde{\sigma}_{zz})_1$. However, if $T_{\text{set}} > 2\Delta t_f$, only one peak will appear. In the present stack, $T_{\text{set}} = 20 \mu\text{s}$ while $2\Delta t_f = 28 \mu\text{s}$, which explains the double peak.

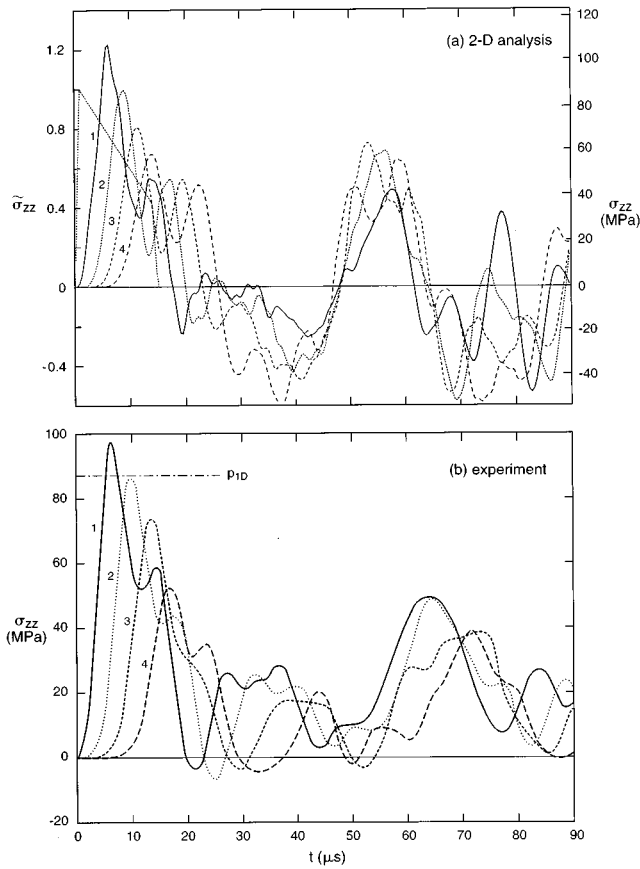


FIG. 8. Comparison of σ_{zz} histories including reflections, from 2-D analysis and experiment.

The preceding 1-D analysis demonstrates that radial propagation from flexure is indispensable for describing wave propagation even in such extreme cases as when the impactor's diameter is half that of the struck tile.

A 2-D simulation¹² based on the geometric and material properties in Table I yielded the histories of $(\tilde{\sigma}_{zz})_1$ shown in Fig. 7(a). Note the following:

- Peak stress of first arrival $(\sigma_{zz})_{1 \max}$ at tile 2 is greater than $(\sigma_{zz0})_{\max}$ with a magnification matching that in Fig. 7(b) of the experiment.
- At the following tiles, $(\sigma_{zz})_{1 \max}$ also matches those in Fig. 7(b).
- Histories of $(\sigma_{zz})_1$ at all tiles include the double peak featured in Fig. 7(b).
- In Fig. 8(a) the second peak is negative and shifted from the first by $20 \mu\text{s}$. It is caused by reflection from the tile's outer boundary. As will be shown below, this second peak in the experiment [see Fig. 8(b)] is positive due to viscoelastic strain of the bond material.
- The third peak at $53 \mu\text{s}$ [see Fig. 8(a)] is caused by reflection from the bottom of the stack, while in Fig. 8(b) that third peak occurs at $63 \mu\text{s}$. The deficit of $10 \mu\text{s}$ is caused by the difference in the number of tiles used in experiment and analysis. The experiment included ten tiles while the 2-D analysis included eight tiles to reduce computational effort. In the experiment, the first pulse has to travel over four additional sets

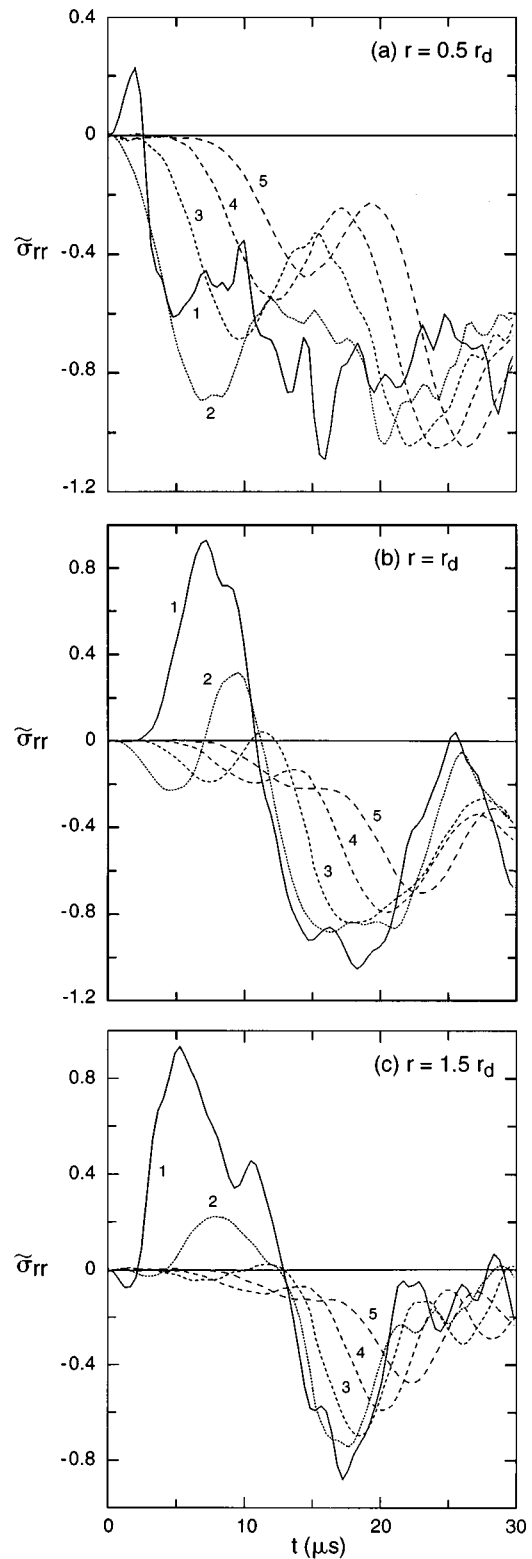


FIG. 9. Normalized radial stress histories $\tilde{\sigma}_{rr}$ on top of first five tiles at radial stations $r = 0.5, r_d, 1.5r_d$.

than in analysis before the reflected pulse reaches the top surface of the stack. Since travel time over a set $\Delta t_s \approx 3 \mu\text{s}$, arrival time in the experiment should be longer by approximately $12 \mu\text{s}$, which is indeed the case.

- Contrary to 1-D where reflection from the bottom of

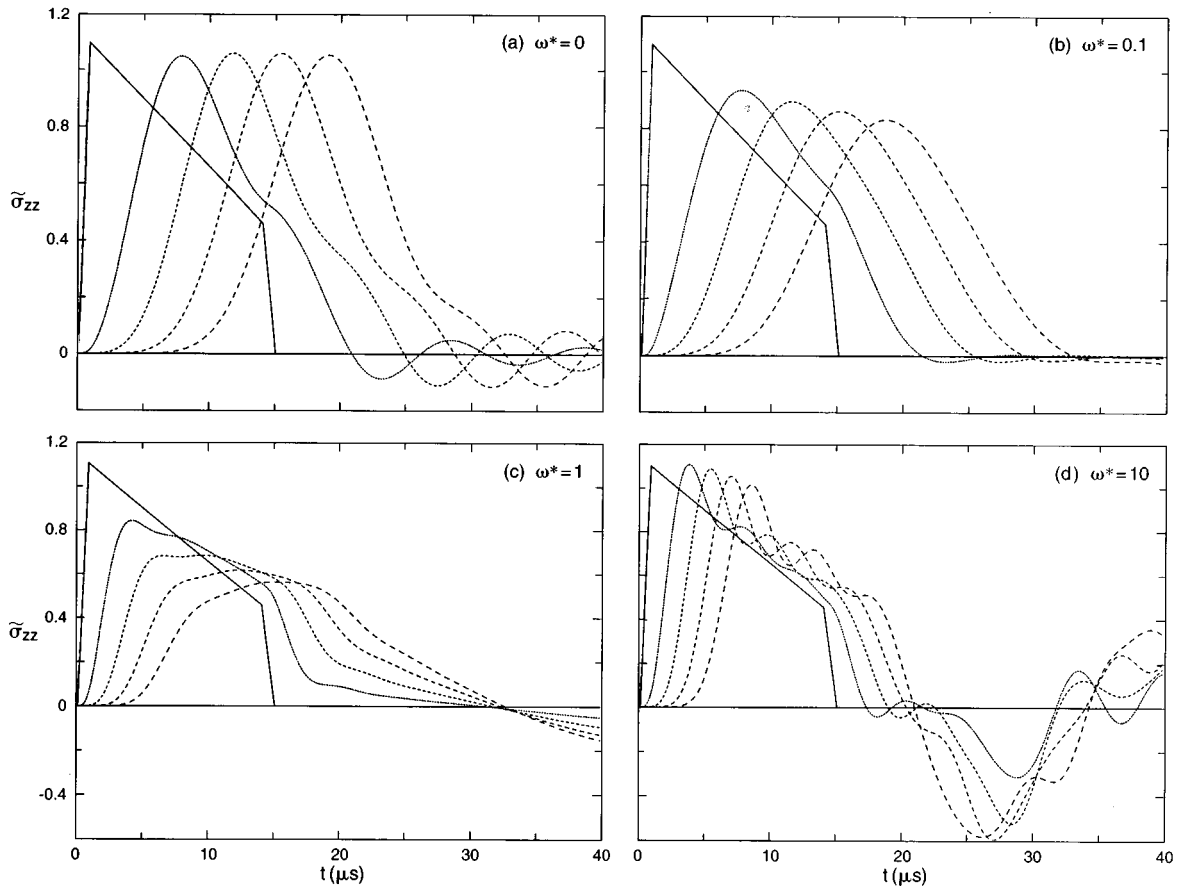


FIG. 10. Histories of $\tilde{\sigma}_{zz}$ in 1-D stack with constant plan from area bonded by viscoelastic layers ($\omega^* = \omega_{\text{set}}\sqrt{\tau_{\sigma}\tau_e}$).

the stack causes tensile stress at the interfacial bond, experiment and 2-D theory reveal that this reflected wave is compressive as shown in Fig. 8(a) and (b). Applied pressure from impact flexes the struck tile as illustrated in Fig. 3. Succeeding tiles also flex but at a time delayed from finite phase velocity along the stack's axis. When the wave reflects from the bottom of the stack, curvature of the bottom tile is reduced. This reduction in curvature then propagates backward toward the top tile at delayed times. The time delay produces a mismatch in curvature between adjacent tiles which in turn compresses the bond.

One discrepancy between histories in Fig. 7(a) and those in Fig. 7(b) is axial phase velocity c_{pz} computed by

$$c_{pz} \approx \frac{(h_c + h_b)}{\Delta t_{\sigma}}, \quad (4)$$

where $(h_c + h_b)$ is total thickness of a periodic set and Δt_{σ} is time interval between peaks at two consecutive tiles. From Fig. 7(b)

$$(c_{pz})_{\text{exp}} \approx \frac{1.3 \times 10^{-5}}{3.5 \times 10^{-6}} = 3.7 \text{ km/s},$$

and from Fig. 7(a)

$$(c_{pz})_{\text{anal}} \approx \frac{1.3 \times 10^{-5}}{2.6 \times 10^{-6}} = 5.0 \text{ km/s}.$$

The source of this discrepancy is the following. The speed of sound in the bond c_b used in the analysis was determined from the experimental phase velocity computed from (4) and the 1-D scaling low:¹¹

$$c_{pz} \approx c_b \left(\frac{\rho_b h_c}{\rho_c h_b} \right)^{1/2}, \quad (5)$$

where (ρ_b, h_b) is bond density and thickness, and (ρ_c, h_c) is ceramic density and thickness. Relation (5) assumes that a ceramic tile acts as an unconstrained rigid mass and the bond acts as a linear spring.¹⁵ In two dimension, only that circular portion of the tile bounded by the flexural wave front moves. The portion outside the wavefront adds its own resistance. Therefore, a value of c_{pz} in two dimensions may be realized by a $c_b < (c_b)_{1D}$ because the total spring reaction includes a contribution from material outside the wavefront. Using $(c_b)_{1D}$ in the 2-D analysis, then, results in a too-stiff bond, so $(c_{pz})_{\text{anal}} > (c_{pz})_{\text{exp}}$.

Another discrepancy is the negative stresses among the analytical histories. As will be demonstrated in the analysis to follow, the reduced tensile stress is caused by viscoelastic strain of the bond material, an effect not included in the 1-D and 2-D simulations.^{11,12}

Figure 9(a)–(c) plots histories of $\tilde{\sigma}_{rr}$ from 2-D analysis on top of the first five tiles in the stack at three radial stations $r = 0.5r_d$, r_d , and $1.5r_d$. Note that on the first tile $\tilde{\sigma}_{rr}$ develops a tensile precursor whose peak increases radially reach-

ing a magnitude close to $|\tilde{\sigma}_{zz0}|_{\max}$ at the perimeter of the disk $r=r_d$. For an impact velocity $v_0=58$ m/s, $|\sigma_{zz0}|_{\max}\approx 1.15\rho_{1D}\approx 203$ MPa, which is above tensile strength of AlN, explaining the formation of circumferential cracks illustrated in Fig. 1(b).

B. Effect of viscoelasticity of bond material

To demonstrate the effect of bond viscoelasticity in one dimension, the elastic bond material is replaced by a linear viscoelastic solid with constitutive law¹⁶

$$\sigma + \tau_\varepsilon \dot{\sigma} = E_{R\varepsilon}(\varepsilon + \tau_\sigma \dot{\varepsilon}), \quad (6)$$

where $(\tau_\sigma, \tau_\varepsilon)$ are time constants of creep and relaxation and $E_{R\varepsilon}$ is rubbery modulus in uniaxial strain when $\dot{\varepsilon}=0$. In the limit when $\dot{\varepsilon}$ and $\dot{\sigma}\rightarrow\infty$, the material becomes glassy and from (6)

$$\sigma = E_{R\varepsilon} \frac{\tau_\sigma}{\tau_\varepsilon} \dot{\varepsilon} = E_{G\varepsilon} \dot{\varepsilon}; \quad \Rightarrow E_{G\varepsilon} = \frac{\tau_\sigma}{\tau_\varepsilon} E_{R\varepsilon}. \quad (7)$$

Treating the tiles as rigid masses, the governing equations are modified to include viscoelasticity of the bond:

$$\begin{aligned} m_1 \ddot{u}_1 &= \sigma_0 - \sigma_1, \\ m_i \ddot{u}_i &= \sigma_{i-1} - \sigma_i, \\ m_n \ddot{u}_n &= \sigma_{n-1}, \\ \sigma_i + \dot{\sigma}_i \tau_\sigma &= E_{R\varepsilon}(\varepsilon_i + \dot{\varepsilon}_i \tau_\sigma), \\ \varepsilon_i &= (u_i - u_{i+1})/h_b, \\ m_i &= \rho_c h_c, \quad \tau_\sigma = \tau_\varepsilon E_{G\varepsilon}/E_{R\varepsilon}, \end{aligned} \quad (8)$$

where u_i is axial displacement of the i th mass m_i , σ_i is axial stress between layers i and $i+1$, and σ_0 is the external stress acting on m_1 . Assume the following bond properties:

$$E_{R\varepsilon} = 1.211 \text{ GPa}, \quad E_{G\varepsilon} = 6.9 \text{ GPa}, \quad \omega^* = 0.1, 1, 10, \quad (9)$$

where $\omega^* = \omega_{\text{set}} \sqrt{\tau_\sigma \tau_\varepsilon}$ and ω_{set} is resonant frequency of the periodic set with rubbery modulus $E_{R\varepsilon}$ (Ref. 15) and $\omega_{\text{set}} = (E_{R\varepsilon}/(\rho_c h_c h_b))^{1/2}$. Figure 10(a)–(c) plots 1-D histories of $(\tilde{\sigma}_{zz})_1$ for the stack with material properties from Table I but with the viscoelastic bond in (9) for three values of ω^* . Clearly the viscoelastic effect is to reduce tensile stress. Note that maximum damping occurs when $\omega^*=1$ (see Ref. 16).

III. CONCLUSION

Nondestructive experiments were performed on periodic stacks of AlN tiles bonded by a thin weak silicone rubber. Pressure measured by carbon gauges on the bottom surface of ceramic tiles was higher than applied pressure on the first tile, and attenuated on all tiles to follow. The close match of experimental histories to 2-D analysis confirmed how flexure controls the evolution of the pulse by spreading it radially. Flexure also modifies the nature of the reflected wave from the bottom of the stack, changing it from tensile to compressive. The absence of normal tensile stress in the experimental histories may be caused by viscoelastic effects of the bond material.

¹W. Thomson, "Transmission of Elastic Waves Through a Stratified Medium," *J. Appl. Phys.* **21**, 89–93 (1950).

²N. A. Haskel, "The Dispersion of Surfaced Waves in Multi-Layered Media," *Bull. Seismic Soc. Am.* **43**, 17–34 (1953).

³D. L. Anderson, "Elastic Wave Propagation in Layered Anisotropic Media," *J. Geophys. Res.* **66**, 2953–2963 (1961).

⁴C. T. Sun, J. D. Achenbach, and G. Herrmann, "Time Harmonic Waves in a Stratified Medium, Propagating in the Direction of the Layering," *J. Appl. Mech.* **35**, 408–411 (1968).

⁵E. H. Lee and W. H. Yang, "On Waves in Composite Materials with Periodic Structure," *SIAM (Soc. Ind. Appl. Math.) J. Appl. Math.* **25**, 492–488 (1973).

⁶T. J. Delph, C. Herrmann, and R. K. Kaul, "Harmonic Wave Propagation in a Periodically Layered Infinite Elastic Body: Antiplane Strain," *J. Appl. Mech.* **45**, 343–349 (1978).

⁷R. C. Engels and L. Meirovitch, "Response of Periodic Structures by Modal Analysis," *J. Sound Vib.* **56**, 481–493 (1978).

⁸A. A. Golebiewska, "On Dispersion of Periodically Layered Composites in Plane Strain," *J. Appl. Mech.* **47**, 206–207 (1980).

⁹A. H. Shah and S. K. Datta, "Harmonic Waves in a Periodically Laminated Medium," *Int. J. Solids Struct.* **18**, 301–317 (1982).

¹⁰A. K. Mal, "Wave Propagation in Layered Composite Laminates Under Periodic Surface Loads," *Wave Motion* **10**, 257–266 (1988).

¹¹M. El-Raheb, "Transient Elastic Waves in Finite Layered Media: One Dimensional Analysis," *J. Acoust. Soc. Am.* **94**, 172–184 (1993).

¹²M. El-Raheb and P. Wagner, "Transient elastic waves in finite layered media: Two-dimensional axisymmetric analysis," *J. Acoust. Soc. Am.* **99**, 3513–3527 (1996).

¹³R. Tham, "Transient Elastic Waves in Finite Layered Media, Experimental Results," EMI Report E (6/95).

¹⁴M. El-Raheb and P. Wagner, "Wave propagation in a plate after impact by a projectile," *J. Acoust. Soc. Am.* **82**, 498–505 (1987).

¹⁵M. El-Raheb, "Simplified Analytical Models of Uniaxial Waves in a Periodic Stack," to appear in *Int. J. Solids Struct.*

¹⁶Y. C. Fung, *Foundations of Solid Mechanics* (Prentice-Hall, Englewood Cliffs, NJ, 1965), 1st ed.

Structural and acoustical wave interaction at a wedge-shaped junction of fluid-loaded plates

A. N. Norris

Department of Mechanical and Aerospace Engineering, Rutgers University, Piscataway, New Jersey 08855

A. V. Osipov

Institute of Radiophysics, The St. Petersburg State University, Uljanovskaja 1-1, Petrodvorets 198904, Russia

(Received 4 March 1996; accepted for publication 4 October 1996)

Two semi-infinite elastic plates are joined along a line forming a wedge structure with unilateral fluid loading in the outer sector of the two plates. The structure is modeled using thin plate theory, allowing freely propagating flexural and longitudinal waves. The junction is mechanically connected with an applied force and moment acting there to simulate a possible internal connection. The general two-dimensional solution is described for incidence of time harmonic structural or acoustical waves. The total pressure is expressed as a Sommerfeld integral, the integrand comprising Malyuzhinets functions and particular solutions of certain difference equations. The junction conditions reduce to a system of four linear equations. Numerical examples indicate the coupling between the modes for welded steel plates in water. Acoustic plane-wave incidence on the flattest junction considered is converted almost equally, in terms of energy, among diffracted flexural and longitudinal waves. The coupling to flexural energy increases with the angle of the water wedge sector, at the expense of the longitudinal energy which vanishes in the limit as the water occupies the entire domain except for a strip comprising the two plates. An incident longitudinal wave generates relatively little acoustic sound for all wedge angles considered, with most of its energy redistributed among structural modes. The acoustical diffraction is generally greater for flexural incidence. Comparison with the dry structural diffraction coefficients indicates that the fluid loading effects for steel and water configurations can be significant for frequencies less than one-fifth of the coincidence frequency, but are small for higher frequencies. © 1997 Acoustical Society of America. [S0001-4966(97)03802-2]

PACS numbers: 43.40.Dx, 43.40.Rj [CBB]

INTRODUCTION

We consider a wedge configuration formed by two elastic plates joined at an angle, with the simplification that the plates are thin and the complication that the structure is loaded unilaterally by an acoustic fluid. The thin plate assumption means that only the basic symmetric and antisymmetric structural modes need to be considered, corresponding to longitudinal and flexural waves. The major difficulty is to simultaneously satisfy the structural dynamic equations and the Helmholtz equation for the acoustic pressure, subject to the continuity conditions at the solid-liquid boundary, and the junction conditions at the vertex. We restrict attention here to the two-dimensional configuration, as depicted in Fig. 1, for which all motion is in the plane normal to the line joining the plates. Our objective is to quantitatively understand the various wave interaction mechanisms, such as structural to structural or acoustic to structural, and the significance of the fluid loading on these interactions.

Similar problems for flat fluid-loaded structural configurations, such as two connected semi-infinite plates¹ or infinite plates with line attachments,^{2,3} have been studied in detail. They differ both physically and mathematically from the present situation. First, there is generally no coupling of the longitudinal structural motion with the acoustic and flexural waves. Thus, the in-plane longitudinal motion is completely

decoupled. Second, conventional Fourier transform and Wiener-Hopf techniques may be used for problems defined on rectangular coordinates, e.g., Ref. 4, but do not suffice for wedge configurations. The general procedure for solving acoustic diffraction from wedges with higher-order boundary conditions has only recently been developed,^{5,6} and has been applied successfully to membrane boundaries,^{6,7} and also to plates. Thus, Osipov⁸ showed that writing the acoustic field as a Sommerfeld integral transform reduces the plate boundary conditions to functional difference equations for the pressure transform. He also provided an explicit procedure for solving these equations using Malyuzhinets functions and Fourier transforms.

In this paper we discuss the general solution for various contact conditions along the line where the plates meet, including the case of welded contact for which displacements and forces are continuous. This case is of most practical significance, but unfortunately, was not considered by Osipov.⁸ The problem involves six continuity conditions at the junction: two for the two velocity components, two more for the force components, and one each for the bending moment and the rotation. We showed in a related paper⁹ that the six continuity conditions can be expressed solely in terms of the transverse plate displacement as a set of four conditions. Approximate results appropriate to wedge configurations that are almost flat were also derived in Ref. 9, but the general

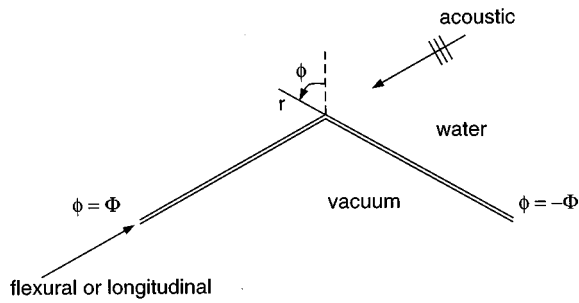


FIG. 1. The wedge configuration.

case was not considered. It is interesting to note that excitation by an incident longitudinal wave produces no forcing in the fluid or flexural equations, but the four junction conditions involve an effective line force at the vertex, the amplitude of which is related to the incident wave amplitude. Thus, longitudinal incidence is equivalent to the radiation problem with a source at the vertex.

The outline of the paper is as follows. The problem is defined in Sec. I, and the general solution procedure based on the Sommerfeld integral transform is described in Sec. II. For a given structure and an incident structural or acoustic wave the problem is reduced to finding eight constants: the values of the normal displacement and its first three derivatives on both plates at the vertex. In Sec. III a system of linear equations for the eight unknowns is obtained by applying appropriate regularity conditions on the Sommerfeld transform and by applying the junction conditions, thus completing the solution. The diffracted structural wave amplitudes are defined and an energy conservation relation is described in Sec. IV. We conclude with a discussion of several illustrative numerical examples in Sec. V.

I. BASIC EQUATIONS

The plate configuration and an incident acoustic wave are depicted in Fig. 1. We are interested in the time harmonic acoustic pressure field $p = p(r, \phi)e^{-i\omega t}$ satisfying the Helmholtz equation outside the wedge,

$$\nabla^2 p + k^2 p = 0, \quad 0 < r < \infty, \quad -\Phi < \phi < \Phi, \quad (1)$$

where $k = \omega/c$ is the acoustic wave number, and r, ϕ are polar coordinates relative to the contact line. The equations of motion and continuity on the wedge faces are

$$-B_{\pm} \frac{d^4 w_{\pm}}{dr^4} + m_{\pm} \omega^2 w_{\pm} = p(r, \pm \Phi), \quad 0 < r < \infty, \quad (2)$$

$$\rho \omega^2 w_{\pm}(r) = \mp \frac{1}{r} \frac{\partial p}{\partial \phi}(r, \pm \Phi), \quad 0 < r < \infty.$$

Here, $w(r)$ is the displacement into the fluid, and m, B , and ρ are the plate density, bending stiffness, and the fluid density. In general, the plate parameters may be different for each face of the wedge, so we denote them as $w_{\pm}, B_{\pm}, m_{\pm}$, where \pm signs correspond to the upper ($\phi = \Phi$) and lower ($\phi = -\Phi$) faces, respectively.

At this stage we define some parameters which simplify the analysis later: the plate flexural wave numbers

$\kappa_{\pm} = (m_{\pm} \omega^2 / B_{\pm})^{1/4}$, and the nondimensional frequency parameters $\Omega_{\pm} = k^2 / \kappa_{\pm}^2 = \omega / \omega_c^{\pm}$ where ω_c^{\pm} are the plate coincidence frequencies, $\omega_c^{\pm} = c^2 \sqrt{m_{\pm} / B_{\pm}}$. The remaining plate dynamics can be represented by frequency independent dimensionless fluid-loading parameters,

$$\epsilon_{\pm} = \frac{\rho \Omega_{\pm}}{k m_{\pm}}, \quad \delta_{\pm} = \frac{c_{\pm}}{c}, \quad (3)$$

where $c_{\pm} = \sqrt{C_{\pm} / m_{\pm}}$ is the longitudinal wave speed and C_{\pm} is the extensional stiffness. Note that both ϵ_{\pm} and δ_{\pm} are also independent of the plate thicknesses: thus, for Kirchhoff thin plate theory $\epsilon_{\pm} = \delta_{\pm} \rho / (\rho_{\pm} \sqrt{12})$ and $\delta_{\pm} = c^{-1} \sqrt{E_{\pm} / [\rho_{\pm} (1 - \nu_{\pm}^2)]}$, where E_{\pm}, ρ_{\pm} , and ν_{\pm} are Young's modulus, volumetric density and Poisson's ratio, respectively.

The excitation may arise from a variety of sources: (i) an incident acoustic plane wave as shown in Fig. 1,

$$p_i(r, \phi, \phi_0) = P_0 \exp[-ikr \cos(\phi - \phi_0)], \quad (4)$$

(ii) an incident subsonic flexural wave on the plate $\phi = \pm \Phi$ is also given by (4) with complex-valued incident angle $\phi_0 = \pm(\Phi - \theta_1^{\pm})$, where θ_1^{\pm} are defined below. Alternatively, (iii) the excitation may be an incident longitudinal wave on either plate,

$$u_{\pm}^{\text{inc}}(r) = U_0^{\pm} \exp(-i\omega r / c_{\pm}), \quad (5)$$

where $u_{\pm}^{\text{inc}}(r)$ are the in-plane displacement components of the plates in the radial direction. In order to make the different incident wave types have consistent amplitudes, let $S_0^{\pm} = \omega k Z_{\pm} U_0^{\pm}$, or

$$\omega k Z_{\pm} u_{\pm}^{\text{inc}}(r) = S_0^{\pm} \exp(-i\omega r / c_{\pm}), \quad (6)$$

where $Z_{\pm} = m_{\pm} c_{\pm}$ are the longitudinal wave impedances. Thus, S_0^{\pm} have the same units (pressure) as P_0 . We note that the Poisson effect is ignored here, and consequently the incident longitudinal waves have no pressure in the fluid. They enter the problem explicitly through the junction conditions. We will see that they can be considered by applying an equivalent force at the junction, see (44) below. In general, any one of the three types of incident waves excites all others. The central problem here is to determine the relative coupling amplitudes.

II. GENERAL SOLUTION

A. Field representation and functional equations

We seek the solution in the form of a Sommerfeld integral

$$p(r, \phi) = \frac{1}{2\pi i} \int_{\gamma} e^{-ikr \cos \alpha} S(\alpha + \phi) d\alpha$$

$$= \frac{1}{2\pi i} \int_{\gamma_+} e^{-ikr \cos \alpha} [S(\alpha + \phi) - S(-\alpha + \phi)] d\alpha. \quad (7)$$

The contour $\gamma = \gamma_+ \cup \gamma_-$, where γ_+ is a loop in the upper half of the complex α plane, beginning at $\pi/2 + i\infty$, ending at $-\pi/2 + i\infty$, with $\text{Im} \alpha$ lying above the maximum value of

$|\text{Im}(\theta_n^\pm)|$, where the complex angles θ_n^\pm $n=1,2,\dots,5$, are defined below. The contour γ_- is the image of γ_+ under inversion about the origin $\alpha=0$. The “transform” $S(\alpha)$ should be a meromorphic function of a complex variable α , have a single pole with residue P_0 at $\alpha=\phi_0$ in the strip $\Pi_0=\{\alpha:|\text{Re } \alpha|\leq\Phi\}$ to reproduce the incident field (4), and be bounded when $\text{Im}\alpha\rightarrow\pm\infty$ satisfying $S(i\infty)=-S(-i\infty)$ without loss of generality.

The Sommerfeld integral (7) is closely related to the Laplace transform. Define the transform

$$\mathcal{A}[f(r)]\equiv\hat{f}(\alpha)=\frac{i}{2}k\sin\alpha\int_0^\infty e^{ikr\cos\alpha}f(r)dr, \quad (8)$$

with inverse transform¹⁰

$$\mathcal{A}^{-1}[\hat{f}]=f(r)=\frac{1}{2\pi i}\int_\gamma e^{-ikr\cos\alpha}\hat{f}(\alpha)d\alpha. \quad (9)$$

Note that $\hat{f}(\alpha)=(i/2)k\sin\alpha F(-ik\cos\alpha)$ where $F(s)$ is the Laplace transform of $f(r)$, and

$$\mathcal{A}\left[\frac{df}{dr}(r)\right]=-ik\cos\alpha\hat{f}(\alpha)-\frac{i}{2}k\sin\alpha f(0). \quad (10)$$

Equation (7) implies that

$$\hat{p}(\alpha,\phi)=\mathcal{A}[p(r,\phi)]=S(\alpha+\phi), \quad (11)$$

and the transform of the normal displacement is

$$\hat{w}_\pm(\alpha)=\pm\frac{ik}{\rho\omega^2}\sin\alpha\hat{p}(\alpha,\pm\Phi). \quad (12)$$

The transform of the boundary conditions (2) is therefore, using (10)–(12),

$$\begin{aligned} \mathcal{A}\left[-B_\pm\frac{d^4w_\pm}{dr^4}+m_\pm\omega^2w_\pm-p\right] \\ =L_\pm(\alpha)S(\alpha\pm\Phi)+\frac{ik}{2}\sin\alpha B_\pm[w_\pm'''(0) \\ -ik\cos\alpha w_\pm''(0)-k^2\cos^2\alpha w_\pm'(0) \\ +ik^3\cos^3\alpha w_\pm(0)], \end{aligned} \quad (13)$$

where

$$L_\pm(\alpha)=\pm i\frac{\Omega_\pm}{\epsilon_\pm}\sin\alpha(1-\Omega_\pm^2\cos^4\alpha)-1. \quad (14)$$

The inverse transform of (13) must be zero for all positive r , implying that the right-hand side of (13) must be an odd function of α . This leads to a pair of functional equations

$$\begin{aligned} L_\pm(\alpha)S(\alpha\pm\Phi)-L_\pm(-\alpha)S(-\alpha\pm\Phi) \\ =2\sin\alpha\sum_{n=1}^4 C_n^\pm\cos^{n-1}\alpha, \end{aligned} \quad (15)$$

with constants C_n^\pm , $n=1,2,3,4$ which depend upon the normal displacement and its derivatives at the tip:

$$C_n^\pm=\frac{B_\pm}{2}(-ik)^n\frac{d^{4-n}w_\pm}{dr^{4-n}}(0). \quad (16)$$

Thus, the problem is reduced to a system of functional equations (15) with eight constants C_n^\pm , $n=1,2,3,4$, which are to be determined.

B. The plate angles

The general solution depends crucially upon the angles θ_n^\pm , $\text{Re } \theta_n^\pm\in(-\pi/2,\pi/2)$, $n=1,\dots,5$, defined by

$$L_\pm(\mp\theta_n^\pm)=0, \quad (17)$$

or $\sin\theta_n^\pm=X_n^\pm$, where X_n^\pm , $n=1,\dots,5$ are the roots of the equation $F_\pm(X_n^\pm)=0$, and

$$F_\pm(X)=X^5-2X^3-(\Omega_\pm^{-2}-1)X+i\epsilon_\pm/\Omega_\pm^3. \quad (18)$$

By analogy with optics, θ_n^\pm may be interpreted as Brewster angles for each plate. They are related to the structural wave numbers of infinite plates through the connection $\gamma=ik\sin\theta_n^\pm$, where γ is the commonly used decay wave number, e.g., Ref. 11. Crighton¹² has examined the root structure of the related fifth-order polynomial equation for γ [Eq. (3.1) of Ref. 12]. Based upon this, we deduce that for real Ω_\pm and ϵ_\pm , there exists one and only one root of $F_\pm(X_n^\pm)=0$ on the negative imaginary axis, say X_1^\pm . The imaginary roots θ_1^\pm have $\text{Im } \theta_1^\pm<0$ and correspond to a subsonic flexural wave which propagates unattenuated along each plate and decays exponentially into the fluid. Of the four remaining X -roots, two lie in the lower and two in the upper half-plane, symmetrically positioned with respect to the imaginary axis.

The two roots in the upper half-plane, X_4^\pm and X_5^\pm , lie on the imaginary axis if the following inequality is satisfied:

$$\frac{4\Omega_\pm^3}{5^{5/2}}\left(\frac{5}{\Omega_\pm^2}-2-\sqrt{4+\frac{5}{\Omega_\pm^2}}\right)\left(\sqrt{4+\frac{5}{\Omega_\pm^2}}-3\right)^{1/2}\geq\epsilon_\pm. \quad (19)$$

This condition is new (we believe), and may be determined as follows. Let $X=-i\eta$, so that $F_\pm(X)=0$ is equivalent to $G_\pm(\eta)=0$. The related equation $G'_\pm(\eta)=0$ has real roots only if $\Omega_\pm\leq 1$ and they occur at $\eta=\sqrt{\zeta_\pm}$, $\eta=-\sqrt{\zeta_\pm}$, where $\zeta_\pm=-\frac{3}{5}+\frac{1}{5}(4+5/\Omega_\pm^2)^{1/2}$. Since $G_\pm(0)<0$ and $G_\pm(\eta)\rightarrow\pm\infty$ as $\eta\rightarrow\pm\infty$, there is only one zero of $G_\pm(\eta)$ on the positive real axis, and either zero or two on the negative real axis. The condition for two roots on the negative axis is that $G_\pm(-\sqrt{\zeta_\pm})\geq 0$, which reduces to (19). This may be rewritten as

$$(\zeta_\pm+1)(5\zeta_\pm+1)^3\zeta_\pm^{-3}\leq 16\epsilon_\pm^{-2}. \quad (20)$$

It can be easily checked that the left member has a unique minimum at $\zeta_\pm=1$, implying that (19) can only hold for systems with $\epsilon_\pm\leq\epsilon_c\equiv 1/\sqrt{27}=0.1925$, and then only for a range of subsonic frequencies, $0<\Omega_\pm^l\leq\Omega_\pm\leq\Omega_\pm^u\leq 1$ where $\Omega_\pm^l(\epsilon)<(12)^{-1/2}=0.2887<\Omega_\pm^u(\epsilon)$ are the values at which the equality holds.

Thus, one of the five θ_n^\pm lies on the negative imaginary axis, and either two or zero lie on the positive imaginary axis depending as (19) holds or not. For example, $\epsilon=0.134$ for

steel and water, and $\epsilon=0.4$ for aluminum and water, and consequently the latter system has only one purely imaginary θ_n , while steel and water has three for $0.0748 < \Omega_{\pm} < 0.5918$ and one otherwise. The ambiguity concerning the values of parameters $s_n^{\pm} = \text{sgn}(\text{Re}\theta_n^{\pm})$ if $\text{Re}X_n^{\pm}=0$ can be removed by introducing a small amount of dissipation. Giving the bending stiffness B_{\pm} a small negative imaginary part shifts these roots from the imaginary axis in the complex X plane to get $\text{Re}X_{1,3,5}^{\pm} > 0$, $\text{Re}X_{2,4}^{\pm} < 0$. Consequently, we have $\text{Re}\theta_{1,3,5}^{\pm} \in (0, \pi/2)$, $\text{Re}\theta_{2,4}^{\pm} \in (-\pi/2, 0)$ and $s_n^{\pm} = (-1)^{n-1}$, $n=1, \dots, 5$. At very low frequency, such that $\Omega_{\pm} \ll 1$, asymptotic approximations to the roots yields $\theta_1^{\pm} \approx -i\lambda_{\pm}$, $\theta_2^{\pm} \approx -\theta_3^{\pm} \approx \theta_4^{\pm} \approx -\theta_5^{\pm} \approx \theta_1^{\pm} - \frac{2}{5}\pi$, where $\lambda_{\pm} = -\frac{3}{5} \ln \Omega_{\pm} + \frac{1}{5} \ln \epsilon_{\pm} + \ln 2$. These limiting values specify the quadrant positions of the angles for finite Ω_{\pm} . We note for future reference that $\text{Im} \theta_2^{\pm} < 0$, $\text{Im} \theta_4^{\pm} > 0$.

C. General solution of the functional equations

The general solution to Eq. (15) is represented as

$$S(\alpha) = \Psi(\alpha) \left(P_0 \frac{\sigma(\alpha, \phi_0)}{\Psi(\phi_0)} + \Lambda(\alpha) \right), \quad (21)$$

where $\Psi(\alpha)$, $\sigma(\alpha, \phi_0)$, and $\Lambda(\alpha)$ are each particular solutions to a pair of difference equations. Thus, $\Psi(\alpha)$ is the unique (up to a multiplicative constant) solution of the homogeneous system

$$L_{\pm}(\alpha)\Psi(\alpha \pm \Phi) - L_{\pm}(-\alpha)\Psi(-\alpha \pm \Phi) = 0, \quad (22)$$

which has no poles or zeros in the strip Π_0 , $\sigma(\alpha, \phi_0)$ is the solution of the homogeneous system

$$\sigma(\alpha \pm \Phi, \phi_0) - \sigma(-\alpha \pm \Phi, \phi_0) = 0, \quad (23)$$

which has a simple pole with unit residue at the single point $\alpha = \phi_0$ in the strip Π_0 , and $\Lambda(\alpha)$ is the particular solution of the nonhomogeneous system

$$\begin{aligned} \Lambda(\alpha \pm \Phi) - \Lambda(-\alpha \pm \Phi) \\ = \frac{2 \sin \alpha}{L_{\pm}(\alpha)\Psi(\alpha \pm \Phi)} \sum_{n=1}^4 C_n^{\pm} \cos^{n-1} \alpha. \end{aligned} \quad (24)$$

The function $\Psi(\alpha)$ is a product of special Malyzhinets functions $\psi_{\Phi}(\alpha)$ which depends upon the Brewster angles for the boundaries, θ_n^{\pm} , $n=1, \dots, 5$. The form of $\Psi(\alpha)$ depends critically upon s_n^{\pm} , defined above, implying the following analytical form of the auxiliary function

$$\Psi(\alpha) = \frac{\Psi_1^+(\alpha)\Psi_3^+(\alpha)\Psi_5^+(\alpha)}{\Psi_2^+(\alpha)\Psi_4^+(\alpha)} \frac{\Psi_1^-(\alpha)\Psi_3^-(\alpha)\Psi_5^-(\alpha)}{\Psi_2^-(\alpha)\Psi_4^-(\alpha)}, \quad (25)$$

$$\begin{aligned} \Psi_n^{\pm}(\alpha) = \psi_{\Phi} \left(\alpha \pm \Phi + \frac{\pi}{2} + (-1)^n \theta_n^{\pm} \right) \\ \times \psi_{\Phi} \left(\alpha \pm \Phi - \frac{\pi}{2} - (-1)^n \theta_n^{\pm} \right), \end{aligned} \quad (26)$$

where $\psi_{\Phi}(\alpha)$ is the Malyzhinets function, which is analytic for $|\text{Re} \alpha| < 2\Phi + \pi/2$.

The required solution of the homogeneous system (23) is

$$\sigma(\alpha, \phi_0) = \frac{(\pi/2\Phi)\cos(\pi\phi_0/2\Phi)}{\sin(\pi\alpha/2\Phi) - \sin(\pi\phi_0/2\Phi)}. \quad (27)$$

Finally, the particular solution of (24) can be deduced as

$$\Lambda(\alpha) = \sum_{n=1}^4 C_n^+ \Lambda_n^+(\alpha) + \sum_{n=1}^4 C_n^- \Lambda_n^-(\alpha), \quad (28)$$

where the procedure to determine the functions $\Lambda_n^{\pm}(\alpha)$ is described in Appendix A, with the result

$$\Lambda_n^{\pm}(\alpha) = \mp \frac{1}{\pi i} \int_0^{i\infty} \frac{\sigma(\alpha, \beta \pm \Phi) \sin \beta \cos^{n-1} \beta}{L_{\pm}(\mp \beta) \Psi(\pm(\Phi - \beta))} d\beta. \quad (29)$$

In the limit as $\text{Im} B_{\pm} \uparrow 0$, the point $\beta = -\theta_1^{\pm}$ lies on the contour of integration, resulting in a singularity of the integrand. This may be handled by taking the limit and evaluating the contribution as a principal value integral. A similar principal value contribution also occurs at $\beta = \theta_5^{\pm}$ when $\epsilon_{\pm} \leq \epsilon_c$ and $0 < \Omega_{\pm}^l \leq \Omega_{\pm} \leq \Omega_{\pm}^u < 1$. Such singularities located on the positive imaginary axis can be avoided by deforming the contour into the region $\text{Im} \beta > 0$, $\text{Re} \beta \in (0, \pi/2)$ where $1/\Psi(\pm(\Phi - \beta))$ by construction is regular and only one zero of $L_{\pm}(\mp \beta)$ occurs at $\beta = \theta_5^{\pm}$. In practice, the integration is performed numerically by deforming to the contour $L(N)$ which goes from 0 to x_0 to $x_0 + iN$, where $x_0 = \frac{1}{2}[\pi/2 + \text{Re}(\theta_5^{\pm})]$ and N need not be very large for fast convergence. The change of contour introduces a residue contribution at the circumscribed pole, thus

$$\begin{aligned} \Lambda_n^{\pm}(\alpha) = - \frac{2\sigma(\alpha, \theta_5^{\pm} \pm \Phi) \sin \theta_5^{\pm} \cos^{n-1} \theta_5^{\pm}}{L'_{\pm}(\mp \theta_5^{\pm}) \Psi(\pm(\Phi - \theta_5^{\pm}))} \\ \mp \frac{1}{\pi i} \int_{L(\infty)} \frac{\sigma(\alpha, \beta \pm \Phi) \sin \beta \cos^{n-1} \beta}{L_{\pm}(\mp \beta) \Psi(\pm(\Phi - \beta))} d\beta. \end{aligned} \quad (30)$$

The previous definitions of the functions $\Psi(\alpha)$ and $\Lambda(\alpha)$, and consequently $S(\alpha)$, are analytic only in the strip Π_0 , but may be analytically continued outside this region by repeated use of the functional relations (15), (21), (22), and (24). For example, the values of these functions in the sectors neighboring Π_0 , $\Pi_{\pm 1} = \{\alpha: \Phi < \text{Re}(\pm \alpha) \leq 3\Phi\}$ are related to themselves in Π_0 by the formulas

$$\Psi(\alpha) = \frac{L_{\pm}(-\alpha \pm \Phi)}{L_{\pm}(\alpha \mp \Phi)} \Psi(-\alpha \pm 2\Phi), \quad \alpha \in \Pi_{\pm 1}, \quad (31)$$

$$\begin{aligned} \Lambda(\alpha) = \Lambda(-\alpha \pm 2\Phi) + \frac{2 \sin(\alpha \mp \Phi)}{L_{\pm}(-\alpha \pm \Phi) \Psi(-\alpha \pm 2\Phi)} \\ \times \sum_{n=1}^4 C_n^{\pm} \cos^{n-1}(\alpha \mp \Phi), \quad \alpha \in \Pi_{\pm 1}, \end{aligned} \quad (32)$$

$$\begin{aligned} S(\alpha) = \frac{L_{\pm}(-\alpha \pm \Phi)}{L_{\pm}(\alpha \mp \Phi)} S(-\alpha \pm 2\Phi) + \frac{2 \sin(\alpha \mp \Phi)}{L_{\pm}(\alpha \mp \Phi)} \\ \times \sum_{n=1}^4 C_n^{\pm} \cos^{n-1}(\alpha \mp \Phi), \quad \alpha \in \Pi_{\pm 1}. \end{aligned} \quad (33)$$

III. DETERMINATION OF CONSTANTS

The eight unknowns can be determined from a linear system of equations of the form

$$\begin{pmatrix} E_{11}^+ & E_{11}^- & E_{12}^+ & E_{12}^- & E_{13}^+ & E_{13}^- & E_{14}^+ & E_{14}^- \\ E_{21}^+ & E_{21}^- & E_{22}^+ & E_{22}^- & E_{23}^+ & E_{23}^- & E_{24}^+ & E_{24}^- \\ \vdots & \vdots & \vdots & \vdots & \vdots & \vdots & \vdots & \vdots \\ \vdots & \vdots & \vdots & \vdots & \vdots & \vdots & \vdots & \vdots \\ E_{81}^+ & E_{81}^- & E_{82}^+ & E_{82}^- & E_{83}^+ & E_{83}^- & E_{84}^+ & E_{84}^- \end{pmatrix} \begin{pmatrix} C_1^+ \\ C_1^- \\ C_2^+ \\ C_2^- \\ C_3^+ \\ C_3^- \\ C_4^+ \\ C_4^- \end{pmatrix} = (g_1 \ g_2 \ g_3 \ g_4 \ g_5 \ g_6 \ g_7 \ g_8)^T. \quad (34)$$

The first four of these equations follow from certain regularity conditions on the integrand $S(\alpha)$, and the remaining four are consequences of the mechanical conditions at the vertex. The two sets of conditions are used below to determine the elements of \mathbf{E} and \mathbf{g} .

A. Regularity conditions

The far-field ($r \rightarrow \infty$) behavior of the Sommerfeld integral (7) can be determined by deforming the contour γ into a pair of contours $\Gamma_\varepsilon(\pm\pi)$, one of which goes from $\pi - \varepsilon + i\infty$ through $\alpha = \pi$ to $\pi + \varepsilon - i\infty$, and the other is symmetric to it about the origin $\alpha = 0$. Assuming that ε is positive and arbitrarily small, one finds that these contours belong totally to those portions of the complex α plane, labeled Π^- , in which $\text{Im} \cos \alpha < 0$, and hence any integral of $\exp(-ikr \cos \alpha)$ taken over the contours $\Gamma_\varepsilon(\pm\pi)$ vanishes as $r \rightarrow \infty$. In deforming the contour certain poles may be captured in the area designated as Π^{ess} which is enclosed by contours γ_\pm at the top and bottom, and by $\Gamma_\varepsilon(\pm\pi)$ at the left and right. If the captured poles include one or more located inside the regions Π^+ where $\text{Im} \cos \alpha > 0$, then the residues at such poles would grow exponentially with r , giving unphysical behavior at infinity. Poles of this type (named in Ref. 4 as ‘‘forbidden’’ poles) violate conditions at $r = +\infty$ for some $\phi \in (-\Phi, \Phi)$ and must be eliminated from the solution.

In the following we assume that $\text{Im} \theta_2^\pm < 0$, $\text{Im} \theta_4^\pm > 0$, then it can be shown that among the forbidden poles which are shared by Π^{ess} and Π^+ are as follows: $\alpha = -\phi + \alpha_p^f$ where $p = 1, 2, 3, 4$, and

$$\begin{aligned} \alpha_1^f &= \theta_2^+ + \pi + \Phi, \\ \alpha_2^f &= -\theta_4^+ + \Phi, \\ \alpha_3^f &= -\theta_2^- - \pi - \Phi, \\ \alpha_4^f &= \theta_4^- - \Phi. \end{aligned} \quad (35)$$

In order to guarantee the correct behavior of the integral (7) as $r \rightarrow +\infty$ we have to cancel the residues of its transform $S(\alpha)$ at the forbidden poles (35) by equating

TABLE I. The junction conditions for clamped, free and hinged plates. In each case four of the eight unknowns are zero, and the remaining four are determined by four linear equations.

| Type | Conditions | Implications | Equations |
|---------|-----------------------------------|-------------------------|-----------|
| Clamped | $w_\pm(0) = 0, w'_\pm(0) = 0$ | $C_3^\pm = C_4^\pm = 0$ | (40) |
| Free | $w''_\pm(0) = 0, w'''_\pm(0) = 0$ | $C_1^\pm = C_2^\pm = 0$ | (41) |
| Hinged | $w_\pm = 0, w''_\pm(0) = 0$ | $C_2^\pm = C_4^\pm = 0$ | (42) |

$$P_0 \frac{\sigma(\alpha_p^f, \phi_0)}{\Psi(\phi_0)} + \Lambda(\alpha_p^f) = 0, \quad p = 1, 2, 3, 4. \quad (36)$$

These provide the first four rows of the matrix \mathbf{E} and the vector \mathbf{g} . Thus,

$$g_p = -P_0 \frac{\sigma(\alpha_p^f, \phi_0)}{\Psi(\phi_0)}, \quad p = 1, 2, 3, 4. \quad (37)$$

The elements of the top half of \mathbf{E} follow by noting that the function $\Lambda(\alpha)$ satisfies the functional equations (24). Thus, $\alpha_1^f, \alpha_2^f \in \Pi_1$, $\alpha_3^f, \alpha_4^f \in \Pi_{-1}$ if $\Phi > \pi/2$ and consequently, using (32),

$$\begin{aligned} E_{pn}^+ &= \Lambda_n^+(-\alpha_p^f + 2\Phi) \\ &+ \frac{2 \sin(\alpha_p^f - \Phi) \cos^{n-1}(\alpha_p^f - \Phi)}{L_+(-\alpha_p^f + \Phi) \Psi(-\alpha_p^f + 2\Phi)}, \end{aligned} \quad (38)$$

$$E_{pn}^- = \Lambda_n^-(-\alpha_p^f + 2\Phi), \quad p = 1, 2, \quad n = 1, 2, 3, 4,$$

and

$$\begin{aligned} E_{pn}^- &= \Lambda_n^-(-\alpha_p^f - 2\Phi) \\ &+ \frac{2 \sin(\alpha_p^f + \Phi) \cos^{n-1}(\alpha_p^f + \Phi)}{L_-(-\alpha_p^f - \Phi) \Psi(-\alpha_p^f - 2\Phi)}, \end{aligned} \quad (39)$$

$$E_{pn}^+ = \Lambda_n^+(-\alpha_p^f - 2\Phi), \quad p = 3, 4, \quad n = 1, 2, 3, 4.$$

The functions $\Lambda_n^\pm(\alpha)$ and $\Psi(\alpha)$ in Eqs. (38) and (39) have arguments only in Π_0 .

B. Junction conditions

1. Clamped, free, or hinged plates

We consider three sets of junction conditions under which the equations simplify considerably. These are listed in Table I as clamped, free, and hinged. In the former case both plates are clamped at the vertex, constraining motion there. The nonzero equations are

$$\begin{pmatrix} E_{11}^+ & E_{11}^- & E_{12}^+ & E_{12}^- \\ E_{21}^+ & E_{21}^- & E_{22}^+ & E_{22}^- \\ E_{31}^+ & E_{31}^- & E_{32}^+ & E_{32}^- \\ E_{41}^+ & E_{41}^- & E_{42}^+ & E_{42}^- \end{pmatrix} \begin{pmatrix} C_1^+ \\ C_1^- \\ C_2^+ \\ C_2^- \end{pmatrix} = \begin{pmatrix} g_1 \\ g_2 \\ g_3 \\ g_4 \end{pmatrix}. \quad (40)$$

Under ‘‘free’’ conditions the shear force and bending moment on each plate vanishes at the tip, and the equations are

$$\begin{pmatrix} E_{13}^+ & E_{13}^- & E_{14}^+ & E_{14}^- \\ E_{23}^+ & E_{23}^- & E_{24}^+ & E_{24}^- \\ E_{33}^+ & E_{33}^- & E_{34}^+ & E_{34}^- \\ E_{43}^+ & E_{43}^- & E_{44}^+ & E_{44}^- \end{pmatrix} \begin{pmatrix} C_3^+ \\ C_3^- \\ C_4^+ \\ C_4^- \end{pmatrix} = \begin{pmatrix} g_1 \\ g_2 \\ g_3 \\ g_4 \end{pmatrix}. \quad (41)$$

The hinged ends constrain the linear motion but not the rotation, and exert no moments, yielding

$$\begin{pmatrix} E_{11}^+ & E_{11}^- & E_{13}^+ & E_{13}^- \\ E_{21}^+ & E_{21}^- & E_{23}^+ & E_{23}^- \\ E_{31}^+ & E_{31}^- & E_{33}^+ & E_{33}^- \\ E_{41}^+ & E_{41}^- & E_{43}^+ & E_{43}^- \end{pmatrix} \begin{pmatrix} C_1^+ \\ C_1^- \\ C_3^+ \\ C_3^- \end{pmatrix} = \begin{pmatrix} g_1 \\ g_2 \\ g_3 \\ g_4 \end{pmatrix}. \quad (42)$$

2. Welded and forced

We now consider the important case of two plates that are mechanically joined at the vertex. The displacements and rotations are continuous, and there is an applied moment M_0 per unit length in the third dimension, and force \mathbf{F} per unit length acting at the tip. The continuity conditions can be expressed in terms of the deflection $w_{\pm}(r)$ and their derivatives at $r=0$:⁹

$$w'_+(0) + w'_-(0) = 0,$$

$$B_+ w''_+(0) - B_- w''_-(0) = M_0, \quad (43)$$

$$\frac{B_{\pm}}{i\omega} w'''_{\pm}(0) + Z_{\pm} w_{\pm}(0) - \frac{(Z_+ + Z_-)}{\sin^2 2\Phi} \times [w_{\pm}(0) + w_{\mp}(0) \cos 2\Phi] = \frac{F_r^{\mp}}{i\omega \sin 2\Phi}.$$

Here, F_r^{\pm} are the radial components of \mathbf{F} along $\phi = \pm\Phi$. For acoustic or flexural wave incidence we have $M_0=0$ and $F_r^{\pm}=0$. Longitudinal waves traveling inwards towards the junction on the \pm plate can be considered by setting $M_0=0$ and

$$F_r^{\pm} = -2i\omega(Z_{\pm}U_0^{\pm} + Z_{\mp}U_0^{\mp} \cos 2\Phi), \quad (44)$$

where U_0^{\pm} is the particle displacement of the incident longitudinal wave at $r=0$ in the radial direction, defined by (5). Using (16) implies

$$\frac{C_3^+}{B_+} + \frac{C_3^-}{B_-} = 0, \quad (45)$$

$$C_2^+ - C_2^- = -\frac{k^2}{2}M_0,$$

$$\frac{k^2}{c}C_1^{\pm} + \frac{Z_{\pm}}{B_{\pm}}C_4^{\pm} - \frac{(Z_+ + Z_-)}{\sin^2 2\Phi} \left(\frac{C_4^{\pm}}{B_{\pm}} + \frac{C_4^{\mp}}{B_{\mp}} \cos 2\Phi \right) = \frac{-ik^3 F_r^{\mp}}{2c \sin 2\Phi},$$

and therefore the bottom half of \mathbf{E} comprises zeros except for the elements

$$E_{53}^{\pm} = \frac{\epsilon_{\pm}}{\Omega_{\pm}^3}, \quad E_{62}^{\pm} = \pm 1, \quad E_{71}^+ = E_{81}^- = -\sin^2 2\Phi,$$

$$E_{74}^+ = \frac{\delta_+}{\Omega_+^2} \left(\cos^2 2\Phi + \frac{\epsilon_+ \delta_- \Omega_-}{\epsilon_- \delta_+ \Omega_+} \right),$$

$$E_{74}^- = \frac{\delta_-}{\Omega_-^2} \cos 2\Phi \left(1 + \frac{\epsilon_- \delta_+ \Omega_+}{\epsilon_+ \delta_- \Omega_-} \right), \quad (46)$$

$$E_{84}^- = \frac{\delta_-}{\Omega_-^2} \left(\cos^2 2\Phi + \frac{\epsilon_- \delta_+ \Omega_+}{\epsilon_+ \delta_- \Omega_-} \right),$$

$$E_{84}^+ = \frac{\delta_+}{\Omega_+^2} \cos 2\Phi \left(1 + \frac{\epsilon_+ \delta_- \Omega_-}{\epsilon_- \delta_+ \Omega_+} \right),$$

while the right-hand members become for longitudinal incidence, using (44) and $M_0=0$,

$$g_5 = 0, \quad g_6 = 0,$$

$$g_7 = (S_0^- + S_0^+ \cos 2\Phi) \sin 2\Phi, \quad (47)$$

$$g_8 = (S_0^+ + S_0^- \cos 2\Phi) \sin 2\Phi.$$

In summary, the right-hand side of the matrix equation (34) is defined by the incident pressures P_0 and S_0^{\pm} , and therefore all coefficients C_n^{\pm} also have units of pressure.

IV. DIFFRACTED STRUCTURAL WAVES

The total longitudinal motion in the plates is defined by the displacement components in either plate in the radial direction:

$$u_{\pm}(r) = u_{\pm}^{\text{inc}}(r) + u_{\pm}^{\text{sc}}(r), \quad (48)$$

where $u_{\pm}^{\text{inc}}(r)$ is the incident wave, from (6), and $u_{\pm}^{\text{sc}}(r)$ is the scattered wave which satisfies

$$\omega k Z_{\pm} u_{\pm}^{\text{sc}}(r) = A_L^{\pm} \exp(i\omega r/c_{\pm}), \quad (49)$$

indicating longitudinal energy radiating outwards. The initial amplitudes are related to the transverse displacements by⁹

$$u_{\pm}(0) = (\sin 2\Phi)^{-1} [w_{\mp}(0) + w_{\pm}(0) \cos 2\Phi], \quad (50)$$

and therefore, using (16), the longitudinal diffraction coefficients are

$$A_L^{\pm} = \frac{2\delta_{\pm}}{\Omega_{\pm}^2 \sin 2\Phi} \left(C_4^{\pm} \cos 2\Phi + C_4^{\mp} \frac{\epsilon_{\mp} \Omega_{\mp}^3}{\epsilon_{\pm} \Omega_{\pm}^3} \right) - S_0^{\pm}. \quad (51)$$

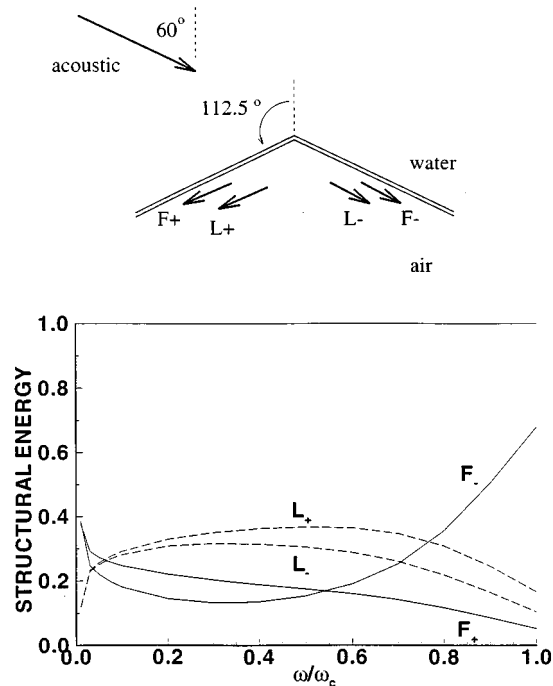


FIG. 2. The fraction of structural energy associated with flexural (F_{\pm}) and longitudinal (L_{\pm}) waves excited at the vertex of a steel and water configuration with $\Phi=112.5^\circ$ for acoustic incidence at angle $\phi_0=60^\circ$. The frequency ω_c is the flexural and acoustic coincidence frequency. The sum of the four energies is 1.

The evaluation of the flexural wave amplitudes requires a little more effort. The integral (7) can be evaluated asymptotically for $kr \gg 1$ by deformation of the contour γ into a pair of steepest descent paths. This yields a representation

$$p(r, \phi) = p_G(r, \phi) + p_D(r, \phi) + p_F^+(r, \phi) + p_F^-(r, \phi), \quad (52)$$

where p_G and p_D are the geometrical and acoustical (vertex) diffraction fields, respectively. The terms $p_F^\pm(r, \phi)$ denote the residues at captured poles of the function $\Psi(\alpha + \phi)$, and they coincide with the zeros of $L_\pm(\alpha + \phi \mp \Phi)$ which lie within the steepest descent paths. The dominant contributions to $p_F^\pm(r, \phi)$ are due to the residues at poles $\alpha = -\phi \pm (\Phi + \pi + \theta_1^\pm)$ that describe the subsonic flexural waves excited at the tip by the incident field and then traveling outwards along both sides of the wedge without dissipation if the material parameters of the plates are assumed to be entirely real, that is $\text{Re} \theta_1^\pm = 0$. The corresponding expressions may be summarized as follows

$$p_F^\pm(r, \phi) = H[\pm \phi - \Phi - \text{Re} \theta_1^\pm - g d(\text{Im} \theta_1^\pm)] A_F^\pm e^{ikr \cos(\Phi \mp \phi + \theta_1^\pm)}, \quad (53)$$

where gd is the Gudermanian function,¹³ and using (33),

$$A_F^\pm = \frac{2}{L'_\pm(\theta_1^\pm)} \left(S(\pm \Phi \mp \pi \mp \theta_1^\pm) \pm \sin \theta_1^\pm \sum_{n=1}^4 C_n^\pm \cos^{n-1}(\theta_1^\pm + \pi) \right). \quad (54)$$

The acoustical diffraction, p_D of (52), is defined by

$$p_D(r, \phi) \approx D(\phi) \frac{\exp(ikr - i3\pi/4)}{\sqrt{2\pi kr}}, \quad (55)$$

where the diffraction coefficient follows from a steepest descents integral as

$$D(\phi) = S(\phi + \pi) - S(\phi - \pi). \quad (56)$$

This term describes the cylindrical wave arising due to diffraction of the incident field by the tip. The acoustical diffraction coefficient must be unchanged under the interchange of the source and observation directions. Thus, when considered as a function of both ϕ and ϕ_0 , it satisfies the reciprocity identity $D(\phi_0, \phi) = D(\phi, \phi_0)$.

The energy of an incident structural wave is defined as twice the flux of energy per cycle in the direction of the incoming wave. For the longitudinal wave this is simply the energy flux in the plate,

$$\mathcal{F}_L^\pm = \omega^2 Z_\pm |U_0^\pm|^2. \quad (57)$$

The flexural wave contains energy in the plate and in the fluid, and it can be shown to yield a flux of

$$\mathcal{F}_F^\pm = \frac{|L'_\pm(\theta_1^\pm)|}{2\rho\omega} |P_0|^2, \quad (58)$$

and $|L'_\pm(\theta_1^\pm)| = \pm i L'_\pm(\theta_1^\pm)$ assuming no dissipation in the system. The energy fluxes of the radiated flexural and longitudinal waves follow from (57) and (58), and the acoustic energy is

$$\lim_{r \rightarrow \infty} \frac{1}{\rho c} \int_{-\Phi}^{\Phi} |p_D(r, \phi)|^2 r d\phi = \frac{1}{2\pi\rho\omega} \int_{-\Phi}^{\Phi} |D(\phi)|^2 d\phi. \quad (59)$$

The total radiated energy, structural and acoustic, is therefore

$$\begin{aligned} \mathcal{F}_s = \frac{1}{2\rho\omega} & \left\{ |L'_+(\theta_1^+)| |A_F^+|^2 + |L'_-(\theta_1^-)| |A_F^-|^2 \right. \\ & + \frac{2\epsilon_+ |A_L^+|^2}{\delta_+ \Omega_+} + \frac{2\epsilon_- |A_L^-|^2}{\delta_- \Omega_-} \\ & \left. + \frac{1}{\pi} \int_{-\Phi}^{\Phi} |D(\phi)|^2 d\phi \right\}. \quad (60) \end{aligned}$$

This defines the energy balance for the wave conversion process.

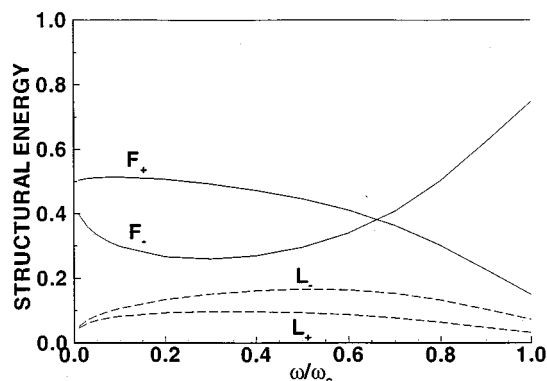


FIG. 3. The same as Fig. 2 but for $\Phi=135^\circ$.

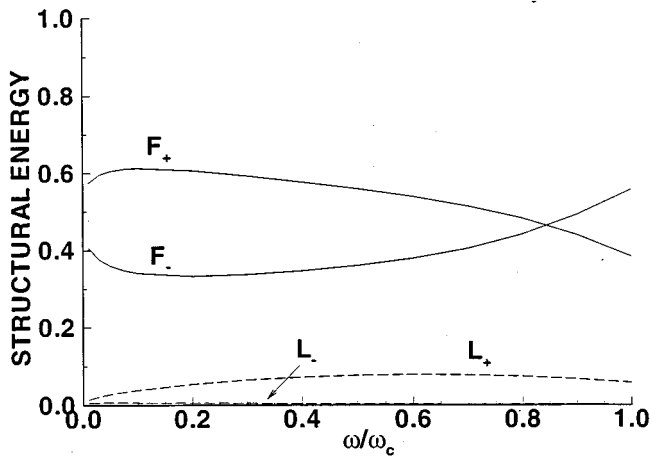


FIG. 4. The same as Fig. 2 but for $\Phi = 157.5^\circ$.

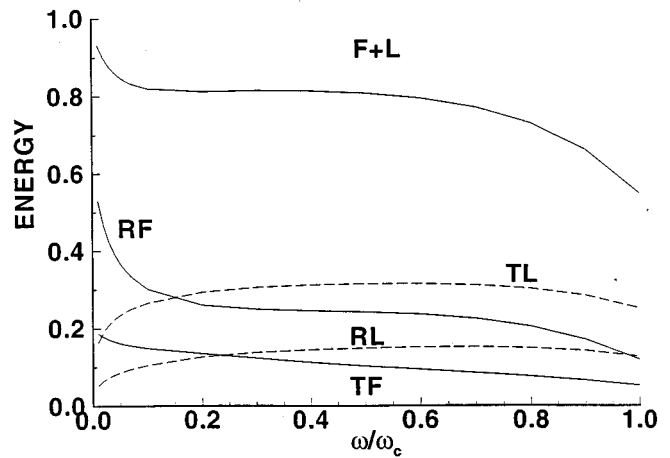


FIG. 6. The same as Fig. 5 for $\Phi = 157.5^\circ$.

V. NUMERICAL RESULTS AND DISCUSSION

We now present some numerically computed results for the particular case of identical steel plates in water ($\epsilon = 0.134$) that are mechanically joined at the contact line (welded contact conditions). Several simplifications result when the plates are identical: thus, $\theta_n^+ = \theta_n^-$ for $n = 1, 2, \dots, 5$, the function $\Psi(\alpha)$ is even,

$$\Lambda_n^+(\alpha) + \Lambda_n^-(-\alpha) = 0,$$

and

$$E_{1n}^+ + E_{3n}^- = 0, \quad E_{2n}^+ + E_{4n}^- = 0.$$

We consider three representative configurations: $\Phi = \frac{5}{8}\pi$, $\frac{3}{4}\pi$, and $\frac{7}{8}\pi$. Figures 2–8 show the energy partition for acoustical, flexural, and longitudinal incidence as a function of the nondimensional frequency $\Omega = \omega/\omega_c$.

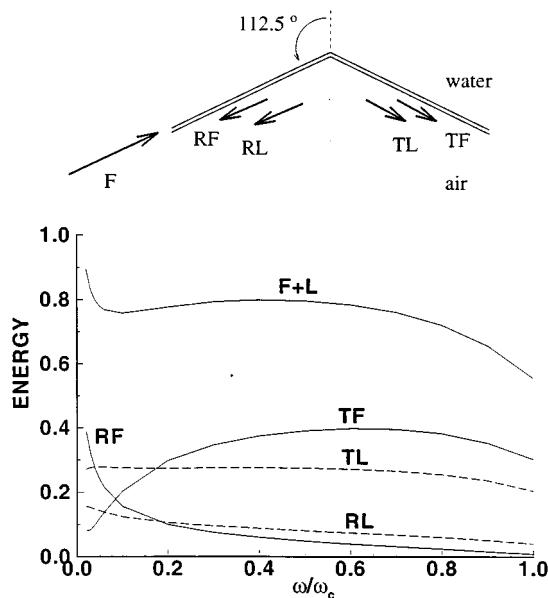


FIG. 5. The structural energy redistribution for flexural wave incidence on the steel and water configuration with $\Phi = 112.5^\circ$. The curves “RF,” “TF,” “RL,” and “TL,” indicate the amounts of reflected flexural, transmitted flexural, reflected longitudinal, and transmitted longitudinal energies, respectively. The sum of these four energies is the curve “F+L.”

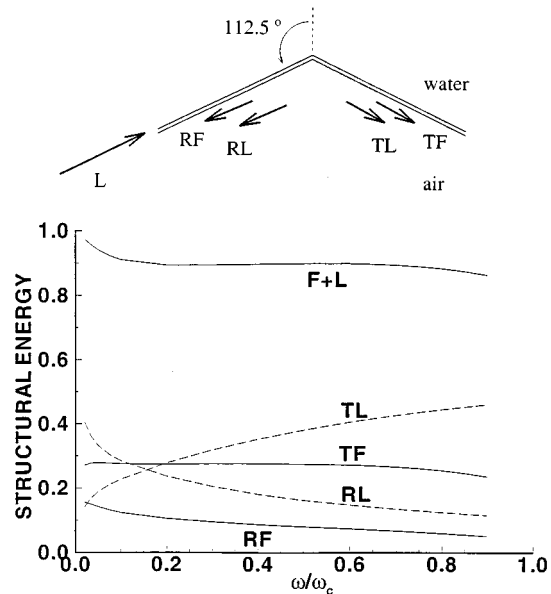


FIG. 7. The same as Fig. 5 but for longitudinal incidence.

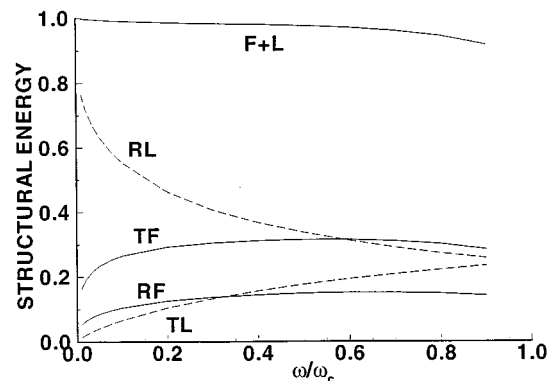


FIG. 8. The same as Fig. 7 for $\Phi = 157.5^\circ$.

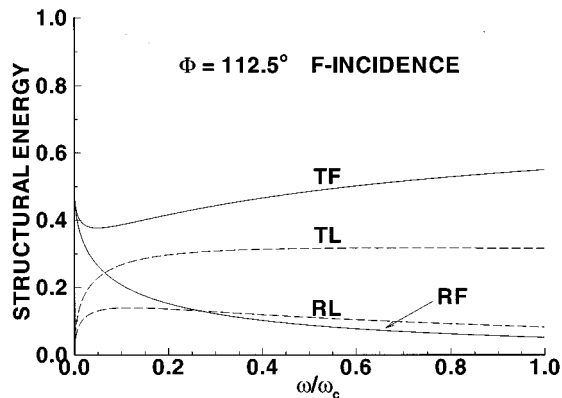


FIG. 9. The same as Fig. 5 but for dry plates (no fluid loading). The same frequency parameter is used for purposes of comparison. In this case the sum of the four fluxes is unity.

The fractional distribution of the diffracted structural energy for acoustic plane-wave incidence with $\phi_0 = 60^\circ$ are shown in Figs. 2–4 for frequencies below critical. In these and subsequent plots the solid curves indicate the flexural energy and the dashed curves show the longitudinal energy fractions. We note from Figs. 2–4 that the relative coupling to flexural energy increases with the wedge angle, at the expense of the longitudinal energy which vanishes as $\Phi \rightarrow 180^\circ$.

The curves in Figs. 5 and 6 show the fraction of incident flexural energy that is converted into the four radiating structural modes. In this case the sum of the flexural and longitudinal fluxes (the curve ‘‘F+L’’) is less than unity. The deficit indicates, from Eq. (60), the fraction of energy converted to acoustic waves. Similar curves for longitudinal incidence are in Figs. 7 and 8. In all cases the total structural energy is conserved at low frequency although it is significantly redistributed among the modes. These and other computations indicate that an incident longitudinal wave generates relatively little acoustic sound for all values of Φ considered, with most of its energy redistributed among structural modes. The acoustical diffraction is generally greater for flexural incidence.

Finally, Figs. 9 and 10 show the structural energy redistribution for two dry configurations (see Appendix B). These

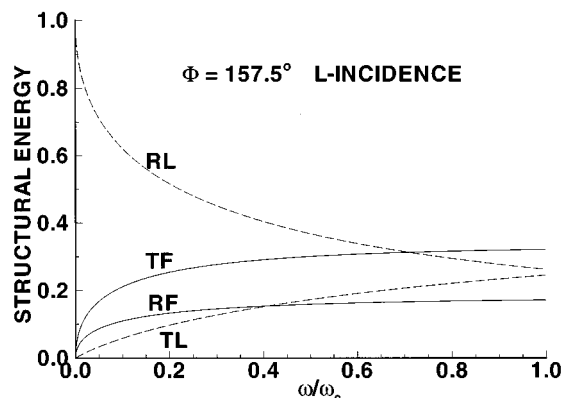


FIG. 10. The same as Fig. 8 but for dry plates.

curves should be compared with the fluid-loaded cases in Figs. 5 and 8. It is interesting to note that the fluid loading does not have much effect for longitudinal incidence. The story is different for flexural incidence, where fluid loading effects can be appreciable for $\omega \leq 0.2\omega_c$. In general, experience shows (e.g., Ref. 11) that fluid loading has a strong influence on radiation and scattering from sources and discontinuities for $\Omega < \epsilon$, and the results presented here are consistent with this conclusion.

The numerical computations presented here indicate the degree of coupling between the modes for different wedge angles and frequencies. Some of the observed trends can be understood by consideration of the special cases (i): $\Phi = \pi$, for which a Wiener–Hopf analysis leads to relatively simple expressions for the acoustical and flexural diffraction coefficients,⁷ and (ii) $\Phi \approx \pi/2$, which can be analyzed by perturbation methods,⁹ with the flat plate $\Phi = \pi/2$ solution as the leading-order term. The latter analysis predicts that acoustic plane-wave incidence on flat junctions ($\Phi \approx 90^\circ$) is converted almost equally, in terms of energy, among diffracted longitudinal waves on the two plates. This is in accord with the almost identical L_+ and L_- curves from the ‘‘exact’’ computations in Fig. 2.

ACKNOWLEDGMENT

The work of A. N. Norris was supported by the Office of Naval Research.

APPENDIX A: THE FUNCTION Λ

The general solution of the pair of difference equations

$$\Lambda(\alpha \pm \Phi) - \Lambda(-\alpha \pm \Phi) = f_{\pm}(\alpha), \quad (\text{A1})$$

can be expressed as $\Lambda(\alpha) = \Lambda^+(\alpha) + \Lambda^-(\alpha)$, where

$$\Lambda^+(\alpha + \Phi) - \Lambda^+(-\alpha + \Phi) = f_+(\alpha),$$

$$\Lambda^+(\alpha - \Phi) - \Lambda^+(-\alpha - \Phi) = 0, \quad (\text{A2})$$

with a similar system for $\Lambda^-(\alpha)$. We will discuss the solution of the pair of simultaneous equations (A2) only, which apply to the functions Λ_n^+

The solution is represented using a modified Fourier transform pair:

$$\Lambda^+(\alpha) = \int_{-i\infty}^{i\infty} e^{-i\alpha t} \eta(t) dt, \quad (\text{A3})$$

$$\eta(t) = -\frac{1}{2\pi} \int_{-i\infty}^{i\infty} e^{i\alpha t} \Lambda^+(\alpha) d\alpha,$$

so that the difference equations (A2) become

$$\int_{-i\infty}^{i\infty} [\eta(t)e^{-it\Phi} - \eta(-t)e^{it\Phi}] e^{-it\alpha} dt = f_+(\alpha), \quad (\text{A4})$$

$$\int_{-i\infty}^{i\infty} [\eta(t)e^{it\Phi} - \eta(-t)e^{-it\Phi}] e^{-it\alpha} dt = 0.$$

Hence, using the modified Fourier transform, we easily obtain

$$\eta(t) = \frac{e^{-it\Phi}}{4\pi i \sin(2\Phi t)} \int_{-i\infty}^{i\infty} e^{i\beta t} f_+(\beta) d\beta, \quad (\text{A5})$$

and so

$$\Lambda^+(\alpha) = \int_{-i\infty}^{i\infty} f_+(\beta) G(\beta, \alpha) d\beta, \quad (\text{A6})$$

where

$$\begin{aligned} G(\beta, \alpha) &= \int_{-i\infty}^{i\infty} \frac{e^{it(\beta-\Phi-\alpha)} dt}{4\pi i \sin(2\Phi t)} \\ &= \int_{-i\infty}^{i\infty} \frac{\sin[(\beta-\Phi-\alpha)t] dt}{4\pi \sin(2\Phi t)}. \end{aligned} \quad (\text{A7})$$

But $f_+(\beta)$ is an odd function of its argument, implying that

$$\Lambda^+(\alpha) = \int_0^{\infty} f_+(\beta) (G(\beta, \alpha) - G(-\beta, \alpha)) d\beta, \quad (\text{A8})$$

while

$$\begin{aligned} G(\beta, \alpha) - G(-\beta, \alpha) &= \frac{i}{\pi} \int_0^{\infty} \frac{\sinh(\beta s) \cosh[(\alpha + \Phi)s]}{\sinh(2\Phi s)} ds \\ &= \frac{i}{4\Phi} \frac{\sin(\beta\pi/2\Phi)}{(\cos(\beta\pi/2\Phi) - \sin(\alpha\pi/2\Phi))}, \end{aligned} \quad (\text{A9})$$

where the latter follows from Eq. (3.511.5) of Ref. 13.

APPENDIX B: DRY PLATES

Consider incident flexural waves on the \pm plate with displacement amplitudes W_0^\pm . The total transverse displacement on each plate can then be written as the sum of the incident wave plus outgoing propagating and evanescent flexural waves:

$$w_\pm(r) = W_0^\pm e^{-i\kappa_\pm r} + A_F^\pm W_0^\pm e^{i\kappa_\pm r} + B_F^\pm W_0^\pm e^{-\kappa_\pm r}. \quad (\text{B1})$$

The following identities are direct consequences of (B1):

$$\begin{aligned} w_\pm''(0) + (1-i)\kappa_\pm w_\pm'(0) - i\kappa_\pm^2 w_\pm(0) \\ = -2(1+i)\kappa_\pm^2 W_0^\pm, \end{aligned} \quad (\text{B2})$$

$$w_\pm'''(0) + \kappa_\pm w_\pm''(0) + \kappa_\pm^2 w_\pm'(0) + \kappa_\pm^3 w_\pm(0) = 0. \quad (\text{B3})$$

The eight unknowns $w_\pm(0)$, $w_\pm'(0)$, $w_\pm''(0)$, $w_\pm'''(0)$, can now be found using the junction conditions (43) supplemented by (B2) and (B3).

We cite some results for the particular case of identical plates, with either flexural or longitudinal incidence, for which we find that

$$\begin{aligned} A_F^\pm &= \frac{(1-i)}{2} w_s^\pm \frac{1}{2} w_d + \frac{(1+i)}{2} W_0^\mp + \frac{(i-1)}{2} W_0^\pm, \\ A_L^\pm &= w_s \cot \Phi \mp w_d \tan \Phi - U_0^\pm, \end{aligned} \quad (\text{B4})$$

where $w_s = \frac{1}{2}[w_+(0) + w_-(0)]$, $w_d = \frac{1}{2}[w_+(0) - w_-(0)]$, or explicitly,

$$w_s = \frac{(U_0^+ + U_0^-) \cot \Phi + (1-i)(W_0^+ + W_0^-) \beta}{\cot^2 \Phi + (1-i)\beta}, \quad (\text{B5})$$

$$w_d = \frac{-(U_0^+ - U_0^-) \tan \Phi + (W_0^+ - W_0^-) \beta}{\tan^2 \Phi + \frac{1}{2}(1-i)\beta}, \quad (\text{B6})$$

with $\beta = \omega/(\kappa c_0)$ and c_0 is the longitudinal wave speed ($=c_\pm$). In terms of the nondimensional parameter Ω for the fluid loaded problem we have $\beta = \sqrt{\Omega}/\delta$. Finally, we note that the total energy balance for the dry plate problem is simply

$$|A_F^+|^2 + |A_F^-|^2 + \frac{1}{2\beta} |A_L^+|^2 + \frac{1}{2\beta} |A_L^-|^2 = 1, \quad (\text{B7})$$

for a single incident flexural wave of unit amplitude ($|W_0^+|$ or $|W_0^-| = 1$), or for incidence of a longitudinal wave of amplitude $|U_0^+|$ or $|U_0^-| = \sqrt{2\beta}$. We refer to Budrin¹⁴ and Maslov¹⁵ for further results concerning the dry structural acoustics problem.

¹A. N. Norris and G. R. Wickham, "Acoustic diffraction from the junction of two flat plates," Proc. R. Soc. London **451**, 631–656 (1995).

²D. M. Photiadis, "Transport of energy across a discontinuity by fluid loading," J. Acoust. Soc. Am. **97**, 1409–1414 (1995).

³D. A. Rebinsky and A. N. Norris, "Acoustic and flexural wave scattering from a three member junction," J. Acoust. Soc. Am. **98**, 3309–3319 (1995).

⁴A. N. Norris, "Acoustic diffraction from the junction of two joined parallel plates," J. Acoust. Soc. Am. **99**, 1475–1483 (1996).

⁵A. V. Osipov, "General solution for a class of diffraction problems," J. Phys. A **27**, L27–L32 (1994).

⁶I. D. Abrahams and J. B. Lawrie, "Traveling waves on a membrane: reflection and transmission at a corner of arbitrary angle. I," Proc. R. Soc. London **451**, 657–683 (1995).

⁷A. V. Osipov and A. N. Norris, "Sound diffraction by a fluid-loaded membrane corner," Proc. R. Soc. London (in press).

⁸A. V. Osipov, "Sound diffraction by an angular joint of thin elastic plates," Prikl. Mat. Mekh. (Russia) (in press).

⁹A. N. Norris and A. V. Osipov, "On acoustic interaction between two thin elastic plates through an angular welded joint," J. Sound Vib. **196**, 75–84 (1996).

¹⁰G. D. Malyuzhinets, "Inversion formula for the Sommerfeld integral," Sov. Phys. Dokl. **3**, 52–56 (1958).

¹¹M. C. Junger and D. Feit, *Sound, Structures, and Their Interaction* (Acoustical Society of America, Woodbury, NY, 1993).

¹²D. G. Crighton, "The free and forced waves on a fluid-loaded elastic plate," J. Sound Vib. **63**, 225–235 (1979).

¹³I. S. Gradshteyn and I. M. Ryzhik, *Table of Integrals, Series, and Products* (Academic, New York, 1980).

¹⁴S. V. Budrin and A. S. Nikiforov, "Wave transmission through assorted joints," Sov. Phys. Acoust. **9**, 333 (1964).

¹⁵V. P. Maslov, "Reflection of a flexural wave from an angular junction of plates," Sov. Phys. Acoust. **14**, 483–486 (1969).

Wave-number space response of a near periodically ribbed shell

Douglas M. Photiadis, Earl G. Williams, and Brian H. Houston
Naval Research Laboratory, Washington, DC 20375-5000

(Received 8 April 1996; accepted for publication 19 September 1996)

Employing near-field acoustic holography measurements, the wave-number space response of a ribbed shell to a point drive is investigated. The data show the dominance of flexural vibration in the mid-frequency range, and demonstrate the prominent role played by the eigensolutions of the periodic structure. The supersonic region of frequency–wave-number space is examined in detail and the fast membrane waves, although suppressed in level relative to the subsonic bending waves, provide a clear highlight in this domain at frequencies below the first radiating flexural passband. The results are also examined in k_z-k_ϕ space for several frequencies. This representation enables an interpretation of the results in terms of the slowness surface of the flexural waves and provides a simple explanation for the various complex beaming and focusing phenomena which occur in this system. [S0001-4966(97)03501-7]

PACS numbers: 43.40.Ey, 43.40.Rj, 43.20.Jr, 43.20.Ks [CBB]

INTRODUCTION

A knowledge of the structural acoustic response of ribbed plates and shells is an important ingredient in the acoustic design and diagnostic analysis of marine vehicles, aircraft, and a number of components of systems such as reinforced piping and support structures. A number of idealized theoretical models have been analyzed to provide at least some guidance in this process; for example, infinite periodically ribbed plates and cylindrical shells,^{1–6} a few finite periodic structures,⁷ and more recently some aperiodic systems.^{8–13} The exact solutions when obtainable are usually quite complex,^{5,6} especially for somewhat realistic fluid loaded systems, and one must resort to approximate solutions if the idealized models are to be of use. Hence, a knowledge of the most important features of the behavior of real systems is quite important. Unfortunately, only a small amount of experimental data^{14–17} shedding light on this issue has been published.

We report here the first near-field acoustic holography¹⁸ measurements of the vibratory response of a ribbed shell to a local excitation. The measurements cover a substantial portion of the mid-frequency range, roughly $\omega_c < \omega < 4\omega_c$ with $\omega_c = c_p/a$ the ring frequency of the cylinder. Here, a is the radius of the shell and c_p is the longitudinal wave speed. The experimental system consists of a thin steel shell with 80 ring stiffeners immersed in water. A drawing of the shell is given in Fig. 1. The rings are identical to within fabrication tolerances and are attached in a near periodic fashion with mean spacing d along the shell. The detailed positions of the rings along the shell are distributed uniformly and randomly within a small region about the nominal periodic location; i.e., the probability density that the position of a particular ring near $x = nd$ has position x is

$$p(x) = \begin{cases} 1/(2\Delta x), & |x - nd| < \Delta x, \\ 0, & \text{otherwise.} \end{cases} \quad (1)$$

The maximum deviation of the position, Δx , of a ring from its nominal periodic location is 2.5% of the rib spacing, $\Delta x/d = 0.025$.

In this paper we examine modes with relatively small azimuthal mode number, $n \leq 11$, which typically are spatially global apart from the effects of radiation damping. In particular, we focus here on the wave-number space behavior of these modes. In the absence of radiation damping, most of the small n modes would indeed be extended over the entire structure (80 ribs), the Anderson localization effects caused by the coordinate irregularity being relatively unimportant over these length scales. The behavior of the larger n helical modes is dramatically different,¹¹ with strong Anderson localization effects^{8,19} resulting from the weak spatial irregularity. These results, along with an examination of the weaker real space Anderson localization effects we have observed for the small n modes, will be given in a subsequent publication.

One would expect the modes of the system to be similar to those occurring on the associated periodic ($\Delta x = 0$) structure for such a small degree of irregularity provided the transmission of energy across the ribs is not too small. Our results confirm that this is indeed the case, at least locally, for the $n \leq 11$ azimuthal modes. The experimental results exhibit great simplicity; a clear dispersion structure dominated primarily by the Bloch or Floquet²⁰ wave-number k of the flexural wave and its replications by scattering from the periodic array, $k + 2\pi n/d$. The observed Bloch wave number differs significantly from the flexural wave number of the unribbed shell, particularly at the lower end of the frequency spectrum. Sizable frequency gaps are typically a dominant feature of the results.

While the approach for obtaining the formal solution of a vibrating periodically ribbed structure has been known for some time, and analytical and numerical solutions have been given by several authors,^{1–6} the physical significance of the Bloch wave number in the context of structural acoustics was probably first noted by Mace⁴ and Hodges *et al.*¹⁴ The importance of the Bloch wave number in the context of the scattering cross section, a direct measure of the supersonic wave-number space response of the structure, was pointed out by Photiadis⁹ and measurements¹⁶ are in accord with the

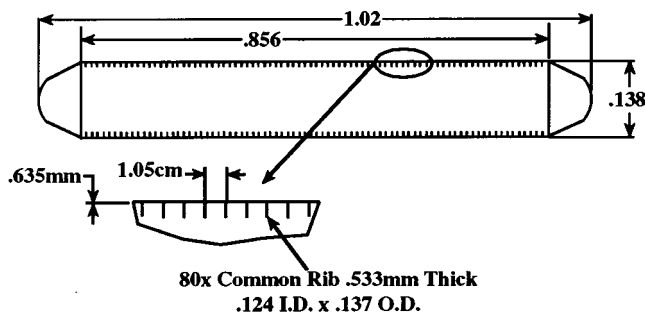


FIG. 1. Drawing of the framed shell. All dimensions are in meters unless otherwise indicated.

theoretical predictions. These experimental results revealed, however, only a piece of the puzzle since they sample such a small region of wave-number–frequency space, and as such, ambiguity concerning what wave numbers are excited on the structure remained. The results we give here provide a nearly complete picture of the physics of the $n \leq 11$ modes in this frequency range.

I. DESCRIPTION OF THE EXPERIMENT

The experiment was carried out at the Laboratory for Structural Acoustics at the Naval Research Laboratory by use of a precision multi-axis in-water robot that is used to scan an omnidirectional hydrophone on a cylindrical surface as indicated in Fig. 2. The electro-mechanical positioning and data acquisition are similar to that which has been previously reported.¹⁸ Two degrees of freedom, θ and z , are exercised to synthesize the cylindrical measurement surface of pressure with a scanning hydrophone under automated control in 0.5-cm steps along the z axis (perpendicular to the water's surface). The acoustic pressure response is recorded at each location along a 512 point line that is one and one-half times the length of the overall cylinder; at the end of

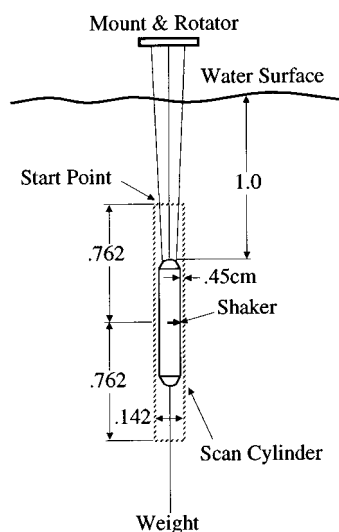


FIG. 2. Drawing of the hologram measurement geometry. All dimensions are in meters. Four support wires are attached to the rim of the endcap and are used to rotate the structure. A ballast weight is attached to the center of the bottom endcap.

each line the cylinder is rotated and the axial scan is repeated. A total of 128 rotations were completed with the 129th line being an overscan of the very first one and allows overall reproducibility to be evaluated.

The two most critical design criteria for a near-field acoustic holographic measurement are the hydrophone spatial aperture and standoff. Generally speaking, a hydrophone must be used that is sufficiently small such that it does not spatially average the highly evanescent pressures in the very near field of the structure. Similarly, the acoustic center of the hydrophone must have a sufficiently small standoff so that these evanescent components can in fact be measured above the intrinsic noise of the hydrophone. Both of these properties are satisfied by the use of a rebuilt Centronics LC-5 hydrophone having a 2.5 mm width that is positioned at a standoff distance of 4.5 mm. In order to estimate the required resolution to obtain high quality reconstructions we use²¹

$$\lambda = 54.6(d/D), \quad (2)$$

where λ is the minimum wavelength of resolution, d is the measurement standoff, and D is the dynamic range (SNR) at each frequency. At the highest frequency of this study (40 kHz), the wavelength of flexural waves on the shell is estimated by a free bending wave of a flat plate to be 1.2 cm and so the required minimum dynamic range for a 4.5-mm standoff is 20 dB.

The overall broadband signal-to-noise ratio achieved was over 55 dB at each of the frequencies in the band of interest. The excess dynamic range was highly desirable in that the wave-number domain filtering to implement GENAH (generalized near-field acoustic holography) was made easier as a result. The very high dynamic range was achieved by use of a linear (FM) chirp 6 ms long that covered a band from 8 to 50 kHz. The chirp was designed in MATLAB, loaded into an arbitrary waveform generator, and synchronously triggered at a 5-Hz repetition rate to clock out the entire waveform at 8-ms sample intervals. The chirp was amplified to a 140-V peak-to-peak level and used to drive a lightweight (8 g) and low moment-of-inertia piezo-electric microshaker mounted directly to the shell near its axial midpoint, midway between two ribs. In order to measure the drive point force and track it throughout the measurement, the shaker was built with a collocated force shell.

The entire hologram consists of $128 \times 512 = 65\,536$ spatial points (not including the overlapping last line). After motion to a new hydrophone measurement position, the scanner was allowed to settle before acquisition and similarly after shell rotation. At each of these hydrophone measurement positions, the shaker was excited with the waveform and the resulting acoustic pressure was recorded 16 times to form an average in order to increase the signal-to-noise ratio. In a similar fashion, the force cell response was recorded together with the pressure response at the beginning of each line, i.e., 128 times. Each of the recorded time histories consisted of 32.768 ms of time data for a spectral resolution of 30.517 Hz. The resulting data files required approximately 1.1 Gbyte of storage.

II. WAVE-NUMBER SPACE (k_z, ω) RESULTS

A. General observations

The normal surface velocity field on the shell obtained from holographic projection, $v(\theta, z, \omega)$, is transformed into wave-number space by Fourier transforming over the straight section of the shell,

$$v_n(k_z, \omega) = \int d\theta dz \exp(-i(k_z z + n\theta)) v(\phi, z, \omega). \quad (3)$$

One may then plot the data as a function of (k_z, ω) for varying fixed values of n . In this way, the natural waves of the system can be directly inferred from the data. In Figs. 3 and 4, the experimental results are shown for $n=0, \dots, 11$. In Fig. 3(a) the near-field response of the shell to the drive has been removed using a notch filter with a Tukey window. This signal processing lowers the broad wave-number background resulting from the shaker near field which especially obscures the supersonic part of the spectrum and makes the membrane waves more difficult to see. The Fourier spectrum including the near field is shown for small values of n in Fig. 3(b) for comparison. Overlaid on the figures are the acoustic wave number and the flexural wave number of an unribbed fluid loaded shell. The dispersion relation for the flexural wave number is shown for only a few of the modes because it changes by only a small amount over this range of n .

The most prominent aspect of the data for the values shown, $n \leq 11$, is the appearance of very strong continuous features in the wave-number–frequency space response. These features are observed to obey a number of rules independent of mode number n . The inferred group speed of the features; the local slope, is slow relative to the speed of the acoustic and membrane waves, corresponding roughly to the group speed of flexural waves on an unribbed fluid loaded shell, or slower. The shapes of the features are smooth, periodic in wave-number space with period $2\pi/d$, and show sizable frequency gaps. Note also that the response is fairly strongly suppressed for wave numbers within the sonic cone because of radiation damping. All of these aspects are expected properties of the flexural Bloch or Floquet waves²⁰ of the associated periodic system, and these results provide the most compelling evidence to date that the (k_z, ω) response of a ribbed fluid loaded cylindrical shell is generally dominated by the flexural Bloch wave number. Note that in the uppermost band, the flexural wave number for the unribbed shell provides a reasonable approximation to the Bloch wave number, but that at lower frequencies the departures from this estimate are order of magnitude effects.

One can also observe horizontal lines passing through all of the data. These features are independent of azimuthal mode number n and reasonably independent of k_z as well, implying that they arise from a small area about the drive point. We suspect that this effect arises from an intrinsic difficulty in measuring the actual force applied to the shell because of the small but finite (≈ 0.5 gm) mass below the force cell, and is not a characteristic of the Green's functions of the system. Based on measurements of the input impedance, the change in the force arising from a mass of this

amount gives rise to small frequency shifts near resonances of the correct order of magnitude to account for the observed venetian blind effect in the holograms. (Such a frequency shift in the measured force produces “venetian blinds” through the normalization operation, $G = v_{\text{meas}}/F_{\text{meas}}$.) In any case, this effect does not substantively effect our interpretation of the data.

The results show a significant dependence on the azimuthal mode number n primarily because of the presence of the ribs. All the mode orders show basically three passbands; for the orders $n=0, \dots, 3$ the lowest band is below the lowest frequency of the data and only the very top of the band is seen. Typically there is a fairly small frequency gap between the two lower bands, and a significant frequency gap separating the middle and upper frequency bands. The lowest frequency band occurs somewhat below the ring frequency (about 11 kHz) for the low mode orders and gradually increases to occur near the ring frequency for the $n=8-11$ modes. This passband is rather narrow. The second passband occurs in the neighborhood of the ring frequency for the low order modes, is typically rather narrow except in the neighborhood of $n=7-9$, and once again increases relatively slowly in frequency as n increases. The third band is quite broad, extending from about $f=18$ kHz all the way up to $f=37$ kHz for the $n=0-8$ modes.

The physical mechanisms underlying most of these results can be inferred by comparison with existing theoretical predictions for the flexural Bloch wave number. The two lower bands are most likely due to near resonant motion of the ribs coupled by flexural motion of the shell. Hodges *et al.*¹⁴ predicted the occurrence of two such low-frequency passbands just as we have observed, the lower band being associated with out-of-plane twisting rib motion and the upper band being associated with in-plane flexural rib motion. Further, the theoretical dispersion curves given by Hodges *et al.*¹⁴ are in reasonable qualitative agreement with our results, despite the fact that their rib geometry differed somewhat from that which we examined, T -ribs rather than simple rings. The near vanishing of the frequency gaps near mode $n=8$ was also predicted theoretically¹¹ and shown to arise from a rib transmission resonance, essentially phase matching to the flexural wave in the rib. The upper passband involves primarily reverberent flexural motion of the shell and, apart from the very significant band gaps, the Bloch wave number in this band can be predicted with reasonable accuracy by the fluid loaded flexural wave number of the unribbed shell scattered into the first Brillouin zone by the near periodic array. This has been noticed previously in the context of acoustic scattering from a ribbed shell.^{16,17} The theoretical approach employed by the above references, directly solving for the Bloch wave number, seems to be quite sufficient for obtaining predictions of the dominant wave numbers excited on nearly periodic ribbed shells in this frequency range.

The explanation for the appearance *only* of the flexural Bloch wave number, ignoring for the moment the weak imprint of the membrane waves which we shall discuss below, is quite simple and has to some extent been given previously.¹⁷ Ignoring radiation damping, the natural waves

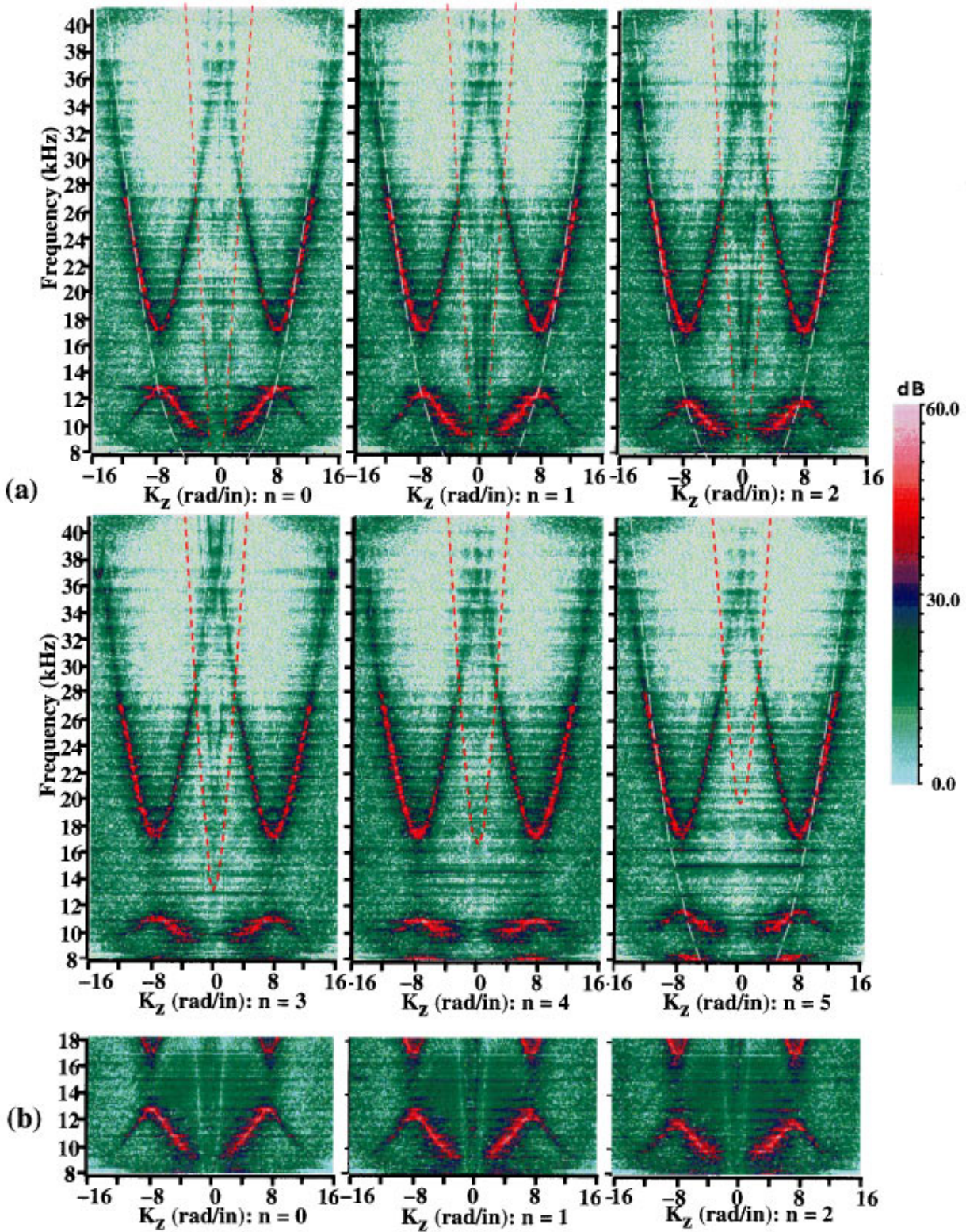


FIG. 3. Magnitude of the measured normal surface velocity field in dB ($20 \log_{10}|v|$) in axial wave-number–frequency space for azimuthal modes $n=0, \dots, 5$. (a) has the shaker near-field filtered out as discussed in the text, while (b) contains the shaker near field for comparison. The white dotted line is the dispersion curve for free flexural waves while the red dotted line encloses the supersonic region.

of the periodic system are Bloch waves of the form²²

$$\psi_{q\alpha}(z) = \exp(iqz)U_{q\alpha}(z), \quad (4)$$

where q is the flexural Bloch wave number, α is the band index, and $U_{q\alpha}(z)$ is periodic with period d ; $U_{q\alpha}(z)$ gives

the mode shape within a single bay. The Bloch wave-number q is determined uniquely up to a sign at each frequency yielding a characteristic dispersion relation $\omega(q)$. The response of the system can be expressed as a superposition of these natural waves, and at frequency ω , will be strongly

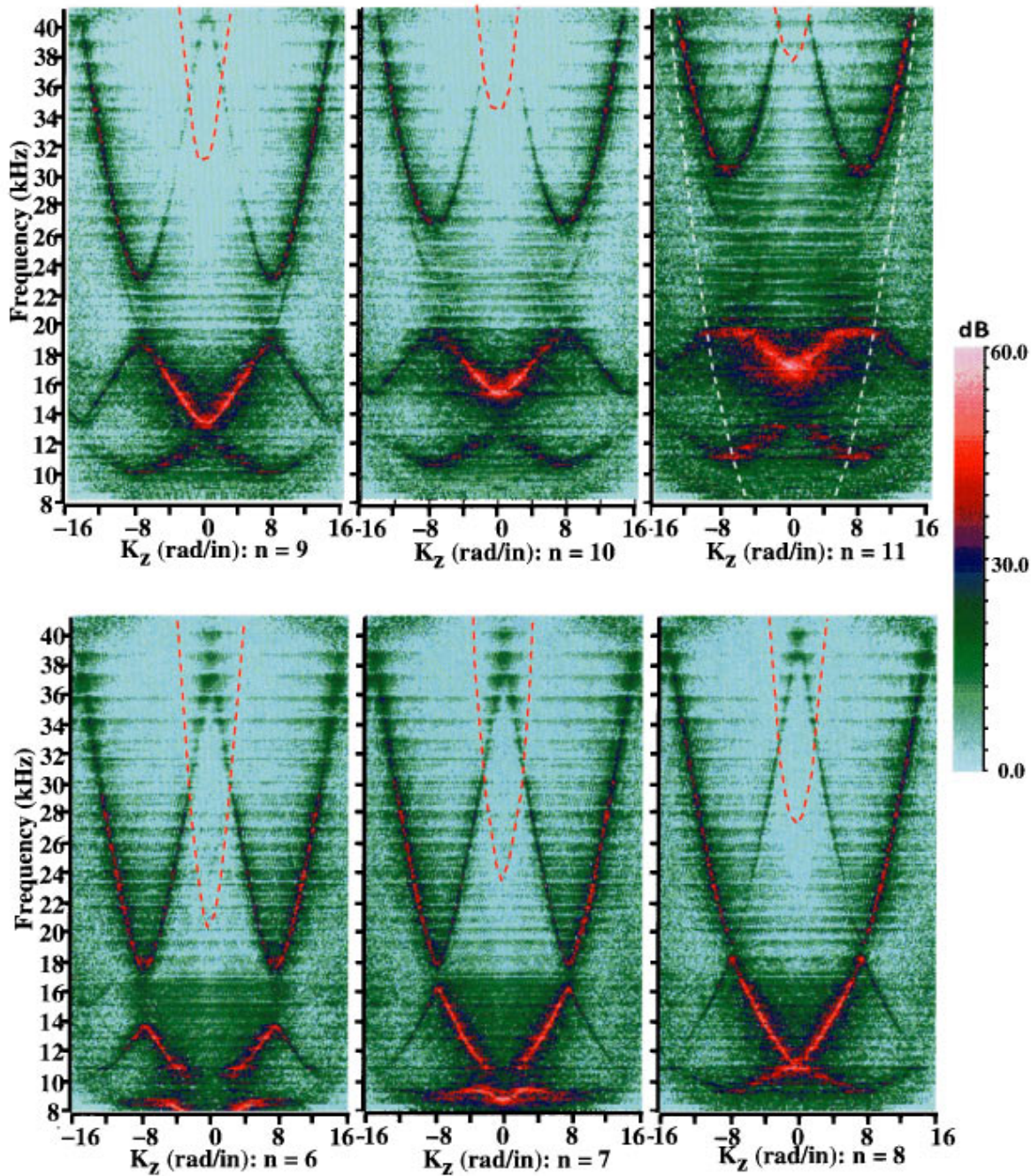


FIG. 4. Magnitude of the measured normal surface velocity field in dB ($20 \log_{10}|u|$) in axial wave-number–frequency space for azimuthal modes $n=6, \dots, 11$. The white dotted line is the dispersion curve for free flexural waves while the red dotted line encloses the supersonic region.

enhanced by the modes most nearly satisfying the dispersion relation, provided such solutions exist. Near a particular feature in (k_z, ω) space, the response is therefore approximately given by a single Bloch mode $\psi_{q\alpha}(z)$, whose Fourier spectrum is

$$\begin{aligned} \psi_{q\alpha}(k_z) &= \int dz \exp(-ik_z z) \psi_{q\alpha}(z) \\ &= \sum_m \alpha_{m\alpha} \delta(q + 2\pi m/d - k_z), \end{aligned} \quad (5)$$

with only the components $q + 2\pi m/d$ appearing as a result of the periodicity of $U_{q\alpha}$.

In the presence of fluid loading, such an expansion is of course not exact, and one might expect significant smearing of the pass/stop bands, indicating the presence of other wave numbers, but the experimental results demonstrate that this is in fact not the case. The observed enhancements are sharp and well defined and trace out a typical dispersion for the Bloch wave number. This result is quite significant since the problem contains at least two other important wave numbers, the flexural wave number of the unribbed shell and the acoustic wave number, and an exact expression for Green's function is quite complicated. The acoustic wave number does make an appearance but by a strong suppression of the

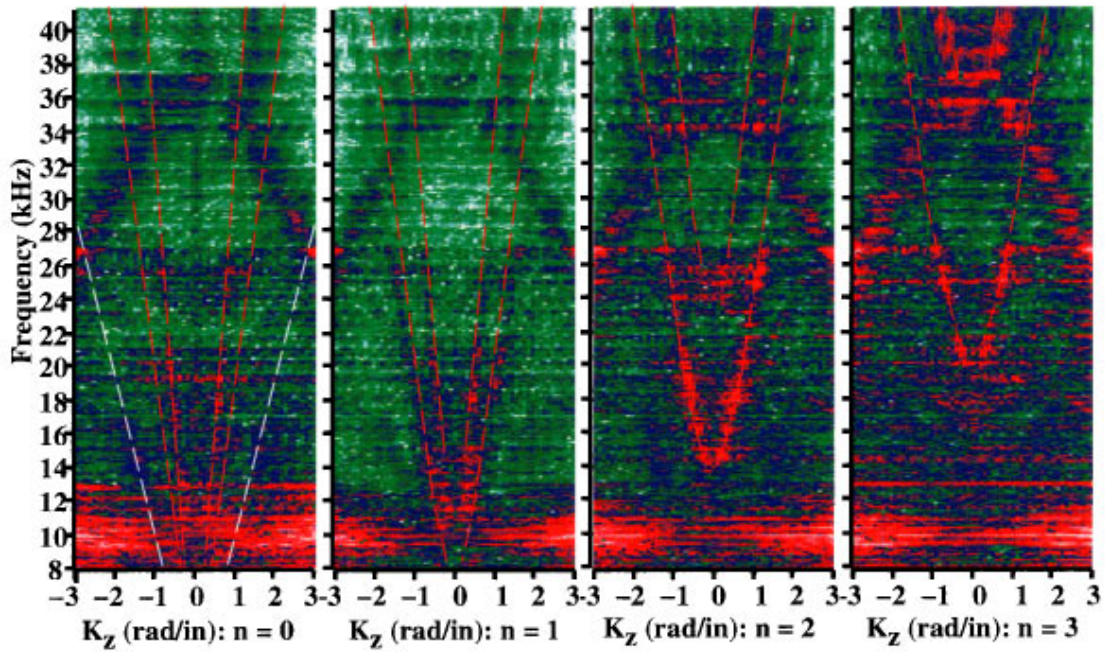


FIG. 5. Magnitude of the measured normal surface velocity field in dB ($20 \log_{10}|v|$) in supersonic region of axial wave-number–frequency space for azimuthal modes $n=0,\dots,3$. The dynamic range has been increased in order to make the features in this region more visible. The white dotted line encloses the supersonic region of wave-number–frequency space and varies slowly with n over most of the frequency range, while the red dotted lines are the dispersion curves for the longitudinal (inner lines) and shear (outer lines) waves. As in Fig. 3(a), the shaker near field has been filtered out.

surface velocity field, rather than an enhancement, just as one would expect.

B. Supersonic wave numbers

The supersonic part of the wave-number space spectrum is of special interest because these components are respon-

sible for the radiation of both interior and exterior noise, and in addition control the elastic part of the scattering cross section. The response of the system is rather strongly suppressed in this region because of radiation damping as shown in Fig. 3(a). To better examine the results, a close up with enlarged dynamic range is shown for the low order modes in

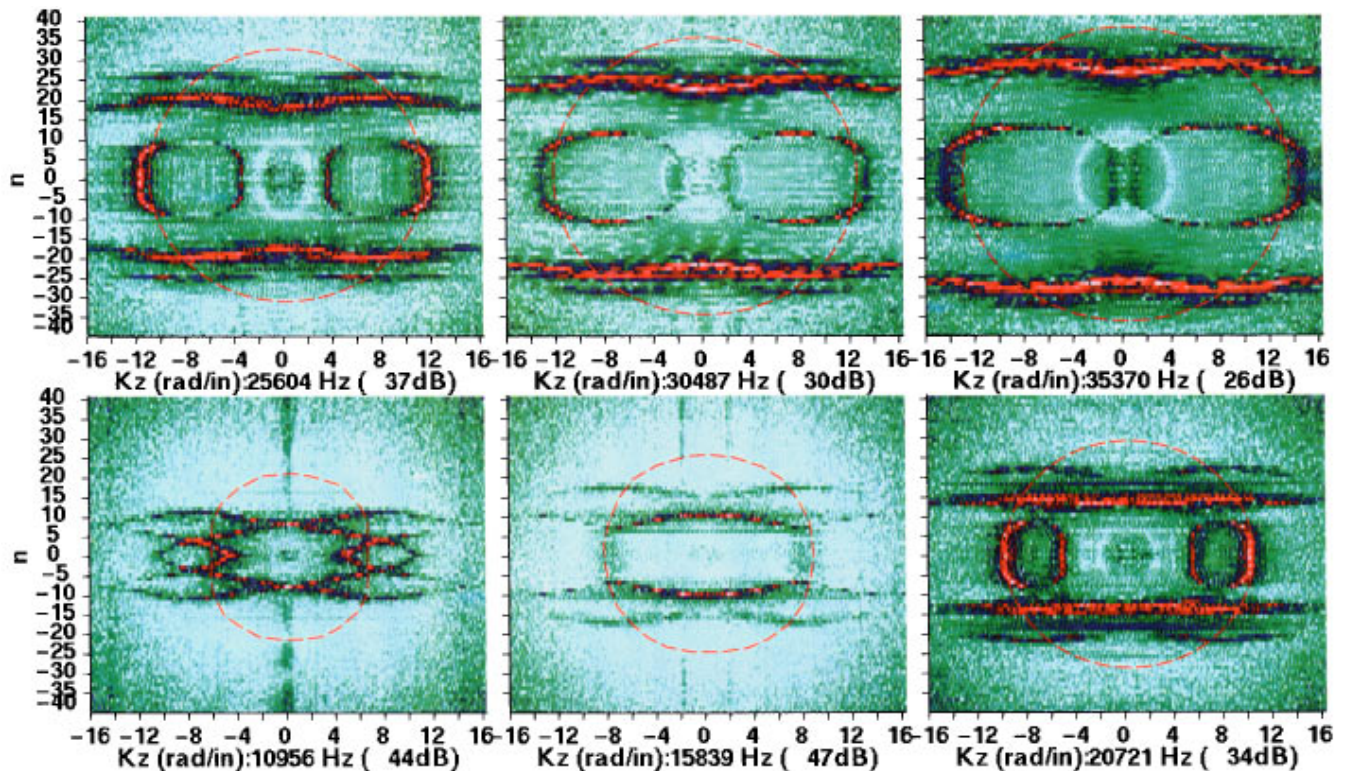


FIG. 6. Magnitude of the measured normal surface velocity field in dB ($20 \log_{10}|v|$) in wave-number space (n, k_z) for various fixed frequencies. The red dotted line encloses the supersonic region of wave-number space. The plots are relative to the maximum dB level at each frequency, indicated below each subplot.

Fig. 5. Superimposed on the figures are dispersion curves for the fast shear and longitudinal waves and the sonic cone. The near field has been filtered out as in Fig. 3(a) in order to better see the traveling wave behavior. Enhancements due to the fast membrane waves²³ are clearly discernable but weaker than they appear in scattering measurements. Typically, just as for an unribbed shell, the flexural waves dominate the response, the levels resulting from the membrane waves being 25–35 dB smaller.

The results show a strong impact of the dispersion curves of the flexural Bloch wave on the enhancements resulting from the fast waves. At relatively low frequencies, $f \leq 27$ kHz, the response due to the shear and longitudinal waves is apparent. As the frequency is increased and the flexural Bloch wave enters the sonic cone, the imprint due to the fast waves is abruptly suppressed and the dominant highlight is due to the supersonic component of the Bloch wave. As the frequency increases into the next stop band at about 34–37 kHz the membrane waves once again become noticeable. Evidently, interaction between the flexural Bloch waves and the membrane waves is important in determining the levels of the membrane waves.

The abrupt suppression of the fast waves when the flexural Bloch waves become supersonic implies that when the Bloch waves are able to radiate energy into the fluid there is a significant energy flow: membrane wave → flexural Bloch wave → radiated acoustic wave. At frequencies for which the flexural Bloch wave cannot radiate such a steady-state energy flow evidently does not occur. A simple explanation for this observation is that in the absence of radiation damping, energy which transfers into the flexural Bloch wave later scatters back into membrane wave energy. Thus, when the flexural Bloch wave is entirely subsonic, an equilibrium situation is set up in which there is no net energy flow between the wave types. This “equilibrium” scattering of vibrational energy back and forth between flexural and membrane motion, wave mixing, is disturbed by acoustic radiation if the flexural Bloch wave has a supersonic component; i.e., there is not time for flexural energy to be scattered back into membrane energy and is instead rather quickly radiated into the fluid. In the reverse direction, there does not appear to be a corresponding energy flow, flexural → membrane → radiated acoustic wave; such a flow would give rise to damping of the subsonic flexural Bloch waves, an effect not seen in the data. This is consistent with theoretical results²⁴ which show enhanced damping of membrane waves at frequencies for which the flexural Bloch wave is radiation damped.

III. SLOWNESS SURFACES

In an earlier paper²⁵ the dispersion curves in (k_z, n) for fixed frequency for an unribbed shell, otherwise similar to the ones discussed in this paper, were presented. The helical wave spectra of the flexural waves in the unribbed shell appear as figure eights in (k_z, n) space which open up to circles as the frequency increases. In the case of the ribbed shell, this picture dramatically changes. Figure 6 presents the k -space results, with $20 \log[v_n(k_z, \omega_i)]$ color coded as before, for the ribbed shell at a set of selected frequencies. These results can be constructed from horizontal cuts

through $k_z - \omega$ plots, shown in Figs. 3 and 4, which helps interpret the very complicated patterns which arise. The red dashed lines indicate the dispersion curve (remnants of the figure eights) of the flexural wave for an unribbed shell. Note also that the acoustic circle, in which the helical waves radiate to the far field, is very apparent at the higher frequencies (corresponding to low levels of the velocity). A major feature of the slowness plots are the circular regions which we refer to as “eyeglasses.” These features arise from flexural Bloch waves, especially from the third passband, appearing first ($n=0$) near 17 kHz. When the eyeglasses enter the acoustic circle, the Bloch waves radiate to the far field, dominating the radiation from the shell. This radiation loading then depresses the level of the associated subsonic Fourier component of the Bloch waves (seen in the left and right vertical segments at the extremities of the eyeglasses).

Another important feature of the dispersion curves are the “eyebrows” above and below the eyeglasses. Note that there are actually two sets, with an outer eyebrow lower in level than the inner one. The outer eyebrow seen in all the panels is due to the first passband. The inner eyebrow, also occurring in all the panels, arises from the second passband. At the lowest frequency shown, 10.9 kHz, this eyebrow closes down, filling in the region around $n=0$.

The measured dispersion curves in (k_z, n) space provide a powerful tool when viewed as slowness surfaces. The high levels which occur can be interpreted as a discretized form of the slowness surfaces, curves in this two-dimensional case, which appear in crystallography.²⁶ Each highlight on the slowness curve corresponds to a helical Bloch wave, and the normals to the curves formed from these highlights provide the direction of waves which beam down the shell. In other words, the helical waves in the slowness curve spatially beat against one another to create beam patterns of energy.

Perhaps it is not as well known that the strength of the beams which are created are proportional to the local radius of curvature of the slowness surface at any given frequency. This can be fairly easily shown²⁷ using a stationary phase approximation to a line integral which represents a sum of the waves over a piece of the slowness surface. That is, assuming continuous wave-numbers k_s in the circumferential direction and letting $s = a\phi$, the resulting shell velocity from that piece is proportional to

$$v(z, s) \approx \int_{\Gamma} V(\mathbf{k}) e^{i\mathbf{k} \cdot \mathbf{r}} d\Gamma, \quad (6)$$

where $\mathbf{r} = (r \cos \beta, r \sin \beta)$ is the position on the shell, and $\mathbf{r} = (k_x(\theta), k_y(\theta))$, a particular point on the slowness curve, gives the direction of the helical wave. Here θ is the angular coordinate in k space. Converting Eq. (6) to an integral over θ gives

$$v(z, s) \approx \int_{\theta} V(\theta) e^{i r [k_x(\theta) \cos \beta + k_y(\theta) \sin \beta]} \times k(\theta) \sqrt{1 + \left(\frac{1}{k} \frac{dk}{d\theta} \right)^2} d\theta. \quad (7)$$

Assuming that $V(\mathbf{k})$ is slowly varying relative to the oscillating exponential, an assumption which fixes the source

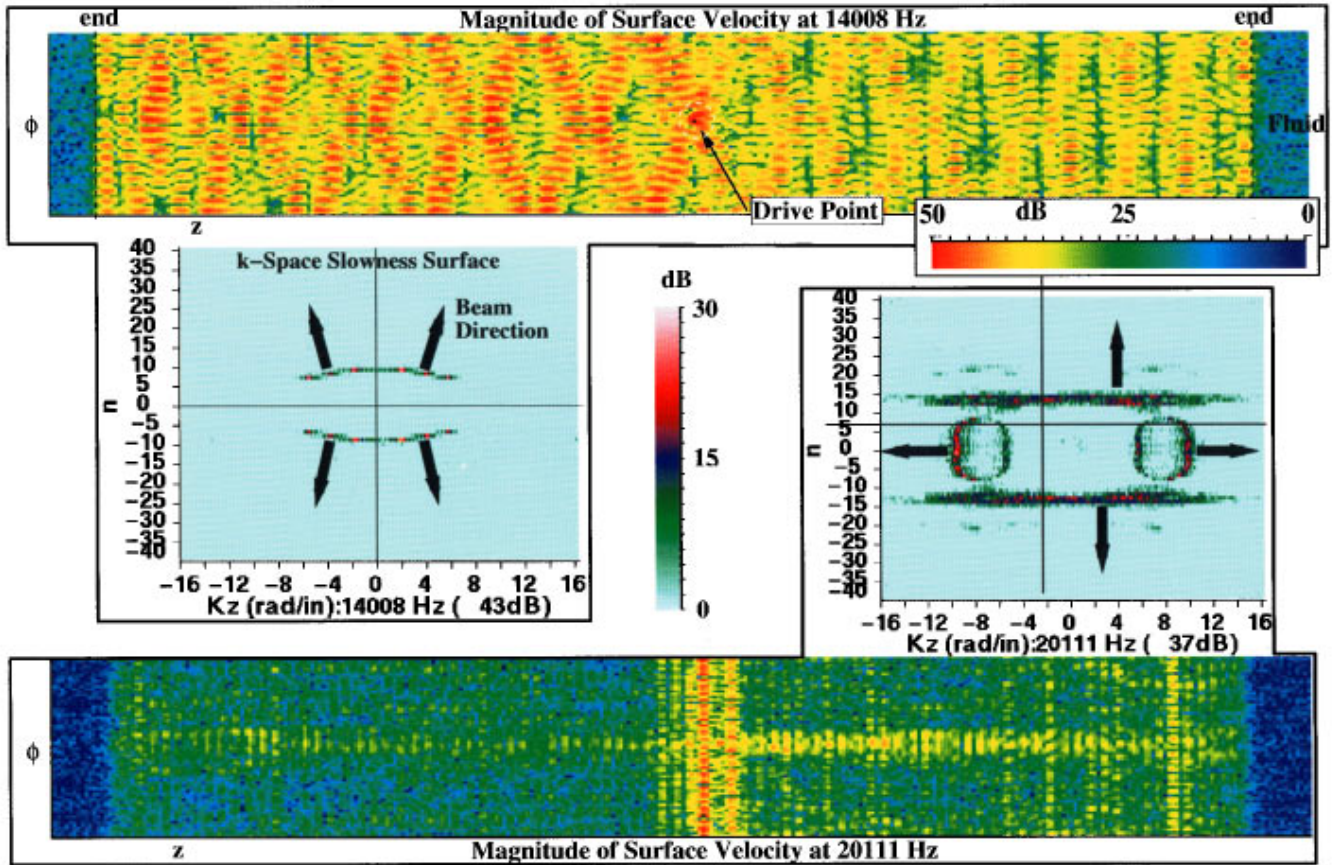


FIG. 7. Real space response of the shell with the accompanying wave-number space (n, k_z) measurements at $f=14$ kHz and $f=20$ kHz.

at $r=0$, and evaluating the integral by the method of stationary phase yields

$$v(z, s) \approx V(\theta_0) e^{ik_0 \cdot r} e^{\pm i\pi/4} \sqrt{\frac{2\pi k_0}{r}} \sqrt{\rho(\theta_0)}, \quad (8)$$

where the stationary phase point, θ_0 , is determined from a solution to

$$\frac{d\mathbf{k}}{d\theta} \cdot \hat{r} = 0, \quad (9)$$

and $\rho(\theta_0)$ is the local radius of curvature of the slowness curve. Hence, when the slowness surface is flat, implying a large radius of curvature, then provided the surface velocity near these wave numbers is sizable, a strong beam of energy is formed. On the other hand, when the slowness surface has a small local radius of curvature, then vibrational energy tends to spread isotropically. The stationary phase point can be easily picked out graphically by employing Eq. (9), which indicates that the normal to the slowness curve points in the direction of the observer at the stationary phase point. These results are directly analogous to those one obtains in a general anisotropic medium.²⁶

We further clarify these concepts in Fig. 7, which shows the slowness surfaces at two different frequencies compared with the corresponding spatial surface velocity on the shell. The displayed amplitude range has been reduced to 30 dB

for the slowness surfaces in this figure. The 14-kHz surface (on the left) is dominated in each quadrant by three helical wave components, seen as the small white-red dots nearly in a straight line. The perpendicular to this straight line provides the direction of propagation of the energy down the shell. These three waves beat against one another to create velocity beams as can be seen in the top panel. The drive point is at the center of the panel. In the 20-kHz example, shown at the bottom of Fig. 7, the dominant pieces of the slowness surface and the corresponding directions of energy flow are shown. These pieces correspond to very large radii of curvature, and thus from the analysis above, provide the dominant directions of energy flow in the shell. The eyeglasses, containing low circumferential orders, lead to wave propagation in the axial direction down the shell, whereas the eyebrows, dominated by $n=\pm 13$ and $n=\pm 14$, lead to a wave in the circumferential direction which tends to get trapped at the drive point. These conclusions are reflected in the surface velocity shown at the bottom of the figure.

In summary, the slowness surface can be used to predict the magnitude and the direction of wave propagation in a shell. Returning to the slowness surfaces of Fig. 6, we can use this insight to predict the dominant directions of wave propagation down the shell by looking for regions of large radius of curvature (and large amplitude) and drawing the normal to the curve in these regions. Observations of the

reconstructed surface velocity, not shown here, bear out the fact that very frequently the second passband leads to wave propagation in the circumferential direction, trapped near the driver, with almost no group velocity in the axial direction. This corresponds to the three panels, at 20.7, 30.5, and 35.4 kHz, in Fig. 6, as well as the 20.1-kHz example in Fig. 7.

IV. CONCLUSION

We have presented measurements of the radial response of a ribbed shell to an internal point drive. The axisymmetry of the system enables the data to be examined one azimuthal mode at a time, an approach which allows the dispersion relation of each mode to be directly observed in wave-number–frequency space. This reveals the overall dominance of the flexural Bloch or Floquet waves in the response of a ribbed shell to a localized source, and further, shows the importance of the Bloch wave-number q and its components $q + 2\pi n/d$ resulting from scattering from the near periodic array.

The supersonic components of the response, which play a dominant role in the radiation and scattering of sound, are strongly suppressed relative to the subsonic components because of the effects of radiation damping. At the low end of the mid-frequency range the small n membrane waves, both quasi-longitudinal and quasi-shear, are visible although rather weakly excited. As the frequency increases and the flexural Bloch waves begin radiating acoustic energy, these modes are strongly suppressed. As the frequency is increased further and one enters the next stop band, the membrane modes once again become apparent. This result provides evidence for significant mixing of flexural and membrane vibrational energy resulting from the ribs: Such wave mixing would suppress the membrane response provided flexural waves are damped. This result may be quite significant in terms of understanding the behavior of more complex structures, since in that scenario flexural vibration would most likely be damped by one mechanism or another.

Within the various passbands, significant beaming and focusing of vibrational energy results from the presence of the ribs. An examination of the response of the system in $k_z - k_\phi$ space enables these effects to be understood relatively easily. The beaming most often occurs in the azimuthal direction, and arises most often in this frequency range from the second flexural Bloch passband. The dynamics in this band consist of in-plane flexural vibration of the ribs coupled to one another by out-of-plane flexural shell motion. Strong focusing also occurs in the axial direction, in this case arising most often from the third flexural passband, the band in which the wave propagation consists of flexural shell vibration multiply scattered by the rib array. This phenomenon leads to the formation of relatively narrow beams of energy traveling along the length of the shell.

The weak deviations of the shell from periodicity (2.5%) do not strongly effect the wave-number spectrum of the system for the relatively small values of n , $n \leq 11$, we have examined here. The principle effects which we have observed in wave-number space are a relatively weak broadening of dispersion relations. This implies that locally, at least for a few structural wavelengths, the wave propagation pro-

ceeds as though the structure were periodic. Modeling efforts based on the infinite periodic structure can most probably be successful in accounting for the results we have presented here. On closer examination in real space, the localizing effects of even this small amount of irregularity can be observed for the small n helical modes, with more dramatic effects occurring for the large n helical modes. We will report on these results in a subsequent publication.

ACKNOWLEDGMENT

This work was supported by the Office of Naval Research.

- ¹M. V. Bernblit, "Sound radiation from a ribbed cylindrical shell," *Sov. Phys. Acoust.* **21**, 518–521 (1976).
- ²C. H. Hodges, J. Power, and J. Woodhouse, "The low frequency vibration of a ribbed cylinder, Part I: Theory," *J. Sound Vib.* **101**, 219–235 (1985).
- ³D. J. Mead, "Wave propagation and natural modes in periodic systems: I. Mono-coupled systems," *J. Sound Vib.* **40**(1), 1–18 (1975).
- ⁴B. R. Mace, "Periodically stiffened fluid-loaded plates, I: Response to convected harmonic pressure and free wave propagation," *J. Sound Vib.* **73**, 473–486 (1980).
- ⁵D. J. Mead, and N. S. Bardell, "Free vibration of a thin cylindrical shell with periodic circumferential stiffeners," *J. Sound Vib.* **115**, 499–520 (1987).
- ⁶C. B. Burroughs, "Acoustic radiation from fluid-loaded infinite cylinders with doubly periodic ring supports," *J. Acoust. Soc. Am.* **75**, 715–721 (1984).
- ⁷S. H. Choi, J. D. Achenbach, and T. Igusa, "The effect of periodically attached substructures on the excitation of submerged cylindrical shells," *J. Sound Vib.* **177**, 339–392 (1994).
- ⁸C. H. Hodges and J. Woodhouse, "Vibration isolation from irregularity in a nearly periodic structure: Theory and measurements," *J. Acoust. Soc. Am.* **74**, 894–905 (1983).
- ⁹D. M. Photiadis, "The effect of irregularity on the scattering of acoustic waves from a ribbed plate," *J. Acoust. Soc. Am.* **91**, 1897–1903 (1992).
- ¹⁰D. M. Photiadis, "Anderson localization of one-dimensional wave propagation on a fluid-loaded plate," *J. Acoust. Soc. Am.* **91**, 771–780 (1992).
- ¹¹D. M. Photiadis, "Localization of helical flexural waves by irregularity," *J. Acoust. Soc. Am.* **96**, 2291–2301 (1994).
- ¹²G. Maidanik and J. Dickey, "Reflection of incident pressure waves from a ribbed panel," *J. Acoust. Soc. Am.* **90**, 2124–2138 (1992).
- ¹³M. B. Sobnack and D. G. Crighton, "Anderson localization effects in the transmission of energy down an irregularly ribbed fluid-loaded structure," *Proc. R. Soc. London, Ser. A* **444**, 185–200 (1994).
- ¹⁴C. H. Hodges, J. Power, and J. Woodhouse, "The low frequency vibration of a ribbed cylinder, Part I: Theory," *J. Sound Vib.* **101**, 219–235 (1985).
- ¹⁵J. R. Chapman, "Model scale measurements of the transmission and radiation of hull-borne vibrational energy using frequency/wave number analysis," in *Shipboard Acoustics* (Martinus Nijhoff, Dordrecht, The Netherlands, 1986).
- ¹⁶D. M. Photiadis, J. A. Bucaro, and B. H. Houston, "Scattering from flexural waves on a ribbed cylindrical shell," *J. Acoust. Soc. Am.* **96**, 2785–2790 (1994).
- ¹⁷B. H. Houston, J. A. Bucaro, and D. M. Photiadis, "Broadband acoustic scattering from a ribbed shell," *J. Acoust. Soc. Am.* **98**, 2851–2853 (1995).
- ¹⁸E. G. Williams, H. D. Dardy, and K. B. Washburn, "Generalized near field acoustic holography for cylindrical geometry: Theory and experiment," *J. Acoust. Soc. Am.* **81**, 389–407 (1987).
- ¹⁹P. W. Anderson, "Absence of diffusion in certain random lattices," *Phys. Rev.* **109**, 1492–1505 (1958).
- ²⁰L. Brillouin, *Wave Propagation in Periodic Structures* (Dover, New York, 1946).
- ²¹E. G. Williams, B. H. Houston, and J. A. Bucaro, "Broadband nearfield acoustic holography for vibrating cylinders," *J. Acoust. Soc. Am.* **86**, 674–679 (1989).
- ²²N. Ashcroft and D. Mermin, *Solid State Physics* (Saunders, Philadelphia, PA, 1976), pp. 131–191.
- ²³M. L. Rumerman, "Contribution of membrane wave reradiation to scat-

- tering from finite cylindrical steel shells in water," J. Acoust. Soc. Am. **93**, 55–65 (1993).
- ²⁴D. M. Photiadis, "Wave mixing effects on a periodically ribbed cylindrical shell," ASME Trans. J. Vib. Acoust. **118**, 100–106 (1996).
- ²⁵E. G. Williams, B. H. Houston, and J. A. Bucaro, "Experimental investigation of the wave propagation on a point-driven submerged capped cylinder using K -space analysis," J. Acoust. Soc. Am. **87**, 513–522 (1990).
- ²⁶B. A. Auld, *Acoustic Fields and Waves in Solids* (Wiley, New York, 1973), Vol I.
- ²⁷D. M. Photiadis, "Acoustic Beaming and Focusing in Nearly Periodic Systems," *Proceedings of the 3rd International Congress on Air and Structure Borne Vibration* (1994), pp. 261–268.

Extension of the tip excitation technique to the rotational compliance measurement of curved structures

L. Cheng and Y. C. Qu

Department of Mechanical Engineering, Université Laval, Québec, Québec G1K 7P4, Canada

(Received 18 December 1995; accepted for publication 20 September 1996)

The present paper presents an extension of the so-called tip excitation technique for measuring the rotational compliance of curved structures. On the basis of the original form of the technique, developed for attached plane structures, the technique is improved to take into account the presence of the in-plane vibration and the rigid motion. Two derivatives of the technique are developed: the first one using two accelerometers allows a more accurate indication of rotational response, thus providing a good accuracy in middle frequency range; the second one using double excitation effectively eliminates the in-plane force excitation, thus providing an excellent measurement accuracy at both low and middle frequencies. Numerical simulations using finite element modeling are performed to analyze different parameters affecting the performance of the technique. Experimental validations are then reported. It is shown that the technique is successfully extended to curved structures while retaining the advantages of the original version of the method in terms of its simplicity and its capacity for mass loading compensations. © 1997 Acoustical Society of America. [S0001-4966(97)00902-8]

PACS numbers: 43.40.Yq, 43.40.At [CBB]

INTRODUCTION

Mechanical compliance and mobility concepts have become one of the standard tools to characterize the dynamic behavior of structures. Their wide application demands that both theoretical and experimental techniques be developed.¹ Compared to the translational compliance, the rotational compliance measurement is much more difficult due to the access to the quantities related to the rotational degrees of freedom. Two major obstacles to overcome include the acquisition of rotational responses and the production of a moment excitation.^{2,3} The situation is even more critical when one handles light thin-walled structures, since any measuring device physically connected to the system will tend to affect the dynamics of the original structure.

Due to these difficulties, there exists only a very short list of references dealing with the rotational compliance or mobility measurement, as reported by some very recent works.⁴⁻⁷ The classical approach is the double-exciter method, using a pair of dynamic exciters operated in phase opposition to provide moment excitation via a simple lever. Since its development, it remains the method that is mostly used. Effort has been made recently to improve the method by taking into account the loading effects of the exciter.^{4,5} However, main difficulties related to the method lie in the production of a perfect phase match between two exciters to ensure a perfect phase opposition. In addition to that, the quality of the excitation can still be poor due to the mass introduced by the exciting configuration.

As an attempt to address the rotational measurement problem, a so-called tip excitation technique (TET), was recently proposed.^{6,7} In this approach, a beamlike tip is used to transfer a force excitation into a torque and the rotational response into a translational one, thus converting a rotational measurement problem into a translational one, permitting the

use of conventional apparatus. Using a single force exciter or an impact hammer, the TET avoids the matching difficulties encountered in the double-exciter method. Also, a dynamic analysis of the tip motion allows one to eliminate the mass effect of the tip on the structure to be measured. On the basis of a cantilevered rectangular plate, the technique was numerically and experimentally assessed, showing that the TET is feasible to use in low- and middle-frequency ranges for plane structures. However, the hypotheses made in the development of the technique restrain its application only to attached plane structures, whose in-plane motion can be mostly neglected compared with the flexible motion. This technique will hereafter be called the original TET.

As a continuation of the previous work, this paper first discusses the applicability of the original TET to curved structures that may involve significant in-plane motion. The so-called in-plane motion, due to the curvature or free boundaries, represents the movement of the measuring point in the tangential plane of the structure. After a brief review of the technique, the original TET without any modification is first applied to a series of curved panels with varying curvatures. Curvature effects are then analyzed, leading to some modifications of the technique. Two alternatives using two accelerometers with single or double excitations are further investigated. The modified TET using two accelerometers with single excitation eliminates unwanted translational response to enhance the accuracy of the rotation measurement, while the modified TET with double excitation eliminates effects of the in-plane force excitation. Finally, experiments using a free panel are carried out to assess the technique. Both numerical and experimental results illustrate the performance of each version of the technique, as well as the applicability of each.

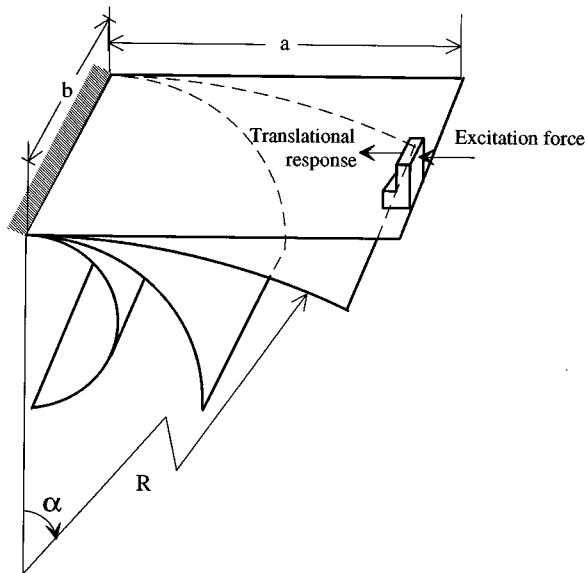
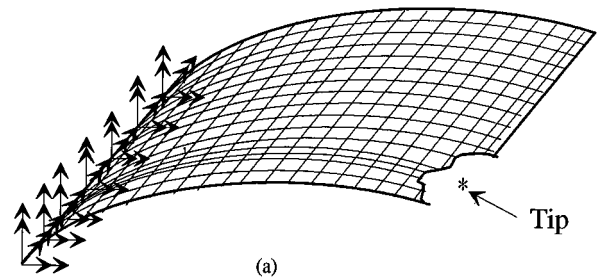
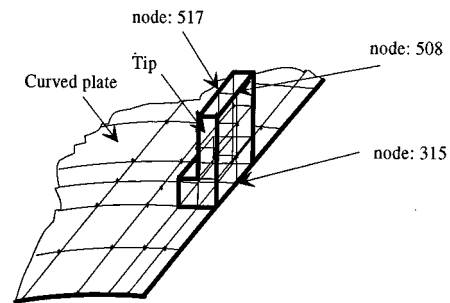


FIG. 1. Curved panels with various curvatures.



(a)



(b)

FIG. 2. FEA mesh of a typical curved panel-tip combination.

I. REVIEW OF THE TECHNIQUE AND DESCRIPTION OF THE PROCEDURE

The TET consists of attaching a small beamlike tip to a point on the structure where the rotational compliance has to be evaluated as illustrated in Fig. 1. For illustrating purpose, assume that the rotational compliance about the free edge is under investigation. By applying a driving force at the tip, an excitation moment is produced at the tip-structure intersection. In addition to that, the tip's motion provides information about the rotation undergone by the structure. On the basis of simultaneous measurements of the exciting force and the resulting acceleration, the rotational compliance of the structure is to be derived. A rigid body dynamic analysis of the tip is then performed, taking into account the coupling at the intersection of the structure and the tip, resulting in analytical formulas for rotational compliance. This procedure yields the following expression for both the compliance amplitude A_{cr} and the phase angle ϕ_{cr} :

$$A_{cr} = \frac{1}{\omega^2} \sqrt{\left(\frac{K}{T}\right)^2 - 2I_{yy} \frac{K}{T} \cos \phi_a + I_{yy}^2}, \quad (1)$$

$$\tan \phi_{cr} = \frac{-I_{yy} \sin \phi_a}{I_{yy} - (K/T) \cos \phi_a}, \quad (2)$$

where I_{yy} is the total effective moment of inertia of the tip about the rotation axis, passing through the contact region between the tip and the panel and parallel to the panel's free edge in the specific configuration shown in Fig. 1; T and ϕ_a are, respectively, the amplitude and the phase angle of the translational acceleration (acceleration/force) measured on the tip; and K is a geometric parameter which depends on the position of the excitation and that of the acceleration response. It is worth noting that the above expressions have proven to be effective in partially eliminating the inertial effects of the tip on the rotational compliance. However, these analytical relations were obtained on the basis of several hypotheses and simplifications, taking advantage of the

fact that the structure under investigation is an attached plane panel so that all quantities relating to the in-plane motion had been neglected.⁶ This should certainly be the main obstacle to remove regarding the extension of the technique to general curved structures.

In order to investigate the applicability of the TET to curved structures, a series of curved panels with varying curvatures are chosen as illustrated in Fig. 1. Taking a plane panel as a starting point, the panel is then bent so that the sector angle α varies from 0° (plane panel) to 180° (semi-cylindrical shell), while keeping all other dimensions and characteristics unchanged (length $a=400$ mm; width $b=300$ mm; thickness $h=3$ mm; density $\rho=7820.0$ kg/m³; Young's modulus $E=2.068E+11$ N/m² and Poisson ratio $\mu=0.30$). An aluminum tip is used to estimate the rotational compliance of the panels at a point 5 cm from the corner along the free straight edge. The tip is designed according to the principles previously developed⁶ and all its dimensions (as indicated in Fig. 5). As to the boundary conditions of the panels at the left end, either clamped edge or a free edge is to be investigated in the analyses.

Finite element analyses (FEA) using I-DEAS software are performed for the curved panels and the curved panel-tip combinations. For the former, the angular response of the panel under a pure moment excitation is calculated to provide the *expected results* of the rotational compliance. For the latter, assuming a unit force excitation on the tip, FEA calculates the quantities that should be measured in practice. The rotational compliance is then calculated using the derived compliance formula [Eqs. (1) and (2) for the original TET or other corresponding expressions that will be derived later when the TET is modified]. The results obtained are referred to as the *simulated results*.

The mesh of the curved panel-tip combination is illustrated in Fig. 2. The panel is discretized into 340 linear thin

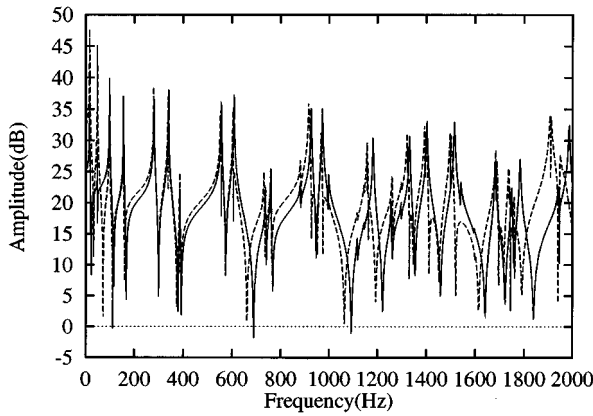


FIG. 3. Comparison of the rotational compliance of the panel with $\alpha=30^\circ$. Original TET. Expected results: (—); simulated results: (-----).

shell elements and the tip is divided into 8 linear solid elements. Convergence tests were made to ensure that the number of elements used was sufficient for the frequency range considered in this paper. For the curved panel, an exciting moment is applied at node 315 where the rotational compliance is to be evaluated. For the panel-tip combination, an exciting force is applied at node 508 and the translational acceleration at node 517 is calculated on the tip, allowing the estimation of the rotational compliance at node 315 on the curved panel.

II. DIRECT APPLICATION OF THE ORIGINAL TET

The original TET previously established is first applied to the curved panels. Figures 3 and 4 show the amplitude of the rotational compliance of the curved panels with two different sector angles: $\alpha=30^\circ$ and $\alpha=180^\circ$, respectively. Curves corresponding to the two cases are plotted for different frequency ranges so that a compatible amount of modes are included. The results are expressed in dB referencing to $1.0E-5$ rad/N m [$10 \log(A_{cr}/1.0E-5)$]. In both cases, the *simulated results* are compared with the *expected results*. It can be seen that although the two panels exhibit different dynamic characteristics, the overall tendency in terms of compliance estimation accuracy is quite similar. Generally speaking, the amplitude level discrepancy varies with the

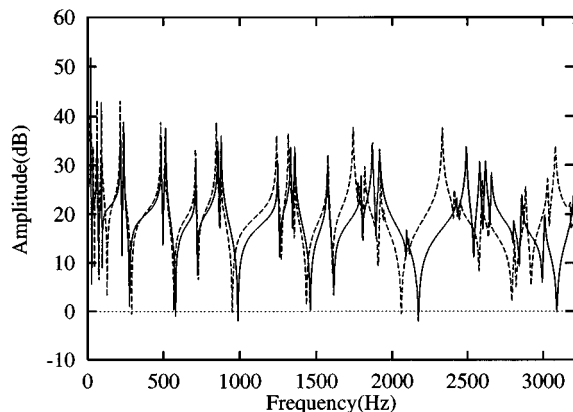


FIG. 4. Comparison of the rotational compliance of the panel with $\alpha=180^\circ$. Original TET. Expected results: (—); simulated results: (-----).

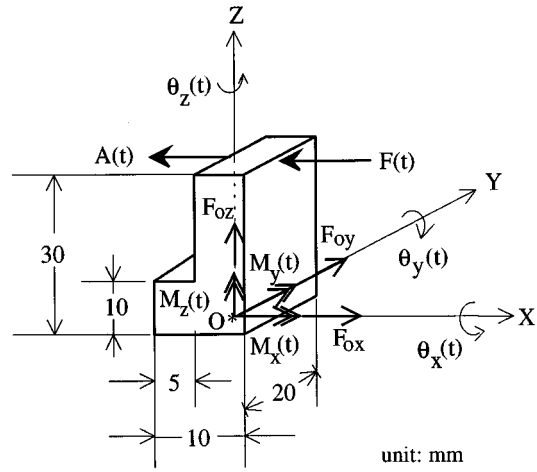


FIG. 5. Dynamic model of the tip.

frequency zone and the curvature. When the curvature becomes greater, the discrepancy seems to increase. More specifically, we notice a very bad accuracy of the technique at low frequencies involving the first 3–4 modes (zone A). In fact, both configurations present a discrepancy oscillating around 10 dB between the expected results and the simulated ones. The rigid motion of the tip in the excitation direction is believed to be the most responsible for this discrepancy, since a single accelerometer is no longer sufficient to accurately indicate the rotational response of the structure. At the middle-frequency range up to 10 modes (zone B), the technique seems to work reasonably well. With the increase of the frequency (zone C), we notice a degradation of the technique, which was also observed in the case of plane structures, mainly resulting from the coupling between the tip and the tested structure. It should be noted that the existence of the three zones is quite obvious while the dividing line between each zone may vary from structure to structure. These results seem to indicate that the original TET can be directly used for the curved structures only in the middle-frequency range (zone B). The advantage consists in its simplicity since only one accelerometer and a single excitation are required. However, modifications must be made to improve the technique at low frequencies.

III. MODIFIED TET USING TWO ACCELEROMETERS

The first step to improve the technique consists in using two accelerometers to get a more accurate indication of the rotational response of the curved structures. To this end, a dynamic analysis is performed for the tip by considering it as a rigid body. Figure 5 illustrates all possible existing forces and moments applied on the tip through the reaction of the curved structure. Note that all these quantities are decomposed into components in three directions in the established coordinate system. The frame is set in a way that the Z axis passes through the mass center of the tip. The complete equation of motion related to the rotation about Y axis is as follows:⁸

$$\begin{aligned}
& m_t(a_{ox}\bar{z} - a_{oz}\bar{x}) + I_{yy}\ddot{\theta}_y + (I_{xx} - I_{zz})\dot{\theta}_x\dot{\theta}_z \\
& + I_{yz}(\dot{\theta}_y\dot{\theta}_x - \ddot{\theta}_z) - I_{xy}(\dot{\theta}_y\dot{\theta}_z + \ddot{\theta}_x) + I_{xz}(\dot{\theta}_x^2 - \dot{\theta}_z^2) \\
& = M_y(t) - h_f F(t), \tag{3}
\end{aligned}$$

where I_{xx} , I_{yy} , I_{zz} , I_{yz} , I_{xy} , I_{xz} are the moments of inertia of tip with respect to different axes; θ_x , θ_y , θ_z the angular displacements about the X , Y , Z axes, respectively; \bar{x} , \bar{z} , \bar{y} the coordinates of the mass center of the tip in O - XYZ frame; a_{ox} , a_{oz} the two acceleration components of the tip at its base along X and Z axis; m_t the mass of the tip; $M_y(t)$ the reacting moment and h_f the distance between the applied force $F(t)$ and the X axis.

Due to the symmetric geometry of the tip about XOZ plane, $I_{xy} = I_{yz} = 0$. Equation (1) becomes

$$\begin{aligned}
& m_t(a_{ox}\bar{z} - a_{oz}\bar{x}) + I_{yy}\ddot{\theta}_y + (I_{xx} - I_{zz})\dot{\theta}_x\dot{\theta}_z + I_{xz}(\dot{\theta}_x^2 - \dot{\theta}_z^2) \\
& = M_y(t) - h_f F(t). \tag{4}
\end{aligned}$$

In the above equation, the last two terms at the left-hand side represent the coupling between the rotation about Y and X axis, and the one between Y and Z axis. Compared with other terms in the equation, these two terms are higher order terms for small amplitude vibration and can therefore be neglected. Additionally, the fact that the Z axis passes through the mass center of the tip yields $\bar{x} = 0$ and $\bar{y} = 0$. Hence Eq. (4) is simplified as

$$m_t a_{ox}(t)\bar{z} + I_{yy}\ddot{\theta}_y(t) = M_y(t) - h_f F(t). \tag{5}$$

For the plane structure, considering the high stiffness in the in-plane direction, the first term at the left-hand side can be neglected since the in-plane acceleration component a_{ox} is much smaller than all other quantities. For curved panels however, it should be kept, which demands the use of another accelerometer along the X axis.

Assuming a harmonic excitation, the reacting moment at the panel-tip intersection can be derived from Eq. (5) as follows:

$$M_y(t) = (h_f F_0 - I_{yy}\theta_0\omega^2 e^{j\phi_\theta} + m_t \bar{z} A_{Ox} e^{j\phi_{Ox}}) e^{j\omega t}, \tag{6}$$

where F_0 is the amplitude of exciting force; ω the angular frequency; θ_0 and ϕ_θ the amplitude and phase angle of the

angular displacement response; A_{Ox} and ϕ_{Ox} the amplitude and phase angle of the linear acceleration at the base of the tip along X axis.

For a point on the tip, the translational acceleration in the X direction can be written as⁸

$$\begin{aligned}
a_x(t) &= a_{Ox}(t) + \ddot{x} - x(\Omega_y^2 + \Omega_z^2) + y(\Omega_x\Omega_y - \dot{\Omega}_z) \\
&+ z(\Omega_x\Omega_z + \dot{\Omega}_y) + 2(\dot{z}\Omega_y - \dot{y}\Omega_z), \tag{7}
\end{aligned}$$

in which Ω stands for the angular velocities with respect to different axes. In principle, the translational acceleration depends not only on the rotation about X , Y , and Z axes but also the translational acceleration at the origin. In the present case where the point of interest is a fixed point on the tip with respect to the reference frame, the coordinates of the point of interest are constants ($x \approx 0$ due to the small thickness of the tip, $y = 0$, $z = h_a$). Hence, $\dot{x} = \dot{y} = \dot{z} = 0$, $\ddot{x} = \ddot{y} = \ddot{z} = 0$. By neglecting the higher order terms and replacing $\dot{\Omega}_y$ by $\dot{\theta}_y$, one obtains the following expression:

$$a_x(t) - a_{Ox}(t) = h_a \ddot{\theta}_y(t). \tag{8}$$

Assuming $\Delta a_x(t) = a_x(t) - a_{Ox}(t) = \Delta A_x e^{j(\omega t + \Delta\phi_a)}$, Eq. (8) becomes

$$\theta_0 \omega^2 = \frac{\Delta A_x}{h_a}, \tag{9}$$

where ΔA_x stands for the amplitude of the difference between $a_x(t)$ and $a_{Ox}(t)$, and h_a is the distance between the X axis and the point of measurement of acceleration.

According to the definition of the rotational compliance and, one can derive the rotational compliance $CR = \theta_y/M_y$ under complex forms:

$$CR = \frac{1}{\omega^2} \left/ \left(I_{yy} - \frac{K}{\Delta T} e^{-j\Delta\phi_a} - K_c e^{j(\phi_{Ox} - \Delta\phi_a)} \right) \right., \tag{10}$$

where $K = h_f h_a$ is a geometric parameter; $\Delta T = \Delta A_x / F_0$, and $K_c = m_t \bar{z} A_{Ox} (h_a / \Delta A_x)$.

From Eq. (10), the rotational compliance can be expressed in terms of amplitude A_{cr} and phase angle ϕ_{cr} as

$$\begin{aligned}
A_{cr} &= \frac{1}{\omega^2} \left/ \sqrt{\left(\frac{K}{\Delta T} \right)^2 - 2I_{yy} \frac{K}{\Delta T} \cos \Delta\phi_a + I_{yy}^2 + K_c^2 + 2K_c \frac{K}{\Delta T} \cos \phi_{Ox} - 2I_{yy} K_c \cos(\phi_{Ox} - \Delta\phi_a)} \right., \\
\tan \phi_{cr} &= - \frac{I_{yy} \sin \Delta\phi_a + K_c \sin(\phi_{Ox} - \Delta\phi_a)}{I_{yy} - (K/\Delta T) \cos \Delta\phi_a + K_c \cos(\phi_{Ox} - \Delta\phi_a)}. \tag{11}
\end{aligned}$$

Compared with the original TET using a single accelerometer expressed by Eqs. (1) and (2), the modified TET requires the use of two accelerometers situated respectively at the top and the base of the tip. By doing so, we hope to measure more accurately the rotation. Furthermore, the additional terms in Eq. (11) with respect to Eqs. (1) and (2)

include the possible rigid motion of the tip along the X axis and therefore help to improve the performance of the added inertia compensation.

The modified TET using two accelerometers is applied to the two curved panels previously investigated. The simulated compliances are again compared with the expected re-

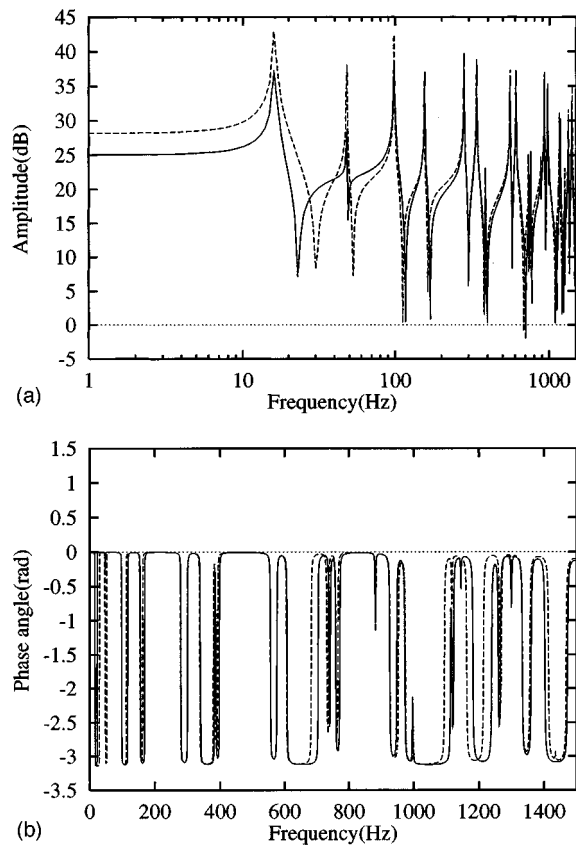


FIG. 6. Comparison of the rotational compliance of the panel with $\alpha=30^\circ$. Modified TET. Expected results: (—); simulated results: (-----). (a) Amplitude; (b) phase angle.

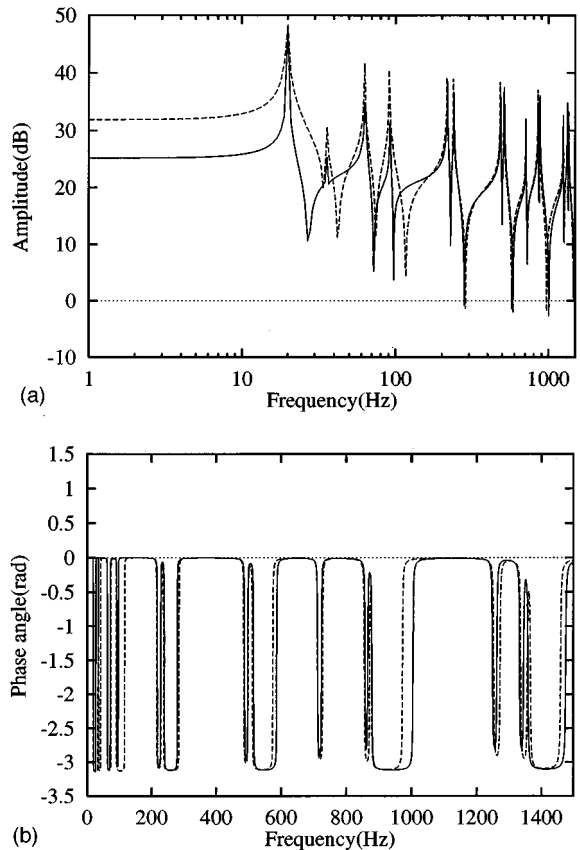


FIG. 7. Comparison of the rotational compliance of the panel with $\alpha=180^\circ$. Modified TET. Expected results: (—); simulated results: (-----). (a) Amplitude; (b) phase angle.

sults for $\alpha=30^\circ$ and $\alpha=180^\circ$ in terms of amplitude and phase angle. The results are presented in Figs. 6(a), (b), 7(a), and (b). In order to better show the performance of the technique at the low-frequency range, the amplitude results are presented in a logarithm frequency scale. It can be seen that the modified TET greatly improves the accuracy of the simulated compliance in amplitude level and the resonance frequency. At very low frequencies, the 10-dB difference noticed previously with the original TET is reduced to some 3 and 7 dB for the 30° panel and 180° panel, respectively.

Before going to further improvement of the technique, we propose several indicators to quantify the errors due to the measurement technique. It is believed that the obtained results should be split out in terms of the modal response to make the conclusions more representative on one hand, and to cover a wider spectrum of panels on the other hand. To this end, the previous expected and simulated results were firstly decomposed into modal responses. Then the errors were calculated for each mode. Two indicators are then proposed to indicate the errors associated with resonance peak positions and the amplitude levels. Figure 8 illustrates two typical modal compliance curves corresponding to the simulated and expected results respectively. The two following indicators are used:

(1) *Amplitude error* relative to the compliance level: For a given mode i , it is defined as $\bar{A}_s^i - \bar{A}_e^i$, where \bar{A}_s^i and \bar{A}_e^i are, respectively, the average amplitude levels of the simulated and expected modal compliance over a band of 100 Hz

around their own resonance frequencies f_s^i and f_e^i . Note that the average result is also expressed in dB. This parameter indicates how close the estimated compliance level is compared with the expected one.

(2) *Resonance frequency error* relative to the resonance frequency shift: For a given mode i , it is defined as $(f_s^i - f_e^i)/f_s^i$ in percentage, where f_s^i and f_e^i are, respectively, the resonance frequencies corresponding to the simulated and expected compliances. This parameter indicates how close the estimated natural frequency is compared with that of the single panel.

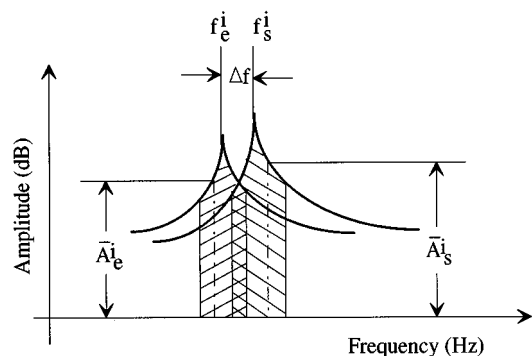


FIG. 8. Illustration of the error indicator definition in terms of modal compliance.

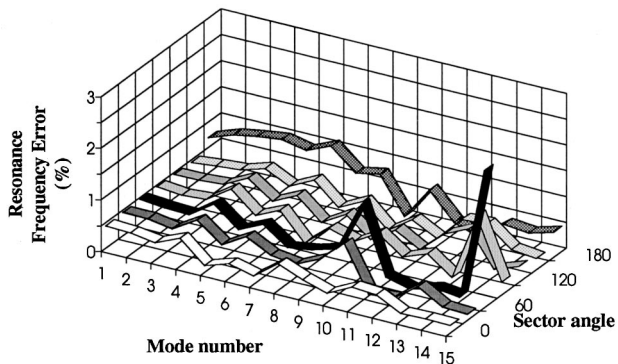


FIG. 9. Comparison of the resonance frequency error of modal response.

Using these definitions, the modified TET using two accelerometers is applied to panels with seven different curvatures ($\alpha=0^\circ; 30^\circ; 60^\circ; 90^\circ; 120^\circ; 150^\circ; \text{ and } 180^\circ$). For each panel, the first 15 modes are investigated. The error results are presented in Figs. 9 and 10 showing, respectively, the variation of the amplitude error and that of the resonance frequency error versus the mode number and the sector angle. It can be seen from Fig. 9 that the technique seems to limit the resonance frequency shift to an acceptable level. In fact, for all panels, the resonance frequency error is usually less than 2% for all modes considered, indicating that the inertia effect due to the tip is well compensated. Figure 10 shows that the amplitude error associated with lower order modes increase with the curvature of the structure. Then the technique seems to work well before going into a zone of high order modes, where the error is somewhat amplified and less dependent on the curvature of the panels. These results are consistent with the conclusions drawn previously, permitting the distinction of three different zones. Considering the inherent limitations of the technique at high frequencies, it is concluded that further improvement is still needed to increase the accuracy of the technique mainly at the very low-frequency range.

IV. MODIFIED TET WITH DOUBLE EXCITATION

In both the original TET and the modified TET using two accelerometers, one of the most important functions of the tip is to transform a force excitation into a moment one. However, by driving the tip, unwanted in-plane force (in the

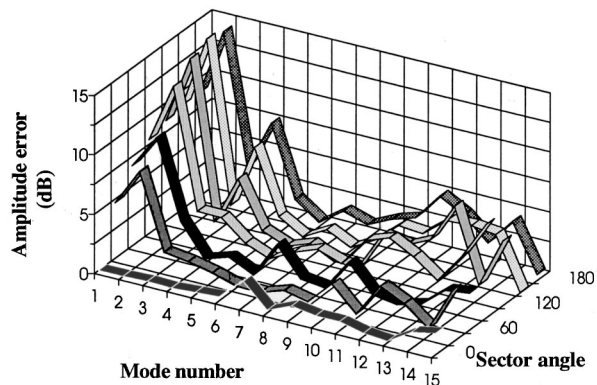


FIG. 10. Comparison of the amplitude error of modal response.

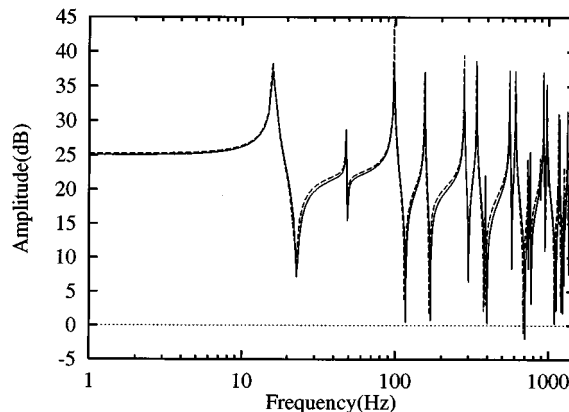


FIG. 11. Comparison of the rotational compliance of the panel with $\alpha=30^\circ$. Modified TET with double excitation. Expected results: (—); simulated results: (-----).

tangential plane for curved panels) and other tip inertia quantities are simultaneously applied. Discussions on the effects of all six inertia forces and moments of the tip have been made using finite element results on an attached panel.⁶ Using a selected configuration, the results seemed to indicate that, compared to $M_y(t)$, the other inertia quantities had negligible effects on the system for most frequencies. The transverse motion (in the Z direction) seemed to have a more noticeable influence on the measurements around the resonant values of the system. In fact, in the present configuration, among these quantities, only the in-plane force and the moment $M_y(t)$ are directly related to the excitation, while all others are produced via the tip motion. By neglecting the effects of other inertial forces and moments, the angular displacement θ_y can be regarded as the resultant of two components: θ_m caused by a pure moment excitation and θ_f by the in-plane force excitation:

$$\theta_y = \theta_m + \theta_f. \quad (12)$$

Therefore, the real angular displacement response due to the moment excitation is the difference between the total angular response θ_y and the angular response due to the force excitation θ_f . The rotational compliance should then be

$$(CR)_m = CR - (CR)_f, \quad (13)$$

where $(CR)_m = \theta_m/M_y$ is the rotational compliance to be measured, CR is the rotational compliance estimated as before, and $(CR)_f = \theta_f/M_y$ is the component resulted from the in-plane force excitation.

Equation (13) shows that it is this in-plane force that results in some rotational compliance error, which is more obvious at low frequencies. To eliminate this unfavorable effect, a so-called modified TET with double excitation is used. It consists in applying the modified TET as has been established previously to obtain the total quantity CR . Then, an exciting force is applied at the base of the tip along the tangential direction of the structure where the tip is connected. With the use of two accelerometers already on the tip, one gets the angle response under the in-plane force excitation as follows:

$$\theta_f = (\Delta A_x)_f / h_a \omega^2, \quad (14)$$

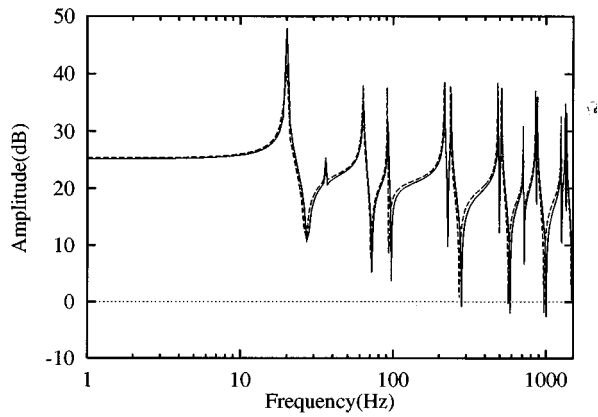


FIG. 12. Comparison of the rotational compliance of the panel with $\alpha=180^\circ$. Modified TET with double excitation. Expected results: (—); simulated results: (----).

in which $(\Delta A_x)_f$ is the same term as defined in Eq. (9) with a subscript f indicating that it is an in-plane force that is applied. By assuming a simple relation between the moment excitation and the exciting force $F(t)$ and neglecting the tip motion, one gets

$$M_y(t) = h_f F(t). \quad (15)$$

$(CR)_f$ can then be estimated by

$$(CR)_f = (\Delta A_x)_f / h_a h_f \omega^2 F_0. \quad (16)$$

Upon obtaining $(CR)_f$, The real rotational compliance of the structure can then be derived from Eq. (13).

Note that it is equally possible to derive a more complete relation instead of Eq. (15) by considering the tip motion since all required quantities are available, resulting in a lengthy expression. However, numerical simulations showed that this treatment was merely necessary since the modifications made aim at low frequencies. It is also important to note that although the technique requires double excitation, it does not mean, however, that the double excitation should be simultaneously applied. As indicated by the technique, two measurements, each one using a single force exciter, can be made quite independently. The results are then made use of to derive the rotational compliance.

The modified TET with double excitation is first validated using numerical simulations on two clamped panels with two sector angles: $\alpha=30^\circ$ and $\alpha=180^\circ$. The obtained results are illustrated, respectively, in Figs. 11 and 12 in terms of compliance amplitude. In both figures we notice a very good agreement between the simulated and expected results. As expected, the modified TET with double excitation seems to completely resolve the problems at low frequencies. No noticeable influences are observed at middle- and high-frequency ranges. To further illustrate the compensation effect, the amplitude errors defined previously were calculated with respect to the results issued from the modified TET and the modified TET with double excitation respectively for 30° and 180° sector angle panels. Again the results were expressed versus the mode number in Figs. 13

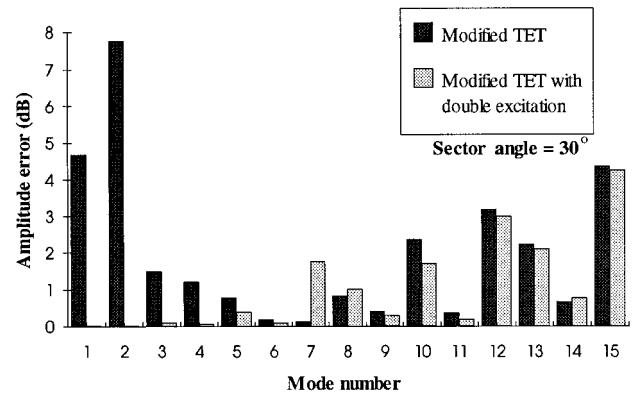


FIG. 13. Amplitude error of modal response for a panel with $\alpha=30^\circ$. Comparison between the modified TET with two accelerometers and the modified TET with double excitation.

and 14, respectively. It can be seen that the compensation effect of the modified TET with double excitation is very effective for the first five modes.

The technique was equally tested using a totally free panel with $\alpha=180^\circ$, which involves more significant rigid motion with respect to the clamped one. The comparison is plotted in Fig. 15 in terms of the compliance amplitude. Again, a very good agreement between the simulated and expected results can be noticed.

V. EXPERIMENTAL STUDY

Experimental measurements were performed to assess the modified TET with double excitation. A free steel semi-cylindrical shell was used. The panel was 416.6 mm long (unfolded length), 300 mm wide, and 3 mm thick. To simulate a free boundary condition, the curved panel was suspended on a steady base frame with four rubber bands of very weak stiffness at the panel's corners. This suspension method has been proved to be effective to simulate free boundaries.⁹ An aluminum tip was fixed with three screws and glued to the panel using high strength fast glue (LEPAGE epoxy syringe). The tip was fixed at a point 5 cm from the corner of the straight edge.

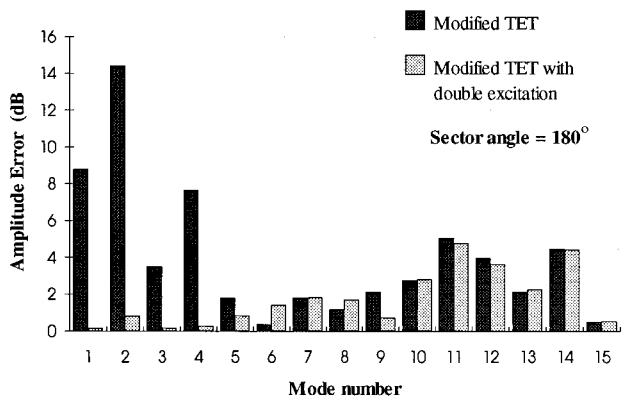


FIG. 14. Amplitude error of modal response for a panel with $\alpha=180^\circ$. Comparison between the modified TET with two accelerometers and the modified TET with double excitation.

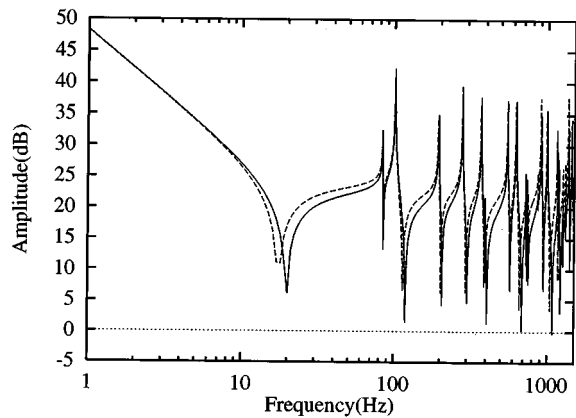


FIG. 15. Comparison of the rotational compliance of the free panel with $\alpha=180^\circ$. Modified TET with double excitation. Expected results: (—); simulated results: (-----).

Details about experimental setup and the measurement block diagram were identical to those reported in Ref. 7. Basically, a B&K 2035 signal analyzer was used to generate a random excitation signal. A B&K 4809 vibration exciter was used to apply a excitation force to the test system and the generated forces were measured by a B&K 8200 force transducer. The acceleration response was measured by a tiny B&K 4393 accelerometer installed in the different places on the tip as specified by the technique. Both force and acceleration signals were then analyzed using the B&K 2035 signal analyzer. Measured data were then transferred to a HP work station to make calculations.

The measured compliance curve using the modified TET with double excitation was compared to the expected results in Fig. 16. The first peak appeared in the spectrum corresponded to the first nonzero natural frequency of the panel. The reason that the curve began at 40 Hz was due to the fact that we could not obtain a good signal-to-noise ratio below this frequency. The agreement between the experimental and expected results are generally good. A good coincidence of

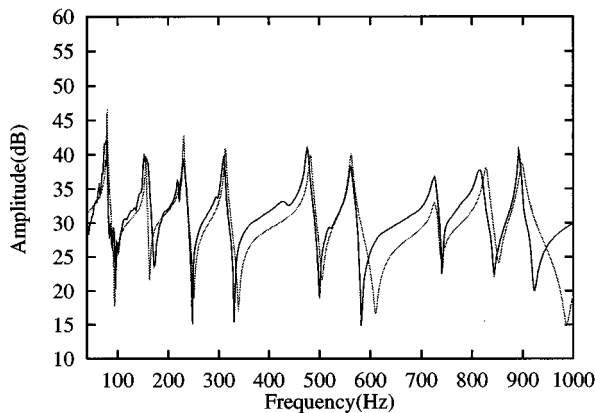


FIG. 16. Comparison of the rotational compliance of the free panel with $\alpha=180^\circ$. Modified TET with double excitation. Experimental results: (—); simulated results: (-----).

the resonance peaks can be observed for the whole frequency range used. The amplitude difference is generally within 3 dB except for some antiresonance regions.

VI. CONCLUSIONS

As an extension of the previously established tip excitation technique, the present work discussed applications of the TET to curved structures. Three versions of the techniques were proposed and assessed via numerical simulations. Experimental validations were also made using a representative configuration. It was demonstrated that the original TET can provide an acceptable accuracy for rotational compliance only in the middle-frequency range. At low frequencies involving a few structural modes, the accuracy was clearly insufficient due to the inaccurate indication of the rotational response and the effect of the in-plane force excitation. Compared with the original TET, the modified TET using two accelerometers brought an obvious improvement at low frequencies. The advantage of these two versions of the technique is their simplicity, since in both cases, only a single excitation is needed at the top portion of the tip. The third version of the TET requires a two-step measurement. It consists in separately exciting the tip both at the top and on the base and measuring the corresponding acceleration responses. These two tests may be performed separately requiring no synchronization. Both numerical and experimental results showed that the modified TET with double excitation ensures a good estimation accuracy for the rotational compliance for all low- and middle-frequency ranges. From this point of view, it becomes possible to apply the modified TET with double excitation to curved structures to reach the same performance as the original TET does to the plane structures. We believe that the obstacles limiting the application of the TET to curved structures are now removed.

¹ANSI S2.34-1984, "American National Standard Guide to the Experimental Determination of Rotational Mobility Properties and the Complex Mobility Matrix" (American National Standards Institute, New York, 1984).

²D. J. Ewins, *Modal Testing: Theory and Practice* (Research Studies Press, Tauton, Somerset, 1984).

³H. G. D. Goyder, "Methods and application of structural modeling from measured structural frequency response data," *J. Sound Vib.* **68**(2), 209–230 (1980).

⁴M. A. Sanderson and C. R. Fredô, "Direct measurement of moment mobility, Part I: A theoretical study," *J. Sound Vib.* **179**(4), 669–684 (1995).

⁵M. A. Sanderson, "Direct measurement of moment mobility, Part II: An experimental study," *J. Sound Vib.* **179**(4), 685–696 (1995).

⁶L. Cheng and Y. C. Qu, "Rotational compliance measurement of a flexible plane structure by means of an attached beamlike tip. Part I: Analysis and numerical simulation," to appear in *J. Vib. Acoust. Trans. ASME* **119** (1997).

⁷Y. C. Qu, L. Cheng, and D. Rancourt, "Rotational compliance measurement of a flexible plane structure by means of an attached beamlike tip. Part II: Experimental study," to appear in *J. Vib. Acoust. Trans. ASME* **119** (1997).

⁸D. A. Wells, *Theory and Problems of Lagrangian Dynamic* (McGraw-Hill, New York, 1967).

⁹L. Cheng and R. Lapointe, "Vibration attenuation of panel structures by optimally shaped viscoelastic coating with added weight consideration," *Thin-Walled Struct.* **21**, 307–326 (1995).

The effect of internal oscillators on the acoustic response of a submerged shell

Douglas M. Photiadis, J. A. Bucaro, and Brian H. Houston
Naval Research Laboratory, Washington, DC 20375-5000

(Received 3 May 1996; accepted for publication 9 September 1996)

The effect of a large number (≈ 1000) of internal mechanical oscillators on the acoustic backscattering cross section of a submerged ribbed shell has been experimentally investigated. A comparison of the backscattering cross section of the shell with oscillators to that of a simple ribbed shell with no oscillators shows a number of significant effects arising from the internal structure and overall a significantly increased average scattering strength. These results are presented and several physical mechanisms which can account for the salient aspects of the observations are discussed. [S0001-4966(97)03601-1]

PACS numbers: 43.40.At, 43.40.Ey, 43.20.Tb [CBB]

INTRODUCTION

Complex internal structure has been predicted to influence the acoustic properties of simple elastic structures in two basic ways: storage/dissipation of structure-borne vibration in the internals,¹⁻⁴ and scattering of structure-borne vibration by the internals.^{1,5-9} These mechanisms have been predicted in one way or another to impact the behavior of a number of real-world mechanical systems. We report here some initial results in an experimental investigation of the acoustic effects of internal structure, a comparison of measurements of the backscattering cross section of a simple ribbed shell to measurements of a similar shell with a large number (≈ 1000) of attached internal oscillators. Even though we have not yet “discovered” the physics leading to the observations, the results are reported here both because they show dramatic changes due to the internal structure, and because we seek to encourage further analysis of these effects.

The base structure consists of a nearly periodically ribbed nickel cylindrical shell of radius $R=7$ cm. The shell is thin, with a thickness to radius ratio $h/R\approx 0.009$, and fairly long, $L/R\approx 12$. The ring frequency of the unribbed shell is approximately 12 kHz, and falls within the experimental frequency range of the measurements, $11\text{ kHz}<f<45\text{ kHz}$. The ribs are simple rings spaced fairly close to one another, with 80 rings in total along the length of the shell. The spacing was chosen to give a rib spacing to diameter ratio typical of that found in underwater naval structures. The mean rib spacing is $d\approx 0.15R=1.05$ cm, and the mean deviation of the spacings from periodicity is small ($\Delta d/d\approx 0.025$). The structural acoustic behavior of this system has been studied in some detail, and measurements of the backscattering cross section¹⁰ and the response of the system to a point drive¹¹ are in qualitative agreement with theoretical expectations. Detailed drawings and additional information concerning the construction of the base model can be found in Ref. 11.

The complex structure consists of the base structure with 11 simple stainless steel beam-mass oscillators attached to each rib—in all, 880 attached oscillators. The 11 oscillators on each beam have different resonance bands, which, taken together, cover a significant portion of the measurement

band. We strove to design the structure so that there would be present the full range of oscillator frequencies within each relevant elastic length scale, viz., within an area of order λ^2 on the shell. Over the measurement band (11–45 kHz) the elastic scales are: longitudinal (46–8.5 cm), shear (27–5.4 cm), and flexural (2–0.9 cm). This issue is discussed more fully below, after additional information concerning the model is given; but generally, full “coverage” was achieved for the shear and longitudinal waves, while the flexural wave is coupled to the entire spectrum of the oscillators only after propagating several wavelengths.

We measured the backscattering cross section of the ribbed shell with no internals (the base structure) and that of the system with attached oscillators (the complex structure). The measurements were made as a function of frequency and incidence angle relative to the axis of the shell. As our results will make clear, the internal structure has had a profound impact on the character of the cross section. At issue is the physical behavior of the complex structure which is responsible for these observations.

I. THE MODEL

In Fig. 1(a), a drawing of a beam-mass oscillator is shown. A typical oscillator has a mass of about 3 g and a net length of about 1.65 cm. The total mass of the attached oscillators is about equal to the mass of the ribbed shell. The lowest resonance frequency of a particular oscillator in isolation is approximately predicted simply by the half-wave bending mode of the beam, and more accurate numerical predictions have been given by Snowdon.¹² The resonance frequency of the oscillators¹³ was varied by changing the thickness of the beam of the dumbbell [see Fig. 1(c)].

The dumbbell oscillators were attached to the structure by laser welding them to the ribs at the midpoint of the oscillator beam, cocked at alternating $\pm 45^\circ$ angles [see Fig. 1(b)]. A depiction of the ribbed shell with the oscillators mounted is shown in Fig. 2. The mounting at a 45° angle ensures that both in-plane and out-of-plane motions of the ring will be well coupled to the flexural mode of the beam-mass oscillator. It is difficult to see the different attachment angles of the attached oscillators in the figure; we have at-

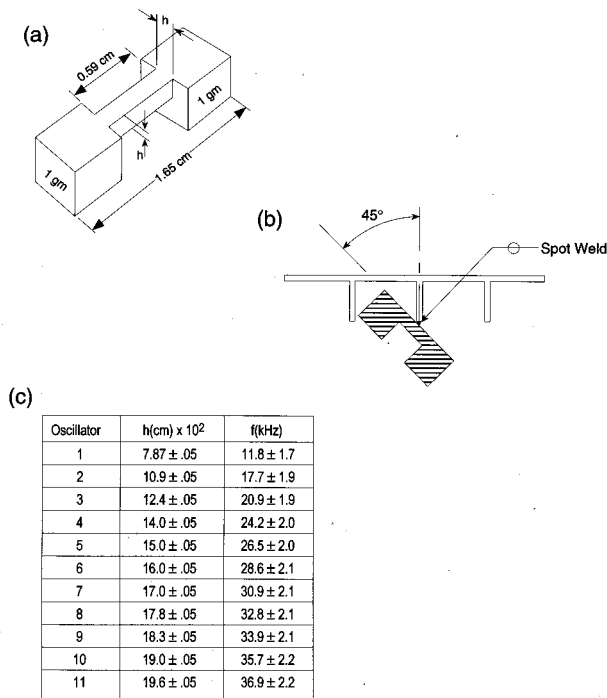


FIG. 1. The internal oscillators: (a) An individual “dumbbell” oscillator; (b) diagram indicating the attachment geometry; (c) table indicating the different beam thicknesses and the corresponding coupled oscillator-frame resonance frequency. Also indicated are the mechanical tolerances and the corresponding shift in the resonance frequency.

tempted to show this graphically by having the oscillators alternate in color between gold and silver. The attachment angle was varied in this fashion to avoid introducing a systematic asymmetry in the rib dynamics.

The *in situ* strain resonances of the individual oscillators mounted on a shell test section were measured by Doppler vibrometry.¹⁴ The shell test section consisted of a relatively short cylindrical shell with a single rib. These results and some elementary theoretical explanations have been separately reported;¹⁵ we summarize the important features here. The attachment of a single oscillator to the test section introduces a cluster of resonances to the system. This occurs because the motion of the oscillator is coupled to the high order modes of the ring. The band of these induced resonances is fairly broad with a bandwidth $\Delta\omega/\omega$ varying from 0.34 for the lowest-frequency oscillators to 0.019 for the highest. The individual resonance peaks within a particular oscillator/frame resonance cluster are very narrow, with a Q at least as large as 100. In order to “cover” a significant portion of the measurement band we chose 11 center frequencies for the oscillators in accordance with our measurements of the effective widths of the induced resonance clusters so that adjacent clusters overlapped. In this sense, rather than in the sense of full modal overlap (not possible for us to achieve with this model), the internal oscillators “cover” the measurement band. A larger number of oscillators would of course be preferable but would have introduced significant additional problems in the model construction.

The dimensions of the 11 oscillators arrived at in this manner, along with the coupled oscillator-frame resonance frequencies are given in the inset table in Fig. 1. The random

spread in the oscillator frequencies arising from errors in the fabrication (primarily the beam thickness) are indicated in the table. On each rib, 11 different oscillators “covering” the measurement bandwidth, one near each center frequency, were evenly spaced around the circumference. A random number generator was used to arrange the oscillator resonance frequencies on each ring in a pseudo-random fashion. Hence, there is no average periodicity, either circumferentially or axially, after attaching the oscillators. Notice that the frequency band spanned by the *in situ* resonance frequencies, $10 \text{ kHz} < f < 40 \text{ kHz}$, is shifted significantly from the band of resonance frequencies of the oscillators in isolation, $3.2 \text{ kHz} < f < 20 \text{ kHz}$. This occurs because each oscillator is so heavy relative to the section of ring supporting it, about three times heavier, and in addition is stiffer than the ring section owing to its much greater thickness.

The distance between the oscillators circumferentially is $\approx 4 \text{ cm}$, while the interframe spacing, and hence the axial distance between the oscillators, is 1.05 cm. Within an area of order the square of the shear wavelength, 50 cm^2 at the highest measurement frequencies, there are roughly 12 oscillators with random frequencies, and a near vanishing probability that the entire band is covered bearing in mind that it takes 11 distinct oscillators to cover the band. Even a slightly greater area, however, rapidly increases the probability that the band is covered to nearly 1, so that one may consider that the band is covered bearing in mind that it takes 11 distinct oscillators to cover the band. Even a slightly greater area, however, rapidly increases the probability that the band is covered to nearly 1, so that one may consider that the band is covered bearing in mind that it takes 11 distinct oscillators to cover the band. A flexural wave, on the other hand, must propagate several wavelengths before interacting with the entire spectrum of oscillators. These simple estimates ignore the effect of the rib in coupling the oscillators to the shell, an aspect which can increase the coupling considerably when the in-plane response of the rib is involved.

II. MEASUREMENTS

Shown in Fig. 3 is the measured backscattering cross section of the base structure (left plot) and the complex structure (right plot). The measurements were carried out at the Naval Research Laboratory in a similar manner as reported previously.¹⁰ The plots give the measured backscattered pressure in decibels as a function of frequency and the incident angle relative to the axis of the cylinder. Also indicated on the figure are two frequency bands associated with characteristics of the oscillator/frame/shell system. The Δf_{iso} band (3.2 kHz, 20 kHz) refers to the fundamental resonance frequencies of the individual dumbbell oscillators in isolation, and Δf_{exp} (10 kHz, 40 kHz) to the measured oscillator strain resonances when attached to the shell test section. We show both frequency bandwidths on the figure because the Δf_{iso} band has physical meaning if one seeks to understand the system as *base structure + oscillators*, while the Δf_{exp} band is relevant if one seeks to decompose the system as *shell + internals*. The significant impact of the attached internal oscillators on the cross section is evident.

The physical mechanisms responsible for the nonspecular highlights in the cross section of the base structure (left plot in Fig. 3) are known. The “chalice” feature which fills in a range of angles $\pm 30^\circ$ about the beam specular return is due to phase matching to shear and longitudinal membrane

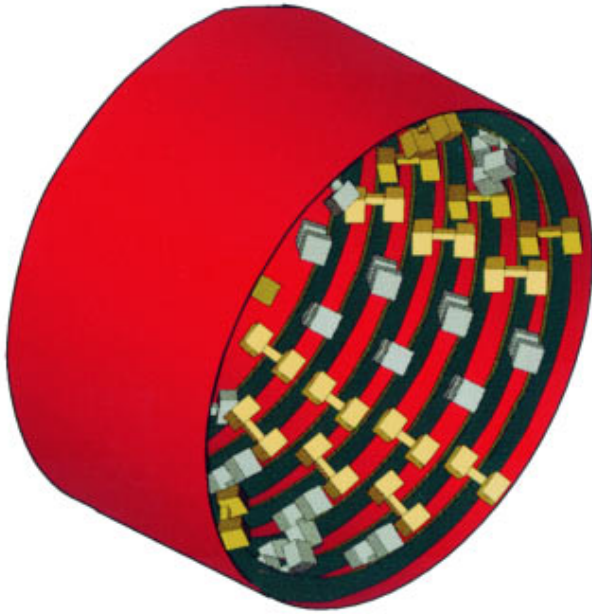


FIG. 2. A depiction of the ribbed shell with attached oscillators.

waves.¹⁶ These features have a characteristic vertical appearance in this display corresponding to the lack of dispersion of individual membrane modes above the cutoff frequency. The high level, more narrow-band features occurring at about twice the ring frequency, result from phase matching to flexural Bloch waves.^{17,18}

Comparison of the cross section of the complex structure with the base structure shows the following significant differences:

(1) In the frequency band Δf_{exp} , the nonbeam scattering cross section of the complex shell is on average significantly increased. Interestingly, the frequency range at which this broadband enhancement begins also coincides with the frequency range in which the “chalice” enhancement due to

membrane waves begins for the simple ribbed shell.

(2) The qualitative appearance of the scattering in frequency-angle space is greatly altered. The “chalice” structure of cross section of the simple ribbed shell has been replaced by a pattern which broadens rather than narrows as the frequency decreases. The response of the complex structure would overall be described as having a “Christmas tree” appearance with branches and all, as opposed to the “chalice” observed in the measurements of the simple shell.

(3) The scattering from the higher-frequency flexural Bloch wave, the rather horizontal feature at about the twice the ring frequency, has been greatly reduced. Most notable is the decrease in the backscattering at large angles relative to beam.

(4) The smooth, discrete structure of the cross section of the simple shell, with patterns of high intensity well predicted by the dispersion of individual modes, has been replaced by a “noisy” speckle pattern of generally increased levels.

III. DISCUSSION

The changes in the backscattering cross section of the structure indicate that the vibrational behavior of the ribbed shell has been significantly altered by the presence of the internal oscillators. The measurements confront us with some basic questions. Do the oscillators primarily absorb and dissipate energy, or is the elastic scattering from the oscillators dominant? What is the nature of the vibrational behavior of the shell in the frequency range in which the nonbeam cross section is enhanced? We will not be able to answer these questions here, but instead will discuss some mechanisms which can give rise to the observed changes in the frequency versus angle plots.

Some candidate mechanisms are:

(1) Simple mass loading and subsequent slowing of the membrane waves;

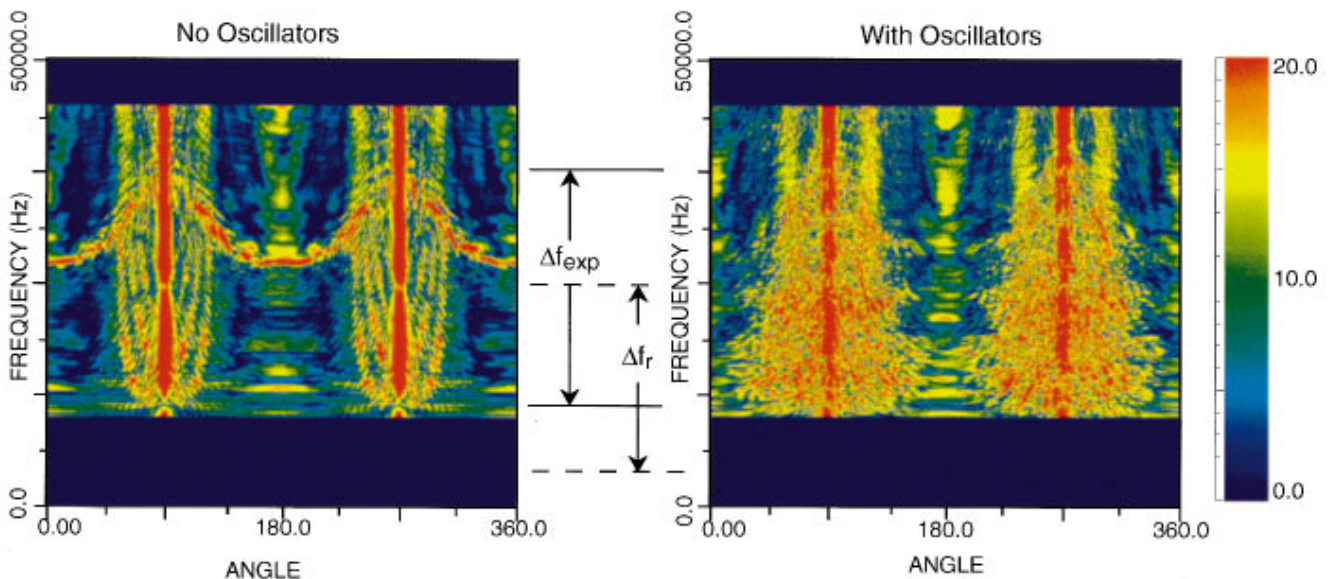


FIG. 3. Comparison of the backscattering cross section of the ribbed shell to that of the ribbed shell with 880 attached oscillators. The color scale gives the magnitude of the backscattered pressure in decibels.

- (2) Increased scattering from flexural waves caused by structural discontinuities;
- (3) Energy storage by the internal vibratory states; and
- (4) Spatial decorrelation.

Consider the first mechanism—simple mass loading. At frequencies below the resonance frequency, a free oscillator appears to be a simple mass. At very low frequencies, this would be the case for all of the dumbbell oscillators, so that the added mass would be large. As the frequency increases, we move through succeeding oscillator frequencies, decreasing the added mass. Thus, the membrane waves would be significantly slowed at low frequencies (of the order observed based on the total mass of the oscillators) with less and less slowing at higher frequencies, producing a Christmas tree effect. However, the membrane cutoff frequency, the base of the chalice in the simple structure, would be significantly lowered as well, an aspect which is not observed.

The second mechanism, increased scattering from flexural waves, is suggested by the fact that the dominant response of the simple ribbed shell to normal forces in this frequency range is flexural. In the simple shell, the flexural waves are typically nonradiating because they are predominantly subsonic in this frequency range. In the complex structure, the attached oscillators will scatter some of the energy of the flexural Bloch waves into supersonic wave numbers, thereby allowing these modes to radiate. The horizontal branches of the Christmas tree could arise from this phenomena. However, the frequency spectrum over which such enhancements would occur is not known, nor is the scattering strength of this mechanism.

The third mechanism has its plausibility rooted in the fact that measurements made on the shell section/frame/oscillator system demonstrate the existence of new internal vibratory states in the band f_{exp} , the frequency band in which the major changes occur. We can show in analogy with vibrational relaxation mechanisms in fluids¹⁹ that interaction with these states could lead to slowing of the membrane waves precisely in this band, and that this slowing would become less important at higher frequencies as long as the energy coupling into these states is large enough. This mechanism does produce a slowing just as arises from a simple added mass, as discussed above, but is in our opinion a different physical phenomena involving an additional time scale, i.e., the time for the internal states to effectively reach equilibrium with the shell vibrational energy. This mechanism could lead to large angular broadening at the lower frequencies and the Christmas tree shape observed. However, whether there exists sufficient coupling of energy into these states is not clear.

The fourth mechanism, spatial decorrelation of the surface velocity field, is indicated by the speckle nature of the scattering cross section. Assuming that vibration along the cylindrical region of the shell is dominant, the scattered pressure is proportional to a sum of axial Fourier transforms of the azimuthal modes of the surface velocity weighted by smooth transfer functions. Hence, the observed speckle pattern must either be present in the individual modes of the surface velocity field or arise from interference between the

various modes. At these frequencies, interference between the various terms in the indicated sum cannot produce such rapid fluctuations because there are too few radiating modes. Therefore, the axial Fourier transforms of individual modes of the surface velocity must possess the observed speckle behavior. This in turn implies that the low order azimuthal modes of the surface velocity field cannot consist of a single traveling wave, nor vary in any simple repetitive fashion. One explanation for this observation is that the low order modes do propagate but that their phase varies in an irregular fashion as a result of scattering by the oscillators. We cannot however rule out alternatives, such as the dominance of local resonances in the cross section, or the propagation of modes with varying azimuthal mode number.

Our discussion in this section is only a cursory examination of the physics which might be involved in this phenomena. A more serious and detailed examination of the data as well as concrete theoretical predictions and perhaps additional experimentation would be required to go beyond this sort of heuristic discussion. We have included it in an attempt to stimulate further work in this area and to indicate the direction of our future research.

IV. CONCLUSION

Measurements of the backscattering cross section of a ribbed shell with a large number of attached oscillators (≈ 1000) have been carried out and compared to measurements of a similar ribbed shell without oscillators. These results should be of interest to those at work trying to understand, predict, and modify the acoustic behavior of complex real world systems, particularly marine vehicles and aircraft: They show how even relatively simple dynamic structure attached to the interior of a framed cylindrical shell can dramatically change the character of the acoustic response of the system. The measurements compared only the scattering cross sections of the two systems, and yet, since vibrational waves play a large role in this phenomena, one may infer that the basic wave propagation characteristics over acoustic length scales have been greatly altered by the internal structure.

We have observed a number of large differences between the simple and complex structure: generally increased nonspecular backscattering levels, a qualitatively different pattern in frequency-angle space—a “Christmas tree” rather than a “chalice,” reduced scattering from flexural Bloch waves, and last but not least, a generally noisy, uniform speckle pattern to the cross section as opposed to the relatively smooth, discrete pattern associated with the simple shell. And although we have described a number of potential mechanisms which can account for some of the observations, the physics underlying the phenomena we have observed remains to be unraveled.

ACKNOWLEDGMENTS

This work was supported by ONR Code 334. The authors would like to acknowledge the contributions of a number of individuals who collaborated in the discussions which led to this experiment. These include: Dr. Geoffrey Main,

Dr. David Feit, Dr. Murray Strasburg, Dr. Earl Williams, Dr. Christian Soize, Dr. Vic Sparrow, Professor Ira Dyer, and Professor Allan Pierce.

- ¹R. H. Lyon, *Statistical Energy Analysis of Dynamical Systems: Theory and Applications* (MIT, Cambridge, MA, 1975).
- ²C. Soize, "Probabilistic structural modeling in linear dynamic analysis of complex mechanical systems. I. Theoretical elements," *J. Recherche Aerospat. (ONERA France)* **5**, 23–48 (1986).
- ³"Vibration damping of large structures induced by attached small resonant structures," *J. Acoust. Soc. Am.* **99**, 335–344 (1996).
- ⁴A. D. Pierce, V. W. Sparrow, and D. A. Russell, "Fundamental structural acoustic idealizations for structures with fuzzy internals," *J. Vib. Acoust. Trans. ASME* **117**, 339–348 (1995).
- ⁵G. Maidanik, "Response of ribbed panels to reverberant pressure fields," *J. Acoust. Soc. Am.* **34**, 809–826 (1962).
- ⁶D. M. Photiadis, "The effect of irregularity on the scattering of acoustic waves from a ribbed plate," *J. Acoust. Soc. Am.* **91**, 1897–1903 (1992).
- ⁷C. H. Hodges and J. Woodhouse, "Vibration isolation from irregularity in a nearly periodic structure: Theory and measurements," *J. Acoust. Soc. Am.* **74**, 894–905 (1983).
- ⁸D. M. Photiadis, "Localization of helical flexural waves by irregularity," *J. Acoust. Soc. Am.* **96**, 2291–2301 (1994).
- ⁹J. A. Turner and R. L. Weaver, "Coupling and attenuation of waves in plates by randomly attached impedances," *J. Acoust. Soc. Am.* (in press).
- ¹⁰B. H. Houston, J. A. Bucaro, and D. M. Photiadis, "Broadband acoustic scattering from a ribbed shell," *J. Acoust. Soc. Am.* **98**, 2851–2853 (1995).
- ¹¹D. M. Photiadis, E. G. Williams, and B. H. Houston, "Wavevector space response of a near periodically ribbed shell," *J. Acoust. Soc. Am.* (in review).
- ¹²J. C. Snowdon, "Transverse vibration of free-free beams," *J. Acoust. Soc. Am.* **35**, 47–52 (1963).
- ¹³The *in vacuo* resonance frequencies of the 11 oscillators on each frame were chosen to be near the frequencies: 4.0 kHz, 7.8 kHz, 10.0 kHz, 12.8 kHz, 14.7 kHz, 16.7 kHz, 18.9 kHz, 20.7 kHz, 21.9 kHz, 23.6 kHz, 25.1 kHz.
- ¹⁴J. F. Vignola and B. H. Houston, "The design of a three-dimensional laser vibrometer," Winter Annual Meeting of the ASME, 1993-WA/NCA-10 (1993).
- ¹⁵D. M. Photiadis, J. A. Bucaro, and B. H. Houston, "Vibrational response of a single oscillator attached to an elastic structure," *J. Acoust. Soc. Am.* **97**, 3415(A) (1995).
- ¹⁶M. L. Rumerman, "Contribution of membrane wave reradiation to scattering from finite cylindrical steel shells in water," *J. Acoust. Soc. Am.* **93**, 55–65 (1993).
- ¹⁷D. M. Photiadis, J. A. Bucaro, and B. H. Houston, "Scattering from flexural waves on a ribbed cylindrical shell," *J. Acoust. Soc. Am.* **96**, 2785–2790 (1994).
- ¹⁸G. Maidanik and J. Dickey, "Reflection of incident pressure waves from a ribbed panel," *J. Acoust. Soc. Am.* **90**, 2124–2138 (1992).
- ¹⁹K. F. Herzfeld and T. A. Litovitz, *Absorption and Dispersion of Ultrasonic Waves* (Academic, New York, 1959).

Structural wave reflection coefficients of cylindrical shell terminations: Numerical extraction and reciprocity constraints

P. W. Smith, Jr., J. Gregory McDaniel, Kevin D. LePage, and Robert Barile
BBN Corporation, 70 Fawcett Street, Cambridge, Massachusetts 02138

(Received 1 July 1996; accepted for publication 12 September 1996)

A fluid-loaded cylindrical shell guides vibratory energy along its axial direction in the form of a finite set of distinct traveling wave types. On a finite shell, the energy incident upon a termination is redirected into reflected waves of all types and into sound radiated into the farfield. (The total field near the termination also includes various evanescent components.) Reflection coefficients relate the amplitudes of individual reflected wave types to the amplitudes of individual incident wave types. In this paper, values for the reflection coefficients of several terminations have been extracted from results of finite element analysis for the forced response of a finite structure excited by a variety of different sources. The numerical results exhibit good agreement with the analytical constraints consequent to the principle of reciprocity. The constraints are developed here by an analysis adaptable to other multimodal waveguides by appropriate modification of detail. © 1997 Acoustical Society of America. [S0001-4966(97)02901-9]

PACS numbers: 43.40.Ey, 43.20.Gp [CBB]

INTRODUCTION

We are concerned with the dynamics of a finite fluid-loaded structure that consists of a long, homogeneous thin cylindrical shell, bounded by terminations at each end and reinforced by a few localized ring discontinuities spaced at large intervals along the shell. In this paper, the shell is forced into vibration by internal mechanical sources. It is plausible to conjecture (subject to later verification) that vibratory energy in such a structure is carried between adjacent terminations or ring discontinuities in the form of natural shell waves, indistinguishable from similar waves on an infinite shell having the same dynamical properties.

It is sometimes argued from asymptotic analysis that grazing sound propagation, with associated forced motion of the shell, must eventually be a more important coupling mechanism than natural shell waves, because the sound amplitude decays only as a power of distance while the shell waves decay exponentially. But our interest lies in their relative strength at a finite distance. Suffice it to say that our numerical results at typical distances and frequencies of interest show no reason to include grazing sound as a coupling mechanism.

A. Multiple reflection model

We are led by this conjecture to a multiple reflection model of the total vibratory field on the structure. Except near the discontinuities, the vibratory field consists of a superposition of natural waves propagating in both directions. When one such wave strikes a discontinuity, energy is sent out into many distinct paths: reflected natural waves of all types, transmitted waves of all types (when the discontinuity is not a termination), and sound radiated into the fluid.

If the discontinuities are widely enough spaced, one expects that the reflection process at any one of them is sensibly independent of the others, except insofar as their presence may affect the amplitudes of the incident waves. The

reflection process at one discontinuity is then indistinguishable from reflection at the same discontinuity located on an infinite shell (or at the end of a semi-infinite shell in the case of a termination) and irradiated by the same incident wave field.

B. Reflection coefficients

The principal goal of this analysis is to evaluate the complex *reflection coefficients*, functions of frequency, which relate the amplitudes of the reflected fields to the amplitudes of all of the incident wave types. Each different discontinuity is characterized by a different set of reflection coefficients, but the values for any one discontinuity are, for widely spaced discontinuities, independent of the presence or the location of other discontinuities. This independence is the pre-eminent advantage of the multiple reflection model.

In general, stringent analytical difficulties arise in trying to evaluate these coefficients. We know of only one class of discontinuity that is amenable to the procedures of classical analysis: a thin interior ring discontinuity that contacts the shell on a single cross section. In this case the interaction of shell and discontinuity can be described by collocated ring forces and moments. A classical formulation expresses the total vibratory field on the infinite shell as the sum of an incident field and a scattered field, and imposes appropriate continuity conditions at the connection between shell and discontinuity. The analysis can be carried out formally in terms of the solutions for two sub-problems: (i) the shell's response to localized ring forcing, and (ii) the discontinuity's response to forcing on its outer perimeter.¹⁻³ The first problem is easily formulated classically, using Fourier analysis, although numerical calculations will often be necessary to evaluate the resulting integral forms. The second problem may also have a simple solution if the design of the discontinuity is sufficiently simple.

In the case of terminations and ring discontinuities that have significant axial extent, two serious complications arise:

(i) elastic deformation occurs within the discontinuity, with the possibility for multiple resonances, and (ii) acoustic coupling arises among the elements of the discontinuity and adjacent shell surfaces. No simple approach is then evident. The solution to this problem is the topic of this paper.

C. This study

This study illustrates a technique by which the reflection coefficients of a discontinuity, specifically a termination, can be extracted from results of finite element analysis (FEA) of a particular finite structure containing that discontinuity. The finite structure used here is a homogeneous fluid-loaded thin shell with a termination on each end. For simplicity in the exposition, both shell and termination are taken as axisymmetric. The analysis, which is clearly based on the multiple reflection model, has several parts.

First, the properties of the natural wave types propagating on the shell are determined by classical analysis for an infinite fluid-loaded shell. The equations for pure-tone vibrations in the absence of external forcing are solved for the complex wave numbers and for the associated wave shapes or “polarizations” that specify the relative amplitudes of the three components of vector displacement in the natural wave.

Second, the velocity pattern associated with forced response of the finite structure is found by FEA. It is useful to think of these calculations as a numerical experiment, in which the target termination is located at one end of a long unobstructed segment of shell and a mechanical source and closing termination are located at the other end. The whole structure thus consists of three sections: a source end, a transmission and measurement section, and the target end. The total velocity pattern in the transmission section is then resolved into a sum of incident and reflected natural waves by making a linear least-square-error fit to the velocity using the previously calculated wave numbers and polarizations.

This second step is repeated using one or more different mechanical sources. For example, source candidates might include a radial ring force, an axial ring force, a ring moment (all on the shell), and various force distributions on the adjacent termination. By superposing the results for a set of these sources it is possible to synthesize a combined source having any desired mix of wave types incident on the target. In particular, we can synthesize an incident wave field that has (in a least squares sense) only a single wave type. Then the measured amplitudes of the reflected waves, suitably normalized, yield the desired reflection coefficients directly.

In this study we focus our attention on a steel shell in water in the frequency range $2 < k_0 a < 10$, where k_0 is the wave number of sound in the water and a is the radius of the shell. In various calculations the shell length L has had values in the range $13 < L/a < 18.5$.

I. NATURAL WAVES

Consider the natural, pure-tone waves that can exist on an infinite fluid-loaded thin shell.⁴⁻⁶ We take a cylindrical coordinate system where z is the axial coordinate, ϕ is the circumferential angle, and r is the radial coordinate; the shell’s midsurface lies at $r = a$. Then the displacement vector $\mathbf{d} = \{u, v, w\}^T$ of any single wave type has the general form

$$\mathbf{d} = A \begin{bmatrix} \cos n(\phi - \phi_0) & 0 & 0 \\ 0 & \sin n(\phi - \phi_0) & 0 \\ 0 & 0 & \cos n(\phi - \phi_0) \end{bmatrix} \times \mathbf{S} e^{i(kz - \omega t)}, \quad (1)$$

where A is an arbitrary complex constant, n is an integer, ϕ_0 is an arbitrary reference angle, \mathbf{S} is a unit “polarization” vector, k is the complex axial wave number, and ω is the real angular frequency. (The diagonal matrix should be replaced by the identity matrix in the case $n = 0$.) Different wave types have distinct characteristic values of k and \mathbf{S} , which vary with frequency.

These characteristic values are found in the customary manner, with numerical algorithms similar to those proposed by Scott.⁵ The differential equations of unforced motion with fluid loading reduce to a matrix equation,

$$\mathbf{Z}\mathbf{d} = \mathbf{0}, \quad (2)$$

which has nontrivial solutions only if the determinant of the impedance matrix \mathbf{Z} vanishes. That determinant is well known to be a function of k^2 . Therefore, if k is a root corresponding to a wave propagating in the positive z direction there is a root $-k$ corresponding to an identical wave propagating in the opposite direction. In the complex k -plane, both upper and lower half-planes have four distinct principal roots of the determinantal equation, $|\mathbf{Z}(k)| = 0$, for each n and every frequency. Once these are found, the polarization vector is evaluated from the cofactors of \mathbf{Z} . In the results reported here, the Donnell–Mushtari thin shell theory has been used.

In contrast to most prior studies, we have included shell dissipation by means of a non-vanishing loss factor in the elastic moduli of the shell material. This enhances both the generality and the realism of the results, and even improves the performance of computer algorithms (the wave number as a function of frequency is not only continuous but has a continuous derivative if the damping is nonzero); there is no possibility of a strictly real root.

A. Natural wave types

Prior studies, omitting shell dissipation, have elucidated the general properties of the roots of the determinantal equation for a fluid-loaded thin shell. In general, the presence of fluid loading or of small dissipation in the shell material leads only to small changes in the wave numbers from the idealized case most often studied.

There are four principal roots in each half of the k plane.⁷ [Scott (Ref. 5, p. 254 ff. and Appendix D) delineates other, highly attenuated roots called “Stokes’ roots” that exist for large values of n . These are intimately related to “creeping waves” in the fluid surrounding the shell.] The principal roots are:

(i) **quasi-longitudinal:** The principal displacement is axial although radial motion is nonvanishing. In the idealized case, the wave can be resolved into a pair of helical traveling waves whose phase speed, at frequencies well above cutoff, is nearly the speed of longitudinal waves in a thin flat plate.

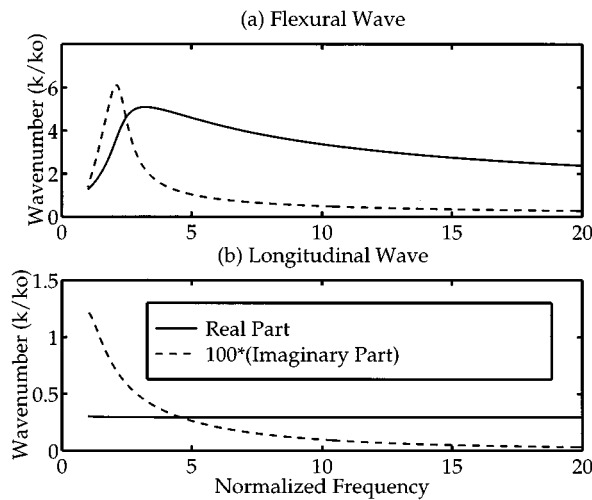


FIG. 1. Axial wave number k normalized by acoustic wave number k_0 versus normalized frequency $k_0 a = \omega a / c_0$ for the (a) $n=0$ flexural wave and (b) $n=0$ longitudinal wave.

(ii) **quasi-shear:** The principal displacement is circumferential although radial motion is nonvanishing except for $n=0$. In the idealized case, the wave can be resolved into a pair of helical travelling waves whose phase speed, at frequencies well above cutoff, is nearly the speed of shear waves in a thin flat plate.

(iii) **quasi-flexural:** The principal displacement is radial. In the idealized case, the wave can be resolved into a pair of helical traveling waves whose phase speed, at frequencies well above both cutoff and ring frequencies, is nearly the speed of bending waves in a thin flat plate.

(iv) **evanescent:** The principal displacement is radial. This wave is highly attenuated in the axial coordinate and is significant only near inhomogeneities. We dismiss it as a means of coupling between discontinuities on the shell. For simplicity, we shall omit the “quasi” prefix in future discussions.

Thus, there are three natural wave types for each value of n that can propagate between the discontinuities, if the frequency is above their cutoff frequencies. (Cutoff frequencies can be roughly estimated from analytical results for a shell *in vacuo* without dissipation.⁷) When the frequency moves below the cutoff frequency of one of these wave types, the wave number acquires an increasingly large imaginary part. At some point, it is necessary for numerical reasons to omit such a wave type from consideration; for example, if $\text{Im } ka \geq 2$, the amplitude attenuates by more than 17 dB in a distance of one radius.

B. Typical results

Some typical numerical results are given in Fig. 1 for $n=0$ waves on a steel shell in water. The nondimensional parameters of the shell are: thickness/radius, $h/a = 0.01$; specific gravity, $\rho/\rho_0 = 7.8$; loss factor, $\eta = 0.02$; relative Young’s modulus, $E/\rho_0 c_0^2 = 88(1 - i\eta)$; Poisson’s ratio, $\nu = 0.3$; where ρ_0 and c_0 are the density and sound speed of the ambient fluid. The graphs show the real and imaginary parts of the natural wave number as functions of frequency

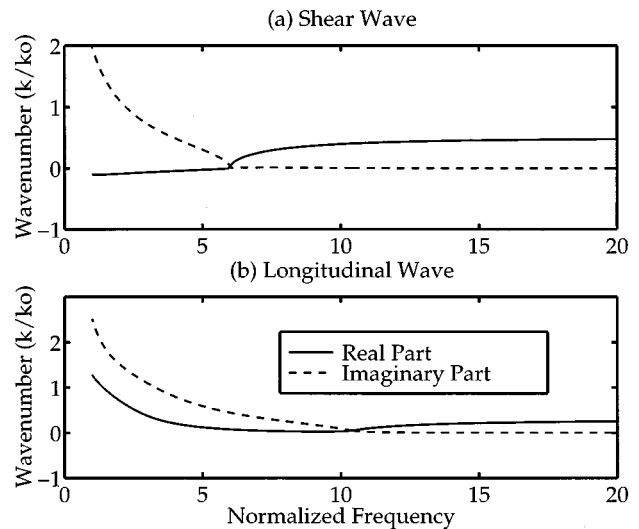


FIG. 2. Axial wave number k normalized by acoustic wave number k_0 versus normalized frequency $k_0 a = \omega a / c_0$ for the (a) $n=3$ shear wave and (b) $n=3$ longitudinal wave.

expressed by the value of $k_0 a$. Figure 1(a) is for the flexural wave. As shown in prior studies, this subsonic wave gains a large phase speed below the ring frequency (about $k_0 a = 3.6$); the dispersion leads to a small group speed and an associated peak in the attenuation rate. Figure 1(b) is for the longitudinal wave. This supersonic wave is only slightly dispersive, and the attenuation is primarily due to radiation. We omit the shear wave which for $n=0$ is purely torsional and unaffected by the ambient fluid.

Figure 2 shows similar results for the shear and longitudinal wave types for $n=3$. Here, each of the three wave types has a cutoff frequency. Cutoff frequencies, estimated for the shell without fluid loading,⁷ are at $k_0 a$ equal to 6.4 for the shear wave and 11.4 for the longitudinal wave. One observes that the wave numbers acquire a large imaginary part below these frequencies. The real part of the shear wave number is negative below cutoff.

II. FINITE ELEMENT EXPERIMENTS

A. The model

The so-called experiments run by FEA determine the response velocity of a simple fluid-loaded shell with two terminations, the shell being excited by mechanical ring sources located near one of the terminations (see Fig. 3). The mechanical ring sources, all of which were distributed about the circumference with specified circumferential harmonic

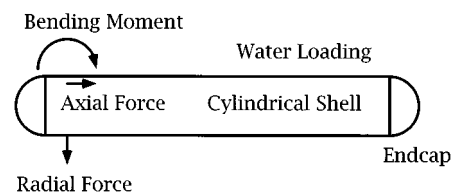


FIG. 3. Water-loaded cylindrical shell with terminations and mechanical ring excitations, concentrated in axial location but distributed circumferentially.

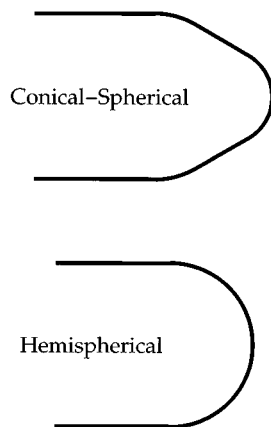


FIG. 4. Termination geometries studied in reflection analysis.

n , consisted of bending moments about the circumferential coordinate, radial forces, and axial forces. These sources have usually been located at a distance of $0.9L$ from the target termination.

Since the shell and terminations are taken as axisymmetric, a 2-D code suffices; calculations are carried out for each circumferential harmonic in isolation. The raw output data consist of the three directional components of complex shell velocity at each axial location along the shell. We have used the 2-D SARA code,⁸ which represents fluid loading by a layer of fluid elements bounded by essentially nonreflective infinite elements.

The shell modeled in the experiments is identical to that used in the analysis of wave numbers. Elastic parameters are appropriate to steel and water and the ratio of shell thickness h to radius a is $h/a=0.01$. The length of the shell is somewhat arbitrary, determined principally by the two requirements that, at all frequencies of interest, (i) evanescent elastic fields near the terminations shall be negligible in the center of the shell, and (ii) the propagating wave types shall not be so highly attenuated in the length of the shell as to give rise to numerical inaccuracies. The ratio of cylindrical length L to radius a in our studies ranged from $13 < L/a < 18.5$.

Two termination geometries have been tested, as shown in Fig. 4. For modeling convenience, the same design is used for the termination at each end. In order to assess the effects of termination dynamics, two studies of the hemispherical termination were conducted. In one study, it was modeled as steel while in the other study it was “rigidized” with a Young’s modulus many times larger than steel, thus highlighting the effects of interior dynamics on the reflection process.

III. EXTRACTION OF REFLECTION COEFFICIENTS

A. Traveling wave amplitudes

The first task is to extract estimates of the traveling wave amplitudes from the FEA data for velocity on the shell in the n th circumferential order. We search for the best fit to the data of an analytical model of the velocity pattern, expressed as a sum of traveling waves having the previously

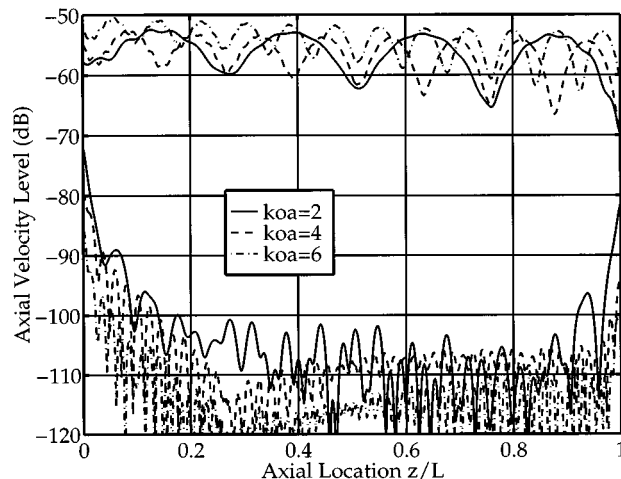


FIG. 5. The upper curves represent axial velocity on the shell in dB versus normalized axial location z/L for $k_0a=2,4,6$ as predicted by the SARA FEA code for a ring axial force at $z/L=0$. The lower curves represent the residual when a natural wave solution is used to represent the axial velocity shown in the upper curves.

determined natural wave numbers. Let the axial coordinates of points on the shell extend from $z=0$ at the source termination to $z=L$ at the target termination. Then the model for, say, total radial velocity is

$$v(z, \phi) = \sum_n \cos(n\phi) \sum_q [V_q^{\text{inc}} e^{ik_q(z-L)} + V_q^{\text{ref}} e^{ik_q(L-z)}], \quad (3)$$

where the unknown complex amplitudes V_q of the q th wave type have superscripts “inc” for the waves incident on the target termination and “ref” for the reflected waves. (Subscripts n on the complex amplitudes and natural wave numbers have been suppressed.)

The values of the V_q are determined by a least-mean-square matching to the data from, typically, $0.1 < z/L < 0.9$, the source region and the ends of the shell being truncated in order to exclude regions where the field is dominated by evanescent terms, including the response to grazing sound. Note that the amplitudes are normalized in magnitude and phase to the values at the discontinuity, $z=L$.

The same procedure can be applied to the axial or circumferential velocity patterns, and the data for all three vector components could be combined in a single extraction process by using the polarization vector \mathbf{S} [see Eq. (1)] determined from analysis of waves on the infinite shell. One must however be careful to distinguish between the polarization vectors of incident and reflected waves. The whole procedure, which must be repeated for all frequencies and all order numbers n of interest, is greatly facilitated by flexible software for manipulating complex matrices.⁹

Figure 5 shows some results of this extraction process. Since the residual after extracting the natural waves has a level more than 50 dB less than the level of the total shell velocity, except near the ends of the shell, it is clear that the natural waves are the dominant mechanism coupling the two ends of the shell. The conjecture in the Introduction is thus confirmed by the data.

B. Reflection coefficients defined

At this point the reflection coefficients can be introduced formally as a square matrix \mathbf{R} relating the reflected amplitudes to the incident amplitudes:

$$\mathbf{V}_k^{\text{ref}} = \mathbf{R} \mathbf{V}_k^{\text{inc}}, \quad (4)$$

where the wave amplitudes for the different wave types have been assembled into vectors:

$$\mathbf{V}_k^{\text{ref}} = \begin{Bmatrix} V_{1,k}^{\text{ref}} \\ V_{2,k}^{\text{ref}} \\ V_{3,k}^{\text{ref}} \end{Bmatrix} \quad \text{and} \quad \mathbf{V}_k^{\text{inc}} = \begin{Bmatrix} V_{1,k}^{\text{inc}} \\ V_{2,k}^{\text{inc}} \\ V_{3,k}^{\text{inc}} \end{Bmatrix}. \quad (5)$$

The subscript k has been added to these variables as a placeholder for an index number identifying the source, for use in the subsequent discussion of multiple sources. (In the axisymmetric case, the shear wave is often omitted and the order of the matrices reduced to two.)

C. Multiple sources; Solution for \mathbf{R}

The wave amplitudes determined for a single source do not determine the desired reflection coefficients. Because each incident wave type can reflect into every wave type, one has in Eq. (4) three scalar equations with nine unknown coefficients. Our procedure for resolving this problem is to use multiple sources, exploiting the fact that the reflection matrix is independent of the values of the incident wave amplitudes.

Suppose that we have wave amplitudes for K different source arrangements on the structure. The result for all the sources are combined into the one matrix equation

$$\mathbf{V}^{\text{ref}} = \mathbf{R} \mathbf{V}^{\text{inc}}, \quad (6)$$

where

$$\mathbf{V}^{\text{ref}} = [\mathbf{V}_1^{\text{ref}}, \dots, \mathbf{V}_K^{\text{ref}}] \quad \text{and} \quad \mathbf{V}^{\text{inc}} = [\mathbf{V}_1^{\text{inc}}, \dots, \mathbf{V}_K^{\text{inc}}]. \quad (7)$$

When the number of sources K is equal to 3 (or 2 for $n=0$), the matrix \mathbf{V}^{inc} can be inverted, if it is not singular or ill-conditioned, and the desired solution found:

$$\mathbf{R} = \mathbf{V}^{\text{ref}} [\mathbf{V}^{\text{inc}}]^{-1}. \quad (8)$$

For larger K , a matrix pseudo-inverse is used.

These mathematical statements have interesting physical interpretations. First, the matrix \mathbf{V}^{inc} is singular if its columns are not linearly independent. This would imply that the mixes of incident wave types achieved in the different experiments are not sufficiently distinct; an examination of the mixes achieved may suggest a more desirable source. Second, postmultiplying \mathbf{V}^{inc} by any matrix is equivalent to synthesizing new compound sources by superposing the original sources (and their responses) in proportion to the columns of that matrix. If the multiplier is the inverse of \mathbf{V}^{inc} , so that the product is the identity matrix, each of those synthetic sources generates a new incident field in which only a single wave type is nonvanishing. We have then achieved those ideal sources which were described in the Introduction.

D. Results

Figure 6 shows the amplitudes of reflection coefficients

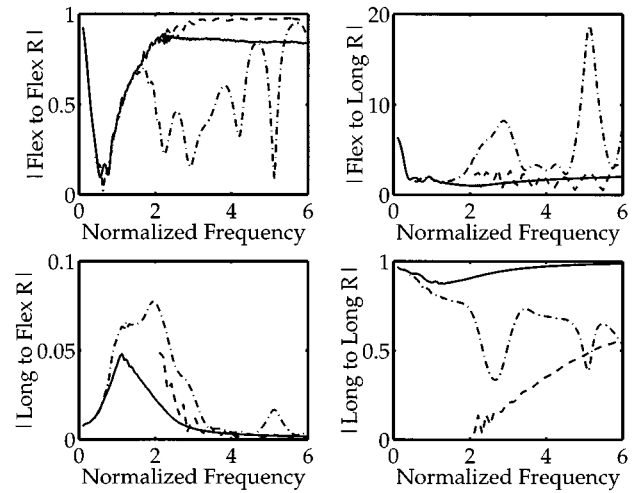


FIG. 6. Magnitudes of reflection coefficients versus normalized frequency $k_0 a$ for $n=0$ flexural and longitudinal waves incident on a rigid hemispherical termination (solid lines), a steel hemispherical termination (dashed lines), and a steel conical-spherical termination (dashed-dotted lines).

for the $n=0$ flexural and longitudinal waves for a rigid hemispherical termination, a steel hemispherical termination, and a steel “conical-spherical” termination. Note the dramatic effects of termination shape as well as flexibility in the direct reflection coefficients (flexural-to-flexural and longitudinal-to-longitudinal). Energy considerations restrict these direct reflection amplitudes to be equal to or less than unity.

IV. RECIPROCITY CONSTRAINTS

One is aware from many studies that the principle of reciprocity constrains the results of any two transmission measurements in which the directions of transmission are reversed (Ref. 10, p. 550 ff.). The objective of this section is to develop analytical expressions of those constraints as applied to the reflection coefficients. The classical statement of reciprocity (Ref. 11, Volume 1, p. 150 ff.) involves transmission between two transducers, each of which can be used either as a source or as a receiver. We shall define a canonical reflection problem of that type, using ring transducers on a semi-infinite shell. However, both incident and reflected fields then involve all the propagating wave types. Further analysis is necessary to find the constraints on individual reflection coefficients, each of which corresponds to a single incident wave type and another single reflected wave type.

A. Transducers

We conceptualize the ideal structural transducer as a ring located at some axial coordinate $z = z_0$ that, as a source, exerts a localized normal traction in the outward radial direction and, as a receiver, measures the outward radial velocity. Transducers having different circumferential orders n are required.

As a source, the transducer of order n applies a generalized force F_n at an axial coordinate z_0 by generating a normal stress or pressure

$$p(z, \phi) = F_n \delta(z - z_0) \Phi_n(\phi), \quad (9)$$

having the ‘‘mode shape’’

$$\Phi_n(\phi) = \frac{\varepsilon_n}{2\pi a} \cos(n\phi), \quad (10)$$

where ε_n is the Neumann factor, equal to 1 for $n=0$ and 2 for $n>0$. (There is no consensus on the normalization of terms in a Fourier series expansion; the one adopted here may differ from that used in any particular finite element program.)

As a receiver excited by an arbitrary radial velocity field $v(z, \phi)$, this same transducer’s output is the generalized velocity

$$V_n = \int_0^{2\pi} v(z_0, \phi) \Phi_n(\phi) a \, d\phi, \quad (11)$$

corresponding to the series expansion for a general velocity field having symmetry in $\phi=0$ in the form

$$v(z_0, \phi) = \sum_{n=0} V_n \cos(n\phi). \quad (12)$$

We pause to verify that the normalization of the generalized variables demanded by the principle of reciprocity has been achieved. [See Rayleigh (Ref. 11, p. 157). Rayleigh expresses this constraint on normalization in the equivalent terms of work done rather than complex power.] The surface integral for time-averaged complex power is readily found to satisfy

$$\frac{1}{2} \int \int p(z, \phi) v^*(z, \phi) a \, d\phi \, dz = \frac{1}{2} F_n V_n^*, \quad (13)$$

where the superscript asterisk denotes complex conjugation. The form on the right side is the desired standard expression for complex power in terms of the generalized variables.

For complete generality, one should simultaneously require transducers with different angular symmetry [$\sin(n\phi)$ as well as $\cos(n\phi)$] and with different orders n , since reflection from a general, non-axisymmetric termination could involve both symmetries and all orders. The added complexity, easily achieved, is unnecessary in the case at hand where the structure is axisymmetric. One could also generalize the analysis by considering transducers that apply different tractions (e.g., axial) to the shell. The reciprocity constraints would be no different, so long as the proper normalization of generalized variables is maintained [cf. Eq. (13)]. In the present case, nothing is gained by that procedure since all wave types except the $n=0$ shear wave have nonvanishing radial motion. Explicit denotation of the circumferential order by means of the subscript n will be dropped in the subsequent discussion.

B. Canonical reflection problem

The canonical reflection problem for coupling between different structural wave types consists of a semi-infinite shell closed by the target termination, with two ring transducers on the shell at a distance from the termination (see Fig. 7). The transducers numbered 1 and 2 are located at large distances d_1 and d_2 from the termination, so that the evanescent nearfields of the transducers do not couple sig-

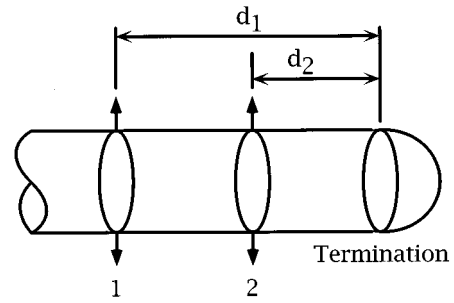


FIG. 7. Semi-infinite shell with two transducers, each capable of operating as a source or receiver, located at large distances from the termination.

nificantly with the termination. Without loss of generality, we assume that both transducers are of the same type (radial force, axial force, etc.).

Now consider two reciprocal experiments, a and b , in which first one then the other transducer is active as a source, exerting generalized forces F_1 and F_2 . The inactive transducer acts as a receiver, measuring generalized velocities V_2 and V_1 , respectively. The mathematical expression of reciprocity is

$$[V_2/F_1]_a = [V_1/F_2]_b. \quad (14)$$

In the absence of trust in Lord Rayleigh, one may readily derive Eq. (14) from Eqs. (9)–(12) with the condition of point-to-point reciprocity in the Green’s function.

The measured velocities in each of these two experiments is the sum of two parts: direct transmission from the source (superscript ‘‘dir’’ below) and the field reflected from the termination (superscript ‘‘ref’’ below). This decomposition is expressed in the equations

$$[V_2]_a = [V_2^{\text{dir}} + V_2^{\text{ref}}]_a \quad \text{and} \quad [V_1]_b = [V_1^{\text{dir}} + V_1^{\text{ref}}]_b. \quad (15)$$

The direct transmission is defined as the transmission for the same source and receiver on an infinite shell of the same design; the reflected transmission is the difference between the results on the semi-infinite and infinite shells.

But, measurements on the infinite shell are also governed by reciprocity, so that the direct components alone must satisfy

$$[V_2^{\text{dir}}/F_1]_a = [V_1^{\text{dir}}/F_2]_b, \quad (16)$$

whence the reflected components alone satisfy a similar equation:

$$[V_2^{\text{ref}}/F_1]_a = [V_1^{\text{ref}}/F_2]_b, \quad (17)$$

This is not the desired final form, mainly because the reflected fields include contributions from all propagating wave types, each of which may have been generated by all propagating wave types in the incident field. The next section unravels that complication.

C. Multiple wave types

In both experiments, a and b , the measured reflected field is a sum over components, each of which represents a signal propagating from the source to the termination in one wave type and propagating from the termination to the re-

ceiver in another wave type (or the same). Hence, the total reflected field is a double sum with exponential phase factors dependent on the distances d_1 and d_2 ; the exponential factors contain the complete dependence on those distances.

The result for experiment *a* can be written as

$$\left[\frac{V_2^{\text{ref}}}{F_1} \right]_a = \sum_q \sum_r Y_r R_{qr} e^{i(k_q d_2 + k_r d_1)}, \quad (18)$$

where the admittance Y_r is defined by the following form for the amplitude of the r -th component of the incident field that is generated by F_1 at a distance d_1 :

$$V_r^{\text{inc}} = F_1 Y_r e^{i k_r d_1}. \quad (19)$$

Note that Y_r , a ‘‘source strength’’ as we shall call it, is independent of the distance from the source although dependent on the type of source and the wave type r . (Sometimes the response to the source on an infinite shell does not have left–right symmetry; a ring moment is a good example. Then the value of Y_r also depends on the orientation of the source. Care is required to avoid mistakes.) Its evaluation is examined below.

The corresponding result for experiment *b* is identical except that the distances d_1 and d_2 must be interchanged. For purposes of the argument it is desirable also to interchange the subscripts r and q inside the summations so that the exponential factor is unchanged; the result is

$$\left[\frac{V_1^{\text{ref}}}{F_2} \right]_b = \sum_q \sum_r Y_q R_{rq} e^{i(k_q d_2 + k_r d_1)}. \quad (20)$$

Now comes the crux of the argument. Equation (17) indicates that the right sides of Eqs. (18) and (20) must be equal—their difference must vanish—at all values of d_1 and d_2 . Since the natural wave numbers are distinct, it can then be argued (see the Appendix) that the constant coefficients of the variable exponentials must be equal term by term:

$$Y_r R_{qr} = Y_q R_{rq}, \quad (21)$$

which can be written in the nondimensional form

$$R_{qr} \sqrt{Y_r / Y_q} = R_{rq} \sqrt{Y_q / Y_r}. \quad (22)$$

D. Source strength

We turn to the evaluation of the wave type source strengths Y_r defined by Eq. (19). For purposes of illustration, consider a radial ring source, as defined in Eq. (9), located at $z_0 = 0$ on an infinite fluid-loaded shell. We must evaluate the strength of the r th wave type at a large distance d_1 from the transducer when it exerts a generalized force F_1 . For convenience, we evaluate the strength of the radial component of shell velocity, other components being related to it by the polarizations determined in Sec. II.

The analysis proceeds by standard means, using a Fourier transform in the z -coordinate. (For examples, see Refs. 1–3.) The transforms of the applied pressure and of the response radial velocity on the shell are related by a spectral impedance determined by the fluid-loaded shell equations:

$$\tilde{Z}(k) \tilde{v}(k) = \tilde{p}(k), \quad (23)$$

where k is the transform wave number. The transform of pressure defined by

$$\tilde{p}(k) = \int_{-\infty}^{\infty} p(z) e^{-ikz} dz \quad (24)$$

is easily evaluated from Eq. (9), with the result $\tilde{v}(k) = F_1 \Phi_n(\phi) \tilde{Z}(k)^{-1}$.

The total velocity at a distance d_1 is given by the inverse transform of $\tilde{v}(k)$:

$$v(d_1, \phi) = F_1 \Phi_n(\phi) \frac{1}{2\pi} \int \frac{e^{ikd_1}}{\tilde{Z}(k)} dk. \quad (25)$$

That part of the total velocity represented by the r th wave type is the pole contribution of the integral (closed in the upper half-plane) at the natural wave number k_r , a simple pole of the integrand where $\tilde{Z}(k)$ vanishes by definition. The pole contribution is readily found and written [using the notation of Eq. (19)] as

$$\begin{aligned} [v(d_1, \phi)]_r &= V_r^{\text{inc}} \cos(n\phi) \\ &= i F_1 \Phi_n(\phi) e^{i k_r d_1} \left[\frac{\partial \tilde{Z}(k)}{\partial k} \right]_{k=k_r}^{-1}, \end{aligned} \quad (26)$$

so that the reciprocal of the desired source strength is given by

$$\frac{1}{Y_r} = \frac{-i 2 \pi a}{\epsilon_n} \left[\frac{\partial \tilde{Z}}{\partial k} \right]_{\tilde{Z}=0; k=k_r}, \quad (27)$$

where ϵ_n is the previously defined Neumann factor.

Surprisingly, an algebraic form can be developed for the derivative of the spectral impedance as a function of wave number, frequency, and n , so that the source strength is readily calculated. The spectral impedance is the sum of a shell impedance, algebraic in the variables, and a transcendental fluid impedance. The derivative of the shell part is easily expressed algebraically. The derivative of the fluid impedance can be shown, by using the differential equation governing Bessel functions, to involve only algebraic factors and the fluid impedance itself. But, at the wave number where the total impedance vanishes, the fluid impedance equals the negative of the shell impedance, so that the desired derivative of the total spectral impedance can be expressed algebraically.¹

In the case of natural waves that are not attenuated by radiation or internal dissipation, it has been shown that the derivative with respect to wave number of the spectral impedance is the dominant factor in the characteristic wave impedance, which relates wave power to the square of response velocity. (See Ref. 12, Section 11.7, and Ref. 13 for further discussion.) Then, the square of Eq. (22) corresponds to requiring equality of the reflection coefficients for power. A similar interpretation for waves with nonvanishing attenuation has not been developed.

E. Results

The values of the reflection coefficients derived in the manner described in Sec. IV have been tested for their con-

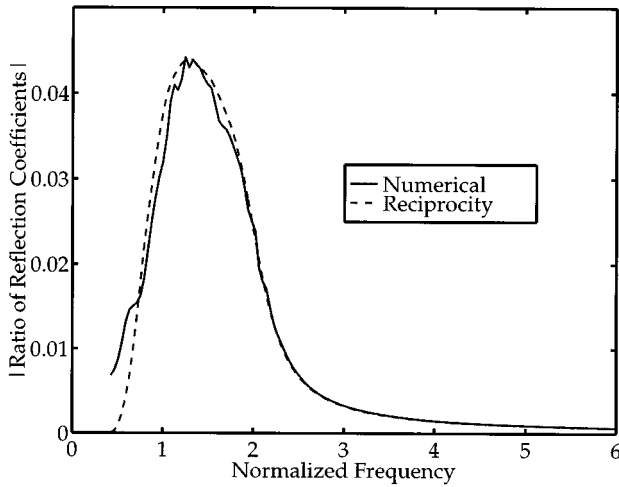


FIG. 8. Absolute value of the ratio of reflection coefficients (longitudinal to flexural divided by flexural to longitudinal) as directly computed and as computed from reciprocity considerations.

sonance with the principle of reciprocity, as expressed in Eqs. (22) and (27). Specifically, Fig. 8 shows the absolute value of the ratio of reflection coefficients (longitudinal-to-flexural divided by flexural-to-longitudinal) predicted both by our numerical experiments and by reciprocity considerations. The agreement is remarkable in that no knowledge of the termination is needed for the reciprocity result.

V. CONCLUDING REMARKS

The literature of acoustics is replete with problems involving the reflections of waves on a waveguide by an isolated inhomogeneity, those results being needed as building blocks for the analysis of some realistic situation involving several discontinuities. The problem is usually selected so as to be amenable to classical methods of analysis. However, in the case at hand the existence of multiple traveling waves, significant fluid loading, and resonant behavior internal to the discontinuity all combine to impede a classical approach to the reflection problem.

We have demonstrated that the essentially analytic multiple-reflection model of response can be retained in such complicated problems, by developing a methodology for evaluating its parameters. Appropriate reflection coefficients are evaluated from an analysis of finite element results for a set of particular problems which share the same discontinuities. The results are tested for agreement with the analytical constraints consequent to the principle of reciprocity.

ACKNOWLEDGMENTS

This paper reports a part of a broader study of the dynamics of fluid-loaded structures supported by the Office of Naval Research, under the supervision and encouragement of Dr. Geoffrey L. Main. The insight of Dr. R. Preuss was critical with respect to the Appendix.

APPENDIX

When the results of the two reciprocal experiments, Eqs. (18) and (20), are subtracted, one obtains a function of the

distances d_1 and d_2 which must vanish for any values of d_1 and d_2 ; it has the form of a double summation over the wave types:

$$g(d_1, d_2) = \sum_{q,r=1}^N A_{qr} e^{ik_q d_2} e^{ik_r d_1} = 0, \quad (\text{A1})$$

where $A_{qr} = Y_r R_{qr} - Y_q R_{rq}$ and N is the number of wave types. It is to be proven that A_{qr} must vanish identically for all values of q and r .

For all pairs of integers (n, m) ranging from 0 to $N-1$, consider the derivatives

$$G_{nm} = \frac{\partial^{n+m} g(d_1, d_2)}{i^{n+m} \partial d_2^n \partial d_1^m}, \quad (\text{A2})$$

which have the form

$$G_{nm} = \sum_{q,r} k_q^n k_r^m A_{qr} e^{i(k_q d_2 + k_r d_1)}. \quad (\text{A3})$$

Since g is constant with value zero, these derivatives all vanish. The result can be written as the matrix equation

$$\mathbf{G} = \mathbf{V}^T \mathbf{B} \mathbf{V} = \mathbf{0}, \quad (\text{A4})$$

where $B_{qr} = [A_{qr} e^{i(k_q d_2 + k_r d_1)}]$ and \mathbf{V} is the Vandermonde matrix:¹⁴

$$\mathbf{V} = \begin{bmatrix} 1 & k_1 & k_1^2 & \cdots & k_1^{N-1} \\ 1 & k_2 & k_2^2 & \cdots & k_2^{N-1} \\ \vdots & \vdots & \vdots & \ddots & \vdots \\ 1 & k_N & k_N^2 & \cdots & k_N^{N-1} \end{bmatrix}. \quad (\text{A5})$$

A Vandermonde matrix in the form of \mathbf{V} is known to be nonsingular, and thus to have an inverse, if $k_q \neq k_r$ for every $q \neq r$. Since the natural wave numbers are known to be distinct, it follows from Eq. (A4) that \mathbf{B} equals the null matrix, $A_{qr} = 0$, and $Y_r R_{qr} = Y_q R_{rq}$ for every r and q , as was to be demonstrated.

¹P. W. Smith, Jr., "Scatter of subsonic waves on a fluid-loaded cylindrical shell from an internal obstacle," J. Acoust. Soc. Am. **89**, 1944 (1991), a summary of Technical Report 978 (Bolt Beranek and Newman Inc., 1987).

²Y. P. Guo, "Effects of structural joints on sound scattering," J. Acoust. Soc. Am. **93**, 857–863 (1993).

³C. N. Corrado, Ph.D. thesis, Massachusetts Institute of Technology, Department of Ocean Engineering, 1993.

⁴M. C. Junger and D. Feit, *Sound, Structures, and Their Interaction* (MIT, Cambridge, MA, 1986), 2nd ed.

⁵J. F. M. Scott, "The Free Modes of Propagation of an Infinite Fluid-Loaded Thin Cylindrical Shell," J. Sound Vib. **125**, 241–280 (1988).

⁶Y. P. Guo, "Approximate solutions of the dispersion equation for fluid-loaded cylindrical shells," J. Acoust. Soc. Am. **95**, 1435–1440 (1994).

- ⁷P. W. Smith, Jr., "Phase velocities and displacement characteristics of free waves in a thin cylindrical shell," *J. Acoust. Soc. Am.* **27**, 1065–1072 (1955).
- ⁸H. Allik and S. Moore, *SARA-3D User's Manual, Version 92-1* (BBN Systems and Technologies, New London, CT, 1992).
- ⁹*Matlab User's Guide* (The Mathworks, Inc., Natick, MA, 1992).
- ¹⁰L. Cremer and M. Heckl, *Structure-Borne Sound* (Springer-Verlag, New York, 1987), 2nd ed., translated and revised by E. E. Ungar.
- ¹¹Lord Rayleigh (John William Strutt), *Theory of Sound* (Dover, New York, 1945), 2nd ed.
- ¹²G. B. Whitham, *Linear and Nonlinear Waves* (Wiley, New York, 1974).
- ¹³K. L. Chandiramani, "Role of Spectral Derivatives of Structure Reactance in Vibration Problems," Technical Report No. 105 (Bolt Beranek and Newman, Inc., Cambridge, MA, 1986).
- ¹⁴K. Nomizu, *Fundamentals of Linear Algebra* (McGraw-Hill, New York, 1966).

Free vibration of a partially fluid-filled cross-ply laminated composite circular cylindrical shell

Z. C. Xi, L. H. Yam, and T. P. Leung

Department of Mechanical Engineering, The Hong Kong Polytechnic University, Hung Hom, Kowloon, Hong Kong

(Received 29 January 1996; accepted for publication 26 September 1996)

Free vibration of a partially fluid-filled cross-ply laminated composite circular cylindrical shell is investigated using a semi-analytical procedure based on the Reissner–Mindlin theory and compressible fluid equations. The shell is modeled using unaxisymmetric shear deformable circular cylindrical shell elements. The fluid is modeled using column fluid elements. The equation of motion of the partially fluid-filled shell is derived using the Hamilton’s variational principle. Numerical examples are given for free vibrations of partially fluid-filled orthotropic and cross-ply laminated composite circular cylindrical shells with various boundary conditions. Numerical results indicate that the fluid filling can reduce significantly the natural frequencies of orthotropic and cross-ply laminated composite circular cylindrical shells. © 1997 Acoustical Society of America. [S0001-4966(97)02502-2]

PACS numbers: 43.40.Ey, 43.20.Tb [CBB]

LIST OF SYMBOLS

| | | | |
|--------------------------------|--|--|--|
| $A_{ij}(i, j = 1, 2, 6)$ | extensional stiffness coefficients of the laminated composite shell | z | radial coordinate for the shell |
| $A_{ij}(i, j = 4, 5)$ | transverse shear stiffness coefficients of the laminated composite shell | β_x, β_θ | rotations of the normal to the middle surface in the x and θ axes |
| $B_{ij}(i, j = 1, 2, 6)$ | extensional-bending coupling stiffness coefficients of the laminated composite shell | $\gamma_{\theta z}, \gamma_{xz}$ | transverse shear strains defined by Eq. (29) |
| $D_{ij}(i, j = 1, 2, 6)$ | bending stiffness coefficients for the laminated composite shell | δ_1, δ_2 | middle surface strains |
| E | Young’s modulus of isotropic material | $\varepsilon_x, \varepsilon_\theta, \varepsilon_{x\theta}$ | circumferential coordinate |
| E_1, E_2 | Young’s moduli of unidirectional composite in the 1 and 2 directions | θ | $\zeta = r/R$ |
| G | shear modulus of isotropic material | ζ | $\eta = x/l$ |
| G_{12}, G_{23}, G_{13} | shear moduli of unidirectional composite in the 1–2, 2–3, and 1–3 planes | η | Poisson’s ratio of isotropic material |
| h | thickness of the shell wall | ν | Poisson’s ratio for unidirectional composite in the 1–2 plane |
| H | height of the fluid | ν_{12} | mass density of unidirectional composite |
| l | length of the shell element | ρ | mass density of the fluid |
| L | length of the shell | ρ_f | middle surface curvatures and twist curvature |
| m | axial half wave number | $\chi_x, \chi_\theta, \chi_{x\theta}$ | ω |
| $M_x, M_\theta, M_{x\theta}$ | moment resultants | ω | circular frequency |
| n | circumferential wave number | \mathbf{a} | vector of nodal displacements |
| N_i, N_j | shape functions of the shell element | $\mathbf{\ddot{a}}$ | vector of nodal accelerations |
| $N_x, N_\theta, N_{x\theta}$ | membrane stress resultants | \mathbf{A} | defined by Eq. (25) |
| P | hydrodynamic pressure | \mathbf{A}_s | defined by Eq. (28) |
| $Q_{\theta z}, Q_{xz}$ | transverse shear stress resultants | \mathbf{B} | defined by Eq. (26) |
| $Q_{ij}(i, j = 1, 2, 4, 5, 6)$ | reduced stiffness coefficients of unidirectional composite | \mathbf{D} | defined by Eq. (27) |
| r | radial coordinate for the fluid | \mathbf{F} | defined by Eq. (32) |
| R | average radius of the shell | \mathbf{H} | defined by Eq. (34) |
| Rc | fundamental natural frequency ratio | \mathbf{I} | defined by Eq. (31) |
| u, v, w | middle surface displacements in axial, circumferential, and radial directions | \mathbf{I}_5 | 5×5 identity matrix |
| $\dot{u}, \dot{v}, \dot{w}$ | middle surface velocities in axial, circumferential, and radial directions | \mathbf{K} | stiffness matrix of the shell element |
| x | axial coordinate | \mathbf{M} | mass matrix of the shell element |
| | | \mathbf{M}_f | defined by Eq. (33) |
| | | \mathbf{N} | shape function matrix of the shell element |
| | | \mathbf{N}_f | shape function matrix of the fluid element |
| | | \mathbf{P} | vector of nodal hydrodynamic pressures |
| | | $\boldsymbol{\theta}$ | triangular function matrix |

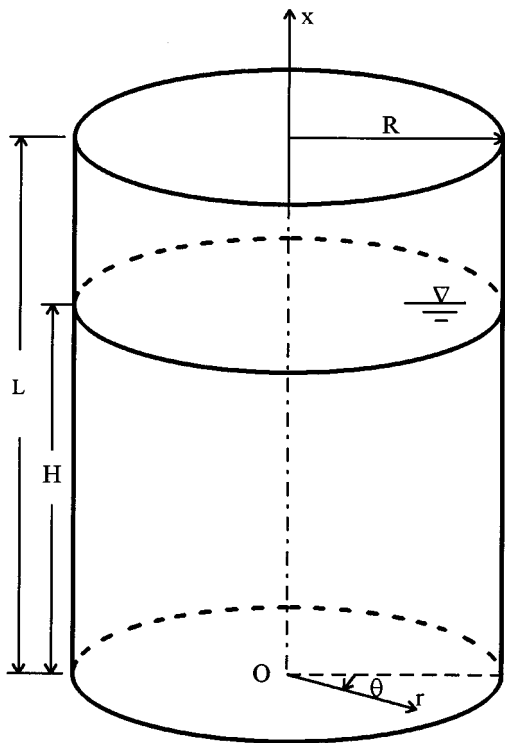


FIG. 1. Geometry of a partially fluid-filled shell and coordinate system of a fluid.

INTRODUCTION

The failure of a partially fluid-filled isotropic circular cylindrical shell due to dynamic loading has received much attention. Advanced composite materials possess high specific strength and stiffness, and super corrosion resistance. The replacement of conventional metal materials by advanced composite materials can improve the bearing capacity of a partially fluid-filled shell. Therefore, in recent years, the use of a partially fluid-filled laminated composite circular cylindrical shell in engineering industry has been steadily increasing. In the design of such a partially fluid-filled composite shell, dynamic response is still a major concern. The free vibration analysis of the partially fluid-filled composite shell is very useful indeed to better study and understand the dynamic behavior.

Owing to the significance of the problem, a few investigators have carried out the vibration analyses of partially fluid-filled laminated composite circular cylindrical shells. On the basis of the first-order shear deformation theory, Jain investigated the vibration of a simply supported fluid-filled circular cylindrical shell composed of multiple isotropic layers using the Rayleigh–Ritz method.¹ Chen and Bert studied the dynamic stability of an orthotropic circular cylindrical shell containing swirling fluid flow using an analytical approach.² Based on the first-order shear deformation theory, Chang and Chiou predicted the natural frequency of a fixed–fixed laminated composite circular cylindrical shell conveying a fluid using the Hamilton’s principle.³ Lakis and Laveau discussed the influence of nonlinearity associated with fluid flow on the natural frequency of a circular cylindrical shell partially filled with a fluid.⁴ Lakis and Sinno dealt with the

axisymmetric and beamlike free vibration problems of an anisotropic circular cylindrical shell partially filled with a liquid.⁵ Lakis, Dyke, and Ouriche analyzed the free vibration of an anisotropic fluid-filled conical shell.⁶ The semi-analytical methods presented in Refs. 4–6 are based on the Sanders’ thin shell theory.

In this paper, free vibrations of partially fluid-filled orthotropic and cross-ply laminated composite circular cylindrical shells are investigated using a semi-analytical procedure based on the Reissner–Mindlin theory and compressible fluid equations. The shell is modeled using unaxisymmetric shear deformable circular cylindrical shell elements. The fluid is modeled using column fluid elements. The equation of motion of the partially fluid-filled shell is derived using the Hamilton’s variational principle. Numerical examples are given for the free vibrations of partially fluid-filled orthotropic and cross-ply laminated composite circular cylindrical shells with various boundary conditions. Parametric studies including circumferential wave number, length-to-radius ratio, radius-to-thickness ratio, material property, and boundary condition are carried out. Emphasis is placed on the effects of the fluid filling on the natural frequencies of orthotropic and cross-ply laminated composite circular cylindrical shells.

I. THEORY

Consider a partially fluid-filled cross-ply laminated composite circular cylindrical shell shown in Fig. 1. Here L and R denote the length and the mean radius of the shell, respectively, and H represents the height of the fluid. The laminated shell is presumed to consist of perfectly bonded shell-like laminae. The laminae are linearly elastic. The deflections are small. The Reissner–Mindlin hypothesis is also adopted, that is, normals to the shell middle surface before deformation remain straight but not necessarily normal to the shell middle surface after deformation, and have constant length. Under these assumptions, the generalized strain-displacement relations are given by

$$\begin{Bmatrix} \varepsilon_x \\ \varepsilon_\theta \\ \varepsilon_{x\theta} \end{Bmatrix} = \begin{Bmatrix} \frac{\partial u}{\partial x} \\ \frac{1}{R} \frac{\partial v}{\partial \theta} + \frac{w}{R} \\ \frac{\partial v}{\partial x} + \frac{1}{R} \frac{\partial u}{\partial \theta} \end{Bmatrix}, \quad (1)$$

$$\begin{Bmatrix} \chi_x \\ \chi_\theta \\ \chi_{x\theta} \end{Bmatrix} = \begin{Bmatrix} \frac{\partial \beta_x}{\partial x} \\ \frac{1}{R} \frac{\partial \beta_\theta}{\partial \theta} \\ \frac{1}{R} \frac{\partial \beta_x}{\partial \theta} + \frac{\partial \beta_\theta}{\partial x} \end{Bmatrix}, \quad (2)$$

$$\begin{Bmatrix} \gamma_{\theta z} \\ \gamma_{xz} \end{Bmatrix} = \begin{Bmatrix} \frac{1}{R} \frac{\partial w}{\partial \theta} - \frac{v}{R} + \beta_\theta \\ \frac{\partial w}{\partial x} + \beta_x \end{Bmatrix}, \quad (3)$$

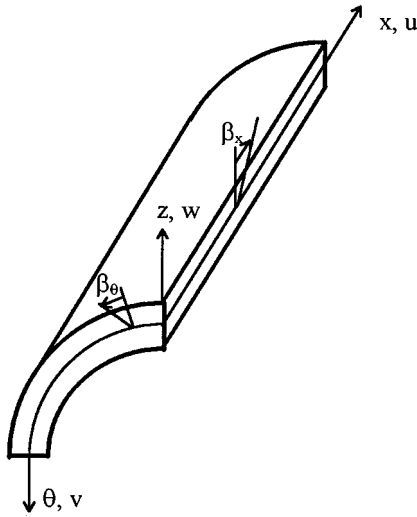


FIG. 2. Sign convention and coordinate system of a shell.

where $\varepsilon_x, \varepsilon_\theta, \varepsilon_{x\theta}$ are the middle surface strains of the shell, $\chi_x, \chi_\theta, \chi_{x\theta}$ are the middle surface curvatures and twist curvature of the shell, $\gamma_{\theta z}, \gamma_{xz}$ are the transverse shear strains of the shell, $u, v,$ and w are the middle surface displacements in the axial, circumferential, and radial directions, respectively, and β_x and β_θ are the rotations of the normal to the middle surface in the x and θ axes, respectively, as is shown in Fig. 2.

The constitutive relations for a cross-ply laminated composite shell are given by⁷

$$\begin{Bmatrix} N_x \\ N_\theta \\ N_{x\theta} \end{Bmatrix} = \begin{bmatrix} A_{11} & A_{12} & 0 \\ A_{12} & A_{22} & 0 \\ 0 & 0 & A_{66} \end{bmatrix} \begin{Bmatrix} \varepsilon_x \\ \varepsilon_\theta \\ \varepsilon_{x\theta} \end{Bmatrix} + \begin{bmatrix} B_{11} & B_{12} & 0 \\ B_{12} & B_{22} & 0 \\ 0 & 0 & B_{66} \end{bmatrix} \begin{Bmatrix} \chi_x \\ \chi_\theta \\ \chi_{x\theta} \end{Bmatrix}, \quad (4)$$

$$\begin{Bmatrix} M_x \\ M_\theta \\ M_{x\theta} \end{Bmatrix} = \begin{bmatrix} B_{11} & B_{12} & 0 \\ B_{12} & B_{22} & 0 \\ 0 & 0 & B_{66} \end{bmatrix} \begin{Bmatrix} \varepsilon_x \\ \varepsilon_\theta \\ \varepsilon_{x\theta} \end{Bmatrix} + \begin{bmatrix} D_{11} & D_{12} & 0 \\ D_{12} & D_{22} & 0 \\ 0 & 0 & D_{66} \end{bmatrix} \begin{Bmatrix} \chi_x \\ \chi_\theta \\ \chi_{x\theta} \end{Bmatrix}, \quad (5)$$

$$\begin{Bmatrix} Q_{\theta z} \\ Q_{xz} \end{Bmatrix} = \begin{bmatrix} A_{44} & 0 \\ 0 & A_{55} \end{bmatrix} \begin{Bmatrix} \gamma_{\theta z} \\ \gamma_{xz} \end{Bmatrix}, \quad (6)$$

where $N_x, N_\theta, N_{x\theta}$ are the membrane stress resultants, $M_x, M_\theta, M_{x\theta}$ are the moment resultants, and $Q_{\theta z}, Q_{xz}$ are the transverse shear stress resultants. The extensional, extensional-bending coupling, bending, and transverse shear stiffnesses are defined as

$$(A_{ij}, B_{ij}, D_{ij}) = \int_{-h/2}^{h/2} \bar{Q}_{ij}(1, z, z^2) dz, \quad i, j = 1, 2, 6, \quad (7)$$

$$A_{ij} = \frac{5}{4} \int_{-h/2}^{h/2} \bar{Q}_{ij} \left(1 - \frac{4z^2}{h^2} \right) dz, \quad i, j = 4, 5, \quad (8)$$

where h is the thickness of the shell wall, and the expressions for the reduced stiffness coefficients \bar{Q}_{ij} ($i, j = 1, 2, 4, 5, 6$) in terms of the material properties of the ply are given in Ref. 7.

For irrotational flow of an inviscid fluid undergoing small motions, the hydrodynamic pressure P satisfies the Helmholtz's equation in the $r, \theta,$ and x coordinates (see Fig. 1),

$$\frac{\partial^2 P}{\partial r^2} + \frac{1}{r} \frac{\partial P}{\partial r} + \frac{1}{r^2} \frac{\partial^2 P}{\partial \theta^2} + \frac{\partial^2 P}{\partial x^2} - \frac{1}{c^2} \frac{\partial^2 P}{\partial t^2} = 0, \quad (9)$$

where c denotes the speed of sound in the fluid.

When surface gravity waves are considered, on the free surface the pressure P satisfies

$$\frac{\partial P}{\partial x} = -\frac{1}{g} \frac{\partial^2 P}{\partial t^2}, \quad (10)$$

where g is the gravity acceleration.

On the interface between the fluid and the shell the pressure P satisfies

$$\frac{\partial P}{\partial \bar{n}} = -\rho_f \frac{\partial^2 w}{\partial t^2}, \quad (11)$$

where \bar{n} is the unit normal to the wetted surface of the shell and ρ_f is the mass density of the fluid.

The Hamilton variational principle is used to derive the equation of motion of a partially fluid-filled shell. The Hamilton variational principle for the free vibration of a partially fluid-filled laminated composite circular cylindrical shell is given by

$$\delta \int_{t_0}^{t_1} (U - T + J) dt = 0, \quad (12)$$

where the times t_1 and t_0 are arbitrary, U and T are the potential energy and kinetic energy of the shell, respectively, and J is the energy stored in the fluid.

The two-node straight axisymmetric circular cylindrical shell element presented by Zienkiewicz *et al.*⁸ is extended here to the unaxisymmetric case in order to consider the coupling between in-plane and transverse variables. For free vibration, the displacement field within an element for circumferential wave number n may be expressed as

$$[u \ v \ w \ \beta_x \ \beta_\theta]^T = \boldsymbol{\theta} \mathbf{N} \mathbf{a}, \quad (13)$$

where the triangular function matrix $\boldsymbol{\theta}$, the shape function matrix \mathbf{N} of the shell element, and the nodal displacement vector \mathbf{a} of the shell element are respectively given by

$$\boldsymbol{\theta} = \begin{bmatrix} \cos n\theta & 0 & 0 & 0 & 0 \\ 0 & \sin n\theta & 0 & 0 & 0 \\ 0 & 0 & \cos n\theta & 0 & 0 \\ 0 & 0 & 0 & \cos n\theta & 0 \\ 0 & 0 & 0 & 0 & \sin n\theta \end{bmatrix}, \quad (14)$$

$$\mathbf{N} = [N_1 \mathbf{I}_5 \quad N_j \mathbf{I}_5], \quad (15)$$

$$\mathbf{a}=[u_i \ v_i \ w_i \ \beta_{xi} \ \beta_{\theta i} \ u_j \ v_j \ w_j \ \beta_{xj} \ \beta_{\theta j}]^T. \quad (16)$$

In Eq. (15) \mathbf{I}_5 is the 5×5 identity matrix, and the shape functions N_i and N_j of the shell element are defined as $N_i=1-\eta$ and $N_j=\eta$ with $\eta=x/l$, where l is the length of the element and subscripts i and j denote the front and rear ends of the shell element, respectively.

When the shell element is filled with a fluid, the potential energy U is given by

$$U = \frac{1}{2} \int_0^{2\pi} \int_0^1 \left(\begin{Bmatrix} \varepsilon_x \\ \varepsilon_\theta \\ \varepsilon_{x\theta} \end{Bmatrix}^T \begin{Bmatrix} N_x \\ N_\theta \\ N_{x\theta} \end{Bmatrix} + \begin{Bmatrix} \chi_x \\ \chi_\theta \\ \chi_{x\theta} \end{Bmatrix}^T \begin{Bmatrix} M_x \\ M_\theta \\ M_{x\theta} \end{Bmatrix} + \begin{Bmatrix} \gamma_{\theta z} \\ \gamma_{xz} \end{Bmatrix}^T \begin{Bmatrix} Q_{\theta z} \\ Q_{xz} \end{Bmatrix} \right) Rl \, d\eta \, d\theta - \int_0^{2\pi} \int_0^1 w P Rl \, d\eta \, d\theta, \quad (17)$$

where P is the hydrodynamic pressure acting on the wall of the shell. The kinetic energy of the shell element T can be expressed as

$$T = \frac{1}{2} \int_0^{2\pi} \int_0^1 \int_{-h/2}^{h/2} \rho [\dot{u}^2 + \dot{v}^2 + \dot{w}^2 + z^2 (\dot{\beta}_x^2 + \dot{\beta}_\theta^2)] Rl \, dz \, d\eta \, d\theta, \quad (18)$$

where ρ is the mass density of the shell and \dot{u} , \dot{v} , \dot{w} are the middle surface velocities in the axial, circumferential, and radial directions, respectively.

The column fluid element presented by Cao and Cheung⁹ is employed to model the fluid. When the effect of fluid sloshing is neglected, the hydrodynamic pressure P within an element for circumferential wave number n may be expressed as

$$P = \mathbf{N}_f \mathbf{p} \cos n\theta, \quad (19)$$

where the shape function matrix \mathbf{N}_f of the fluid element and the vector \mathbf{p} of nodal hydrodynamic pressures are respectively given by

$$\mathbf{N}_f = [N_i \zeta \quad N_i \zeta^2 \quad N_i \zeta^3 \quad N_i \zeta^4 \quad N_j \zeta \quad N_j \zeta^2 \quad N_j \zeta^3 \quad N_j \zeta^4], \quad (20)$$

$$\mathbf{p} = [p_{1i} \ p_{2i} \ p_{3i} \ p_{4i} \ p_{1j} \ p_{2j} \ p_{3j} \ p_{4j}]^T. \quad (21)$$

In Eq. (20) $\zeta=r/R$. The energy stored in the fluid element is given by

$$J = \int_0^{2\pi} \int_0^1 \int_0^1 \left\{ \frac{1}{2} \left[\left(\frac{\partial P}{R \partial \zeta} \right)^2 + \left(\frac{\partial P}{R \zeta \partial \theta} \right)^2 + \left(\frac{\partial P}{l \partial \eta} \right)^2 \right] + \frac{P}{c^2} \frac{\partial^2 P}{\partial t^2} \right\} R^2 l \zeta \, d\zeta \, d\eta \, d\theta + \int_0^{2\pi} \int_0^1 \frac{P}{g} \frac{\partial^2 P}{\partial t^2} \times R^2 \zeta \, d\zeta \, d\theta + \int_0^{2\pi} \int_0^1 \frac{\partial^2 w}{\partial t^2} \rho_f P Rl \, d\eta \, d\theta. \quad (22)$$

Substituting Eqs. (17), (18), and (22) into Eq. (12), performing variational operations, and using the orthogonal property

of the trigonometric functions give the equation of motion of the partially fluid-filled shell,

$$\begin{bmatrix} \mathbf{M} & \mathbf{0} \\ \rho_f \mathbf{F}^T & \mathbf{M}_f \end{bmatrix} \begin{Bmatrix} \ddot{\mathbf{a}} \\ \ddot{\mathbf{p}} \end{Bmatrix} + \begin{bmatrix} \mathbf{K} & -\mathbf{F} \\ \mathbf{0} & \mathbf{H} \end{bmatrix} \begin{Bmatrix} \mathbf{a} \\ \mathbf{p} \end{Bmatrix} = \mathbf{0}, \quad (23)$$

where the stiffness matrix \mathbf{K} of the shell element is given by

$$\mathbf{K} = \int_0^1 [\mathbf{B}_m^T \mathbf{A} \mathbf{B}_m + \mathbf{B}_m^T (\mathbf{B} + \mathbf{B}^T) \mathbf{B}_b + \mathbf{B}_b^T \mathbf{D} \mathbf{B}_b + \mathbf{B}_s^T \mathbf{A}_s \mathbf{B}_s] Rl \, d\eta. \quad (24)$$

In Eq. (24) the strain-displacement matrices $\mathbf{B}_m = [\mathbf{B}_{mi} \ \mathbf{B}_{mj}]$, $\mathbf{B}_b = [\mathbf{B}_{bi} \ \mathbf{B}_{bj}]$, and $\mathbf{B}_s = [\mathbf{B}_{si} \ \mathbf{B}_{sj}]$ are shown in Ref. 10, and

$$\mathbf{A} = \begin{bmatrix} A_{11} \delta_1 & A_{12} \delta_1 & 0 \\ A_{12} \delta_1 & A_{22} \delta_1 & 0 \\ 0 & 0 & A_{66} \delta_2 \end{bmatrix}, \quad (25)$$

$$\mathbf{B} = \begin{bmatrix} B_{11} \delta_1 & B_{12} \delta_1 & 0 \\ B_{12} \delta_1 & B_{22} \delta_1 & 0 \\ 0 & 0 & B_{66} \delta_2 \end{bmatrix}, \quad (26)$$

$$\mathbf{D} = \begin{bmatrix} D_{11} \delta_1 & D_{12} \delta_1 & 0 \\ D_{12} \delta_1 & D_{22} \delta_1 & 0 \\ 0 & 0 & D_{66} \delta_2 \end{bmatrix}, \quad (27)$$

$$\mathbf{A}_s = \begin{bmatrix} A_{44} \delta_2 & 0 \\ 0 & A_{55} \delta_1 \end{bmatrix}, \quad (28)$$

where

$$\delta_1 = \begin{cases} 2\pi, & n=0, \\ \pi, & n \neq 0, \end{cases} \quad \delta_2 = \begin{cases} 0, & n=0, \\ \pi, & n \neq 0. \end{cases} \quad (29)$$

In Eq. (23) the mass matrix \mathbf{M} of the shell element is given by

$$\mathbf{M} = \int_0^1 \mathbf{N}^T \mathbf{I} \mathbf{N} Rl \, d\eta, \quad (30)$$

where

$$\mathbf{I} = \int_{-h/2}^{h/2} \begin{bmatrix} \delta_1 \rho & 0 & 0 & 0 & 0 \\ 0 & \delta_2 \rho & 0 & 0 & 0 \\ 0 & 0 & \delta_1 \rho & 0 & 0 \\ 0 & 0 & 0 & \delta_1 \rho z^2 & 0 \\ 0 & 0 & 0 & 0 & \delta_2 \rho z^2 \end{bmatrix} dz. \quad (31)$$

In Eq. (23) the coupling term \mathbf{F} due to the hydrodynamic pressure is given by

$$\mathbf{F} = \delta_1 \int_0^1 \mathbf{N}^T \mathbf{n}^T \mathbf{N}_f|_{\zeta=1} Rl \, d\eta, \quad (32)$$

where $\mathbf{n}=[0 \ 0 \ 1 \ 0 \ 0]$.

In Eq. (23) \mathbf{M}_f and \mathbf{H} are respectively given by

TABLE I. Natural frequency (in Hz) of a clamped–free ($0^\circ/90^\circ$) laminated composite circular cylindrical shell.^a

| n | m | Number of elements used | | | | |
|-----|-----|-------------------------|-----|-----|-----|-----|
| | | 7 | 14 | 21 | 28 | 32 |
| 1 | 1 | 640 | 641 | 642 | 642 | 642 |
| 11 | 1 | 565 | 670 | 704 | 705 | 705 |

^a $L/R=2$, $R/h=200$.

$$\mathbf{M}_f = \frac{\delta_1}{c^2} \int_0^1 \int_0^1 \mathbf{N}_f^T \mathbf{N}_f R^2 l \zeta d\zeta d\eta + \frac{\delta_1}{g} \int_0^1 (\mathbf{N}_f^T \mathbf{N}_f)|_{\eta=1} R^2 \zeta d\zeta, \quad (33)$$

$$\mathbf{H} = \int_0^1 \int_0^1 \left[\delta_1 \left(\frac{\partial \mathbf{N}_f^T}{R \partial \zeta} \right) \left(\frac{\partial \mathbf{N}_f}{R \partial \zeta} \right) + n^2 \delta_2 \left(\frac{\mathbf{N}_f^T}{R \zeta} \right) \left(\frac{\mathbf{N}_f}{R \zeta} \right) + \delta_1 \left(\frac{\partial \mathbf{N}_f^T}{l \partial \eta} \right) \left(\frac{\partial \mathbf{N}_f}{l \partial \eta} \right) \right] R^2 l \zeta d\eta d\zeta. \quad (34)$$

Putting $\mathbf{a} = \bar{\mathbf{a}} \cos \omega t$ and $\mathbf{p} = \bar{\mathbf{p}} \cos \omega t$ and inserting them into Eq. (23) give the characteristic equation of the partially fluid-filled shell

$$\left| \begin{bmatrix} \mathbf{K} & -\mathbf{F} \\ \mathbf{0} & \mathbf{H} \end{bmatrix} - \omega^2 \begin{bmatrix} \mathbf{M} & \mathbf{0} \\ \rho_f \mathbf{F}^T & \mathbf{M}_f \end{bmatrix} \right| = 0, \quad (35)$$

where ω is the circular frequency of the partially fluid-filled shell.

II. NUMERICAL RESULTS AND DISCUSSION

In this section, the influence of the fluid filling on the natural frequencies of orthotropic and cross-ply laminated composite circular cylindrical shells is studied numerically using the foregoing theory. A lamina numbering increases from the outer to the inner shell surface. The 0° and 90° layers have all-axial and all-circumferential fiber orientations, respectively. An orthotropic shell is composed of 0° layers only. The lamina material properties used are¹¹ $E_1=206.9$ GPa, $E_2=18.62$ GPa, $G_{12}=4.48$ GPa, $G_{13}=G_{12}$, $G_{23}=0.5G_{12}$, $\nu_{12}=0.28$, and $\rho=2048$ kg m⁻³. The fluid is taken as water with the mass density, ρ_f , of 1000 kg m⁻³.

A convergence study is made to find the number of elements required for the analyses. Table I shows the natural frequency of a clamped–free ($0^\circ/90^\circ$) laminated composite circular cylindrical shell. The clamped boundary condition implies $u=v=w=\beta_x=\beta_\theta=0$, while at the free end all the nodal degrees of freedom are unconstrained. It can be seen that with 28 elements, the frequencies are converged to a very good degree of accuracy. In the subsequent calculations, the shell is divided axially into 28 elements. The length of the fluid element is the same as that of the shell element.

First, three examples are used to clarify the validity of the present analysis. The first two examples are for simply supported orthotropic and cross-ply laminated composite circular cylindrical shells. The simply supported boundary condition implies that at one end the boundary conditions are $u=w=\beta_\theta=0$, whereas at the other end the boundary condi-

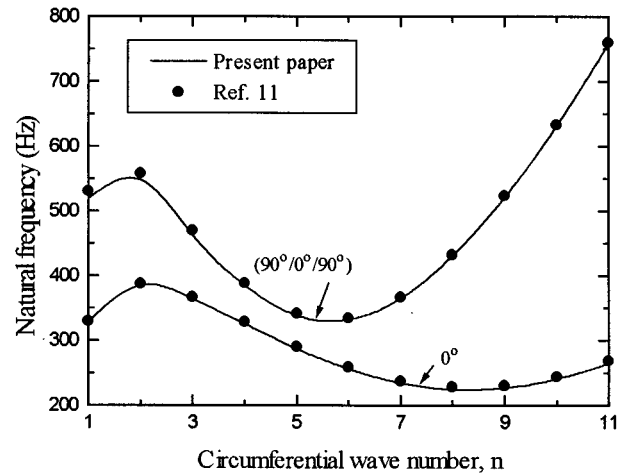


FIG. 3. Natural frequencies of simply supported laminated composite circular cylindrical shells ($L=0.381$ m, $R=0.1905$ m, $h=0.501 \times 10^{-3}$ m, $m=1$).

tions are $w=\beta_\theta=0$. The natural frequencies are shown in Fig. 3 and compared with those given by Sheinman and Weissman.¹¹ These results are obtained for longitudinal mode $m=1$. Good agreement is achieved.

The third example is for a clamped–free thin circular cylindrical shell partially filled with a fluid. The natural frequency is shown in Fig. 4 and compared with the experimental results provided by Chiba, Yamaki, and Tani.¹² These results are obtained for circumferential wave number $n=5$ and longitudinal mode $m=1$. The agreement between the present and experimental results is very good.

Now natural frequencies of partially fluid-filled orthotropic and cross-ply laminated composite circular cylindrical shells with various boundary conditions are calculated.

Figures 5 and 6 show the variations of the natural frequencies with circumferential wave number for clamped–free orthotropic and ($0^\circ/90^\circ$) laminated composite circular cylindrical shells partially filled with a fluid, respectively. For the sake of comparison, the natural frequencies of the corresponding empty shells are also plotted in these figures. As can be seen from these figures, the fluid filling can reduce significantly the magnitude of the natural frequencies of the shells. This phenomenon may be explained intuitively. For a partially fluid-filled shell, the fluid filling increases the total mass of the shell, hence the natural frequencies of the shell decrease. In addition, from Figs. 5 and 6 it can also be seen that the variations of the natural frequencies with circumferential wave number for partially fluid-filled orthotropic and cross-ply laminated composite circular cylindrical shells are similar to those for the corresponding empty shells. For these numerical examples, the natural frequencies of both partially fluid-filled and empty shells first decrease to a minimum and then increase with circumferential wave number. The fluid filling cannot shift the lowest natural frequencies of these shells. This indicates that the fluid filling has negligible effect on the distribution of the natural frequencies of the shells.

Figures 7 and 8 show the effect of the fluid filling on the

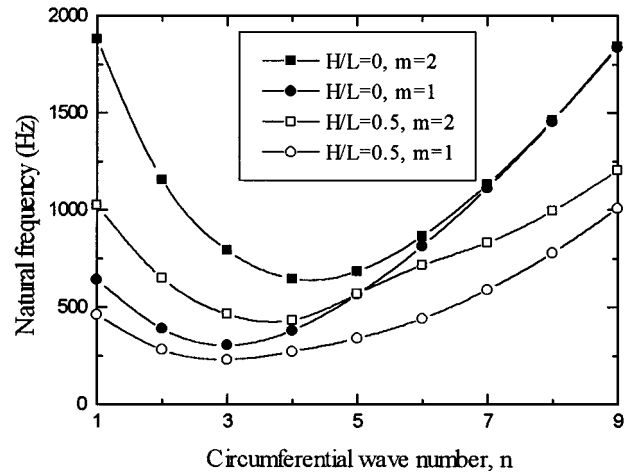
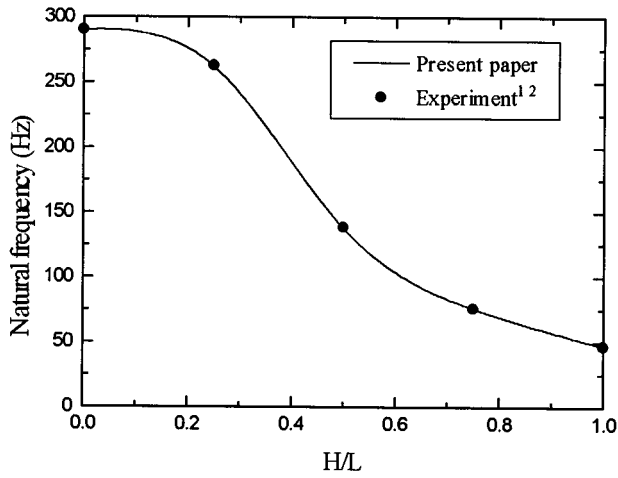


FIG. 4. Natural frequency of a clamped-free isotropic circular cylindrical shell partially filled with a fluid ($R=0.1$ m, $L=0.1139$ m, $h=0.247 \times 10^{-3}$ m, $E=5.56$ GPa, $\nu=0.3$, $\rho=1405$ kg m $^{-3}$, $n=5$, $m=1$).

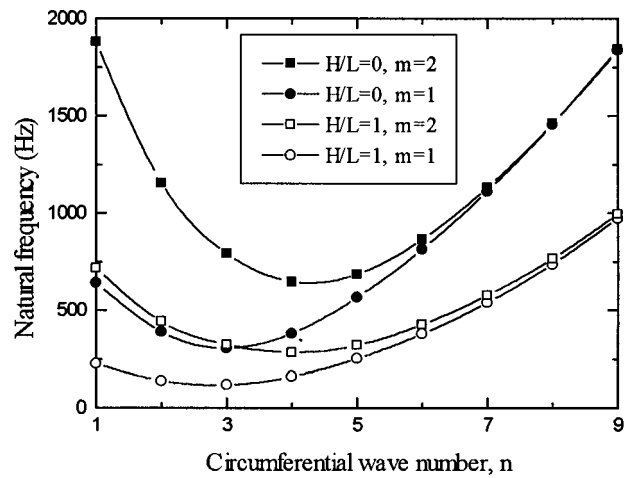
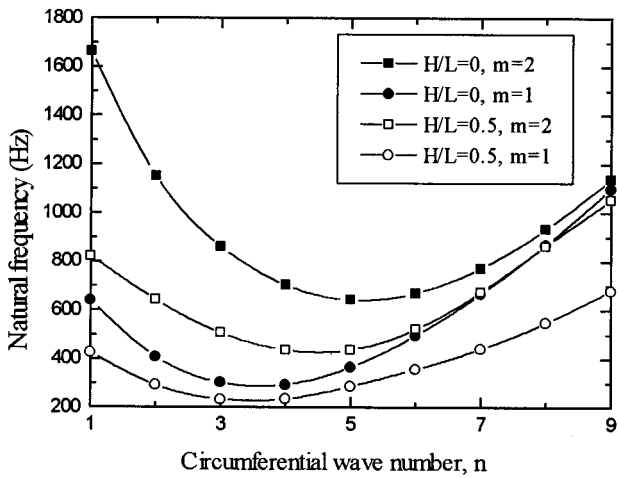


FIG. 6. Natural frequency of a clamped-free ($0^\circ/90^\circ$) laminated composite circular cylindrical shell partially filled with a fluid ($L/R=2$, $R/h=50$).

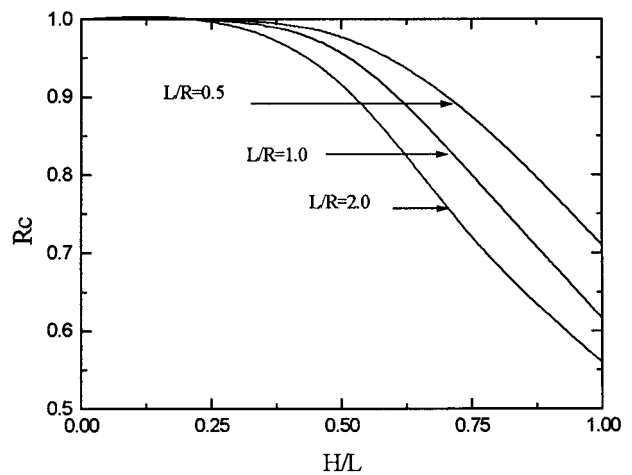
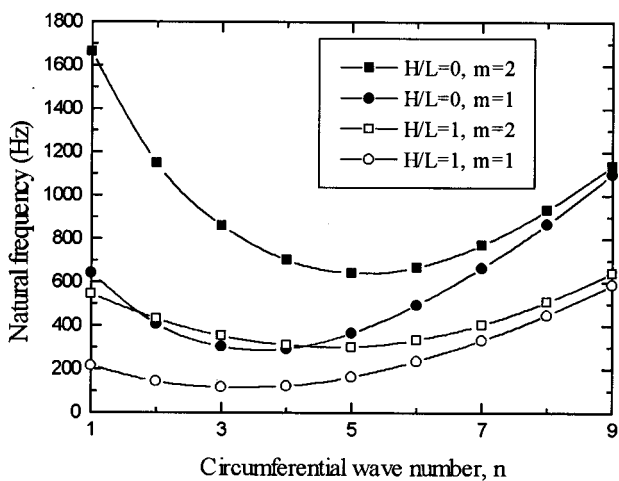


FIG. 5. Natural frequency of a clamped-free orthotropic circular cylindrical shell partially filled with a fluid ($L/R=2$, $R/h=50$).

FIG. 7. Effect of the fluid filling on the fundamental natural frequencies of clamped-free orthotropic circular cylindrical shells with different length to radius ratios ($R/h=20$).

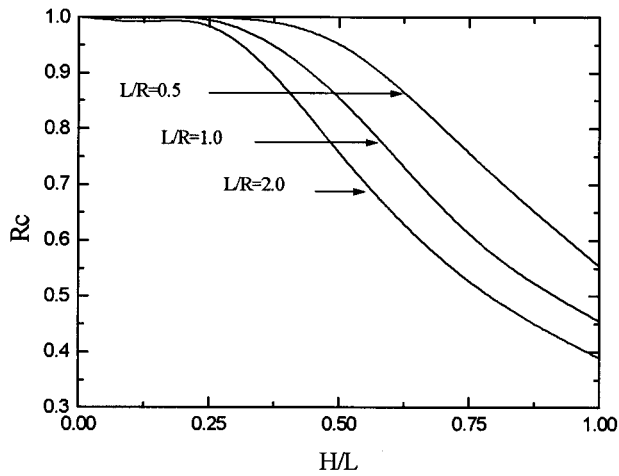


FIG. 8. Effect of the fluid filling on the fundamental natural frequencies of clamped-free ($0^\circ/90^\circ$) laminated composite circular cylindrical shells with different length to radius ratios ($R/h=50$).

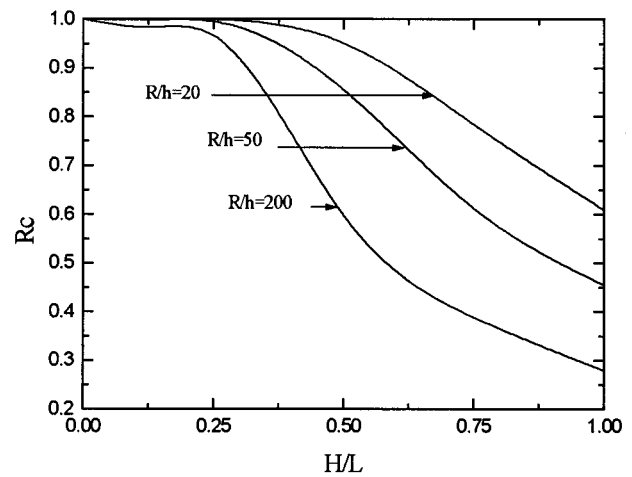


FIG. 10. Effect of the fluid filling on the fundamental natural frequencies of clamped-free ($0^\circ/90^\circ$) laminated composite circular cylindrical shells with different radius to thickness ratios ($L/R=1$).

fundamental natural frequencies of clamped-free orthotropic and ($0^\circ/90^\circ$) laminated composite circular cylindrical shells with different length to radius ratios, respectively. The fundamental natural frequency ratio R_c is defined as the ratio of the natural frequency of the partially fluid-filled shell to that of the corresponding empty shell. The curves in these figures reveal that the influence of the fluid filling on the natural frequencies of the shells becomes strong with the length to radius ratio. The behavior is due to the change in the stiffness of the shell. As the ratio of length to radius increases, the shell becomes flexible. Accordingly, the shell is sensitive to the fluid filling.

In addition, from Figs. 7 and 8 it can be seen more clearly how the reduction of the natural frequencies of the shells varies with the height of the fluid filling. For these numerical examples, as the height of the fluid filling increases, the natural frequencies of the shells decrease first slightly and then quickly.

Figures 9 and 10 show the effect of the fluid filling on

the fundamental natural frequencies of clamped-free orthotropic and ($0^\circ/90^\circ$) laminated composite circular cylindrical shells with different radius to thickness ratios, respectively. It is obvious that the influence of the fluid filling on the natural frequencies of the shells becomes strong as the ratio of radius to thickness increases. This behavior may be explained from the change of the stiffness of the shell. As the ratio of radius to thickness increases, the stiffness of the shell reduces. As a result, the reduction of the natural frequency of the shell becomes large.

Besides, it can also be seen from Figs. 9 and 10 that as the height of the fluid filling increases, the pattern of the variation of the natural frequency of a thinner shell is different from that of a thicker shell. For example, for $H/L > 0$, the natural frequencies of the shells with $R/h=200$ begin to reduce, while for $H/L > 0.25$, the natural frequencies of the shells with $R/h=20$ and 50 begin to decrease.

Figures 11 and 12 show the effect of the fluid filling on

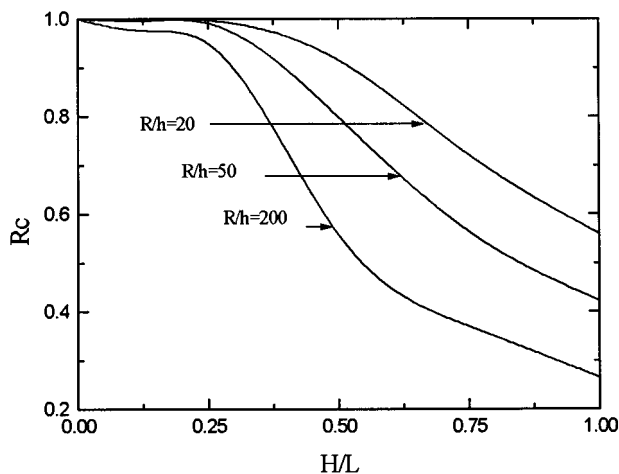


FIG. 9. Effect of the fluid filling on the fundamental natural frequencies of clamped-free orthotropic circular cylindrical shells with different radius thickness ratios ($L/R=2$).

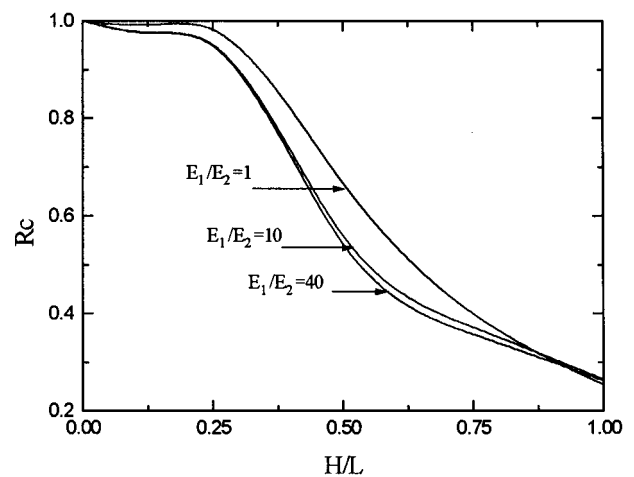


FIG. 11. Effect of the fluid filling on the fundamental natural frequencies of clamped-free orthotropic circular cylindrical shells with different material properties ($G_{12}/E_2=0.24$, $\nu_{12}=0.28$, $G_{13}=G_{12}$, $G_{23}=0.5G_{12}$, $L/R=2$, $R/h=200$).

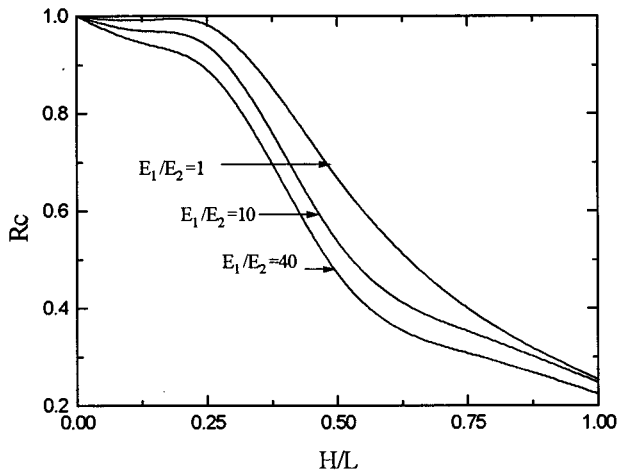


FIG. 12. Effect of the fluid filling on the fundamental natural frequencies of clamped-free ($0^\circ/90^\circ$) laminated composite circular cylindrical shells with different material properties ($G_{12}/E_2=0.24$, $\nu_{12}=0.28$, $G_{13}=G_{12}$, $G_{23}=0.5G_{12}$, $L/R=2$, $R/h=200$).

the fundamental natural frequencies of clamped-free orthotropic and ($0^\circ/90^\circ$) laminated composite circular cylindrical shells with different material properties, respectively. Clearly, the influence of the fluid filling on the natural frequencies of the shells becomes strong as E_1/E_2 increases. Comparison of two figures shows that as E_1/E_2 increases, the reduction of the natural frequencies of the orthotropic shell is different from that of the cross-ply shell. As can be seen from Fig. 11, the reduction of the natural frequencies of the orthotropic shell is remarkable when E_1/E_2 increases from 1 to 10. When E_1/E_2 continues to increase, the natural frequencies reduce only slightly. However, the results in Fig. 12 indicate that the reduction of the natural frequencies of the cross-ply shell is remarkable all the way as E_1/E_2 increases.

Figures 13 and 14 show the effect of the fluid filling on the fundamental natural frequencies of orthotropic and ($0^\circ/90^\circ$) laminated composite circular cylindrical shells with dif-

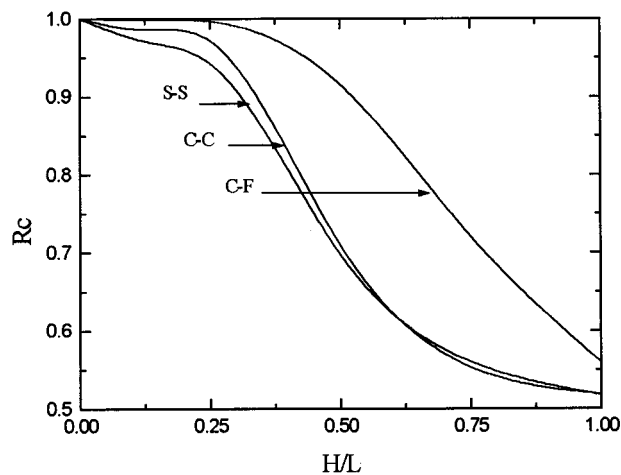


FIG. 13. Effect of the fluid filling on the fundamental natural frequencies of orthotropic circular cylindrical shells with different boundary conditions ($L/R=2$, $R/h=20$).

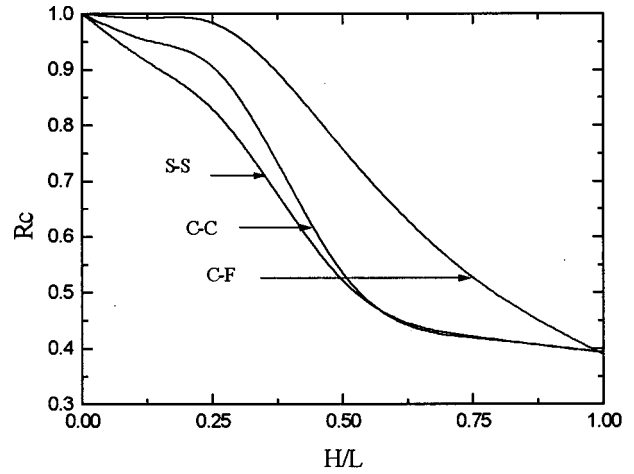


FIG. 14. Effect of the fluid filling on the fundamental natural frequencies of ($0^\circ/90^\circ$) laminated composite circular cylindrical shells with different boundary conditions ($L/R=2$, $R/h=50$).

ferent boundary conditions, respectively. At two simply supported ends the boundary conditions imply $w=\beta_\theta=0$. From these figures it can be found that the fluid filling has more considerable influence on the natural frequencies of the simply supported and clamped-clamped shells than on those of the clamped-free shell. This shows that relaxing one end constraint can reduce the effect of the fluid filling on the natural frequencies of the shells. Besides, the natural frequencies of the simply supported shells are different from those of the clamped-clamped shells. For $H/L \leq 0.5$, the reduction of the natural frequencies of the simply supported shells due to the fluid filling is more remarkable than that for the clamped-clamped shells. It can be seen that the simply supported shells are more sensitive to the fluid filling than the clamped-clamped shells when the shells become half-full from empty. For $H/L > 0.5$, the reductions of the natural frequencies of the simply supported and clamped-clamped shells due to the fluid filling are almost identical. In other words, the influences of the fluid filling on the natural frequencies of the simply supported and clamped-clamped shells are almost the same when the shells become full from half-full.

III. CONCLUSIONS

Free vibrations of partially fluid-filled orthotropic and cross-ply laminated composite circular cylindrical shells with various boundary conditions are studied using a semi-analytical method based on the Reissner-Mindlin shell theory and compressible fluid equations. Based on the numerical results presented in this paper, the following conclusions may be drawn:

- The fluid filling can reduce significantly the natural frequencies of orthotropic and cross-ply laminated composite circular cylindrical shells, but it has negligible effect on the distribution of the natural frequencies of these shells.
- As the ratio of length to radius increases, the effect of

the fluid filling on the natural frequencies of orthotropic and cross-ply laminated composite circular cylindrical shells becomes strong.

- (c) The influence of the fluid filling on the natural frequencies of orthotropic and cross-ply laminated composite circular cylindrical shells increases with the ratio of radius to thickness.
- (d) The influence of the fluid filling on the natural frequencies of orthotropic and cross-ply laminated composite circular cylindrical shells increases as E_1/E_2 increases.
- (e) When the other parameters are the same, the fluid filling has more considerable effect on the natural frequencies of orthotropic and cross-ply laminated composite circular cylindrical shells with simply supported and clamped–clamped boundary conditions than on those of the corresponding clamped–free shells.

ACKNOWLEDGMENTS

The authors are grateful to the Research Committee of The Hong Kong Polytechnic University for the support of this investigation. The authors would like to thank Professor G. Lin of Dalian University of Technology, China, for the helpful discussions.

¹R. K. Jain, "Vibration of fluid-filled, orthotropic cylindrical shells," *J. Sound Vib.* **37**, 379–388 (1974).

- ²T. L. C. Chen and C. W. Bert, "Dynamic stability of isotropic or composite material cylindrical shells containing swirling fluid flow," *J. Appl. Mech.* **44**, 112–116 (1977).
- ³J. S. Chang and W. J. Chiou, "Natural frequencies and critical velocities of fixed-fixed laminated circular cylindrical shells conveying fluids," *Comput. Struct.* **57**, 929–939 (1995).
- ⁴A. A. Lakis and A. Laveau, "Non-linear dynamic analysis of anisotropic cylindrical shells containing a flowing fluid," *Int. J. Solids Struct.* **28**, 1079–1094 (1991).
- ⁵A. A. Lakis and M. Sinno, "Free vibration of axisymmetric and beam-like cylindrical shells partially filled with liquid," *Int. J. Num. Meth. Eng.* **33**, 235–268 (1992).
- ⁶A. A. Lakis, P. V. Dyke, and H. Ouriche, "Dynamic analysis of anisotropic fluid-filled conical shells," *J. Fluids Struct.* **6**, 135–162 (1992).
- ⁷S. W. Tsai and H. T. Hahn, *Introduction to Composite Materials* (Technomic, Westport, CT, 1980).
- ⁸O. C. Zienkiewicz, J. Bauer, K. Morgan, and E. Onate, "A simple and efficient element for axisymmetric shells," *Int. J. Num. Meth. Eng.* **11**, 1545–1558 (1977).
- ⁹Z. Y. Cao and Y. K. Cheung, "A semi-analytical method for structure-internal liquid interaction problems," *Appl. Math. Mech.* **6**, 1–8 (1985) (in Chinese).
- ¹⁰Z. C. Xi, L. H. Yam, and T. P. Leung, "Semi-analytical study of free vibration of composite shells of revolution based on the Reissner–Mindlin assumption," *Int. J. Solids Struct.* **33**, 851–863 (1996).
- ¹¹I. Sheinman and S. Weissman, "Coupling between symmetric and anti-symmetric modes in shells of revolution," *J. Compos. Mater.* **21**, 988–1007 (1987).
- ¹²M. Chiba, N. Yamaki, and J. Tani, "Free vibration of a clamped-free circular cylindrical shell partially filled with liquid—part 3: Experimental analysis," *Thin-Walled Struct.* **3**, 1–14 (1985).

Sensitivity analysis of coupled structural-acoustic problems using perturbation techniques

Steven R. Hahn and Aldo A. Ferri

School of Mechanical Engineering, Georgia Institute of Technology, Atlanta, Georgia 30332

(Received 26 June 1995; accepted for publication 5 September 1996)

The analysis of acoustic radiation and scattering from submerged elastic structures is an important and challenging problem. Often, numerical solutions are hampered by the fact that the acoustic pressure field can be very sensitive to structural detail. In this paper, a procedure for obtaining the sensitivity of a structural-acoustic system to structural perturbations is presented. The theoretical development assumes a finite element description of the structure and a boundary element description of the fluid. The analysis includes full coupling between the fluid and the structure, and can accommodate both internal and/or external fluid regions. The types of perturbations are limited to those that do not alter the geometry of the wetted surface, but are otherwise completely general in nature. The technique is then applied to acoustic scattering from a cylindrical shell. Two perturbations are considered: A change in the shell thickness and a change in the elastic modulus. The effect of these structural perturbations on the surface pressure, surface normal velocity, and scattered pressure are examined for plane-wave scattering. © 1997 Acoustical Society of America. [S0001-4966(97)02601-5]

PACS numbers: 43.40.Rj [CBB]

INTRODUCTION

Although structural analysis tools such as finite element and boundary element techniques are well developed, their use in the analysis of large scale coupled structural-acoustic systems is relatively new. Because boundary elements are adept at modeling exterior fluids and finite elements can accurately model complicated elastic structures, these two numerical techniques are often coupled together to analyze acoustic scattering and radiation from submerged elastic bodies. Amini *et al.*¹ provide a comprehensive presentation of the coupled finite element/boundary element (FE/BE) technique. To date, the FE/BE technique has been implemented in several commercially available computer codes. When applied to simple elastic structures, for example shells of revolution, the FE/BE technique has proven to be accurate in the low-frequency range. In terms of wave numbers $k = \omega/c$ (where ω is the harmonic frequency in rad/s and c is the wavespeed in the surrounding fluid), the low-frequency regime is generally considered to be the range $0 < ka < 10$, where “ a ” is a length dimension. For structures that are more complicated, for example nonaxisymmetric structures or elastic shells with significant internal structure, and for structures of moderate complexity in the mid-frequency range ($10 < ka < 20$), the accuracy of FE/BE predictions when compared to experimental results is known to be less reliable. Although there are many theories for why FE/BE techniques have difficulty in predicting radiated or scattered pressures from fluid-loaded structures, one possibility is the high sensitivity of the physical system to structural detail.

As the acoustic frequency gets large, the size of the computational model likewise grows. Thus, in the mid-frequency range where the structure is many wavelengths in dimension, the size of the computational model becomes very large. Given limited computational time/power, it is desirable to understand what parts of the structure need to be

modeled accurately and which parts are less important from the standpoint of far-field acoustic radiation and scattering. With respect to design, it is desirable to know which parts of a structure have the strongest effect on the scattered pressure; presumably, design modifications in this area would offer the greatest potential to alter the scattering characteristics. Being able to accomplish this without the need to run extensive parametric studies would greatly facilitate design refinement and optimization.

The purpose of this paper is to develop perturbation techniques suitable for numerical models of fluid-loaded structures. The perturbation technique allows one to predict the effect of small structural modifications on acoustic radiation and scattering. This, in turn, makes it possible to identify critical features of the model which can be targeted for model refinement. The perturbation information can also be used to provide guidance for design changes.

Perturbation theory for linear systems and linear operators is a fairly mature field (see, for example, the reference texts by Kato² and Baumgartel³). For the case of statically loaded elastic structures, Saigal⁴ calculated the change in response stemming from changes in design parameters using a boundary element description of the system. In the areas of vibration theory and structural dynamics, many authors have studied the application of perturbation theory to a system's free response characteristics; see, for example, Fox and Kapoor,⁵ Collins and Thomson,⁶ or the survey article of Ibrahim.⁷ Several authors have considered the effect of perturbations on the forced response to harmonic excitation; for example, Ryland and Meirovitch,⁸ Sinha,⁹ Wei and Pierre,¹⁰ Mignolet and Lin.¹¹

In the context of acoustic and structural-acoustic systems, several authors have considered the effects of structural modifications on radiated and/or scattered pressures. The influence of isolated point masses on the vibration of

fluid-loaded plates has been studied (Sandman,¹² Feit,¹³ Ginsberg *et al.*¹⁴). The influence of rib stiffeners on fluid-loaded plates has also received attention (Mace,¹⁵ Ginsberg and McDaniel¹⁶). The influence of more complicated internal substructures on acoustic radiation and scattering is also relevant to the present discussion (Achenbach *et al.*,¹⁷ Rebillard *et al.*¹⁸).

The aforementioned references pertaining to acoustics and structural-acoustic systems have studied the effect of the structural perturbation through a complete reanalysis of the modified system. No attempt was made to derive expressions for the perturbed radiated or scattered pressure, which is the subject of this paper. Some prior work in this area, however, should be noted. Ma and Hagiwara¹⁹ developed eigenmode and frequency response sensitivity analysis methods for use in optimization schemes. The work is based on a finite element description of both the fluid and the structure and examines only internal fluid cavities; no external radiation or scattering is considered. St. Pierre and Koopmann²⁰ calculated sensitivity derivatives due to the addition of point masses to a fluid-loaded baffled plate. Vlahopoulos²¹ derived acoustic sensitivities with respect to structural shape and impedance. These sensitivities are based on finite element/boundary element models and are particularly concerned with scattering problems. The sensitivity calculations ignore any coupling between the fluid and the structure, so their use is limited. The sensitivities are used in an optimization scheme to reduce scattering. A procedure that is suitable to *light fluid loading* was developed recently by Filippi *et al.*²² The method treats the influence of the fluid loading to the vibratory response as a perturbation to the *in vacuo* response.

The remainder of the paper is organized as follows. The next section develops the mathematical model which is used to describe the structural acoustic problem. A perturbation technique is then presented, and the method is applied to the problem of scattering from an infinite elastic cylinder. The approximate response obtained from the perturbation analysis is compared to solutions obtained from a full reanalysis of the perturbed structure. Some observations and concluding remarks are presented in the final section.

I. MODEL FORMULATION

This paper considers linear structural-acoustic problems where the fluid motion can be represented by the acoustic wave equation,

$$\nabla^2 p - \frac{1}{c^2} \frac{\partial^2 p}{\partial t^2} = 0, \quad (1)$$

where p is the pressure, t is time, and c is the acoustic wave speed. The corresponding wave equation for a linear elastic, isotropic material is, in vector form,

$$\mu \nabla^2 \mathbf{u} + (\lambda + 2\mu) \nabla(\nabla \cdot \mathbf{u}) = \rho \frac{\partial^2 \mathbf{u}}{\partial t^2}, \quad (2)$$

where \mathbf{u} is a displacement vector, ρ is the mass density, and μ and λ are the Lamé constants relating stress to strain. The constant frequency case, with time dependence $e^{-i\omega t}$ results in

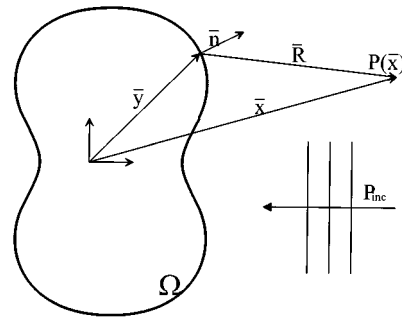


FIG. 1. Geometry for acoustic radiation and scattering using the Helmholtz integral.

$$\nabla^2 p + k^2 p = 0 \cdots k = \frac{\omega}{c} \text{ (fluid)} \quad (3)$$

and

$$\mu \nabla^2 \mathbf{u} + (\lambda + 2\mu) \nabla(\nabla \cdot \mathbf{u}) = -\omega^2 \rho \mathbf{u} \text{ (structure)}. \quad (4)$$

The equations are coupled at the fluid-structure interface by the following continuity conditions:

$$u_n^{\text{struc}} = u_n^{\text{fluid}} = \frac{1}{\rho \omega^2} \frac{\partial p}{\partial n} \text{ continuity of normal displacement}$$

$$\sigma_{nn} = p; \quad \sigma_{nt} = 0 \text{ continuity of normal and tangential stress.} \quad (5)$$

Analysis of sound radiation and scattering can often be facilitated by a mathematical theorem due to Kirchhoff and Helmholtz. Using Eq. (1) along with a vector identity and Gauss' theorem, the following integral equation can be derived:

$$\alpha p(\mathbf{x}) = -\frac{1}{4\pi} \int_{\Omega} \left[G(\mathbf{x}, \mathbf{y}) \frac{\partial p(\mathbf{y})}{\partial n_{\mathbf{y}}} - p(\mathbf{y}) \frac{\partial G(\mathbf{x}, \mathbf{y})}{\partial n_{\mathbf{y}}} \right] d\Omega(\mathbf{y}) + p_{\text{inc}}(\mathbf{x}), \quad (6)$$

where p is the total pressure and p_{inc} is the pressure due to an incident plane at point \mathbf{x} . The factor α accounts for the jump condition across the surface boundary, Ω ,

$$\alpha = \begin{cases} 1, & \mathbf{x} \text{ exterior to } \Omega, \\ \frac{1}{2}, & \mathbf{x} \text{ on } \Omega \text{ (smooth surface)}, \\ 0, & \text{interior to } \Omega. \end{cases} \quad (7)$$

The Green's function, $G(\mathbf{x}, \mathbf{y})$, is the free space Green's function,

$$G(\mathbf{x}, \mathbf{y}) = \frac{e^{ik|\mathbf{x}-\mathbf{y}|}}{|\mathbf{x}-\mathbf{y}|}. \quad (8)$$

The geometry for such a scattering problem is shown in Fig. 1. This integral, known as the Helmholtz integral, forms the basis for most boundary element methods (BEM) in acoustics. The BEM solves Eq. (6) by discretizing the surface into L patches or elements that are commonly small relative to an acoustic wavelength. This allows the surface pressure and

normal velocity within each element to be approximated by simple functions, typically polynomial distributions of second order or less. The surface pressure, p , can be expressed in terms of the local isoparametric coordinates ξ and η ,

$$p(\xi, \eta) = \sum_{i=1}^M N_i(\xi, \eta) p_i. \quad (9)$$

A similar expression is used to describe $\partial p / \partial n$. The N_i are called shape or interpolation functions since they interpolate the value of p and $\partial p / \partial n$ between the nodal values. Equation (6) can now be written as

$$\alpha p(\mathbf{x}) = \frac{1}{4\pi} \sum_{i=1}^L \int_{\Omega_i} \left[G \sum_{j=1}^M N_j \left(\frac{\partial p}{\partial n} \right)_j - \frac{\partial G}{\partial n} \sum_{j=1}^M N_j p_j \right] d\Omega_i + p_{\text{inc}}(\mathbf{x}). \quad (10)$$

Repeated application of Eq. (10) with \mathbf{x} taken to be the position of each of the acoustic nodes in turn results in a set of algebraic equations,

$$\left(\frac{1}{2}I - H\right)p = -Gv_n + p_{\text{inc}}, \quad (11)$$

where p and v_n are vectors denoting the nodal pressures and normal velocities, respectively, I is the identity matrix, G and H are complex, full, nonsymmetric matrices, and p_{inc} is a vector of incident pressure at the nodes. Advantage is taken of Euler's equation of motion for a fluid which requires that $\partial p / \partial n = i\omega\rho v_n$. Note that in the interest of notational clarity, matrices will be denoted by upper case letter and vectors and scalars will be denoted by lower case letters.

Upon specification of the boundary conditions, Eq. (11) can be solved for p and v_n . Once the surface pressures and normal velocities are known, the scattered radiated pressures can be found from Eq. (10) with $\alpha=1$. Using asymptotic versions of the free space Green's function, far-field scattered pressures can be calculated,

$$p_{\text{ff}} = h^T p - g^T v_n. \quad (12)$$

The elastic structure can be modeled approximately using the finite element method (FEM). The FEM is a variational technique in which an energy functional is minimized. The structural volume is discretized into many small volumes or elements in a manner similar to that of the surface discretization of the BEM. Simple interpolation functions are used to represent the displacement field in each element. The minimization of the energy functional resulting from the displacement field results in a matrix relationship between structural displacements and various structural loadings including point forces, body forces, and surface tractions,

$$(K - \omega^2 M)d = f, \quad (13)$$

where K is the stiffness matrix, M is the mass matrix, d is a vector of nodal displacements, and f is a vector of nodal forces due to point forces, surface tractions, and body forces. In order to maintain consistent unknowns between the boundary element matrices and the finite elements matrices, Eq. (13) can be expressed as a structural impedance,

$$Sv = f \text{ where } S = (i/\omega)K - i\omega M \text{ and } v = -i\omega d. \quad (14)$$

The continuity conditions of Eq. (5) are enforced by requiring that

$$f = f_s + Ap, \quad v_n = \tilde{N}v, \quad (15)$$

where f_s represents all structural loading except that due to acoustic pressures, A is a matrix that transforms surface pressures to nodal forces, and \tilde{N} is a matrix consisting of normal vectors that transforms the global structural velocity vector into a vector containing only wetted surface normal velocities. Combining Eqs. (11), (13), and (15) results in a set of equations in p and v ,

$$Sv = f_s + Ap, \\ \left(\frac{1}{2}I - H\right)p = -G\tilde{N}v + p_{\text{inc}}.$$

These equations are typically reduced by solving for v in terms of p ,

$$\left(\frac{1}{2}I - H + G\tilde{N}S^{-1}A\right)p = -G\tilde{N}S^{-1}f_s + p_{\text{inc}}. \quad (16)$$

II. PERTURBATION METHOD

This section details the development of a first-order perturbation method which may be applied directly to the FE/BE system description. After formulating the perturbed solution for arbitrary structural models, the method will be simplified for the more specialized case of structures which can be modeled by a local impedance condition.

Consider an acoustic plane wave impinging on a submerged elastic structure resulting in a far-field scattered pressure, p_{ff} . Using Eq. (16) with $f_s=0$, a structural impedance condition can be found which relates surface normal velocities to surface pressures,

$$v_n \equiv \tilde{N}v = \tilde{N}S^{-1}Ap. \quad (17)$$

Substituting this into Eq. (12) gives an expression for the scattered pressure solely in terms of the surface pressure,

$$p_{\text{ff}}(S) = (h^T - g^T \tilde{N}S^{-1}A)p, \quad (18)$$

where the dependence on the structural matrix, S , has been indicated explicitly. Now consider the effect on p_{ff} of perturbing the structural matrix S by an amount $\epsilon\Delta S$, where ϵ is a small scalar ($\epsilon \ll 1$) and the perturbation is a matrix which is assumed to be on the same order of the original structure; i.e., $\|\Delta S\| \approx \|S\|$, according to some appropriate norm. The inverse of the perturbed structural matrix can be found as follows:

$$I = (S + \epsilon\Delta S)(S + \epsilon\Delta S)^{-1}, \\ S(S + \epsilon\Delta S)^{-1} = I - \epsilon\Delta S(S + \epsilon\Delta S)^{-1}, \\ (S + \epsilon\Delta S)^{-1} = S^{-1} - \epsilon S^{-1}\Delta S(S + \epsilon\Delta S)^{-1}, \\ (S + \epsilon\Delta S)^{-1} = S^{-1} - \epsilon S^{-1}\Delta S(S^{-1} - \epsilon S^{-1} \\ \times \Delta S(S + \epsilon\Delta S)^{-1}), \\ (S + \epsilon\Delta S)^{-1} = S^{-1} - \epsilon S^{-1}\Delta S S^{-1} + \epsilon^2(S^{-1}\Delta S)^2 \\ \times (S + \epsilon\Delta S)^{-1}.$$

Since $\epsilon \ll 1$, the inverse can be approximated by

$$(S + \epsilon \Delta S)^{-1} \approx S^{-1} - \epsilon S^{-1} \Delta S S^{-1}. \quad (19)$$

Note that the existence of S^{-1} is assured by the inclusion of a small amount of structural damping, but if S is nearly singular, ϵ will have to be extremely small for the first-order approximation to be valid. Using Eq. (19) in Eq. (11) and again ignoring higher order terms, the surface pressure perturbation can be found:

$$\begin{aligned} (\frac{1}{2}I - H)p + Gv_n &= p_{\text{inc}}, \\ (\frac{1}{2}I - H)p + G\tilde{N}S^{-1}Ap &= p_{\text{inc}}, \\ \{(\frac{1}{2}I - H) + G\tilde{N}[S^{-1} - \epsilon S^{-1} \Delta S S^{-1}]A\}(p + \epsilon \Delta p) &= p_{\text{inc}}, \\ \{[(\frac{1}{2}I - H) + G\tilde{N}S^{-1}A] - \epsilon G\tilde{N}S^{-1} \Delta S S^{-1}A\}(p + \epsilon \Delta p) & \\ = p_{\text{inc}}, & \quad (20) \\ -\epsilon G\tilde{N}S^{-1} \Delta S S^{-1}Ap + \epsilon [(\frac{1}{2}I - H) + G\tilde{N}S^{-1}A] \Delta p &\approx 0, \\ [(\frac{1}{2}I - H) - G\tilde{N}S^{-1}A]^{-1}[G\tilde{N}S^{-1} \Delta S S^{-1}A]p &= \Delta p. \end{aligned}$$

Substituting the above expressions into Eq. (18) yields an expression for the perturbed scattered pressure as a function of the structural matrix, S ,

$$\begin{aligned} p_{\text{ff}}(S + \epsilon \Delta S) & \\ = [h^T - g^T \tilde{N}(S^{-1} - \epsilon S^{-1} \Delta S S^{-1})A](p + \epsilon \Delta p) & \\ = p_{\text{ff}}(S) + \epsilon g^T \tilde{N}S^{-1} \Delta S S^{-1}Ap + \epsilon (h^T - g^T \tilde{N}S^{-1}A) [(\frac{1}{2}I & \\ - H) - G\tilde{N}S^{-1}A]^{-1}(G\tilde{N}S^{-1} \Delta S S^{-1}A)p + \epsilon^2(\dots). & \quad (21) \end{aligned}$$

After dropping higher order terms in ϵ , this equation can be further simplified by noting that $S^{-1}Ap = v$ and defining an impedance matrix, Z , such that $\tilde{N}S^{-1}A = Z^{-1}$,

$$\begin{aligned} \Delta p_{\text{ff}} &= p_{\text{ff}}(S + \epsilon \Delta S) - p_{\text{ff}}(S) \\ &= \epsilon [(h^T - g^T Z^{-1})[(\frac{1}{2}I - H) - GZ^{-1}]^{-1}G + g^T] \\ &\quad \times \tilde{N}S^{-1}(\Delta S)v \\ &= \epsilon \text{tr}\{v[(h^T - g^T Z^{-1})[(\frac{1}{2}I - H) - GZ^{-1}]^{-1}G + g^T] \\ &\quad \times \tilde{N}S^{-1}(\Delta S)\}. \quad (22) \end{aligned}$$

If ΔS is known, then Eq. (22) can be used to calculate, to first order, changes in the far-field scattered pressure, p_{ff} . In fact, for specified ΔS , equations in the form of Eq. (22) can be used to evaluate the effect of ΔS on various acoustic metrics. Often, however, one may wish to evaluate the effect of a variety of structural perturbations on a given metric. For these cases, where ΔS is not specified, an important relationship attributed to Kleinman²³ is useful.

Kleinman's Lemma: Let $f(X)$ be a trace function of X where X is an m by n matrix. If for any variations ΔX it is possible to write, $f(X + \epsilon \Delta X) - f(X) = \epsilon \text{tr}(D(X)^T \Delta X)$ as $\epsilon \rightarrow 0$; where $D(X)$ is an m by n matrix, then, $\partial f(X)/\partial X = D(X)$.

Applying Kleinman's Lemma to Eq. (22), it is seen that the derivative of the scattered pressure with respect to the structural matrix, S , is

$$\begin{aligned} D_S = \frac{\partial p_{\text{ff}}}{\partial S} &= \left\{ v \left[(h^T - g^T Z^{-1}) \left[\left(\frac{1}{2} I - H \right) - GZ^{-1} \right]^{-1} G \right. \right. \\ &\quad \left. \left. + g^T \tilde{N}S^{-1} \right]^T \right\}. \quad (23) \end{aligned}$$

Equation (23) can be used to investigate the sensitivity of the far-field scattered pressure to changes in S . In contrast, Eq. (22) can be used as a means of calculating a scalar derivative of p_{ff} with respect to ϵ for a particular, i.e., specific, ΔS . In other words, an equation such as (22) is most useful in determining the effect of a specified perturbation on various metrics of interest, and Eq. (23) is most useful when the effect of an unspecified perturbation on a given metric is of interest. Although Eqs. (22) and (23) may appear intimidating, they are actually fairly easy to compute. All of the large matrices and matrix inversions are computed in the analysis of the nominal system and can be saved for later calculation of the sensitivities. Also, although $\partial p_{\text{ff}}/\partial S$ is a large fully populated matrix, it can be efficiently stored as the outer product of two vectors so that the required matrix elements can be quickly calculated as needed. The calculation of the sensitivities takes only a small fraction of the time required to analyze the nominal system.

A modeling simplification that is often justified is that the surface impedance reacts locally; i.e., the motion at one point on the surface does not affect the motion at other points on the surface. An example of such a system is a body surrounded by a highly damped acoustic coating.²⁴ For such local impedance models, the impedance matrix, $[Z]$, is diagonal and the value of the diagonal terms can be calculated using a one dimensional spring, mass, damper model. For such structures Eq. (23) can be simplified to,

$$\begin{aligned} D_Z = \frac{\partial p_{\text{ff}}}{\partial Z} &= \left\{ v_n \left[(h^T - g^T) \left[\left(\frac{1}{2} I - H \right) - GZ^{-1} \right]^{-1} G \right. \right. \\ &\quad \left. \left. + g^T Z^{-1} \right]^T \right\}. \quad (24) \end{aligned}$$

III. NUMERICAL EXAMPLE

As a numerical example of structural perturbations, consider a thin cylindrical steel shell submerged in water [Fig. 2(a)]. A plane wave, $p_{\text{inc}} = p_0 e^{-ikx}$, is scattered by the cylinder, and it is desired to know how changing the thickness of the cylinder affects the far-field back scattered pressure. For this example the nominal shell has a radius of 1 m and is 0.03 m thick. The perturbation corresponds to a 33% increase in shell thickness, from $t_0 = 0.03$ m to $t_0 + \Delta t = 0.04$ m. For these numerical studies, three models will be compared with one another: (1) the nominal model, $p_{\text{ff}}(S)$; (2) the perturbed model using full reanalysis, $p_{\text{ff}}(S + \Delta S)$; and (3) the perturbed model using perturbation theory [Eq. (22)], $p_{\text{ff}}(S) + \Delta p_{\text{ff}}$.

As shown in Fig. 2(b), the perturbation, ΔS , corresponds to the addition of a layer of elements on the inner surface of

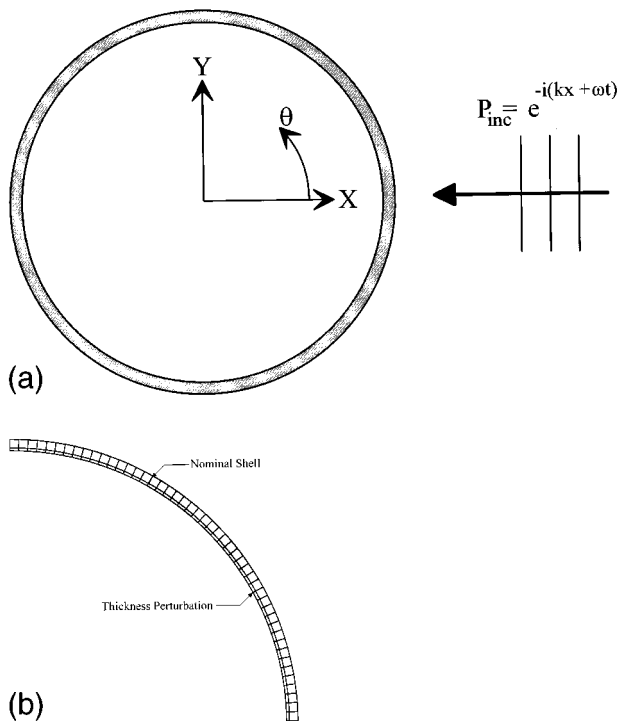


FIG. 2. Scattering from a cylindrical shell. (a) Geometry. (b) Finite element mesh.

the nominal model. In order to calculate p_{ff} using Eq. (22), ΔS must have the same degrees of freedom (i.e., nodes) as S . For the example considered here, this was accomplished by augmenting the nominal shell to include the inner layer of elements which describe the perturbation. To these elements a very small Young's modulus and zero density is assigned so that they are structurally insignificant but numerically stable. A more elegant approach would be to use substructuring techniques to condense out of the perturbation matrix all the nodes not shared on the common boundary with the nominal structure before applying Eq. (22).

In Fig. 3, the far-field back scattered pressure is examined as a function of frequency. The far-field back scattered pressure is normalized by the magnitude of the incident wave, p_0 , and the cylindrical spreading term, e^{ikR}/\sqrt{R} . It is

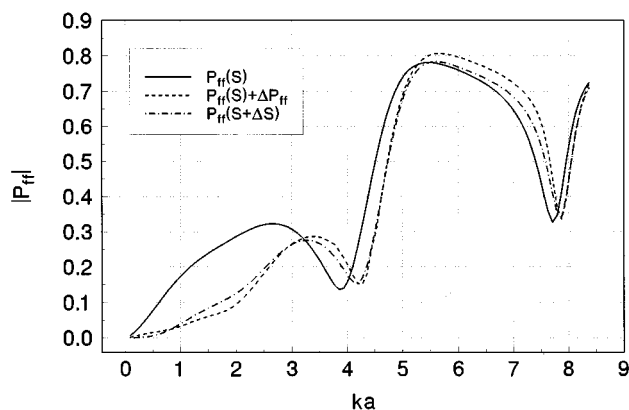


FIG. 3. Changes in far-field back scattered pressure due to thickness perturbation.

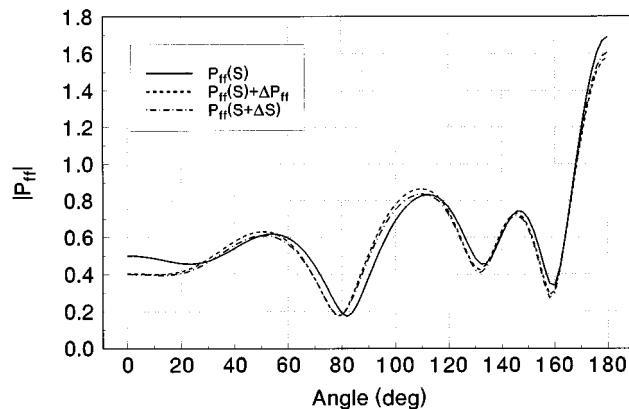


FIG. 4. Changes in far-field scattered pressure due to thickness perturbation as a function of angle at $ka=8$.

seen that the first-order perturbation estimate is quite accurate over the entire frequency range and correctly predicts the direction of back scattered null and peak movement. Note that the back scattered pressure is most sensitive to thickness changes at low frequencies and that low-frequency back scatter decreases as the cylinder surface looks less like a pressure release surface.

For a frequency of 1910 Hz ($ka=8$) Fig. 4 shows the magnitude of scattered pressure as a function of azimuthal angle; an angle of 0° is back scatter whereas an angle of 180° is forward scatter. Again, the first-order perturbation estimation is in close agreement with a complete reanalysis. Also for $ka=8$, Figs. 5 and 6 show the surface pressures and surface normal velocity, respectively. The surface pressure is normalized by the magnitude of the incident pressure wave, p_0 , and the surface normal velocity is normalized by the velocity of the incident pressure wave, $p_0/\rho c$. One would expect that the surface quantities would be much more sensitive to structural perturbation than scattered pressures, and this is indeed the case. Both the surface pressure and normal velocity change significantly when the thickness of the shell is increased, but the perturbation analysis still does a good job of predicting these changes. Note that some of the finer structure of the perturbed surface quantities, particularly the surface normal velocity, is not captured by the perturbation

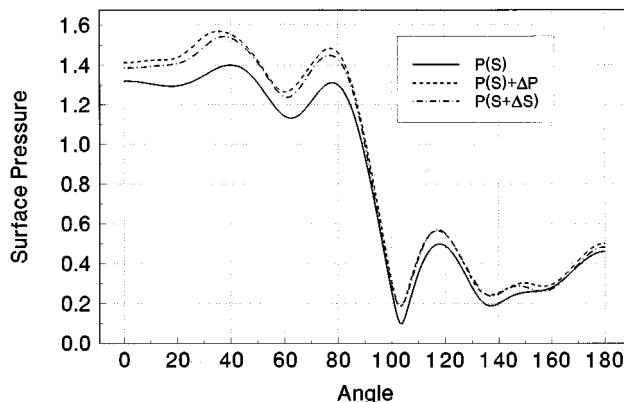


FIG. 5. Changes in surface pressure due to thickness perturbation.

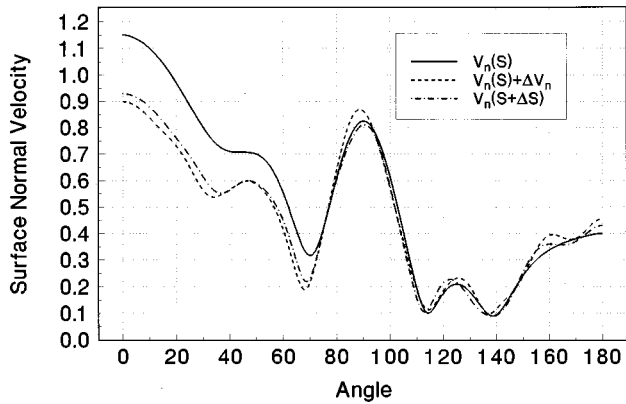


FIG. 6. Changes in surface normal velocity due to thickness perturbation.

estimate, but the overall changes are well predicted. This is particularly encouraging since the size of the structural perturbation is relatively large.

As a second example, the same nominal cylinder of Fig. 2 is again perturbed, with the perturbation corresponding to a 5% increase in the magnitude of the Young's modulus (both the real and imaginary parts are increased so that the proportional damping factor remains the same). Figure 7 shows the far-field back scattered pressure for the nominal and perturbed models as a function of ka . As in the previous example, the first-order perturbation analysis agrees very well with the complete reanalysis. The only areas of poor agreement are the frequencies in the vicinity of the sharp dips in the backscattered pressure. These dips occur at frequencies where the longitudinal wavelength in the cylinder is an integer multiple of the circumference of the cylinder. Since changing the Young's modulus changes the longitudinal sound speed, it is not surprising that the back scattered pressure exhibits high sensitivity to changes in the Young's modulus near the dips. The original perturbation of shell thickness, however, did not alter the longitudinal sound speed in the cylinder, and high sensitivity was not seen. This illustrates how a sensitivity analysis can aid in identifying underlying physical processes in complicated scattering problems.

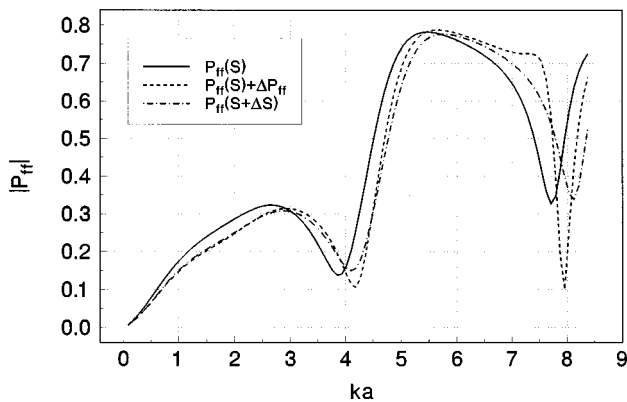


FIG. 7. Changes in far-field back scattered pressure due to Young's modulus perturbation.

IV. CONCLUDING REMARKS

A perturbation technique has been developed for the analysis of structural-acoustic systems. The technique assumes that the structure has been modeled by a finite element method and that the fluid has been modeled by a boundary element method. The method gives a closed-form expression for the derivative of various acoustic quantities with respect to arbitrary structural perturbations. Two examples of structural perturbations to a cylindrical shell are presented to demonstrate the technique. In particular, it is shown that first-order perturbation theory can be used to estimate changes in both far-field and near-field scattered pressure as well as surface pressures and normal velocities in the low-frequency range. It is important to note that the sensitivity information described above may be obtained with very little computational effort. All of the matrices and matrix inversions used in the formulation are generally available from the analysis of the nominal model. These matrices can be saved for later calculation of sensitivity data. In the examples above, calculations of the sensitivities took only a small fraction of the time required for the original analysis.

- ¹S. Amini, P. J. Harris, and D. T. Wilton, *Coupled boundary and finite element methods for the Solution of the Dynamic Fluid-Structure Interaction Problem*, Lecture Notes in Engineering (Springer-Verlag, New York, 1992).
- ²T. Kato, *Perturbation Theory for Linear Operators* (Springer-Verlag, New York, 1966).
- ³H. Baumgarte, *Analytic Perturbation Theory for Matrices and Operators* (Birkhauser-Verlag, Boston, 1985).
- ⁴S. Saigal, "Reanalysis for structural modifications in boundary-element response and design sensitivity analysis," *AIAA J.* **28**, 323-328 (1990).
- ⁵R. L. Fox and M. P. Kapoor, "Rates of change of eigenvalues and eigenvectors," *AIAA J.* **6**, 2426-2429 (1968).
- ⁶J. D. Collins and W. T. Thomson, "The eigenvalue problem for structural systems with statistical properties," *AIAA J.* **7**, 642-648 (1969).
- ⁷R. A. Ibrahim, "Structural dynamics with parameter uncertainties," *Appl. Mech. Rev.* **40**, 309-328 (1987).
- ⁸G. Ryland, II and L. Meirovitch, "Response of vibrating systems with perturbed parameters," *AIAA J. Guid. Control Dynam.* **3**, 298-303 (1980).
- ⁹A. Sinha, "Calculating the statistics of forced response of a mistuned bladed disk assembly," *AIAA J.* **24**, 1797-1801 (1986).
- ¹⁰S.-T. Wei and C. Pierre, "Statistical analysis of the forced response of mistuned cyclic assemblies," *AIAA J.* **28**, 861-868 (1990).
- ¹¹M. P. Mignolet and C.-C. Lin, "The combined closed form-perturbation approach to the analysis of mistuned bladed disks," *ASME J. Turbomachine.* **115**, 771-780 (1993).
- ¹²B. E. Sandman, "Fluid-loaded vibration of an elastic plate carrying a concentrated mass," *J. Acoust. Soc. Am.* **61**, 1503-1510 (1977).
- ¹³D. Feit, "The scattering of sound by a non-homogeneous plate," presented at the 1990 ASME Winter Annual Meeting, Dallas, Texas, 25-30 Nov., ASME Paper #90-WA/NCA-11.
- ¹⁴J. H. Ginsberg, K. A. Cunefare, and H. Pham, "Spectral description of inertial effects in fluid-loaded plates," *ASME J. Vib. Acoust.* **117**, 206-212 (1995).
- ¹⁵B. R. Mace, "Sound radiation from a plate reinforced by two sets of parallel stiffeners," *J. Sound Vib.* **71**, 435-441 (1980).
- ¹⁶J. H. Ginsberg and J. G. McDaniel, "An acoustic variational principle and component mode synthesis applied to the analysis of acoustic radiation from a concentrically stiffened plate," *ASME J. Vib. Acoust. Stress Reliab. Design* **113**, 401-408;1991).
- ¹⁷J. D. Achenbach, J. Bjarnason, and T. Igusa, "Effect of a vibrating substructure on acoustic radiation from a cylindrical shell," *ASME J. Vib. Acoust.* **114**, 312-318 (1992).
- ¹⁸E. Rebillard, B. Laulagnet, and J. L. Guyader, "Influence of an embarked spring-mass system and defects on the acoustic radiation of a cylindrical shell," *Appl. Acoust.* **36**, 87-106 (1992).

- ¹⁹Z.-D. Ma and I. Hagiwara, "Sensitivity analysis methods for coupled acoustic-structural systems. Part I: Modal sensitivities and Part II: Direct frequency response and its sensitivities," *AIAA J.* **29**, 1787–1801 (1991).
- ²⁰R. L. St. Pierre, Jr. and G. H. Koopmann, "Minimization of radiated sound power from plates using distributed point masses," presented at the 1993 ASME Winter Annual Meeting, New Orleans, LA, 28 Nov.–3 Dec., ASME Paper # 93-WA/NCA-11.
- ²¹N. Vlahopoulos, "Boundary element formulations for acoustic sensitivities with respect to structural design variables and acoustic impedance," Second International Conference on Recent Developments in Air- and Structure-Borne Sound and Vibration, Auburn University, USA, 4–6 March 1992, pp. 1019–1026.
- ²²P. J. T. Filippi, O. Lagarrigue, and P.-O. Mattei, "Perturbation method for sound radiation by a vibrating plate in a light fluid: Comparison with the exact solution," *J. Sound Vib.* **177**, 259–275 (1994).
- ²³W. S. Levine and M. Athans, "On the determination of the optimal constant output feedback gains for linear multivariable systems," *IEEE Trans. Automat. Control* **AC-15**, 44–48 (1970).
- ²⁴A. D. Pierce, *Acoustics: An Introduction to Its Physical Principles and Applications* (Acoustical Society of America, New York, 1989), p. 110.

The application of analytical/numerical matching to structural discontinuities in structural/acoustic problems

Rickard C. Loftman and Donald B. Bliss

Department of Mechanical Engineering, Duke University, Durham, North Carolina 27708-0300

(Received 11 March 1996; accepted for publication 9 September 1996)

Analytical/numerical matching (ANM) is introduced to more efficiently model structural discontinuities in structural/acoustic problems. The general method is explained in detail for the simple example problem of normal incidence acoustic scattering from a periodically line-supported elastic membrane. A modal series solution exists for this problem. The most slowly convergent part of this solution, the dominant high-resolution (large wave number) content, is removed from the series representation and summed in closed form in what is called the ANM local solution. This local solution is represented by a piecewise polynomial that is zero outside of a small region. The remaining part of the solution, containing the overall low resolution content, is called the ANM global solution and converges very rapidly. In the present example, the series representing the global solution falls by three powers of the index faster than the classical modal solution. The result is an ANM composite (local plus global) solution that requires far less computational effort to resolve. In addition to providing a clear abstraction of the method, the example problem allows the equivalence of the ANM solution to be verified, and indicates the importance of resolving the fine scale effects of discontinuities in constrained scattering problems. © 1997 Acoustical Society of America. [S0001-4966(97)00202-6]

PACS numbers: 43.40.Rj, 43.20.Tb [CBB]

INTRODUCTION

Analytical/numerical matching (ANM) is a general analysis method that separates a problem into a global numerical solution and a local analytical solution. The method achieves high accuracy using low resolution numerics. ANM achieves greater convergence rates than conventional methods by treating the most rapidly varying parts of a system analytically, and separately, from the overall computational evaluation of the system.

A simple problem with relevant physical behavior was chosen to illustrate ANM for structural acoustics, that of scattering of a normally incident plane acoustic wave from a periodically line-supported elastic membrane. This is a basic problem of fundamental interest in structural acoustics. It is investigated in the text by Morse and Ingard for the more general case involving obliquely incident waves¹ using a Green's function formulation, and also by other authors such as Leppington,² who uses a transform method which is approximately inverted for large and small fluid loading. In the case of normal incidence, the solution is periodic and reduces to an infinite modal series. The present work is concerned with the details of the constraint condition, which applies a line force to the membrane. The physics of the line-driven fluid-loaded membrane has been extensively treated by Crighton.^{3,4} Other configurations of the fluid-loaded membrane problem have also been studied by other authors.⁵⁻⁷

The intent of this paper is not primarily to investigate the physics of the particular problem geometry, but rather, to use this simple case to clearly present a method for more efficiently modeling structural discontinuities in scattering problems. In regard to the way in which computational advantage is attained, the present work is similar to the mode

acceleration method.^{8,9} Both methods improve computational efficiency by capturing most of the high wave number content of a total solution in a separate constituent solution. In the mode acceleration method, the high resolution content is contained in the solution of the equivalent pseudo-static problem. In the present work, the high resolution content is contained in a separate analytic solution of local extent, which is associated directly with a discontinuity. This local solution has the advantages of being derived independently of overall problem geometry and being very efficiently expressed.

Analytical/numerical matching is a general analysis method originally developed by Bliss. The method was first applied to problems in vortex dynamics and rotorcraft free wake analysis.¹⁰⁻¹⁴ More recently, ANM has been applied to wing aerodynamics for compressible unsteady flow,^{15,16} and to the development of an acoustic boundary element method.¹⁷ The present work is part of a broad research effort to apply ANM to structural acoustic problems with structural discontinuities.^{18,19} The ANM approach leads to an accurate alternative formulation of the basic problem, with a large reduction in computational cost. In addition, the alternative formulation can lead to an improved understanding of the effect of discontinuities.

The ANM methodology allows for more efficient treatment of structural discontinuities in the solution of coupled structural/acoustic vibration problems. The motivation for applying ANM to structural acoustics begins with the realization that there is a small region, characterized by rapid spatial variation, around any discrete load applied to an elastic structure. In fact, certain properties of the response of an elastic structure are discontinuous at the point of application of a discrete load. This rapidly varying region requires very

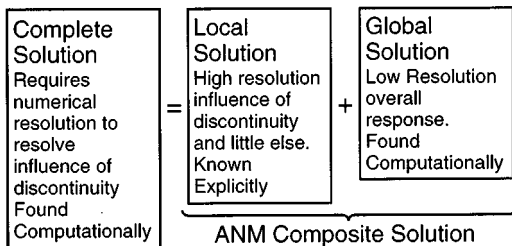


FIG. 1. Summary of ANM constituents.

high resolution to capture its features accurately, and therefore challenges the accuracy of any numerical technique used to solve the problem. Resolving the small region about a discontinuity requires far greater resolution, and therefore computational effort, than is otherwise warranted by the overall system under consideration. Compounding this issue is that in many situations, especially in the event of a discontinuous constraint on motion, failure to properly resolve the small region about the discontinuity can cause significant errors throughout the system. This paper will show that structural/acoustic scattering is an important example of a problem in which a failure to converge locally can lead to global errors. Structural acoustic scattering is therefore an example of a problem in which overall accuracy can be significantly hindered by a very local phenomenon.

ANM alleviates much of the difficulty of resolving the influence of a discontinuity on a structure by treating the rapidly varying region separately, in what is called the local solution. The local solution is solved analytically, before determining the overall system response, and is known without approximation. Once the local solution is found, the overall system response is computed using conventional methods, except that the discrete load is replaced by a special smooth distributed load. Isolating the rapidly varying part of the problem within the local solution allows the remaining overall response to be solved with less computational effort. The smoothed overall solution is called the global solution, and is usually found by numerical means. The overall assembly of the ANM composite solution is summarized in Fig. 1.

The important feature required to separate local and global parts of a problem having discrete constraints is the disparity in the length scales that characterize the discontinuity and the overall response. The characteristic scales of the overall response, which must be resolved computationally, are associated with the structural and acoustic wavelengths and the overall geometry of the system. In contrast, the length scale characterizing the structural discontinuity (for instance, a point of attachment) is very small, or even infinitesimal. The approach taken by ANM is to introduce an intermediate smoothing length scale used to generate the local solution and capture the most rapidly varying effects of the discontinuity analytically. The same smoothing scale also appears as the smallest scale in the global solution. When the composite solution is constructed, the smoothing effects cancel out, and the final result is independent of the choice of smoothing.

This paper demonstrates the application of ANM to the structural acoustic problem of scattering from a fluid-loaded

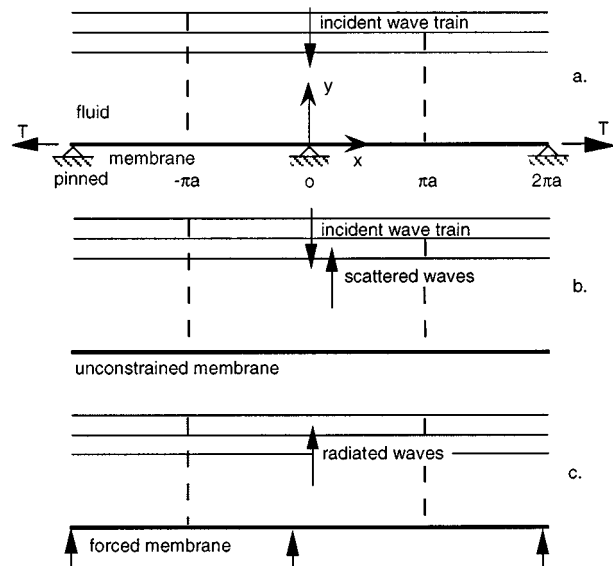


FIG. 2. (a) Example problem geometry, scattering from constrained membrane. (b) Unconstrained scattering problem. (c) Driven problem.

membrane fixed along periodic parallel lines. Since the purpose is to illustrate the method, this example problem is intentionally chosen to be simple, and easily solvable by classical modal means. However, it turns out that this problem also illustrates the sensitivity of scattering problems to accurate resolution at points of discontinuity. Understanding this sensitivity is a valuable insight, and it is particularly important in the present context because ANM is a very effective way to address this difficulty.

In the following sections, the problem geometry and mathematical formulation are first presented, and the problem is solved classically by modal expansion. Next, the problem is formulated using the ANM methodology. Finally, the ANM and classical exact solutions are compared in terms of their accuracy and computational efficiency. The sensitivity of scattering problems to solution convergence is discussed and illustrated at several points throughout the paper.

I. MATHEMATICAL FORMULATION

The problem under consideration is the acoustic scattering from a periodically constrained fluid-loaded elastic membrane. The problem geometry is illustrated in Fig. 2(a). The membrane lies in the xy plane, has area density σ_m , and tension T . The normal displacement of the membrane is given by $\eta(x, y, t)$. The membrane is rigidly fixed along periodic lines parallel to the y axis, $\eta(x = m2\pi a, y, t) = 0$, where m is the integers. The membrane is bounded above ($z > 0$) by a half-space of acoustic medium with density ρ_f and acoustic phase speed c_f . A light fluid of negligible effect is assumed to bound the other side of the membrane ($z < 0$). A normally incident, acoustic plane wave train originating at $z = -\infty$ drives the membrane harmonically with magnitude P and frequency ω , $p_{\text{incident}} = P e^{i\omega(t + y/c_f)}$. Transients are assumed to have decayed, and a time dependence of $e^{i\omega t}$ can be assumed for all quantities. No variation is exhibited in the y direction, reducing it mathematically to a problem in two

dimensions, x and z . Furthermore, this problem is periodic in x on the interval of $2\pi a$, and symmetric about all $x = m\pi a$.

A force balance on the membrane yields the following governing equation:

$$\sigma_m \frac{\partial^2 \eta}{\partial t^2} = T \nabla^2 \eta + p_a - p_f. \quad (1)$$

The pressure applied to the membrane is broken into two parts. The fluid pressure on the surface of the membrane, $p_f(x, y, t)$, represents the hydrodynamic and radiation loading. Other external loading, including the influence of the constraint line discontinuities, is represented by $p_a(x, y, t)$.

Since there is no dependence on the y coordinate, the equation of motion governing the membrane reduces to a one-dimensional wave equation. Assuming harmonic time dependence allows the differentiation in time to be performed, and the time dependence to be dropped. Using a as the characteristic length scale, the dimensionless form of the membrane equation is given by

$$-\frac{\partial^2 \bar{\eta}}{\partial \bar{x}^2} - K_m^2 \bar{\eta} = \bar{p}_a - \bar{p}_f, \quad (2)$$

where $\bar{\eta}(x) = \eta(x, t)/ae^{i\omega t}$, $\bar{p}(x) = ap(x, t)/\sigma_m c_m^2 e^{i\omega t}$, $K_m = k_m a = (\omega/c_m)a$, and c_m is the *in vacuo* wave speed on the membrane, given by $c_m = \sqrt{T/\sigma_m}$.

In the acoustic medium, the governing equation of motion is the familiar acoustic wave equation, which reduces to Helmholtz's equation in space with the assumption of harmonic time dependence, as follows:

$$(\nabla^2 + k_f^2) \bar{p}_f = 0, \quad (3)$$

where $k_f^2 = \omega^2/c_f^2$ is the acoustic wave number and c_f is the acoustic wave speed.

The acoustic momentum equation relates the fluid pressure distribution to its velocity field, \mathbf{V}_f .

$$\rho_f \frac{\partial \mathbf{V}_f}{\partial t} = -\nabla p_f. \quad (4)$$

This relationship provides the means to apply the boundary condition of continuous normal velocity at the fluid/membrane interface.

A. Solution of the scattering problem

The response of the membrane can be separated into two parts: the response of the unconstrained membrane, Fig. 2(b), and the response due to the force influence of the discontinuity, Fig. 2(c). The free response of the membrane is a simple one-dimensional problem with the following solution:

$$\bar{\eta}_{\text{freeresponse}} = \frac{2Pa}{T} \frac{-1}{\alpha i K_f - K_m^2}, \quad (5)$$

where $\alpha = a\rho_f c_f^2/\sigma_m c_m^2$ is the fluid-loading parameter, and $K_f = k_f a = (\omega/c_f)a$.

Reasoning that a line discontinuity can only influence the membrane by applying a line force to it, the part of the response due to the periodic line discontinuities must be satisfied by a periodically line-driven membrane solution. Therefore, the response is found for a membrane driven at

the discontinuities with unit strength. This solution is then scaled so that the response at the discontinuities is equal and opposite that of the unconstrained problem. The unconstrained problem and the forced problem are superimposed to yield the net constrained membrane subject to the incident plane wave train, given by

$$\bar{\eta} = \bar{\eta}_{\text{freeresponse}} \left[1 - \frac{\bar{\eta}_{\text{driven}}}{\bar{\eta}_{\text{driven}}|_{\bar{x}=0}} \right]. \quad (6)$$

It is important to note that because the constraint condition is written in terms of the net response at the discontinuity, namely $\bar{\eta}_{\text{driven}}|_{\bar{x}=0}$; the amplitude of the forced solution used to model the constraint is inversely proportional to the response value of this solution at the driving points. Therefore, the entire forced solution will be corrupted by any numerical error that is associated with calculating the forced response right at the driving points. This sensitivity is significant because the response at the location of the discrete load is considerably more difficult to resolve (converge) than the overall system response. Therefore, in the constrained scattering problem, the error of the overall solution can be dominated by the accuracy with which the rapidly varying region about the discrete force is resolved. In particular, when the forced system exhibits near-resonant behavior, the response at the drive points will be much smaller than the overall response. In this situation, the overall scattering response will be dominated by the discretely forced part of the solution, and any error in this small denominator will have a profound effect on the accuracy of the entire problem. It is this sensitive, rapidly varying region about the driving points that ANM is designed to treat more accurately and efficiently.

B. Solution of the driven problem

An exact solution for the membrane driven by spatially periodic forcing exists in the form of an infinite modal expansion. Assume the following expansion for the membrane displacement:

$$\bar{\eta}_{\text{driven}} = \sum_{n=0}^{\infty} A_n \bar{\eta} \cos(n\bar{x}). \quad (7)$$

The trigonometric dependence of this series in \bar{x} creates an orthogonal set of basis functions that take advantage of the natural symmetry and periodicity of the problem.

Once the form of the membrane response has been assumed, the fluid solution resulting from membrane motion can be determined. The technique of separation of variables is used to determine the form of the fluid solution. The resulting solution is restricted on physical grounds to allow only outward propagating waves and only finite values as z becomes large. The z component of the momentum equation and the property of orthogonality are then used to apply the boundary condition of equal normal velocities at the membrane, which determines the fluid solution. The fluid pressure, in terms of the assumed membrane response, is given by

$$\bar{p}_f(\bar{x}, \bar{z}) = \sum_{n=0}^{\infty} -i\alpha A_n \bar{\eta} \frac{K_f^2}{K_{y_n}} \cos(n\bar{x}) e^{i(K_{y_n}\bar{z})}, \quad (8)$$

where

$$K_{y_n} = \begin{cases} -\sqrt{K_f^2 - n^2}, & K_f > n \\ \sqrt{K_f^2 - n^2}, & K_f < n. \end{cases} \quad (9)$$

Substituting the expressions for membrane displacement [Eq. (7)] and fluid loading [Eq. (8)] into the membrane governing equation [Eq. (2)], and utilizing orthogonality, the coefficients of membrane displacement for the driven membrane are given by the following relations:

$$A_n \bar{\eta} = \frac{A_n \bar{p}_a}{n^2 - K_m^2 - i\alpha K_f^2 / K_{y_n}}, \quad (10)$$

where

$$A_n \bar{p}_a = \frac{\epsilon_n}{2\pi} \int_{-\pi}^{\pi} \bar{p}_a \cos(n\bar{x}) d\bar{x}, \quad (11)$$

and ϵ_n is the Neumann factor, defined as 1 if $n=0$ and 2 otherwise.

The periodic discrete driving forces are modeled with the use of the Dirac delta function in x ; the coefficients of driving pressure [Eq. (11)] for this configuration are found to be

$$A_n \bar{p}_a = \frac{F}{\sigma_m c_m^2} \frac{\epsilon_n}{2\pi}. \quad (12)$$

II. ANM FORMULATION OF DRIVEN PROBLEM

In order to more efficiently model the rapidly varying regions around the driving point discontinuities, ANM will attack the discretely driven portion of the solution. The discretely driven problem can be separated into two parts. The overall response, called the global solution, will be modeled by classical methods except that the driving force will be spatially smoothed and, therefore, will converge more efficiently. Meanwhile, the exact difference between the original discretely driven problem and the smoothed problem will be represented by the local solution, as follows.

A. The local solution

Construction of the local solution is the most crucial step in synthesizing the ANM composite solution. It is also, perhaps surprisingly, the first step. This may seem counterintuitive, since the local solution is defined as the difference between the system response when driven by the original discrete loads and the response when driven by the smoothed pressure distribution. But indeed, the local solution is not just this difference, it is also the tool that generates the smoothed driving distribution.

In order to smooth the discrete load in the proper manner, the mechanical system will, in effect, be solved backwards. The local solution is prescribed so that it represents the local high-resolution effect of the discrete load, and little else. Once the local displacement is known, the loading that is required to enforce it is found by simple substitution into

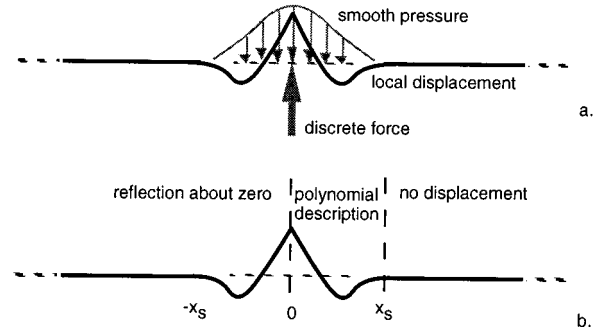


FIG. 3. (a) Local solution and applied loads. (b) Local solution description regions.

the governing equation. By the definition of the local solution, this loading is the discrete load minus the smoothed load. Since the discrete load is known, so now is the smoothed load. A schematic of this approach is included in Fig. 3(a).

Central to the ANM method for structural acoustics is the ability to identify and isolate the particular effect of a discontinuous loading on the mechanical system at its point of application. For instance, in this example problem, a line force is applied to a membrane. It is shown from the governing equation that this implies a discontinuous slope in membrane displacement, as follows. Integrating the governing equation in \bar{x} from $-\epsilon$ to ϵ yields

$$\int_{-\epsilon}^{\epsilon} -K_m^2 \bar{\eta} d\bar{x} = \left[\frac{\partial \bar{\eta}}{\partial \bar{x}} \right]_{-\epsilon}^{\epsilon} + \int_{-\epsilon}^{\epsilon} \frac{a}{\sigma_m c_m^2} \times \{F \delta(0) - p_{\text{fluid}}\} d\bar{x}. \quad (13)$$

Assuming $\bar{\eta}$ is finite and continuous, dimensionless frequency, K_m , is finite, and taking the limit as $\epsilon \rightarrow 0$ yields

$$-\left[\frac{\partial \bar{\eta}}{\partial \bar{x}} \right]_{0^-}^{0^+} = \frac{F}{\sigma_m c_m^2}. \quad (14)$$

Knowing the precise manifestation of the discrete load on the mechanical system allows it to be treated as a boundary condition when generating the local solution.

With the discrete load accounted for, there remain three goals for generating the local solution. First, the local solution must be known without numerical approximation. Second, the local solution must be prudent in the most basic sense. When prescribing a local solution, it is possible to erroneously try to enforce a solution that is not physically realizable, or inadvertently incorporates unintentional discrete loads. Third, foresight of the ultimate goal must be maintained. Using the governing equation, the local solution will be prescribed so that the smooth driving distribution it implies will be continuous and well behaved. This condition will enhance the convergence characteristics of the global solution to come. Also, the range of influence of the local solution through the fluid medium must be limited, for instance, by requiring it to be acoustically compact. This condition assures that the smooth driving pressure implied by the local solution will be localized.

1. Assuming a form

The local solution is generated by assuming a polynomial form to one side of a discontinuity within a prescribed smoothing region. The local solution is defined to be zero outside this smoothing region. The local solution is then completed within the smoothing region by the appropriate even or odd reflection about zero. The regions of the assumed local solution description are illustrated in Fig. 3(b). The extent of the smoothing region is somewhat arbitrary and is chosen based on convergence considerations, as will be discussed in Sec. II C. In the case of the present example, the local solution is even about zero. Of course, it is also periodically reproduced for each discontinuity. For simplicity, consider only the ANM treatment of the discrete force at the origin.

It is convenient to normalize \bar{x} by the smoothing half-width, \bar{x}_s , when describing the local solution, $\bar{x} = \bar{x}/\bar{x}_s$. This will simplify the solution of the polynomial coefficients. The piecewise polynomial description of local displacement is written as follows:

$$\bar{\eta}_l = \begin{cases} \sum_{q=0}^Q a_q |\bar{x}|^q, & |\bar{x}| \leq 1 \\ 0, & 1 < |\bar{x}|. \end{cases} \quad (15)$$

In order to satisfy the continuity conditions that will follow, note that the value and derivatives of this assumed form can only be discontinuous at the boundaries of the piecewise regions, that is $\bar{x} = 0, \pm 1$. At these boundaries, the desired conditions will be applied in order to generate a useful local solution. The order of the polynomial, Q , is set as a result of the number of constraints imposed on the local solution, as will be seen in the following sections. Note during the following that there is some discretion involved in choosing these constraints and, therefore, the choice of local solution is not entirely unique.

2. Constraints on the local solution

It has been shown that a discrete line force is balanced in the membrane by a discontinuous jump in slope. Therefore, the line force is included in the local solution by requiring such a jump in slope. Referring to Eq. (14), and recalling that the local solution is even, the discrete force is included by satisfying the following slope condition as \bar{x} approaches zero from the positive side:

$$\left. \frac{\partial \bar{\eta}_l}{\partial \bar{x}} \right|_{\bar{x}=0^+} = \frac{1}{\bar{x}_s} \left. \frac{\partial \bar{\eta}_l}{\partial \bar{x}} \right|_{\bar{x}=0^+} = \frac{a_1}{\bar{x}_s} = -\frac{1}{2} \frac{F}{\sigma_m c_m^2}. \quad (16)$$

Just as important as ensuring that the discrete force at zero is included in the local solution, no discrete force is allowed at the outer edge of the smoothing region, $\bar{x} = 1$. Therefore, recalling the local solution is zero outside the smoothing region, the following condition must be met:

$$\left. \frac{\partial \bar{\eta}_l}{\partial \bar{x}} \right|_{\bar{x}=\bar{x}_s} = \frac{1}{\bar{x}_s} \sum_{q=1}^Q q a_q = 0. \quad (17)$$

The local solution must, of course, be continuous in value. This condition is automatically satisfied at zero be-

cause the solution is even, but must be imposed at $\bar{x} = 1$:

$$\bar{\eta}_l \Big|_{\bar{x}=\bar{x}_s} = \sum_{q=0}^Q a_q = 0. \quad (18)$$

The next constraint is that the total area under the local solution be zero. The condition of no net area ensures that there will be no net monopole strength in the fluid due to the local solution. Radiated pressure from the local solution will be small when the smoothing region is chosen to be acoustically compact, approaching that of a baffled quadrupole. This property ensures that the fluid motion accompanying the local displacement of the membrane is also quite local. This local behavior will prove beneficial in implementing the smoothed driving pressure in the global solution, which will be partly due to the radiated pressure from the local solution:

$$\int_0^{\bar{x}_s} \bar{\eta}_l d\bar{x} = \bar{x}_s \sum_{q=0}^Q \frac{a_q}{q+1} = 0. \quad (19)$$

Higher moments of area may be required to vanish, further weakening the radiation from this local region; however, current experience indicates that this refinement is not necessary.

Note that due to the infinite periodicity of this problem geometry, there is a particular issue regarding infinite fluid pressures in the event that the local solution has nonzero harmonic content in a mode that corresponds to a fluid mode at coincidence ($K_f = n$). This situation requires careful consideration of the mathematical limits, or a more complex local solution to avoid the problem. However, because this is an example problem that was introduced in order to demonstrate the ANM method for structural acoustics in a simplified manner, and because the geometries which are the ultimate goal of this method will not display this particular problem, this issue of coincidence is not considered here in depth.

The previous constraints are sufficient to create a local solution that allows the discretely driven membrane problem to be replaced by one driven by a pressure distribution over the smoothing region. But, looking ahead to the solution of the problem driven by this pressure distribution, it is also possible to impose constraints on the local solution that will ensure that this pressure distribution be continuous and smooth, which will further enhance the convergence of the associated global solution. Omitting the influence of the fluid for the moment, since it will certainly be continuous and smooth already, the governing equation for the membrane is given by

$$-K_m^2 \bar{\eta} = \frac{\partial^2 \bar{\eta}}{\partial \bar{x}^2} + \frac{P_a a}{\sigma_m c_m^2}. \quad (20)$$

A continuous applied pressure is guaranteed at zero due to symmetry. But, at $\bar{x} = 1$ the second derivative of displacement in \bar{x} must be set to zero in order to ensure that the applied pressure is also zero and thus continuous (the displacement is already zero):

$$\left. \frac{\partial^2 \bar{\eta}_l}{\partial \bar{x}^2} \right|_{\bar{x}=\bar{x}_s} = \frac{1}{\bar{x}_s^2} \sum_{q=2}^Q q(q-1)a_q = 0. \quad (21)$$

Further refinement is possible by requiring that the slope of the applied pressure is also continuous. Taking the derivative of the membrane governing equation with respect to \bar{x} yields

$$-K_m^2 \frac{\partial \bar{\eta}}{\partial \bar{x}} = \frac{\partial^3 \bar{\eta}}{\partial \bar{x}^3} + \frac{a}{\sigma_m c_m^2} \frac{\partial p_a}{\partial \bar{x}}. \quad (22)$$

Since the slope of displacement is already zero at $\bar{x}=1$, the third derivative of displacement in \bar{x} needs to be set to zero in order to ensure continuity of slope of the applied pressure:

$$\left. \frac{\partial^3 \bar{\eta}_l}{\partial \bar{x}^3} \right|_{\bar{x}=\bar{x}_s} = \frac{1}{\bar{x}_s^3} \sum_{q=3}^Q q(q-1)(q-2)a_q = 0. \quad (23)$$

At $\bar{x}=0$, the slope of displacement is not zero. The sum of terms must equal zero to ensure a continuous slope in applied pressure:

$$\left[K_m^2 \frac{\partial \bar{\eta}}{\partial \bar{x}} + \frac{\partial^3 \bar{\eta}}{\partial \bar{x}^3} \right]_{\bar{x}=0} = K_m^2 \frac{a_1}{\bar{x}_s} + \frac{6a_3}{\bar{x}_s^3} = 0. \quad (24)$$

It is seen from the development of the constraint conditions that the choice of local solution is not unique. In the present example, the only constraints that are necessary to create a physically reasonable local solution that will effectively replace the discrete force by a distributed pressure are given by Eqs. (16)–(18). That is, the discrete force at the origin and no others must be included, and the local displacement must be continuous. The other conditions, however, such as requiring a slope continuous implied pressure, enhance the effectiveness of the method by creating a global solution that is more rapidly convergent. The system under consideration dictates the minimum requirements of the local solution. In the present example, for instance, it is clear that the local displacement needs to be continuous, while in the case of a plate, slope of displacement must also be continuous in order to avoid a fatal singularity. It is a practical consideration of diminishing returns, however, that dictates how many steps should be taken to further refine the solution. It is possible to require higher derivatives to be continuous, but only at the expense of an increasingly complex formulation. The present choice of conditions is simply the result of judgment based on experience.

3. Solving for the local solution

The complete set of constraints on the local solution is now known. A sixth-order polynomial, $Q=6$, having seven unknown coefficients, is required for the displacement in the upper half of the smoothing region to satisfy this set of constraints. It is now only a matter of linear algebra to determine the coefficients and, therefore, the local displacement. The constraint equations in matrix form are as follows:

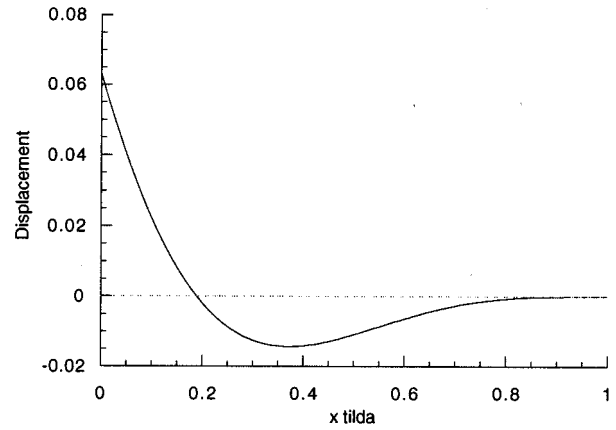


FIG. 4. Local displacement.

$$\begin{bmatrix} 0 & 1/\bar{x}_s & 0 & 0 & 0 & 0 & 0 \\ 0 & 1 & 2 & 3 & 4 & 5 & 6 \\ 1 & 1 & 1 & 1 & 1 & 1 & 1 \\ 1 & 1/2 & 1/3 & 1/4 & 1/5 & 1/6 & 1/7 \\ 0 & 0 & 2 & 6 & 12 & 20 & 30 \\ 0 & 0 & 0 & 6 & 24 & 60 & 120 \\ 0 & K_m^2 & 0 & 6/\bar{x}_s^2 & 0 & 0 & 0 \end{bmatrix} \begin{Bmatrix} a_0 \\ a_1 \\ a_2 \\ a_3 \\ a_4 \\ a_5 \\ a_6 \end{Bmatrix} = -\frac{1}{2} \frac{F}{\sigma_m c_m^2} \begin{Bmatrix} 1 \\ 0 \\ 0 \\ 0 \\ 0 \\ 0 \\ 0 \end{Bmatrix}. \quad (25)$$

The solution of this system is given by

$$\{a_q\} = \frac{\bar{x}_s}{2} \frac{F}{\sigma_m c_m^2} \begin{Bmatrix} (120 + K_m^2 \bar{x}_s^2)/960 \\ -1 \\ 3(40 - K_m^2 \bar{x}_s^2)/64 \\ K_m^2 \bar{x}_s^2/6 \\ -5(40 + 3K_m^2 \bar{x}_s^2)/64 \\ 3(20 + K_m^2 \bar{x}_s^2)/20 \\ -7(24 + K_m^2 \bar{x}_s^2)/193 \end{Bmatrix}. \quad (26)$$

A plot of this shape, for characteristic parameters, is shown in Fig. 4.

B. The global solution

As already noted, the global solution is defined as the system response when driven by the smoothed forcing implied by the local solution. Upon solving for the local solution, determining the associated forces is a matter of substitution into Eq. (2) which governs the membrane. These forces are, by definition, the original point force minus the smoothed driving force that will replace it, plus the fluid forces generated by the local solution, so:

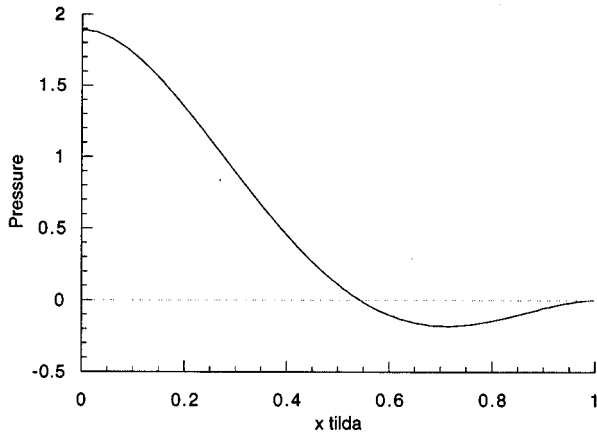


FIG. 5. Smooth pressure due to structural terms.

$$\frac{ap_{a \text{ smooth}}}{\sigma_m c_m^2} = K_m^2 \bar{\eta}_l + \frac{\partial^2 \bar{\eta}_l}{\partial \bar{x}^2} + \frac{a(p_{a \text{ discrete force}} - p_f \text{ due to } \bar{\eta}_l)}{\sigma_m c_m^2}. \quad (27)$$

The addition of the discrete load is simple in practice. Recall that the structural terms of the local solution have been defined so that they exactly counteract the discrete force at zero, namely,

$$\left[\frac{\partial^2 \bar{\eta}_l}{\partial \bar{x}^2} + \frac{ap_{a \text{ discrete force}}}{\sigma_m c_m^2} \right]_{\bar{x}=0} = 0. \quad (28)$$

Substituting the polynomial representation of the local solution into the governing equation, and realizing that the discrete force cancels the resulting infinite value at zero, gives the smooth pressure. Because the local solution region is small, and a poor radiator by design, the structural part of the smooth pressure is the dominant influence. In addition, because the velocity itself is always finite and continuous, the contribution of the fluid loading will always be quite smooth. A plot of the shape of the smooth applied pressure due to the structural terms is shown in Fig. 5 for characteristic values.

The fluid terms in the applied smooth pressure are computed in a manner consistent with the solution technique used to solve the global problem. In the present case, the fluid terms can be solved exactly by modal decomposition of the local solution. Although tedious, the integration may be carried out in closed form. Alternatively, the coefficients may be determined by formula, since there are only a finite number of known jumps in the derivatives of the function. Similarly, the component of smoothed applied pressure due to structural terms will need to be cast in a form consistent with the global solution method, in this case by Fourier decomposition:

$$A_n^{\bar{p}_{a \text{ smooth structural}}} = \frac{\epsilon_n}{\pi} \int_0^{\bar{x}_s} \bar{p}_{a \text{ smooth structural}} \cos(n\bar{x}) d\bar{x}. \quad (29)$$

This integration is over a polynomial defined on the positive half of the smoothing region, and makes use of symmetry

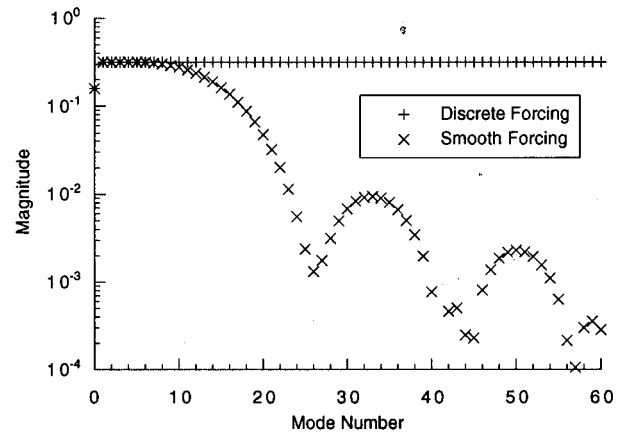


FIG. 6. Magnitude of Fourier coefficients; discrete and smooth forcings.

and the fact that the pressure due to structural terms is zero outside the smoothing region. A logarithmic plot of the magnitude of the Fourier harmonics of this smoothed forcing, and the original discrete forcing is shown in Fig. 6. The smoothed forcing, unlike the discrete forcing, is lacking in significant high mode number content. The structural response to this smoothed forcing, which is the global solution, will be similarly lacking in high mode number content, and will therefore converge rapidly. Note, also, that the smooth forcing is identical to the discrete forcing for low mode numbers. This property ensures that the global solution has the same low resolution, or overall response, as the discretely driven problem. The point at which the harmonic content of the smooth pressure begins to fall off is controlled by the smoothing width.

With the smoothed driving distribution in hand, the solution procedure for the global problem is identical to the solution for the discontinuous driving. The coefficients of membrane response are given by Eq. (10), where, for the smooth driving forces,

$$A_n^{\bar{p}_{a \text{ smooth}}} = \frac{\epsilon_n}{\pi} \int_0^{\pi} \bar{p}_{a \text{ smooth}} \cos(n\bar{x}) d\bar{x} = A_n^{\bar{p}_{a \text{ smooth structural}}} + i\alpha \frac{K_f^2}{K_{y_n}} A_n^{\bar{\eta}_l}. \quad (30)$$

The global solution contains all of the large scale features of the original exact solution, but not the high-resolution detail around the point of application of the discrete load.

C. Assembling the ANM composite solution

The ANM composite solution is given by the smooth global solution plus the local solution. This is illustrated for a sample case by the surface velocity magnitude plots in Fig. 7 of the global solution, the local solution, and the resulting sum, which is the complete solution.

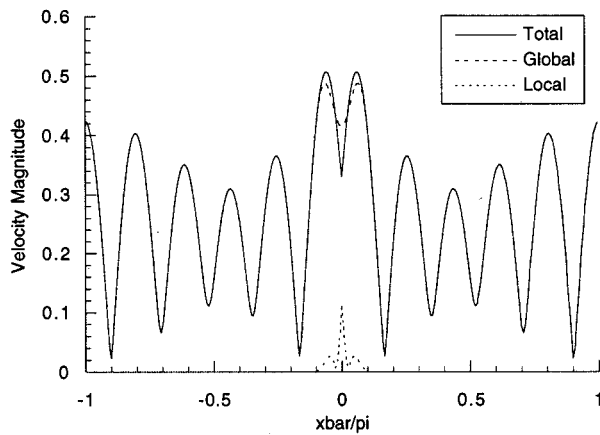


FIG. 7. Surface velocity magnitude distributions, driven membrane; complete, global, and local solutions.

Another very illustrative way of presenting how the global and local solutions combine to form the aggregate exact solution is to plot the magnitude of the Fourier coefficients of surface velocity for all three solutions, as shown in Fig. 8. It is clear from this plot that the global solution completely dominates the solution in the low-resolution region, or low mode numbers. The local solution, however, rises to capture the high-resolution content of the solution, associated with the high mode numbers. The point of crossover between local and global solutions is controlled by the choice of smoothing width. A smaller smoothing width shifts the point of crossover to a higher mode number. In the limit of no smoothing, the global solution reduces to the exact solution, and the local solution disappears. Experience indicates that the most effective choice of smoothing width is one that yields a crossover point at a mode number just higher than the predominant vibrational modes. That is to say, as expected, the smoothing region should be just smaller than the length scale associated with the predominant structural waves.

Decomposing the local solution into a modal series for illustrative purposes, as above, elicits an important advantage of demonstrating ANM on an example problem that can be

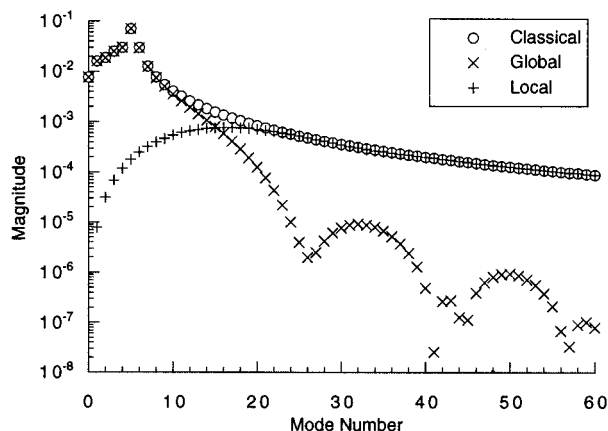


FIG. 8. Magnitude of surface velocity harmonics, driven membrane; exact, global, and local solutions.

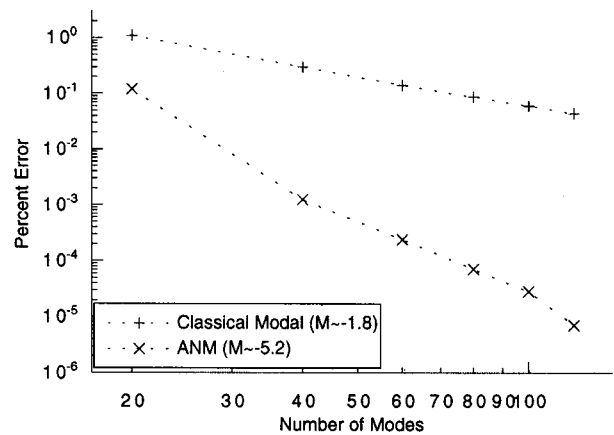


FIG. 9. Surface velocity convergence, driven membrane; classical, and ANM composite.

solved by modal methods. The present problem is an example for which the modal response amplitudes of the discretely forced system are known exactly. It can be shown in analytic closed form that, in the absence of truncation, the ANM composite solution is exactly equivalent to the classical exact series solution. The modal response amplitudes of the exact, local, and global solutions may all be expressed analytically, i.e., all integrals can be performed. Therefore, it can be shown in closed form that, mode for mode, the exact solution is equivalent to the local solution plus the global solution. By the uniqueness of the Fourier series, the classical modal solution and the ANM composite solution are identical in the absence of truncation.

It is important to note that the local solution has been decomposed harmonically only for illustrative purposes. When applying the method, the piecewise polynomial representation is used, since it contains no truncation error.

III. COMPARISON OF ANM AND CLASSICAL METHOD

The application of ANM to structural acoustics has been designed to treat structural discontinuities more efficiently by moving high resolution effects into a local solution, which is expressed without the need for approximation. In order to clearly illustrate the ability of the method to achieve this goal, attention is focused first on the discretely driven structure, where the modal response coefficients are known exactly (an example of this situation is the case illustrated in Fig. 7). In this discretely driven problem, the only source of error is due to the inevitable truncation of terms in the series representation of response. Figure 8 has already been referred to to illustrate the ability of ANM to effectively separate the overall, low-resolution content from the high-resolution content of this solution. Error is introduced into the classical and ANM solutions by the truncation of the series representing the classical and ANM global solutions, respectively (no truncation is associated with the ANM local solution). These truncation errors, the computational errors associated with the two methods, are shown in Fig. 9. The case shown is the same as that shown in Fig. 7. Error is plotted against the number of modes calculated. Percent error is calculated relative to a series solution that was converged

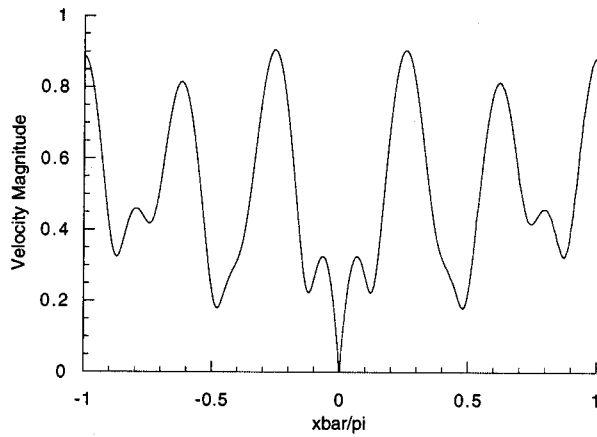


FIG. 10. Surface velocity magnitude distribution, scattering problem.

to an accuracy well beyond the error associated with the plotted cases. Absolute error has been spatially averaged in x before determining the percentage. Computing the surface velocity of the driven problem with ANM yields less error for a given number of calculated modes, and the error also decreases more rapidly as the number of modes is increased, by better than a power of 3 in mode number.

Attention is now focused on the scattering problem, an example of which is illustrated by the surface velocity magnitudes plotted in Fig. 10.

The most interesting feature of the scattering problem, and the feature that makes ANM particularly useful to the scattering problem, is the sensitivity of the overall solution to the accuracy with which the local region near the discontinuity is resolved, as explained in Section I A. This sensitivity occurs because the entire forced solution that is used to model the constraints is inversely proportional to the displacement of the unit driven solution at zero, $\overline{\eta}^{\text{driven}}|_{\bar{x}=0}$. In the forced problem, it was possible to arrive at algebraic expressions for the modal response coefficients that were exact. In the scattering problem, however, each modal coefficient in the solution contains the term $\overline{\eta}^{\text{driven}}|_{\bar{x}=0}$, which is given by an infinite series. Therefore, every coefficient in the solution must contain truncation error associated with this term. Also, this truncation error is that associated with the displacement at the point of application of the discrete load, precisely the high-resolution part of the problem that ANM is designed to treat more efficiently. In problems with a constraint condition that is dependent upon the response of the system at a discontinuity, the entire problem is strongly influenced by the accuracy with which the motion at the discontinuity is modeled.

In addition, when the forces applied to the system due to the constraints are driving a nearly resonant system, inaccuracy in the response of the driven point will produce an especially profound effect on the entire solution. This strong effect is observed because the component of the response associated with the constraint forces is inversely proportional to the response of the driven solution at the driven point [illustrated by Eq. (6)]. Furthermore, a nearly resonant system is characterized by large motions overall, relative to a small drive point response. Therefore, in a nearly resonant

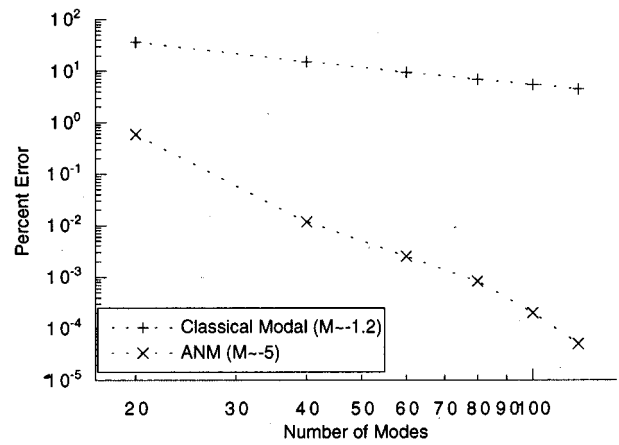


FIG. 11. Surface velocity convergence, scattering problem; classical, and ANM composite.

situation, any absolute error associated with the small driven point response will be more significant on a fractional basis, and will multiply a large overall forced response.

The result of these factors is that the convergence of the scattering problem can be quite sensitive to the difficulty of resolving the influence of the discontinuous constraint. The errors associated with calculating the response in the scattering problem using finite numbers of modes are shown for a sample case in Fig. 11. Errors, in general, are seen to be much larger, and to fall less rapidly than in the forced case. The advantage of the ANM method is seen to be more significant in this problem, where the accuracy of the response at the discontinuity is so important. With only a small number of calculated modes, the error associated with the ANM composite solution is orders of magnitude smaller than that associated with the classical modal solution having the same number of modes. Also, Fig. 11 shows that the rate at which this error falls is faster than that of the classical solution by better than a power of 3 in mode number.

A further point regarding the scattering problem involves the acoustic field observed far from the membrane relative to wavelength, the far field. The geometry of the present example problem exhibits the phenomenon of acoustic cutoff, implying that for a given frequency, only a finite number of modes in the series solution generate propagating acoustic waves, while the remaining infinite number of modes are evanescent. This behavior has important ramifications if one is concerned with the fluid solution far from the structure. In a driven structural problem in which the modal amplitudes are known exactly, the fluid motion far from the structure can be calculated without truncation error by considering only the finite number of modes that propagate. However, this is not the case for the scattering problem, since each modal amplitude contains the term, $\overline{\eta}^{\text{driven}}|_{\bar{x}=0}$, which introduces truncation error. The far-field fluid pressure in the scattering problem is dependent upon the accuracy with which the response of the structure at the point of the discontinuity is modeled. The convergence of scattered power is shown for the sample case in Fig. 12 for classical and ANM methods. Because the error of the scattered power is so sharply dominated by the $1/\overline{\eta}^{\text{driven}}|_{\bar{x}=0}$ term in the co-

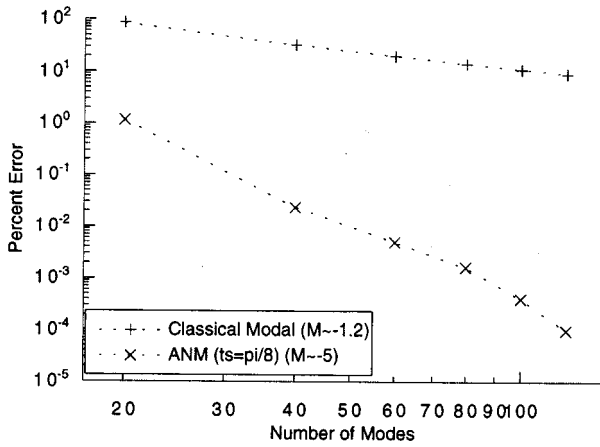


FIG. 12. Convergence of scattered power; classical, and ANM composite.

efficients of the first few modes, this figure is almost identical to the convergence plot of $1/\sqrt{\eta}^{\text{driven}}|_{\bar{x}=0}$ itself.

In the present problem, the influence of the periodic discrete forces leads to uncoupled structural modes and, therefore, a formally exact solution as an infinite modal series. This is very advantageous for showing the effect of the ANM method. In general, though, modes are coupled through fluid loading in structural acoustic problems. This situation is not problematic for the ANM treatment of a discretely forced structure, since the added complications due to coupled modes arise in the classical solution of the forced global problem. The generation of the local solution is independent of the issue of modal coupling.

IV. SUMMARY AND CONCLUSION

The construction of an ANM composite solution has been explained and demonstrated in detail in the context of a simple example of structural acoustic scattering. In a perhaps unlikely way, a smoothing of the original problem has been performed so that the exact difference between the original solution and the smoothed global solution is known in the form of a piecewise polynomial.

It was observed that there exists at the point of application a particular manifestation of discontinuous loading in the physical system. This manifestation, which in the present example is a discontinuous slope of displacement, causes the series representation of the solution to converge slowly. In order to enhance convergence, a local solution was generated that captures this hard to converge detail of the discrete load, and is very smooth in every other respect. Moreover, the local solution is generated in such a way that it is known without the need of approximation. It is expressed exactly as a piecewise polynomial, not an infinite series.

The advantage of generating this local solution is fully realized by the ability to also generate the complementary smoothed global solution. The smoothed global solution is the overall response of the system, less the particular local detail associated with the discrete load. The global solution is solved by conventional methods, with the discrete force of the discontinuity replaced by a smoothed loading. In this way, the hard to converge details of the discrete load have

been absorbed into the local solution, which is by the nature of its description already converged. As a result, the global solution and therefore the ANM composite solution converges significantly faster than the original exact solution.

The advantage of ANM is apparent only with the realization that in practice, a perfectly converged answer for the system does not exist. In the limit of a fully converged solution, there is absolutely no difference in the result, whether ANM or the original direct approach is used. Both are exact in the limit of an infinite number of summed modes, but ANM converges much more rapidly. A slowly convergent modal series has been replaced by a rapidly convergent modal series, plus a piecewise polynomial, which is of course identically converged.

Beyond the application of ANM to structural acoustics, an interesting outcome of this work is the demonstration of the sensitivity of scattering problems to accurate modeling (solution convergence, in this case) around structural discontinuities. It is shown in the paper that displacement constraints at discontinuities can lead to global errors, if the solution is not locally converged. These errors are not limited to the fine scales in the vicinity of the discontinuity, but significantly affect the lower modes which radiate the scattered sound.

Ongoing research involves the application of ANM to more complex configurations, including insonified fluid-loaded shells with structural discontinuities. It should be noted that the advantages illustrated in the present work are not limited to problems solved by modal analysis. The convergence of other numerical methods is generally improved by solving problems with smoothly varying loads, rather than problems with discrete loads and rapid spatial variations. Therefore, it is expected that ANM will be used to benefit a variety of numerical solution methods.

ACKNOWLEDGMENTS

This work was sponsored by the Office of Naval Research. The authors would especially like to thank Dr. L. Couchman and Dr. G. Main.

- ¹P. M. Morse and K. U. Ingard, *Theoretical Acoustics* (McGraw-Hill, New York, 1968), Sec. 10.3.
- ²F. G. Leppington, "Acoustic Scattering by Membranes and Plates With Line Constraints," *J. Sound Vib.* **58**, 319-332 (1978).
- ³D. G. Crighton, "The Green Function of an Infinite, Fluid Loaded Membrane," *J. Sound Vib.* **86**, 411-433 (1983).
- ⁴D. G. Crighton, "Approximations to the Admittances and Free Wavenumbers of Fluid-Loaded Panels," *J. Sound Vib.* **68**, 15-33 (1979).
- ⁵D. G. Crighton and D. Innes, "The Modes, Resonances and Forced Response of Elastic Structures Under Heavy Fluid Loading," *Philos. Trans. R. Soc. London, Ser. A* **312**, 295-341 (1984).
- ⁶D. G. Crighton and D. Innes, "Low Frequency Acoustic Radiation and Vibration Response of Locally Excited Fluid-Loaded Structures," *J. Sound Vib.* **91**, 293-314 (1983).
- ⁷D. G. Crighton and G. Maidanik, "Acoustic and Vibration Fields Generated by Ribs on a Fluid-Loaded Panel, I: Plane-Wave Problems for a Single Rib," *J. Sound Vib.* **75**, 437-452 (1981).
- ⁸J. L. Humar, *Dynamics of Structures* (Prentice-Hall, Engelwood Cliffs, NJ, 1968), pp. 567-572.
- ⁹R. L. Blisplinghoff and H. Ashley, *Principles of Aeroelasticity* (Dover, New York, 1962), pp. 350, 471.
- ¹⁰D. B. Bliss and W. O. Miller, "Efficient Free Wake Calculations Using

- Analytical/Numerical Matching," J. Am. Helicopter Soc. **38**, 870–879 (1993).
- ¹¹W. O. Miller, "Analytical/Numerical Matching and Periodic Inversion: Two Advances in Free Wake Analysis," Doctoral thesis, Duke University, 1990.
- ¹²T. R. Quackenbush and D. B. Bliss, "Free Wake Calculation of Rotor Flow Fields for Interactional Aerodynamics," *Vertica* **14**, 313–327 (1990).
- ¹³T. R. Quackenbush, C-M. G. Lam, and D. B. Bliss, "Vortex Methods for Computational Analysis of Rotor/Body Interaction," J. Am. Helicopter Soc. **39**, 14–24 (1994).
- ¹⁴D. B. Bliss and R. J. Epstein, "Free Vortex Problems Using Analytical/Numerical Matching with Solution Pyramiding," AIAA J. **33**, 894–903 (1995).
- ¹⁵D. B. Bliss and R. J. Epstein, "Novel Approach to Aerodynamic Analysis Using Analytical/Numerical Matching," in AIAA J. **34**, 2225–2232 (1996).
- ¹⁶R. J. Epstein and D. B. Bliss, "An Aeroacoustic Boundary Element Method Using Analytical/Numerical Matching," in *Proceedings of the First Joint CEAS/AIAA Aeroacoustics Conference*, Munich, Germany, June 1995 (German Society for Aeronautics and Astronautics, 1995).
- ¹⁷R. J. Epstein and D. B. Bliss, "An Acoustic Boundary Element Method Using Analytical/Numerical Matching," J. Acoust. Soc. Am. **101**, 92–106 (1997).
- ¹⁸R. C. Loftman, "Analytical/Numerical Matching for Structural Acoustics," Masters thesis, Duke University, 1994.
- ¹⁹D. B. Bliss and R. C. Loftman, "Local and Global Effects in Structural-Acoustic Scattering Using Analytical/Numerical Matching," in *Proceedings of the 15th International Congress on Acoustics*, Trondheim, Norway, June 1995 (Acoustical Society of Norway, 1995).

Wave propagation and attenuation in Herschel–Venturi tubes

A. Selamet and V. Easwaran

The Ohio State University, Department of Mechanical Engineering and The Center for Automotive Research, 206 West 18th Avenue, Columbus, Ohio 43210-1107

(Received 29 April 1996; accepted for publication 27 August 1996)

Wave propagation and attenuation in a classical flow metering device, the Herschel–Venturi tube, is investigated analytically and experimentally. The analytical results are shown to compare well with the experimental observations for anechoically terminated Herschel–Venturi tubes. In the absence of flow, the Taylor series approximations to the governing differential equations and the stepwise expansion and contraction method are shown to be identical. The effect of mean flow on the wave attenuation performance of Herschel–Venturi tubes is also studied in terms of a solution obtained by the Runge–Kutta method, and the applicability of the stepwise expansion and contraction method is discussed with the mean flow through the duct. © 1997 Acoustical Society of America. [S0001-4966(97)02101-2]

PACS numbers: 43.50.Gf, 43.20.Mv [GAD]

INTRODUCTION

Nonuniform ducts are used in many applications such as the breathing system of reciprocating engines and compressors. The nonuniformity may be due to the variation of area along the ducted system, or to the variation of lining impedance along a uniform area duct, or to a combination of both. The Herschel–Venturi tube (HVT) is a typical example of a variable-area duct. The use of Herschel–Venturi tubes for flow measurements is well known (ISO Recommendation, 1980). Though the flow performance of these Venturi tubes has been studied in detail (Bean, 1971; Blevins, 1992), the wave attenuation performance of the same configuration has received very little attention despite the fact that the theory of wave propagation in individual variable-area ducts such as conical, exponential, and catenoidal is well established (Morse, 1981, for one-parameter solution; Munjal, 1987, for one-dimensional solution). Since ducts of these types are the basis for horns as waveguides, extensive literature is available starting with Webster and Rayleigh in 1910s (see, for example, Easwaran and Munjal, 1992; Easwaran, 1993; and Post and Hixon, 1993). The classic NACA report of Davis *et al.* (1954) mentions Venturi tubes only briefly in conjunction with the attenuation improvement of a Helmholtz resonator connected to a Venturi throat.

Davis and Johnson (1974) investigated the one-dimensional wave propagation in duct-nozzle-duct configurations. Standing waves in the duct were decomposed into two traveling waves: one moving along the flow, and the other against the flow. A “shooting method” was then used to obtain the solution for wave propagation of each wave, given the boundary conditions. The work of Davis and Johnson was restricted primarily to the study of pressure and velocity fluctuations along the duct and to the variation of energy flux due to the propagation of either of the traveling waves.

Eversman (1995) describes in detail many of the theoretical models available for the analysis of variable-area flow ducts. The sound transmission through nonuniform ducts carrying a high speed subsonic compressible flow was inves-

tigated by Eversman and Astley (1981), who used the method of weighted residuals. In a companion paper, Astley and Eversman (1981) addressed the same problem using the finite element method. The intent of the investigations reported by Eversman and his co-workers was to determine the suitability of the method of weighted residuals and the finite-element method to a computationally difficult problem. Also, these references assume that the sound speed does not vary with the axial distance. The quasi-one-dimensional wave propagation in varying area ducts was investigated by Lumsdaine and Ragab (1977). They used the power series method and the Runge–Kutta method to solve the governing equations for a given mean flow distribution, rather than for a given duct shape. Miles (1981) addressed the issue of wave propagation in exponential ducts. His method is based on solving the governing differential equations by dividing the duct into smaller segments, each having an exponential area variation. The flow within each segment was assumed to be constant, while allowing for mean flow discontinuity across the duct segments. In such a case, multiplying the transfer matrices sequentially without accounting for the effect of discontinuities can lead to erroneous results as illustrated by Gupta *et al.* (1995).

As shown in Fig. 1, the Herschel–Venturi tube consists of a converging conical section, a uniform duct, and a diverging conical section, designated by lengths L_1 , L_{throat} , and L_2 , respectively. Radiused transitions (fillets) as indicated by R_1 , R_2 , and R_3 , are provided to blend the uniform and conical sections, thereby ensuring a gradual variation of area from one section to the other, which were ignored in an earlier work (Selamet *et al.*, 1994a). This earlier work was also limited to only one configuration and neglected the effect of flow. Since Herschel–Venturi tubes are primarily used for flow measurements, it is imperative to investigate the effect of flow on the acoustic performance of these tubes. The objective of the present study is then: (1) to consider a number of different Herschel–Venturi tubes with main duct to throat cross-sectional area ratios of $m=2, 4, 9$, and 16 ; (2) to incorporate the effect of mean flow analytically; and (3) to

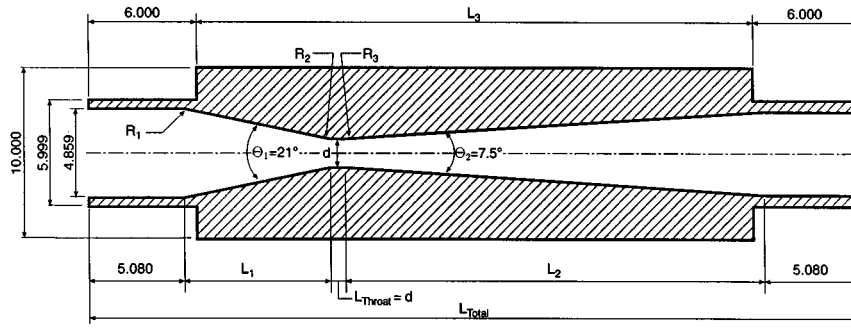


FIG. 1. Schematic of a Herschel–Venturi tube.

examine the effect of fillets. The fillets are represented by a sequence of conical duct sections. Thus the Herschel–Venturi tube is modeled as a series of converging duct sections, followed by a uniform duct, and by a series of diverging duct sections. These are then combined with upstream and downstream straight ducts. Relationships are developed to account for the subsonic mean flow through a variable-area duct. Analytical results for the transmission loss are presented for (1) the limit of quiescent medium along with the experimental results; and (2) for the subsonic flow through the Herschel–Venturi tube. Following the illustration of the fillet effect, the study is concluded by some final remarks.

I. THEORY

The present analysis assumes steady, one-dimensional, and homentropic flow. When the taper, or the rate of change of area with distance is gradual, the mass and momentum conservation equations can be written as (Shapiro, 1953)

$$\frac{\partial \rho^*}{\partial t} + \frac{1}{A} \frac{\partial}{\partial x} (\rho^* u^* A) = 0 \quad (1)$$

and

$$\rho^* \frac{\partial u^*}{\partial t} + \rho^* u^* \frac{\partial u}{\partial x} + \frac{\partial p^*}{\partial x} = 0, \quad (2)$$

respectively. Here, p^* is the pressure, u^* is the fluid velocity, ρ^* is the fluid density, and A is the cross-sectional area. Perturbing Eqs. (1) and (2) in terms of $p^* = p_0 + p$, $u^* = u_0 + u$, and $\rho^* = \rho_0 + \rho$, and retaining only the first-order terms, yields

$$\begin{aligned} \frac{\partial \rho}{\partial t} + u_0 \frac{\partial \rho}{\partial x} + u \frac{\partial \rho_0}{\partial x} + \rho_0 \frac{\partial u}{\partial x} + \rho \frac{\partial u_0}{\partial x} + \frac{\rho u_0}{A} \frac{dA}{dx} \\ + \frac{\rho_0 u}{A} \frac{dA}{dx} = 0 \end{aligned} \quad (3)$$

and

$$\rho_0 \frac{\partial u}{\partial t} + \rho_0 u \frac{\partial u_0}{\partial x} + \rho_0 u_0 \frac{\partial u}{\partial x} + \rho u_0 \frac{\partial u_0}{\partial x} + \frac{\partial p}{\partial x} = 0, \quad (4)$$

respectively, where subscript “0” indicates the mean or the steady-state quantities, and p , u , and ρ are, respectively, the acoustic pressure, the acoustic particle velocity, and the acoustic density. While the steady-state variables are of zeroth

order in magnitude, the acoustic quantities are of order one. Similarly, the linearized version of the isentropic pressure density relationship is (Shapiro, 1953),

$$\frac{p}{\rho} = \gamma \frac{p_0}{\rho_0} = c_0^2, \quad (5)$$

where γ is the ratio of specific heats and c_0 is the speed of sound. The corresponding steady-state equations (zeroth-order equations) are

$$\frac{d}{dx} (\rho_0 u_0 A) = 0 \quad \text{and} \quad \frac{dp_0}{dx} + \rho_0 u_0 \frac{du_0}{dx} = 0. \quad (6)$$

Assuming a time dependence of $\exp(i\omega t)$, Eqs. (3)–(5) can be combined to yield

$$\begin{aligned} \begin{bmatrix} \frac{u_0}{\rho_0 c_0^2} & 1 \\ 1 & u_0 \end{bmatrix} \begin{bmatrix} \frac{dp}{dx} \\ \frac{du}{dx} \end{bmatrix} \\ + \begin{bmatrix} \frac{i\omega}{\rho_0 c_0^2} + \frac{u_0}{\rho_0 c_0^2} \frac{d}{dx} [\ln u_0 + \ln A - (\gamma - 1) \ln \rho_0] & \frac{d}{dx} (\ln \rho_0 + \ln A) \\ \frac{u_0^2}{\rho_0 c_0^2} \frac{d}{dx} \ln u_0 & i\omega + u_0 \frac{d}{dx} \ln u_0 \end{bmatrix} \\ \times \begin{bmatrix} p \\ u \end{bmatrix} = 0. \end{aligned} \quad (7)$$

Note, however, that p_0 , ρ_0 , and hence c_0 are all functions of the axial distance “ x .” Equation (7) differs from that derived by Miles (1981) since he had assumed a constant c_0 .

Equations (5) and (6) can be combined to give

$$\frac{d}{dx} \ln u_0 = \frac{-1}{1 - M_0^2} \frac{d}{dx} \ln A$$

and

$$\frac{d}{dx} \ln \rho_0 = \frac{M_0^2}{1 - M_0^2} \frac{d}{dx} \ln A,$$

where $M_0 = u_0/c_0$ is the mean flow Mach number. Substituting Eq. (8) in Eq. (7), yields

$$\begin{Bmatrix} \frac{dp}{dx} \\ \frac{du}{dx} \end{Bmatrix} = [B] \begin{Bmatrix} p \\ u \end{Bmatrix}, \quad (9)$$

where the components of matrix $[B]$ are

$$\begin{aligned} B_{11} &= \frac{ik_0 M_0}{1-M_0^2} + \frac{M_0^2(1-\gamma M_0^2)}{(1-M_0^2)^2} \frac{d \ln A}{dx}, \\ B_{12} &= -\frac{i\omega\rho_0}{1-M_0^2} + \frac{2c_0 M_0 \rho_0}{(1-M_0^2)^2} \frac{d \ln A}{dx}, \\ B_{21} &= -\frac{ik_0}{\rho_0 c_0 (1-M_0^2)} + \frac{(\gamma-1)M_0^3}{\rho_0 c_0 (1-M_0^2)^2} \frac{d \ln A}{dx}, \\ B_{22} &= \frac{ik_0 M_0}{1-M_0^2} - \frac{(1+M_0^2)}{(1-M_0^2)^2} \frac{d \ln A}{dx}. \end{aligned} \quad (10)$$

The matrix $[B]$ is a function of the mean flow Mach number M_0 , the local sound speed c_0 , the density ρ_0 , the frequency ω , and the rate of change of area with axial distance, $d \ln A / dx$. If the initial conditions are known, the values of p and u at any given axial distance x can then be evaluated numerically. Runge–Kutta method is ideally suited for such initial value problems.

Representing the inlet and exit conditions by subscripts i and e , respectively, the pressure and particle velocity at both ends may be related to each other by

$$\begin{Bmatrix} p \\ u \end{Bmatrix}_i = \begin{bmatrix} T_{11} & T_{12} \\ T_{21} & T_{22} \end{bmatrix} \begin{Bmatrix} p \\ u \end{Bmatrix}_e, \quad (11)$$

where T_{ij} 's are the components of the transfer matrix $[T]$. Thus

$$\begin{aligned} T_{11} &= \left. \frac{p_i}{p_e} \right|_{u_e=0}, & T_{12} &= \left. \frac{p_i}{u_e} \right|_{p_e=0}, \\ T_{21} &= \left. \frac{u_i}{p_e} \right|_{u_e=0}, & T_{22} &= \left. \frac{u_i}{u_e} \right|_{p_e=0}. \end{aligned} \quad (12)$$

By prescribing values of zero and unity for p_e and u_e the transfer matrix components can be readily evaluated. For a configuration comprising of “ n ” ducts, an overall transfer matrix relating the inlet and exit conditions may be obtained through a sequential multiplication of all the transfer matrices. Such a multiplication is possible only when there is a continuity of mean flow Mach numbers between two duct segments (Gupta *et al.*, 1995). The values of M_0 , ρ_0 , and c_0 are to be computed at every interval required for the Runge–Kutta method. From the conventional definitions (Shapiro, 1953), the stagnation temperature T_s and the density ρ_s may be written as

$$\begin{aligned} T_s &= T_0 \left[1 + \frac{\gamma-1}{2} M_0^2 \right], \\ \rho_s &= \rho_0 \left[1 + \frac{\gamma-1}{2} M_0^2 \right]^{1/(\gamma-1)}, \end{aligned} \quad (13)$$

where the mean speed of sound for the calculation of M_0 is given by

$$c_0 = \sqrt{\gamma R T_0}. \quad (14)$$

Here, T is the gas temperature and R is the gas constant. Thus by knowing the stagnation conditions at the exit and the Mach numbers at locations required by the Runge–Kutta method, the density and the sound speed can be evaluated at these locations. The Mach number at any location within a duct of a given shape can be determined from

$$\frac{A}{A^*} = \frac{1}{M_0} \left[\left(\frac{2}{\gamma+1} \right) \left(1 + \frac{\gamma-1}{2} M_0^2 \right) \right]^{(\gamma+1)/2(\gamma-1)} \quad (15)$$

(Shapiro, 1953). Here, A^* represents the area where the Mach number becomes unity. Thus at every integration step required by the Runge–Kutta method the Mach number at that location can be evaluated by using the area ratio given by Eq. (15). The corresponding density ρ_0 and the local sound speed c_0 can be evaluated from Eqs. (13) and (14).

Representing the inlet and exit conditions of the Herschel–Venturi tube by subscripts “1” and “2,” respectively, and assuming that the inlet and exit ducts are terminated by ducts of uniform area, one can write

$$p_1 = C_1^+ + C_1^- \quad \text{and} \quad u_1 = \frac{C_1^+ - C_1^-}{\rho_{01} c_{01}} \quad (16)$$

and

$$p_2 = C_2^+ + C_2^- \quad \text{and} \quad u_2 = \frac{C_2^+ - C_2^-}{\rho_{02} c_{02}}, \quad (17)$$

where C_1^+ , C_2^+ , C_1^- , and C_2^- are all constants and depend on the boundary conditions. When the termination is anechoic, $C_2^- = 0$. In terms of these constants the input power P_1 and the output power P_2 are given (Munjaj, 1987) by

$$P_1 = \frac{1}{2} (1 + M_{01})^2 A_1 |C_1^+|^2, \quad P_2 = \frac{1}{2} (1 + M_{02})^2 A_2 |C_2^+|^2. \quad (18)$$

Transmission loss, defined by

$$\text{TL} = 10 \log_{10} \left| \frac{P_1}{P_2} \right|, \quad (19)$$

can be expressed in terms of the transfer matrix as

$$\begin{aligned} \text{TL} &= 20 \log_{10} \left[\frac{1}{2} \sqrt{\frac{A_1}{A_2}} \left| T_{11} + \frac{T_{12}}{\rho_{02} c_{02}} + \rho_{01} c_{01} T_{21} \right. \right. \\ &\quad \left. \left. + \frac{\rho_{01} c_{01}}{\rho_{02} c_{02}} T_{22} \left[\frac{(1+M_{01})}{(1+M_{02})} \right] \right| \right]. \end{aligned} \quad (20)$$

By definition, transmission loss is independent of the source as well as termination. Therefore, unless the flow direction is reversed, it does not depend on the location of the source: i.e., upstream or downstream of the Herschel–Venturi tube.

The Taylor series expansion may be used to write

$$p(x - \Delta x) = p(x) - \frac{dp}{dx} \Delta x, \quad (21)$$

$$u(x - \Delta x) = p(x) - \frac{du}{dx} \Delta x, \quad (22)$$

and

$$A(x - \Delta x) = A(x) - \frac{dA}{dx} \Delta x. \quad (23)$$

Combining Eqs. (21)–(23) with Eqs. (9) and (10) results in

$$\begin{Bmatrix} p(x - \Delta x) \\ v(x - \Delta x) \end{Bmatrix} = [\Delta T] \begin{Bmatrix} p(x) \\ v(x) \end{Bmatrix}, \quad (24)$$

where $v(x) = A(x)u(x)$ is the volume velocity and the components of the $[\Delta T]$ matrix are given by

$$\begin{aligned} \Delta T_{11} &= 1 - \frac{iM_0 k_0 \Delta x}{1 - M_0^2} - \frac{M_0^2(1 - \gamma M_0^2)}{(1 - M_0^2)^2} \frac{1}{A} \frac{dA}{dx} \Delta x, \\ \Delta T_{12} &= \frac{\rho_0 c_0}{A} \left(\frac{ik_0 \Delta x}{1 - M_0^2} - \frac{2M_0}{(1 - M_0^2)^2} \frac{1}{A} \frac{dA}{dx} \Delta x \right), \\ \Delta T_{21} &= \frac{A}{\rho_0 c_0} \left(\frac{ik_0 \Delta x}{1 - M_0^2} - \frac{(\gamma - 1)M_0^3}{(1 - M_0^2)^2} \frac{1}{A} \frac{dA}{dx} \Delta x \right), \\ \Delta T_{22} &= 1 - \frac{iM_0 k_0 \Delta x}{1 - M_0^2} + \frac{1 + M_0^2}{(1 - M_0^2)^2} \frac{1}{A} \frac{dA}{dx} \Delta x - \frac{1}{A} \frac{dA}{dx} \Delta x. \end{aligned} \quad (25)$$

The overall transfer matrix of a varying area duct can then be obtained by multiplying sequentially the corresponding $[\Delta T]$ matrices. Note that, at all points the mean flow Mach numbers are continuous. In the absence of flow the ΔT matrix reduces to

$$\Delta T_{M_0=0} = \begin{bmatrix} 1 & \frac{i\rho_0 c_0 k_0}{A} \Delta x \\ \frac{ik_0 A \Delta x}{\rho_0 c_0} & 1 \end{bmatrix}. \quad (26)$$

The transfer matrix of a uniform area duct with mean flow is given (Munjaj, 1987) by

$$T_{dA=0} = \exp(-ik_c M_0 l) \begin{bmatrix} \cos k_c l & i \frac{\rho_0 c_0}{A} \sin k_c l \\ \frac{iA}{\rho_0 c_0} \sin k_c l & \cos k_c l \end{bmatrix}, \quad (27)$$

where $k_c = k_0/(1 - M_0^2)$. If $k_c l \ll 1$, then Eq. (27) reduces to

$$T_{dA=0} = \left(1 - i \frac{k_0 M_0 l}{1 - M_0^2} \right) \begin{bmatrix} 1 & \frac{i\rho_0 c_0 k_0 l}{A(1 - M_0^2)} \\ \frac{ik_0 A l}{\rho_0 c_0(1 - M_0^2)} & 1 \end{bmatrix}. \quad (28)$$

Equation (26) is then the limiting case of a uniform area duct of length $l = \Delta x$. Therefore, multiplying the transfer matrices for segments with length Δx and uniform cross-sectional area essentially leads to the solution of the actual governing differential equations. Such approach is known in the literature as the ‘‘stepwise contraction and expansion method’’ and was used, for example, by Alfredson (1972), and by Selamet *et al.* (1994a, b).

If the mean flow is nearly incompressible, i.e., $M_0^2 \ll 1$, it can easily be shown that the transfer matrix for the uniform

duct of length $l = \Delta x$ [refer to Eq. (28)], does not identically reduce to the $[\Delta T]$ matrix. However, when the taper is quite small, these matrices compare relatively well. When the flow is compressible, the transfer matrix of uniform duct of length Δx given by Eq. (28) does not reduce to that given by Eq. (24). Thus the stepwise expansion and contraction method can be used only in the limit of incompressible flow and a gradual taper. How well this method compares with the actual solution of the governing equations in the presence of flow depends on the Mach number and the taper. Thus in the presence of flow, instead of using the limiting case of a uniform area duct of infinitesimal length, it would be more appropriate and accurate to use Eq. (24) to evaluate the transfer matrix $[\Delta T]$.

Since the stepwise expansion and contraction [assuming that the transfer matrix defined by Eq. (24) is used rather than the limiting case of the transfer matrix defined by Eq. (27)] is essentially a Taylor series method truncated after the first-order terms, the resulting error would be of the order of $(\Delta x)^2$. However, in the Runge–Kutta method the corresponding error would be of the order of $(\Delta x)^5$. The advantage of Runge–Kutta method over the stepwise expansion and contraction depends on how small the value of Δx should be for a given problem. The smaller the value, the superior the Runge–Kutta method. For the Herschel–Venturi tube considered in this paper the number of segments required for the stepwise expansion and contraction method was found to be almost the square of the number of discretizations required by the Runge–Kutta method. Hence, in the present paper, computations have been carried out using the Runge–Kutta method. The Runge–Kutta method converges faster than the stepwise expansion and contraction method in the presence of flow, while the difference between the two methods diminishes in the absence of flow.

II. CLOSED FORM SOLUTION

In the absence of flow, for a conical duct, Eq. (9) can be shown to reduce to

$$\frac{d^2 p}{dx^2} + \frac{2}{x} \frac{dp}{dx} + k_0^2 p = 0, \quad (29)$$

where $k_0 = \omega/c_0$ is the wave number. The solution of this equation is

$$p = \frac{1}{x} [C_1 e^{-ik_0 x} + C_2 e^{ik_0 x}] \quad (30)$$

and hence

$$u = \frac{1}{i\omega\rho_0 x^2} [(1 + ik_0 x)C_1 e^{-ik_0 x} + (1 - ik_0 x)C_2 e^{ik_0 x}]. \quad (31)$$

The expression for the transfer matrix of a conical duct segment becomes (Selamet *et al.*, 1996)

TABLE I. Dimensions (cm) of the Herschel–Venturi tube ($R_1=5.345$ cm and $L_{\text{throat}}=d$).

| m | d | L_1 | L_2 | L_3 | R_2 | R_3 |
|-----|-------|-------|--------|--------|--------|--------|
| 2 | 3.436 | 3.839 | 10.857 | 16.292 | 12.025 | 17.179 |
| 4 | 2.430 | 6.554 | 18.534 | 25.677 | 8.503 | 12.148 |
| 9 | 1.620 | 8.739 | 24.711 | 33.230 | 5.669 | 8.098 |
| 16 | 1.215 | 9.831 | 27.800 | 37.006 | 4.252 | 6.074 |

$$\begin{aligned}
 & \begin{Bmatrix} p \\ u \end{Bmatrix}_{r=r_1} \\
 &= \begin{bmatrix} \frac{r_2}{r_1} \cos(k_0 l) - \frac{\tan \theta}{k_0 r_1} \sin(k_0 l) & i \rho_0 c_0 \frac{r_2}{r_1} \sin(k_0 l) \\ -i \frac{l \tan^2 \theta}{k_0 r_1^2} \frac{\cos(k_0 l)}{\rho_0 c_0} + & \frac{r_2}{r_1} \cos(k_0 l) + \\ i \left(\frac{r_2}{r_1} + \frac{\tan^2 \theta}{k_0^2 r_1^2} \right) \frac{\sin(k_0 l)}{\rho_0 c_0} & \frac{\tan \theta}{k_0 r_1} \sin(k_0 l) \end{bmatrix} \\
 & \times \begin{Bmatrix} p \\ u \end{Bmatrix}_{r=r_2}, \tag{32}
 \end{aligned}$$

where $l=x_2-x_1$, and $r=x \tan \theta$. Here, θ is the angle between the axis and the wall, often referred to as ‘‘cone half-angle.’’

In the absence of flow, Eq. (32) is used to evaluate the transmission loss of HVTs, as it is much faster. Two conical segments were found to adequately represent the short fillet transitions. These predictions are then used for comparison with the experimental results. The Runge–Kutta method and the stepped duct approach would also yield the same results. This fact is used to determine the step size for the Runge–Kutta method and also for the stepped duct approach. The closed form solution was also used to benchmark the numerical results.

Four Herschel–Venturi tubes were used in the analytical study with the duct to throat cross-sectional area ratios varying from $m=2$ to 16. While the fillet radius R_1 , the reducer and the diffuser included cone angles (Θ_1 and Θ_2) are kept the same, the throat diameter d , and as a result, various lengths L_1 , L_2 , L_3 , and the remaining fillet radii R_2 and R_3 are varied as illustrated in Table I. The radii of curvature follows the lower bound of the recommendation for the cast-convergent design. Thus $R_1=1.1D$, $R_2=3.5d$, and $R_3=5d$, where $D=4.859$ cm is the main duct diameter. Clearly, the inner dimensions in Fig. 1 define the Herschel–Venturi tube configurations, while the outer dimensions are for fabrication/installation purposes and hence are of secondary importance here. Configurations with $m=4$, 9, and 16 were also fabricated (on a cubital machine) as single units and the transmission loss characteristics were measured using an anechoically terminated impedance tube setup. The details of the experimental results are discussed elsewhere (see, for instance, Selamet *et al.*, 1994c) and hence will not be elaborated here. The next section discusses the results from the analytical and experimental work.

III. RESULTS

Figure 2 compares the analytical transmission loss of Herschel–Venturi tubes with area ratios of $m=4$, 9, and 16 with the experimental results for a quiescent medium. The analytical predictions from the preceding section agree reasonably well with the experimental observations. The deviation of the analytical predictions from the experimental results appears to be significant above 1250 Hz and at large values of m . Since transmission loss tends to diminish at high frequencies, any deviation in this range will become relatively important. The deviation may possibly be attributed to the fact that at high frequencies, curvature effects may no longer be neglected and the assumption of plane waves therefore needs to be modified. Viscous damping which increases with frequency may also affect the results in a similar way. Since the analytical treatment is restricted to the ideal case of zero damping, the discrepancy between the analytical and the experimental results is expected to increase at higher frequencies. The transmission loss characteristics exhibit a dominant first peak followed by a weak second peak. These peaks, however, have broad frequency bands. Though for a given area ratio the Herschel–Venturi tube would exhibit smaller peaks compared to the simple expansion chamber type of silencers, the bands are wider. The Herschel–Venturis can hence be used as a broadband acoustic filters.

The transmission loss characteristics of the Herschel–Venturi tubes with area ratios of 2, 4, 9, and 16 for different mean flow Mach numbers are calculated by using the Runge–Kutta method, as described earlier in Sec. I. The results are shown in Figs. 3–6, where the Mach number M corresponds to the downstream conditions, i.e., conditions at the exit duct. In Fig. 3 the transmission loss curve for Mach number of 0.3 is included to show the effect of choking. The phenomenon occurs at $M=0.3059$ at the throat for the present configuration. Thus for flow speeds near this number, the TL values show a sharp rise. In all cases, while the mean flow increases the transmission loss peaks to some degree and shifts them toward lower frequencies, the overall char-

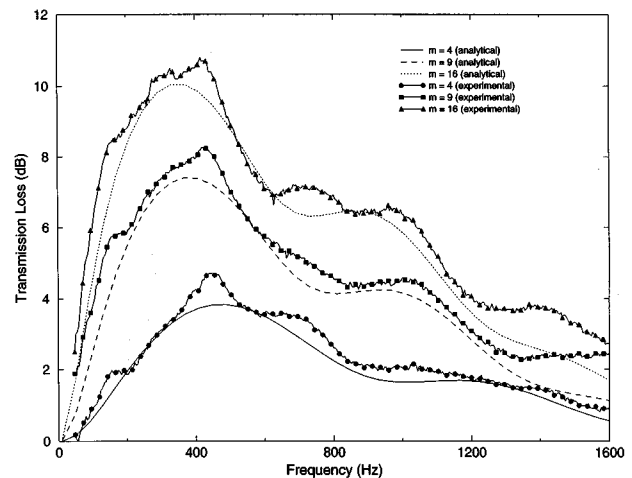


FIG. 2. Comparison of the analytical and the experimental results for the Herschel–Venturi tube with main duct-to-throat cross-sectional area ratios of $m=4$, 9, and 16.

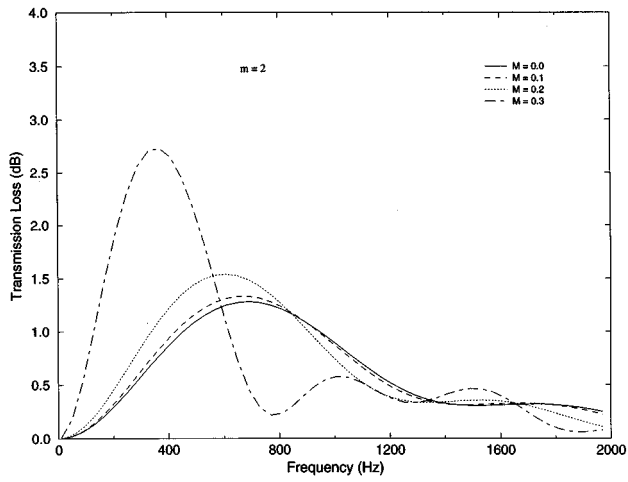


FIG. 3. Effect of flow on the Herschel-Venturi tube with $m=2$.

acteristics of the attenuation behavior continue to resemble those of no flow case. For a given Mach number at the inlet or exit, the effect of mean flow is predominant for ducts with higher area ratios as expected since the Mach numbers at the throat become quite significant. For computations to converge in the frequency range of interest, a step length of 1 mm was found to be sufficient. Finally, the effect of fillets is illustrated in Fig. 7 in terms of an HVT with area ratio $m=9$. The fillets either raise or lower the transmission loss peaks and troughs slightly.

IV. CONCLUDING REMARKS

The present study has developed an analytical treatment to characterize the wave propagation in variable-area flow ducts. The transmission loss characteristics of the Herschel-Venturi tube have been investigated both analytically and experimentally. It has been shown that, in the absence of flow, the Taylor series approximations to the governing differential equations and the stepwise contraction and expansion method are identical. The extension of the stepwise con-

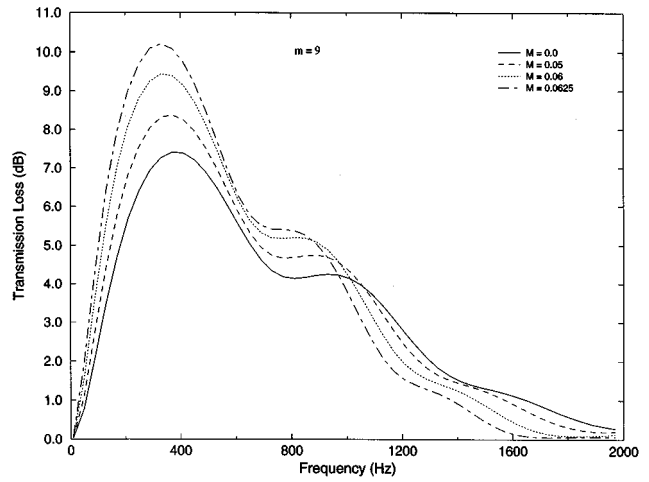


FIG. 5. Effect of flow on the Herschel-Venturi tube with $m=9$.

traction and expansion method to study wave propagation in variable-area ducts with mean flow is shown to be, at best, applicable to the case where the flow is almost incompressible and the duct taper is very small if one were to use the transfer matrix corresponding to that of a uniform area duct of infinitesimal length. This problem can, however, be overcome if the transfer matrix defined by Eq. (24) is used in the computations. The theoretical predictions have been shown to agree reasonably well with the experimentally observed trends. An increase in the mean flow is shown to raise the transmission loss peaks and shifts them to lower frequencies.

For the frequency range of interest, for example, in the intake and the exhaust ducts of an internal combustion engine (<1000 Hz), the deviation from the one-dimensional behavior is known to be negligible. Therefore, the present one-dimensional study is expected to prove to be useful in designing venturi silencers for noise reduction in ducts, particularly in the presence of fluid flow. The magnitude of noise suppression, however, needs to be carefully examined against the flow efficiency of these configurations where the cross-sectional area decrease has a detrimental effect on the

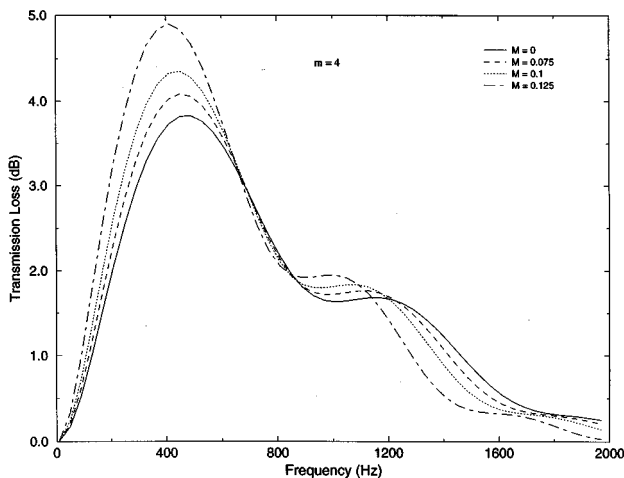


FIG. 4. Effect of flow on the Herschel-Venturi tube with $m=4$.

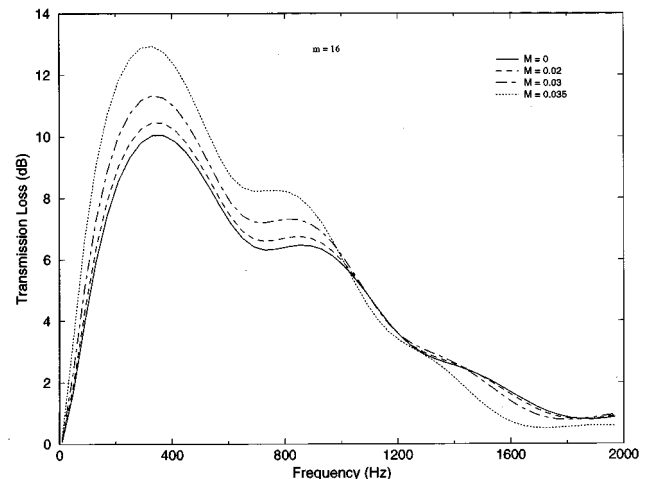


FIG. 6. Effect of flow on the Herschel-Venturi tube with $m=16$.

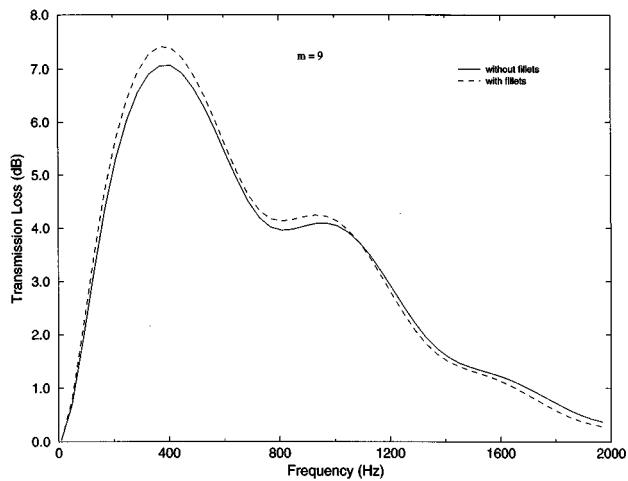


FIG. 7. Effect of the fillets (for $m=9$).

flow performance due mainly to the separation of flow from boundaries. The need for the compromise, or a change to an alternative configuration, becomes more important with increasing flow rates and larger duct-to-throat cross-sectional area ratios.

Alfredson, R. J. (1972). "The propagation of sound in a circular duct of continuously varying cross-sectional area," *J. Sound Vib.* **23**, 433–442.

Astley, R. J., and Eversman, W. (1981). "Acoustic transmission in non-uniform ducts with flow. Part II: The finite element method," *J. Sound Vib.* **74**, 103–121.

Bean, H. S. (1971). *Fluid Meters, Their Theory and Applications* (ASME, New York), 6th ed.

Blevins, R. D. (1992). *Applied Fluid Dynamics Handbook* (Kreiger, Boca Raton, FL).

Davis, D. D., Stokes, G. M., Moore, D., and Stevens G. L. (1954). "Theoretical and experimental investigation of mufflers with comments on engine exhaust muffler design," NACA Report No. 1192.

Davis, S. S., and Johnson, M. L. (1974). "Propagation of plane waves in a

variable area duct carrying a compressible subsonic flow," *J. Acoust. Soc. Am. Suppl.* **1** **55**, S74.

Easwaran, V. (1993). "Analysis of Variable Area Flow Ducts and Anechoic Linings," Ph.D. thesis, Indian Institute of Science, Bangalore, India.

Easwaran, V., and Munjal, M. L. (1992). "Plane wave analysis of conical and exponential pipes with incompressible mean flow," *J. Sound Vib.* **152**, 73–93.

Eversman, W. (1995). "Theoretical models for duct acoustic propagation and radiation," *Aeroacoustics of Flight Vehicles* (Acoustical Society of America, Woodbury, NY), pp. 101–163.

Eversman, W., and Astley, R. J. (1981). "Acoustic transmission in non-uniform ducts with flow. Part I: Method of weighted residuals," *J. Sound Vib.* **74**, 89–101.

Gupta, V. H., Easwaran, V., and Munjal, M. L. (1995). "A modified segmentation approach for plane wave propagation in non-uniform ducts with mean flow," *J. Sound Vib.* **182**, 697–707.

ISO Recommendation 5167 (1980). *Measurement of Fluid Flow by Means of Orifice Plates, Nozzles and Venturi Tubes Inserted in Circular Cross-Section Conduits Running Full* (Global Engineering, California).

Lumsdaine, E., and Ragab, S. (1977). "Effect of flow on quasi-one-dimensional acoustic wave propagation in a variable area duct of finite length," *J. Sound Vib.* **53**, 47–61.

Miles, J. H. (1981). "Acoustic transmission of a variable area duct or a nozzle carrying a compressible subsonic flow," *J. Acoust. Soc. Am.* **69**, 1577–1586.

Morse, P. M. (1981). *Vibration and Sound* (Acoustical Society of America, Woodbury, NY), pp. 265–285.

Munjal, M. L. (1987). *Acoustics of Ducts and Mufflers* (Wiley, New York).

Post, J. T., and Hixon, E. L. (1993). "Rayleigh's horn equation," *J. Acoust. Soc. Am.* **94**, 1803.

Selamet, A., and Dickey, N. S. (1994c). "The Herschel–Quincke tube: A theoretical, computational, and experimental investigation," *J. Acoust. Soc. Am.* **96**, 3177–3185.

Selamet, A., Kim, Y., Dickey, N. S., and Novak, J. M. (1994a). "The Herschel–Venturi tube," *Proc. Noise-Con* **94**, 255–260.

Selamet, A., Kim, Y., Dickey, N. S., and Novak, J. M. (1994b). "Venturi tubes: acoustic attenuation versus flow losses," *Proc. Intl. Mech. Eng. Cong.*, ASME, Chicago.

Selamet, A., Dickey, N. S., and Novak, J. M. (1996). "Wave attenuation by universal venturi tubes: an analytical, computational, and experimental investigation," *Noise Control Eng. J.* **44**(5), 224–230.

Shapiro, A. H. (1953). *The Dynamics and Thermodynamics of Compressible Fluid Flow* (Wiley, New York), Vol. I.

Status of road traffic noise in Calcutta metropolis, India

Debashis Chakrabarty, Subhas Chandra Santra, and Abirlal Mukherjee

Department of Ecological Studies, School of Environmental Science, University of Kalyani,
Kalyani-741235, India

Biva Roy

Department of Physics, Bose Institute, Calcutta-700009, India

Prasun Das

SQC & OR Unit, Indian Statistical Institute, Calcutta-700016, India

(Received 13 February 1996; revised 6 August 1996; accepted 8 August 1996)

Road traffic noise was measured at 24 traffic junctions of Calcutta, India during the summer of 1993, with the simultaneous recording of the number of vehicles passing. The A-weighted values of $L_{eq(24)}$, L_{dn} , L_{10} , L_{90} , L_{99} , L_{np} and TNI were determined. Statistical regression equations of $L_{eq(h)}$ were developed as a function of logarithm of the equivalent number of light/heavy vehicles per hour for the entire city and for zones within the city. © 1997 Acoustical Society of America.

[S0001-4966(97)03012-9]

PACS numbers: 43.50.Lj [GAD]

INTRODUCTION

Calcutta, a metropolis of 10 million, is the most populous city in India and the fourth largest in world population. The city is more than 300 years old and expands in a linear orientation on the north-south axis along the bank of the river Hooghly, resulting in unplanned settlement pattern and narrow roads. The road transport system consists of trucks, buses, mini-buses, cars, taxis, trams, auto-rickshaws, motor-cycles coupled with slow moving traffic like rickshaws and bicycles, besides thousand of pedestrians.

The traffic noise level of Calcutta was previously measured by Pancholy *et al.* (1967); Roy *et al.* (1984); Prabhu and Muni Chakrabarty (1978); CPCB (1991); and others. But these measurements were made only for 2 to 3 h during the morning, afternoon, and night. Among the available reports on the environmental noise studies in different Indian cities like Delhi (Mohan, 1987; Kumar and Jain, 1994), Bombay (Dixit, *et al.*, 1982), Ahmedabad (Shrivastava *et al.*, 1987) Visakhapatnam (Rao *et al.*, 1989; Rao and Rao, 1990, 1991), etc. Only a systematic and comprehensive study of the road traffic noise level of Visakhapatnam was made by Rao *et al.* (1989) who developed regression equations for predicting the noise levels of Visakhapatnam. The present study includes the development of similar equations for predicting the ambient noise levels of Calcutta with the necessary consideration of the effect of plying traffic distance from the measurement point. The average speed of movement of the vehicles on Calcutta city roads rarely exceeds 20 km/hr. It is assumed to a first approximation, that the traffic noise is a function of traffic volume only, if the plying traffic distance remains the same. Accordingly, regression equations connecting the hourly equivalent continuous noise level $L_{eq(h)}$, combined with the term representing plying traffic distance and the traffic density (N_i/h) are proposed.

I. MEASUREMENT LOCATIONS

Twenty four locations spread over the city of Calcutta from south suburb to north suburb were chosen. The names

of these 24 road intersections are given in Table I and they are indicated by the corresponding site numbers in the map of Calcutta shown in Fig. 1. Sites 1, 23, and 24 lie in suburbs not shown on the map. Sites 1 to 10 have been selected in the south, sites 11 to 15 are in central Calcutta, and sites 16 to 24 are in the north.

The 24 measurement sites have been divided into five zones according to the particular use of the area, as follows:

- (1) residential (7, 10, and 20),
- (2) commercial (2, 11, 12, 13, and 17),
- (3) residential-commercial (1, 3, 5, 6, 8, 15, 16, 18, 19, 21, and 23),
- (4) residential-industrial (4, 22, and 24),
- (5) office complex (9 and 14).

II. METHOD OF MEASUREMENT

Most of the roads of Calcutta are unplanned and are not alike. Some of the roads in a traffic junction are narrow, while some others are wide. The sketches of three typical representative sites with the plying traffic center-line, microphone location, and the surrounding buildings have been shown in Fig. 2. For studying the characteristic of the sound field at different sites, simultaneous measurements of sound-pressure levels (SPL) at different points around a particular location were made. It was observed that in the majority of the sites the effect of plying traffic distance on measured SPL values was approximately the same as that in a free-field condition, though at a few points in some sites the effects of reflection from surrounding structures were prominent.

Measurements of A-weighted sound-pressure level (SPL) were made for 24 h at an interval of 30 s in which 1800 pieces of data were recorded in the day time (7 a.m.–10 p.m.) and 1080 data were recorded during the night time (10 p.m.–7 a.m.). The sound level meter used in this traffic noise level measurement was a digital sound level meter, Lutron SL-4001 (an IEC 651 type I instrument). The portable sound

TABLE I. Traffic noise monitoring locations in Calcutta metropolis.

| Site number(s) | Site name(s) | Location of sites in the city |
|----------------|--|-------------------------------|
| 01 | Garia More | South East |
| 02 | Jadavpur 8B Bus Terminus on Raja S.C. Mallick Road | South East |
| 03 | Behala 14 No. Bus Terminus on D.H. Road | South West |
| 04 | Taratala Road—D.H. Road Crossing | South West |
| 05 | Gariahat More | South East |
| 06 | Rashbehari Avenue—S.P. Mukherjee Road Crossing | South |
| 07 | Hazra More | South |
| 08 | Khidirpur Road—D.H. Road Crossing | South West |
| 09 | J.N. Road—A.J.C. Bose Road Crossing | South Central |
| 10 | Park Circus VII Point Crossing | South East |
| 11 | Chowringhee—Park Street Crossing | Central |
| 12 | Esplanade—Lenin Sarani Crossing | Central |
| 13 | Moulali More | Central |
| 14 | B.B.D. Bag S.E.—Mission Row Crossing | Central |
| 15 | Bowbazar—College Street Crossing | Central |
| 16 | Sealdah—Mirjapur Crossing | North Central |
| 17 | Strand Road—M.G. Road Crossing | North West |
| 18 | Ganesh Talkie—Chitpur More | North |
| 19 | Manicktala More | North |
| 20 | Ultadanga V.I.P. More | North East |
| 21 | Shyambazar V Point Crossing | North |
| 22 | Chiria More on B.T. Road | North |
| 23 | Nagerbazar More | North East |
| 24 | Dunlop Bridge More | North |

level meter was placed on a rigid stand. The microphone was 1.2 m above the ground and 1 m from the facade of the building at each site. The distance of the microphone from the plying traffic center-line was different for different sites, depending on the width of footpath and road. The actual distance of microphone from the plying traffic center-line for each site has been given in Table II. Sound-pressure levels were manually recorded at intervals of 30 s using A-weighting network and slow meter speed. The sound level meter was calibrated before and after the data recording at each site. The counts of number of vehicles that crossed the point of measurement from either direction on the road was also recorded concurrently with the noise level. Vehicles traveling the roads in the city were divided into three categories on the basis of their size and engine capacity:

light vehicles (LV)—moped, motor cycle, auto-rickshaw,

medium vehicles (MV)—car, taxi, matador van,

heavy vehicles (HV)—Mini-bus, bus, tram, and truck.

The average A-weighted noise emitted by the individual vehicles in the three categories traveling the roads of Calcutta under actual conditions of the noise monitoring site was determined at five different measurement locations when a single vehicle in each category was passing at its free speed. These five measurement locations were selected to represent all the 24 traffic junctions according to the similarity of road conditions and noise-reflecting surfaces. Since the distance of the microphone from the traffic centerline traveled are different for different sites (see Fig. 2) all the recorded values of sound-pressure levels have been converted to the value it would have been at a distance of 4.6 m (15 ft), which

was the minimum distance observed. The statistical average of all these converted sound-pressure levels for vehicles of a particular category was determined to get the mean noise emission level L_m for the same category. Data were recorded for 50 vehicles of a particular category at each location. The total number of mixed vehicles per hour was converted to an equivalent number of vehicles N_i of a particular category, i being l or h representing LV or HV.

III. DATA COMPUTATION

Data recorded for 24 h at each site of measurement were used to compute the hourly equivalent continuous noise level $L_{eq(h)}$, 24 h equivalent continuous noise level $L_{eq(24)}$, and day-night average sound level L_{dn} , traffic noise index (TNI), noise pollution level L_{np} , and the noise exceedence levels L_{10} , L_{50} , L_{90} , and L_{99} . The different formulas used for computation of these parameters are given below:

$$L_{(h)} = L_{eq(h)} = 10 \log \frac{1}{n} \sum_{i=1}^n 10^{L_i/10}, \tag{1}$$

where n = total number of recorded data in the period of 1 h and L_i = the i th sound-pressure level data:

$$L_{eq(24)} = 10 \log \frac{1}{24} \sum_{i=1}^{24} 10^{L_{(h)i}/10}, \tag{2}$$

$$L_{dn} = 10 \log \frac{1}{24} \left[\sum_{i=1}^{15} 10^{L_{(h)i}/10} + \sum_{i=16}^{24} 10^{L_{(h)i} + 10/10} \right], \tag{3}$$

$$\mathbf{TNI} = 4(L_{10} - L_{90}) + L_{90} - 30, \tag{4}$$

CALCUTTA CITY(major roads)

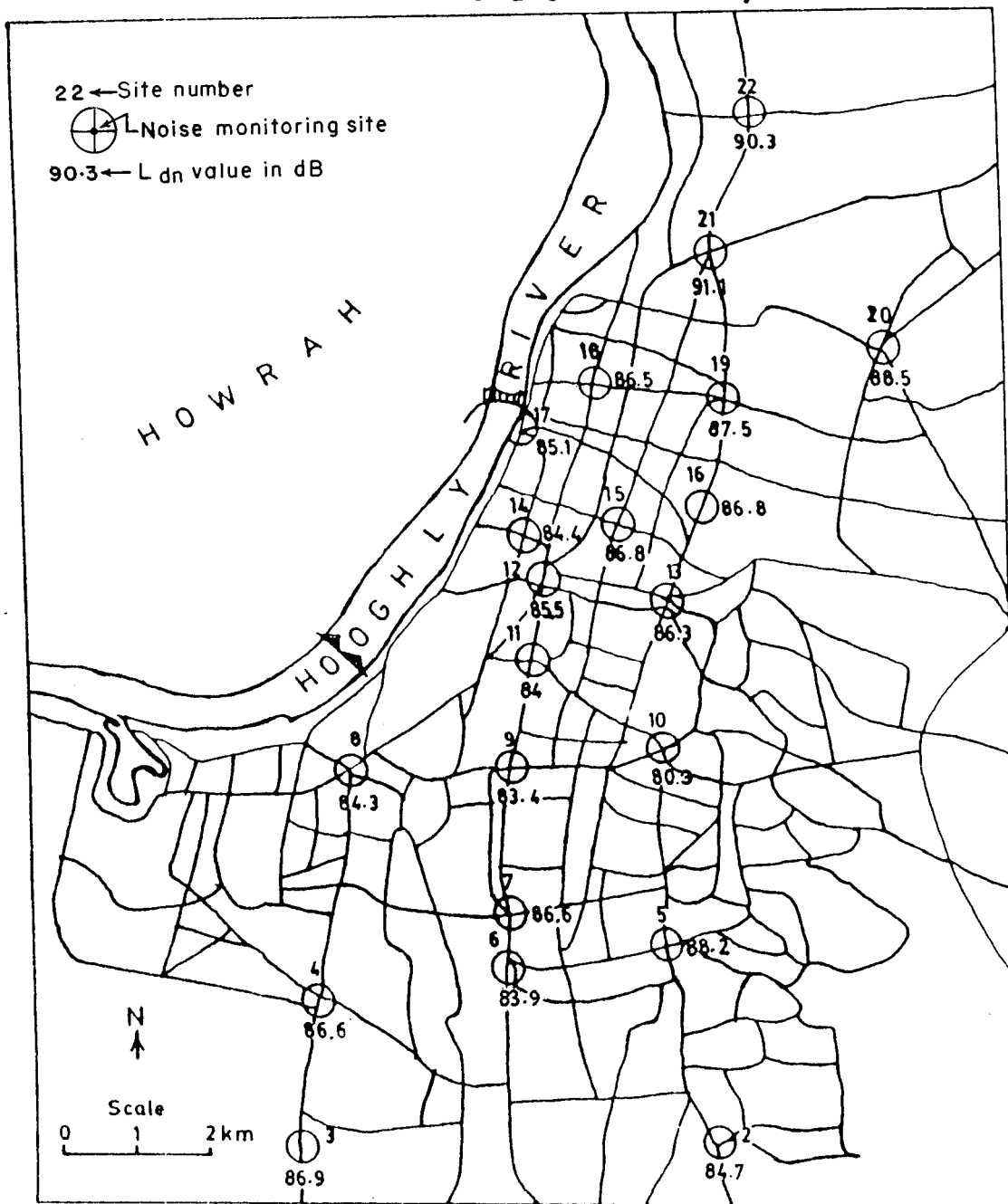


FIG. 1. Location of noise-monitoring sites with corresponding observed L_{dn} values on the map of Calcutta City. The road intersections of the monitoring sites are circled.

$$L_{np} = L_{eq(24)} + (L_{10} - L_{90}). \quad (5)$$

For converting the sound-pressure level, recorded at a particular distance r from the road centerline to its value at 15 ft, the relation used was

$$(L_{eq})_{15 \text{ ft}} = (L_{eq})_r - 20 \log(15/r), \quad (6)$$

with the assumption of free-field condition.

It was assumed that a plot of hourly $L_{eq(h)}$ combined with a term representing the distance to the traffic as a func-

tion of the log of an equivalent number of light/heavy vehicles should be a straight line of the form

$$L_{eq(h)_n} + 20 \log r_n = a \log N_i + b, \quad (7)$$

r_n being the distance of microphone from the plying traffic centerline for the site number n , where n may vary from 1 to 24.

All the noise monitoring sites have been divided into five different zones according to land use. Statistical linear regression analysis was performed on the computed hourly

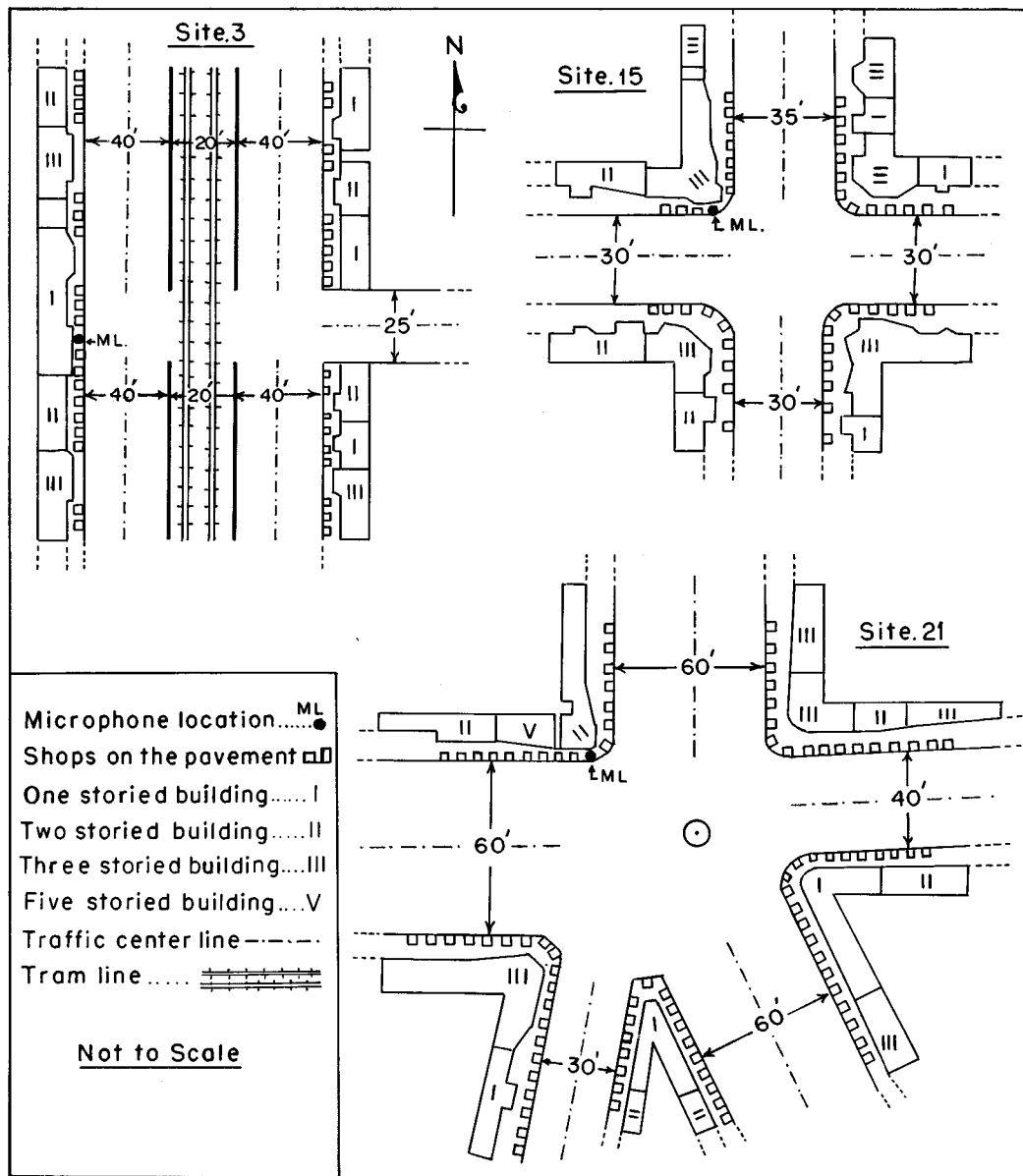


FIG. 2. Three typical representative sites showing the traveled traffic centerline, microphone location, and the surrounding buildings.

$L_{eq(h)}$ data combined with the site-specific $20 \log r_n$ term with $\log(N_i/h)$, i representing either heavy or light vehicles. Regression coefficients were obtained for the five zones and for the entire city, with each set having a and b values both for an equivalent number of light and heavy vehicles. Two sets of regression data were also obtained for L_{dn} and $L_{eq(24)}$ for the entire city.

IV. RESULTS AND DISCUSSION

Table II presents the computed results of $L_{eq(24)}$, L_{dn} , L_1 , L_{10} , L_{50} , L_{90} , L_{99} , L_{np} , and TNI for all 24 measurement locations. The different monitoring sites (circled) have been shown in the map of Calcutta in Fig. 1 with corresponding L_{dn} values posted against each. The measured data of Table II shows that for the entire city, the values of L_{dn} are higher than the corresponding values of $L_{eq(24)}$ by 2–3 dB. The variability of the measured $L_{eq(24)}$ for all the locations are

indicated by the values of L_{np} and TNI given in Table II. Figure 3 shows the variation of noise level ($L_{eq(h)}$), at a fixed distance of 15 ft from the traveled traffic centerline, as a function of the time of day of 24 h for all five zones. The typical dip in the curves for all five zones during 2:00–3:00 a.m. during the night time should be noted. The graph also indicates a lowering of noise level during the afternoon time from 1:00 p.m. to 2:00 p.m. for almost all four zones, except at the residential-industrial zone, where the values of $L_{eq(h)}$ are very random, due to the industrial activities.

The average noise levels L_m for different categories of vehicles on the roads of Calcutta, and their equivalent number of light/heavy vehicles in terms of the average noise emission levels, are given in Table III. Utilizing these conversion factors the hourly traffic density at each locations was converted to the equivalent number of light/heavy vehicles per hour (N_i/h). The hourly $L_{eq(h)}$ values for all sites

TABLE II. Computed values of noise indices in dB for 24 measuring locations of Calcutta metropolis: (using 2880 measured SPL data recorded for each location).

| Study site no. (s) | Distance of SLM from road center-line in feet | Exceedence levels (percentiles) | | | | | | | | |
|--------------------|---|---------------------------------|----------|----------|-------|----------|----------|----------|----------|-------|
| | | $L_{eq(24)}$ | L_{dn} | L_{np} | TNI | L_{99} | L_{90} | L_{50} | L_{10} | L_1 |
| 01 | 15.0 | 83.0 | 85.7 | 101.8 | 112.2 | 58.4 | 67.0 | 78.1 | 85.8 | 94.5 |
| 02 | 15.0 | 82.2 | 84.7 | 103.3 | 119.0 | 53.9 | 64.3 | 78.6 | 85.4 | 93.0 |
| 03 | 20.0 | 84.5 | 86.9 | 104.3 | 117.1 | 58.1 | 68.1 | 80.4 | 87.8 | 95.6 |
| 04 | 37.5 | 84.4 | 86.6 | 103.3 | 114.3 | 56.5 | 68.8 | 80.0 | 87.6 | 95.9 |
| 05 | 32.0 | 86.2 | 88.2 | 108.7 | 127.7 | 57.7 | 67.7 | 81.6 | 90.2 | 97.3 |
| 06 | 45.0 | 81.3 | 83.9 | 102.0 | 117.5 | 54.4 | 64.4 | 78.0 | 85.2 | 91.1 |
| 07 | 30.0 | 84.0 | 86.6 | 104.4 | 118.7 | 56.2 | 67.0 | 80.4 | 87.4 | 94.5 |
| 08 | 25.0 | 84.3 | 87.7 | 104.3 | 118.4 | 54.9 | 68.2 | 80.6 | 88.3 | 94.2 |
| 09 | 25.0 | 83.4 | 86.0 | 102.9 | 115.8 | 57.1 | 67.9 | 79.7 | 87.4 | 93.3 |
| 10 | 23.0 | 80.3 | 83.0 | 99.2 | 111.0 | 59.3 | 65.4 | 77.5 | 84.3 | 89.0 |
| 11 | 42.5 | 84.0 | 86.1 | 107.0 | 127.5 | 53.1 | 65.5 | 80.8 | 88.5 | 94.2 |
| 12 | 20.0 | 85.5 | 87.5 | 108.0 | 126.4 | 57.1 | 66.2 | 81.0 | 88.8 | 96.5 |
| 13 | 40.0 | 86.3 | 89.2 | 105.3 | 117.1 | 58.7 | 71.3 | 81.9 | 90.3 | 97.2 |
| 14 | 40.0 | 84.4 | 86.7 | 109.8 | 134.4 | 55.2 | 63.1 | 80.5 | 88.4 | 94.8 |
| 15 | 15.0 | 86.8 | 89.3 | 113.0 | 140.0 | 53.6 | 65.2 | 82.4 | 91.4 | 97.2 |
| 16 | 32.0 | 86.8 | 89.3 | 111.4 | 135.9 | 56.9 | 67.7 | 82.5 | 92.3 | 97.8 |
| 17 | 15.0 | 85.1 | 87.8 | 106.8 | 123.9 | 58.8 | 67.2 | 81.8 | 88.9 | 95.6 |
| 18 | 15.0 | 86.5 | 89.5 | 105.5 | 117.6 | 61.4 | 71.5 | 82.1 | 90.5 | 96.9 |
| 19 | 30.0 | 87.5 | 90.6 | 108.5 | 124.7 | 58.7 | 70.7 | 83.0 | 91.7 | 97.8 |
| 20 | 30.0 | 88.5 | 90.0 | 117.5 | 150.2 | 52.9 | 64.5 | 82.7 | 93.4 | 99.1 |
| 21 | 30.0 | 91.1 | 93.1 | 113.3 | 132.9 | 63.6 | 74.0 | 85.4 | 96.2 | 101.2 |
| 22 | 40.0 | 90.3 | 93.4 | 110.4 | 125.1 | 63.6 | 74.9 | 86.3 | 94.9 | 100.3 |
| 23 | 20.0 | 92.1 | 95.4 | 119.9 | 150.4 | 55.6 | 69.2 | 87.1 | 97.0 | 101.7 |
| 24 | 40.0 | 92.0 | 94.1 | 116.5 | 140.4 | 61.9 | 72.2 | 86.2 | 96.8 | 102.5 |

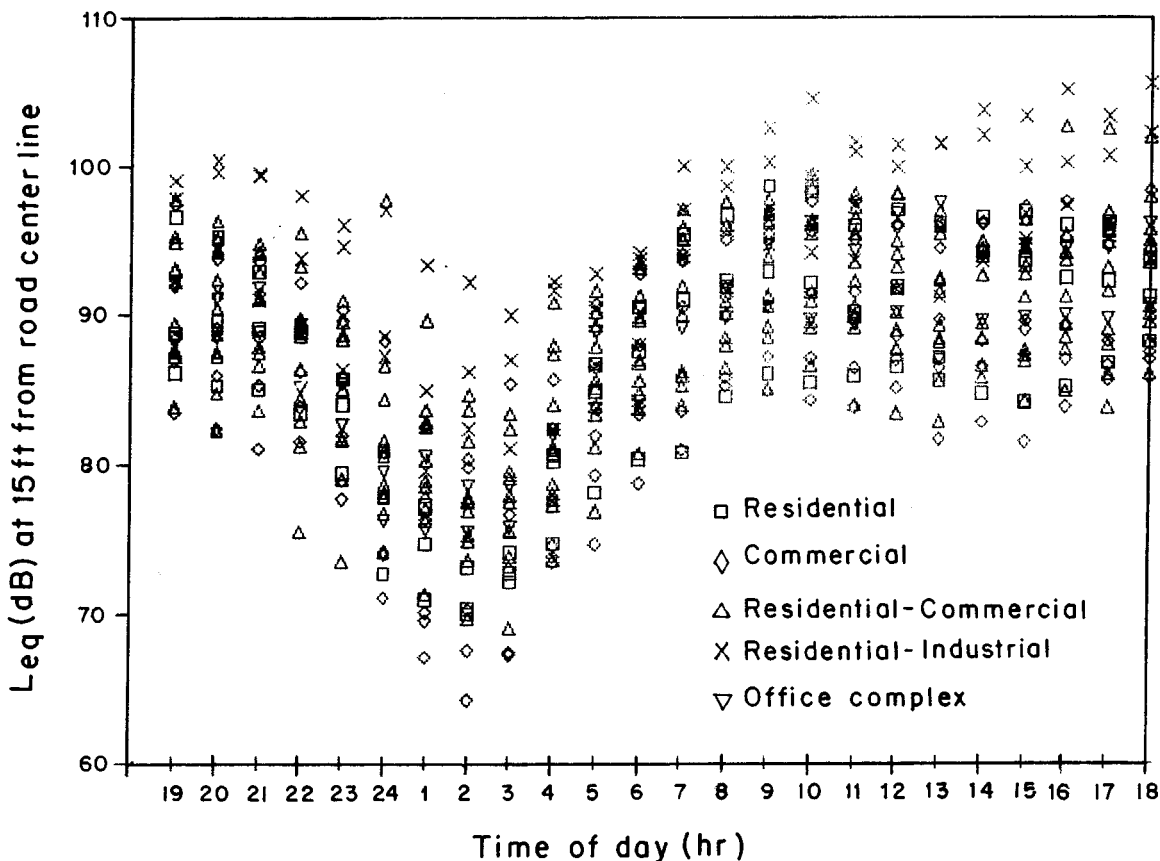


FIG. 3. Variation of hourly $L_{eq(h)}$ at a distance of 15 ft from the traveled traffic centerline over a 24-h period for five zones of Calcutta.

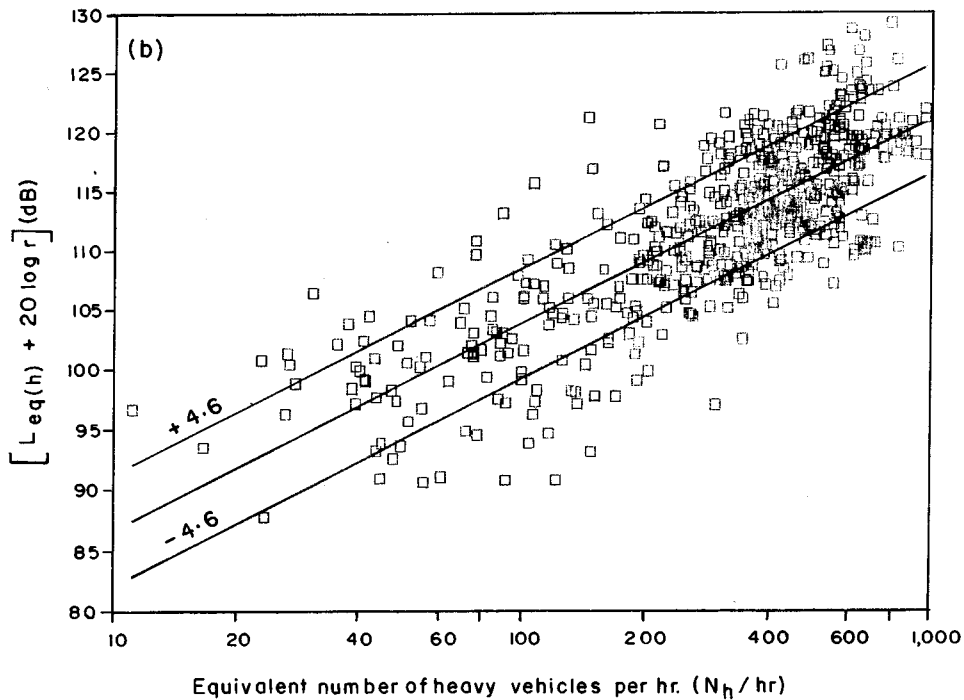
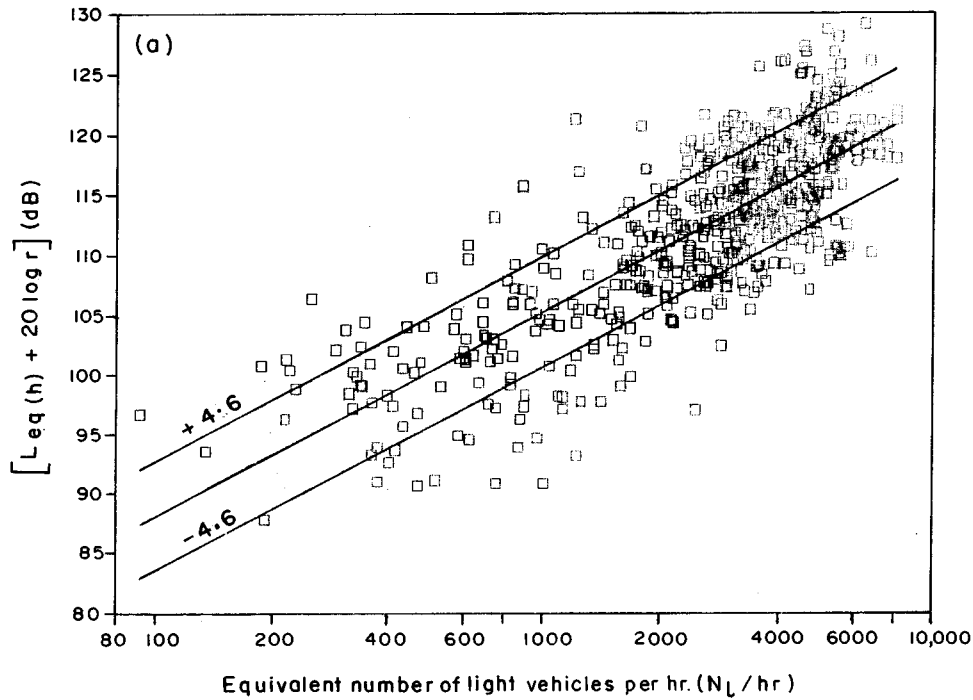


FIG. 4. Variation of $[L_{eq(h)} + 20 \log r]$ as a function of equivalent number of (a) light vehicles per hour and (b) heavy vehicles per hour for the entire city.

were added with the site-specific $20 \log r_n$ values and the results were plotted against the logarithms of corresponding equivalent traffic densities per hour. The plots with their regression fit lines for equivalent light vehicle density and heavy vehicle density have been shown in Fig. 4(a) and (b), respectively. Table IV presents the regression analysis data, a and b for different zones, entire city, $L_{eq(24)}$ and L_{dn} . Different regression equations for different zones can be ob-

tained by substituting the corresponding values of a and b in Eq. (7). The regression equation for the entire city can be written as

$$L_{eq(h)} + 20 \log r = 53.8 + 17.2 \log N_L, \quad (8a)$$

$$L_{eq(h)} + 20 \log r = 69.6 + 17.2 \log N_h, \quad (8b)$$

TABLE III. Mean noise emission level of three different categories of vehicles on roads of Calcutta with the conversion factors for equivalent number of light and heavy vehicles.

| Category of vehicles | Average noise level (L_m) in dB (at 15 ft from vehicle) | Equivalent number of light vehicles | Equivalent number of heavy vehicles |
|----------------------|---|-------------------------------------|-------------------------------------|
| Light vehicles (LV) | 83.2 | 1.00 | 0.12 |
| Medium vehicles (MV) | 85.8 | 1.82 | 0.22 |
| Heavy vehicles (HV) | 92.4 | 8.32 | 1.00 |

at a distance r from the traveled traffic centerline. The value of $[L_{eq(h)} + 20 \log r]$ was predicted using these regression equations. In Fig. 4, the line graphs correspond to the predicted values and from the distribution of measured data points it can be seen that almost 70% of the data points lie within ± 4.6 dB of the predicted values. Therefore the regression model developed here can be used for the prediction of the extent of noise level generation, at any distance r from the traveled traffic centerline, to a first approximation with the confidence interval given by twice the standard error (as

TABLE IV. Regression analysis data for $L_{eq(h)} + 20 \log r$ and (N_i/h) for different zones and the entire city [Calcutta metropolis].

| Serial no. | Zones | Equivalent vehicle category | Intercept (b) | Standard error of b | Slope (a) | Standard error of a |
|------------|------------------------|-----------------------------|-------------------|-----------------------|---------------|-----------------------|
| 1 | Residential | Light | 56.9 | ± 4.2 | 16.2 | ± 1.2 |
| | | Heavy | 71.7 | ± 4.2 | 16.2 | ± 1.2 |
| 2 | Commercial | Light | 41.7 | ± 4.5 | 19.7 | ± 1.2 |
| | | Heavy | 59.8 | ± 4.5 | 19.7 | ± 1.2 |
| 3 | Residential-commercial | Light | 57.2 | ± 4.0 | 16.3 | ± 0.7 |
| | | Heavy | 72.2 | ± 4.0 | 16.7 | ± 1.7 |
| 4 | Residential-industrial | Light | 59.6 | ± 4.0 | 16.7 | ± 1.7 |
| | | Heavy | 75.0 | ± 4.0 | 16.7 | ± 1.7 |
| 5 | Office complex | Light | 59.3 | ± 3.0 | 15.2 | ± 1.3 |
| | | Heavy | 73.4 | ± 3.0 | 15.2 | ± 1.3 |
| 6 | Entire city | Light | 53.8 | ± 4.6 | 17.2 | ± 0.6 |
| | | Heavy | 69.6 | ± 4.6 | 17.2 | ± 0.6 |
| 7 | $L_{eq(24)}$ all sites | Light | 13.0 | ± 3.9 | 29.1 | ± 7.7 |
| | | Heavy | 39.8 | ± 3.9 | 29.1 | ± 7.7 |
| 8 | L_{dn} all sites | Light | 18.6 | ± 3.9 | 28.2 | ± 7.7 |
| | | Heavy | 44.6 | ± 3.9 | 28.2 | ± 7.7 |

in the Table IV). The regression equations for $L_{eq(24)}$ and L_{dn} for the entire city are

$$L_{eq(24)} + 20 \log r = 13.0 + 29.1 \log N_1, \quad (9a)$$

$$L_{eq(24)} + 20 \log r = 39.8 + 29.1 \log N_h, \quad (9b)$$

$$L_{dn} + 20 \log r = 18.6 + 28.2 \log N_1, \quad (10a)$$

$$L_{dn} + 20 \log r = 44.6 + 28.2 \log N_h. \quad (10b)$$

These equations enable an easy and quick prediction of the ambient noise level at any distance r from the traveled traffic centerline by knowing the equivalent number of light/heavy vehicle density.

V. CONCLUSION

Characterization of road traffic noise level of Calcutta during 1993, in terms of standard noise indices, have been made. Regression equations for predicting the ambient noise levels, at any distance r from the traveled traffic centerline, by knowing the equivalent number of light/heavy vehicles per hour have been developed.

ACKNOWLEDGMENTS

One of the authors, particularly Biva Roy, is grateful to her colleague Dr. B. K. Chatterjee of the Dept. of Physics, Bose Institute for some helpful discussions on data analysis and she also acknowledges the help of Mr. Dhritiman Roy in bulk data handling. This work was partially supported by the financial assistance of University of Kalyani.

- Anonymous (1991). "Noise level in metropolitan cities Part III Calcutta," Report of Central Pollution Control Board, Delhi, Control of Urban Pollution Series, CUPS, 1-19.
- Dixit, G. R., Mahadevan, T. N., and Kapoor, R. K. (1982). "A noise pollution survey of Bombay," Scavenger **12** (2), 20-25.
- Kumar, V., and Jain, V. K. (1994). "A study of noise in various modes of transport in Delhi," Appl. Acoust. (U.K.) **43** (1), 57-65.
- Mohanan, V. (1987). "Acoustics of Domestic Environments," J. Acoust. Soc. Ind. **15** (1), 221-223.
- Pancholy, M., Chhapgar, A. F., and Singhal, S. P. (1967). "Noise Survey in Calcutta," J. Sci. Ind. Res. **26**, 314-316.
- Prabhu, B. T. S. and Muni Chakrabarty, R. L. (1978). "An urban noise model for planners," J. Sound Vib. **58**, 595-596.
- Rao, M. G. S., Rao, P. R., Dev, K. S., and Rao, K. V. (1989). "A model for computing environmental noise level due to motor vehicle traffic in Visakhapatnam City," Appl. Acoust. (U.K.) **27**, 129-136.
- Rao, P. R., and Rao, M. G. S. (1990). "Traffic noise pollution in the city of Visakhapatnam," Scavenger **21** (1), 9-13.
- Rao, P. R., and Rao, M. G. S. (1991). "Prediction of L_{A10T} traffic noise levels in the city of Visakhapatnam, India," Appl. Acoust. (U.K.) **34**, 101-110.
- Roy, B., Santra, S. C., Chandra, S., and Mitra, B. (1984). "Traffic Noise Level in Calcutta," Sci. Cult. **50**(8), 62-64.
- Shrivastava, J. P., Shah, R. K., and Desai, M. N. (1986). "Noise Pollution in Ahmedabad city," J. Acoust. Soc. Ind. **14**(2), 41-47.

A re-examination of risk estimates from the NIOSH Occupational Noise and Hearing Survey (ONHS)

Mary M. Prince, Leslie T. Stayner, Randall J. Smith, and Stephen J. Gilbert
*Education and Information Division, National Institute for Occupational Safety and Health,
4676 Columbia Parkway, Cincinnati, Ohio 45226*

(Received 13 July 1994; revised 9 April 1996; accepted 20 September 1996)

This paper describes a new analysis of data from the 1968–72 National Institute for Occupational Safety & Health (NIOSH) Occupational Noise and Hearing Survey (ONHS). The population consisted of 1172 (792 noise-exposed and 380 “controls”) predominately white male workers from a cross section of industries within the United States. The analysis focused on how risk estimates vary according to various model assumptions, including shape of the dose-response curve and the amount of noise exposure among low-noise exposed workers (or controls). Logistic regression models were used to describe the risk of hearing handicap in relation to age, occupational noise exposure, and duration exposed. Excess risk estimates were generated for several definitions of hearing handicap. Hearing handicap is usually denoted as an average hearing threshold level (HTL) of greater than 25 dB for both ears at selected frequencies. The frequencies included in the binaural averages were (1) the articulation-weighted average over 1–4 kHz, (2) the unweighted average over 0.5, 1, and 2 kHz, and (3) the unweighted average over 1, 2, and 3 kHz. The results show that excess risk estimates for time-weighted average sound levels below 85 dB were sensitive to statistical model form and assumptions regarding the sound level to which the “control” group was exposed. The choice of frequencies used in the hearing handicap definition affected the magnitude of excess risk estimates, which depended on age and duration of exposure. Although data were limited below 85 dB, an age-stratified analysis provided evidence of excess risks at levels ranging from 80 to 84 dB, 85–89 dB, and 90–102 dB. Due to uncertainty in quantifying risks below 85 dB, new data collection efforts should focus on better characterization of dose-response and longitudinal hearing surveys that include workers exposed to 8-hour time-weighted noise levels below 85 dB. Results are compared to excess risk estimates generated using methods given by ANSI S3.44-1996.

[S0001-4966(97)01102-8]

PACS numbers: 43.50.Qp, 43.64.Wn [GAD]

INTRODUCTION

The most common goal for protecting workers from the auditory effects of occupational noise has historically been the preservation of hearing for speech discrimination. With this protection goal in mind, the National Institute for Occupational Safety and Health (NIOSH) defined hearing handicap as a *binaural average* of hearing levels exceeding 25 dB at the audiometric test frequencies of 1, 2, and 3 kHz and 0.5, 1, and 2 kHz (NIOSH, 1972). Here, the term “binaural average” is used to identify the mean value for the left and right ears. Using these definitions, NIOSH (1972) estimated the excess risk of hearing handicap as a function of age, sound levels and duration of occupational noise exposure. Excess risk, also known as percentage risk, is defined as the percentage of individuals with hearing handicap among individuals exposed to daily 8-hour occupational noise exposure after subtracting the percentage of individuals who would typically incur such a handicap due to aging in an unexposed population. For a 40-year lifetime exposure to average daily (8-hour) noise levels of 80, 85, and 90 dB in the workplace, NIOSH (1972) estimated the excess risk to be 3%, 15%, and 29%, respectively for the binaural average over 1, 2, and 3 kHz. [Unless otherwise noted, “dB” implies an A-weighted 8-hour time-weighted average sound level.] Table I compares the NIOSH (1972) excess risk estimates for the binaural

average over 0.5, 1, and 2 kHz to those developed by other organizations at approximately the same time.

Since the publication of the 1972 NIOSH Criteria Document, statistical methods for analyzing categorical data outcomes have been improved to assess risk of disease (Breslow and Day, 1980a). The aim of this paper is to reevaluate the models used to generate excess risk estimates from data collected for the NIOSH 1968–72 Occupational Noise and Hearing Survey (ONHS) (Lempert and Henderson, 1973). Using these newer statistical methods, the paper examines the relationship between exposure to noise and risk of noise-induced hearing handicap (NIHH) and highlights areas of uncertainty in estimating risks. These results will be compared to the 1972 NIOSH analysis (NIOSH, 1972) and to the ANSI S3.44 (ANSI, 1996) standard, which adopted the methods developed by the International Standards Organization (ISO 1971, 1990). The data collected in the NIOSH survey are of continuing interest since they were obtained before hearing protection devices were widely used in the U.S. Observations by NIOSH investigators during sound level surveys and management’s impressions of their respective plants did not indicate that participating companies had policies *requiring* hearing protection use. Use of protectors, if available at all, were left to the discretion of the workers. No mass use of hearing protectors was noted in any of the

TABLE I. Comparison of excess risk estimates by organization.^a

| Average daily exposure level (dB) | Excess risk estimates (%) | | |
|-----------------------------------|---|-----------------|------------------|
| | Hearing handicap defined as HTLs > 25 dB for the average of 0.5, 1, 2 kHz | | |
| | NIOSH (1972) | ISO 1999 (1971) | EPA ^b |
| 80 | 3 | 0 | 5 |
| 85 | 15 | 10 | 12 |
| 90 | 29 | 21 | 22.3 |
| 95 | 43 | 29 | not available |

^aThese excess risk estimates are for a 40-year lifetime exposure to noise.

^bFrom Federal Register, Vol. 39, No. 244, 1974.

companies surveyed (Cohen, personal communications, 1996).

I. RELEVANCE TO COMPARABLE STUDIES OF NOISE-INDUCED HEARING LOSS

Several investigators (Robinson and Sutton, 1975; Royster and Thomas, 1979; NCHS, 1965; Robinson, 1970; Yerg *et al.*, 1978) have examined the relationship of noise-induced permanent threshold shift (NIPTS) and occupational

noise exposure. Studies similar to the NIOSH 1968–72 Noise Survey with respect to time period and methods of data collection include Baughn (1973), Passchier-Vermeer (1968) and Burns and Robinson (1970). These studies will be the main focus of our review of the relevant noise and hearing surveys from this period. These studies have been used by ISO 1999 (1971) and ANSI S3.44 (ANSI, 1996) to estimate the risk of NIHH or NIPTS. Table II presents major study characteristics of each of these studies.

As shown in Table II, only the Baughn (1973) study did not screen their workers for otologic abnormalities. These studies report that their populations were restricted to workers with daily constant levels of steady state noise exposure for the entire length of employment. A review of these studies' limitations has been addressed by Ward and Glorig (1975) and Yerg *et al.* (1975). They include possible contamination of non-steady state noise exposure in the population and small sample sizes for subjects exposed to continuous steady state for daily sound levels below 90 dB. The Passchier-Vermeer report (1968) reviewed published studies and was not specifically designed to address criteria for a noise standard. The NIOSH study (Lempert and Henderson, 1973) was specifically designed to examine risk of noise-

TABLE II. Overview of selected noise and hearing studies used to assess risk of hearing handicap.

| Study | Population examined in risk analysis | Exposure characteristics | Screening of subjects |
|-------------------------------|---|---|---|
| NIOSH ONHS study ^a | 1172 predominately white males from a cross section of industries within the U.S.
792 noise-exposed
380 low noise-exposed | Workers exposed to steady state noise for up to 41 years of exposure to daily noise levels from 80–102 dB.
Workers exposed to impact or impulse noise were excluded. | Workers were excluded if they had previous noisy jobs, significant firearm exposure (military or recreational), ear disease or other otologic abnormalities, incomplete job histories or unknown noise exposures. |
| Baughn, 1973 | 6,835 audiograms on Caucasian male employees from a Midwestern auto parts plant: 1960–65. Stable work force, light turnover. Employees drawn from surrounding farming-industrial community. Age range: 18–68 yrs. | Workers assigned to three 8-hour TWA exposure levels: 78, 86, and 92 dB:
N=852–78 dB
N=5150–86 dB
N=833–92 dB
Age used as uniform measure of exposure duration. | No Otological screening of subjects.
2/3 of available tests were excluded due to significant known or unknown exposures. |
| Passchier-Vermeer, 1968 | 4557 Caucasian workers from an industrial population in The Netherlands:
4096 males
461 females | Include only workers with constant noise exposure levels for an 8-hour shift for all exposure years considered. | Workers excluded if they had previous noise exposure during other jobs, otologic abnormalities. |
| Burns & Robinson, 1970 | 759 noise-exposed workers and 97 non-noise exposed controls from a variety of occupations. Subjects were volunteers.
422 males
337 females | Exposed daily to steady state noise for periods of up to 50 years. | Excluded individuals with existing or previous ear disease or abnormality, exposure to firing weapons, workers whose noise exposure could not be quantified, and those with language difficulty. |

^aLempert and Henderson, 1972.

induced hearing handicap as a basis for establishing health based occupational standards. The following summary of the study methods is from a NIOSH technical report by Lempert and Henderson (1973).

II. STUDY METHODOLOGY

A. Survey population

In 1968, the U.S. Public Health Service undertook a nationwide study, called the Occupational Noise and Hearing Survey (ONHS). The study was continued and completed by NIOSH in 1972. The aim of the survey was "to characterize noise exposure levels in a variety of industries, to describe the hearing status of workers exposed to such noise conditions, and to establish a relationship between occupational noise exposure and hearing handicap that would be applicable to general industry." Subjects for the study were recruited through notices at industrial hygiene conferences and through the regional offices of the U.S. Public Health Service. All companies interested in participating were considered if certain priority considerations applied. These included (1) existence of a factory or occupational noise conditions having noise levels relevant to developing noise standards and criteria, and (2) a work force with a wide range of years of exposure to such noise levels.

The data collected in the survey included noise measurements, personal background information, medical and otological data and audiometric examinations. Noise level measurements (using Bruel-Kjaer Sound Level Meters) were taken at different areas of each plant and tape recordings were used for laboratory analysis of noise characteristics. A questionnaire was used to obtain information on each worker's job history, military service, hobbies, and medical history pertinent to ear abnormalities and hearing difficulty. An otoscopic inspection of the ears was also made, usually after the completion of the questionnaire. Measurements of hearing levels (using a Rudmose RA-108 audiometer) for pure tone frequencies of 0.5, 1, 2, 3, 4, and 6 kHz in the right and left ears of the workers were conducted in a Rudmose audiometric travel van (model RA-113). Workers from noisy workplaces were always tested at the beginning of their work shift.

For plants with less than 500 employees, the entire work force was tested. For larger plants, a random sample was selected. Individuals from each plant who worked in offices or other quiet work areas were also included in the survey to provide control data.

B. Screened population for analysis

The survey population was "screened" to exclude individuals with prior noise exposure (from occupational and non-occupational sources) and medical or otologic conditions that might affect a person's risk of hearing loss, independent of occupational noise levels at the time of the survey. Criteria for data exclusion included (1) uncertainty in the noise exposure history or validity of audiometric tests and (2) evidence that hearing loss might have been caused by factors other than occupational noise exposure (e.g., military history, other non-occupational noise exposures, head

trauma, other audiological/otologic medical conditions). Workers exposed to noise that was not continuous (e.g., discrete impact sounds or noise with highly variable and unpredictable levels) and all maintenance workers were also excluded. Due to the relatively small number of females in the survey population, all analyses were limited to 1172 males (792 noise-exposed and 380 controls).

C. Variable definitions

1. Definition of hearing handicap

The major outcome of interest is hearing handicap, defined as a binaural average hearing threshold level of greater than 25 dB for a selected set of frequencies. In this analysis, the set of frequencies includes (a) 0.5, 1, and 2 kHz, (b) 1, 2, and 3 kHz and (c) 1, 2, 3, and 4 kHz (herein denoted as 1-4 kHz). The 1-4 kHz frequency average was recommended by an American Speech-Language-Hearing Association (ASHA) Task Force (ASHA, 1981), which focused on the need to include frequencies most affected by noise exposure. The ASHA Task Force recommended that percentage formulas should include hearing threshold levels for 1, 2, 3, and 4 kHz, with low and high fences of 25 and 75 dB, representing 0 percent and 100 percent hearing handicap boundaries, respectively (ASHA, 1981). In this analysis, the ASHA recommendation was modified by calculating a weighted average across frequencies rather than an arithmetic average over the test frequencies of 1, 2, 3, and 4 kHz. Weights were assigned according to frequency specific articulation indexes (ANSI, 1969). The articulation index (AI) is a weighted fraction representing (for a given listening situation) the effective proportion of the speech signal that is available (above a masking noise level or hearing threshold) to a listener for conveying speech intelligibility (ANSI, 1969).

Average hearing threshold levels (HTL_{avg}) using the articulation indexes as weights were calculated [Eq. (1)] and then averaged over both ears:

$$HTL_{avg} = \frac{HTL_{1k}W_1 + HTL_{2k}W_2 + HTL_{3k}W_3 + HTL_{4k}W_4}{W_1 + W_2 + W_3 + W_4}, \quad (1)$$

where, $W_1 = 0.24$, $W_2 = 0.38$, $W_3 = 0.34$, and $W_4 = 0.24$ are the weights at 1, 2, 3, and 4 kHz, respectively. This definition will be referred to as the "1-4 kHz AI average" definition of NIHH.

2. Measurement of noise exposure

Daily 8-hour time-weighted average (TWA) noise exposure was estimated for each worker or worker group using (1) area survey samples, (2) interviews with workmen and supervisors to establish typical workday patterns and (3) time-study charts. These charts segmented the workday into a succession of exposures at specific noise levels and for specified durations. Discussions with both management and workmen were necessary to determine changes in noise exposure over the course of many years. Consideration was given to variations in occupational noise conditions due to placement or relocation of machinery and as well as changes in workers' work routine and locations. The reported noise

TABLE III. Covariates considered for inclusion in the analysis of the NIOSH survey.

| Variables | Coding conventions |
|---|--|
| Age at examination | Continuous variable: age in years |
| | Categorical: ^a |
| | 17–27 years |
| | 28–35 years |
| | 36–45 years |
| 45–54 years | |
| >54 years | |
| Duration of noise exposure | Continuous variable: duration in years |
| | Categorical: ^{a,b} |
| | 0–1 years |
| | 2–4 years |
| | 5–10 years |
| 11–20 years | |
| > 20 years | |
| Sound level, L_{NE} , A-weighted 8-hour, time-weighted Average (TWA) sound level—dB, where L_{NE} =average sound levels for exposed workers; L_0 =average sound levels for control population | Continuous variable |
| | “Centered” at L_0 , dB: ($L_{NE}-L_0$) |
| | L_0 was initially fixed to 79 dB but then estimated in models presented in the text. |
| | |
| | |

^aCategories were the same as NIOSH, 1972.

^bIn the 1972 NIOSH analysis, those exposed to noise for less than 6 months were coded as “0” for duration of exposure. In the current analysis, controls were coded as “0” for duration of exposure and exposed individuals with less than 6 months of exposure were given a value of 0.25.

levels for the study population represent A-weighted eight hour TWA sound levels calculated assuming a 5 dB exchange rate (i.e., 5 dB increase in sound level is exchanged against a factor of 2 in duration within the workday). All levels were measured with sound level meters set to “slow” response. The A-weighted daily noise levels were available on the 792 noise-exposed individuals but not available for the 380 controls. Although sound levels for the control population were not recorded, they were reported to be below 80 dB (Lempert and Henderson, 1973).

3. Other covariates

Other covariates of interest in this paper were age and duration of exposure in years. The risk of hearing handicap was examined in relation to the covariates defined in Table III. For models that included categorical variables for age (reference: 17–27 years) and duration (reference: 0–1 years), four indicator variables were created for different levels of age and duration exposed (Table III). For models that included continuous variables for duration exposed, all controls were reassigned a duration value of zero because it was assumed that duration has no effect on the hearing of the controls. Exposed individuals with less than six months were coded as 0.25 years (midpoint between 0 and 0.5 years).

D. Statistical models

Logistic regression models were used to analyze hearing handicap, defined as the proportion of individuals whose binaural hearing level is greater than 25 dB for averages over selected frequencies. These logistic regression models were fit using the SAS LOGISTIC procedure (SAS Institute, Inc., 1989) and the nonlinear minimization (NLMINB) routine in S-PLUS (Statistical Sciences, Inc., 1993).

Stratified contingency table analyses (Breslow and Day, 1980a) were performed to assess these data for qualitative evidence of hearing handicap due to exposure to noise after controlling for age. The 2×2 contingency tables were stratified by one year age groups and the prevalence of hearing handicap among the three noise-exposed categories of 80–84 dB, 85–89 dB, and 90–102 dB were contrasted to the prevalence among controls. One-sided tests for detecting increased risks were computed using Mantel–Haenszel methods. Further details of this method are found in Breslow and Day (1980a).

The quantitative relationship between hearing handicap and the covariates (defined below) was modeled using logistic regression methods (Breslow and Day, 1980b). These models can be expressed as

$$p = \Pr(Y = 1 | X) = \frac{e^{F(X; \alpha, \beta, \phi, L_0)}}{1 + e^{F(X; \alpha, \beta, \phi, L_0)}}, \quad (2)$$

where, p = the expected proportion with average hearing level greater than 25 dB (indicated by $Y=1$), given \mathbf{X} . ($Y = 0$ indicates an average hearing level is less than or equal to 25 dB);

\mathbf{X} = a vector of explanatory variables containing information on age, sound level, and duration of exposure;

$$F(X; \alpha; \beta; \phi; L_0) = \alpha + \beta_1 (\text{Age}) + [\beta_{2j} (L_{NE} - L_0)^\phi], \quad (3)$$

where

L_{NE} = A-weighted 8-hour TWA sound level for noise-exposed workers in dB;

L_0 = parameter for nominal TWA sound level in control population in dB;

ϕ = shape parameter on dB effect;

α = intercept parameter;

β_1 = slope coefficient for age effect;

β_{2j} = the slope coefficient for the j th duration of exposure (years) interval, where $j=1,2,3$ represent exposure intervals of 2–4 years, 5–10 years, and > 10 years of exposure, respectively.

1. Model development

The first step in the analysis was to fit several hierarchical logistic regression models and compare nested models using likelihood ratio tests (LRTs) to identify which parameters significantly improved the fit to the data (Fienberg, 1987). The fit of the model to the data was evaluated using a likelihood ratio test and examining the log likelihood statistic, \mathbf{G} , which is defined by the expression

$$\mathbf{G} = -2\sum\{Y \log p + (1 - Y)\log(1 - p)\}, \quad (4)$$

where the summation is over all individuals in the sample (Breslow and Day, 1980b).

In general, the lower the value of G , the better the fit between the model and the data. Differences in G statistics for nested models may be interpreted as chi-squares (Breslow and Day, 1980b).

To be consistent with the methodology used in the 1972 NIOSH Noise Criteria Document (NIOSH, 1972), the model was initially fit assuming that the sound level for the control population (L_0) was 79 dB and the shape parameter (ϕ) was 1. This was accomplished by first fitting models with main effects only and then adding interaction terms between (a) duration exposed and daily TWA sound level (L); (b) duration exposed and age; and (c) age and sound level. These interaction terms tested whether there should be allowance for differing slopes by levels of other variables. Models with linear main effect of age, duration exposed, and sound levels were fit with an assumption that all control 8-hour TWA sound levels (L_0) were 79 dB. This assumption was made because individual noise exposure data for controls were unavailable but were known to be less than 80 dB (Lempert and Henderson, 1973). Other models with categorical main effects of age and duration were also examined. The final steps of the analysis involved further model refinements that included (1) assuming there is a nondecreasing relationship of prevalence with sound level and duration; (2) refitting functional forms identified by the LRT strategy accordingly; (3) assuming more flexible models for incorporating the effects of sound level by permitting the shape parameter (ϕ) to vary; (4) permitting the control sound level (L_0) to vary from 79 dB; and (5) conducting sensitivity analyses of the impact of critical assumptions.

A final form of the model was fit such that all the parameters (including L_0 and ϕ) were solved for simultaneously. This model form was fit with the following restriction: the control level, L_0 , was bounded at 55 dB and 79 dB. For the final model, a two-sided 90 percent confidence interval was calculated for several noise levels using the parametric percentile bootstrap method (Efron and Tibshirani, 1986; Efron, 1982). The same restrictions on L_0 were applied to 1000 bootstrap samples generated to obtain the confidence limits for excess risk. Graphical displays of bootstrap-based confidence limits were smoothed using localized linear regression smoothers in S-PLUS (Statistical Sciences, Inc., 1993).

2. Excess risk estimation

Excess risk for a particular age is defined as the difference between the risk of hearing handicap for the noise-exposed population, given exposure duration, and the exposure sound level, L_{NE} (where $L_{NE} > L_0$), and the risk of hearing handicap among controls. The excess risk associated with exposure to noise evaluated at a given age was estimated from logistic models using the following relationship:

$$\text{Excess Risk} = \Pr[Y = 1 | \text{age, duration, and intensity of exposure}] - \Pr[Y = 1 | \text{age, control}]. \quad (5)$$

Hence, excess risk is assumed to be equivalent to the increase in risk of hearing handicap associated with noise exposure.

3. Sensitivity analyses

Sensitivity analyses were performed to examine how model assumptions may affect the results (i.e., excess risk estimates). Assumptions evaluated in this analysis included (1) the shape of the dose-response relationship; (2) the sound level, L_0 , for the control population; and (3) the effect of using different definitions of hearing handicap. The first two issues were addressed during model development, where each assumption was varied while the other remained fixed.

A comparison of how excess risk estimates varied with different definition of hearing handicap was also examined in this analysis. The new definition (1–4 kHz AI average) was compared to definitions previously used by NIOSH (1972)—binaural hearing levels averaged over 1–3 kHz and 0.5–2 kHz. The analyses of different hearing handicap definitions were based on our final model for each definition of hearing handicap: the model in which the control sound level (L_0) and shape parameter (ϕ) were simultaneously estimated.

III. RESULTS

Figure 1 shows the hearing threshold level distributions (10th, 50th, 90th percentiles) for different frequencies by age and sound level categories for exposed and control workers. All hearing thresholds shown are averages over the left and right ears. Data are classified into five age groups and three noise exposure categories (80–87 dB, 88–92 dB, 92–102 dB). The boundaries for the age and sound level categories were selected to provide adequate sample size (i.e., at least 30) in each cell. Sample sizes for the noise-exposed [$n(NE)$] groups are provided for each graph with median exposure duration. The sample sizes for the controls [$n(C)$] are the same within age groups (shown in top panel of each column). The graphs show similar exposure durations within each age cell and increasing trends for median hearing threshold levels with age and sound level. In all cases, control hearing threshold levels are lower than the noise-exposed population. The tendency of median hearing thresholds to increase with increasing age and sound level is also illustrated. The spread of the distribution (given by the 10th and 90th percentiles) is most marked at 3 and 4 kHz.

A scatter plot of the ONHS data showing years of duration versus TWA sound level, L_{NE} , is presented in Figure 2. The vast majority of the data points are at sound levels above 85 dB. Almost 50% of the noise-exposed population had 8-hour TWA sound levels between 85 and 89 dB, while only 27% were exposed below 85 dB. There are also very few data points corresponding to 40 or more years of noise exposure. This lack of data in the low exposure region (80–84 dB) and among workers with long duration of exposure (> 40 years) imposes limitations for quantifying the risks for workers exposed to noise throughout their working lifetime (e.g., 45 years, assuming a worker starts work at 20 years of age and ends at 65 years).

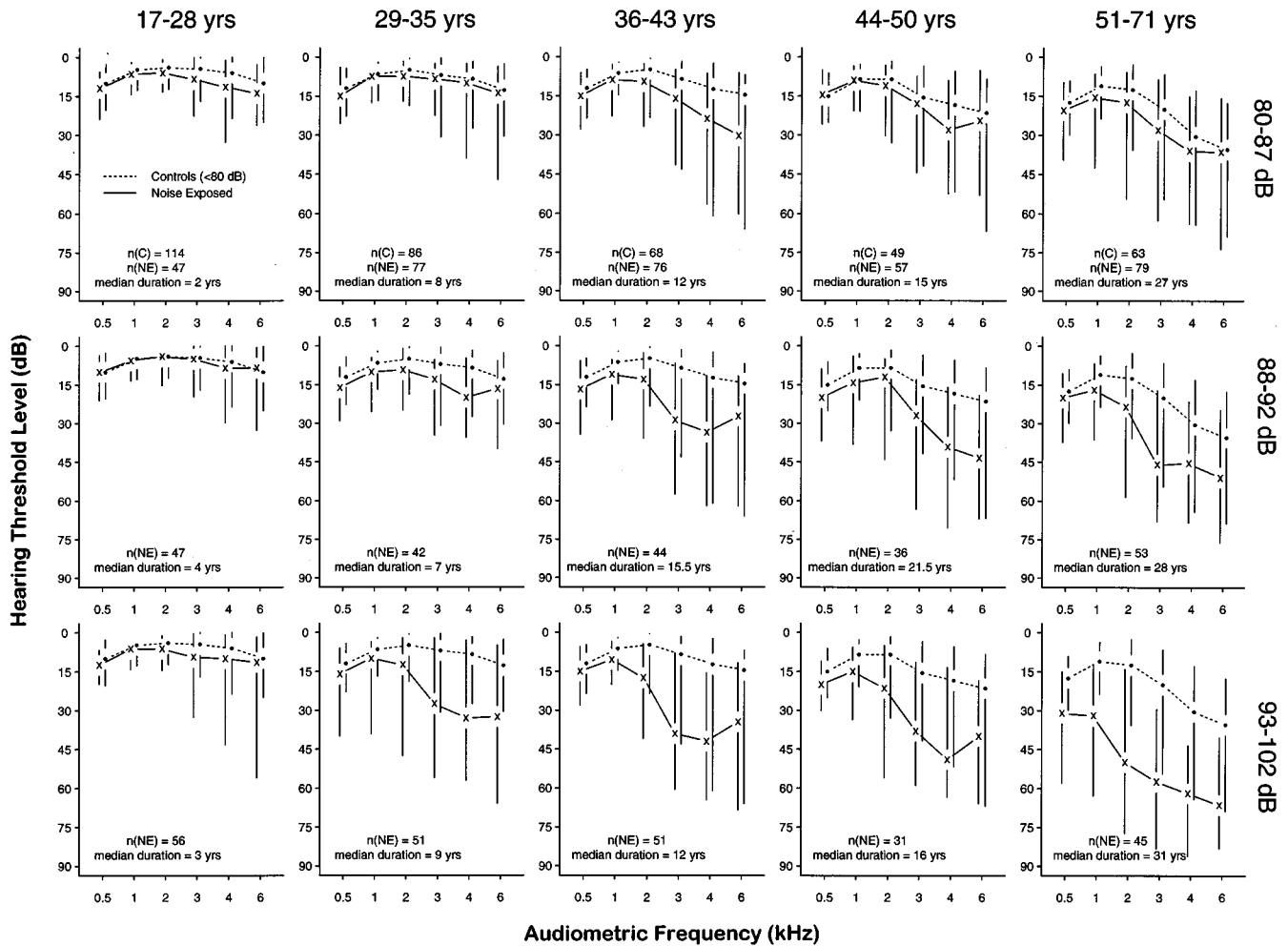


FIG. 1. Distribution of hearing levels (10th, 50th, and 90th percentiles) by age and average daily sound level (L_{NE}) categories from the NIOSH 1968–72 survey.

Despite the limited amount of data in the low exposure region, the Mantel–Haenszel age-stratified analysis provided evidence of positive excess risk associated with sound levels ranging from 80 to 84 dB ($p=0.02$), as well as 85 to 89 dB ($p=0.02$) and 90 to 102 dB ($p<0.001$).

Age was found to be a highly significant predictor of hearing handicap due to noise whether it was modeled using a continuous variable ($\chi^2=211$, $df=1$) or a set of categorical variables ($\chi^2=213$, $df=4$). The fitted categorical effects for age suggested a linear trend (data not shown). This trend was also apparent when models including sound level and duration were fit. Therefore, the simpler models with linear effects for age (as a continuous variable) were subsequently considered in the final models. The addition of either years of exposure or sound level (L_{NE}) significantly improved the fit of the model containing age. The addition of both terms further increased the goodness of fit. A statistically significant interaction ($\chi^2=29.6$, $df=4$) was observed between sound level and categories of years of exposure. No significant interactions between age and duration exposed, nor age and sound level were observed in this data set.

Based on this preliminary analysis, the best fitting linear model is a function of continuous age, categorical levels of duration of exposure, and sound level. However, this model

initially appeared to be inappropriate for risk assessment because the excess risk of hearing handicap predicted by this model decreased over limited ranges of sound level and duration of exposure. For example, the parameter estimates of this model suggested that the risk of hearing handicap was lower for individuals with greater than 20 years of exposure than it was for individuals with 11–20 years of exposure when the sound level was above 90 dB. We found no statistically significant difference between the fit of the model that combined the two highest duration categories (11–20 years and > 20 years combined to > 10 years) and the model with separate parameters for each duration category. This suggested that risks remain essentially flat after 10 years of exposure, and that these two categories could be combined. This initial model was further refined to describe predicted risks of hearing handicap as a nondecreasing function of exposure duration and sound level. The models also assume that the effects of sound level depend on durations greater than or equal to two years.

To test whether a linear sound level effect ($\phi=1$) adequately described the relationship between noise exposure and risk of hearing handicap, higher order terms for the sound level effect were tested in the analysis. Using a quadratic sound level term for exposure ($\phi=2$) appreciably im-

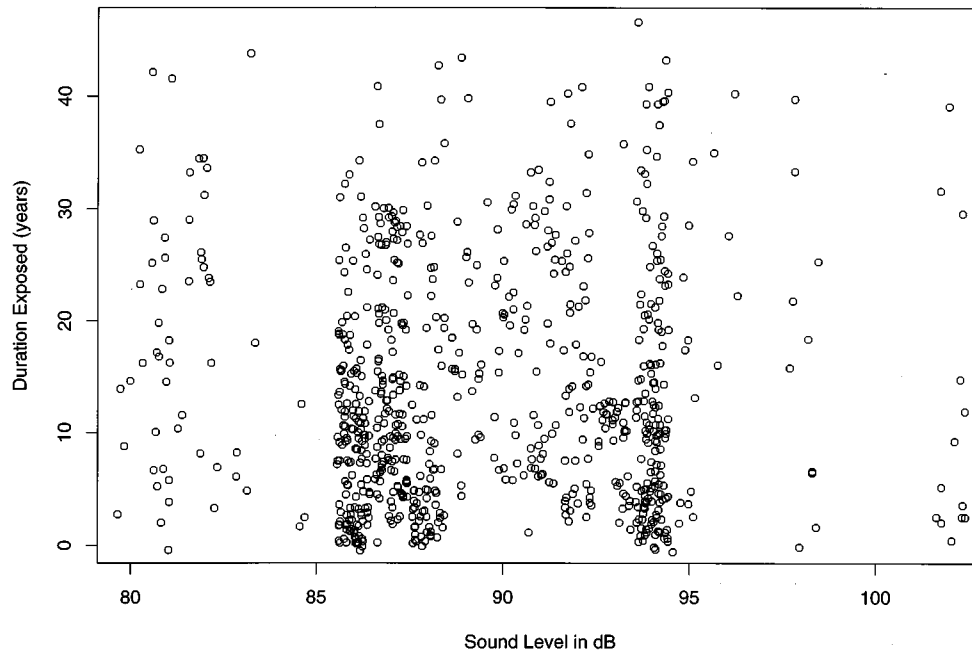


FIG. 2. Scatter plot of exposure sound levels (L_{NE}) versus exposure duration of 792 noise-exposed workers from the NIOSH 1968–72 survey.

proved the goodness of fit of the model relative to the linear model. Using a cubic sound level term ($\phi=3$) resulted in only a slight improvement in the goodness of fit over the quadratic model. The final results from fitting models with linear, quadratic, or cubic sound level terms and assuming control sound levels, L_0 , of 79 dB are presented in Table IV. Also shown are the results from fitting a final model in which the control value and the shape parameter were found to be 73 dB and 3.4, respectively (model 4, Table IV). Model 4 is denoted as the “best fitting model,” because it produced the best fit to the data. These results indicate considerable variability in excess risk estimates depending on model form and is likely due to lack of data at lower sound levels. This was most marked at average daily sound levels less than or equal to 85 dB. Figure 3 presents excess risk estimates with smoothed 90 percent confidence limits for 65-year-old males with greater than 10 years of exposure as a function of sound level for the “best fitting model” (model 4).

A. Sensitivity analyses

1. Assumption regarding control 8-hour TWA sound levels

To examine the sensitivity of risk estimates to the assumed sound level for the control group, the value of L_0 was varied from 60 to 79 dB and optimum values of the shape parameter, ϕ , were estimated. As L_0 is varied, there is very little variation in the log likelihood statistic, G , whereas the excess risk estimate for noise exposure at a level of 80 dB varies between 0.06 and 2.9 (Table V). The results also show that the optimum value of ϕ decreases considerably as the assumed value of L_0 increases. This analysis suggests that information regarding the distribution of occupational sound levels within the control population is important in estimating the risk of noise-induced handicap in noise-exposed populations. The variability of excess risk estimates below 85 dB seen in Fig. 3 may be attributed to the lack of accurate

TABLE IV. Excess risk percent of noise-induced hearing handicap for workers aged 65 with 10 or more years of noise exposure at various time-weighted average sound levels for linear, quadratic, cubic, and best fitting models.

| Exposure sound level (L_{NE}) in dB | Excess risk estimates for various models | | | | |
|---|--|-----------------------------|---|-------------------------------|--------------|
| | Quadratic (model 2)
$\phi=2$ | Cubic (model 3)
$\phi=3$ | Best fitting (model 4) ^a
$\phi=3.4$ | Linear dB models ($\phi=1$) | |
| | | | | Present analysis | NIOSH (1972) |
| 80 | 0.2 | 0.02 | 1.2 | 3.4 | 3 |
| 85 | 8.3 | 3.2 | 7.6 | 19.6 | 15 |
| 90 | 24.5 | 17.8 | 22.3 | 32.2 | 29 |
| 95 | 28.5 | 36.2 | 38.3 | 40.6 | 43 |
| 100 | 44.1 | 41.2 | 44.0 | 45.5 | 56 |

^aRisk estimates can be generated using the following equation: $Logit [Pr(Y > 25 \text{ dB HL})] = -5.0557 + 0.0812(\text{Age}) + [\beta_j (\text{Duration}=1)] * [(L_{NE} - L_0) / (102 - 73)]^\phi$, where, $\beta_j = 2.6653, 3.989,$ and 6.4206 , respectively, for the j th duration of exposure for 2–4 years, 5–10 years, and >10 years, respectively and Y is the AI-weighted binaural average over 1–4 kHz. For the best fitting model, ϕ was estimated to be 3.4 and $L_0 = 73$ dB. The term $(102 - 73)$ in the denominator of the coefficient describing the effect of duration and sound level, standardizes the exposure term such that the maximum exposure equals one. This was done for ease of comparison to models with differing estimates for L_0 and ϕ .

TABLE V. Excess risk percent of hearing handicap from logistic regression models assuming different sound level values for controls with corresponding shape parameters: Male workers aged 65 with duration exposure greater than 10 years.

| Exposure sound level
(L_{NE}) in dB | Control sound levels (L_R) in dB and corresponding shape parameters (ϕ) | | | | |
|--|--|--------------------|--------------------|--------------------|--------------------|
| | 60 ($\phi=5.46$) | 65 ($\phi=4.67$) | 70 ($\phi=3.88$) | 75 ($\phi=3.10$) | 79 ($\phi=2.49$) |
| 80 | 2.9 | 2.4 | 1.8 | 0.8 | 0.06 |
| 85 | 9.6 | 9.1 | 8.3 | 7.0 | 5.2 |
| 90 | 23.4 | 23.2 | 22.8 | 22.1 | 21.0 |
| 95 | 39.2 | 39.0 | 38.6 | 38.1 | 37.3 |
| 100 | 45.2 | 44.9 | 44.4 | 43.6 | 42.6 |
| Log likelihood statistic, G | 1039.794 | 1039.715 | 1039.645 | 1039.631 | 1039.754 |

sound level data among control subjects and the sparseness of the data for workers exposed at sound levels below 85 dB.

2. Definition of hearing handicap

To examine whether excess risk estimates varied by the definition of hearing handicap used, we compared the 1–4 kHz AI average definition to two other definitions using the same fence (> 25 dB HL), the unweighted binaural frequency averages of 0.5–2 kHz and 1–3 kHz. All three definitions were examined using a model that included age and a dose metric effect defined as $(L_{NE} - L_0)^\phi$ times duration categories (e.g., 2–4, 5–10, and > 10 years). The resultant estimated shape parameters for the 0.5–2 kHz and 1–3 kHz binaural averages were 4.5 and 4.9, respectively, with L_0 equal to 55 dB for both.

Under these models, excess risk estimates were affected by both the definition of hearing handicap and the age of the

worker. We also found that changing from the articulation index to a simple average of 1–4 kHz did not substantially affect excess risk estimates (results not shown). For workers aged 65 years (with > 10 years of exposure), excess risks for the 1–3 kHz definition are higher than excess risk for the new definition, particularly for sound levels above 85 dB (Fig. 4A). However, among workers aged 45 with similar years of exposure, excess risk estimates are similar for all sound levels for the 1–3 kHz definition and the new definition (Fig. 4B). For younger workers (aged 30 years) with 5 to 10 years of exposure, excess risk estimates for the definitions that included 3 kHz and/or 4 kHz, are similar for all sound levels (Fig. 4C).

IV. DISCUSSION

The results of these analyses indicate that there is an excess risk of noise-induced hearing handicap (NIHH) at 8-hour time-weighted average (TWA) sound levels greater than or equal to 85 dB. The excess risk below 85 dB was not well defined in our analysis. However, the Mantel–Haenszel test result suggests that there is a positive and statistically significant excess risk at levels between 80 and 84 dB.

These findings also indicate two major areas of uncertainty for quantifying the risk of noise-induced hearing handicap. The first concerns the sensitivity of the analysis to the assumed sound level for the control group (L_0). The second relates to the shape of the dose-response relationship between the sound levels among the noise-exposed group (L_{NE}), duration exposed, and the risk of NIHH. Risk estimates were found to vary considerably for values of L_{NE} below 85 dB, depending on the assumed control sound level (L_0), and the shape parameter (ϕ) for the sound level effect (e.g., linear, quadratic, or cubic) in the models.

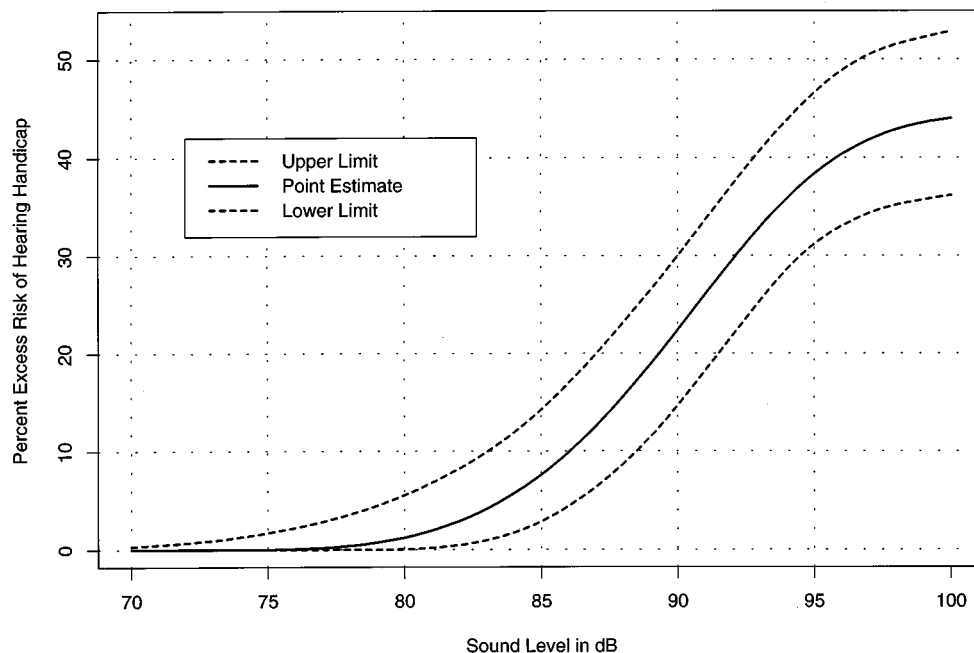


FIG. 3. Excess risk (percent) of hearing handicap (AI-weighting, 1–4 kHz) and bootstrap-based 90% confidence limits from model 4 (Table IV) for 65-year-old males exposed for greater than 10 years to varying levels of noise (L_{NE}).

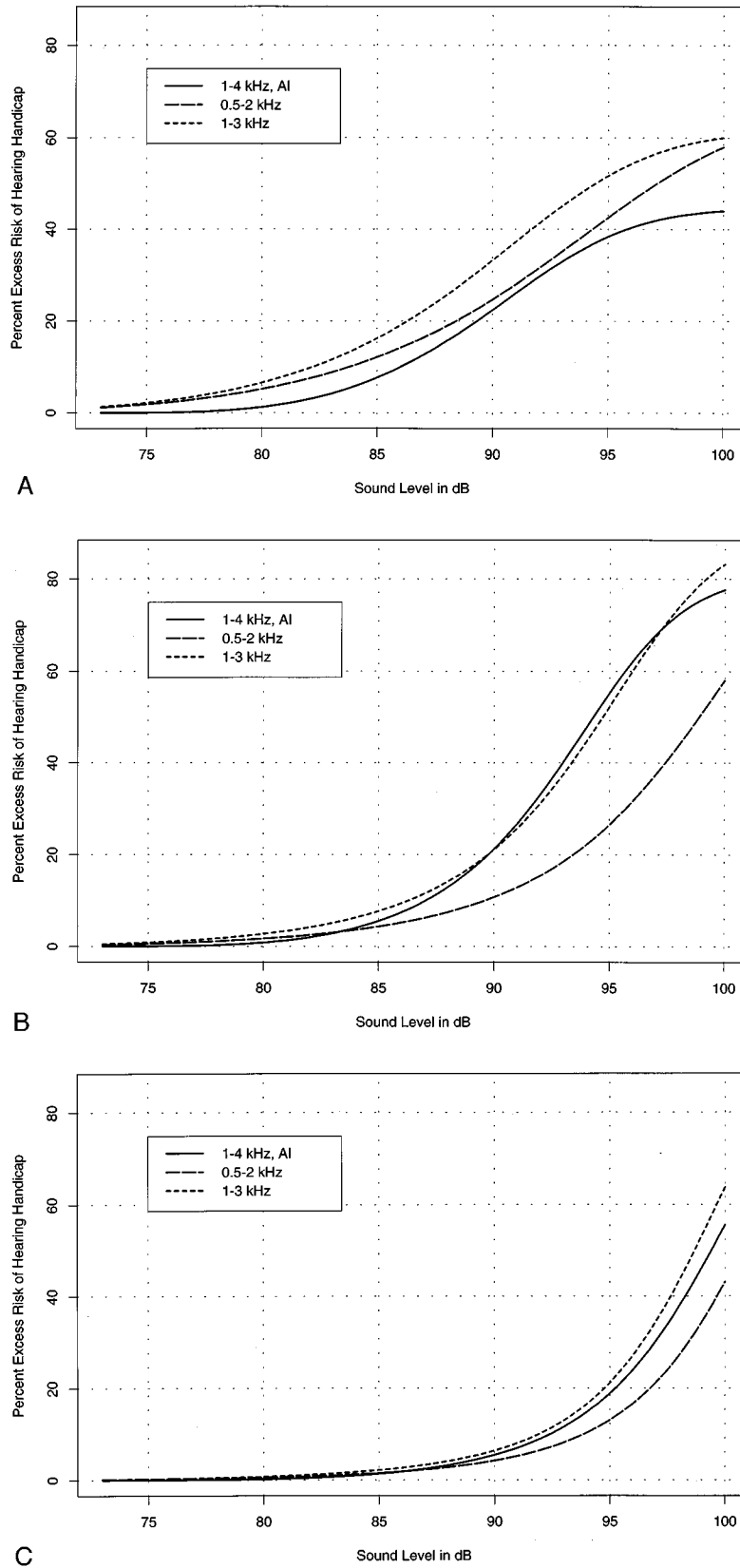


FIG. 4. Excess risk percent from model 4 (Table IV) as a function of varying sound levels (L_{NE}) for different definitions of hearing handicap. Panel A: Age 65 years, duration exposure >10 years. Panel B: Age 45, duration exposure >10 years. Panel C: Age 30 years, duration exposure 5–10 years.

The previous NIOSH (1972) estimate of excess risk for a 40-year working lifetime of exposure to noise was approximately 15 percent at 85 dB. A linear regression model of log hearing levels was used in the previous analysis (NIOSH, 1972) to estimate the risk of hearing handicap. NIHH was defined as an average binaural hearing level greater than 25 dB based on unweighted averages of 0.5–2 kHz or 1–3 kHz. The model described in the 1972 NIOSH criteria document (NIOSH, 1972) is mathematically equivalent to a probit model in which the risk of a hearing level greater than 25 dB is of interest. The results from the previous NIOSH analysis (NIOSH, 1972) also appear to be consistent with the assumption that the control group was exposed to sound levels near 79 dB.

It is clear that models which include a quadratic or cubic effect for the sound level effect fit significantly better than the linear effect model and produce lower excess risk estimates for sound levels below 85 dB than similar models used in the 1972 NIOSH analysis (NIOSH, 1972). As shown in Table IV, the point estimates of excess risk at 85 dB from the quadratic and cubic models are 8 percent and 3 percent, respectively. The quadratic and cubic models fit better than the linear model, mainly due to the effect of sound level in the low exposure region. For sound levels less than or equal to 90 dB, the excess risk estimates from fitting a linear model (Table IV) are slightly higher than those in the NIOSH (1972) analysis. Thus, the disparity in excess risk estimates presented in Table IV may be attributed primarily to the different functional forms (i.e., shape of the sound level effect) of the fitted models. The logistic model used in this analysis assumes the existence of a plateau in risk after 10 years of exposure duration.

The analysis comparing different indicators of NIHH show that patterns of excess risk as a function of average daily sound level depend on age. Differences in excess risk were nominal for the 1–4 kHz average, irrespective of whether HTLs were weighted by the frequency-specific articulation indexes. These differing results by age may be attributable to the fact that the effect of aging on risk of hearing handicap may overshadow any incremental increases in excess risk due to noise exposure. In the upper range of duration and sound level, the dose-response curve shows signs of a plateau effect. The analysis also suggests that the effect of sound intensity and duration of exposure is dependent on frequency. Hearing damage at 3 and 4 kHz is expected to occur sooner than loss at lower frequencies (0.5, 1, or 2 kHz). Definitions that exclude the higher frequencies tend to be less sensitive to noise damage and may require longer durations of exposure to a given sound level to see significant excess risks in the population.

Figure 4A and B suggests that the most suitable definition of hearing handicap may depend on the population characteristics, such as age, exposure duration, and degree of hearing handicap already accrued, as well as whether one chooses to identify preclinical or later stages of hearing handicap. The addition of the most sensitive frequencies to a hearing handicap definition is a valid option if the goal is to have a measure that addresses both prevention and identification of hearing handicap.

A. Data limitations

The cross-sectional design of this study presented limitations for estimating the risk of noise-induced hearing handicap. For example, the 8-hour TWA sound levels, L_{NE} , were determined at one point in time and are assumed to be representative of exposure over the entire length of an employee's job experience. This may have introduced a substantial source of error in the estimation of L_{NE} . As a means of reducing this error, the screened ONHS population included only workers who remained in the same job for the entire time that they worked at the study facility. These workers were then assigned an 8-hour TWA sound level based on noise measurements and job activities at the time of the survey. It is possible that larger errors in estimating 8-hour TWA sound levels over a long period of time may have occurred for workers with longer durations of exposure. It is also possible that the workers with long durations included in this study represented a population which may have been less sensitive to the adverse effects of noise on hearing. This may have contributed to the observed decrease in risk with increasing sound level, L_{NE} , for durations greater than 20 years. Hence, the cross-sectional design of the survey introduces areas of concern for predicting NIHH risks over a working lifetime.

B. Modeling caveats

The data limitations described above also placed limitations on the modeling approach and interpretations presented in this paper. One data limitation with implications for modeling the risk of noise-induced hearing handicap, was the lack of information on the distribution of 8-hour TWA sound levels among the control population. This is a crucial omission because all excess risk estimates depend on the risk of handicap among workers with low levels of occupational noise exposure (in this study, defined as exposure to sound levels less than 80 dB).

Due to this lack of data, a very simplistic assumption was made: sound levels in the control population could be represented by a single number. This is problematic in terms of model interpretation. First, it ignores the possibility that there may be a distribution of sound levels below 80 dB for this population. Second, this assumption results in a model that implies that the estimated value (L_0) is a threshold sound level at which no excess risk of noise-induced hearing handicap is predicted regardless of the duration of exposure. Hence, the statistical criteria used in model development are valid only if all of the controls were below a defined threshold.

These modeling issues underscore the fact that all models are likely to be dependent on assumptions used to account for uncertainty in the available data. This analysis did not model hearing threshold levels as a continuous variable. Therefore, calculation of NIPTS using these models are not possible. The analysis also did not extensively explore other possible shapes for the sound level function other than $(L_{NE} - L_0)^\phi$. Furthermore, modeling exposure duration as a categorical variable limits finer examination of the relationship of duration of exposure on risk of hearing handicap.

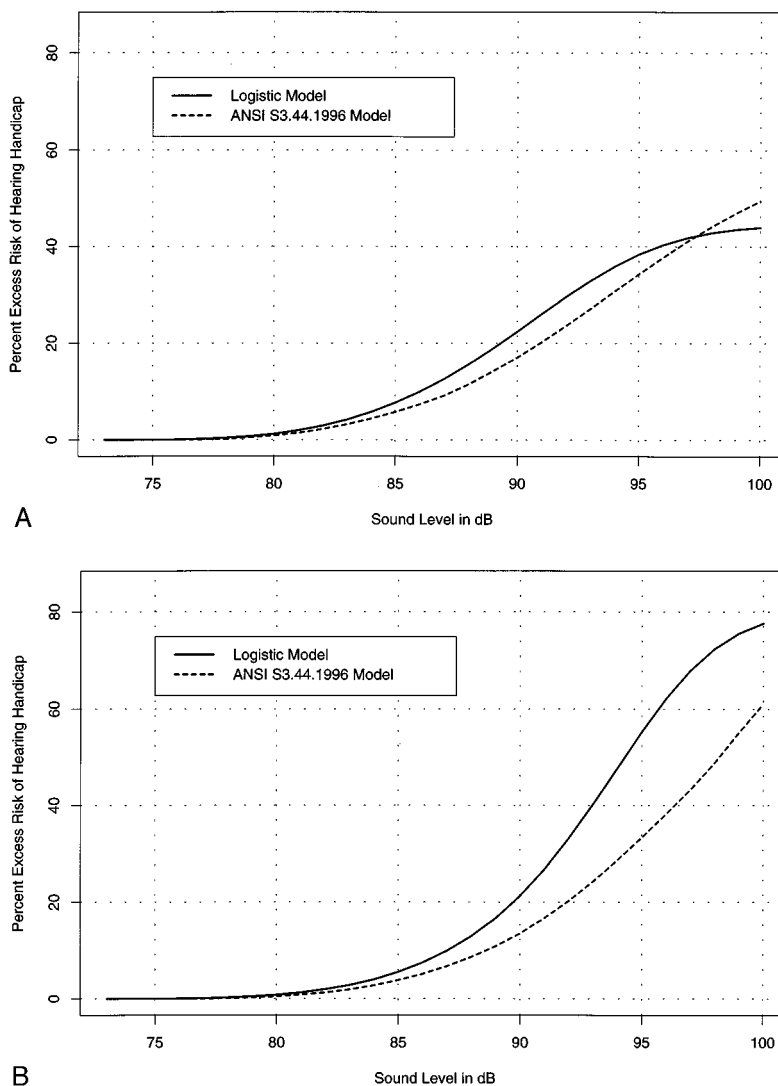


FIG. 5. Excess risk (AI-weighting, 1–4 kHz) as a function of sound level (L_{NE}) according to model 4 (Table IV), in comparison with curves derived from ANSI S3.44.1996 using Annex A database. Panel A: age 65 years, exposure duration 45 years. Panel B: age 45 years, exposure duration 25 years.

The models described in this paper were developed on the basis of this particular data set. Inferences based on the ONHS data set are also limited by its cross-sectional nature and the fact that exposure data was absent for the control population exposed to 8-hour TWA sound levels below 80 dB. As a result, the use of this model for other data sets with differing characteristics and different methods of data collection would not necessarily provide similar results.

C. Comparison of new risk estimates to ANSI S3.44

Given this updated analysis of the NIOSH (1972) data, it is of interest to compare these results to estimates generated using methodology developed by the International Standards Organization (ISO 1971, 1990), which was adopted in the ANSI S3.44 standard (ANSI, 1996). This standard was issued to provide a more accurate and more generalized model of the relationship between NIPTS and occupational noise exposure for people at different ages and duration of exposure. ANSI S3.44 (ANSI, 1996) provides mathematical pro-

cedures for estimating hearing handicap due to noise exposure for populations free from auditory impairment (other than that due to noise).

The data from studies by Passchier-Vermeer (1968) and by Burns and Robinson (1970) are the basis of the ANSI S3.44 (ANSI, 1996) standard for estimating NIPTS. As with the NIOSH (1972) study, most of the noise-exposed workers were exposed to daily noise levels ranging from 85 to 95 dB.

The Passchier-Vermeer (1968) and Robinson (1970) models are represented by different mathematical equations which include an aging (non-noise) component in dB and a NIPTS component in dB. For each model, the equation for NIPTS was determined by age correcting the noise-exposed workers' hearing threshold levels to get the NIPTS component. An empirical equation was developed for NIPTS in terms of noise level and exposure time. For each model, the aging and NIPTS components were combined to compute total hearing threshold level in dB (ANSI, 1996). A simple arithmetic average of the NIPTS values of Passchier-Vermeer and Robinson are used to predict NIPTS for ANSI

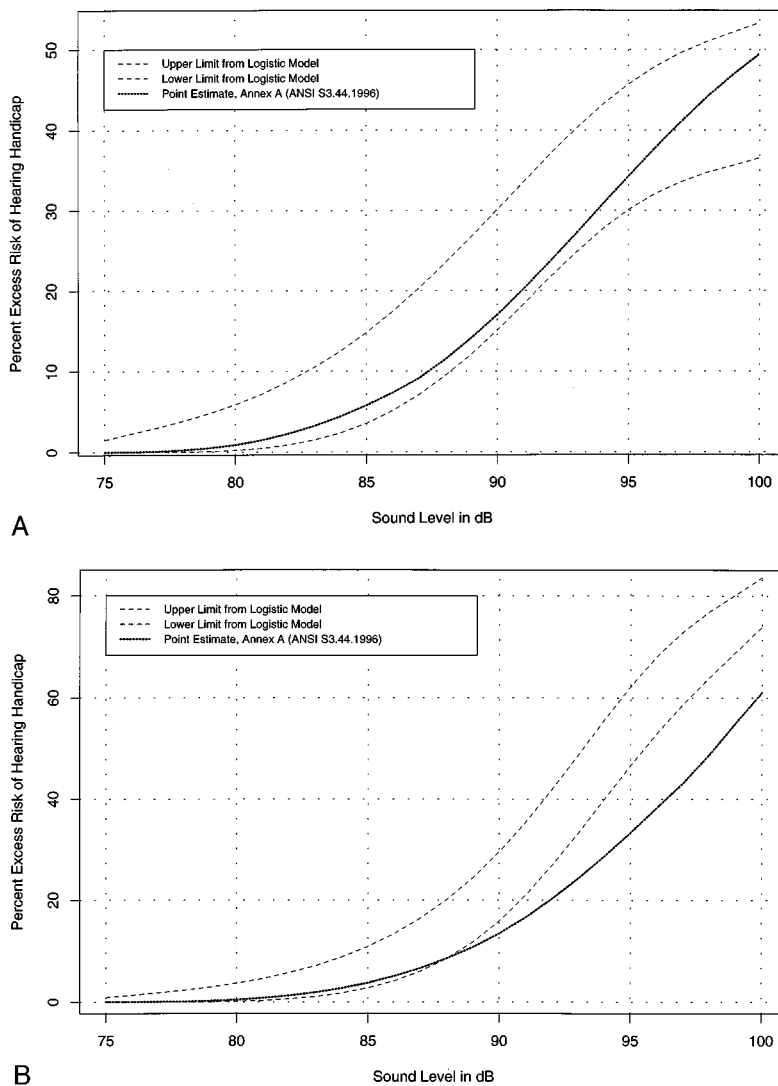


FIG. 6. Bootstrap-based 90% lower and upper confidence limits for excess risk (AI-weighting, 1–4 kHz) as a function of sound level (L_{NE}) according to model 4 (Table IV), in comparison with curves derived from ANSI S3.44.1996 using Annex A database. Panel A: age 65 years, exposure duration 45 years. Panel B: age 45 years, exposure duration 25 years.

S3.44 (ANSI, 1996). Johnson (1978) provides the methodology used to develop risk percent calculations using the percentage of the population expected to exceed a specific hearing threshold level (e.g., 25 dB) for a given population.

The excess risks generated from our analysis of the 1–4 kHz AI definition are compared to excess risk estimates generated using the ANSI S3.44 (ANSI, 1996) methodology and Annex A as the unexposed population. Annex A was chosen over Annex B since the NIOSH study population was highly screened. Hence, the Annex A highly screened control population is the most appropriate comparison to our study population. As shown in Fig. 5, excess risk estimates from our best fitting model are similar to those estimated by ANSI S3.44 (ANSI, 1996) for workers aged 65 years with 45 years of exposure. However, among workers aged 45 years with 25 years of exposure, excess risk estimates at sound levels greater than 90 dB are higher for this analysis as compared to ANSI S3.44 (ANSI, 1996). These results particularly in the range of 80–90 dB are not surprising given the similarities in

study design, data collection and time period for all of these studies. Although these are qualitative comparisons, the differences in estimates of lifetime excess risk between ANSI S3.44 (ANSI, 1996) and this analysis do not appear to be substantial. This is illustrated in Fig. 6, which shows that excess risk estimates generated from ANSI S3.44 are located between the bootstrap-based 90% upper and lower confidence limits from the best fitting logistic model. At age 45 years and 25 years of exposure, excess risk estimates below 89 dB are within the lower bound of the confidence limits from the logistic model. Thereafter, point estimates from ANSI S3.44 are found to be lower, particularly at sound levels greater than 92 dB.

For other definitions of hearing handicap (0.5–2 kHz and 1–3 kHz), ANSI S3.44 estimates of excess risk are considerably lower at 85 dB for workers aged 65 years with 25 years of exposure. For the 0.5–2 kHz definition, excess risks at 85 dB from our logistic model and ANSI S3.44 (ANSI, 1996) are 12% and 1%, respectively. For the 1–3 kHz defi-

dition, the values are 16% for our model and 4% using ANSI S3.44 (ANSI, 1996) methods. At 80 dB, ANSI S3.44 generates excess risks of 0% for both definitions, while estimates from this analysis are 5% and 6% for the 0.5–2 kHz and 1–3 kHz definitions, respectively. Some of the divergent results may be due to differences in population characteristics of the studies used to generate excess risks. The NIOSH data set represented a heterogeneous population of workers from a variety of geographic regions and worksites within the United States. The study populations used to develop the ANSI S3.44 (ANSI, 1996) models were likely to be more homogeneous with respect to industry, demographic and socioeconomic (e.g., access to medical care) characteristics.

D. Future directions and data needs

This analysis indicates a need to collect and analyze data from populations exposed to noise at sound levels below 85 dB to learn more about the shape of the dose-response relationship below 85 dB. Like similar studies conducted in the late 1960 and early 1970's, the screened ONHS data set had few subjects with exposures at levels below 85 dB. This contributed to a high degree of instability in the risk estimates as the modeling assumptions were varied. Although logistic modeling techniques were used in this analysis, other methods for evaluating excess risks can reasonably be applied to these data. Nonetheless, it seems plausible that the observed instability below 85 dB would persist using other modeling methods. Risk estimates in the range of 88–95 dB are probably more reliable than the estimates for the lower ranges of sound level. More recent longitudinal data sets may be useful in examining risk below 85 dB. To examine whether noise-induced hearing handicap remains a problem for workers enrolled in OSHA-mandated hearing conservation programs (Department of Labor, 1981a, 1981b), we are currently examining appropriate longitudinal audiometric databases. The present analysis indicates that new studies should be implemented to (1) characterize noise exposure for presumably “non-noise” or low noise populations (including populations exposed to nonoccupational sources of noise); and (2) examine dose-response relationships for noise and hearing handicap among workers exposed to noise levels below 90 dB.

ACKNOWLEDGMENTS

The authors wish to thank Dr. John Franks for his useful comments and advice in the development of this work and Barry Lempert for supplying an electronic version of the data for this analysis.

ANSI (1969). ANSI S3.5-1969, “American National Standard Methods for the Calculation of the Articulation Index (American National Standards Institute, New York).
ANSI (1996). ANSI S3.44-1996, American National Standard Determination of Occupational Noise Exposure and Estimation of Noise-Induced Hearing Impairment (American National Standards Institute, New York).

ASHA (1981). American Speech-Language-Hearing Association Task Force on the Definition of Hearing Handicap, “On the definition of hearing handicap,” *Asha* **23**, 293–297.
Baughn, W. L. (1973). “Relation between daily noise exposure and hearing loss as based on the evaluation of 6835 industrial noise exposure cases,” AMRL-TR-73-53, Aerospace Medical Research Laboratory, Wright-Patterson Air Force Base, Ohio.
Breslow, N. E., and Day, N. E. (1980a). “Classical Methods of Analysis of Grouped Data,” in *Statistical Methods in Cancer Research: Vol. I—The Analysis of Case-control Studies (International Agency for Research on Cancer, Lyon, France)*, IARC Publication No. 32, Chap. 4, pp. 140–148.
Breslow, N. E., and Day, N. E. (1980b). “Unconditional Logistic Regression for Large Strata,” in *Statistical Methods in Cancer Research: Vol. I—The Analysis of Case-control Studies (International Agency for Research on Cancer, Lyon, France)*, IARC Publication No. 32, pp. 192–247.
Burns, W., and Robinson, D. W. (1970). *Hearing and Noise in Industry* (Her Majesty’s Stationary Office, London).
Cohen, A. (1996). Personal communication. August 1996.
Department of Labor (1981a). 46 Fed. Reg. 11, “Occupational noise exposure; Hearing Conservation amendment, rule, and proposed rule, part III,” pp. 4078–4179.
Department of Labor (1981b). “Final regulatory analysis of the hearing conservation amendment,” Report number 723-860/752 1-3, U.S. Government Printing Office, Washington, D.C.
Efron, B. (1982). *The Jackknife, the Bootstrap and Other Resampling Plans (Society for Industrial and Applied Mathematics, Philadelphia, PA)*.
Efron, B., and Tibshirani, R. (1986). “Bootstrap methods for standard errors, confidence intervals, and other measures of Statistical Accuracy.” *Stat. Sci.* **1**(1), 54–77.
Federal Register (1974). “Environmental Protection Agency comments on Proposed OSHA Occupational Noise Exposure Regulation,” Vol. 39, No. 244, pp. 43802–43809.
Fienberg, S. E. (1987). *The Analysis of Cross-Classified Categorical Data* (MIT, Cambridge, MA).
ISO 1999 (1971). “Assessment of occupational noise exposure for hearing conservation purposes,” First Edition, International Organization for Standardization, ISO/R 1999–1971.
ISO 1999 (1990). “Acoustics—Determination of occupational noise exposure and estimation of noise-induced hearing impairment,” International Organization for Standardization.
Johnson, D. L. (1978). “Derivation of presbycusis and noise induced permanent threshold shift (NIPTS) to be used for the basis of a standard on the effects of noise on hearing,” AMRL-TR-78-128, Aerospace Medical Research Laboratory, Wright-Patterson Air Force Base, Ohio.
Lempert, B. L., and Henderson, T. L. (1973). “Occupational Noise and Hearing 1968 to 1972: A NIOSH Study,” U.S. Department of Health, Education, and Welfare, Public Health Service, Center for Disease Control, National Institute for Occupational Safety and Health, Division of Laboratories and Criteria Development, Cincinnati, OH.
NCHS (National Center for Health Statistics) (1965). “Hearing Levels of Adults by Age and Sex, United States, 1960–72,” *Vital and Health Statistics*, Public Health Service Publication No. 1000-Series 11-Np. 11, U.S. Government Printing Office, Washington, D.C.
NIOSH (1972). “NIOSH criteria for a recommended standard: occupational exposure to noise,” Cincinnati, OH: U.S. Department of Health, Education, and Welfare, Public Health Service, Center for Disease Control, National Institute for Occupational Safety and Health, DHSS(NIOSH) Publication No. HIM 73-11001.
Passchier-Vermeer, W. (1968). “Hearing loss due to exposure to steady-state broadband noise,” Report No. 35 and Supplement to Report No. 35, Institute for Public Health Engineering, The Netherlands.
Robinson, D. W. (1970). “Relations between hearing loss and noise exposure,” in *Hearing and Noise in Industry*, edited by W. Burns and D. W. Robinson (Her Majesty’s Stationary Office, London), pp. 100–151.
Robinson, D. W., and Sutton, G. O. (1975). “A comparative analysis of data on the relation of pure-tone audiometric thresholds to age,” NPL Acoustics Report AC84, England, April 1978.
Royster, L. H., and Thomas, W. G. (1979). “Age effect hearing levels for a

white non-industrial noise exposed population (NINEP) and their use in evaluating hearing conservation programs," *Am. Ind. Hyg. Assoc. J.* **40**, 504–511.

SAS Institute, Inc. (1989). "SAS/STAT User's Guide," Version 6, Fourth Edition Volume 2. SAS Institute, Cary, NC, pp. 1071–1125, pp. 1135–1193.

Statistical Sciences, Inc. (1993). *S-PLUS for Windows Users Manual, Version 3.1* (Statistical Science Inc., Seattle).

Ward, W. D., and Glorig, A. (1975). "Protocol of inter-industry noise study," *J. Occup. Med.* **17**(12), 760–770.

Yerg, R. A., Sataloff, J., Glorig, A., and Menduke, H. (1978). "Inter-industry noise study," *J. Occup. Med.* **20**(5), 351–358.

Sound transmission through a double leaf partition with edge flanking

R. J. M. Craik

Department of Building Engineering and Surveying, Heriot-Watt University, Riccarton, Edinburgh EH14 4AS, United Kingdom

T. R. T. Nightingale

Acoustics Laboratory, Institute for Research in Construction, National Research Council Canada, Ottawa, Ontario K1A 0R6, Canada

J. A. Steel

Department of Mechanical and Chemical Engineering, Heriot-Watt University, Riccarton, Edinburgh EH14 4AS, United Kingdom

(Received 8 January 1996; revised 2 September 1996; accepted 24 September 1996)

Lightweight double leaf partitions are widely used and with proper design give good sound isolation. However, when these walls are used as party walls between dwellings, then precautions are necessary to prevent the transmission of fire and smoke. This is usually carried out by placing a firestop in the cavity. This firestop introduces flanking transmission paths reducing the airborne transmission loss of the wall. A simple model is developed which can predict vibration transmission across this type of structural connection. The structural vibration transmission loss can then be used with a more general statistical energy analysis model to give the sound transmission through the entire system. Predicted airborne transmission loss results for a variety of different materials are compared with measured results and good agreement is obtained. © 1997 Acoustical Society of America. [S0001-4966(97)01002-3]

PACS numbers: 43.55.Ti, 43.55.Rg, 43.55.Vj [JDQ]

INTRODUCTION

Double walls are widely used both as internal partitions and as high performance walls separating two different dwellings. They normally consist of a frame of wood or profiled metal channel covered with one or more layers of gypsum board. If the wall is to have good sound isolating properties, then there will usually be sound absorbing material in the cavity which will increase the airborne transmission loss. Sound insulation will be further improved if two separate frames are used to support the gypsum board so that there is no physical connection between the two leaves of the wall. It is these high performance walls that are considered in this paper.

When properly designed these partitions work well and give good sound isolation. However, in walls that separate dwellings, fire and smoke must also be considered as the cavity can allow the spread of fire throughout the dwelling. To prevent this, a physical barrier called a firestop is usually placed in the cavity as shown in Fig. 1. Typical materials used are plywood, gypsum board, or steel.¹ When the firestop is at floor level (as shown in Fig. 1) the simplest method of construction is to make the plywood floor deck continuous under the wall. When the firestop is a vertical edge (in which case Fig. 1 is a plan rather than a section and the floor is another wall), then the gypsum board that covers the flanking wall can be continuous across the cavity of the separating wall.

Measurements made in real buildings show that the airborne transmission loss of a wall when a firestop has been fitted is less than when there is no firestop. This is confirmed

by laboratory measurements made on standard forms of construction.²

In this paper a model is developed which enables the vibration transmission across a continuous firestop to be predicted. The predicted structural transmission loss results from this model are then used within a more general statistical energy analysis framework. This enables noise transmission between the two rooms through the partition system and also across the firestop to be determined.

A comparison of measured results with these calculations shows good agreement. It is shown that there are considerable differences in sound transmission depending on which firestop materials are used and that this difference can be predicted. The model enables appropriate firestop materials to be selected.

I. THEORY OF STRUCTURE-BORNE TRANSMISSION

The actual construction of the joint between the two leaves of the wall and the two parts of the floor at the firestop is complex and some simplifications are necessary if useable models are to be developed. A floor will usually consist of wood joists with a floor covering (typically a plywood deck) and a gypsum board ceiling. Each leaf of the wall will generally have a metal or wooden frame with gypsum board covering. For simplicity, the effects of the joists in the floor and the frame in the walls have not been considered. Their omission greatly simplifies the calculation but can lead to some errors.

In the test structure the frame reduced vibration propagation across both the gypsum board wall and the plywood

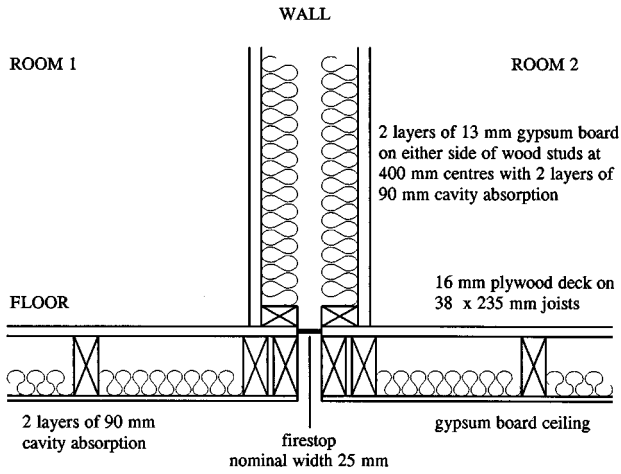


FIG. 1. Section through a double wall resting on a wood floor with a firestop to prevent the passage of fire and smoke.

floor. If a panel is excited by airborne sound then the vibration energy will be uniformly distributed across the panel and there will be no net power flow between different sections so that the effect of the frame will be negligible. However, in flanking paths the excitation of the receiving room wall and floor is along an edge. In this case the effect of the frame and the joists will be more important. In the test constructions the joists were parallel to the test joint and so affected the propagation of energy away from the joint. In the walls (both the common wall and the flanking wall) the frame members were vertical. If the firestop element is at floor level then the wall frame will have a small effect on the distribution of energy across the panel. If the firestop is a vertical edge then the effect will be larger.

Another approximation that simplifies the calculations is to ignore in-plane vibration. Where a floor and a wall meet at a right angle it is reasonable, as a first approximation, to assume that each will prevent lateral motion of the other. Thus, the floor will prevent in-plane motion of the wall that is at right angles to it and *vice versa*. The wall and floor are still free to rotate but there is no lateral motion of the actual joint. This assumption prevents the generation of in-plane displacements and power is then transmitted by moments only. With these assumptions the structural transmission at the joint can be determined.

The parameter used to describe transmission is the transmission coefficient, τ , defined as the ratio of the power transmitted across a joint to the power incident on it. This is then related to the structural transmission loss, $H = 10 \log(1/\tau)$.

The method commonly used to determine the structural transmission loss at the joints between plates is to examine the behavior of semi-infinite plates connected at a joint.³ In this case there are four plates (two walls and two floors). It is assumed that there is a bending wave incident on the joint and that the objective of the analysis is to calculate the amplitude of the waves leaving the joint and hence the structural transmission loss. This is a standard procedure for calculating structural transmission loss.^{3,4}

The general coordinate system used for the calculations is shown in Fig. 2. On each plate there will be a traveling

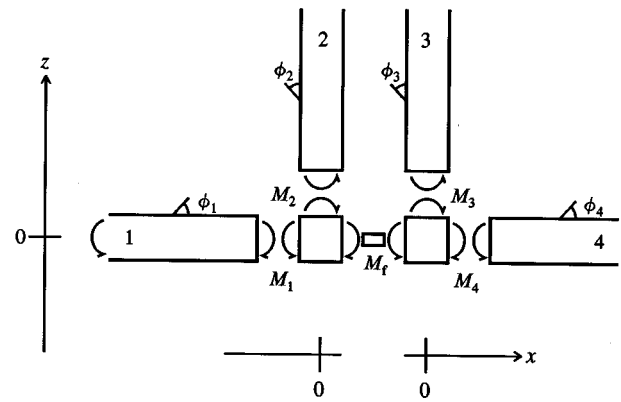


FIG. 2. Coordinate system used to calculate the structural transmission loss.

bending wave with amplitude T and a near-field bending wave with amplitude T_n . In addition on plate 1 there is assumed to be a wave incident on the joint with unit amplitude. The displacement on plates 1–4 (ξ_1 to ξ_4) can then be given as

$$\xi_1 = (e^{-ik_1 \cos \theta_1 x} + T_1 e^{ik_1 \cos \theta_1 x} + T_{n1} e^{k_{n1} x}) \times e^{-ik_1 \sin \theta_1 y} e^{i\omega t}, \quad (1)$$

$$\xi_2 = (T_2 e^{-ik_2 \cos \theta_2 z} + T_{n2} e^{-k_{n2} z}) e^{-ik_2 \sin \theta_2 y} e^{i\omega t}, \quad (2)$$

$$\xi_3 = (T_3 e^{-ik_3 \cos \theta_3 z} + T_{n3} e^{-k_{n3} z}) e^{-ik_3 \sin \theta_3 y} e^{i\omega t}, \quad (3)$$

$$\xi_4 = (T_4 e^{-ik_4 \cos \theta_4 x} + T_{n4} e^{-k_{n4} x}) e^{-ik_4 \sin \theta_4 y} e^{i\omega t}, \quad (4)$$

where k is the wave number.

Since power is transmitted only by moments in this model the orientation of the plates can be changed without affecting the structural transmission loss. Thus, the numbering can be changed so that plate 1 is the wall and plate 2 is the floor. The only necessary assumption is that plates 1 and 2 are on one side of the firestop and that 3 and 4 are on the other.

If the sound field on plate 1 is diffuse then all angles of incidence are possible. For a given angle of incidence θ_1 (measured from the normal) on plate 1 the angle of transmission of the other waves can be found from the relationship

$$k_1 \sin \theta_1 = k_2 \sin \theta_2 = k_3 \sin \theta_3 = k_4 \sin \theta_4. \quad (5)$$

k_n is the near-field wave number in the x or z direction and can be found for any plate from³

$$k_{ni} = \sqrt{k_i^2 + k_i^2 \sin^2 \theta_i}. \quad (6)$$

The requirement that the displacement of all the plates be zero at the boundary (where x and $z=0$) gives, from Eqs. (1)–(4),

$$1 + T_1 + T_{n1} = T_2 + T_{n2} = T_3 + T_{n3} = T_4 + T_{n4} = 0, \quad (7)$$

so that the amplitude of the near-field waves can be given in terms of the traveling wave amplitude for each plate.

At the boundary it is assumed that the plates on the left of the joint and those on the right are rigidly bonded together so that the angle between them is preserved. This leads to two equations linking the slope, ϕ , on plates 1 and 2 and the

slopes on plates 3 and 4. Equating the slopes on plates 1 and 2 gives $\phi_1 = \phi_2$. Expressing the slope as the derivative of the displacement³ gives

$$\frac{\partial \xi_1}{\partial x} = \frac{\partial \xi_2}{\partial z}. \quad (8)$$

Evaluating this at the origin where x , and $z=0$ gives

$$T_1[-k_{n1} + ik_1 \cos \theta_1] + T_2[-k_{n2} + ik_2 \cos \theta_2] = k_{n1} + ik_1 \cos \theta_1. \quad (9)$$

Similarly, equating the slopes of plates 3 and 4, so that $\phi_3 = \phi_4$, gives

$$\frac{\partial \xi_3}{\partial z} = \frac{\partial \xi_4}{\partial x}, \quad (10)$$

which can be given as

$$T_3[k_{n3} - ik_3 \cos \theta_3] + T_4[-k_{n4} + ik_4 \cos \theta_4] = 0. \quad (11)$$

Two other equations can be written relating the moments. Summing the moments about each side in turn and using the coordinate system shown in Fig. 2 gives

$$M_1 - M_2 - M_f = 0 \quad (12)$$

and

$$M_3 + M_4 - M_f = 0, \quad (13)$$

where M_i is the moment acting on the firestop from plate i and M_f is the moment acting on the plates due to the firestop.

The moment (per unit width) acting on the boundary due to wave motion on a plate can be given by³

$$M = -B \left[\frac{\partial^2 \xi}{\partial x^2} + \mu \frac{\partial^2 \xi}{\partial y^2} \right], \quad (14)$$

so that, by substituting the displacement into Eq. (14) and evaluating at x , y and $z=0$, the moment due to each plate can be found. For moments on plates 2 and 3 the x dependence in Eq. (14) is changed to z . Here, B is the material stiffness per unit width and is given in terms of Young's modulus E , the thickness h , and Poisson's ratio μ , as

$$B = \frac{Eh^3}{12(1-\mu^2)}. \quad (15)$$

The moment (per unit width) acting on the plates due to the firestop can be written in terms of the change in slope across its width ($\phi_1 - \phi_4$) and the stiffness (per unit width) of the firestop component. This depends on both the stiffness of the firestop material B_f and the cavity depth d to give

$$M_f = \frac{B_f}{d} (\phi_1 - \phi_4), \quad (16)$$

where d , the width of the firestop, is taken as the separation between the sole plates of the wall (25 mm for the test structure). At normal incidence the bending stiffness of the firestop can be found from Eq. (15). At other angles of incidence there also will be bending along the y axis which will increase the overall stiffness. Accounting for this more correctly would increase the overall complexity of the model and is not justified, given the other approximations and as-

sumptions that have been made. Therefore in all calculations the simple approximation of Eq. (15) has been used.

Inserting Eqs. (14) and (16) into Eqs. (12) and (13), and substituting for the displacement, gives the two moment equations as

$$T_1[2B_1k_1^2 + B_fk_{n1}/d - iB_fk_1 \cos \theta_1/d] + T_2[-2B_2k_2^2] + T_4[B_fk_{n4}/d - iB_fk_4 \cos \theta_4/d] = -2B_1k_1^2 - B_fk_{n1}/d - iB_fk_1 \cos \theta_1/d \quad (17)$$

and

$$T_1[B_fk_{n1}/d - iB_fk_1 \cos \theta_1/d] + T_3[2B_3k_3^2] + T_4[2B_4k_4^2 + B_fk_{n4}/d - iB_fk_4 \cos \theta_4/d] = -B_fk_{n1}/d - iB_fk_1 \cos \theta_1/d. \quad (18)$$

The four equations, (9), (11), (17), and (18), can be solved numerically to give the amplitude of the waves leaving the joint from which the structural transmission coefficient τ can be found using

$$\tau_{12}(\theta) = \frac{\rho_{s2}k_1 \cos \theta_2 |T_2|^2}{\rho_{s1}k_2 \cos \theta_1}, \quad (19)$$

where ρ_s is the surface density.

The angular averaged transmission coefficient can then be found from³

$$\tau_{av} = \int_0^{\pi/2} \tau(\theta) \cos \theta d\theta. \quad (20)$$

As the four plates that make up the joint are often very similar a useful approximation is to assume that all the plates are made from the same materials and have the same thickness. In this case, the normal incidence solution for the structural transmission loss can be given as

$$H_{13} = H_{14} = 10 \log \left[\frac{16B^2k^2d^2}{B_f^2} + \frac{16Bkd}{B_f} + 8 \right]. \quad (21)$$

This can be used to give an estimate of the structural transmission loss and can be used to quickly rank different materials.

The relation between the parameter Bkd/B_f and the structural transmission loss can be seen in Fig. 3 for the case where all four plates are assumed to have the same material properties. The results show both the random incidence solution and the normal incidence approximation. It can be seen that the normal incidence approximation is about 2 dB less than the random incidence solution. At low frequencies or for stiff firestops (the left of Fig. 3) the structural transmission loss tends to a constant value. The limits are 9 dB for the normal incidence solution and 10.8 dB for the random incidence solution and are the same as the result for a rigid cross joint. As the frequency increases or the stiffness gets less so the structural transmission loss increases.

The solution given above is for four plates connected at a joint. In some cases there may be additional plates if for example the walls under the floor were included. For each

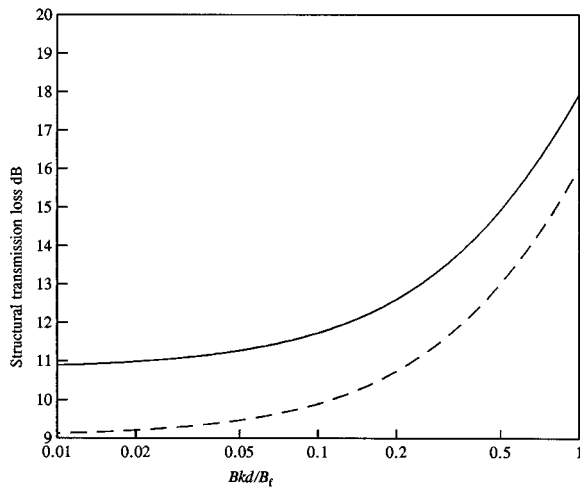


FIG. 3. Structural transmission loss between plates 1 and 3 (or 4) at a joint where all the plates are made from the same material and have the same thickness. —, random incidence; ----, normal incidence.

additional plate there is one additional equation relating the slope of the new plate to an existing plate and one additional term in one of the moment equations.

II. TEST FACILITY

In order to test the theory given in the previous section measurements were carried out in the flanking laboratory of the National Research Council of Canada.² The test facility consists of four rooms (two up and two down) with volumes from 35 to 50 m³. The test joint shown in Fig. 1 formed the only link between two pairs of otherwise separate rooms. The walls were made from wood frames covered with two layers of gypsum board and the floors were constructed from 38- × 235-mm joists with 16-mm plywood on the top and 2 layers of 13-mm gypsum board on the ceiling attached using resilient furring strips. The separating wall (13.5 m²) had independent frames with two layers of plasterboard on each side and the cavity between the two leaves was filled with sound absorbing material.

Sound transmission was measured between the upper pairs of rooms and the firestop was either at floor level or at a wall edge. When the firestop was at floor level the joint is like that shown in Fig. 1, except that there are rooms underneath. Due to the method of construction it was not appropriate to include the walls below the floor in the analysis, as there was no significant physical connection between the floor assembly and the lower party wall.

Sound transmission between the test rooms was predicted using a statistical energy analysis model. Statistical energy analysis modeling is described in more detail by Craik⁴ and details of the model used are given in Ref. 5.

The firestops used were all 25 mm wide and were 0.38-mm steel, 16-mm plywood or 26-mm gypsum board (made from 2 sheets of 13-mm gypsum board).

III. RESULTS

All of the tests carried out were of airborne sound transmission between two rooms separated by a test wall, as

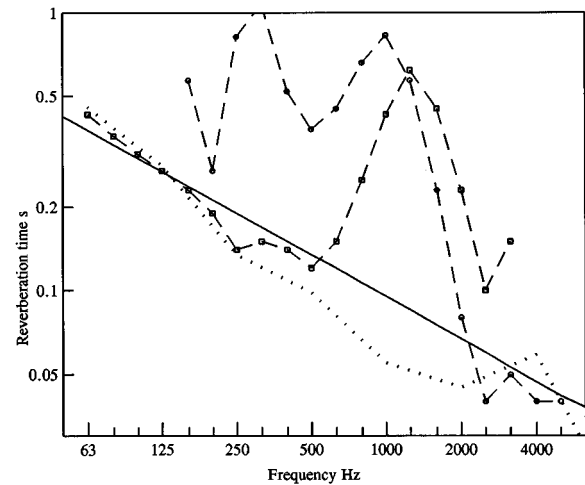


FIG. 4. Reverberation time measured in the cavity of the double wall and floor. --□--, measured in the wall; --○--, measured in the floor; —, estimated curve $3/\sqrt{f}$; ·····, measured in an isolated cavity.

shown in Fig. 1 but with additional rooms underneath. A noise source was placed in room 1 and a standard sound transmission test⁶ was carried out to give the airborne transmission loss of the wall.

The first tests were carried out when there was no firestop connecting the two leaves of the separating wall so that direct transmission through the wall together with any minor flanking paths through the rest of the laboratory could be determined.

As the dominant transmission path is the direct path through the wall, the absorption in the cavity is important. Transmission through the double wall can be considered as transmission into the cavity followed by transmission out of the cavity. The sound-pressure level in the cavity is inversely proportional to the cavity damping so that the overall airborne transmission loss is inversely proportional to the reverberation time of the cavity.

The reverberation time, T , that was measured in the wall cavity and in one of the floor cavities can be seen in Fig. 4. The reverberation time was much less than would be expected for a normal room and was very difficult to measure. A standard decay rate method was used with a small loudspeaker placed in the cavity. There was considerable interference in the cavity decay curve from energy returning from the rooms and the rest of the structure making the decay curves difficult to interpret. It was assumed that the high readings of around 0.5 s were due to the reverberation time of the rooms and that the true reverberation time was the lowest of the measured readings. A best fitting estimate of $T = 3/\sqrt{f}$ was therefore used as this passed through the lowest readings. Subsequent measurements were made on an isolated test structure that reproduced the conditions in the cavity without interference from any surrounding structure. The results for the isolated cavity (also shown in Fig. 4) confirm that the estimate is a good one.

Using these data and a standard SEA model, sound transmission through the basic partition was predicted. This is shown together with the measured airborne transmission loss in Fig. 5. It can be seen that there is good agreement

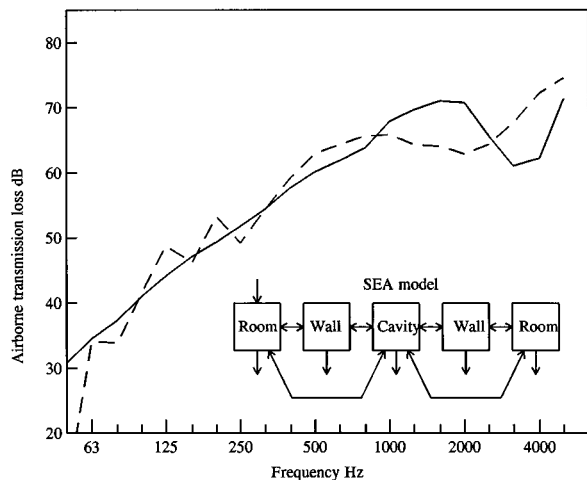


FIG. 5. Airborne transmission loss of a double wall with no firestop. A simplified SEA model is shown in the insert. —, predicted; ----, measured.

between the measured and predicted data, although the predicted dip at around 3 kHz associated with the critical frequency is not at the correct frequency. The SEA model used included all of the surrounding structure (using 20 subsystems) and is therefore more complex than the 5 subsystem model shown in the insert. However, the 5 subsystem model describes the direct paths through the partition and is sufficient for most purposes. In the SEA model the arrows from the room to the cavity represent the nonresonant (mass-law) transmission path and will dominate transmission at frequencies below the critical frequency.

Using the 5 subsystem model the airborne transmission loss due to the direct path can be given as⁴

$$R = R_1 + R_2 + 10 \log \frac{1}{fT_c} + 14.4, \quad (22)$$

where R is the overall airborne transmission loss, $R_{1,2}$ is the airborne transmission loss of the individual leaves of the wall and can be approximated to the mass-law equation⁷ below the critical frequency, and T_c is the reverberation time of the cavity. This equation assumes that the cavity is sufficiently narrow that it behaves as a two dimensional space. f is the band center frequency (usually $\frac{1}{3}$ octaves).

When the firestop is introduced then sound is transmitted by additional paths which decrease the overall airborne transmission loss. The model is then much more complex and there is no single simple algebraic expression for the sound reduction index equivalent to Eq. (22). Either a full SEA model has to be set up or else a path by path analysis carried out.⁴ The results of such calculations can be seen in Fig. 6, which shows the measured results for no firestop (shown in Fig. 5) together with the measured and predicted results for situations where there is a steel firestop and a plywood firestop at floor level.

At low frequencies sound is mainly transmitted via the direct paths so that the additional flanking paths through the firestop make little difference. At higher frequencies the results show clearly the effect of the additional flanking paths. The steel firestop provides very weak coupling and gives

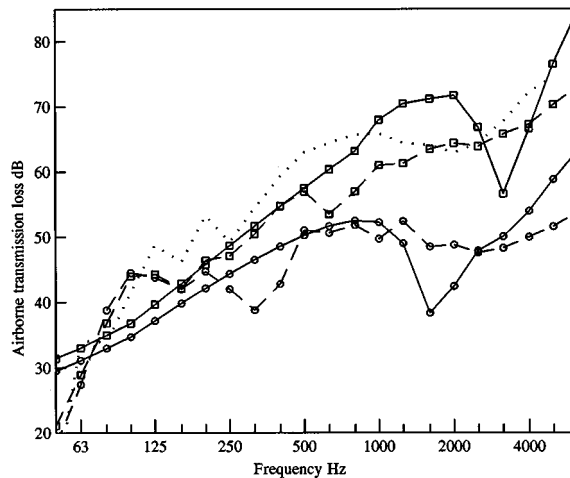


FIG. 6. Airborne transmission loss for a wall with a steel and a plywood firestop at floor level. --□--, measured with a steel firestop; —□—, predicted with a steel firestop; --○--, measured with a plywood firestop; —○—, predicted with a plywood firestop; measured with no firestop.

results that are more or less the same as the results for no firestop. The results for the plywood firestop show a significant decrease in airborne transmission loss at the higher frequencies. This result shows that the best method of reducing flanking is to use a flexible firestop such as a thin steel plate.

An analysis of the different transmission paths associated with transmission between the two rooms when there is a plywood firestop can be seen in Fig. 7. The figure shows the predicted airborne transmission loss when there is no firestop together with the four main paths associated with the firestop. The least important is the path from source room to the wall in the source room across the firestop to the wall in the receiving room followed by radiation into the receiving room. The most important of the flanking paths is from the source room, into the floor of the source room, across the joint into the floor of the receiving room, followed by radiation into the receiving room. The other two flanking paths

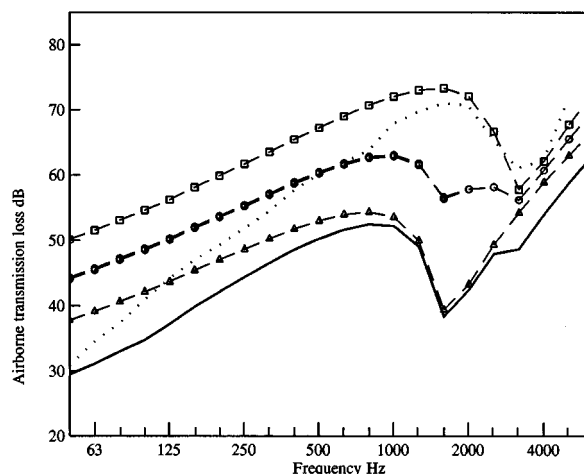


FIG. 7. Transmission paths associated with the plywood firestop. —, sum of all paths; --□--, wall-wall path; --○--, wall-floor path; --△--, floor-wall path; --◇--, floor-floor path; prediction with no firestop.

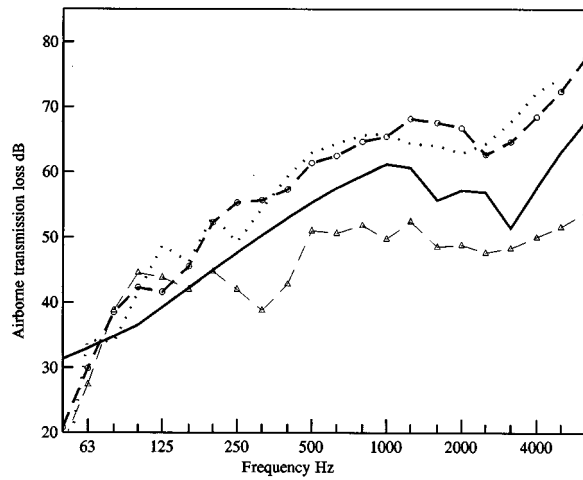


FIG. 8. Airborne transmission loss for transmission between the two rooms when a floating floor is placed over the floor to reduce excitation of and radiation from the floor., measured with no firestop; --○--, measured with a plywood firestop and a floating floor; --△--, measured with a plywood firestop; —, predicted.

from the source room wall to the receiving room floor and from the source room floor to the receiving room wall are approximately equal and lie midway between the other two flanking curves. As was shown in the measured data in Fig. 6, the transmission at low frequencies is dominated by the direct path through the wall. In this figure the prediction for the wall with no firestop is shown for comparison. At the higher frequencies, above about 125 Hz, the dominant path is the flanking path involving transmission from one floor to the other and shows clearly the effect of this path on transmission between the two rooms.

Given that the dominant flanking path involves the floor in each room then one method of improving the overall transmission loss between the two rooms would be to place a floating floor on top of the structural floor to reduce excitation of the floor and radiation from it. The results for such a floor can be seen in Fig. 8. This shows the measured and predicted results for the case where there is a floating floor on the receiving side only. For simplicity it was assumed that the floating floor only eliminated coupling between the floor and the room (effectively eliminating two of the four main flanking paths). The predicted results are lower than the measured results but both show a significant increase in the airborne transmission loss compared to that for a plywood firestop.

Figure 9 shows results for flanking along the external wall where the firestop was two sheets of gypsum board carried through from the wall of one room to the wall of the other. Again the results are shown for a system with and without a firestop. In this case the firestop has little effect except at the higher frequencies.

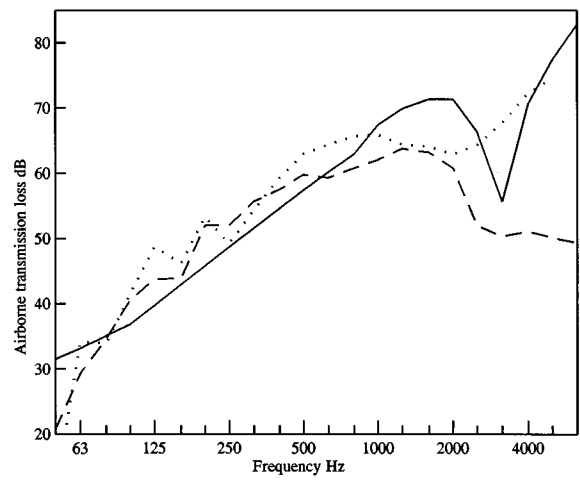


FIG. 9. Airborne transmission loss of the double wall when there is a gypsum board firestop providing flanking along the external wall. ----, measured; —, predicted;, measured with no firestop.

IV. CONCLUSIONS

Despite the simplicity of the model used for the calculation of structural transmission loss, it gives reasonable agreement between the measured and predicted results. The theory predicts the correct trends and therefore allows a comparison of the effect of different firestop materials. The plywood firestop is the simplest method of forming a firestop at floor level and leads to significant flanking paths for double partition constructions. In the test construction these could be reduced by placing a floating floor on top of the structural floor. Alternatively a thin steel sheet can be used as a firestop to minimise flanking transmission.

An estimate of the structural transmission loss can be found from Eq. (21) which can be used to rank different test materials.

- ¹National Building Code of Canada 1990, Part 9, Section 9.10.15 Firestops, Associate Committee on the National Building Code, National Research Council, Canada, 1991.
- ²T. R. T. Nightingale, "Methods for measuring and identifying flanking transmission in wood-framed constructions," Proc. INTERNOISE **93**, 953–956 (1993).
- ³L. Cremer, M. Heckl, and E. E. Ungar, *Structure-Borne Sound* (Springer-Verlag, Berlin, 1988).
- ⁴R. J. M. Craik, *Sound Transmission Through Buildings Using Statistical Energy Analysis* (Gower, Aldershot, United Kingdom, 1996).
- ⁵R. J. M. Craik, J. A. Steel, and T. R. T. Nightingale, "Sound transmission through framed buildings," IRC internal report IRC-IR-672, Institute for Research in Construction, National Research Council, Ottawa, Canada, 1995.
- ⁶ASTM E336-90, "Standard test method for measurement of airborne sound insulation in buildings," 1995 (also ISO 140 1978).
- ⁷L. L. Beranek and I. L. Ver, *Noise and Vibration Control Engineering* (Wiley, New York, 1992).

A study of the transmission of ultrasound across solid–rubber interfaces

Bruce Drinkwater

Department of Mechanical Engineering, University of Bristol, Bristol BS8 1TR, England

Rob Dwyer-Joyce

Department of Mechanical and Process Engineering, University of Sheffield, Sheffield S1 3JD, England

Peter Cawley

Department of Mechanical Engineering, Imperial College, London SW7 2BX, England

(Received 12 January 1996; accepted for publication 12 September 1996)

The reflection coefficient at the solid–rubber interface of a rubber coupled ultrasonic transducer may be used as a measure of its coupling performance; the lower the solid–rubber reflection coefficient, the better the coupling. An experimental and theoretical study of the transmission of ultrasound across dry coupled solid–rubber interfaces, and in particular the effect of surface roughness and particulate contaminants on solid coupling, is described. The effect of surface roughness is modeled using a numerical contact model of the solid–rubber interface from which the static stiffness is calculated. The calculated interfacial stiffness is then used in a spring model of the interface to predict the solid–rubber reflection coefficient behavior. By repeating this process for different loads applied to the solid–rubber interface the variation of reflection coefficient with interfacial pressure is found. The agreement between these predictions and the experiments is shown to be reasonable in general and good at higher pressures. The numerical contact model is then used to predict the pressure required to achieve a given level of coupling on a variety of surfaces. This modeling procedure can now be used to provide the operator of a dry coupled system with an estimate of the pressure which must be applied to a dry coupled transducer on a given system to achieve the required coupling. The effect of dust and dirt on the transmission of ultrasound across solid–rubber interfaces has been considered experimentally. These experiments showed that particulate contaminants at a solid coupled interface significantly reduce the degree of coupling and this effect is quantified. © 1997 Acoustical Society of America. [S0001-4966(97)02301-1]

PACS numbers: 43.58.Vb, 43.35.Yb, 43.38.Ar [SLE]

INTRODUCTION

The authors are currently working on a project to improve the performance of solid coupled ultrasonic transducers. This work has already enabled the construction of a rubber coupled wheel probe¹ that operates at a center frequency of 4 MHz. In this device a rubber tyre conforms around the surface roughness contours of the test structure hence providing coupling. Coupling can be improved by increasing the pressure across the rubber–solid interface or by reducing the surface roughness of the test structure. Dust and dirt increase the effective roughness of the surface, providing additional obstacles around which the rubber must conform in order to couple to the test structure. For an efficient solid coupled system transmission across the rubber–solid boundary must be maximized. Unfortunately, transmission coefficient measurements on this system are difficult as the transducers will approach one another as the pressure across the interface is increased and the rubber deforms. This makes transmission coefficient measurement inaccurate and so reflection coefficient measurements were performed in this study. It is assumed that the proportion of the wave scattered obliquely is negligible and so the solid–rubber reflection coefficient measured at normal incidence will determine the proportion of the wave transmitted into the test structure. This assumption is valid if the size of the scatterer is small compared to the

wavelength because the amount of scattering decreases as the scatterer size decreases relative to the wavelength.² Reflection coefficients are, therefore, used to measure the degree of coupling across the rubber–solid interface, maximum coupling occurring when the reflection coefficient is a minimum. In this paper results are presented in which the solid–rubber reflection coefficient is measured for various surface roughnesses and for interfaces contaminated with a variety of particulate contaminants.

Reflection coefficients from solid–solid interfaces and the similar case of reflection from a layer of embedded pores have been studied by many authors. Baik and Thompson³ describe a spring model approximation to calculate reflection coefficients in the low-frequency range, the spring constants being determined from the static stiffness of the solid–solid interface; this is termed the quasistatic model (QSM). Margetan *et al.*⁴ verified this type of model experimentally by measuring the reflection coefficient from artificially introduced defects of simple geometry and known size. Angel and Achenbach⁵ have derived a closed form solution for the reflection coefficient from a regular array of equally sized defects which is valid at all frequencies, and have demonstrated that this model is in good agreement with the quasistatic approximation at low frequencies. Nagy⁶ used both longitudinal and shear waves to classify interfacial imperfec-

tions and showed that by using both these wave types it is possible to gain additional information about the state of the interface.

Other authors have investigated the reflection coefficient from the interface between randomly rough surfaces under pressure. Haines⁷ considered the reflection coefficients from rough solid–solid interfaces. He described a statistical model of the rough surface and calculated the true area of contact by considering the independent elastic, and elastic-plastic, contact of each asperity. From the true area of contact a spring model was used to calculate the reflection coefficient. At high percentages of contact the neighboring asperities interact, hence limiting this model to low percentages of contact. Krolikowski⁸ attempted to measure contact parameters by measuring the reflection coefficient from the solid–solid interface and by using a similar model of the contact to Haines.

This paper describes a link between the reflection coefficient from a solid–rubber interface, surface roughness and interfacial pressure. It advances on previous work^{3–8} in this area by describing a method by which the stiffness of a solid–rubber interface can be predicted and used to calculate the reflection coefficient if the surface profiles and elastic properties of the materials are known. Rubber–solid contact provides an example of elastic contact and so an elastic contact model can be used. The surface profiles of the two substrates are measured and a numerical contact model is then used to predict the size and distribution of the noncontacting regions (gaps) along the rubber–solid interface as a function of applied load. Measurements of the reflection coefficients at varying loads, together with the results from the numerical contact model, then allow the variation of the reflection coefficient with changes in the contact conditions (e.g., percentage contact) to be determined. Interfacial stiffnesses have been calculated from the information provided by the numerical contact model and from simplifying assumptions about the interfacial geometry. These stiffnesses are then used in spring models to calculate reflection coefficients which are then compared to those measured experimentally.

I. BACKGROUND

The normal incidence reflection coefficient from a bonded interface between materials 1 and 2 when a wave is incident on the interface from medium 1 can be written as⁹

$$R_{12} = \frac{Z_1 - Z_2}{Z_2 + Z_1}, \quad (1)$$

where Z_1 and Z_2 are the acoustic impedances of the media on either side of the interface. Attenuation has been neglected in the derivation of Eq. (1), but even for high loss materials like rubber its effect is negligible on the rubber–solid reflection coefficient.¹⁰ From Eq. (1) it can be seen that the reflection coefficient from such an interface is independent of frequency.

If an ultrasonic wave is incident on a partially contacting interface the reflection coefficient cannot be calculated using Eq. (1). Where the surfaces are in contact, the ultrasonic wave will “see” a continuous piece of material, and where

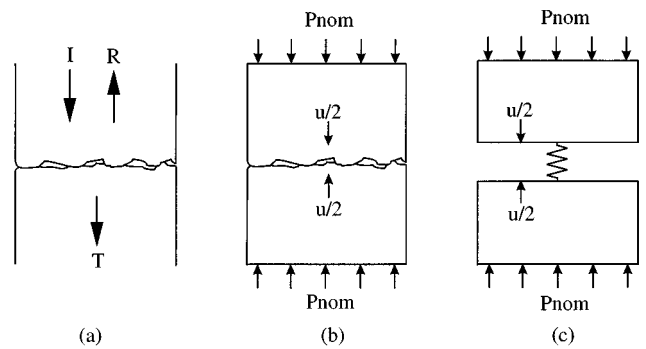


FIG. 1. Representation of partially contacting interfaces by a spring: (a) geometry of the experimental setup; (b) static model of the interface; (c) spring model of the interface.

the surfaces are out of contact it will “see” an impenetrable air gap. Each air gap will scatter the incoming wave and so the reflected and transmitted acoustic fields will be the net result of many wave–scatterer interactions. The precise nature of these interactions is governed by the ratio of the wavelength to the size of the scatterers (air gaps) in the plane of the interface. If the wavelength of the incident ultrasonic wave is large compared to the size of the air gaps then Rayleigh scattering occurs. The Rayleigh scattering regime is perhaps the simplest regime to work in as many factors become less significant at low frequency (long wavelength) and in particular, spring approximations apply.³ As the wavelength is large compared to the length of the gaps and the wave falls over many gaps it is no longer necessary to consider the individual effects of all the gaps. The overall effect of the gaps is to change the stiffness of the material across the interface. The mass of the interfacial layer can be ignored as the air gaps are very thin in the direction normal to the interface and the density of the interface layer is low due to the presence of the air. The imperfect interface can then be replaced by a spring with a stiffness equivalent to the overall interfacial stiffness. Also as the frequency is low, dynamic effects are ignored and so the quasistatic approximation can be taken in which the interfacial stiffness can be replaced by the static stiffness of the interface. This approximation, which is exact in the limit when frequency tends to zero, has been shown to describe well the observed frequency dependence⁷ and is in good agreement with more rigorous scattering models.⁵

A schematic diagram of the spring description of a partially contacting interface is shown in Fig. 1. The spring stiffness per unit area, k , for a given interface can be described as

$$k = \frac{\sigma}{\delta_l}, \quad (2)$$

where σ is the average stress across the interface and δ_l is the extra displacement caused by the partially contacting interface. If a stress is applied across a poorly contacting interface, the resulting interfacial displacement will be large and hence give a low spring stiffness. If a stress is now applied across an almost perfect interface, the extra displacement at the interface will be small and hence give a high interfacial spring stiffness. This model can now be incorpo-

rated into the definition of reflection coefficient. Equation (1) was derived assuming continuity of stresses and displacements across the boundary as is the case for a perfectly coupled interface. For a partially contacting interface this boundary condition is replaced by the spring boundary condition,

$$\delta_2 - \delta_1 = \frac{\sigma_b}{k} \quad (3a)$$

and

$$\sigma_1 = \sigma_2 = \sigma_b, \quad (3b)$$

where δ_1 and δ_2 are the amplitudes of the displacements of the waves either side of the interface, σ_b is the stress at the boundary and k is the interfacial stiffness per unit area. Following the analysis of Tattersall¹¹ the reflection coefficient can now be described as

$$R_{12} = \frac{Z_1 - Z_2 + i\omega(Z_1 Z_2 / k)}{Z_1 + Z_2 + i\omega(Z_1 Z_2 / k)}, \quad (4)$$

where ω is the angular frequency and $i = \sqrt{-1}$. From this equation it can be seen that as the interfacial stiffness tends to infinity, the reflection coefficient tends to the perfect contact value. Also as the interfacial stiffness tends to zero, so the reflection coefficient tends to unity, indicating complete reflection. Frequency dependence of the reflection coefficient has also been introduced. When the frequency tends to zero (the static case) so the reflection coefficient tends to the perfect contact value indicating that the wave will not “see” the imperfections of the interface. As the frequency is increased, the amplitude of the reflection coefficient increases toward unity, though before it reaches this value, the quasistatic approximation itself becomes invalid.

II. MEASUREMENT OF REFLECTION COEFFICIENT VERSUS PRESSURE

In this section the measurement of the solid–rubber reflection coefficient variation with pressure is described. Also the effect of surface roughness is considered. Knowledge of this variation is an important parameter in the design of solid coupled ultrasonic devices. Although a specific case of a rubber and a solid is described in this section the experimental procedure described is generic and is not dependent on the end application.

A. Measurement technique

The material used as a solid couplant must be both soft and have an acceptable material attenuation level. The rubber used in this work was typical of a soft rubber containing only low levels of additives such as fillers. It had a low frequency Young’s modulus of 1.3 MPa, a Poisson’s ratio of 0.5 and a density of 980 kg/m³. The longitudinal wave speed in the material was 1500 m/s. Perspex (or Plexiglas) was used as the solid as it is reasonably well acoustically matched to the rubber so the reflection coefficient changes significantly between the no contact and contact conditions. It also has a high enough Young’s modulus compared to rubber to be considered as rigid in the analysis.

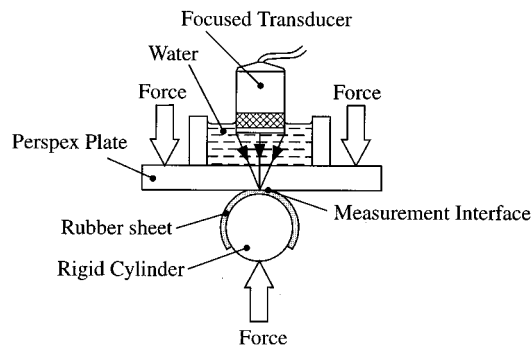


FIG. 2. Experimental setup used to measure the perspex–rubber reflection coefficient from a line contact.

In order to measure the variation of solid–rubber reflection coefficient with pressure the first stage is to construct experimental apparatus with which the pressure across a solid–rubber interface can be varied in a known way and from which the reflection coefficient can be measured. The contact pressure will be calculated from the applied load and so it is important that the pressure distribution across the contact region is simple in form and repeatable. This is difficult to achieve when two flat plates contact as they must be perfectly aligned and perfectly flat in two axes.¹² If the plates are not flat or are misaligned, unknown pressure variations are developed across the contact region. With this situation it is impossible to determine the pressure corresponding to the measured reflection coefficient. The likelihood of this problem occurring is increased if either solid is soft, as soft solids are less dimensionally stable. In order to surmount this problem the apparatus shown in Fig. 2 was used in which a 2-mm-thick rubber sheet was bonded to a 12-mm-diam solid cylinder. This rubber-coated cylinder makes contact with an interchangeable perspex plate. Using this technique a line contact was made. Such a contact is only sensitive to misalignments in one plane and has a simple pressure distribution. A 5-MHz center frequency, focused transducer was placed in a water bath above the perspex plate. The transducer had a diameter of 10 mm and a focal length of 35 mm. The water bath enabled coupling between the transducer and the perspex to be achieved and enabled the transducer to be scanned over the perspex–rubber contact. Care was taken to ensure the transducer was focused on the perspex–rubber (or perspex–air) interface. The amplitude of the reflection from the perspex–rubber interface was compared with that from a perspex–air interface (where the reflection coefficient equals unity) and hence the reflection coefficient was calculated. Figure 3 shows the measured variation of reflection coefficient over the contact region for different applied loads in tests on a smooth perspex plate of roughness average, $R_a = 0.19 \mu\text{m}$. The roughness average is defined as the mean of the vertical (z) departure of the profile from the center line,

$$R_a = \frac{1}{L} \int_0^L |z(x)| dx, \quad (5)$$

where L is the length of the profile and all the other symbols have their usual meanings. Each reflection coefficient profile

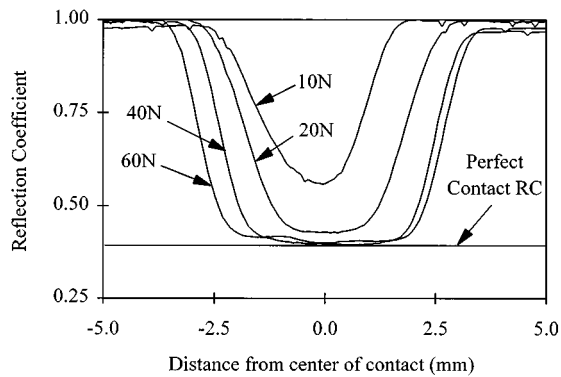


FIG. 3. Measured perspex-rubber reflection coefficient under different loads ($R_a=0.19 \mu\text{m}$).

shown in Fig. 3 is an average of five profiles taken at different positions along the axis of the cylinder. It can be seen that at low loads the minimum of the reflection coefficient profile is of parabolic form. Where no contact is made the reflection coefficient is equal to unity; as the contact pressure increases toward the center of the cylinder, so more energy is transmitted into the rubber and the reflection coefficient decreases. Once the contact pressure is sufficient to cause perfect contact, the reflection coefficient reaches a minimum value equal to the reflection coefficient calculated from Eq. (1) and shown in Fig. 3. The correct measurement of the perfect contact reflection coefficient provides a good means of verifying the reflection coefficient measurement procedure.

B. Prediction of pressure profiles

In order to relate the measured reflection coefficient to pressure the pressure distribution across the contact zone must be found. The geometry considered is the contact of a cylindrical layered body on a flat plate. Unfortunately there is no simple analytical solution for this case. However, Meijers¹³ presented an approximate iterative scheme which showed that the expected pressure distribution is semielliptical. A finite-element model of this geometry was constructed by the authors which also showed that the pressure distribution was semielliptical. Both these models need inputs that are unknown, for example the coefficient of friction between the substrates. However, it is possible to reduce the need for these numerical models by measuring the contact width optically with a traveling microscope. The contact pressures can then be calculated as the load and contact width are known and the profile can be assumed to be semielliptical.

The transducer, despite being focused, will not measure the reflection coefficient at a point but will give a weighted average across its focal zone. Hence, at a given measurement position the pressure corresponding to the measured reflection coefficient is a weighted average of the point pressures across the width of the focal zone. The focal length of the transducer was 35 mm and its width was 6.4 mm which gave focal spot size¹⁴ of 3.2 mm (width of the central lobe) with a standard Bessel function pressure field distribution. Figure 4 shows a semielliptical pressure distribution for 40N load applied to the system shown in Fig. 2 and the weighted average

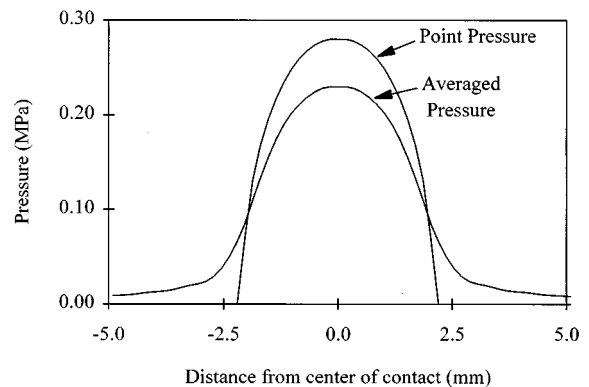


FIG. 4. Predicted pressure across the contact region.

pressure over the focal region for the same case. The effect of averaging over the focal region is to lower the peak pressure and widen the apparent contact width.

Figure 5 shows the variation of reflection coefficient with pressure for different loads applied to the system shown in Fig. 2 using a perspex plate of roughness average $0.19 \mu\text{m}$. At a given load, a range of pressures from zero to the peak pressure are generated and the corresponding reflection coefficients are measured. Note that as the reflection coefficient (Fig. 3) and pressure profiles (Fig. 4) are symmetric about the maximum reflection coefficient and pressure, respectively, it is only necessary to plot half this data in Fig. 5. Most values of pressure are repeated at higher loads and in this way most of the reflection coefficient measurements at a given pressure are repeated. If the predicted pressure profiles are correct then these repeat measurements should give the same reflection coefficient. It can be seen from Fig. 5 that the agreement of these repeated measurements is good. The worst discrepancy is between the readings at 10N and those at other loads in region "A" as indicated in Fig. 5.

C. The effect of different surface roughnesses

At least two parameters are needed to describe a rough surface, one describing the height of the asperites and one describing their distribution in the plane of the surface. There are many such parameters to choose from¹⁵ and two of the most common have been chosen in this paper. The roughness

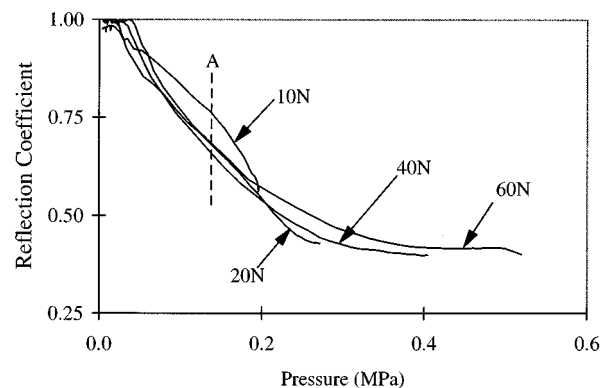


FIG. 5. Measured variation of reflection coefficient with pressure for a number of different applied loads ($R_a=0.19 \mu\text{m}$).

TABLE I. Measured roughness parameters of the perspex plates.

| Method of abrasion | Maximum peak to valley height (μm) | R_a (μm) | β^* (μm) | R_a/β^* |
|----------------------------|---|-------------------------|-----------------------------|---------------|
| p1000 grade emery paper | 1.44 | 0.19 | 2.48 | 0.10 |
| p800 grade emery paper | 4.37 | 0.47 | 6.92 | 0.09 |
| n/wr/100 grade emery cloth | 10.21 | 1.61 | 24.53 | 0.08 |

average or center line average (R_a or CLA) has been used to describe the height of the roughness and the correlation length (β^*) has been used to describe its distribution. These parameters do not uniquely describe a surface but do enable the character of a surface to be grasped quickly. They also provide a route by which dissimilar surfaces can be more easily compared and contrasted.

The roughness average was defined in Eq. (5) and the correlation length is defined as the wavelength when the autocorrelation function has decayed to some specific fraction of its peak ($1/e$ has been used in this paper). The autocorrelation function, $R(\lambda)$, can be written as

$$R(\lambda) = \frac{1}{(L-\lambda)} \int_0^{L-\lambda} z(x)z(x+\lambda)dx, \quad (6)$$

where λ is the wavelength for which the autocorrelation function is being determined and all other symbols have their usual meanings.

The surface profiles of both the solid and the rubber were measured using a stylus profilometer to provide a discretised height map of the sample surface along a line. A Form Talysurf stylus profilometer was used with a $0.2\text{-}\mu\text{m}$ -radius stylus and a finely balanced arm so that minimum force was applied to the specimen but the surface contours were still followed. The profile line was assumed to be statistically representative of the roughness of the whole sample. The length of line determines the long wavelength roughness limit of the measurement, and the horizontal sampling interval and stylus radius determine the short wavelength limit. The shortest possible sampling interval was chosen as it was thought that roughness on a small scale determines the acoustic contact. For the surface roughness measurements described in this paper the sampling interval used was $1\ \mu\text{m}$ and the sample length was $1000\ \mu\text{m}$. The surface profiles were then statistically evaluated to find the roughness parameters. Surfaces of different surface roughness were manufactured by abrading perspex plates with different grades of glass paper and emery cloth. The measured parameters are shown in Table I. Unabraded perspex was not tested as this requires loads to cause perfect coupling below that due to the mass of the perspex plate and water bath (2.5N) shown in Fig. 2. The roughness caused by abrasion with the finest emery paper is still a very smooth surface in engineering terms and is typical of that produced by grinding. The coarser emery papers cause roughness typical of that caused by lower quality machining processes such as turning or shaping.

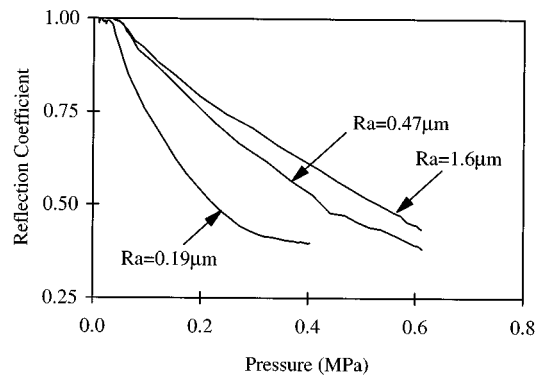


FIG. 6. Measured reflection coefficient variation with pressure for three different surface roughnesses.

Note from Table I that the ratio, R_a/β^* , is approximately constant; this is a factor of the abrasion method. Although different grades of emery paper have different sized abrading particles the shape of the particles remains approximately constant.

The plates described in Table I were used in turn to provide the measurement interface of the apparatus shown in Fig. 2 and hence the effect of surface roughness was studied. All reflection coefficient profiles of the contact region had a similar form to that shown in Fig. 3 for the smoothest plate, but the loads needed to achieve a given level of reflection coefficient below unity were higher for increased roughness. Figure 6 shows the effect of increased surface roughness on the reflection coefficient variation with pressure. Only the highest load case has been plotted for each roughness to avoid confusion. As expected, for each surface roughness, the reflection coefficient can be seen to decrease with increasing pressure toward the perfect contact value. It can be seen that increased surface roughness increased the pressure needed to achieve a given level of coupling. The pressure needed to achieve perfect contact varies from about $0.35\ \text{MPa}$ when $R_a=0.19\ \mu\text{m}$ to over $0.6\ \text{MPa}$ when $R_a=1.61\ \mu\text{m}$. If such a rubber is to be used in a dry coupled system these pressures need to be achieved at the dry coupled interface to allow consistent coupling.

III. PREDICTION OF REFLECTION COEFFICIENT VERSUS PRESSURE

A. Description of the numerical contact model

The numerical contact model used is a two-dimensional, linear elastic model developed by Webster and Sayles.¹⁶ The inputs are measured surface profiles obtained, in the case of this work, by a stylus profilometer. In order to simplify the analysis the following assumptions are made:

- (1) the contact is linear elastic,
- (2) friction effects, i.e., stick-slip effects, are neglected,
- (3) horizontal displacements are neglected,
- (4) the surface slopes are small and so local roughness does not affect global displacements,
- (5) the displacements are small compared to the sizes of the bodies.

The surface profiles of the two surfaces are summed to create a ‘‘composite’’ surface and contact is then modeled between

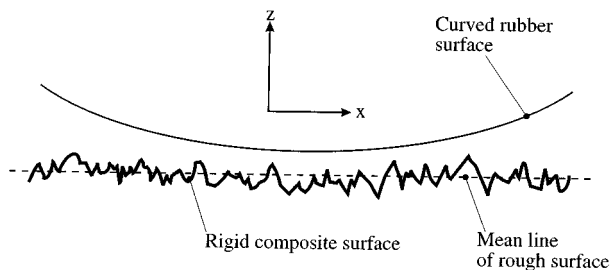


FIG. 7. Inputs to the numerical contact model.

this surface and a smooth surface. As the analysis is two dimensional, each “point” on the digitized profile is represented by a line. Where a point on the composite surface profile touches the flat surface, the relationship between the surface deflection and the applied load is given by the equation for line loading of a semi-infinite half-space.¹⁷ The deflection of the surface due to a pressure distribution can be found by superposition of the deflections caused by a number of line loadings. The geometry of the contact is shown in Fig. 7 where it can be seen that the contact is between a smooth, curved surface and a rough plane. The software was written to handle the contact of two curved surfaces but in the work described here the radius of curvature of one of these surfaces was set to infinity to model a plane surface. The other surface must remain curved such that all the contact between the two bodies remains within the length of surface modeled. Solution proceeds by making an initial guess for the surface displacements of each point on the two surfaces based on the geometric overlap of the surfaces. The pressures across the surface are then calculated, some of which will be negative (tensile) as the initial displacement guess is an underestimate. The terms corresponding to the negative pressures are removed and a reduced set of equations formulated. The solution is then repeated with the reduced set of equations and an extra test is carried out to ensure that points removed from the set would not be in contact under the new conditions. Iteration continues until all pressures are positive and the above test is satisfied. The total load on the system is calculated by summing the calculated pressures. If the total load taken by the interface is equal to the applied load then the solution is complete, and if it is not then the overlap of the bodies is changed in the appropriate direction and the above iteration repeated until the required load is reached.

B. Interfacial stiffness direct from the numerical contact model

The aim of the modeling is to predict the reflection coefficient as a function of interfacial geometry. The numerical contact model can be used to calculate the interfacial geometry at a given applied pressure. Then, at each pressure, and hence each interfacial geometry, it is necessary to determine the interfacial spring stiffness, and hence the reflection coefficient. The interfacial spring stiffness can be obtained from the numerical contact by applying a load to the interface and hence developing an interfacial pressure distribution and deformed interfacial geometry. The load is then increased (or

decreased) slightly causing a small amount of deflection of the interface. The change in pressure, ΔP , and the resulting interfacial closure, $\Delta \delta_I$ are recorded from which the interfacial stiffness per unit area is obtained by

$$k = \frac{\Delta P}{\Delta \delta_I}. \quad (7)$$

The stiffness obtained will be approximately that of the interface at a pressure equal to the average pressure over the increment. In the limit as the size of the pressure increment becomes zero so the value of interfacial stiffness obtained becomes that corresponding exactly to the applied pressure.

Ideally the interfacial closure is assessed remotely by considering the “approach” of distant points on the two bodies with and without the roughness. When the roughness is included, the “approach” will be greater due to the extra displacement caused by the interface. By subtracting these two “approaches,” the displacement due to the interface can be found and this measurement is then in line with the definition presented by Baik and Thompson.³ Unfortunately the “approach” due to body deflections is many orders of magnitude above that due to the interface and so when this calculation is attempted using the numerical contact model the numerical errors are large and dominate the result.

The average interfacial closure, measured at the interface can be used as an alternative definition of deflection due to the interface. Using this definition the deflection of the interface can easily be calculated by considering in turn the separation of the points that make up the interface. At each position along the interface there will be two points, one on the rigid body and one on the rubber body. If these points are initially apart, then, as the load on the system is increased, these points will approach one another until they meet, at which point the gap is closed and contact pressure is developed. The change in separation of these two points, due to a change in pressure, is termed the interfacial closure. The average interfacial closure is then given by

$$\Delta \delta_{I(\text{ave})} = \frac{1}{N} \sum_{n=1}^{n=N} (\Delta \delta_I)_n, \quad (8)$$

where N is the number of points over which the average is taken. This average interfacial closure can now be used in Eq. (7).

The Young’s modulus of rubbers increases significantly with strain rate and hence frequency. The low-frequency Young’s modulus determines the contact geometry, but it is the high-frequency Young’s modulus which determines the propagation characteristics of the interface. The high-frequency Young’s modulus was determined from a measurement of the shear wave velocity of the rubber assuming a Poisson’s ratio of 0.5 (the longitudinal wave velocity was not used as the relationship between this velocity and Young’s modulus is highly sensitive to Poisson’s ratio in the region where $\nu \approx 0.5$). The low-frequency Young’s modulus (1.3 MPa) is used in the numerical contact model to determine the interfacial geometry for a given load and then, assuming this interfacial geometry, the Young’s modulus at 5 MHz (13 MPa) is used in the numerical contact model to find the

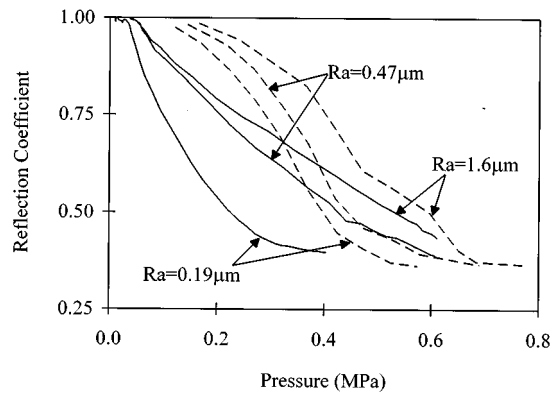


FIG. 8. Measured (solid lines) and numerical contact model predicted (dashed lines) perspex–rubber reflection coefficient variation with pressure for three different surface roughnesses.

interfacial stiffness. As the system is elastic the same result can be obtained by calculating the interfacial stiffness purely with the low-frequency Young's modulus and then scaling up the stiffness by the ratio of the 5-MHz Young's modulus to the low-frequency Young's modulus.

This stiffness can then be used in a spring model to predict the reflection coefficient of the interface. Figure 8 shows the predicted variation of reflection coefficient with pressure plotted on the same graph as the experimental results. Note that the predicted lines are not smooth due to the limited number of points at which calculations were performed. From this figure it can be seen that for the medium and high roughness perspex plates the agreement is good at high loads and reasonable at low loads. The prediction for the low roughness perspex plate is poor indicating pressures 50% greater than those measured to achieve a given reflection coefficient. This inaccuracy could be because the sampling interval used to discretize the roughness profile was not adequate to describe the surface. This is likely as the sampling interval used was $1 \mu\text{m}$ which is comparable to the correlation length of the profile. Sampling intervals smaller than $1 \mu\text{m}$ were not available on the high quality stylus profilometer used.

C. Interfacial stiffness from crack models

Angel and Achenbach⁵ and Baik and Thompson³ modeled imperfect interfaces as a series of cracks. They then used fracture mechanics analysis to calculate the stiffness of the cracks and hence the interface assuming a quasistatic model. Data on the stress fields around cracks and the forces required to open them are widely published.¹⁸ From these data, the extra deflection due to the presence of a given crack and hence, the stiffness of the cracked specimen, can be calculated. The gaps left at an imperfect interface are generally long and thin in shape and so can be approximated by cracks in the plane of the interface with little error. As the numerical contact model allows the interfacial geometry of a partially contacting solid–rubber interface to be predicted, it is now possible to test the proposition that crack models can be used to predict the stiffness of such interfaces.

A partially contacting solid–rubber interface can be modeled as a series of cracks, each crack representing one of

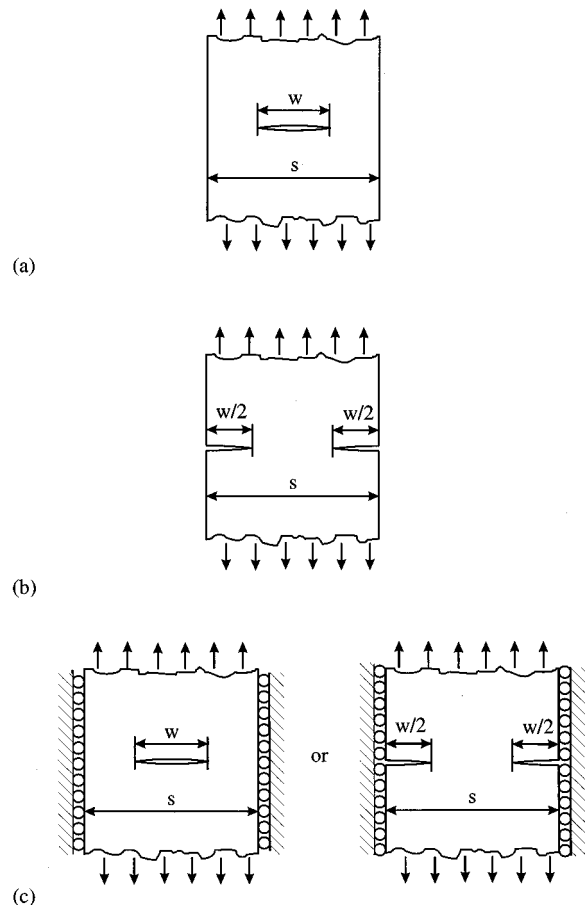


FIG. 9. Unit cell crack models of partially contacting interfaces; (a) center crack model; (b) double edge crack model; (c) plane strain crack model.

the gaps left at the solid–rubber interface. Figure 9 shows three possible unit cell crack models that could be used to represent one of the gaps from an imperfect interface. In each case, the cracks shown are in the plane of the interface. Figure 9(a) is called the center crack model, Fig. 9(b) is called the edge crack model, and Fig. 9(c) shows two plane strain crack models. Models (a) and (b) have free-vertical edges, whereas the models shown in (c) have plane strain boundary conditions on the vertical edges such that these edges are constrained to move only in the vertical plane. Note that the plane strain center crack and plane strain edge crack models are equivalent. The real boundary conditions of a gap at an imperfect interface will be somewhere between free and plane strain depending on the effect of neighboring gaps. The stiffnesses of such cracks can be found from standard fracture mechanics handbooks, for example Tada *et al.*¹⁸ At low percentages of contact, the interface will consist of many, approximately circular, contacts and so, in three dimensions a circumferential edge crack model, which would leave a circular contact region, would seem to be a good approximation. The two-dimensional equivalent of this is the edge crack model. At high percentages of contact, the interface will consist of many, approximately circular, gaps and so, a circular crack model would seem to be a good approximation. The two-dimensional equivalent of this is the center crack model.

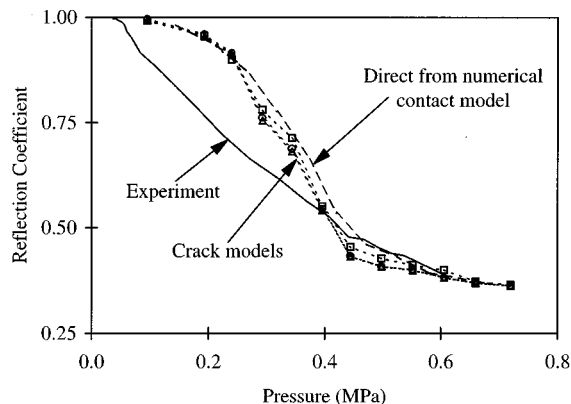


FIG. 10. Comparison between the reflection coefficient variation with pressure predicted by crack based models, predicted using the numerical contact model and experiment ($R_a=0.47 \mu\text{m}$). The edge crack model is shown by the hollow square, the center crack prediction by the hollow circle and the plane strain crack model by the hollow triangle.

Once a crack model of the interface has been chosen, the next step is to link these unit cell models to describe the whole interface. Using the stiffness per unit area of the average gap unit cell is one possibility, but this will be incorrect if the relationship between gap or contact size and stiffness is nonlinear. Using the unit cell of average stiffness is another possibility, but this model cannot cope with the effect of small gaps which may have stiffnesses approaching infinity just before they close. A more robust approach is, first to calculate the stiffnesses of all the unit cells, and then to apply a pressure across the interface such that it acts equally on each unit cell. Each unit cell will deflect due to the crack, and the resulting average interfacial deflection across all unit cells can be found and used in Eq. (7) to find the overall interfacial stiffness. This is effectively how the stiffness was calculated directly from the numerical contact model. This procedure was implemented as follows; first the deflection of one unit cell due to the average applied pressure was calculated,

$$\delta_1 = \frac{P_{\text{ave}}}{k_1}, \quad (9)$$

where the subscript refers to the particular unit cell under consideration. This deflection was then weighted according to the width of the unit cell, s , to calculate the length averaged deflection,

$$\delta_{\text{ave}} = \sum_{m=1}^{m=M} \frac{P_{\text{ave}} s_m}{k_m L}, \quad (10)$$

where M is the total number of unit cells along a length L of the interface, s_m is the width of the m th unit cell, and k_m is the stiffness of the m th unit cell. The overall interfacial stiffness can then be written as

$$k_{\text{ave}} = \frac{P_{\text{ave}}}{\Delta_{\text{ave}}} = \frac{L}{\sum_{m=1}^{m=M} (s_m / k_m)}. \quad (11)$$

This stiffness can then be used to calculate reflection coefficient by using Eq. (4). Figure 10 shows the variation of reflection coefficient with pressure as predicted from the

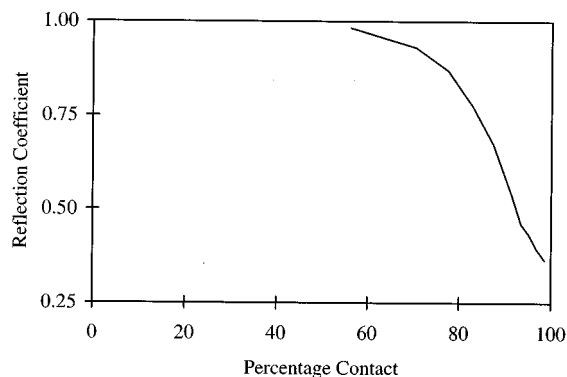


FIG. 11. Numerical contact model prediction of the variation of the perspex-rubber reflection coefficient with percentage contact for the perspex plate of $R_a=0.47 \mu\text{m}$.

three crack models in this way plotted on the same graph as the experimental data and the prediction direct from the numerical contact model. Note that the experimental data and the predictions shown in this figure correspond to the perspex plate of $R_a=0.47 \mu\text{m}$ and that the spring model prediction lines are not smooth due to the limited number of points at which calculations were performed. The agreement between these predictions and the experimental results is reasonable in general and good at the higher loads. These crack model based predictions follow similar curves to those obtained directly from the numerical contact model showing that crack based models can be used to predict the stiffness of partially contacting solid-rubber interfaces if the interfacial geometry is known.

D. True area of contact

Figure 11 shows the predicted variation of reflection coefficient with percentage contact (proportional to the true area of contact) for the case of the perspex plate of roughness $R_a=0.47 \mu\text{m}$. The percentage contact was calculated from the output of the numerical contact model by considering the percentage of points across a given interface where contact pressure exists. An interesting point to note from this figure is that the reflection coefficient only decreases slightly up to 70% contact and then decreases rapidly toward the perfect contact value as percentage contact is increased above 70%. This means that in a solid coupled system where good coupling is essential, the percentage contact must be above 70%. Note that the line is not smooth due to the limited number of points at which the calculation was performed (the percentage contact required for good coupling is a function of the correlation length; the 70% value obtained here is typical for correlation lengths in the region shown in Table I).

It is interesting to note that the graph of percentage contact versus reflection coefficient shown in Fig. 11 is vastly different to that predicted by the authors for an aluminum-aluminum contact.¹⁹ For an aluminum-aluminum contact perfect coupling was achieved at 10%–15% contact for the same ratio of wavelength to interfacial geometry. This comparison was made by using the measured surface profile of the $R_a=0.47\text{-}\mu\text{m}$ perspex plate in the numerical contact model with aluminum material properties. When calculating

the reflection coefficient of the aluminum–aluminum contact from Eq. (4) the frequency was adjusted such that the wavelength in the aluminum was the same as in the rubber at 5 MHz. This reduction in percentage contact to achieve perfect coupling in the case of aluminum–aluminum contact as compared with the case of perspex–rubber contact is not intuitive and so warrants further thought. Equation (4) can be rewritten for the case when the material either side of the partially contacting interface is the same,

$$|R_{12}| = \frac{1}{\sqrt{(4K/\omega z)^2 + 1}}, \quad (12)$$

where all symbols have their usual meanings. The controlling parameter, Π , of this equation is

$$\Pi = K/\omega z. \quad (13)$$

For the case of rubber–perspex contact, Eq. (12) does not apply as rubber and perspex have different acoustic impedances so for the sake of this discussion consider the case of rubber–rubber contact. Baik and Thompson³ showed that the interfacial stiffness obtained from crack models is of the form

$$K = \frac{E'}{s} f\left(\frac{w}{s}\right), \quad (14)$$

where E' is the plane strain modulus, s is the separation of the gaps, w is the width of the crack, and $f(w/s)$ is a function of the percentage contact (see Fig. 9 for some examples of typical crack models). Substituting Eq. (14) into Eq. (13) and rewriting frequency in terms of wavelength gives

$$\Pi = \left(\frac{\lambda}{s}\right) \left(\frac{f(w/s)}{2\pi}\right) \left(\frac{E'}{\rho c^2}\right). \quad (15)$$

The first term is the ratio of the gap separation to the wavelength, the second term is a function of the percentage contact of the interface and the third term is governed by the material properties of the propagating medium. The third term of Eq. (15) can be rewritten by substituting the relationship between longitudinal velocity, Young's modulus, and Poisson's ratio which gives

$$\frac{E'}{\rho c^2} = \frac{(1-2\nu)}{(1-\nu)^2}. \quad (16)$$

Now if the Poisson's ratio of the surface is equal to 0.34, as it is for aluminum then the term shown in Eq. (16) is equal to 0.73. As Poisson's ratio tends toward 0.5 this term tends toward 0 and from Eq. (4) the reflection coefficient then tends toward unity. The Poisson's ratio of rubber is close to 0.5 and so if all the other terms in Eq. (15) are equal then the rubber–rubber reflection coefficient will be higher than the aluminum–aluminum reflection coefficient.

For the case of rubber–perspex contact the dependence on Poisson's ratio is the same but the proof is more complicated than that presented above. The difference between the aluminum–aluminum and the perspex–rubber reflection coefficient variations with percentage contact can therefore be explained as a Poisson's ratio effect. This causes the difference between the longitudinal wave velocity of aluminum

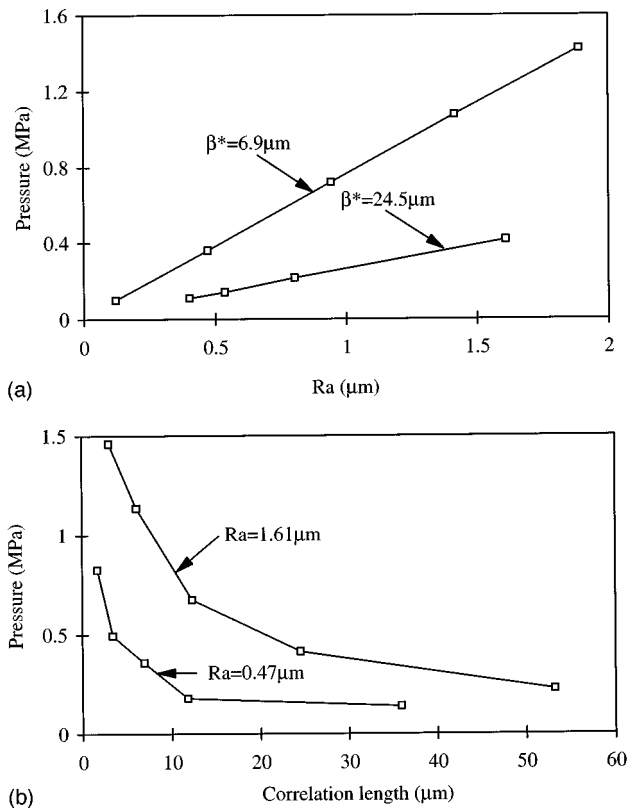


FIG. 12. Variation of pressure required to achieve 90% acoustic contact with R_a of the surface for two different correlation lengths. (b) Variation of pressure required to achieve 90% acoustic contact with correlation length of the surface for two different values of R_a .

and rubber to be small (i.e., 6000 m/s in aluminum and 1500 m/s in rubber) compared to the difference between their Young's moduli (i.e., 70 GPa for aluminum and 0.013 GPa for rubber).

IV. IMPLICATIONS FOR DRY COUPLED SYSTEMS

A. The effect of surface roughness

The effect on coupling of changing the R_a and β^* of the surfaces was investigated by creating artificial surface profiles by magnifying and stretching those measured from the perspex plates and then putting them in the numerical contact model. Magnifying the surface profiles increased the R_a leaving β^* unchanged, whereas stretching the profiles had the opposite effect, increasing β^* and leaving R_a unchanged. For each surface the numerical contact model was used to form a graph of reflection coefficient versus pressure, from which the pressure required to achieve a reflection coefficient within 10% (90% acoustic contact) of the perfect coupling value was taken. Figure 12(a) shows that the variations of the predicted pressure required to achieve 90% acoustic contact with R_a are approximately straight lines through the origin. This can be explained as the contact model is based on linear elastic theory and only vertical movement of the points is permitted. This means that if the R_a is increased by, say, a factor of 2, then the displacement of a given point required to achieve a given level of contact will double and, as the material is linear elastic, so the force required to displace it will

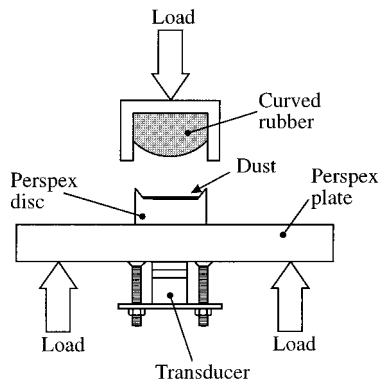


FIG. 13. Experimental setup used to measure reflection coefficients from a layer of dust trapped at a perspex–rubber interface.

also increase by a factor of 2. Deviation from a linear relationship indicates inaccuracies in the model. The variation in pressure required to achieve 90% acoustic contact with β^* can be seen in Fig. 12(b) from which it can be seen that when β^* is high the pressure to achieve 90% acoustic contact is low and as β^* is decreased, it becomes increasingly difficult to achieve 90% acoustic contact. These results quantitatively describe the observation that it is easier to conform around shallow, long asperities than it is to conform around deep narrow asperities. This procedure could be used to create a contour map showing the pressure required to achieve a given level of coupling for any combination of R_a and β^* .

B. Experiments to consider the effect of dust and dirt

Under laboratory conditions it is easy to ensure that all surfaces are kept clean and free from surface contamination such as dust, dirt, and oxide layers. In a typical industrial environment a surface may have all of these contaminants to some degree and so it is important that their effects are considered. The aim of these experiments is to determine the effect of particulate contaminants such as dust and dirt on the coupling performance of solid coupled ultrasonic devices. The particulate contaminants become trapped between the test structure and the rubber couplant hence decreasing the level of coupling. Particulate contaminants come in all shapes and sizes but it is expected that in any nondestructive testing system the larger particles (over 150 μm) will be removed from the surface prior to inspection by, for example, wire brushing. In many industrial environments smaller particles, such as airborne dust, are unavoidable and so particles in the diameter range 1–150 μm will be considered in this study.

In a series of experiments particles of known size were spread over a 15-mm-diam polished perspex disk shown in Fig. 13. The particles, made from silica, brass, iron, or diamond, had been sieved by the supplier and sorted into groups with tight size ranges. The particles were evenly spread over the perspex disk with a brush giving the surface a coating that was “light” and even in appearance. A rubber disk was then loaded against the perspex disk trapping the particles at the rubber–perspex interface. A wideband 5-MHz plane transducer was used, this frequency being representative of

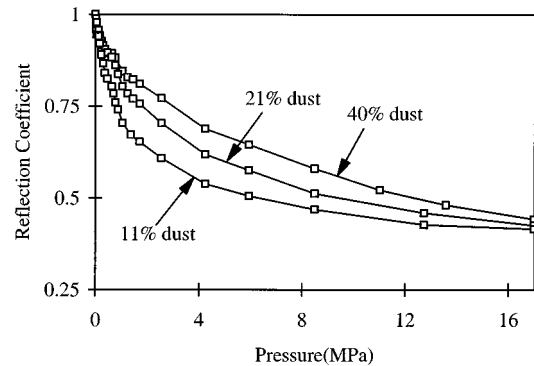


FIG. 14. Measured perspex–rubber reflection coefficient variation with pressure for different masses of 5- μm dust particles. Number of particles expressed as percentage of the surface covered.

the operating frequency of dry coupled devices. The signal reflected from the perspex–rubber interface was compared with the signal reflected from the perspex interface when no rubber was present, and the reflection coefficient known to be unity, and hence the perspex–rubber reflection coefficient was calculated.

Figure 14 shows the variation of reflection coefficient with pressure when the perspex disk was coated with a number of different masses of 5- μm particles. It can be seen that, as expected, the reflection coefficient decreases with pressure and that for a given pressure the greater the mass of particles used the higher the reflection coefficient. The reflection coefficient at high pressures approaches the perfect contact reflection coefficient of 0.38 indicating that the proportion of the wave scattered obliquely at this point is small.

Figure 15 shows the variation of reflection coefficient with pressure when 0.002 g of a range of different particle sizes were spread over the perspex disk shown in Fig. 13. It can be seen that, as expected, the reflection coefficient falls with increased pressure for all particle sizes. For particle sizes other than 1.5- μm diameter, large pressures are needed to achieve a reflection coefficient from the interface approaching that of a perfectly bonded perspex–rubber interface. Figure 16 shows the reflection coefficient variation with

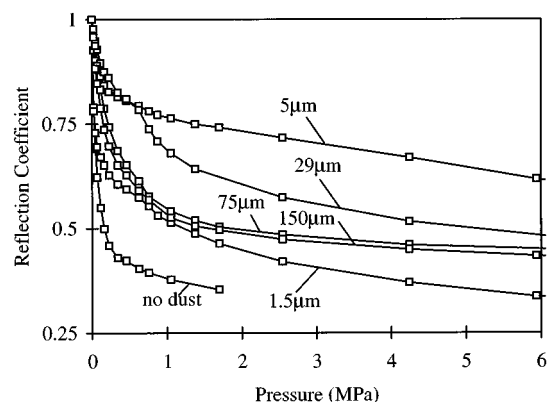


FIG. 15. Measured perspex–rubber reflection coefficient variation with pressure for a number of different dust particle sizes and a constant mass (0.002 g) of dust.

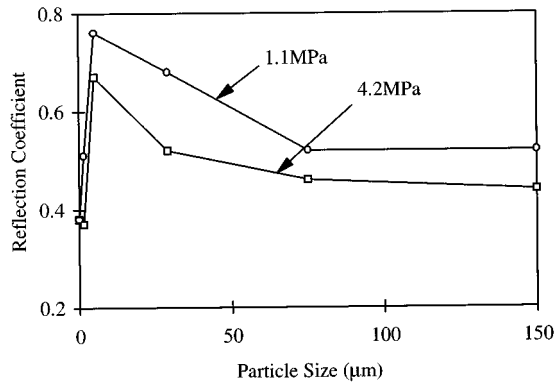


FIG. 16. Measured perspex-rubber reflection coefficient variation with particle size at two different loads and 0.002 g of dust particles.

particle size at pressures of 1.1 and 4.2 MPa. This shows that there appears to be a “worst” possible dust size of approximately 5 μm and that the large particle sizes appear to present less of a barrier to the ultrasound.

This latter effect can be described qualitatively by considering the load needed to embed a rigid cylinder into an elastic half-space. The deflected shape of the surrounding material is given by Johnson²⁰ as,

$$U_z(r) = \frac{W}{\pi E' a} \sin^{-1}\left(\frac{a}{r}\right) \quad \text{for } r \geq a, \quad (17)$$

where $U_z(r)$ is the vertical displacement of the elastic solid at a distance r from the center of the cylinder, W is the applied load, a is the radius of the cylinder, and E' is the plain strain modulus of the half-space. From this equation the load required to embed the full height of the particle into the rubber can be found by setting $U_z(a) = h$, where h is the height of the cylinder. The load is given by

$$W = 2haE'. \quad (18)$$

If the height of the particle is equal to the diameter of the particle then from Eq. (18) it can be seen that the force required to embed the particle increases as the square of particle size. For a given mass of particles the number of particles decreases as the cube of particle size. This means that the force needed to embed a given mass of particles is inversely proportional to the particle size. Of course there is a limit to this effect as the particles become so small that the air gaps they create present a reduced barrier to the ultrasonic wave. This appears to happen when the particle size becomes comparable with the surface roughness, and it could be imagined that such small particles disappear into the roughness contours. This fitting together of the particles and the surface roughness will further reduce the size of the remaining air gaps and could explain the why the 1- to 2- μm particles had significantly less effect than the 5- μm particles.

An “effective” R_a of the dust-covered surfaces can be calculated by considering the dust as a series of rectangles on a flat surface of height, width, and separation equal to those of the dust. If a surface 21% covered by 5- μm particles is modeled in this way the “effective” $R_a = 1.6 \mu\text{m}$ and the required separation of the particles (rectangles) is 25 μm .

From Fig. 14 the pressure required to achieve 90% acoustic contact (reflection coefficient is 0.44) for this case is 15 MPa. From Fig. 6 it can be seen that the pressure required to achieve 90% coupling on a rough surface of $R_a = 1.6$ and $\beta^* = 24.5 \mu\text{m}$ is approximately 0.6 MPa. It can be seen that this rough surface has similar characteristics to the dust covered surface but that considerably less pressure is required to achieve 90% coupling. This is due to the steep surface gradients around the dust particles which are more difficult to conform around than the much lower surface gradients of a typical rough surface which are typically around 10 deg. This explains the severely detrimental effect of dust and dirt on the coupling performance of dry coupled devices.

V. CONCLUSIONS

Measurements of perspex-rubber reflection coefficient variations with pressure have been described. These measurements now mean that the interfacial pressure required to achieve a given level of coupling is known for a typical soft rubber and a range of surface roughnesses. To achieve perfect coupling with these materials, an interfacial pressure of 0.5 MPa is required on a surface of $R_a = 0.47 \mu\text{m}$ and $\beta^* = 6.9 \mu\text{m}$. These measurements could now be repeated on any prospective coupling material in order to assess its coupling performance on a given test structure.

Measured surface profiles have been used in a numerical contact model to predict the perspex-rubber contact geometry under load. This model can then be used to predict the static stiffness of the interface. This stiffness was then used in a quasi-static model to predict the reflection coefficient variation with predicted percentage contact. The reflection coefficient was predicted from stiffness obtained directly from the numerical contact model and from a number of simple interfacial models. These predictions were in good agreement with the reflection coefficient measurements, particularly at high pressures.

The effect of dust and dirt on the coupling performance of dry coupled devices has been studied experimentally. The variation of perspex-rubber reflection coefficient with pressure for different amounts and sizes of particles was measured. This showed, for example, that the pressure required to achieve 90% acoustic contact when 0.006 g (21% covered) of 5- μm particles are trapped is approximately 15 MPa. This is an indication of the severely detrimental effect of particulate contamination on coupling. For this reason a dry coupled wheel probe will require a built-in brushing device to clean the surface in front of the tire.²¹

¹B. W. Drinkwater and P. Cawley, “An Ultrasonic Wheel Probe Alternative to Liquid Coupling,” *Insight* **36**, 430–433 (1994).

²B. Fay, “Ultrasonic Backscattering: Fundamentals and Applications,” in *Physical Acoustics*, edited by O. Leroy and M. A. Breazeale (Plenum, New York, 1991).

³J. M. Baik, and R. B. Thompson, “Ultrasonic Scattering from Imperfect Interfaces: a Quasi-Static Model,” *J. Non-Destruct. Eval.* **4**, 177–196 (1984).

⁴F. J. Margetan, R. B. Thompson, J. H. Rose, T. A. Gray, “The Interaction of Ultrasound with Imperfect Interfaces: Experimental Studies of Model Structures,” *J. Non-Destruct. Eval.* **11**, 109–126 (1992).

⁵Y. C. Angel, and J. D. Achenbach, “Reflection and Transmission of Elas-

- tic Waves by a Periodic Array of Cracks," J. Appl. Mech. **52**, 33–40 (1985).
- ⁶P. B. Nagy, "Ultrasonic Classification of Imperfect Interfaces," J. Non-Destruct. Eval. **11**, 127–139 (1992).
- ⁷N. F. Haines, "The Theory of Sound Transmission and Reflection at Contacting Surfaces," CEGB Berkely Nuclear Laboratories, Report No. RD/B/N4744, 1980.
- ⁸J. Krolikowski and J. Szczepek, "Prediction of Contact Parameters Using Ultrasonic Method," Wear **148**, 181–195 (1991).
- ⁹L. E. Kinsler, and A. R. Frey, *Fundamentals of Acoustics* (Wiley, New York, 1962).
- ¹⁰T. P. Pialucha, "The Reflection Coefficient from Interface Layers in NDT of Adhesive Joints," Ph.D., University of London, 1992.
- ¹¹H. G. Tattersall, "The Ultrasonic Pulse-Echo Technique as Applied to Adhesion Testing," J. Appl. Phys. D: Appl. Phys. **6**, 819–832 (1973).
- ¹²B. W. Drinkwater, T. P. Pialucha, and P. Cawley, "The Transmission of Ultrasound Across Solid–Solid Interfaces—Practical Measurement Considerations," Rev. Prog. Quant. NDE **13**, 1399–1405 (1994).
- ¹³P. Meijers, "The Contact Problem of a Rigid Cylinder on an Elastic Layer," Appl. Sci. Res. **18**, 353–383 (1968).
- ¹⁴M. G. Silk, *Ultrasonic Transducers for Nondestructive Testing* (Hilger, Bristol, 1984).
- ¹⁵R. S. Sayles, "The Profile as a Random Process," in *Rough Surfaces*, edited by T. R. Thomas (Longman Group, London, 1982), pp. 91–108.
- ¹⁶M. N. Webster and R. S. Sayles, "A Numerical Model for the Elastic Frictionless Contact of Real Rough Surfaces," Trans. ASME—J. Tribol. **108**, 314–320 (1986).
- ¹⁷S. Timoshenko, *Theory of Elasticity* (McGraw-Hill, London, 1951).
- ¹⁸H. Tada, P. Paris, and G. Irwin, *The Stress Analysis of Cracks Handbook* (Del Research Co., St. Louis, 1973).
- ¹⁹B. W. Drinkwater, R. Dwyer-Joyce, and P. Cawley, "A Study of the Interaction Between Ultrasound and a Partially Contacting Solid–Solid Interface," Proc. R. Soc. London (in press).
- ²⁰K. L. Johnson, *Contact Mechanics* (Cambridge U.P., Cambridge, 1985).
- ²¹B. W. Drinkwater and P. Cawley, "The Effect of Dust and Surface Roughness on the Efficiency of Solid Coupled Ultrasonic Transducers," Rev. Prog. Quant. NDE **15**, 955–962 (1996).

Optimal binaural processing based on point process models of preprocessed cues

Lin Yue and Don H. Johnson

Computer and Information Technology Institute, Department of Electrical and Computer Engineering, Rice University, Houston, Texas 77005-1892

(Received 23 August 1995; revised 8 June 1996; accepted 30 September 1996)

Toward localizing high-frequency tonal signals in the horizontal plane, the lateral superior olive (LSO) encodes the interaural level differences, the crucial cue for azimuthal angle extraction by more central nuclei in the binaural pathway. This paper derives optimal processors for localization using inputs from the LSO and anteroventral cochlear nucleus. Both Poisson and non-Poisson point processes are developed to model cellular responses. The LSO projection is shown to be the only input needed in maximum likelihood angle estimation, and it is processed similarly under different LSO response models. However, localization performance depends strongly on the model's regularity, with increasing regularity improving localization accuracy and precision. © 1997 Acoustical Society of America. [S0001-4966(97)05302-2]

PACS numbers: 43.64.Bt, 43.66.Qp, 43.66.Pn, 43.64.Qh [RDF]

INTRODUCTION

In sound localization, binaural hearing is superior to monaural hearing because differences between the stimuli at the two ears provide crucial cues that supplement those available in the monaural case. Neurophysiological studies have shown that most lateral superior olive (LSO) units are high-frequency sensitive ($CF \geq 3$ kHz). They are excited by ipsilateral input from anteroventral cochlear nucleus (AVCN) and inhibited by contralateral input from medial nucleus of trapezoid body (MNTB) (Boudreau and Tsuchitani, 1968; Guinan *et al.*, 1972). LSO cells are presumed to be involved in the localization of high-frequency tonal stimuli using binaural cues. The potential role of LSO in encoding interaural level differences (ILD) between ipsilateral and contralateral stimuli is suggested by the sensitivity of unit discharge rates to ILD (Tsuchitani and Boudreau, 1969). Theoretical studies (Dabak, 1990; Johnson *et al.*, 1990) describe the role of LSO in localization as an optimal processor that provides the sufficient statistic related to ILD to some higher auditory center responsible for extracting lateral angle. The inferior colliculus (IC) is believed to be one such center because, among the numerous pathways that converge on the contralateral IC, the ipsilateral LSO and ipsilateral AVCN provide major ascending projections (Adams, 1979; Irvine, 1986).

In this paper, we theoretically investigate how a higher center localizes a sound source, i.e., produces an estimate of lateral angle, using LSO and AVCN discharges (Yue, 1995). By approaching the localization problem from an estimation theoretic point of view, we consider the higher center as an optimal processor that produces an angle estimate by processing inputs from LSO and AVCN (Fig. 1). Our work is mainly concerned with three aspects of the optimal processor: what information it uses in localization, how the representation of this information impacts its processing, and how well it performs. This work departs from previous studies (Johnson *et al.*, 1990) in that more accurate point process models are used throughout, especially when we model LSO

discharge patterns. This additional precision allows comparison of performance differences among optimal processors designed for Poisson inputs, which are typically assumed in modeling efforts for analytic tractability, and for non-Poisson (renewal and nonrenewal) inputs.

I. NEURONAL DISCHARGE MODELING

A. Binaural acoustics

The complex geometry of the torso, head, and pinna produces direction-dependent information of sound waves in terms of both amplitude and time-of-arrival discrepancies at the two ears. The head-baffle and head-shadow effects give rise to interaural level differences (ILD) and interaural time differences (ITD), which are major cues for sound localization. Defined as the ratio between sound pressure at the left ear and sound pressure at the right ear, ILD is a reliable localization cue at high frequencies when significant level differences are present at the two ears (Kuhn, 1987). We focus our attention on ILD instead of ITD since high-frequency sound signals incident in the horizontal plane are not generally localized on the basis of ITD (Green, 1976; Kuhn, 1987).

A simplified geometry of incident plane wave relative to the head is depicted in Johnson *et al.* (1990). A denotes the amplitude of the sound source. The lateral angle is denoted by θ , with 0° corresponding to midline and positive angles corresponding to the right hemisphere. We study here the localization performance of the lower auditory pathway and restrict the sound source to lie in the right quadrant ($0^\circ \leq \theta \leq 90^\circ$), taking the right side as ipsilateral. In our modeling, the directivity function is idealized to be $D(\theta) = \exp\{k \sin \theta\}$ with $k=1$ (Dabak, 1990; Johnson *et al.*, 1990). Ignoring the time-of-arrival difference at the two ears, the signal amplitudes are $AD(\theta)$ and $AD(-\theta)$ at the right ear and the left ear, respectively. Thus, ILD measured with respect to the right ear is given by the ratio of the directivity functions

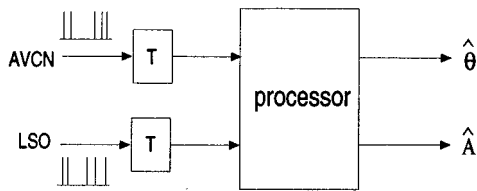


FIG. 1. Block diagram of the localization processing. Inputs to the location processor are LSO and AVCN discharges averaged over a fixed time interval of length T . Outputs are the lateral angle estimate $\hat{\theta}$ and the sound amplitude estimate \hat{A} .

$$\text{ILD} = \frac{D(\theta)}{D(-\theta)} \quad (1)$$

and is expressed in decibels. The ILD resulting from our idealized directivity function only approximates measured ILDs, which are highly frequency dependent and may be nonmonotonic (Irvine, 1987).

B. Auditory anatomy and physiology

The major nuclear divisions of the brainstem auditory pathway that concern us here are shown schematically in Fig. 2. The AVCN, one of the major divisions of the cochlear nucleus (CN), receives ascending projections from auditory-nerve fibers, and sends afferent discharges to the ipsilateral LSO and the contralateral MNTB. The AVCN input excites LSO neurons. The LSO also receives inhibitory input from the homolateral MNTB. The IC receives ascending projections from many nuclear divisions, including AVCN and LSO.

There are two types of large neurons, bushy cells and stellate cells, located in the AVCN (Bourk, 1976; Brawer *et al.*, 1974; Tolbert *et al.*, 1982). Firm correspondence between physiological response and cellular morphology has been observed: bushy cells are mainly primarylike units, and

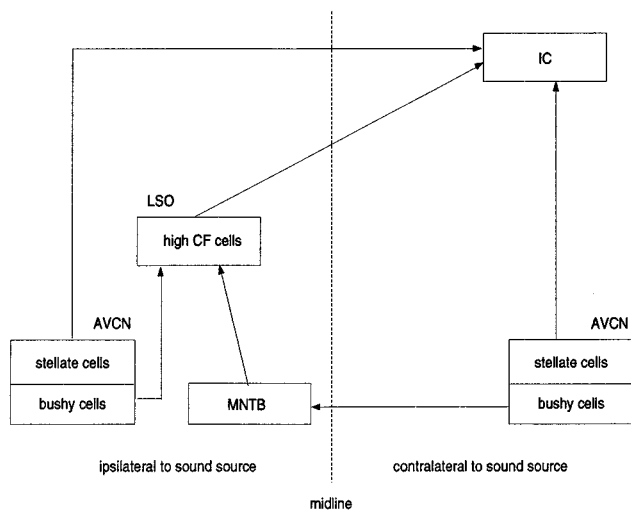


FIG. 2. Auditory pathway from periphery to IC. LSO receives excitatory inputs from ipsilateral AVCN bushy cells and inhibitory inputs from contralateral AVCN bushy cells via homolateral MNTB. High-CF LSO cells project contralaterally to IC. AVCN stellate cells send major projections contralaterally and minor projections ipsilaterally to IC.

stellate cells are choppers (Adams, 1976; Rhode *et al.*, 1983; Pfeiffer, 1966). The spherical bushy cells, heavily concentrated in the rostral part of the AVCN, project to the ipsilateral LSO (Cant and Casseday, 1986; Warr, 1966). The globular bushy cells, found in the interstitial nucleus and the posterior part of the AVCN, project to the contralateral LSO via the contralateral MNTB (Warr, 1972). The spherical cells are primarylike units, while the globular cells are primarylike-with-notch units (Bourk, 1976; Goldberg and Brownell, 1973; Pfeiffer, 1966). Poisson process models describe well these cells' responses to continuous tone stimuli (Bourk, 1976).

Unlike the bushy cells, the stellate cells in AVCN exhibit chopping responses to tone burst stimuli; this transient chopping response to stimulus onset can persist for over 20 ms (Irvine, 1986; Pfeiffer, 1966; van Gisbergen *et al.*, 1975). Both the spontaneous and the driven activity of chopper units are more regular than those of primarylike units. Poisson processes are inadequate to model these discharge patterns, even after the chopping ceases. Stellate cells provide major ascending projections to the contralateral IC and minor projections to the ipsilateral IC.

The LSO and medial superior olive (MSO) are believed to be the first centers of binaural processing in the auditory pathway. Most LSO units are high-frequency sensitive. The projections to LSO from AVCN and MNTB both have primarylike discharge patterns (Guinan *et al.*, 1972; Rhode *et al.*, 1983). LSO units are excited by ipsilateral inputs and inhibited by contralateral inputs (E/I characteristic) (Boudreau and Tsuchitani, 1968; Guinan *et al.*, 1972), and the sustained discharge rates of LSO units are related to ILD (Boudreau and Tsuchitani, 1968; Johnson *et al.*, 1990). The initial discharges of LSO cells to tone bursts are of the chopper type. Two types of LSO units have been defined according to the width and spacing of initial peaks in the PST histogram (Tsuchitani, 1982): fast choppers have narrow, closely spaced peaks, and slow choppers exhibit relatively broad, widely spaced peaks. The statistical properties of LSO discharges and previous LSO modeling work (Zacksenhouse, 1993) force non-Poisson models of LSO discharge patterns: interspike intervals (ISIs) are not even approximately exponentially distributed, and they are serially correlated. LSO neurons project to IC ipsilaterally and contralaterally, and these are partially segregated in that only a small percentage of LSO units send collaterals to both sides. The majority of the high-CF LSO units project to the contralateral IC (Glendenning and Masterton, 1983).

C. Point process models

Typical of single-neuron responses, the outputs of AVCN and LSO cells consist of trains of action potentials (spikes); these spike trains can be well described by point processes (Cox and Lewis, 1966). The signal conveyed by neuronal discharges is encoded in the intensity of the corresponding point process. To describe neuronal discharges statistically, point process models should well approximate measures such as the poststimulus time (PST) histogram, the ISI histogram and its associated hazard function,¹ and any ISI correlation (Johnson, 1996). Although it ignores the re-

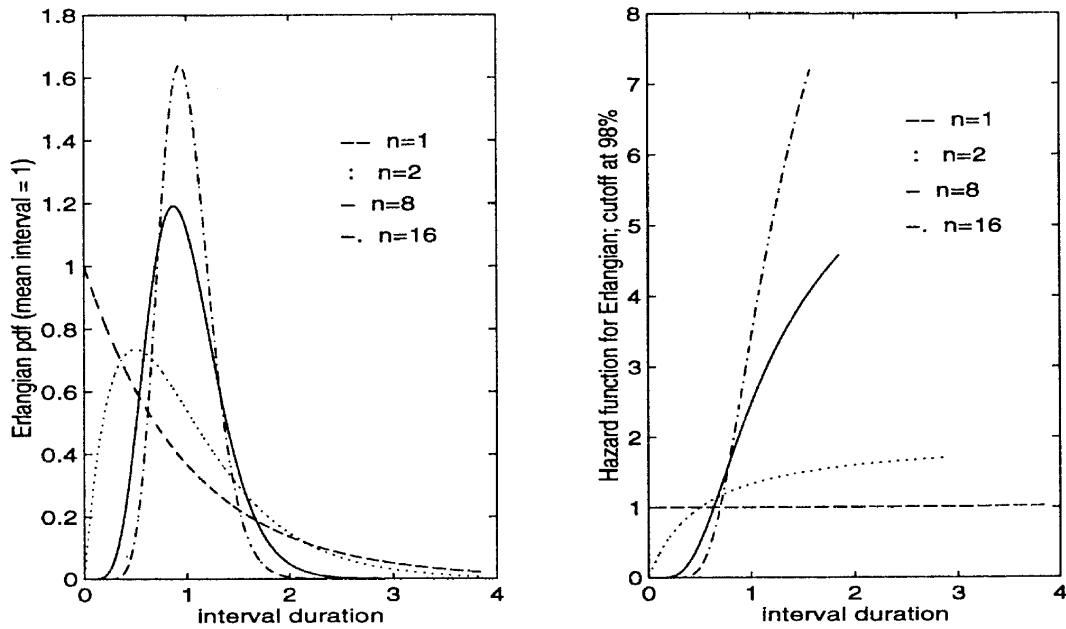


FIG. 3. Erlangian densities and the corresponding hazard functions. Left panel: Erlangian pdfs with average 1 and parameter $n=1,2,8,16$ are shown [see Eq. (2)]. As n increases with the mean held constant, the variance of the density decreases, and the density becomes more Gaussian-like. Right panel: hazard functions of the point processes with Erlangian intervals given in the left panel. $n=1$ corresponds to Poisson process, with constant hazard function.

factory properties of neural discharges, the simplest point process—the Poisson—has been used to model the responses of auditory-nerve fibers and primarylike units (Bourk, 1976; Kiang *et al.*, 1965). Using τ to represent an interevent interval, a homogeneous Poisson process is characterized by exponentially distributed intervals [$p_\tau(\tau) = \lambda e^{-\lambda\tau}$], which corresponds to a constant hazard function, and independent, identically distributed (i.i.d.) intervals.

A point process having i.i.d. intervals with an arbitrary interval distribution is known as a renewal process. Non-Poisson renewal processes result when intervals are i.i.d., but not exponentially distributed. We are particularly interested in Erlangian and Gaussian ISI renewal processes because of their capability of modeling regular discharge patterns. Stein (1965) employed the Gamma density to provide an excellent fit to the ISI distribution of some neuronal data. The Erlangian, a special Gamma density, is consistent with neuron temporal integration mechanisms (van Gisbergen *et al.*, 1975). One of these mechanisms, integrate-and-fire, assumes that an integrating neuron gives one output spike for every n input spikes: each output interval is the sum of n input intervals. If the input process is Poisson, each output ISI is the sum of n i.i.d. exponential random variables, and the resulting interval distribution of the output has an Erlangian density

$$p_\tau(\tau) = \frac{\lambda(\lambda\tau)^{n-1}e^{-\lambda\tau}}{(n-1)!}, \quad (2)$$

which defines an Erlangian process. The left panel of Fig. 3 shows several Erlangian densities with different values for n and constant mean interval of 1 (i.e., $\lambda=n$); the right panel shows hazard functions of the corresponding point processes.

For large n , the Erlangian density is approximately Gaussian because of the central limit theorem (CLT). Here,

we want to approximate the Erlangian by a Gaussian density $\mathcal{N}(\mu, \sigma^2)$, with μ representing the average interval duration and σ^2 interval variance. The complication introduced by this approximation is that negative intervals, a physical impossibility, have a nonzero probability. For a renewal Gaussian ISI point process, the probability of a negative interval is $Q(\mu/\sigma)$, with $Q(x)$ denoting the probability that a zero-mean, unit-variance, Gaussian random variable exceeds x . For $5 \leq \mu/\sigma \leq 10$, this probability lies between 10^{-6} and 10^{-23} , meaning that negative intervals almost never occur, and that the Gaussian model can be used. Figure 4 illustrates

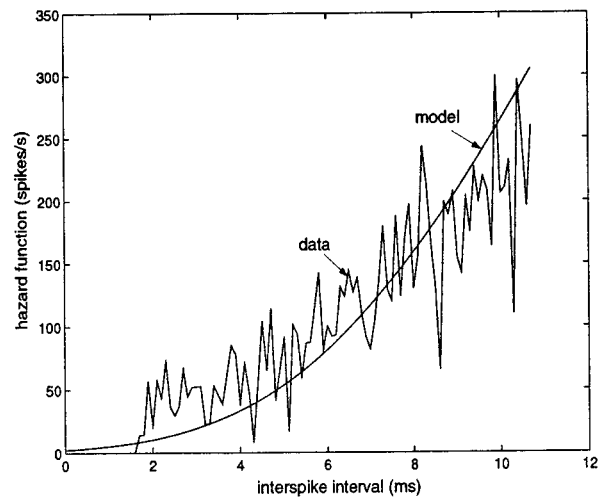


FIG. 4. Hazard functions of LSO data and Gaussian ISI model. The hazard function of the Gaussian ISI model matches with that of LSO data. The parameters for the Gaussian model are $\mu=10$ ms and $\sigma=\mu/5$. The LSO data are obtained from Dr. Tsuchitani, the Medical School of University of Texas at Houston. Cell recording number is t108-1c.r3.

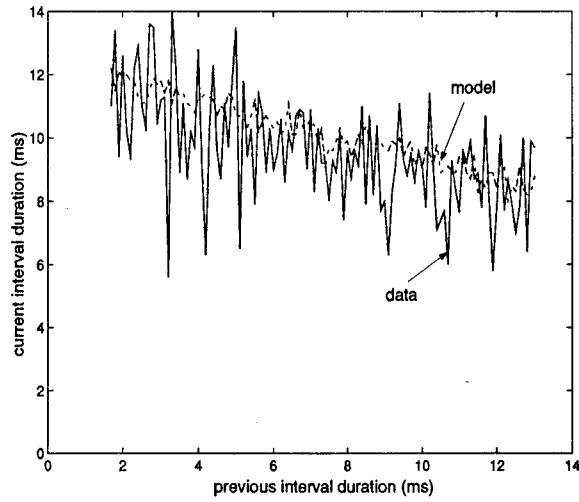


FIG. 5. Conditional mean functions of LSO data and nonrenewal model. The conditional mean function obtained from the nonrenewal Gaussian ISI model matches with that of LSO data (t108-1c.r3). The parameters of the Gaussian model are the same as in Fig. 4. The negative correlation coefficient between successive intervals in the nonrenewal model is -0.3 , approximating that measured from data.

a hazard function for a Gaussian ISI renewal process along with a hazard function obtained from a cat LSO slow chopper. Because it simplifies our analysis and does seem to yield hazard functions that approximate data well, we use the Gaussian ISI point process to describe nonprimarylike discharge patterns, all the while making sure that negative interval probabilities remain vanishingly small.

The regularity of a stationary renewal point process is quantified by the interevent interval's coefficient of variation (CV), defined as the ratio of the standard deviation and the mean of the interevent interval distribution (Johnson, 1996). For a renewal point process, the larger the CV, the greater the irregularity. A Poisson process is an irregular point process with $CV=1$; Erlangian and Gaussian ISI processes are much more regular because they have smaller CVs. For example, a Gaussian ISI process with $CV=0.2$ produces the hazard function in Fig. 4. The temporal integration mechanism suggests that the neuron is capable of producing discharges more regular than its input process: if the integration process involves n input intervals, the CV of the output process is reduced to $1/\sqrt{n}$ times of the input process's CV. Thus, for the Erlangian process case, $CV=1/\sqrt{n}$. A nonrenewal point process is more regular than a renewal point process having the same interval distribution: the interinterval correlation means that the next interval's duration can be partially predicted from the current one.

To represent the correlation found between successive ISIs in LSO data (Johnson *et al.*, 1986), we define a nonrenewal Gaussian ISI process. If successive ISIs are jointly Gaussian with correlation coefficient ρ , the conditional mean equals

$$E[\tau_i|\tau_{i-1}] = \rho\tau_{i-1} + (1-\rho)\mu. \quad (3)$$

A negative ρ makes the conditional mean function $E[\tau_i|\tau_{i-1}]$ a linearly decreasing function, which matches the data well (Fig. 5). Another direct consequence of negative

correlation is that the conditional hazard function

$$h(\tau_i|\tau_{i-1}) = \frac{\exp\left(-\frac{(\tau_i - (\rho\tau_{i-1} + (1-\rho)\mu))^2}{2(1-\rho^2)\sigma^2}\right)}{\sqrt{2\pi(1-\rho^2)}\sigma Q\left(\frac{\tau_i - (\rho\tau_{i-1} + (1-\rho)\mu)}{\sqrt{(1-\rho^2)}\sigma}\right)}, \quad (4)$$

which is shifted horizontally by the duration of the conditioning interval τ_{i-1} . Specifically, larger τ_{i-1} shifts $h(\tau_i|\tau_{i-1})$ toward shorter interval durations. This shifting property has been found in LSO slow chopper data (Johnson *et al.*, 1986).

For our subsequent theoretical work, we need an expression for the probability of N events occurring in a time interval of length T . The general result is (Cox, 1962)

$$\Pr\{N_T=N\} = \Pr\left\{\sum_{i=1}^{N+1} \tau_i > T\right\} - \Pr\left\{\sum_{i=1}^N \tau_i > T\right\}, \quad N=0,1,\dots \quad (5)$$

For the homogeneous Poisson process with intensity λ , this probability is given by

$$\Pr\{N_T=N\} = \frac{e^{-\lambda T}(\lambda T)^N}{N!}, \quad N=0,1,\dots \quad (6)$$

For the Gaussian ISI point process with $p_\tau(\tau) \sim \mathcal{N}(\mu, \sigma^2)$ and correlation coefficient ρ , we have $\sum_{i=1}^N \tau_i \sim \mathcal{N}(N\mu, (N+2\rho(N-1))\sigma^2)$, which yields

$$\Pr\{N_T=N\} = Q\left[\frac{T - (N+1)\mu}{\sqrt{N+1+2\rho N}\sigma}\right] - Q\left[\frac{T - N\mu}{\sqrt{N+2\rho(N-1)}\sigma}\right]. \quad (7)$$

D. AVCN and LSO discharge modeling

We investigate the Poisson process model first because it is the simplest point process, and the characteristics of the resulting optimal processor provide a reference for comparing the predictions of more complicated, but more accurate, point process models. The responses of AVCN bushy cells and MNTB units are primarylike, and are well modeled by homogeneous Poisson processes. We focus our study on the effect of interaural levels on localization, and assume that no interaural time information is conveyed to the optimal processor. In addition, we assume that the stimulus amplitude A at the midline is an unknown constant. Under these assumptions, the discharge rates of AVCN cells under a high-frequency stimulus are monotonically related to the signal amplitudes present at the ears (Dabak, 1990; Johnson *et al.*, 1990),

$$\lambda_{lp}(t, \theta) = R[AD(-\theta)], \quad \lambda_{rp}(t, \theta) = R[AD(\theta)], \quad (8)$$

where $\lambda_{lp}(t, \theta)$ and $\lambda_{rp}(t, \theta)$ denote the intensities of the Poisson processes characterizing discharges of a single bushy cell (primary units) in the left and right AVCN, respectively. The rate-level function $R[\cdot]$ is an increasing function until the

discharge rate saturates at high sound levels (Dabak, 1990; Johnson *et al.*, 1990).

In modeling AVCN stellate cell responses, we first employ Poisson processes with intensities given in formula (8). Since the input to a stellate cell comes from auditory-nerve fibers, whose responses are well modeled by Poisson processes, the Gaussian ISI process models the regularity underlying the output process, thereby producing a non-Poisson discharge model far superior to the Poisson one. If ISIs are identically distributed as a Gaussian [$p_r(\tau) \sim \mathcal{N}(\mu, \sigma^2)$], the average discharge rate is approximately $1/\mu$. Relating AVCN discharge rate to this quantity, we define the Gaussian parameters μ and σ according to the responses of a single AVCN stellate cell by $\mu = 1/R[AD(\theta)]$, $\sigma = \mu/a$, where a is the reciprocal CV ($a = 1/\text{CV}$).

Our first model for LSO responses is the Poisson process. Previous studies (Boudreau and Tsuchitani, 1970; Colburn and Moss, 1981; Johnson *et al.*, 1990) highlighted the E/I characteristics of high-CF LSO cells and the representation of ILD by their sustained discharges. We model the Poisson process intensities as

$$\lambda_{\text{lso}}(t, \theta) = f\left[\frac{D(-\theta)}{D(\theta)}\right], \quad \lambda_{\text{rso}}(t, \theta) = f\left[\frac{D(\theta)}{D(-\theta)}\right], \quad (9)$$

where $\lambda_{\text{lso}}(t, \theta)$ and $\lambda_{\text{rso}}(t, \theta)$ correspond to responses of a single cell in the left LSO and the right LSO, respectively (Dabak, 1990; Johnson *et al.*, 1990). The function $f[\cdot]$ describes the transformation from ILD to a LSO cell's discharge rate. To simplify the empirical relationship between a single LSO cell's discharge rate and ILD (Boudreau and Tsuchitani, 1968), we assume that the discharge rate increases monotonically until it saturates at the highest discharge rate possible for the neuron when a large ILD is reached. For the 20-dB ILD range in our study, the saturation point is not reached for almost all LSO cells.

We investigated several possibilities for the transformation $f[\cdot]$, including linear

$$(\lambda_{\text{rso}}(t, \theta) = b_1[[D(\theta)/D(-\theta)] - 1]),$$

logarithmic

$$\lambda_{\text{rso}}(t, \theta) = b_2 \log[D(\theta)/D(-\theta)],$$

and square root

$$(\lambda_{\text{rso}}(t, \theta) = b_3[[D(\theta)/D(-\theta)] - 1]^{1/2});$$

see Fig. 6. Here b_i , $i=1,2,3$ are constants selected to produce a specified maximum discharge rate. Each functional form ensures the monotone property of the discharge rate with respect to lateral angle. These one-to-one mappings between LSO discharge rate and lateral angle avoid any ambiguity in angle estimation using LSO responses. Preliminary data analysis suggests that the discharge rate is linear with ILD on a log-log scale, and the slope of the line is measured to be approximately 1/2 (Johnson *et al.*, 1990). The square-root model describes this relationship quantitatively. Despite uncertainties in the form of $f[\cdot]$, we found that these various transformations have little effect on the performance of the optimal angle estimator. Hence, we choose the simplest

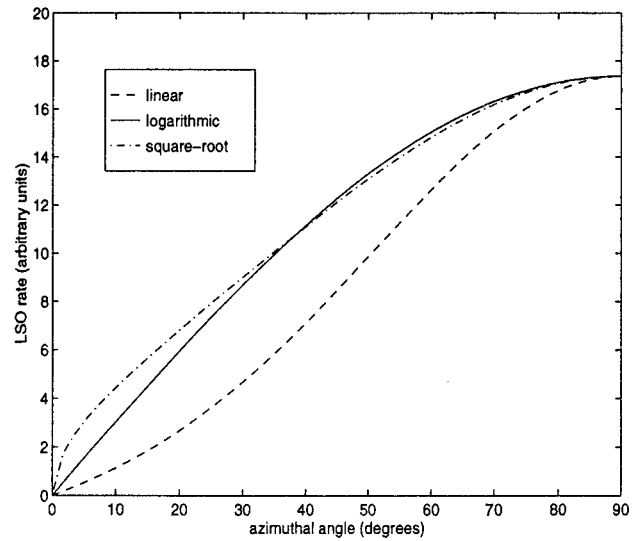


FIG. 6. Transformation from lateral angle to LSO discharge rate. The discharge rate of a single LSO cell decreases monotonically as lateral angle changes from 90° (directly on the subject's right) to 0° (frontal), and goes to zero at midline.

model, the linear one, to describe the sustained discharge rate of a single LSO cell.

To model more accurately the non-Poisson nature of LSO cell discharges, we use the analytically tractable Gaussian ISI point process as a more precise model. The Gaussian parameters are selected according to two criteria: the average rate of the point process model depends on ILD, and the probability of negative intervals occurring under the model is negligibly small ($\leq 10^{-6}$). If $0^\circ \leq \theta \leq 90^\circ$, $D(\theta)$ is proportional to the ipsilateral stimulus level, and $D(-\theta)$ to the contralateral level. For a right (ipsilateral) LSO cell, we define

$$\mu = \frac{1}{f[D(\theta)/D(-\theta)]} = \frac{1}{b(D(\theta)/D(-\theta) - 1)}, \quad \sigma = \mu/a, \quad (10)$$

where a and b are constants, θ is the lateral angle, $f[\cdot]$ is the linear rate-ILD function. The probability of negative intervals can be ignored if $a > 5$. The discharge rate of the LSO cell modeled by this point process is implicitly determined by the Gaussian parameters μ and σ . The average discharge rate is related to ILD and is approximately $1/\mu$.²

Note also that the resulting hazard function of the model agrees with the shifting and scaling characteristics described in Tsuchitani (1987) and Zacksenhouse (1993) for LSO binocular stimuli responses: stronger contralateral stimuli tend to scale down the hazard function, and stronger ipsilateral stimuli shift the hazard function toward shorter intervals and scale up the hazard function to have a higher slope. The slope of the Gaussian ISI point process's hazard function is

$$\lim_{\tau \rightarrow \infty} \frac{d}{d\tau} h(\tau) = \frac{1}{\sigma^2} = \left[ab \left(\frac{D(\theta)}{D(-\theta)} - 1 \right) \right]^2. \quad (11)$$

Clearly, a stronger ipsilateral stimulus [$D(\theta)$ increases] increases the slope, while stronger contralateral stimulus [$D(-\theta)$ increases] reduces it. Also, at stronger ipsilateral

levels, μ decreases, shifting the hazard function to shorter intervals [formula (4)].

To refine our model further, we take into account ISI correlation observed in LSO responses by using a first-order negative correlation in the Gaussian ISI model. A value for the correlation coefficient between successive intervals of -0.3 typifies the slope of measured conditional mean functions.

II. MAXIMUM LIKELIHOOD ESTIMATION OF LATERAL ANGLE

A. Estimator derivation

In our localization problem, the angle is a deterministic but unknown parameter, of which we have no *a priori* knowledge except for its range (the front of the subject). We use maximum likelihood estimation not only because it suits the situation, but also because it is the only systematic estimation method known in nonrandom parameter estimation. The maximum likelihood estimate is asymptotically unbiased, consistent, and asymptotically efficient (van Trees, 1968). These properties ensure that as the duration T of the observation interval increases, the mean of the angle estimate approaches the actual lateral angle, and that the variance of the angle estimate approaches zero. Therefore, the maximum likelihood estimate is asymptotically optimal.

Suppose the point processes representing the outputs of two different cells, LSO and AVCN cells, are conditionally independent given a sound signal; the joint probability of the number of events occurring in each of the two processes is

$$p_{N_1, N_2 | \theta, A}(N_1, N_2 | \theta, A) = p_{N_1 | \theta, A}(N_1 | \theta, A) \cdot p_{N_2 | \theta, A}(N_2 | \theta, A), \quad (12)$$

where N_1 and N_2 are the total number of discharges of the two cells within observation interval of length T for specific values of θ and A . The maximum likelihood estimates of θ and A are those at which this joint probability reaches its maximum value.

As discussed in the Appendix, the angle estimate is solely determined by LSO discharges (if nonzero) regardless of AVCN discharges. Because the model for AVCN discharges does not affect the optimal angle estimator when LSO discharges are available, we assume for simplicity a Poisson model for AVCN discharges and focus on different models of LSO discharge patterns. The impact of AVCN discharge regularity on localization is discussed later when both LSOs are totally inhibited. Under the assumption of nonzero input from LSO, the maximum likelihood angle estimate occurs when the joint probability associated with only LSO cell(s) is maximized.

Under the Poisson model for LSO discharges with the intensity given in formula (9), the maximum likelihood estimator of lateral angle based on AVCN and LSO discharges is given by

$$\hat{\theta} = \sin^{-1} \left[\frac{1}{2k} \ln \left(f^{-1} \left[\frac{N_{\text{rlso}}}{T} \right] \right) \right], \quad (13)$$

where N_{rlso} is the total number of discharges observed in the right LSO cell's output during the time interval of length T , and $f^{-1}[\cdot]$ is the inverse of the rate-ILD function. Letting $f[x] = b(x-1)$, the linear relation between the discharge rate and ILD (Fig. 6), we have

$$\hat{\theta} = \sin^{-1} \left[\frac{1}{2k} \ln \left(1 + \frac{N_{\text{rlso}}}{bT} \right) \right]. \quad (14)$$

The spike count of LSO outputs, N_{rlso} , provides the sufficient statistic for angle estimation. Since LSO discharges are directly related to ILD, ILD plays the crucial role in localization. Another observation is that, as long as it is not saturated,³ the AVCN discharge rate-level function $R[\cdot]$ does not influence the lateral angle estimate. Therefore, in this range, the absolute signal amplitudes at each ear do not matter in sound direction estimation. However, when the signal amplitude is desired, we need both $R[\cdot]$ and N_{rp} , the spike count from the right AVCN cell during the same interval of length T ,

$$\hat{A} = \frac{R^{-1}[N_{\text{rp}}/T]}{\sqrt{f^{-1}[N_{\text{rlso}}/T]}}. \quad (15)$$

While a single LSO cell is theoretically capable of providing the information sufficient for the higher center to localize the sound source, higher neural centers process the responses of a neural population to extract the lateral angle. To study how populations of neurons, as opposed to a single neuron, would be processed, we start by assuming that the population consists of two identical (i.e., same CF, same threshold) neurons producing conditionally independent discharges given a sound signal. No matter whether there is an input from AVCN or not, the maximum likelihood estimator of lateral angle is

$$\hat{\theta} = \sin^{-1} \left[\frac{1}{2k} \ln \left(f^{-1} \left[\frac{N_{\text{rlso1}} + N_{\text{rlso2}}}{2T} \right] \right) \right]. \quad (16)$$

Generalizing this result to M identical LSO inputs, we have

$$\hat{\theta} = \sin^{-1} \left[\frac{1}{2k} \ln \left(f^{-1} \left[\frac{\sum_{i=1}^M N_{\text{rlso}_i}}{MT} \right] \right) \right]. \quad (17)$$

When we have only one LSO cell projecting to the optimal processor with a discharge rate M times as large, the maximum likelihood angle estimator is given by

$$\hat{\theta} = \sin^{-1} \left[\frac{1}{2k} \ln \left(f^{-1} \left[\frac{N_{\text{rlso}}}{MT} \right] \right) \right]. \quad (18)$$

Comparing formulae (17) and (18), we find that, as far as angle estimation is concerned, having a large number of identical convergent LSO cells is equivalent to having one cell with a correspondingly high discharge rate. Hence, superposition holds under the Poisson model in that the optimal processor would superimpose (add) its LSO inputs and produce the angle estimate based on the sum. The straight solid lines in Fig. 7 demonstrate the superposition result for two LSO cells.

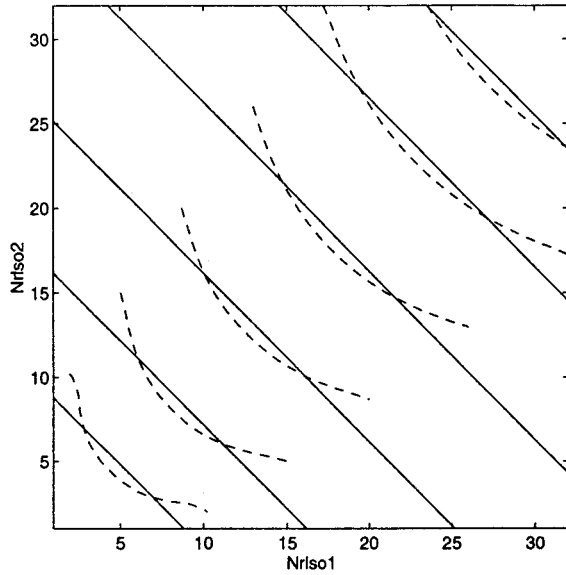


FIG. 7. Superposition under LSO Poisson model and nonsuperposition under LSO Gaussian ISI model: contour plot. Iso-angle-estimate contours of the optimal estimator are shown as a function of the spike counts produced by two LSO inputs. The solid lines correspond to the Poisson model, where the angle estimate remains constant when the sum of the spike counts from the two cells is constant. The dashed lines are under the Gaussian ISI model, where the angle estimate is not constant when the sum of discharges of the two cells is constant.

We now describe a LSO cell's responses as Gaussian ISI point processes. With ρ representing ISI correlation, the single-input maximum likelihood estimator of lateral angle is, for the linear choice for $f[\cdot]$,

$$\hat{\theta} = \sin^{-1} \left[\frac{1}{2k} \ln \left(1 + \frac{N_{\text{rlso}}}{bT} + \frac{c}{abT} \right) \right], \quad (19)$$

where c is a root of the quadratic equation

$$(2\rho + 1)c^2 + 2aBc + \left[C \ln \left(\frac{B}{C} \right) - a^2 \right] B = 0,$$

with $B = (1 + 2\rho)N_{\text{rlso}} - 2\rho$, $C = (1 + 2\rho)N_{\text{rlso}} + 1$ (see the Appendix). As in the Poisson case, the ILD, which determines the spike count of the LSO input, is the only important factor in estimating the lateral angle. Using $\rho = 0$ to model the renewal case, the angle estimator simplifies into

$$\hat{\theta} = \sin^{-1} \left[\frac{1}{2k} \ln \left(1 + \frac{\sqrt{N_{\text{rlso}}(N_{\text{rlso}} + 1)}(a^2 + \ln(1 + 1/N_{\text{rlso}}))}{abT} \right) \right]. \quad (20)$$

Except when the average discharge rate is low or the observation interval of length T is short, we can assume the total spike count $N_{\text{rlso}} \gg 1$.⁴ Thus, the angle estimator in formula (20) further simplifies into formula (14), the angle estimator under the Poisson model. For the more realistic nonrenewal Gaussian model, we use $\rho = -0.3$ and $a = 5$ to yield $\text{CV} = 0.2$. By choosing these parameters, we have $aN_{\text{rlso}} \gg c$ [except when N_{rlso} is small (one or two spikes)], with the result that the angle estimator also reduces to formula (14) in the Poisson model.

We approach neural population localization by considering the two-input case. Analytic difficulties in dealing with non-Poisson models forced us to obtain maximum likelihood angle estimates numerically for the two-input case. In our simulations, the numerical approach converged easily, and the maximum found is global because of the unimodal property of the joint probability function in the Gaussian case. Shown in Fig. 7 by the dashed lines, the angle estimate does not remain constant when the total spike count $N_{\text{rlso1}} + N_{\text{rlso2}}$ is constant. Unlike the Poisson case, the inputs of the two LSO units are *not* simply superimposed together: superposition does not hold under the LSO Gaussian ISI model. Flatness in the curvature suggests that the suboptimal superposition rule may give localization performance similar to that of the optimal processor when the number of discharges from each neuron are roughly equal.

B. Performance analysis

The discharges of LSO and AVCN cells are assumed to be observed over a time interval of length T , and the total spike counts are the sole information available to the optimal processor. We chose the observation interval length $T = 100$ ms and the maximum discharge rate of a single LSO cell about 320 spikes/s. Although localization within a shorter period of time is possible, a higher LSO discharge rate would be required for the optimal angle estimator to produce small localization error. For example, the mean spike count of a Poisson process with intensity λ over interval T is λT , and the standard deviation of the spike count is $\sqrt{\lambda T}$. Any decrease in the product λT results in a bigger CV of the spike distribution ($1/\sqrt{\lambda T}$), a more random spike count to the optimal processor, and thus a larger localization error. The existence of cell spontaneous activity, ignored in our study, offers another reason for using a relatively long observation window: if both the discharge rate and the observation window length are small, it becomes difficult for the higher center to distinguish between driven activity and spontaneous activity of its inputs, leading to large localization errors.

The optimal processor retains a similar form under each single-input LSO model. Moreover, the nonlinear processing of LSO responses to extract lateral angle under each model is the same if the spike count from the LSO is not too small. Despite of the similarity in estimator form, we found that the localization performance depends strongly on the point process model of LSO responses. The performance of an optimal estimator is evaluated by its bias and the standard deviation of the angle estimates. These criteria correspond to localization accuracy and precision respectively. In Fig. 8, the mean of angle estimate under each LSO model is shown. The bias near $\theta = 90^\circ$ is an artifact due to our assumption that the sound always comes from the front. The other extreme situation occurs when the sound source is located near the midline and the cell produces no input to the processor because of strong inhibition. Except for these artifacts, the optimal estimator under each LSO model is approximately unbiased, and the Gaussian ISI models give rise to less biased angle estimates than the Poisson model.

The optimal estimator under the Gaussian ISI model

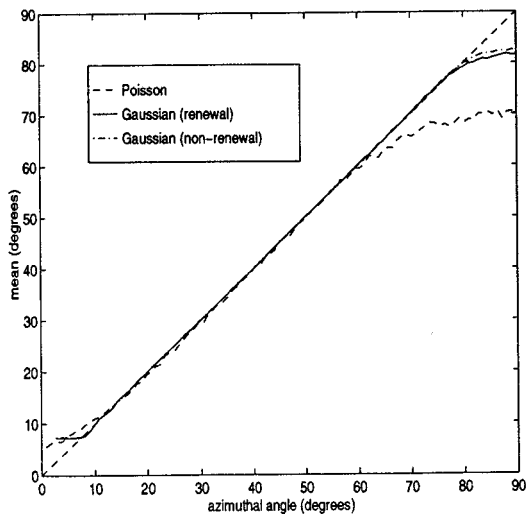


FIG. 8. Different LSO models: mean of angle estimate. The mean of angle estimate under different LSO models is shown as a function of lateral angle. The diagonal dashed line indicates unbiased estimates. The significant bias near 90° is an artifact of the estimator's assumption about the sound direction. The Gaussian ISI models result in much smaller bias than the Poisson model, while the nonrenewal factor does not contribute as much. All the performance results shown in this paper are based on the statistics of 50 trials per angle point.

yields much smaller variance than that under the Poisson model, and the nonrenewal Gaussian ISI model results in even smaller variances (Fig. 9). Only the approximately unbiased angle estimate portion is included for reasonable comparison. Because regularity is the only prominent factor that varies from model to model, we attribute the performance improvements in localization to the regular discharge patterns of LSO units.

Under both the Poisson and Gaussian LSO models, neuron ensemble processing tends to result in an optimal angle estimator with better performance than that of a single-input

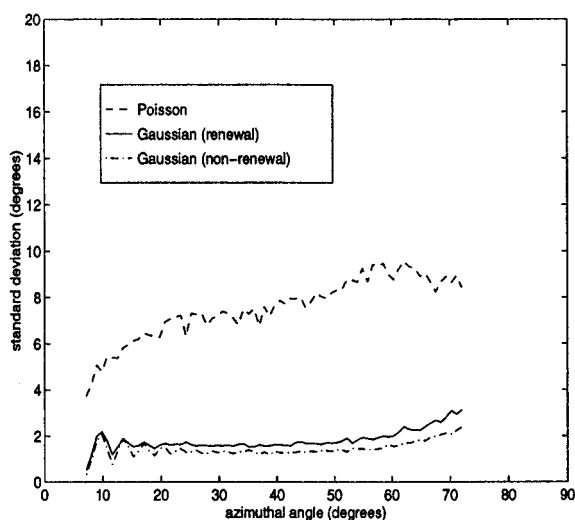


FIG. 9. Different LSO models: standard deviation of angle estimate. The standard deviation of angle estimate under different LSO models is quite different. Similar to the comparison of bias results, Gaussian ISI models result in much less variable estimator than the Poisson model, while the nonrenewal factor does not contribute as much.

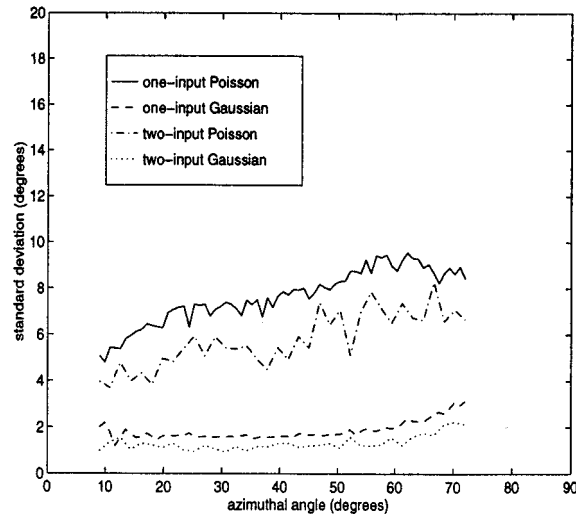


FIG. 10. LSO neuron population improves localization capability of the higher neural center. In addition to the result demonstrated in Fig. 9, localization with inputs from two LSO cells gives rise to less variable angle estimator than one LSO cell under either point process model.

estimator. It is reasonable to expect that a larger neuron population can improve the localization performance even more. However, we do expect a limit in the number of convergent cells because the higher center might be saturated by the total LSO response producing high discharge rates. The reduction in localization error by multineuron inputs processing suggests that spatial integration among input cells improves the localization capability of the higher center. Figure 10 demonstrates the result by comparing the standard deviation of angle estimates produced by processor having one input or two inputs under each LSO model.

C. Localization at midline

Contralateral LSO cells are usually totally inhibited, and both ipsilateral and contralateral LSO cells may be totally inhibited if the ILD is small (Boudreau and Tsuchitani, 1970). The small ILD situation is encountered with a midline source. Thus, a midline problem arises: how does the optimal processor localize a source when the LSO provides no input? For all the previous models, the inputs to the contralateral optimal estimator arise from only the ipsilateral LSO and ipsilateral AVCN, and only identical LSO neurons are considered. In the following, we first address what happens if the contralateral AVCN input is also used, and then consider LSO cells with different thresholds to help solve the midline problem.

1. Ipsilateral LSO and both AVCNs

If LSO input is nonzero, the maximum likelihood angle estimator with inputs from ipsilateral LSO and both AVCNs is the same as one AVCN case, and the direct projection to the IC from the AVCNs does *not* contribute to localization. Now suppose the optimal processor receives inputs from both AVCNs, but no LSO input is available. If the AVCN inputs were Poisson, the IC-based optimal processor estimates the ILD to produce the angle estimate as in Dabak (1990) and Johnson *et al.* (1990) for LSO-based localization. The inconsistency between the Poisson model and AVCN

projections to the IC indicates the possibility of different localization capability of the higher center and the LSO. If the AVCN discharges are modeled by the more regular Gaussian ISI point process, the functional form of the optimal estimator could not be derived, but numerical results do show that the performance of the optimal processor for the higher center is greatly improved over that for the LSO.

The optimal estimator with regular inputs from AVCN produces almost unbiased angle estimates, while the Poisson model (also corresponding to LSO-like localization) results in very biased angle estimates. In addition, the variance of angle estimates at the higher center having only AVCN inputs is similar to that with only LSO inputs, given the same regularity condition. Thus, localization performance is preserved when LSO discharges are not available to the higher center.

2. Ipsilateral AVCN and different ipsilateral LSO cells

Experimental data indicate that LSO cells are not identical. In particular, the threshold level at which the cell is excited may be different from cell to cell (Kiang *et al.*, 1973; Tsuchitani, 1996). Experiments also show that neurons with different threshold and/or different CF may be excited simultaneously. Hence, it is reasonable to assume that, within the neuron population that project to the higher center, some LSO cells with certain thresholds do not get totally inhibited when ILD is small. We model this possibility by supplying discharges of two LSO cells with different inhibitory thresholds (same CF) to the optimal estimator along with the input from the ipsilateral AVCN. If at least one of the LSO cells is not totally inhibited, the input from AVCN is ignored in angle extraction. The performance improvement over the one LSO case for the optimal estimator in this case is similar to that with same-threshold inputs.

Assuming the nonzero discharge rate crosses the midline, some contralateral LSO cells may provide inputs to the higher center with near-midline source. However, the projections from contralateral LSO cells are minor with relatively low discharge rates compared with those of ipsilateral LSO cells, and our simulations show no observable effect on localization performance.

III. CONCLUSIONS

We have investigated, in certain aspects, the role of a higher center after LSO in binaural localization with LSO and AVCN discharges. Non-Poisson point processes were developed to model cell responses more accurately. The theoretical result that LSO encodes sufficient statistics (the ILD cue) for localization is confirmed in this study, and the nonlinearity of processing LSO discharges optimally is obtained under both LSO Poisson and non-Poisson models. Our study suggests that regularity of the point process has significant impact on the localization performance of the corresponding angle estimator: the more regular the point process, the smaller the bias and the standard deviation of the angle estimate, resulting in greatly improved localization accuracy and precision. Empirically, we found that the reduction factor of the CV of the discharge pattern approximately equals

the improvement in localization error. For example, the reduction is about 0.2 in Fig. 9, a value equaling the CV reduction of the Gaussian model with respect to the Poisson. By considering the correlation between successive intervals, localization performance is improved even more. However, because the correlation is small, this improvement yields little localization performance gain. These results mean that regular discharge patterns can give rise to improved processing performance by later stages in the binaural pathway.

The significance of discharge regularity in localization is demonstrated again by the result of one of our solutions to the midline problem. When both LSOs are totally inhibited and provide no input to the optimal processor, localization is still possible if the processor receives inputs from both AVCNs. Simulations show that localization accuracy and precision at the higher center using AVCN regular inputs are much better than at the LSO using AVCN irregular discharges with the same mean discharge rates. We attributed discharge regularity to input integration, and we have shown that spatial integration is another mechanism that improves localization performance. Because of the impact of the regularity difference of AVCN responses, it is clear that the higher center is not simply a replica of LSO, even if AVCNs were the only nuclei providing ascending projections.

The well-accepted duplex theory argues that ILD is primarily responsible for localization of high-frequency signals, and that ITD is used in localization of low-frequency ones. The theoretical study of optimal localization of high-frequency signals at LSO implies that the level cue should be processed separately from the phase cue, and that level-based processing is more effective than phase-based processing (Dabak and Johnson, 1993). Although it is reasonable to consider ILD as the most important cue in high-frequency localization at the higher center, we leave out other possible localization information conveyed in LSO responses by using only the sustained portion of cell responses. One of the prominent cues possibly used by the higher center is the highly structured chopping responses obvious in PST histograms of LSO data. A recent study (Zacksenhouse *et al.*, 1995) points out that the chopping discharge pattern can be produced by the joint effect of the deadtime and the driven process with an exponentially decaying intensity. Furthermore, one consequence of a regular discharge pattern, which yields high-performance (small interval CV) lateral angle estimation, is a chopping response to step changes in stimulus amplitude (Johnson *et al.*, 1986). Another important cue in LSO responses is the tightly distributed time-of-occurrence of the first spike, which accurately represents the ipsilateral stimulus onset. How the chopping information is represented and what effect the timing of initial discharges has on localization are interesting and unexplored research topics.

ACKNOWLEDGMENT

The funding of this research was provided by NSF Grant No. IBN-9309263.

APPENDIX

We show here that the presence of AVCN discharges does not affect the optimal angle estimate. Assume LSO discharges are modeled by the renewal Gaussian ISI point process and that the input from AVCN is Poisson. Assuming a linear $R[\cdot]$, the joint pmf of two inputs is given by

$$p_{N_{\text{rlso}}, N_{\text{tp}} | \theta, A}(N_{\text{rlso}}, N_{\text{tp}} | \theta, A) = \left(\frac{e^{-AD(\theta)T} (AD(\theta)T)^{N_{\text{tp}}}}{N_{\text{tp}}!} \right) \cdot \left(Q \left[\frac{T - (N_{\text{rlso}} + 1)\mu}{\sqrt{N_{\text{rlso}} + 1 + 2\rho N_{\text{rlso}}\sigma}} \right] - Q \left[\frac{T - N_{\text{rlso}}\mu}{\sqrt{N_{\text{rlso}} + 2\rho(N_{\text{rlso}} - 1)\sigma}} \right] \right), \quad (\text{A1})$$

where μ and σ are defined in formula (10). Evaluating the partial derivative of the logarithm of this joint pmf with respect to A , we have

$$\frac{\partial \ln p}{\partial A} = -TD(\theta) + \frac{N_{\text{tp}}}{A}. \quad (\text{A2})$$

So, the maximum likelihood estimates of A and θ must satisfy

$$\hat{A}D(\hat{\theta}) = \frac{N_{\text{tp}}}{T}. \quad (\text{A3})$$

By evaluating the partial derivative of the joint pmf with respect to θ , we have

$$\frac{\partial \ln p}{\partial \theta} = \left(\frac{e^{-AD(\theta)T} (AD(\theta)T)^{N_{\text{tp}}}}{N_{\text{tp}}!} \right) \cdot \left(\frac{d}{d\theta} (Q[t_1] - Q[t_2]) \right) + (Q[t_1] - Q[t_2]) \cdot \left(\frac{\partial}{\partial \theta} \frac{e^{-AD(\theta)T} (AD(\theta)T)^{N_{\text{tp}}}}{N_{\text{tp}}!} \right), \quad (\text{A4})$$

where

$$t_1 = \frac{T - (N_{\text{rlso}} + 1)\mu}{\sqrt{N_{\text{rlso}} + 1 + 2\rho N_{\text{rlso}}\sigma}} = \frac{abT(D(\theta)/D(-\theta) - 1) - a(N_{\text{rlso}} + 1)}{\sqrt{N_{\text{rlso}} + 1 + 2\rho N_{\text{rlso}}\sigma}},$$

$$t_2 = \frac{T - N_{\text{rlso}}\mu}{\sqrt{N_{\text{rlso}} + 2\rho(N_{\text{rlso}} - 1)\sigma}} = \frac{abT(D(\theta)/D(-\theta) - 1) - a(N_{\text{rlso}})}{\sqrt{N_{\text{rlso}} + 2\rho(N_{\text{rlso}} - 1)}}.$$

The partial derivative in the second term of formula (A4) equals

$$\frac{\partial}{\partial \theta} \frac{e^{-AD(\theta)T} (AD(\theta)T)^{N_{\text{tp}}}}{N_{\text{tp}}!} = \frac{e^{-AD(\theta)T} (AD(\theta)T)^{N_{\text{tp}} - 1}}{N_{\text{tp}}!} \cdot \frac{dD(\theta)}{d\theta} \cdot A(N_{\text{tp}} - ATD(\theta)). \quad (\text{A5})$$

Note that $N_{\text{tp}} - ATD(\theta)$ explicitly appears as a product term. Because the maximum likelihood solution must satisfy formula (A3), this term must be zero for the maximum likelihood estimates of θ and A . Combining with formula (A4), we have

$$\frac{d}{d\theta} \left(Q \left[\frac{abT(D(\theta)/D(-\theta) - 1) - a(N_{\text{rlso}} + 1)}{\sqrt{N_{\text{rlso}} + 1 + 2\rho N_{\text{rlso}}\sigma}} \right] - Q \left[\frac{abT(D(\theta)/D(-\theta) - 1) - a(N_{\text{rlso}})}{\sqrt{N_{\text{rlso}} + 2\rho(N_{\text{rlso}} - 1)}} \right] \right) \Big|_{\hat{\theta}} = 0. \quad (\text{A6})$$

Solving Eq. (A6) for $\hat{\theta}$ yields formula (19). For other models of inputs to the higher center from AVCN and LSO, similar structures occur in solving for maximum likelihood estimates of θ and A , and the AVCN input is always discarded in angle estimation.

¹We have found that the hazard function, although directly computed from the interval histogram, provides much more information about point process models than does its progenitor.

²The mean rate of a Gaussian ISI point process cannot be derived analytically. The numerical mean of spike count in time interval of length T is T/μ if the number of spikes is large. In our simulations, the difference between T/μ and the mean spike count of simulated data is always less than 0.5 spike on average. In addition, the optimal processor we study later doesn't directly rely on the mean rate.

³If either the rate-level function $R[\cdot]$ or the rate-ILD function $f[\cdot]$ is saturated, we have a degenerate localization problem, and the optimal processor can't localize the sound source without ambiguity.

⁴The average discharge rate of a typical LSO cell is low only when the sound source is located near the midline. From the estimation viewpoint, a smaller value of the input to the angle estimator incurs a larger localization error. If the LSO input is small, it is very probable that the higher center incorporates responses from some other lower neural centers for more reliable localization.

Adams, J. (1976). "Single unit studies on the dorsal and intermediate acoustic striae," *J. Comp. Neurol.* **170**, 97–106.

Adams, J. (1979). "Ascending projections to the inferior colliculus," *J. Comp. Neurol.* **183**, 519–538.

Boudreau, J., and Tsuchitani, C. (1968). "Binaural interaction in the cat superior olive S segment," *J. Neurophysiol.* **31**, 442–454.

Boudreau, J., and Tsuchitani, C. (1970). "Cat superior olive S segment cell discharge to tonal stimuli," *Contributions to Sensory Physiology*, edited by W. Neff, Vol. 4 (Academic, New York), pp. 143–213.

Bourk, T. (1976) "Electrical Responses of Neural Units in the Anteroventral Cochlear Nucleus of the Cat," Ph.D. thesis, Dept. EECS, Mass. Inst. Tech., Cambridge, MA.

Brawer, J., Morest, D., and Kane, E. (1974). "The neuronal architecture of the cochlear nucleus of the cat," *J. Comp. Neurol.* **155**, 251–299.

Cant, N., and Casseday, J. (1986). "Projections from the anteroventral cochlear nucleus to the lateral and medial superior olivary nuclei," *J. Comp. Neurol.* **247**, 457–476.

Colburn, H., and Moss, P. (1981). "Binaural interaction models and mechanisms," *Neuronal Mechanisms of Hearing*, edited by J. Syka and L. Aitkin (Plenum, New York), pp. 283–288.

Cox, D. (1962). *Renewal Theory* (Methuen, London).

Cox, D., and Lewis, P. W. (1966). *The Statistical Analysis of Series of Events* (Methuen, London).

- Dabak, A. (1990). "Binaural localization using interaural cues," Master's thesis, Department of Electrical and Computer Engineering, Rice University, Houston, TX.
- Dabak, A., and Johnson, D. (1993). "Function-based modeling of binaural interactions: Level and time cues," *J. Acoust. Soc. Am.* **94**, 2604–2616.
- Glendenning, K., and Masterton, R. (1983). "Acoustic chiasm: Efferent projections of the lateral superior olive," *J. Neurosci.* **3**, 1521–1537.
- Goldberg, J., and Brownell, W. (1973). "Discharge characteristics of neurons in anteroventral and dorsal cochlear nuclei of cat," *Brain Res.* **64**, 35–54.
- Green, D. (1976). *An Introduction to Hearing* (Wiley, New York).
- Guinan, J., Norris, B., and Guinan, S. (1972). "Single auditory units in the superior olivary complex. II. Locations of unit categories and tonotopic organization," *Int. J. Neurosci.* **4**, 147–166.
- Irvine, D. (1986). *The Auditory Brainstem*, Vol. 7 of *Progress in Sensory Physiology*, edited by D. Otoson (Springer-Verlag, Berlin).
- Irvine, D. (1987). "Interaural intensity differences in the cat: Changes in sound pressure level at the two ears associated with azimuthal displacements in the frontal horizontal plane," *Hear. Res.* **26**, 267–286.
- Johnson, D. (1996). "Point process models of single-neuron discharges," *J. Comput. Neurosci.* **3**, 275–299.
- Johnson, D., Dabak, A., and Tsuchitani, C. (1990). "Function-based modeling of binaural interactions: Interaural level," *Hear. Res.* **49**, 301–320.
- Johnson, D., Tsuchitani, C., Linebarger, D., and Johnson, M. (1986). "Application of a point process model to responses of cat lateral superior olive units to ipsilateral tones," *Hear. Res.* **21**, 135–159.
- Kiang, N., Morest, D., Godfrey, D., Guinan, J., and Kane, E. (1973). "Stimulus coding at caudal levels of the cat's auditory nervous system: I. Response characteristics of single units," in *Basic Mechanisms in Hearing*, edited by A. Møller (Academic, New York), pp. 455–478.
- Kiang, N. S., Watanabe, T., Thomas, E., and Clark, L. (1965). *Discharge Patterns of Single Fibers in the Cat's Auditory Nerve* (MIT, Cambridge, MA).
- Kuhn, G. (1987). "Physical acoustics and measurements pertaining to directional hearing," in *Directional Hearing*, edited by W. Yost and G. Gourevitch (Springer-Verlag, New York), Chap. 1.
- Pfeiffer, R. (1966). "Classification of response patterns of spike discharges for units in the cochlear nucleus: Tone-burst stimulation," *Exp. Brain Res.* **1**, 220–235.
- Rhode, W., Oertel, D., and Smith, P. (1983). "Physiological response properties of cells labeled intracellularly with horseradish peroxidase in cat ventral cochlear nucleus," *J. Comp. Neurol.* **213**, 448–463.
- Stein, R. (1965). "The theoretical analysis of neuronal variability," *Biophys. J.* **5**, 173–194.
- Tolbert, L., Morest, D., and Yurgelun-Todd, D. (1982). "The neuronal architecture of the anteroventral cochlear nucleus of the cat in the region of the cochlear nerve root: Golgi and Nissl methods," *Neuroscience* **7**, 3013–3030.
- Tsuchitani, C. (1982). "Discharge patterns of cat lateral superior olivary units to ipsilateral tone-burst stimuli," *J. Neurophysiol.* **47**(3), 479–500.
- Tsuchitani, C. (1987). "The inhibition of cat lateral superior olive unit excitatory responses to binaural tone bursts. II. The sustained discharges," *J. Neurophysiol.* **19**, 184–211.
- Tsuchitani, C. (1996). "Input from the medial nucleus of the trapezoid body to an interaural level detector," *Hear. Res.* (to appear).
- Tsuchitani, C., and Boudreau, J. (1969). "Stimulus level of dichotically presented tones and cat superior olive S-segment cell discharge," *J. Acoust. Soc. Am.* **46**, 979–988.
- van Gisbergen, J., Grashuis, J., Johannesma, P., and Vendrik, A. (1975). "Statistical analysis and interpretation of the initial responses of cochlear nucleus neurons to tone bursts," *Brain Res.* **23**, 407–423.
- van Trees, H. (1968). *Detection, Estimation, and Modulation Theory, Part I* (Wiley, New York).
- Warr, W. (1966). "Fiber degeneration following lesions in the anterior ventral cochlear nucleus of the cat," *Exp. Neurol.* **14**, 453–474.
- Warr, W. (1972). "Fiber degeneration following lesions in the multipolar and globular areas in the ventral cochlear nucleus of the cat," *Brain Res.* **40**, 247–270.
- Yue, L. (1995). "Optimal binaural processing based on point process models of preprocessed cues," Master's thesis, Department of Electrical and Computer Engineering, Rice University, Houston, TX.
- Zacksenhouse, M. (1993). "Point-Process Modeling of Excitatory/Inhibitory Interactions in LSO Neurons," Ph.D. thesis, Department of Electrical and Computer Engineering, Rice University, Houston, TX.
- Zacksenhouse, M., Johnson, D., and Tsuchitani, C. (1995). "Transient effects during the chopping response of LSO neurons," *J. Acoust. Soc. Am.* **98**, 1410–1422.

Auditory-nerve fiber responses to clicks in guinea pigs with a damaged cochlea

Huib Versnel,^{a)} Vera F. Prijs, and Ruurd Schoonhoven

ENT Department, University Hospital, P.O. Box 9600, 2300 RC Leiden, The Netherlands

(Received 12 January 1996; accepted for publication 6 August 1996)

This paper describes auditory-nerve single-fiber responses to clicks in noise-damaged cochleas. Poststimulus time histograms (PSTHs) were recorded for various click intensities and for the two click polarities. The PSTHs found in fibers with elevated thresholds are discussed in relation to the frequency threshold curves (FTCs) measured in these fibers. Five types of abnormal FTCs are distinguished. Type I is elevated as a whole, type II has an elevated (and often broadened) tip and a tail at normal level, type III has low thresholds in the tail (often hypersensitive), type IV represents a flat tuning, and type V has no tip but shows a clear appearance of the tail (often hypersensitive). The click PSTHs of abnormal fibers were compared to normal PSTHs at equal sound-pressure levels, and various abnormal trends were found corresponding to the type of FTC. PSTHs for type I have longer dominant-peak latencies and smaller amplitudes; PSTHs for type II were normal well above the fiber's threshold; PSTHs for type III revealed remarkable patterns with multiple peaks, part of them with a latency strongly varying with polarity; PSTHs for type IV showed narrow peaks and steep amplitude/intensity curves; PSTHs for type V showed a multiple peaked pattern and large amplitudes and steep amplitude/intensity curves to rarefaction polarity. The various features in the click responses were in most cases consistent with the type of FTC. The results can be used to explain deviations in whole-nerve recordings in abnormal cochleas. © 1997 Acoustical Society of America. [S0001-4966(97)01301-5]

PACS numbers: 43.64.Pg, 43.64.Wn [RDF]

INTRODUCTION

The effects of cochlear damage on responses of auditory-nerve fibers have been studied extensively, in particular the effects on frequency selectivity, two-tone suppression, and rate-intensity profiles (e.g., Evans, 1975; Dallos and Harris, 1978; Schmiedt *et al.*, 1980; Schmiedt and Zwislocki, 1980; Harrison, 1981; Harrison and Evans, 1982; Robertson, 1982; Salvi *et al.*, 1983; Liberman and Dodds, 1984b; Liberman and Kiang, 1984). Changes of frequency tuning as a consequence of damage can be dramatic and can take a variety of forms. Single-neuron labeling experiments allowed Liberman and Dodds (1984b) to associate specific hair cell lesions with abnormal types of frequency threshold curves (FTCs), which contributed to our understanding of the morphological causes of changes in frequency selectivity. These findings fit well with current ideas about the function of hair cells (for reviews see, e.g., Patuzzi, 1992; Dallos, 1992). Outer hair cells (OHCs) can be considered to be active transducers which give positive mechanical feedback to enhance sensitivity for specific frequencies and thus damage to these cells leads to frequency-dependent changes in the FTC such as broadening and elevation of the tip. Inner hair cells (IHCs) can be considered to be passive transducers which convert the mechanical vibrations into voltages which in turn cause release of neurotransmitter. Damage to IHCs leads to frequency-independent threshold shifts.

Temporal aspects of pathological responses have re-

ceived much less attention than the spectral aspects, despite the importance arising from phase-locking of nerve-fiber responses. Phase locking may play a critical role in the neural coding of sounds (Young and Sachs, 1979; Shamma, 1985). Further, knowledge of temporal response patterns of single fibers is relevant for interpretation of the compound action potential (CAP) or auditory brain-stem response (ABR) often applied to examine cochlear functioning in pathology (Eggermont, 1976; Chiappa, 1989). A few reports have presented responses to clicks in noise-damaged cochleas with specific types of abnormal FTCs (broad tips: Salvi *et al.*, 1979; W-shaped FTCs: Schoonhoven *et al.*, 1994).

We used broadband clicks to study temporal response patterns of single fibers in noise-damaged cochleas in guinea pigs. The click responses, presented as poststimulus time histograms (PSTHs), were examined for fibers with a range of abnormal FTC shapes. One obvious question is whether certain deviations in the temporal patterns correspond to certain FTC shapes. A simple example of such correspondence in the normal cochlea is the interpeak distance in click PSTHs of fibers with a low characteristic frequency (CF) measuring about $1/CF$ (Kiang *et al.*, 1965; Pfeiffer and Kim, 1972). Another example is changes in click PSTHs resulting from cochlear damage: abnormal PSTHs could be ascribed to changed FTCs assuming that neural click PSTHs reflect a well-known (nonlinear) transformation of the impulse response of the cochlear filter (Salvi *et al.*, 1979; Schoonhoven *et al.*, 1994).

It would be useful for electrocochleography to be able to derive from deviations in CAPs abnormal local temporal response patterns. It would be of extra value when one is able

^{a)}Present address: University Laboratory of Physiology, Parks Road, Oxford, OX1 3PT, UK. Electronic mail: hv@physiol.ox.ac.uk

to even estimate morphological anomalies on the basis of abnormal temporal patterns which underlie the CAP. Having that in mind we will discuss PSTHs by associating them to FTCs and in turn to morphological changes assessed from FTCs relying on the data of Liberman and Dodds (1984b).

I. METHODS

A. Noise exposure

The data presented in this paper were collected in 13 female, albino guinea pigs weighing between 200 and 800 g. In order to induce a hearing loss each animal was first exposed to loud sounds. The animal was lightly anaesthetized and positioned in a small sound attenuating chamber ($0.8 \times 0.6 \times 0.5 \text{ m}^3$) with the right pinna about 3 cm from a speaker (Fane type Classic 10-125T). The left ear canal was plugged to minimize contralateral damage. The exposure level was measured by means of a 12.7 mm (0.5 in.) condenser microphone (Bruël & Kjaer 4134) placed at the position of the exposed ear. The animals were exposed for 2 h, eight to a tone of 6.0 kHz at 121–123 dB SPL, five to a tone of 1.4–1.7 kHz at 112–122 dB SPL. Before and immediately after the acoustic overstimulation thresholds to short tone bursts over a range from 2.8 to 11 kHz were estimated by auditory brain-stem responses (ABR). A needle placed closely behind the pinna served as active ABR electrode and a needle on the vertex was the reference electrode. Acute recordings from the auditory nerve were performed after a survival time of 14–123 days.

B. Preparation, acoustic stimuli, recordings

The procedures and equipment were the same as for previous experiments we performed in normal hearing guinea pigs and are described in detail in Versnel *et al.* (1990). The guinea pigs were intraperitoneally anaesthetized with Nembutal® (27 mg/kg). A silver ball electrode was positioned at the round window and the cochlear nerve was intracranially approached as described by Evans (1979). Ear canals were clean and there were no indications of middle ear infections (after the experiment the bulla was routinely opened to check).

Sound stimuli were presented in a closed field by a dynamic earphone of Standard Telephones and Cables (4026A). The earphone, calibrated with the 0.5-in. Bruël & Kjaer condenser microphone, showed a frequency characteristic with less than 10-dB variation up to 10 kHz, and a high-frequency roll-off of about 50 dB/oct. The roll-off was such that thresholds above 50 dB SPL in a frequency range above 12 kHz could not be measured properly. Consequently, it was possible to measure an FTC tip with a normal threshold above 12 kHz [as normal values for high-SR fibers are around 20 dB SPL, see Fig. 9(A)] but an FTC tip with an abnormal threshold (e.g., above 50 dB SPL) might not be identified. Rectangular pulses of 100- μs width were used for the generation of clicks; the acoustic click spectrum was relatively flat within 15 dB up to about 9 kHz where it fell off rapidly (see Fig. 1 in Versnel *et al.*, 1992). The level of the click was expressed in dB nSL, where nSL is the level relative to the average click-evoked CAP threshold for nor-

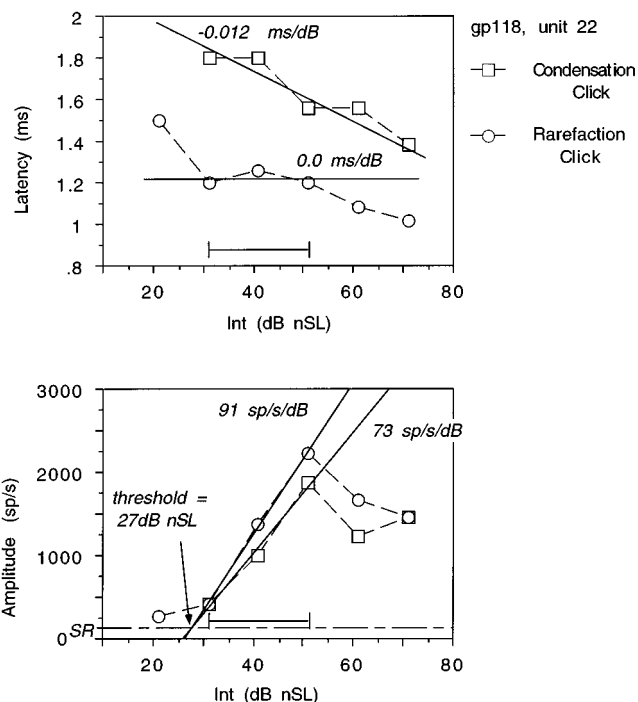


FIG. 1. Example of input/output curves of the latency (*top*) and amplitude (*bottom*) of PSTHs to condensation and rarefaction clicks recorded in a single fiber. The slopes of the input/output curves are computed at three levels over a 20-dB interval with the lowest level at 0–10 dB above threshold. The bold bar marks the 20-dB interval over which the slopes are computed. The click threshold is estimated by linear extrapolation of the three amplitude data points to the spontaneous rate (dash-dotted line).

mal hearing animals (Versnel *et al.*, 1990). The peak amplitude of the click at normal threshold (0 dB nSL) was equal to the peak pressure of a sinusoidal tone of 41 dB SPL. The threshold audiogram of the averaged CAP was determined using 4-ms tone bursts and a 1- μV threshold criterion. Frequency threshold curves (FTCs) were determined by an automated threshold tracking procedure (see Evans, 1979) using tone bursts of 50-ms duration and a threshold criterion of 20% increase above spontaneous activity.

The single-fiber recordings were made with glass micropipettes filled with 0.5 M KCl/0.1 M TRIS buffer (*in situ* resistance 30–60 M Ω). Bursts of broadband noise with a level of 80 dB SPL were used as search stimuli. After an FTC of a fiber was determined, PSTHs to condensation and rarefaction clicks were recorded using 256 sweeps and a bin width of 60 μs .

C. Data analysis

The recordings in the noise-exposed guinea pigs are compared to data in 14 normal hearing animals which are described in Versnel *et al.* (1990, 1992). The cochlea of a noise-exposed animal was considered to be abnormal when, for any frequency, tone thresholds determined by CAP recordings from the round window, were raised by more than 2 s.d. (≈ 15 dB) from average thresholds in the normal hearing animals (Versnel *et al.*, 1990). The single-fiber thresholds in abnormal cochleas were compared to average thresholds of fibers within the same CF range (<0.5 kHz, 0.5–3 kHz, >3 kHz) and the same category of spontaneous discharge rate

(SR) (<5 sp/s, 5–30 sp/s, >30 sp/s) in the normal-hearing guinea pigs. Fibers with a threshold at CF raised by more than 2 s.d. (typically about 20 dB) from the normal values were considered abnormal.

The distinction of tip, notch and tail is important for the analysis of abnormal FTCs. The tip is a (local) minimum near the high-frequency cutoff, the tail is the low-frequency section where the slope is minimal or even changes its sign resulting in a second local FTC minimum. The notch of the FTC is defined as the point where tip and tail meet, often manifesting as a local maximum (hence the term “notch”). The terms tail frequency and tail level will be used to refer to the frequency and level at the minimum of the tail, or in case of a relatively flat tail, to refer to an average value of the tail thresholds. Other parameters of the FTC used are the CF, threshold at CF, and $Q_{10\text{ dB}}$ (ratio of CF and bandwidth at 10 dB above the threshold at CF).

The PSTHs were smoothed using a sliding three-point (1/4, 1/2, 1/4) window, and were normalized to firing probability density by dividing the number of spikes by the number of sweeps and the bin width. The main PSTH parameters derived were the latency, t_p , and amplitude, A_p , of the largest peak which we introduced previously for click PSTHs in normal cochleas (Versnel *et al.*, 1990). We chose these parameters since they are analogous to commonly used CAP parameters, and since they can be used to simulate CAPs (Versnel *et al.*, 1992; Versnel, 1993). The latency, defined at the peak's maximum, is referred to the start of the cochlear microphonics in order to eliminate acoustic and middle-ear delays. The amplitude A_p is the normalized spike rate the time t_p in spikes/s. These parameters were analyzed at fixed levels (in dB nSL) and polarities. Furthermore parameters were derived which reflect the dependence of t_p and A_p on click intensity and polarity. The slopes of the input/output curves were computed using three levels with 10-dB intervals with the lowest one at 0–10 dB above threshold. Figure 1 illustrates how slope values were determined. The dependence on polarity was expressed by the difference of latencies to condensation (C) and to rarefaction (R) clicks, $t_p(C) - t_p(R)$, and by a ratio of amplitudes, $A_p(C)/A_p(R)$, the latter analyzed on a logarithmic scale. Also, the absolute latency difference and absolute ratio were analyzed. The duration of the PSTH is defined from the onset of the response to the last point where the instantaneous rate is above the spontaneous rate.

The various response parameters of abnormal fibers are statistically compared to those of normal fibers. Since the parameters might depend not only on FTC-type, but also on CF and SR (Versnel *et al.*, 1990, 1992), a multiple regression analysis is applied with $\log(\text{CF})$ and SR category as independent variables in addition to the FTC category that distinguishes abnormal from normal.

We present PSTHs to both click polarities as compound histograms (cf. Pfeiffer and Kim, 1972). If compound PSTHs revealed an oscillatory pattern [which normally is the case for low-CF fibers; CF below 3 kHz; see, e.g., Fig. 2(B),(C)], difference PSTHs were computed by subtracting PSTHs to rarefaction clicks from PSTHs to condensation clicks. Subsequently, the Fourier power spectrum of these difference

PSTHs was computed by an FFT procedure (Versnel *et al.*, 1992), and the frequency at the peak of the power spectrum is defined as the best frequency (BF) according to Eggermont *et al.* (1983). We compare the peaks of the power spectrum to the FTC in order to find out whether the impulse response of the (abnormal) cochlear filter is at least partly represented in the (abnormal) temporal response patterns, and thus whether changes in the PSTHs can be ascribed to the changes in the cochlear filter. We assume that the nonlinear transformation of the cochlear filter's impulse response to the PSTH does not prohibit a comparison of synchrony and rate measures as reflected in PSTH and FTC, respectively (Schoonhoven *et al.*, 1994). The validity of our analysis of low-frequency periodicities in the PSTH was illustrated for normal low-CF fibers in Versnel *et al.* (1992).

II. RESULTS

A. FTCs and click PSTHs in normal cochleas

The main points of normal FTCs and click PSTHs are described here as reference for the responses in damaged cochleas. Details can be found in previous papers (Versnel *et al.*, 1990, 1992).

The fibers are divided into three groups with respect to their spontaneous discharge rate (SR) with boundaries at 5 and 30 spikes/s; in normal cochleas the distribution of fibers over the low-, medium-, and high-SR ranges is about 15%–20%–65%, respectively. Low-SR fibers have significantly higher thresholds than high-SR fibers and medium-SR fibers have intermediate thresholds. The $Q_{10\text{ dB}}$ increases with CF and is described as $Q_{10\text{ dB}} = 2.7f_c^{0.3}$ where f_c is the CF (in kHz).

On the basis of two distinct click-response patterns we distinguished low- and high-CF fibers with a frequency boundary of 3 kHz. Figure 2 shows representative examples of normal click PSTHs for a high-CF (A) and two low-CF (B) and (C) fibers. The PSTHs are presented in compound mode with PSTHs to condensation clicks plotted upward and to rarefaction clicks downward. The PSTHs of high-CF fibers are similar for condensation and rarefaction clicks [Fig. 2(A)]. The PSTHs have a single peak with a short latency often followed by a smaller peak. Low-CF fibers show click responses which differ with click polarity [Fig. 2(B) and (C)]. The PSTHs have several peaks (usually more than two) which alternate with polarity, and interpeak intervals are about $1/f_c$. Compared to the high-CF fibers the PSTH latency is longer for low-CF fibers, the peak amplitude is larger, and the duration of the response is longer. Responses of fibers with a CF around 3 kHz [see (B)] show a transition between the two response patterns.

B. Classification of frequency threshold curves in abnormal cochleas

Thirteen animals had a significant CAP threshold shift at one or more frequencies and thus their cochleas were regarded as abnormal (see Sec. I). The maximum threshold shift per audiogram varied across animals from 22 to 51 dB. Most of the losses were in frequency regions around and above the frequency of the exposure, and most animals had

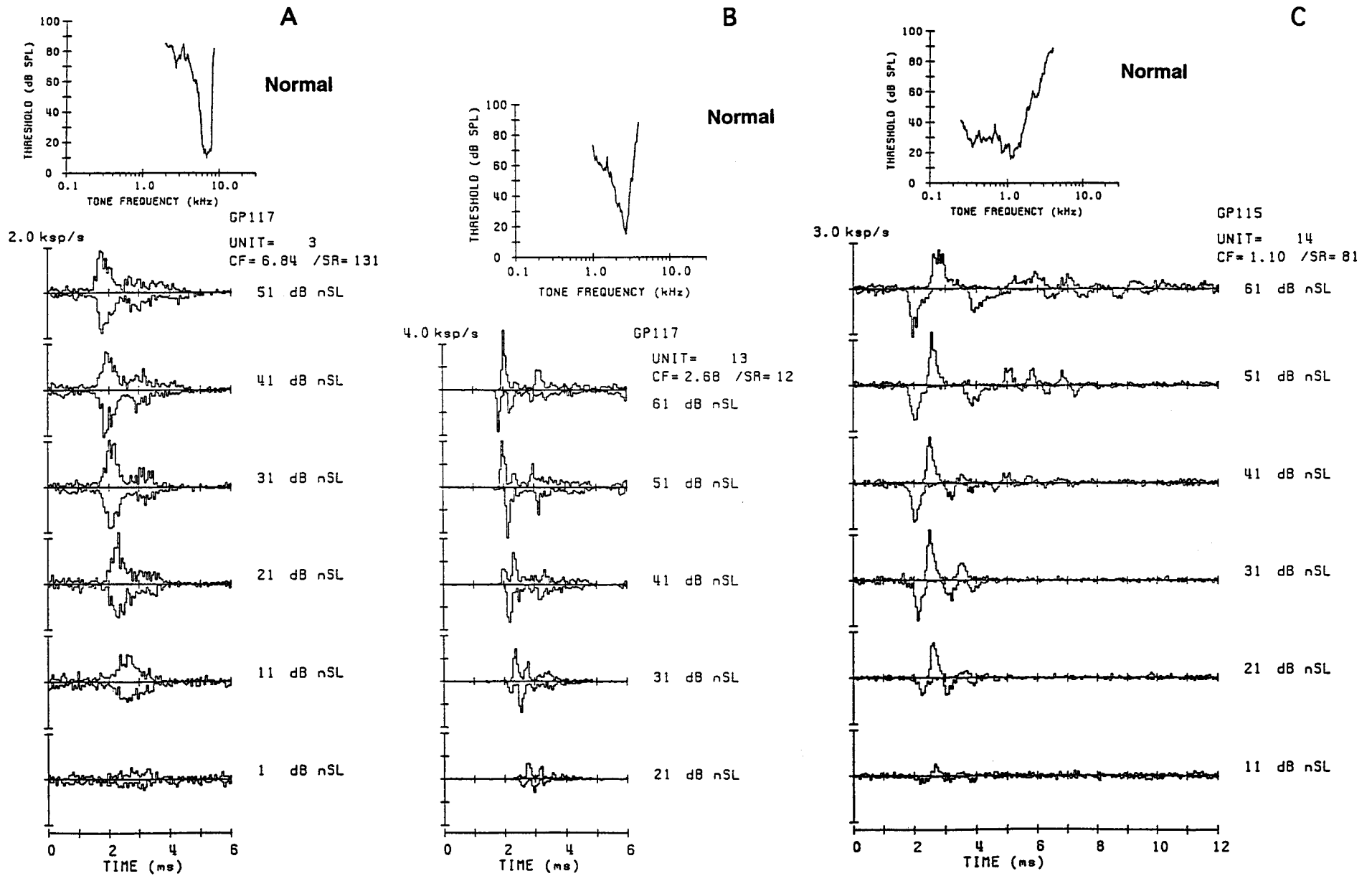


FIG. 2. Frequency threshold curve (FTC) and compound poststimulus time histograms (PSTHs) in normal cochleas. The resolution of the FTC is 50 points per octave. The condensation-click PSTHs are plotted upward, the rarefaction-click PSTHs downward; the compound PSTHs are arranged in order of decreasing click intensity. The bin width of the PSTH is 60 μ s. The ordinate represents the instantaneous firing probability density (number of spikes per sweep, divided by the bin width). (A) Responses of a fiber with a high CF (6.8 kHz); the PSTHs are similar for the two click polarities. (B) Responses of a fiber with a low CF (2.6 kHz); the PSTH-peak latencies are different for the two polarities. (C) Responses of another fiber with a low CF (1.1 kHz); the PSTHs vary with click polarity more distinctly than in (B).

TABLE I. Criteria for FTC classification. A distinct tip is defined as a region in the curve which is at least 10 dB lower than a maximum at lower frequency (often the notch) and where a slope along higher frequencies is at least 30 dB/oct over $\frac{1}{3}$ oct. The notch refers to the point where tip and tail meet, often appearing as local maximum. The tail is defined as low-frequency region at least one octave below the tip.

| Type | Distinct tip | Tail threshold (dB SPL) | Tail-notch level difference | Global shape |
|------|--------------|-------------------------|-----------------------------|------------------------------------|
| I | present | > 80 | < 20 | entire curve elevated |
| II | present | 65–80 | < 20 | tip elevated |
| III | present | ≤ 65 | ≥ 20 | tip elevated/tail low |
| IV | not present | > 65 | < 20 | entirely flat |
| V | not present | ≤ 65 | ≥ 20 | flat for high frequencies/tail low |

normal ABR thresholds before exposure. However, two animals exposed to 6 kHz had, in addition to a high-frequency loss, low-frequency losses (below 1 kHz). Two other animals had abnormal ABR thresholds at high frequencies before exposure.

In the abnormal cochleas we recorded from 90 single fibers which were considered to be abnormal on the basis that their thresholds were elevated relative to normal values in comparable CF and SR regions (see Sec. I). The CF-tone thresholds of these fibers are shown with normal thresholds of high-SR fibers in Fig. 9(A). Most abnormal thresholds ($N=71$) were found in fibers with a high CF (above 3 kHz), which was expected from the most often used frequency of exposure (6 kHz).

The FTCs of the abnormal fibers are classified into five types on the basis of the tip shape and tail threshold. The criteria applied for the classification are presented in Table I, and the five types of abnormal FTCs are schematically shown in Fig. 3. Types I, II, and III all have distinct tips with elevated thresholds; these are further distinguished by their tail: type I shows elevation of the tail threshold, type II a normal tail level, and type III an abnormally low tail threshold. Types IV and V are lacking a tip that can be associated with a CF (implying an extreme broadening or total loss of tuning at CF); of these two, type IV has a tail segment at a similar level to the high-frequency thresholds, and type V shows, as type III, a distinct tail with a low threshold. The tail level is compared to normal tail levels (for high-CF fibers with a high SR in normal ears: 74 ± 7 dB SPL, $N=19$), and it is compared to the level of the “notch” which connects tip and tail. The criteria with regard to the tail did not apply to FTCs with CFs below about 2 kHz where the tail level is difficult to define because of the sloping character of the tail. In such cases we compared to tails of normal FTCs with a similar CF. Note that a CF and $Q_{10\text{ dB}}$ cannot be determined for type-IV and type-V FTCs because of the absence of the tip. The lowest threshold at the high-frequency section of the FTC are used as “threshold at CF” of types IV and V.

Because of the high-frequency roll-off in the earphone spectrum (see Sec. I), above 12 kHz only thresholds below 50 dB SPL could be detected. This raises questions about the FTCs classified as type IV and V which almost all responded to frequencies up to about 10 kHz but where a high-frequency slope could not be detected: these FTCs might actually represent fibers with a CF above 12 kHz and an

elevated tip threshold. However, seven out of nine type-IV FTCs were recorded in animals which had both near-normal CAP thresholds and near-normal single-fiber thresholds above 12 kHz. Thus it can be assumed that in these animals most fibers with medium or high SR and a CF above 12 kHz had FTC tips close to normal and therefore their tips could have been detected. Hence, we believe that at least those seven type-IV FTCs, which were recorded in fibers with a medium or high SR, probably were genuine types IV with an original CF up to about 10 kHz.

The largest percentage of abnormal FTCs was of type III (38%), and relatively few fibers were found with type IV (10%) or type V (7%). Each FTC type could be found at any place in a hearing-loss region of the CAP audiogram, except for regions below 1 kHz where only FTCs of type I were classified (details in Versnel, 1993). Each type occurred in both moderate (20–40 dB) and severe hearing losses (40–60 dB), except for type V which was only found for severe losses.

C. FTCs and corresponding click PSTHs, typical examples

In this subsection we present examples of different types of FTCs and click PSTHs which were found with these types. Next Secs. II D, E present the FTC and PSTH parameters statistically compared to normal values. Figures 4–8 show responses for each type, mostly of both low- and high-CF fibers. Aspects of the click PSTHs considered are: duration of the response, occurrence of multiple peaks, and latency and amplitude of peaks, with particular attention to the polarity and intensity dependence of these aspects. We describe deviations from the normal response behavior (summarized in Sec. II A) based on visual inspection of the temporal response patterns. A common feature in all examples in Figs. 4–8 is that click thresholds are elevated.

Figure 4 shows the PSTHs for two fibers with type-I FTC, one with a high CF (A), and the other with a low CF (B). Both for the high-CF and low-CF case the PSTHs have normal patterns.

Figure 5 shows an example of type-II responses of high-CF fiber. The PSTHs have changed in several respects. The duration of the response is shorter than normal at all intensities: e.g., at 51 dB nSL it is about 1 ms whereas a normal value is about 2 ms [see Fig. 2(A)]. The peak amplitude shows a large increase with intensity, such that it

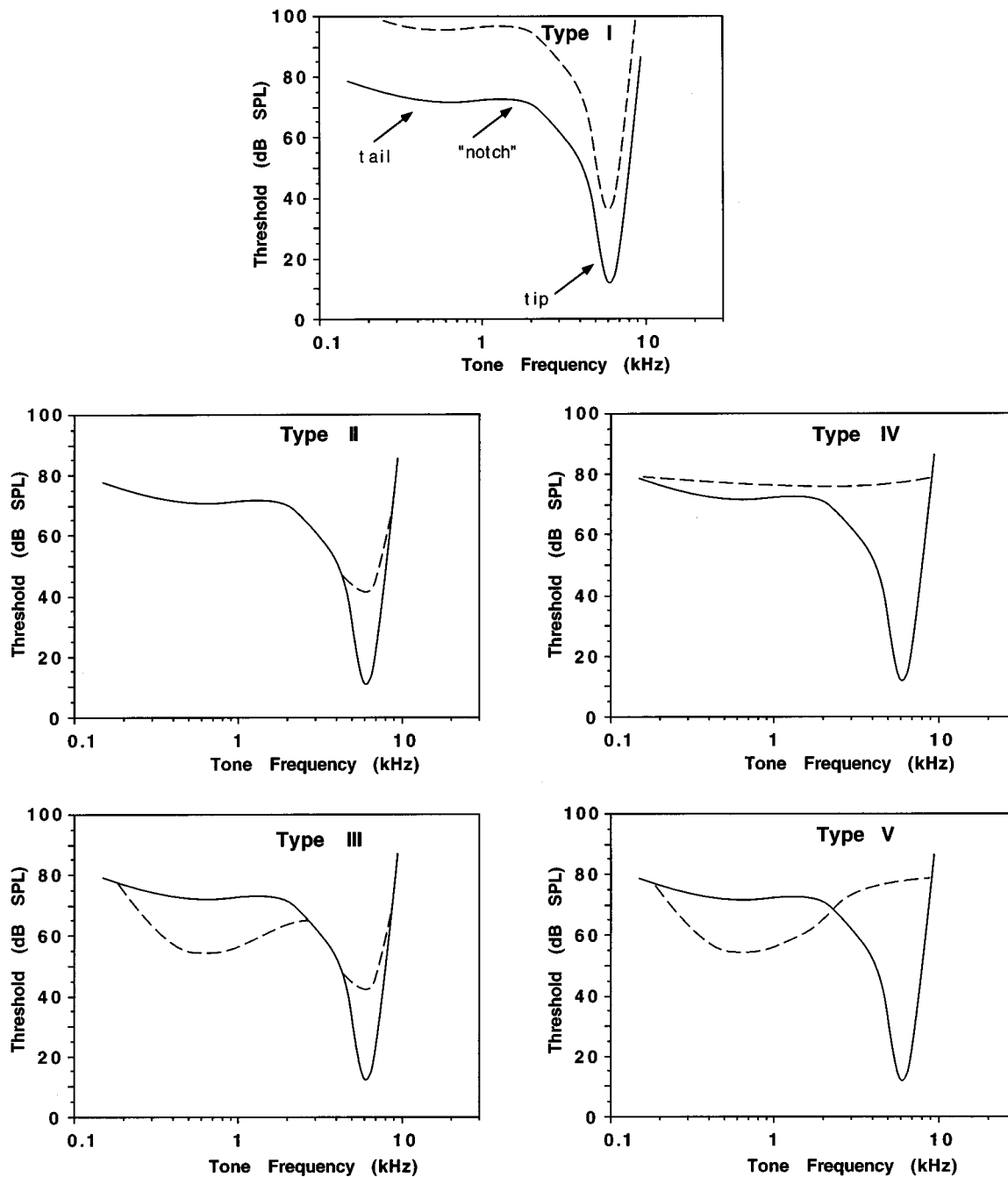


FIG. 3. Schematic representation of five types of FTCs found in fibers with a raised threshold. The solid line represents the normal FTC. The dashed lines represent the segments of the curve that deviate from normal. The arrows in the top plot point to the tip and tail regions of the FTC and to the notch which connects the tip and tail. Note that for the type classification the explicit criteria given in Table I are applied.

reaches a normal level at 20–30 dB above the threshold. The click PSTHs of a low-CF fiber with a type-II FTC [Fig. 5(B)] show similar deviations: a short duration of the responses [e.g., at 51 dB nSL the response ceases after 3 ms whereas normally it continues after 4 ms, see Fig. 2(B)], and a rapid amplitude increase to normal values.

Figure 6(A) presents a prominent example of type-III responses. The FTC clearly exhibits the double tuning to tip and tail frequencies, and the corresponding click responses reveal remarkable deviations. The main anomaly in the PSTHs is the dissimilarity of the responses to condensation and rarefaction clicks. The latency of the dominant rarefac-

tion peak is shorter than that of the condensation peak, and the early peaks alternate with click polarity. Furthermore, at higher intensities the rarefaction-click PSTHs show an isolated second peak with a long latency, whereas in normal high-CF fibers second peaks occur early [cf. Fig. 2(A)]. Abnormal behavior as a function of intensity is demonstrated by a smaller latency decrease than normal and a larger increase of peak amplitude. All of these aspects are characteristic for low-CF fibers rather than for high-CF fibers [cf. Fig. 2(A) and (C)]. Figure 6(B) shows type-III responses for a low-CF fiber. The tail has a threshold (50 dB SPL) that is even lower than the CF threshold (70 dB SPL). Here the click threshold

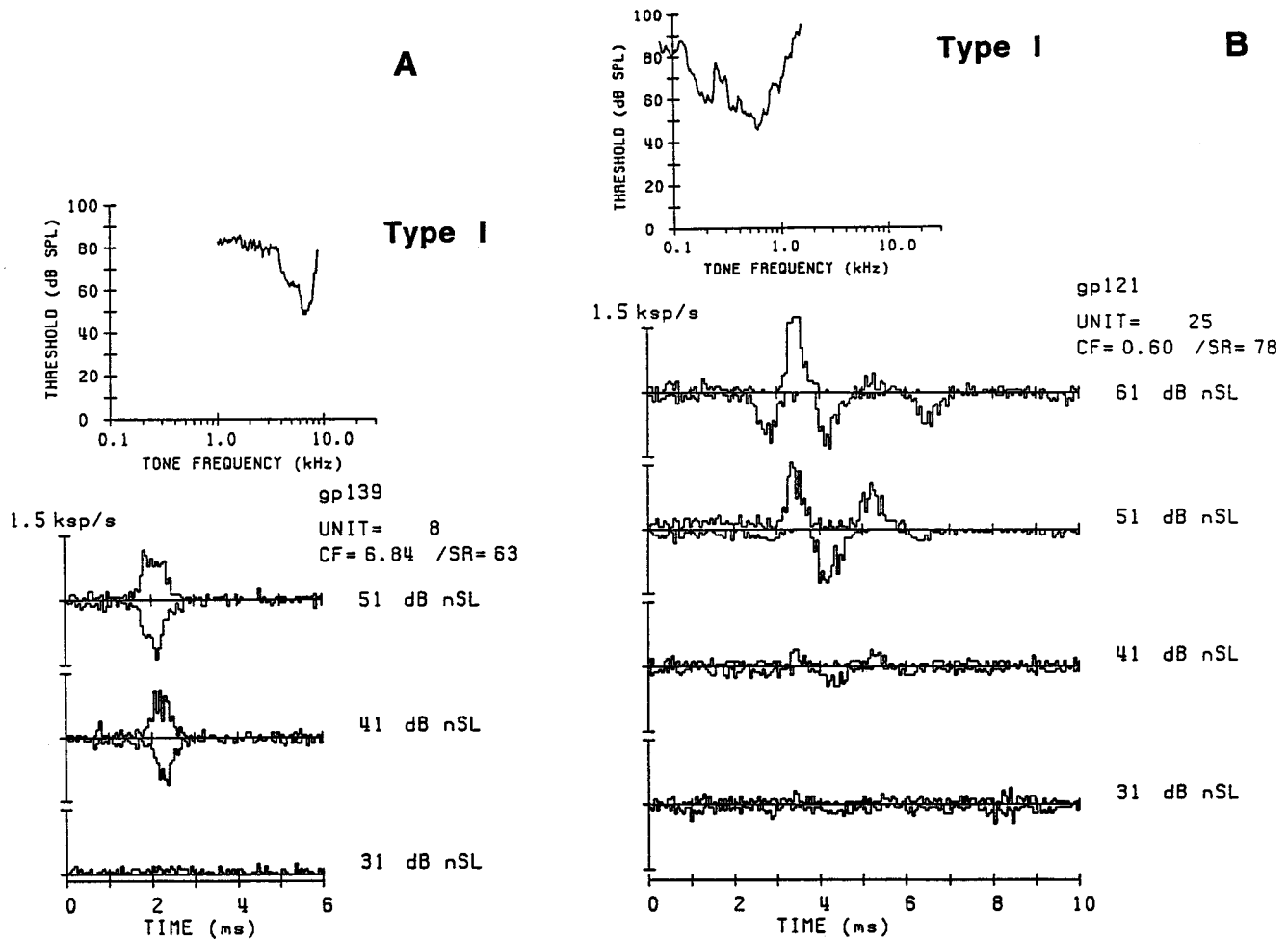


FIG. 4. Two examples of abnormal FTC type I (top) with the corresponding compound click PSTHs. The FTCs are classified as type I according to the criteria described in Table I. The condensation-click PSTHs are plotted upward, the rarefaction-click PSTHs downward. The ordinate represents the instantaneous rate (number of spikes per sweep divided by the bin width). The compound PSTHs are arranged in order of decreasing click intensity (expressed in an absolute measure, dB nSL or dB *re*: normal click threshold). (A) Responses for a fiber with a high CF (6.9 kHz) and high SR (63 spikes/s). (B) Responses for a fiber with a low CF (0.60 kHz) and high SR (78 spikes/s).

(40 dB nSL) does not correspond to the tip threshold but rather to the tail threshold (as tone and click thresholds typically differ 10 dB according to Versnel *et al.*, 1992). Just above threshold the compound click PSTHs show an oscillatory pattern corresponding to the tail frequency (0.7 kHz). For higher intensities the pattern changes such that the interpeak intervals for rarefaction are longer than for condensation clicks.

Figure 7 illustrates click responses of a fiber with a type-IV FTC, i.e., where tuning is lost. The PSTHs were normal for high-CF fibers in view of a very short and polarity independent latency and a second peak at an interpeak time of about 1.0 ms. However, in comparison to normal high-CF fibers [e.g., Fig. 2(A)], the dominant peaks were only half as wide as normal. Also, the amplitude increase with intensity was larger than normal for both polarities, and in turn, larger for the PSTH peak to condensation clicks than to rarefaction clicks.

Type-V FTCs show loss of tuning to high-frequency tones as in type IV, and relatively high sensitivity to low frequencies as in type III. The click PSTHs (compared with responses of normal high-CF fibers) showed abnormal prop-

erties reflecting both aspects of type-III and type-IV response behavior [Fig. 8(A)]. Similarly to type III, the PSTHs markedly varied with polarity, while the large amplitude and the small width of the dominant peaks observed from 20 dB above threshold were characteristic for type IV. We found one fiber with a type-V FTC which did not respond to high frequencies, implying a low original CF (i.e., below 3 kHz). Figure 8(B) shows the responses of this fiber. The high-frequency slope of the FTC at 2–3 kHz indicates that the CF tip might have been originally between 1 and 2 kHz, which is supported by the PSTH latencies. The PSTHs were abnormal in that they had two distinct interpeak intervals: one in the rarefaction-click PSTHs of about 3 ms, and the other in the early condensation-click response of about 0.5 ms. These intervals might be associated to the two frequencies where the fiber is slightly more sensitive (around 0.3 and 2 kHz).

D. FTC parameters and SR

Threshold at CF, $Q_{10\text{ dB}}$ and SR distribution, which are plotted in Fig. 9(A)–(C), varied significantly with FTC type. The $Q_{10\text{ dB}}$ and SR distributions of abnormal fibers were sta-

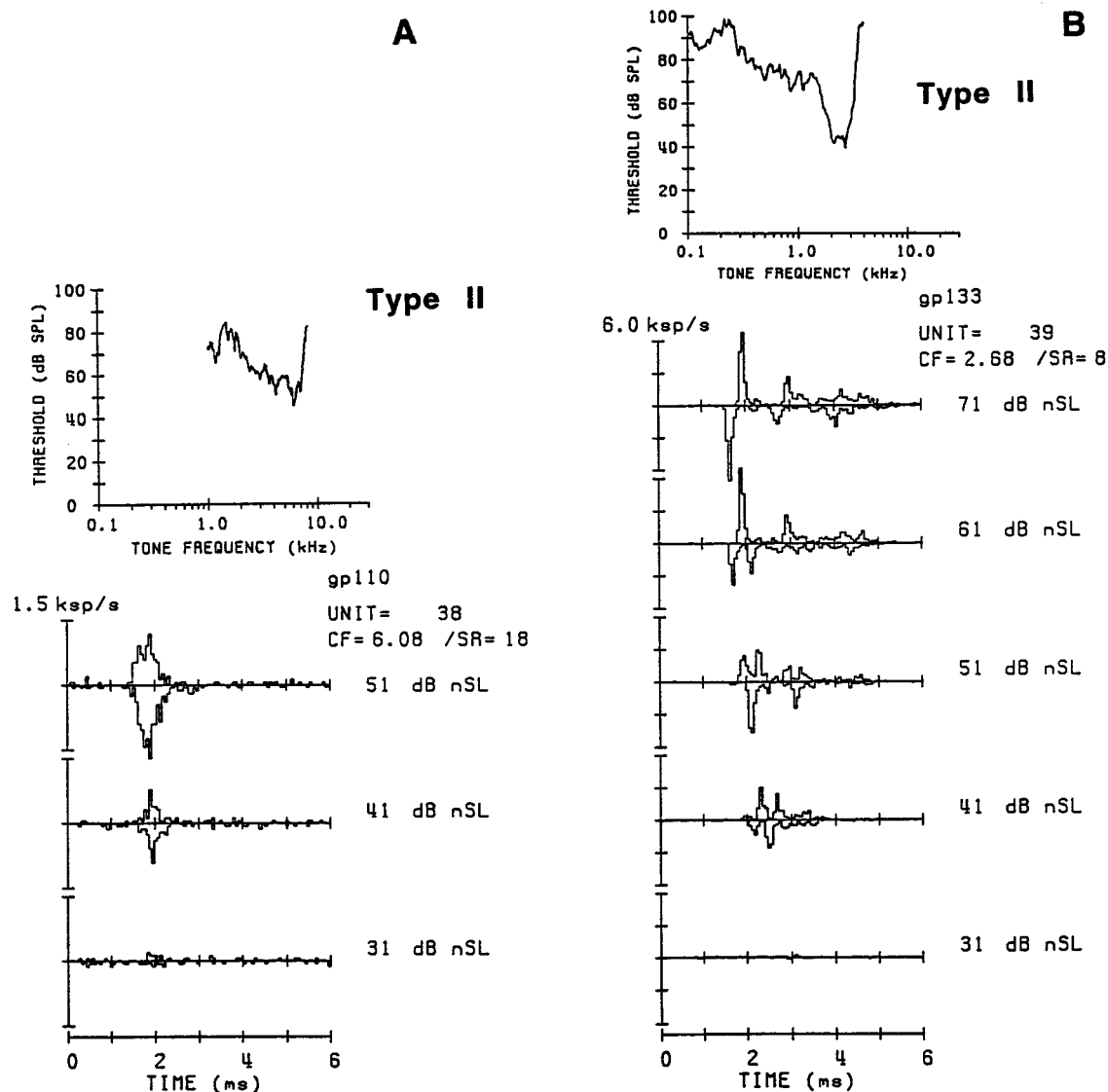


FIG. 5. Examples of FTCs and click PSTHs for abnormal type II; for explanation of plots see Fig. 4. (A) Responses for a fiber with a high CF (6.1 kHz) and medium SR (18 spikes/s). (B) Responses for a fiber with a low CF (2.7 kHz) and medium SR (8 spikes/s). Note the differences in ordinate scales between A and B.

tistically compared to normal for each type separately, and the thresholds at CF were compared among pairs of abnormal FTC types. Since threshold at CF and $Q_{10\text{ dB}}$ did not only possibly depend on FTC type, but also on CF and SR, a multiple regression analysis was applied with $\log(\text{CF})$, SR-category (medium and high), and FTC type (normal and tested type) as independent variables. The CF variable was excluded for types IV and V. The type-III FTCs showed higher thresholds at CF than type-II FTCs ($P < 0.05$), the type-IV and -V FTCs had the highest thresholds ($P < 0.05$) where the lowest threshold at the high-frequency section of the FTC was used as “threshold at CF” [see Fig. 9(A)]. Type-I FTCs had normal $Q_{10\text{ dB}}$ values, and both type-II and -III FTCs had a $Q_{10\text{ dB}}$ which was significantly lower than normal ($P < 0.05$). Note in Fig. 9(B) that abnormal FTCs can have very high $Q_{10\text{ dB}}$ s as exhibited here by some type-III FTCs. An unpaired Student’s t test was performed for the SR distribution with the values 1, 2, 3 representing high, medium, and low SR, respectively. Fibers with a type-III FTC

had more often a high SR than normal fibers ($P < 0.05$), whereas the SR distribution of type-V fibers showed the opposite trend ($P < 0.05$) [Fig. 9(C)].

E. PSTH parameters

The click threshold is elevated in most cases such as those described in Sec. II (C). The relation with the tonal threshold is examined in Fig. 10 by plotting the difference between the threshold at CF (or high-frequency tones in case of types IV and V) and click threshold as a function of CF. The trend of this parameter with CF globally follows the frequency spectrum of the click stimulus (see Versnel *et al.*, 1992). Several abnormal fibers have a larger threshold difference than the normal fibers (shown by the open circles in Fig. 10), especially the fibers with a type-III or type-V FTC. This means that the click threshold for abnormal fibers can be lower than expected on the basis of the threshold at CF

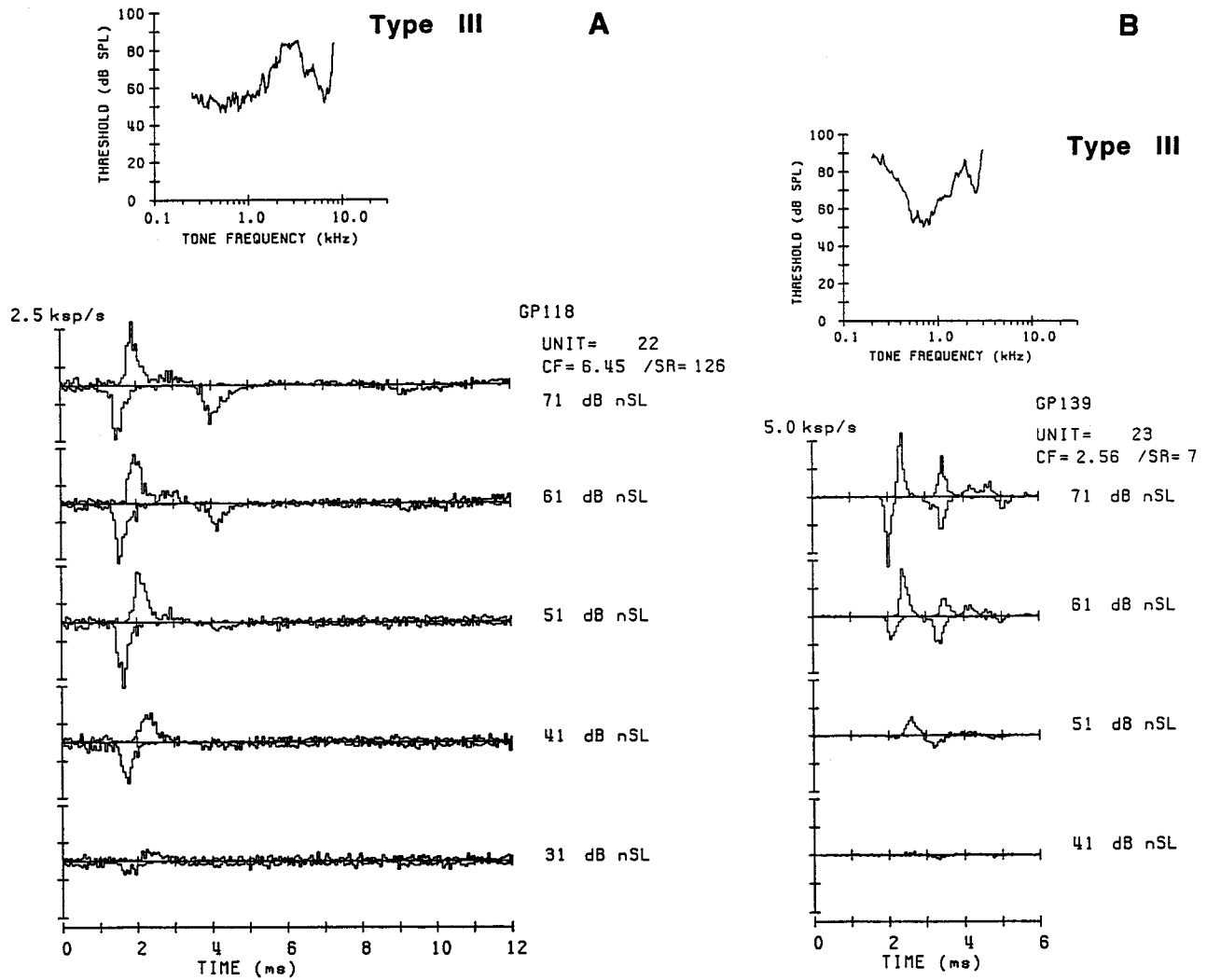


FIG. 6. Examples of FTCs and click PSTHs for abnormal type III; for explanation of plots see Fig. 4. (A) Responses for a fiber with high CF (6.5 kHz) and a high SR (126 spikes/s). Input/output curves of the PSTHs of this fiber are shown in Fig. 1. (B) Responses for a fiber with a low CF (2.6 kHz) and medium SR (7 spikes/s). Note the differences in ordinate scales between (A) and (B).

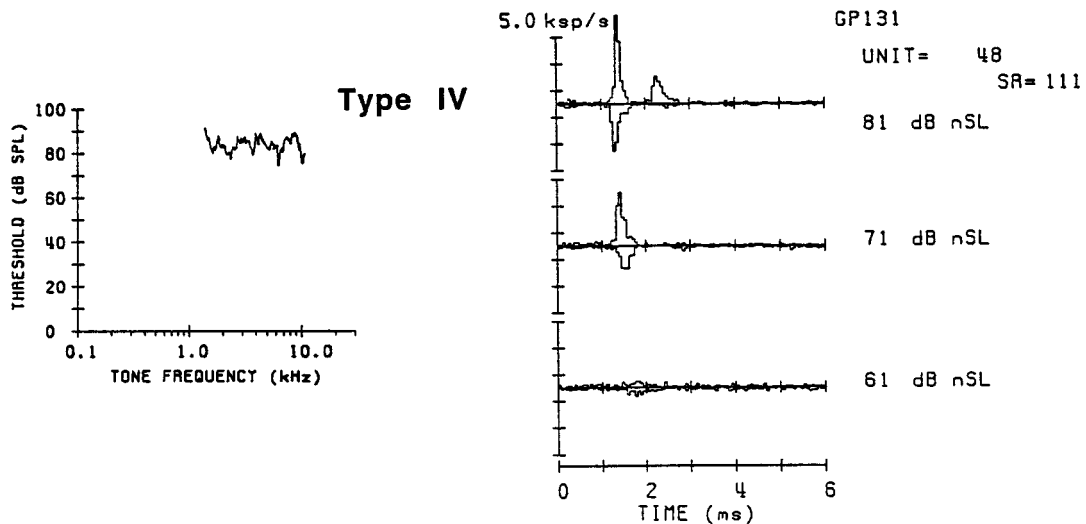


FIG. 7. Example of a type-IV fiber. The fiber's CF is unknown (cannot be determined), and the fiber has a high SR (111 spikes/s).

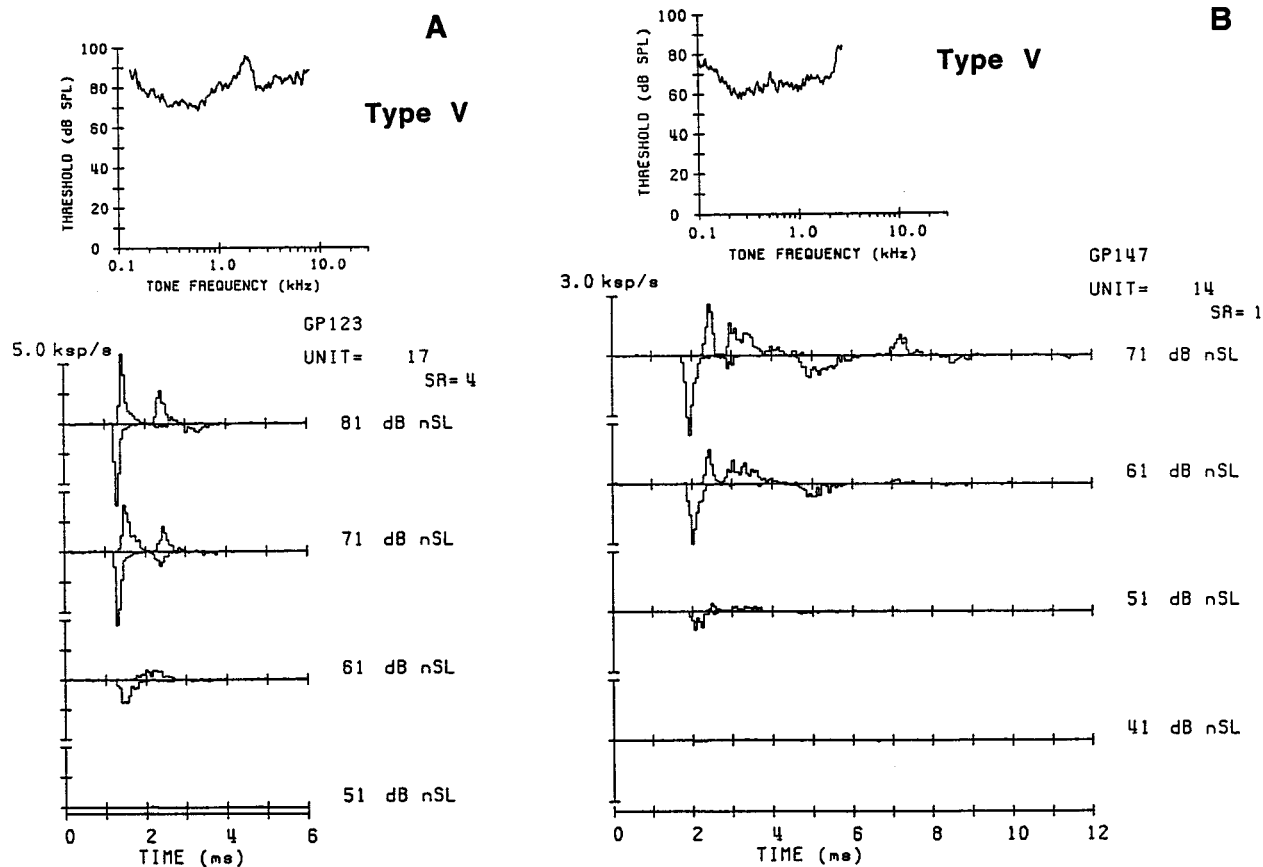


FIG. 8. Two examples of FTCs and click PSTHs for abnormal type V; for explanation of plots see Fig. 4. The CFs cannot be determined. (A) The minimum (tail) threshold is found at 0.63 kHz, and the fiber has a low SR (4 spikes/s). (B) The FTC has a distinct high-frequency slope which indicates that the CF probably lies between 1 and 3 kHz. The minimum (tail) threshold lies at 0.25 kHz, and the fiber has a low SR (1 spike/s).

and the click spectrum. This particularly occurs when the threshold of the FTC tail is lower than the threshold at CF [see Fig. 6(B)].

Figures 11 and 12 present the latency and amplitude of the PSTHs as well as their dependence on click intensity and polarity. Figure 11 shows the parameters of types I–III compared to normal, and Fig. 12 shows the parameters of types IV and V, in both figures compared to normal (circles). Statistical significance is tested using a multiple regression analysis with $\log(\text{CF})$, SR category (high and medium) and FTC type (normal and tested type) as independent variables. The statements in the next paragraph are based on 95% confidence intervals.

Click responses of type I had longer latencies and the decrease of latency with intensity was smaller than normal [see Fig. 11(A), (B)]. The amplitude at a fixed level was smaller than normal [Fig. 11(D)]. For type II all parameters had normal average values, but for individual fibers the parameters could significantly deviate from normal [see, e.g., in Fig. 11(A)]. Most deviations from normal are found for type III. The absolute latency difference with polarity was larger than normal, in most cases because the condensation click latencies were longer than normal [Fig. 11(A)]. The decrease of latency with intensity was small, sometimes the latency was even constant or increased with intensity [Fig. 11(B)]. The amplitude was smaller than normal but its increase with intensity was larger [Fig. 11(D), (E)]. The

type-IV responses exhibited very steep amplitude versus intensity functions [Fig. 11(E)]. Also, the polarity dependence of the amplitude is larger than normal, with either a strong preference for condensation or rarefaction polarity [Fig. 12(F)]. The type-V responses were larger than normal to rarefaction clicks, and their amplitude increase with intensity was larger. Also, the rarefaction click amplitudes were larger than the condensation click amplitudes, whereas the opposite trend was found for normal fibers [Fig. 12(F)].

F. Abnormal multiple peaked click response patterns and the FTC tail

For normal low-CF fibers the Fourier transform of a difference PSTH shows an amplitude peak around the CF. Specifically, at low click intensities the peak frequency or best frequency (BF) is about equal to CF, and with increase of intensity the BF decreases. Figure 13(A) illustrates an example of this trend. The PSTHs of type-III or type-V responses show a multiple peak pattern, which might be related to the increased sensitivity to low frequencies. However, this pattern does not have such an obvious (e.g., equidistant) interpeak interval as that found in low-CF fibers which can be associated with the CF. Instead, the Fourier transform of the difference PSTH might be more appropriate to reveal a correspondence of the PSTH to the FTC. Figure

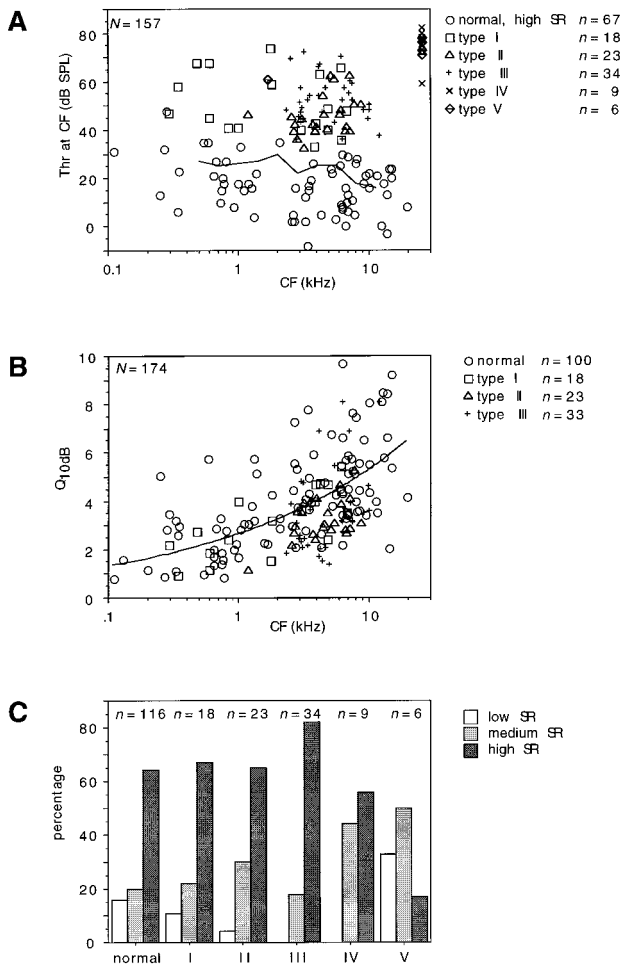


FIG. 9. (A) The threshold at CF versus CF for normal and abnormal fibers. For clarity the normal fibers are only represented by the high-SR group which has the lowest thresholds. A CF cannot be ascribed to types IV and V [except for one around 1.7 kHz, see Fig. 8(B)], hence minimum thresholds at the high-frequency section of these FTCs are used as “threshold at CF” and plotted at the right side. The solid line represents the average tone audiogram in normal guinea pigs as measured by compound-action-potential recordings from the round window. Multiple regression analysis with type of FTC and SR category (low, medium, and high) as independent variables shows that the thresholds of types IV and V are significantly higher than those of types I, II, and III ($P < 0.01$). (B) The Q_{10dB} versus CF for normal and abnormal fibers of types I–III (Q_{10dB} cannot be ascribed to types IV and V). The solid curve represents an exponential fit to normal values: $Q_{10dB}(f_c) = 2.7f_c^{0.3}$ where f_c is the CF. Multiple regression analysis with $\log(f_c)$, SR category (medium and high) and type of FTC as independent variables shows that Q_{10dB} is significantly smaller than normal for both type II and III ($P < 0.01$). Q_{10dB} of type-I FTC does not significantly differ from normal ($P > 0.05$). (C) SR distributions for normal and abnormal fibers. The distributions of types I, II, and IV are normal, the distribution of type III is abnormally skewed toward high SR, the distribution of type V is abnormally skewed toward low SR (according to unpaired Student’s t tests with values 1, 2, and 3 representing low, medium, and high SR, respectively).

13(B) shows an example of the Fourier power spectra of a fiber with a type-III FTC. The power spectrum at intensities near threshold closely mirrors the FTC tail, and with increasing intensity the spectrum broadens. Figure 14 shows a scatter plot of the BF near threshold versus tail frequency for a group of fibers with type-III or type-V FTCs. For all but one fiber there is a close correspondence between the BF and the tail frequency.

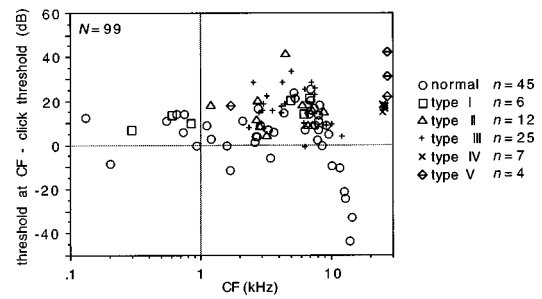


FIG. 10. Difference between CF-tone threshold (in dB SPL) and click threshold (in dB nSL) versus CF for normal and abnormal fibers. The threshold differences of types IV and V are plotted at the right side. Types III and V have significantly higher threshold differences than normal (unpaired Student’s t test, $P < 0.01$), i.e., the click thresholds are lower than normally expected on the basis of the threshold at CF.

III. DISCUSSION

We described single-fiber responses to clicks in relation to different abnormal shapes of tuning curves in impaired guinea-pig cochleas. We distinguished five types of abnormal FTCs, and to each of these we could associate specific (often abnormal) features in the click responses (see Figs. 4–8, 11, 12). Important assumptions to interpret these findings are that OHCs behave as active transducers which give frequency-dependent positive mechanical feedback, and IHCs are passive transducers which convert the mechanical vibrations into release of neurotransmitter (see e.g., Patuzzi, 1992; Dallos, 1992). A direct consequence of these assumptions is that damage to OHCs would lead to frequency-dependent changes of the single-fiber response, and damage to IHCs to frequency independent changes. Furthermore, we will interpret the click responses and their relation to the FTCs in the context of assumed cochlear lesions. Liberman and Dodds (1984b) correlated the various shapes of FTCs to various stages of hair cell lesions on the basis of intracellular labeling experiments, and we will rely on these correlations to make assumptions about the kind of damage for each type of FTC we found. Three of the four types of tuning curves given by Liberman and Dodds (see their Fig. 14) correspond closely to our types I, III, V, respectively, and their fourth curve corresponds to II or IV.

Within the above described conceptual framework, we will first discuss the type-I and type-II cases which can simply be associated to IHC or OHC damage, respectively, and subsequently, we discuss the more complex cases of types III, IV, and V.

A. Type I

Type-I FTCs are characterized by a frequency-independent threshold shift, and thus, they are probably caused by disruption of passive transduction mechanisms, e.g., occurring by damage to the IHC or afferent synapse (Liberman and Dodds, 1984b; Patuzzi *et al.*, 1989). Such damage effectively induces a higher detection threshold of the passive transducer. The findings in the corresponding click PSTHs seem to support this view. Damage to the IHC presumably affects the depolarization process and consequently reduces the postsynaptic generator potential (Liber-

Normal and types I, II, and III

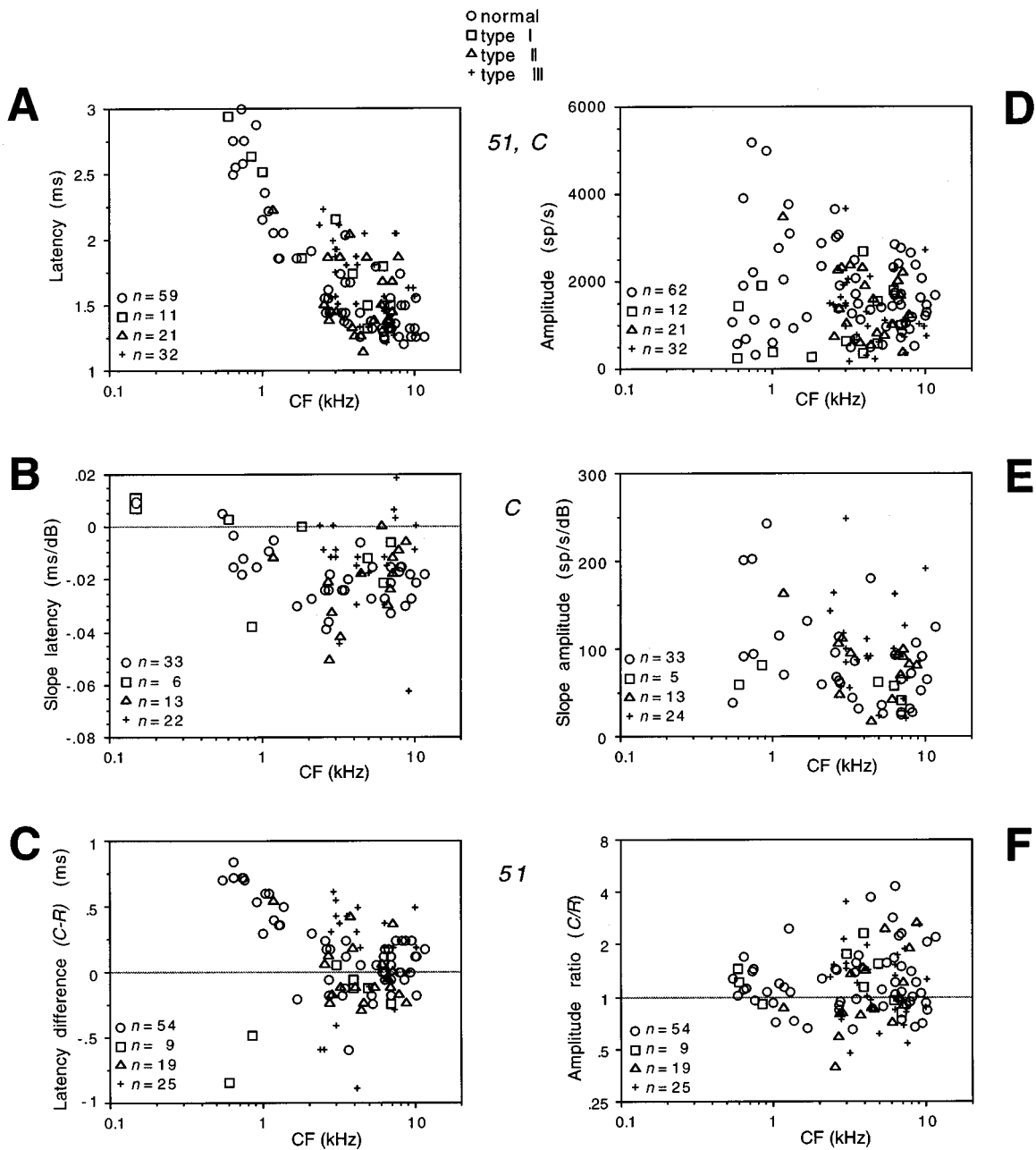


FIG. 11. Parameters of click PSTHs versus CF for normal and abnormal responses. The FTC types associated to the abnormal responses are I, II, and III. The responses of low-SR fibers are excluded. (A) Latency for condensation clicks at 51 dB nSL. For type I and type III the latencies are significantly longer than normal ($P < 0.05$; multiple regression analysis with $\log(\text{CF})$, SR category and FTC type as independent variables). (B) Slope of latency-intensity function for condensation clicks. For type I and type III the slopes are significantly shallower than normal ($P < 0.05$). (C) Difference between latencies to both click polarities at 51 dB nSL. For type III the absolute difference is significantly larger than normal ($P < 0.001$). (D) Amplitude of PSTH for condensation clicks at 51 dB nSL. For type I and type III the amplitude is significantly smaller than normal ($P < 0.05$). (E) Slope of amplitude-intensity function for condensation clicks. For type III the slope is significantly larger than normal ($P < 0.05$). (F) Ratio of amplitudes to both click polarities at 51 dB nSL.

man and Dodds, 1984a). Assuming a certain build-up time of the generator potential, the excitation threshold will be reached later and with a lower probability. In other words, the latency will be longer and the amplitude will be smaller, which is indeed what we found in the click responses.

B. Type II

The type-II FTCs have broad elevated tips and normal thresholds to frequencies below CF, which is typical for

cochlear regions with OHC damage (Robertson, 1983; Liberman and Dodds, 1984b; Patuzzi *et al.*, 1989). Our click PSTHs from type II seem to be consistent with OHC dysfunction, since, first, Salvi *et al.* (1979) recorded similar click PSTHs (normal latency, shorter response) in chinchilla cochleas where they observed predominant damage to OHCs, and, second, basilar membrane responses to clicks in noise exposed cochleas reveal comparable features (Ruggero *et al.*, 1993). We elaborate here on the latter point.

Normal and types IV and V

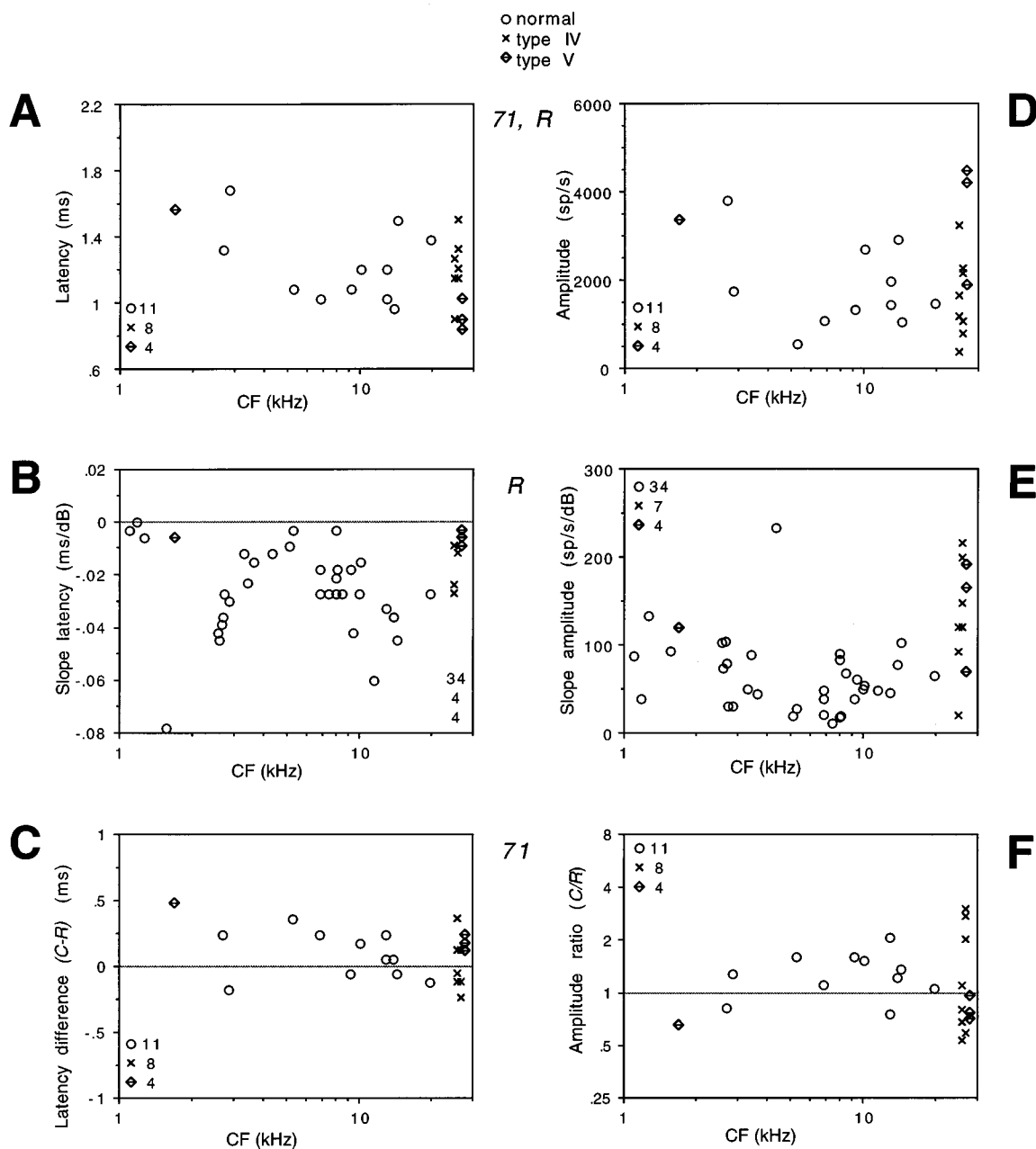


FIG. 12. Parameters of click PSTHs versus CF for normal and abnormal responses. The FTC types associated to the abnormal responses are IV and V. The responses of type IV and V are plotted to the right as their CF is not known (except for one case). (A) Latency for rarefaction clicks at 71 dB nSL. (B) Slope of latency-intensity function for rarefaction clicks. (C) Difference between latencies to both click polarities at 71 dB nSL. (D) Amplitude of PSTH for rarefaction clicks at 71 dB nSL. The amplitude is significantly larger than normal for type V ($P < 0.05$; multiple regression analysis with SR category and FTC type as independent variables). (E) Slope of amplitude-intensity function for rarefaction clicks. For both type IV and V the slope is steeper than normal ($P < 0.05$). (F) Ratio of amplitudes to both click polarities at 71 dB nSL. For type IV the absolute ratio of amplitudes, $|\log(A_p(C)/A_p(R))|$, is smaller than normal ($P < 0.05$), and for type V the absolute ratio is larger than normal ($P < 0.05$).

In deteriorated cochleas which likely involve loss of active transduction mechanisms (associated with dysfunction of OHC) the mechanical response to CF tones is reduced at low levels but is virtually the same as normal at high levels (Sellick *et al.*, 1982; Ruggero *et al.*, 1993). One could say that in a normal cochlea the OHC function is reduced at high levels making the input to the IHC independent of the state

of OHCs. In agreement with this argument, the mechanical click response in the pathological cochlea was very similar to the early component of the normal response (Ruggero *et al.*, 1993) and accordingly, we found for fibers with a type-II FTC a normal latency and amplitude. However, the late (nonlinear) component which Ruggero *et al.* (1993) distin

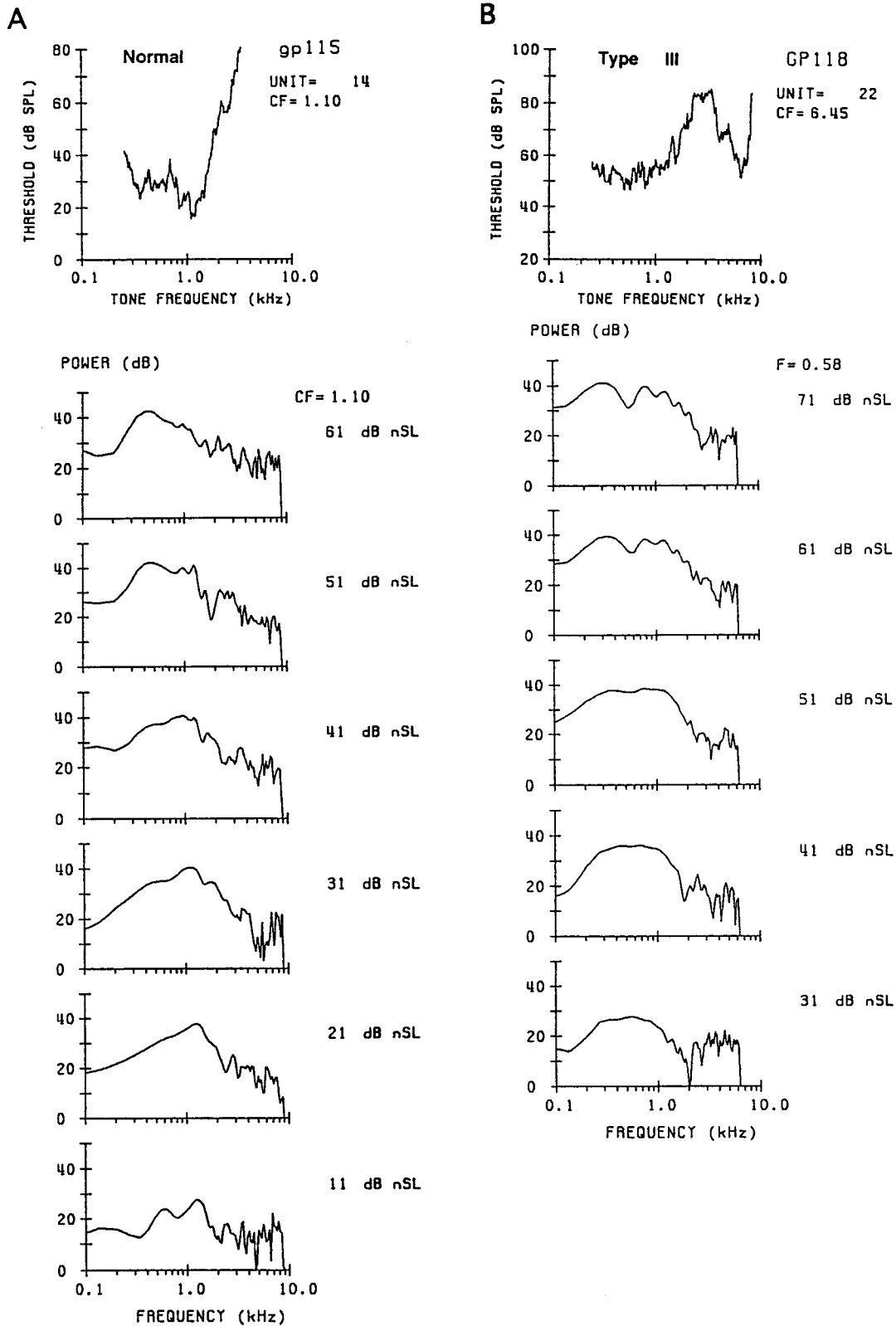


FIG. 13. Magnitude of Fourier transform of difference PSTHs (response to rarefaction click subtracted from response to rarefaction click) and the corresponding FTC (top). Fourier spectra are shown in order of descending click intensity. (A) Spectra for a normal fiber with a CF of 1.1 kHz. The corresponding PSTHs are shown in Fig. 2(C). (B) Spectra of fiber with a type-III FTC, a CF of 6.5 kHz and a tail frequency of 0.58 kHz [original PSTHs in Fig. 6(A)].

guished in the normal click response has disappeared in the abnormal cochlea, and accordingly, the duration of the single-fiber click responses of type II was shorter than normal (see also Salvi *et al.*, 1979). This implies that OHCs

somehow play a role in the response to high-intensity transient sounds. We suggest that during the first oscillations the cochlea is in a "high-intensity state" where the OHC condition is not crucial, and that after a few oscillations the

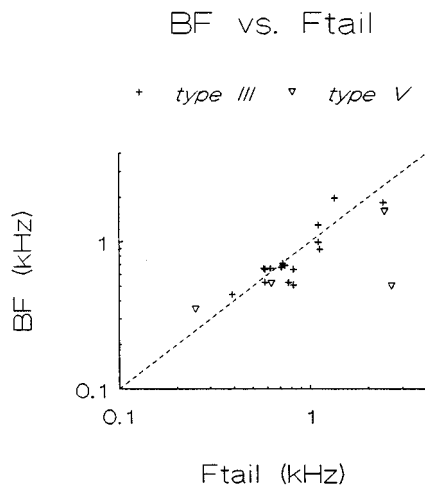


FIG. 14. Best frequency (BF) of Fourier power spectra of difference PSTHs versus frequency of FTC tail for 20 fibers. The PSTHs are considered at relatively low click levels, usually 5–20 dB above threshold, which can vary from 31 to 61 dB nSL. FTCs are of type III and V, types with a relatively sensitive tail. The dashed line represents BF equal to tail frequency.

cochlea falls into a “low-intensity state,” in which the response depends on the condition of the OHC.

C. Type III

Tuning curves of type III, i.e., W-shaped possibly including a hypersensitive tail, have been found in cochleas damaged by noise (Liberman and Kiang, 1978; Robertson, 1982; Salvi *et al.*, 1983; Liberman and Dodds, 1984b), ototoxic drugs (Schmiedt *et al.*, 1980) or endolymphatic hydrops (Harrison and Prijs, 1984). In agreement with the reports of Liberman and colleagues we found that type-III FTCs were far from exceptional and that they tended to have a higher SR [Fig. 9(C)]. It has been suggested that hypersensitivity is caused by selective severe damage to OHCs with IHCs functionally intact (Liberman and Kiang, 1978; Liberman and Dodds, 1984b; Schmiedt *et al.*, 1980; Smith *et al.*, 1988). Various cochlear models support this suggestion as they simulate hypersensitivity by manipulating OHC mechanics (Zwislocki, 1984; Geisler, 1991).

Schoonhoven *et al.* (1994) showed that if cochlear mechanics is simulated by two parallel linear filter components mimicking the (elevated) tip and (hypersensitive) tail of the type-III FTC the single-fiber responses PSTHs could be predicted fairly well over a large intensity range: the simulated response shows the multiple peak pattern with first peaks to opposite polarities partly overlapping and shortest latency to rarefaction polarity. Thus their model strongly suggests that the aberrant click response patterns were primarily caused by changes in the mechanics, which would imply damage to OHCs. The drawback of a mechanical explanation of type-III tuning is that such tuning has never been reported for basilar-membrane recordings. This paradox might be explained by the existence of a second filter, possibly provided by interaction of cilia and tectorial membrane, which gives rise to the notch between tip and tail but the effect of which is not present in the motion of the basilar membrane (Allen and Fahey, 1993). Irrespective of the precise type and location of

morphological changes underlying the pronounced double tuning, the model of Schoonhoven *et al.* (1994) demonstrated that the increased sensitivity to low frequencies lead to the aberrant response patterns. This notion is supported by several response characteristics which are typical for low-CF fibers: a multiple peaked click response pattern, power spectra of click difference PSTHs corresponding to the tail (Figs. 13 and 14), and a small decrease of latency with intensity (Fig. 11). Furthermore, the click threshold is lower than expected on the basis of the CF tone threshold [Figs. 6(B), 10] in cases of a low tail threshold.

D. Type IV

The type-IV FTC might be considered to be an extreme form of type-I and/or type-II FTCs. The loss of tuning indicates severe OHC damage and the elevated low-frequency thresholds indicate IHC damage (Robertson, 1983; Liberman and Dodds, 1984b; Patuzzi *et al.*, 1989). In combined damage it is more difficult to predict the effect on the click responses. IHC damage might have the effect as described for type I (longer latency and smaller amplitude), and OHC damage might have the effect as described for type II (normal at high levels, shorter response duration). The features of the type-IV responses pointed to the latter rather than to the former. Several aspects of the type-IV click responses are reminiscent of the postmortem basilar-membrane recordings of Ruggero *et al.* (1992). Like our single-fiber data, their mechanical responses were asymmetric with largest amplitude for either of the click polarities, their duration was short (less than 1 ms) and they showed a larger increase with intensity near threshold. The resemblance to responses in a passive postmortem system supports that OHC damage was the dominant cause for the type-IV responses.

E. Type V

Liberman and Dodds (1984b) found that FTCs only consisting of a hypersensitive tail, like type-V, accompany cochlear regions which show a total loss of OHCs and intact IHCs. With the active feedback system knocked out, one would expect a mechanical response which is the same as in a postmortem cochlea. However, this is obviously not true since a postmortem response does not show significant hypersensitivity (e.g., Sellick *et al.*, 1982; Ruggero *et al.*, 1992, 1993). Moreover, our click responses confirm that type V is not postmortem-like since, e.g., the response duration is much longer than postmortem click responses (Ruggero *et al.*, 1992).

As we saw for type III, the click responses in many ways reflect low-CF response behavior: the peak of the power spectrum of the click difference PSTH corresponds to the tail over a large intensity range (Fig. 14), the amplitude versus intensity function is steep, and the amplitude (to the rarefaction click) is larger than normal. The low-frequency tuning is a plausible cause of the large amplitude since the saturation level of the IHC receptor potential is larger for low than for high frequencies (Palmer and Russell, 1986) allowing a larger neural response (see also Schoonhoven *et al.*, 1994). The same effect contributes to the larger slope of the I/O function.

F. Relevance of click PSTHs for CAP and speech processing

Our results can be related to certain features in CAPs from abnormal cochleas. For instance, CAP latencies to clicks at high intensities are often found to be normal in pathology (Wang and Dallos, 1972; Eggermont, 1976; Elberling and Salomon, 1976; Salvi *et al.*, 1979), which can be explained by our finding that for most abnormal response types the click latencies are virtually normal. Abnormally short latencies even in cochleas with a high-frequency loss might occur if there is a significant number of fibers with response types III or V. An example of abnormal CAPs in humans which can be ascribed to such response types is reported by Eggermont (1979) who found abnormally short narrow-band derived CAP latencies to clicks in subjects with a severe flat hearing loss.

The temporal pattern of the response to click showed abnormal features especially in the type-III and type-V cases. Single-neuron responses to complex sounds such as speech may change accordingly. Temporal cues probably play a significant role in speech processing (Young and Sachs, 1979; Shamma, 1985). Hence, it is conceivable that in cochlear hearing loss including type-III like abnormalities, speech processing is not only disturbed by a change in spatial response patterns (resulting from threshold audiogram changes and broadening of tuning) but also by a change in temporal patterns. Whereas in the literature most attention is paid to changes in tuning to account for impaired speech perception (e.g., Tyler, 1986), we suggest that temporal aspects as discussed in this paper might be considered as well.

ACKNOWLEDGMENTS

This study was supported by the Netherlands Organization for Scientific Research (NWO) and by the Heinsius Houbolt Fund. The authors are grateful to Victor Gerritsma, Aart van Wijngaarden, and Pim Schotel for technical assistance. We thank Egbert de Boer, Jos Eggermont, Flint Boettcher, Tim Denison, and Alan Palmer for their useful comments on earlier versions of the manuscript.

- Allen, J. B., and Fahey, P. F. (1993). "A second cochlear-frequency map that correlates distortion product and neural tuning measurements," *J. Acoust. Soc. Am.* **94**, 809–816.
- Chiappa, K. H. (1989). "Brain stem auditory evoked potentials: interpretation," in *Evoked Potentials in Clinical Medicine*, edited by K. H. Chiappa (Raven, New York), pp. 223–284.
- Dallos, P., and Harris, D. (1978). "Properties of auditory nerve responses in absence of outer hair cells," *J. Neurophysiol.* **41**, 365–383.
- Dallos, P. (1992). "The active cochlea," *J. Neurosci.* **12**, 4575–4585.
- Eggermont, J. J. (1976). "Electrocochleography," in *Handbook of Sensory Physiology*, edited by W. D. Keidel and W. D. Neff (Springer-Verlag, Berlin), pp. 626–705.
- Eggermont, J. J. (1979). "Narrow band AP latencies in normal and recruiting human ears," *J. Acoust. Soc. Am.* **65**, 463–470.
- Eggermont, J. J., Johannesma, P. I. M., and Aertsen, A. M. H. J. (1983). "Reverse-correlation techniques in auditory research," *Q. Rev. Biophys.* **16**, 341–414.
- Elberling, C., and Salomon, G. (1976). "Action potentials from pathological ears compared to potentials generated by a computer model," in *Electrocochleography*, edited by R. Ruben, C. Elberling, and G. Salomon (University Park Press, Baltimore), pp. 439–455.
- Evans, E. F. (1975). "The sharpening of cochlear frequency selectivity in the normal and abnormal cochlea," *Audiology* **14**, 419–442.

- Evans, E. F. (1979). "Single unit studies of mammalian cochlear nerve," in *Auditory Investigation: The Technological and Scientific Basis*, edited by H. A. Beagley (Clarendon, Oxford), pp. 324–367.
- Geisler, C. D. (1991). "A cochlear model using feedback from motile outer hair cells," *Hear. Res.* **54**, 105–117.
- Harrison, R. V. (1981). "Rate versus intensity functions and related AP responses in normal and pathological guinea pig and human cochleas," *J. Acoust. Soc. Am.* **70**, 1036–1044.
- Harrison, R. V., and Evans, E. F. (1982). "Reverse correlation study of cochlear filtering in normal and pathological guinea pig ears," *Hear. Res.* **6**, 303–314.
- Harrison, R. V., and Prijs, V. F. (1984). "Single cochlear fibre responses in guinea pigs with long term endolymphatic hydrops," *Hear. Res.* **14**, 79–84.
- Kiang, N. Y. S., Watanabe, T., Thomas, E. C., and Clark, L. F. (1965). *Discharge Patterns of Single Fibers in the Cat's Auditory Nerve* (MIT, Cambridge, MA).
- Lieberman, M. C., and Dodds, L. W. (1984a). "Single neuron labeling and chronic cochlear pathology. II. Stereocilia damage and alterations of spontaneous discharge rates," *Hear. Res.* **16**, 43–53.
- Lieberman, M. C., and Dodds, L. W. (1984b). "Single neuron labeling and chronic cochlear pathology. III. Stereocilia damage and alterations of threshold tuning curves," *Hear. Res.* **16**, 55–74.
- Lieberman, M. C., and Kiang, N. Y. S. (1978). "Acoustic trauma in cats," *Acta Otolaryngol. Suppl.* **358**, 1–63.
- Lieberman, M. C., and Kiang, N. Y. S. (1984). "Single neuron labeling and chronic cochlear pathology. IV. Stereocilia damage and alterations in rate and phase level functions," *Hear. Res.* **16**, 75–90.
- Palmer, A. R., and Russell, I. J. (1986). "Phase locking in the cochlear nerve of the guinea pig and its relation to the receptor potential of inner hair cells," *Hear. Res.* **24**, 1–15.
- Patuzzi, R. B. (1992). "Effect of noise on auditory nerve responses," in *Noise-Induced Hearing Loss*, edited by A. L. Dancer, D. Henderson, R. J. Salvi, and R. P. Hemernik (Mosby Year Book, St. Louis), pp. 45–59.
- Patuzzi, R. B., Yates, G. K., and Johnstone, B. M. (1989). "Outer hair cell receptor current and sensorineural hearing loss," *Hear. Res.* **42**, 47–72.
- Pfeiffer, R. R., and Kim, D. O. (1972). "Response patterns of single cochlear nerve fibers to click stimuli: descriptions for cat," *J. Acoust. Soc. Am.* **52**, 1669–1677.
- Robertson, D. (1982). "Effects of acoustic trauma on stereocilia structure and spiral ganglion cell tuning properties in the guinea pig cochlea," *Hear. Res.* **7**, 55–74.
- Robertson, D. (1983). "Functional significance of dendritic swelling after loud sounds in the guinea pig cochlea," *Hear. Res.* **9**, 263–278.
- Ruggero, M. A., Rich, N. C., and Recio, A. (1992). "Basilar membrane responses to clicks," in *Auditory Physiology and Perception, Advances in the Biosciences*, edited by Y. Cazals, L. Demany, and K. C. Horner (Pergamon, Oxford), pp. 85–92.
- Ruggero, M. A., Rich, N. C., and Recio, A. (1993). "Alteration of basilar membrane responses to sound by acoustic overstimulation," in *Biophysics of Hair Cell Sensory Systems*, edited by H. Duifhuis, J. W. Horst, P. v. Dijk, and S. M. v. Netten (World Scientific, Singapore), pp. 258–265.
- Salvi, R. J., Henderson, D., and Hamernik, R. P. (1979). "Single auditory nerve fiber and action potential latencies in normal and noise treated chinchillas," *Hear. Res.* **1**, 237–251.
- Salvi, R. J., Hamernik, R. P., and Henderson, D. (1983). "Response patterns of auditory nerve fibers during temporary threshold shift," *Hear. Res.* **10**, 37–67.
- Schmiedt, R. A., and Zwislocki, J. J. (1980). "Effects of hair cell lesions on responses of cochlear nerve fibers. II. Single- and two-tone intensity functions in relation to tuning curves," *J. Neurophysiol.* **43**, 1390–1405.
- Schmiedt, R. A., Zwislocki, J. J., and Hamernik, R. P. (1980). "Effects of hair cell lesions on responses of cochlear nerve fibers. I. Lesions, tuning curves, two-tone inhibition, and responses to trapezoidal-wave patterns," *J. Neurophysiol.* **43**, 1367–1389.
- Schoonhoven, R., Keijzer, J., Versnel, H., and Prijs, V. F. (1994). "A dual filter model describing single-fiber responses to clicks in the normal and noise-damaged cochlea," *J. Acoust. Soc. Am.* **95**, 2104–2121.
- Sellick, P. M., Patuzzi, R. B., and Johnstone, B. M. (1982). "Measurement of basilar membrane motion in the guinea pig using the Mössbauer technique," *J. Acoust. Soc. Am.* **72**, 131–141.

- Shamma, S. A. (1985). "Speech processing in the auditory system II: Lateral inhibition and the central processing of speech evoked activity in the auditory nerve," *J. Acoust. Soc. Am.* **78**, 1622–1632.
- Smith, D. W., Moody, D. B., and Stebbins, W. C. (1988). "Effects of selective outer hair cell lesions on the frequency selectivity of the auditory system," in *Basic Issues in Hearing*, edited by H. Duifhuis, J. W. Horst, and H. P. Wit (Academic, London), pp. 448–456.
- Tyler, R. S. (1986). "Frequency resolution in hearing-impaired listeners," in *Frequency Selectivity in Hearing*, edited by B. C. J. Moore (Academic, London), pp. 309–371.
- Versnel, H. (1993). "The effects of abnormal single-fibre responses on the compound action potentials in damaged cochleas," Ph.D. thesis, University of Leiden.
- Versnel, H., Prijs, V. F., and Schoonhoven, R. (1990). "Single-fibre responses to clicks in relationship to the compound action potential in the guinea pig," *Hear. Res.* **46**, 147–160.
- Versnel, H., Schoonhoven, R., and Prijs, V. F. (1992). "Single-fibre and whole-nerve responses as a function of sound intensity in the guinea pig," *Hear. Res.* **59**, 138–156.
- Wang, C.-Y., and Dallos, P. (1972). "Latency of whole-nerve action potentials: influence of hair-cell normalcy," *J. Acoust. Soc. Am.* **52**, 1678–1686.
- Young, E. D., and Sachs, M. B. (1979). "Representation of steady-state vowels in the temporal aspects of the discharge patterns of populations of auditory-nerve fibers," *J. Acoust. Soc. Am.* **66**, 1381–1403.
- Zwislocki, J. J. (1984). "How OHC lesions can lead to neural cochlear hypersensitivity," *Acta Otolaryngol.* **97**, 529–534.

Masking of a brief probe by sinusoidal frequency modulation

Brent W. Edwards^{a)} and Neal F. Viemeister

Department of Psychology, University of Minnesota, Minneapolis, Minnesota 55455

(Received 7 August 1995; revised 12 September 1996; accepted 7 October 1996)

Contrary to level detection models, the thresholds for a brief-duration probe masked by a sinusoidal frequency modulation (FM) masker increases as the modulation index (β) of FM increases [Zwicker, *Acustica* **31**, 243–256 (1974)]. In this paper the reason for this phenomenon is investigated. In experiment 1, a 10-ms, 1-kHz probe was detected in the presence of an FM masker centered at 1 kHz and sinusoidally modulated at 16 Hz. Thresholds increased by over 15 dB with increasing β , consistent with Zwicker's findings. In experiment 2, the instantaneous frequency changes of the masker used in experiment 1 were clipped and the resulting thresholds indicated that detection was determined primarily by the masker's total frequency excursion rather than by its instantaneous sweep rate. In experiment 3, the FM maskers from the first two experiments were passed through a roex filter centered at 1 kHz and the resulting envelope was used to amplitude modulate a 1-kHz tone, producing approximately the same effective envelope at 1 kHz as the FM maskers. Threshold functions for the amplitude modulated (AM) maskers were similar to those for their corresponding FM maskers. Thresholds increased by over 15 dB while the total energy of the AM masker decreased by over 10 dB, again contrary to standard level-detection models. The results from these experiments can be explained, at least qualitatively, by a model based on envelope shape discrimination: similarities between the envelopes of the masker alone and masker-plus-probe at the output of an auditory filter centered on the frequency of the probe are primarily responsible for the observed masking, particularly at large β 's. © 1997 Acoustical Society of America. [S0001-4966(97)03902-7]

PACS numbers: 43.66.Ba, 43.66.Dc, 43.66.Mk [LLF]

INTRODUCTION

An old, and common, assumption is that the detectability of a pure-tone signal is determined by the amount of masker passed by an auditory filter, or critical band, centered at the frequency of the signal. This notion dates back at least to Fletcher (1940) and is described in more recent formulations such as the energy detector model (Green and Swets, 1966) and the power spectrum model (Moore, 1989). There is evidence that in certain circumstances this notion is incorrect, that information other than a simple change in the overall filter output ("level detection," henceforth) is the basis for monaural detection. For example, adding "comodulated" noise to frequencies far removed from the signal frequency can lead to an improvement in pure-tone detection in narrow-band noise (Hall *et al.*, 1984). Until recently such discrepancies generally have been considered minor and level-detection schemes have been taken as useful approximate descriptions of the detection process. Indeed, psycho-physical measurements of auditory frequency selectivity, most of which rely heavily on such assumptions (e.g., Patterson and Moore, 1986), are considered to be reasonably valid.

Recent evidence indicates, however, that level detection may be the exceptional case. Several studies have shown, for example, that randomizing the noise level over a wide range has little effect on detection performance when the signal-to-noise ratio is fixed (Gilkey, 1987; Kidd *et al.*, 1989; Richards *et al.*, 1991). Such presentation-by-presentation "roving"

would wreak havoc on the performance of a simple single-channel level detector. Current research has moved in the direction of examining other possible cues used in detection and has returned, in a more sophisticated way, to earlier concerns about this fundamental problem (Jeffress, 1964; Ahumada and Lovell, 1971).

A striking discrepancy with the level-detection scheme antedates many of these recent studies but, surprisingly, has been addressed only in passing. The discrepancy is shown in studies on the masking of a brief probe by sinusoidal frequency modulation (FM) and by frequency sweeps. These studies (Zwicker, 1974; Smoorenburg and Coninx, 1980; Kemp, 1982) show that when the instantaneous frequency of the masker is equal to the probe frequency, an increase in the sweep rate may cause an *increase* in threshold.

Figure 1 plots a spectrographic representation of the masker and probe for two conditions similar to those investigated by Zwicker. A 10-ms, 1-kHz probe is presented when the instantaneous frequency of the masker increases through 1 kHz. The probe detection threshold when the masker's total frequency excursion (TFE) equals 1024 Hz [Fig. 1(a)] is more than 15 dB *higher* than when the TFE is 64 Hz [Fig. 1(b)]. Clearly, the masker energy in a narrow-band centered at 1 kHz is less for the larger TFE. For example, the masker energy, or average power, passed by a typical auditory filter centered at 1 kHz is 10 dB less for the masker with a TFE of 1024 Hz than the masker with 64-Hz TFE. The simple level detector therefore would show a 10 dB lower threshold for the larger TFE; the discrepancy with the data is 25 dB.

Although Zwicker investigated the effects of modulation

^{a)}Current address: ReSound Corp., 220 Saginaw Dr., Redwood City, CA 94063.

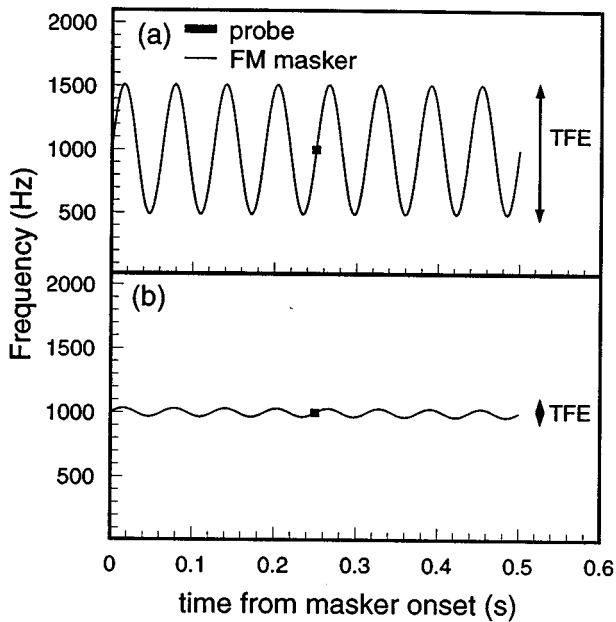


FIG. 1. Spectrographic representations of stimuli demonstrating the masking phenomenon. The total frequency excursions (TFE) of the FM masker is (a) 1024 Hz, and (b) 64 Hz. While the masker in (b) has 10 dB more energy through a critical band centered at 1 kHz than the masker in (a), 15 dB more masking is produced by the masker in (a).

frequency and later Kemp (1982) investigated the effects of modulator phase, neither discussed the reason for the unexpected effect of increased thresholds with increased TFE. This paper investigates this phenomenon and presents a possible explanation. In experiment 1, conditions similar to those used by Zwicker (1974) and by Kemp (1982) are run with a 16-Hz modulation frequency. Results from this experiment are used as a comparison for the results obtained in the next two experiments. In experiment 2, the FM masker is processed to separate correlated characteristics of the masker, specifically, the frequency sweep rate and TFE, and to determine the relevancy of each to the masking of the probe. In experiment 3, a filter model is used to account for the data and thresholds are obtained with a single-channel representation of the stimuli used in the first and second experiments.

I. EXPERIMENT 1: SINUSOIDAL FM MASKER

A. Stimuli

The FM masker was 500 ms in duration with 20-ms raised-cosine on and off ramps. The steady-state portion of the masker was generated using

$$A \sin[2\pi f_c t - \beta \cos(2\pi f_m t)], \quad (1)$$

where f_c is the carrier frequency, f_m is the modulation frequency, and A is a constant set such that the level of the masker was 60-dB sound-pressure level (SPL). The TFE of the masker is $2\beta f_m$. This dependence of the TFE on modulation frequency is a result of the way β is typically defined and is one reason why FM detection thresholds decrease as a function of β but remain relatively constant as a function of TFE (for small f_m). Throughout the following experiments, f_m was fixed at 16 Hz and TFE was changed by varying β .

The carrier frequency was 1 kHz for all experiments.

The probe was a 1-kHz tone with 5-ms raised-cosine ramps and a total duration of 10 ms. Probe levels were defined as the SPL at the maximum portion of the probe. The temporal center of the probe coincided with the temporal center of the masker, i.e., the onset of the probe was 245 ms after the onset of the masker. The instantaneous frequency of the masker was increasing through 1 kHz at the temporal center of the probe (as shown in Fig. 1). This condition provides maximum masking of the probe (Zwicker, 1974) and was used for all of the present experiments.

Since the phase of the FM masker changes during presentation of the probe, it is not clear what probe phase should be used. The problem is compounded because the phase changes in the masker depend on TFE, a variable of primary interest in the present studies. Therefore, to minimize systematic phase-related effects on probe threshold, the phase of the probe was randomly chosen (rectangular distribution, $0-2\pi$) for each probe presentation and for all conditions (including TFE=0). Pilot data indicated that there was little difference between threshold functions obtained with random phases and threshold functions obtained with phase fixed at 90° (the orthogonal condition for TFE=0).

The stimuli were generated digitally on a NeXT computer using its 16-bit D/As and a sampling rate of 44.1 kHz. The NeXT's programmable attenuators were used to increase the effective dynamic range of the D/A. Stimuli were presented monaurally using Sony MDR-V6 headphones.

B. Procedure

A 3IFC task was used, with each 500-ms observation interval separated by 500 ms of silence. An identical masker was presented in each interval, and the probe was added to the masker in one of the intervals chosen at random with equal probability.

A two-down, one-up tracking procedure was used to estimate the 70.7% correct point on the psychometric function. The level of the probe was adjusted in 3-dB steps until four reversals were achieved, then the probe was adjusted in 1-dB steps. The procedure terminated after a total of 12 reversals; the first four reversals were ignored and the levels of the last eight reversals were averaged to estimate the threshold for that block of trials. Threshold estimates were discarded if the standard deviation of the reversals within a block exceeded 4 dB.

The masker was fixed within a block and the masker TFE was randomized across blocks. Thresholds from four blocks with the same TFE were averaged to estimate the final threshold for a condition.

Visual cues denoted the observation intervals (for the entire 500 ms) and provided correct answer feedback.

C. Subjects

The three subjects had normal hearing (within 10 dB of laboratory norms). S1 was an experienced subject; S2 and S3 received five hours of training using a variety of conditions from experiment 1, during which their probe thresholds stabilized.

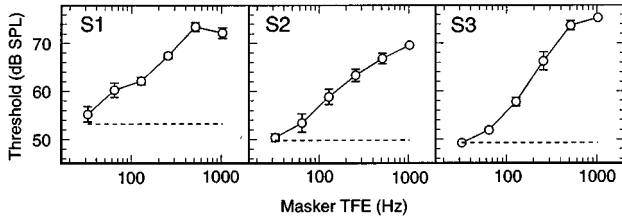


FIG. 2. Probe threshold as a function of masker TFE for experiment 1.

D. Results

Figure 2 shows the probe detection thresholds as a function of the masker TFE. Each panel represents a different subject, and the dashed line represents detection threshold when the masker is a 1-kHz tone, i.e., TFE=0. Error bars denote the standard deviation of the threshold estimates.

For the condition which results in the lowest threshold, TFE=32 Hz, the masker sweeps through less than 16 Hz in the 10-ms window during possible probe presentation; for the condition which results in the highest threshold, TFE =1024 Hz, the masker sweeps through more than 490 Hz during this window. These results demonstrate the general phenomena which is contradictory to the simple level-detection scheme: probe-detection thresholds increase while the masker energy near the frequency of the probe decreases. The data are consistent with those of Zwicker (1974) and Kemp (1982) which demonstrate the same phenomenon at different modulation frequencies.

II. EXPERIMENT 2: CLIPPED FM MASKER

While the results from the previous experiment indicate that the masking of a tonal probe by an FM signal increases as the TFE of the masker increases, it is unclear what underlying property of the masker causes the threshold increase. Specifically, as the masker TFE increases, so does the rate of change of frequency during the probe presentation. When the instantaneous frequency of the masker is 1 kHz, occurring at the temporal center of the probe, the rate of change of the masker's frequency, or sweep rate, is proportional to the TFE of the masker:

$$\begin{aligned} \frac{d}{dt} f(t)|_{1000 \text{ Hz}} &= 2\pi f_m^2 \beta \text{ Hz/s} \\ &= \pi f_m \times \text{TFE} \text{ Hz/s.} \end{aligned} \quad (2)$$

The results from experiment 1 demonstrate that thresholds increase as masker TFE increases. Because of the relationship between masker TFE and sweep rate shown in Eq. (2), it is unclear if the increase in threshold is due only to the TFE *per se* or, as hypothesized by Smoorenburg and Coninx (1980) for linear-sweep FM, results from the increase in the masker's sweep rate during the probe presentation. Experiment 2 was intended to isolate these two effects.

A. Stimuli

The probe and masker were similar to those in the previous experiment except that the instantaneous frequency of the masker was "clipped" such that the masker's instantane-

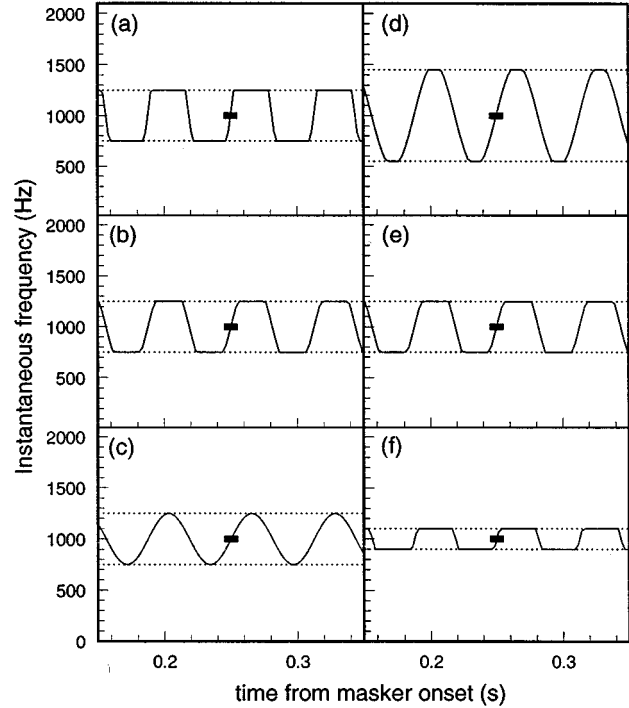


FIG. 3. Panels (a)–(c) demonstrate stimuli conditions for experiment 2 where the masker TFE is held constant while the sweep rate during probe presentation varies; panels (d)–(f) demonstrate conditions where the masker sweep rate is held constant while the TFE varies.

ous frequency deviation from 1 kHz did not exceed a predefined limit, f_{cl} . Before clipping, the masker was defined in the same manner as experiment 1. For a fixed TFE (or fixed β), the instantaneous frequency of the masker was then restricted such that

$$\begin{aligned} f(t) &= f_c + f_{cl}, & \text{for } f_c + f_m \beta \sin(2\pi f_m t) > f_c + f_{cl}, \\ &= f_c - f_{cl}, & \text{for } f_c + f_m \beta \sin(2\pi f_m t) < f_c - f_{cl}, \\ &= f_c + f_m \beta \sin(2\pi f_m t), & \text{otherwise.} \end{aligned} \quad (3)$$

By fixing f_{cl} , the masker's actual TFE was held constant while the sweep rate was changed by varying β in Eq. (3) [or by varying the TFE before clipping; see Eq. (2)]. Figure 3(a)–(c) demonstrates this situation: the sweep rate during the probe presentation in each figure is different while the masker TFE is the same. Figure 3(d)–(f) displays the opposite case, where the TFE in each figure is different while the sweep rate during probe presentation remains unchanged. It should be noted that clipping the instantaneous frequency did not result in the spectral splatter that would result from a similar clipping of the envelope. In addition, care was taken not to introduce any discontinuities in the phase of the stimuli which would result in splatter and noticeable clicks.

B. Procedure

The procedure was the same as in experiment 1, with the following exceptions. Within a set of blocks, the masker always had the same TFE. Different blocks within a set had different masker sweep rates. TFE and sweep rate were varied in a pseudorandom manner and at least four threshold

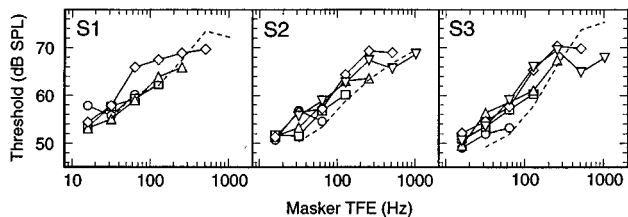


FIG. 4. Data for the conditions shown in Fig. 3. Each symbol represents a different sweep rate during the probe presentation: 1024 (circles), 2048 (squares), 4096 (up-triangles), 8192 (diamonds), and 16 384 (down-triangles) Hz/s. The abscissa represents the TFE of the masker after its instantaneous frequency has been clipped. Thus, different data points but with the same symbol correspond to panels (d)–(f) in Fig. 3. The dashed line plots the data from Fig. 2 as a function of sweep rate.

estimates were obtained for each condition. Final thresholds were obtained for each condition by averaging the four threshold estimates.

C. Subjects

The subjects from experiment 1 participated in this experiment.

D. Results

The results are shown in Fig. 4, which plots probe threshold versus actual (post-clipped) masker TFE. The parameter is the masker sweep rate when the frequency is increasing through 1 kHz. Also shown in Fig. 4 with the dashed lines are the thresholds from Fig. 2, i.e., thresholds when the masker was unclipped. To simplify the figures, standard deviations are not shown, but were all less than 3 dB.

One result obvious from Fig. 4 is that when the masker sweep rate is fixed, thresholds still increase with increasing masker TFE. The thresholds are similar to the thresholds obtained using unclipped maskers with the same TFE (dashed line). If thresholds from experiment 1 were dependent upon the sweep rate and not the TFE, then (1) the lines would be flat as a function of TFE, and (2) the lines would be ordered according to the sweep rate they represent, with lines corresponding to higher sweep rates falling above lines corresponding to lower sweep rates. This last property is only seen with a single-condition for subject 1, where thresholds from the fastest sweep rate are higher than all the thresholds from all the other sweep rates.

Figure 5 further demonstrates the roles of TFE and sweep rate. Here, the thresholds from Fig. 4 are replotted as a function of sweep rate, with masker TFE as the parameter. If the data were dependent upon sweep-rate and not post-clipped TFE, then all of the lines would coincide. Instead, thresholds for a given post-clipped TFE are nearly constant; the lines are separated and ordered, with a few exceptions, such that lines corresponding to higher clipped TFEs have higher thresholds. This figure further illustrates that the sweep rate has little effect on threshold.

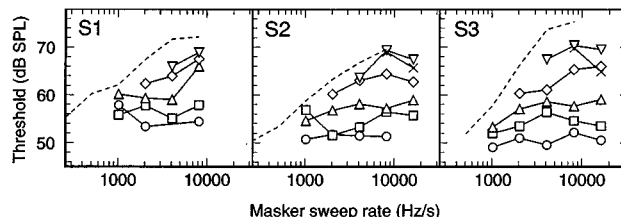


FIG. 5. The data from Fig. 4, replotted in a different manner. The abscissa represents the frequency sweep rate of the masker during probe presentation. The parameter is the actual masker TFE: 16 (circles), 32 (squares), 64 (up-triangles), 128 (diamonds), 256 (down triangles), and 512 (crosses) Hz. Different data points but with the same symbol correspond to (a)–(c) in Fig. 3.

III. EXPERIMENT 3: EQUIVALENT AM MASKERS

The results of experiment 2 indicate that the masker’s TFE, and not the masker’s sweep rate, is the primary factor in determining the amount of masking of the probe. Why thresholds increase with increasing TFE, the fundamental problem motivating this paper, is still not clear.

One possible explanation is based on the following. As the masker sweeps through an auditory filter, a brief increase occurs in the envelope of the signal at the output of the filter. This envelope “pulse” is similar to that caused by a brief probe whose frequency is at the center frequency of the filter. It is possible that the listener has difficulty detecting the envelope fluctuation produced by adding the probe because the masker is causing similar fluctuations. That is, we hypothesize that the subject is basing decisions on differences between the temporal structure of the envelopes; the task is effectively envelope-shape discrimination. As the envelope of the filtered masker becomes more similar in shape to that of the probe, the envelope of the masker-plus-probe will be, at least roughly, more similar to that of the masker and detectability will deteriorate.

To examine this hypothesis, the FM maskers from the previous two experiments are transformed into AM maskers to simulate the form of the envelope fluctuations that the masker produces at the output of an auditory filter. A carrier of 1 kHz is used so the envelope seen at the output of an auditory filter due to the AM masker will be approximately the same as that due to an FM masker.

A. Stimuli

The probe was the same as in the previous two experiments. The masker was obtained by passing the FM maskers from the previous two experiments through a roex filter (Patterson *et al.*, 1982) with a transfer function defined by

$$H(f) = (1 + p|f_c - f|/f_c) \exp(-p|f_c - f|/f_c), \quad (4)$$

where f_c is the center frequency of the filter (1 kHz), and p is a constant which determines the attenuation rate of the filter (fixed here at 30; Rosen *et al.*, 1992).

Figure 6 demonstrates the signal processing of the masker. Once an FM signal was filtered, the envelope was extracted using a Hilbert transform. The envelope was then used to amplitude modulate a 1-kHz tone, creating an AM signal with no frequency modulation. The envelope of the

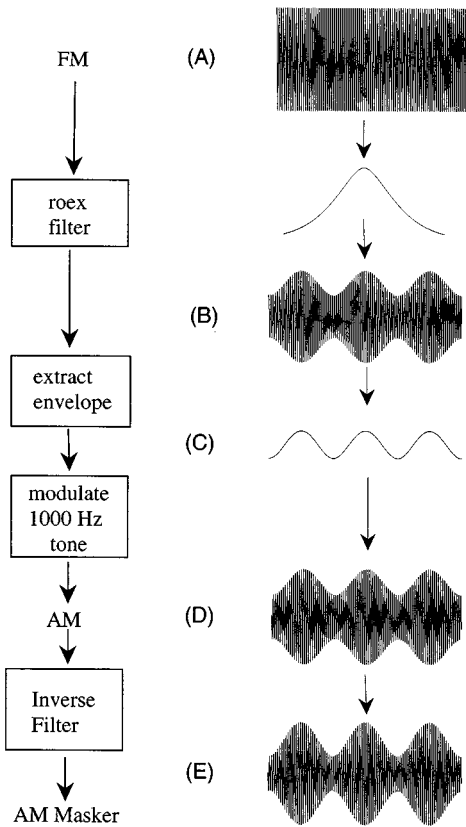


FIG. 6. Processing done on FM maskers from experiments 1 and 2 to obtain their equivalent AM maskers for experiment 3.

AM signal (point D in Fig. 6) is identical to the envelope of the FM masker after it is filtered (point B). Finally, the AM signal was filtered by the inverse of Eq. (4) to negate the effect of further filtering by the listener's own auditory filter. The intent of this processing scheme is that the envelope at the output of the listener's auditory filter due to the AM masker will be similar to the envelope of the auditory filter's output due to the corresponding FM masker. After the AM masker was generated, the probe was then added such that the temporal center of the probe corresponded to the temporal center of the masker, i.e., the point equivalent to the probe's location in the previous two experiments.¹

Again, the general goal is to evaluate whether the observed increases in probe threshold with increasing TFE are at least qualitatively consistent with a single-channel, envelope-extraction scheme. Although it might be desirable to measure filter functions for each subject and to use those in the processing, such an effort seems unnecessary at this stage of inquiry. Thus, the simulated auditory filter and subsequent processing were the same for all subjects.

B. Procedure

The procedure was similar to that of experiments 1 and 2, and the same subjects participated.

C. Results

Figure 7 shows the results obtained when the sinusoidal FM maskers from experiment 1 were used to generate the

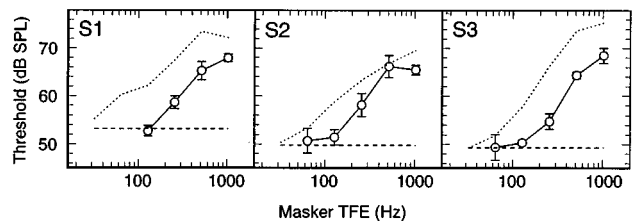


FIG. 7. Probe detection thresholds for AM maskers that were created by processing the FM maskers used in experiment 1. The abscissa represents that TFE of the masker before it was processed. The AM maskers have the same envelope fluctuations at 1 kHz as their FM equivalents from experiment 1. The dashed line represents threshold when the masker was a 1-kHz pure tone. The data from Fig. 2 are replotted with dotted lines.

AM maskers. The abscissa represents the TFE of the masker before it was transformed to an AM signal (i.e., the TFE at point A in Fig. 6); the actual masker presented to the subjects had no instantaneous frequency fluctuations.² The dashed line represents threshold when the masker is an unmodulated tone, i.e., TFE=0. The dotted line represents the average of the data from Fig. 2, i.e., data from the FM maskers used to create the AM equivalents. The relationship between this line and the data from experiment 3 will be discussed in the next section.

As can be seen, thresholds increased as the pre-processed³ TFE of the masker increased. It should be noted that the total energy of the masker decreased as the pre-processed TFE increased. This is because more of the FM signal is filtered by the roex filter as more of the FM signal's energy occurs outside of the filter's bandwidth. Thus, thresholds in Fig. 7 are increasing while the total energy of the AM masker is decreasing, once again contradictory to the level-detection scheme.

Figure 8 shows the thresholds obtained when the clipped-FM maskers of experiment 2 are used to generate the AM masker. The TFE of the post-clipped, pre-processed masker is plotted along the abscissa; the pre-processed sweep rate is the parameter. The dashed line is the data from Fig. 7. Most of the lines tend to coincide, except for S1's where the data parallel the dashed line but are shifted to the left. Consistent with experiment 2, the results indicate that the TFE of the FM masker has more effect on probe threshold than the sweep rate.

This is confirmed in Fig. 9, which replots the data from

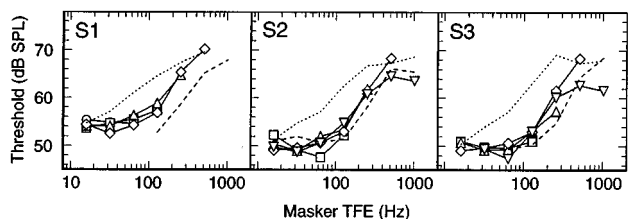


FIG. 8. Probe-detection thresholds for AM maskers that were created by processing the FM maskers used in experiment 2. The abscissa represents the TFE of the FM masker after its frequency was clipped but before it was processed. The symbols represent the same frequency sweep rates as in Fig. 4. The data from Fig. 7 are replotted with the dashed line. The averages of the data in Fig. 4 are plotted with dotted lines.

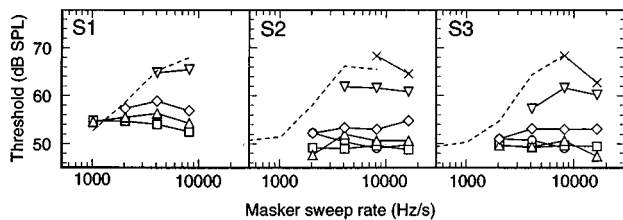


FIG. 9. Replotting of data in Fig. 8, but with the pre-processed frequency sweep rate as the abscissa and the pre-processed TFE as the parameter; the symbols represent the same TFEs as in Fig. 5. The dashed line replots the data from Fig. 7.

Fig. 8 using pre-processed sweep rate as the abscissa and the post-clipped, pre-processed TFE as the parameter; this plot is similar to the plot in Fig. 5. As in Fig. 5, the data indicate the dominance of FM TFE over FM sweep rate. The dotted lines in Figs. 8 and 9 represent the average of the data in Figs. 4 and 5, respectively.

IV. DISCUSSION

Experiment 1 replicated the phenomenon that is the focus of this paper: the increased masking of a probe with increased masker TFE. The results are consistent with those of Zwicker.

Experiment 2 was designed to determine which properties of the masker were related to the increased thresholds. Two previously correlated properties of the masker, sweep rate during probe presentation and TFE, were independently manipulated and thresholds were found to be much more dependent upon TFE than sweep rate. This is somewhat surprising since it had been previously thought that increased sweep rate was responsible for the increased thresholds. Smoorenberg and Coninx (1980) noted that the increased sweep rate increased the frequency region which is excited by the masker during the probe presentation; since they demonstrated that the loudness of a frequency sweep increases with the width of the region swept (Coninx and Smoorenberg, 1979), they suggested that the increased thresholds were due to the increased loudness of the masker.

Since thresholds are relatively unaffected by the sweep rate of the masker during probe presentation, the properties of the masker either before or after probe presentation are responsible for the increased thresholds, possibly suggesting forward or backward masking. The results are in contrast to standard frequency effects for these types of masking, however, in that the most masking in our experiment is produced for maskers that reach frequencies most distant from the probe's frequency.

A. Detection of energy splatter

Although a simple account in terms of masking seems untenable, a consideration of the possible role of energy splatter may make such an account more plausible. Specifically, it may be that the thresholds obtained at small-masker TFEs are relatively low because the subject is listening "off frequency" and is detecting energy splatter produced by adding the probe. As the TFE increases this strategy becomes less advantageous, partly because the signal-to-masker ratio

at the nominal frequency of the probe becomes increasingly large, and partly because the splatter is being masked. We at first discounted this possibility because, even though the probe is brief (10 ms), its equivalent rectangular bandwidth is only 150 Hz and all but 1 dB of its energy is in a 146-Hz band centered at 1 kHz. However, subsequent observations seem consistent with splatter detection at low TFEs. First, varying the phase of addition of the probe to a zero-TFE masker (increment detection) had little effect on threshold. If the subject was basing decisions on the output of a filter centered at the probe frequency, this phase manipulation might be expected to produce a significant change in threshold; the task would be increment detection, a situation where the relative phase of addition would have a large effect. If, however, the subject were detecting splatter then, because of the similarity in the spectra, little phase effect might be seen. Second, adding a broadband noise whose level was sufficient to raise the probe-alone threshold by 20 dB, and thus presumably to mask the splatter, raised the probe threshold more at low masker TFEs than at high. This is also consistent with the detection of splatter at low TFEs. Finally, reducing the masker level from 60 to 35 dB reduced the probe threshold less at low TFEs than at high. Again this is consistent with the splatter hypothesis: the thresholds are "artificially" low at the higher masker level and low TFE because of splatter detection.

The question raised by these observations is whether the splatter detection at low TFEs, together with simple level detection at large TFEs, can account for all of the TFE effect. This is very unlikely. In both the noise and 35-dB masker conditions, the threshold at a TFE of 512 Hz was still at least 10-dB higher than at a TFE of zero. Thus, there is still a substantial effect of TFE even when splatter detection is almost certainly not involved.⁴ Also, it seems that level detection cannot account for the basic phenomenon: the large amount of masking seen for FM maskers with large TFEs. Even with *no* auditory filtering, the average level of the masker is approximately 5–7 dB lower than that expected based on level detection.⁵ In summary, splatter detection may be involved in the present experiments, but we think that it affects only the magnitude of the TFE effect, not the presence of the effect itself.

B. Envelope fluctuations

The results from experiment 2 discounted some possible causes of the general masking phenomenon shown in experiment 1, but they did not suggest an account for the data. Experiment 3 examined the hypothesis that the TFE effect reflects changes in the envelope fluctuations at the output of an auditory filter centered at the frequency of the probe. The AM maskers used in experiment 3 attempted to simulate *only* the envelope fluctuations due to the masker that might occur at the output of such a filter.

Threshold changes obtained with AM maskers in experiment 3 were similar to those obtained with their corresponding FM maskers. Thresholds increased by as much as 20 dB and the slopes of the threshold functions were similar to those found in experiments 1 and 2. We have suggested that detection of energy splatter may partially account for the

relatively low thresholds at small TFEs. Such would also be the case in experiment 3: In the limiting case of $TFE=0$, where splatter detection is most likely, the maskers used in all the experiments are identical.

It should be noted that the point at which the thresholds begin to increase above the pure-tone masker threshold is at a larger TFE in experiment 3 than experiment 2 (compare data with dotted lines in Figs. 7–9), i.e., the thresholds obtained with the AM masker are generally lower than those obtained with the FM masker. This could be for a number of reasons. Although the masker energy at 1 kHz is the same for both the FM masker and its AM equivalent, the AM masker has less energy at the frequency locations above and below 1 kHz because of the processing done to transform the masker from a wideband FM signal to a narrow-band AM signal.⁶ Thus, excitation or splatter from the probe that has spread to these other frequency regions is not masked as well by the AM masker and thresholds will be lower than for the FM masker. Another possibility, of course, is that the roex filter used to obtain the AM equivalent is not correct. At this point, we consider the discrepancy in thresholds to be of secondary importance: the important aspect is the similarity in the form of the functions for FM and the AM equivalent, specifically those relating probe threshold to TFE and to pre-processed TFE.

C. Envelope-shape discrimination

Consistent with the hypothesis that motivated experiment 3, we propose that in the present experiments detection of the probe, particularly at large TFEs, involves detecting differences between the envelopes produced by the masker and the masker-plus-probe. Such envelope-shape discrimination qualitatively accounts for the differences in detectability shown for maskers with different TFEs. Figure 10 illustrates the notion of envelope-shape discrimination, here when clipped FM was used to produce the AM masker. In Fig. 10 the envelopes have been normalized to have equal total areas and a dc shift has been added in the upper panel (one of the curves was lowered) to facilitate comparison of the envelope shapes. The solid lines show one period of the envelopes of two different AM maskers used in experiment 3; the dashed lines show the envelopes of the masker plus probe⁷ over the same interval. Clearly, the addition of the same probe produces a larger change in envelope shape for the masker with the smaller TFE (upper panel). This should lead to higher detectability of the probe or, consistent with the data, a lower probe threshold.

D. Envelope spectra

Another possibility is suggested by Green *et al.* (1992) who argue that in certain circumstances detection may be based on differences in the amplitude spectrum of the envelope. Envelope spectral-shape discrimination also provides a qualitative account of the present data. Figure 11 shows the normalized spectra of the envelopes from Fig. 10. Clearly,

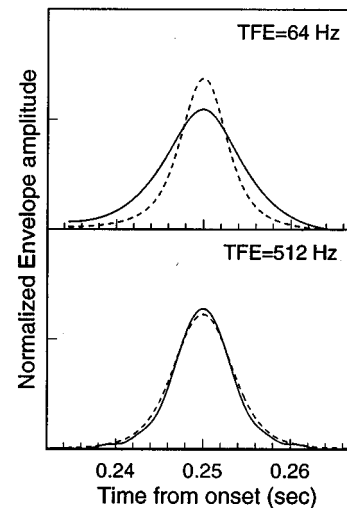


FIG. 10. The response of a roex filter centered at 1 kHz to stimuli used in experiments 1 and 2. The lines represent one period of the response's envelope. The solid lines are responses to only maskers. The dashed line represents the average response to masker+probe, where the envelopes were averaged across probe phase. The probe in both panels was at 65 dB. The pre-clipped TFE for both panels is 1024 Hz. The masker in the upper panel has an actual TFE of 64 Hz while the masker in the lower panel has an actual TFE of 512 Hz. The envelopes have been normalized to unit area for comparison purposes.

the spectra shown in the upper figure differ more than those shown in the lower figure and, consistent with the data, should yield lower probe thresholds.

Although both the envelope-shape and the envelope amplitude spectrum provide a basis of accounting for the present data, we believe that waveshape is more realistic. The argument against a role for envelope spectrum is similar to that regarding the long-term amplitude spectrum of sounds. For example, sounds with identical amplitude spectra, such as a waveform and its time-reversed version, generally sound considerably different. Similarly, sounds with identical envelope-amplitude spectra but different phase

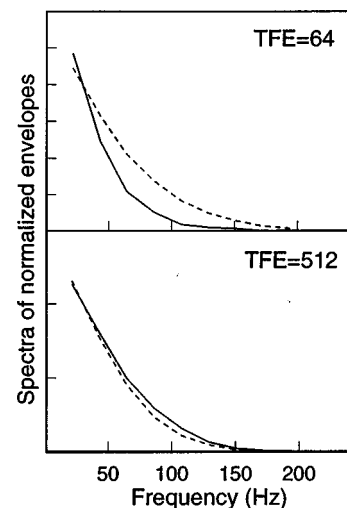


FIG. 11. The spectra of the envelopes in Fig. 10. The solid line corresponds to the spectra of the masker envelope; the dashed line corresponds to the spectra of the masker+probe envelope.

spectra may sound considerably different. A concrete example is the recent work by Patterson (1994a,b) on ramped versus damped sinusoids in which the envelopes are time-reversed versions of each other. The envelope amplitude spectra are thus identical but the sounds can be readily discriminable. We argue that this indicates sensitivity to the temporal structure of the envelope.

E. Final observations

The envelope-shape model is preliminary and needs considerable refinement and quantitative implementation. In a sense the present model is rather trivial: It argues that the more dissimilar the envelopes of the waveforms, the more discriminable they will be. A visually based argument, such as we have done in discussing Fig. 10, is not satisfactory. Clearly, "envelope shape" needs more precise specification. One difficulty in such refinement stems from the nonadditivity of envelopes: the envelope of the masker-plus-probe is generally not the sum of the envelopes of the masker and of the probe. This appears to preclude an analytic examination of various decision strategies, such as envelope cross-correlation, and thus makes such an examination a rather tedious simulation exercise. More importantly, the data from the present experiments are not ideal for developing the model. First, there is the complication of splatter detection. Second, the envelopes used in experiment 3 are not simple and, in the context of a model, derivation of the envelopes, especially for the FM maskers, requires assumptions about the characteristics of the auditory filter. This is somewhat secondary to the basic notion of the model. Other experiments, perhaps using amplitude modulated broadband noise, may provide a basis for examining envelope-shape discrimination models with minimal dependence on assumptions about the shape of the auditory filter.

As a qualitative account, however, envelope-shape discrimination is quite appealing. It provides a description of the counter-intuitive results of the present experiments. It also offers the possibility of describing the problematic results, described in the Introduction, obtained with swept-frequency maskers. Finally, the basic notion of the importance of envelope shape generalizes to other detection and discrimination tasks and, using the strategy of experiment 3, provides a testable alternative hypothesis.

lead;1V. SUMMARY AND CONCLUSIONS

(1) Probe detection thresholds increased substantially as the amount of FM in the masker increased, consistent with Zwicker's (1974) findings.

(2) Thresholds increased in the same manner when masker frequency sweep rate was fixed and the total frequency excursion (TFE) increased, while thresholds remained approximately constant when TFE was fixed and sweep rate increased. Thus, TFE, not sweep rate, primarily determines the amount of masking.

(3) Detection of energy splatter at small TFEs appears to account for part of the TFE effect. When splatter detection is unlikely, however, the thresholds at large TFEs were still

substantially higher (10 dB) than those at small TFEs and were too large to be explained by simple level detection.

(4) When the FM maskers from the first two experiments were transformed to AM maskers in such a way that the simulated envelope fluctuations at 1 kHz were the same for both, thresholds increased similarly with TFE.

(5) The results are consistent with the concept that detection of a brief probe in an FM masker involves envelope-shape discrimination.

ACKNOWLEDGMENTS

This research was supported by research Grant No. DC00683 from the National Institute on Deafness and Other Communication Disorders, National Institutes of Health. The authors would like to thank the anonymous reviewers for their helpful comments on improving this paper.

¹The probe was added at the end of the processing and not at the beginning because the inverse filter would improve the ability of the listener to use off-frequency masking: Significant energy in the signal interval would exist distant from 1 kHz, and since the gain of the inverse filter is much larger for these frequencies, the probe would be enhanced at frequencies distant from 1 kHz.

²The inverse filter does not introduce any instantaneous frequency fluctuations in the AM signal because the filter is symmetric around 1 kHz and has zero phase response.

³The term "pre-processed" will be used from here on to indicate the FM signal that is used to generate the AM masker before filtered by the roex filter, i.e., at point (A) in Fig. 6.

⁴There are two strong indications that splatter detection was not occurring when the masker level was 35 dB. First, the expected change in threshold with probe phase (approximately 7 dB) was observed with a TFE of zero, indicating that simple level detection (or envelope-shape discrimination), and not splatter detection, was occurring. Second, the probe threshold observed with zero-TFE, 90° probe phase, was only 6 dB above detection threshold for the probe in quiet. At such a relatively low probe level, splatter almost certainly would have been inaudible.

⁵The prediction based on level detection requires an estimate of the Weber fraction obtained when splatter detection is not involved. The estimates used were based on: (1) increment detection in the 20-dB noise ($10 \log \Delta I/I = 5$ dB); (2) intensity discrimination with a pedestal gated identically to the 10-ms probe ($10 \log \Delta I/I = 4$ dB), which was corrected for the effects of gating with the raised-cosine window; (3) increment detection with a 35-dB masker ($10 \log \Delta I/I = 3$ dB). With TFE=512 Hz the observed threshold for this subject was 68 dB. Thus, assuming level detection, the effective masker level was 65–67 dB. The level of the (unfiltered) masker was 60 dB, 5–7 dB lower than that based on level detection. The discrepancy will increase, of course, if the masker is filtered, as it certainly is by the auditory system.

⁶The inverse filter was bandlimited around 1 kHz because the enormous gain of the inverse filter at frequencies distant from 1 kHz would unnecessarily amplify noise and negligible frequency components.

⁷Since phase of the probe was randomized during the experiments, the probe and masker were added 72 different times, with the phase of the probe incremented by 5° each time, spanning the full range of 360°. The envelopes of each summation were calculated using the Hilbert transform and the 72 envelopes were averaged to produce the envelopes displayed with the dashed lines in Fig. 10.

Ahumada, Jr., A., and Lovell, J. (1971). "Stimulus features in signal detection," *J. Acoust. Soc. Am.* **49**, 1751–1756.

Coninx, F., and Smoorenburg, G. F. (1979). "Masking of short probe sounds by tone bursts with a sweeping frequency," *J. Acoust. Soc. Am. Suppl.* **1** **66**,

Fletcher, H. (1940). "Auditory patterns," *Rev. Mod. Phys.* **12**, 47–65.

Gilkey, R. H. (1987). "Spectral and temporal comparisons in auditory masking," in *Auditory Processing of Complex Sounds*, edited by W. A. Yost and C. S. Watson (Erlbaum, Hillsdale, NJ).

- Green, D. M., and Swets, J. A. (1966). *Signal Detection Theory and Psychophysics* (Wiley, New York).
- Green, D. M., Berg, B. G., Huanping, D., Eddins, D. A., Onsan, Z., and Nguyen, Q. (1992). "Spectral shape discrimination of narrow-band sounds," *J. Acoust. Soc. Am.* **92**, 2586–2597.
- Hall, J. W., Haggard, M. P., and Fernandes, M. A. (1984). "Detection in noise by spectro-temporal pattern analysis," *J. Acoust. Soc. Am.* **76**, 50–56.
- Jeffress, L. A. (1964). "Stimulus-oriented approach to detection," *J. Acoust. Soc. Am.* **36**, 766–774.
- Kemp, S. (1982). "Masking period patterns of frequency modulated tones of different frequency deviations," *Acustica* **50**, 63–69.
- Kidd, Jr., G., Mason, R., Brantley, M. A., and Owen, G. A. (1989). "Roving-level tone-in-noise detection," *J. Acoust. Soc. Am.* **86**, 1310–1317.
- Moore, B. C. J. (1989). *An Introduction of the Psychology of Hearing* (Academic, London).
- Patterson, R. D., Nimmo-Smith, I., Weber, D. L., and Milroy, R. (1982). "The deterioration of hearing with age: Frequency selectivity, the critical ratio, the audiogram, and speech threshold," *J. Acoust. Soc. Am.* **72**, 1788–1803.
- Patterson, R., and Moore, B. C. J. (1986). "Auditory filters and excitation patterns as representations of frequency resolution," in *Frequency Selectivity in Hearing*, edited by B. C. J. Moore (Academic, London), pp. 123–177.
- Patterson, R. D. (1994a). "The sound of a sinusoid: Spectral models," *J. Acoust. Soc. Am.* **96**, 1409–1418.
- Patterson, R. D. (1994b). "The sound of a sinusoid: Time-interval models," *J. Acoust. Soc. Am.* **96**, 1419–1428.
- Richards, V. M., Heller, L. M., Green, D. M. (1991). "Detection of a tone in a narrow band of noise: The energy model revisited," *Q. J. Psychol.* **43A**, 481–501.
- Rosen, S., Baker, R. J., and Kramer, S. (1992). "Characterizing changes in auditory filter bandwidth as a function of level," in *Auditory Physiology and Perception*, edited by Y. Cazals, L. Demany, and K. Horner (Pergamon, London), pp. 171–177.
- Smooenburg, G. F., and Coninx, F. (1980). "Masking of short probe sounds by tone bursts with a sweeping frequency," *Hear. Res.* **3**, 301–316.
- Zwicker, E. (1974). "Mithörschwellen und Erregungsmuster stark frequenzmodulierter töne," *Acustica* **31**, 243–256.

A new way to account for binaural detection as a function of interaural noise correlation

Marcel van der Heijden and Constantine Trahiotis

Surgical Research Center, Department of Surgery (Otolaryngology) and Center for Neurological Sciences, University of Connecticut Health Center, Farmington, Connecticut 06030

(Received 21 June 1996; revised 11 September 1996; accepted 2 October 1996)

The purpose of this communication is to describe a new method for predicting masking level differences (MLDs) as a function of the interaural correlation of the masking noise. The general idea is to decompose a binaural noise masker having an arbitrary value of interaural correlation into two parts: an No constituent and an $N\pi$ constituent. It is shown that the amount of masking produced by a noise having an arbitrary interaural correlation is equal to the *addition of the masking effects* produced by the No and $N\pi$ constituents that compose the masker. The new approach was used to generate predictions of MLDs for $N\rho S\pi$ and $N\rho So$ conditions. Those predictions accounted for 98% of the variance in the classical data of Robinson and Jeffress [J. Acoust. Soc. Am. **35**, 1947–1952 (1963)]. Finally, it is shown that the “additivity of masking” method is mathematically equivalent to assuming that binaural detection consists of a stage of errorless binaural processing preceded by a corrupted representation of the stimulus. © 1997 Acoustical Society of America. [S0001-4966(97)04202-1]

PACS numbers: 43.66.Ba, 43.66.Pn, 43.66.Rq [RHD]

INTRODUCTION

The binaural detectability of tones masked by noise is known to be strongly dependent on the interaural correlation of the masking noise. For example, a signal presented in the interaurally phase-reversed ($S\pi$) configuration is easy to detect against a background of diotic noise (No , interaural correlation of one), yet difficult to detect against a background of noise that is also interaurally phase-reversed ($N\pi$, interaural correlation of minus one). The converse relation holds when the signal is presented interaurally in-phase (So). The differences in thresholds of detectability among such conditions (i.e., $NoS\pi$ vs $N\pi S\pi$ and $NoSo$ vs $N\pi So$) are called masking level differences or MLDs. The size of the MLD depends on details concerning the stimuli, but MLDs of 15–25 dB are often reported (Jeffress *et al.*, 1956; Durlach and Colburn, 1978).

The purpose of this communication is to describe a new method for predicting the size of the MLD for intermediate values of interaural correlation of the masking noise. The general idea is to decompose a binaural noise masker having an arbitrary value of interaural correlation (ρ) into two parts: an No constituent and an $N\pi$ constituent. We will show that the amount of masking produced by a noise having an arbitrary interaural correlation is equal to the *addition of the masking effects* produced by the No and $N\pi$ constituents that compose the masker. Stated in terms of MLDs, we will show that the MLD produced by a noise having a given interaural correlation reflects the additivity of masking of the signal by the (separate) No and $N\pi$ constituents that are conceived of as making up the total masking noise.

After describing the approach, we generate predictions of MLDs for $N\rho S\pi$ and $N\rho So$ conditions and compare the predictions to the classical data of Robinson and Jeffress (1963). We then show that this approach utilizing an “additivity of masking” method is consistent with common con-

ceptions of the processing of binaural information.

I. ADDITIVITY OF BINAURAL MASKING

We assume the masker is a Gaussian noise having equal power at the two ears and an interaural correlation ρ . We begin by noting that such a stimulus ($N\rho$) can always be decomposed into two components: one component having an interaural correlation of +1 (No) and a second component having an interaural correlation of $-1(N\pi)$.¹ We write this decomposition symbolically as

$$N\rho = No + N\pi.$$

The powers of No and $N\pi$, in each channel, respectively, add up to the total power of the noise (N_{total}) in that channel. Different values of ρ correspond to different *relative* powers of components No and $N\pi$. If we denote the powers of components No and $N\pi$ at each ear, expressed as ratios relative to the *total* noise power at each ear, by No/N_{total} and $N\pi/N_{\text{total}}$ respectively, then the relation between these power ratios and interaural correlation ρ is given by [see the Appendix, Eqs. (A1a) and (A1b)]

$$No/N_{\text{total}} = \frac{1}{2}(1 + \rho), \quad N\pi/N_{\text{total}} = \frac{1}{2}(1 - \rho).$$

The ability to decompose $N\rho$ into No and $N\pi$ components suggested to us that it might be possible to regard MLDs obtained as a function of ρ as stemming from an “addition” of the masking effects produced by each of the separate components. That is, it occurred to us that the power of the signal required for detection in the presence of a noise having an interaural correlation ρ could be equal to the sum of the powers of signals that would be required for detection in the presence of the underlying components No and $N\pi$. Denoting the signal power at threshold by T , with an appropriate subscript to specify the masker configuration, this additivity is expressed by

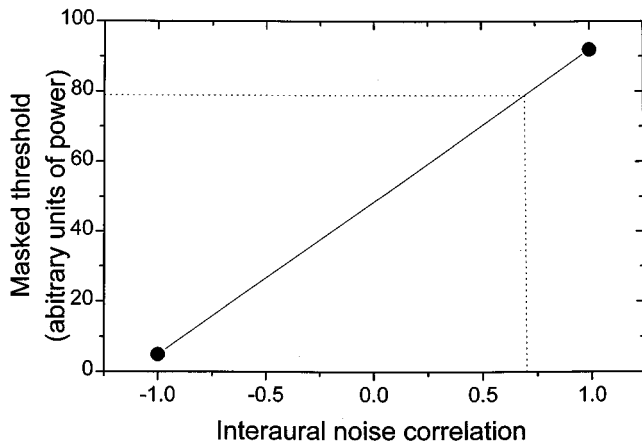


FIG. 1. A way of relating binaural thresholds to interaural noise correlation. The amount of power required to reach threshold (in arbitrary units of power) is plotted against interaural noise correlation. As indicated by the dotted lines in the figure and as discussed within the text, the straight line joining thresholds measured with an interaural correlation of -1 and an interaural correlation of $+1$ can be used to predict thresholds for all intermediate interaural correlations by simple interpolation.

$$T_{N\rho} = \frac{1}{2}(1 + \rho)T_{No} + \frac{1}{2}(1 - \rho)T_{N\pi}. \quad (1)$$

The factors $\frac{1}{2}(1 + \rho)$ and $\frac{1}{2}(1 - \rho)$ are weights that reflect the relative amounts of the No and $N\pi$ components, as shown immediately above.

Equation (1) states a linear relation between signal power at threshold (plotted in linear units) and interaural correlation of the masking noise (also plotted in linear units). Figure 1 shows how one can obtain a prediction of threshold for any value of interaural correlation by simply reading off values from a line drawn between the two thresholds obtained with interaural correlations of $+1$ and -1 , respectively.

We compared predictions of MLDs obtained with Eq. (1) to data obtained in the classic study of Robinson and Jeffress (1963), who measured thresholds for several values of interaural noise correlation. In order to facilitate a comparison between predictions and data, it is useful to restate Eq. (1) in terms of MLDs. When the stimuli are presented in an $N\rho S\pi$ configuration, the MLD, *re: NπSπ*, is given by the ratio of the signal powers at threshold, $T_{N\pi}/T_{N\rho}$. Expressing this MLD in dB, we obtain

$$\text{MLD}_{N\rho S\pi} = -10 \log\left[\frac{1}{2}(1 - \rho) + \frac{1}{2}(1 + \rho)T_{No}/T_{N\pi}\right]. \quad (2)$$

The ratio $T_{No}/T_{N\pi}$ in this equation reflects the MLD obtained with the $NoS\pi$ stimulus configuration (again, *re: NπSπ*) and can be expressed in dB as

$$10 \log[T_{No}/T_{N\pi}] = -\text{MLD}[NoS\pi \text{ re: } N\pi S\pi]. \quad (3)$$

The analogous equations for the $N\rho So$ configuration are

$$\text{MLD}_{N\rho So} = -10 \log\left[\frac{1}{2}(1 + \rho) + \frac{1}{2}(1 - \rho)T_{N\pi}/T_{No}\right], \quad (4)$$

with

$$10 \log[T_{N\pi}/T_{No}] = -\text{MLD}[N\pi So \text{ re: } NoSo]. \quad (5)$$

A comparison of the predictions with the data of Robinson and Jeffress is presented in Fig. 2. The predictions ac-

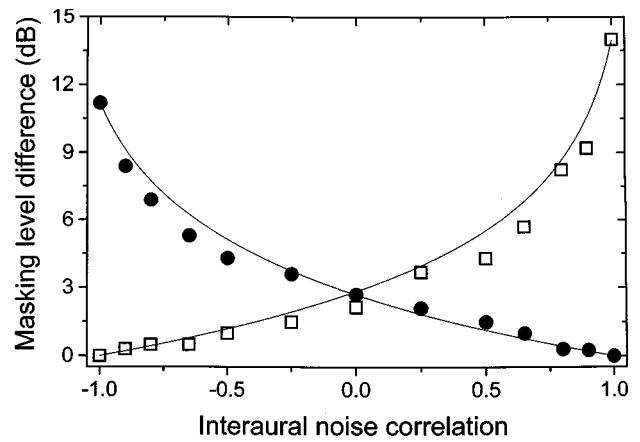


FIG. 2. Comparison of masking data reported by Robinson and Jeffress (1963, Fig. 3) with predictions obtained resolving $N\rho$ into components No and $N\pi$ as expressed by Eqs. (2)–(5). Robinson and Jeffress used continuous wide-band (100–3000 Hz) noises as maskers. Interaural correlation, ρ , was manipulated by suitably mixing three independent sources of noise. The signal was a 150-ms tone at 500 Hz presented either interaurally in-phase (So , circles) or interaurally out-of-phase ($S\pi$, squares). The $N\rho S\pi$ MLDs are referenced to $N\pi S\pi$, and the $N\rho So$ MLDs are referenced to $NoSo$. The ascending and descending lines in the figure depict the predictions for the $N\rho S\pi$ and $N\rho So$ conditions, respectively.

count for 98% of the variance in the data.² The predictions are remarkably accurate considering that the only parameters determined by the data were the two MLDs appearing in Eqs. (3) and (5).

Accounting for binaural detection thresholds in terms of additivity of masking, as described above, may seem to be *ad hoc*. This is not the case, as will be demonstrated in the next section where we relate our additivity of masking approach to common conceptions of the processing of binaural information.

II. INTERPRETING ADDITIVITY OF MASKING AS RESULTING FROM AN ERRORLESS BINAURAL PROCESSOR DEALING WITH AN IMPERFECT INPUT

We consider binaural processing to be a stage of internal processing that is optimal. Optimal processing in the $NoS\pi$ condition would result in a cancellation of the masking noise (say by subtraction) without any loss of information concerning the signal. As a result of such optimal binaural processing, the masked threshold of the $S\pi$ signal would be the same as its unmasked threshold. In fact, masked thresholds obtained with the $NoS\pi$ condition are much higher than their unmasked counterparts. We account for those masked thresholds by assuming that a stage of errorless cancellation is preceded by some other, imperfect, transformation of the input that effectively corrupts the information available in the stimulus. Although this assumption is reminiscent of, and conceptually similar to, assumptions within Durlach's model (Durlach, 1963; Durlach, 1972), we wish to make it clear that it is not the case that our approach and his are equivalent. Our assumptions are quite general and quite few. The corruption of the stimuli is assumed to be relatively small and to be independent of the binaural configuration of the external stimulus including its interaural correlation. We make no further assumptions concerning the nature of the

corruption including its realization as an additive and/or multiplicative “internal noise.” In contrast, Durlach’s model is quite precise regarding the specification of internal noise and contains many more parameters. With regard to stating whether our approach is compatible with or mathematically equivalent to other models of binaural hearing, we choose to refrain. We do so in light of Domnitz and Colburn’s (1976) arguments and demonstrations concerning conditions under which different-appearing models of binaural processing make mathematically identical predictions.

Our intent is to show that a model incorporating a corruptive stage of processing preceding an optimal stage of binaural processing is mathematically equivalent to the “additivity masking method” described in Sec. I. In order to succeed, we need to compute the “effective” interaural correlation of the *corrupted stimulus* that serves as input to the cancellation device. Unfortunately, we do not have detailed knowledge concerning the corruption of the stimulus. Therefore, we cannot precisely convert the actual correlation of the stimulus, ρ , to its *effective* interaural correlation, ρ' . However, all is not lost. We can obtain a useful estimate of ρ' by employing the following reasoning. First, large MLDs commonly obtained with the standard $NoS\pi$ configuration could only have occurred if the interaural correlation of the stimulus were not unduly diluted. Second, given that fact, it is reasonable to assume that the corruption of the stimulus is of such relative small magnitude that it can be adequately modeled *as though it resulted from an additive process*.³ A straightforward calculation (described in the Appendix) then leads to the simple rule [see the Appendix, Eq. (A2)]

$$\rho' = \rho\rho_D,$$

where ρ_D is the effective correlation that would result from a diotic stimulus.

Within our scheme, the external noise is transformed by the initial stage of corruptive processing to have an “effective correlation,” ρ' . Using the method described in Sec. I, the effective masker having a correlation ρ' is decomposed into an No component and an $N\pi$ component. The optimal processor cancels the No component, but is unable to cancel the $N\pi$ component without also canceling the $S\pi$ signal. Therefore, binaural detection of the $S\pi$ signal is constrained by the $N\pi$ component of the internal, corrupted stimulus. Functionally, the effect of having the optimal binaural processor is to cancel the No component of the noise, thereby transforming the actual stimulus configuration into a new one, $N\pi S\pi$. Analogously, the detection of an So signal would be constrained by the No component of the internal, corrupted stimulus. For an So signal, the effect of having the optimal binaural processor is to cancel the $N\pi$ component, thereby transforming the actual stimulus configuration into $NoSo$. In the case of the $N\rho S\pi$ configuration, the relative power of the effective $N\pi$ component is equal to $\frac{1}{2}(1 - \rho\rho_D)$; in the case of the $N\rho So$ configuration, the relative power of the effective No component is equal to $\frac{1}{2}(1 + \rho\rho_D)$.

We are now in a position to evaluate the predictions of a model that incorporates a corruptive stage of processing having an output that serves as input to an optimal stage of

binaural processing. We will use the detection of an $S\pi$ signal for our discussion.⁴

The signal power at threshold for an $S\pi$ signal masked by a noise having an interaural correlation, ρ , is denoted by $T_{N\rho}$ and, according to our scheme, is expected to be proportional to the power of the $N\pi$ component:

$$T_{N\rho} = (C/2)(1 - \rho\rho_D).$$

The two unknowns C and ρ_D can be eliminated by evaluating this equation for two special cases: $\rho=1$ and $\rho=-1$. The $\rho=1$ case corresponds to the stimulus condition $NoS\pi$, while the $\rho=-1$ case corresponds to the stimulus condition $N\pi S\pi$:

$$T_{No} = (C/2)(1 - \rho_D), \quad T_{N\pi} = (C/2)(1 + \rho_D).$$

The elimination of C and ρ_D immediately leads to Eq. (1), previously introduced in Sec. I in the context of “additivity of masking.”

ACKNOWLEDGMENTS

This research was supported by research Grant No. NIH DC-00234. We thank Dr. Les Bernstein for his comments and appreciate the suggestions offered during review.

APPENDIX

1. Notation

Given a waveform $x(t)$ having duration T , we use the following notation:

$$\bar{x} = \frac{1}{T} \int dt x(t).$$

Note that \bar{x}^2 is the total power of waveform $x(t)$. Using this notation, the normalized cross correlation between two waveforms $x(t)$ and $y(t)$ is

$$\rho = \overline{xy} / \sqrt{\overline{x^2} \overline{y^2}}.$$

Note that if x and y have equal power, the denominator in this expression is equal to this power.

2. Decomposition of a binaural stimulus into diotic and phase-reversed components

Consider a binaural stimulus consisting of two waveforms n_L (left ear) and n_R (right ear) having equal power P . The interaural correlation ρ of the stimulus is

$$\rho = \overline{n_L n_R} / P.$$

Now we construct waveforms a and b as follows:

$$a = \frac{1}{2}(n_L + n_R), \quad b = \frac{1}{2}(n_L - n_R).$$

Using these definitions, we can express the original stimulus in terms of waveforms a and b :

$$n_L = a + b, \quad n_R = a - b.$$

These equations provide a decomposition of the original binaural stimulus (n_L and n_R) into a diotic component (a) and an interaurally phase-reversed component (b). Components a and b are uncorrelated, because:

$$\overline{ab} = \frac{1}{4}(n_L + n_R)(n_L - n_R) = \frac{1}{4}(\overline{n_L^2} - \overline{n_R^2}) = 0.$$

The powers of each of the components *re* the total power P are given by

$$\begin{aligned} \overline{a^2}/P &= \frac{1}{4}(n_L + n_R)^2/P \\ &= \frac{1}{4}(\overline{n_L^2} + \overline{n_R^2} + 2\overline{n_L n_R})/P = \frac{1}{2}(1 + \rho), \end{aligned} \quad (\text{A1a})$$

$$\begin{aligned} \overline{b^2}/P &= \frac{1}{4}(n_L - n_R)^2/P \\ &= \frac{1}{4}(\overline{n_L^2} + \overline{n_R^2} - 2\overline{n_L n_R})/P = \frac{1}{2}(1 - \rho). \end{aligned} \quad (\text{A1b})$$

3. Effect of additive uncorrelated noise on the interaural correlation of a stimulus

Given a binaural stimulus consisting of waveforms n_L (left ear) and n_R (right ear) having equal power P and an interaural correlation ρ , let us consider the effect of adding other noise waveforms u_L (left ear) and u_R (right ear) to form

$$n'_L = n_L + u_L, \quad n'_R = n_R + u_R.$$

Further assume that u_L and u_R have equal power U and that they are uncorrelated with each other and with n_L and n_R . The purpose of adding u_L and u_R is to evaluate effects due to corruption of the information in the external stimulus, as described in the text.

The interaural correlation of n'_L and n'_R is

$$\begin{aligned} \rho' &= \overline{n'_L n'_R} / P' = \overline{(n_L + u_L)(n_R + u_R)} / (P + U) \\ &= \overline{n_L n_R} / (P + U) \\ &= \overline{n_L n_R} / P \cdot P / (P + U) \\ &= \rho [P / (P + U)]. \end{aligned}$$

For the purpose of measuring effects solely due to changes in stimulus correlation, ρ , it is important to note that ρ can be manipulated without affecting the overall stimulus power P . Under these conditions, ρ' is linearly related to ρ because the factor $P/(P + U)$ does not depend on ρ . Now, by

substituting $\rho=1$ into the above equation, we can see that the factor $P/(P + U)$ is the *effective binaural correlation that would result if the external stimulus were diotic*. Denoting this quantity by ρ_D , we arrive at the following relation between the *stimulus* interaural correlation ρ and the *effective* correlation ρ' :

$$\rho' = \rho \rho_D. \quad (\text{A2})$$

¹The mathematical explanation of this decomposition is given in the Appendix. The Appendix also includes other derivations and arguments that clarify and justify our main points. It appears to be worth noting that one could reverse the process and produce a desired interaural correlation ρ by mixing suitable amounts of No and $N\pi$, given that those two components are taken from independent sources.

²The amount of variance accounted for could be considered artificially high because the predictions guarantee an exact match at the endpoints of the curves. In that regard, it is important to note that ‘‘predictions’’ obtained by drawing a straight line between the endpoints accounts for only 44% of the variance in the data.

³This is not to imply that the internal decorrelation results from an additive ‘‘internal noise’’ whose presence and characteristics are independent of the stimulus. As a matter of fact, in the present approach, such an assumption would once again lead to the equality of $NoS\pi$ and absolute thresholds! If one prefers to think of the internal decorrelation as stemming from ‘‘internal noise,’’ then one has to assume that the internal noise depends on the external stimulus.

⁴The choice of an $S\pi$ signal in the derivation is not essential. An So signal leads to the same logical conclusion.

Domnitz, R. H., and Colburn, H. S. (1976). ‘‘Analysis of binaural detection models for dependence of interaural target parameters,’’ *J. Acoust. Soc. Am.* **59**, 598–601.

Durlach, N. I. (1963). ‘‘Equalization and cancellation theory of binaural masking-level differences,’’ *J. Acoust. Soc. Am.* **35**, 1206–1218.

Durlach, N. I. (1972). ‘‘Binaural signal detection: Equalization and cancellation theory,’’ in *Foundations of Modern Auditory Theory*, Volume II, edited by J. V. Tobias (Academic, New York), pp. 365–466.

Durlach, N. I., and Colburn, H. S. (1978). ‘‘Binaural phenomena,’’ in *Handbook of Perception*, Volume IV, Hearing, edited by E. C. Carterette and M. P. Freedman (Academic, New York), pp. 365–466.

Jeffress, L. A., Blodget, H. C., Sandel, T. T., and Wood III, C. L. (1956). ‘‘Masking of tonal signals,’’ *J. Acoust. Soc. Am.* **28**, 416–426.

Robinson, D. E., and Jeffress, L. A. (1963). ‘‘Effect of varying the interaural noise correlation on the detectability of tone signals,’’ *J. Acoust. Soc. Am.* **35**, 1947–1952.

Asymmetry of masking revisited: Generalization of masker and probe bandwidth

Joseph L. Hall

Acoustics Research Department, AT&T Bell Laboratories, Murray Hill, New Jersey 07974

(Received 22 February 1996; revised 24 June 1996; accepted 30 September 1996)

A band of noise masked by a tone is audible at a much lower intensity increment between masker alone and masker plus just-detectable probe than is a tone masked by a band of noise. To better understand the mechanisms responsible for this asymmetry of masking, we measured thresholds of probe signals ranging in bandwidth from 0 to 256 Hz in the presence of masking signals also ranging in bandwidth from 0 to 256 Hz. Masker and probe center frequencies were 1 kHz in all cases. Two versions of the experiment are reported: (1) masker intensity constant at 70 dB SPL and (2) masker intensity roved over the range 65–75 dB SPL. The results confirm and extend previous results. For a fixed masker bandwidth, threshold intensity increments are essentially constant, and accounted for by a model based on long-term average energy, so long as probe bandwidth does not exceed masker bandwidth. If probe bandwidth exceeds masker bandwidth, threshold intensity increments decrease sharply for all masker bandwidths tested. Roved-intensity results are consistent with the hypothesis that detection is based on long-term average energy for probe bandwidth equal to or less than masker bandwidth, but that for probe bandwidth greater than masker bandwidth other cues are utilized. In addition, we investigated the possible contribution of off-frequency listening by developing and presenting results from a frequency-selective model of peripheral masking. Model results argue against detection based on spectral cues associated with off-frequency listening for signal bandwidths less than a critical band. The conclusion is that detection must utilize the temporal structure of the signal for probe bandwidth greater than masker bandwidth. © 1997 Acoustical Society of America. [S0001-4966(97)03102-0]

PACS numbers: 43.66.Dc, 43.66.Ba, 43.66.Fe [WJ]

INTRODUCTION

A problem that arises for models of masking and sound quality based on long-term average energy of the stimulus is that a band of noise and a tone have quite different masking properties. As pointed out by Hellman (1972), a tone probe masked by a narrow (one critical band or less) band of noise is audible only at high probe-to-masker ratios, as high as -4 dB. If the roles of masker and probe are reversed, so that the tone is masker and the noise is probe, the noise is audible at probe-to-masker ratios as low as -20 to -30 dB. For perceptual coders, the coding noise being masked is audible at lower probe-to-masker ratios when the signal being encoded is tonelike than when it is noiselike in nature. Johnston, for example (1988), finds it necessary to compute the “tonality” of the masking signal as well as its long-term average spectrum and to vary the masking criterion accordingly. (By “long-term,” we are referring to integration times in the range of a few tens of milliseconds.) While this empirically based procedure gives useful results in most cases, it would be desirable to have an improved understanding of the mechanisms of hearing responsible for this asymmetry.

Studies of this asymmetry of masking have concentrated on the extreme cases of noise masking tone and tone masking noise. These studies leave unanswered the question of whether the essential distinction is tone versus noise or whether the effect is in fact graded and changes in some smooth manner with bandwidth of masker and of probe. The answer to this question would put some important constraints on modeling efforts and would be useful in attempting to

understand the underlying mechanisms. To this end, we have carried out a series of psychophysical listening experiments with five stimuli ranging in bandwidth from 0 to 256 Hz (pure tone to substantially greater than a critical band at the center frequency of 1 kHz). Each of the five stimuli served as masker for each of the five stimuli as probe, so that all 25 combinations of masker and probe bandwidth were tested. The stimulus conditions can be visualized as lying on a 5×5 matrix with noise masking tone at one corner, tone masking noise at the opposite corner, and intermediate conditions in between. Conditions on the main diagonal of this matrix, in which masker and probe are identical, can be interpreted as intensity difference limens as a function of stimulus bandwidth.

We ran two versions of this experiment. In the first version, intensity of the masker was held constant at 70 dB SPL. In the second version, intensity of the masker varied randomly from presentation to presentation over the range 65–75 dB SPL, so that the intensity of the masker in a “masker only” presentation and in a “masker plus probe” presentation could differ by as much as 10 dB. This procedure, known as “roving level,” weakens the salience of overall intensity as a cue and thus puts additional constraints on possible underlying mechanisms of hearing involved in the detection task.

Two subjects participated in the experiment. While there are quantitative differences between the two subjects, the overall trends for the two subjects are similar. In agreement with results in the literature, the threshold intensity incre-

ment for 256-Hz bandwidth noise masked by a pure tone is approximately -23 dB, while the threshold intensity increment for a pure tone masked by 256-Hz bandwidth noise is much higher: -4 dB for one subject and -11 dB for the other. More interestingly, for unroved stimuli it appears that the essential distinction is not whether the stimuli are tones or noises, but rather whether or not the bandwidth of the probe is greater than the bandwidth of the masker. For a given bandwidth of masker, the threshold intensity increment does not depend strongly on probe bandwidth as long as probe bandwidth is equal to or less than masker bandwidth. However, the threshold intensity increment drops sharply when probe bandwidth exceeds masker bandwidth.

Roving the intensity of the masker had surprisingly little effect on performance. When masker and probe are identical except for amplitude, roving the intensity of the masker severely degrades performance, as indeed it must because in this case overall intensity is the only available cue. Roving also degrades performance, although to a lesser extent, when probe bandwidth is slightly greater than masker bandwidth. For all other cases, roving has little effect. It is possible to predict from the unroved thresholds what the roved thresholds would be if the subject were responding solely on the basis of change of overall intensity. For masker bandwidth less than probe bandwidth, and for masker bandwidth much greater than probe bandwidth, roved thresholds are closer to unroved thresholds than to the thresholds that are predicted under this assumption.

It can be argued that the low intensity increments at threshold for probe bandwidth greater than masker bandwidth are the result of off-frequency listening: The probe excites regions of the basilar membrane that are not excited by, and not masked by, the masker. In order to test this hypothesis, we adapted an existing frequency-selective model of peripheral masking based on long-term average energy to the present experiment. While the model accounts very satisfactorily for published results on masking of tones and accounts reasonably well for results observed in the present experiment with masker bandwidth at least as wide as probe bandwidth, it does not account for results observed in the present experiment with masker bandwidth narrower than probe bandwidth. We conclude that a model based on long-term average energy is inadequate for these stimuli, and that something else, such as a waveform-based model, is required.

The results presented here should be useful in improving our understanding of masking. A comprehensive model of masking should be able to account for these results, and in addition these results point up the shortcomings of some existing models of masking. The primary purpose of this paper is to make these results accessible. Modeling efforts using these results are currently in progress (Goldstein, 1995; Goldstein and Hall, 1995).

I. PROCEDURES

A. Stimuli

A 16 384-point FFT with a sampling rate of 16 384 Hz was used to generate three groups of five 1-s long stimuli, to

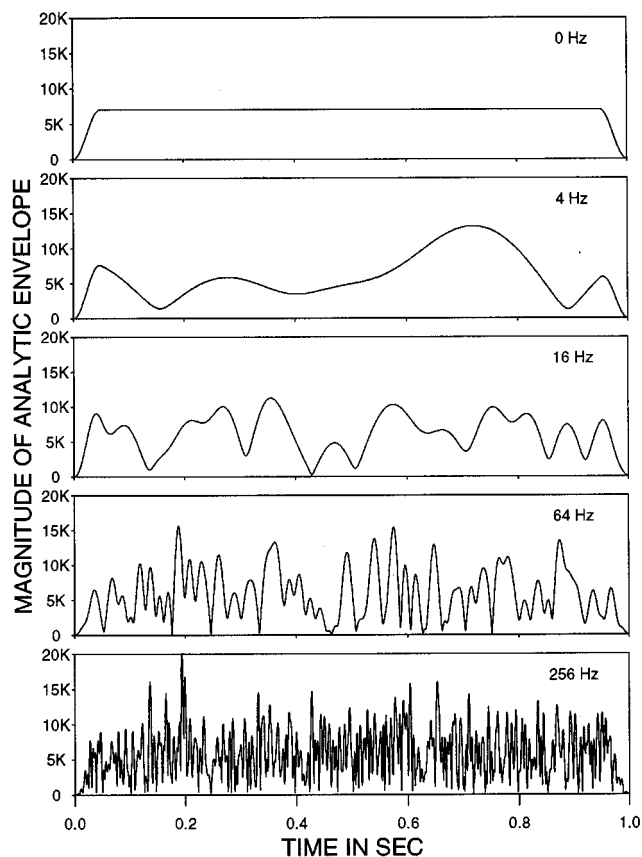


FIG. 1. Representative analytic envelopes for the five stimulus bandwidths.

be used in three replications of the experiment, with a frequency resolution of 1 Hz. All stimuli had an arithmetic center frequency of 1 kHz, and the five stimuli in each group had bandwidths of 0, 4, 16, 64, and 256 Hz. Each stimulus had equal-intensity components over the specified bandwidth. The 0-Hz bandwidth signal, for example, consisted of a single component at 1 kHz, and the 256-Hz bandwidth signal consisted of 257 equal-intensity components at 872, 873, ..., 1128 Hz. The phase ϕ of each component was chosen at random over the interval $-\pi < \phi \leq \pi$ subject to the constraint that the phase at a particular frequency was the same for each of the five stimuli in a group. Consider the stimulus of group g ($g=1, 2, 3$) and bandwidth b ($b=0, 4, 16, 64, 256$ Hz). Designate the amplitude of its component at frequency f ($f=872, 873, \dots, 1128$ Hz) by $a_{g,b,f}$ and the phase of that component by $\phi_{g,b,f}$. Then $a_{g,b,f}$ depends only on b , so that $a_{g,b,f} = a_b$ for $1000 - b/2 \leq f \leq 1000 + b/2$ and $a_{g,b,f} = 0$ otherwise. $\phi_{g,b,f}$ depends only on g and f , so that $\phi_{g,b,f} = \phi_{g,f}$. Figure 1 shows the analytic envelopes of the five stimuli in one group.

The effect of this phase assignment is that, although each stimulus in a group is noiselike in that the phases of its frequency components are chosen at random, still when two stimuli of the same group are added together all common frequency components add in phase. If the phase of common frequency components of masker and probe are not constrained to be equal (as is the case in analog-controlled masking experiments in which a tone generated by one piece of equipment is masked by noise generated by another piece of

equipment), then an uncontrolled source of variability is produced (Jeffress, 1970; Sydorenko and Allen, 1994). It may very well be that in the practical case we do not have control over phase to this extent, so that the statistics of random phase assignments would have to be taken into consideration; for the present case we regard this variability as a property of the stimulus, rather than of the auditory system, and choose to eliminate it.

In addition to using the same phase assignments for masker as for probe, we used the same phase assignments in each block of trials, so that only three sets of phases were tested. Another way to design the experiment would have been to randomly vary the phases on each trial, so that the results would have been an average over many different phases. Each experiment is perfectly valid, but they measure two different things. Our goal in the present study is to minimize stimulus variability so as to concentrate on limitations of the auditory system *per se*. It is not even clear that we could relate results from the two experiments by repeating the measurements made in the present study with many different phase assignments and looking at the statistics of the experimental results, because the design of the present study facilitates the subject's use of the most effective cue in a complex percept. This point is discussed further in Sec. III.

After the time waveforms were computed, their leading and trailing edges were windowed with 50-ms raised cosines to eliminate audible transients. This windowing introduces some irregularities into the spectra. Each stimulus functioned interchangeably as masker and probe. In the nonroved version of the experiment, the masker was always at 70 dB SPL. This means that for the masker stimuli $\alpha_b = \alpha_0 / \sqrt{b+1}$, with appropriately chosen α_0 .

B. Stimulus presentation

Stimuli were generated and controlled by a Concurrent MC5400 computer fitted with a DA04H 16-bit digital-to-analog converter operating at a sampling frequency of 16 384 Hz. The D/A output passed through two sections of a Wavetek 552A low-pass filter with a rolloff of greater than 53 dB/octave/section above the cutoff frequency of 5 kHz and a Crown D-75 power amplifier. The amplifier output was fed into a double-walled Industrial Acoustics Company soundproof booth. Inside the booth, the signal passed through a fixed 5-dB pad (to reduce line noise), a $\frac{1}{8}$ -A fuse (to protect the ER-2 earphone), and an Etymotic ER-2 insert earphone with an ER1-14 foam eartip.

The ER-2 earphone was calibrated with a DB-100 (Zwislocki) coupler. The frequency response of the acoustic system agreed with the manufacturer's specifications for the ER-2 earphone: essentially flat up to the cutoff frequency of the low-pass filter.

Stimuli were presented with a four-alternative forced-choice paradigm. A *trial* consisted of four stimulus *presentations*, each 1 s long, separated by silent intervals of approximately 200 ms.¹ Three of the four presentations consisted of masker alone. One of the four, selected at random, consisted of masker plus probe. The subject sat inside the booth holding a button box with lighted pushbuttons for

communicating with the computer. Each of the four buttons corresponding to the four alternatives lit up in turn during the four stimulus presentations. At the end of each trial, the subject pushed the button corresponding to the stimulus that was judged different from the other three stimuli. The subject was given feedback: When the subject pushed one of the four buttons, the button corresponding to the correct response lit up. The subject was not allowed to repeat a trial.

This procedure, in which multiple presentations of masker alone provide a reference, eliminates problems that can arise in a two-interval forced-choice paradigm in which the subject has to be given instructions along the line of "select the louder stimulus" or "select the stimulus that has more noise added to it." We do not necessarily know *a priori* what the subjective attribute corresponding to addition of probe is, so instructions that specify a subjective attribute to listen for can introduce problems.

A *run* consisted of 42 trials. All 42 trials in a run used the same masker and the same probe. We used a maximum-likelihood psychophysical procedure (Hall, 1981) to control probe intensity and to estimate thresholds. Probe intensity relative to masker was controlled by the PEST adaptive procedure (Taylor and Creelman, 1967) with a target performance level of probability of correct response $P_c = 0.625$ (halfway between chance level of $P_c = 0.25$ and perfect performance of $P_c = 1$). At the end of each run, an estimate of P_c was obtained by fitting an assumed parametric form of the psychometric function to the data.

Monaural measurements were made on two subjects, JH and MS. Subject MS is a male in his twenties, subject JH is a male in his fifties. While both subjects have audiological normal hearing according to the 1969 ANSI reference (average hearing level at 500, 1000, and 2000 Hz less than 26 dB) (Green, 1978) in the ear used for the tests, subject JH has presbycusis resulting in a threshold elevation of approximately 18 dB at 1 kHz. This threshold elevation is essentially constant over the range of frequencies of interest in this experiment. Some of the differences in results obtained for the two subjects (for example, the difference between the two subjects in threshold intensity increment for a pure tone masked by 256-Hz bandwidth noise seen in Fig. 2) may be attributable to this presbycusis. Results from the two subjects are similar in all respects that are central to the thesis of this paper.

For each of the two versions of the experiment (unroved and roved), each of the 25 combinations of masker bandwidth and probe bandwidth were measured three times, once with phase assignments from each of the three groups described above. The exception to this is that for the roved version with subject MS the only masker and probe bandwidths used were 0, 16, and 256 Hz, so that only 9 combinations of masker bandwidth and probe bandwidth were measured. The unroved version of the experiment was done first for both subjects.

II. RESULTS

A. No intensity rove

As described above, the independent variables controlled during an experimental run were masker intensity I_m

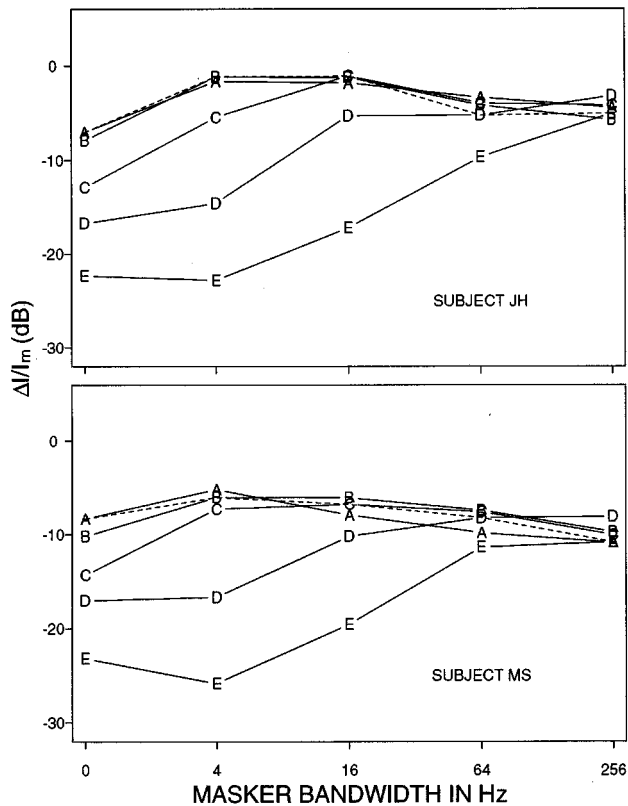


FIG. 2. Threshold intensity increment ΔI in dB *re:* masker intensity I_m vs masker bandwidth in Hz, with probe bandwidth as parameter. A: 0 Hz; B: 4 Hz; C: 16 Hz; D: 64 Hz; E: 256 Hz. The dotted line connects points for which masker and probe bandwidths are equal. No intensity rove. Upper panel: Subject JH. Lower panel: Subject MS.

and probe intensity I_p . Results are presented in units of masker intensity I_m and intensity increment at threshold $\Delta I = I_{m+p} - I_m$. (See Appendix A for a discussion of computation and presentation of experimental results.) Figure 2 shows experimental results for the no intensity rove condition. Masker bandwidth appears on the abscissa, intensity increment ΔI *re:* masker intensity I_m (in dB) appears on the ordinate, and probe bandwidth appears as a parameter. The dotted lines connect points for which masker and probe bandwidth are equal. The upper panel shows results for subject JH and the lower panel shows results for subject MS. Each point is the average of three measurements, one for each of the three phase-assignment groups described in Sec. I A. A simple analysis of variance gives a 90% confidence interval of ± 1.1 dB for subject JH and ± 1.4 dB for subject MS. Since we made only one measurement for each phase-assignment group, we do not have enough degrees of freedom to determine if there was a group effect for any of the masker/probe combinations.

The asymmetry between masking of a tone by a band of noise and masking of a band of noise by a tone is apparent in the two extreme conditions. For subject JH, a 256-Hz band of noise masked by a tone is audible at an intensity increment of -22.3 dB *re:* masker, while a tone masked by a 256-Hz band of noise is audible at an intensity increment of -4.4 dB *re:* masker. For subject MS, a 256-Hz band of noise masked by a tone is audible at an intensity increment of

-23.2 dB *re:* masker, while a tone masked by a 256-Hz band of noise is audible at an intensity increment of -10.9 dB *re:* masker. These values are in general agreement with results in the literature (Hellman, 1972; Zwislocki, 1965).

The crucial feature of Fig. 2 is the transition between the two extreme conditions. Note that, for each subject, thresholds are approximately constant as long as masker bandwidth is at least as great as probe bandwidth. For $b_p = 0$ Hz (points labeled "A"), data points are in almost every case within 1 dB of points for which masker and probe bandwidth are equal (points connected by the dotted line). This is also the case for $b_p = 4$ Hz (points labeled "B"), except for a slight departure for subject MS for $b_m = 0$ Hz. As probe bandwidth increases still further, the departure from the equal-bandwidth case becomes more pronounced. However, for any fixed value of probe bandwidth greater than 4 Hz, thresholds increase toward the equal-bandwidth thresholds monotonically as masker bandwidth increases, up until the point where masker and probe bandwidths are equal. [An exception to this last statement is a slight decrease in intensity increment at threshold for $b_p = 256$ Hz (points labeled "E") as masker bandwidth increases from 0 to 4 Hz. This effect is seen for both subjects, but it is on the edge of significance. It may be a real effect caused by detection of the 256-Hz probe in minima of the slowly varying envelope of the 4-Hz masker (see Fig. 1).]

An interesting effect in Fig. 2 that appears for both subjects is the nonmonotonic intensity jnd as signal bandwidth increases from 0 to 256 Hz with probe and masker bandwidths equal. For both subjects, $\Delta I/I_m$ is largest for signal bandwidths equal to 4 and 16 Hz and decreases for lower and higher signal bandwidths. For subject JH, the corresponding intensity jnd I_{m+p}/I_m is at a minimum of approximately 0.8 dB for 0-Hz bandwidth, increasing to a maximum of approximately 2.5 dB for 4- and 16-Hz bandwidths, and decreasing to approximately 1.2 dB for 256-Hz bandwidth. For subject MS, the intensity jnd is approximately 0.6 dB for 0-Hz bandwidth, increasing to a maximum of approximately 1 dB for 4- and 16-Hz bandwidths, and decreasing to a minimum of approximately 0.4 dB for 256-Hz bandwidth. The interpretation of this effect is beyond the scope of the present study. Our speculation is that for these long-duration stimuli the 0- and 256-Hz bandwidth signals are in some sense steady-state signals, while the 4- and 16-Hz bandwidth signals are not (Fastl, 1992), and the fluctuation of loudness at 4- and 16-Hz bandwidths results in increased intensity jnds.

B. ± 5 -dB intensity rove

For this version of the experiment, we reduced the influence of overall level as a cue by randomly varying the intensity of the stimulus from presentation to presentation over a ± 5 -dB intensity range. As before, a trial consisted of four stimulus presentations. For each of the four presentations, the masker intensity was, with equal probability, 65, 66, ..., 75 dB SPL. As before, three of the presentations consisted of masker alone, while one of the four consisted of masker plus probe. The probe level relative to the masker was the experimentally controlled variable. This version of the experiment is conceptually equivalent to the nonroved

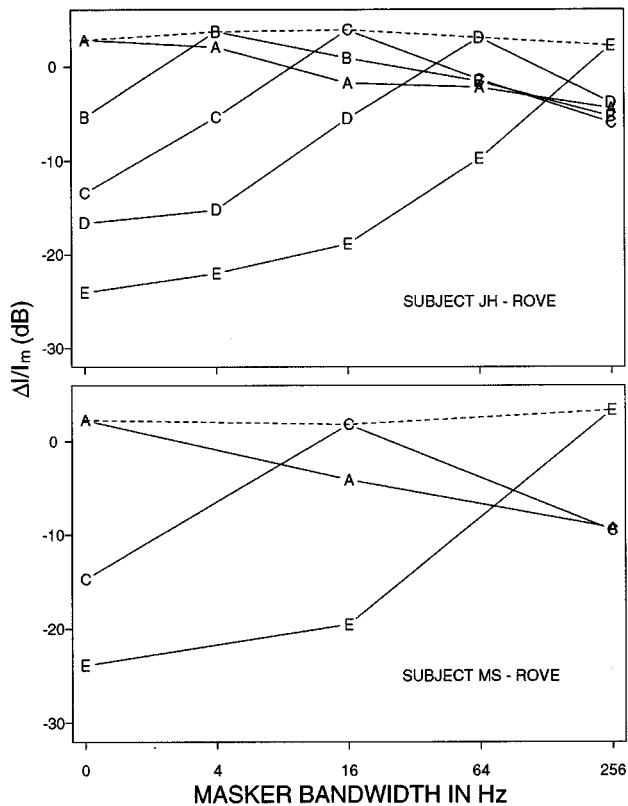


FIG. 3. Identical to Fig. 2, except that masker is presented with ± 5 -dB intensity rove.

version with the addition of a gain element in the signal path that varies from one stimulus presentation to the next over the range -5 to $+5$ dB, in 1-dB steps.

Figure 3 shows experimental results for this version of the experiment. The results are shown in the same format as in Fig. 2: increment ΔI in dB *re*: masker intensity I_m . As in Fig. 2, each point is the average of three measurements, one with each of the three phase assignment groups described in Sec. I A. We did not make a complete set of measurements with subject MS. Instead of the complete set of five bandwidths, we used only bandwidths of 0, 16, and 256 Hz.

Figure 4 shows the difference between thresholds obtained with a ± 5 -dB intensity rove and thresholds obtained with no rove. For masker and probe identical, the differences are substantial. The increment ΔI increases by amounts ranging from 4.9 to 14.2 dB. This large effect is to be expected. For these conditions overall intensity is the only cue available to the subject, so the change of intensity produced by addition of the probe has to be great enough to override the ± 5 -dB intensity rove. For masker bandwidth less than probe bandwidth, intensity roving has almost no effect. There is only one condition, probe bandwidth 4 Hz and masker bandwidth 0 Hz for subject JH, for which the difference between roved and unroved thresholds exceeds 0.0 dB. For masker bandwidth greater than probe bandwidth, the intensity rove produces an elevation of threshold that decreases as difference between probe and masker bandwidth increases.

It is instructive to compare thresholds in the rove case

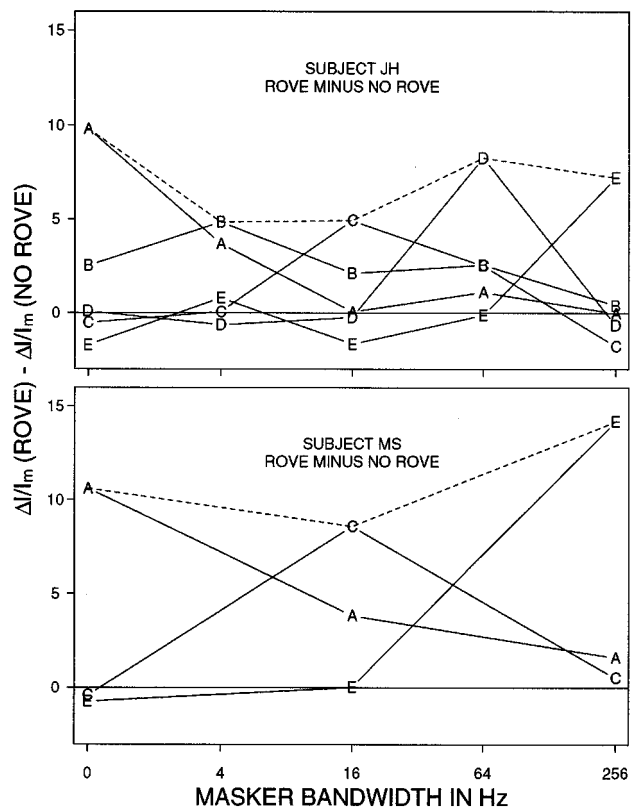


FIG. 4. Difference between threshold intensity increment with ± 5 -dB intensity rove (Fig. 3) and threshold intensity increment with no intensity rove (Fig. 2).

with thresholds predicted from the no-rove case under the assumption that judgments are made solely on the basis of average level. This prediction is based on the standard detection-theory model applied to stimulus intensity (Green, 1988). In this model, presentation of masker alone elicits an internal decision variable drawn from a distribution D_m with mean $\mu_m = I_m$ and standard deviation σ_m (μ_m and σ_m in dB), while presentation of masker plus probe elicits an internal decision variable drawn from a distribution D_{m+p} with mean $\mu_{m+p} = I_{m+p}$ and standard deviation σ_{m+p} . For simplicity we will assume $\sigma_m = \sigma_{m+p} = \sigma$. The subject's response is based on a comparison of these decision variables. For a two-interval forced-choice paradigm, the subject's response is correct if and only if the sample drawn from distribution D_{m+p} is greater than the sample drawn from distribution D_m . For the four-interval forced-choice paradigm used here, the subject's response is correct if and only if the sample drawn from distribution D_{m+p} is greater than the greatest of three independent samples drawn from distribution D_m . We first computed values of σ for each stimulus condition that would give the results shown in Fig. 2 for the no-rove case under the above model. We then convolved the resulting distributions D_m and D_{m+p} with a distribution flat over the range -5 to $+5$ dB to obtain the distributions of the hypothesized decision variables in the roved-intensity case. From these distributions, we computed values of ΔI that would result in the target probability of correct response $P_c = 0.625$.

The predicted results are thus influenced by two components: One is uncertainty caused by variability of the internal

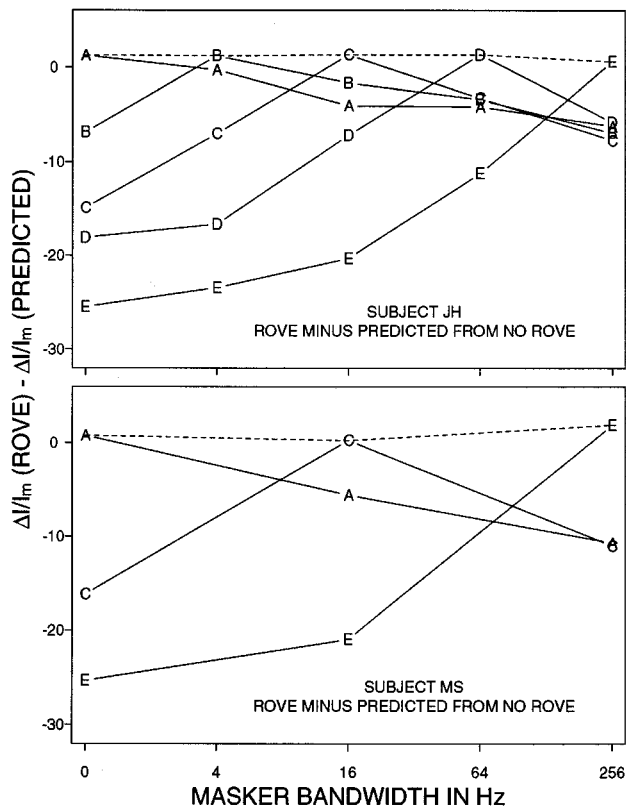


FIG. 5. Difference between threshold intensity increment with ± 5 -dB intensity rove (Fig. 3) and threshold increment predicted from no-rove case (Fig. 2) under the assumption that judgments are based on intensity alone.

decision variable over an ensemble of identical stimulus presentations, and the other is uncertainty introduced by the ± 5 -dB intensity rove. This analysis establishes that the ± 5 -dB intensity rove is large enough to be the dominant component if judgments are actually made on the basis of intensity. In the limiting case, as the unroved intensity difference limen approaches 0 dB, the intensity difference limen I_{m+p}/I_m with a ± 5 -dB intensity rove approaches 3.8 dB, which corresponds to an increment $\Delta I/I_m$ of 1.4 dB. This means that a 1.4-dB intensity increment will result in masker plus probe being more intense than the most intense of three samples of masker alone with probability 0.625.

The ± 5 -dB intensity rove is large enough to be the dominant component of the predicted results for subject MS. His no-rove thresholds are all small enough that the predicted increments range from a minimum of 1.4 dB to a maximum of 1.7 dB. Subject JH's no-rove thresholds are in some cases high enough to have an appreciable influence on predicted thresholds. Predicted difference limens for subject JH range from 1.4 to 2.6 dB. Still, in every case the predicted threshold is dominated by the intensity rove.

Figure 5 shows, for the two subjects, actual threshold increments obtained with a ± 5 -dB rove minus threshold increments predicted from the no-rove case under the assumption that intensity is the only cue. For probe and masker identical except for intensity, when in fact intensity is the only available cue, roving increases threshold increments by a small amount, 0.3–1.9 dB, above the increase predicted from the no-rove case. This result is to be expected: Because

of the additional burden placed on higher processes such as memory, we would expect it to be more difficult to pick out the most intense of four stimuli if the other three were at widely differing intensities than it would be if the other three were all at the same intensity. For all conditions where probe and masker bandwidths are different, roving increases thresholds by less than would be predicted from the no-rove case. The curves drop off steeply for masker bandwidth less than probe bandwidth, less steeply for masker bandwidth greater than probe bandwidth.

III. DISCUSSION OF EXPERIMENTAL RESULTS

The most significant finding of this investigation is that the essential distinction that must be made with reference to asymmetry of masking is not tone versus noise but rather the apparent qualitative difference between the two cases of (1) probe bandwidth equal to or less than masker bandwidth and (2) probe bandwidth greater than masker bandwidth. For the first case, results are consistent with the idea that judgments are based in large part on change of overall level. For masker and probe identical, there is a variation of threshold intensity increment ΔI with stimulus bandwidth that is presumably a central effect and is beyond the scope of this paper, but for any fixed masker bandwidth, threshold intensity increment ΔI is approximately equal for all probe bandwidths equal to or less than masker bandwidth. Intensity roving produces an elevation of threshold if probe bandwidth is equal to or slightly smaller than masker bandwidth, which would occur only if judgments were based at least in part on overall level. Interestingly, if probe bandwidth is much less than masker bandwidth, the effect of roving decreases, which implies that judgments are being made on something other than overall level. This is true even though in the unroved case the threshold intensity increment for probe bandwidth much less than masker bandwidth was approximately equal to the threshold intensity increment for probe bandwidth equal to or slightly less than masker bandwidth, where the effect of intensity roving implies that judgments are based on overall intensity.

It has been established (Zwislicki *et al.*, 1958) that subjects can, with practice, use more than one qualitative cue in a detection task. The stimulus percept in the present experiment is complex, and the experimental design (same masker and probe used in all 42 trials in a run, feedback to the subject after each trial) facilitates the subject's use of the most effective cue. The naive interpretation, which is all we have to offer at the present time, is that the cue used when probe bandwidth is much less than masker bandwidth is not intensity, but by coincidence it gives results that in the unroved case are indistinguishable from judgments based on intensity. This interpretation is unsatisfactory, and the situation needs to be investigated further.

For the second case, probe bandwidth greater than masker bandwidth, results both with and without an intensity rove indicate very strongly that judgments are made on the basis of something other than overall level. Unroved threshold intensity increments are much smaller in this stimulus region, and intensity roving has virtually no effect on threshold. Goldstein (1995) has been successful in modeling some

of these effects with a model that operates on maxima of the temporal waveform. This work will be the subject of a future paper.

IV. POSSIBLE EFFECT OF OFF-FREQUENCY LISTENING

Our thesis in this paper is that a model based on long-term average spectrum is inadequate to account for the observed asymmetry of masking. A counterargument that could be made is that the reduced threshold observed when probe bandwidth is greater than masker bandwidth results from off-frequency listening. That is, the masker plus probe, being of wider bandwidth, excites a broader region of the basilar membrane than does the masker alone. According to this argument, the difference between masker plus probe and masker alone is detected at the edges of the region excited by masker plus probe.

In order to evaluate the possible effect of off-frequency listening, we modified a model previously used by Schroeder *et al.* (1979). In this model, the masking stimulus, on a critical-band scale, was convolved with a “spreading function” obtained from masking data to produce an “excitation pattern” supposed to be thought of as “... energy distributions along the basilar membrane” (Schroeder *et al.*, 1979, p. 1648). Through a series of nonlinear operations on this excitation pattern, an estimate could then be obtained of the loudness of a probe signal. Our modification differs from this model in several respects. (1) Rather than the spreading function used by Schroeder *et al.* (lower and upper skirts asymptotically +25 and -10 dB per critical band, respectively), we used two more recently suggested filters. One was the gammatone filter, defined by Patterson (1994) in the time domain by its impulse response

$$\gamma(t) = at^{(n-1)} \exp(-2\pi bt) \cos(2\pi f_0 t + \phi) \quad (t > 0). \quad (1)$$

This function has been designed to provide a reasonable approximation to a variety of physiological and psychological data. We generated the impulse response for $f_0 = 1$ kHz in the time domain, determined its magnitude in the frequency domain $|\bar{\Gamma}(f)|$, and mapped from $|\bar{\Gamma}(f)|$ on a frequency scale to $|\Gamma(x)|$ on a Bark (critical band) scale using the relationship $x = 7 \times \ln(f/650) + \sqrt{(f/650)^2 + 1}$ (Schroeder *et al.*, 1979, p. 1648). n was set equal to 4 and b was set equal to 147.1 (values recommended by Patterson). We set the scale factor a to make the maximum magnitude of $|\Gamma(x)|$ be equal to one. The phase ϕ is immaterial since we are interested only in the magnitude. The other filter we used was Allen’s two-dimensional resonant tectorial membrane (2-D RTM) filter (Allen, 1980) which at 1 kHz has a steeper high-frequency slope and a less steep low-frequency slope than the gammatone filter. The two filters are compared in Fig. 6. (2) Rather than the approach used by Schroeder *et al.* of considering masker and probe separately to determine if the probe is detectable in the presence of the masker, we compared excitation patterns obtained from the power spectrum of the masker and from the power spectrum of probe plus masker to determine if the difference is detectable, as described in Appendix B. This is an important distinction, be-

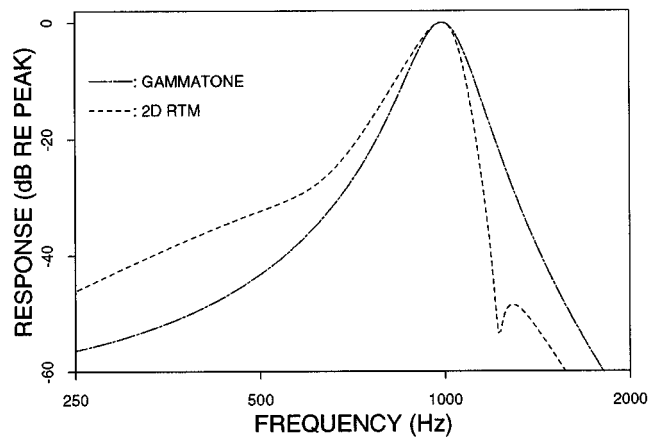


FIG. 6. Frequency response of gammatone and 2-D RTM filters centered at $f_0 = 1$ kHz.

cause treating masker and probe independently ignores the influence of phase relationships between probe and masker. (3) The criterion for determining that probe plus masker was distinguishable from probe alone was that the excitation pattern resulting from probe plus masker differed by at least one intensity jnd from the excitation pattern resulting from probe alone at some place along the length of the model basilar membrane. The excitation pattern comprises a response with the units of stimulus intensity at each place on the model basilar membrane. We know from psychophysical measurements what change of intensity of a stimulus presented to the ear is detectable. The crucial assumption for this criterion is that intensity jnd’s as measured for a stimulus presented to the ear can be applied to differences of excitation patterns at a single point along the length of the model basilar membrane.

There are various ways in which this model could be implemented. One way, which is influenced by Hellman and Hellman’s (1990) generalization of the McGill–Goldberg (1968) counting model, is described in Appendix B. When we apply this model with the two different filters to the present data, the results are as shown in Fig. 7. The gammatone filter, shown in the upper panel, fails completely. Predicted thresholds are almost totally independent of masker or probe bandwidth unless at least one of the two bandwidths is equal to 256 Hz. Furthermore, the change of threshold with change of masker bandwidth for the 256-Hz-wide probe is much less than was observed experimentally. The 2-D RTM filter, shown in the lower panel, predicts results very close to the experimental results for the 256-Hz-wide probe, but it still fails completely for all narrower probes.

It is difficult to prove a negative, but these results strongly suggest that a model based on long-term average spectrum is inadequate to account for the experimentally observed asymmetry of masking. The gammatone filter, which accounts reasonably well for masking of tones, does not provide anything near the required frequency selectivity for the present data. The 2-D RTM filter is at the same time too sharply tuned to account for masking of tones and too broadly tuned to account for the present data for probe bandwidths less than one critical band. We do not claim that we

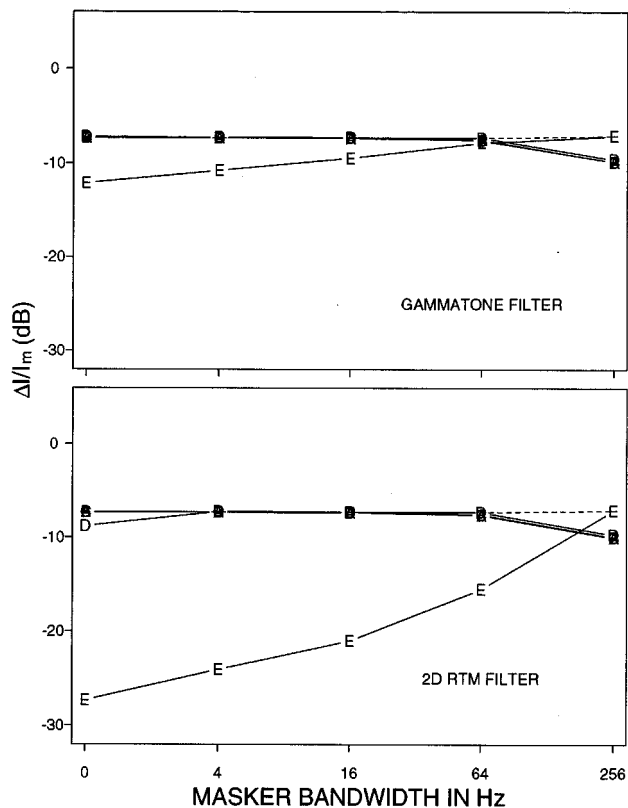


FIG. 7. Threshold intensity increment as predicted by model with gammatone filter (upper panel) and with 2-D RTM filter (lower panel) versus masker bandwidth in Hz, with probe bandwidth as parameter. Symbols same as in Fig. 2.

have used the “best” possible filter. We claim that it is impossible to find a filter, any filter, that could account for these experimental results in a model based on long-term average spectrum.

V. CONCLUSIONS

Results presented here confirm and expand on results already in the literature. A band of noise masked by a tone is audible at a much lower probe-to-masker ratio than is a tone masked by a band of noise, as was already known. A more general statement is that over the range of bandwidths explored here, probe-to-masker ratios are only weakly dependent on bandwidth as long as the bandwidth of the probe does not exceed the bandwidth of the masker. When the bandwidth of the probe does exceed the bandwidth of the masker, threshold probe-to-masker ratios decrease sharply.

These results are consistent with the hypothesis that detection is based on long-term average energy as long as the bandwidth of the probe is equal to or is slightly less than the bandwidth of the masker, but that other cues are utilized for probe bandwidth greater than masker bandwidth or probe bandwidth much less than masker bandwidth. This hypothesis is strengthened by the observation that random variation of masker intensity (“level roving”), which reduces the salience of long-term average energy, degrades performance for probe bandwidth equal to or slightly less than masker bandwidth but has almost no effect on performance for probe bandwidth greater than masker bandwidth. Level roving also

has little effect on performance for probe bandwidth much less than masker bandwidth, which is puzzling because it suggests that long-term average energy is not the relevant cue even though results for this condition in the absence of level roving can be described accurately in terms of long-term average energy.

It would be useful to repeat these experiments with a larger number of subjects and with a larger number of phase assignments. Because of the small number of subjects (two) and of phase assignments (three), we are unable to make some potentially interesting statistical decisions. Another extension would be to repeat these experiments at other intensities: Hellman’s 1972 results show that the asymmetry of masking can be dependent on stimulus level.

Results from a frequency-selective model based on long-term average energy argue against spectral cues associated with off-frequency listening as a cue for the condition of probe bandwidth greater than masker bandwidth. The gammatone filter, which was designed to provide a reasonable approximation to a variety of physiological and psychophysical data, does not provide the required frequency selectivity. The 2-D RTM filter, which was derived from a physical model of the cochlea, provides reasonable predictions for the widest probe signal but it is too sharply tuned to account for the data reported here. The conclusion is that a perceptual coder should consider some stimulus measure other than long-term spectral content, such as the temporal structure of the signal. Goldstein’s theoretical analysis of these data (Goldstein, 1995; Goldstein and Hall, 1995), in which he has been able to reproduce many of these experimental results with a model that operates on maxima of the temporal waveform, provides support for this view.

APPENDIX A: COMPUTATION AND PRESENTATION OF EXPERIMENTAL RESULTS

As Jesteadt *et al.* (1977) have pointed out in their Appendix A, these results could be presented in any one of several forms, including the increment relative to the masker (in dB) $10 \times \log(\Delta I/I_m)$ and the difference in dB between masker and masker plus probe $10 \times \log(I_{m+p}/I_m)$. The second of these forms is more natural when discussing intensity jnd’s, but, as Jesteadt *et al.* observe, it is highly compressive and makes recovery of the data difficult. We have chosen to present these results in terms of $10 \times \log(\Delta I/I_m)$.

In order to avoid any possible ambiguity, let us be very specific about how these numbers were computed. Consider two signals of the type described in Sec. I A, s_1 and s_2 . (Whether s_1 is masker and s_2 is probe or vice versa will be seen to depend on whether masker or probe is of wider bandwidth.) s_1 has rms amplitude a_1 and N_1 equal-amplitude components each of amplitude $a_1/\sqrt{N_1}$. s_2 has rms amplitude a_2 and N_2 equal-amplitude components each of amplitude $a_2/\sqrt{N_2}$. s_1 has power $I_1 = a_1^2$ and s_2 has power $I_2 = a_2^2$. We can assume, without loss of generality, that $N_2 \geq N_1$. Since components at the same frequency add in phase, it follows that the combined signal $s_1 + s_2$ has N_1 components of amplitude $a_1/\sqrt{N_1} + a_2/\sqrt{N_2}$ and $N_2 - N_1$ components of

amplitude $a_2/\sqrt{N_2}$, and the power of the combined signal $I_{1+2} = a_1^2 + a_2^2 + 2a_1a_2\sqrt{N_1/N_2}$. What is plotted in these figures is $10 \times \log_{10}[(I_{m+p} - I_m)/I_m]$, the power of the combined signal minus the power of the masker, relative to the power of the masker, in dB. Note that measures involving the power of the probe by itself are not meaningful, because of the variation of coherence between probe and masker.

APPENDIX B: COMPUTATION OF MODEL RESULTS FOR OFF-FREQUENCY LISTENING

The psychophysical measurements we used to carry out this evaluation are Jesteadt *et al.*'s (1977) measurements as fit by their Eq. (1), $\Delta I/I = 0.463 \times (I/I_0)^{-0.072}$, where I_0 is their threshold intensity at 1 kHz of 14.7 dB SPL. This equation is plotted on a decibel scale in the top panel of Fig. B1. [Jesteadt *et al.* actually provide, in their Eq. (2), a straight-line fit to their data on a decibel scale, but we have chosen to use their Eq. (1) instead because it provides a better fit to their data.]

The most straightforward way to determine if the two excitation patterns differ by at least one intensity jnd is, for each position along the length of the model basilar membrane, to compare I and ΔI from the model results with Jesteadt *et al.*'s Eq. (1). This process is cumbersome. It is easier to define a mapping $g(I)$ that has the property that if ΔI is equal to one jnd as defined by Jesteadt *et al.*'s Eq. (1) then $g(I + \Delta I)$ exceeds $g(I)$ by a fixed constant value k . Such a function can be obtained by integrating $I/\Delta I$ in Jesteadt *et al.*'s Eq. (1):

$$g(I) = g(I_0) + k \int_{I_0}^I \frac{d\xi}{\Delta I}. \quad (\text{B1})$$

An interesting mapping results if we define a new variable $N(I) = g^2(I)$, with $k=0.5$. Equation (B1) then becomes

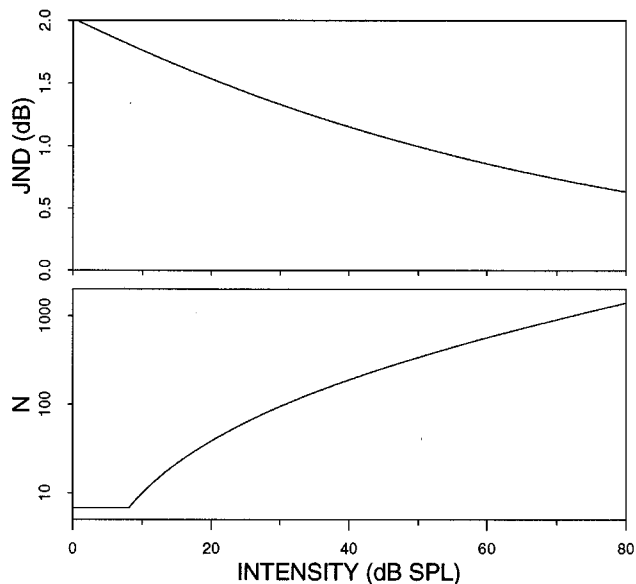


FIG. B1. Top panel: Intensity jnd in dB as specified by Jesteadt *et al.* (1977) Eq. (1). Bottom panel: $N(I)$ to give absolute threshold of 10 dB SPL and intensity jnd's as specified by Jesteadt *et al.* using criterion specified in text.

$$\sqrt{N(I)} = \sqrt{N(I_0)} + 0.5 \int_{I_0}^I \frac{1}{\Delta I} d\xi, \quad (\text{B2})$$

from which it follows that

$$\frac{1}{\sqrt{N}} \frac{dN}{dI} \Delta I = 1 \quad (\text{B3})$$

and

$$\frac{N(I + \Delta I) - N(I)}{\sqrt{N(I)}} \approx 1. \quad (\text{B4})$$

It can be argued that the quantity on the left side of Eq. (B4) can be identified with the detectability index d' . The ratio of difference between means to standard deviation for samples from two Poisson processes, one with mean and variance N_1 and the other with mean and variance N_2 (an approximate description of the integrated output of auditory-nerve fibers), is equal to $(N_2 - N_1)/\sqrt{N_2}$ (assuming $N_1 \approx N_2$). If the samples are large enough that their distributions are approximately Gaussian, then this ratio is approximately equal to the detectability index d' . This measure is appealing because it has been suggested that under some conditions a count N with this property corresponds to neural firing rates integrated over some interval and can be identified with loudness (McGill and Goldberg, 1968; Hellman and Hellman, 1990). However, as used here the function $N(I)$ should be regarded simply as a mapping of stimulus intensity that facilitates the determination of intensity jnds.

Note that there is an unconstrained constant of integration $N(I_0) = N_0$. We can set this constant to be whatever we please and still get the right answer, since our only requirement is that the condition $(N_2 - N_1)/\sqrt{N_2} = 1$ at one intensity jnd be satisfied. As Hellman and Hellman (1990) point out, an attempt to identify N or a transformation of N with loudness puts constraints on this constant.

The bottom panel of Fig. B1 shows N plotted versus intensity in dB SPL. Our approach is slightly different from that used by Hellman and Hellman in that we set the constant of integration N_0 to be equal to one at 0 dB SPL, and then artificially forced an elevation of absolute threshold to 10 dB SPL by putting a floor on N such that a signal at 10 dB SPL met our criterion for detection. For the conditions given here, a signal at 10 dB SPL corresponds to $N=9.96$. This value of N is at threshold if the value of N in the absence of acoustic stimulation is equal to 6.80, because $(9.96 - 6.80)/\sqrt{9.96} = 1$. The value of 6.80 could be regarded as corresponding to a spontaneous neural firing rate, and a signal at 10 dB SPL that elicited a count of 9.96 would result in a d' of one.

The four panels of Fig. B2 illustrate how this procedure is applied. The gammatone filter was used for this example. The procedure is identical for the 2-D RTM filter. Panel (a) shows excitation patterns resulting from a 1-kHz tone at 70 dB SPL (the masker) and from the sum of a 1-kHz tone at 70 dB SPL and an 800-Hz tone at 38.5 dB SPL (masker plus threshold-level probe). These two excitation patterns are identical except for a very slight difference in the neighborhood of $x=7.3$ Barks, the position maximally excited by an 800-Hz tone. For reference, this panel also shows the exci-

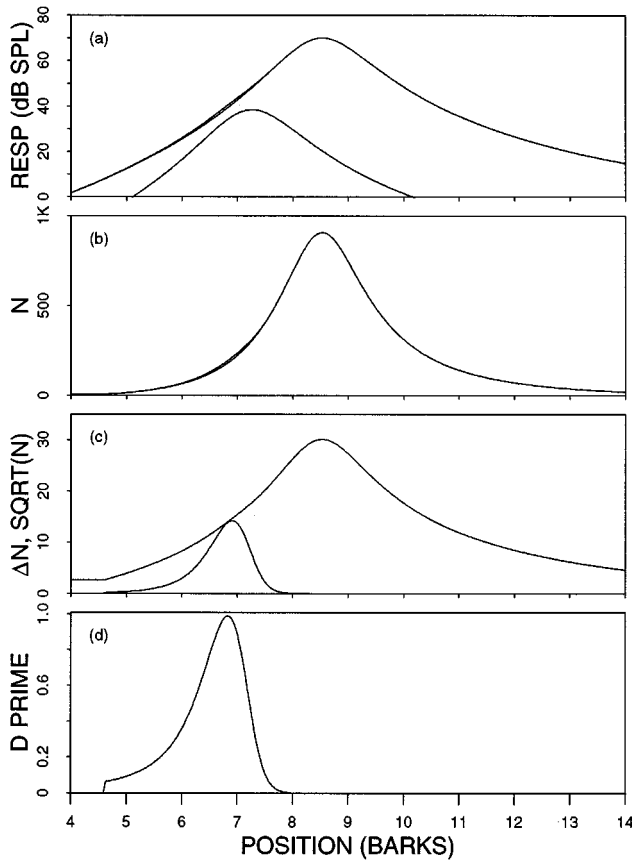


FIG. B2. (a) Excitation patterns resulting from masker, masker plus probe, and probe, as described in text. (b) $N(I)$ elicited by masker and by masker plus probe. (c) Difference between, and square root of, values shown in (b). (d) d' as determined from ratio of curves shown in (c).

tation pattern resulting from an 800-Hz tone at 38.5 dB SPL presented alone. Panel (b) shows count as a function of position for these same two signals, masker alone (N_1) and masker plus probe at threshold (N_2), as obtained from the mapping shown in the bottom panel of Fig. B1. Panel (c) shows $N_2 - N_1$, the difference between the two curves in panel (b), and it also shows $\sqrt{N_2}$. The difference $N_2 - N_1$ is zero over most of the length of the simulated basilar membrane, but it reaches a maximum of 14.2 at $x = 6.9$ Barks that is just equal to $\sqrt{N_2}$ at this position so that the ratio $(N_2 - N_1) / \sqrt{N_2}$, shown in panel (d), is equal to one. To check on this result, we note that the response to masker alone shown in panel (a) is 41.1 dB SPL at $x = 6.9$ Barks and the response to masker plus probe is 42.2 dB SPL. The difference between the two is 1.1 dB, which is equal to the intensity jnd at 42 dB SPL shown in the top panel of Fig. B1.

Note that, because of the slope of the excitation patterns, the position of maximum detectability of the 800-Hz tone is somewhat apical to the 800-Hz place. In general, for any given experimental condition, we have to look for the position of maximum detectability across the entire length of the simulated basilar membrane (the model analogue of off-frequency listening).

We can get some sense as to whether or not the gammatone and the 2-D RTM filters may be appropriate by comparing, in Fig. B3, masking of pure tones by a narrow-band

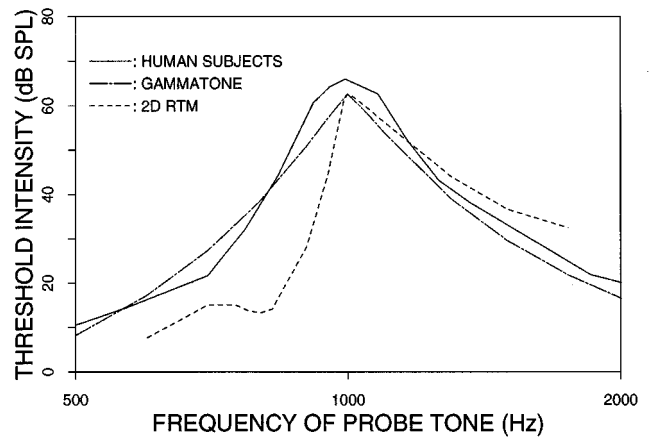


FIG. B3. Masking by narrow-band 1-kHz 70 dB SPL signal as determined by human listening experiments (Scharf, 1971) and as predicted by model with gammatone filter and with 2-D RTM filter.

masker at 70 dB SPL centered at 1 kHz as determined in human listening experiments (Scharf, 1971, cited in Scharf 1978) with model predictions for masking by a 70 dB SPL 1-kHz pure tone with the gammatone filter and the 2-D RTM filter. The agreement between model and experiment is excellent, in general within ± 5 dB, for the gammatone filter. The 2-D RTM filter, because of its steep high-frequency slope, predicts too little masking for probe frequency less than masker frequency. We conclude that for steady-state pure-tone probe signals this model gives reasonable results with the gammatone filter and too sharply tuned results with the 2-D RTM filter.

¹Note that this interstimulus interval is not long enough to rule out post-stimulus effects. We did in fact observe some order effects. Both subjects noted that detection was more difficult when the probe was added to the first of the four presentations than when it was added to one of the other three. We did not explore this facet in detail, and we are unable to say whether increase of the interstimulus interval would have reduced this order effect.

Allen, J. B. (1980). "Cochlear micromechanics—A physical model of transduction," *J. Acoust. Soc. Am.* **68**, 1660–1670.
 Fastl, H. (1992). "Fluctuation strength of narrow band noise," in *Advances in the Biosciences* (Pergamon, London), Vol. 83, pp. 331–336.
 Goldstein, J. L. (1995). "Comparison of peak and energy detection for auditory masking of tones by narrow-band noise," *J. Acoust. Soc. Am.* **98**, 2907(A).
 Goldstein, J. L., and Hall, J. L. (1995). "Peak detection for auditory sound discrimination," *J. Acoust. Soc. Am.* **97**, 3330(A).
 Green, D. M. (1988). *Profile Analysis. Auditory Intensity Discrimination* (Oxford U.P., New York).
 Green, D. S. (1978). "Pure tone air-conduction testing," in *Handbook of Clinical Audiology*, 2nd ed., edited by J. Katz (Williams & Wilkins, Baltimore/London), p. 105.
 Hall, J. L. (1981). "Hybrid adaptive procedure for estimation of psychometric functions," *J. Acoust. Soc. Am.* **69**, 1763–1769.
 Hellman, R. P. (1972). "Asymmetry of masking between noise and tone," *Percept. Psychophys.* **11**, 241–246.
 Hellman, W. S., and Hellman, R. P. (1990). "Intensity discrimination as the driving force for loudness. Application to pure tones in quiet," *J. Acoust. Soc. Am.* **87**, 1255–1265.
 Jeffress, L. A. (1970). "Masking," in *Foundations of Modern Auditory Theory*, edited by J. V. Tobias (Academic, New York), Vol. 1, pp. 87–114.

- Jesteadt, W., Wier, C. G., and Green, D. M. (1977). "Intensity discrimination as a function of frequency and sensation level," *J. Acoust. Soc. Am.* **61**, 169–177.
- Johnston, J. D. (1988). "Transform coding of audio signals using perceptual noise criteria," *IEEE J. Sel. Areas Commun.* **6**, 314–323.
- McGill, W. J., and Goldberg, J. P. (1968). "Pure-tone intensity discrimination and energy detection," *J. Acoust. Soc. Am.* **44**, 576–581.
- Patterson, R. D. (1994). "The sound of a sinusoid: Spectral models," *J. Acoust. Soc. Am.* **96**, 1409–1418.
- Scharf, B. (1971). "Fundamentals of auditory masking," *Audiology* **10**, 30–40.
- Scharf, B. (1978). "Loudness," in *Handbook of Perception*, edited by E. C. Carterette and M. P. Friedman (Academic, New York), Vol. IV, pp. 187–242.
- Schroeder, M. R., Atal, B. S., and Hall, J. L. (1979). "Optimizing digital speech coders by exploiting masking properties of the human ear," *J. Acoust. Soc. Am.* **66**, 1647–1652.
- Sydorenko, M. R., and Allen, J. B. (1994). "The relationship between the just noticeable difference (jnd) in intensity and the masked threshold of sub-critical bandwidth signals" (in preparation).
- Taylor, M. M., and Creelman, C. D. (1967). "PEST: Efficient estimates on probability functions," *J. Acoust. Soc. Am.* **41**, 505–508.
- Zwislocki, J., Maire, F., Feldman, A. S., and Rubin, H. (1958). "On the effect of practice and motivation on the threshold of audibility," *J. Acoust. Soc. Am.* **30**, 254–262.
- Zwislocki, J. (1965). "Analysis of some auditory characteristics," in *Handbook of Mathematical Psychology*, edited by R. D. Luce, R. R. Bush, and E. Galanter (Wiley, New York), Vol. 3, pp. 1–97.

On the Duifhuis pitch effect

Jian-Yu Lin and William M. Hartmann

Department of Physics and Astronomy, Michigan State University, East Lansing, Michigan 48824

(Received 12 July 1995; revised 11 July 1996; accepted 14 October 1996)

An effect discovered by Duifhuis [J. Acoust. Soc. Am. **48**, 888–893 (1970)], wherein an omitted high harmonic of a periodic complex tone is found to have an audible pitch, is extended to a variety of new broadband signal conditions. The effect is found to exist for flat spectra and spectra decreasing at 6 dB/octave, independent of phases as long as they are constant. The effect exists for alternating phases and Schroeder phases. It can generate a missing-fundamental pitch. Pitch and loudness matching experiments support the status of the omitted harmonic as an objective tone in the signal. Further experiments using narrower bands challenge the traditional explanation for the effect, which attributes it to short-term frequency analysis by peripheral auditory filters. Instead, the experiments suggest that different peripheral channels must be combined, maintaining some phase information, to generate the effect. © 1997 Acoustical Society of America.

[S0001-4966(97)05202-8]

PACS numbers: 43.66.Hg, 43.66.Ba, 43.66.Nm [LLF]

INTRODUCTION

Duifhuis (1970, 1971) described a delightful psychoacoustical effect that might be called the “pitch of the harmonic that is not there.” It was created by a periodic train of narrow pulses to which was added a sine tone, phase locked, and adjusted so as to cancel one of the harmonics of the pulse train. The spectrum of the signal therefore looked like Fig. 1(a). When the fundamental frequency was low enough and the cancelled harmonic number was high enough, listeners perceived a pitch corresponding to the cancelled harmonic.

A priori, Duifhuis’s effect is surprising. What is heard by listeners is exactly what is *not* present in the signal. On second thought, the effect seems easy to understand. An oscillographic tracing of the waveform, shown in Fig. 1(b) shows a clear periodic component corresponding to the cancelled harmonic. The trace looks like a pulse with added sine. The oscilloscope is, of course, a very broadband system. The auditory system, however, is not broadband in this way. Instead, the auditory system begins with tuned channels, represented as an array of auditory filters. The filters analyze incoming signals into separate bands, and therefore the entire oscillographic representation never appears within the auditory system.

The explanation for the audible effect given by Duifhuis is that when the frequency spacing between harmonics is considerably less than the bandwidth of relevant auditory filters, the tuned auditory channels appear to be broadband

too. Then the output of the auditory filter bank retains an impulsive character, and the cancelled harmonic appears in the temporal gap between ringing responses to successive pulses. The cancelled harmonic is present in the output just as though the cancellation tone were an objective sine signal.

The present article is a study of the Duifhuis pitch effect (DPE) consisting of two parts. The first uses broadband signals to explore the DPE for a variety of new conditions. The conclusions of these broadband tests are consistent with the idea that the DPE results from an objective added cancellation tone. The second part is a band-narrowing experiment that tests the concept of the cancellation tone as an isolated component appearing in the output of the auditory filter bank during the temporal gap. It is shown that this concept fails. Instead, the DPE appears to be a segregation process that depends both on the cancellation tone in the gap and on the broadband complex tone that establishes a background including multiband phase coherence.

I. BROADBAND DPE EXPERIMENTS

The broadband experiments were undertaken to extend the experiments by Duifhuis to new signal conditions. The first goal was to distinguish between those conditions in which the DPE can be heard and those condition in which it cannot. The second goal was to determine the pitch and loudness of the DPEs.

A. Method

It is well known that changes in the spectrum (turning a harmonic on and off, amplitude modulating a single harmonic, mistuning a harmonic or suddenly shifting its phase) can cause a harmonic to be heard out from a complex tone (Pierce, 1960; Kubovy and Jordan, 1979; McAdams, 1984; Hartmann, 1988; Moore and Glasberg, 1989; Alcantara and Moore, 1995). Such effects occur both for harmonics that are spectrally resolved and for harmonics that are not. They are “attention” effects caused by the contrast between “before” and “after” conditions.

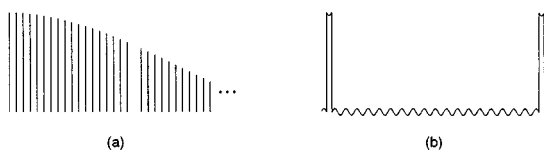


FIG. 1. (a) The amplitude spectrum of a periodic narrow pulse train with the 19th harmonic omitted; (b) waveform generated by the spectrum in (a) with all harmonics having cosine phase.

The Duifhuis pitch effect is not such a contrast effect, and to guard against a contrast artifact our formal experiments did not permit the listener to compare omitted-harmonic signals with complete-spectrum signals. Instead they were matching experiments. The listener heard an omitted-harmonic tone and was required to match its pitch with a sine tone. In the end it was concluded that the listener could hear the DPE if the matches were consistent.

1. General procedure

The listener was seated in a sound-treated room, holding a response box that controlled the events of an experimental trial. When the listener pressed a yellow button there was a pause of 200 ms and then a 700-ms complex tone having an omitted harmonic. When the listener pressed an orange button there was a pause of 200 ms and then a 700-ms sine tone with a frequency that could be adjusted by means of a ten-turn potentiometer on the box. The listener's task was to tune the sine tone so as to match the pitch of the DPE. The level of the matching tone could also be easily controlled from the response box. The listener could call up the complex tone or the matching tone as often as he liked. When the listener was satisfied with his match he pressed the green button to finish the trial. The target and matching frequencies were recorded, and then the next trial with a different omitted harmonic began. There was no feedback to the listener.

Trials were blocked into runs. Each experimental run included four trials. It took about 1–5 min for a listener to finish a run. Runs for each of the conditions below continued until the results appeared to be stable. The final data reported here are based on the final five matches.

2. Stimuli

Duifhuis created an omitted-harmonic tone by adding a cancellation sine tone to a pulse train. Therefore, the amplitude spectrum decreased slowly with increasing frequency as shown in Fig. 1(a). Our experiments were similar except that they used a flat amplitude spectrum. The computer added a large number, N , of harmonics with equal amplitudes and cosine phases to make signal $x(t)$,

$$x(t) = \sum_{n=1}^N A_n \cos(2\pi n f_0 t + \phi_n), \quad (1)$$

where all the amplitudes A_n , except for the highest two, were equal to 1. The amplitudes of the highest two harmonics in the spectrum were tapered to reduce edge pitches (Klein and Hartmann, 1981) and Gibbs phenomena ($A_N=0.3$ and $A_{N-1}=0.7$). All the phases, ϕ_n , were equal to zero, and the fundamental frequency, f_0 , was 50 Hz. To generate the DPE, one harmonic, called n' , was omitted by setting the corresponding amplitude $A_{n'}$ equal to zero. Although our technique of signal generation did not explicitly add a cancellation tone to a complex tone, we will continue to refer to the omitted harmonic as the result of an added "cancellation tone."

The digital waveform was loaded into a digital-to-analog converter (TDT-DD1) and cycled indefinitely (16 bits, 50 000 samples/s). The signal was low-pass filtered below 20 kHz (–115 dB/octave) and sent to headphones, Sennheiser

HD480, where it was heard diotically. The signal level was set so that each component had a level of 45 dB SPL.

The matching tone was generated by a Wavetek VCG116 function generator. Its frequency was controlled by a voltage from the listener's response box and was read by the computer through a reciprocal reading frequency counter on the computer bus. The matching tone was passed through a computer-controlled attenuator (TDT-PA4) so that its level could also be controlled and read by the computer.

3. Listeners

Three male listeners LB, LD, and LJ participated in the experiments. Their ages were 56, 20, and 34, respectively. LJ and LB were the authors. Audiograms showed that LD and LJ had normal hearing through 6 kHz, but that LB had a high-frequency hearing loss typical of males of his age. All the listeners had some training as performers of musical instruments and could perform a standard pitch matching task accurately.

B. Experiment 1: The frequency range of the DPE

To study the frequency range of the DPE, we used a flat spectrum with $N=170$ harmonics. To create the DPE, one harmonic, which could be as low as the 8th or as high as the 145th, was omitted from the complex tone spectrum. The purpose of this experiment was to test the frequency limits of the DPE for a 50-Hz complex tone.

The results are shown in Fig. 2. There are three panels in the figure, one for each subject. The vertical axis gives the matching ratio, defined as the listener's matching frequency divided by the frequency of the omitted harmonic. Therefore, when the ratio is unity the listener has made a perfect match.

The left four data points were tests of the low-frequency end of the DPE. The dot-dashed lines are the edges of the spectral gap created by omitting a harmonic. For example, when harmonic 10 is omitted, the edges of the spectral gap are harmonic 9 (ratio of 0.9) and harmonic 11 (ratio of 1.1). For omitted harmonics with very low harmonic number listeners seem to hear the edges and match them. Our criterion for the existence of the DPE at low frequency is that the listener's match should be closer to the omitted harmonic than to one of the edges. The data show that the three different listeners have different low ends: harmonic 13 for LB, 15 for LD, and 19 for LJ. Duifhuis (1972) found that the low-frequency limit of the DPE decreases with increasing signal level. From his results one would expect a lower limit between harmonics 10 and 20 for the levels used here.

The middle four points test the performance of the listeners at the middle range. All the listeners could make successful matches, although there is a small systematic pitch shift. The shift is positive as expected (Terhardt and Fastl, 1971). Such pitch shifts were also reported in the thesis by Duifhuis (1972). Informal comments by the listeners indicated that in the middle range the DPE was clear and loud, and there was no ambiguity in its pitch.

The four points on the right were intended to test the high-frequency end of the effect. Successful matches as high

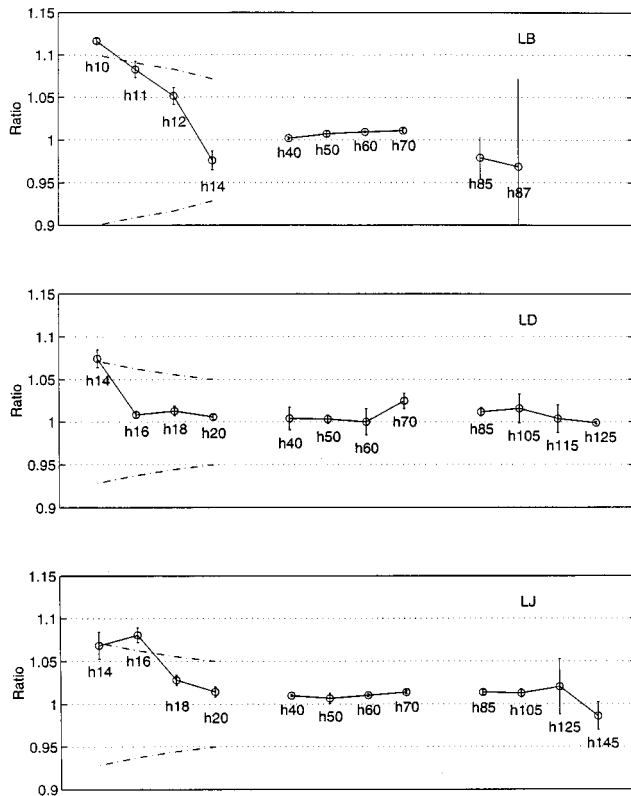


FIG. 2. Frequency matching results for experiment 1 showing matches. Each panel is for one subject. The *Ratio* is defined as the matching frequency divided by the frequency of the omitted harmonic. The symbol “h...” tells which harmonic is omitted in the complex tone. The left four points are for the low-frequency end of the effect. The dashed lines there show the edges of the spectral gap. The middle four points are in middle range of the effect. The right four points show an attempt to explore the high-frequency end of the effect.

as the 125th harmonic (6250 Hz) for LD and the 145th harmonic (7250 Hz) for LJ indicate a DPE at high frequency. However, matching became difficult and time consuming at these high frequencies, perhaps because of the unavailability of timing information above 5000 Hz (Johnson, 1980; Pickles, 1982; Moore, 1973). In the end, no upper limit was found for these two listeners. Listener LB made large errors for an omitted 87th harmonic (4350 Hz) and could not reliably detect the presence of a DPE for omitted harmonics 89 or 92. This high-frequency failure is possibly related to a high-frequency hearing loss. At 4500 Hz, LB showed a bilateral loss of about 16 dB. However, as shown in the next section, an effective reduction of 16 dB is not, by itself, enough to eliminate the DPE.

C. Experiment 2: Level effect

The purpose of the level effect experiment was to see whether the strength of the DPE is determined by the level of the cancellation tone. In this experiment the listener adjusted both the frequency and the level of a sine tone to match the DPE. The matching level was controlled through two buttons on the response box; pressing one increased the level by 1 dB, and pressing the other decreased the level by 1 dB.

Omitted harmonics at the lower end of the middle range, 25–40, were chosen for this experiment. The top harmonic

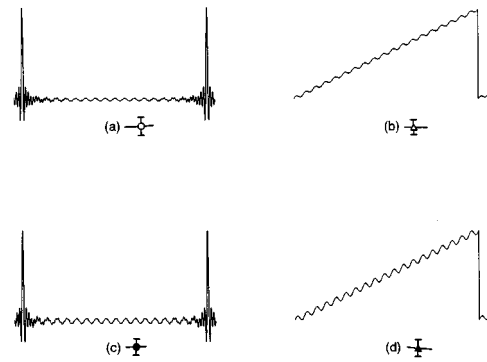


FIG. 3. Waveforms for experiment 2. (a) Waveform of a flat-spectrum cosine-phase complex tone with the 19th harmonic omitted; (b) sawtooth waveform with 19th harmonic omitted; (c) waveform of flat-spectrum cosine-phase complex tone with 19th harmonic phase inverted; (d) sawtooth waveform with 19th harmonic phase inverted. The damped high-frequency oscillations for flat-spectrum cases (a) and (c) are Gibbs phenomena from the upper end of the spectra. The high-frequency ends of the spectra were tapered to reduce this effect. Symbols with the letters are guides to Fig. 4.

number was reduced to 70, which had the effect of increasing the loudness of the DPE compared to the stimulus with 170 harmonics. All phase angles were again zero.

1. Spectra

Four spectra were used in this experiment. The illustrative waveforms are plotted in Fig. 3. Stimulus (a) was 70-component pulse train with one of its harmonics omitted. The amplitude spectrum was flat but tapered at the top to reduce the edge pitch. Stimulus (c) was the same as (a) except that the target harmonic was phase inverted instead of omitted. Therefore, there was no gap in the spectrum; the amplitude spectrum of (c) was identical to the amplitude spectrum of a pulse with all its harmonics equal.¹ For stimulus (c) the cancellation tone was 6 dB greater than in condition (a), and this fact can easily be seen in the waveform in Fig. 3(c). The oscillations between the pulses there have twice the amplitude as in Fig. 3(a). Stimulus (b) was a 70-component sawtooth wave with one of its harmonics omitted. The sawtooth wave is the integral of the pulse waveform (without its dc component), and so the amplitude of a harmonic in a sawtooth wave is inversely proportional to the harmonic number. For example, the 20th harmonic has twice the amplitude of the 40th. We expected to see a corresponding loudness variation in the DPE since the cancellation tone for different harmonic numbers has a different amplitude. Stimulus (d) was the same as stimulus (b) except that phase inversion replaced omission. The sawtooth waveforms were presented at the same level as the pulse train. Therefore, the original sawtooth waveform was given by

$$x(t) = - \sum_{n=1}^{70} \frac{6.552}{n} \sin(2\pi n f_0 t). \quad (9)$$

2. Results

The level experiment produced both pitch matching data and loudness matching data. The pitch matches were consistent, as expected for this range of harmonic numbers. The

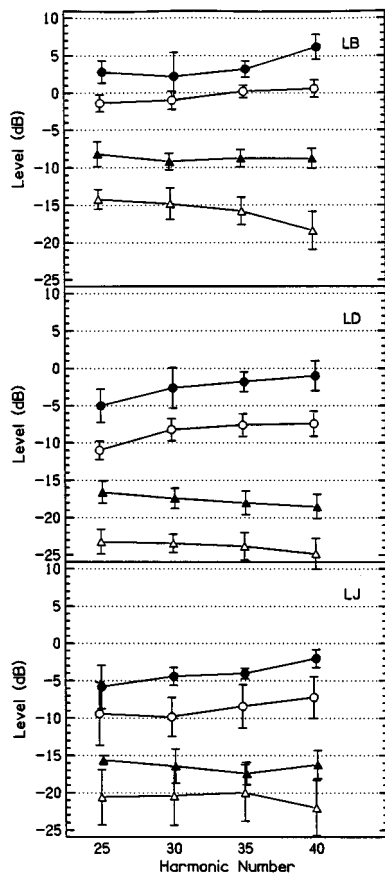


FIG. 4. Results of experiment 2. Each panel is for one subject. Matching levels of the DPE are plotted as a function of the harmonic number of the anomalous harmonic. Symbols identify waveforms *per* Fig. 3. Circle symbols are for a flat-spectrum pulse train, and triangles are for the sawtooth waveform. Open symbols are for omitted harmonics, and filled symbols are for phase-inverted harmonics. (Only relative levels for LD were available. The absolute levels shown here were adjusted *per* the analysis for LJ because early runs by LD and LJ were very similar.)

standard deviations were less than 1% of the matching frequency, and the pitch shifts were less than 2%. Of primary interest are the level matches, and these are shown in Fig. 4. There are three panels in the figure, one for each subject. The level matching scale on the vertical axis is in decibels referenced to the level of one component in a flat-spectrum complex tone, i.e., 45 dB SPL, corresponding to an amplitude of unity in Eq. (2).

For all three listeners, the relative level matches agree with the expected values for an objective cancellation tone. For both the flat spectrum and the sawtooth, the matches made with an inverted harmonic lie about 6 dB above the matches for the omitted harmonic. The average of the 24 differences is 5.4 dB (s.d.=1.5) to be compared with the expected value of 6 dB. Further, the matching levels for the sawtooth waveform agree with expectation when compared to the matching levels for the flat spectrum. The expected level differences (saw-flat) for n' values of 25, 30, 35, and 40 are, respectively: -11.6, -13.2, -14.6, and -15.7 dB. The measured values are -11.4 (1.0), -13.0 (1.9), -14.2 (2.2), and -16.3 (1.9) dB.

The absolute values of the level matches made by LB agreed with the actual level of the cancellation tones. Abs-

olute levels matched by LD and LJ were lower by about 8 dB. The difference is possibly caused by a different treatment of the loudness reduction due to partial masking among the listeners. Quite generally the data from the level experiment support the idea that the loudness of the DPE is determined by the level of the cancellation tone.

3. Further level tests

Informal experiments found that the level of the DPE can be matched by the best beats method, in which the listener adjusts the level of an added sine tone to maximize beats. However, the level range for best beats was found to be rather wide, as large as 4 dB, especially in the omitted-harmonic condition. As Duifhuis (1970) noted, it is significant that an added sine tone can form beats with the DPE because this implies an objective character for the cancellation tone.

The sawtooth waveform has a particular phase spectrum, where all ϕ_n are equal to 90 degrees. Informal experiments showed that a DPE could also be heard for other constant values of the phase. Then the base waveform no longer has the straight sides of the sawtooth, but the base waveform is smooth so that omitted or inverted harmonics are still apparent on an oscilloscope.

The integral of a sawtooth is a parabola wave (Hartmann, 1997), with amplitudes decreasing at 12 dB/octave. The triangle wave has odd harmonics with amplitudes that also decrease at 12 dB/octave; the waveform is composed of straight line segments like the sawtooth. When harmonics of these waveforms were either omitted or inverted, no DPE could be found.

D. Experiment 3: The effect of harmonic phases

The phases of the harmonics play a critical role in the DPE. Duifhuis (1972) found that if the phases are randomized no effect can be heard at all. The purpose of the experiments of this section was to determine the behavior of the DPE under several coordinated changes of phase.

1. Spectra of the stimuli

The formal pitch matching experiments used a 100-component complex tone with four different phase conditions: (a) All the harmonics were cosine phase ($\phi_n=0$). (b) All the harmonics were sine phase ($\phi_n=\pi/2$). (c) All the harmonics had a 45-deg initial phase ($\phi_n=\pi/4$). (d) The harmonics were in Schroeder phase (Schroeder, 1970). For an equal-amplitude complex tone Schroeder phases are given by the equation

$$\phi_n = -\frac{\pi}{N} n^2. \quad (3)$$

To create a DPE one harmonic was omitted. The omitted harmonic numbers were in the middle range, 40-70.

2. Results

The consistency in tuning a matching frequency was used to determine the existence and strength of the DPE. The consistency of matches showed that all three listeners could

hear the tone equally well in all four conditions. Frequency matching ratios for LB and LJ were in the range 1.00–1.02; for LD the range was 50% wider. Matching ratios increased somewhat with increasing harmonic number, and this tendency was greatest for the Schroeder phase condition. Otherwise, nothing special could be found in the matching frequencies or their variance to distinguish among the four phase conditions. The standard deviation of the ratio was about 0.005 for LB and LJ and about twice as large for LD.

For conditions (b) and (c), with common phase angles of 90° or 45°, the tone color of the background pulse became “fuller” than in condition (a) with zero phase. However, the DPE did not change. Waveforms made with different common phases are similar in that they all are quite spiky. They all have the same envelope with a temporal gap.

Unlike the other three waveforms, there is no time gap in the waveform with Schroeder phases. Therefore, no cancellation tone can be seen in an oscillographic representation of the waveform. Nevertheless, the experiments showed that the DPE exists. An explanation is proposed in the next section.

E. Additional phase effects

In addition to the formal phase experiments of the previous section, some informal phase experiments were done.

1. High and low omitted harmonics

We found it strange that the formal experiments revealed no difference between constant phase and Schroeder phase. Therefore, we performed informal matching experiments with omitted harmonics near 90 and 15 comparing cosine and Schroeder phases. No difference was found near harmonic 15, but the DPE was weaker for the Schroeder phase compared to cosine phase for omitted harmonics near 90, although this difference in strength was hardly noticeable in the matching data.

2. Low-fluctuation pulses

The Schroeder phase condition leads to a waveform with small power fluctuation. An alternative way to generate a waveform with small fluctuation is the low-noise noise method (Pumplin, 1985; Hartmann and Pumplin, 1991). Phase angles from the latter article were taken to make a signal having 36 equal-amplitude harmonics. Exploration with half a dozen values of n' found no DPE for either omitted or inverted harmonics. We conclude that the existence of the DPE for Schroeder phase is not solely the result of the small-fluctuation character of Schroeder-phase signals.

3. Random phases

When all the harmonics had random phases, the three listeners agreed that no DPE could be heard. In order to confirm this quantitatively, LB and LJ tried the matching experiment for ten different random-phase complex tones with omitted harmonics in the range 40–70. The results of their matches had a wide distribution. The average matching

frequency for a given omitted harmonic showed no correlation with the frequency of the omitted harmonic, verifying that no DPE exists.

4. Alternating phases

When all even-numbered harmonics had phases of 0 and all odd-numbered harmonics had phases of 90°, or vice versa (*per* Plomp and Steeneken, 1969), a DPE could easily be heard for omitted or inverted harmonics with numbers greater than 33 in informal experiments. We concluded that the change from constant phases to alternating phases affected the low-frequency end of the DPE but not the high-frequency end. Qualitatively such a result is not unexpected because a waveform with alternating phases has two evenly spaced spikes per cycle, hence quiet gaps between ringing responses are half as long.

F. Experiment 4: The missing-fundamental DPE

A famous result in pitch research is that a complex periodic tone in which the fundamental is absent nevertheless has a pitch equal to the fundamental frequency. We attempted to create a missing-fundamental pitch using the DPE. When harmonics 18, 24, and 30 of the 50-Hz fundamental are omitted or inverted, the spectrum of the cancellation tones resembles the 3rd, 4th, and the 5th harmonics of 300 Hz. Informal experiments showed that such stimuli produce a pitch at 300 Hz, clearly suggesting a missing-fundamental DPE. The following experiment was a formal test of this phenomenon using phase inversion. Because the amplitudes were unchanged by this experiment, the amplitude spectrum was simply that of a 100-component equal-amplitude cosine-phase pulse train.

1. Spectra of the stimuli

There were four different conditions, each of which inverted the phases of three harmonics: (a) harmonics 18, 24, and 30; (b) harmonics 27, 36, and 45; (c) harmonics 36, 48, and 60; and (d) harmonics 42, 56, and 70. These harmonics resemble the third, fourth, and fifth harmonics of 300, 450, 600, and 700 Hz, respectively.

2. Results

Results from the three listeners are plotted in Fig. 5. The scale on the vertical axis is the ratio of the matching frequency to the frequency of the missing fundamental. The plot shows that all the listeners could match the missing-fundamental frequency with good reproducibility. The actual matching ratios tend to be less than 1, especially for LB. This result can be compared with the measurements of Terhardt (1971) showing that the pitch of the missing fundamental of a complex tone is about 2% below the pitch of a sine tone with the frequency of the fundamental. LJ and LD show a shift that is less than 2%; LB shows a shift that is larger than 2%.

II. PERIPHERAL FILTER MODEL FOR THE DPE

The explanation for the DPE by Duifhuis (1970, 1971) is that when the frequency spacing between harmonics is considerably less than the bandwidth of relevant peripheral

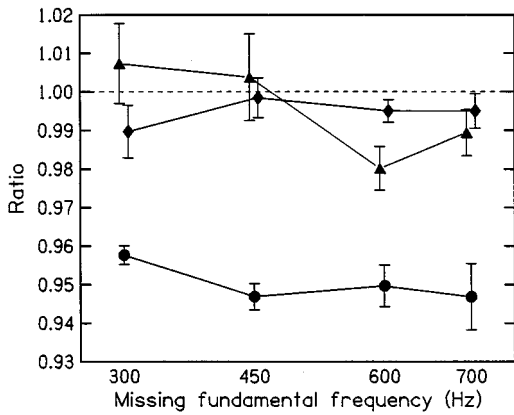


FIG. 5. Results of experiment 4. Matches to the missing fundamental tone are shown for each subject: circles for LB, triangles for LD, and diamonds for LJ. The matches are plotted as the ratio of matching frequency to missing-fundamental frequency.

auditory filters, the peripheral filters can be said to be broadband. A broadband frequency analyzing system has a short impulse response time, substantially less than the period of the input signal. Therefore, when the input is a pulse train with an omitted harmonic, there is a portion of time in each period during which the output of the peripheral filter is dominated by the small oscillations of the cancellation tone. That portion of the output in each period can be detected as a sine tone. A bank of such filters therefore produces a short-term frequency analysis of the input signal.

To get a clearer picture of the short-term frequency analysis, we implemented the idea with a realistic auditory filter bank—the gammatone filter bank (Patterson, 1987).

Figure 6 is a three-dimensional plot of the output of a gammatone filter bank. The bandwidths of the filters are determined by the ERBs from Glasberg and Moore (1990). The input to the filter bank is the 50-Hz complex tone with harmonics from 1 to 45. The x axis is a time axis. Its unit is the period of the input signal, 20 ms. Therefore, the plot shows exactly one period of the output. The y axis is the center frequency of a filter in the filter bank. The unit is chosen to be 50 Hz so that harmonics of the signal appear at integer values on this axis. Harmonic n appears at integer value n . The z axis shows the output, normalized to a maximum value of one. The output is half-wave rectified to improve the three-dimensional impression in the figure.

The response shown in Fig. 6 is essentially the impulse response of the auditory filter bank. Filters with a high center frequency, e.g., $26 \times 50 = 1300$ Hz, are relatively broad and have a short impulse response. There is a decided gap in their output. Filters with a lower center frequency, e.g., $10 \times 50 = 500$ Hz, have a longer ring time and no appreciable gap in their output.

Figure 7 is similar to Fig. 6 except that the 19th harmonic (950 Hz) of the input tone is omitted. Figure 7 shows a valley in the ringing region of the output, and a “peak” appears in the previously quiet region. This peak is actually the same response as would be obtained had the input been a 950-Hz sine tone. It is this peak that is the traditional explanation of the DPE.

The traditional explanation may also be applied to the DPE heard in the Schroeder-phase condition. The Schroeder phase leads to a frequency sweep (chirp) with the duration of a period. The sweep moves continuously from the highest frequency in the band to the lowest. Therefore, there is some

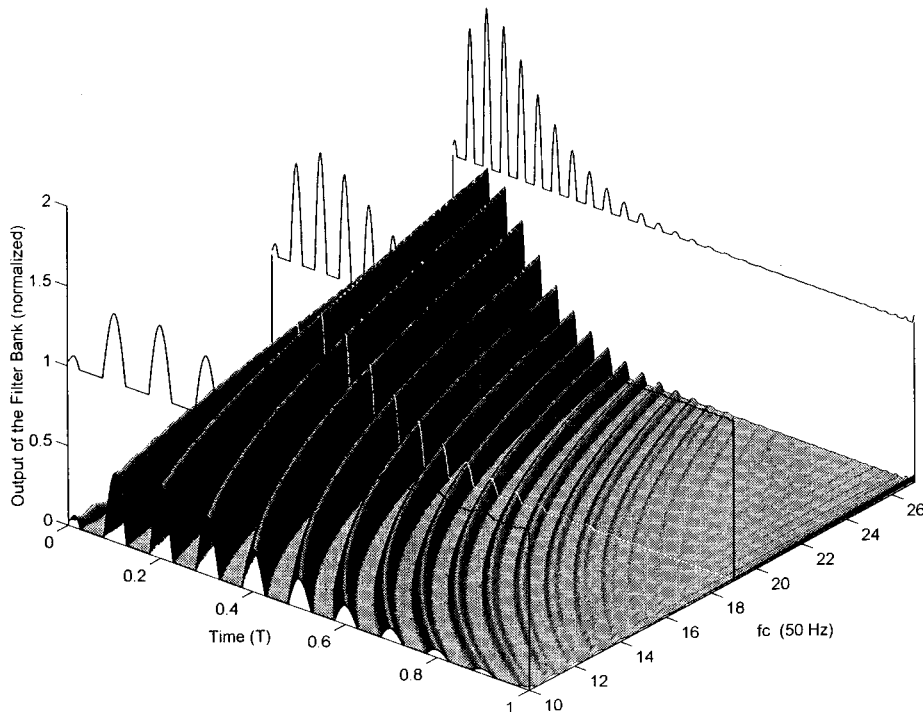


FIG. 6. Three-dimensional plot of the output of the model peripheral auditory filter bank. The input signal is a 45-harmonic flat-spectrum complex tone with a fundamental frequency of 50 Hz. All the harmonics have cosine phase. The elevated functions show the time-dependent outputs of model filters centered on reference harmonic numbers.

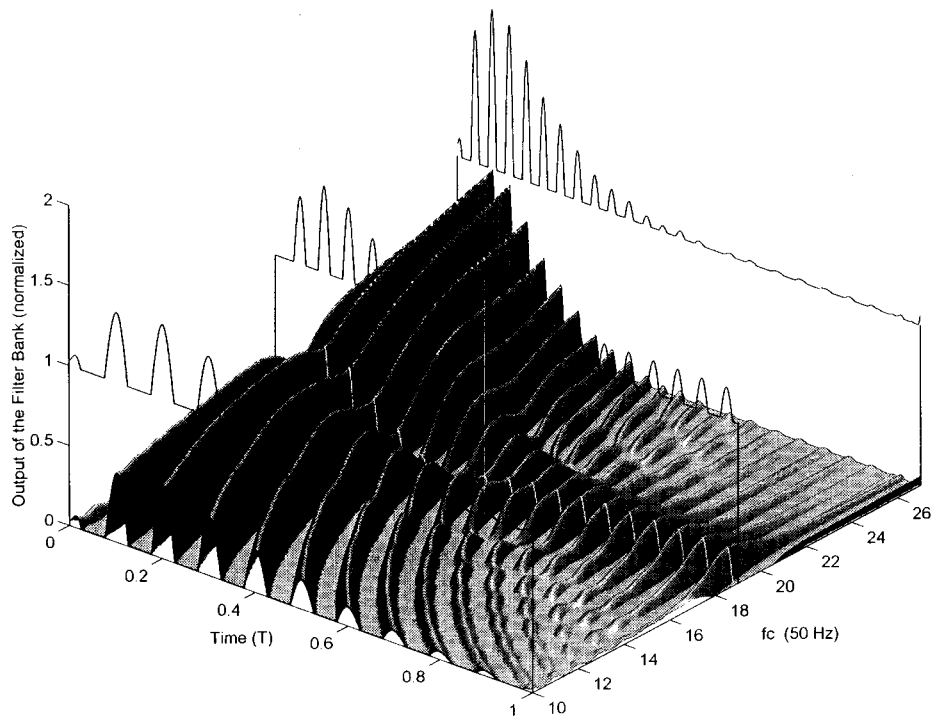


FIG. 7. Three-dimensional plot of the output of the model peripheral auditory filter bank. The input signal is the same as for Fig. 6 except that the 19th harmonic is omitted.

fraction of the period within which the instantaneous frequency of the stimulus differs greatly from the center frequency of any particular auditory filter. Therefore, there is a quiet gap in the temporal output of any auditory filter, but different filters experience the gap at different times within the signal period, as shown in Fig. 8. When a harmonic is omitted or inverted, a peak can appear across the quiet gap in the output of filters having their center frequencies in the range of the anomalous harmonic, as shown for an omitted

19th harmonic in Fig. 8. This transitory peak might well produce a DPE.

III. CHALLENGE TO THE PERIPHERAL FILTER MODEL OF THE DPE

According to the traditional explanation, the DPE is the result of the sine-tonelike peak in the quiet gap in the output of a peripheral filter bank. The challenge to this explanation

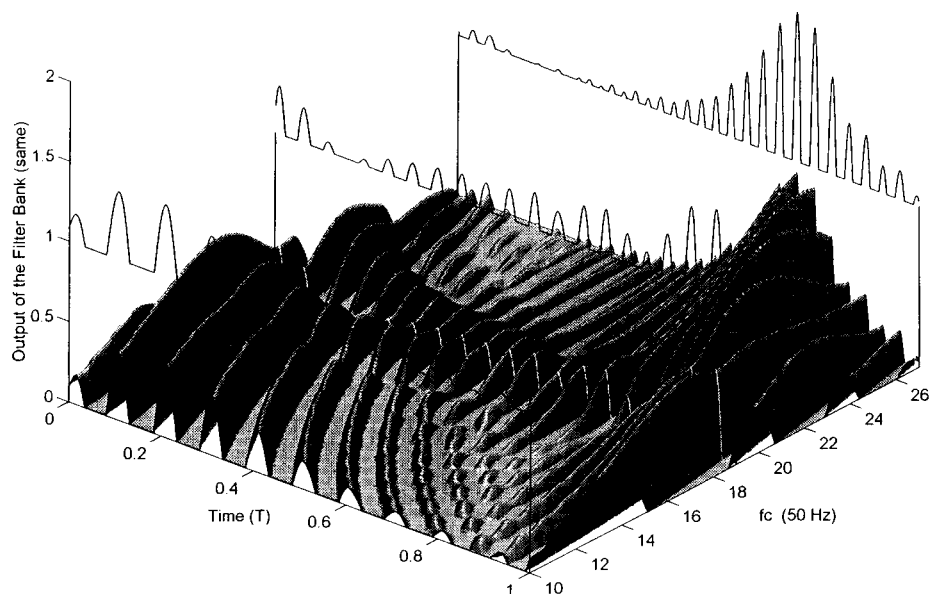


FIG. 8. Three-dimensional plot of the output of the model peripheral auditory filter bank when the harmonics of the complex tone are in Schroeder phase and the 19th harmonic is omitted.

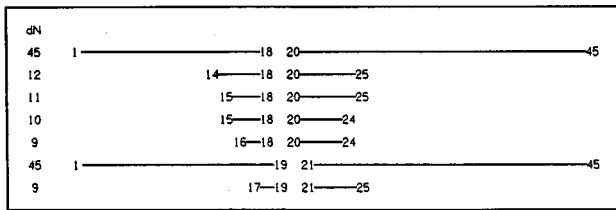


FIG. 9. The seven spectral bands for the band-narrowing experiment. For example, the fourth line shows the spectrum for $dN=10$ harmonic numbers in the band. They are harmonics 15–18 and 20–24, where 19 has been omitted.

begins with the observation that the peak involves only a limited number of harmonics. For the omitted 19th in Fig. 7, for example, only the harmonics in the range 17–22 make an important contribution. Therefore, it follows that if all the harmonics outside this range were removed, the DPE should be unchanged. It might even be stronger because there would be less competition from the other harmonics of the pulse train. The first of our challenge experiments systematically deleted harmonics outside the range of the omitted harmonic.

A. Experiment 5: Band narrowing

The band-narrowing experiment was a matching experiment like those previously described. However, because the central issue in the band-narrowing experiment was the existence of the DPE, we took particular precautions to avoid cuing a harmonic. Therefore, the listener was not allowed to alternate between the complex tone and the matching sine tone. The listener was allowed to listen to the complex tone as many times as he wanted, but once he decided to do the matching and heard a matching sine tone, he was not allowed to listen to the complex tone again. As a further precaution,

the sampling rate of the digital to analog converter was randomized by $\pm 5\%$ on each trial to reduce the possibility of cues across trials.

1. Complex tones

There were seven complex tones in the experiment. Five of them had an omitted 19th harmonic, and two had an omitted 20th. Their spectra are described by Fig. 9. Each harmonic had cosine phase and a level of 45 dB SPL as before. Therefore, the narrowed signals were bandpassed versions of the pulse-train signals used previously. The high and low edges of the spectrum were tapered (0.7, 0.3, as before). Figure 10 shows the effect of narrowing the spectrum in the output of the auditory filter bank. The input for Fig. 10 was the signal on the fourth line of Fig. 9 with $dN=10$ harmonics, numbers 15–24 with the 19th omitted. A comparison between the calculated output for Figs. 7 and 10 shows that the sine-tonelike peak in the filter centered on the 19th harmonic changes very little. We expect correspondingly little change in the DPE.

Each of the three listeners did 20 runs of the band-narrowing experiment. Each run required seven matches, one match for each of the complex tones in Fig. 9.

2. Results

The matching data for each listener and each complex tone were plotted in a histogram with its bin width equal to the harmonic spacing (50 Hz). The histograms for the broadband signals (harmonics 1–45) were concentrated on the omitted harmonic, indicating that listeners could easily hear the DPE. As the spectrum was narrowed, the histograms widened considerably, rapidly approaching half the bandwidth of the entire stimulus. The dependence of the 21 histograms in the experiment are here summarized in Fig. 11 by plotting the percentage of matches in the central histogram

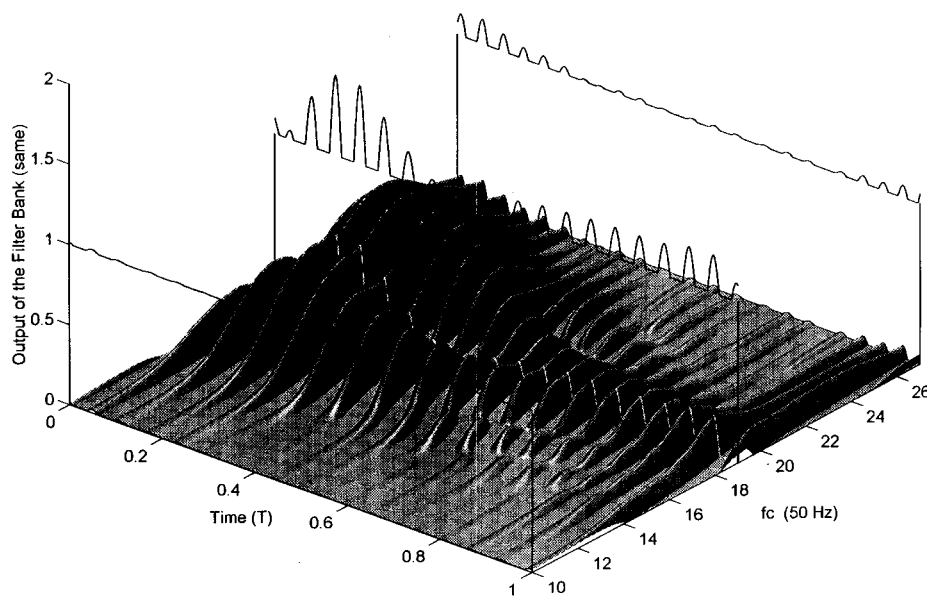


FIG. 10. Three-dimensional plot of the output of the model peripheral auditory filter bank. The input signal is the signal with $dN=10$ from Fig. 9, where all the harmonics, 15–24, have cosine phase, and the 19th harmonic is omitted. Therefore, the input signal was the same as in Fig. 7 passed through a bandpass filter. The region around harmonic 19 can be seen to be similar to Fig. 7, where the signal is broadband.

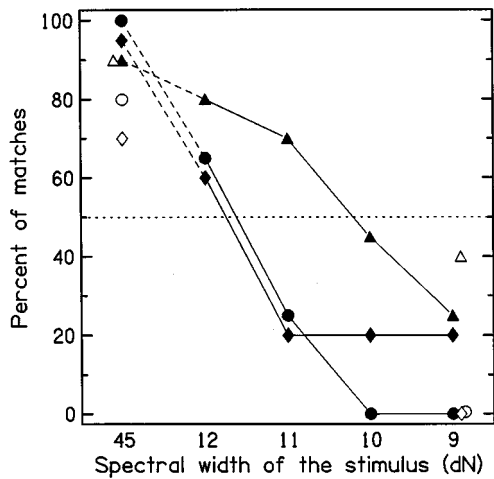


FIG. 11. Plots of the percentages of the matches to a missing 19th harmonic that are in the 19th harmonic bin as a function of the bandwidth of the stimulus. Circles are for LB, triangles are for LD, and diamonds are for LJ. Spectra for different values of dN are defined by Fig. 9. Open symbols are for the missing 20th harmonic.

bin (matching ratio=1) for the five complex tones with an omitted 19th harmonic. That is, the percentage of the matches that are closer to the 19th harmonic than to any other harmonic. Open symbols show the percentages for the omitted 20th harmonic, which serve as supplementary data. It is evident from Fig. 11 that as the band was narrowed, the listeners were unable to make accurate matches to the DPE.

For all the listeners the steepest slope in Fig. 11 occurs near the 50% point. Therefore, we define this as the boundary for hearing the DPE, i.e., if the number of matches in the central bin is greater than 50% of the total, the pitch is said to be “heard,” otherwise it is “not heard.” Applying this criterion to our results, we find that none of the listeners could hear the DPE for dN equal to 9 or 10 (*per* Fig. 10). This result came as no surprise to the listeners themselves; informally they remarked that no DPE was heard for these narrow bands. The conclusion of the band-narrowing experiment is that the peripheral filter model fails the challenge.

B. Experiment 6: Narrowing the phase-coherence region

Because the DPE exists with a broadband tone with constant harmonic phases but does not exist for random phases, there is another way to narrow the effective band of the stimulus. The narrowed-phase coherence-region (NPCR) experiment retained cosine phases for the harmonics near the omitted harmonic, but randomized the phases of all the other harmonics in the signal. Harmonics 1–45 all had unit amplitude, except for an omitted harmonic. The regions of cosine phase were exactly the spectral regions shown in Fig. 9. Thus, the NPCR experiment paralleled the band-narrowing experiment. The three listeners each did 20 runs using the protocol of the band-narrowing experiment.

1. Results

The matching data from the NPCR experiment were plotted in histograms like the data for the band-narrowing experiment. Unlike the matches in the band-narrowing experiment,

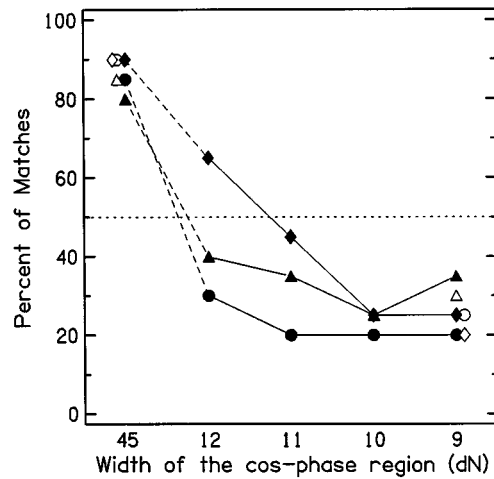


FIG. 12. Plots of the percentages of the matches to a missing 19th harmonic that are in the 19th harmonic bin as a function of the bandwidth of the phase coherence region. Circles are for LB, triangles are for LD, and diamonds are for LJ. Open symbols are for a missing 20th harmonic.

experiment, which were confined because of the narrowed stimulus spectrum, the matches in the NPCR experiment were spread over a very wide frequency range.

The percent of matches in the central bin for the omitted 19th harmonic is plotted in Fig. 12 as a function of the bandwidth of the cosine-phase region, dN . The percentage decreases as the bandwidth decreases. Again, defining 50% as the boundary, we find that none of the listeners could hear the pitch resulting from Duifhuis effect for dN equal to 9, 10, or 11. This result shows that phase information from components that are distant from the omitted harmonic is needed in order for the DPE to exist.

IV. DISCUSSION AND CONCLUSION

The Duifhuis pitch effect (DPE), as studied in this report, is created by starting with a low-frequency complex tone having many harmonics and then omitting a harmonic or inverting the phase of a harmonic. This spectral change is perceived as an added pure tone with a pitch equal to the frequency of the omitted or inverted harmonic. The traditional explanation for the DPE can be regarded as a two-step process. The first step considers the response of a broadband system to the stimulus, and the second step considers the circumstances in which the peripheral auditory system adequately approximates such a broadband system.

The first step essentially considers the waveform of the stimulus as it would appear on an oscilloscope. It establishes the general rule that to generate a DPE, the phases of the original complex tone must be chosen so that the waveform includes a quiescent time interval in which the omitted harmonic can be heard as a cancellation tone. The experiments by Duifhuis used a pulse train for the original complex tone. The experiments of Sec. I in the present report used a variety of original complex tones.

Many of the results from Sec. I were consistent with the cancellation tone concept. The DPE was found to exist when the waveform included some form of quiescent interval: flat-spectrum pulse with constant phase, sawtooth, Schroeder-

phase chirp, or alternating-phase pulse. The DPE was found not to exist in the absence of such characteristic time structure, specifically for random phases or phases producing minimum power fluctuation.

The continuation of the DPE well above 5 kHz makes it unlikely that the effect is caused by some aspect of neural timing because jitter causes neural synchrony to vanish above this frequency (Johnson, 1980; Pickles, 1982; Moore, 1973). The generation of a DPE by phase changes alone, while leaving the power spectrum unchanged (inverted harmonic case), rules out an explanation based on simple autocorrelation of the waveform. Instead, the effect appears to result from an objective cancellation tone. The good agreement between the loudness matches and the level of the cancellation tone for the different complex tones in experiment 2 supports this interpretation; so does the generation of a missing-fundamental DPE in experiment 4.

The second step in the traditional explanation of the DPE requires that the omitted or inverted harmonic be in a frequency range where the bandwidth of peripheral auditory filters is considerably greater than the fundamental frequency of the complex tone. Only then do the auditory filters contain enough harmonics to produce a quiescent time interval in which the cancellation tone can be heard. This idea predicts that the effect should exist only for harmonics too high to be resolved.

Experiments by Duifhuis (1972) found a low-frequency limit near the 10th harmonic for 50-dB, 50-Hz tones; experiment 1 of this report suggests a limit near the 15th. Calculations using gammatone auditory filters (Lin, 1996) show that a lower limit near 15 is not unreasonable for a 50-Hz tone. The observation (Duifhuis, 1972) that the low-frequency limit depends on level then suggests that the bandwidth of auditory filters increases significantly with increasing level. There is some evidence that the level dependence of bandwidth is particularly prominent for impulsive signals of this kind (Hartmann and Rakerd, 1993).

The band-narrowing experiments of Sec. III challenged the traditional explanation for the DPE because they showed that no DPE exists for narrowed-spectrum complex tones. By contrast, an auditory filter model shows that the cancellation tone in the quiescent interval is essentially the same for the narrowed-spectrum tones as for the broadband tones for which the DPE is always observed. Thus, although it seems to be *necessary* for auditory filters near the omitted harmonic to isolate the cancellation tone in a quiescent interval, it is not *sufficient*.

The band-narrowing experiments showed that the existence of the DPE depends on the presence of harmonics well outside the range of frequencies passed by auditory filters near the omitted harmonic. The DPE therefore appears to be a broadband effect in which information is combined across different auditory channels. What is especially notable is that this cross-channel combination must include phase information. Experiment 6 showed that the DPE requires phase coherence over a broad frequency region. Cross-channel phase comparison is an unusual idea in auditory theory. However, the phase coordination of separate channels by a broadband

impulsive signal does not seem implausible. Possibly even the nonsimultaneous, but regular, temporal pattern generated by Schroeder-phase signals could lead to a coordinated response.

ACKNOWLEDGMENTS

We are grateful to Dr. Hendrikus Duifhuis and Dr. Roy Patterson for helpful discussions. This work was supported by the National Institute on Deafness and Other Communicative Disorders, Grant No. DC00181.

¹Inversion can lead to amplitude spectrum changes if there is nonlinear distortion. The amplitude spectrum, measured at the headphones with a microphone, revealed no changes caused by inversion within the precision of our measuring process, 0.25 dB.

- Alcantara, J. I., and Moore, B. C. J. (1995). "The identification of vowel-like harmonic complexes: Effects of component phase, level and fundamental frequency." *J. Acoust. Soc. Am.* **97**, 3813–3824.
- Duifhuis, H. (1970). "Audibility of high harmonics in a periodic pulse," *J. Acoust. Soc. Am.* **48**, 888–893.
- Duifhuis, H. (1971). "Audibility of high harmonics in a periodic pulse. II. Time effect," *J. Acoust. Soc. Am.* **49**, 1155–1162.
- Duifhuis, H. (1972). "Perceptual analysis of sound," thesis, University of Eindhoven, The Netherlands, unpublished.
- Glasberg, B. R., and Moore, B. C. J. (1990). "Derivation of auditory filter shapes from notched noise data," *Hear Res.* **47**, 103–138.
- Hartmann, W. M. (1988). "Pitch perception and the segregation and integration of auditory entities," in *Auditory Function*, edited by G. M. Edelman, W. E. Gall, and W. M. Cowan (Wiley, New York), pp. 623–645.
- Hartmann, W. M. (1997). *Signals, Sound and Sensation* (AIP Press, New York).
- Hartmann, W. M., and Pumplin, J. (1991). "Periodic signals with minimal power fluctuations," *J. Acoust. Soc. Am.* **90**, 1986–1999.
- Hartmann, W. M., and Rakerd, B. (1993). "Auditory spectral discrimination and the localization of clicks in the sagittal plane," *J. Acoust. Soc. Am.* **94**, 2083–2092.
- Johnson, D. H. (1980). "The relationship between spike rate and synchrony in responses of auditory-nerve fibers to single tones," *J. Acoust. Soc. Am.* **68**, 1115–1122.
- Kubovy, M., and Jordan, R. (1979). "Tone segregation by phase: On the phase sensitivity of the single ear," *J. Acoust. Soc. Am.* **66**, 100–106.
- Klein, M. A., and Hartmann, W. M. (1981). "Binaural edge pitch," *J. Acoust. Soc. Am.* **70**, 51–61.
- Lin, J.-Y. (1996). "Psychoacoustical theory and experiments on human auditory organization of complex sounds and the critical bandwidth," thesis, Michigan State University, unpublished.
- McAdams, S. (1984). "The auditory image: A metaphor for musical and psychological research on auditory organization," in *Cognitive Processes in the Perception of Art* (North-Holland, Amsterdam).
- Moore, B. C. J. (1973). "Frequency difference limens for short duration tones," *J. Acoust. Soc. Am.* **54**, 610–619.
- Moore, B. C. J., and Glasberg, B. R. (1989). "Difference limens for phase in normal and hearing impaired listeners," *J. Acoust. Soc. Am.* **86**, 1351–1365.
- Patterson, R. D. (1987). "A pulse ribbon model of monaural phase perception," *J. Acoust. Soc. Am.* **85**, 1560–1586.
- Pickles, J. O. (1982). *An Introduction to the Physiology of Hearing* (Academic, London).
- Pierce, J. R. (1960). "Some work on hearing," *Am. Scientist* **48**, 40–45.
- Plomp, R., and Steeneken, H. J. M. (1969). "Effect of phase on the timbre of complex tones," *J. Acoust. Soc. Am.* **46**, 409–421.
- Pumplin, J. (1985). "Low-noise noise," *J. Acoust. Soc. Am.* **78**, 100–104.
- Schroeder, M. R. (1970). "Synthesis of low-peak-factor signals and binary sequences with low autocorrelation," *IEEE Trans. Inf. Theory* **IT-16**, 85–89.
- Terhardt, E. (1971). "Die Tonhöhe harmonischer Klänge und das Oktaveintervall," *Acustica* **24**, 126–136.
- Terhardt, E., and Fastl, H. (1971). "Zum Einfluss von Stortönen und Storgerauschen auf die Tonhöhe von Sinustönen," *Acustica* **25**, 53–61.

The relation between gap detection, loudness, and loudness growth in noise-masked normal-hearing listeners

Joseph W. Hall III and John H. Grose

The Division of Otolaryngology/Head and Neck Surgery, University of North Carolina Medical School, Chapel Hill, North Carolina 27599-7070

(Received 9 May 1996; accepted for publication 24 September 1996)

Gap detection was measured for 50 and 1000-Hz-wide noise markers arithmetically centered on 1000 Hz. The markers were presented in a lowpass background noise having a high-frequency cutoff of 2000 Hz. The pressure spectrum level of the background noise was either 0 or 40 dB/Hz. Gap detection was determined at sensation levels (SLs) of 10, 15, 20, and 30 dB in the 0-dB/Hz background, and at SLs of 10, 15, and 20 dB in the 40-dB/Hz background. Because loudness increased more steeply in the higher level noise background, the markers in the 40-dB/Hz background were at higher loudness (and at a steeper portion of the loudness growth function) than markers in the 0-dB/Hz background, for markers matched in terms of SL. The main goal of the experiment was to determine whether gap detection would be relatively poor at steep portions of the loudness growth function due to the gap being confused with ongoing random dips. Such confusion might be particularly great when the noise bandwidth was narrow (and therefore characterized by prominent fluctuation) and the growth of loudness was steep. Gap detection was poorer for the 50-Hz-wide marker than for the 1000-Hz-wide marker. For a given marker bandwidth at a given SL, gap detection was similar whether the marker was presented in the 0-dB/Hz noise or the 40-dB/Hz noise. Supplementary conditions indicated that (1) gap detection results for 50-Hz-wide markers presented at equal SL's were also similar between a 0-dB/Hz noise background and a 55-dB/Hz noise background, and that (2) gap detection for 50- and 1000-Hz-wide markers was poorer in a 40-dB/Hz background than in a 0-dB/Hz background when markers were matched for loudness. The results generally indicated similar gap detection thresholds for markers presented at similar SLs across a relatively wide range of background noise levels. Gap detection was related more closely to the marker-to-noise ratio than to the loudness relation between markers or the steepness of loudness growth. © 1997 Acoustical Society of America. [S0001-4966(97)01902-4]

PACS numbers: 43.66.Mk, 43.66.Cb [WJ]

INTRODUCTION

Several studies have indicated that temporal gap detection for noise markers can be relatively poor in listeners with hearing loss of cochlear origin (Buus and Florentine, 1985; Fitzgibbons and Wightman, 1982; Florentine and Buus, 1984; Glasberg and Moore, 1992; Grose *et al.*, 1989; Moore and Glasberg, 1988). Although reduced temporal gap detection in cochlear-impaired listeners can often be accounted for in terms of the reduced audibility of the stimulus (Buus and Florentine, 1985; Florentine and Buus, 1984), some instances of reduced gap detection performance appear to be related to poor analysis of the dynamic aspects of the stimulus waveform (Buus and Florentine, 1985; Glasberg and Moore, 1992; Glasberg *et al.*, 1987).

Gap detection may be particularly poor in cochlear-impaired listeners when the bandwidth of the noise marker is narrow (Glasberg and Moore, 1992; Moore and Glasberg, 1988), and therefore characterized by prominent, random fluctuation. Gap detection for narrowband noise markers may be difficult (even in normal-hearing listeners) because of the ambiguity in distinguishing the gap from the ongoing random dips in the noise. In cochlear hearing-impaired listeners, it has been hypothesized (Moore and Glasberg, 1992) that the effects of loudness recruitment augment the perceived amplitude fluctuations of the narrowband noise, mak-

ing the detection of the gap even more difficult than for a normal ear.

The present study examined gap detection in normal-hearing listeners using both a relatively wideband noise marker (associated with the perception of a relatively smooth sound) and a narrowband noise marker (associated with the perception of a highly fluctuant sound). In some conditions, stimuli were presented so that recruitmentlike effects were present, while in other conditions, stimuli were presented such that recruitmentlike effects were minimal. In conditions that did not result in a recruitmentlike effect, gap detection was expected to be poorer for the narrowband noise marker than for the wideband marker, for reasons related to perceived fluctuation. If loudness recruitment acts to amplify the perceived fluctuations of the stimulus, then the disparity in gap detection performance between wideband and narrowband noise is expected to be even greater in the conditions resulting in a recruitmentlike effect. Loudness recruitment was simulated by using a 40-dB/Hz background noise. The growth of loudness for stimuli presented in such a background noise is steeper than that which occurs in quiet (Gleiss and Zwicker, 1964; Hellman and Zwislocki, 1964; Scharf, 1964; Steinberg and Gardner, 1937; Stevens and Guirao, 1967). Testing was also conducted in a 0-dB/Hz

background noise, where recruitmentlike effects were expected to be minimal.

I. METHOD

A. Subjects

Six normal-hearing subjects, two male and four female, participated in gap detection measures. Five of these subjects also participated in measures of loudness growth. All subjects had participated previously in psychoacoustic experiments.

B. Conditions and procedure

1. Gap detection

The gap marker had a bandwidth of 50 Hz (where prominent fluctuations might be particularly troublesome under recruitmentlike conditions), or a bandwidth of 1000 Hz (where the smoother sounding stimulus might be relatively less troublesome under recruitmentlike conditions). Gaps were created by gating a wideband noise off and on abruptly (rise/fall time of approximately 10 μ s), and then passing the gated wideband noise through an IHR universal digital filter (Trinder, 1983) having a bandwidth of either 50 or 1000 Hz (Grose *et al.*, 1989). This procedure insures that cues related to "spectral splatter" are not available to the listener. The filtered noise bands were centered on 1000 Hz. The sampling frequency of the digital filter was 5 kHz. The filtering procedure essentially imposed a rise-fall time on the gap, the duration of which was inversely proportional to the bandwidth of the noise marker (Grose *et al.*, 1989). Each stimulus trial was composed of three 1-s intervals. In one interval, at random, a gap was introduced 500 ms after the beginning of the marker, and the gap duration was subtracted from the remainder of the marker. Intervals were separated by a 200-ms interstimulus interval. Visual feedback was provided after each response. The presentation order of conditions was random.

A 3AFC adaptive procedure was used to determine gap threshold. Gap size was varied by a factor of 1.2. Threshold estimates were based upon the geometric mean of the final eight reversals in a run. The threshold for a particular condition was the geometric mean of at least three (usually four) estimates. A background noise (0–2 kHz) was continuously present. The level of the background noise was either 0 or 40 dB/Hz SPL. Gap detection was determined as a function of the sensation level (above masked threshold) of the marker. Sensation levels of 10, 15, 20, and 30 dB were tested for the 0-dB/Hz background, and 10, 15, and 20 dB for the 40-dB/Hz background.

Detection thresholds were obtained using a 3AFC procedure to estimate 0 dB SL for the 50- and 1000-Hz-wide noise markers in each of the two background noise conditions (0- and 40-dB/Hz SPL). An initial step-size of 8 dB was reduced to 4 dB after two reversals, and further reduced to 2 dB after two more reversals. Each threshold run was stopped after 12 reversals, with the average of the last 8 reversals taken as the threshold for that run. Four thresholds were averaged to compute the final threshold.

2. Loudness growth

A measure of loudness growth was also obtained in order to confirm the expectation that loudness growth would be relatively steeper in the 40-dB/Hz background noise than in the 0-dB/Hz background noise, and to obtain measurements that could provide approximate loudness ratings for the stimuli used in the gap detection experiment. The LGOB (loudness growth in $\frac{1}{2}$ -oct bands) measure of loudness growth (Allen *et al.*, 1990) was used for this purpose. Allen *et al.* found that the LGOB method was an efficient method of measuring loudness growth and loudness recruitment. They also suggested that line segment fits to the LGOB data appeared to be functionally equivalent to more time-consuming sone functions. In our implementation of the LGOB method, the threshold level and the uncomfortable listening level (both in dB SPL) for a 600-ms stimulus (20-ms rise/fall) burst were first determined (Allen *et al.*, 1990). The stimulus was a 50-Hz-wide noise band or 1000-Hz-wide noise band arithmetically centered on 1000 Hz [we used stimuli like those used in the gap detection study rather than the $\frac{1}{2}$ -oct band noises used by Allen *et al.* (1990)]. The range between the threshold level and the discomfort level was then divided into 15 steps, equispaced on a dB scale. The fifteen different levels were presented in a quasi-random order, such that each level was presented three times during a run. Four runs were undertaken for each condition, resulting in 12 judgments at each of the 15 stimulus levels of each condition. The stimulus was gated on three times in each presentation, with a 200-ms pause between stimulus bursts. After each stimulus presentation, the listener rated the loudness of the sound on a scale from 0 to 6. Ratings of 0, 1, 2, 3, 4, 5, and 6 corresponded to judgments of "did not hear," "very soft," "soft," "ok," "loud," "very loud," and "too loud," respectively. Measurements were performed in both the 0- and the 40-dB/Hz noise backgrounds. Loudness measures were obtained from five of the six subjects. In all experiments and conditions, stimuli were delivered via Sony MDR-V6 headphones.

II. RESULTS AND DISCUSSION

A. Loudness

We used "the response-average level" method of Allen *et al.* (1990) to determine the SPL values corresponding to the loudness categories between 1 and 5. Values for the extreme categories (0 and 6) are not determined because the stimulus levels in this range are necessarily limited by the procedure. The values were similar across listeners, and average data are shown in Table I. An obvious finding was that loudness growth was steeper in the 40-dB/Hz background than in the 0-dB/Hz background. For example, the range between very soft to very loud was spanned by about 60–65 dB in the 0-dB/Hz background, but by only about 30 dB in the 40-dB/Hz background. Thus, for a given SL, the loudness was higher in the 40-dB/Hz background. Whereas the 10–20 dB SL markers were associated with loudness in the "very soft" to "soft" regions for the 0-dB/Hz noise back-

TABLE I. Average (over five subjects) SPL values corresponding to loudness ratings from 1–5. The intersubject standard deviations are shown in parentheses.

| | 0-dB/Hz background | | | | | 40-dB/Hz background | | | | |
|---------|--------------------|----------------|---------------|---------------|---------------|---------------------|---------------|---------------|---------------|---------------|
| | 1 | 2 | 3 | 4 | 5 | 1 | 2 | 3 | 4 | 5 |
| 50 Hz | 30.9
(4.8) | 56.4
(6.9) | 75.8
(2.9) | 88.1
(2.5) | 94.8
(2.9) | 64.5
(2.9) | 76.0
(2.9) | 85.0
(2.3) | 91.7
(2.1) | 96.0
(3.5) |
| 1000 Hz | 31.9
(9.7) | 55.7
(10.5) | 75.9
(6.9) | 88.1
(3.0) | 93.5
(3.5) | 68.1
(3.1) | 78.2
(2.8) | 85.7
(2.3) | 92.0
(1.5) | 95.7
(1.7) |

ground, the same SLs were more typically associated with loudness in the “soft” to “ok” regions for the 40-dB/Hz background.

Past research has shown that a wideband noise is generally louder than a narrowband noise when both bands are presented at a moderate or high fixed SPL (Cacace and Margolis, 1985; Zwicker *et al.*, 1957). Although the present study was not intended to examine this question specifically, the data obtained are relevant. Interestingly, the present data indicate that a particular loudness rating was usually associated with a similar SPL for a 50-Hz wide noise and a 1000-Hz wide noise (see Table I). Launer (1995) did report evidence of loudness summation for band-limited noise stimuli that were rated for loudness on a categorical scale. However, the range of bandwidths used in his study (210–1880 Hz wide) was quite different than that used in the present study. Further research using the LGOB method, specifically examining the effect of noise bandwidth, would be useful.

B. Gap detection

In agreement with previous studies (Buus and Florentine, 1985; Fitzgibbons, 1983; Plomp, 1964), gap detection

generally improved with increasing SL, for both masking noise bandwidths and at both background noise levels (see Fig. 1). Also, as expected, gap detection was better for the 1000-Hz-wide noise marker than for the 50-Hz-wide marker. The question of central interest to the present investigation concerned comparisons in performance between the 0-dB/Hz background noise condition and the 40-dB/Hz background noise condition. The loudness growth measures (see Table I) indicated that loudness grew more steeply with increasing stimulus level in the 40-dB/Hz noise than in the 0-dB/Hz background noise. However, at matched SLs, gap detection performance was typically no worse under conditions associated with a recruitmentlike effect (40-dB/Hz background), than under the low-level masking condition. In fact, at relatively low SLs, some listeners showed slightly better performance in the 40-dB/Hz background (see Fig. 1). Masked detection thresholds for the noiseband markers are shown in Table II.

Fitzgibbons (1984) also examined gap detection in normal-hearing listeners, using various levels of background masking noise. In contrast to the present study, Fitzgibbons used only a relatively wideband noise marker, an octave-wide noise band centered on 1000 Hz. Comparing results for background noise levels of 12, 32, and 47 dB/Hz, Fitzgibbons found that a criterion level for gap detection performance was obtained at relatively lower SLs as the masking

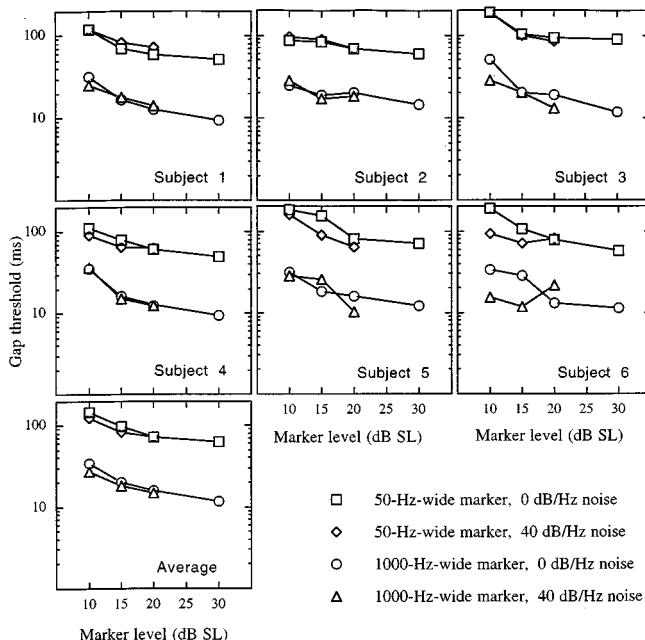


FIG. 1. Gap detection thresholds as a function of SL for the 50- and 1000-Hz-wide markers presented in the 0- and 40-dB/Hz noise backgrounds.

TABLE II. Individual and average detection thresholds (dB SPL) for the 50- and 1000-Hz-wide markers presented in the 0- and 40-dB/Hz noise backgrounds. Numbers in brackets are intrasubject standard deviations for individual data and intersubject standard deviations for average data.

| | 50-Hz-wide marker | | 1000-Hz-wide marker | |
|----------------|-----------------------------|-----------------------------|-----------------------------|-----------------------------|
| | 0-dB/Hz background | 40-dB/Hz background | 0-dB/Hz background | 40-dB/Hz background |
| Subject 1 | 18.0
(0.5) | 60.3
(1.2) | 23.6
(1.0) | 65.8
(0.6) |
| Subject 2 | 22.2
(1.2) | 62.2
(1.3) | 27.0
(1.5) | 68.1
(1.4) |
| Subject 3 | 19.7
(1.3) | 62.0
(0.5) | 23.0
(1.3) | 66.8
(0.4) |
| Subject 4 | 16.7
(1.0) | 59.0
(0.7) | 22.0
(1.2) | 63.0
(1.9) |
| Subject 5 | 18.7
(1.4) | 60.0
(0.9) | 26.0
(1.1) | 66.2
(1.4) |
| Subject 6 | 17.2
(0.4) | 59.4
(0.8) | 25.0
(0.7) | 67.6
(0.1) |
| Average | 18.8
(2.0) | 60.5
(1.3) | 24.3
(1.9) | 66.2
(1.8) |

TABLE III. Data for conditions where markers were presented at levels determined from alternate binaural loudness matches to 40- and 60-dB SPL reference stimuli. The table shows the bandwidth of the marker (in Hz), the marker to noise ratio (I/N_0 in dB), the approximate SL of the marker (in dB), and the gap detection threshold (in ms).

| Sub. | BW | 40-dB reference level | | | 60-dB reference level | | | 40-dB reference level | | | 60-dB reference level | | |
|------|------|-----------------------|------|------|-----------------------|------|------|-----------------------|------|-------|-----------------------|------|-------|
| | | I/N_0 | SL | Gap | I/N_0 | SL | Gap | I/N_0 | SL | Gap | I/N_0 | SL | Gap |
| 1 | 50 | 45.3 | 27.3 | 49.9 | 57.7 | 39.7 | 53.4 | 31.5 | 11.2 | 96.9 | 35.5 | 15.2 | 92.0 |
| 2 | 50 | 40.0 | 17.8 | 68.6 | 58.5 | 36.3 | 58.7 | 27 | 4.8 | 177.5 | 33.5 | 11.3 | 103.3 |
| 1 | 1000 | 44.5 | 20.9 | 10.8 | 56.2 | 32.7 | 11.0 | 33.0 | 7.2 | 41.5 | 37.2 | 11.6 | 22.6 |
| 2 | 1000 | 39.0 | 12.0 | 20.3 | 58.2 | 31.2 | 16.4 | 30.7 | 2.6 | 48.0 | 37.2 | 9.1 | 24.8 |

noise level increased. Whereas most of the present data are consistent with an interpretation that gap detection is similar at similar SLs, some of the present data did indicate slightly better performance in the higher than the lower level background masking noise when markers were presented at equivalent SLs. This indicates a degree of agreement between the present study and that of Fitzgibbons (1984). However, the trend for gap detection performance to improve with increasing background noise level appears to be more consistent in the study of Fitzgibbons.

C. Supplementary conditions examining gap detection at equal, low loudness

It is of interest to determine whether markers that are associated with similar loudnesses also are associated with similar gap detection thresholds. This question is not particularly pertinent for relatively high loudness because of the likelihood of being near the asymptote for gap threshold. However, the question is pertinent for relatively low loudness, where gap detection threshold is still improving with increasing marker level. The data in the main experiment indicated that similar gap detection thresholds occurred for the 0-dB/Hz noise background and the 40-dB/Hz noise background when the markers were presented at matched, relatively low, SLs. Because the markers were at a higher loudness in the 40-dB/Hz noise background than the 0-dB/Hz noise background (for comparisons made at equal SLs), it follows that, for markers of relatively low equal loudness, gap detection would be worse in the higher level background. To examine this question directly, we determined gap thresholds in the 0-dB/Hz noise and the 40-dB/Hz noise for markers that were matched for loudness.

Whereas it is possible to estimate equal loudness levels across the two background noise levels from the data obtained in the LGOB procedure of the main experiment, such estimates might be regarded as imprecise due to the relatively coarse nature of the rating scale. Therefore, a binaural method of adjustment was used to obtain loudness matches. In this method, the standard (40 or 60 dB SPL in level) was presented to the right ear, and, 300 ms later, the level-adjustable target was presented to the left ear. Both the standard and the target were 600 ms in duration with 20-ms rise/fall times. Following stimulus presentation, the subject pressed one button to make the target louder on the next presentation, and another button to make the target softer. The button press initiated a new trial. The subject was in-

structed to bracket the equal loudness point (by alternately adjusting the target to be louder and softer than the standard) before converging upon the point of equal loudness judgment. The subject pressed a third button when satisfied that a loudness match had been made. This procedure was carried out both for a 50-Hz-wide noise band centered on 1000 Hz, and a 1000-Hz-wide noise band centered on 1000 Hz. The 40 or 60 dB SPL standard was always presented in quiet, and the target was presented either in the 0-dB/Hz background noise or the 40-dB/Hz background noise. The standard and target always had the same bandwidth. Gap detection was then determined for the 50- and 1000-Hz-wide markers presented in either the 0- or 40-dB/Hz noise backgrounds. In each case, the marker was set to the level corresponding to the loudness match that had been obtained previously. Two subjects (subject 1 and subject 2) participated.

The hypothesis investigated in this experiment was that gap detection for a narrowband noise marker might be worse in the 40-dB/Hz noise than in the 0-dB/Hz noise for reasons related to the relatively steeper growth of loudness in the higher level background noise. Table III indicates that markers presented at equal, relatively low loudness resulted in poorer gap detection in the 40-dB/Hz noise background than in the 0-dB/Hz background. One might interpret this poorer performance in the higher level noise background as being related to loudness growth. However, there are at least two considerations that make such an interpretation questionable. One is that the loudness-growth hypothesis is associated with a prediction of a larger effect for the narrowband marker than for the wideband marker (see Introduction). The data of Table III indicate that gap detection was poorer in the 40-dB/Hz background than in the 0-dB/Hz background by similar factors for both the narrowband marker (by a factor of approximately 2.0 across subjects and conditions) and for the wideband marker (by a factor of approximately 2.4 across subjects and conditions). The second consideration is that the marker-to-noise ratio probably provides a sufficient explanation for the relatively poorer gap detection performance in the 40-dB/Hz background noise (see Table III). For the 50-Hz-wide noise band, I/N_0 was about 40–58 dB in the 0-dB/Hz background (SLs ranging from about 18–40 dB), but was only about 27–35 dB in the 40-dB/Hz background (SLs ranging from about 5–15 dB). For the 1000-Hz-wide noise band, I/N_0 was about 39–58 dB in the 0-dB/Hz background (SLs ranging from about 12–33 dB), but was only about 31–37 dB in the 40-dB/Hz background (SLs ranging

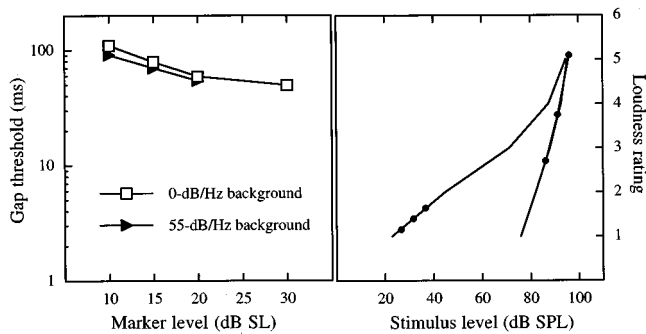


FIG. 2. The left panel shows gap detection data for the 50-Hz-wide marker presented in the 0-dB/Hz noise background and in the 55-dB/Hz noise background. The right panel shows the loudness growth line segments obtained in the 0-dB/Hz noise (left-hand function) and in the 55-dB/Hz noise (right-hand function). The dots placed on the functions indicate the SPLs at which the 10, 15, and 20-dB gap markers were presented in the gap detection condition.

from about 3–12 dB). Thus, the gap detection findings of this supplementary experiment are in good agreement with previous results, indicating an improvement in gap detection with increasing marker level (Plomp, 1964).

D. Supplementary conditions examining gap detection in 55-dB/Hz background noise

Most of the present data indicated that gap detection was similar in the 0- and 40-dB/Hz noise backgrounds, when markers were presented at similar SLs. This finding does not support the idea that gap detection should be poorer in the 40-dB/Hz background, due to an effect related to steep loudness growth (recruitmentlike effect). One possibility, however, is that the 40-dB/Hz background noise level was too low to result in a sufficiently steep loudness growth function. To assess this possibility, one of the subjects (subject 4) was run on additional conditions using a background noise level of 55 dB/Hz (88 dB SPL overall). Because an effect of recruitment was expected to be more likely for the 50-Hz-wide marker than the 1000-Hz-wide marker, loudness growth and gap detection conditions were run only for the 50-Hz-wide marker. Figure 2 summarizes the loudness growth and gap detection results for these conditions (gap detection results for the 0-dB/Hz noise background are also shown to aid comparison). The gap detection results indicated very similar performance between the 0- and 55-dB/Hz noise backgrounds, despite the fact that loudness growth was considerably steeper in the 55-dB/Hz background (see Fig. 2).

III. GENERAL DISCUSSION

The main issue investigated in this study was whether performance for a narrowband marker (50-Hz-wide noise-band) would be particularly poor under conditions of relatively steep loudness growth. When markers were presented at relatively low, matched SLs, performance was generally similar between the high-level noise background (40 dB/Hz) and the low-level noise background (0 dB/Hz). Similar results were found for the limited conditions repeated with a background noise level of 55 dB/Hz.

The correspondence between gap detection and loudness was not strong. Gap detection was not comparable for markers in 0 and 40-dB/Hz backgrounds when stimuli were matched to the loudness of 40 or 60 dB SPL standards. Here, performance was worse in the higher-level noise background. It is likely that the poor gap detection performance in the 40-dB/Hz background was due to the relatively low signal-to-noise ratio that was associated with these conditions.

The overall findings of this study do not support a relation between steep loudness growth and gap detection where the steep loudness growth is produced by background noise. This result could be interpreted as undermining the suggestion that loudness recruitment contributes to poor gap detection in cochlear hearing-impaired listeners. However, it is also possible that loudness recruitment does have a deleterious effect on gap detection in cochlear-impaired listeners, but that the “recruitment-like effect” that occurs in partial masking of normal ears is functionally *dissimilar* to the loudness recruitment associated with cochlear hearing loss. For example, it has been demonstrated that whereas physiological correlates of loudness recruitment can be seen at the level of the auditory nerve in cases of cochlear hearing loss, such effects are not seen until higher levels of auditory processing in cases of masking simulation (Phillips, 1987).

In conclusion, the use of masking noise to simulate hearing loss and associated recruitment does not result in a deleterious effect on gap detection. However, it remains to be determined whether loudness recruitment in hearing-impaired listeners may affect gap detection in some manner that is not adequately simulated by testing normal-hearing listeners in a background masking noise.

ACKNOWLEDGMENTS

This research was supported by a grant (R01DC00418) from NIH NIDCD. Two reviewers, Mary Florentine and Peter Fitzgibbons, provided helpful criticisms of a previous version of this manuscript. We thank Rhona Hellman and Brian Moore for helpful suggestions. We thank Debora Hatch for helpful discussion and technical contributions.

- Allen, J. B., Hall, J. L., and Jeng, P. S. (1990). “Loudness growth in $\frac{1}{2}$ -octave bands (LGOB)—a procedure for the assessment of loudness,” *J. Acoust. Soc. Am.* **88**, 745–753.
- Buus, S., and Florentine, M. (1985). “Gap Detection in normal and impaired listeners: The effect of level and frequency,” in *Time Resolution in Auditory Systems*, edited by A. Michelsen (Springer-Verlag, New York).
- Cacace, A. T., and Margolis, R. H. (1985). “On the loudness of complex stimuli and its relationship to cochlear excitation,” *J. Acoust. Soc. Am.* **78**, 1568–1573.
- Fitzgibbons, P. J. (1983). “Temporal gap detection in noise as a function of frequency, bandwidth and level,” *J. Acoust. Soc. Am.* **74**, 67–72.
- Fitzgibbons, P. J. (1984). “Temporal gap resolution in masked normal ears as a function of masker level,” *J. Acoust. Soc. Am.* **76**, 67–70.
- Fitzgibbons, P. J., and Wightman, F. L. (1982). “Gap detection in normal and hearing-impaired listeners,” *J. Acoust. Soc. Am.* **72**, 761–765.
- Florentine, M., and Buus, S. (1984). “Temporal gap detection in sensorineural and simulated hearing impairment,” *J. Speech Hear. Res.* **27**, 449–455.
- Glasberg, B. R., and Moore, B. C. J. (1992). “Effects of envelope fluctuations on gap detection,” *Hear. Res.* **64**, 81–92.

- Glasberg, B. R., Moore, B. C. J., and Bacon, S. P. (1987). "Gap detection and masking in hearing-impaired and normal-hearing subjects," *J. Acoust. Soc. Am.* **81**, 1546–1556
- Gleiss, N., and Zwicker, E. (1964). "Loudness function in the presence of masking noise," *J. Acoust. Soc. Am.* **36**, 393–393.
- Grose, J. H., Eddins, D. A., and Hall, J. W. (1989). "Gap detection as a function of stimulus bandwidth with fixed high-frequency cutoff in normal-hearing and hearing-impaired listeners," *J. Acoust. Soc. Am.* **86**, 1747–1755.
- Hellman, R. P., and Zwislocki, J. (1964). "Loudness function of a 1000-cps tone in the presence of a masking noise," *J. Acoust. Soc. Am.* **36**, 1618–1627.
- Launer, S. (1995). "Loudness perception in listeners with sensorineural hearing impairment," Doctoral dissertation, University of Oldenburg.
- Moore, B. C. J. and Glasberg, B. R. (1988). "Gap detection with sinusoids and noise in normal, impaired and electrically stimulated ears," *J. Acoust. Soc. Am.* **83**, 1093–1101
- Moore, B. C. J. and Glasberg, B. R. (1992). "Simulation of the effects of loudness recruitment on temporal resolution," *Br. J. Audiol.* **26**, 195.
- Phillips, D. P. (1987). "Stimulus intensity and loudness recruitment: Neural correlates," *J. Acoust. Soc. Am.* **82**, 1–12.
- Plomp, R. (1964). "Rate of decay of auditory sensation," *J. Acoust. Soc. Am.* **36**, 277–282.
- Scharf, B. (1964). "Partial masking," *Acustica* **14**, 16–23.
- Steinberg, J. C. and Gardner, M. B. (1937) "The dependence of hearing impairment on sound intensity," *J. Acoust. Soc. Am.* **9**, 11–23.
- Stevens, S. S., and Guirao, M. (1967). "Loudness functions under inhibition," *Percept. Psychophys.* **2**, 459–465.
- Trinder, J. R. (1983). "Hardware–software configuration for high performance digital filtering in real time," *Proc. IEEE Int. Conf. Acoust. Speech Sig. Process.* **2**, 687–690.
- Zwicker, E., Flottorp, G., and Stevens, S. S. (1957). "Critical bandwidth in loudness summation," *J. Acoust. Soc. Am.* **29**, 548–557.

Monaural sound localization revisited

Frederic L. Wightman

Department of Psychology and Waisman Center, University of Wisconsin—Madison, Madison, Wisconsin 53705

Doris J. Kistler

Waisman Center, University of Wisconsin—Madison, Madison, Wisconsin 53705

(Received 23 February 1996; revised 2 August 1996; accepted 25 September 1996)

Research reported during the past few decades has revealed the importance for human sound localization of the so-called “monaural spectral cues.” These cues are the result of the direction-dependent filtering of incoming sound waves accomplished by the pinnae. One point of view about how these cues are extracted places great emphasis on the spectrum of the received sound at each ear individually. This leads to the suggestion that an effective way of studying the influence of these cues is to measure the ability of listeners to localize sounds when one of their ears is plugged. Numerous studies have appeared using this monaural localization paradigm. Three experiments are described here which are intended to clarify the results of the previous monaural localization studies and provide new data on how monaural spectral cues might be processed. Virtual sound sources are used in the experiments in order to manipulate and control the stimuli independently at the two ears. Two of the experiments deal with the consequences of the incomplete monauralization that may have contaminated previous work. The results suggest that even very low sound levels in the occluded ear provide access to interaural localization cues. The presence of these cues complicates the interpretation of the results of nominally monaural localization studies. The third experiment concerns the role of prior knowledge of the source spectrum, which is required if monaural cues are to be useful. The results of this last experiment demonstrate that extraction of monaural spectral cues can be severely disrupted by trial-to-trial fluctuations in the source spectrum. The general conclusion of the experiments is that, while monaural spectral cues are important, the monaural localization paradigm may not be the most appropriate way to study their role. © 1997 *Acoustical Society of America*. [S0001-4966(97)02902-0]

PACS numbers: 43.66.Qp, 43.66.Pn, 43.66.Yw [RHD]

INTRODUCTION

While human sound localization is generally acknowledged to be a process that depends predominately on acoustical stimulation of both ears, the study of monaural sound localization has captured the interest of hearing scientists since the turn of the century (Angell and Fite, 1901). In the past three decades, for example, more than 25 empirical studies have been published that deal explicitly with monaural localization. These studies are typically motivated by referring to weaknesses in the well-entrenched “duplex theory” of sound localization (Strutt, 1907). This theory holds that the apparent position of a sound is determined entirely by interaural time and level differences (ITDs and ILDs, respectively). It has been clear for some time that there are essential features of human sound localization that cannot be explained by ITDs and ILDs alone. That localization does not seem to be dramatically impaired on the median plane, where ITDs and ILDs are minimal, is one obvious example. The direction-dependent filtering provided by the pinnae is now acknowledged to be one of the most salient of the localization cues not incorporated in the duplex theory. Pinna filtering provides spectral shape cues at each ear individually, and the monaural localization paradigm, which typically requires normal hearing listeners to localize sound sources while one ear is plugged, is used as a way of studying how these monaural spectral cues are processed.

The monaural localization paradigm has some significant weaknesses that lead us to question the extent to which the results of such experiments can inform us about the mechanisms and processes that subserve sound localization in normal binaural conditions. The first problem is that complete “monauralization” of a listener is difficult to achieve, and this leads to the choice of very low stimulus levels (20–30 dB SL) in most monaural localization studies. While it is difficult to know the amount of attenuation provided by the typical “plug and muff” used in monaural localization studies, it is almost certainly lowest in the low frequencies. Given the documented importance of low frequencies for determining the extent to which listeners rely on ITD cues (Wightman and Kistler, 1992), a small amount of low-frequency energy leaking through the “plug and muff” could complicate interpretation of the results considerably. An additional complication is that sound will reach the occluded ear via bone conduction, and while the bone-conducted components would be more than 45 dB below the air-conducted sound at all frequencies (e.g., Hood, 1962), they cannot be ignored at high stimulus levels. Also, given the importance of both the low frequencies (for ITD coding) and the high frequencies (where monaural spectral cues are represented), the use of very low overall stimulus levels to circumvent the leakage and bone conduction issues is problematic. If the stimulus is wideband, its threshold would be

determined primarily by the mid frequencies, where the auditory system is most sensitive. Thus, an overall stimulus level of 30 dB SL would limit the availability of cues at low and high frequencies, since these frequencies would be close to or below threshold. The second problem is that while monauralization is usually described as “removing” ITD and ILD cues, thus forcing listeners to attend to monaural spectral cues, it is probably more accurate to say that monauralization produces very unnatural ITD and ILD cues. Plugging one ear obviously causes a large ILD. It is an unnatural localization cue because the pattern of ILD across frequency produced by a plug is very different from that produced by a real sound source at any position in auditory space. The effect of monauralization on ITD is less obvious, but it seems just as appropriate to describe it as producing an infinite ITD as to say it removes ITD altogether. In any case, the result of monauralization is a situation in which the monaural spectral cues are usually in conflict with (i.e., signal different spatial positions) one or both of the interaural difference cues. Whether or not listeners will attend to the former and disregard the latter may depend on other factors such as task variables (range of stimulus positions and response alternatives, experience, expectation, context) or stimulus frequency content (bandwidth, low-frequency content, trial-to-trial spectral uncertainty). A third complicating factor in previous studies of monaural localization is the frequent emphasis on localization *accuracy*, typically measured by the extent to which a listener successfully identifies the specific loudspeaker in a small set of loudspeakers that actually produced the stimulus. Localization accuracy can be a useful metric, but in some conditions, monaural listening being one of them, reporting accuracy alone conceals large perceptual or response biases. For example, it is often reported that monaural localization accuracy is high for sources directly opposite the functioning ear and low for sources in front or behind. While true, the statement obscures the fact that the apparent origin of nearly all sounds heard monaurally is pulled strongly toward the unoccluded ear. Thus, accurate localization on the unoccluded side may be little more than an epiphenomenon produced by the large perceptual bias. Because of the issues raised above, it is difficult to interpret the results of many previous monaural localization studies as reflecting the salience of monaural spectral cues in normal binaural localization.

Monaural spectral cues are produced by the directionality of pinna filtering. Since the characteristics of pinna filtering change dramatically with changes in source position, those characteristics could potentially serve as cues (monaural spectral cues) to source position. The viability of monaural spectral cues depends on a listener’s ability both to extract the pinna filtering characteristics from an incoming sound and to associate those characteristics with the appropriate source position. The latter process is usually thought to involve some form of comparison between the extracted pinna characteristics and a set of templates or feature lists stored in memory (e.g., Middlebrooks, 1992). Whether the stored representations of pinna characteristics are built up through experience or hard wired in the neural circuitry is not of concern here. However, there is ample evidence for

the existence of some kind of stored representation that links apparent sound position and pinna characteristics.

Extraction of pinna filtering characteristics from an incoming sound requires knowledge of the spectrum of the sound source. The spectrum of a sound at the eardrum is the product of the pinna filter and the source spectrum. Thus, the only way a listener could deconvolve the two in order to process the characteristics of the pinna filter is by knowing the spectrum of the source. It is clearly unreasonable to postulate that listeners know, in any precise sense, the spectra of all potential sounds. However, it may not be unreasonable to suggest that laboratory experiments which require listeners to localize a noise burst or click, the spectrum of which is simple and constant for many trials, may offer listeners an opportunity to learn the source spectrum. In everyday life, when the source spectrum is uncertain and highly variable, listeners may make certain assumptions about the source spectrum in order to accomplish the deconvolution.

A large body of work on monaural localization shows that under certain circumstances information about sound source position is extracted from the sound at one ear. This clearly suggests that the auditory system is deconvolving from the sound transduced at the eardrum the separate contributions of the sound source and the pinna filtering. Whether the deconvolution is based on assumptions about or prior knowledge of source characteristics is unclear. Some studies, such as those in which narrow bands of noise were used as the stimulus (Belendiuk and Butler, 1977; Butler and Flannery, 1980; Flannery and Butler, 1981; Musicant and Butler, 1984, 1985; Butler, 1986), suggest that assumptions are made about the source spectrum. Others, such as those in which a white noise was the stimulus. (Oldfield and Parker, 1986; Butler *et al.*, 1990), are inconclusive, since white noise, which has a flat spectrum with minimal trial-to-trial spectral uncertainty, may allow listeners to learn the source spectrum. The fact that some process like deconvolution can occur to extract monaural spectral cues is an important result that emerges from past work on monaural sound localization.

Another important finding contributed by previous monaural localization experiments is that in certain conditions some or all features of monaural localization are nearly normal, as if the listener was binaural. For example, when the sound source is on the side of the functioning ear, the elevation component of the apparent position is near normal (Oldfield and Parker, 1986; Butler *et al.*, 1990; Slattery and Middlebrooks, 1994). With long-term experience, some monaural listeners, such as the unilaterally deaf listeners studied by Slattery and Middlebrooks (1994), demonstrate near normal localization in both azimuth and elevation components and not only on the side of the functioning ear, but on the side of the occluded ear as well. Clearly these listeners have learned sophisticated strategies for extracting and processing the monaural spectral cues.

The research described here revisits the monaural localization paradigm. Our purpose is not only to address some of the problems with the earlier work, but also to use the monaural paradigm to learn more about how the monaural cues contribute to normal binaural localization. The hallmark of our approach is the use of the virtual sources, i.e., sounds

presented over headphones that include nearly all of the spatial attributes of sounds presented in free field and that evoke realistic, externalized spatial percepts (Wightman and Kistler, 1989a, b). The use of virtual sources provides considerably more interaural attenuation than a plug for monaural presentation (see below for data on this point) and allows for stimulus configurations not possible with real sources. The experiments described below will exploit these advantages.

Three experiments are described. The first measures the apparent positions of both real and virtual sources in monaural listening conditions. This is essentially a replication of previous work, with the added feature that in the virtual source conditions monaural stimuli are intermingled with binaural stimuli in an attempt to promote natural binaural localization strategies. The second experiment explores the influence of the spectral uncertainty of the stimulus to be localized in monaural listening conditions. The rationale is that some degree of spectral uncertainty is always present in everyday listening conditions, and this spectral uncertainty must interfere with a listener's ability to extract monaural spectral cues. The third experiment examines the influence on apparent position judgments of increasing amounts of unilateral attenuation. The aim of this experiment is to better understand the effects of various degrees of monauralization (such as obtained with a plug or over headphones).

I. GENERAL METHOD

A. Listeners

University of Wisconsin students participated as paid listeners in these experiments. Selection criteria consisted of normal hearing (as verified by complete audiometric exam), clean ear canals, and willingness to participate for 4–6 h per week for at least a semester. There were different numbers of listeners in each experiment; not all listeners participated in all three experiments. Most of the listeners were experienced, having participated in other localization experiments conducted in this laboratory.

B. Stimuli

In order to produce the virtual sources, a set of head-related transfer functions was measured on each listener. The measurement procedure was nearly identical to that described by Wightman and Kistler (1989a); the reader is referred to the earlier article for complete details. In short, a small (1-mm-diam) probe tube was held in position close to the listener's eardrum, while a wideband periodic noise test stimulus was presented from a loudspeaker. A microphone connected to the probe tube recorded the response to the test stimulus and a computer averaged the responses to multiple periods to improve signal-to-noise ratio. The two ears were measured simultaneously and the HRTFs from 266 source positions (roughly evenly spaced on the sphere, at 15° azimuth intervals all around the listener and at 12° elevation intervals from -48° to +72° relative to the horizontal plane) were measured during a single session. The transfer characteristics of the headphones used in the experiments (Sennheiser HD430) were measured in a similar way on each listener.

The procedures used to produce the virtual sources used as stimuli in these experiments were identical to those described in a previous publication (Wightman and Kistler, 1989a), so they will only be summarized here. A virtual source is synthesized by passing the desired stimulus (in these experiments a noise burst) through a pair of digital filters. Each digital filter consists primarily of the listener's own HRTF for the desired source position and ear divided by the headphone characteristic for that listener and ear. The result is two stimulus waveforms, one for each ear, which when presented simultaneously to the listener over the headphones produce an externalized sound image at an apparent spatial position very close to that which would have been produced by the comparable free-field source (Wightman and Kistler, 1989b).

The basic stimulus in all the experiments was a 250-ms noise burst with 20-ms cosine-squared on/off ramps. The noise was bandpassed between 200 Hz and 14 kHz and in the passband its spectrum was either flat or "scrambled." The scrambled spectrum was produced by randomizing the noise spectrum level within each critical band from trial-to-trial (uniform distribution, 20-dB or 40-dB range). Thus, in the case of 20-dB scrambling, adjacent critical bands could differ in level by as much as 20 dB. The noise burst was repeated four times on each trial with 300 ms of silence between the bursts. In free-field conditions the stimulus was presented from one of 12 small loudspeakers (Realistic Minimus 3.5) mounted on a vertical semicircular arc (as described in Wightman and Kistler, 1989b), at 12° elevation intervals. Since the arc could be rotated around the listener, the free-field stimulus could be presented from any azimuth and from one of 12 elevations ranging from -48 to +72. In virtual source conditions the stimulus was presented over Sennheiser headphones (HD 430). The overall stimulus level in both free-field and virtual source conditions was approximately 70 dB SPL.

C. Procedure

In free-field conditions listeners were seated in the anechoic chamber with their heads at the center of the loudspeaker arc and asked to keep their heads as still as possible. In the virtual source conditions, listeners were tested either in the anechoic chamber or in an IAC soundproof chamber. In both conditions the listeners were blindfolded. The task required listeners to report verbally, using standard spherical coordinates, the apparent azimuth and elevation (in degrees) of each stimulus immediately following the four noise bursts. In some, but not all, of the virtual source conditions, a few listeners were also asked to report apparent source distance in feet. A short training session was used to familiarize the listeners with the coordinate system. This session was conducted informally outside the anechoic chamber and included visual and auditory cues and feedback. Following the familiarization session, listeners were given about 6 h of experience listening and responding to free-field stimuli before any data were taken. No feedback was given either during this "training" phase or during any of the experimental conditions. A single 1.5-h session typically involved 180 trials, presented in 5 blocks of 36. All stimulus conditions were

constant during a block, but could be changed between blocks. In many of the virtual source conditions, the test stimuli, which were either monaural or otherwise abnormal, were “interlaced” with normal stimuli. The normal stimuli were virtual sources with all the natural localization cues intact. The interlacing was random so that on any one trial there was a 0.5 probability of a test stimulus and a 0.5 probability of a normal stimulus being presented. At least eight blocks of trials were completed by each listener in each test condition. In conditions in which test stimuli were interlaced with normal stimuli, 16 blocks per condition were completed.

D. Data analysis

Data from localization experiments frequently include substantial numbers of what have come to be known as “front-back” confusions. These are responses indicating a perceived position in the front hemifield (azimuths between -90 on the left and $+90$ on the right) for a rear hemifield (azimuths from -90 to -180 on the left and between 90 and 180 on the right) target position. Given the roughly conical symmetry of the ITD cue such confusions are not entirely unexpected (cf. the “cone of confusion” described in Mills, 1972). However, the rate of front-back confusions varies considerably from listener to listener and from condition to condition (Wightman and Kistler, 1989b, Makous and Middlebrooks, 1990), and it is often difficult to distinguish between confusions and true error variance (e.g., for target positions near $+90^\circ$ and -90° azimuth). Consequently, analysis of apparent position data is problematic. Our choice is to avoid measures of central tendency and variability (which would be inappropriate with bimodal response distributions) and to restrict analysis of the data to the descriptive level. Thus, we display the raw data and draw conclusions on the basis of the appearance of those displays.

Data are displayed, condition by condition and listener by listener, on a three-pole coordinate system (Kistler and Wightman, 1992). Thus, each individual response is represented by a point on three separate graphs. The azimuth component of the response is decomposed into a “left-right” component and a “front-back” component, each expressed in degrees and plotted in separate graphs. The left-right component is the angle between the judgment vector and the median plane, and the front-back component is the angle between the judgment vector and the transverse plane (the vertical plane that goes through the ears). The elevation component of each response is plotted untransformed and is called the up-down component. In this coordinate system the extremes on each of the three dimensions are represented similarly, by angles of $+90^\circ$ and -90° .

II. EXPERIMENT 1: MONAURAL LOCALIZATION OF REAL AND VIRTUAL SOURCES

The general conclusion of all recent studies of monaural localization is that apparent azimuth is dramatically affected by the monauralization and apparent elevation is less affected (Oldfield and Parker, 1986; Butler *et al.*, 1990; Slattery and Middlebrooks, 1994). Apparent azimuth is pulled

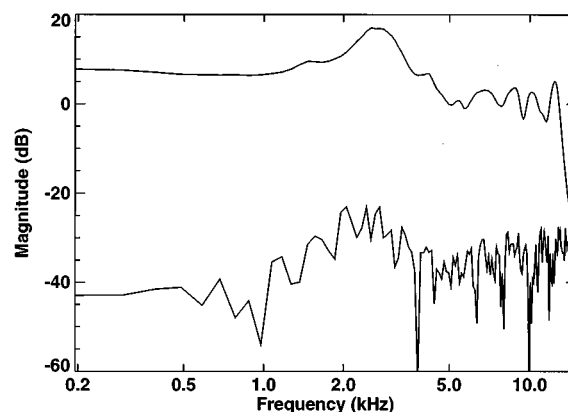


FIG. 1. The magnitude spectrum of a virtual monaural flat-spectrum noise stimulus measured in the ear canals of a representative listener. The upper curve shows the measurement made in the stimulated ear and the lower curve shows the measurement made in the nonstimulated ear. The nonstimulated ear measurements are obviously corrupted by the noise level of the measuring system (and sound room) which had a spectrum level of approximately -40 dB on this scale.

strongly toward a position directly opposite the open ear. While only one of these experiments (Slattery and Middlebrooks, 1994) evaluated the effect of monauralization on apparent positions of sources on the occluded side, the azimuth effect there was the same as on the unoccluded side. Our first experiment constitutes a replication of the essential features of the previous studies with both free-field and virtual sources.

A. Method

All general aspects of stimulus generation and presentation and listener response were as described above. There were six conditions in this experiment, four free-field conditions involving real sources, and two virtual source conditions. Of the four free-field conditions, two involved binaural listening, one at an overall stimulus level of approximately 70 dB SPL, and one at an overall level 40 dB lower. The other two free-field conditions required listeners to localize with the left ear occluded. Occlusion was accomplished in the usual way by plugging the ear with an EAR compressible foam plug, and covering it with a muff (EAR NRR26). Stimuli for the two “monaural” free-field conditions were at the same levels (about 70 dB SPL and 40 dB lower) as in the comparable binaural conditions. The two virtual source conditions involved binaural and monaural stimulus presentation (achieved by disconnecting the left headphone) at an overall level of approximately 70 dB SPL. In the monaural virtual source condition, monaural stimuli were interlaced with binaural stimuli as described above.

The monaural virtual source condition achieves excellent isolation of the nonstimulated ear, probably better than is possible with any plug-muff combination in the free field. Figure 1 shows measurements of ear canal sound pressure produced by a flat-spectrum noise stimulus in both the stimulated and nonstimulated ears of a typical listener in this experiment. Note that even at low frequencies the isolation exceeds 50 dB. This analysis does not consider the influence of bone-conducted sound which would effectively reduce the

TABLE I. Listener participation in the test conditions of experiment 1.

| Conditions | | | Listeners | | | | | | | | | |
|------------|----------|----|-----------|-----|-----|-----|-----|-----|-----|-----|-----|-----|
| | Level | | SDL | SDO | SDP | SER | SET | SGE | SGG | SHD | SHG | SIK |
| | dB SPL | | | | | | | | | | | |
| Free field | Binaural | 70 | X | X | X | X | X | X | X | X | X | X |
| Free field | Binaural | 30 | X | | | | | X | X | X | | X |
| Free field | Monaural | 70 | X | X | X | | | X | X | X | X | X |
| Free field | Monaural | 30 | X | | X | | | X | X | X | X | X |
| Virtual | Binaural | 70 | X | X | X | X | X | X | X | X | X | X |
| Virtual | Monaural | 70 | X | X | X | X | X | X | X | X | X | X |

isolation at the lowest frequencies to about 40 dB (Hood, 1962). Thus, with the 70 dB SPL stimulus, which would have a spectrum level of less than 30 dB, the level in the nonstimulated ear is close to or below threshold at all frequencies. The plug-muff combination conventionally used to monauralize listeners cannot be expected to produce the same degree of isolation, especially at low frequencies.

The spectra of the noise-burst stimuli in this experiment were scrambled in an effort to approximate the spectral uncertainty typical of everyday listening. The scrambling was as described previously (Wightman and Kistler, 1989b). In this experiment the level in each critical band was randomized (from trial to trial) within a 20-dB range. The potential effect of this spectral scrambling on monaural localization is the subject of experiment 2.

Because the experiment was conducted over a long period of time, not all listeners participated in all conditions. However, we feel that enough listeners participated in each condition to represent the full range of individual differences we observed. Ten listeners in all were tested and Table I lists the conditions in which each listener participated. Six of the ten listeners contributed distance judgments in the virtual source conditions. No distance judgments were obtained in the free-field conditions since these were run before distance reporting was implemented.

B. Results

The data from the high level (70 dB SPL) binaural conditions are unremarkable, and data from comparable conditions have been described before (Wightman and Kistler, 1989b). The apparent positions of free-field sources match their actual positions reasonably well, with the exception of a few front-back confusions and greater variance in the up-down dimension than in the other two dimensions. The results from the virtual source condition are nearly identical to those from the free-field condition, attesting to the adequacy of the simulation. Figure 2 shows the results from a typical listener in the high-level binaural conditions.

The high level monaural conditions produced several intriguing results. In contrast to the binaural conditions, the monaural conditions revealed considerable individual differences. Figures 3 and 4 show data from two listeners (SGG and SIK, respectively) that represent the range of performance we obtained from the listeners who participated in these conditions. Note that in the case of the monaural free-

field condition, responses to sources on the side of the open ear are plotted separately from the responses to the sources on the occluded side.

It is clear that, in general, localization as reflected by the match between target and response position is degraded in the monaural condition. One obvious effect is that the variance of the responses is much larger in the monaural conditions. A second is that in many cases the responses do not cluster along the major diagonal. In these cases there is little correspondence between target and response positions. In the free-field conditions, this is true primarily for listener SGG (Fig. 3). Note that for this listener, on both the open and

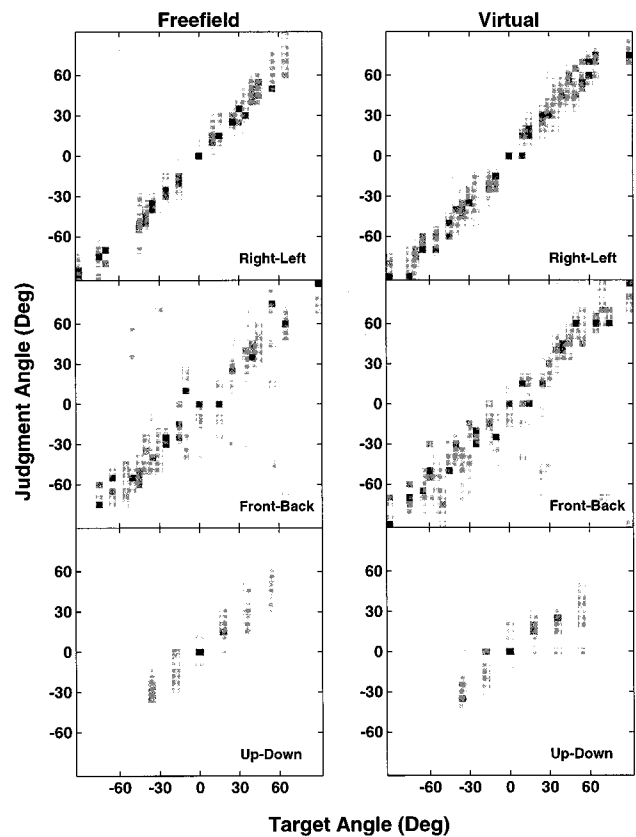


FIG. 2. Scatter plots of judged direction versus target direction from a typical listener in the high-level binaural condition of experiment 1. As described in the text, the judged and target directions are represented in terms of three angles, right-left, front-back, and up-down. Each data cell includes all the judgments within a 5° wide interval. The darker the cell, the more judgments represented in that cell. The lightest cells represent a single judgment. There are at least 288 judgments shown in each panel.

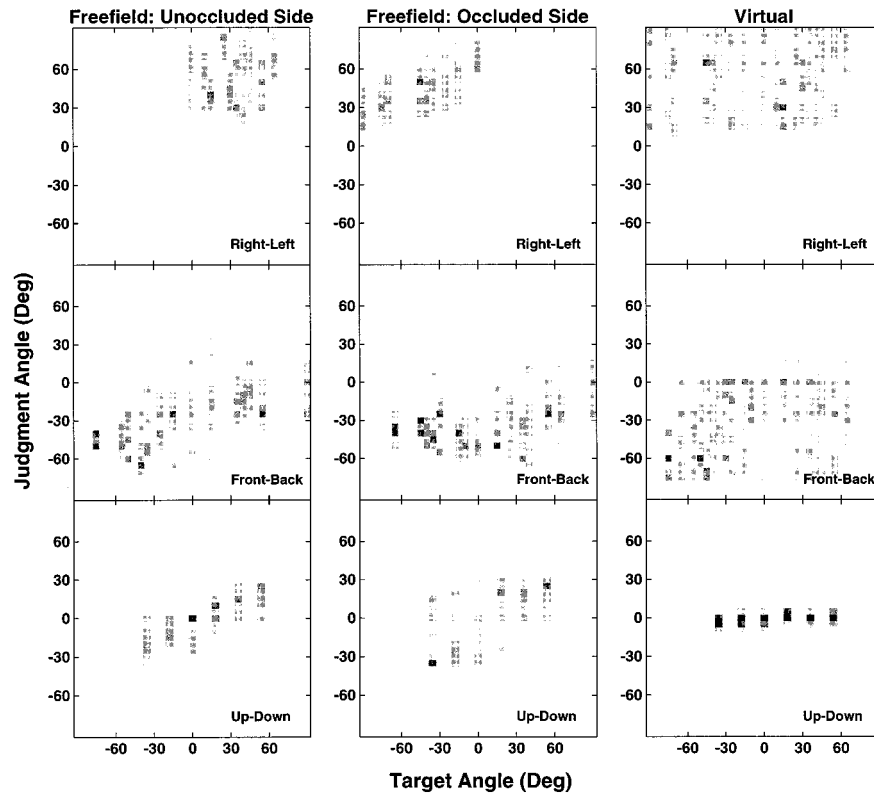


FIG. 3. Scatter plots of data from listener SGG in the high-level monaural conditions. Note that in the case of stimuli presented in free field, responses to stimuli on the occluded and unoccluded sides are plotted separately.

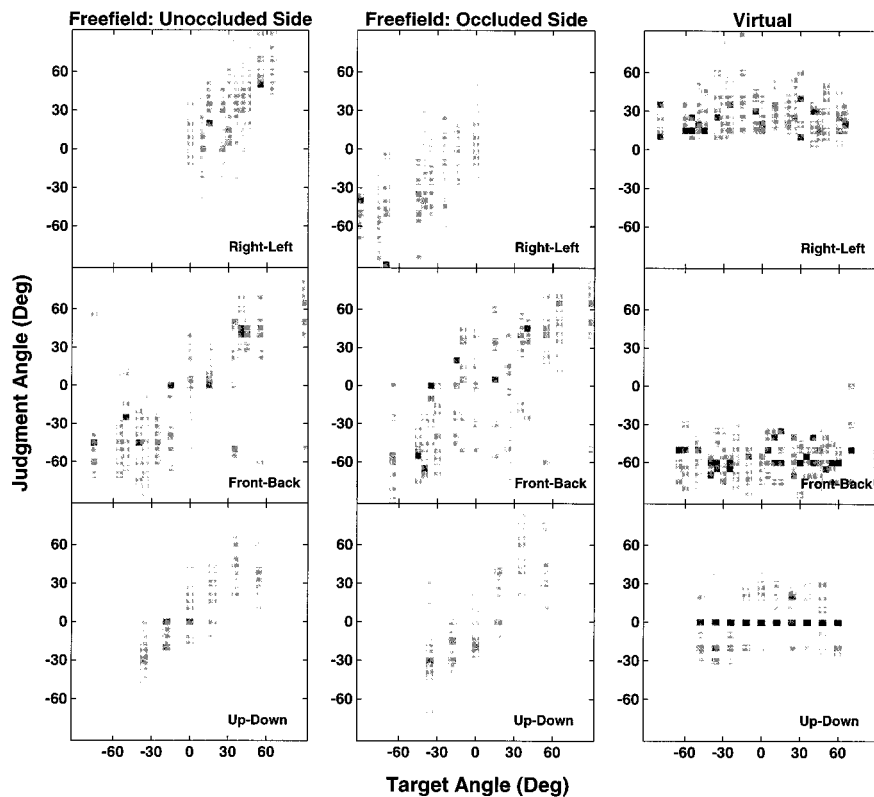


FIG. 4. Same as Fig. 3, but data are from listener SIK.

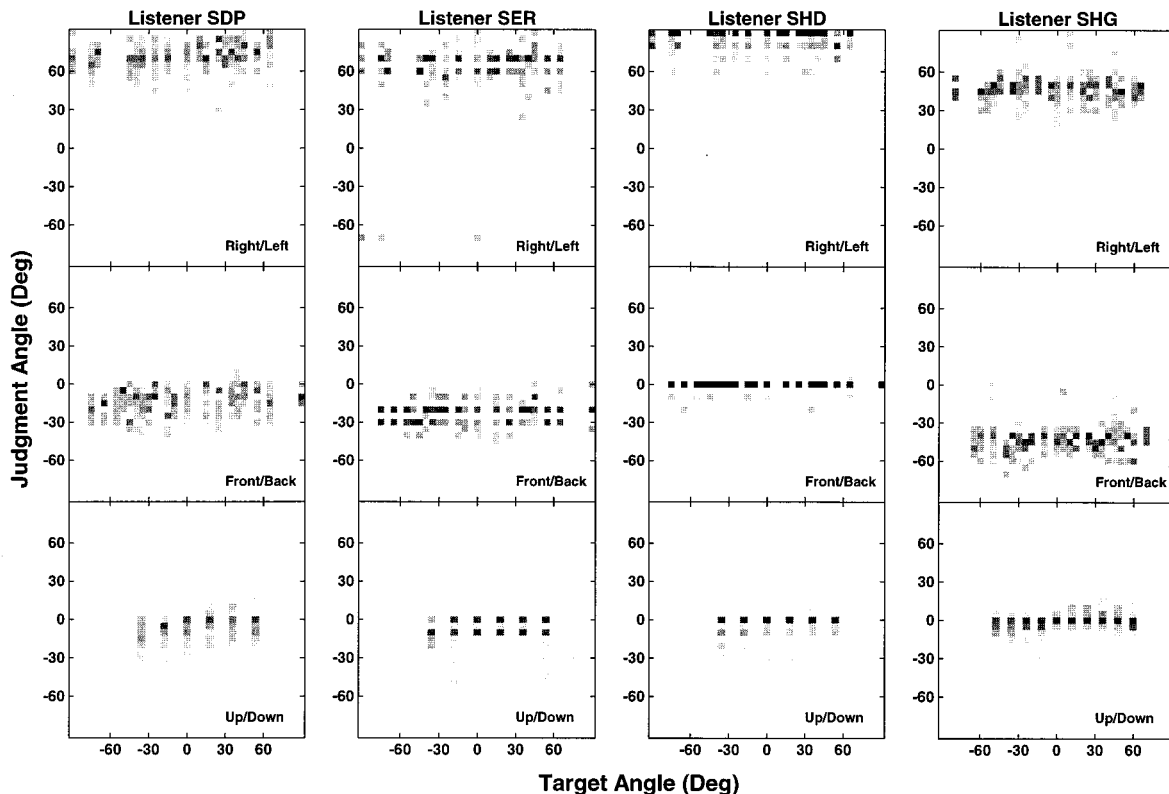


FIG. 5. Scatter plots of data from four additional listeners in the monaural virtual source condition.

occluded side, the responses, while showing the usual bias toward the open side and a hint of up-down perception on the open side, appear randomly distributed around a position roughly centered on the front-back and up-down dimensions. In the case of listener SIK (Fig. 4), however, responses to stimuli on the open ear side suggest nearly normal localization (although with increased variance in the responses). Even more remarkable is this listener's responses to stimuli on the occluded side. Not only are the up-down and front-back components of the responses nearly the same as on the open side, but the left-right components of the responses do not show the usual bias toward the open side (right, or positive angles on the left-right dimension). The reason for this is almost certainly inadequate "monauralization" by the plug and muff, an issue that will be discussed in connection with the results from the low-level free-field conditions.

The apparent position judgments from the monaural virtual source condition are quite different than those from the comparable free-field condition. For both of the listeners whose data are shown in Figs. 3 (SGG) and 4 (SIK), responses to all stimuli are more or less randomly distributed on the side of the stimulated ear (positive angles on the left-right dimension), toward the rear of the interaural axis (negative angles on the front-back dimension), and more or less close to zero elevation (zero angle on the up-down dimension). Thus, we conclude that localization is essentially abolished in the monaural virtual source condition. Distance judgments were obtained from both SGG and SIK in the virtual source conditions. In the binaural virtual source condition (data not shown) the mean source distance reported by SGG was 4.5 ft (s.d.=0.8) and by SIK it was 3.9 ft (s.d.

=0.7). In the monaural virtual source condition (Figs. 3 and 4), SGG reported a mean source distance of 2.6 ft (s.d.=0.9), and SIK reported a mean distance of 2.7 ft. (s.d.=1.6). Thus, even though the monaural virtual sources were not localizable, they were apparently externalized by these listeners.

Not all listeners in the monaural virtual source condition distributed their azimuth judgments as widely as those shown in Figs. 3 and 4. In fact, a more typical pattern was a tight clustering of judgments around a single azimuth. To illustrate this trend the data from four additional listeners in the monaural virtual source condition are shown in Fig. 5. The overall conclusion that localization is abolished in the monaural virtual source condition is the same for these listeners as for those whose data are shown in Figs. 3 and 4. Distance judgments are available for three of these four listeners (all but SER) and confirm that all monaural virtual sources were externalized. The mean reported source distances were 3.1, 28.5, and 0.5 ft (s.d.=1.7, 18.0, and 1.5) for SDP, SHD, and SHG, respectively.

The results from the low-level free-field conditions reveal the inadequacy of the plug and muff in achieving effective monauralization. Figures 6 and 7 show the data from two listeners, SGG and SIK, respectively, whose data from the high-level free-field condition were displayed in Figs. 3 and 4. Note first that the apparent position judgments in the low-level binaural condition are nearly identical to the judgments in the high-level binaural condition (cf. Figs. 2 and 6, both from listener SGG). While this comparison is shown for only one listener, the data from all the other listeners are consistent with this observation. Also note that for listener SGG, the monaural judgments are the same at low and high

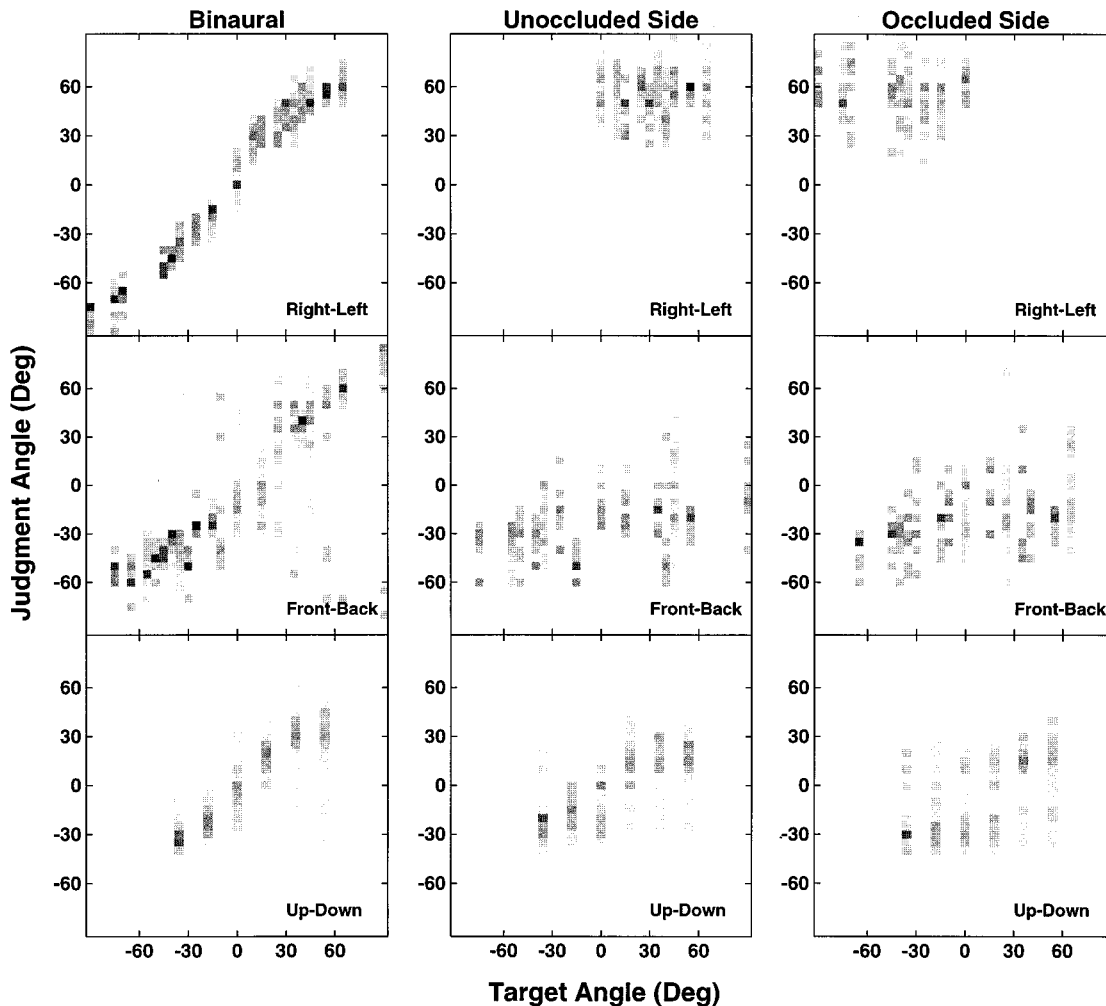


FIG. 6. Scatter plots of data from listener SGG in the low-level free-field conditions.

levels for stimuli on both the open and occluded side (cf. Figs. 3 and 6). However, for listener SIK, whose monaural judgments in the high-level condition suggested near normal localization (Fig. 4), the reduction in level had a dramatic effect. While this listener's judgments to stimuli on the open side are about the same at the two levels, the responses to stimuli on the occluded side are completely different at the lower level: Azimuth is strongly biased toward the open side, and elevation is nearly eliminated (clustered around 0°). We interpret this result as suggesting that for some listeners the plug and muff typically used to monauralize listeners may not be completely effective in preventing stimulation of the occluded ear. This in turn would allow the listener to use some interaural cues, most likely low-frequency ITDs. Of course, if the stimulus had not contained low frequencies, as was the case in the experiment reported by Slattery and Middlebrooks (1994), the consequences of inadequate interaural attenuation would probably have been quite different.

C. Discussion

The results of this experiment led us to two conclusions which we feel are important. One is that interpretation of the results of experiments in which listeners are monauralized by using an ear plug and muff must take into account the

amount and frequency dependency of the attenuation produced by the plug and muff. In the case of localization studies, inadequate attenuation forces investigators to present stimuli at very low levels. At these low levels, the accessibility of spectral cues may depend critically on stimulus spectral content, spectral variability, and sensitivity of the listener at high frequencies. A second conclusion is that monaurally presented virtual sources are not localizable. Whatever differences exist between free-field and virtual sources seem to be magnified in the monaural condition. While even at low levels there is some hint of localizability for monaural free-field sources, a monaural virtual source cannot be localized.

III. EXPERIMENT 2: INFLUENCE OF SPECTRAL UNCERTAINTY ON THE SALIENCE OF MONAURAL SPECTRAL CUES

The spectrum of a sound at each eardrum is the product of the pinna filtering and the spectrum of the sound source itself. The only way the two components of the product can be deconvolved, to extract the spectral cue produced by pinna filtering, is through knowledge of the spectrum of the source. The clearest evidence of the importance of prior knowledge of the stimulus spectrum comes from research on

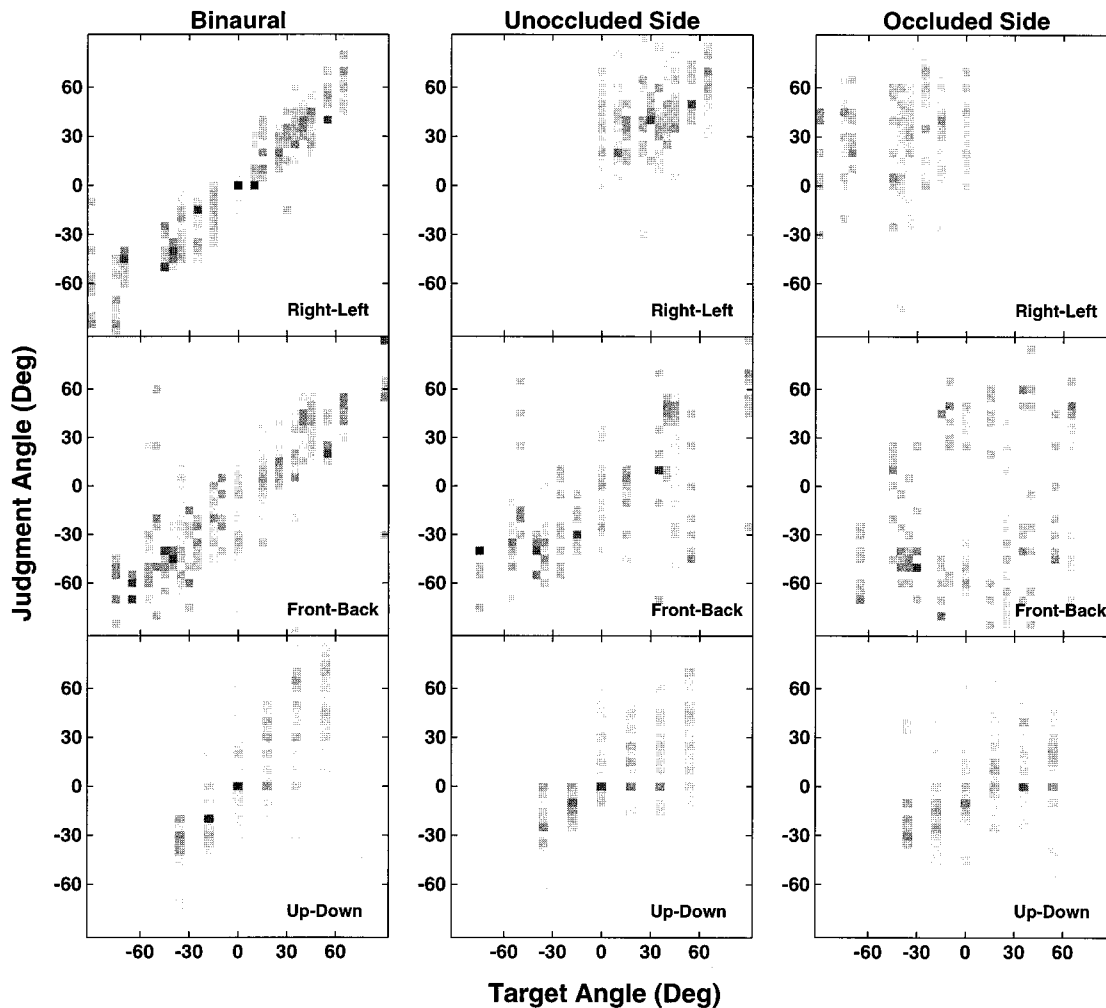


FIG. 7. Same as Fig. 6, but data are from listener SIK.

the apparent positions of narrow-band sounds (e.g., Blauert, 1969; Middlebrooks, 1992). Results from such studies consistently show that the apparent position of a narrow-band sound, especially its apparent elevation, is determined primarily by its center frequency and not by its actual position. The apparent position is one at which the pinna filter has a prominent peak at that frequency (Middlebrooks, 1992). These results imply that listeners know the characteristics of their own pinna filters and that they assume the spectrum of an incoming stimulus is relatively flat.

Many of the studies that demonstrate the importance of monaural spectral cues have used stimuli with spectra which were both relatively smooth over a broad frequency range and unchanging from presentation to presentation. It is possible that these conditions are optimal for extraction of monaural spectral cues, since the stimulus spectrum can be considered “known” to the listener and since it has no prominent spectral peaks or valleys. In more realistic conditions listeners encounter numerous stimuli which have non-flat spectra and must deal with considerable uncertainty about the stimulus spectrum. Both of these factors could interfere with the use of monaural spectral cues.

There has been very little research on the role of listeners’ prior knowledge of or expectations about stimulus spec-

tral characteristics. One study, reported by Hebrank and Wright (1974), showed that localization of flat-spectrum median plane sources was significantly degraded when random peaks and valleys were introduced into the sound spectra. The conclusion was that the uncertainty of the stimulus spectrum from trial-to-trial prevented extraction of monaural spectral cues.

A. Method

In this experiment the role of *a priori* knowledge of stimulus characteristics was studied by comparing listener’s judgments of the apparent positions of real free-field sources with flat or randomly scrambled spectra in both monaural and binaural listening conditions (thus, four conditions in all). The essential features of the stimuli and experimental procedure were as described above. The stimulus level in this experiment was the same as the low level in experiment 1 (40 dB SPL). In the scrambled-spectrum conditions the range of randomization of critical band levels was 40 dB (it was 20 dB in experiment 1). Six listeners participated in this experiment. One listener, SIK, also participated in experiment 1.

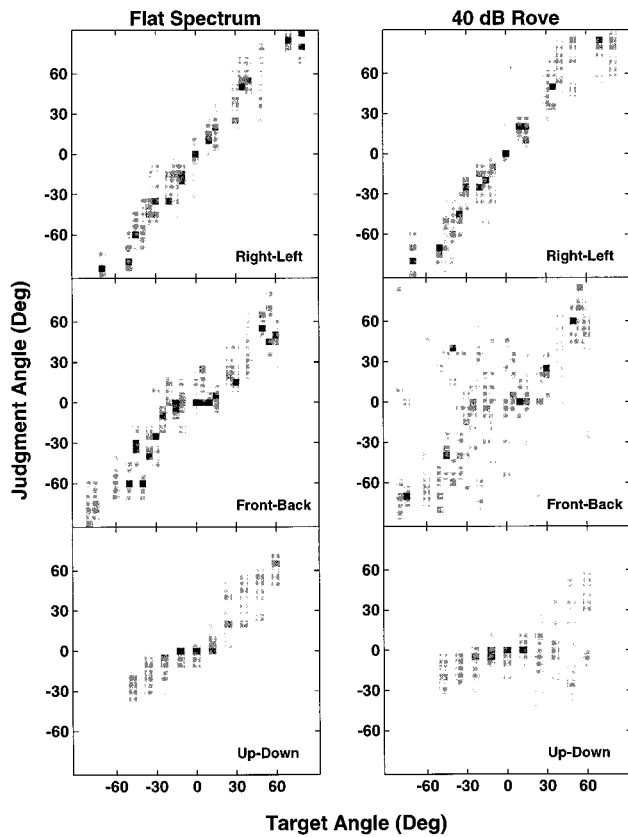


FIG. 8. Scatter plots of data from a typical listener in the flat- and scrambled-spectrum binaural conditions.

B. Results

Figure 8 shows the judgments from a typical listener in the flat and scrambled binaural conditions. Note that for this listener the effect of scrambling is to increase the number of front-back confusions (off-diagonal judgments in the “front-back” panels) and to degrade the perception of apparent elevation. Both of these effects are indicative of the way monaural spectral cues are being used. Scrambling the stimulus spectrum would presumably reduce the effectiveness of monaural spectral cues, since listeners would be unable to learn the spectral characteristics of the stimuli. The effects of scrambling are greater for some listeners than for others and thus may reflect the extent to which each listener relies on monaural spectral cues.

Figure 9 shows the judgments from the same listener in the flat and scrambled monaural conditions. In the flat condition, note that the most dramatic effect of the monauralization is in the right-left component of the judgment. It is clear that nearly all the stimuli were perceived to be on the right side (positive right-left judgment angles). Moreover, even when the source itself was on the right side, there was little correspondence between the target angle and the judgment angle. The consistent lateralization of monaural stimuli to the side of the unplugged ear agrees with many previous findings (Musicant and Butler, 1980; Hebrank and Wright, 1974; Butler *et al.*, 1990; Oldfield and Parker, 1986; Blauert, 1983; Butler, 1975) and probably reflects the perceptual salience of the large ILD caused by plugging one ear. The front-back and up-down components of the judgments were affected

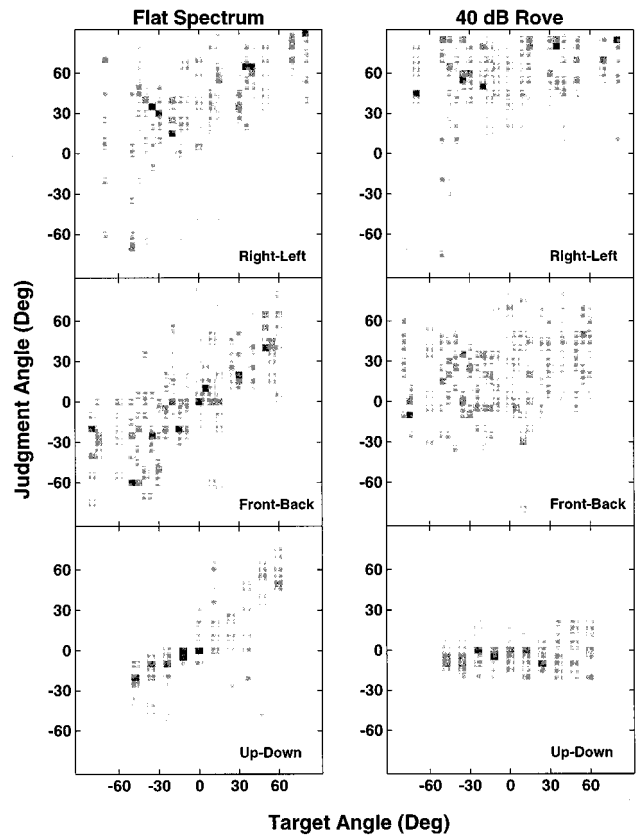


FIG. 9. Same as Fig. 8, but data are from the same listener in the flat- and scrambled-spectrum monaural conditions.

less by the monauralization of the listener, confirming the importance of monaural spectral cues for front-back and up-down perception. This result is also consistent with other monaural localization data in the literature (e.g., Oldfield and Parker, 1986; Butler *et al.*, 1990; Slattery and Middlebrooks, 1994). In the scrambled-spectrum condition both front-back and up-down perception is severely degraded, presumably because the monaural spectral cues have been rendered ineffective by the scrambling. Scrambling the spectrum over a smaller range (e.g., 20 dB, as in experiment 1) produces less severe disruption of free-field monaural localization, leaving the up-down components of the judgments only slightly degraded (cf. Figs. 6 and 7).

C. Discussion

The results of this experiment suggest that spectral uncertainty interferes with a listener’s ability to extract monaural spectral cues. Thus, the results of experiments which present flat-spectrum stimuli, which are near optimal for extraction of monaural spectral cues, may not be generalizable to more typical listening conditions which include some uncertainty about the stimulus spectrum. This is especially important when considering experiments such as monaural localization experiments in which apparent position judgments may be unusually dependent on monaural spectral cues. Whether or not the 20-dB spectral scrambling we chose for experiment 1 more accurately represents natural spectral uncertainty is unknown. Unfortunately, it is difficult to estimate the extent of spectral uncertainty in everyday sounds. Since

most everyday sounds are time variant, both analysis of their spectra and determination of which components determine their apparent position are complex problems with no obvious solutions.

IV. EXPERIMENT 3: LOCALIZATION WITH INTERAURAL LEVEL IMBALANCE

The results of experiment 1 suggest that small energy levels in a nominally occluded ear can have a dramatic impact on the apparent position judgments of some listeners. Because it is difficult to know precisely the attenuation characteristics of a plug and muff, and because those characteristics almost certainly are different for each listener, it is not possible to determine the extent to which our results and the results of previous studies of monaural localization might be affected. For this reason, and to aid a more complete understanding of the various factors which affect sound localization in natural listening situations, we carried out an experiment on the effects of various degrees of interaural intensity imbalance on sound localization.

A. Method

The only feasible way to conduct a localization experiment in which interaural level difference are varied is with the virtual source technique. Since the signals delivered to the two ears via headphones are essentially independent (see Fig. 1), independent control of the overall level at the two ears is straightforward. In this experiment, scrambled-spectrum (20-dB range) virtual sources were presented with the average overall level in the right ear set at approximately 70-dB SPL. In separate conditions the signal being delivered to the left ear was attenuated by 10, 20, 30, or 40 dB. In order to avoid problems of response bias, trials involving unilaterally attenuated virtual sources were interlaced (as in experiments 1) with trials involving “normal” virtual sources. The seven listeners who participated in this experiment had been tested in experiment 1, so data from both normal and monaural virtual source conditions were available for comparison.

B. Results

While the details in the patterns of responses were different for each of the seven listeners, the general trend was the same for all. Therefore, only the data from one listener will be shown here. Figure 10 shows the judgments from this listener in the binaural and monaural virtual source conditions (data from experiment 1). Note that the binaural data from this listener are normal, and that the monaural data suggest a complete elimination of normal localization. Regardless of nominal target position, the apparent positions of all stimuli are concentrated at 90° azimuth (90° left–right and 0° front–back) and 0° elevation, directly opposite the stimulated ear. This is the typical pattern of judgments in the monaural virtual source condition, as discussed above in connection with experiment 1. Figure 11 shows the data from the same listener in the conditions in which the signal to one ear was attenuated. Note a unilateral level imbalance of as much as 40 dB results in a pattern of responses that is

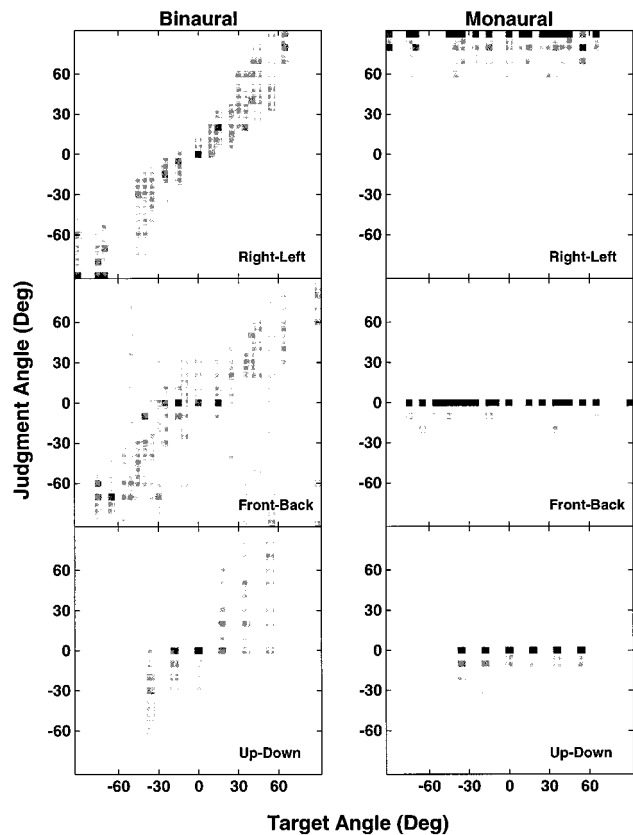


FIG. 10. Scatter plots of data from a representative listener in the binaural and monaural virtual source conditions of experiment 1.

clearly different from that obtained in the monaural condition, especially in the right–left components of the judgments. An imbalance of 10 dB produces a pattern of responses that is nearly “normal” (i.e., like that obtained with no unilateral attenuation).

The sensitivity to interaural level imbalance varied somewhat from listener to listener. For some, an imbalance of 40 dB was equivalent to the monaural condition, but for most it was not. Also, for some an imbalance of 10 dB had very little impact (as for the listener whose data are shown in Fig. 11), and for others the effect was more obvious. Finally, sensitivity to interaural level imbalance seems to be inversely correlated with the ability to extract interaural cues in the free-field monaural condition. Our data on this point are limited since not all listeners who participated in experiment 3 were also tested in experiment 1. However, a qualitative analysis of the available data suggests that those listeners whose localization judgments (especially the left–right components) were most accurate in the high-level free-field monaural condition of experiment 1 were among those whose judgments were least affected by interaural intensity imbalance. To the extent that monauralization with an earplug and muff is equivalent to creating an interaural level imbalance, such a correspondence would be expected.

C. Discussion

The results of this experiment are somewhat unexpected. Lateralization experiments, which involve presentation of

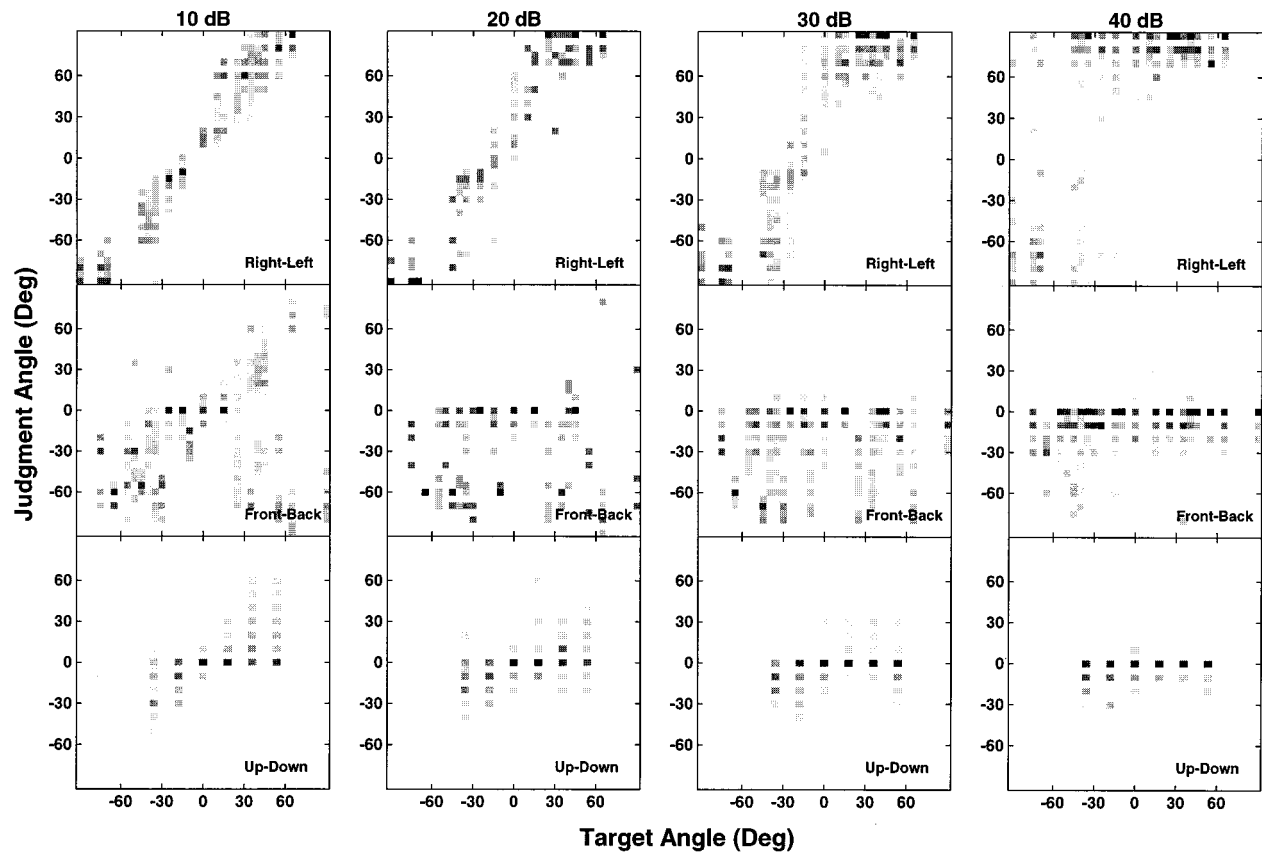


FIG. 11. Scatter plots of data from the same listener whose data are shown in Fig. 10 showing the effects of progressive attenuation of the signal at one ear. The amount of attenuation is indicated at the top of each panel.

nonspatialized stimuli (i.e., stimuli devoid of the spectral cues provided by pinna filtering), suggest that an interaural imbalance of 10–15 dB is sufficient to cause complete lateralization of the sound image, a shift of its apparent position all the way to one side (e.g., Yost and Hafter, 1987). In this experiment, with all the naturally occurring localization cues present, a 10-dB imbalance has a generally small effect on the apparent position of the sound image. However, this result is consistent with previous data on the apparent positions of virtual sources presented with conflicting localization cues (Wightman and Kistler, 1992). Those data suggest that with low frequencies present in the stimulus, as in the current experiment, the ITD cue was dominant, and the ILD and spectral cues were essentially ignored. If the effect of a 10–15 dB interaural level imbalance on the ITD cue is negligible, the results of the present experiment are less surprising.

The most important result from this experiment is the observation that even very low signal levels delivered to the attenuated ear can have a measurable influence on judgments of the apparent positions of virtual sources. This finding not only broadens our understanding of how the various localization cues are extracted and processed, but also complicates the interpretation of the results of many free-field monaural localization experiments.

V. GENERAL DISCUSSION AND CONCLUSIONS

Sound localization is a perceptual process that involves integration of several different types of information: audi-

tory, visual, and cognitive, at least. The auditory substrate of sound localization derives from what we call the acoustical cues: ITD, ILD, and the spectral cues. Much is known about the auditory system's sensitivity to these cues and about how at least the interaural difference cues are extracted from acoustical stimuli. However, the extent to which, in any given situation, each contributes to the perception of the apparent position of a sound source is not well understood.

The monaural localization paradigm is thought to represent a situation in which the contributions of the spectral cues is emphasized. However, because monaural listening actually provides conflicting and unnatural cues to sound source position, one cannot be certain that a listener's judgments of apparent sound source position will reflect only the influence of spectral cues. Thus, interpretation of the results of monaural localization experiments strictly in terms relating to the use of spectral cues is not straightforward.

The three experiments reported here focus on various aspects of the monaural localization paradigm with the aims of clarifying the results of such experiments and increasing our general understanding of the processing of spectral cues. Experiments 1 and 3 deal with the consequences of the incomplete monauralization achieved by plugging a listener's ear. The results suggest that even very low stimulus levels in the occluded ear provide access to interaural cues for some listeners. Studies with the virtual source technique, which offers considerably improved monauralization, suggest that localization is essentially eliminated in monaural listening.

This result conflicts with the results of all monaural localization experiments (including our own) conducted in the free field, even those which used stimulus levels low enough to assure no stimulation of the occluded ear. The free-field experiments suggest that at least some residual localization, particularly in the up-down dimension, is maintained in monaural listening conditions. We will return to a discussion of this discrepancy shortly.

Experiment 2 is concerned with the role of prior knowledge of the stimulus spectrum. Extraction of reliable monaural spectral cues requires knowledge of the source spectrum. However, there is ample evidence from experiments involving narrow-band stimuli (e.g., Middlebrooks, 1992; Rogers and Butler, 1992) that, even without explicit information about source characteristics, the spectral shaping provided by an individual's own pinnae influences apparent position judgments. This suggests that listeners make certain assumptions about the source spectrum in order to extract the monaural spectral cue. The results of experiment 2, in which source spectrum is directly manipulated, suggest that extraction of monaural spectral cues is a process that, as expected, can be disrupted by uncertainty in the source spectrum.

There remains a curious discrepancy between the free-field results, which suggest that vertical localization is only moderately degraded by monauralization, and the virtual source results, which suggest that localization is effectively eliminated by monaural listening. There are two differences between free-field and virtual source conditions which we feel could be the source of this discrepancy. One is the fact that interlacing of monaural and binaural stimuli was done only in the virtual source conditions. It is possible that without the frequent exposure to normal binaural localization cues provided by the interlacing, listeners attended more to the available spectral cues. However, an informal pilot experiment which involved localization of monaural virtual sources without interlacing convinces us that this explanation is not correct. There were no differences between performance with and without the interlacing. The other major difference between listening in free field and listening to virtual sources lies in the consequences of small head movements. With the static, non-head-coupled virtual sources used here, head movements cause no change in the stimulus reaching the eardrum. In free-field conditions the eardrum stimulus is constantly changing since all listeners move their heads slightly when listening to the stimuli, even though they are asked to hold their heads still. We have monitored this movement with a magnetic head tracker and find that for some listeners the standard deviation of head azimuth during a stimulus presentation (which consists of four bursts of noise) is as large as 2°. Head movements of this magnitude, while small, could easily provide useable cues in the form of changes in the spectrum of the stimulus at the eardrum. At 6 kHz, for example, the frequency response of the outer ear changes at the rate of at least 0.25 dB/deg on the horizontal plane (Middlebrooks *et al.*, 1989). Since a 0.25-dB difference between spectra at high frequencies is detectable (Leshowitz, 1971), we conclude that very small head movements could produce detectable spectral changes, which could influence apparent position judgments in the free-field

condition. That head movements cause no change in the stimulus in virtual source conditions is unnatural, and the effects of this, if any, on apparent position judgments are unknown.

In summary, while there can be no doubt about the importance of monaural spectral cues for sound localization, the monaural localization paradigm may not be the best means for studying their role. Problems of implementation and problems of interpretation greatly complicate the endeavor and argue for finding alternatives.

ACKNOWLEDGMENTS

The authors gratefully acknowledge the assistance of Marianne Arruda and Ramona Agrawal in the technical phases of the work, and the very helpful comments of Ewan Macpherson on an earlier version of this paper. Financial support was provided by NASA (Cooperative Agreement No. NCC2-542) and the NIH-NIDCD (DC00116).

- Angell, J. R., and Fite, W. (1901). "The monaural localization of sound," *Psychol. Rev.* **8**, 225–246.
- Belendiuk, K., and Butler, R. A. (1977). "Spectral cues which influence monaural localization in the horizontal plane," *Percept. Psychophys.* **22**, 353–358.
- Blauert, J. (1969). "Sound localization in the median plane," *Acustica* **22**, 205–213.
- Blauert, J. (1983). *Spatial Hearing The Psychophysics of Human Sound Localization* (MIT, Cambridge, MA), pp. 1–427.
- Butler, R. A. (1975). "The influence of the external and middle ear on auditory discriminations," in *Handbook of Sensory Physiology*, edited by W. D. Keidel and W. D. Neff (Springer-Verlag, Berlin), pp. 247–260.
- Butler, R. A. (1986). "The bandwidth effect on monaural and binaural localization," *Hear. Res.* **21**, 67–73.
- Butler, R. A., and Flannery, R. (1980). "The spatial attributes of stimulus frequency and their role in monaural localization of sound in the horizontal plane," *Percept. Psychophys.* **28**, 449–457.
- Butler, R. A., Humanski, R. A., and Musicant, A. D. (1990). "Binaural and monaural localization of sound in two-dimensional space," *Perception* **19**, 241–256.
- Flannery, R., and Butler, R. A. (1981). "Spectral cues provided by the pinna for monaural localization in the horizontal plane," *Percept. Psychophys.* **29**, 438–444.
- Hebrank, J. H., and Wright, D. (1974). "Are two ears necessary for localization of sound sources on the median plane?," *J. Acoust. Soc. Am.* **56**, 935–938.
- Hood, J. D. (1962). "Bone conduction: A review of the present position with especial reference to the contributions of Dr. Georg. Von Békésy," *J. Acoust. Soc. Am.* **34**, 1325–1332.
- Kistler, D. J., and Wightman, F. L. (1992). "A model of head-related transfer functions based on principal components analysis and minimum-phase reconstruction," *J. Acoust. Soc. Am.* **91**, 1637–1647.
- Leshowitz, B. (1971). "Measurement of the two-click threshold," *J. Acoust. Soc. Am.* **49**, 462–466.
- Makous, J. C., and Middlebrooks, J. C. (1990). "Two-dimensional sound localization by human listeners," *J. Acoust. Soc. Am.* **87**, 2188–2200.
- Middlebrooks, J. C. (1992). "Narrow-band sound localization related to external ear acoustics," *J. Acoust. Soc. Am.* **92**, 2607–2624.
- Middlebrooks, J. C., Makous, J. C., and Green, D. M. (1989). "Directional sensitivity of sound-pressure levels in the human ear canal," *J. Acoust. Soc. Am.* **86**, 89–108.
- Mills, A. W. (1972). "Auditory localization," in *Foundations of Modern Auditory Theory—Volume II*, edited by J. V. Tobias (Academic, New York), pp. 301–345.
- Musicant, A. D., and Butler, R. A. (1980). "Monaural localization: An analysis of practice effects," *Percept. Psychophys.* **28**, 236–240.
- Musicant, A. D., and Butler, R. A. (1984). "The psychophysical basis of monaural localization," *Hear. Res.* **14**, 185–190.

- Musicant, A. D., and Butler, R. A. (1985). "Influence of monaural spectral cues on binaural localization," *J. Acoust. Soc. Am.* **77**, 202–208.
- Oldfield, S. R., and Parker, S. P. A. (1986). "Acuity of sound localization: A topography of auditory space. III. Monaural hearing conditions," *Perception* **15**, 67–81.
- Rogers, M. E., and Butler, R. A. (1992). "The linkage between stimulus frequency and covert peak areas as it relates to monaural localization," *Percept. Psychophys.* **52**, 536–546.
- Slattery III, W. H., and Middlebrooks, J. C. (1994). "Monaural sound localization: acute versus chronic unilateral impairment," *Hear. Res.* **75**, 38–46.
- Strutt, J. W. (1907). "On our perception of sound direction," *Philos. Mag.* **13**, 214–232.
- Wightman, F. L., and Kistler, D. J. (1989a). "Headphone simulation of free-field listening II: psychophysical validation," *J. Acoust. Soc. Am.* **85**, 868–878.
- Wightman, F. L., and Kistler, D. J. (1989b). "Headphone simulation of free-field listening I: stimulus synthesis," *J. Acoust. Soc. Am.* **85**, 858–867.
- Wightman, F. L., and Kistler, D. J. (1992). "The dominant role of low-frequency interaural time differences in sound localization," *J. Acoust. Soc. Am.* **91**, 1648–1661.
- Yost, W. A., and Hafter, E. R. (1987). "Lateralization," in *Directional Hearing*, edited by W. A. Yost and G. Gourevitch (Springer-Verlag, New York), pp. 49–84.

Toward articulatory-acoustic models for liquid approximants based on MRI and EPG data. Part I. The laterals

Shrikanth S. Narayanan^{a)} and Abeer A. Alwan^{b)}

Speech Processing and Auditory Perception Laboratory, Department of Electrical Engineering, School of Engineering and Applied Sciences, UCLA, 405 Hilgard Avenue, Los Angeles, California 90095

Katherine Haker

Imaging Medical Group, Cedars-Sinai Medical Center, 8700 Beverly Boulevard, Los Angeles, California 90048

(Received 11 March 1996; accepted for publication 26 September 1996)

Magnetic resonance images of the vocal tract during the sustained phonation of /l/ (both dark and light allophones) by four native American English talkers are employed for measuring lengths, area functions, and cavity volumes and for the analysis of 3-D vocal tract and tongue shapes. Electropalatography contact profiles are used for studying inter- and intra-talker variabilities and as a source of converging evidence for the magnetic resonance imaging study. The general 3-D tongue body shapes for both allophones of /l/ are characterized by a linguo-alveolar contact together with inward lateral compression and convex cross sections of the posterior tongue body region. The lateral compression along the midsagittal plane enables the creation of flow channels along the sides of the tongue. The bilateral flow channels exhibit somewhat different areas, a characteristic which is talker-dependent. Dark /l/s show smaller pharyngeal areas than the light varieties due to tongue-root retraction and/or posterior tongue body raising. The acoustic implications of the observed geometries are discussed. © 1997 Acoustical Society of America.

[S0001-4966(97)02202-9]

PACS numbers: 43.70.Aj, 43.70.Bk [AL]

INTRODUCTION

Accurate articulatory-to-acoustic modeling of speech production requires a detailed knowledge of the 3-D geometry of the human vocal tract. Magnetic resonance imaging (MRI) is a powerful tool in obtaining the vocal-tract geometry and does not involve any known radiation risks. The images have good signal-to-noise ratio (SNR) and are amenable to computerized 3-D modeling of the vocal tract. The low image sampling rate (i.e., high acquisition time), however, has restricted MRI use to the study of sustained speech sounds, corresponding to “static” tract shapes. In parts I and II of this paper, an analysis of the vocal-tract geometry obtained from magnetic resonance imaging in axial, coronal, and sagittal planes, of the liquid approximants in American English is reported. Due to similarities in certain phonetic and phonological properties, the lateral /l/ and the rhotic /r/ are classified as “liquids” (Ladefoged, 1993). For example, both laterals and rhotics can be syllabic in word-final positions, and both are sonorous oral sounds. Part I focuses on the laterals, and part II on the rhotics. Linguopalatal contact profiles obtained through electropalatography (EPG) are used for the analysis of inter- and intra-speaker variabilities and to provide a source of converging evidence for the results of the MRI study.

I. PRODUCTION MECHANISMS OF LATERALS

Laterals are sounds which are typically produced with a lingual contact along the midsagittal line such that air flows

along one or both sides of the tongue. The contact is made with the anterior tongue tip or blade in the anterior region of the roof of the oral cavity. In English, the lateral approximant¹ /l/ is voiced and has been broadly classified into two canonical allophones, namely the light and dark varieties, which will be referred to by the symbols [l] and [ɫ], respectively, in this paper. The light allophone [l] occurs in prevocalic contexts (for example, as in “led”) and the dark allophone [ɫ] occurs in postvocalic and syllabic cases (for example, as in “bell”). Acoustically, [ɫ] is characterized by a relatively lower F_2 and higher F_1 when compared to the F_2 and F_1 values of [l] (Lehiste, 1964; Espy-Wilson, 1992). The exact details of the vocal-tract geometry and the aerodynamics of these sounds are not well-known. Previous articulatory studies have indicated that there is a greater retraction of the anterior tongue body in the dark /l/ when compared to the light variety (Giles and Moll, 1975; Gartenberg, 1984). Although there has been some evidence for the raising of the posterior tongue body (dorsum) toward the velum (“velarization”) in [ɫ], such behavior has not been observed consistently (Sproat and Fujimura, 1993).

Articulatory and acoustic properties that are intermediate in nature to those associated with the canonical dark and light variants have been known to exist. In fact, it has been argued that the dark and light variants of /l/ are not distinct elements, either from a phonological or a physiological point of view, but rather are manifestations of phonetically predictable contextual characteristics (such as syllable-initial versus syllable-final) suggesting that an allophonic distinction in describing them may not be necessary (Sproat and Fujimura, 1993).

^{a)}Now at AT&T Labs, Murray Hill, NJ.

^{b)}Corresponding author.

Articulatory evidence from previous studies have shown differences in the production patterns of the laterals across different English dialects. For example, Giles and Moll (1975) report that lingual contact in the front region of the oral activity is often not observed in the dark variant of American English; results of Gartenberg (1984), on the other hand, indicate a significant front region linguopalatal contact for postvocalic /l/s in British English.

The primary objective of this study is to provide a characterization of the 3-D geometry of dark and light variants of /l/ so that better acoustic models for these sounds can be developed. Investigation of coarticulation and other dynamic properties are not within the scope of this study.

II. METHOD

A. Subjects

Four phonetically trained, native American English speakers [2 males (MI, SC) and 2 females (AK, PK)] served as subjects. Subjects AK and MI, both in their twenties at the time of the experiments, were raised in Northern California and have spent the 7 years preceding this study in Southern California. Subject SC, in his thirties, spent the first 10 years of his life in Indiana and has since been in California. Subject PK, in her early forties, lived in New Jersey and Ohio her first 3 years, and in the Boston area through her thirties. She has been living in the Los Angeles area for 14 years. All subjects have professional working knowledge of phonetics: PK for more than 20 years, and is an expert phonetician; SC and AK for more than 10 years through teaching and research; and MI for more than 5 years through phonetics classes and work experience. All have been subjects for various production and listening experiments.

B. Magnetic resonance imaging (MRI)

A detailed description of the acquisition and analysis procedures is provided in Narayanan *et al.* (1995). Magnetic resonance (MR) images were collected using a GE 1.5 T SIGNA machine with a fast SPGR (radio frequency spoiled GRASS) protocol in the coronal, axial, and sagittal planes. The image slice thickness was 3 mm with no interscan spacing. Each image was represented by a 256×256 pixel matrix, yielding a resolution of 0.0081 cm² per pixel for an FOV=24 cm. The subjects, in supine position, sustained dark or light /l/ for about 13–16 s enabling four to five image slices to be recorded in a particular plane (about 3.2 s/image). Dark and light /l/s were produced in a neutral vowel context, and the subjects repeated each sound six to nine times, with a pause of three to ten seconds between repetitions, to enable the entire vocal tract to be scanned. The data set comprised 28–35 images/sound/subject in the sagittal plane, and 40–45 images/sound/subject in the axial and coronal planes.

Scanning of each subject in any one particular plane (axial, for example), was completed within the same session. Scanning in each of the three orthogonal planes was carried out in different sessions. A special head-neck coil helped maintain the subjects' heads in a fixed position. Stability of the articulators could not be monitored during scanning. Instead, analysis results of EPG data, which were collected on

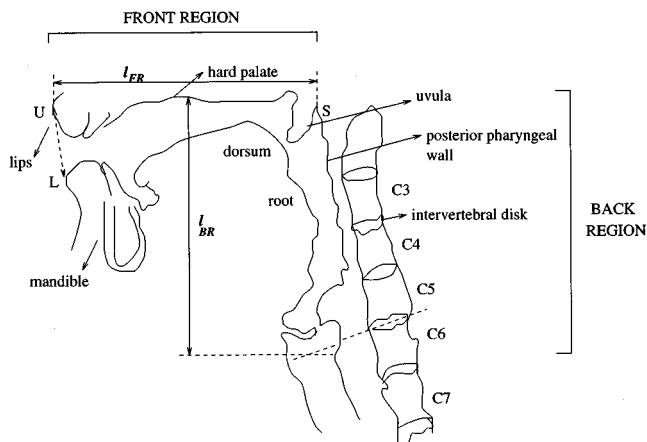


FIG. 1. Tracing of the midsagittal profile of the vocal tract during the production of the vowel /a/ (subject MI) highlighting terminologies and landmarks used for measurements.

a different day, suggest that our phonetically trained subjects maintained stable gestures while sustaining these sounds. In addition, a comparison of the EPG data for /l/s obtained from sustained utterances with those from in-context words (described in the Appendix) helped justify the use of sustained utterances for studying the articulatory geometry during the production of these sounds.

In order to provide a convenient reference to key anatomical landmarks in the vocal tract, a tracing of a sample midsagittal MR image of the vocal tract for the vowel /a/ spoken by a male subject is shown in Fig. 1. The scanning region for the coronal and axial planes included the region between the lips and the posterior pharyngeal wall along the anteroposterior axis and the region between the top of the hard palate and just below the eighth vertebra along the inferosuperior axis. Coronal and axial scans were taken approximately perpendicular to the vocal-tract midlines, in the oral and pharyngeal regions, respectively, based on a midsagittal localizer image for each subject. Similarly, the scanning region for the sagittal plane was based on axial and/or coronal localizer images. In addition, reformatting of the raw images was used to obtain cross sections along any desired (oblique) plane. Since midsagittal profiles provide the most convenient reference for specifying grid locations for performing area calculations, sagittal scans were chosen for area calculations along the vocal-tract bend from reformatted images. Midsagittal data were also used for length measurements.

Automatic segmentation of the vocal-tract regions in the images was followed by careful manual verification of the selected regions in each image. Following segmentation, three-dimensional reconstructions of the entire vocal tract, or specific regions such as the sublingual cavities, could be made by computer-aided concatenation of the selected regions of interest. Length, area, and volume measurements could be made directly using a pixel counting algorithm.

Articulatory analysis and measurements were performed in several steps. Overall vocal tract and tongue shapes were first analyzed using raw images, and complete 3-D models were then reconstructed from appropriately segmented raw

scans. All the 3-D reconstructions reported in this study were constructed using coronal scans. Interactive slicing of the 3-D objects, along any desired plane, facilitated the morphological analyses. Area measurements were made in two stages: in the first, cross-sectional areas were directly measured from the coronal and axial scans to provide information on the front (oral) and back (pharyngeal/laryngeal) regions, respectively; in the second, sagittal scans were reformatted to obtain areas along the planes perpendicular to the midline of the vocal-tract bend. To enable comparative graphical analyses across the various sounds and subjects, a simplified representation of the area function is considered. Areas up to the laryngeal inlet (glottal opening), defined by the section showing the complete separation of the piriform sinuses by the ary-epiglottic fold, were considered. Furthermore, the “effective” area of the airway was obtained by a simplification of the morphology: subtracting tissue areas, such as the uvula, and the various epiglottal folds, from the total pharyngeal cavity areas. Areas of the lateral channels, along the sides of the tongue, were measured using coronal scans. These areas were calculated using the airway segmentation technique aided by appropriate tracings of the teeth similar to that described in Narayanan *et al.* (1995).

C. Electropalatography (EPG)

1. Data acquisition

EPG data from the subjects were recorded on a later date using Kay Elemetrics Palatometer. Each subject has a custom-fitted acrylic palate with 96 sensing electrodes. The sweep rate of this system is 1.7 ms and the sampling period is 10 ms. The data for each subject were collected in a single session that lasted for about one and a half to two hours. The data were collected over a month (post-MRI experiments).

The speech material consisted of the lateral approximant (dark and light allophones) sustained for about 4 s/token. The sounds were produced preceded by the neutral vowel /ə/. The subjects assumed a supine position, similar to that assumed inside the MRI machine, while phonating the sustained utterances.² In addition, EPG data for dark and light /l/s from spoken words were collected for comparative analyses (described in the Appendix). Eight repetitions of each condition were obtained.

2. Data analysis

For the purposes of this study, the total region covered by the electrodes was broadly divided into front and back regions. A schematic of the region definitions is given in Fig. 2. The front region comprises the alveolar and prepalatal regions while the back region comprises the midpalatal and postpalatal regions. In addition, these regions could be further divided into left and right lateral zones, with respect to the midsagittal line, in order to study the symmetry in the linguopalatal contact profiles. The percentage of electrodes that are contacted in each of these regions served as a basis for our analysis.

The EPG data were used to study the stability of the articulatory gestures during sustained phonation and intertoken variabilities in each subject’s production, and to compare

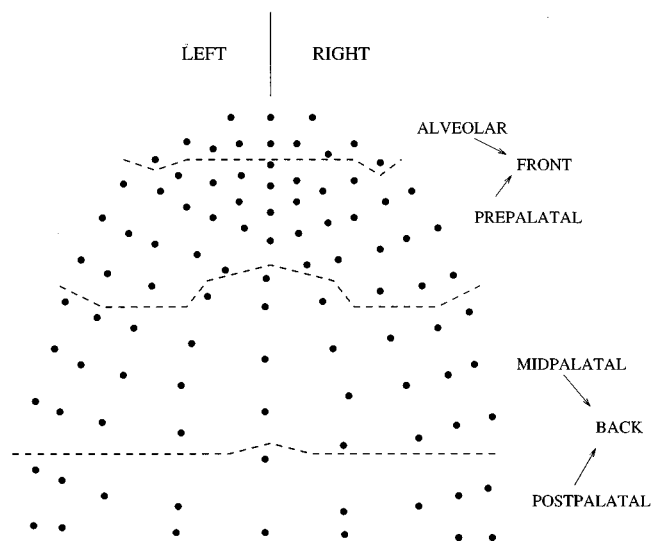


FIG. 2. Schematic of electrode placement on the pseudopalate used in electropalatography with region definitions.

sustained versus in-context phonations. The linguopalatal contact profiles provided by the EPG data were studied using repeated-measures multifactorial ANOVA (Analysis of VAriance) techniques (SYSTAT, 1992). Furthermore, wherever necessary, Tukey-HSD posthoc tests were used to isolate the potential sources of variations. Note that EPG only measures linguopalatal contacts, and is limited to the region between the teeth and the anterior part of the velum.

III. RESULTS

Articulatory analysis of the laterals is based on MRI and EPG data of sustained productions of the light [l] and dark [ɫ] allophones. Tracings obtained from midsagittal MR images of [l] and [ɫ] for the different subjects are shown in Fig. 3, and the corresponding area functions are shown in Fig. 4. Sample linguopalatal contact profiles for [l] and [ɫ] are shown in the Appendix.

Analysis of the midsagittal images reveals, for both [l] and [ɫ], that the tongue shapes are significantly different across the four subjects. Nevertheless, a detailed analysis of the cross-sectional shapes and the lingual contact patterns reveals several common characteristics. Moreover, for each subject, the tongue shapes for the dark and light allophones showed many similar characteristics, particularly in the oral region, but certain systematic differences were also found, such as in the degree of posterior tongue body raising in the velar region, and tongue-root retraction in the pharyngeal region.

A. The light [l]

1. The linguo-alveolar contact

For [l], all subjects revealed lingual contact along the midsagittal line, beginning in the region behind the front incisors and continuing over the majority of the alveolar region (starting at approximately 1 cm away from the lip opening and extending up to about 1.8, 1.8, 2.1, and 1.5 cm from the lip opening for AK, PK, MI, and SC, respectively). This linguo-alveolar contact was established either with a raised

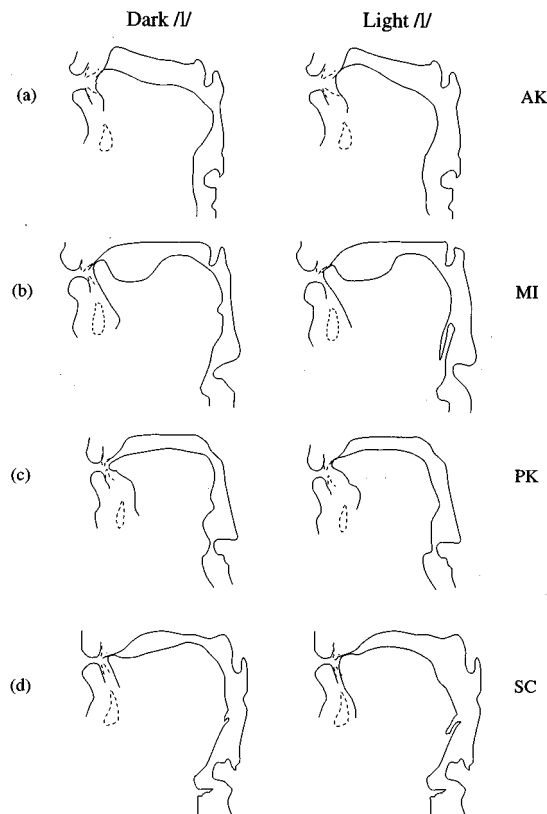


FIG. 3. Tracings of the midsagittal profiles of the vocal tract of the different subjects during the production of the lateral approximants [ɬ] (left side) and [l] (right side): (a) AK, (b) MI, (c) PK and, (d) SC. The front incisors and the jaw are shown in dashed lines.

tongue blade (i.e., a *laminal* articulation), as observed in AK and PK [Fig. 3(a) and (c)] or with a raised tongue tip (i.e., an *apical* articulation), as observed in MI and SC [Fig. 3(b) and (d)]. The MRI data also showed that the linguo-alveolar contact for the laminal [l]s of AK and PK extended laterally through the midpalatal region (up to about 5.4 cm and 4 cm from the lips, for AK and PK, respectively). The lateral extension of the alveolar contacts for apical [l]s of MI and SC, on the other hand, was smaller and confined to the prepalatal region (up to about 2.8 and 2.4 cm from the lips, for MI and SC, respectively). Note that *lateral* lingual contacts cannot be observed in midsagittal images (Fig. 3).

Analysis of the EPG data showed greater front-region linguopalatal contacts for the laminally articulated [l]s of AK and PK when compared to the more apical articulations of MI and SC (see for example, Fig. A1 in the Appendix). On average, about 75%–80% of the front-region electrodes were contacted in subjects AK and PK when compared to about 60% in MI and 40% in SC. ANOVA results showed that the front-region contacts of PK were significantly different ($p < 0.001$) from those of MI and SC. Similarly, the front-region contacts of AK were significantly different from those of SC.

Sample MRI coronal cross sections for subject MI are shown in Fig. 5. Linguo-alveolar contact can be seen in the three contiguous sections starting at the leftmost panel of the bottom row. Lateral linguopalatal contacts are observed in the panels following, and the loss of the linguopalatal contact

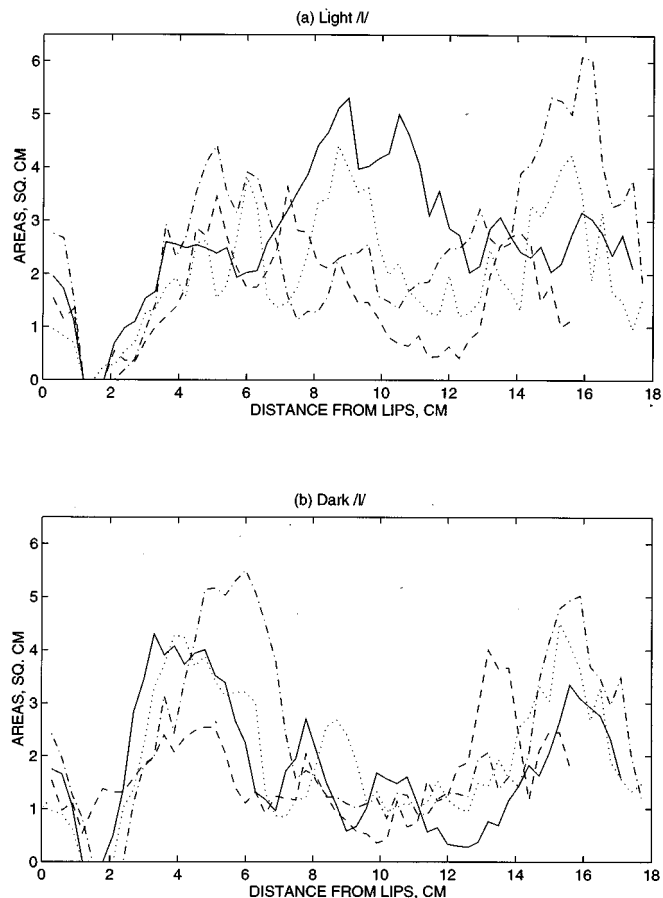


FIG. 4. Area functions, in cm^2 , for the laterals of the different subjects: solid (AK), dashed (PK), dot-dashed (MI), dotted (SC). Top panel: [l], bottom panel: [ɬ]. Areas of the lateral openings around the alveolar contact are not included in these figures, but areas of the lateral openings behind the contact, if present, are included. The abscissa for the area functions are distances (in cm) from the outer lip opening. Approximately, the region about 1.5–2.5 cm from the lips is the alveolar region, 2.5–6 cm is the palatal region, 6–8.5 cm is the velar region, 8.5–13 cm is the uvular and upper-pharyngeal region, and 13–15 cm is the lower-pharyngeal region. For PK, 1–2 cm is the alveolar region, 2–5 cm is the palatal region, 5–7 cm is the velar region, 7–10 cm is the uvular and upper pharyngeal region, and 10–12.5 cm is the lower-pharyngeal region. The laryngeal region is posterior to the lower-pharyngeal region.

is first observed in the 2nd rightmost panel in row 3 (from bottom). Around either side of the linguo-alveolar contact, small lateral openings were observed in the coronal scans until the lateral contacts ended. These lateral channels can be observed in a side perspective of MI's 3-D vocal tract shown in Fig. 6 in the region of the alveolar contact, behind the lips, and these channels extend to the oral region.

The cross-sectional areas of the lateral channels alongside the alveolar contact, for all subjects, are summarized in Table I. The areas vary between 0.1–0.5 cm^2 depending on the subject's oral morphology and how the lingual contact was formed, such as apically or laminally. Note that the left and right lateral channels have, in general, different areas.

2. Region behind the linguo-alveolar contact

The midsagittal tongue body contours for [l] were found to be quite different across the four subjects (Fig. 3). For example, the middle and posterior tongue body were gradu-

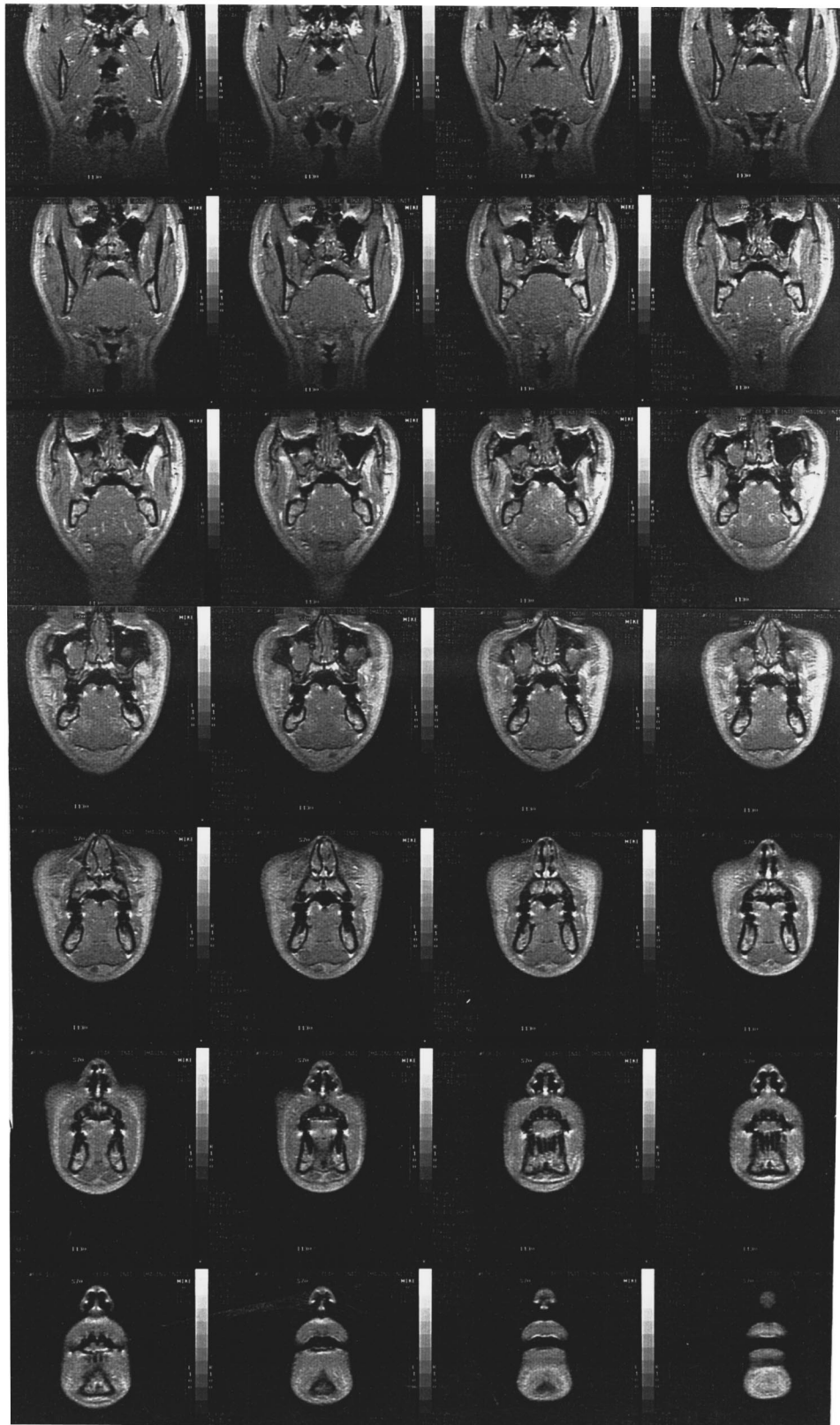


FIG. 5. Coronal profiles of the vocal tract during the production of [l] (subject MI) taken along contiguous sections in the oral cavity at every 3 mm starting from 3 mm from the outer lip opening and ending at the uvular region. The figure is arranged such that the cross section closest to the lips appears in the rightmost panel of the bottom row and successive cross sections, moving away from the lips, are placed right-to-left in each row. Linguo-alveolar contact can be seen in the three contiguous sections starting at the leftmost panel of the bottom row. Grooving along the midsagittal line is observed in the panels of rows 3 and 4 (from bottom), and the convex tongue surface is apparent in row 6 panels.

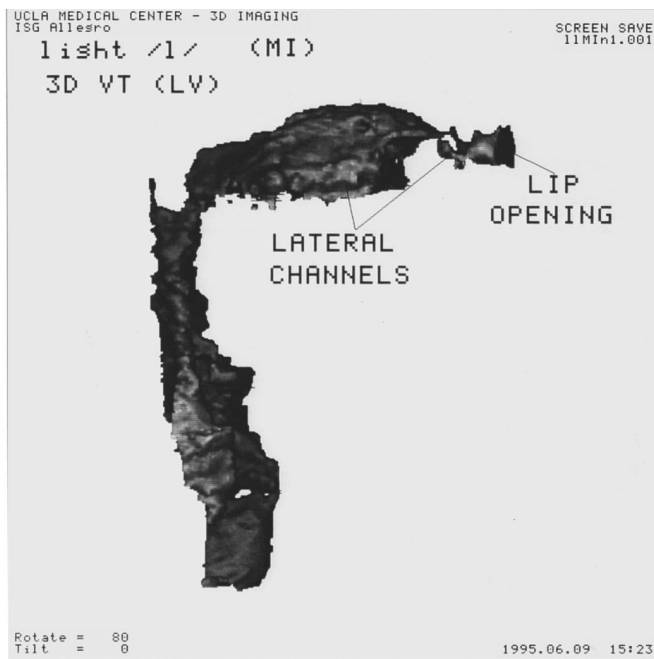


FIG. 6. A lateral (side) perspective of the 3-D vocal tract for subject MI's [l]. Small lateral channels can be seen in the region of the alveolar contact, just behind the lips. Also notice the presence of lateral channels in addition to the central airway in the oral region.

ally lowered toward the posterior pharyngeal wall for AK, while for PK, the entire tongue body behind the alveolar contact was maintained at the same height. For MI, on the other hand, the middle tongue body appears significantly

TABLE I. Areas (in cm^2) of the lateral channels in the alveolar contact region for [l] and [h] (L:left channel, R:right channel) from coronal MR images. x_l is the distance from the lips in cm. Note that no lateral areas for PK's [h] are reported due to difficulty in area measurements because of the absence of a complete alveolar contact.

| [l] | | | | | |
|-------|--------|--------|-------|--------|--------|
| x_l | AK (L) | AK (R) | x_l | PK (L) | PK (R) |
| 1.2 | 0.214 | 0.256 | 1.2 | 0.223 | 0.180 |
| 1.5 | 0.197 | 0.209 | 1.5 | 0.107 | 0.280 |
| 1.8 | 0.246 | 0.238 | 1.8 | 0.085 | 0.432 |
| x_l | MI (L) | MI (R) | x_l | SC (L) | SC (R) |
| 1.2 | 0.514 | 0.177 | 1.2 | 0.153 | 0.111 |
| 1.5 | 0.197 | 0.159 | 1.5 | 0.357 | 0.307 |
| 1.8 | 0.116 | 0.145 | ... | ... | ... |
| 2.1 | 0.137 | 0.136 | ... | ... | ... |
| [h] | | | | | |
| x_l | AK (L) | AK (R) | x_l | PK (L) | PK (R) |
| 1.2 | 0.165 | 0.226 | ... | ... | ... |
| 1.5 | 0.182 | 0.128 | ... | ... | ... |
| 1.8 | 0.212 | 0.279 | ... | ... | ... |
| x_l | MI (L) | MI (R) | x_l | SC (L) | SC (R) |
| 1.5 | 0.150 | 0.136 | 1.2 | 0.131 | 0.200 |
| 1.8 | 0.119 | 0.057 | 1.5 | 0.249 | 0.398 |
| 2.1 | 0.235 | 0.111 | 1.8 | 0.100 | 0.122 |
| 2.4 | 0.409 | 0.382 | 2.1 | 0.131 | 0.171 |

lowered with respect to the anterior contact and the raised posterior tongue body. For SC, a slight raising of the middle tongue body was observed. In order to provide a clearer picture of the articulatory patterns, a detailed analysis of the cross-sectional shapes and the 3-D tongue and vocal-tract shapes becomes essential.

For MI, the coronal cross sections (Fig. 5) in the region immediately posterior to the contact revealed a flat tongue shape and grooving along the midsagittal line which extended over the majority of the palatal region (approximately 2.4–4.5 cm from the lip opening). Grooving can be observed in the panels of rows 3 and 4, from bottom, in the figure.

The 3-D tongue body shape revealed a tongue which was drawn *laterally* inwards, directed toward the midsagittal plane, and this inward movement was particularly prominent in the posterior tongue-body region where the lateral linguopalatal contact ended. This lateral tongue compression facilitates air flow along the sides of the tongue behind the alveolar contact. The overall tongue-body shape exhibits a convex³ contour especially in the posterior tongue body region. The convex shape, clearly observed in row 6 panels in Fig. 5, perhaps aid the lateral flow along the tongue sides in this region. This results in an airway opening that is more or less “crescent” shaped, at least until lateral lingual contacts are reestablished with the roof of the oral cavity in the velar region. Similar observations were made by Stone and Vatikiotis-Bateson (1995). The linguovelar contact can be observed in the leftmost panel in row 6, and above.

The overall tongue-shape behavior for the other subjects was similar to that of MI:

(1) For SC, grooving in the region immediately behind the alveolar contact was not marked and extended over only a short region (about 0.5 cm). The overall 3-D tongue body behind the contact exhibited a convex contour, and was drawn laterally inwards (toward the midsagittal plane). Asymmetry was observed in the lateral flow channel with more opening on the left side than on the right. Lateral channels extended till the linguovelar contact was established.

(2) For PK, the cross-sectional tongue surface which appeared flat, but nonconcave, until about 5 cm from the lip opening turned distinctly convex in the middle part of the tongue body. Behind the alveolar contact, lateral channels were not evident until lateral linguopalatal contact ended at about 4 cm from the lip opening. Asymmetry in the tongue shape and airway areas was noticed in the posterior region (4.2–5.7 cm). Lateral channels disappeared again in the region where lateral lingual bracing against the roof of the oral cavity was reestablished in the velar region, at about 5.7 cm away from the lips.

(3) For AK, the tongue surface, in general, was distinctly convex. Like PK, the appearance of lateral flow channels in the region behind the contact coincided with the disappearance of the lateral linguopalatal contact (at about 5.4 cm from the lip opening). The lateral contribution started decreasing in the velar region with the establishment of lingual bracing with the roof of the oral cavity. Furthermore, coronal scans illustrated a medial notch on the posterior tongue surface once the linguopalatal contact disappeared. This, perhaps, is a consequence of the inward lateral com-

pression of the tongue body toward the midsagittal plane and lateral linguo-velar bracing.

The area functions were similar in their patterns across the four subjects, particularly up to about 4 cm from the lips [Fig. 4(a)]. Lateral openings alongside the tongue, created by inward lateral compression of the tongue body, contributes to increased airway areas in that region. For subjects SC and MI, grooving along the midsagittal line immediately behind the alveolar contact contributes to the increased areas as well. Subjects showed some area decrease in the velar region which is attributed to the disappearance of the lateral channels due to lingual bracing against the roof of the oral cavity. Decreased areas in the uvular and upper-pharyngeal region [at about 10–11 cm in Fig. 4(a)] for MI and SC result from a slightly raised and retracted posterior tongue body, perhaps a consequence of their apical articulation. The decreased areas in the upper- to lower-pharyngeal region for PK [8–12 cm in Fig. 4(a)], and for AK (approximately, 12–15 cm), on the other hand, is due to a slight tongue-root retraction; a probable consequence of their laminal articulation. Note the large areas in the velar- to upper-pharyngeal region for AK [7–12 cm in Fig. 4(a)]; this is probably due to her lowering the middle and posterior tongue body.

Analysis of the EPG data showed that the total (percentage) contacts were smaller for MI and SC when compared to PK and AK (on average, 60% in AK and PK compared to 40% in MI and 25% in SC). ANOVA results showed that differences in the back region contacts of AK and PK were significant ($p < 0.001$) when compared to those of MI and SC implying that indeed the lateral contacts of AK and PK extend further back. Systematic asymmetry in linguopalatal contacts was only found for subject PK with the right side more favored than the left.

B. The dark [ɖ]

1. The linguo-alveolar contact

The [ɖ] articulations of subjects AK and PK were laminal while those of MI and SC were apical (Fig. 3). The MRI data showed no lingual contact in the anterior (dental/alveolar) region for subject PK, while for AK medial lingual contact was seen in the anterior alveolar region (extending between 1.2–1.8 cm from the lip opening). Analysis of the EPG data of subjects AK and PK showed little or no front-region linguopalatal contact in [ɖ] with only about 10%–25% of the front-region electrodes contacted on an average (see for example Fig. A1 in the Appendix). The linguo-alveolar contact along the midsagittal line for MI's and SC's [ɖ], on the other hand, extended between 1.5–2.4 cm and between 1.2–2.1 cm from the lip opening, respectively. EPG data showed that MI and SC consistently showed linguo-alveolar bracing with 50%–75% front-region contacts on an average. Except for SC, the linguo-alveolar contact did not extend laterally through the palatal region.

Coronal profiles of the vocal tract during the production of [ɖ] (subject MI) are shown in Fig. 7. Medial linguo-alveolar contact is observed in the panels of the second row

from the bottom. Areas of the lateral channels, found on either side of the linguo-alveolar contact, for all subjects are given in Table I.

2. Region behind the linguo-alveolar contact

For subject MI, prominent convex tongue body shapes are observed at and behind the linguo-alveolar contact (from about 1.8–3.3 cm from the lips.) Although the medial surface of the tongue body shows a slight flattening in the post-palatal region (row 4 panels and the 2 rightmost panels in row 5 in Fig. 7) the tongue body shape turned convex again in the vicinity of the velar region (2 leftmost panels in row 5, from bottom, and above). Grooving along the midsagittal line (observed in the 3 leftmost panels in row 4 from bottom) is not as prominent as that observed in [l]. Lateral bracing with the roof of the oral cavity in the velar region, at about 7.5 cm away from the lips, can be seen in rightmost panel of row 7.

The cross-sectional tongue shapes of the other speakers were as follows:

(1) For SC, there was a slight concave cross section of the tongue behind the linguo-alveolar contact, from about 2.1–2.4 cm, which changed into convex at the end of the lateral linguopalatal contact. The medial tongue surface, in general, was flat with the sides relatively rounded. A small notch on the tongue surface (along the midsagittal line) was observed in the vicinity of the postpalatal region, although it was found not to alter the overall convex shaping of the tongue body. Lateral lingual bracing with the roof of the oral cavity was established in the velar region.

(2) For PK, the cross-sectional surface of the anterior tongue body was convex. A slight flattening of the surface was found behind the alveolar contact (between 2.7–4.5 cm from the lip opening), although the surface turned significantly convex again, in the middle and posterior tongue body regions. No linguo-velar bracing was observed.

(3) For AK, the tongue body showed distinct convex shapes in the anterior region (1.2–2.4 cm) with a tendency toward decreased convexity (flattening of the surface) in the middle part of the tongue body (2.7–3.6 cm from the lips). The overall cross-sectional shapes of the posterior tongue body were also convex with slight grooving along the midsagittal line, and significant asymmetry which resulted in greater right-side openings in the airway. No linguo-velar bracing was observed.

The overall 3-D tongue shapes and linguopalatal contact patterns suggest that the grooving found sometimes in the region immediately behind the alveolar contact (in MI's /l/s, SC's [l], and AK's [ɖ]) is, most likely, a secondary effect of the anterior lingual contact and the lateral compression of the tongue body, rather than a primary characteristic to satisfy an aerodynamic requirement. Grooving along the midsagittal line did not appear to be actively controlled during production, and, hence, is susceptible to intra- and inter-subject variabilities. Groove dimensions (width and depth) were small and did not exceed 5 mm for any of the subjects.

Analysis of the area functions, shown in Fig. 4(b), indicates similarities in the overall patterns across all subjects except for PK. For the other three subjects there was an

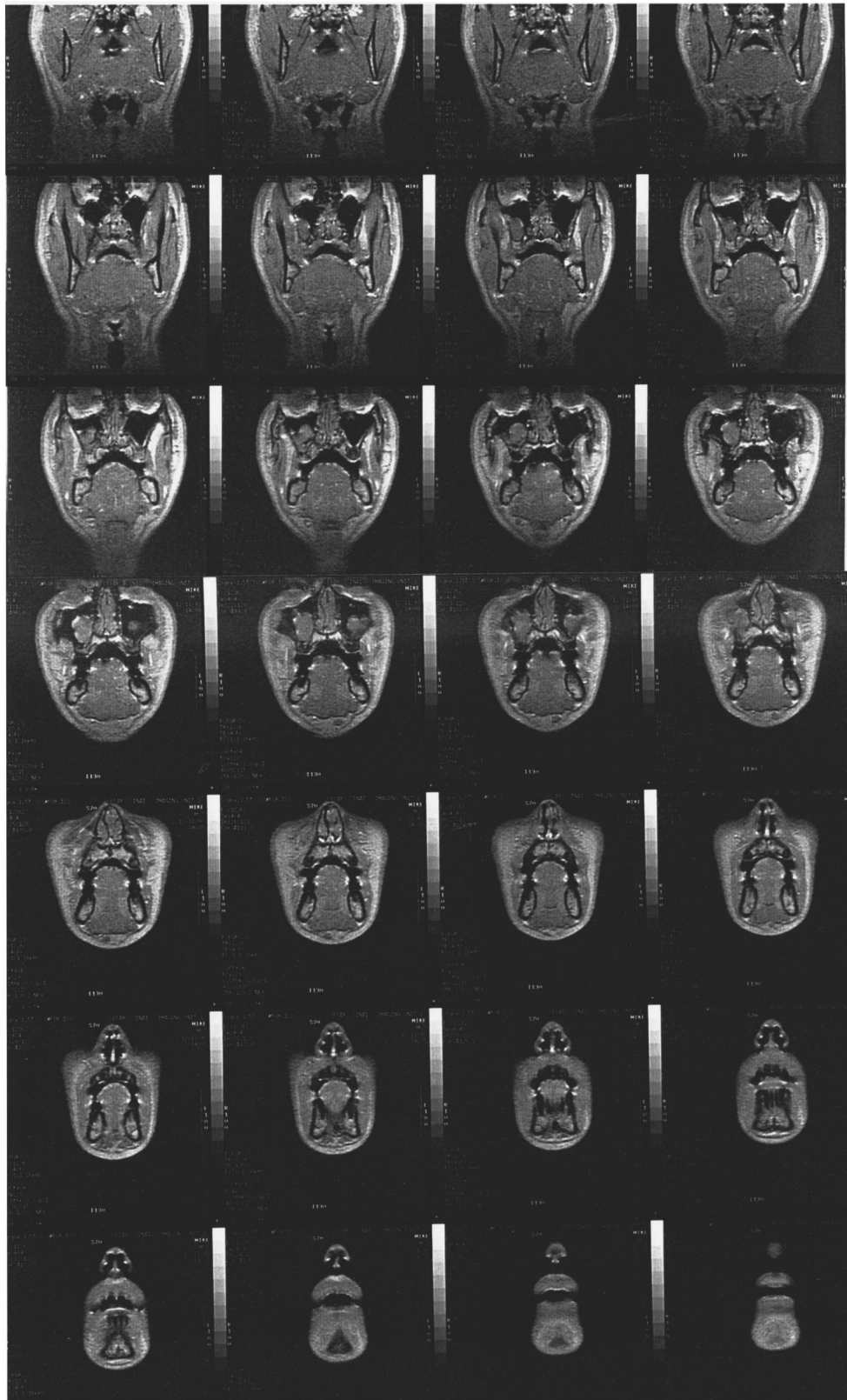


FIG. 7. Coronal profiles of the vocal tract during the production of [ɬ] (subject MI) taken along contiguous sections in the oral cavity at every 3 mm starting from 3 mm from the outer lip opening. The figure is arranged such that the cross section closest to the lips appears in the rightmost panel of the bottom row and successive oral-cavity cross sections, moving away from the lips, are placed right-to-left in each row. Linguo-alveolar contact is observed in the panels of the second row from the bottom of the page. Prominent convex tongue body shapes can be seen at and behind the linguo-alveolar contact. Grooving along midsagittal line (see panels in row 4 from the bottom) is not as prominent as that observed in [l] (Fig. 5). Lateral lingual bracing with the roof of the oral cavity is seen in the rightmost panel of row 7 (from the bottom).

abrupt increase in the areas in the region immediately posterior to the alveolar contact, and large areas in the palatal region due to the contribution of lateral openings alongside the tongue (created by the inward tongue compression). For PK, the area change was more gradual than the other subjects due to the absence of a linguo-alveolar contact in the MRI data. The EPG data, however, showed that PK's [ɫ] may or may not be produced with a complete linguo-alveolar contact.

All subjects reveal a distinct narrowing of the airway in the uvular and upper-pharyngeal region. For subjects MI and SC, the decreased areas, which extend to the velar region for MI, are due to a significantly raised tongue body in the velar region. For PK and AK, on the other hand, the decreased areas are a consequence of a retracted posterior tongue body. The area functions also reveal decreased pharyngeal areas which result from tongue-root retraction. The extent of the pharyngeal region affected by the tongue-root retraction varied across subjects. The upper- and lower-pharyngeal regions [9–14 cm in Fig. 4(b)] showed small areas in the [ɫ]s of AK and MI. For SC and PK, the area reduction is mostly confined to the uvular and upper-pharyngeal region [10–12 cm, and 9–10 cm, respectively, in Fig. 4(b)], especially when compared to their [ɫ]s.

Analysis of the area functions shows that narrowing of the vocal tract at the uvular and upper-pharyngeal region is a consistent correlate of [ɫ]. This narrowing may not necessarily be due to velarization [defined as the raising of the posterior tongue body (dorsum) in the velar region], since only subjects MI and SC showed velarization. It may be that velarization only occurs for apically produced [ɫ]s.

Analysis results of the EPG data were consistent with those of the MRI study. ANOVA results showed the mean contact patterns of subjects AK and PK were significantly different from those of MI and SC.

C. Comparing light [l] and dark [ɫ]

The midsagittal tongue contours for [l] and [ɫ] were similar in the front region but showed noticeable differences in the back region. The front region EPG contact for [l] and [ɫ], on the other hand, showed different behavior across subjects: laminal light [l]s (AK and PK) exhibited significantly more front-region contacts than the laminal dark variety, while these contacts were comparable for the apically-produced [l]s and [ɫ]s (MI and SC). ANOVA results confirmed the statistical significance of this observation. Moreover, [l] exhibited greater lateral contacts in the palatal region for all subjects. These results imply variabilities in strategies used by different speakers to achieve similar tongue shapes.

The inter- and intra-speaker variabilities observed in the total electrode contacts appeared to be greater in [ɫ] than in [l]. For example, PK produced [ɫ] either without any contact in the alveolar region (in 3 out of the 8 tokens) or with linguo-alveolar contact (in the remaining tokens). The other subjects, on the other hand, consistently exhibited linguo-alveolar contact. The total linguopalatal contacts for the dark allophone of subjects AK and PK were much smaller than those of MI and SC while the reverse was true for the light

allophones. ANOVA results showed significant differences in the front, back, and total linguopalatal contacts of the dark and light allophones of both AK and PK.

The overall 3-D tongue body *shape*—alveolar contact (constriction), lateral compression, and convex tongue body—for [l] and [ɫ] were similar although the tongue body *position* in the velar and pharyngeal regions were different. The area functions of [ɫ] contrast with those of [l] in two ways: (1) [ɫ]s show somewhat larger areas in the palatal region immediately behind the alveolar contact due to a greater inward lateral compression of the tongue body and less lateral contacts; the greater compression is also evidenced by somewhat larger sizes of postcontact lateral openings in [ɫ], and (2) [ɫ] exhibit significantly decreased areas in the uvular and upper-pharyngeal region, with effects extending either as far as the velar region and/or the lower-pharyngeal region depending on the part of the tongue body used in forming the pharyngeal “constriction.” Involvement of the upper part of the tongue root and/or posterior tongue body results in decreased velar to upper-pharyngeal areas while retraction of the whole tongue root influences most of the pharyngeal region. Figure 8 contrasts 3-D tongue shapes for MI's [l] and [ɫ]; both posterior and anterior views of the tongue are shown. Note the greater lateral compression for MI's [ɫ] when compared to [l] [parts (a) and (c)] and the convex shape of the posterior tongue body for both sounds [parts (b) and (d)].

D. Length measurements

The vocal-tract length (l_{VT}) and the vertical lip-opening (l_{VO}) measurements are summarized in Table II. Dark [ɫ]s have somewhat greater l_{VT} values when compared to light [l]s due to tongue-root retraction and/or posterior tongue body raising. Recall that the length of the vocal tract is measured along the midline and, hence, raising or backing of the tongue increases the effective length of the back region, and hence increases the overall length. The l_{VO} values appear to be subject dependent, and no contrastive differences are noticed among these values for the different sounds.

E. Summary of the results

MR images for both the light allophone [l] and the dark allophone [ɫ] indicate that the midsagittal tongue contours can be different across subjects. Common characteristics, however, were revealed in cross-sectional and 3-D tongue shapes, area functions, and linguopalatal contact profiles. These sounds were characterized by a complete linguo-alveolar contact or, just a constriction as observed in some cases of the [ɫ] of subject PK. The contact location was about 1–1.5 cm away from the lip opening and the contact length, 0.6–1.5 cm in the alveolar region with relatively small openings around both sides of the contact. These “*lateral channels*” alongside the tongue appeared in the alveolar contact, or constriction, region and, in general, continued posteriorly until the lateral linguovelar contact was established. The right and left channels were, in general, unequal and their areas started increasing behind the alveolar contact (due to

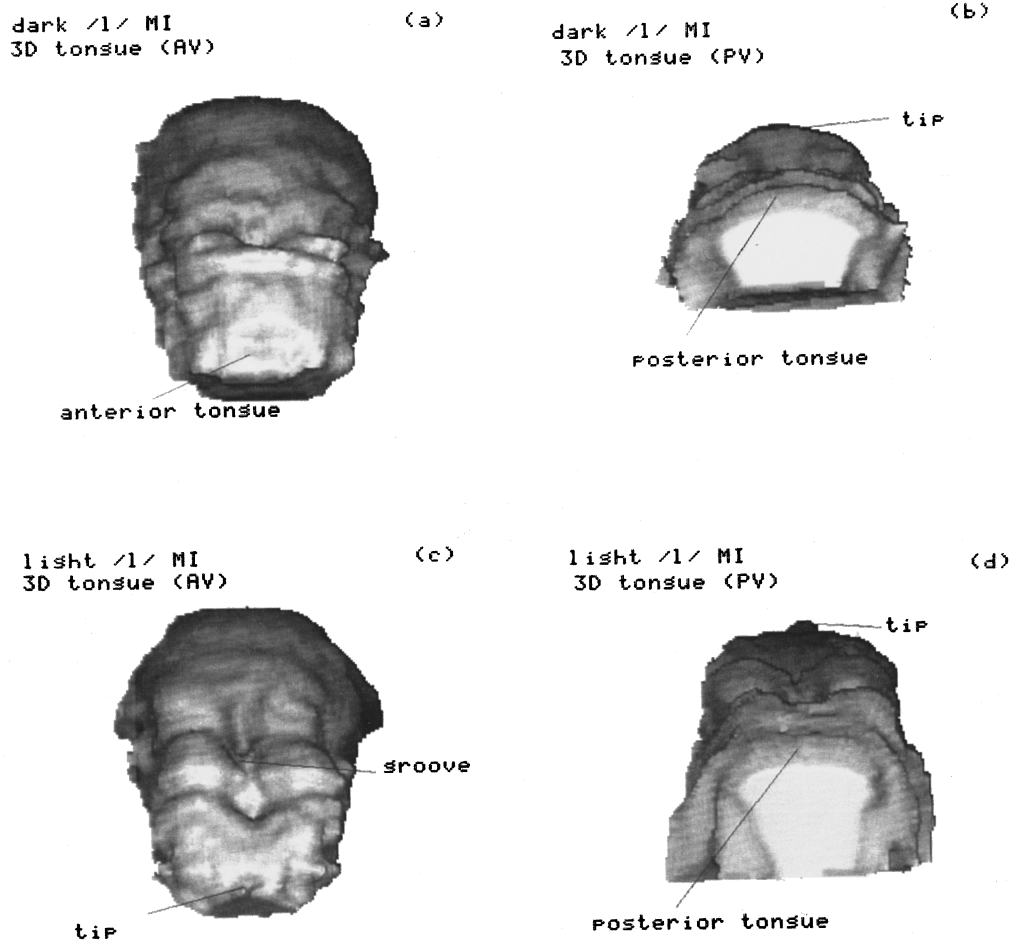


FIG. 8. The 3-D tongue shapes for the MI's dark and light lateral approximants. (a), (b) Anterior (AV) and posterior views (PV) for [ɫ]. (c), (d) Anterior and posterior views for [l].

inward lateral compression of the tongue body), and started decreasing again as the region of the lateral linguo-velar contact, if present, was approached.

The merging of the lateral channels with the central opening along the palatal region resulted in crescent-shaped cross sections and relatively large areas. The extent of the lateral flow channel in the palatal region behind the linguo-alveolar contact was limited by the extent of the lateral linguopalatal contact: [ɫ] typically revealed more lateral contact than [l], thus explaining, in part, the smaller areas consistently observed in the palatal region of [ɫ].

The posterior tongue body, as observed in 3-D tongue shapes, showed *inward lateral compression* which was directed toward the midsagittal plane. This lateral compression enables the creation of the lateral flow channels along the curved sides of the tongue. This observation is perhaps related to the tongue blade narrowing which is hypothesized to

be a feature for the laterals (Sproat and Fujimura, 1993). The overall 3-D tongue shape behind the contact tended to be convex. For some subjects, the cross-sectional coronal tongue shapes immediately behind the linguo-alveolar contact appeared flat due to lateral linguopalatal bracing. In addition, some subjects showed grooving along the midsagittal line. Grooving along the midsagittal line or tongue-surface flattening, which appear sometimes, may be viewed as a “superposition” on the otherwise basic convex tongue body shape. The anterior grooving is less prominent than that observed in alveolar sibilants such as /s/ (Narayanan *et al.*, 1995). Unlike alveolar fricatives, the grooving, if present, does not continue through the posterior tongue region as a concave surface, suggesting that it is not a key component of a medial airflow channel. Hence, the modification of the tongue body contour, in terms of surface flattening and/or grooving, observed in some portions of the tongue surface for some subjects, is not a primary articulatory characteristic satisfying an aerodynamic constraint, but merely represents secondary effects of the linguopalatal bracing and the lateral inward compression of the posterior tongue body.

It is important to note here that midsagittal tongue shapes can be misleading in characterizing /l/. Similar 3-D tongue shapes (convex surface, lateral compression, and alveolar contact) with somewhat different groove characteris-

TABLE II. Vocal-tract length (l_{VT}) and vertical lip opening (l_{VO}) measurements (in mm).

| Sound | Subject AK | | Subject MI | | Subject PK | | Subject SC | |
|-----------|------------|----------|------------|----------|------------|----------|------------|----------|
| | l_{VT} | l_{VC} | l_{VT} | l_{VO} | l_{VT} | l_{VO} | l_{VT} | l_{VO} |
| Light [l] | 170.7 | 22.7 | 178.1 | 22.9 | 153.7 | 7.5 | 178.4 | 14.1 |
| Dark [ɫ] | 173.2 | 26.1 | 184.9 | 23.5 | 156.7 | 6.8 | 179.6 | 13.3 |

tics along the midsagittal line may look vastly dissimilar in midsagittal slices. Conversely, similar groove lengths and depths in two somewhat different 3-D tongue body shapes may appear similar in the midsagittal plane.

The back region areas for [l] showed significant inter-subject variability. In the case of [ɫ], on the other hand, all subjects revealed decreased areas in the uvular and upper-pharyngeal regions due to significant retraction of the tongue root and/or raising of the posterior tongue body. In addition, the effect of this pharyngeal “constriction” was found to extend either as far as the velar region and/or through the lower-pharyngeal region depending on the particular part of the tongue body actively involved in the constriction formation. These results indicate that velarization, which is typically associated with [ɫ], is not necessarily a consistent characteristic across speakers although decreased uvular and upper-pharyngeal areas, when compared to those of [l], is a consistent feature for all subjects.

IV. DISCUSSION

It appears that the primary tongue-shaping mechanisms for laterals are responsible for the alveolar contact, inward-lateral compression, and convex shaping of the middle and posterior tongue body. These features seem to be invariant across subjects. Flattening or grooving of the tongue body immediately behind the alveolar contact, appear to be *secondary* features. We speculate that these secondary features are influenced by the extent and force of front-region linguopalatal contact and the muscular activity of the middle and posterior tongue body. For example, a tendency toward a greater grooving in the middle tongue body was observed in the apically articulated [l]s that showed smaller lateral linguopalatal contacts than laminally articulated [l]s; laminal [l]s were characterized by a somewhat flat middle tongue body shape.

Although there were differences in the tongue body *position* of the dark and light /l/s in the back region, the overall 3-D tongue body *shapes* comprising the alveolar contact and convex middle and posterior tongue body with inward-lateral compression, were, in general, similar. These tongue body shapes were, however, quite distinct from those of the vowels /a,i,u/ (Narayanan *et al.*, in preparation). Hence, the similarity in the midsagittal tongue contours of the laterals and vowels observed by Giles and Moll (1975) does not, most likely, translate to similarity in the corresponding overall tongue shapes. Further corroborating evidence for this observation regarding the tongue shapes of the vowels and laterals is provided by ultrasound data (Stone, 1991; Stone *et al.*, 1992).

Acoustic implications: Some preliminary speculations regarding the acoustic characteristics of the laterals can be made based on these articulatory data. The observed supraglottal “constriction” areas (lateral channel areas and/or areas along the midsagittal line) together with the relatively low flow rates, typically 100–200 cm³/s (Stevens, to be published), suggest no significant pressure drop in the supraglottal constriction region, and hence, negligible chances for friction. The absence of a significant supraglottal pressure drop also implies a sustained, and almost uniform, transglot-

tal flow through the entire duration of the sound. Most of the spectral energy of the laterals is below 5 kHz, with the low-frequency behavior greatly influenced by the cavity posterior to the primary supraglottal constriction (back cavity). The first formant frequency (F_1), which typically occurs between 250–500 Hz, can be associated with the Helmholtz resonance between the relatively large back-cavity volume and the oral-constriction space. The losses at the oral constriction contribute to relatively high bandwidth for F_1 which in turn tends to reduce the amplitude of the spectrum. Furthermore, the anterior tongue body shape suggests that changes in F_1 at the consonant’s release (for example, into a following vowel) can be expected to be somewhat abrupt in /l/ due to abrupt changes in the corresponding area functions. The second formant frequency (F_2) can be associated with the half-wavelength resonance of the back cavity (for example, lengths of 12–14 cm would approximately correspond to resonances in the range 1250–1460 Hz). Retracting or raising the posterior tongue body observed in the case of [ɫ] result in an increase in the effective length of the back cavity, and hence, a lowering of the F_2 values.

The acoustic characteristics of the lateral channels in /l/ have not yet been studied in detail. The pole-zero cluster observed in the acoustic spectra of /l/s (around 3–5 kHz) most likely results from both back-cavity and lateral channel effects. A simple approximate analysis suggests that the two lateral channels, which, in general, have different areas, would contribute a pole-zero-pole cluster in the frequencies below 5 kHz (Stevens, to be published). Variability, however, is expected in the structure of the high-frequency cluster due to intra- and inter-subject differences in the shapes and sizes of the back cavity and the lateral channels. Effects of coarticulation and speech rate may further influence these variabilities (Giles and Moll, 1975).

In this paper, a detailed account of the 3-D vocal tract and tongue shapes for the laterals in American English was presented. The results of this investigation may be used as a baseline for studying articulatory-to-acoustic relations of these sounds and will be reported in the future.

ACKNOWLEDGMENTS

The cooperation and support of the Cedars-Sinai medical imaging group, the UCLA Department of Radiology, and the UCLA Phonetics Laboratory is gratefully acknowledged. We are grateful to our subjects AK, MI, PK, and SC for their help. We thank Patricia Keating and Peter Ladefoged for useful discussions and for use of EPG facilities. Thanks to Carol Espy-Wilson, Anders Lofqvist, and Maureen Stone for valuable suggestions. The assistance of Makkalon Em with the EPG data analysis is appreciated. This work was supported in part by UCLA and by NSF.

APPENDIX: VARIABILITY ANALYSES THROUGH EPG STUDIES

In this Appendix, we describe the results of an EPG study which is aimed at investigating:

- (1) Intra-token articulatory (temporal) stability during sustained phonation of light and dark /l/s.

- (2) Inter-token articulatory variabilities of these sounds.
- (3) Differences and similarities between these sounds produced in sustained utterances with respect to the sounds produced in naturally spoken words. Both inter-subject differences in the articulatory patterns for each sound and differences and similarities between light versus dark /l/ are investigated. Our focus here is to study the variabilities of sustained sounds with respect to those occurring in natural contexts, and not to investigate specific coarticulatory effects.
- (4) Inter-subject differences in the articulatory patterns for each sound.

1. Data analysis

EPG data from the sustained utterances (eight repetitions) were collected from the subjects in a supine posture (simulating the position assumed inside the MRI scanner). EPG data were also collected for the words {*elitist, freely, Robert E. Lee*} for light /l/, and the words {*paul, peel, pool*} for dark /l/, all of which were spoken embedded in the carrier phrase “Say—again”. These utterances were spoken by the subjects in their normal upright posture.

The total percentage of electrodes contacted in the front and back regions (refer to Fig. 2 for region definitions) were calculated and used for variability analyses. Temporal averaging of the contact measures was done over the middle 3.8 s of each sustained data segment.

It should be noted that, given differences in individual oral morphologies (such as palate structure), the intersubject comparisons using EPG contacts can be justified since: (a) region definitions for each subject were selected based on their individual palate structure instead of an arbitrary assignment of electrodes to particular regions, (b) comparisons were based on normalized “percentage” contacts in each region, and (c) intersubject comparisons are intended to give, at a gross level, differences in the tongue-palate interactions (e.g., whether light /l/ is characterized with greater contact in one subject compared to another). Due to the data “normalization,” such comparisons should reflect differences in gestural rather than anatomical differences.

Sample EPG contact profiles are shown in Fig. A1. For the sustained utterances, the mean and standard deviation of the *total* (i.e.,=front+back) linguopalatal contact were calculated. For [l], the total linguopalatal contact (expressed in percentage relative to the total number of electrodes) across tokens was 60% in AK and PK when compared to 40% in MI and 25% in SC. Token-to-token variability was less than 5%, and within-token variations were within 4%, assuring both within- and across-token consistency. For [ɫ], the total contact was 20%, 40%, and 25% for AK, MI, and SC, respectively. Token-to-token variability was less than 7%, and within-token variations were within 3.7%. Subject PK produced [ɫ] with no lingual contact (in 3 tokens) or with minimal contact (5%–10% total contact in 5 tokens). Recall that the “sampling time” for EPG is 10 ms. Hence, about 400 EPG profile samples were averaged in each token.

These results indicate that our phonetically trained subjects produced the sustained sounds in a consistent manner assuring a degree of articulatory stability during the MRI

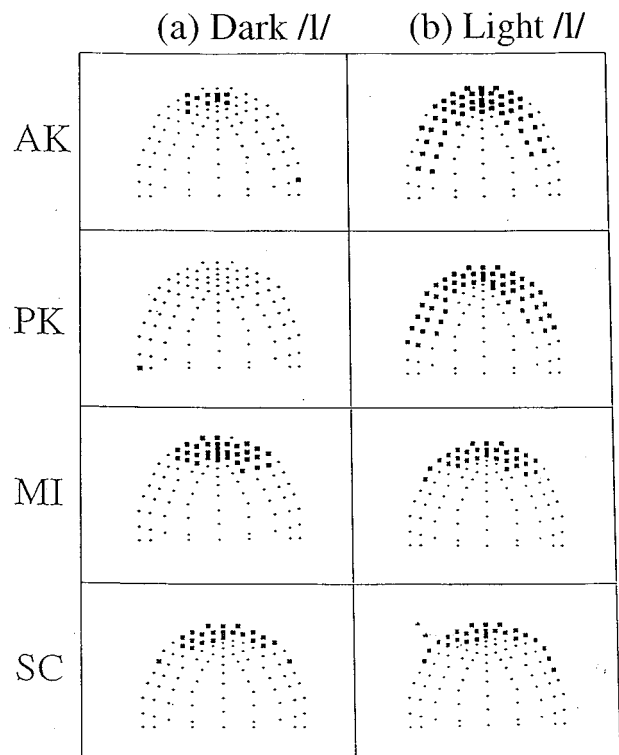


FIG. A1. Sample linguopalatal contact profiles for the dark and light lateral allophones of the different subjects.

experiments. Further detailed analysis of intra- and inter-token variabilities was done using repeated measures ANOVA with total linguopalatal contact as the dependent variable.

The first set of these tests used sustained utterances. Results showed no significant intra-token variations in the total contact values for both dark and light /l/ ($F=0.183$, $p=0.903$) for all the subjects.

ANOVA results (one-way repeated measures using allophone type as factor and total linguopalatal contact as the dependent variable) for between-subjects variation in the total contact of the sustained light versus dark /l/ may be considered somewhat statistically significant ($F=4.092$, $p=0.092$). The absence of a high significance in these variabilities is not surprising since the contact patterns for the dark and light /l/ of subject MI, and to a lesser degree, of subject SC, are comparable. This may have resulted due to either the tongue shaping and bracing associated with the apical nature of the /l/s produced by these subjects, and/or a greater tongue bracing in the artificial scenario of sustaining the lateral sounds (the latter hypothesis may be verified by comparing sustained and in-context EPG data). The analysis also showed variations in the total contacts of dark versus light cases for each subject with similar statistical significance levels ($F=1.984$, $p=0.080$). There was an equally significant interaction with the sound-type factor ($F=2.198$, 0.054) which may be due to the fact that not all subjects showed the same contrast in tongue-palate contact patterns between [l] and [ɫ].

In the second of these tests, EPG data corresponding to the laterals extracted from naturally spoken words were com-

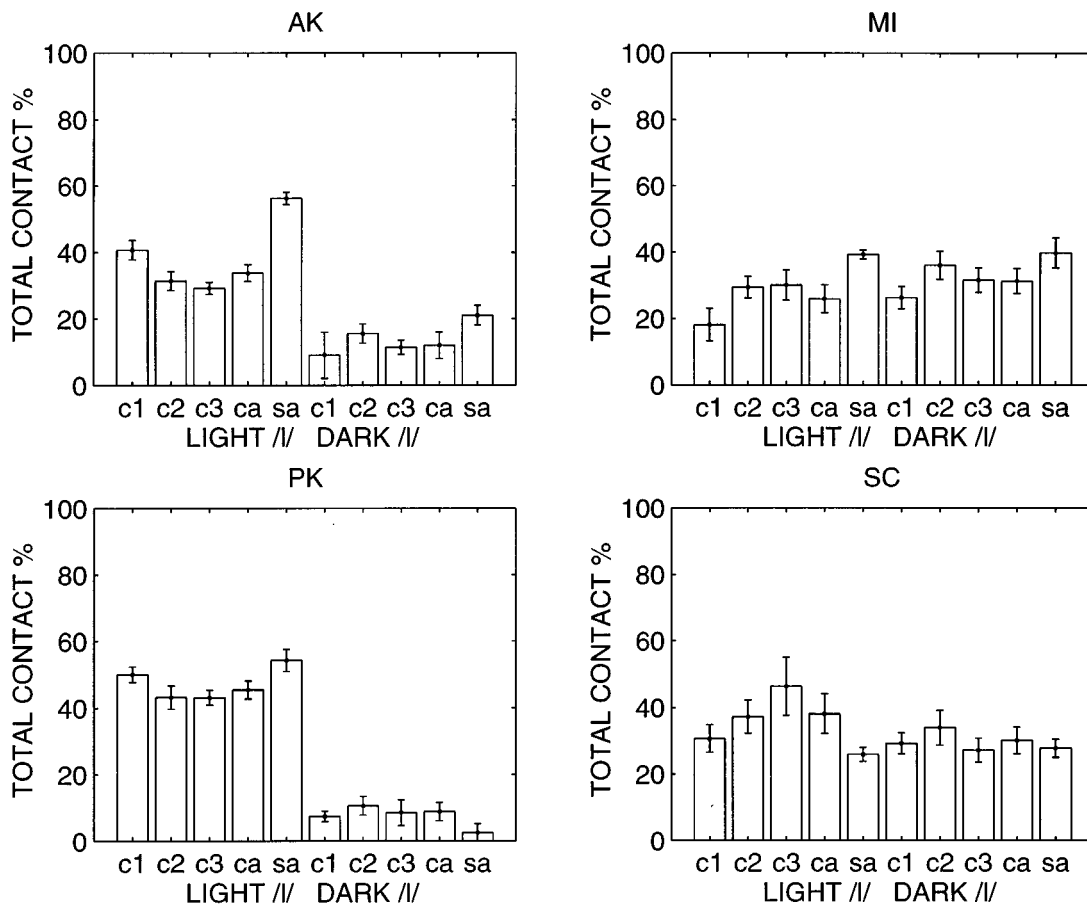


FIG. A2. Total linguopalatal contact expressed in percent relative to the total number of electrodes for light and dark /l/ obtained from both naturally spoken words and sustained utterances, averaged across eight repetitions for each subject. The first five bins in each panel correspond to light /l/ while the last five correspond to dark /l/. For light /l/, c1, c2, c3 represent contact values extracted from the words {*elitist*, *freely*, *Robert E. Lee*}, respectively, while for dark /l/, they represent contact values extracted from the words {*paul*, *peel*, *pool*}. ca and sa represent the pooled average values for the in-context and the sustained utterances, respectively. The error bars represent the variations in linguopalatal contact across repetitions. Further data analysis was based on ANOVA techniques (see text for details).

pared against the sustained ones. Segmentation from each word was done manually using time-aligned displays of the acoustic waveform, spectrograms, and EPG data. The total contact for each token was then obtained by (temporal) averaging over the segmented duration and used for variance analyses. The variabilities within the eight repetitions of each token were found to be statistically insignificant, and the results reported in this paper are based on averages of the total contacts across the eight repetitions. The average total linguopalatal contact values for each of the in-context cases, along with their pooled average and the average value for the sustained utterances, are shown in Fig. A2. ANOVA on total average contact (dependent variable) for [l] with respect to context showed no significant variation ($F=0.554$,

$p=0.655$). Similar tests for [ɫ] with respect to context (words vs sustained) also showed no significant variation between the various cases ($F=2.098$, 0.154). Matrices of comparison probabilities computed following Tukey *post hoc* tests (Tables AI and AII, for [l] and [ɫ], respectively) showed that, although statistically not significant, relatively greater variability was found when the in-context cases were compared with the sustained cases. The reason for this may be the somewhat greater (but not significant) tongue bracing seen in the sustained utterances of all subjects, except subject SC.

The final set of tests were comparisons (two-way ANOVA followed by Tukey *post hoc* tests) based on pooled averages across the various in-context cases with respect to averages for sustained cases. The resulting matrix of com-

TABLE AI. Matrix of pairwise comparison probabilities from Tukey *post hoc* tests following ANOVA of average total linguopalatal contact for [l] across various contexts and sustained utterances ($F=0.554$, $p=0.655$).

| | <i>elitist</i> | <i>freely</i> | <i>Robert E. Lee</i> | sustained |
|----------------------|----------------|---------------|----------------------|-----------|
| <i>elitist</i> | 1.000 | | | |
| <i>freely</i> | 1.000 | 1.000 | | |
| <i>Robert E. Lee</i> | 0.991 | 0.995 | 1.000 | |
| sustained | 0.675 | 0.707 | 0.831 | 1.000 |

TABLE AII. Matrix of pairwise comparison probabilities from Tukey *post hoc* tests following ANOVA in average total linguopalatal contact for [ɫ] across various contexts and sustained utterances ($F=2.098$, $p=0.154$).

| | <i>paul</i> | <i>peel</i> | <i>pool</i> | sustained |
|-------------|-------------|-------------|-------------|-----------|
| <i>paul</i> | 1.000 | | | |
| <i>peel</i> | 0.864 | 1.000 | | |
| <i>pool</i> | 0.987 | 0.693 | 1.000 | |
| sustained | 0.250 | 0.638 | 0.151 | 1.000 |

TABLE AIII. Matrix of pairwise comparison probabilities from Tukey post hoc tests following a two-way ANOVA in average total linguopalatal contact for [ɸ] and [l] across various contexts (pooled averages) and sustained utterances. ANOVA results: For, the factor *allophone*={[ɸ],[l]}, ($F=34.108$, $p=0.000$); for the factor *type*={in-context, sustained}, ($F=6.243$, $p=0.019$); for the interaction between allophone and type, ($F=0.174$, $p=0.680$).

| | | [ɸ]
context | [ɸ]
sustained | [l]
context | [l]
sustained |
|---|-----------|----------------|------------------|----------------|------------------|
| ɸ | context | 1.000 | | | |
| ɸ | sustained | 0.190 | 1.000 | | |
| l | context | 0.000 | 0.108 | 1.000 | |
| l | sustained | 0.000 | 0.020 | 0.467 | 1.000 |

parison probabilities (Table AIII) helps us to further isolate some of the variabilities. No significant differences were found between the sustained and in-context cases for both [l] and [ɸ]. The differences in the total linguopalatal contact were significantly different between [l] and [ɸ] in both sustained and in-context cases ($p<0.005$). A two-way ANOVA with respect to the different subjects and sound type (dark, light) showed significant differences ($p<0.01$) between [l] and [ɸ] for subjects AK, PK, and SC (Table AIV).

In summary, the EPG analyses indicate significant intra- and inter-token articulatory stability in the production of [l] and [ɸ] by our phonetically trained subjects. Furthermore, no significant differences were found in the linguopalatal contact patterns of the artificially sustained utterances of /l/ and those that occurred in natural contexts. These results give credibility to our using MR images of sustained laterals to

TABLE AIV. Matrix of pairwise comparison probabilities from Tukey post hoc tests following a two-way ANOVA in average total linguopalatal contact (pooled across various contexts) for [ɸ] and [l] across various subjects. ANOVA results: For, the factor *allophone*={[ɸ],[l]} ($F=44.231$, $p=0.000$); for the factor *subject*={AK,MI,PK,SC} ($F=1.044$, $p=0.391$); for the interaction between allophone and subject ($F=1.358$, $p=0.279$).

| | | [ɸ]
AK | [ɸ]
MI | [ɸ]
PK | [ɸ]
SC | [l]
AK | [l]
MI | [l]
PK | [l]
SC |
|-----|----|-----------|-----------|-----------|-----------|-----------|-----------|-----------|-----------|
| [ɸ] | AK | 1.000 | | | | | | | |
| [ɸ] | MI | 1.000 | 1.000 | | | | | | |
| [ɸ] | PK | 1.000 | 1.000 | 1.000 | | | | | |
| [ɸ] | MI | 1.000 | 1.000 | 1.000 | 1.000 | | | | |
| l | AK | 0.031 | 0.035 | 0.024 | 0.033 | 1.000 | | | |
| l | MI | 0.437 | 0.470 | 0.374 | 0.454 | 0.836 | 1.000 | | |
| l | PK | 0.002 | 0.002 | 0.002 | 0.002 | 0.933 | 0.206 | 1.000 | |
| l | SC | 0.111 | 0.124 | 0.089 | 0.118 | 0.998 | 0.991 | 0.638 | 1.000 |

capture “canonical” tongue shapes for these sounds. The caveats of our study, however, should be reiterated. The coarticulatory influences in the production of liquid consonants are well-known, and EPG data provides only limited articulatory information. Our study, however, is an attempt to provide insights into the three-dimensional vocal tract and tongue shapes during speech production and to gather quantitative data that can be useful for articulatory-to-acoustic modeling.

¹An approximant is a sound that is characterized by the approach of one articulator toward another but without the tract being narrowed to such an extent that a turbulent air stream is produced (Ladefoged, 1993).

²Data from sustained utterances were also collected from the subjects in upright position, but no significant differences in the linguopalatal contact patterns of these sounds produced in the two postures were found. Some of the minor differences found for [l] include: for PK, a tendency toward relatively larger linguo-alveolar contacts in the upright articulations when compared to the supine ones; for AK, slightly greater lateral linguopalatal contacts were observed in supine position; and for SC, lateral contact in the postpalatal region, which is probably due to the anterior extension of the linguo-velar bracing, were found in supine position.

³A convex shape refers to doming of the tongue surface as viewed from the palate, whereas concave refers to curving of the surface inwards as viewed from the palate.

Espy-Wilson, C. Y. (1992). “Acoustic measures for linguistic features distinguishing the semivowels /wjr/ in American English,” *J. Acoust. Soc. Am.* **92**, 736–757.

Gartenberg, R. (1984). “An electropalatographic investigation of allophonic variation in English /l/ articulations,” in *Work in Progress*, Vol. 4 (Phonetics Laboratory, University of Reading), pp. 135–157.

Giles, S. B., and Moll, K. L. (1975). “Cinefluorographic study of selected allophones of English /l/,” *Phonetica* **31**, 206–227.

Ladefoged, P. (1993). *A Course in Phonetics* (Harcourt Brace Jovanovitch College, Fort Worth), 3rd ed.

Lehiste, I. (1964). “Acoustical characteristics of selected English consonants,” *Folklore and Linguistics* **34**, 10–50. Indiana University Research Center in Anthropology.

Narayanan, S., Alwan, A., and Haker, K. (in preparation). “Articulatory-acoustic data, analysis, and models: Vowels” (in preparation).

Narayanan, S. S., Alwan, A. A., and Haker, K. (1995). “An articulatory study of fricative consonants using magnetic resonance imaging,” *J. Acoust. Soc. Am.* **98**, 1325–1347.

Sproat, R., and Fujimura, O. (1993). “Allophonic variation in English /l/ and its implications for phonetic implementation,” *J. Phon.* **21**, 291–311.

Stevens, K. N. (to be published). *Acoustic Phonetics* (to be published).

Stone, M. (1991). “Toward a model of three-dimensional tongue movement,” *J. Phon.* **19**, 309–320.

Stone, M., Faber, A., Raphael, L. J., and Shawker, T. H. (1992). “Cross-sectional tongue shapes and linguopalatal contact patterns in [S], [s] and [l],” *J. Phon.* **20**, 253–270.

Stone, M., and Vatikiotis-Bateson, E. (1995). “Trade-offs in tongue, jaw, and palate contributions to speech production,” *J. Phon.* **23**, 81–100.

SYSTAT for Windows: Statistics. (1992). SYSTAT Inc., Evanston, IL, version 5 ed.

Toward articulatory-acoustic models for liquid approximants based on MRI and EPG data. Part II. The rhotics

Abeer Alwan^{a)} and Shrikanth Narayanan^{b)}

*Speech Processing and Auditory Perception Laboratory, Department of Electrical Engineering,
School of Engineering and Applied Sciences, UCLA, 405 Hilgard Avenue, Los Angeles, California 90095*

Katherine Haker

*Imaging Medical Group, Cedars-Sinai Medical Center, 8700 Beverly Boulevard, Los Angeles,
California 90048*

(Received 11 March 1996; accepted for publication 26 September 1996)

Magnetic resonance images of the vocal tract during sustained production of [ɹ] by four native American English talkers are employed for measuring vocal-tract dimensions and for morphological analysis of the 3D vocal tract and tongue shapes. Electropalatography contact profiles are used for studying inter- and intra-talker variabilities. The vocal tract during the production of [ɹ] appears to be characterized by three cavities due to the presence of two supraglottal constrictions: the primary one in the oral cavity, and a secondary one in the pharyngeal cavity. All subjects show a large volume anterior to the oral constriction, which results from an inward-drawn tongue body, an anterior tongue body that is characterized by convex cross sections, and a concave posterior tongue body shape. Inter-subject variabilities are observed in the oral-constriction location and the way the constriction is formed. No systematic differences are found between the 3-D vocal tract and tongue shapes of word-initial and syllabic [ɹ]s. Tongue-shaping mechanisms for these sounds and their acoustic implications are discussed. © 1997 Acoustical Society of America.

[S0001-4966(97)02302-3]

PACS numbers: 43.70.Aj, 43.70.Bk [AL]

INTRODUCTION

In this paper, an analysis of the vocal-tract geometry obtained from magnetic resonance imaging of the American English rhotic approximant [ɹ] is reported. Linguopalatal contact profiles obtained through electropalatography (EPG) are used for analyzing inter- and intra-speaker variabilities and for providing a source of converging evidence for the magnetic resonance imaging (MRI) study.

I. PRODUCTION MECHANISMS OF THE RHOTICS

The class of rhotics comprises different varieties such as trills, taps and flaps, approximants, and fricatives, exhibiting a wide range of manners and places of articulation (Ladefoged and Maddieson, 1986). The voiced approximant [ɹ] is the most prevalent form in the majority of American English (AE) dialects. Cineradiographic investigations from various English dialects suggest the presence of a variety of midsagittal tongue shapes for [ɹ] (Delattre and Freeman, 1968; Lindau, 1985) with varying locations for a supraglottal constriction in the oral cavity. These tongue shapes range between the “bunched” (where the anterior tongue body is lowered and drawn inwards, away from the front incisors, and the oral constriction is made by raising the middle part of the tongue body in the palatal region) and “retroflex” (where the oral constriction is formed by a raised tongue tip) shapes. The retroflex and bunched [ɹ]s have very similar formant frequencies. The extreme form of retroflexion in En-

glish [ɹ]s, where the oral constriction is made with a curled-up tongue tip, is considered to be more common in British English than in AE dialects. In addition, the AE [ɹ] demonstrates a secondary constriction in the pharyngeal region (Delattre and Freeman, 1968) and, frequently, a lip-rounding behavior. These observations suggest that the AE [ɹ] may be characterized by a vocal-tract model with three cavities that are formed as a result of the oral and pharyngeal constrictions. Acoustically, [ɹ] is characterized by a low F_3 ; Delattre and Freeman (1968) reported F_3 values between 1500 and 2600 Hz, and Espy-Wilson (1992) reported F_3 values of less than 1900 Hz.

The articulatory-to-acoustic relations for [ɹ]s are not well-understood. Moreover, contextual effects, such as pre-vocalic vs syllabic positions, on the sound's tongue shapes are not clear: previous x-ray studies of [ɹ]s in different contexts have demonstrated both consistency *and* variability of tongue shapes with respect to contextual variations across different subjects (Delattre and Freeman, 1968; Lindau, 1985).

The primary objective of this study is to provide a detailed characterization of the 3-D vocal-tract geometry for the rhotic approximants in AE based on MRI and EPG data. Coarticulatory effects on 3-D shapes cannot, unfortunately, be examined due to the limitations of MRI and the limited information provided by EPG.

II. SUBJECTS AND METHOD

The same four phonetically trained subjects [MI, SC, AK, PK] who were described in a previous paper (Narayanan *et al.*, 1997) participated in these experiments. The MRI and

^{a)}Corresponding author.

^{b)}Now at AT&T Labs, Murray Hill, NJ.

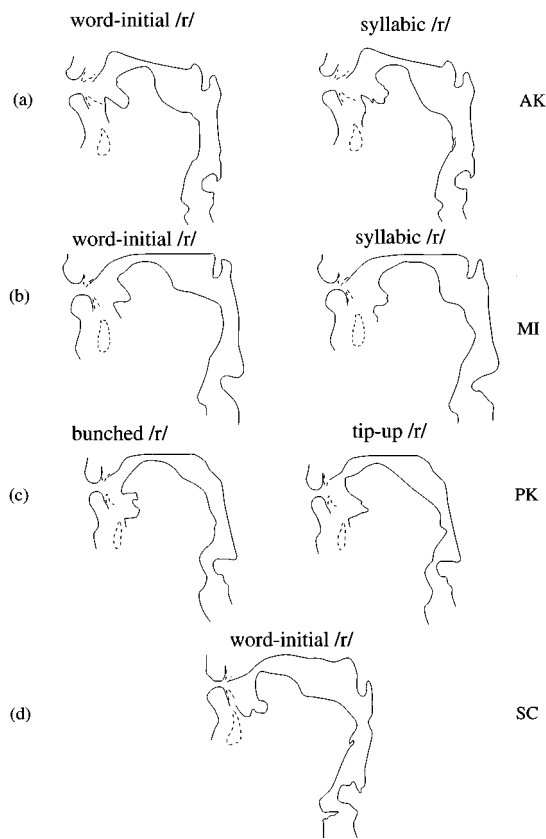


FIG. 1. Midsagittal profiles of the vocal tract during the production of the AE rhotic approximant. (a), (b) Tracings of word-initial [ɹ] (left side) and syllabic [ɹ] (right side) by subjects AK and MI, respectively. (c) Tracings of a “bunched” and tongue “tip-up” [ɹ] by subject PK. (d) Tracing of word-initial [ɹ] by subject SC. The front incisors and the jaw are shown in dashed lines. MRI data for SC’s syllabic [ɹ] are not available.

EPG data acquisition and analysis techniques were similar to those described in that paper. The speech material consisted of sustained productions of [ɹ].

III. RESULTS

Analysis of the rhotic approximant is based on the following data:

(1) Subjects AK and MI produced [ɹ]s as they would occur in word-initial and syllabic positions in a neutral vowel environment (/ə/). For subject SC, MRI data for [ɹ] are available for the word-initial case only since, at the time of the MRI experiments, he reported feeling no differences in his productions of [ɹ] in the word-initial and syllabic cases.

(2) Subject PK deliberately attempted to produce two varieties of [ɹ]s that correspond to the “retroflex” (tongue tip curled up) and “bunched” tongue shapes. The subject reported that, in her speech, the retroflex [ɹ] occurs in most contexts, while the bunched [ɹ] typically occurs in clusters with velars. In fact, the subject prepared herself to produce the bunched [ɹ] during the experiments by first making such a cluster.

Tracings of midsagittal profiles of the [ɹ]s for the different subjects are shown in Fig. 1. In parts (a) and (b), tracings of [ɹ] in word-initial and syllabic positions as anticipated by subjects AK and MI are shown, while part (c) shows tracings

of a “bunched” and tongue “tip-up” [ɹ] by subject PK. Tracing of SC’s [ɹ] in word-initial position is shown in part (d). Sample linguopalatal contact profiles for [ɹ] are shown in the Appendix.

These tracings reveal a consistency in the various [ɹ] productions. The tongue body is drawn inwards (away from the lips) thereby creating a relatively large volume in the region anterior to it. The vocal tract can be characterized by three cavities separated by two supraglottal constrictions: one in the oral region and the other in the pharyngeal region. The front-region (oral) constriction occurs over a range of palatal locations, from the prepalatal region in subject SC to the postpalatal region in subjects AK and MI, and is made by raising the anterior and/or middle part of the tongue body. The pharyngeal constriction, formed by a retracted tongue root, appears in the midpharyngeal region. Details of the articulatory shapes for the different subjects are given in the following sections. The tip-up and bunched [ɹ]s of PK are first discussed, followed by an analysis of the word-initial and syllabic varieties produced by the other three subjects.

A. Tongue tip-up and bunched [ɹ]s

Three-dimensional vocal-tract and tongue shapes for the bunched and tip-up [ɹ] of subject PK are shown in Fig. 2. The figure shows lateral perspectives of 3-D vocal tracts [(a) and (c)] and 3-D tongues [(b) and (d)] for the two [ɹ]s. A relatively large volume in the region anterior to the oral constriction is observed for both [ɹ]s [Fig. 2(a) and (c)]. The anterior cavity was larger for the tip-up case: the cavity’s volume was 4.5 cm³, and 6.1 cm³ for the bunched, and tip-up [ɹ], respectively.

The deliberately-produced bunched [ɹ] revealed an oral constriction that was formed by raising the tongue in the midpalatal region, accompanied by a lowered anterior tongue body [Fig. 2(a) and (b)]. Interestingly, the [ɹ] produced with a raised tongue-tip was characterized by an oral constriction that was formed by raising the middle part of the tongue body and the tongue tip [Fig. 2(c) and (d)]. The location of the maximum constriction (minimum cross-sectional area) in the tip-up case was more posterior when compared to that of the bunched case (4.8 cm vs 3.3 cm from the lip opening, for the tip-up versus bunched [ɹ], respectively). Nevertheless, analysis of the corresponding area functions, shown in Fig. 3, suggests that the precise location of the maximum constriction may not be crucial but the constriction length, which is about 2–2.5 cm (slightly longer in the tip-up case) might be important.

Differences in the cross-sectional areas within the constriction region (approximately 2–4.5 cm in Fig. 3) are minimal, particularly relative to the large volumes present both anterior and posterior to the constriction region. The slightly larger area observed within the constriction region in the tip-up case is attributed to a relatively flatter surface of the anterior tongue body compared to a more convex surface of the bunched [ɹ] [refer to Fig. 2(b) and (d)].

The back-region areas for the bunched and tip-up varieties were similar. The posterior tongue body was significantly lowered and revealed a concave surface when compared to the more convex surface observed in the raised

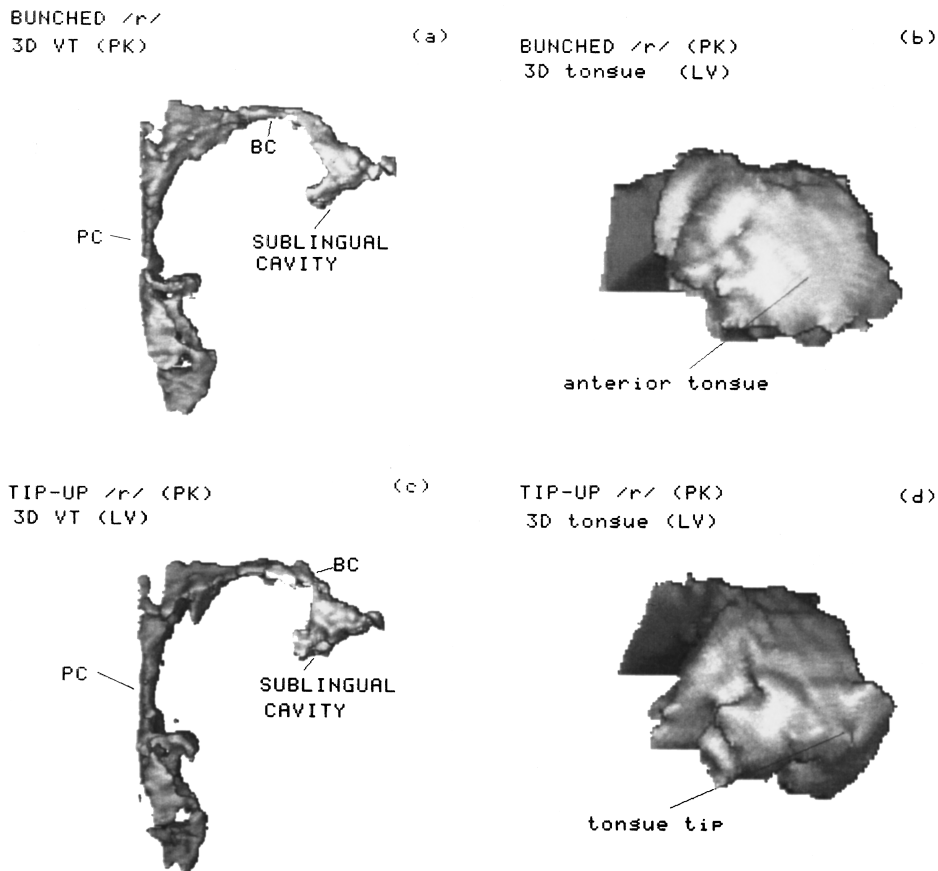


FIG. 2. Lateral perspectives of 3-D vocal tracts [(a) and (c)] and 3-D tongues [(b) and (d)] for subject PK. [(a) and (b)] “bunched” [ɹ], and (c) and (d) “tip-up” [ɹ]. BC refers to the oral constriction and PC refers to the pharyngeal constriction in the vocal tract.

tongue body region, thereby resulting in a large volume posterior to the oral constriction. The abrupt transition in the tongue body cross-sectional shapes behind the oral constriction, from convex to concave, resulted in an abrupt increase in the corresponding area function (at about 4.5 cm in Fig.

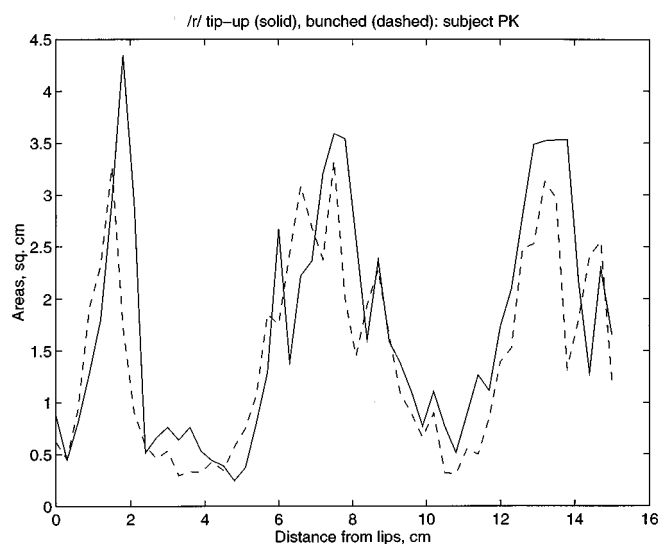


FIG. 3. Area functions, in cm^2 , for subject PK's [ɹ]: tongue “tip-up” (solid) and “bunched” (dashed). The abscissa for the area functions are distances (in cm) from the outer lip opening. Approximately, the region about 1–2 cm from the lips is the alveolar region, 2–5 cm is the palatal region, 5–7 cm is the velar region, and 7–10 cm is the uvular and upper-pharyngeal region.

3). The degree of posterior tongue body concavity appeared slightly greater in the bunched [ɹ] when compared to the tip-up case. The corresponding areas, in the region posterior to the oral constriction, were, however, comparable due to a relatively lower height of the posterior tongue body in the tip-up case. Some asymmetry in the posterior tongue was observed, with the right side at a higher position than the left, particularly in the bunched [ɹ]. A secondary supraglottal constriction, formed by a retracted tongue root, was observed in the midpharyngeal region at about 2.5 cm from the glottal opening.

ANOVA (Analysis of VAriance) analysis of the EPG data for the tip-up and bunched [ɹ]s indicated that most of the linguopalatal contacts were restricted to the back lateral region (see for example, Fig. A1 in the Appendix); average percentage contacts were 3%–10% for the front region versus 60%–75% in the back region. Recall that the back region in EPG profiles comprises the midpalatal and postpalatal regions, whereas the front region comprises the alveolar and prepalatal regions. Also note that these lateral contacts cannot be observed in midsagittal images (Fig. 1). The MRI data show that the relatively small lingual contact in the front palatal region is due to an anterior tongue body that is retracted away from the lips. The prominent lateral contact in the back region is due to the raised middle part of the tongue body that helps in the creation of the primary oral constriction. The contact patterns of the tip-up and bunched cases

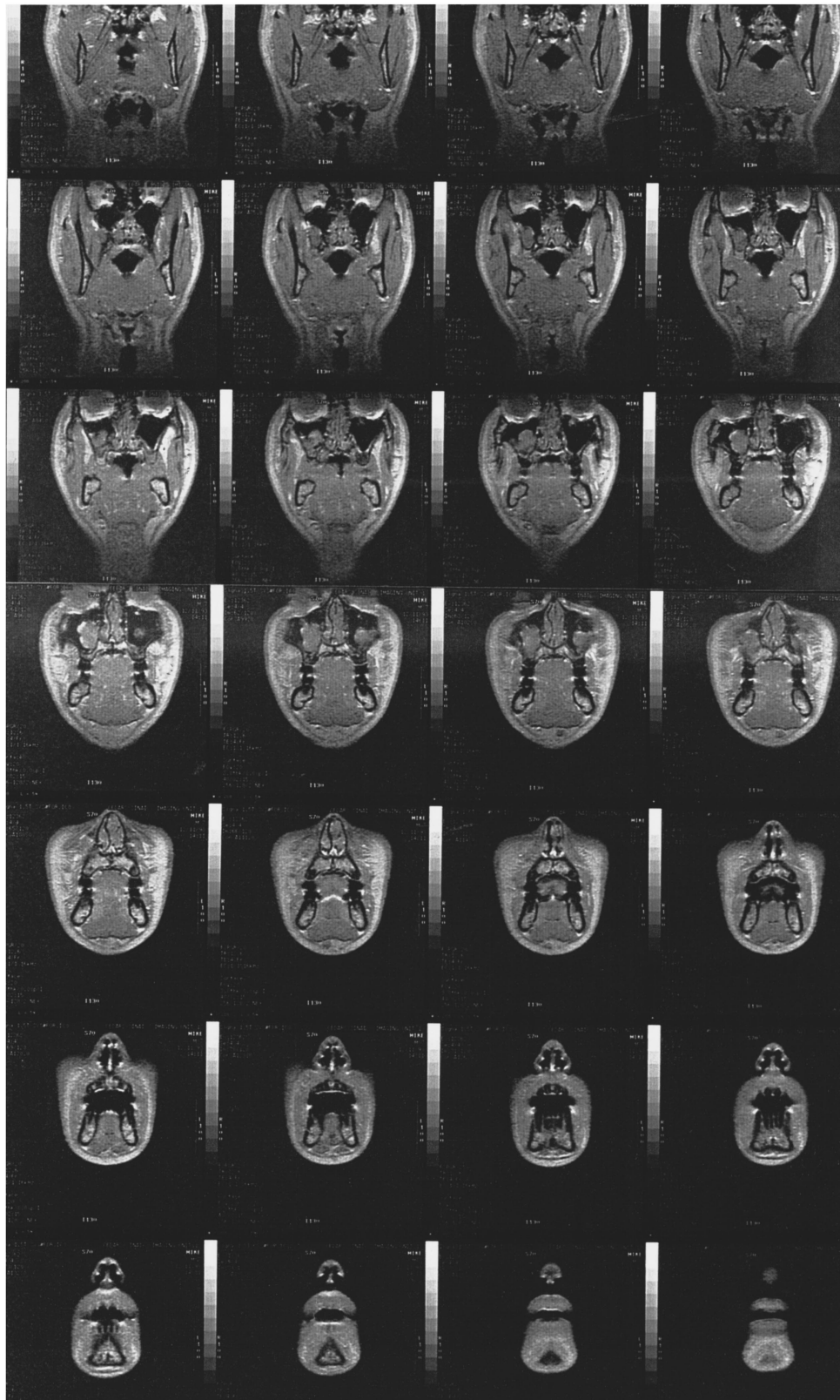


FIG. 4. Coronal profiles of the vocal tract during the production of word-initial [ɹ] (subject MI) taken along contiguous sections in the oral cavity at every 3 mm starting from 3 mm from the outer lip opening. The figure is arranged such that the cross section closest to the lips appears in the rightmost panel of the bottom row and successive oral-cavity cross sections, moving away from the lips, are placed right-to-left in each row. The anterior tongue body first appears in the rightmost panel of row 3 (from the bottom), and sublingual space can be observed in the two rightmost panels in row 3. The convex tongue body surface in the constriction region (panels in rows 3 and 4, and the first two panels of row 5) changes abruptly to concave in the posterior region (starting from the second leftmost panel in row 5).

were not statistically different although the tip-up [ɹ] showed less contact than the bunched [ɹ].

B. Word-initial and syllabic effects

1. The oral constriction and the region anterior to it

The anterior tongue body of [ɹ] in both word-initial and syllabic positions was, in general, retracted away from the lips, resulting in the creation of a large anterior volume. No prominent differences were found in the volumes of this anterior cavity between the word-initial and syllabic cases. The large anterior cavity can be seen in panels of the bottom two rows in Fig. 4. The figure shows coronal profiles of the vocal tract for MI's word-initial [ɹ] taken along contiguous sections in the oral cavity starting at 3 mm away from the outer lip opening and ending at the uvular region. The panels are arranged such that the cross section closest to the lips appears in the rightmost panel of the bottom row and successive oral-cavity cross sections, moving away from the lips, are placed right-to-left in each row. The anterior tongue body first appears in the rightmost panel of row 3 (counting from the bottom of the figure) and sublingual space can be observed in the 2 rightmost panels in that row.

The oral constriction in subjects AK and MI was made with a raised middle part of the tongue body, while lowering the anterior tongue body, in both word-initial and syllabic cases. The tongue body shapes clearly resembled a bunched [ɹ]. SC's [ɹ], on the other hand, was produced with a raised anterior tongue body (both the tip and blade) which resulted in a more anterior oral constriction when compared to MI and AK. Area functions for subjects AK, MI, and SC are shown in Fig. 5. As shown in the figure, the oral constriction of MI and AK extended for about 1.5–2.5 cm, beginning at about 3 cm from the lips, with the syllabic [ɹ] having a somewhat longer constriction. The constriction region for SC's [ɹ], which was made with a raised anterior tongue in the prepalatal region, was the shortest of all subjects extending for less than 1 cm.

2. The region posterior to the oral constriction

For AK and MI, the posterior tongue body (dorsum) was significantly, and abruptly, lowered behind the oral constriction thereby creating a large cavity in that region (between 6–10 cm in Fig. 5). Examination of the 3-D tongue shapes revealed convex shapes of the anterior tongue body which turned significantly concave in the region behind the oral constriction, resulting in a pitlike cavity in the lowered posterior tongue body region. The transition from the convex to the prominent, concave shapes was abrupt for both word-initial and syllabic [ɹ]s. For example, Fig. 4 shows a convex tongue body surface in MI's constriction region (panels in rows 3 and 4, and the two rightmost panels in row 5, from bottom) which changes abruptly to concave in the posterior region (starting from the second leftmost panel in row 5). The convex shape of the anterior tongue body and the concave shape of the posterior tongue body can also be seen in the 3-D tongue shapes shown in Fig. 6. The figure shows anterior and posterior views of MI's syllabic [ɹ] 3-D tongue.

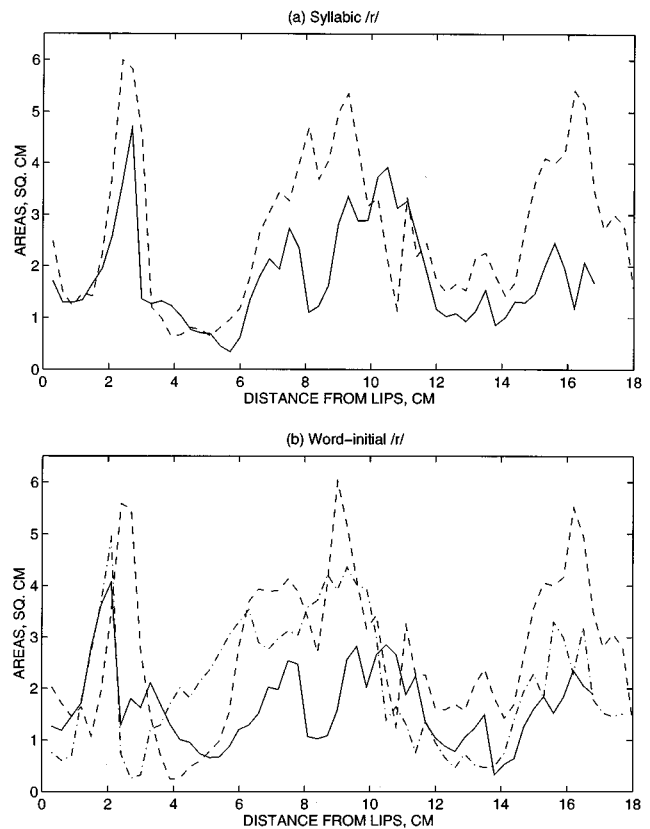


FIG. 5. Area functions for different subjects, in cm^2 (a) syllabic [ɹ], (b) word-initial [ɹ] (solid: AK, dashed: MI, dot-dashed: SC). The abscissa for the area functions are distances (in cm) from the lip opening. Roughly, the region about 1.5–2.5 cm from the lips is the alveolar region, 2.5–6 cm is the palatal region, 6–8.5 cm is the velar region, and 8.5–13 cm is the uvular and upper-pharyngeal region. Note that the area function for subject SC is available only for the word-initial [ɹ].

For SC, on the other hand, the lowering of the tongue body behind the oral constriction appeared less abrupt than the other subjects due to the more anterior oral constriction. The transition from the convex shapes of the raised anterior body to the concave shapes was more gradual, resulting in a relatively gradual area increase into the cavity posterior to the oral constriction [Fig. 5(b)]. Figure 7 shows right-lateral, anterior, and posterior perspectives of the 3-D vocal tract and tongue shapes for SC's [ɹ]. The convex shape of the anterior tongue body and the concave shape of the middle and posterior tongue body can be clearly seen in parts (b)–(d). This figure also illustrates how SC involves both his tongue blade and tip in forming the oral constriction.

A secondary supraglottal constriction was found in the midpharyngeal region (at about 2 cm for AK and MI and 3 cm for SC away from the glottal opening). A retracted tongue root caused this “pharyngealization.” The dimensions of the cavity formed between the oral and pharyngeal constrictions do not appear to be significantly different between the word-initial and syllabic cases for MI and AK, although AK showed larger areas in the syllabic case (between 6–10 cm in Fig. 5). The pharyngeal constriction for SC, on the other hand, occurred at a more superior location in the pharyngeal cavity than that observed in MI and AK, resulting in relatively smaller areas in the upper and midpha-

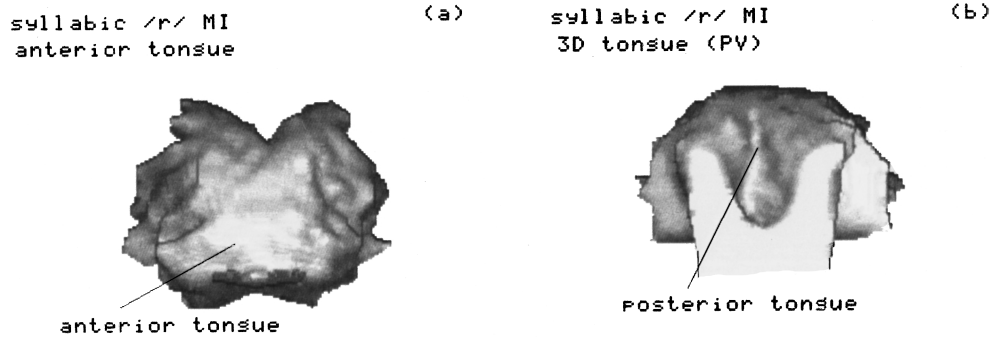


FIG. 6. The 3-D tongue shapes for subject MI's syllabic [ɹ]: (a) anterior view, and (b) posterior view. The anterior tongue body shows convex shaping while the posterior tongue shows concave shaping.

ryngeal region [approximately between 11–14 cm in Fig. 5(b)]. It appears that a more anterior primary oral constriction is associated with a more superior secondary pharyngeal constriction, and with smaller degrees of posterior tongue body concavity (and hence, smaller areas in the corresponding region). These observations suggest somewhat comparable volumes of the cavity between the primary and secondary constrictions, which in turn may imply similarities in the

acoustics in spite of differences in the actual constriction locations.

3. EPG results

Analysis of linguopalatal contact profiles for the word-initial and syllabic [ɹ]s revealed greater lateral contacts in the back palatal region than in the front. The average front-

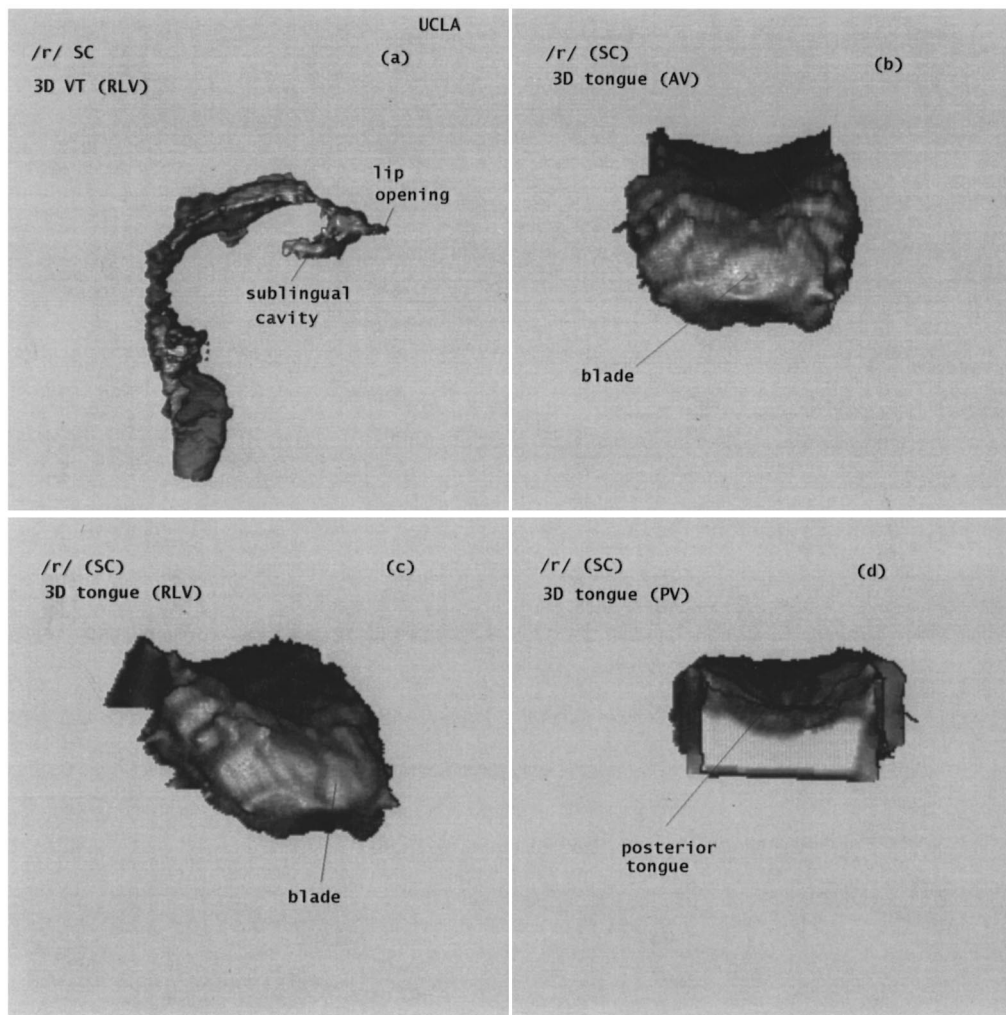


FIG. 7. The 3-D vocal tract and tongue shapes for subject SC's "word-initial" [ɹ]. (a) Right lateral perspective of the 3-D vocal tract. (b) Anterior view (AV) of the 3-D tongue. (c) Right lateral view (RLV) of the 3-D tongue. (d) Posterior view of the 3-D tongue. Note the convex shape of the anterior tongue body and the concave shape in the region posterior to it in parts (b)–(d).

TABLE I. Vocal-tract length (l_{VT}) and vertical lip opening (l_{VO}) measurements (in mm). WI and SY refer to the word-initial and syllabic cases, respectively [AK, MI, and SC (WI case only)], while TU and BU refer to the tip-up and bunched cases, respectively, (PK).

| Sound | Subject AK | | Subject MI | | Subject PK | | Subject SC | |
|-----------|------------|----------|------------|----------|------------|----------|------------|----------|
| | l_{VT} | l_{VO} | l_{VT} | l_{VO} | l_{VT} | l_{VO} | l_{VT} | l_{VO} |
| /ɪ/:WI/TU | 175.3 | 23.3 | 179.7 | 18.4 | 157.8 | 7.5 | 182.5 | 13.7 |
| /ɪ/:SY/BU | 173.9 | 20.9 | 181.3 | 19.8 | 159.3 | 7.7 | | |

region contacts were negligible for subject AK, 3%–10% for MI and 15%–30% for SC; the greater front-region contact in SC is attributed to a more forward anterior body when compared to the other subjects. ANOVA results also indicated that inter-subject differences in the front-region contacts were statistically significant ($p < 0.001$). Although word-initial [ɪ]s showed a tendency toward greater front-region contact than the syllabic cases, differences between the two cases were not statistically significant.

All subjects showed considerable lateral linguopalatal contact in the back region (50%–60%, on average) as can be seen in Fig. A1 in the Appendix. Inter-subject differences in linguopalatal contact profiles in this region were not statistically significant. Furthermore, there were no significant differences in the back-region contacts of the word-initial and syllabic cases. Subject MI showed greater lateral contact (implying a smaller medial opening) in the postpalatal region in the syllabic [ɪ]. This, perhaps, explains the slightly larger area values of the word-initial [ɪ] in the region behind the oral constriction when compared to the syllabic case. The opposite was true for AK: the lateral contact in the postpalatal region is relatively smaller for the syllabic [ɪ] resulting in larger areas in that region when compared to the word-initial case.

The lateral linguopalatal contact for subject SC, in both word-initial and syllabic cases¹ started as early as the prepalatal zone, similar to what was observed in his MRI data. A relatively wide medial opening was seen in the postpalatal region corresponding to decreased back lateral contacts. The contact patterns for the word-initial and syllabic cases appeared similar, in general, although the contacts for the syllabic [ɪ] in the prepalatal region started slightly later when compared to the word-initial case suggesting a more posterior tongue body.

Asymmetry in linguopalatal contacts was subject dependent; some asymmetry was found in the contact patterns of AK. ANOVA results, however, indicated that the left and right lateral contacts were not statistically different for our subjects.

C. Length and sublingual area measurements

Details of the vocal-tract length (l_{VT}) and the vertical lip-opening (l_{VO}) measurements are given in Table I. The l_{VO} values appear to be subject dependent: AK and MI show greater vertical lip opening than PK and SC. No contrastive differences are noticeable among the length values of these sustained sounds.

TABLE II. Areas (in cm^2) of the sublingual space for [ɪ] measured from coronal MR images. x_l is the distance from the lips in cm.

| x_l | Word-initial [ɪ] | | | Syllabic [ɪ] | |
|-------|------------------|-------|-------|--------------|-------|
| | AK | MI | SC | AK | MI |
| 2.4 | 1.272 | ... | 1.239 | ... | ... |
| 2.7 | 0.847 | 1.019 | 0.987 | 1.302 | ... |
| 3.0 | 0.421 | 0.148 | 0.267 | 0.764 | 1.468 |
| 3.3 | 0.442 | ... | ... | 0.223 | 0.075 |

| x_l | Tip-up [ɪ] | | Bunched [ɪ] | |
|-------|------------|-------|-------------|--|
| | PK | x_l | PK | |
| 2.7 | 2.036 | 2.1 | 0.497 | |
| 3.0 | 0.904 | 2.4 | 0.453 | |
| 3.3 | 0.295 | 2.7 | 0.203 | |

The cross-sectional areas of the sublingual space are summarized in Table II. The areas vary between 0.2–2.0 cm^2 depending on the subject's oral morphology and how the oral constriction was formed.

D. Summary

During the production of the American English [ɪ], the vocal tract is characterized by three cavities due to the presence of two supraglottal constrictions. The primary constriction occurs in the oral cavity and the secondary constriction, in the pharyngeal cavity. The oral constriction may occur anywhere in the palatal region: the more forward ones are typically formed by raising the anterior tongue body and the posterior ones by raising the middle part of the tongue body. In all cases, a large volume anterior to the oral constriction result from a tongue body that is drawn inwards, away from the lips, an anterior tongue body characterized by convex cross sections, and a concave posterior tongue body shape. Inter-subject variabilities were observed in the location and the way the primary oral constriction was formed.

Comparison of the bunched and tip-up [ɪ]s produced by subject PK revealed that, in spite of the raised tongue tip in the latter case, the primary oral constriction was attributed mainly to raising the middle part of the tongue body in both cases, and a three-cavity vocal tract description still holds. For AK and MI, the oral constriction was produced with a raised midtongue body and a lowered anterior tongue, resulting in a tongue body shape that resembled a bunched [ɪ]. SC's [ɪ], on the other hand, was produced with a raised anterior tongue body (tip and blade), resulting in a more anterior and shorter oral constriction when compared to the other subjects. For our subjects, the oral constriction extended over approximately 1–2.5 cm with minimum cross-sectional areas ranging between 0.25–0.7 cm^2 .

The secondary constriction typically occurred in the midpharyngeal region due to an advanced tongue root ("pharyngealization"). This constriction extended over 1–2 cm with minimum areas ranging between 0.25–2 cm^2 . A large volume posterior to the oral constriction (and superior to the pharyngeal constriction) was created by a significantly lowered posterior tongue body that exhibited a prominent concave shaping. The change in the cross sections, from the

convex anterior shapes to the more concave posterior shapes, appeared to be more abrupt for the oral constrictions that were at a more posterior location, resulting in more abrupt changes in the area functions. General tongue body shapes and area functions were similar for both word-initial and syllabic [ɹ]s, although AK's syllabic [ɹ] showed larger areas in the cavity between the oral and pharyngeal constrictions.

These observations suggest an interplay between the relative locations of the oral and pharyngeal constrictions and the 3-D tongue shapes. Variabilities in the details of the relative cavity sizes and their locations largely depend on the individual's articulation patterns and oral morphology.

IV. DISCUSSION

The observed vocal-tract and tongue shapes of [ɹ] are consistent with those of other articulatory studies (Delattre and Freeman, 1968; Lindau, 1985; Westbury *et al.*, 1995). These results suggest the presence of a wide range of tongue shapes that is fundamentally dictated by the location of the primary oral constriction. The canonical "retroflex" and "bunched" vocal-tract configurations correspond to two extreme oral-constriction locations: the most anterior with the constriction formed by raising only the tongue tip, and the most posterior formed by raising the middle part of the tongue body with the tongue-tip down, respectively. None of our subjects showed a retroflexed [ɹ]: AK, MI, and one of PK's tokens were bunched, while SC's oral constriction was formed by raising the tongue tip and blade, and PK's tip-up case used both the tongue tip and midtongue body to form the constriction. The results of previous cineradiographic studies (Delattre and Freeman, 1968; Lindau, 1985) and this MRI study suggest that the extreme form of retroflex [ɹ] may not be prevalent in American English.

It also appears that the pharyngeal constriction is likely to be more superior in cases where the oral constriction is formed by raising the anterior tongue body. Moreover, the degree of concavity of the tongue shapes posterior to the oral constriction is smaller for the more anterior oral constrictions. In fact, a canonical retroflex variety may not show a secondary constriction in the pharyngeal region, and the tongue concavity behind the oral constriction may not be prominent. Evidence supporting these observations can be found in Delattre and Freeman (1968) and in the results of a recent study of Tamil liquids, that included retroflex rhotics, using MRI, Electro Magnetic Midsagittal Articulator, and palatography (Narayanan *et al.*, 1996) which showed that if the oral constriction is formed only with the tongue tip, the pharyngeal constriction is not prominent and the degree of concavity of the posterior tongue body is relatively small.

These results indicate that [ɹ] tongue shapes belong to a continuum of possible shapes created between the two "extreme" configurations, namely, the canonical retroflex and bunched varieties with a greater tendency towards the bunched configuration in the present data. As a result, the rhotic approximant in American English can be specified by a three-cavity model wherein a more anterior primary oral constriction is associated with a more superior secondary pharyngeal constriction. Furthermore, the vocal tract of a canonical retroflex [ɹ], which may occur in other English dia-

lects or in other languages, can be treated as a special case of the three-cavity model, wherein the secondary pharyngeal constriction, corresponding to the anteriorly-located tongue tip-up oral constriction, is absent.

A. Tongue-shaping mechanisms

The wide range of tongue shapes for the American English [ɹ] imply possible differences in the underlying muscular mechanisms. The anterior tongue body is drawn inwards, away from the lips, with little linguopalatal contact, likely due to the contraction of the longitudinal muscle fibers. The constriction in the oral cavity may be produced with a raised anterior or middle tongue body; this is related to the extent of contraction of the longitudinal fibers and, probably, the geni-glossus. The flat and/or convex cross-sectional shapes in the region of the constriction, and the region anterior to it, are perhaps influenced by the contraction of the transverse muscle (Stone, 1996). The lateral linguopalatal contact in the midpalatal and postpalatal regions aid in maintaining the flat and convex anterior tongue body shapes. The concave posterior tongue body shapes are likely due to the pulling up of the lateral margins of the posterior tongue by the styloglossus and palatoglossus. The posterior tongue body surface accompanying oral constrictions located further backward in the oral cavity is characterized by a greater degree of concavity. This suggests an interplay between the extent of the contraction of longitudinal muscle fibers and the geni-glossus, and the effectiveness of the styloglossus and the palatoglossus in pulling up the lateral margins of the posterior tongue body. Furthermore, it was observed that more posterior oral constrictions require a relatively higher (middle) tongue body position and the effect of raising the tongue seems to further enhance the degree of concavity in the back region. Retraction of the posterior tongue body, which results in the secondary pharyngeal constriction, may be due to the hyoglossus pulling the tongue back and down.

B. Acoustic implications

Some preliminary speculations regarding the acoustic characteristics of the rhotic approximant can be made based on the articulatory data. The first formant frequency (F_1) can be associated with the Helmholtz resonance between the oral-constriction space and the relatively large cavity posterior to it. The second formant frequency (F_2) can be either associated with the half-wavelength resonance of the cavity posterior to the oral constriction (for cases where the pharyngeal constriction is not narrow) or, in the case of a narrow pharyngeal constriction, to a Helmholtz resonance between the pharyngeal constriction and the cavity posterior to it. F_3 is probably associated with the large front cavity volume with possible additional contributions from sublingual components (Stevens, to be published) and lip rounding. The correlation between low F_3 values and the "dorsal bunched cases with dip" observed by Delattre and Freeman (1968) in American English [ɹ] is mostly likely due to the large front-cavity volume associated with relatively posterior oral constrictions. Abrupt transitions in the area function between cavities can affect the bandwidths of the cavities' resonances.

In this paper, a detailed account of the 3-D vocal tract and tongue shapes for sustained rhotic approximants in American English is presented. The results of this investigation can be used as a baseline for studying articulatory-to-acoustic relations of these sounds.

ACKNOWLEDGMENTS

The cooperation and support of the Cedars-Sinai medical imaging group, the UCLA Department of Radiology, and the UCLA Phonetics Laboratory are gratefully acknowledged. We are grateful to our subjects AK, MI, PK, and SC for their help. We thank Patricia Keating and Peter Ladefoged for many useful discussions and for use of EPG facilities. Thanks to Carol Espy-Wilson, Anders Lofqvist, and Maureen Stone for valuable suggestions. The assistance of Makkalon Em with EPG data analysis is appreciated. This work was supported in part by NSF.

APPENDIX: VARIABILITY ANALYSES THROUGH EPG STUDIES

In this Appendix, we describe the results of an EPG study which was conducted to investigate:

- (1) Intra-token articulatory (temporal) stability during sustained word-initial and syllabic /ɹ/. Subject PK, a trained phonetician since 1972, deliberately produced bunched and tongue tip-up /ɹ/s; both productions occur in her speech.
- (2) Inter-token articulatory variabilities to quantify the subjects' consistency in reproducing the /ɹ/.
- (3) Differences and similarities between /ɹ/s produced in sustained utterances with respect to those produced in words. It should be noted that the main focus of this study is the variability of artificially sustained sounds with respect to those occurring in natural contexts, and not specific coarticulatory effects.
- (4) Inter-subject differences in the articulatory patterns for each sound.
- (5) Differences and similarities between word-initial versus syllabic /ɹ/.

1. Data analysis

EPG data from the sustained utterances, typically 4 s long with eight repetitions per token, were collected from subjects producing these sounds in a supine posture² (simulating the position assumed inside the MRI scanner). Sample linguopalatal contact profiles for the rhotic approximants are shown in Fig. A1. EPG data were also collected for the words (eight repetitions per word) {*rod, read, rude*} for word-initial /ɹ/, {*turd, turk, kirk, perk*} for word-medial (syllabic) /ɹ/, and {*beater, beaker, beeper*} for word-final (syllabic) /ɹ/. All words were spoken embedded in the carrier phrase "Say—again." The words were spoken by the subjects in their normal upright posture.

The total percentage of the electrodes contacted in the front and back regions (refer to Fig. 2 in Part I for region definitions) were calculated and used for variability analyses. Temporal averaging of the contact measures was done over the middle 3.8 s of each sustained data segment.

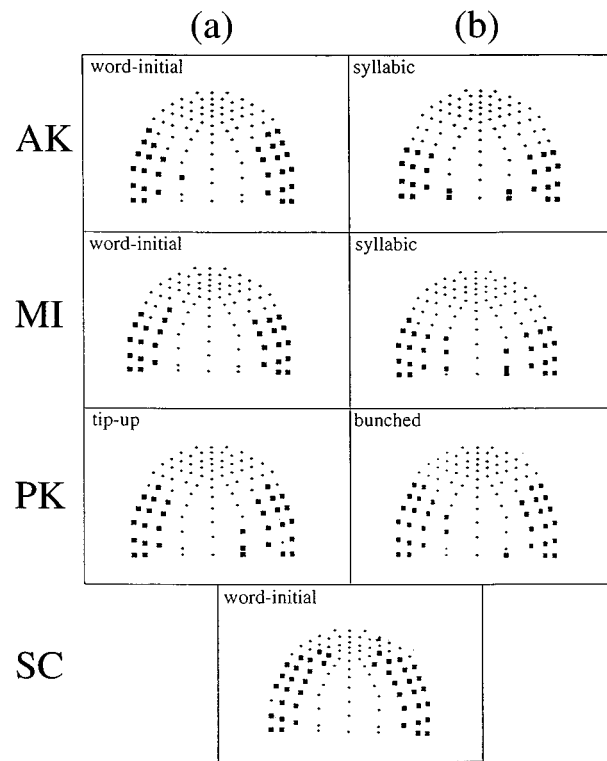


FIG. A1. Sample linguopalatal contact profiles for the rhotic approximants. For subjects AK, MI, and SC the left and right panels correspond to word-initial and syllabic /ɹ/, respectively. For subject PK, the left and right panels correspond to the tip-up and bunched versions, respectively.

To investigate the gross intra-token (temporal) stability of the sustained utterances, the mean and standard deviation of the *total* (i.e., =front+back) linguopalatal contact were calculated over the duration of the utterance (one EPG contact profile for every 10 ms yielding 380 frames for the 3.8 s data segment considered for analysis). For word-initial /ɹ/, total (percentage) contact was about 27% for AK and MI and 30% for SC. For syllabic /ɹ/, the total contact was about 28% for AK and MI, and 33% for SC. The total contact for PK's tip-up and bunched /ɹ/ was 40% and 30%, respectively. Within-token variations for all cases, except for one of MI's tokens, were less than 3%, while across-token variations were less than 7%. The variations in one of MI's word-initial /ɹ/ tokens varied by 8%.

Results indicate that, in general, our phonetically trained subjects produced the sustained sounds in a consistent manner assuring some degree of articulatory stability (both within and across each repetition) during the MRI experiments. Further detailed analysis of intra- and inter-token variabilities was done using repeated measures ANOVA with total linguopalatal contact as the dependent variable.

The first set of these tests used the sustained utterances. Results showed no significant intra-token variations in the total contact values for both word-initial and syllabic cases for all subjects. Repeated measures ANOVA with total EPG contact as the independent variable and the consonant position (word-initial, syllabic) showed no significant differences between the subjects ($F=0.016$, $p=0.902$). In addition, within subjects, there was no significant variation in the total contact between the word-initial and syllabic cases (F

=1.469, $p=0.204$) and no significant interaction with the consonant position ($F=0.765$, $p=0.619$). The somewhat greater (although nonsignificant) variability between word-initial cases is probably due to subjects PK and SC.

The absence of any significant intra-token variations in the contact patterns warranted using the pooled average values of total contact for further analyses. ANOVA repeated using the average total contact measures followed by Tukey post hoc tests confirmed no significant differences between the syllabic and word-initial sustained sounds ($F=0.016$, $p=0.902$). To investigate the variabilities in the contact patterns with respect to the subjects, ANOVA with the subjects as the factor was carried out using average total contact as the dependent variable (followed by Tukey post hoc tests). No significant effects of the factor subjects were found ($F=1.283$, $p=0.394$). Although statistically insignificant, the matrix of comparison probabilities (Table AI) showed that PK's /ɪ/s were more different than those of the other subjects. Recall that subject PK deliberately produced the tongue-tip version (grouped with word-initial /ɪ/s of the other subjects) and the tongue body bunched version (grouped with syllabic /ɪ/s of the others).

TABLE AI. Matrix of pairwise comparison probabilities from Tukey post hoc tests following ANOVA in average total linguopalatal contact for sustained /ɪ/s with respect to different subjects ($F=1.283$, $p=0.394$).

| | AK | MI | PK | SC |
|----|-------|-------|-------|----|
| AK | 1 | | | |
| MI | 0.99 | 1 | | |
| PK | 0.41 | 0.49 | 1 | |
| SC | 0.756 | 0.856 | 0.872 | 1 |

For a more detailed analysis, EPG data corresponding to the rhotic approximants extracted from naturally-spoken words were compared against the sustained productions. Segmentation of the consonant from each word was done manually using time-aligned displays of the acoustic waveform, spectrograms (with the option of obtaining spectral slices), and EPG data. The total contact for each token was then obtained by (temporal) averaging over the segmented duration and used for variance analyses. The variabilities within the eight repetitions of each token was found to be statistically insignificant, and the results reported in this paper are based on averages of total contact across the eight

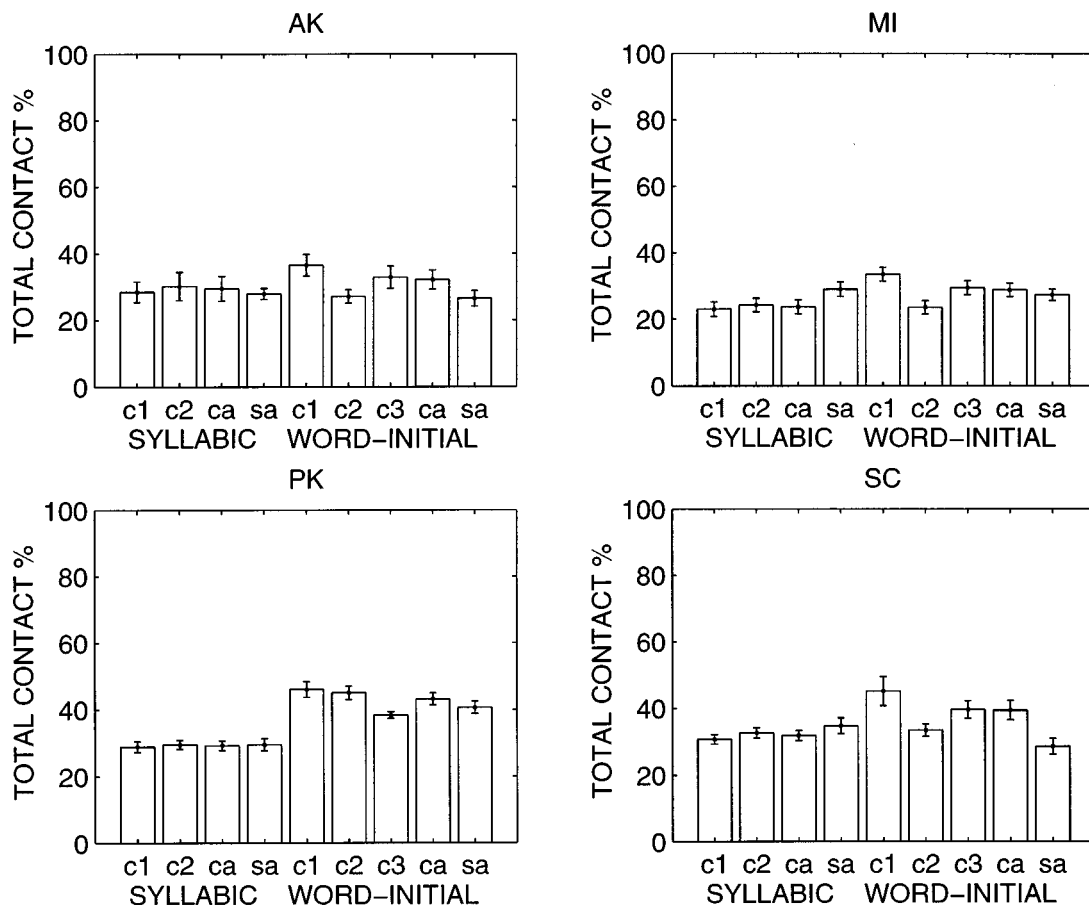


FIG. A2. Total linguopalatal contact (expressed in percent relative to the total number of electrodes) for syllabic and word-initial /ɪ/ obtained from both naturally spoken words and sustained utterances, using eight repetitions for each token. Note that contact measures for each token were based on a temporal average over the duration of the appropriately segmented consonant. The first four bins in each panel correspond to syllabic /ɪ/ while the last five correspond to word-initial /ɪ/. For /ɪ/s occurring in words, contact values were averaged across eight tokens and all words for each condition. For syllabic /ɪ/, c1 represents contact values for word-final cases while c2 represents values for word-medial cases. For word-initial /ɪ/, c1, c2, and c3 represent /ɪ/ in /reed/, /rod/, /rude/ respectively. ca and sa represent the average values for the in-context (words) and the sustained cases, respectively. Note that PK's sustained bunched and tip-up /ɪ/s are very similar to the syllabic and word-initial in-context cases, respectively, for the other subjects. Error bars represent variations in contact across repetitions and were further analyzed using ANOVA.

TABLE AII. Matrix of pairwise comparison probabilities from Tukey post hoc tests following ANOVA in average total linguopalatal contact (pooled across various contexts) for syllabic /ɹ/ across various contexts and sustained utterances ($F=0.817$, $p=0.583$).

| | beaker | beeper | beater | kirk | perk | turd | turk | sustained |
|-----------|--------|--------|--------|-------|-------|-------|-------|-----------|
| beaker | 1.000 | | | | | | | |
| beeper | 1.000 | 1.000 | | | | | | |
| beater | 1.000 | 1.000 | 1.000 | | | | | |
| kirk | 1.000 | 1.000 | 1.000 | 1.000 | | | | |
| perk | 0.999 | 1.000 | 1.000 | 1.000 | 1.000 | | | |
| turd | 0.995 | 0.912 | 0.963 | 0.915 | 0.891 | 1.000 | | |
| turk | 0.972 | 0.801 | 0.891 | 0.806 | 0.770 | 1.000 | 1.000 | |
| sustained | 0.997 | 0.929 | 0.973 | 0.932 | 0.911 | 1.000 | 1.000 | 1.000 |

repetitions. The average total linguopalatal contact values for the in-context cases (word-medial and word-final cases are pooled), along with their overall average and the average value for the sustained utterances, are shown in Fig. A2 for the syllabic and word-initial /ɹ/s of all the subjects. These figures suggest that (1) the variation across repetitions for each condition (as represented by the standard deviation error bars) are minimal. (2) The differences between the in-context cases and the sustained cases for each subject and consonant position in the word (syllabic, word-initial) appear to be minimal. (3) The total linguopalatal contact for the word-initial and syllabic cases of subjects AK, MI, and SC appear to be comparable. For PK, the total contact for the in-context word-initial case are somewhat greater than the in-context syllabic cases. Furthermore, the two cases of sustained utterances that were (deliberately) produced with the tongue tip up and a bunched tongue body, respectively, show comparable EPG contact patterns to those of the in-context word-initial and syllabic cases, respectively.

To verify the statistical significance of these observations, ANOVA was carried out. In the analysis, the data for PK's sustained tip-up /ɹ/ were grouped with the word-initial ones from the other subjects, and her bunched /ɹ/ data were grouped with the others' syllabic /ɹ/s.

ANOVA on total average contact (dependent variable) for syllabic /ɹ/ with respect to context (words: {beaker, beeper, beater, kirk, perk, turk, turd} versus sustained), showed no significant variation between them ($F=0.817$, $p=0.583$). The matrix of comparison probabilities computed following Tukey post hoc tests (Table AII) showed no specific condition as contributing to any highly significant variation. Similar tests for word-initial /ɹ/ with respect to context (words: {reed, rod, rude} vs sustained) showed a greater variation than the syllabic cases (although statistically not

TABLE AIII. Matrix of pairwise comparison probabilities from Tukey post hoc tests following ANOVA of average total linguopalatal contact for word-initial /ɹ/ across various contexts and sustained utterances ($F=5.164$, $p=0.016$).

| | reed | rod | rude | sustained |
|-----------|-------|-------|-------|-----------|
| reed | 1.000 | | | |
| rod | 0.017 | 1.000 | | |
| rude | 0.433 | 0.227 | 1.000 | |
| sustained | 0.048 | 0.925 | 0.508 | 1.000 |

TABLE AIV. Matrix of pairwise comparison probabilities from Tukey post hoc tests following a two-way ANOVA in average total linguopalatal contact for syllabic /ɹ/ and word-initial /ɹ/ across various contexts (pooled averages) and sustained utterances. ANOVA results: For, the factor *consonant position in word*={syllabic, word-initial} ($F=1.893$, $p=0.176$); for the factor *type*={in-context, sustained} ($F=0.263$, $p=0.610$); for the interaction between consonant position in word and context ($F=2.597$, $p=0.114$).

| | | Syllabic context | Syllabic sustained | Word-initial context | Word-initial sustained |
|--------------|-----------|------------------|--------------------|----------------------|------------------------|
| syllabic | context | 1.000 | | | |
| syllabic | sustained | 0.850 | 1.000 | | |
| word-initial | context | 0.008 | 0.576 | 1.000 | |
| word-initial | sustained | 0.920 | 0.999 | 0.477 | 1.000 |

significant) ($F=5.164$, $p=0.016$). The matrix of comparison probabilities computed following Tukey post hoc tests (Table AIII) showed that the differences were mainly due to the word *reed*, and to a lesser degree, the word *rude*. This is probably due to the somewhat greater linguopalatal bracing because of coarticulatory effects of /i/ (*reed*) and /u/ (*rude*) that have a higher tongue body when compared to /a/ (*rod*) (recall that the sustained utterances were produced in a /ə/ context).

With these observations in mind, another experiment aimed at finding the (gross) overall differences for the word-initial and syllabic /ɹ/s between the in-context (all data pooled together) and sustained cases was carried out. The results of two-way ANOVA followed by Tukey post hoc tests are shown in Table AIV and indicate: (1) no significant differences between the in-context and sustained cases ($F=0.263$, $p=0.610$) for both word-initial and syllabic /ɹ/s. (2) Some indication of variability between the syllabic and word-initial cases ($F=2.597$, $p=0.114$) with an interaction of the context and consonant position in the word with a similar level of statistical significance. Probabilities of pairwise comparison showed significant differences between the word-initial and syllabic cases, mostly due to the coarticulatory influences of the vowels in the word-initial /ɹ/ data.

Finally, a two-way ANOVA with respect to the different subjects and consonant position in word (word-initial versus syllabic) showed significant between-subject differences for syllabic and word-initial /ɹ/s (Table AV). The Tukey *post*

TABLE AV. Matrix of pairwise comparison probabilities from Tukey post hoc tests following a two-way ANOVA in average total linguopalatal contact (pooled across various contexts) for syllabic and word-initial /ɹ/ across various subjects. ANOVA results: For, the factor *consonant position in word*={syllabic, word-initial} ($F=12.743$, $p=0.001$); for the factor *subject*={AK, MI, PK, SC} ($F=8.216$, $p=0.000$); for the interaction between consonant position in word and subject ($F=0.581$, $p=0.631$).

| | | Syllabic | | | | Word-initial | | | |
|--------------|----|----------|-------|-------|-------|--------------|-------|-------|-------|
| | | AK | MI | PK | SC | AK | MI | PK | SC |
| syllabic | AK | 1.000 | | | | | | | |
| syllabic | MI | 0.308 | 1.000 | | | | | | |
| syllabic | PK | 0.993 | 0.061 | 1.000 | | | | | |
| syllabic | MI | 0.939 | 0.025 | 1.000 | 1.000 | | | | |
| word-initial | AK | 0.994 | 0.162 | 1.000 | 1.000 | 1.000 | | | |
| word-initial | MI | 1.000 | 0.618 | 0.995 | 0.966 | 0.995 | 1.000 | | |
| word-initial | PK | 0.195 | 0.002 | 0.539 | 0.730 | 0.771 | 0.316 | 1.000 | |
| word-initial | SC | 0.019 | 0.000 | 0.094 | 0.178 | 0.260 | 0.054 | 0.988 | 1.000 |

hoc tests help to isolate the specific sources for these differences. For both syllabic and word-initial /ɹ/, subject MI was different compared to subjects PK and SC, and to a lesser extent with respect to AK. The raw contact pattern values shows that MI has somewhat smaller percentage of electrodes contacted. This may be due to the limitation of EPG: recall from the MRI data that the tongue body for MI was further back in the oral cavity than the other subjects, and probably was out of the EPG pseudopalate's range. None of the subjects, however, showed significant differences between word-initial and syllabic /ɹ/s.

In summary, the EPG analyses show significant intra- and inter-token articulatory stability in the production of word-initial and syllabic /ɹ/s by our four phonetically trained subjects (except subject PK who produced the sustained utterances with the tongue tip up and tongue body bunched). Furthermore, no significant differences were found in the linguopalatal contact patterns of the artificially sustained utterances of /ɹ/ and those that occurred in words. These results justify the use of MRI to study the human vocal tract and tongue shape during sustained production of the rhotic approximants.

¹Although the MRI data for SC is available for only the word-initial [ɹ], EPG data were collected for both word-initial and syllabic [ɹ].

²Data were also collected from the subjects in an upright position, but not used or reported in this paper since our analyses indicated no significant differences in the linguopalatal contact patterns of the sounds produced in a supine posture versus those produced in an upright posture. Subjects AK and SC showed some tendency towards greater contact in the postpalatal region in the supine posture, but these differences were not statistically significant.

Delattre, P. and Freeman, D. C. (1968). "A dialect study of American r's by x-ray motion picture," *Linguistics, An international review* **44**, 29–68.

Espy-Wilson, C. Y. (1992). "Acoustic measures for linguistic features distinguishing the semivowels in American English," *J. Acoust. Soc. Am.* **92**, 736–757.

Ladefoged, P., and Maddieson, I. (1986). "Some of the sounds of the world's languages," *UCLA Working Papers in Phonetics*, 64; Also, *Sounds of the world's languages*, in preparation.

Lindau, M. (1985). "The story of /r/," in *Phonetic Linguistics, Essays in Honor of Peter Ladefoged*, edited by V. A. Fromkin (Academic, New York).

Narayanan, S., Kaun, A., Byrd, D., Ladefoged, P., and Alwan, A. (1996). "Liquids in Tamil," in *Proceedings of the International Conference on Spoken Language Processing*, New Castle, Delaware, pp. 797–800.

Narayanan, S., Alwan, A., and Haker, K. (1997). "Toward articulatory-acoustic models for liquid approximants based on MRI and EPG data. Part I. The laterals," *J. Acoust. Soc. Am.* **101**, 1064–1077.

Stevens, K. N. (to be published). *Acoustic Phonetics* (to be published).

Westbury, J. R., Hashi, M., and Lindstrom, M. J. (1995). "Differences among speakers in articulation of American English /r/: An x-ray micro-beam study," in *Proceedings of XIII International Congress of Phonetic Sciences*, Stockholm, Sweden, Vol. 4, pp. 50–53.

Stone, M. (1996). Personal communication.

Perceptual magnet effect in the light of behavioral and psychophysiological data

Olli Aaltonen

Centre for Cognitive Neuroscience and Department of Phonetics, University of Turku, FIN-20014 Turku, Finland

Osmo Eerola

Centre for Cognitive Neuroscience, University of Turku, FIN-20014 Turku, Finland

Åke Hellström

Department of Psychology, Stockholm University, S-106 91 Stockholm, Sweden and Centre for Cognitive Neuroscience, University of Turku, FIN-20014 Turku, Finland

Esa Uusipaikka

Centre for Cognitive Neuroscience and Department of Statistics, University of Turku, FIN-20014 Turku, Finland

A. Heikki Lang

Centre for Cognitive Neuroscience, University of Turku, FIN-20014 Turku, Finland and Department of Clinical Neurophysiology, Turku University Central Hospital, FIN-20014 Turku, Finland

(Received 19 July 1993; revised 22 April 1996; accepted 16 October 1996)

Finnish speaking adults categorized synthetic vowels, varying in the frequency of the second formant ($F2$), as either /y/ or /i/. Two subject groups emerged: “good” and “poor” categorizers. In a /i/ rating experiment, only the good categorizers could consistently label their best /i/ (the prototype, P), being low in the $F2$ continuum. Poor categorizers rated /i/’s with high $F2$ values as Ps. In a same/different (AX) discrimination experiment, using the individual Ps and nonprototypes (NPs), it was more difficult for good categorizers to detect small $F2$ deviations from the P than from an NP (the “perceptual magnet effect”). For poor categorizers, the opposite effect was found. The same stimuli were used to record the mismatch negativity (MMN), an ERP component reflecting preattentive detection of deviations from a standard sound. For the good categorizers the MMNs were lower for Ps than for NPs; for the poor categorizers the MMNs for Ps and NPs did not differ significantly. The results show that individual listeners behaved differently in categorization and goodness rating but in the same way in attentive (AX) discrimination, being the poorest at about the same $F2$ location. The perceptual magnet effect was indicated in the good categorizers both by behavioral and psychophysiological (MMN) discrimination data. © 1997 Acoustical Society of America. [S0001-4966(97)05502-1]

PACS numbers: 43.71.Es, 43.71.An, 43.64.Qh [RAF]

INTRODUCTION

In a series of papers, Kuhl and her collaborators (e.g., Kuhl, 1991; Kuhl *et al.*, 1992; Kuhl, 1993a) have suggested that speech perception is governed not only by the functional principles of the auditory system, but also by speech prototypes in long-term memory. The proponents of the prototype approach (e.g., Eimas and Corbit, 1973; Massaro and Oden, 1989; Kuhl, 1991) hold that classification into a phonetic category is based on a mental representation that contains information about its characteristic and ideal attributes, rather than about its boundaries against other categories (Rosch and Mervis, 1975; Mervis and Rosch, 1981; Medin and Barsalou, 1987). The application of prototype theory has diverted the emphasis of speech perception from the boundaries of categories to their centers.

In the boundary-based approach, the mental representation of a category is thought to hold information only about its boundaries (e.g., Studdert-Kennedy *et al.*, 1970; Maddox and Ashby, 1993). Hence, discrimination is assumed pos-

sible only for pairs of sounds whose members can be identified as belonging to different phoneme categories. This relation between identification and discrimination has been interpreted as a consequence of categorial perception, which is also reflected as an increased sensitivity to stimulus differences at the boundaries. In contrast, the prototype-based approach holds that members of a given phonetic category are discriminable in terms of their goodness as category exemplars, that is, some are perceived to be better exemplars than others (e.g., Grieser and Kuhl, 1989). Reaction times to identification judgements of stimuli within a category depend on this goodness (Massaro, 1987). It also appears that members of a category can vary in their perceptual potency, providing an internal structure to the category. For example, some category exemplars are more effective than others in selective adaptation (Samuel, 1982; Miller *et al.*, 1983) and in dichotic competition (Repp, 1977).

Kuhl (1991) provided the first evidence suggesting that discrimination is affected not only by physical factors but also by stimulus typicality. She showed that a vowel judged

to be a prototype of its category was more difficult to discriminate from its neighbors than a less prototypical one, a nonprototype. The recent experiments of Iverson and Kuhl (1995), using signal detection theory and multidimensional scaling of choice reaction times, convincingly demonstrate how perceptual distances within a category shrink and stretch in the regions of the best and the worst instances, respectively. The effect is even stronger for vowels in a word context than for isolated ones (Eyraud and Kuhl, 1994). With respect to discrimination, the prototype thus seems to act like a "perceptual magnet" by pulling other stimuli toward itself and by that means it strengthens category coherence. Moreover, the magnet effect was found in infants of only six months of age, while monkeys failed to show it (Kuhl, 1991). Therefore, Kuhl (1991, 1993a) concludes that the magnet effect must be caused by mental representations unique to humans rather than to general auditory ones, shared by humans and animals. Kuhl suggests that infants either are biologically endowed with phonetic prototypes, or develop such prototypes through experience with spoken language.

To test the language-experience hypothesis, Kuhl *et al.* (1992) synthesized a set of vowels surrounding, in formant space, the American English prototypic /i/ and another set surrounding the Swedish prototypic /y/. (American English /i/ is not prototypical of any Swedish vowel; neither is Swedish /y/ prototypical of any American English vowel.) Both American and Swedish six-month-old infants showed poorer detection of deviations from their native vowel than from the foreign one. Similar results were obtained by Polka and Werker (1994) with American and German infants. Thus, phonetic prototypes seemed to develop in infants prior to word acquisition, as a result of their exposure to ambient speech. Kuhl (1993a, 1993b) hypothesized that this occurs because infants are neurophysiologically prepared to respond to linguistic stimuli.

Recent evidence questions some of Kuhl's findings. First, the subjects' qualitative ratings of category goodness may not be stable, although the location of the prototype seems to be determined by long-term exposure to language. Thus, rating experiments may not provide accurate measures of the true internal structure of a phonetic category. For example, vowels with high *F2* frequencies, rather than those central in the category, were rated with highest prototypicality in the experiments of Lively (1993), Iverson and Kuhl (1995), and Sussman and Lauckner-Morano (1995). Also, Lively (1993) found that the prototype location varied as a function of context. Attempts to replicate the magnet effect, using Kuhl's vowels and the subjects' own prototypes, have failed (Lively, 1993). Furthermore, Sussman and Lauckner-Morano (1995) argued that results usually interpreted as demonstrating the magnet effect can be explained by varying auditory resolution over the formant space, as found by Macmillan *et al.* (1988).

The findings of Kuhl and her colleagues are of great significance for evaluating the traditional division of the speech perception process into distinct auditory and phonetic stages. According to this dual-process approach, the phonetic stage is needed to transform the initial auditory representa-

tion into a categorical one that corresponds to the perceived segments of the utterance (e.g., Fujisaki and Kawashima, 1970; Pisoni, 1973; Sawusch *et al.*, 1980). Auditory coding processes are sensitive to physical differences, whereas phonetic processes depend on such factors as learning, linguistic experience, memory, and attention (Repp, 1987). In light of this evidence, it has been proposed that the acoustic properties of vowels favor auditory coding, whereas those of consonants do not (Studdert-Kennedy, 1976, 1993).

Kuhl (1991) suggested, however, that the magnet effect for vowels, which was found only in humans, not in animals, must reside at the phonetic stage, subsequent to the auditory analyses. In contrast, categorical perception, shared by humans and animals, has to have the characteristics of the auditory stage (e.g., Kuhl and Miller, 1975). Thus, in Kuhl's view, the magnet effect offers a tool for behaviorally dissociating the two distinct and ordered analysis stages. There is, however, a methodological problem in realizing this dissociation. Standard behavioral measures are based on the final output of the categorization process (e.g., Meyer *et al.*, 1988) and cannot yield information about its components. In addition, these measures require that the subjects attend to the stimuli. Attending affects discrimination performance by way of numerous factors such as strategies, previous learning, and the nature of the experimental task (Creelman and Macmillan, 1979; Pisoni and Luce, 1986) and thus make the measures hard to interpret.

Looking for the magnet effect in subjects who are ignoring the stimuli should therefore help to clarify the role of the auditory component in speech perception. In conditions when attention is not being paid to the stimuli there may be too little spread of activation from the acoustic detectors to the neurons underlying phonetic perception (Maiste *et al.*, 1995). Thus, ignoring the stimuli has the advantage that the auditory processing is not affected by the phonetic processing, which otherwise would always be superimposed on the concordant auditory processing. If the magnet effect could be demonstrated by examining sensitivity to ignored stimuli, this would support the view (e.g., Massaro, 1987; Rosner and Pickering, 1994) that auditory prototypes, rather than more abstract ones, are used by listeners in categorizing speech sounds. In the developing brain, auditory prototypes might be built up by synaptic modifications resulting from some form of simple unsupervised learning of phonetic categories (e.g., Hebb, 1949; Lieberman, 1984; Kluender, 1994). The human auditory system thus becomes customized to human speech sounds, just as those of animals become customized to species-typical animal sounds (Konishi, 1985; Suga, 1988). The role of common auditory coding processes in the formation of category prototypes for speech sounds is also indicated by animal studies of categorization. For example, Kluender *et al.* (1987) have shown that birds (quails) can learn to categorize speech sounds in a way that parallels that found in studies of human categorization (for a review, see Kluender, 1994). Furthermore, the recent results of Sussman and Lauckner-Morano (1995) using a paradigm less conducive to phonetic processing than that of Kuhl (1991) suggest an important auditory factor behind the perceptual magnet effect.

One promising method of measuring cortical information processing “on line” is to record event-related potentials (ERPs), transient voltage fluctuations in brain tissue, generated by neural events. There are two general classes of ERP components: exogenous and endogenous (Hillyard and Kutas, 1983). According to Meyer *et al.* (1988) the exogenous components occur within 100 ms or so after the stimulus onset, and they are believed to reflect relatively peripheral sensory mechanisms, while the endogenous components, occurring 100 ms or more after stimulus onset, are thought to reflect more central processes such as perception, attention, and decision.

One of the endogenous ERP components, the mismatch negativity (MMN), is of particular interest for the study of auditory processes, because it reflects preattentive detection of deviations from sounds in sensory memory, and can therefore be elicited even when the subject ignores the stimuli (for reviews, see Näätänen, 1990, 1992; Ritter *et al.*, 1995). Thus, the MMN makes it possible to study automatic auditory discrimination without influences from higher-level psychological factors.

Näätänen (1992) claims that each auditory stimulus leaves a memory trace which is formed automatically, without conscious perception or selective attention, and that this trace accurately represents the physical features of the stimulus. In an automatic comparison process, with a neuronal memory trace left by a repetitive standard stimulus, the MMN process is triggered by an occasional stimulus that deviates from the standard (the oddball paradigm). This neuronal mismatch process, reflected by the MMN, is capable of causing an attention switch. The MMN consists of an increased negativity in the 100–200 ms poststimulus range of the ERP, its amplitude increasing with the magnitude of the deviation. Magnetoencephalographic recordings (Hari *et al.*, 1984; Sams *et al.*, 1991) and source analyses of scalp-recorded electrical potentials (Scherg *et al.*, 1989) suggest that the MMN is mainly generated in the supratemporal plane (for a review, see Alho, 1995). It can be obtained from simple sounds as well as from speech signals such as vowels and consonant–vowel syllables (e.g., Aaltonen *et al.*, 1987, 1992; Lang *et al.*, 1990; Sams *et al.*, 1990; Sharma *et al.*, 1993; Lawson and Gaillard, 1981; Maiste *et al.*, 1995). The correlation of the MMN with reported behavioral discrimination measures is high even with stimulus differences close to detection thresholds (Aaltonen *et al.*, 1994; Kraus *et al.*, 1992).

MMN recordings from guinea pigs suggest that certain speech features require processing at the cortical level (e.g., rapid spectral changes typical to stop consonants), whereas others (e.g., slow varying spectral changes typical to suprasegmental aspects of speech) are processed at the thalamic level (Kraus *et al.*, 1994). Thus, different acoustic features underlying speech are represented by different neural processes in the auditory system. Likewise, results from aphasic patients (Aaltonen *et al.*, 1993) indicate that the MMN to vowels, but not to sine tones, disappears after left temporoparietal lesions.

The present study is a series of four experiments with the same Finnish-speaking subjects, using synthetic vowel

stimuli varying only in the second formant (F_2). In experiment 1, the subjects categorized the stimuli as either /i/ or /y/. In experiment 2, the stimuli previously categorized consistently as /i/ were rated for their goodness as exemplars of /i/. For each subject, the best scoring exemplar was designated the prototype (P) and the lowest scoring the nonprototype (NP). In experiment 3, the individual P and NP were used as referents, and they were discriminated, using a same–different procedure (AX discrimination), from deviants spaced in equal mel steps. Finally, in experiment 4, using the same P, NP, and deviants, preattentive auditory discrimination was studied by MMN recordings.

I. EXPERIMENT 1: CATEGORIZATION

It is essential that in locating the prototype of a phonetic category, all employed stimuli represent this category (Kuhl, 1991). However, in earlier studies of the categorization of Finnish vowels (e.g., Aaltonen and Suonpää, 1983), in group data the phoneme boundary between /i/ and /y/ was not sharp but gradual, indicating that listeners differ in their categorization of the same sounds. Therefore, the purpose of this experiment was to determine what stimuli are consistently categorized as /i/ by speakers of Finnish. The *quality* of the Finnish closed front vowels /i/ and /y/ is mainly dependent on the frequencies of F_2 and F_3 . To make the interpretation of the results straightforward and comparable to our earlier experiments studying the effects of F_2 on the MMN and on the labeling of synthetic vowel stimuli (e.g., Aaltonen *et al.*, 1987), we used stimuli varying only in the frequency of F_2 .

A. Method

1. Subjects

Thirteen Finnish-speaking young adults with normal hearing (aged 21–32 years, mean age 23.5 years, 9 females, 4 males) volunteered. All spoke the modern educated Finnish of the Turku area. Before the experiment, they were screened for possible hearing defects by routine audiometric tests.

2. Stimuli

Nineteen long vowels (duration 500 ms) in the Finnish /y/–/i/ continuum (Aaltonen and Suonpää, 1983) were synthesized by a parallel mode speech synthesizer (Klatt, 1980) embedded in a UNIX workstation. The duration of each stimulus was 500 ms with a linearly ramped 30-ms onset and offset in the beginning and at the end of the stimulus. The synthesis parameters given by Kuhl (1991) were followed with the exception that only the F_2 value varied from 1520 Hz to 2966 Hz in steps of 30 mels (Table I). The other formants were fixed at the following frequencies: $F_1=250$ Hz, $F_3=3010$ Hz, $F_4=3300$ Hz, $F_5=3850$ Hz. A 100-ms rise–400-ms fall contour was used for F_0 ; that is, it rose from 112 Hz to 132 Hz in 100 ms and dropped to 92 Hz during the remaining 400 ms of the vowel duration.

3. Apparatus

The stimuli were played with a NeuroStim PC-based stimulus presentation device at 10-kHz playback rate. A 12-bit digital-to-analog converter with an integrated reconstruc-

TABLE I. The $F2$ values of the stimuli used in the experiments in the Hz and mel scales. Center frequencies of the critical bands, according to Scharf (1970), associated with the $F2$ frequency range. Frequency differences of adjacent stimuli in the Hz and mel scale.

| Stimulus unit | $F2$ frequency | | Critical band Hz | Frequency difference | |
|---------------|----------------|------|------------------|----------------------|-----|
| | Hz | mel | | Hz | mel |
| 1 | 1520 | 1290 | 1480 | | |
| 2 | 1582 | 1320 | | 62 | 30 |
| 3 | 1646 | 1350 | | 64 | 30 |
| 4 | 1712 | 1380 | 1720 | 66 | 30 |
| 5 | 1780 | 1410 | | 68 | 30 |
| 6 | 1850 | 1440 | | 70 | 30 |
| 7 | 1922 | 1470 | | 72 | 30 |
| 8 | 1996 | 1500 | 2000 | 74 | 30 |
| 9 | 2071 | 1530 | | 75 | 30 |
| 10 | 2149 | 1560 | | 78 | 30 |
| 11 | 2230 | 1590 | | 81 | 30 |
| 12 | 2313 | 1620 | 2320 | 83 | 30 |
| 13 | 2400 | 1650 | | 87 | 30 |
| 14 | 2488 | 1680 | | 88 | 30 |
| 15 | 2578 | 1710 | | 90 | 30 |
| 16 | 2670 | 1740 | 2700 | 92 | 30 |
| 17 | 2766 | 1770 | | 96 | 30 |
| 18 | 2864 | 1800 | | 98 | 30 |
| 19 | 2966 | 1830 | | 102 | 30 |

tion filter fed the stimuli through calibrated insert earphones (Ear Tone 3A) at a sound-pressure level of 75 dB(A). The audio system was calibrated with a Bruel & Kjaer artificial ear (type 4152) and a precision sound level meter (type 2230). Like in all experiments, the subjects sat in a quiet soundproof room (sound-pressure level of ambient noise lower than 40 dB).

4. Procedure and analysis

Each of the 19 vowel variants was randomly repeated 15 times, i.e., each variant occurred in a random order 15 times in a series of 285 vowel variants. The subjects were to identify each variant as /y/ or /i/ by pressing one of two buttons during a 2000-ms period after the stimulus. Pressing the button paced the next stimulus. The maximum interstimulus interval (ISI) was thus 2000 ms, i.e., those responses given after the 2000-ms period were not counted, but the next stimulus was played instead. Half of the subjects used the left thumb for /y/ and the right thumb for /i/, and the other half vice versa.

To evaluate the reliability of the identifications, Subjects 3, 4, 5, and 12 were selected at random to repeat the test within a few days from the first recording.

B. Results and discussion

The categorization data are presented in Fig. 1. The percentage of /y/ and /i/ categorizations in the 15 occurrences of each variant is plotted against the $F2$ frequency.

All the subjects were able to make the categorization. The categorization changed in an orderly manner: Stimuli with low $F2$ values were predominantly called /y/, and those with higher $F2$ values were called /i/. At a $F2$ of about 2000 Hz the subjects categorized stimuli equally often as /i/ and as /y/. Considerable interindividual variation can be seen in the

steepness of the categorization function and in the boundary location. For example, subjects 3 and 10 consistently categorized the stimulus with $F2=2000$ Hz as /y/, whereas the same stimulus was categorized as /i/ by subjects 5 and 12. The retest results for subjects 3, 4, 5, and 12 demonstrate that the categorization functions were quite stable.

The plot shapes indicate that subjects differed greatly in the consistency with which they made the categorizations. On the basis of the categorization consistency and the boundary width (defined as the difference between the $F2$ values yielding 75% /i/ and 75% /y/), the subjects were classified as good categorizers (subjects 1, 2, 3, 5, 9, 11, and 12) and poor categorizers (subjects 4, 6, 7, 8, 10, and 13). The mean boundary width of the good categorizers was 112 Hz (s.d. 39.5 Hz, range 68–182). Thus, they made phonemic distinctions with $F2$ differences much smaller than the standard critical bandwidth, one bark (e.g., Zwicker and Feldtkeller, 1967). The poor categorizers had a mean boundary width of 339.5 Hz (s.d. 115.5 Hz, range 250–363) indicating that they needed more than one bark of difference in $F2$ to be certain about the phonemic quality of the vowel stimuli used in the experiment. Subject 4 was inconsistent in categorizing most of the stimuli. Subject 7 was least consistent in categorizing vowels as /y/, for this subject there were no clear exemplars of /y/ and some of the stimuli in the boundary area were not responded to at all within 2000 ms (hence the less than 50% in Fig. 1). Subject 10 behaved in the opposite way; for this subject there were more clear exemplars of /y/ than of /i/. The individual differences in the location and width of the boundary resulted in a gently sloping categorization function for /i/ in the group data, with a boundary width of approximately 1.2 bark.

As shown in Fig. 1, there is no clear relationship between the location of the boundary and its width. For instance, subjects 3 and 5 were equally consistent in categorizing the stimuli in the range of 1750–2300 Hz although they did this in opposite ways. The phonetic category boundaries, defined by the point at which the stimuli were labeled equally often as /i/ and /y/, were at the same location for subjects 3 and 7. However, the boundary was sharper for subject 3.

Three main findings emerge. First, the location of the /y/–/i/ boundary in the $F2$ continuum varied greatly between subjects. However, it was quite stable within each subject, which is consistent with the results of Ganong and Zatorre (1980). It is generally agreed that several factors influence the location of phonetic category boundaries on physical stimulus continua. For example, subjects may be differently sensitive to effects of the stimulus sequence, their internal category representations may be different, or they may have adopted different criteria for deciding between two competing categories (for a review, see Repp and Liberman, 1987).

Second, some subjects made distinctions for $F2$ differences much smaller than one bark, indicating that the standardized critical bandwidth does not limit individual categorization performance (cf. Weitzman, 1992). Third, the frequency of $F2$ alone was a sufficient cue for the good categorizers to classify the vowels as /i/ or /y/. For the poor categorizers the stimuli apparently were not natural enough,

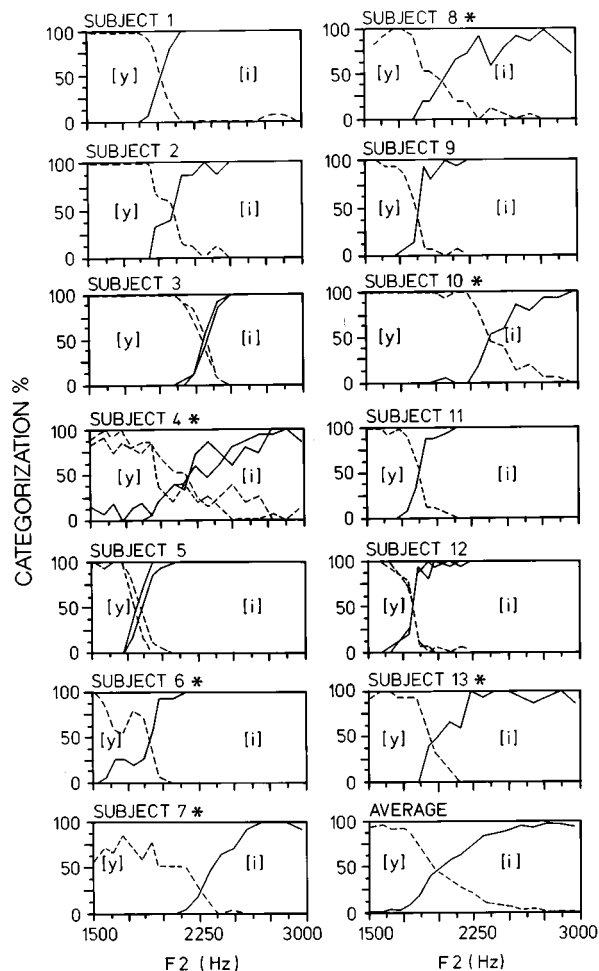


FIG. 1. Individual categorization percentages as a function of F_2 in the frequency range of 1520–2966 Hz. Repetitions for subjects' 3, 4, 5, and 12 are shown in the corresponding frames. The averaged categorization data for all subjects are presented in the lowermost panel on the right. The F_2 step size between successive stimuli is 30 mels. The F_2 scale ticks indicate intervals of 125 Hz. Poor categorizers are marked by *.

which may have led these subjects to feel uncertain about the categorization task. This may have been due to the absence of the information which in natural vowels is provided by the higher formants. In a naturally spoken /y/, the lip rounding lowers the frequencies of the higher formants (Fant, 1960). These (especially F_3) contribute to the perceptual distinctiveness of /y/ and /i/ (e.g., Aaltonen, 1984). Furthermore, many researchers (e.g., Carlson *et al.*, 1970; Chistovich *et al.*, 1979) have suggested that the higher formants are perceptually integrated with F_2 , forming a single “effective” formant (F_2'), which is higher for /i/ than for /y/.

II. EXPERIMENT 2: GOODNESS RATING

While it is a long-standing tradition to focus on subjects' relative inability to detect within-category differences, the prototype approach, as discussed above, holds that stimuli within a category differ in their representativeness as category members (e.g., Eimas and Corbit, 1973; Oden and Massaro, 1978; Samuel, 1982; Miller and Volaitis, 1989). If the prototype location, defined as the location of the token with the highest rated goodness, is determined by long-term

exposure to language (Kuhl *et al.*, 1992) it should be relatively stable across subjects and contexts. In Kuhl's (1991) study, the prototype was found in the center of the category and rated goodness decreased symmetrically from that point. On the other hand, the results of Lively (1993), Iverson and Kuhl (1995), and Sussman and Lauckner-Morano (1995) indicate that prototypes can reside at more extreme locations in the vowel space. The location of the prototype may be influenced by for instance, the particular set of stimuli used (Iverson and Kuhl, 1995). Moreover, Lively (1993) found that the subjects' prototypes may be unstable, whereas the subjects of Iverson and Kuhl had a stable prototype location across trials, although their identification responses were influenced by the context and also showed individual differences. Finally, Sussman and Lauckner-Morano (1995) suggest that experienced listeners may judge the “goodness” of stimuli in a different way from naive listeners, because knowledge of phonetics plays a role in identification. Altogether, these contradictory results support the notion of graded internal structure of vowel categories, but they also call into question whether rating experiments yield accurate measures of this structure.

In experiment 2, the subjects rated the stimuli previously labeled as /i/, using a “category goodness” metric. We expected the good categorizers, with their steeper categorization functions, to give higher ratings than the poor categorizers, as was found by Nàbelek *et al.* (1993). We also expected that the poor categorizers, who could reliably categorize only stimuli high in the F_2 continuum as /i/, would tend to select those stimuli as the best instances of /i/. For the good categorizers, a wider range of stimuli received a high percentage of /i/ responses, and therefore they should have more choices.

A. Method

1. Subjects and stimuli

The same subjects as in experiment 1 participated. Each subject evaluated those vowels that were consistently (in more than 75% of the cases) categorized by him/herself as /i/ (see Table I). Because there was large variation in the individual location of the /y/-/i/ boundary, the number of /i/ variants differed between subjects.

2. Procedure and analysis

The stimuli were played via the same stimulus presentation device as in experiment 1. The minimum ISI was 2000 ms although stimulus presentation was self-paced. The variants were presented in random order, 15 times each. The stimuli were rated using the scale 1–7 (1=poor category exemplar, 7=good category exemplar) and the results were marked on a form. The ratings were to be done with reference to a good pronunciation of /i:/ in the Finnish word *tilli* /ti:li/ “brick.” To check the reliability of the ratings, the test was repeated with subjects 1, 3, 4, 5, 7, and 10 within a few days from the first session. The individual ratings were plotted against the F_2 frequency (see Fig. 2). For each subject, the stimulus with the highest rating was called the P and the

one with the lowest the NP. The significance of the difference in mean rating between the P and NP was *t* tested for each subject.

B. Results

The individual rating data are presented in Fig. 2, and Table II. The Ps and the NPs obtained average ratings of 5.7 and 2.1, respectively. Although goodness is a relative measure usable only within a given stimulus set, the rating values obtained are lower than those reported by Kuhl (1991), using the same scale. This is probably, at least partly, due to our subjects' inexperience with synthetic speech. The difference in goodness rating between the Ps and the NPs is substantial and comparable to that found by Kuhl. Apart from the Ps themselves, ratings were highest for their closest neighbors, and consistently decreased with increasing distance from the Ps.

Individual goodness ratings show that, as was hypothesized on the basis of the categorization data, the perceptual organization of the /i/ category was not the same across subjects. Subjects 4, 6, 7, 8 and 10 (the high-P group) selected the stimulus with highest *F*₂ as the best /i/ with ratings decreasing with lower *F*₂ values. Thus, they showed a category structure similar to that reported by Lively (1993). However, except for subject 6, *t* tests for the difference between P and NP in rated goodness showed no significance for the subjects in the high-P group. Subjects 1, 2, 3, 11, and 13 (the Down group) yielded an opposite pattern. For them, stimuli close to the boundary against /y/ were rated as the best /i/ and those with highest *F*₂ as the worst. Subjects 5, 9, and 12 (the Hill group) had similar P positions but lower category boundaries; therefore the stimuli they rated as the best /i/ were close to their category center. Thus, their ratings indicate a category structure for /i/ similar to that obtained by Kuhl (1991). The Down and Hill groups (henceforth, the low-P group) showed significant differences in rated goodness between the P and the NP, which indicates that, unlike the high-P group, they could reliably distinguish the best /i/ from the worst. The replications for subjects 1, 3, 4, 5, 7, and 10 yielded virtually identical results.

The goodness ratings and categorization data were compared. As expected, the subjects in the high-P group were the poor categorizers of experiment 1. The subjects of the low-P group were the good categorizers [with subject 13, a poor categorizer (boundary width 272 Hz), as an exception]. The mean width of the boundary for the low-P group was 132 Hz (s.d. 67 Hz, range 68–272) and for the high-P group 353 Hz (s.d. 124 Hz, range 250–363). The lower the boundary, the lower was the location of the P ($r=0.67$, $p<0.05$). Also, the sharper the boundary, the lower was the P ($r=0.67$, $p<0.05$). The location of the NP correlated significantly only with the boundary width ($r=-0.59$, $p<0.05$).

C. Discussion

Our subjects' ability to perceive and label goodness differences within-category was related to their performance in the identification task. The good categorizers were more able to distinguish the best category exemplars from the poor

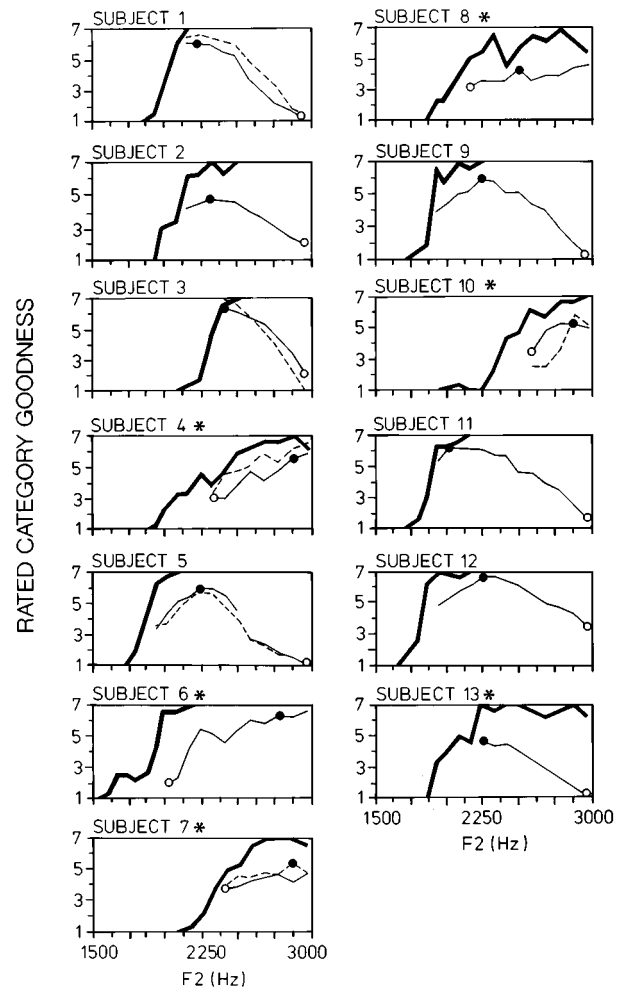


FIG. 2. Individual goodness ratings in the scale of 1–7 (7 is the best rating) for the stimuli categorized by the subject as /i/ in more than 75% of the cases. Dashed lines represent repetitions. The individual *F*₂ values (Hz) of prototypes (P) and nonprototypes (NP) are shown in Table II as well as the *p*-value of the significance of their difference. The *F*₂ step size between successive stimuli is 30 mels. The *F*₂ scale ticks indicate intervals of 125 Hz. Poor categorizers are marked by *. The /i/ category boundary is indicated by a thick line.

ones than the poor categorizers. As indicated by the goodness ratings, only the good categorizers exhibited an internal category structure. However, for the Down (sub)group this structure was not concordant with that reported by Kuhl (1991), because the vowels close to their boundary were rated as having the highest prototypicality, not those in the center of the category.

It can be doubted, however, whether goodness rating of synthetic stimuli is an adequate method for revealing the true internal structure of vowel categories. The P and NP determined in this way are most likely based on a rather abstract level of information processing guided by experience and with principles varying between subjects. The subjects in our high-P group may have been chasing after the most distinct example of /i/ (as compared to /y/), instead of the most natural /i/, because they could categorize with certainty only the extreme stimuli. Setting *F*₂ close to *F*₃ typically increases the distinctiveness of /i/ sounds, but at the cost of losing their status as typical members of the Finnish /i/ category. Addi-

TABLE II. The $F2$ values and the mean goodness ratings for the best rated (prototype, P) and the worst rated stimuli (nonprototype, NP) for each subject. t and p values for the differences between mean ratings of P and NP. Poor categorizers are marked by *. Ns=not significant ($p>0.05$).

| Subject | $F2$ value (Hz) | | Mean goodness ratings on scale 1–7 | | | | t | df | p |
|---------|-----------------|------|------------------------------------|------------|------|------------|--------|------|--------|
| | P | NP | P | σ^2 | NP | σ^2 | | | |
| 1 | 2230 | 2966 | 6.00 | 6.34 | 1.00 | 0.00 | 7.692 | 28 | <0.001 |
| 2 | 2313 | 2966 | 4.87 | 1.84 | 2.00 | 0.00 | 8.200 | 28 | <0.001 |
| 3 | 2400 | 2966 | 6.87 | 1.84 | 1.00 | 0.00 | 16.771 | 28 | <0.001 |
| 4* | 2864 | 2313 | 5.53 | 8.21 | 3.00 | 38.40 | 1.435 | 28 | ns |
| 5 | 2230 | 2966 | 6.00 | 0.00 | 1.07 | 1.01 | 18.926 | 28 | <0.001 |
| 6* | 2766 | 1996 | 6.27 | 7.35 | 1.93 | 28.98 | 2.789 | 28 | <0.01 |
| 7* | 2864 | 2400 | 5.47 | 8.21 | 4.00 | 23.44 | 1.012 | 28 | ns |
| 8* | 2488 | 2149 | 4.27 | 37.45 | 3.07 | 22.33 | 0.601 | 28 | ns |
| 9 | 2230 | 2966 | 5.87 | 14.70 | 1.13 | 1.84 | 5.790 | 28 | <0.001 |
| 10* | 2864 | 2578 | 5.13 | 4.06 | 3.4 | 40.34 | 1.006 | 28 | ns |
| 11 | 1996 | 2966 | 6.20 | 8.89 | 1.53 | 6.14 | 4.664 | 28 | <0.001 |
| 12 | 2230 | 2966 | 6.60 | 3.90 | 3.23 | 2.52 | 5.196 | 28 | <0.001 |
| 13* | 2230 | 2966 | 4.60 | 10.33 | 1.00 | 0.00 | 4.337 | 28 | <0.001 |

tional information of the *vowel quality*, and thus for the sufficient contrast between the *natural* /i/ and /y/, is hidden among higher formants, although $F1$ and $F2$ are considered to convey more information than any other formant in categorizing natural vowel sounds.

The lack of additional information may have made these subjects particularly susceptible to the ‘‘hyperspace effect’’ discovered by Johnson *et al.* (1993): Listeners’ perceptual vowel space is expanded relative to their production space, reflecting hyperarticulated vowels rather than vowels of normal effortless speech. Johnson *et al.* also found that goodness ratings of synthetic stimuli can be affected by the instructions given. Subjects who were asked to find the ‘‘best’’ vowel for each word were more critical to the stimuli than those instructed to find the vowel sound most closely matching their own pronunciation. Thus, our subjects may have interpreted the instructions in two different ways: The subjects in our high-P group may have meant as the ‘‘best’’ the ‘‘most distinct,’’ and consequently, rated the stimuli with reference to more abstract linguistic representations than the subjects in the low-P group did, for whom the vowels probably sounded more natural or closer to their own pronunciation. For the low-P group the goodness ratings at the phonetic level may be based on an internal category structure at the auditory level, as was earlier suggested by the adaptation study of Miller *et al.* (1983).

III. EXPERIMENT 3: DISCRIMINATION

As was discussed earlier, Kuhl (1991) found that detecting deviations from the P was more difficult than from the NP; thus, discrimination performance was determined not only by the mel difference but also by the prototypicality of the referent. A signal detection analysis of the discrimination results of Sussman and Lauckner-Morano (1995, p. 551) partly supports this conclusion, but these authors also suggest that ‘‘an auditory processing component may be an important part of the ‘perceptual magnet’ effect’’ (p. 551). In contrast, Lively (1993) found that discrimination performance, as measured by the percentage of misses, was similar for the P and the NP, and depended solely on the mel difference. Experiment 3 (the same–different discrimination test)

studied the relation between the discriminability of $F2$ differences for /i/ tokens and their rated goodness.

A. Method

1. Subjects

The same subjects as in experiments 1 and 2 participated.

2. Stimuli

The discrimination performance of each subject was studied using a same–different (AX) paradigm. The individual Ps and NPs, and stimuli differing from them by 30, 60, 90, or 120 mels in $F2$ (for the $F2$ values in Hz see Table I) were used as stimulus pairs. The presentation of the stimulus pairs is indicated in Table III. Different sessions were used for Ps (rows 1–4 in Table III) and NPs (rows 6–10 in Table III). All P and NP stimuli served as referents [the columns marked ‘‘A(standard)’’ in Table III] as well as deviants [the columns marked ‘‘X(deviant)’’ in Table III]. In addition X could be identical to A, i.e., the difference was 0 mel. When the referent was high in $F2$ (close to $F3$) only lower deviants were used; when it was low (close to the boundary) only higher ones. The AX pairs were presented in random order, 15 times each in each direction, that is, A=referent/X=deviant and A=deviant/X=referent. Thus, each subject heard 8×15 pairs of different stimuli and 15 pairs of equal stimuli in two different sessions of randomly ordered pairs.

3. Procedure and analysis

The stimuli were presented with a pause of 1000 ms between stimuli, and 2000 ms between stimulus pairs. The responses were collected using the NeuroStim reaction time keypad. The subjects were asked to press, as quickly as possible, the ‘‘same’’ button when they heard the stimuli as being the same and the ‘‘different’’ button when they heard them as different. Half of the subjects used the left thumb for ‘‘same’’ and the right thumb for ‘‘different,’’ and the other half vice versa.

TABLE III. The stimulus pairs in experiment 3 (AX discrimination), and experiment 4 (MMN recordings). In both experiments two separate sessions were used: the prototype session (cases 1–5) and the nonprototype session (cases 6–10). In the AX discrimination sessions nine stimulus pairs were used. In the MMN recording sessions only eight stimulus pairs were used because equal stimuli (P-P or NP-NP) do not elicit MMN responses.

| | A (standard) | X (deviant) | A (standard) | X (deviant) |
|----|--------------|----------------------|----------------------|--------------|
| 1 | prototype | prototype | | |
| 2 | prototype | prototype+30 mel | prototype+30 mel | prototype |
| 3 | prototype | prototype+60 mel | prototype+60 mel | prototype |
| 4 | prototype | prototype+90 mel | prototype+90 mel | prototype |
| 5 | prototype | prototype+120 mel | prototype+120 mel | prototype |
| 6 | nonprototype | nonprototype | | |
| 7 | nonprototype | nonprototype+30 mel | nonprototype+30 mel | nonprototype |
| 8 | nonprototype | nonprototype+60 mel | nonprototype+60 mel | nonprototype |
| 9 | nonprototype | nonprototype+90 mel | nonprototype+90 mel | nonprototype |
| 10 | nonprototype | nonprototype+120 mel | nonprototype+120 mel | nonprototype |

B. Results

Table IV gives, for each subject, the number of responses “different” and “same” for each referent and deviant combination (P=P, P≠P, and NP=NP, NP≠NP) along with the values of d' , read off from the tables of Kaplan *et al.* (1978) for AX experiments. As recommended by Macmillan and Creelman (1991), percentages of hits and false alarms below 1% were changed to 1%, and those above 99% to 99%.

A MANOVA (multivariate approach to repeated measures) on the d' values with factors referent (P and NP) and P level (low-P and high-P) yielded a nonsignificant effect of referent [$F(1,11)=3.00$, ns]. The effect of the P level was significant [$F(1,11)=10.06$; $p<0.01$], which is due to higher d' values in the low-P group (mean=4.54, s.d.=0.53) than in the high-P group (mean=3.54, s.d.=0.59). Individual d' values correlated significantly with the width of the boundary: $r=-0.68$, $p<0.05$ (two tailed).

The referent \times P level interaction was highly significant [$F(1,11)=69.38$; $p<0.001$]. To explore the nature of this interaction in more detail, for each subject the relative difference in d' between NP and P,

$$\Delta_{d'} = 2[d'_{NP} - d'_P] / [d'_{NP} + d'_P] \quad (1)$$

and the corresponding $F2$ difference in Hz between NP and P,

$$\Delta_{F2} = F2_{NP} - F2_P \quad (2)$$

were computed. An effect of $F2$ on discriminability will show up in the regression term, and an effect of the designation of the referents (the one with higher $F2$ as P and the one with lower $F2$ as NP, or vice versa) in the intercept (the value of $\Delta_{d'}$ that obtains for $F2_{NP}=F2_P$). The linearity of this plot, and thus also the estimate of its intercept, is quite insensitive to a possible nonlinearity of the relation between d' and $F2$.

The computed regression line was:

$$\Delta_{d'} = -0.022 + 0.501 \times \Delta_{F2}, \quad r = 0.912. \quad (3)$$

The regression coefficient differed highly significantly from zero [$t(11)=7.39$; $p<0.001$] whereas the intercept did not [$t(11)=-0.48$, ns]. This implies that the detectability of

deviations increased with the $F2$ frequency of the referent, but was independent of its designation as P or NP. Thus, for each group, discrimination was easiest for the referent with the highest $F2$ frequency: for the low-P group, NP; for the high-P group, P.

C. Discussion

Our aim with experiment 3 was to investigate whether the discriminability of the /i/ tokens is related to their rated goodness. In other words, are equal mel deviations more difficult to detect from the P than from the NP? The answer from the analysis of the data as a whole seems to be negative. For both the high-P and low-P groups, the poorest discrimination occurred at about the same location in the $F2$ continuum, which made the best-rated /i/ for the low-P group, and was therefore used as their P, but which was also the worst-rated /i/ for the high-P group and used as their NP. Thus, only the data from the low-P group are possible to explain as resulting from a prototype-based magnet effect. The high-P group showed an opposite effect. For these subjects, it was more difficult to detect deviations from their NP than from their P.

The simplest conclusion, then, from the evidence collected so far seems to be that discriminability, rather than being ruled by the prototypicality of the referent as indicated by goodness ratings, depends on its location in the $F2$ continuum. Furthermore, our results can neither be explained by categorical perception, which predicts that discrimination of identically labeled stimuli should be equally poor (Fry *et al.*, 1962; Pisoni and Tash, 1974; Repp *et al.*, 1979), nor by the listeners' strategy to use such stimuli that are easy to label consistently (“perceptual anchors”) for discriminating speech stimuli (Macmillan *et al.*, 1988). Although the theories of categorical perception, perceptual magnets, and perceptual anchors are based on fundamentally different approaches to speech perception, they all predict peaks in discrimination near the category boundary. Thus, none of these theories can explain the discrimination behavior of the Finnish listeners, who were more sensitive to stimulus differences far from the boundary than close to it.

An important point, as made by a reviewer, is that for

TABLE IV. Number of responses in categories “different” and “same” (total for all deviants), the d' estimates, and differences of d' estimates for NP and P referents.

| Subject No. (Type) | Referent | Deviant | Different | Same | d' | $d'_{NP} - d'_P$ |
|--------------------|----------|---------|-----------|------|------|------------------|
| 1 (low-P) | P | = | 5 | 67 | 3.21 | |
| | P | ≠ | 80 | 40 | | +2.28 |
| | NP | = | 0 | 75 | 5.49 | |
| 2 (low-P) | NP | ≠ | 104 | 11 | | |
| | P | = | 0 | 68 | 4.42 | |
| | P | ≠ | 80 | 33 | | +0.92 |
| 3 (low-P) | NP | = | 0 | 75 | 5.34 | |
| | NP | ≠ | 108 | 14 | | |
| | P | = | 2 | 73 | 4.61 | |
| 11 (low-P) | P | ≠ | 102 | 18 | | +0.89 |
| | NP | = | 3 | 72 | 5.50 | |
| | NP | ≠ | 116 | 4 | | |
| 13 (low-P) | P | = | 8 | 67 | 2.80 | |
| | P | ≠ | 77 | 43 | | +1.52 |
| | NP | = | 3 | 72 | 4.32 | |
| 5 (low-P) | NP | ≠ | 101 | 19 | | |
| | P | = | 21 | 53 | 3.03 | |
| | P | ≠ | 103 | 17 | | +2.19 |
| 9 (low-P) | NP | = | 9 | 66 | 5.22 | |
| | NP | ≠ | 117 | 2 | | |
| | P | = | 3 | 72 | 3.75 | |
| 12 (low-P) | P | ≠ | 87 | 33 | | +1.29 |
| | NP | = | 1 | 74 | 5.04 | |
| | NP | ≠ | 103 | 17 | | |
| 4 (high-P) | P | = | 0 | 66 | 4.33 | |
| | P | ≠ | 112 | 8 | | +1.52 |
| | NP | = | 1 | 74 | 5.85 | |
| 6 (high-P) | NP | ≠ | 114 | 6 | | |
| | P | = | 10 | 65 | 3.81 | |
| | P | ≠ | 106 | 14 | | +2.06 |
| 7 (high-P) | NP | = | 5 | 69 | 5.87 | |
| | NP | ≠ | 119 | 1 | | |
| | P | = | 11 | 61 | 3.64 | |
| 8 (high-P) | P | ≠ | 96 | 14 | | -0.61 |
| | NP | = | 14 | 71 | 3.03 | |
| | NP | ≠ | 110 | 32 | | |
| 10 (high-P) | P | = | 17 | 58 | 3.45 | |
| | P | ≠ | 106 | 13 | | -0.60 |
| | NP | = | 8 | 66 | 2.85 | |
| 8 (high-P) | NP | ≠ | 79 | 41 | | |
| | P | = | 8 | 67 | 3.85 | |
| | P | ≠ | 104 | 16 | | -1.21 |
| 10 (high-P) | NP | = | 14 | 61 | 2.64 | |
| | NP | ≠ | 83 | 34 | | |
| | P | = | 7 | 67 | 3.78 | |
| 10 (high-P) | P | ≠ | 101 | 19 | | -0.82 |
| | NP | = | 10 | 64 | 2.96 | |
| | NP | ≠ | 87 | 33 | | |
| 10 (high-P) | P | = | 0 | 60 | 5.55 | |
| | P | ≠ | 82 | 8 | | -1.93 |
| | NP | = | 2 | 58 | 3.62 | |
| | NP | ≠ | 60 | 30 | | |

similar $F1$ frequencies the Finnish listeners in our study showed a discrimination pattern opposite to that of American listeners: Finnish listeners are least sensitive to acoustic differences for /i/ tokens with low $F2$; American listeners for those with high $F2$ (Kuhl, 1991; Iverson and Kuhl, 1995; Sussman and Lauckner-Morano, 1995). Thus, the pattern of differential sensitivity along the $F2$ continuum observed in the present study is not due to common auditory processing, as suggested by Sussman and Lauckner-Morano, but rather

seems to result from the specific linguistic experience of the Finnish-speaking subjects. Macmillan *et al.* (1988) have suggested that listeners use perceptual anchors for discriminating speech stimuli, which leads to increased discrimination near perceptual anchors and poor discrimination far from them. According to this, our discrimination results suggest that Finnish listeners have perceptual anchors located at high rather than low frequencies of $F2$ for /i/ tokens. Increased auditory resolution for higher formant frequencies is needed

in Finnish, which has an opposition between /i/ and /y/ based on higher versus lower values of $F2$ and $F3$ (or of $F2'$). No such opposition is found in English, which instead has an opposition (not found in Finnish) between /i/ and /I/ based on $F1$ and $F2$ (Wiik, 1965).

Sussman and Lauckner-Morano (1995) suggest that the direction of the intrapair change in formant frequency plays a role in determining differential sensitivity, and that this may have contributed to the perceptual magnet effect they found. Subjects who made frequency comparisons in pairs with a change from high to low showed better sensitivity than those who heard the same standard but with an upward frequency change. Dooley and Moore (1988) found the same asymmetry in glide detection. These results suggest that, in the present study, the measured sensitivity to $F2$ changes in the regions close to $F3$ might have been somewhat overestimated due to the fact that only downward changes in $F2$ were used. Nord (1980) also showed that Swedish listeners are more sensitive to an $F2$ fall than to a rise, whereas in Flanagan's (1955) study the same type of stimuli produced the opposite pattern with American listeners. Thus, linguistic experience as well as acoustic factors may make listeners more sensitive in their vowel discrimination to a shift of a formant frequency in one direction than in the other.

IV. EXPERIMENT 4: MMN RECORDINGS

According to Kuhl's (1991, 1993a) hypothesis, the perceptual magnet effect is restricted to a phonetic process component that uses abstracted mental representations of prototypical speech sounds. An alternative hypothesis is that auditory (sensory) prototypes are linked with phonetically good tokens. The assumption is supported, at least partly, by theories that emphasize the role of lower-level articulatory and auditory constraints in shaping phonetic inventories (e.g., Liljencrants and Lindblom, 1972; Stevens, 1989; Diehl *et al.*, 1990). To test the latter hypothesis, auditory discrimination was measured by recording MMNs using the same (P and NP) referents (in MMN literature: standards) and deviants as in experiment 3. In order to rule out attention effects during the MMN recording, the subjects were instructed to watch a silent subtitled movie and to ignore the vowel stimuli.

A. Method

1. Subjects and stimuli

The same subjects and the same stimuli as in experiment 3 were used. Using the oddball paradigm, either the P or the NP served as a standard and vowels deviating from it by 30, 60, 90, or 120 mel in $F2$ as deviants, or vice versa (see Table III). For each subject there were two sessions, each with eight stimulus pairs, which were separately randomized for Ps and NPs. The duration of each stimulus was 500 ms; the time interval from the beginning of one stimulus to the next was 850 ms, so the presentation of one block (100 deviants and 900 referents) took about 15 min. The duration of a recording session was thus about 2 h excluding a 30-min preparing time for electrode fittings. The subject watched a silent, subtitled movie (of their own choice) on a 21-in. TV

screen 2.5-m apart and was instructed to ignore the vowel stimuli presented binaurally in earphones. All subjects had normal vision.

2. Equipment and procedure

Continuous EEG was recorded and stored using a Braintronics 32-channel EEG-amplifier connected to the Neuro Scan EEG data acquisition and analysis computer. Ag/AgCl electrodes were used, and they were placed according to the international 10/20 system, using linked ears as the reference. The electrodes were placed at $Fp1$, $Fp2$, $F7$, $F3$, Fz , $F4$, $F8$, $T3$, $C3$, Cz , $C4$, $T4$, $T5$, $P3$, Pz , $P4$, $T6$, $O1$, Oz , and $O2$ (Figs. 4 and 5). The electrode impedance was regularly checked during the sessions in order to keep it below 5 k Ω . At the beginning of each session the amplifiers were calibrated. The amplifier bandwidth was set to 0.1–70 Hz (–3 dB) and a sampling frequency of 200 Hz was used. The EEG averaging was triggered by the stimulus onset, and response epochs of 800-ms duration were averaged off-line and stored in separate files for standard and deviant stimuli. A 50-ms pretrigger period was used to evaluate the EEG background activity, which was subtracted as a dc baseline from the response epoch. A level-sensitive (± 50 - μ V) artifact rejection was applied prior to the summing of the trials. The averaged ERP responses to standard and deviant stimuli were digitally filtered (using a time-domain bandpass filter of 24 dB/octave in a band of 0.1–21 Hz) to further reduce noise.

The experimenter (an experienced EEG laboratory technician) continuously monitored the subject's EEG and performance (via a video system). Eyeblinks, drowsiness, and alfa activity were specifically controlled. In a few cases, the experiment was stopped because a subject did not watch the movie or got tired. The session was then restarted after a few minutes' break.

For each stimulus block, the response epoch to the standard preceding the deviant was subtracted (point-by-point) from that to the deviant, and the MMN peak amplitude and latency were measured from the difference curves (from onset to peak) manually by two scorers blind as to the behavioral performance of the subject. Both were professional EEG laboratory technicians experienced with MMN experiments. The amplitude values were fed to a computer for statistical analysis.

B. Results

1. MANOVA

The analysis was done with SAS software using the MANOVA approach to repeated measures (Bock, 1975). This method eliminates interindividual differences normally present in ERP recordings (e.g., Lang *et al.*, 1995). The MMN peak amplitudes and latencies from the same subject in different conditions and in different electrodes were the repeated measures. These were structured by within-factors referent (P,NP), position (standard; deviant), distance (30, 60, 90, and 120 mel), laterality [left ($F3,C3$); middle (Fz,Cz); right ($F4,C4$)], and sagittal [front ($F3,Fz,F4$);

central (C3,Cz,C4)]. The rest of the electrodes were excluded from the statistical analysis, because they showed no MMN.

The subjects were grouped by two between-subject factors, gender (male; female) and P level [low-P (8 subjects); high-P (5 subjects)]. Distance had a significant effect on MMN amplitude [$F(3,7)=17.31$; $p<0.01$] and on MMN latency [$F(3,29)=7.98$; $p<0.001$]. The MMN amplitude increased and latency decreased with the difference between standard and deviant. The linear effect of distance on MMN amplitude was highly significant [$F(1,9)=45.25$; $p<0.0001$]. The MMN latency was not affected by any other factor than distance.

For MMN amplitudes, the effects of position and sagittal factors were nonsignificant, whereas that of laterality factor was highly significant [$F(2,6)=47.50$; $p<0.001$]. The mean MMN amplitudes were $-2.65 \mu\text{V}$ for the left (F3,C3), $-2.79 \mu\text{V}$ for the middle (Fz,Cz), and $-2.68 \mu\text{V}$ for the right (F4,C4) electrodes. Thus, the significance resulted from a difference between the middle electrodes and those to the left and to the right.

There was also a significant main effect on MMN amplitude due to gender [$F(1,7)=12.03$; $p<0.05$]. The mean MMN amplitudes were higher for females ($-2.79 \mu\text{V}$) than for males ($-2.49 \mu\text{V}$). The main effect of referent was not significant [$F(1,9)=0.61$]. This effect was significant for the low-P group [$F(1,9)=6.79$; $p<0.05$] but not for the high-P group [$F(1,9)=1.65$]. The referent \times P level interaction was significant [$F(1,9)=7.26$; $p<0.05$].

The mean MMNs for P and NP as a function of distance are plotted in Fig. 3. As shown in the low-P group the mean MMN amplitude is systematically less negative for P (mean = $-2.77 \mu\text{V}$) than for NP (mean = $-3.40 \mu\text{V}$), reflecting a magnet effect. The MMN becomes less affected by stimulus prototypicality as the difference between the standard (referent) and deviant increases. The MMN data from the high-P group are less systematic than those from the low-P group. The difference curves in Figs. 4 and 5 illustrate the difference between the P and the NP as a standard (referent) at different electrodes in the low-P and high-P groups when the deviation was 30 mels. For the low-P group, with the NP as referent, there is a clear MMN recorded at the F and C electrodes, peaking around 200 ms. No such peaks are visible for the P. The low-P group shows no P300 (an ERP component reflecting attentive discrimination in an oddball paradigm), which indicates that the 30-mel deviation from the P did not trigger attentional processes. As illustrated by Fig. 5, there is a different MMN pattern in the high-P group: The MMNs at the F and C electrodes are clearly larger for the P than for the NP. In addition, a P3 component is visible, indicating that for the same stimulus differences the mismatch process was sensitive enough to cause an attention switch in the high-P group but not in the low-P group. There is also a clear negative peak at a latency of 400 ms in the low-P group, but no such component is visible in the high-P group (Figs. 6 and 7). This late negative peak may thus be related particularly to preattentive discrimination. However, these conclusions are based only on the qualitative inspection of the grand average difference curves.

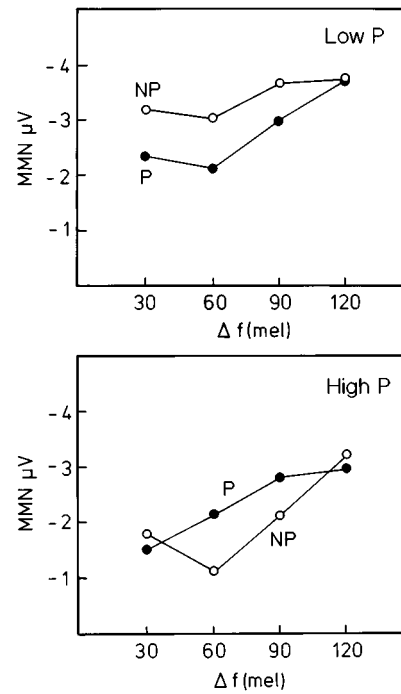


FIG. 3. Mean MMN amplitudes for the low-P and high-P groups recorded from electrodes F3, F4, C3, C4, Fz and Cz in the P and NP conditions.

2. Regression analysis

In analogy with the analyses for the d' values from experiment 3 [see Eqs. (1) and (2)], the within-subject relative difference in MMN between NP and P,

$$\Delta_{\text{MMN}} = 2[\text{MMN}_{\text{NP}} - \text{MMN}_{\text{P}}] / [\text{MMN}_{\text{NP}} + \text{MMN}_{\text{P}}] \quad (4)$$

for each electrode position, and the corresponding $F2$ difference in Hz,

$$\Delta_{F2} = F2_{\text{NP}} - F2_{\text{P}} \quad (5)$$

were calculated (using amplitudes as well as latencies). In a linear regression of MMN on Δ_{F2} , an effect of the $F2$ difference between the standards (referents) would show up in the regression term, and an effect of the designation of the standard (referent) with the higher and lower $F2$ as P and

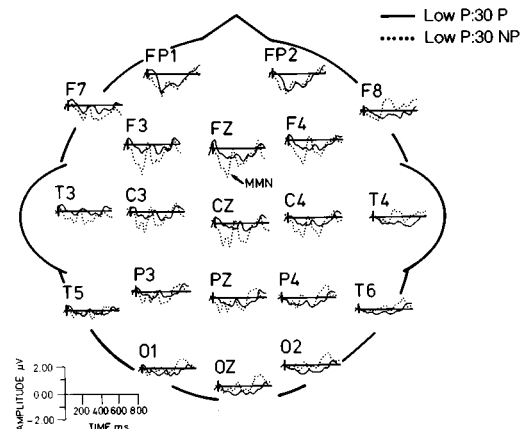


FIG. 4. Difference curves for P and NP at different electrodes for the low-P group with 30-mel deviance.

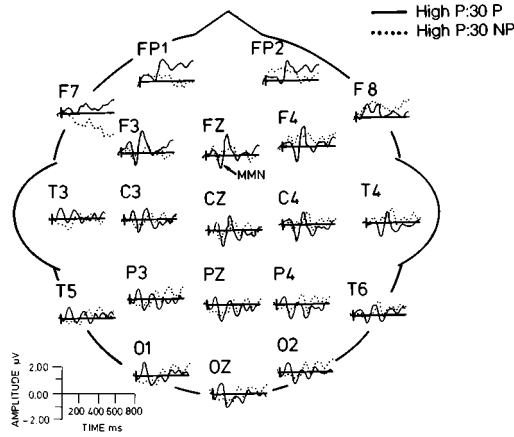


FIG. 5. Difference curves for P and NP at different electrodes for the high-P group with 30-mel deviance.

NP, or vice versa, in the intercept (the value of Δ_{MMN} for $F2_{NP}=F2_P$). The correlations were higher for the amplitudes than for the latencies. The computed correlation coefficients (two-tailed p values in parentheses) between Δ_{MMN} (absolute amplitudes) and Δ_{F2} were: $F3$: 0.346 (ns); Fz : 0.430 (ns); $F4$: 0.531 ($p < 0.10$); $C3$: 0.534 ($p < 0.10$); $C4$: 0.570 ($p < 0.05$). For $C4$, which showed the highest correlation, the regression line was:

$$\Delta_{MMN} = 0.0004 + 7.44 \times \Delta_{F2}, \quad r = 0.569. \quad (6)$$

The regression coefficient differed significantly from zero ($p < 0.05$) whereas the intercept did not. Thus, similarly as for the behavioral discrimination measures, for the subject group as a whole, only the $F2$ frequency of the referent, not its designation as P or NP, determined the MMN evoked by the deviants.

Also, for each electrode, the correlations were computed between the subjects' mean d' values and their mean MMN latencies and amplitudes. The coefficients and two-tailed p values were for the MMN latencies: $F3$: 0.494 ($p < 0.10$); Fz : 0.520 ($p < 0.10$); $F4$: 0.512 ($p < 0.10$); $C3$: 0.523 ($p < 0.10$);

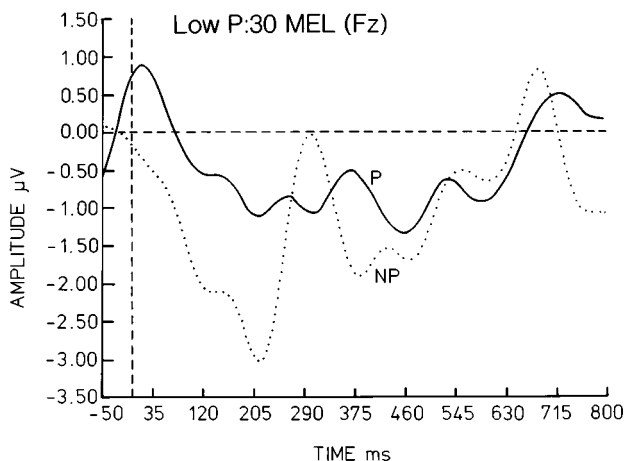


FIG. 6. Difference curves for P and NP at Fz for the low-P group with 30-mel deviance.

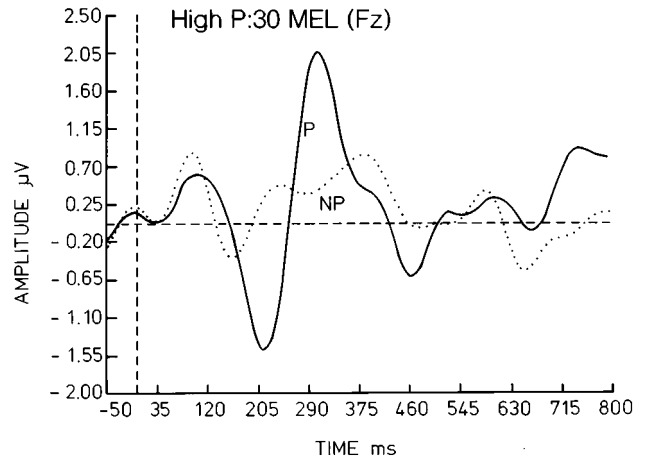


FIG. 7. Difference curves for P and NP at Fz for the high-P group with 30-mel deviance.

< 0.10); Cz : 0.514 ($p < 0.10$); $C4$: 0.507 ($p < 0.10$). For the MMN amplitudes all correlations were small and nonsignificant.

The correlations between MMNs and category widths were also computed; none of these correlations was significant.

C. Discussion

The MMN recordings showed that preattentive processing is sensitive to differences within a vowel category. The MMN amplitude increased with the difference between standard (referent) and deviant. The subjects' MMN latencies correlated with their discrimination performance as measured by d' , which suggests that conscious and preattentive discrimination of vowel sounds works in much the same way. The MMN amplitudes were highest in the middle of the head, and tended to be higher for females than for males. For d' , there was no appreciable gender difference.

Prior evidence suggested that the MMN reflects the physical parameters of the stimuli, and not their phonetic categories (e.g., Aaltonen *et al.*, 1992; Sams *et al.*, 1990; Sharma *et al.*, 1993; Maiste *et al.*, 1995). For example, increased sensitivity at phonetic boundaries, reflecting categorical perception, has not been reported for MMN; neither are there any differences between MMNs elicited by phonetically relevant (e.g., $F2$) and irrelevant stimuli (e.g., $F0$) (Aaltonen *et al.*, 1994). Typically, the choice of stimuli in earlier studies was based on the boundary-oriented approach (using stimuli from opposite categories or from the boundary area as standards), whereas in the present study it was guided by the prototype-oriented approach (using stimuli within one category). The most interesting result of experiment 4, then, is that the position of the stimuli in the phonetic continuum plays a role in the generation of the MMN. Equal mel differences between standard and deviant stimuli elicited larger MMNs at the higher end of the $F2$ continuum than at the lower end. Earlier MMN studies indicate equal discrimination both across and within categories. Moreover, in the low-P group the MMN amplitudes not only reflected the difference between referent and deviant, but also correlated

with the rated goodness of the stimuli. This gives further support to the hypothesis that the prototypes of the high-P group were based on more abstract levels of processing than such prototypes as yield a perceptual magnet effect. This might also explain the attention shift, which was not shown by the low-P group.

An important feature of the MMN is that its amplitude increases with training (Kraus *et al.*, 1995). Perhaps the MMNs were larger in the good categorizers (the low-P group) because these had properly learned to discriminate the stimuli. In the high-P group, as well as in the low-P group, the MMN tended to be diminished for stimuli in the low $F2$ region. Applying the perceptual magnet theory, this could mean that this region has features that are related to stimulus prototypicality—although subjects may not recognize this—and therefore impair discrimination.

V. GENERAL DISCUSSION

In earlier studies it has generally been assumed that the processes underlying the MMN are based primarily on acoustical stimulus differences (e.g., Näätänen, 1992; Aaltonen *et al.*, 1994). Our results suggest that this may not be true. The low-P group demonstrated what may be interpreted as a perceptual magnet effect, not only behaviorally but also in terms of MMN amplitudes. For this group, equal mel differences between standard (referent) and deviant stimuli elicited lower MMNs when the standard was the P than when it was the NP. On the other hand, the high-P group behaved in the opposite way: Both as indicated by MMN amplitudes and behaviorally, it was easier for them to detect differences from their Ps than from their NPs.

The MMN reflects aspects of sensory processing that are assumed to be relatively independent of cognitive, linguistic, and attentional factors. Nevertheless, according to our results, it is modified by the listener's experience with spoken language. One interpretation is that on the auditory processing level this experience is organized into clusters of similar, frequently heard speech sounds. The ability to discriminate sounds within the same cluster is impaired—the perceptual magnet effect—and at the subsequent phonetic processing level the category limits are adjusted to fit the pattern of clusters.

Morais and Kolinsky (1994) suggest that there are two functionally distinct phonological systems underlying language processing: an unconscious one for speech perception and production, and a conscious one for reading and writing. One explanation for the results of the high-P group might be that these subjects used unconscious (auditory) phoneme representations for discrimination, resulting in interindividually consistent MMNs and d' values but conscious (phonetic) representations, which are more difficult to use, for categorization and goodness rating, yielding inter- and intraindividually inconsistent results.

In the study of Lang *et al.* (1990) the MMN elicited by a given set of pure-tone stimuli varied greatly between normally hearing listeners; as in the present study, one-third of their subjects showed lower MMN amplitudes than the others. The MMNs correlated with frequency discrimination performance. It is possible that, for some reason, the memory

traces generating the MMN were not equally well developed in our poor categorizers as in our good ones. To compensate for this deficit at the preattentive level of perception, the poor categorizers may have been inclined to rely on abstract representations of the vowels, different from the auditory ones used by the good categorizers; therefore, attentional processes were triggered by the poor categorizers to activate the corresponding neuronal assemblies.

One counterargument against the interpretation we offer for our results might be that the mechanism that generates the MMN may not be fully independent of attention; subjects may have attended to the stimuli although they were asked to ignore them. However, there is a bulk of literature on the MMN (e.g., Näätänen, 1992) indicating that the MMN represents preattentive processes. This view is supported by the fact that the MMN is elicited even when the subject concentrates on a difficult problem solving task (Lyytinen *et al.*, 1992), or tries to recognize visual stimuli (Woods *et al.*, 1992) or stimuli in another auditory modality (Paavilainen *et al.*, 1993). A strong piece of evidence for the independence of the MMN from the direction of the subject's attention comes from a recent study by Cheour-Luhtanen *et al.* (1995) who recorded an MMN-like response to vowels in quietly sleeping newborns. In the present study, the lack of the $P3$ component in the low-P group strongly suggests that they did not attend to the stimuli.

Our study also showed that listeners are not all alike in identifying vowels and in rating their category goodness. About one-third of our subjects (the poor categorizers) were uncertain about the phonetic quality of the stimuli. In addition, their mean MMN amplitude over all electrodes ($-2.1 \mu\text{V}$) was lower than that of the other subjects ($-2.9 \mu\text{V}$). However, this difference was not significant, probably because of the small number of subjects (Lang *et al.*, 1995). Nevertheless, separate t tests for each electrode showed differences approaching statistical significance between the groups at Fz [$t(11)=-2.05$, $p<0.10$] and $F4$ [$t(11)=-1.86$, $p<0.10$]. As expected, the mean d' also differed significantly (2.94 for the high-P group, 3.39 for the low-P group) [(9.10) (unequal variances)=2.90, $p<0.05$].

High goodness ratings require that most formants ($F1$, $F2$, $F3$, etc.) are close to their prototypical values. However, as indicated by our results, the perceptual magnet effect works at a lower level of processing than the goodness ratings. The level of the magnet effect may be also lower than that where the formant cues are integrated to form a single percept of a vowel. If so, then the magnet effect can be elicited when the stimulus vowel has the same $F2$ frequency as the prototype (cf. Lively, 1993), not requiring a match to occur for $F3$ as well. The latter match may depend on interindividually varying principles. Our stimuli turned out to sound quite unnatural for many subjects, and for those subjects the $F3$ match may not have occurred. The elicitation of the magnet effect by a single formant match reminds of the principle in visual perception that the presence of a single depth cue can evoke size scaling to achieve constancy, without eliciting any conscious experience of depth (see Coren *et al.*, 1994).

VI. CONCLUSIONS

Taken together, our results show that individual listeners were inconsistent in categorization and goodness rating but consistent in discrimination. For all our subjects, the poorest discrimination occurred at about the same location in the $F2$ continuum, but only the data from the good categorizers are possible to explain as resulting from a prototype-based magnet effect. In speech perception research, the absence of decisive evidence often leads to a long-standing competition between phonetic explanations and more general and simple auditory ones (Diehl *et al.*, 1990). In the case of the perceptual magnet effect, more evidence from electrophysiological, as well as, behavioral measures is obviously needed before the locus of the effect can be unambiguously determined. However, for similar $F1$ frequencies the Finnish listeners of our study show a discrimination pattern opposite to that of American listeners. Thus, the pattern of differential sensitivity along the $F2$ continuum observed in the present study seems to result from language experience affecting basic sensory capabilities of listeners, as demonstrated by our MMN recordings.

ACKNOWLEDGMENTS

The study was supported by the Academy of Finland and by the Swedish Council for Research in the Humanities and Social Sciences (Åke Hellström). We wish to thank Jari Riitala, M.Sc., for vowel synthesization, Tuula Järnstedt, Mia Ek, M.Sc., and Anne Hjort for making the recordings, Pasi Hakulinen for writing the analysis software for the behavioral experiments, and Lea Heinonen-Eerola, M.A., for editing the English language of the manuscript. Dr. Altti Salmivalli, M.D., has kindly allowed the hearing tests of the subjects at the Hearing Centre of Turku University Hospital.

Aaltonen, O. (1984). "The effect of relative amplitude levels of $F2$ and $F3$ on the categorization of synthetic vowels," *J. Phon.* **13**, 1–9.

Aaltonen, O., and Suonpää, J. (1983). "Computerized two-dimensional model for Finnish vowel identifications," *Audiology* **22**, 410–415.

Aaltonen, O., Niemi, P., Nyrke, T., and Tuhkanen, M. (1987). "Event-related brain potentials and the perception of a phonetic continuum," *Biol. Psychol.* **24**, 197–207.

Aaltonen, O., Paavilainen, P., Sams, M., and Näätänen, R. (1992). "Event-related brain potentials and discrimination of steady-state vowels within and between phoneme categories: a preliminary study," *Scand. J. Logopedics Phoniatrics* **17**, 107–112.

Aaltonen, O., Tuomainen, J., Laine, M., and Niemi, P. (1993). "Cortical differences in tonal versus vowel processing as revealed by an ERP component called mismatch negativity (MMN)," *Brain Lang.* **44**, 139–152.

Aaltonen, O., Eerola, O., Lang, H., Uusipaikka, E., and Tuomainen, J. (1994). "Automatic discrimination of phonetically relevant and irrelevant vowel parameters as reflected by mismatch negativity," *J. Acoust. Soc. Am.* **96**, 1489–1493.

Alho, K. (1995). "Cerebral generators of mismatch negativity (MMN) and its magnetic counterpart (MMNm) elicited by sound changes," *Ear Hear.* **16**, 38–50.

Bock, R. D. (1975). *Multivariate Statistical Methods in Behavioral Research* (McGraw-Hill, New York).

Carlson, R., Granström, B., and Fant, G. (1970). "Some studies concerning perception of isolated vowels," *Speech Transmission Laboratory Quarterly Progress Report, Stockholm, KTH*, **2–3**, 1–8.

Cheour-Luhtanen, M., Alho, K., Kujala, T., Sainio, K., Reinikainen, K., Renlund, M., Aaltonen, O., Eerola, O., and Näätänen, R. (1995). "Mismatch negativity shows discrimination of speech stimuli in newborns," *Hear. Res.* **82**, 53–58.

Chistovich, L. A., Sheikin, R. L., and Lublinskaya, V. V. (1979). "'Center of gravity' and spectral peaks as the determinants of vowel quality," in *Frontiers of Speech Communication Research, Festschrift for Gunnar Fant*, edited by B. Lindblom and S. Öhman (Academic, London), pp. 143–157.

Coren, S., Ward, L. M., and Enns, J. T. (1994). *Sensation and Perception* (Harcourt Brace Jovanovich, New York), 4th ed.

Creelman, C. D., and Macmillan, N. A. (1979). "Auditory phase and frequency discrimination: A comparison of nine procedures," *J. Exp. Psychol. Hum. Percept. Perform.* **5**, 146–156.

Diehl, R. L., Kluender, K. R., and Walsh, M. A. (1990). "Some auditory bases of speech perception and production," in *Advances in Speech; Hearing and Language Processing*, edited by W. A. Ainsworth, Vol. 1 (JAI London), pp. 243–267.

Dooley, G. J., and Moore, B. C. J. (1988). "Detection of linear frequency glides as a function of frequency and duration," *J. Acoust. Soc. Am.* **84**, 2045–2057.

Eimas, P. D., and Corbit, J. D. (1973). "Selective adaptation of linguistic feature detectors," *Cogn. Psychol.* **4**, 99–109.

Eyraud, R., and Kuhl, P. (1994). "Extending the perceptual magnet effect to a CVC word context," Paper presented at the 128th meeting of the Acoustical Society of America, November 30, 1994, Austin, TX.

Fant, G. M. C. (1960). *Acoustic Theory of Speech Production* (Mouton, The Hague).

Flanagan, J. (1955). "A difference limen for vowel formant frequency," *J. Acoust. Soc. Am.* **27**, 613–617.

Fry, D. B., Abramson, A. S., Eimas, P. D., and Liberman, A. M. (1962). "The identification and discrimination of synthetic vowels," *Lang. Speech* **5**, 171–189.

Fujisaki, H., and Kawashima, T. (1970). "Some experiments on speech perception and a model for the perceptual mechanism," Annual Report of the Engineering Research Institute, Faculty of Engineering, University of Tokyo.

Ganong, W. F., and Zatorre, R. J. (1980). "Measuring phoneme boundaries four ways," *J. Acoust. Soc. Am.* **68**, 431–439.

Grieser, D., and Kuhl, P. K. (1989). "Categorization of speech by infants: Support for speech-sound prototypes," *Dev. Psychol.* **25**, 577–588.

Hari, R., Hämäläinen, M., Ilmoniemi, R., Kaukoranta, E., Reinikainen, K., Salminen, J., Alho, K., Näätänen, R., and Sams, M. (1984). "Responses of the primary auditory cortex to pitch changes in a sequence of tone pips: Neuromagnetic recordings in man," *Neurosci. Lett.* **50**, 127–132.

Hillyard, S. A., and Kutas, M. (1983). "Electrophysiology of cognitive processing," *Ann. Rev. Psychol.* **45**, 188–196.

Hebb, D. O. (1949). *The Organization of Behavior* (Wiley, New York).

Iverson, P., and Kuhl, P. (1995). "Mapping the perceptual magnet effect for speech using signal detection theory and multidimensional scaling," *J. Acoust. Soc. Am.* **97**, 553–561.

Johnson, K., Flemming, E., and Wright, R. (1993). "The hyperspace effect: phonetic targets are hyperarticulated," *Language* **69**, 505–528.

Kaplan, H. L., Macmillan, N. A., and Creelman, C. D. (1978). "Tables of d' for variable-standard discrimination paradigms," *Behav. Res. Methods Instrum.* **10**, 796–813.

Klatt, D. (1980). "Software for a cascade/parallel formant synthesizer," *J. Acoust. Soc. Am.* **67**, 971–995.

Kluender, K. R. (1994). "Speech perception as a tractable problem in cognitive science," in *Handbook of Psycholinguistics*, edited by M. A. Gernsperger (Academic, New York), pp. 173–217.

Kluender, K. R., Diehl, R. L., and Killeen, P. R. (1987). "Japanese quail can learn phonetic categories," *Science* **237**, 1195–1197.

Konishi, M. (1985). "Birdsong: from behavior to neuron," *Ann. Rev. Neurosci.* **8**, 125–170.

Kraus, N., McGee, T., Carrell, T., and Sharma, A. (1995). "Neurophysiologic bases of speech discrimination," *Ear Hear.* **16**, 19–37.

Kraus, N., McGee, T., Sharma, A., Carrell, T., and Nicol, T. (1992). "Mismatch negativity event-related potential elicited by speech stimuli," *Ear Hear.* **13**, 158–164.

Kraus, N., McGee, T., Carrell, T., King, C., Littman, T., and Nicol, T. (1994). "Discrimination of speech-like contrasts in the auditory thalamus and cortex," *J. Acoust. Soc. Am.* **96**, 2758–2768.

Kuhl, P. K. (1991). "Human adults and human infants show a 'perceptual

- magnet effect' for the prototypes of speech categories, monkeys do not," *Percept. Psychophys.* **50**, 93–107.
- Kuhl, P. K. (1993a). "Early linguistic experience and phonetic perception: implications for theories of developmental speech perception," *J. Phon.* **21**, 125–139.
- Kuhl, P. K. (1993b). "Psychoacoustics and speech perception: internal standards, perceptual anchors, and prototypes," in *Developmental Psychoacoustics*, edited by L. A. Werner and E. Rubel (Academic, San Francisco), pp. 293–332.
- Kuhl, P., and Miller, J. (1975). "Speech perception by the chinchilla: Voiced-voiceless distinction in alveolar plosive consonants," *Science* **190**, 69–72.
- Kuhl, P. K., Williams, K. A., Lacerda, F., Stevens, K. N., and Lindblom, B. (1992). "Linguistic experience alters phonetic perception in infants by 6 months of age," *Science* **255**, 606–608.
- Lang, H., Nyrke, T., Ek, M., Aaltonen, O., Raimo, I., and Näätänen, R. (1990). "Pitch discrimination performance and auditive event-related potentials," in *Psychophysiological Brain Research*, edited by C. H. M. Brunia, A. W. K. Gaillard, and A. Kok, Vol. 1 (University, Tilburg), pp. 294–298.
- Lang, H., Eerola, O., Korpilahti, P., Holopainen, I., Salo, S., Uusipaikka, E., and Aaltonen, O. (1995). "Practical issues in the clinical application of mismatch negativity," *Ear Hear.* **16**, 118–130.
- Lawson, E. A., and Gaillard, A. W. K. (1981). "Mismatch negativity in a phonetic discrimination task," *Biol. Psychol.* **13**, 281–288.
- Lieberman, P. (1984). *The Biology and Evolution of Language* (Harvard U.P., Cambridge, MA).
- Liljencrants, J., and Lindblom, B. (1972). "Numerical simulation of vowel quality systems: the role of perceptual contrast," *Language* **48**, 839–862.
- Lively, S. E. (1993). "An examination of the perceptual magnet effect," *J. Acoust. Soc. Am.* **93**, 2423.
- Lyytinen, H., Blomberg, A.-P., and Näätänen, R. (1992). "Event-related potentials and automatic responses to a change in unattended auditory stimuli," *Psychophysiology* **29**, 523–534.
- Macmillan, N. A., and Creelman, C. D. (1991). *Detection Theory: A User's Guide* (Cambridge U.P., New York).
- Macmillan, N. A., Goldberg, R. F., and Braida, L. D. (1988). "Resolution for speech sounds: Basic sensitivity and context memory on vowel and consonant continua," *J. Acoust. Soc. Am.* **84**, 1262–1280.
- Maddox, W. T., and Ashby, F. G. (1993). "Comparing decision boundaries and exemplar models of categorization," *Percept. Psychophys.* **53**, 49–70.
- Massaro, D. W. (1987). "Categorical partition: A fuzzy logical model of categorization behaviour," in *Categorical Perception: The Groundwork of Cognition*, edited by S. Harnad (Cambridge U.P., New York).
- Massaro, D., and Oden, G. (1980). "Evaluation and integration of acoustic features in speech perception," *J. Acoust. Soc. Am.* **67**, 996–1013.
- Maiste, A., Wiens, A., Hunt, M., Scherg, M., and Picton, T. (1995). "Event-related potentials and the categorical perception of speech sounds," *Ear Hear.* **16**, 68–90.
- Medin, D. L., and Barsalou, L. W. (1987). "Categorization processes and categorical perception," in *Categorical Perception: The Groundwork of Cognition*, edited by S. Harnad (Cambridge U.P., New York).
- Mervis, C. B., and Rosch, E. (1981). "Categorization of natural objects," *Ann. Rev. Psychol.* **32**, 89–115.
- Meyer, D. D., Osman, A. M., Irwin, D. E., and Yantis, S. (1988). "Modern mental chronometry," *Biol. Psychol.* **26**, 3–67.
- Miller, J. L., and Volaitis, L. E. (1989). "Effect of speaking rate on the perceptual structure of a phonetic category," *Percept. Psychophys.* **46**, 505–512.
- Miller, J. A., Connine, C. M., Schermer, T. M., and Kluender, K. R. (1983). "A possible auditory basis for internal structure of phonetic categories," *J. Acoust. Soc. Am.* **73**, 2124–2133.
- Morais, J., and Kolinsky, R. (1994). "Perception and awareness in phonological processing: the case of the phoneme," *Cognition* **50**, 287–297.
- Nábelek, A. K., Czyzewski, K., and Crowley, H. J. (1993). "Vowel boundaries for steady-state and linear formant trajectories," *J. Acoust. Soc. Am.* **94**, 675–687.
- Näätänen, R. (1990). "The role of attention in auditory information processing as revealed by event-related potentials and other brain measures of cognitive function," *Phys. Behav. Brain Sci.* **13**, 210–288.
- Näätänen, R. (1992). *Attention and Brain Function* (Erlbaum, Hillsdale, NJ).
- Nord, L. (1980). "Analysis and prediction of difference limen data for formant frequencies. The testing of two distance metrics," Working Papers, 19, Papers given at the seventh Swedish-Danish symposium, Lund, April 25–26, 1980, Phonetics Laboratory, Department of General Linguistics, Lund University, pp. 49–53.
- Oden, G. C., and Massaro, D. W. (1978). "Integration of featural information in speech perception," *Psychol. Rev.* **85**, 172–191.
- Paavilainen, P., Jiang, D., Lavikainen, J., and Näätänen, R. (1993). "Stimulus duration and the sensory memory trace: an event-related potential study," *Biol. Psychol.* **35**, 139–152.
- Pisoni, D. B. (1973). "Auditory and phonetic codes in the discrimination of vowels and consonants," *Percept. Psychophys.* **13**, 253–260.
- Pisoni, D. B., and Luce, P. A. (1986). "Principal issues in speech perception," in *Pattern Recognition by Humans and Machines: Speech Perception*, edited by E. C. Schwab and H. C. Nusbaum, Vol. 1 (Academic, New York), pp. 1–50.
- Pisoni, D. B., and Tash, J. (1974). "Reaction times to comparisons within and across category," *J. Acoust. Soc. Am.* **15**, 285–290.
- Polka, L., and Werker, J. F. (1994). "Developmental changes in perception of non-native vowel contrasts," *J. Exp. Psychol. Hum. Percept. Perform.* **20**, 421–435.
- Repp, B. H. (1977). "Dichotic competition of speech sounds: the role of acoustic stimulus structure," *J. Exp. Psychol. Hum. Percept. Perform.* **3**, 37–50.
- Repp, B. (1987). "The role psychophysics in understanding speech perception," in *The Psychophysics of Speech Perception*, edited by M. E. H. Schouten (Nijhoff, Dordrecht, The Netherlands), pp. 3–27.
- Repp, B. H., and Liberman, A. M. (1987). "Phonetic boundaries are flexible," in *Categorical Perception: the Groundwork of Cognition*, edited by Stevan Harnad (Cambridge U.P., New York), pp. 89–112.
- Repp, B. H., Healey, A. F., and Crowder, R. G. (1979). "Categories and context in the perception of isolated steady-state vowels," *J. Exp. Psychol.: Hum. Percept. Perform.* **5**, 129–145.
- Ritter, W., Deacon, D., Gomes, H., Javitt, D., and Vaughan, Jr., H. (1995). "The mismatch negativity of event-related potentials as probe of transient auditory memory: A review," *Ear Hear.* **16**, 52–67.
- Rosch, E. H., and Mervis, C. B. (1975). "Family resemblances: Studies in the internal structure of categories," *Cogn. Psychol.* **7**, 573–605.
- Rosner, B. S., and Pickering, J. B. (1994). *Vowel Perception and Production*, Oxford Psychology Series, 23 (Oxford U.P., New York).
- Sams, M., Aulanko, R., Aaltonen, O., and Näätänen, R. (1990). "Event-related potentials to infrequent changes in synthesized phonetic stimuli," *J. Cogn. Neurosci.* **2**, 344–357.
- Sams, M., Kaukoranta, E., Hämäläinen, M., and Näätänen, R. (1991). "Cortical activity elicited by changes in auditory stimuli: different sources for the magnetic N100m and mismatch responses," *Psychophysiology* **28**, 21–29.
- Samuel, A. G. (1982). "Phonetic prototypes," *Percept. Psychophys.* **31**, 307–314.
- Sawusch, J. R., Nusbaum, H. C., and Schwab, C. E. (1980). "Contextual effects in vowel perception II: Evidence for two processing mechanisms," *Percept. Psychophys.* **27**, 421–434.
- Scharf, B. (1970). "Critical bands," in *Foundations of Modern Auditory Theory*, edited by J. V. Tobias, Vol. 1 (Academic, New York), pp. 157–202.
- Scherg, M., Vajsar, J., and Picton, T. W. (1989). "A source analysis of the human auditory evoked potentials," *J. Cogn. Neurosci.* **1**, 336–355.
- Sharma, A., Kraus, N., McGee, T., Carrell, T., and Nicol, T. (1993). "Acoustic versus phonetic representation of speech as reflected by the mismatch negativity event-related potential," *Electroencephalogr. Clin. Neurophysiol.* **88**, 64–71.
- Stevens, K. N. (1989). "On the quantal nature of speech," *J. Phon.* **17**, 3–45.
- Studdert-Kennedy, M. (1976). "Speech perception," in *Contemporary Issues in Experimental Phonetics*, edited by N. J. Lass (Academic, New York), pp. 243–293.
- Studdert-Kennedy, M. (1993). "Discovering phonetic function," *J. Phon.* **21**, 147–155.
- Studdert-Kennedy, M., Liberman, A. M., Harris, K. S., and Cooper, F. S. (1970). "Motor theory of speech perception: A reply to Lane's critical review," *Psychol. Rev.* **77**, 234–249.
- Suga, N. (1988). "Auditory neuroethology and speech processing: complex-sound processing by combination-sensitive neurons," in *Auditory Function: Neurobiological Bases of Hearing*, edited by G. M. Edelman, W. E. Gall, and W. M. Cowan (Wiley, New York), pp. 679–720.
- Sussman, J. E., and Lauckner-Morano, V. J. (1995). "Further tests of the 'perceptual magnet effect' in the perception of [i]: Identification and

- change/no-change discrimination,” J. Acoust. Soc. Am. **97**, 539–552.
- Weitzman, R. S. (1992). “Vowel categorization and the critical band,” Lang. Speech **35**, 115–125.
- Wiik, K. (1965). Finnish and English Vowels Annales Universitatis Turkuensis, Series B, 94. Polytypos, Turku.
- Woods, D. L., Alho, K., and Algazi, A. (1992). “Intermodal selective attention I: effects of event-related potentials to lateralized auditory and visual stimuli,” Electroencephalogr. Clin. Neurophysiol. **82**, 341–355.
- Zwicker, E., and Feldtkeller, R. (1967). *Das Ohr als Nachrichtenempfänger* (S. Hirzel Verlag, Stuttgart).

Improving discrimination of confusable words using the divergence measure

Philipos Loizou

Department of Applied Science, University of Arkansas at Little Rock, Little Rock, Arkansas 72204-1099

Andreas Spanias

Department of Electrical Engineering, Arizona State University, Tempe, Arizona 85287-7206

(Received 18 October 1995; revised 26 July 1996; accepted 20 September 1996)

This paper describes the use of the divergence measure as a criterion for finding a transformation matrix which will map the original speech observations onto a subspace with more discriminative ability than the original. A gradient-based algorithm is also proposed to compute the transformation matrix efficiently. The subspace approach is used as a preprocessing step in a hidden Markov model (HMM) based system to enhance discrimination of acoustically similar pairs of words. This approach is compared with standard linear discriminant analysis (LDA) techniques and shown to yield as much as 4.5% improvement. The subspace approach is also applied successfully to a more general recognition problem, i.e., discrimination of K confusable words, using the average divergence measure. © 1997 Acoustical Society of America. [S0001-4966(97)04501-3]

PACS numbers: 43.72.Ne [JS]

INTRODUCTION

Linear discriminant analysis is a well-known technique in statistical pattern recognition which has been applied recently to speech recognition to improve recognition performance (Brown, 1987; Yu *et al.*, 1990; Zahorian *et al.*, 1991; Hunt and Lefebvre, 1989; Umbach and Ney, 1992). The idea in linear discriminant analysis (LDA) is to find a transformation matrix which projects feature vectors from an n -dimensional space to an m -dimensional space ($m < n$) such that a class separability criterion is maximized. Criteria such as the ratio of overall-class (or between-class) variance to the average within-class variance are often used in LDA. Ideally, we would like to use the error probability as a criterion for finding this transformation matrix. Unfortunately, the error probability is either unknown or too difficult to compute. In this paper, we propose the divergence measure as an alternative criterion which, unlike previously proposed criteria, is related to the Bayes' error (Kailath, 1967). In addition, the divergence measure criterion makes no assumption about the normality of the input features since it is formulated for any distribution. We note that similar measures have been used in signal selection (Kailath, 1967) and character recognition applications (Tou and Heydorn, 1967). We show here that the use of the divergence measure yields considerable improvement in recognition of confusable pairs of words. The requirements for the computation of the transformation matrix in the proposed method are rather high. In order to reduce the complexity, we propose a gradient algorithm for the efficient computation of the transformation matrix. The above approach has also been applied to a more general recognition problem, i.e., discrimination of K confusable words, using the average divergence measure. The rest of the paper is organized as follows. Section I presents the derivation of the transformation matrix used to enhance discrimination of pairs of confusable words, and also gives simulation results. Section II extends the idea presented in

Sec. I, and derives the transformation matrix used to enhance the discrimination of K confusable words. Section III gives the conclusion.

I. DIVERGENCE MEASURE

The divergence is a measure of dissimilarity between two pattern classes, and also a measure of difficulty in discriminating between two classes (Kullback, 1958). Consider two classes, ω_1 and ω_2 , characterized by the conditional probability density functions, $p_1(\mathbf{x})=p(\mathbf{x}|\omega_1)$ and $p_2(\mathbf{x})=p(\mathbf{x}|\omega_2)$, respectively. Now consider a linear transformation matrix \mathbf{A} which maps the original observations \mathbf{x} into \mathbf{y} , that is

$$\mathbf{y} = \mathbf{A}^T \mathbf{x}, \quad (1)$$

where \mathbf{x} is an n -dimension vector, \mathbf{y} an m -dimension vector, $m < n$, and \mathbf{A} is $n \times m$ matrix with m linearly independent columns. The divergence between the two classes in the subspace is given by (Kullback, 1958)

$$Y_{12} = \int_{\mathbf{y}} [p_1(\mathbf{y}) - p_2(\mathbf{y})] \ln \left[\frac{p_1(\mathbf{y})}{p_2(\mathbf{y})} \right] d\mathbf{y}. \quad (2)$$

Assuming that the conditional density functions $p_i(\mathbf{x})$ are normally distributed according to $N(\boldsymbol{\mu}_i, \boldsymbol{\Sigma}_i)$ with means $\boldsymbol{\mu}_i$ and covariance matrices $\boldsymbol{\Sigma}_i$ ($i=1,2$), then it can be shown that the corresponding density functions $p_i(\mathbf{y})$ are also normally distributed according to $N(\mathbf{A}^T \boldsymbol{\mu}_i, \mathbf{A}^T \boldsymbol{\Sigma}_i \mathbf{A})$. The divergence Y_{12} is then given by (see Kailath, 1967, p. 59)

$$Y_{12} = \frac{1}{2} \text{tr}[\mathbf{C}_1^{-1} \mathbf{C}_2 + \mathbf{C}_2^{-1} \mathbf{C}_1] - m + \frac{1}{2} \text{tr}[(\mathbf{C}_1^{-1} + \mathbf{C}_2^{-1}) \boldsymbol{\Delta}_1], \quad (3)$$

where $\mathbf{C}_1 = \mathbf{A}^T \boldsymbol{\Sigma}_1 \mathbf{A}$, $\mathbf{C}_2 = \mathbf{A}^T \boldsymbol{\Sigma}_2 \mathbf{A}$, $\boldsymbol{\Delta}_1 = \mathbf{A}^T \boldsymbol{\Delta} \mathbf{A}$ are $m \times m$ matrices, and $\boldsymbol{\Delta} = (\boldsymbol{\mu}_1 - \boldsymbol{\mu}_2)(\boldsymbol{\mu}_1 - \boldsymbol{\mu}_2)^T$ is an $n \times n$ matrix, and $\text{tr}[\cdot]$ is the trace of a matrix. We are seeking a transformation matrix \mathbf{A} such that the divergence Y_{12} given in (3) is maximized. This can be done by taking the partial derivative of

Y_{12} with respect to the matrix \mathbf{A} and setting it equal to zero, i.e.,

$$\mathbf{G} \equiv \frac{\partial Y_{12}}{\partial \mathbf{A}} = \Sigma_1 \mathbf{A} (\mathbf{C}_2^{-1} - \mathbf{C}_1^{-1} (\mathbf{C}_2 + \Delta_1) \mathbf{C}_1^{-1}) + \Sigma_2 \mathbf{A} (\mathbf{C}_1^{-1} - \mathbf{C}_2^{-1} (\mathbf{C}_1 + \Delta_1) \mathbf{C}_2^{-1}) + \Delta \mathbf{A} (\mathbf{C}_1^{-1} + \mathbf{C}_2^{-1}). \quad (4)$$

Matrix \mathbf{A} can be obtained by solving the equation $\mathbf{G} = \mathbf{0}$ for \mathbf{A} , which is difficult. Therefore we propose a gradient ascent algorithm for finding matrix \mathbf{A} , i.e., given an initial matrix $\mathbf{A}^{(0)}$ update matrix $\mathbf{A}^{(k)}$ in the following manner:

$$\mathbf{A}^{(k+1)} = \mathbf{A}^{(k)} + \gamma \mathbf{G}^{(k)} \quad (5)$$

for $k=0,1,2,\dots$, where k is the iteration index, and γ is a constant step size. This algorithm is terminated when an appropriately chosen convergence criterion is met. The computation of the \mathbf{G} matrix can be simplified a great deal if the initial matrix $\mathbf{A}^{(0)}$ is chosen properly. This can be done as follows. The divergence J_{12} between two normally distributed probability densities is given by (see Kailath, 1967, p. 59)

$$J_{12} = \frac{1}{2} \text{tr}[\Sigma_1^{-1} \Sigma_2 + \Sigma_2^{-1} \Sigma_1] - n + \frac{1}{2} \text{tr}[(\Sigma_1^{-1} + \Sigma_2^{-1}) \Delta], \quad (6)$$

and using the fact that the trace of a matrix is the sum of its eigenvalues, Eq. (6) can be written as

$$J_{12} = \frac{1}{2} \sum_{i=1}^n \left(\lambda_i + \frac{1}{\lambda_i} \right) - n + \frac{1}{2} (\delta_1 + \delta_2), \quad (7)$$

where λ_i are the eigenvalues of the matrix $\Sigma_2^{-1} \Sigma_1$, δ_1 is the nonzero eigenvalue of $\Sigma_1^{-1} \Delta$, and δ_2 is the nonzero eigenvalue of $\Sigma_2^{-1} \Delta$. Hence, $\mathbf{A}^{(0)}$ can be initialized with the m eigenvectors of $\Sigma_2^{-1} \Sigma_1$, corresponding to the eigenvalues λ_i for which

$$\lambda_i + \frac{1}{\lambda_i} \geq \lambda_k + \frac{1}{\lambda_k} \quad i=1,2,\dots,m \quad \text{and} \quad k=1,2,\dots,n \quad i \neq k. \quad (8)$$

With this $\mathbf{A}^{(0)}$ as the initial matrix in (5), the \mathbf{G} matrix computation (4) can be simplified significantly using the following result from linear algebra (Searle, 1982). Since Σ_i are positive definite, the eigenvector matrix \mathbf{U} of $\Sigma_2^{-1} \Sigma_1$, simultaneously diagonalizes the matrices Σ_1 and Σ_2 , that is

$$\mathbf{U}^T \Sigma_1 \mathbf{U} = \Lambda \quad \text{and} \quad \mathbf{U}^T \Sigma_2 \mathbf{U} = \mathbf{I}, \quad (9)$$

where Λ is the diagonal eigenvalue matrix of $\Sigma_2^{-1} \Sigma_1$ and \mathbf{I} is the identity matrix. Therefore, the covariance matrices will initially be diagonalized when the matrix $\mathbf{A}^{(0)}$ is initialized with the m eigenvectors of \mathbf{U} . There is no guarantee that the matrix $\mathbf{A}^{(k)}$ in (5) will also diagonalize the covariance matrices for every k . We found, however, that $\mathbf{A}^{(k)T} \Sigma_i \mathbf{A}^{(k)}$ is approximately diagonal, and therefore $\mathbf{C}_i^{(k)}$ can be approximated by the diagonal of $\mathbf{A}^{(k)T} \Sigma_i \mathbf{A}^{(k)}$, i.e., $\mathbf{C}_1^{(k)} \approx \text{diag}(\mathbf{A}^{(k)T} \Sigma_1 \mathbf{A}^{(k)})$ and $\mathbf{C}_2^{(k)} \approx \text{diag}(\mathbf{A}^{(k)T} \Sigma_2 \mathbf{A}^{(k)})$. Letting $S_1(i) = (\mathbf{A}^T \Sigma_1 \mathbf{A})_{ii}$ [$(\mathbf{F})_{ii}$ denotes the diagonal element of the i th row of matrix \mathbf{F}], $S_2(i) = (\mathbf{A}^T \Sigma_2 \mathbf{A})_{ii}$ ($i=1,2,\dots,m$) and defining the diagonal matrices $\mathbf{E}_j (m \times m)$, $j=1,\dots,4$, with diagonal elements given by

$$(\mathbf{E}_1)_{ii} = \frac{1}{S_1(i)} - \frac{S_1(i)}{S_2^2(i)}, \quad (10)$$

$$(\mathbf{E}_2)_{ii} = \frac{1}{S_2(i)} - \frac{S_2(i)}{S_1^2(i)}, \quad (11)$$

$$(\mathbf{E}_3)_{ii} = \frac{1}{S_1(i)}, \quad (12)$$

$$(\mathbf{E}_4)_{ii} = \frac{1}{S_2(i)}, \quad (13)$$

the \mathbf{G} matrix can be approximated by $\hat{\mathbf{G}}$

$$\hat{\mathbf{G}} \approx \Sigma_1 \mathbf{A} (\mathbf{E}_2 - \mathbf{E}_3 \Delta_1 \mathbf{E}_3) + \Sigma_2 \mathbf{A} (\mathbf{E}_1 - \mathbf{E}_4 \Delta_1 \mathbf{E}_4) + \Delta \mathbf{A} (\mathbf{E}_3 + \mathbf{E}_4). \quad (14)$$

Note that the $\hat{\mathbf{G}}$ matrix computation no longer requires matrix inversions for each iteration, but only matrix multiplications. Therefore the $\hat{\mathbf{G}}$ matrix, and consequently the transformation \mathbf{A} matrix, can be computed efficiently. It should also be noted that the matrix $\hat{\mathbf{G}}$ (14) and Eqs. (10)–(13) are valid under the assumption that the covariance matrices Σ_i are symmetric and positive definite. Simulation results are presented next which compare the performance obtained using the exact matrix \mathbf{G} and its approximation $\hat{\mathbf{G}}$.

A. Training

The divergence-based approach can be used in general to enhance the discrimination of confusable pairs of phonemes, words, etc. For instance, it can be used to enhance the recognition of phonemes /b/-/d/, /p/-/t/, /m/-/n/, etc., which are known to be highly confusable. In this paper, we will apply our approach to the discrimination of the letters M and N in the alphabet (i.e., discrimination of /m/-/n/), which are considered to be the second most confusable set in the alphabet after the E-set (Cole *et al.*, 1990a; Loizou *et al.*, 1995a; Loizou and Spanias, 1994). Sixty speakers from the ISOLET database (Cole *et al.*, 1990b), speaking the alphabet letters M and N twice in isolation, were used to test and train our phoneme-based HMM recognizer. Half of the speakers were used in training, and half for testing, with an equal number of female and male speakers. There was a total 60 training utterances (30 of letter M and 30 of letter N) and 120 testing utterances (60 of letter M and 60 of letter N).

The original feature vectors used to derive the transformation matrix consisted of 26 log-filterbank energies obtained by applying 26 mel-spaced triangular windows to the magnitude spectrum. Training involved a three step procedure. The training data were first manually segmented into the phonemes [eh], [m], and [n]. Feature vectors corresponding to segments [m] and [n] were then used to estimate the sample mean vectors, μ_1 and μ_2 , and covariance matrices, Σ_1 and Σ_2 , respectively. In the second step, the transformation matrix was estimated using the gradient ascent algorithm (the final transformation matrix was obtained within six iterations using the gradient based algorithm) described in the previous section, and then used to project the original n -dimensional feature vectors of letters M and N to an m -dimensional space ($m < n$). In the last step, the projected

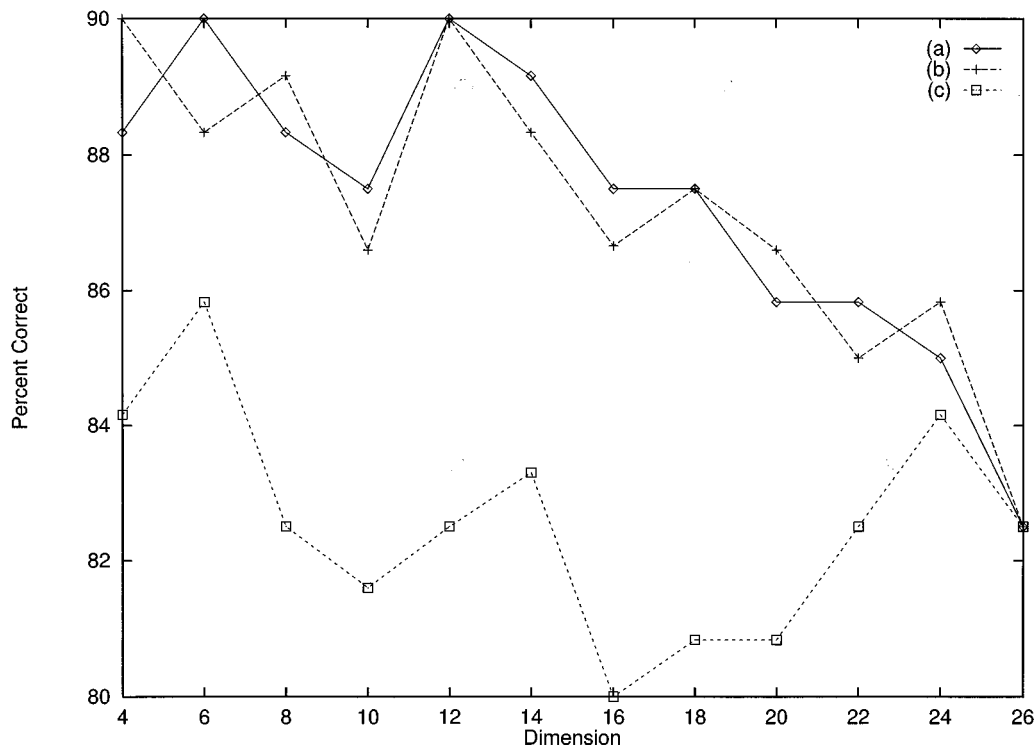


FIG. 1. Comparative performance, in terms of percent correct classification of letters M and N , between our proposed approach [plots (a) and (b)] and the LDA method [plot (c)] as a function of the projected feature dimension. Plots (a) and (b) give the performance obtained with our approach when the transformation matrix in (5) is estimated using the exact \mathbf{G} matrix (4) and approximate $\hat{\mathbf{G}}$ matrix (14), respectively. Plot (c) gives the performance obtained when the LDA transformation matrix is used to project the feature vectors.

feature vectors, appended with a normalized energy term, were used to train phoneme-based HMMs using conventional HMM training techniques (e.g., the Baum–Welch algorithm). A single state, single Gaussian mixture, continuous HMM was used to model each of the phonemes [eh], [m], and [n]. Recognition was performed using the Viterbi algorithm.

It should be noted here that the proposed approach is used as a preprocessing step in an HMM-based system. It is therefore not optimal, in the sense that the transformation matrix is obtained independently of the HMM training. An optimal linear-transformation approach has been proposed by Schukat-Talamazzini *et al.* (1995) where the transformation matrix was included in the model (called feature transform hidden Markov model), and incorporated in the maximum likelihood HMM parameter estimation. A similar approach has also been proposed by Rathinavelu and Deng (1996) for discriminative training of confusable classes.

B. Results

A series of experiments were run to determine the best (in terms of recognition performance) feature dimension m to use in recognition of M and N . This is an important issue in subspace projection approaches, which can be resolved experimentally by varying the dimension of the transformed features and observing the performance. Figure 1, plot (a), shows the percentage of correct classifications of letters M and N , as a function of feature dimension. Figure 1, plot (b), gives the recognition performance obtained when the trans-

formation matrix in (5) is computed using the approximate \mathbf{G} matrix (14). The difference in performance is small, which shows that the transformation matrix can be estimated efficiently without considerable loss of performance. In order to compare the divergence-based approach with the standard LDA approach, we ran a few additional experiments using the LDA transformation matrix, in place of the divergence-based LDA transformation matrix, to project the feature vectors [see Fig. 1, plot (c)]. The LDA transformation matrix was estimated from within-class and total scatter matrices as in (Brown, 1987; Yu *et al.*, 1990; Umbach and Ney, 1992). It should be noted that in our experiments the total scatter matrix was computed using only the /m/ and /n/ observations, and not the /eh/ observations. As shown in Fig. 1, the divergence-based approach outperformed the LDA method for all feature dimensions, with maximum performance of 90% obtained with $m=12$ or 6.

So far, we used context-independent models and assumed that each phoneme was characterized with a single Gaussian distribution, i.e., with a single state HMM. Additional experiments revealed, however, that further improvement in performance could be achieved by modeling each phoneme with a three-state HMM, and by using context-dependent models rather than context-independent models. Figure 2 shows the performance obtained [using the exact matrix \mathbf{G} (4)] with three-state context-independent models and three-state context-dependent models ([eh+m], [eh+n], [n+sil], [m+sil]). As shown in Fig. 2 the context-dependent models outperformed the context-independent models for all

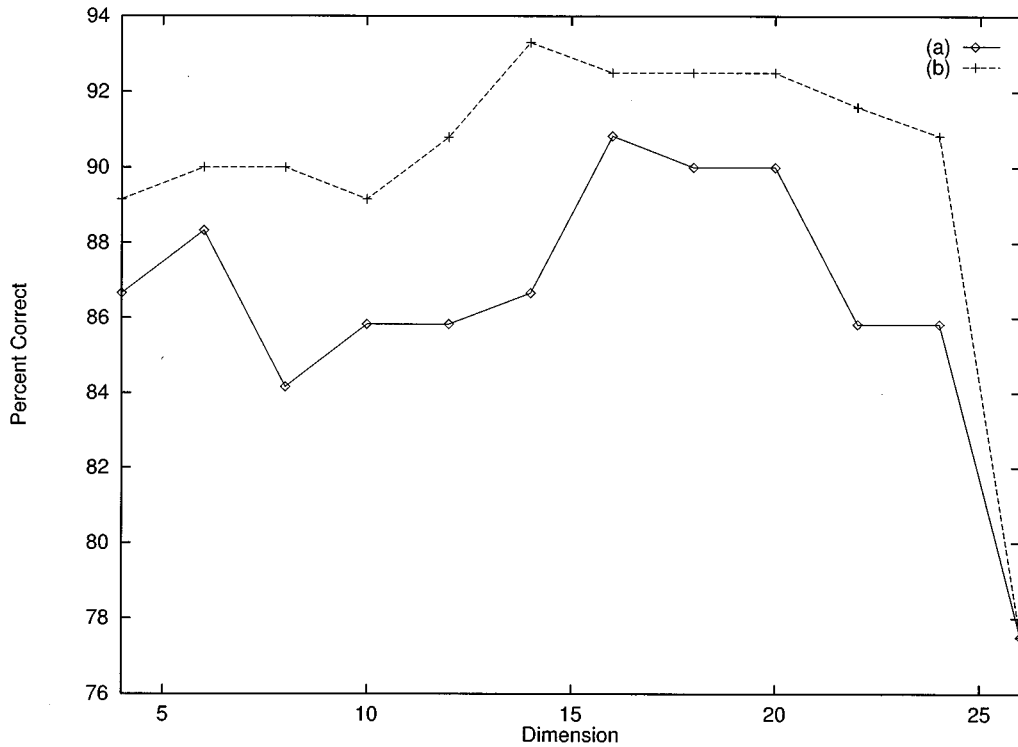


FIG. 2. Comparative performance, in terms of percent correct classification of letters M and N, of the divergence-based approach using three-state context-independent models [plot (a)] and three-state context-dependent models [plot (b)].

feature dimensions by as much as 6%. The maximum performance achieved with the context-dependent models was 92.5% with $m=16$. Further improvement was realized by appending to the projected feature vector the delta feature vector and delta energy terms. This improved the performance to 94.1% (obtained with $m=14$).

II. AVERAGE DIVERGENCE MEASURE

In the previous section, we discussed how to use the divergence measure in a two-class classification problem, where the two classes are highly confusable. In this section, we extend this idea to K -class classification problems, using the average divergence measure (Loizou and Spanias, 1995b).

The average divergence measure (ADIV) can be defined as (Grettenberg, 1963),

$$\bar{J} = \sum_{i=1}^K \sum_{j=1}^K P_i P_j J(i, j), \quad (15)$$

where K is the number of classes (e.g., words, phonemes, etc.), P_i is the *a priori* probability of class i and $J(i, j)$ is the divergence between classes i and j . Assuming that all the classes are normally distributed, $J(i, j)$ can be given as in (3), i.e.,

$$J(i, j) = \frac{1}{2} \text{tr}[\mathbf{C}_i^{-1} \mathbf{C}_j + \mathbf{C}_j^{-1} \mathbf{C}_i] - m + \frac{1}{2} \text{tr}[(\mathbf{C}_i^{-1} + \mathbf{C}_j^{-1}) \mathbf{A}^T \mathbf{\Delta}_{ij} \mathbf{A}], \quad (16)$$

where $\mathbf{C}_i = \mathbf{A}^T \mathbf{\Sigma}_i \mathbf{A}$, $\mathbf{C}_j = \mathbf{A}^T \mathbf{\Sigma}_j \mathbf{A}$ are $m \times m$ matrices, and $\mathbf{\Delta}_{ij} = (\boldsymbol{\mu}_i - \boldsymbol{\mu}_j)(\boldsymbol{\mu}_i - \boldsymbol{\mu}_j)^T$ is an $n \times n$ matrix. Assuming a com-

mon covariance matrix \mathbf{V} among all classes, the average divergence reduces to

$$\bar{J} = \sum_{i=1}^K \sum_{j=1}^K P_i P_j \text{tr}[(\mathbf{A}^T \mathbf{V} \mathbf{A})^{-1} \mathbf{A}^T \mathbf{\Delta}_{ij} \mathbf{A}]. \quad (17)$$

The average divergence \bar{J} can be considered to be a statistical measure of how clustered or dispersed the K classes are. Misclassifications often occur because the classes are closely clustered. Naturally, in order to minimize the recognition errors, the classes need to be separated from each other as much as possible. This can be done by finding a transformation matrix \mathbf{A} that will maximize the average divergence \bar{J} . Matrix \mathbf{A} can be found as follows. Let the matrix \mathbf{M} ($n \times n$) be defined as

$$\mathbf{M} = \sum_{i=1}^K \sum_{j=1}^K P_i P_j (\boldsymbol{\mu}_i - \boldsymbol{\mu}_j)(\boldsymbol{\mu}_i - \boldsymbol{\mu}_j)^T, \quad (18)$$

then the averaged average divergence in (17) can be written as

$$\bar{J} = \text{tr}[(\mathbf{A}^T \mathbf{V} \mathbf{A})^{-1} (\mathbf{A}^T \mathbf{M} \mathbf{A})]. \quad (19)$$

The matrix \mathbf{A} that maximizes the average divergence \bar{J} can be formed by selecting the m eigenvectors of the matrix $\mathbf{V}^{-1} \mathbf{M}$ corresponding to the m largest eigenvalues. It is noted here that the criterion \bar{J} is not the same as Fisher's discriminant ratio (F ratio) because the matrix \mathbf{M} is different from the between-class scatter matrix used in the F ratio.

TABLE I. Recognition performance of the ADIV measure as a function of projected feature dimension. The results shown in the first row ($m=22$) correspond to the case where no transformation is applied to the input feature vectors (baseline results).

| Dimension (m) | Percent correct |
|-------------------|-----------------|
| 22 | 40.73% |
| 8 | 53.00% |
| 4 | 51.68% |

A. Training

The ADIV measure was applied in speaker-independent recognition of the E-set letters (B, C, D, E, G, P, T, V, Z) recorded over the telephone. This is a challenging task, because of the existing acoustic similarities among the letters. E-set letters, taken from a telephone-based alphabet database (Cole *et al.*, 1992), were used to train a phoneme-based HMM recognizer. A total of 100 speakers were used for training and testing, 60 for training and 40 for testing with equal number of female and male speakers. The original features used in training were the log-filterbank energies obtained by applying 22 mel-spaced triangular windows to the magnitude spectrum. The feature vector consisted of 22 log-filterbank energies appended by a normalized energy term. These features were used to derive the transformation matrix \mathbf{A} as follows:

Compute the common sample covariance matrix \mathbf{V} and the sample mean vectors $\boldsymbol{\mu}_i$ ($i=1, \dots, K$) from the training data. In our application, $K=9$ corresponding to the nine consonants in the E-set.

Construct matrix \mathbf{M} as per (18), and compute the eigenvalues and eigenvectors of $\mathbf{V}^{-1}\mathbf{M}$. Use the m eigenvectors corresponding to the m largest eigenvalues of $\mathbf{V}^{-1}\mathbf{M}$ as the m columns of matrix \mathbf{A} .

Matrix \mathbf{A} was then used to project the original observations $\mathbf{x}(n \times 1)$ to \mathbf{y} , of dimension $m < n$. The projected observations \mathbf{y} , appended with a normalized energy term, were used to train phoneme-based HMMs.

There is a total of 11 phonemes in the E-set, namely /iy/, /b/, /s/, /d/, /q/, /jh/, /p/, /t/, /v/, /z/, and /pv/. (The label /pv/ is used for prevoicing, occurring sometimes in letters B, D, and G.) Each phoneme was characterized with a three-state continuous density HMM with diagonal covariance and one mixture per state. A two-state HMM was used for /b/ and /q/. Context-independent models were trained by first running five iterations of the segmental k -means procedure, followed by five iterations of the Baum-Welch algorithm. The context-independent models were then used to obtain context-dependent models by running one iteration of the Baum-Welch reestimation procedure. The context-dependent models were used for recognition. The Viterbi algorithm was employed at recognition with a bigram language model.

B. Results

We first established the baseline performance, namely the performance obtained without using the average divergence to project the original features. Baseline performance

TABLE II. Performance of the ADIV measure obtained after appending to the projected features the delta coefficients and the delta energy.

| Feature dimension (m) | Percent correct |
|---------------------------|-----------------|
| 22+22+2 | 51.96% |
| 8+8+2 | 67.69% |
| 4+4+2 | 65.73% |

of 40.73% was obtained with the original features, i.e., with $m=22$. Results obtained with the average divergence are given in Table I for various values of m . As it can be seen a 13% improvement was realized with the average divergence. This clearly illustrates the effectiveness of the ADIV measure in enhancing discrimination of confusable words.

Further overall improvement was achieved by appending to the projected feature vectors the delta coefficients and the delta energy. Results are given in Table II, showing a big improvement in performance. This was not surprising, given that the delta coefficients are known to be effective features in tracking dynamic spectral information, which is very important in E-set discrimination.

Finally, we compared the performance of a conventional feature representation, such as the cepstrum coefficients, with the performance obtained with projected features derived from the ADIV measure. A 50% and 47% correct performance was obtained using cepstrum coefficients of dimension 8 and 4, respectively. These results are lower than the ones obtained with the ADIV measure (see Table I).

III. DISCUSSION

We showed how the divergence measure can be used in a subspace projection approach to enhance discrimination of confusable pairs of words. A 4.5% improvement over standard LDA techniques was achieved when applied in the recognition of letters M and N, a highly confusable pair in alphabet recognition. The proposed approach has also been applied successfully to a more general classification problem, i.e., discrimination of K confusable words, using the average divergence measure. This approach could therefore be applied more generally to continuous speech recognition to enhance phoneme discrimination.

- Brown, P. (1987). "The Acoustic-Modeling Problem in Automatic Speech Recognition," Ph.D. thesis, Carnegie Mellon University.
- Cole, R., Fanty, M., Muthusamy, Y., and Gopalakrishnan, M. (1990a). "Speaker independent recognition of spoken English letters," Proc. Int. Joint Conf. Neural Networks 2, 45-51.
- Cole, R., Muthusamy, Y., Fanty, M. (1990b). "The ISOLET spoken letter database," Tech. Rep. 90-004, Oregon Graduate Institute.
- Cole, R., Fanty, M., and Roginsky, K. (1992). "A telephone speech database of spelled and spoken names," Proceedings of ICSLP-92, 891-893.
- Grettenberg, T. L. (1963). "Signal selection in communication and radar systems," IEEE Trans. Inf. Theory IT-9, 265-275.
- Haeb-Umbach, R., and Ney, H. (1992). "Linear discriminant analysis for improved large vocabulary speech recognition," Proc. IEEE Int. Conf. Acoust. Speech Signal Process. I, 13-16.
- Hunt, M., and Lefebvre, C. (1989). "A comparison of several acoustic representations for speech recognition with degraded and undegraded speech," Proc. IEEE Int. Conf. Acoust. Speech Signal Process., 262-265.
- Kailath, T. (1967). "The divergence and Bhattacharyya distance measures in signal selection," IEEE Trans. Commun. Technol. COM-15, 52-60.

- Kullback, S. (1958). *Information Theory and Statistics* (Wiley, New York).
- Loizou, P., and Spanias, A. (1994). "Context-dependent modeling in alphabet recognition," Proc. IEEE Int. Symp. Circuits Syst. **2**, 189–192.
- Loizou, P., Dorman, M., and Spanias, A. (1995a). "Automatic recognition of syllable-final nasals preceded by /eh/," J. Acoust. Soc. Am. **3**, 1925–1928.
- Loizou, P., and Spanias, A. (1995b). "Improved speech recognition using the weighted average divergence measure," Proc. Int. Conf. Digital Signal Process. **1**, 90–95.
- Rathinavelu, C., and Deng, L. (1996). "HMM-based speech recognition using state-dependent, linear transforms on Mel-warped DFT features," IEEE Int. Conf. Acoust. Signal Speech Process. **1**, 9–12.
- Searle, S. (1982). *Matrix Algebra Useful For Statistics* (Wiley, New York).
- Schukat-Talamazzini, E., Hornegger, J., and Niemann, H. (1995). "Optimal linear feature transformations for semi-continuous Hidden Markov models," IEEE Int. Conf. Acoust. Signal Speech Process. **1**, 369–372.
- Tou, J., and Heydorn, R. (1967). "Some approaches to optimum feature extraction," in *Computer and Information Sciences II*, edited by J. Tou (Academic, New York).
- Yu, G., Russell, W., Schwartz, R., and Makhoul, J. (1990). "Discriminant analysis and supervised vector quantization for continuous speech recognition," Proc. IEEE Int. Conf. Acoust. Signal Speech Process. 685–688.
- Zahorian, S., Qian, D., and Jagharghi, A. (1991). "Acoustic-phonetic transformations for improved speaker-independent isolated word recognition," Proc. IEEE Int. Conf. Acoust. Signal Speech Process. **1**, 561–564.

Materials for guitar back plates made from sustainable forest resources

Hiroyuki Yano, Yuuzoh Furuta, and Hiroyuki Nakagawa

Department of Forestry, Kyoto prefectural University, Shimogamo, Sakyo-ku, Kyoto, 606 Japan

(Received 16 April 1996; accepted for publication 14 August 1996)

A new type of wood-based material for guitar back plates as a substitute for Brazilian rosewood was produced based on Japanese cedar logs with a small diameter, of which the utilization is limited despite its availability. The sapwood portion of logs with a diameter of 20 cm was processed to veneers of 2 mm thickness using a rotary lathing machine. The veneers were impregnated with a low-molecular-weight phenolic resin, laminated in parallel, and compressed perpendicular to their plane. When the veneers were treated with a 3% or 5% aqueous solution and compressed to a density of 0.8 without adhesives, the specific dynamic Young's modulus (E/γ , ratio of stiffness to specific gravity) and $\tan \delta$ (damping) of the materials became almost the same as those of Brazilian rosewood in the lower-frequency range, not only in the longitudinal direction but also across the longitudinal direction. However, the frequency dependencies of the specific Young's modulus and $\tan \delta$ of the materials differed from those of Brazilian rosewood, which may be partially related to the higher values of E/G of laminated compressed wood as a result of the increased density induced by deformation of the cell walls. © 1997 Acoustical Society of America.

[S0001-4966(97)02801-4]

PACS numbers: 43.75.Gh [WJS]

INTRODUCTION

The tone quality of wooden stringed instruments is highly dependent on the acoustic properties of the materials used. Therefore, materials are carefully selected by musical instrument producers. For example, German spruce has been found to be the best suited material for the top plate of violins and guitars, as well as for soundboards of pianos. In addition, historical evidence suggests that Brazilian rosewood has suitable acoustic properties for the back plate of guitars. However, the availability of high quality resonance wood has recently decreased. The acquisition of Brazilian rosewood especially has become difficult, because the cutting and export of this material has been prohibited due to conservation of the tropical rain forest. Therefore, substitute materials have been sought, but most of these are also endangered species. At present, there is little hope of improvement of these conditions. To maintain the quality of musical instruments while preserving forest resources, a wood-based material with acoustic properties similar to Brazilian rosewood must be produced from easily reproducible and fast-growing forest resources.

We have studied the acoustic properties of wood used for various musical instruments and clarified the mechanisms defining their particular acoustic properties (Yano *et al.*, 1990, 1992, 1995; Yano, 1994). Some chemical treatments were found to be effective in improving the acoustic properties of wood (Yano and Minato, 1992; Yano *et al.*, 1994). In this study we produced a new type of wood-based material from Japanese cedar, of which the utilization is limited despite its availability, as a substitute for Brazilian rosewood.

I. ACOUSTIC PROPERTIES OF BRAZILIAN ROSEWOOD

To produce a wood-based material for guitar back plates, one must clarify the desired acoustic properties of Brazilian rosewood. Hence, in previous studies we analyzed the acoustic properties of Brazilian rosewood as well as those of Indian rosewood (Yano *et al.*, 1995). The acoustic properties of wood used for guitar top and back plates, evaluated by the free-free vibration method at 20 °C and 65% R.H., are summarized in Table I.

The specific gravity (γ) of Brazilian rosewood was distributed around 0.9, which is about 1.1, 2, and 2.5 times higher than the gravity of Indian rosewood, German spruce, and Western red cedar, respectively. As the maximum specific gravity of wood is around 1.1–1.2, these observations show that a high specific gravity is vital for materials for guitar back plates. Furthermore, as the Young's modulus (E) of wood generally increases with increasing specific gravity, higher acoustic impedance (γE) also seems to be a requirement for high-quality back plates.

Differences were also observed in the value of $\tan \delta$ (damping, inverse of Q factor) in the longitudinal direction between Brazilian rosewood and Indian rosewood; the mean value of Brazilian rosewood was 20% lower than that of Indian rosewood. In comparison with other woods, Brazilian rosewood has a lower $\tan \delta$ in both the longitudinal and across the longitudinal directions. Thus, low $\tan \delta$ values are also important for substitute materials. On the other hand, no significant differences were observed in the specific dynamic Young's modulus between Brazilian rosewood and Indian rosewood, the values for both were 30% lower than that of German spruce, which is well known to have a high specific dynamic Young's modulus in the longitudinal direction. This

TABLE I. Acoustic properties of wood used for guitar top and back plates (Yano *et al.*, 1990, 1995). [AVE: Mean value, s.d.: Standard deviation. Subscripts *L* and *CL* imply longitudinal and cross-longitudinal direction, respectively.]

| Species | | γ | E_L/γ
(GPa) | E_{CL}/γ
(GPa) | $\tan \delta_L$
($\times 10^{-3}$) | $\tan \delta_{CL}$
($\times 10^{-2}$) |
|---|---------|----------|-----------------------|--------------------------|---|--|
| Brazilian rosewood
<i>Dalbergia nigra</i> | AVE | 0.864 | 18.1 | 2.32 | 5.83 | 1.47 |
| | s.d. | 0.083 | 3.3 | 0.42 | 1.57 | 0.43 |
| | samples | 113 | 113 | 59 | 113 | 59 |
| Indian rosewood
<i>Dalbergia latifolia</i> | AVE | 0.775 | 17.4 | 3.00 | 7.37 | 1.46 |
| | s.d. | 0.050 | 2.9 | 0.60 | 1.16 | 0.23 |
| | samples | 72 | 72 | 71 | 72 | 71 |
| German spruce
<i>Picea abies</i> | AVE | 0.426 | 26.0 | 1.78 | 6.86 | 1.80 |
| | s.d. | 0.041 | 3.4 | 0.40 | 0.76 | 0.12 |
| | samples | 179 | 179 | 30 | 179 | 30 |
| Western red cedar
<i>Thuja plicata</i> | AVE | 0.354 | 20.7 | 1.79 | 4.84 | 1.04 |
| | s.d. | 0.023 | 2.8 | 0.42 | 0.52 | 0.08 |
| | samples | 164 | 164 | 55 | 164 | 55 |

shows that a high specific dynamic Young's modulus is not indispensable for materials for guitar back plates. On the basis of these results, Brazilian rosewood appears to be a suitable material for guitar back plates due to its high density, high modulus of elasticity, and low damping.

The oven-dry weight of Brazilian rosewood specimens immersed in methanol was reduced by up to 30%, and the value of $\tan \delta$ in the longitudinal and across longitudinal directions increased linearly by up to 120% with the reduction in oven-dry weight. Thus, the acoustic properties which are peculiar to Brazilian rosewood are highly dependent on methanol extractives.

II. PRODUCTION OF PHENOLIC RESIN-IMPREGNATED VENEER LAMINATED BOARD

The specific gravity of wood cell walls is approximately 1.45 regardless of species. Thus, a high density and a high modulus of elasticity of wood are results of a high volumetric ratio of cell walls. On the other hand, as mentioned above, the pronounced low damping of Brazilian rosewood results from methanol extractives, which are maintained in the cell wall and increase the cohesive forces between the wood constituents. Therefore, a combination of compression and low-molecular-weight phenolic resin treatment to enhance the acoustic properties may be effective in producing substitutes for Brazilian rosewood.

A. Material and production of veneer

Japanese cedar (*Cryptomeria japonica*) was used as the raw material. Japanese cedar is easily reproduced and grows quickly. Therefore, a stable supply could be available in the future. However, the utilization of Japanese cedar in building construction has been limited because of its low specific gravity and poor mechanical properties, even though it is the most commonly cultivated tree in Japan. Logs of Japanese cedar with a small diameter (less than 30 cm) have not been used commercially up to this date. For this reason, logs with a diameter of 20 cm and an age of 27 years were obtained from the experimental forest of Kyoto Prefectural University and were used as raw materials in this study.

Increasing the wood density is achieved by deformation and collapse of cells, as shown in Fig. 1. Thus, compression of wood must be performed in the radial direction where the latewood portion (thick cell walls) and earlywood portion (thin cell walls) are distributed in series. In addition, to obtain a guitar back plate with no side-to-side-grain joint, the logs must be processed to veneers. Hence, the sapwood portion of the logs was processed to veneer with a thickness of 2 mm with a rotary lathing machine. Veneers produced by the machine has two sides—outer or tight and inner or loose; the latter has fine or large checks (fissures) called “lathe checks” (Tsoumis, 1991). These checks increase the permeability of the veneers, which results in a uniform chemical treatment of the material; however, on the other hand, these

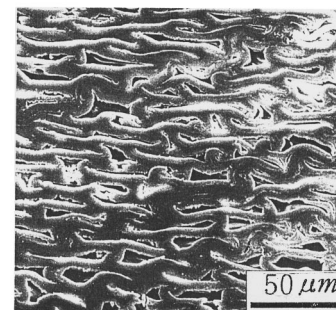
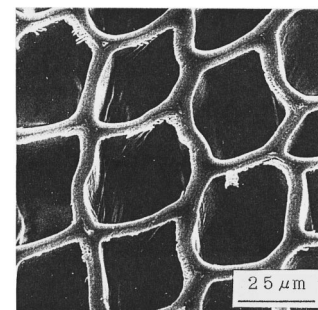


FIG. 1. Deformation of wood cell walls by compression (Japanese cedar, courtesy of Dr. Ikuho Iida).

TABLE II. Acoustic properties of the specimens. [AVE: Mean value, s.d.: Standard deviation. Subscripts L and T imply longitudinal and tangential directions, respectively. *: Unable to measure.]

| Specimens | | γ | E_L/γ
(GPa) | E_T/γ
(GPa) | $\tan \delta_L$
($\times 10^{-3}$) | $\tan \delta_T$
($\times 10^{-2}$) |
|----------------------|---------|----------|-----------------------|-----------------------|---|---|
| Check-free specimens | AVE | 0.298 | 21.7 | | 6.44 | |
| | s.d. | 0.015 | 0.7 | | 0.32 | |
| | samples | 8 | 8 | | 8 | |
| Veneer specimens | AVE | 0.269 | 12.9 | * | 12.36 | * |
| | s.d. | 0.022 | 2.1 | * | 3.78 | * |
| | samples | 114 | 114 | | 27 | |

checks greatly increase the internal friction of veneers.

Two types of specimens were processed from the veneers; longitudinal specimens with the dimensions 240 (longitudinal, L) \times 40 (tangential, T) \times 2 mm (radial, R) and tangential specimens with the dimensions 60 \times 160 \times 2 mm (L , T , R). The average specific gravity of the specimens was 0.27. Quarter sawn longitudinal specimens with the dimensions 160 \times 12 \times 3 mm (L , R , T) were also prepared from the same logs as lathe check-free control specimens, to clarify the effects of lathe checks on the acoustic properties of the veneer laminated materials.

The acoustic properties of the veneer and the quarter sawn specimens evaluated by the free-free vibration method (Hearmon, 1958) at 20 °C and 65% R.H. are summarized in Table II. Table II shows that the specific dynamic Young's modulus in the longitudinal direction decreased and $\tan \delta$ in the longitudinal direction increased markedly due to the lathe checks. Table II also shows that the differences in acoustic properties between Japanese cedar and Brazilian rosewood became wider after veneer lathing. The acoustic properties of tangential veneer specimens could not be measured because of the lathe checks. Thus, an important objective in this study was to reduce the influence of lathe checks on the acoustic properties.

B. Resin impregnation and increase of density

Phenolic resin impregnation was carried out on the veneers. Low-molecular-weight phenolic resin treatment is known to decrease $\tan \delta$ of wood, and to decrease the hygroscopicity of wood, resulting in stabilization of acoustic properties against changes in humidity (Yano *et al.*, 1994). Furthermore, the treatment is effective in fixing the compressed condition when the curing of the resin is carried out during compression (Stamm, 1964).

The veneer specimens were soaked in 1%, 3%, 5%, or 10% aqueous solutions of phenolic resin with a number average molecular weight of about 200 for 10 days. Thereafter, they were air-dried for 10 days followed by drying at 70 °C for 12 h. Several veneer specimens were layered with a parallel orientation and compressed at 150 °C for 15 min to make boards with a thickness of 4 mm thick along with heating. The effects of the concentration of the aqueous solution were studied in specimens composed of six veneers. The effects of the compression were studied using specimens composed of 2–6 veneers which were soaked in a 5% aqueous phenolic resin solution. The degree of compression was

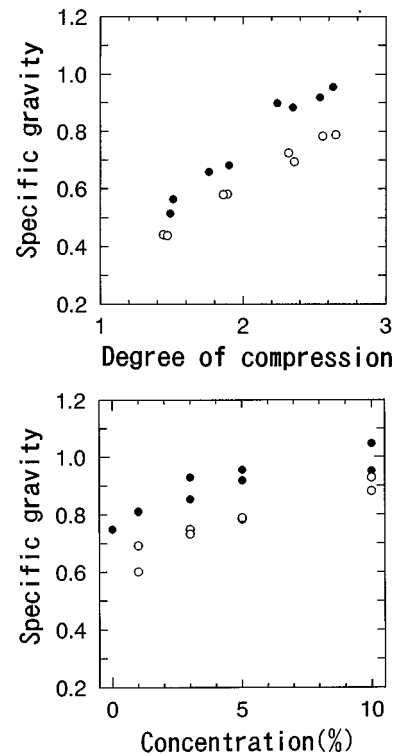


FIG. 2. Specific gravity of veneer-laminated material versus degree of compression and resin concentration. \circ , without adhesives; \bullet , with adhesives.

evaluated by dividing the total thickness of the resin-impregnated veneers dried at 70 °C for 12 h, by the oven-dried thickness of the boards obtained.

Some veneer specimens were laminated after spraying 100 g/m² of phenolic resin adhesives on one side of the veneer.

III. ACOUSTIC PROPERTIES AND DIMENSIONAL STABILITY OF RESIN-IMPREGNATED VENEER LAMINATED BOARD

The laminated and compressed veneer boards were processed into two types of specimens: longitudinal specimens with the dimensions 200 \times 15 mm (L , T) and tangential specimens with the dimensions 150 \times 15 mm (T , L). The specimens were oven-dried for 24 h at 50 °C before measuring the oven-dry weight and dimensions. Thereafter, they were conditioned at 20 °C and 65% R.H. for 3 weeks before measuring the air-dry weight and dimensions, as well as acoustic properties. The acoustic properties, such as the specific Young's modulus and $\tan \delta$, were evaluated using the free-free vibration method mainly at the first mode of vibration where shearing deformation is negligible. Several specimens were subjected to measurement of the apparent frequency dependence of specific Young's modulus and $\tan \delta$. The resonance frequency of the specimens was varied by changing their vibrational mode.

A. Specific gravity

The changes in specific gravity versus compression and resin concentration are shown in Fig. 2.

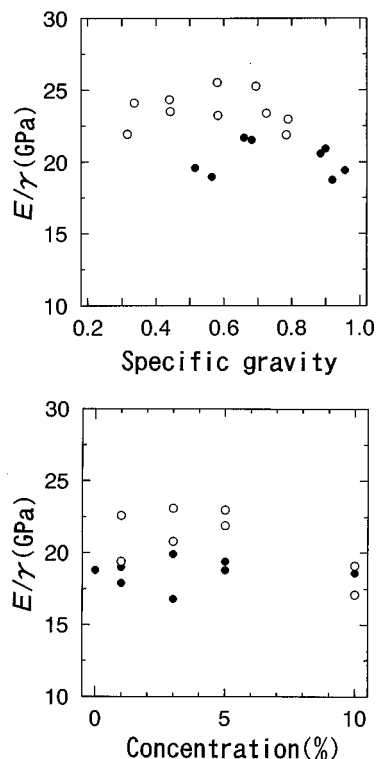


FIG. 3. Specific dynamic Young's modulus of veneer-laminated material in the longitudinal direction versus specific gravity and resin concentration. \circ , without adhesives; \bullet , with adhesives.

The specific gravity of specimens treated with resin at a concentration of 5% increased with increasing degree of compression. The specific gravity of specimens laminated without adhesives reached a specific gravity of around 0.8 at a degree of compression of 2.7. The specimens laminated with adhesives had specific gravities that were 0.1–0.15 higher than those for the specimens without adhesives at the same degree of compression. This can be attributed to the additional weight of the adhesives.

The effects of resin concentration were compared at a degree of compression of about 2.5. The degree of compression was evaluated by dividing the total thickness of the resin-impregnated veneers by the distance between the hot-press plates, which was 4 mm. As can be seen in Fig. 2, the specific gravity increased with increasing resin concentration. This result can be accounted for by the increase in the amount of resin absorbed by the wood with increasing resin concentration, and by the effects of the recovery of the thickness which occurred when the resin content was insufficient to fix the cell wall deformation.

B. Specific dynamic Young's modulus

The relationships between specific dynamic Young's modulus in the longitudinal direction and the specific gravity and resin concentration are shown in Fig. 3.

In specimens treated with a 5% resin solution, the values of the specific dynamic Young's modulus were almost constant regardless of the degree of compression. This suggests that the Young's modulus in the longitudinal direction in-

creased in proportion to the increase in specific gravity. Furthermore, the adhesive lowered the specific dynamic Young's modulus by about 10%.

The specific dynamic Young's modulus did not change with increasing resin concentration until 5%. However, specimens treated with a 10% resin solution exhibited a lower specific dynamic Young's modulus than those treated with a 5% resin solution. Decreases in the specific dynamic Young's modulus were also observed when the veneers were laminated with adhesives. Hence, this decrease was attributed to excessive impregnation of phenolic resin in the cell cavities, which was not effective in increasing the Young's modulus significantly.

As mentioned above, to convert the veneer into a material suitable for soundboards, one must eliminate the influence of lathe checks on the specific dynamic Young's modulus. As shown in Table II, the average values of the specific dynamic Young's modulus of the check-free specimens and the veneer specimens were 20.6 and 12.9 GPa, respectively. This difference indicates a significant influence of lathe checks. Due to treatment with a 5% phenolic resin solution, the specific dynamic Young's modulus of the check-free specimens decreased by 5% and became 19 GPa. Since the specific dynamic Young's modulus of wood does not change with compression as shown in Fig. 3, the specific dynamic Young's modulus of the laminated specimens should be around 19 GPa when the influence of lathe checks are removed. Figure 3 shows that the specific dynamic Young's modulus of specimens laminated without adhesives reached more than 19 GPa even at a resin concentration of 1%. This suggests that the influence of lathe checks on the specific dynamic Young's modulus in the longitudinal direction was eliminated by the combination of impregnation with a low-molecular-weight phenolic resin and compression.

As shown in Fig. 4, the specific dynamic Young's modulus in the tangential direction, in contrast to that in the longitudinal direction, increased linearly with increasing specific gravity, i.e., with increasing degree of compression. Furthermore, the specific Young's modulus also increased with increasing resin concentration, and reached 5 GPa after treatment with a 10% resin solution. This value was 3 GPa higher than that of Brazilian rosewood. Thus, to obtain a material with the same specific gravity and specific dynamic Young's modulus as Brazilian rosewood in both the tangential and the longitudinal direction, the resin concentration must be kept below 5%. The increases in specific dynamic Young's modulus with increasing density or resin concentration may be related to the increase in resin content in a unit volume of compressed wood. However, the precise mechanisms are as yet unclear.

C. $\tan \delta$

The relationships between $\tan \delta$ in the longitudinal direction and the specific gravity and resin concentration are shown in Fig. 5. When the specimens were treated with a 5% resin solution, the values of $\tan \delta$ were almost the same regardless of the degree of compression. Furthermore, the values for the specimens laminated without adhesives were almost equivalent to those of check-free specimens treated

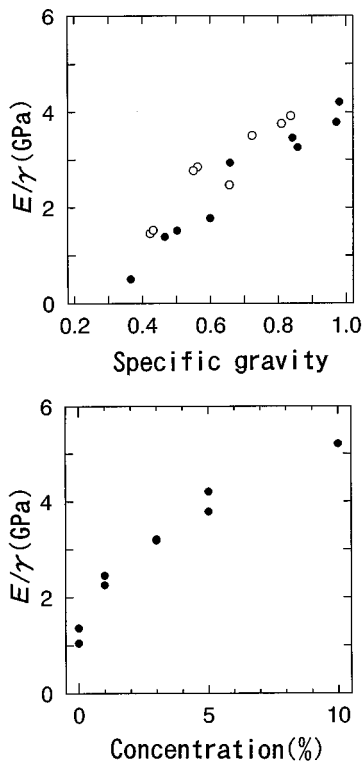


FIG. 4. Specific dynamic Young's modulus of veneer-laminated material in the tangential direction versus specific gravity and resin concentration. \circ , without adhesives; \bullet , with adhesives.

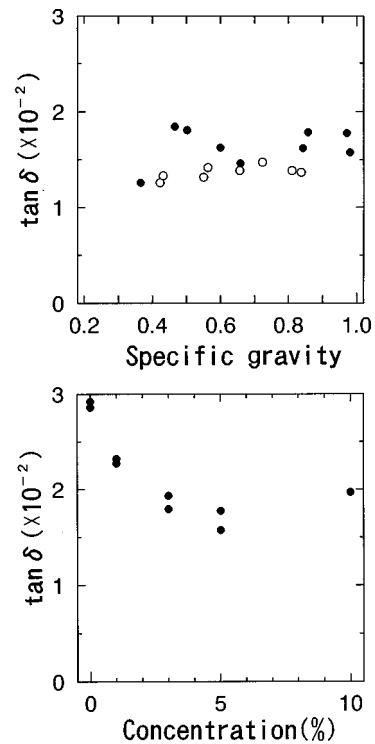


FIG. 6. $\tan \delta$ of veneer-laminated material in the tangential direction versus specific gravity and resin concentration. \circ , without adhesives; \bullet , with adhesives.

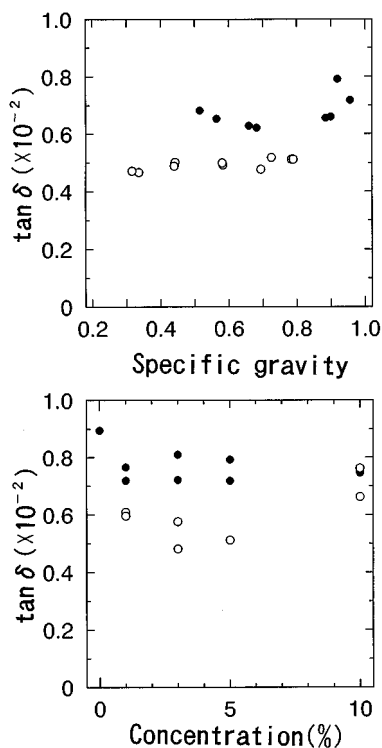


FIG. 5. $\tan \delta$ of veneer-laminated material in the longitudinal direction versus specific gravity and resin concentration. \circ , without adhesives; \bullet , with adhesives.

with a 5% resin solution, the values of which were comparable to that of Brazilian rosewood. This suggests that the influence of lathe checks on $\tan \delta$ were eliminated by impregnation with a 5% resin solution even at a low degree of compression.

As shown in Fig. 5, the values of $\tan \delta$ decreased with increasing resin concentration up to 5%. However, the specimens treated with a 10% resin solution showed higher values than those treated with a 5% solution. As reported previously (Yano *et al.*, 1994), the decrease in $\tan \delta$ was small with increasing average molecular weight of the resin in the case of low-molecular-weight phenolic resin treatment. This result could be explained by a decrease in the amount of resin maintained in the cell walls and by an increase in resin content in the cell cavities. Thus, the higher values of $\tan \delta$ obtained with a 10% phenolic resin treatment may have been due to excessive impregnation by the resin in the cell cavities.

The values of $\tan \delta$ were increased by 20% with adhesives at the same degree of compression and same resin concentration. For the manufacture of laminated wood, the influences of adhesives must therefore be considered.

The values of $\tan \delta$ in the tangential direction are shown in Fig. 6. The relationships between specific gravity and $\tan \delta$ shows that after a 5% resin treatment, similarly to the results observed in the longitudinal direction, lower values comparable to those of Brazilian rosewood were attained even at lower compressive condition. However, the values of

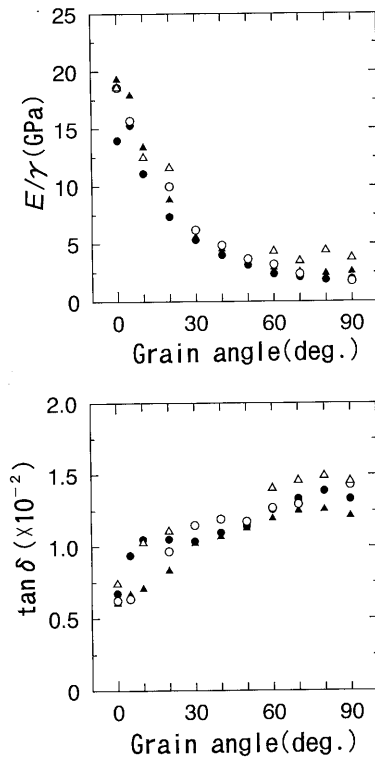


FIG. 7. Angular distributions of specific dynamic Young's modulus and $\tan \delta$. \circ , Δ , veneer-laminated material; \bullet , \blacktriangle , Brazilian rosewood.

$\tan \delta$ for specimens without resin impregnation and those treated with a 1% resin solution were higher than the values of 3% resin-treated specimens irrespective of the degree of compression. This suggests that impregnation with a low-molecular-weight phenolic resin is effective in eliminating the influence of lathe checks on the acoustic properties of veneer not only in the longitudinal direction but also in the tangential direction.

D. The angular distribution of specific dynamic Young's modulus and $\tan \delta$

On the basis of these results, we concluded that materials with the same acoustical properties as Brazilian rosewood in the lower-frequency range can be obtained when the veneers are processed with a 3%–5% low-molecular-weight phenolic resin and compressed to a degree of compression of 2–2.5 without adhesives. Hence, five pieces of 5% phenolic resin-impregnated veneers half the size of a guitar back plate were laminated in parallel and compressed to a degree of compression of 2.3 without adhesives. The distributions of acoustic properties within the plane of the veneer laminated material are compared with those of Brazilian rosewood in Fig. 7. The angular distribution of specific dynamic Young's modulus and $\tan \delta$ in the veneer-laminated boards resembled those of Brazilian rosewood. This suggests that a material with similar acoustic properties as Brazilian rosewood in the lower-frequency range can be produced from logs of Japanese cedar with a small diameter.

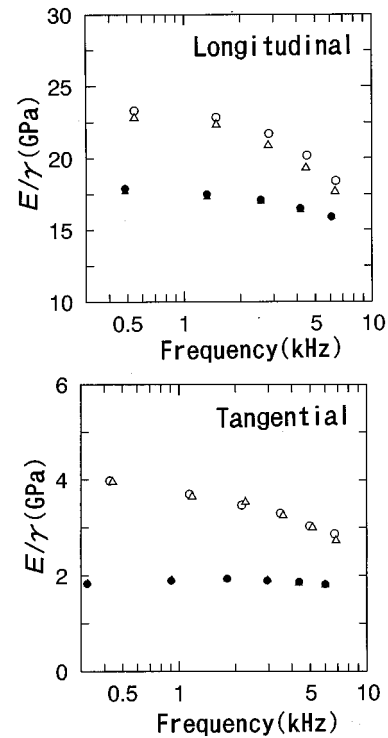


FIG. 8. Frequency dependencies of specific dynamic Young's modulus. \circ , Δ , veneer-laminated material; \bullet , \blacktriangle , Brazilian rosewood.

E. Frequency dependencies of acoustic properties

To be able to use veneer-laminated boards as a back plate material for guitar, the acoustic properties in a wide frequency range must be clarified and compared with those of Brazilian rosewood. Hence, the frequency dependencies of specific dynamic Young's modulus and $\tan \delta$ were studied in the longitudinal and tangential specimens treated with a 5% phenolic resin solution and compressed to a degree of compression of 2.5, and the results were compared with the frequency dependencies of longitudinal and tangential specimens of Brazilian rosewood. The dimensions of the longitudinal specimens were 200 mm (L) \times 15 mm (T) \times 4.5 mm (R), and those of tangential specimens were 140 mm (T) \times 15 mm (L) \times 4.5 mm (R).

Figure 8 shows that, in the longitudinal direction, the specific dynamic Young's modulus of both laminated specimens and Brazilian rosewood decreased with increasing frequency. The specific dynamic Young's modulus of the wood evaluated by the longitudinal vibration method did not depend on the frequency (Tonosaki *et al.*, 1983). In addition, the frequency dependencies of the specific dynamic Young's modulus of wood did not change due to a phenolic resin treatment (Yano *et al.*, 1994). Thus, this reduction may be related to the effects of shearing deformation, the importance of which increases with increasing frequency; that is, the decreases in the distance between the nodes of the vibrating beams with increasing vibrational mode. Furthermore, the decrease was larger in laminated wood specimens than in Brazilian rosewood. As the dimensions of the specimens were the same, this difference indicates that the ratio of Young's modulus to the shearing modulus (E_L/G_{LR}) was

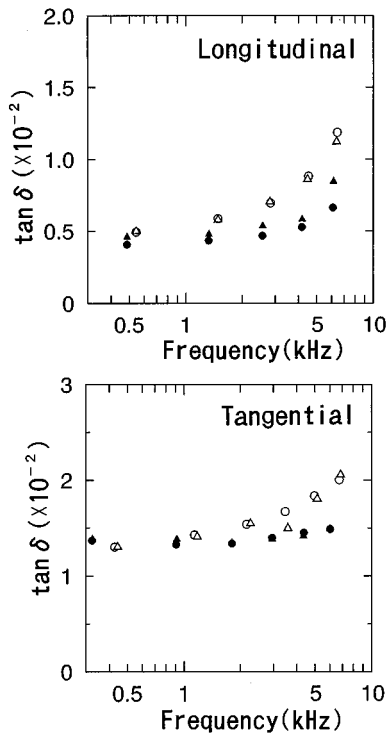


FIG. 9. Frequency dependencies of $\tan \delta$. \circ , \triangle , veneer-laminated material; \bullet , \blacktriangle , Brazilian rosewood.

higher in the laminated specimens than in Brazilian rosewood.

The differences in the frequency dependencies of the specific dynamic Young's modulus were more pronounced in the tangential specimens. The specific Young's modulus of the Brazilian rosewood specimens did not depend on the frequency. On the other hand, the values of the laminated veneer specimens decreased with increasing frequency. As the dimension of laminated veneer and Brazilian rosewood specimens were the same, this difference may have resulted from differences in the value of E_T/G_{TR} .

Generally, the rolling shear stiffness becomes large with increasing cell wall thickness. Hence, above a specific gravity of 1 the value of E_T/G_{TR} of wood reaches 3.5 (Yano and Yamada, 1985), which approaches the value of isotropic materials, which is 2.6–2.8. This means that the differences in the values of E_T/G_{TR} observed between Brazilian rosewood and laminated veneer specimens cannot be explained by differences in specific gravity. So, we must take into account the higher density of Brazilian rosewood which arises from thicker cell walls. However, the higher density for compressed wood results from the deformation of cells as shown in Fig. 1. This deformation seems to give rise to lower G_{TR} and G_{LR} in comparison to the values of Brazilian rosewood, which results in high values of E_T/G_{TR} and E_L/G_{LR} . The effects of the higher values of E/G on the radiated sound from musical instruments must be considered.

The values of $\tan \delta$ for laminated veneer and Brazilian rosewood specimens increased with increasing frequency in both the longitudinal and tangential directions (Fig. 9). However, the increase was higher in the laminated veneer speci-

TABLE III. Dimensional stability of laminated and compressed wood. [MC: Moisture content at 20 °C and 65% R.H.; SE: Swelling efficiency from oven-dry to 20 °C and 65% R.H.; Spring back: Changes in oven-dry thickness due to boiling in water for 5 h.]

| | Degree of compression | γ | MC (%) | SE (%) | Spring back (%) |
|----------------------|-----------------------|----------|--------|--------|-----------------|
| Resin-treated veneer | 1.5 | 0.504 | 4.7 | 0.75 | 0.1 |
| | 2.0 | 0.763 | 4.7 | 0.71 | -0.2 |
| | 2.7 | 0.967 | 4.8 | 0.78 | 2.6 |
| Untreated veneer | 1.3 | 0.468 | 8.2 | 1.47 | 8.1 |
| | 1.8 | 0.752 | 7.7 | 1.39 | 24.3 |
| Brazilian rosewood | | 0.886 | 7.0 | 1.86 | |

mens. This may be the result of the higher values of E/G and changes in frequency dependencies of $\tan \delta$ due to phenolic resin treatment as reported previously (Yano *et al.*, 1994b). From the viewpoint of acoustic characteristics of materials, the phenolic resin-treated veneer-laminated board diminishes sound radiation at high frequency.

F. Dimensional stability

Table III shows the swelling efficiency (the degree of dimensional changes due to moisture absorption) in the tangential direction from a oven-dry condition to 20 °C and 65% R.H., and the equilibrium moisture content at 20 °C and 65% R.H.

In general, the moisture content of wood at 20 °C and 65% R.H. is in the range of 10%–12%. The moisture content of the 5% aqueous-solution-treated specimens was 4.78%, which is less than half the value of untreated wood and lower than that of Brazilian rosewood, the moisture content of which is reduced by a large heartwood content. The reduction of the moisture content in the treated wood is caused by impregnation of phenolic resin in the cell walls which reduces the absorption of moisture into the cell walls. The results obtained here imply that low-molecular-weight phenolic-resin-treated laminated boards have higher dimensional stability, and that the acoustic properties of the material thus would be stabilized against atmospheric changes.

The results of boiling tests performed in each type of specimen in water for 5 h are listed in Table III. The oven-dry thickness of untreated laminated specimens, compressed to a specific gravity of 0.75, recovered by 24.3%. On the other hand, the thickness recovery of the 5% resin-treated wood, which was compressed to a specific gravity of 0.8, was less than 2%. This shows that the compression of the wood is fixed permanently by low-molecular-weight phenolic-resin treatment.

IV. CONCLUDING REMARKS

The low-molecular-weight phenolic-resin-treated veneer compressed boards exhibited the same acoustic properties as Brazilian rosewood in the lower-frequency range. Differences in the acoustic properties between the compressed wood and Brazilian rosewood were observed in the higher-frequency range. However, both guitar makers and players



FIG. 10. Guitar with a veneer-laminated back plate.

felt that the tone quality of guitars with a back plate of resin-impregnated compressed board (Fig. 10) is comparable to that of guitars with a back plate of Brazilian rosewood.

The reduction of the influence of lathe checks on the acoustic properties of the specimens by slight compression of veneer treated with a 3% or 5% aqueous solution of phenolic resin would enable the production of material for the top plate of guitars based on logs of Japanese cedar with a small diameter with an appropriate selection of adhesives. In future studies, the compression pressure, amounts of the adhesives, and aqueous condensation conditions of the phenolic resin need to be clarified.

ACKNOWLEDGMENTS

The authors thank the members of Takamine Gakki Co., Ltd. and AICA KOGYO Co., Ltd. for their useful suggestions. We also thank the Nara Prefectural Forest Experiment Station for the assistance in using the veneer lathing machine. This research was supported in part by a Grant-in-Aid for Scientific Research (C) No. 06660219 from the Ministry of Education, Science, and Culture of Japan.

- Hearmon, R. F. S. (1958). "The influence of shear and rotatory inertia on the free flexural vibration of wooden beams," *Brit. J. Appl. Phys.* **9**, 381–388.
- Stamm, A. J. (1964). *Wood and Cellulose Science* (Ronald, New York), pp. 346–353.
- Tonosaki, M., Takeshi, O., and Asano, I. (1983). "Vibrational properties of Sitka spruce with longitudinal vibration and flexural vibration," *Mokuzai Gakkaishi* **29**, 547–552.
- Tsoumis, G. (1991). *Science and Technology of Wood* (Van Nostrand Reinhold, New York).
- Yano, H. (1994). "The changes in the acoustic properties of Western red cedar due to methanol extraction," *Holzforschung* **48**, 491–495.
- Yano, H., and Minato, K. (1992). "Improvement of the acoustic properties and hygroscopic properties of wood by a chemical treatment and application to the violin parts," *J. Acoust. Soc. Am.* **92**, 1222–1227.
- Yano, H., and Yamada, T. (1985). "The dynamic mechanical properties of wood in the radial direction," *Mokuzai Gakkaishi* **31**, 222–230.
- Yano, H., Oonishi, K., and Mukudai, J. (1990). "Acoustic properties of wood for the top plate of guitar," *J. Soc. Mater. Sci. Jpn.* **39**, 1207–1212.
- Yano, H., Matsuoka, I., and Mukudai, J. (1992). "Acoustic properties of wood for violin," *Mokuzai Gakkaishi* **38**, 122–127.
- Yano, H., Kajita, H., and Mianto, K. (1994). "Chemical treatment of wood for musical instruments," *J. Acoust. Soc. Am.* **96**, 3380–3391.
- Yano, H., Kyou, K., Furuta, Y., and Kajita, H. (1995). "Acoustic properties of Brazilian rosewood used for guitar back plates," *Mokuzai Gakkaishi* **41**, 17–24.

A passive nonlinear digital filter design which facilitates physics-based sound synthesis of highly nonlinear musical instruments

John R. Pierce and Scott A. Van Duyne

Center for Computer Research in Music and Acoustics, Stanford University, Stanford, California 94305

(Received 31 May 1996; revised 16 September 1996; accepted 17 September 1996)

Recent work has led to highly efficient physics-based computational models of wave propagation in strings, acoustic tubes, membranes, plates, and rooms using the digital waveguide filter, the 2-D digital waveguide mesh, and the 3-D tetrahedral digital waveguide mesh, all of which are suitable for real-time musical synthesis applications. A simple first-order nonlinear filter structure derived from a passive nonlinear impedance circuit is described which extends the usefulness of these models, and which avoids the difficulties of energy conservation when memoryless nonlinearities are inserted in resonant feedback systems. © 1997 Acoustical Society of America.

[S0001-4966(97)01602-0]

PACS numbers: 43.75.Tv [WJS]

INTRODUCTION

Among the various approaches to the digital synthesis of musical sounds, some involve the production and excitation of linear resonances which are characteristic of a musical instrument. One fruitful notion has been that of considering the vibrating string as an electrical transmission line (Koch, 1937). The Karplus–Strong plucked-string algorithm (Karplus and Strong, 1983; Jaffe and Smith, 1983) models the vibrating string as a delay line loop. This is a special case of the traveling-wave-based digital waveguide modeling technique (Smith, 1992) which is applicable to many kinds of strings and acoustic tubes (Smith, 1987; Cook, 1990). The vibrating membrane and other two- and three-dimensional (2-D and 3-D) musical structures or reverberant environments have been modeled, and efficiently computed, using the multiply-free, parallel-computable, 2-D digital waveguide mesh (Van Duyne and Smith, 1993) and 3-D tetrahedral extension (Van Duyne and Smith, 1996). It is in the context of these kinds of wave-decomposed, computationally efficient digital modeling schemes that the current work on passive nonlinear filters most naturally resides.

While properly excited resonances of *linear* systems can closely approximate the tones of some musical instruments, *nonlinearity* plays an essential part in the sound of other musical instruments. Some nonlinearities are associated with the maintenance of oscillations in blown or bowed instruments (Smith, 1987). Others nonlinearities may be found in the excitation means of struck strings and percussion instruments, for example, the nonlinear compression force of piano hammer felt which leads to a greater spectral brightness of the sound with greater strike force (Chaigne and Askenfelt, 1994a, 1994b; Van Duyne *et al.*, 1994). The nature of the nonlinearity under present consideration is not to initiate, drive or maintain oscillation, but rather to modify the spectral energy distribution naturally and passively over time by transferring energy among resonating modes during the decay portion of the tone.

Fletcher and Rossing (1991) observe that after striking

cymbals, Chinese gongs, or tam-tams, the spectra become brighter with time. The higher portions of the spectra rise in comparison with the lower portions. The relative rise in higher frequencies, which is essential to the timbre of the sound, comes about because nonlinearities transfer vibrational energy from lower frequency to higher frequency modes. Beyond this, Lagge and Fletcher (1984) have shown that the compliance of a bridge supporting one end of a vibrating string can cause the transfer of energy among modes of vibration. Further, it has been known for some time that the flexible string is intrinsically nonlinear, except for the smallest vibrational amplitudes (Carrier, 1945). Thus, nonlinearities may have a smaller but nonetheless important effect on the tones of some stringed instruments.

We have found that the addition of passive nonlinearities to an otherwise linear digital synthesis algorithm can cause the transfer of energy among modes, and can lead to large and interesting alterations and evolutionary changes in timbre. In real physical instruments nonlinearities are necessarily passive because physical nonlinearities cannot cause an increase in total energy, but can only transfer energy among modes. The use of nonlinearities that are inherently passive in digital sound synthesis is important because other ways of adding nonlinearity can result in instability, oscillation, or unwanted energy loss.

A method has been found to incorporate an efficiently computable, energy conserving, first-order nonlinearity into a resonant feedback system. In particular, the first-order nonlinearity is a digital filter simulation of a spring which is stiffer for deflection in one direction than in the other, or alternatively, a capacitance which has a different value for positive than for negative voltages. Such an element stores no energy at zero deflection (spring) or at zero voltage (capacitor). Any energy that is stored by an increase in deflection or voltage will be given up as the deflection or voltage returns to zero. The element can store and release energy, but it cannot produce energy. The use or addition of this simple element is economical in computation and effective in causing energy transfer among otherwise linear modes. It can

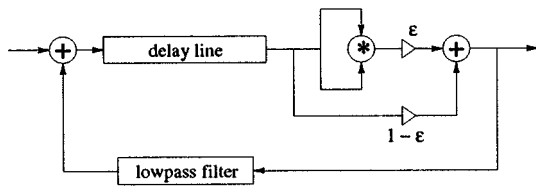


FIG. 1. Delay loop string model with square law nonlinearity.

lead to a substantial and pleasing alteration in the sound produced in an otherwise linear resonant feedback system. It has proven musically useful for both the qualitatively correct simulation of certain traditional instrument tones, and for the development of new and more exotic nonlinear synthetic tones.

I. PROBLEM OVERVIEW

A. Memoryless nonlinearity

Many spectral modifications, as occur during the time evolution of cymbal or gong tones, may be achieved by inserting *memoryless* nonlinearities into feedback loop systems. These kinds of nonlinearities have been used with success to induce auto-oscillation of feedback loops (Rodet, 1994). Nevertheless, energy conservation is out of control without additional amplitude tracking and/or scaling elsewhere in the loop. For example, Fig. 1 illustrates a simple nonlinear sound synthesis model based on the linear Karplus–Strong plucked-string algorithm (Karplus and Strong, 1983). The length of the delay line determines the fundamental pitch of the sound. The lowpass attenuation filter summarizes frequency-dependent loss per period in the string system. The simple linear loop model has been modified to include a square law nonlinearity within the feedback loop. The ϵ and $1 - \epsilon$ scalings allow some control over how much nonlinearity shall be present in the loop. The loop is linear for ϵ set to 0. For small, nonzero ϵ , a pleasant spectral brightening may occur over time. Interpreted physically, a memoryless scaling in the feedback loop may represent the transfer function at a terminating dashpot (or terminating resistor, in the transmission line case) between the left- and right-going traveling force waves (voltage waves). Figure 1 would then correspond to a string terminated on one end with a dashpot whose coefficient varies with the force applied to it, or to an oscillating transmission line terminated with a resistor whose coefficient depends on the voltage drop across it.

In Fig. 1, the choice of scaling coefficients, ϵ and $1 - \epsilon$, will guarantee passivity of the system, understanding that the digital signal levels are restricted to between 1 and -1 ; however, as we increase ϵ , thereby increasing the amount of nonlinearity in the system, the nonlinear dashpot becomes more and more lossy. Yet, for important classes of musical instruments, such as gongs and cymbals, a large, nonlossy nonlinear effect is required. The scaling factors might be adjusted to allow more nonlinearity without as much loss by choosing, for example, ϵ and $1.1 - \epsilon$, but this would correspond to a physical system where the terminating dashpot

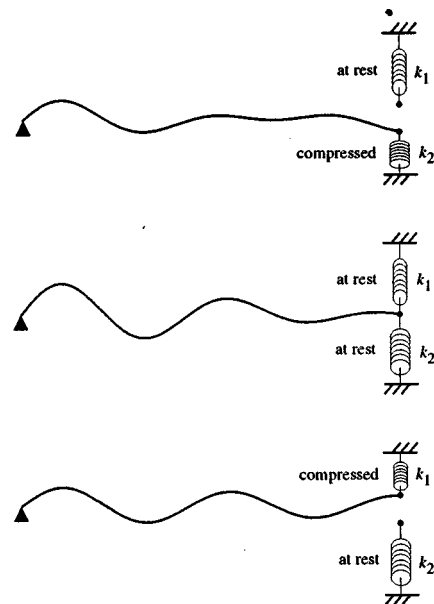


FIG. 2. String terminated with passive nonlinear double spring.

has an active impedance for certain forces and we risk instability in the loop without a careful monitoring of the overall loop gain.

In general, a memoryless nonlinearity may be formulated as a look-up table indexed by the samples of the incoming digital signal. There is no easy way to guarantee that the total energy of the input signal will equal the total energy of the output signal.

B. First-order nonlinearity

In order to resolve this dilemma of having to trade off a musically desirable large nonlinear effect against the risk of system instability, while still maintaining a practical level of computational cost for real-time musical sound synthesis applications, the problem has been approached through the physical modeling of a passive nonlinear lumped termination impedance which has an internal state, that is, which is *not memoryless*. A passive nonlinear loop filter has been derived based on a real physical system constructed from passive, lossless elements only, namely, two springs of differing stiffness.

Consider a string terminated by a double-spring apparatus as shown in Fig. 2. Three states of the system are shown in the figure: First, the lower spring is compressed, while the upper spring is at rest; second, both springs are at rest; and, third, the upper spring is compressed, while the lower spring is at rest. In effect, the spring termination apparatus is equivalent to a single nonlinear spring whose stiffness constant is k_1 when the displacement is positive and k_2 when the displacement is negative.

Now consider what is happening to the energy in the system. When the lower spring is compressed, some energy from the string is converted to potential energy stored in the spring. When the lower spring returns to its rest state, the stored spring energy is entirely returned to the string, and the spring contains no stored energy. When the upper spring is

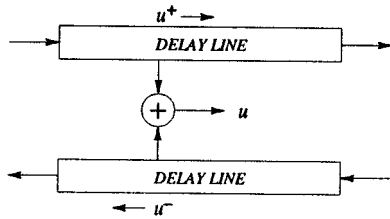


FIG. 3. The digital waveguide.

then compressed, exactly the same kind of energy exchange occurs. This ideal system is physically passive and lossless since energy is neither created nor destroyed.

If the spring stiffness constant had changed while stored potential energy was still in the spring, i.e., when one of the springs was still compressed, the stored energy would be scaled by the new relative stiffness of the spring. In this case, the stored energy before the stiffness change would be different from the stored energy after the stiffness change, leading to the creation or loss of energy, possibly resulting in a nonpassive system. In any model of this nonlinear system, care must be taken to change the spring stiffness coefficient at the right time in order to preserve passivity and losslessness.

Passivity is the requirement that no energy be created by the system. When energy is created in a feedback loop, stability problems may ensue. We have specifically tried to discover a nonlinear system which is passive, and which is lossless, so the system loss may be decoupled from the nonlinear effect, and designed separately.

II. NONLINEAR FILTER DERIVATION

A. The digital waveguide string model

The one-dimensional wave equation may be solved as the sum of two waves traveling in opposite directions (Morse and Ingard, 1968). The traveling wave solution has led to the digital modeling of string and acoustic tube oscillations using a pair of bi-directional delay lines, each delay line implementing one of the traveling waves. This efficient filter structure is known as the digital waveguide (Smith, 1992, 1987). The traveling may represent displacement, velocity, slope, force, or other physical variables. Traveling waves are mathematical constructs, the actual physical values at any point on the string being the sum of the right- and left-going traveling components at that point. Figure 3 illustrates a physical variable, u , as the sum of its traveling components, u^+ and u^- , at some point on the waveguide. The delay lines represent both a sampled delay in time and a sampled position in space. The digital waveguide filter structure permits an exact band-limited reconstruction of the continuous traveling wave in time and space.

If transverse velocity or displacement waves on a string are being modeled, then, on reaching a rigid termination, the traveling wave in the right-going delay line will invert and turn into the left-going delay line. This is to say that the velocity wave transfer function at a rigid termination is -1 . Similarly, if transverse force waves are being modeled, then the force wave transfer function at a rigid termination is $+1$,

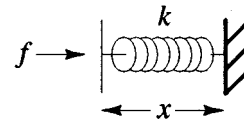


FIG. 4. Simple linear spring system.

that is, there is no inversion of force waves at a rigid termination. The case of a springy termination is considered below.

There is a *wave impedance* relationship between the traveling components of force and velocity in the string, corresponding to the wave impedance relation between pressure and flow in acoustic tubes, or voltage and current in electrical transmission lines (Magnusson, 1970), which can be written

$$f^+ = R_0 v^+ \quad \text{and} \quad f^- = -R_0 v^-, \quad (1)$$

where f^\pm and v^\pm are the traveling wave components of force and velocity, respectively, and where the wave impedance is $R_0 = \sqrt{K\epsilon}$, K being the constant tension on the string and ϵ being the mass density per unit length. Intuitively, these equations say that when a force is applied transversely to a string, the resultant transverse velocity should be less for greater string mass and for greater string tension. The change in sign for the left-going components is due to coordinate system choice. Note that no matter whether velocity or force waves are being modeled in the system loop, both physical force and physical velocity at any point along the string may be computed from the resident traveling wave components using Eq. (1) to make the change of variables,

$$v = v^+ + v^- = (1/R_0)(f^+ - f^-), \quad (2)$$

$$f = f^+ + f^- = R_0(v^+ - v^-). \quad (3)$$

B. The linear spring termination

The force equation for the ideal linear spring shown in Fig. 4 is

$$f(t) = kx(t) \Rightarrow \frac{df(t)}{dt} = kv(t), \quad (4)$$

where $f(t)$ is the force applied on the spring at time t , $x(t)$ is the compression distance of the spring, $v(t)$ is the velocity of compression, and k is the spring stiffness constant.

Taking the Laplace transform mapping $f(t)$ to $F(s)$ and $v(t)$ to $V(s)$, and further assuming no initial force on the spring, we get

$$F(s) = (k/s)V(s). \quad (5)$$

Here, k/s is the lumped impedance of the spring. Setting $s = j\omega$ will give the frequency response of this system.

Figure 5 shows a string terminated by a spring. As was suggested in Eqs. (2) and (3), the physical force at the string termination is the sum of the transverse force waves on the string at that point, $f = f_r + f_l$, while the physical velocity at the termination is the difference between the force waves scaled by $1/R_0$, $v = (1/R_0)(f_r - f_l)$. We may, therefore, reformulate Eq. (5) as a transfer function from F_r to F_l ,

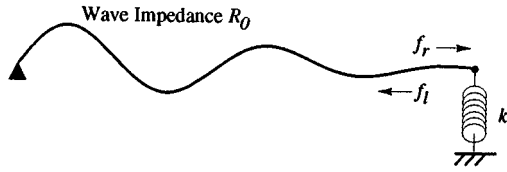


FIG. 5. String terminated by simple spring.

$$F(s) = (k/s)V(s), \quad (6)$$

$$F_r(s) + F_l(s) = \left(\frac{k}{s}\right) \frac{F_r(s) - F_l(s)}{R_0}, \quad (7)$$

$$F_l(s) = \frac{k/s - R_0}{k/s + R_0} F_r(s). \quad (8)$$

The force wave transfer function is stable allpass since its pole is at $s = -k/R_0$ and its zero is at $s = k/R_0$, where k and R_0 are defined to be positive real numbers.

C. Moving to the digital domain

While it is appropriate simply to sample the continuous traveling waves to form the digital waveguide filter structure, it is convenient to make a conformal bilinear transform when taking the spring system from the s plane to the z plane (Parks and Burrus, 1987; Nehari, 1952),

$$s \leftarrow \alpha \frac{1 - z^{-1}}{1 + z^{-1}}. \quad (9)$$

This bilinear transform maps DC in the continuous system to DC in the digital system, while mapping infinite frequency in the continuous system to half the sampling rate, or the Nyquist limit frequency, in the digital system. Further, the system retains its allpass characteristics, which is essential for the present purpose. The parameter α is a degree of freedom which may be used to control the frequency warping. It is usual to choose $\alpha = 2/T$ to obtain faithful frequency response at the low end of the frequency range (Parks and Burrus, 1987).

The bilinear transform is applied to Eq. (8) to obtain

$$F_l(z) = H(z)F_r(z), \quad (10)$$

where

$$H(z) = \frac{a_0 + z^{-1}}{1 + a_0 z^{-1}} \quad \text{and} \quad a_0 = \frac{k - \alpha R_0}{k + \alpha R_0}. \quad (11)$$

The filter coefficient a_0 ranges from -1 to 1 as the spring stiffness parameter k ranges from 0 to ∞ . The frequency domain transfer function, Eq. (10), corresponds to a time domain difference equation of the form

$$f_l(n) = a_0 f_r(n) + f_r(n-1) - a_0 f_l(n-1), \quad (12)$$

where n is the sampled time index. Figures 6 and 7 show two alternative implementations of this allpass difference equation. The z^{-1} blocks indicate a delay of one time sample.

Since the filter coefficient, a_0 , represents the spring stiffness, only a_0 need be changed to modify the stiffness of the spring termination. However, to preserve physical and digital

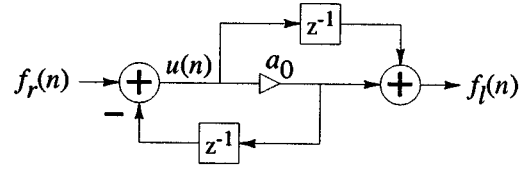


FIG. 6. Allpass filter implementation.

passivity and losslessness this change must be made just at the point where the spring passes through its rest position.

D. Physically correct coefficient modulation

Consider the internal filter signal $u(n)$ in the allpass filter implementation of $H(z)$ shown in Fig. 6. From the diagram, it may be seen that

$$f_l(n) = a_0 u(n) + u(n-1), \quad (13)$$

$$u(n) = f_r(n) - a_0 u(n-1). \quad (14)$$

The actual physical force applied to the spring termination is equal to the sum of the input and output force waves, as defined in Eq. (3). Using (13) and (14), an expression of the actual force on the spring, $f(n)$, may be found:

$$f(n) \triangleq f_r(n) + f_l(n) \quad (15)$$

$$= (1 + a_0)[u(n) + u(n-1)]. \quad (16)$$

Equation (16) indicates that the actual physical force on the spring is proportional to a linearly interpolated value of signal u at time $n-0.5$. From Eq. (4), displacement of the spring termination is zero when force is zero, and $f(n)$ is zero when $u(n) + u(n-1)$ is zero. Therefore, when u changes sign between times $n-1$ and n , the spring displacement is closest to zero. Hence, this is as close as we can get to the physically correct time to change the spring stiffness coefficient in order to model the nonlinear spring termination system shown in Fig. 2.

In some computational circumstances, the alternative filter structure shown in Fig. 7 may be preferable to that in Fig. 6. From the diagram in Fig. 7, it may be seen that

$$f_l(n) = w(n-1) + a_0 f_r(n), \quad (17)$$

$$w(n) = f_r(n) - a_0 f_l(n). \quad (18)$$

Combining (17) and (18) as before, the termination force may be found:

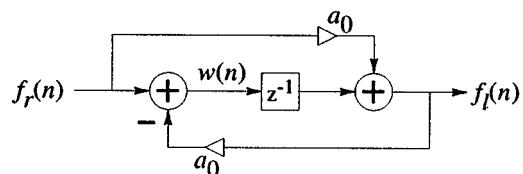


FIG. 7. Alternative allpass filter implementation.

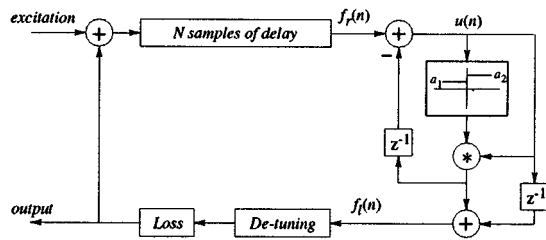


FIG. 8. Nonlinear string/spring system.

$$f(n) \triangleq f_r(n) + f_f(n) \quad (19)$$

$$= \left(\frac{1}{1-a_0} \right) [w(n) + w(n-1)], \quad (20)$$

and the same arguments apply as above. The physically correct time to change the allpass filter coefficient is when the spring force is nearest to zero, which is when the state signal, $w(n)$, changes sign.

E. Digitally correct coefficient modulation

The internal filter state signal, $u(n)$ in Fig. 6, or $w(n)$ in Fig. 7, represents the digital energy stored in the filter at any given time, n . Assume that the allpass coefficient a_0 is to be changed at time $n = T_c$. Also, assume that there is no input signal after time T_c , i.e., $f_r(n) = 0$ for $n > T_c$, and that there is some nonzero internal state value at time $n = T_c$. Then the output of the filter caused only by this internal energy state value is proportional to the decaying exponential, $a_0^{n-T_c}$, and the corresponding energy is the sum of squares of this output signal.

If the coefficient, a_0 , is suddenly changed at time $n = T_c$, it is clear that the internal state energy will ring out of the filter with a different decay rate than if the coefficient had not been changed, and hence, the energy will not be conserved. Such coefficient changes, if made arbitrarily, may lead to instability in a feedback loop. However, if the internal state, $u(T_c)$ for Fig. 6, or $w(T_c)$ for Fig. 7, is zero or near zero when the coefficient a_0 is changed, then the resultant discontinuity in the state energy will be minimal or zero. Therefore, to maintain the desired passivity in the nonlinear allpass filter, the filter coefficient change is gated on the sign of the state. This method of gating the coefficient change is both *physically correct*, since when the state is near zero, the modeled force on the element is correspondingly near zero, and *digitally correct*, since it minimizes energy discontinuities arising from the internal state.

Figure 8 shows a digital system diagram for the nonlin-

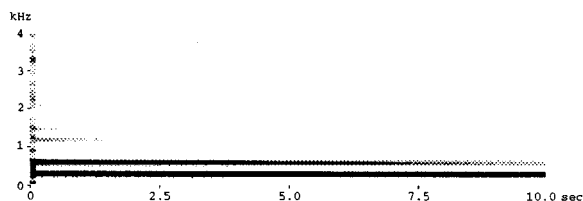


FIG. 9. Spectrogram of harmonic loop with lowpass filter.

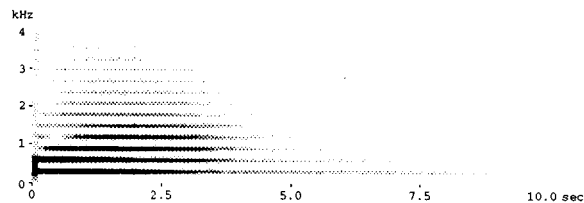


FIG. 10. Spectrogram of harmonic loop with lowpass filter and passive nonlinear filter.

ear string/spring system of Fig. 2 using the allpass filter variant given in Fig. 6. For graphical convenience, a look-up table notation is used to show how $u(n)$ gates the coefficient change, but, in general, this would be implemented in simple conditional logic. Also shown in the loop are a delay line block which determines the fundamental pitch of the loop, a loss filter block which generally is a lowpass filter used to model a frequency dependent attenuation per period, and a detuning filter block representing some static allpass filters which may make a fractional sample delay correction or, otherwise, introduce inharmonicities into the loop.

III. MUSICAL EXAMPLES

The passive nonlinear filter was tested in a variety of musical situations. Shown here are comparisons of the spectral evolution, with and without nonlinearity, of two sounds generated by essentially the model in Fig. 8. In the first example, Fig. 9 shows the spectral evolution of a simple delay line plus lowpass filter loop excited in such a way that the third harmonic is highly attenuated, and in which the nonlinear filter is deactivated. We see a natural exponential decay with higher frequency modes decaying faster than low frequency modes. In Fig. 10, the passive nonlinear filter has been activated with the result that the spectrum brightens over time; in particular, the initially missing third harmonic builds up energy, as do several higher harmonics. After a few seconds, the effect of the lowpass filter in the loop takes over and the loop decays out.

In a second example, the same system is used with the addition of an allpass filter in the loop to detune the modes slightly, giving it a more bell-like tone. Figure 11 shows the spectral evolution when the nonlinear filter is deactivated. Figure 12 shows the result when the nonlinear filter is operating. Note that the modes exchange energy among themselves in a more dynamic manner in this inharmonic case.

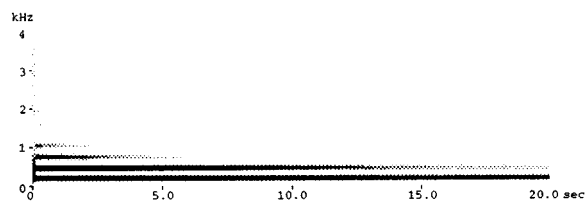


FIG. 11. Spectrogram of inharmonic loop with lowpass filter.

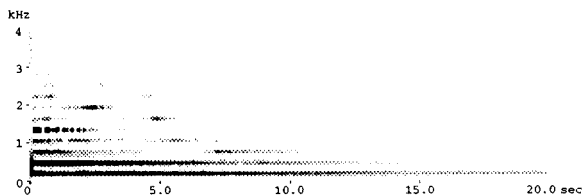


FIG. 12. Spectrogram of inharmonic loop with lowpass filter and passive nonlinear filter.

In addition to these simple loop cases, promising gong- and cymbal-like sounds have been generated by incorporating these passive nonlinear filters into the 2-D digital waveguide mesh membrane model (Van Duyne and Smith, 1993; Van Duyne *et al.*, 1994).

IV. PHASE MODULATION ANALYSIS

The time-varying allpass termination filter shown in Fig. 8 is essentially lossless and passive. However, for it to be useful it must behave in the desired manner. Energy in existing resonant modes of the main system must be caused to spread locally in the spectrum to nearby modes of the system, as is observed in real musical instruments (Fletcher and Rossing, 1991). Empirically, this seems to happen, as seen in Figs. 9–12. However, this filter is difficult to analyze strictly, due to its signal-dependent time variation and due to its inclusion in a feedback loop system. Nonetheless, an intuitive understanding of its operation may be gleaned by considering a simpler, but nonpassive, form.

The termination filter in Fig. 8 is a one-pole allpass filter with a time-varying coefficient. Consider the frequency response of an allpass filter of the same form with a *sinusoidally* varying coefficient taking on values between a_1 and a_2 . Intuitively, this filter will be performing a phase modulation on the input signal. Hence, the output signal of the filter should contain sidebands generated by this phase modulation at multiples of the modulation frequency. Figure 13 shows the dB magnitude spectrum of the output signal of this filter with an input sine wave “center frequency” of 8000 Hz and a coefficient “modulating frequency” of 2000 Hz. The resultant sidebands of the output signal are just as expected.

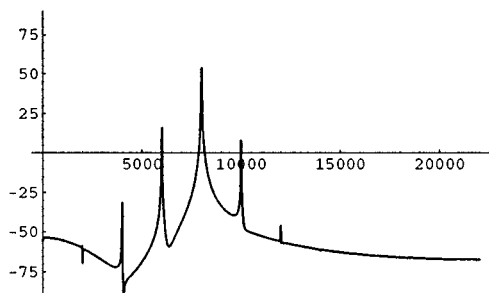


FIG. 13. Output dB magnitude spectrum of sinusoidally driven allpass filter with sinusoidally modulated coefficient.

Modulating the coefficient, $a_0(n)$, with a square wave, instead of a sine wave, should result in an output signal spectrum containing some greater emphasis in the odd sidebands, due to the odd harmonics in the square wave coefficient modulation signal.

In the passive nonlinear filter form of Fig. 8, where the coefficient change is controlled by the change in sign of the internal signal, $u(n)$, the modulating signal is quasi-square wave in that it flips between two distinct values, and it has a “fundamental frequency” related to the input signal to the filter, since $u(n)$ is just a filtered version of the input signal, $f_r(n)$, as indicated in Eq. (14). The filter output signal will, therefore, contain sidebands corresponding to sum and difference frequencies of the input signal, generally grouping near frequencies in the input signal. Further, the choice of a_1 and a_2 may be used to determine the rate of energy spreading and the spectral region where it is most active, by simple analysis of the relative phase response variation between the first-order allpass filters with these two coefficients.

For coupling to occur in the resonant system, the sidebands produced by the modulated allpass filter must fall on supported modes of the system. When a sideband coincides with a supported mode, that mode will be driven by the energy from the appropriate sideband. Energy from sidebands which do not fall on supported modes will not drive any particular mode and will simply be absorbed back into the system. Since the passive nonlinear filter produces sum and difference frequencies of the input signal, we can expect that at least some of the main system modes will be hit and energy spreading will occur.

V. CONCLUSIONS

A first-order, physically motivated, nonlinear digital filter has been developed which is passive and energy conserving. It may be incorporated easily into linear resonant filter-based sound synthesis algorithms such as the Karplus–Strong plucked-string algorithm, and the various one-, two-, and three-dimensional digital waveguide filter structures. The nonlinear effect is pleasing, natural, and qualitatively similar to that which may be observed in real musical instruments, namely, a gradual spreading of spectral energy from existing modes to their neighbor modes. The rate of energy spreading and spectral region of greatest activity may be tuned using the two filter parameters. The filter is computationally efficient and suitable for real-time sound synthesis applications.

Carrier, G. F. (1945). “On the non-linear vibration problem of the elastic string,” *Q. Appl. Math.* **3**, 157–165.
 Chaigne, A., and Askenfelt, A. (1994a). “Numerical simulations of piano strings. I. A physical model for a struck string using finite difference methods,” *J. Acoust. Soc. Am.* **95**, 1112–1118.
 Chaigne, A., and Askenfelt, A. (1994b). “Numerical simulations of piano strings. II. Comparisons with measurements and systematic exploration of some hammer-string parameters,” *J. Acoust. Soc. Am.* **95**, 1631–1640.
 Cook, P. R. (1990). *Identification of Control Parameters in an Articulatory Vocal Tract Model*, with Applications to the Synthesis of Singing, Stanford Univ. Music Dept., Center for Computer Research in Music and Acoustics, Report No. STAN-M-68.
 Fletcher, N. H., and Rossing T. D. (1991). *The Physics of Musical Instruments* (Springer-Verlag, New York).

- Jaffe, D. A., and Smith, J. O. (1989). "Extensions of the Karplus–Strong plucked-string algorithm," in *The Music Machine*, edited by C. Roads (MIT, Cambridge, MA), reprinted from *Comput. Music J.* **7**(2) (1983).
- Karplus, K., and Strong, A. (1989). "Digital synthesis of plucked-string and drum timbres," in *The Music Machine*, edited by C. Roads (MIT, Cambridge, MA), reprinted from *Comput. Music J.* **7**(2) (1983).
- Kock, W. E. (1931). "The vibrating string considered as an electrical transmission line," *J. Acoust. Soc. Am.* **8**, 227–233.
- Lagge, K. A., and Fletcher, N. H. (1984). "Nonlinear generation of missing modes on a vibrating string," *J. Acoust. Soc. Am.* **76**, 5–12.
- Magnusson, P. (1970). *Transmission Lines and Wave Propagation* (Allyn and Bacon, Boston).
- Morse, P., and Ingard, K. (1968). *Theoretical Acoustics* (McGraw-Hill, New York).
- Nehari, Z. (1952). *Conformal Mapping* (McGraw-Hill, New York).
- Parks, T. W., and Burrus, C. S. (1987). *Digital Filter Design* (Wiley, New York).
- Rodet, X. (1994). "Stability/instability of periodic solutions and chaos in physical models of musical instruments," *Proc. International Computer Music Conference* (Århus, 1994).
- Smith, J. O. (1992). "Physical modeling using digital waveguides," *Comput. Music J.* **16**(4).
- Smith, J. O. (1987). *Music Applications of Digital Waveguides*, Stanford Univ. Music Dept., Center for Computer Research in Music and Acoustics, Report No. STAN-M-39.
- Van Duyne, S. A., and Smith, J. O. (1996). "The 3D tetrahedral digital waveguide mesh with musical applications," *Proc. International Computer Music Conference* (Hong Kong, 1996).
- Van Duyne, S. A., Pierce, J. R., and Smith, J. O. (1994). "A passive nonlinear mode-coupling circuit and the wave digital hammer," *Proc. International Computer Music Conference* (Århus, 1994).
- Van Duyne, S. A., and Smith, J. O. (1993). "Physical modeling with the 2D digital waveguide mesh," *Proc. International Computer Music Conference* (Tokyo, 1993).

Can acoustic multipath explain finback (*B. physalus*) 20-Hz doublets in shallow water?

V. Premus^{a)} and J. L. Spiesberger

Department of Meteorology and Applied Research Laboratory, 503 Walker Building, The Pennsylvania State University, University Park, Pennsylvania 16802

(Received 20 December 1995; accepted for publication 28 August 1996)

A broadband acoustic propagation code is combined with an empirically derived geoacoustic seafloor model for the purpose of interpreting finback doublet sequences recorded in the northern Gulf of California by Thompson *et al.* in 1987 [Thompson *et al.*, *J. Acoust. Soc. Am.* **92**, 3051–3057 (1992)]. The result is that for ranges less than 30 km, it is plausible to explain the appearance of the finback doublet in this environment in terms of multipath propagation through the water column and the seafloor. For a channel depth as shallow as 50 m, the detection range of the subbottom arrival may exceed that of the water-borne arrival. This result may have important implications for the accuracy of hyperbolic localization algorithms which assume a sound speed consistent with a water-borne propagation path. When doublet propagation is supported, the interpulse delay is demonstrated to be strongly range dependent. With prior knowledge of the geoacoustic environment, the interpulse delay may provide a practical tool for the real-time passive ranging of finbacks using only a single hydrophone or sensor array. Scientists might consider the impact the multipath-induced doublet has on long distance communication between whales based on temporal cues encoded in patterned 20-Hz pulse sequences. © 1997 Acoustical Society of America. [S0001-4966(97)03202-5]

PACS numbers: 43.80.Ka, 43.30.Sf [FD]

INTRODUCTION

Until now, the bioacoustics literature has presented no evidence to contradict the position that the doublets commonly observed in the patterned 20-Hz vocalizations of fin whales are emitted by the whale itself. Consider the following excerpt from Thompson *et al.*:¹ “The 20-Hz fin whale pulses and interpulse intervals recorded in this gulf [of California], which we found to be unique in comparison with other Pacific and with Atlantic regions, constitute corroborating evidence [that] Gulf of California fin whales may be a separate population, distinct from fin whales in nearby Pacific regions.” From this statement, it is straightforward to conclude that the authors attribute the appearance of the 20-Hz doublet to the calling behavior of the finback. We offer an alternative hypothesis—the occurrence of the doublet and the uniqueness of interpulse intervals observed by Thompson in the Gulf of California may be accounted for by acoustic propagation conditions. For the first time, a broadband acoustic propagation code is combined with an empirically derived geoacoustic seafloor model for the purpose of interpreting finback doublet sequences recorded in the northern Gulf of California by Thompson *et al.* in 1987 (Ref. 1). While the model cannot rule out the possibility that doublets are indeed emitted by fin whales, the results show that for ranges less than 30 km, it is plausible to explain the appearance of the finback doublet in terms of multipath propagation through the water column and seafloor. The interpulse delay of the multipath-induced doublet is demonstrated to be

strongly range dependent. With prior knowledge of the mean geoacoustic environment, it is possible to estimate the animal’s range from the interpulse delay using only a single hydrophone or sensor array. This range estimate is found to be insensitive to the depth of the whale. However, the signal-to-noise ratio (SNR) of the first arrival is sensitive to destructive interference effects related to surface reflections for source depths approaching integer multiples of $\lambda/2$, where λ is the acoustic wavelength. Contrary to intuition, the range of support for doublet propagation in shallow water appears to be limited by the detection range of the water-borne pulse, rather than by that of the subbottom pulse. The subbottom multipath mechanism leads to temporal spreading at ranges of $O(10\text{ km})$ that would be comparable to that experienced at ranges of $O(1000\text{ km})$ in the deep ocean.

I. THE FINBACK DOUBLET: A DATA-MODEL COMPARISON

The data interpreted in this modeling study were collected by Thompson *et al.* off Puerto Libertad, Mexico in the northern Gulf of California in August 1987 (Ref. 1). Figure 1 depicts the location of this recording session, identified by the northernmost asterisk. Data were collected using a single hydrophone. Ambient noise levels, although not explicitly reported in Ref. 1, were known to be low.² The water depth was estimated to be 30–100 m. The receiver depth was unknown but estimated to be 10 m (Ref. 2).

Sonograms of patterned 20-Hz doublet sequences reported in Thompson *et al.*¹ are depicted in Fig. 2. These data come from 25 min of contiguous recordings made on the morning of 8 August 1987. Interpulse intervals are approximately 5.5 s (*A–B*) and 17.5 s (*B–A*), respectively. The

^{a)}Present address: MIT Lincoln Laboratory, 244 Wood Street, Lexington, MA 02173.

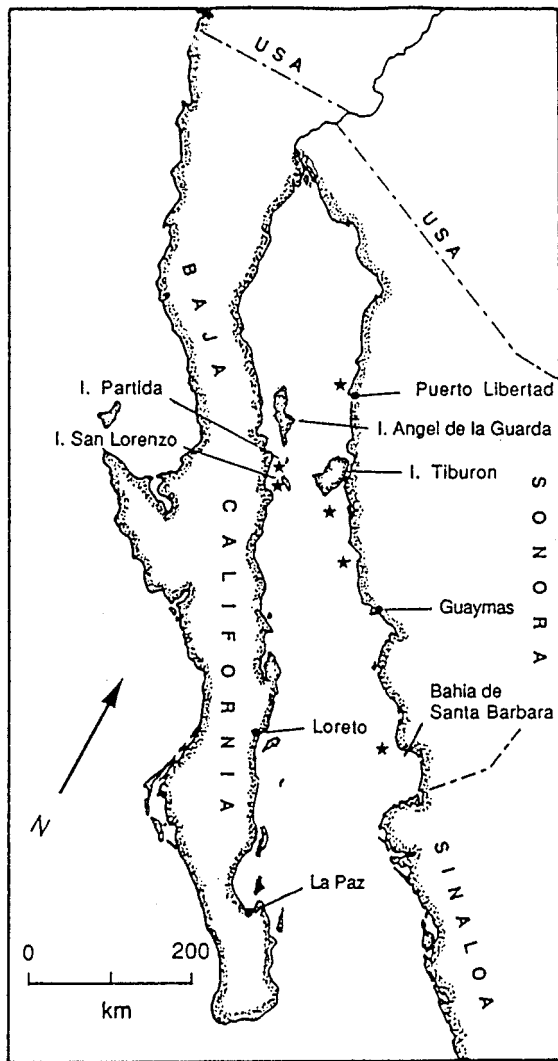


FIG. 1. Gulf of California. Asterisks denote locations of finback data collected by Thompson *et al.* (Ref. 1) during three recording sessions between March 1985 and August 1987. The northernmost asterisk denotes data set that is the subject of this study. Reprinted from Thompson *et al.* (Ref. 1), with permission of AIP.

actual range to the whale was not known. In Ref. 1, Thompson *et al.* reported on the variability of interpulse intervals within the patterned 20-Hz pulse sequences recorded in the Gulf of California in 1985 and 1987. Table II of Ref. 1 summarizes their findings, assembled from approximately 10 h of finback data collected over two recording sessions. For example, in March 1985, doublet sequences with $A-B/B-A$ intervals of 9-s/12-s and 1.5-s/7.5-s were reported, very different from those obtained in August 1987. Thompson² has subsequently confirmed the variable nature of doublet intervals in Gulf of California finback recordings.

Consider Fig. 2. The hypothesis propounded herein is that some or all of these doublets may not have been emitted by the whale, but may instead be attributed to acoustic multipath propagation. The modeling result which supports this hypothesis is shown in Fig. 3. Figure 3(a) depicts a sonogram of the hypothesized call emitted by a finback. The signal consists of a train of *single* 20-Hz pulses, each down-swept from 25 to 17 Hz, with 1-s duration and a source level of 185 dB *re*: 1 μ Pa @ 1 m (Ref. 3). For lack of evidence to

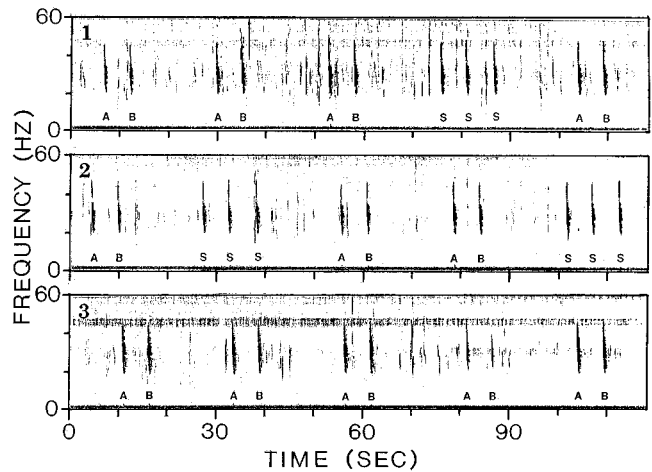


FIG. 2. Sonograms of finback data collected by Thompson *et al.* in August 1987 in the Gulf of California, NW of Puerto Libertad, Mexico. Each panel depicts the doublet pulse train of a nearby whale. Observe that triplets are interspersed within the doublet train. The animal's range is unknown. Interpulse intervals are measured to be 5.5 s ($A-B$) and 17.5 s ($B-A$). Reprinted from Thompson *et al.*, 1992, with permission of AIP.

the contrary, the source is assumed to be omnidirectional. The period between pulses was chosen to conform to the interarrival times between successive *A* pulses in panel 3 of Fig. 2. Figure 3(b) illustrates the acoustic model output, computed using the Ocean Acoustic and Seismic Exploration Synthesis (OASES) code⁴ for the Gulf of California environment at a range of 17 km. The OASES input file used to generate this result is given in Table I. The simulated time

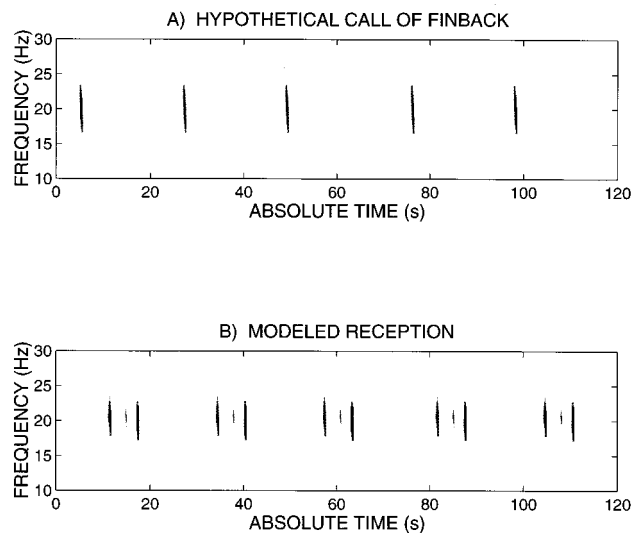


FIG. 3. Sonograms of input and output time series for the Gulf of California model. (a) Hypothetical finback call consisting of a train of *single* 20-Hz pulses, down-swept from 25 to 17 Hz, with 1-s duration and a source level of 186 dB *re*: 1 μ Pa @ 1 m. The interpulse spacing is chosen to conform to the interarrival times between successive *A* pulses in Fig. 2. (b) The model output illustrating the effect of acoustic multipath. The whale is located at a range of 17 km and a depth of 20 m. The receiver depth is 20 m. The channel depth is 50 m. The ambient noise level is 60 dB *re*: 1 μ Pa in 1-Hz band. Single pulses have been transformed into doublets by the impulse response function of the acoustic channel. The early arrival is due to a sediment-refracted/basement-reflected path. It arrives earlier than the waterborne arrival due to the higher sound speed of the sediment and subbottom layers. Compare to panel 3 of Fig. 2.

TABLE I. OASES input file for full geoacoustic model including shear. Beginning with row 5, columns 1–6 specify the acoustic environmental parameters as follows: (1) depth of interface relative to sea surface in meters; (2) compressional wave speed, c_p (m/s); (3) shear wave speed, c_s (m/s); (4) compressional wave attenuation, α_p (dB/ λ_p), where λ_p is the compressional wavelength; (5) shear wave attenuation, α_s (dB/ λ_s), where λ_s is the shear wavelength; and (6) density, ρ (g/cm³). For additional information regarding input parameters, refer to the OASES Application and Upgrade Notes (Ref. 4).

| Gulf of California. Full geoacoustic model, 50-m water depth. | | | | | | |
|---|------|-------|--------|------|------|----|
| J | K | | | | | |
| 20 | 0 | | | | | |
| 25 | | | | | | |
| 0 | 0 | 0 | 0 | 0 | 0 | 0 |
| 0 | 1531 | -1521 | 0 | 0 | 1 | 0 |
| 50 | 1740 | 400 | 0.435 | 6.16 | 1.80 | 0 |
| 125 | 1808 | 440 | 0.220 | 2.78 | 1.82 | 0 |
| 200 | 1876 | 482 | 0.205 | 2.31 | 1.84 | 0 |
| 275 | 1944 | 526 | 0.197 | 2.01 | 1.86 | 0 |
| 350 | 2013 | 572 | 0.194 | 1.80 | 1.88 | 0 |
| 425 | 2081 | 619 | 0.194 | 1.64 | 1.90 | 0 |
| 500 | 2149 | 668 | 0.194 | 1.50 | 1.92 | 0 |
| 575 | 2217 | 719 | 0.195 | 1.38 | 1.94 | 0 |
| 650 | 2286 | 773 | 0.197 | 1.29 | 1.96 | 0 |
| 725 | 2354 | 827 | 0.199 | 1.20 | 1.98 | 0 |
| 800 | 2422 | 884 | 0.201 | 1.13 | 2.00 | 0 |
| 875 | 2490 | 942 | 0.203 | 1.06 | 2.02 | 0 |
| 950 | 2559 | 1003 | 0.206 | 1.00 | 2.04 | 0 |
| 1025 | 2627 | 1065 | 0.209 | 0.95 | 2.06 | 0 |
| 1100 | 2695 | 1129 | 0.211 | 0.90 | 2.08 | 0 |
| 1175 | 2763 | 1195 | 0.214 | 0.85 | 2.10 | 0 |
| 1250 | 2832 | 1263 | 0.217 | 0.81 | 2.12 | 0 |
| 1325 | 2900 | 1332 | 0.220 | 0.78 | 2.14 | 0 |
| 1400 | 2968 | 1404 | 0.223 | 0.74 | 2.16 | 0 |
| 1475 | 3036 | 1477 | 0.226 | 0.71 | 2.18 | 0 |
| 1550 | 4130 | 2065 | 0.200 | 0.60 | 2.40 | 0 |
| 3550 | 5430 | 2715 | 0.110 | 0.32 | 2.60 | 0 |
| 7550 | 6640 | 3320 | 0.130 | 0.38 | 2.90 | 0 |
| 20 | | | | | | |
| 10 | 50 | 5 | | | | |
| 1400 | 1E8 | | | | | |
| -1 | 1 | 4096 | 0 | | | |
| 4096 | 10. | 30. | .00625 | 1 | 1 | 30 |

series were obtained by convolving the time domain finback call representation due to Watkins³ with the impulse response function for the channel.

Since the actual range to the subject was unknown, range is used as a free parameter to fit the model to the data. White Gaussian noise was added to the model output at a level of 60 dB *re*: 1 μ Pa in a 1-Hz band, a typical value at 20 Hz under light shipping conditions.⁵ Notice that the train of single pulses emitted by the finback has been transformed into a train of doublets by the impulse response function of the acoustic channel. A time series depicting a doublet from the OASES model is shown in Fig. 4. The peak-signal-to-rms-noise ratio, denoted from here on as SNR_{peak} , is approximately 20 dB for each arrival. The rms-signal-to-rms-noise ratio, denoted from here on as SNR_{rms} , is somewhat less, about 11 dB. As discussed in the next section, the first arrival can be attributed to a sediment-refracted/basement-reflected path. It arrives earlier than the water-borne pulse, despite its longer path length, due to the higher compressional wave speed in the sediment and subbottom layers. At this range, the (A-B) interpulse spacing is approximately

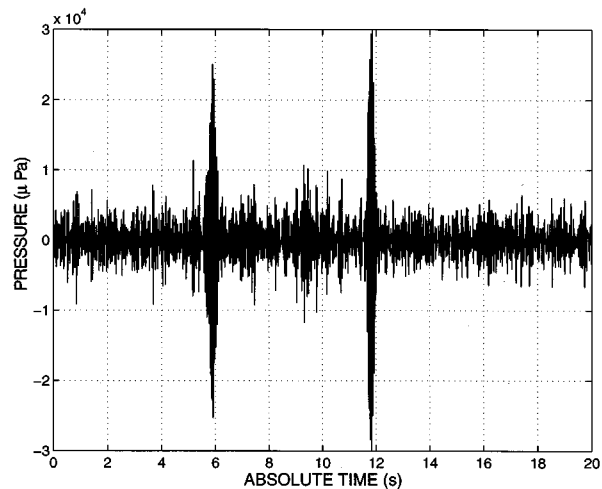


FIG. 4. Time series representation of modeled doublet at a range of 17 km. The peak SNR of the first arrival is 20.1 dB (11.6-dB rms). The peak SNR of the second arrival is 21.7 dB (13.2-dB rms).

5.5–6 s, in good agreement with the (A-B) interval observed by Thompson *et al.* Such multipath time spread at a range of 17 km would ordinarily require a source/receiver separation in excess of 1000 km in the deep ocean.⁶

The triplets interspersed within the patterned doublet sequences of panels 1 and 2 of Fig. 2 may also be accounted for with the acoustic model. An example of a triplet occurrence in the model is shown in Fig. 5. One hypothesis is that the data in panels 1 and 2 of Fig. 2 depict two whales counter calling, with slightly different propagation conditions existing between each caller and the hydrophone. The only changes made to the environmental model of Table I to produce the triplet were: (1) a decrease in the compressional wave attenuation, k_p , in layer 2 from 0.2 to 0.124 dB/m/kHz; and (2) a proportionate increase in $k_p(0)$ in layer 1 from 0.25 to 0.3 dB/m/kHz, to maintain the same total attenuation

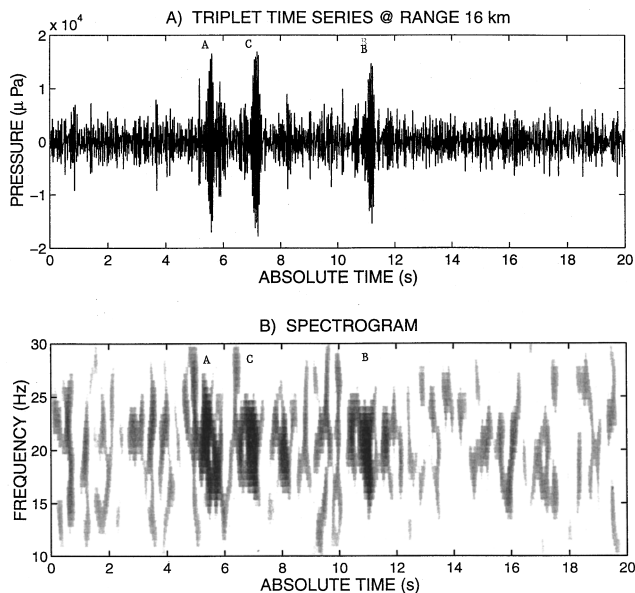


FIG. 5. OASES model triplet. The range is 16 km. The corresponding OASES input file is given in Table I, with two exceptions: (a) $k_p(0)$ in layer 1 was increased from 0.25 to 0.3 dB/m/kHz, and (b) k_p for layer 2 was decreased from 0.03 to 0.02 dB/m/kHz. For clarity, only the top 20 dB of the colormap are shown.

along the subbottom path. These modifications fall well within the tolerances admitted by environmental data for this region (Appendix A). The decrease in compressional wave attenuation in layer 2 enhances the impedance discontinuity at the layer 2–3 interface. This change is enough to enable a reflection from this interface, labeled C in Fig. 5, to propagate to the hydrophone approximately 2 s after the basement-reflected A pulse. The A pulse still arrives at the receiver before the C pulse because it encounters the higher sound speed of layer 3. By decreasing the sound speed or increasing the thickness of layer 2, the arrival time of the C pulse could be adjusted to better approximate the triplet pulse spacing observed in Fig. 2.

The identification of low-frequency, subbottom propagation paths as important contributors to the received field is not without precedent. Urick⁷ was among the first to point out the importance of such paths for low-frequency propagation in a shallow water environment. In that work, Urick compared transmission loss data at 63 Hz taken at two sites, one in the Gulf of Mexico, and one off the U.S. East coast. While there was nothing markedly different about the two acoustic environments with respect to water column properties or bathymetry, transmission loss was observed to decay at a much slower rate for the East coast site. For example, at a range of approximately 50 km, the transmission loss differed by as much as 40 dB. In an effort to explain this anomalous difference in transmission loss, the author pointed out that “anomalies of this sort appear to be not uncommon in shallow water at long ranges, where penetration of the earth by low frequency sound to great depths can be expected to occur.”⁷ Velocity profiles of the ocean bottom down to a depth of about 5.5 km revealed major differences in the subbottom structure of the two sites, particularly with regard to the thickness of unconsolidated sediment (900 m versus 3000 m), with the thicker sediment site corresponding to the more gradual decay in transmission loss.

II. RANGE AND DEPTH DEPENDENCE OF FINBACK DOUBLET

In this section, the range and depth dependence of the doublet structure is investigated. The importance of including the shear properties of the seafloor in the acoustic model is also highlighted. As mentioned in the previous section, the channel impulse response function for the Gulf of California environment is computed using OASES.⁴ OASES is a wave number integration acoustic model for seismo-acoustic propagation in a horizontally stratified waveguide. It computes the full-wave solution to the depth-separated wave equation by (1) partitioning the acoustic environment into a set of discrete, range independent layers, (2) solving for an exact analytical expression of the field in each layer, and (3) simultaneously matching the boundary conditions at each interface using a direct global matrix approach.⁴ It is an efficient algorithm for cases involving a significant degree of bottom interaction.

A. The geoacoustic model

The geoacoustic environmental model for the Gulf of California was assembled from Van Andel,⁸ Phillips,⁹ and

Hamilton.¹⁰ The geoacoustic model includes compressional wave speed, c_p , compressional wave attenuation, α_p , shear wave speed, c_s , shear wave attenuation, α_s , and density, ρ , as a function of depth, down to a depth of 10 km. The northern Gulf of California is a shallow water basin with a sediment/subbottom cross section composed of four layers.⁹ The uppermost layer, denoted layer 1, is an unconsolidated sediment supporting a large positive sound-speed gradient to a depth of 1.5 km. This unconsolidated layer is underlain by semi-consolidated and consolidated sediments, denoted layers 2 and 3, of thickness 2 and 4 km, respectively. The main crustal layer or basement, denoted layer 4, begins at a depth of 7.5 km beneath the seafloor.⁹ A detailed account of the assumptions made in constructing the geoacoustic model is given in Appendix A.

The sound-speed dependence in the water column is based on Levitus' database.¹¹ During summer, when the observations depicted in Fig. 2 were made, ocean temperature, and hence sound speed, increases toward the surface. Since sound bends toward the sound-speed minimum, a call emitted by a whale in this environment is refracted downward toward the seafloor. Due to the shallow extent of the basin, a negative sound-speed gradient spans the entire water column, giving rise to a completely bottom interacting pressure field beyond a range of about 1 km.

B. Range dependence of received call: Fluid bottom

Figure 6 depicts a set of range stacked spectrograms for the Gulf of California environment. For the moment, the bottom is modeled as a fluid, i.e., the shear properties of the bottom are ignored. Since the maximum received level changes by tens of dB over a range of 30 km, it is useful to employ a different colormap to represent the spectrogram at each range. For each range strip, the colormap is chosen to represent a dynamic range of exactly 60 dB. For reference, the color scale corresponding to the spectrogram at a range of 17 km is shown at the bottom of the figure. Each range strip depicts frequency content from 10 to 30 Hz for a time window of 25 s. The water depth is 50 m, source depth is 20 m, and the receiver depth is 20 m. The OASES input file corresponding to Fig. 6 is given in Table I, with the exception that all values for shear wave speed (column 3) and shear attenuation (column 5) are set to zero.

At ranges less than 5 km, the water-borne path, consisting of one or more bottom reflections, is the dominant path. At a range of about 5 km, refraction of the source pulse in the higher velocity, unconsolidated sediment begins to contribute to a temporal spread of acoustic energy which precedes the water-borne arrival. As the source range increases beyond 10 km, this component of the received signal is attenuated due to multiple interactions with the lossy sediment. At a range of about 10 km, a distinct early arrival begins to be identifiable. This arrival becomes a distinct contributor to the received field at a range of approximately 17 km, giving rise to the “doublet” structure. At this range, the interpulse delay is observed to be about 5.5–6 s. The first pulse has a SNR_{peak} of approximately 20 dB, or a SNR_{rms} of about 12 dB. The second pulse has a SNR_{peak} of about 30 dB, or a

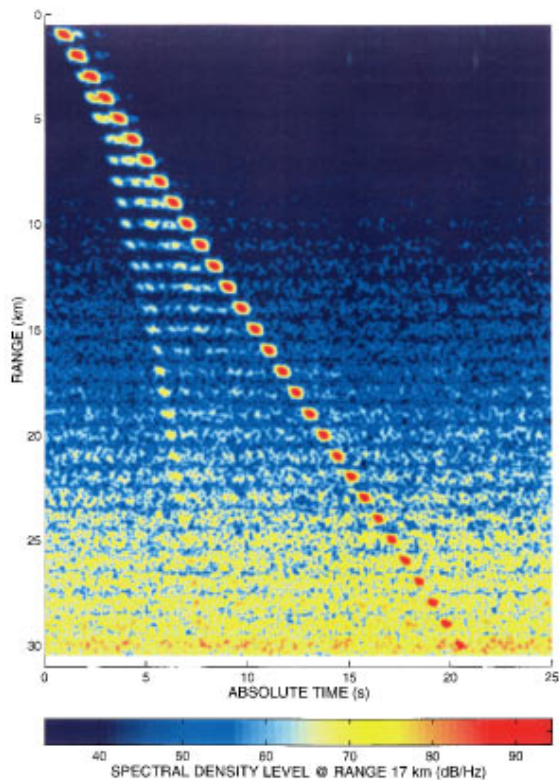


FIG. 6. Range stacked spectrogram depicting spectral density level in dB/Hz for Gulf of California environment with fluid bottom model. Each range strip depicts frequency content from 10 to 30 Hz for a time window of 25 s. The colormap at each range step is chosen to represent a dynamic range of exactly 60 dB. The colormap corresponding to a range of 17 km is shown at the bottom. The whale's depth is 20 m. The receiver depth is 20 m. The channel depth is 50 m. The noise level is 60 dB *re*: 1 μ Pa in 1-Hz band. The bottom penetrating early arrival is visible to a range of 30 km, with a corresponding interpulse spacing of 12 s.

SNR_{rms} of 22 dB. The distinct early arrival is visible to a range of about 25 km, with a corresponding interpulse spacing of 10 s.

C. Range dependence of received call: Elastic bottom

Elastic properties of the seafloor are important to acoustic propagation in shallow water due to the fact that compressional waves propagating in water can be partially converted to shear waves upon interaction with a solid boundary. Figure 7 depicts the set of range stacked spectrograms when shear is added to the geoacoustic model. Again, the colormap has been chosen to represent a dynamic range of exactly 60 dB at each range. Shear waves excited in the bottom will not be detected by a near surface acoustic receiver, as a fluid medium will not support the propagation of shear waves. However, bottom shear acts to enhance the reflection loss incurred with each bottom bounce along the path of the water-borne arrival. The elasticity of the sediment decreases its acoustic impedance relative to a fluid sediment model with the same compressional velocity profile.¹² The importance of sediment shear on the appearance of the received call is made clear by comparing Figs. 6 and 7. At 17 km, the energy in the water-borne pulse, with its multiple bottom bounces, has been reduced significantly relative to that observed in the fluid sediment model. Its detection range has been reduced from greater than 30 to 20

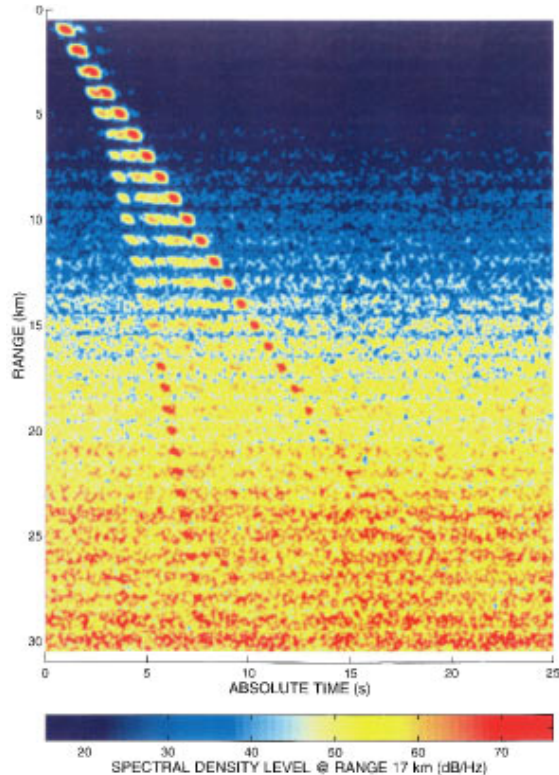


FIG. 7. Range stacked spectrogram depicting spectral density level in dB/Hz for Gulf of California environment with full geoacoustic model including shear. Each range strip depicts frequency content from 10 to 30 Hz for a time window of 25 s. The colormap at each range step is chosen to represent a dynamic range of exactly 60 dB. The colormap corresponding to a range of 17 km is shown at bottom. The whale's depth is 20 m. The receiver depth is 20 m. The channel depth is 50 m. Noise level is 60 dB *re*: 1 μ Pa in 1-Hz band. Shear conversion loss has rendered the water-borne arrival undetectable beyond a range of 20 km. In this case, a doublet is supported for ranges of 17–20 km. In contrast to the fluid sediment model of the previous figure, for ranges of 17–19 km the SNR of each pulse in the doublet is about equal.

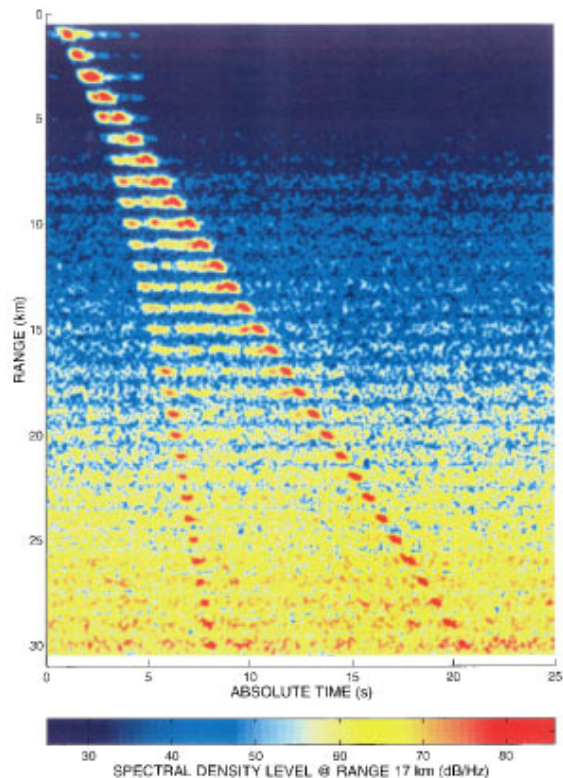


FIG. 8. Range stacked spectrogram depicting spectral density level in dB/Hz for Gulf of California environment with full geoacoustic model including shear. The only difference from the previous figure is that the water depth has been increased from 50 to 100 m. As a result, each pulse is received with a higher SNR. With the increased detection range of the water-borne arrival, the range of support for the doublet has been extended from 17–20 km to 17–30 km.

km. However, the amplitude of the early, bottom-refracted arrival is essentially unaffected by the inclusion of shear properties in the model. At 17 km it is received with a SNR_{peak} of about 20 dB, or a SNR_{rms} of 12 dB. The range of support for the doublet is 17–20 km, limited not by the detection range of the subbottom path, but by that of the waterborne path. Note also that the amplitudes of the two pulses composing the doublet are nearly equal between 17 and 19 km.

The sensitivity of the finback doublet to shear properties in the model points toward the utility of low-frequency whale calls for estimating geoaoustic parameters of seafloor sediments. For example, the finback doublet may be useful in placing an upper bound on the shear wave speed of the unconsolidated sediment layer. If c_s is chosen too large in the geoaoustic model, the resulting excess bottom reflection loss will attenuate the water-borne arrival at a range that is too small to fit the modeled interpulse delay to the data.

Figure 8 illustrates the impact of water depth on the range dependence of the doublet. Shear is included in this geoaoustic model. The channel depth has been increased from 50 to 100 m. The doublet is now easily visible to a range of 30 km. With the deeper channel, two things occur. First, higher-order acoustic normal modes associated with the steep trajectory of the subbottom arrival are more fully excited. Thus, the first pulse is received with a slightly higher signal-to-noise ratio than before. Second, due to the increased water depth, there are fewer bottom interactions along the water borne path. Thus, there is less attenuation due to shear conversion, causing the second pulse to also be received with a higher signal-to-noise ratio at the hydrophone. This increases the detection range of the late arrival. The set of ranges which support doublet propagation is consequently extended from 17–20 km (Fig. 7) to 17–30 km (Fig. 8).

D. The subbottom path

1. Geometry

Travel time calculations summarized in Appendix B support the hypothesis that a 5.5–6 s interpulse delay at a range of 17 km is accounted for by a subbottom path that is partially refracted in the unconsolidated sediment and reflected from the basement interface at critical incidence. The incidence angle is defined as the angle between the wavefront normal and the normal to the interface. The hypothesized trajectory of the subbottom-refracted arrival is depicted in Fig. 9. The mechanism for this path has been confirmed by a sequence of spectrograms computed by building the full geoaoustic model layer by layer, beginning with the unconsolidated sediment, layer 1. These results are depicted in Fig. 10. Note that in this case the same grayscale applies to all four figures and covers a dynamic range of 30 dB. The sequence of spectrograms shows that at the given source range, refraction in the 1500-m-thick unconsolidated sediment layer alone, Fig. 10(a), is insufficient to account for the return of the early arrival to the water column. The early

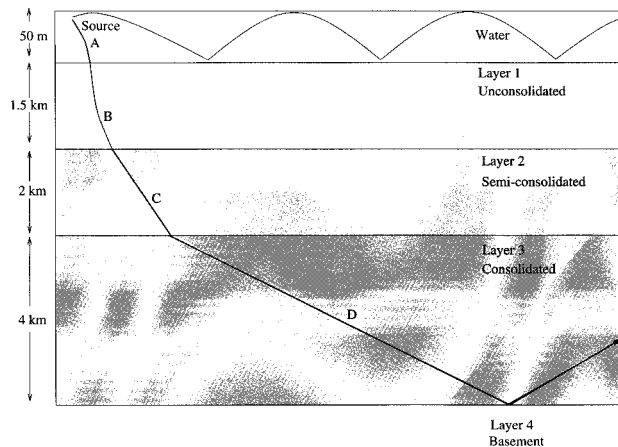


FIG. 9. Propagation paths traversed by the water-borne and sediment-refracted arrivals. For the subbottom path, the positive gradient in the unconsolidated sediment refracts the downward propagating acoustic pulse such that a condition of total internal reflection is satisfied at the basement interface.

arrival is clearly discernible only in the full geoaoustic model which includes the main crustal layer, as seen in Fig. 10(d).

2. Signal-to-noise ratio

In this section, an assumption of plane-wave propagation is used to estimate the contributions of attenuation, reflection, and geometric spreading loss to the total transmission loss along the subbottom path. The expected signal-to-

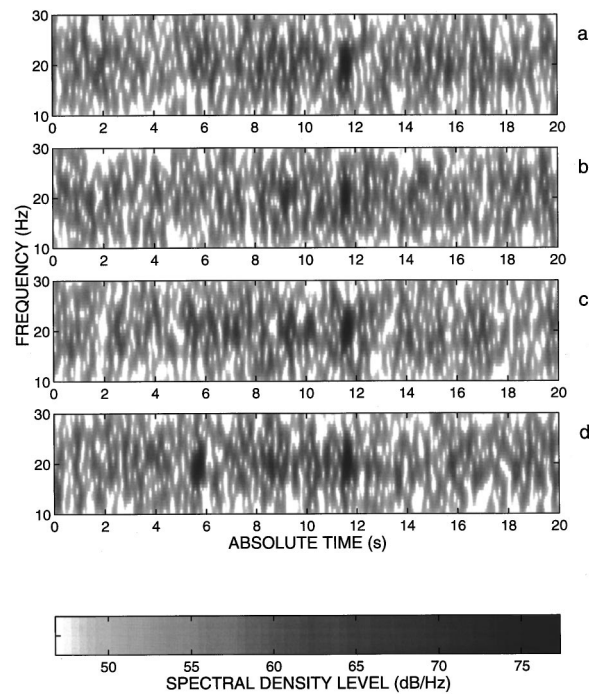


FIG. 10. Sequence of modeled spectrograms depicting the contribution of successive layers in the geoaoustic model: (a) layer 1 only; (b) layers 1 and 2; (c) layers 1, 2, and 3; (d) complete model. The result confirms the hypothesis that refraction due to the positive sound speed gradient in the 1500-m unconsolidated sediment alone is insufficient to account for the appearance of the doublet at the receiver. The doublet appears in the modeled reception only after the basement is included in the geoaoustic model.

TABLE II. Estimate of loss mechanisms in each layer based on an assumption of plane-wave propagation. The source range is 17 km. The total length of the subbottom-refracted path at this range is approximately 22 km. The attenuation loss in each layer is obtained by multiplying the two-way path length in each layer, in compressional wavelengths, by the attenuation coefficient in dB/ λ . The path lengths for layers 1, 2, and 3 used in the calculation were 30λ , 22λ , and 52λ , respectively. The attenuation coefficients used in the calculation were 0.2, 0.2, and 0.11, respectively. Reflection loss corresponds to signal energy lost upon entering/departing the indicated layer. Geometric spreading loss is assumed to be due to spherical spreading. The estimated transmission loss for the subbottom path at this range is 105.5 dB, in good agreement with the OASES model result in Fig. 4.

| Loss mechanism | Layer 1 | Layer 2 | Layer 3 | Total |
|-----------------------|---------|---------|---------|-------|
| Attenuation loss (dB) | 6.0 | 4.4 | 5.7 | 16.0 |
| Reflection loss (dB) | 1.1 | 0.7 | 0.9 | 2.7 |
| Spreading loss (dB) | ... | ... | ... | 86.8 |
| Total (dB) | | | | 105.5 |

noise ratio of the first arrival will then be computed and compared to that obtained from Fig. 4 to yield a coarse consistency check of the OASES model result. The transmission loss, TL, along the subbottom path is defined by¹³

$$TL = \int_{\Gamma} \alpha_p(s) ds + RL + GL, \quad (1)$$

where the integral represents total attenuation loss in dB along the path, Γ , traversed by the acoustic pulse in the subbottom, RL denotes reflection loss in dB, and GL denotes geometric spreading loss in dB. The contributions of each loss term in (1) to the total transmission loss are summarized in Table II. Using Snell's law⁵ to determine the pulse trajectory, the total length of the path through the subbottom is 22 km for a source/receiver separation of 17 km. Given the compressional wave attenuations in Table I, the estimated attenuation loss incurred along this path is calculated to be 16 dB. This estimate is confirmed with OASES by comparing the received level obtained with the geoacoustic model of Table I with that obtained with all attenuations set to zero. Next, the reflection loss at each interface is computed using the formula for the plane-wave reflection coefficient at oblique incidence,⁵

$$\mathfrak{R} = \frac{Z_{j+1} \sin \theta_j - Z_j \sin \theta_{j+1}}{Z_{j+1} \sin \theta_j + Z_j \sin \theta_{j+1}}, \quad (2)$$

where $Z_j = \rho_j c_j$ is the acoustic impedance, ρ_j is the density, c_j is the sound speed, and θ_j is the incidence angle in layer j . The reflection loss at each interface is then given by

$$RL = -10 \log_{10}(1 - |\mathfrak{R}|^2). \quad (3)$$

The total reflection loss along the path is computed to be approximately 2.7 dB. Lastly, geometric spreading loss, assuming spherical spreading for a path length of 22 km, is 86.8 dB. Thus, the total transmission loss along the path assuming plane-wave propagation is estimated to be 105.5 dB. From the passive sonar equation,¹³ the rms-signal-to-rms-noise ratio of the received pulse is defined as

$$SNR_{rms} = SL - TL - NL - 10 \log \Delta f, \quad (4)$$

where SL denotes rms source level in dB, NL denotes noise spectrum level in dB in a 1-Hz band, and Δf is the noise bandwidth. For an rms finback source level of 186 dB, an ambient noise spectral level of 60 dB *re*: $1 \mu\text{Pa}$ in a 1-Hz band, and a noise bandwidth equal to the call bandwidth of 6 Hz, the subbottom pulse in the plane-wave calculation is received with a SNR_{rms} of 12.8 dB. This result should be compared with the SNR_{rms} of the first arrival computed directly from the time series of Fig. 4. From Fig. 4, the SNR_{rms} of the subbottom pulse in the OASES model is computed by

$$SNR_{rms} = 20 \log_{10}(|p_{rms}|^2) - NL - 10 \log_{10} \Delta f. \quad (5)$$

This calculation yields an SNR_{rms} of 10.7 dB, in good agreement with the plane-wave calculation. The 2-dB discrepancy may be related to inaccuracies in the plane-wave reflection loss calculation, e.g., (3) does not account for shear conversion loss at the seafloor. While this calculation is only approximate, it independently confirms that it is plausible for a 20-Hz finback pulse to penetrate to great depths beneath the seafloor and still be detected by a single hydrophone upon returning to the water column.

E. Depth dependence of received call

Given the proximity of the calling individual to the ocean surface, it is important to assess the sensitivity of the detected call to interference effects related to surface reflections. With an estimate of the source departure angle corresponding to the first pulse arrival in the doublet pattern, it is possible to calculate the interference pattern as a function of water depth. The geometry of the calculation is shown in Fig. 11. Using a geometric optics calculation (see Appendix B), it is found that the early arrival detected at a range of 17 km corresponds to a source departure angle of $\theta_d = 13.3^\circ$. Assuming plane-wave propagation as a reasonable first-order approximation, the phase difference, $\Delta\phi$, between the direct and surface reflected paths is given by

$$\Delta\phi = k \left(\frac{z}{\cos \theta_d} \right) (1 + \cos 2\theta_d), \quad (6)$$

where k is the wave number of the medium and z is the source depth. The complex envelope of the net pressure signal propagating downward into the sediment at an angle θ_d , normalized by the peak source pressure, may then be written as

$$p = 1 - e^{j\Delta\phi}. \quad (7)$$

The corresponding interference pattern, which plots the depth dependence of the normalized received level, given by $10 \log pp^*$, where $(*)$ denotes complex conjugate, is depicted in Fig. 12. Notice the deep null at a source depth of 40 m. For this acoustic environment, a finback calling at a depth of 40 m would not be expected to produce a doublet at the receiver. Figure 13 depicts a set of depth stacked spectrograms for the Gulf of California environment at a range of 17 km. Again, each depth strip depicts frequency content from 10 to 30 Hz for a time window of 25 s. Channel depth is 50 m, receiver depth is 20 m, and the source depth is varied from 10 to 50 m. Consistent with the interference pattern shown in Fig. 12, the received levels of the first arrival for

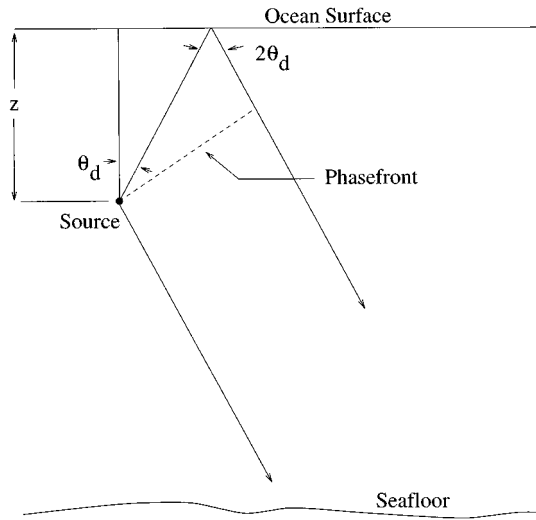


FIG. 11. Geometry of interference cancellation effect between downward propagating ray with source departure angle $-\theta_d$ and surface reflection with departure angle θ_d .

source depths of 10, 20, 30, and 50 m are similar, to within 3 dB. However, at a source depth of 40 m, the first arrival is essentially indistinguishable above the noise floor. Thus, at a range of 17 km, a call emitted at a depth of 20 m is detected as a doublet at the receiver, while a call emitted at a depth of 40 m is detected as a single pulse. Lastly, from Fig. 13, it is observed that in this shallow water environment, the inter-pulse spacing is insensitive to source depth.

III. DISCUSSION

A. Effect on long distance communication between whales

Fine *et al.* discuss evidence that the temporal patterning of fish sounds is of paramount importance in their coding.¹⁴ They suggest that analyses of the swimbladder's role in hearing, in particular its inability to selectively favor any given frequency, support the contention that "the temporal nature of sound, rather than variations in its frequency content, is

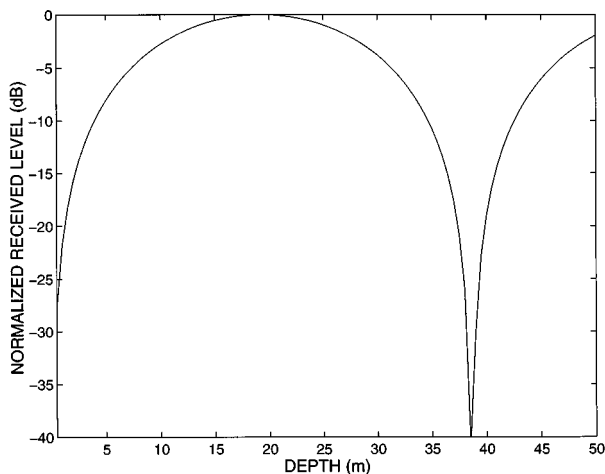


FIG. 12. Interference pattern depicting normalized received level versus source depth. The frequency is 20 Hz. The source departure angle is 13.3° . The channel depth is 50 m.

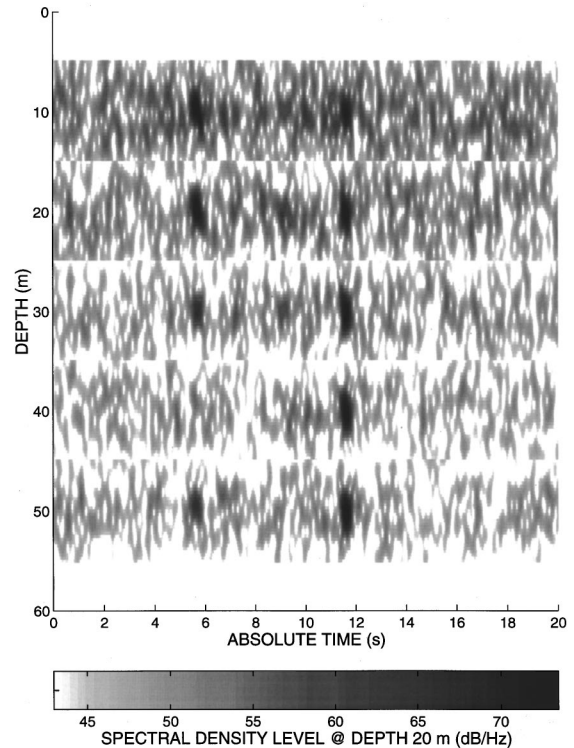


FIG. 13. Depth stacked spectrogram depicting spectral density level in dB/Hz for Gulf of California environment. Each depth strip depicts frequency content from 10 to 30 Hz for a time window of 25 s. The same grayscale applies for all depths. The whale's range is 17 km. The receiver depth is 20 m. The channel depth is 50 m. The noise level is 60 dB *re*: $1 \mu\text{Pa}$ in 1-Hz band. The depth dependence is due to the interference of the (nearly) vertically propagating early arrival and its reflection from the ocean surface. At a range of 17 km, a call emitted at a depth of 20 m would be detected as a doublet at the receiver, while a call emitted at a depth of 40 m would be detected as a single pulse.

important for communication in fishes.”¹⁴ If finbacks rely on temporal cues encoded in patterned 20-Hz pulse sequences for long distance communications, then the findings of this paper present some interesting questions for whale biologists to consider. For instance, biologists might consider whether the periodic insertion of a multipath arrival within a patterned 20-Hz pulse sequence changes the meaning of the sequence. Perhaps, the finback's auditory system is capable of recognizing and discarding such an arrival as redundant. On the other hand, the multipath arrival may provide the animal with some useful information concerning the nature of the seabed below it, perhaps for navigational purposes.

B. Hyperbolic localization

It was shown in Fig. 7 that in a shallow channel it is possible for the detection range of the subbottom penetrating arrival to exceed that of the water-borne arrival. This implies that it may be possible to misinterpret a single 20-Hz finback pulse as being water borne, when it is in fact subbottom penetrating. This finding could have a significant impact on the interpretation of hyperbolic localization results. Hyperbolic fixing methods estimate source position by intersecting two or more hyperbolic loci derived from acoustic pulse travel time differences between pairs of acoustic receivers.¹⁵ Each hyperbola represents a set of candidate positions for a

whale relative to a given pair of receivers. The shape of each hyperbola depends on an assumption for the sound speed of the surrounding medium. If a subbottom penetrating pulse is misinterpreted as a water-borne pulse, and incorrectly associated with the sound speed for water, the shape of the resulting hyperbola will be greatly distorted from its true shape. From Tables I and II, it can be shown that the path integrated sound speed for the subbottom arrival can be as much as 4.2 km/s, almost three times that of water. With such a disparity between the effective sound speeds along the two paths, a hyperbolic fix based on an incorrect path assumption would incur a gross position estimation error.

C. Passive ranging using a single hydrophone or array

When the acoustic environment supports a subbottom-refracted multipath, the interpulse delay may be useful for passive ranging of finbacks using a single hydrophone. Passive localization then becomes possible with only a pair of hydrophones.

The source/receiver geometry for a passive localization experiment based on this premise is depicted in Fig. 14. The source/receiver separation must be sufficient to support doublet propagation, or at least a significant degree of multipath spread. If the animal is sufficiently distant, the geoacoustic model for the site maps the doublet interpulse interval at each receiver to a locus of possible whale positions relative to each receiver. The loci are circles in a perfectly known, isotropic sound-speed environment. In practice, environmental uncertainty will cause these circles to look like annuli of finite thickness. If the same call is detected by each receiver, the set of possible whale locations is narrowed to two points by intersecting the range annuli for receivers R1 and R2. In shallow, coastal waters, it is likely that additional environmental constraints may be available to reject one of these two points. For example, one point may be on land.

If a timebase is recorded at each receiver, it is possible to provide a consistency check for the passive range estimate based on interpulse intervals. With two time-synchronized receivers, a cross correlation of the two measurements will yield the difference in acoustic travel time for each multipath arrival. With the geoacoustic model, this travel time difference can be mapped to a hyperbola which traces a different locus of possible whale locations.¹⁵ This set of locations is independent of that determined from the doublet interpulse delays. Theoretically, the hyperbola should pass through the intersection regions of the range annuli, as shown in Fig. 14. Environmental modeling errors will cause the hyperbola to deviate from the intersection points by a small degree.

IV. CONCLUSION

Using an empirically derived geoacoustic model for the northern Gulf of California, the OASES acoustic propagation model has been used to interpret finback data collected by Thompson *et al.* in 1987. The results support the hypothesis that it is plausible to explain the appearance of the doublet in the Gulf of California finback data in terms of multipath propagation through the seafloor. Of course, these results

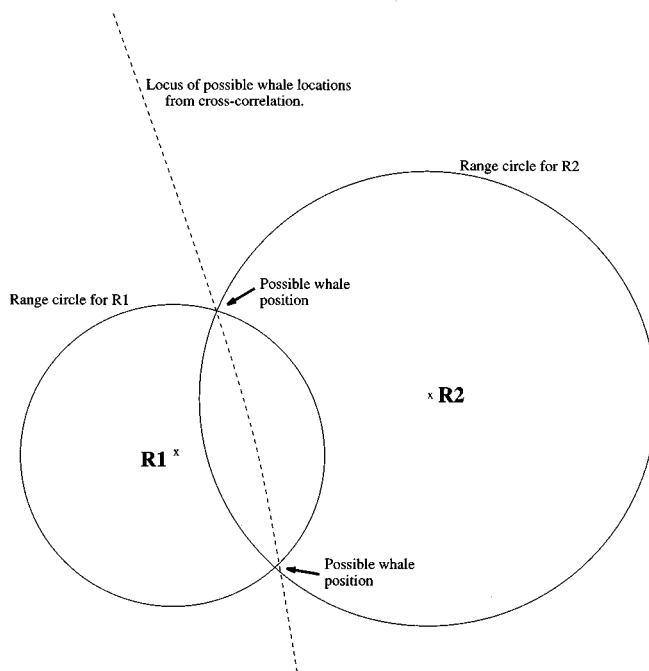


FIG. 14. Source/receiver geometry for passive localization experiment using doublet interpulse delays. Range circles indicate the set of possible whale positions relative to each receiver. In practice, due to environmental uncertainty, circles will be represented by annuli of finite thickness. The hyperbola (dotted line) represents the set of possible whale positions determined from the difference in arrival times between the two receivers. The whale's location will correspond to the intersection of the two circles. The hyperbola should pass very near to each intersection point.

cannot rule out the possibility that finbacks emit doublets. It was found that under moderate ambient noise conditions, the multipath-induced finback doublet may be detectable at ranges up to 30 km. It was also shown that, contrary to intuition, the detection range of the subbottom path could exceed that of the water-borne path. These results have many interesting acoustic and biological implications. For example, it is conceivable that one could receive a singlet from a finback pulsing on the opposite side of an island. Further, the received call was shown to be sensitive to the acoustic properties of the ocean bottom. Future studies could consider the use of the low-frequency vocalizations of *Balaenoptera* whales to bound geoacoustic parameters of the seafloor.

The acoustic model predicts a high degree of variability for the doublet interpulse interval that is caused by multipath. However, this magnitude of variability is supported by observations made by Thompson *et al.* in the Gulf of California. Model predictions for interpulse interval variability in other regions should be calculated and compared with data.³

The interpulse spacing was observed to be insensitive to the whale's depth. However, the signal-to-noise ratio of the first arrival was shown to be very sensitive to depth-dependent interference effects related to surface reflections. The sensitivity of the interpulse spacing to the animal's range points toward its potential as a practical tool for the passive ranging of whales using a single receiver. The geoacoustic model presented in this paper suggests that the range to the finback whose call is depicted in Fig. 2 was 17 km. If the geoacoustic properties of the seafloor remain stationary

over spatial scales on the order of tens of kilometers, a single measurement of the compressional wave speed profile beneath the seafloor in the survey area would be sufficient to yield first-order estimates of the caller's range when a sub-bottom propagation path leading to a doublet is supported. We speculate that finbacks may also rely on the interpulse spacing to estimate the distance to neighboring callers for reasons related to social behavior.

Some biological implications of the findings presented in this paper were suggested. For example, scientists might consider the impact the multipath-induced doublet has on long distance communication between whales based on temporal cues encoded in patterned 20-Hz pulse sequences. Also, due to the strong range dependence of the $A-B$ interval in the multipath-induced doublet, it may be possible to infer swim rate from $A-B$ interval statistics. Finally, it is known that biologists sometimes use song dialects to reveal differences in genetic constitution.¹⁶ In this work, it has been shown that the ocean environment may significantly affect the temporal structure of finback 20-Hz pulse sequences. This suggests that an understanding of the acoustic environment is crucial before differences in sound production can be used for purposes of identifying speciation in *Balaenoptera* whales.

ACKNOWLEDGMENTS

The authors would like to extend their gratitude to Dr. William Watkins of WHOI for encouragement and technical insights shared during many fruitful discussions. We would like to thank Paul Thompson for discussing the details of his Gulf of California finback experiment. The authors also thank Mary E. Putt for reviewing the manuscript and Peter Tyack for his useful comments.

APPENDIX A: OASES MODEL FOR GULF OF CALIFORNIA

Assumptions made in the construction of the Gulf of California geoacoustic model for the Peurto Libertad recording site are outlined. For illustration, Table I depicts the OASES input file used to calculate the pressure time series associated with Fig. 7.

A. Sound speed in water

The speed of sound in the water column was approximated using the Levitus database.¹¹ The coordinates of the Peurto Libertad recording site were estimated to be 30°00'N, 247°12'E. The season was Levitus summer, which represents the mean ocean climatology over the months August, September, and October. Bathymetric data published by Van Andel⁸ indicate that water depths in this area range from 30 to 100 m. For the input file in Table I, a water depth of 50 m was assumed. An n^2 -linear sound-speed profile¹² was fitted to sound-speed values extracted from the Levitus database at depths of 0 and 50 m.

B. Compressional wave speed in bottom

Values for thickness and compressional wave speed in each layer of the model were taken from Phillips.⁹ For the

isovelocity layers, 1a, 2, and 3, these values were determined from Table I-B of Ref. 9 and the seismic velocities reported at the bottom of page 94 of Ref. 9. The expression for the sound-speed dependence in layer 1 was taken directly from the equation at the top of page 97 of Ref. 9.

C. Shear wave speed in bottom

The shear speed profile in layer 1 of the model was approximated by imposing a depth dependence on the ratio c_p/c_s equivalent to that reported in Table VIA of Hamilton.¹⁰ The actual depth dependence of shear speed used in the model is given by

$$c_s(z) = c_p(z) \left[0.23 + 0.0135 \left(\frac{z}{75} \right) \right], \quad (\text{A1})$$

where z is the depth in meters below the seafloor in layer 1. This condition was chosen due to the similarities in total layer thickness and compressional wave speed gradient of the two environments. For shear speeds in layers 1a, 2, and 3, reference was made to the statement on page 1324 of Hamilton: "At compressional wave velocities greater than 3.4 km/s, a $[c_p/c_s]$ ratio 2.0 can be used."¹⁰

D. Compressional wave attenuation

Figure 21 of Van Andel⁸ indicates that surface sediments in the vicinity of the Peurto Libertad recording site consist mainly of sand or silty sand. From Hamilton,¹⁰ the compressional attenuation k_p , specified in units of dB/m/kHz, varies between about 0.25 and 0.60 for surface sands. For most of the figures presented in this paper, a value for $k_p(0)$ of 0.25 dB/m/kHz was adopted. The subbottom refracted arrival was confirmed to be easily visible for $k_p(0)$ as large as 0.45 dB/m/kHz. Data from Van Andel⁸ on the distribution of grain sizes in the northern Gulf support the selection of a k_p value at the low end of the range given by Hamilton. According to Fig. 42 of Van Andel,⁸ sediments around the recording site are dominated by grain sizes in the range $\phi=0.5$ to 1 and $\phi=2$ to 2.5, where $\phi = -\log_2$ (size in mm). Cross referencing this information with Fig. 19 from Hamilton,¹⁰ it is seen that a value of $k_p=0.25$ is not inconsistent with Van Andel's data.

The depth dependence of k_p in layer 1 of the model was assumed to follow a $z^{-1/6}$ power law, in accordance with the discussion on page 1330 of Hamilton.¹⁰ Values for k_p in model layers 1a, 2, and 3 were chosen based on values reported in Table VIA of Hamilton¹⁰ for sedimentary rock and basalt.

Compressional wave attenuation, α_p , in units of dB/wavelength as required by OASES, was obtained from k_p by the conversion

$$\alpha_p(z) = k_p(z) f_c \lambda_p(z), \quad (\text{A2})$$

where f_c is the center frequency of the whale call in kHz and λ_p is the depth-dependent compressional wavelength of the call.

E. Shear wave attenuation

Shear wave attenuations, α_s , were obtained by computing the maximum values allowed under the constraint given by Schmidt¹² for physically meaningful attenuations,

$$\frac{\alpha_s}{\alpha_p} = \frac{3}{4} \left(\frac{c_p}{c_s} \right)^2. \quad (\text{A3})$$

This condition guarantees a bulk modulus that has a positive imaginary component.¹² This condition insures that a pure dilatational wave propagating in the elastic bottom does not increase in amplitude.

F. Density

The density of each layer in the model was determined based on Fig. 26 of Hamilton¹⁰ which relates compressional wave velocity to density. For layers 1, 1a, and 2, the curve labeled ND in Fig. 26 was used. For simplicity, a linear density gradient was assumed for layer 1, with a value of 1.8 g/cm³ at a depth of 0 m below the seafloor and a value of 2.18 g/cm³ at a depth of 1425 m below the seafloor. For layer 3, the basement layer, curve B was used to obtain a density of 2.9 g/cm³, corresponding to a c_p of 6640 m/s.

APPENDIX B: GEOMETRIC OPTICS CALCULATION OF INTERPULSE DELAY TIME

In this appendix, the calculation of the interpulse delay time for the finback doublet is outlined. The calculation proceeds on the assumption that the path of the first arrival is sufficiently refracted in the unconsolidated sediment layer to meet the condition of total internal reflection at the basement interface within a source/receiver separation of 17 km.

Using the theory of geometric optics for acoustic propagation in a medium characterized by a linear sound-speed gradient,¹⁷ we first solve the following set of equations for the travel time of the subbottom arrival, τ_{bot} :

$$\tau_3 = \frac{L_3}{c_3}, \quad L_3 = \sqrt{\Delta x_3^2 + \Delta z_3^2}, \quad \Delta x_3 = \Delta z_3 \tan^{-1} \theta_4, \quad (\text{B1})$$

$$\tau_2 = \frac{L_2}{c_2}, \quad L_2 = \sqrt{\Delta x_2^2 + \Delta z_2^2}, \quad \Delta x_2 = \Delta z_2 \tan^{-1} \theta_3, \quad (\text{B2})$$

$$\tau_1 = -\frac{1}{p_1} \ln \left(\frac{z_{10}}{z_{11}} \frac{1 + \sqrt{1 - z_{11}^2/R_1^2}}{1 + \sqrt{1 - z_{10}^2/R_1^2}} \right), \quad (\text{B3})$$

$$\Delta x_1 = R_1 (\cos \theta_{10} - \cos \theta_{11}), \quad (\text{B4})$$

$$\tau_0 = -\frac{1}{p_0} \ln \left(\frac{z_{00}}{z_{01}} \frac{1 + \sqrt{1 - z_{01}^2/R_0^2}}{1 + \sqrt{1 - z_{00}^2/R_0^2}} \right), \quad (\text{B4})$$

$$\Delta x_0 = R_0 (\cos \theta_{00} - \cos \theta_{01}), \quad (\text{B4})$$

$$\tau_{\text{tot}} = 2(\tau_0 + \tau_1 + \tau_2 + \tau_3), \quad (\text{B5})$$

where θ_4 denotes the incidence angle at the basement, layer 4, θ_3 denotes the incidence angle at layer 3, Δx_i is the horizontal distance traversed by the pulse in layer i , and Δz_i is

the thickness of layer i , $i=0, \dots, 4$ (see Fig. 9). z_{ij} is defined by

$$z_{ij} = R_i \sin \theta_{ij}, \quad (\text{B6})$$

where θ_{ij} denotes the ray angle in the i th layer at depth z_{ij} , and R_i denotes the radius of curvature for the i th layer defined in terms of the Snell invariant, a_i , and the sound-speed gradient, p_i , for that layer as follows:

$$R_i = \frac{1}{a_i p_i}, \quad (\text{B7})$$

$$a_i = \frac{\sin \theta_{ij}}{c(z_{ij})}. \quad (\text{B8})$$

The travel time for the water-borne pulse, τ_{water} may be approximated by

$$\tau_{\text{water}} = \frac{R}{\bar{c}}, \quad (\text{B9})$$

where \bar{c} is the mean sound speed in the water column, and R represents the source range defined by

$$R = 2(\Delta x_0 + \Delta x_1 + \Delta x_2 + \Delta x_3). \quad (\text{B10})$$

Note that $i=0$ corresponds to the water column. The interpulse delay time, $\Delta \tau$, follows directly as

$$\Delta \tau = \tau_{\text{water}} - \tau_{\text{tot}}. \quad (\text{B11})$$

For the geoacoustic model in Table I, the above set of equations can be used to compute the interpulse delay at a range R equal to 17 km. The critical angle at the basement interface is given by $\theta_c = \sin^{-1}(5430/6640) = 54.8^\circ$. Using Snell's law,⁵ the corresponding source departure angle, θ_d , is computed to be 13.3° . For a path which encounters the basement interface at critical incidence, (B5) yields a first pulse travel time of $\tau_{\text{tot}} = 5.3$ s. Accounting for filter delay through the fin source model of 0.5 s, this corresponds to an absolute arrival time for the first pulse of 5.8 s. Similarly, using (B9) and \bar{c} equal to 1526 m/s, the arrival time for the water-borne pulse is found to be 11.6 s. This yields an interpulse delay time of 5.8 s, in good agreement with the result of Fig. 6.

¹P. O. Thompson, L. T. Findley, and O. Vidal, "20-Hz pulses and other vocalizations of fin whales, *balaenoptera physalus*, in the Gulf of California," *J. Acoust. Soc. Am.* **92**, 3051–3057 (1992).

²P. Thompson (personal communication).

³W. A. Watkins, P. Tyack, K. E. Moore, and J. E. Bird, "The 20-Hz signals of finback whales (*balaenoptera physalus*)," *J. Acoust. Soc. Am.* **82**, 1901–1912 (1987).

⁴H. Schmidt, OASES Version 1.7 Application and Upgrade Notes. Technical report, Massachusetts Institute of Technology (1995).

⁵W. S. Burdic, *Underwater Acoustic System Analysis*, 2nd ed. (Prentice-Hall, Englewood Cliffs, NJ, 1991).

⁶F. Tappert, J. L. Spiesberger, and L. Boden, "New full-wave approximation for ocean acoustic travel time predictions," *J. Acoust. Soc. Am.* **97**, 2771–2782 (1995).

⁷R. J. Urick, "Underwater sound transmission through the ocean floor," *Physics of Sound in Marine Sediments*, edited by L. Hampton (Plenum, New York, 1973).

⁸T. H. van Andel, "Recent marine sediments of Gulf of California," *Marine Geology of the Gulf of California*, edited by T. H. van Andel and G. C. Shor, Jr. (American Associates of Petroleum, Geology, 1964), pp. 216–310.

⁹R. P. Phillips, "Seismic refraction studies in Gulf of California," *Marine Geology of the Gulf of California*, edited by T. H. van Andel and G. C.

- Shor, Jr. (American Association of Petroleum, Geology, 1964), pp. 90–121.
- ¹⁰E. L. Hamilton, “Geoacoustic modeling of the sea floor,” *J. Acoust. Soc. Am.* **68**, 1313–1340 (1980).
- ¹¹S. Levitus, “A climatological atlas of the world ocean,” NOAA Prof. Paper **13** (1982).
- ¹²F. Jensen, W. Kuperman, M. Porter, and H. Schmidt, *Computational Ocean Acoustics* (AIP Press, Woodbury, NY, 1994).
- ¹³R. J. Urick, *Principles of Underwater Sound* (McGraw-Hill, New York, 1983), 3rd ed.
- ¹⁴M. Fine, H. Winn, and B. Olla, “Communication in fishes,” In *How Animals Communicate*, edited by T. A. Sebeok (Indiana U.P., Bloomington, IN, 1978).
- ¹⁵J. L. Spiesberger and K. M. Fristrup, “Passive localization of calling animals and sensing of their acoustic environment using acoustic tomography,” *Am. Nat.* **135**, 107–153 (1990).
- ¹⁶M. C. Baker, “Genetic structure of two populations of white-crowned sparrows with different song dialects,” *Condor* **76**, 351–356 (1974).
- ¹⁷I. Tolstoy and C. S. Clay, *Ocean Acoustics: Theory and Experiment in Underwater Sound* (American Institute of Physics, New York, 1987).

Error analysis in acoustic elastography. I. Displacement estimation

Mehmet Bilgen and Michael F. Insana

Department of Radiology, University of Kansas Medical Center, Kansas City, Kansas 66160

(Received 22 May 1996; accepted for publication 21 September 1996)

Correlation between acoustic echo signals obtained before and after application of an external compressional force provides information about the internal deformation of an elastic medium. In this paper, the variance for displacement estimated from an echo data segment and the covariance between two windowed segments that may overlap are derived. The signal and noise spectra are Gaussian and independent. The dependence of the displacement variance on input signal-to-noise ratio (SNR_i), time-bandwidth product W , fractional bandwidth Y^{-1} , and the rate of displacement variation with depth a is investigated. The relationship between a and the other experimental parameters is crucial for understanding how signal decorrelation affects displacement error. The expression for displacement variance reduces to the Cramer-Rao lower bound result when $a=0$ and $W \gg 1$ for both bandpass and base-band signals. When $a \neq 0$ displacement variance increases, and there is an optimal window length at $W = \sqrt{20/a} \sqrt{1+Y^2}$ for which the displacement variance is minimum. Narrow-band signals produce larger errors than broadband signals for long observation windows when $a \neq 0$ and just the opposite when $a=0$. Errors are greatest for displacements estimated from the envelope of narrow-band signals. Finally, a general expression for the minimum displacement variance for arbitrary signal and noise spectra is derived as a function of the experimental parameters. These results form a framework for analyzing strain estimates in elastography, the subject of a companion paper. © 1997 Acoustical Society of America. [S0001-4966(97)03602-3]

PACS numbers: 43.80.Cs, 43.80.Ev, 43.80.Qf [FD]

LIST OF SYMBOLS

| | | | |
|---------------|---|------------------------------------|--|
| a_i | linear compression parameters for observation windows 1 and 2, where $a_i = s_i / (1 - s_i)$ and $i = 1, 2$ | L_s | length scale for strain variation |
| A, B | special functions used in Appendix B | n_I, n_{II} | additive noise processes for the pre- and post-compression signals |
| B_z | bandwidth for flat bandpass spectrum | p, q | special functions used in Eq. (19) |
| c | speed of sound | r_I, r_{II} | pre- and post-compression ultrasonic echo signals |
| D, \hat{D} | tissue displacement and its estimate | s, \hat{s} | tissue strain and its estimate, where $\hat{s} = (\hat{D}_2 - \hat{D}_1) / \Delta Z$ |
| D_t | time delay | SNR _i | input signal-to-noise ratio = σ_f^2 / σ_n^2 |
| f | reflectivity profile as determined by the acoustic scattering structure of the medium | W | time-bandwidth product = Z/L |
| g | a function of experimental parameters in the numerator of the covariance expression | Y | inverse of the fractional bandwidth = $(1/k_0 L)^{-1}$ |
| G_f, G_n | power spectral density functions for signal and noise processes | z | spatial variable along the ultrasonic beam axis |
| h | point spread function of the ultrasonic imaging system | $Z, \Delta Z$ | observation window length and separation between window centers |
| k | spatial frequency variable | β | general (nonlinear) tissue displacement |
| L_f, L_h, L | correlation lengths characteristic of the reflectivity profile f , acoustic pulse h , and the convolution $h \otimes f$ | ϕ | cross-correlation function |
| | | σ_f^2, σ_n^2 | signal and noise variances |
| | | τ | spatial cross-correlation variable |
| | | $\Delta \tilde{Z} = \Delta Z / Z,$ | |
| | | $\tilde{\tau} = \tau / Z,$ | |
| | | $\tilde{D} = D / Z,$ | |
| | | $\tilde{\hat{D}} = \hat{D} / Z$ | are dimensionless quantities |

INTRODUCTION

Time-delay estimation is a problem of great importance in many areas of research.^{1,2} This paper discusses the related

topic of displacement estimation, where ultrasonic echo signals are analyzed to estimate movement within a compressed viscoelastic medium. In acoustic elastography, time-delay measurements D_t are related to local displacements D

through the speed of sound c according to the expression $D = cD_t/2$. Displacement is estimated by applying correlation techniques to windowed segments of echo waveforms obtained before and after compression.

Figure 1 shows typical pre-compression (solid line) and post-compression (dotted line) signals obtained in an elastographic experiment. The echo signals in the figure are segmented into overlapped windows of length Z . The second window has been shifted a distance ΔZ , where $0 \leq \Delta Z \leq Z$. Assuming that the displacement varies linearly with position, the pre-compression $r_I(z)$ and post-compression $r_{II}(z)$ echo waveforms within the first observation window are modeled as

$$\begin{aligned} r_I(z) &= h(z) \otimes f(z) + n_I(z); \\ r_{II}(z) &= h(z) \otimes f((1+a_1)z + D_1) + n_{II}(z) \end{aligned} \quad 0 \leq z \leq Z, \quad (1)$$

where f is the reflectivity function that is determined by the internal scattering structure of the medium, h is the point spread function of a broadband ultrasonic imaging system, n_I and n_{II} are additive, signal-independent noise processes, z is the position along the axis of the sound beam, and \otimes denotes convolution. The subscript 1 indicates the first of two observation windows. The effects of compressing the medium are represented by a shifting and scaling of the axial reflectivity profile. The shifting parameter D_1 accounts for the displacement accumulated between the compressor and the center of the window, and includes the effects of any prior compressions. The scaling parameter a_1 defines the rate at which the displacement varies along z . The linear displacement assumption is related to the more general model of tissue deformation $f(z + \beta(z))$ described previously³ by the series expansion $\beta(z) = D + az + bz^2 \dots$. In this model, the parameter a is given in terms of the applied strain s as $a = s/(1-s) \approx s$ for small s . Notice that a is the input strain parameter that modifies the signal and ultimately determines the quality of the strain estimate \hat{s} .

Similarly, for the second observation window

$$\begin{aligned} r_I(z) &= h(z) \otimes f(z) + n_I(z), \\ r_{II}(z) &= h(z) \otimes f((1+a_2)z + D_2) + n_{II}(z) \end{aligned} \quad \Delta Z \leq z \leq Z + \Delta Z, \quad (2)$$

where a_2 and D_2 are the corresponding displacement parameters.

We assume that (1) $f(z)$ and $n(z)$ are weakly stationary, bandlimited, zero mean random processes that are uncorrelated with each other. The corresponding power spectral densities are $G_f(k)$ and $G_n(k)$, respectively. (2) The gate length Z is large compared to the correlation length of the tissue scattering structure L_f and the length of the acoustic pulse L_h . (3) The pulse bandwidth L_h^{-1} is large so that $h(z) \approx \delta(z)$ in Eqs. (1) and (2) and therefore $r(z) = f(z) + n(z)$. (4) The input signal-to-noise ratio SNR_i is large and a is small to ensure that sidelobe amplitudes of the cross-correlation function between $r_I(z)$ and $r_{II}(z)$ are smaller than the main lobe.⁴

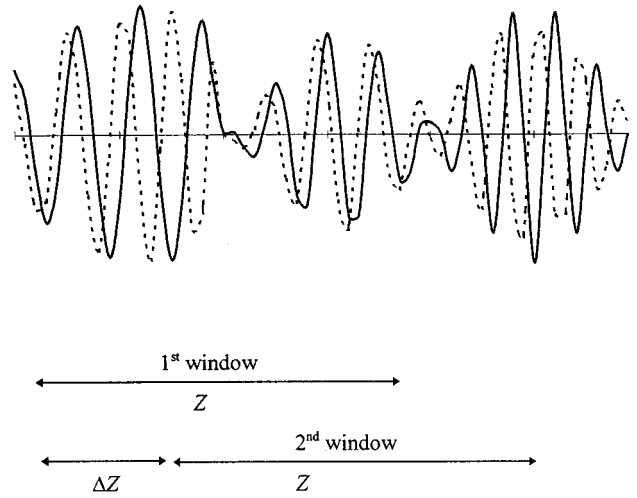


FIG. 1. Examples of a precompression echo signal $r_I(z)$ (solid line) and postcompression echo signal $r_{II}(z)$ (dotted line) are illustrated. Observation windows of length Z are overlapped by an amount $Z - \Delta Z$.

In this paper, our goal is to derive the mean of the displacement difference

$$E[\hat{D}_2 - \hat{D}_1] \quad (3)$$

and the covariance between estimated displacements

$$\text{cov}(\hat{D}_1, \hat{D}_2) = E[(\hat{D}_1 - D_1)(\hat{D}_2 - D_2)] \quad (4)$$

in terms of the important experimental parameters when tissue motion varies linearly with position. The variance of the displacement estimates in each window is obtained by setting $D_1 = D_2$ in Eq. (4). As discussed in the companion paper,⁵ the displacement covariance fully characterizes the variance of the strain estimate $\hat{s} = (\hat{D}_2 - \hat{D}_1)/\Delta Z$ in elastography. Furthermore, the tradeoff between elastographic resolution and strain noise is determined by the displacement covariance through the window separation ΔZ . Consequently, displacement covariance is central to understanding the statistical properties of strain images.

Céspedes *et al.*⁶ investigated the axial strain estimation error from time-delay measurements. They formulated the strain variance in terms of time-delay variance and covariance. A lower bound on the strain variance is given by assuming the ideal conditions of large window length and infinitesimal strain, and a covariance function that decays linearly with window separation for $0 \leq \Delta Z \leq Z$. In this work, the displacement variance and covariance are rigorously derived for the more realistic conditions of finite strain and arbitrary window length.

The paper is structured as follows. In Sec. I, we describe the problem of estimating displacements by cross-correlating the pre- and post-compression echo signals, and we introduce various approximations to simplify the derivation of the displacement covariance. In Sec. II, we provide a covariance expression for echo signals with bandpass Gaussian spectra. We present numerical calculations in Sec. III that illustrate

how changes in experimental parameters affect displacement variance and covariance. Those results are discussed in Sec. IV. Finally, a Gaussian approximation of a sinc(x) function is described in Appendix A, and a general minimum-variance expression for the displacement variance is derived in Appendix B.

I. DISPLACEMENT COVARIANCE

In this section, we derive the covariance between displacements estimated from echo data in two neighboring observation windows that might overlap. The analysis framework parallels that of Azaria and Hertz⁷ who studied time-delay estimation for constant delay ($a=0$). The cross-correlation function between the pre- and post-compression echo signals, r_I and r_{II} is

$$\phi_i(\tau_i) = \int_{-Z/2+(i-1)\Delta Z}^{Z/2+(i-1)\Delta Z} dz r_I(z+\tau_i)r_{II}(z) \quad \text{for } i=1,2, \quad (5)$$

where the subscript $i=1$ denotes the window on the left in Fig. 1 and $i=2$ denotes the window on the right. The displacement estimate \hat{D} is given by τ at the peak of the cross-correlation function, i.e.,

$$\phi_i(\hat{D}_i) = \max_{\tau} \phi_i(\tau_i). \quad (6)$$

Within the limits of the above assumptions, the cross-correlation function may be divided into two terms:

$$\phi_i(\tau_i) = \phi_{iff}(\tau_i) + \phi_{ifn}(\tau_i), \quad (7)$$

where

$$\phi_{iff}(\tau_i) = \int_{-Z/2+(i-1)\Delta Z}^{Z/2+(i-1)\Delta Z} dz f(z+\tau_i)f((1+a_i)z+D_i) \quad (8)$$

and

$$\phi_{ifn}(\tau_i) = \int_{-Z/2+(i-1)\Delta Z}^{Z/2+(i-1)\Delta Z} dz \{f(z+\tau_i)n_{II}(z) + n_I(z+\tau_i) \times f((1+a_i)z+D_i) + n_I(z+\tau_i)n_{II}(z)\}. \quad (9)$$

$\phi_{iff}(\tau_i)$ can be expanded in Taylor series up to second-order around $\tau_i=D_i$, i.e., $\phi_{iff}(\tau_i) \approx \phi_{iff}(D_i) + \frac{1}{2}(\tau_i - D_i)^2 \phi_{iff}''(D_i)$, since $\phi_{iff}'(D_i) \triangleq [d\phi_{iff}/d\tau_i]_{\tau_i=D_i} = 0$. Assuming variations in $\phi_{iff}(\tau_i)$ about the expected value are small, then $\phi_{iff}''(D_i) \approx E[\phi_{iff}''(D_i)]$. Let \hat{D}_i be the estimate of D_i that maximizes $\phi_i(\tau_i)$. Substituting the expansion into Eq. (7), differentiating with respect to τ_i , setting the result equal to zero, and rearranging terms, the displacement error $\hat{D}_i - D_i$ can be expressed as⁷

$$\hat{D}_i - D_i = - \frac{\phi_{ifn}'(\hat{D}_i)}{E[\phi_{iff}''(D_i)]}. \quad (10)$$

The denominator is calculated for the i th window from the cross-correlation of the noise-free pre- and postcompression echo signals evaluated at the true displacement D_i .

From Eq. (10) and assumption 1, the expected deviation is

$$E[\hat{D}_i - D_i] = - \frac{E[\phi_{ifn}'(\hat{D}_i)]}{E[\phi_{iff}''(D_i)]} = 0, \quad (11)$$

which shows that \hat{D}_i is an unbiased estimate of D_i . It should be noted that the interpolation required to locate the cross-correlation peak using sampled data can introduce a bias.^{8,9} Also from Eq. (10),

$$\begin{aligned} \text{cov}(\hat{D}_1, \hat{D}_2) &= E[(\hat{D}_1 - D_1)(\hat{D}_2 - D_2)] \\ &= \frac{E[\phi_{ifn}'(\hat{D}_1)\phi_{ifn}'(\hat{D}_2)]}{E[\phi_{iff}''(D_1)]E[\phi_{iff}''(D_2)]}. \end{aligned} \quad (12)$$

The numerator and denominator in Eq. (12) can be calculated separately. The numerator is written as

$$E[\phi_{ifn}'(\hat{D}_1)\phi_{ifn}'(\hat{D}_2)] = \left[\frac{d^2}{d\tau_2 d\tau_1} g(\tau_1, \tau_2, D_1, D_2, \Delta Z, Z, a_1, a_2, G_f, G_n) \right]_{\tau_1=\hat{D}_1, \tau_2=\hat{D}_2}, \quad (13)$$

where

$$\begin{aligned} g(\tau_1, \tau_2, D_1, D_2, \Delta Z, Z, a_1, a_2, G_f, G_n) &= Z^2 \int_{-\infty}^{\infty} \int_{-\infty}^{\infty} dk_1 dk_2 \exp[-jk_1(\tau_2 - \tau_1)] \{ [G_f(k_1)G_n(k_2) \\ &+ G_n(k_1)G_n(k_2)] \text{sinc}^2[(k_1+k_2)Z/2] \exp[-j(k_1+k_2)\Delta Z] \\ &+ G_n(k_1)G_f(k_2) \text{sinc}[(k_1+(1+a_1)k_2)Z/2] \text{sinc}[(k_1+(1+a_2)k_2)Z/2] \\ &\times \exp[-j(k_1+a_2k_2)\Delta Z - jk_2(D_2 - D_1)] \} \end{aligned} \quad (14)$$

is a function of important parameters related to intrinsic properties of the medium and instrumentation. G_f and G_n represent the signal and noise spectra. The factors in the denominator of Eq. (12) can be written as

$$E[\phi''_{iff}(D_i)] = Z \left[\frac{d^2}{d\tau_i^2} \int_{-\infty}^{\infty} dk G_f(k) \text{sinc}(ka_i Z/2) \right. \\ \left. \times \exp[-jk(\tau_i - D_i)] \right]_{\tau_i = D_i} \quad \text{where } i = 1, 2. \quad (15)$$

Equation (15) clearly shows that the effect of the rectangular window on the cross-correlation function is to introduce a low-pass filter via the sinc function. However, if the displacement is constant along z , i.e., $a_i = 0$, then the signal is ergodic and the correlation function is not filtered. Variances are obtained from Eq. (12) by setting $i = 1 = 2$. Using the equations above, we give the lower bound on displacement variance in Appendix B for general signal and noise spectra.

It should be noted that once Eq. (14) is substituted into Eq. (13), the displacement covariance, Eq. (12), becomes a function of estimated displacements \hat{D}_1 and \hat{D}_2 . Variances in some time-delay estimation algorithms can depend on the unknown delays. The performance of such algorithms and their dependence on the unknown delays have been discussed in the literature.⁹ In our analysis presented below, it turns out that the covariance expression depends on unknown displacements through the difference $\hat{D}_2 - \hat{D}_1$.

II. CALCULATIONS FOR GAUSSIAN SPECTRA

In this section, we calculate the variance and covariance for displacements estimated from signals having bandpass and base-band Gaussian spectra. Examples of bandpass signals are the rf echo signal $r(z)$ and its analytic signal representation. Examples of base-band signals are the echo envelope and the reflectivity profile $f(z)$. We assume the bandpass Gaussian form

$$G_l(k) = \frac{\sigma_l^2}{2} \{ \exp[-(k + k_0)^2 L^2] \\ + \exp[-(k - k_0)^2 L^2] \}, \quad l = f, n, \quad (16)$$

where σ_l^2 is proportional to the variance of the random process l and k_0 is the center frequency of the spectra. L denotes the correlation length of the process, either bandpass or base-band, and $1/L$ can be considered as a measure of bandwidth. The envelope of the signal is described by the base-band spectrum and obtained by setting $k_0 = 0$ in Eq. (16).

It is convenient to work with the following dimensionless parameters:

$$\Delta\tilde{Z} = \Delta Z/Z, \quad \tilde{\tau} = \tau/Z, \quad \tilde{D} = D/Z, \quad W = Z/L, \quad Y = k_0 L. \quad (17)$$

The last two parameters have important implication for error estimation. W is the spatial equivalent of the time-band product; it specifies the number of independent samples per observation window. Y^{-1} is the fractional bandwidth of the echo signal. Since the bandwidth of the tissue reflectivity profile is usually much greater than that of the ultrasonic imaging system, i.e., $L_f^{-1} \gg L_h^{-1}$, the time-bandwidth product and fractional bandwidth of echo signals are limited by the acoustic pulse length, i.e., $W = Z/L_h$ and $Y = k_0 L_h$. To investigate

properties of the echo envelope, we set $W = Z/L_h$ and $Y = 0$. The motion of the compressed medium can also be studied independent of the ultrasonic system properties, as in this paper, by setting $W = Z/L_f$ and $Y = 0$. Therefore, the interpretation of L in Eq. (17) depends on the form of the data.

Using the approximations of Appendix A, we evaluate the integrals in Eqs. (14) in terms of the dimensionless parameters defined in Eq. (17). The result is

$$g(\tilde{\tau}_1, \tilde{\tau}_2, \tilde{D}_1, \tilde{D}_2, \Delta\tilde{Z}, a_1, a_2, W, Y, \text{SNR}_i) \\ = \frac{\sigma_f^4 W^2 e^{-2Y^2}}{4\pi \text{SNR}_i} \sum_{\substack{m=-1,1 \\ n=-1,1}} \left[\frac{[1 + (1/\text{SNR}_i)]}{q_3} \right. \\ \left. \times \exp\left\{ \frac{q_2^2}{q_1^2} + \frac{q_4}{q_3} \right\} + \frac{1}{p_3} \exp\left\{ \frac{p_2^2}{p_1^2} + \frac{p_4}{p_3} \right\} \right], \quad (18)$$

where

$$\text{SNR}_i = \frac{\sigma_f^2}{\sigma_n^2}, \quad (19a)$$

$$q_1^2 = 4(1 + 0.1W^2), \quad (19b)$$

$$q_2 = W \left[j\Delta\tilde{Z} + 2n \left(\frac{Y}{W} \right) \right], \quad (19c)$$

$$q_3^2 = 4(1 + 0.2W^2), \quad (19d)$$

$$q_4 = W^2 q_1^2 [j(\tilde{\tau}_2 - \tilde{\tau}_1 + \Delta\tilde{Z}) + 2m(Y/W) \\ - 0.1W^2(q_2/q_1^2)]^2, \quad (19e)$$

$$p_1^2 = 4\{1 + 0.05[(1 + a_1)^2 + (1 + a_2)^2]W^2\}, \quad (19f)$$

$$p_2 = W \left[j(\tilde{D}_2 - \tilde{D}_1 + (1 + a_2)\Delta\tilde{Z}) + 2n \left(\frac{Y}{W} \right) \right], \quad (19g)$$

$$p_3^2 = 4[p_1^2 + 0.1W^2 + 0.0025(a_1 - a_2)^2 W^4], \quad (19h)$$

$$p_4 = W^2 p_1^2 [j(\tilde{\tau}_2 - \tilde{\tau}_1 + \Delta\tilde{Z}) + 2m(Y/W) \\ - 0.05W^2(p_2/p_1^2)(2 + a_1 + a_2)]^2. \quad (19i)$$

Similarly, the correlation function for the reflectivity profile in Eq. (15) may be calculated for the first and second window:

$$E[\phi_{iff}(\tau_i, D_i, a_i, W, Y)] \\ = \frac{1}{2\sqrt{\pi}} \frac{\sigma_f^2 W e^{-Y^2}}{\sqrt{1 + 0.05a_i^2 W^2}} \\ \times \text{Re} \left[\exp \left\{ - \frac{W^2 [j(\tilde{D}_i - \tilde{\tau}_i) + 2(Y/W)]^2}{4(1 + 0.05a_i^2 W^2)} \right\} \right], \quad (20)$$

where $\text{Re}[\cdot]$ indicates the real part of the complex argument. The displacement covariance of Eq. (12) is obtained by combining Eqs. (13), (18), and the second derivative of Eq. (20). These are tedious calculations and the resulting expression is too lengthy to give explicitly. However, for base-band signals $Y = 0$, a concise expression for the displacement variance can be obtained by substituting $\tilde{D}_1 = \tilde{D}_2$ and $\Delta\tilde{Z} = 0$ into the covariance expression:

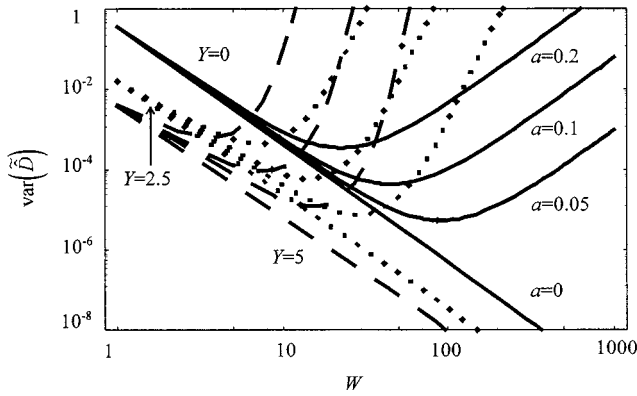


FIG. 2. Displacement variance is plotted as a function of the time-bandwidth product W for the four different values of a indicated on the graph. Solid lines represent base-band results, $Y=0$; dotted lines are bandpass results for $Y=2.5$; and dashed lines are bandpass results for $Y=5.0$. In all cases, $\text{SNR}_i=10$ and the minimum variance occurs at $W = \sqrt{20/a}\sqrt{1+Y^2}$.

$$\begin{aligned} \text{var}(\tilde{D}_i) &= E[(\tilde{D}_i - \bar{D}_i)^2] \\ &= \frac{2(1+0.05a_i^2W^2)^3}{W^2\text{SNR}_i} \left\{ \left(1 + \frac{1}{\text{SNR}_i}\right) \frac{(1+0.1W^2)}{(1+0.2W^2)^{3/2}} \right. \\ &\quad \left. + \frac{[1+0.1(1+a_i)^2W^2]}{[1+0.2(1+a_i+0.5a_i^2)W^2]^{3/2}} \right\}. \end{aligned} \quad (21)$$

Equation (21) offers a considerable amount of intuition about displacement errors, as discussed in Sec. IV.

III. RESULTS

Displacement variance and covariance are described in this section with respect to their dependence on the experimental parameters SNR_i , a , W , and Y .

A. Displacement variance

Displacement variance $\text{var}(\tilde{D}_i)$ is plotted as a function of window length (via W) in Fig. 2, where we have fixed $\text{SNR}_i=10$. The solid lines are the base-band results of Eq. (21), where $Y=0$, for four different scaling parameters $a=0.0, 0.05, 0.1, \text{ and } 0.2$. When $a=0$, the medium is not strained within the windowed echo segment, and the lowest variance is obtained with the longest observation window (Z) and largest bandwidth ($1/L$) achievable. However, for $a>0$, the minimum variance is achieved at the window length $Z = \sqrt{20L/a}$. Above this value, displacement error is dominated by the loss of signal coherence. Removing the strain from $r_{II}(z)$ before cross correlation with $r_I(z)$, i.e., companding, maximizes signal coherence, particularly for large Z , and results in less displacement error.⁵

The dotted and dashed curves in Fig. 2 show the corresponding displacement variances for bandpass signals where $Y=2.5$ and $Y=5.0$, respectively. Increasing Y for fixed pulse length is equivalent to shifting the center frequency of the ultrasonic pulse k_0 to higher values. Higher k_0 yields lower displacement variance at all window lengths when $a=0$. [Note that the three straight lines in Fig. 2 correspond to

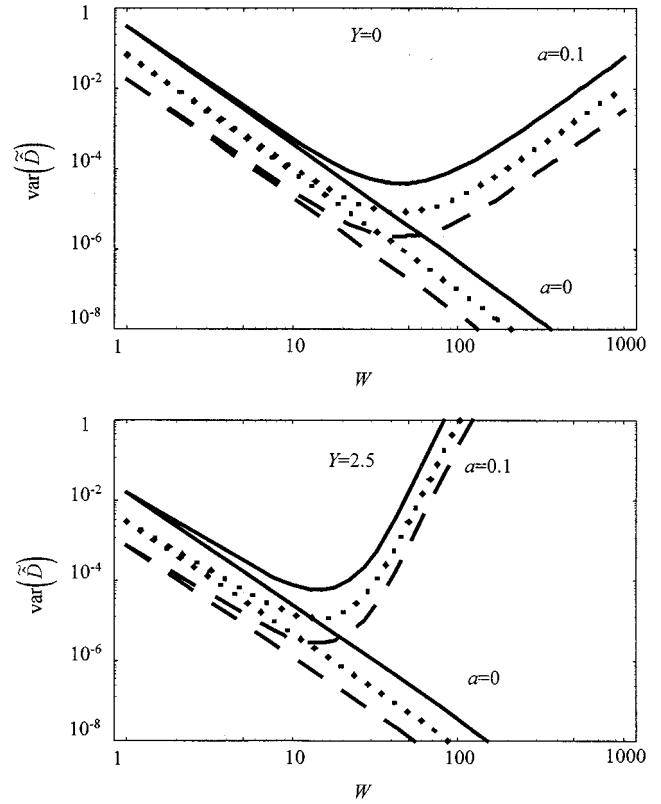


FIG. 3. Displacement variance versus W for three values of $\text{SNR}_i=10$ (solid), 50 (dotted), and 200 (dashed). Results for base-band signals (top) and bandpass signals (bottom) are presented.

$a=0$, where $Y=0$ (solid line), $Y=2.5$ (dotted line), and $Y=5.0$ (dashed line).] As a increases, however, greater displacement error is found for larger Y values, and minimum variance is obtained at

$$Z = \sqrt{20L/a}\sqrt{1+Y^2}. \quad (22)$$

Figure 3 illustrates how displacement variance depends on SNR_i for base-band signals (top) and bandpass signals (bottom). The solid lines are for $\text{SNR}_i=10$, the dotted lines are for $\text{SNR}_i=50$, and the dashed lines are for $\text{SNR}_i=200$. In each case, the error is inversely proportional to SNR_i for all W . However, as shown below, the error is inversely proportional to SNR_i^2 for $\text{SNR}_i<10$ (not shown in Fig. 3).

B. Displacement covariance

The covariance between displacements estimated in two overlapping windows is plotted in Fig. 4 as a function of $\Delta\tilde{Z}$. The results are calculated for $\text{SNR}_i=10$, $\tilde{D}_1=\tilde{D}_2$, and $\tilde{D}_1 = \tilde{D}_2$, therefore the covariance equals the variance at $\Delta\tilde{Z}=0$ where the windows overlap 100%. The upper curves (thick lines) are the base-band results and the lower curves (thin lines) are the bandpass results. As the overlap in the data for the two windows is reduced, so too is the covariance. At $\Delta\tilde{Z}\geq 1$, where the windows are completely uncorrelated, the covariance should be zero. However, examination of Fig. 4 shows that the long tails on the Gaussian approximations to the sinc functions (Appendix A) produce a small error. The

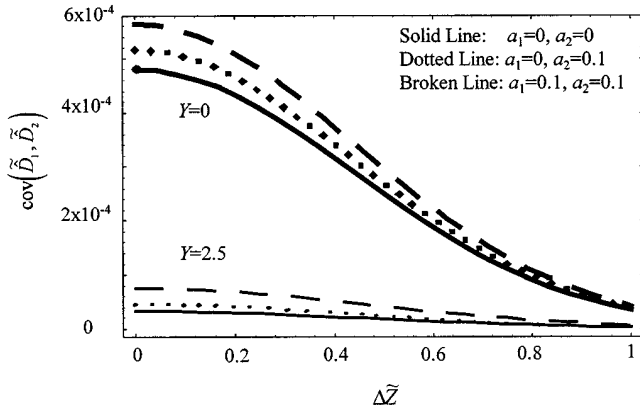


FIG. 4. Displacement covariance is plotted as a function of the window separation $\Delta\bar{Z} = \Delta Z/Z$. The displacements are $\bar{D}_2 = \bar{D}_1$ and $\bar{D}_2 = \bar{D}_1$. The scaling parameter a_1 applies to the first observation window and a_2 applied to the second window. However, as $\Delta\bar{Z} \rightarrow 0$, $a_2 \rightarrow a_1$ and $D_2 \rightarrow D_1$.

figure also shows that straining the medium within one or both windows ($a_i > 0$) produces a slight increase in displacement covariance.

IV. DISCUSSION

The foundation of this analysis is Eq. (10), which provides valuable intuition about the nature of displacement errors. For example, the denominator of Eq. (10) is the expected second derivative with respect to τ of the cross-correlation function between the pre- and post-compression reflectivity profiles $f(z)$ evaluated at $\tau = D$. The second derivative is monotonic with the curvature or sharpness of the correlation peak. Large curvatures produce small deviations in the displacement estimate from the true value. For jointly stationary processes, e.g., $a = 0$, sharp correlation peaks are consistent with long observation windows and high-frequency sound waves.

The numerator of Eq. (10) is the first derivative of the noise and noise-signal cross terms, $\phi'_{ifn}(\hat{D}_i)$. The expected value of the derivative is zero only at the correlation peak $\tau_i = D_i$. As SNR_i decreases, spurious peaks in the cross-correlation function occur where the magnitude of the numerator is large, and that predicts an increase in displacement error.

Equation (21) provides additional insights into the nature of errors. This expression is the displacement variance for base-band signals, and, while it does not include the effects of k_0 as with the full bandpass expression, it does clearly describe the effects of Z , L , a , and SNR_i . Also the base-band expression is isomorphic with the bandpass expression as seen by comparing the data for $Y=0$ with that for $Y \neq 0$ in Figs. 2–4. Examination of Eq. (21) shows that the decorrelation between pre- and post-compression echo signals that is caused by straining r_{II} is the dominant source of displacement estimation error at large W . The trend is clear, although Eq. (21) may not accurately predict $\text{var}(\bar{D}_i)$ at $W \gg 1$ and $a_i \neq 0$ since assumption 4 is violated.

The base-band results of Fig. 2 yield the same minima in the displacement variance versus W curves as those found by Remley (Ref. 10, Fig. 3) who studied the W dependence of a

quantity proportional to the mean-square error in the correlation peak $E[(\phi(\hat{D}_i))^2]$. Remley assumed ideal measurement conditions except for linear displacement. It follows that the error in determining the height of the correlation peak should be highly coupled with the displacement error. Currently, too little is understood about strain variations in typical elastographic imaging situations to know if the linear model of Eqs. (1) and (2) is sufficient to model displacement variance or if the additional information justifies the added complexity of including quadratic displacement variations.¹¹

We can also show that Eq. (21) reduces to the displacement variance given by the Cramer-Rao lower bound (CRLB) for base-band Gaussian spectra. Setting $a_i = 0$ and $W \gg 1$ (which does not violate the assumptions) we find:

$$\text{var}(\hat{D}_i) = \frac{\sqrt{5}L^3}{Z \text{SNR}_i} \left(2 + \frac{1}{\text{SNR}_i} \right). \quad (23)$$

From the analysis of Quazi¹² for base-band flat spectra of bandwidth B_z , the lower bound on variance at high SNR_i signals is given by $\text{var}_{\text{CRLB}}(\hat{D}) \geq 3/(\pi^2 Z \text{SNR}_i B_z^3)$ and at low SNR_i by $\text{var}_{\text{CRLB}}(\hat{D}) \geq 3/(2\pi^2 Z \text{SNR}_i^2 B_z^3)$. Using an equivalent bandwidth measure¹³ to convert B_z for flat spectra to L^{-1} for Gaussian spectra, viz., $B_z = (2\sqrt{\pi}L)^{-1}$, it is straightforward to show that Eq. (23) reduces to the CRLB results for both high and low SNR_i within 4%. Therefore, the straight lines at $a_i = 0$ in Fig. 2 yield $\text{var}(\bar{D}) \cong \text{var}_{\text{CRLB}}(\bar{D})$ for base-band (solid line) and bandpass (broken lines) signals.

The most interesting result from the variance analysis is the occurrence of a minimum at the time bandwidth product $W = \sqrt{20/a} \sqrt{1 + Y^2}$, where the displacement errors from additive noise are comparable to those from signal decorrelation. The variance is dominated by additive noise at smaller W and by signal decorrelation at larger W . This simple result is valid for bandpass and base-band signals, and includes the effects of the acoustic pulse center frequency k_0 and bandwidth L^{-1} , observation window length Z , and scaling parameter a . Betz¹⁴ provides a cogent explanation for the deviation of $\text{var}(\hat{D}_i)$ from the $\text{var}_{\text{CRLB}}(\hat{D}_i)$ with increasing a . For fixed $W \gg 1$ and $a = 0$, $\text{var}(\bar{D}) \cong \text{var}_{\text{CRLB}}(\bar{D})$. As a increases, yet remains small, the peak of the cross-correlation function broadens as predicted by Eq. (15) and consequently $\text{var}(\bar{D}) > \text{var}_{\text{CRLB}}(\bar{D})$. However, when the linear rate of displacement exceeds $a = \sqrt{20}L/Z \sqrt{1 + k_0^2 L^2}$, the cross-correlation peak becomes bimodal, and $\text{var}(\bar{D}) \gg \text{var}_{\text{CRLB}}(\bar{D})$. Displacement variance can be kept to a minimum by choosing a window length given by the expression above, which suggests an intrinsic compromise between resolution and noise. However, adaptive companding techniques that minimize a throughout the measurement range lessen the effects of the compromise. Adaptive companding is critically important to elastography.

For large Y , Eq. (22) reduces to $Z = \sqrt{20/ak_0}$, which has the same form as the expression predicted intuitively by Cespedes¹⁵ for narrow-band spectra. However, Eq. (22) is

more general since it holds for broadband as well as base-band signals.

Although the presence of minima is intuitive and well-documented in the time-delay literature,^{4,10,11,14,15} the dependence of displacement variance on all essential elastographic parameters has not been derived previously. These results are the foundation for specifying elastographic imaging performance.⁵

ACKNOWLEDGMENTS

The authors gratefully acknowledge many helpful discussions with Timothy J. Hall. This work was supported by NIH Grant No. P01 CA64597 (through the University of Texas) and by the Clinical Radiology Foundation at KUMC.

APPENDIX A: SINC APPROXIMATION

Empirically we find that

$$\text{sinc}(x) \approx \exp(-x^2/5) \quad (\text{A1})$$

$$\begin{aligned} & \int_{-Z/2}^{Z/2} \int_{-Z/2+\Delta Z}^{Z/2+\Delta Z} dz_1 dz_2 \exp[j(k_1+(1+a_1)k_2)z_1 - j(k_1+(1+a_2)k_2)z_2] \\ &= Z^2 \text{sinc}[(k_1+(1+a_1)k_2)Z/2] \text{sinc}[(k_1+(1+a_2)k_2)Z/2] \exp[-j(k_1+a_2k_2)\Delta Z - jk_2(D_2-D_1)] \\ &\approx Z^2 \exp\{-[(k_1+(1+a_1)k_2)^2 + (k_1+(1+a_2)k_2)^2]Z^2/20 - j(k_1+a_2k_2)\Delta Z - jk_2(D_2-D_1)\}. \end{aligned} \quad (\text{A4})$$

APPENDIX B: MINIMUM VARIANCE FOR DISPLACEMENT ESTIMATION

The lower bound on displacement variance is derived in this section for arbitrary signal and noise spectra. The results follow the methods of Azaria and Hertz,⁷ except that we do not prefilter the signals but we do allow for linear displacement variation within the observation window, i.e., $a \neq 0$.

Beginning with Eq. (12) and combining Eqs. (13), (18), and (20), we let $a_1 = a_2 = a$, $D_1 = D_2 = D$, and $\Delta Z = 0$. The displacement variance can be written as

$$E[(\hat{D} - D)^2] = \frac{E[(\phi'_{fn}(\hat{D}))^2]}{(\phi''_{ff}(D))^2} = \frac{\int_{-\infty}^{\infty} dk_1 A(k_1)}{(\int_{-\infty}^{\infty} dk_1 B(k_1))^2}, \quad (\text{B1})$$

where

$$B(k_1) = k_1^2 G_f(k_1) \text{sinc}[k_1(1-a)Z/2] \quad (\text{B2})$$

and

$$\begin{aligned} A(k_1) = & \int_{-\infty}^{\infty} dk_2 [\{G_f(k_1)G_n(k_2) \\ & + G_n(k_1)G_n(k_2)\} \text{sinc}^2[(k_1+k_2)Z/2] \\ & + G_n(k_1)G_f(k_2) \text{sinc}^2[(k_1+ak_2)Z/2]]. \end{aligned} \quad (\text{B3})$$

The Schwartz inequality for the real functions $\sqrt{A(k)}$ and $B(k)/\sqrt{A(k)}$ is

and

$$\text{sinc}(x) \approx \exp(-2x^2/5). \quad (\text{A2})$$

These approximations specify a Gaussian function of width comparable to the main lobe of the sinc function. Hence, a Gaussian-weighted window function with spectral properties similar to that of a rectangular window function is identified.

Therefore,

$$\begin{aligned} & \int_{-Z/2}^{Z/2} \int_{-Z/2+\Delta Z}^{Z/2+\Delta Z} dz_1 dz_2 \exp[-j(k_1+k_2)(z_2-z_1)] \\ &= Z^2 \text{sinc}^2[(k_1+k_2)Z/2] \exp[-j(k_1+k_2)\Delta Z] \\ &\approx Z^2 \exp[-(k_1+k_2)^2 Z^2/10 - j(k_1+k_2)\Delta Z] \end{aligned} \quad (\text{A3})$$

and

$$\begin{aligned} & \left(\int_{-\infty}^{\infty} dk_1 \sqrt{A(k_1)} \frac{B(k_1)}{\sqrt{A(k_1)}} \right)^2 \\ &\leq \int_{-\infty}^{\infty} dk_1 (\sqrt{A(k_1)})^2 \int_{-\infty}^{\infty} dk_1 \left(\frac{B(k_1)}{\sqrt{A(k_1)}} \right)^2. \end{aligned} \quad (\text{B4})$$

Applying Eq. (B4) to Eq. (B1) gives the following lower bound for the displacement variance:

$$E[(\hat{D} - D)^2] \geq \left[\int_{-\infty}^{\infty} dk_1 \frac{B^2(k_1)}{A(k_1)} \right]^{-1}. \quad (\text{B5})$$

The general expression of Eq. (B5) includes the important experimental parameters that contribute to measurement uncertainty. However, when $a=0$ and $Z \gg 1$, Eq. (B5) reduces to the variance given by the Cramer-Rao lower bound:

$$\begin{aligned} E[(\hat{D} - D)^2] \geq & \left[Z \int_{-\infty}^{\infty} dk_1 k_1^2 \left/ \left(2 \frac{G_n(k_1)}{G_f(k_1)} \right. \right. \right. \\ & \left. \left. + \left(\frac{G_n(k_1)}{G_f(k_1)} \right)^2 \right) \right]^{-1} \approx \text{var}_{\text{CRLB}}(\hat{D}). \end{aligned} \quad (\text{B6})$$

¹G. C. Carter, *Coherence and Time Delay Estimation: An Applied Tutorial for Research, Development, Test, and Evaluation Engineers* (IEEE, Piscataway, NJ, 1993).

²IEEE Trans. Ultrason. Ferroelectr. Freq. Control, Special Issue on Correlation Techniques and Applications to Ultrasonics **41**, 577-663 (1994).

- ³M. Bilgen and M. F. Insana, "Deformation models and correlation analysis in elastography," *J. Acoust. Soc. Am.* **99**, 3212–3224 (1996).
- ⁴J. W. Betz, "Comparison of the deskewed short-time correlator and the maximum likelihood correlator," *IEEE Trans. Acoust. Speech Signal Process.* **32**, 285–294 (1984).
- ⁵M. Bilgen and M. F. Insana, "Error analysis in acoustic elastography. II. Strain estimation and SNR analysis," *J. Acoust. Soc. Am.* **101**, 1147–1154 (1997).
- ⁶I. Cespedes, M. F. Insana, and J. Ophir, "Theoretical bounds on strain estimation in elastography," *IEEE Trans. Ultrason. Ferroelectr. Freq. Control* **UFFC-42**, 969–972 (1995).
- ⁷M. Azaria and D. Hertz, "Time delay estimation by generalized cross correlation methods," *IEEE Trans. Acoust. Speech Signal Process.* **32**, 280–285 (1984).
- ⁸I. Cespedes, Y. Huang, J. Ophir, and S. Spratt, "Methods for estimation of subsample time delays of digitized echo signals," *Ultrason. Imag.* **17**, 142–171 (1995).
- ⁹D. Hertz, "Time delay estimation by combining efficient algorithms and generalized cross correlation methods," *IEEE Trans. Acoust. Speech Signal Process.* **34**, 1–7 (1986).
- ¹⁰W. R. Remley, "Correlation of signals having a linear delay," *J. Acoust. Soc. Am.* **35**, 65–69 (1963).
- ¹¹W. B. Adams, J. P. Kuhn, and W. P. Whyland, "Correlator compensation requirements for passive time-delay estimation with moving sources or receivers," *IEEE Trans. Acoust. Speech Signal Process.* **28**, 158–168 (1980).
- ¹²A. H. Quazi, "An overview on the time delay estimate in active and passive systems for target localization," *IEEE Trans. Acoust. Speech Signal Process.* **29**, 527–533 (1981).
- ¹³K. S. Shanmugan and A. M. Breipohl, *Random Signals: Detection, Estimation and Data Analysis* (Wiley, New York, 1988).
- ¹⁴J. W. Betz, "Effects of uncompensated relative time companding on a broad-band cross correlator," *IEEE Trans. Acoust. Speech Signal Process.* **33**, 505–510 (1985).
- ¹⁵I. Cespedes, "Elastography: Imaging of Biological Tissue," Ph.D. dissertation, University of Houston, TX, 1993.
- ¹⁶C. H. Knapp and G. C. Carter, "Estimation of time delay in the presence of source or receiver motion," *J. Acoust. Soc. Am.* **70**, 1545–1549 (1977).

Error analysis in acoustic elastography. II. Strain estimation and SNR analysis

Mehmet Bilgen and Michael F. Insana

Department of Radiology, University of Kansas Medical Center, Kansas City, Kansas 66160

(Received 22 May 1996; accepted for publication 21 September 1996)

Accurate displacement estimates are required to obtain high-quality strain estimates in elastography. In this paper the strain variance is derived from the statistical properties of the displacement field to define a point signal-to-noise ratio for elastography (SNR_0). Displacements caused by compressional forces applied along the axis of the transducer beam are modeled by scaling and shifting the axial reflectivity profile of the tissue. The strain variance is given as a function of essential experimental parameters, such as the amount of tissue compression, echo waveform window length, and the amount of window overlap. SNR_0 is defined in terms of applied compression and strain variance and normalized by the input signal-to-noise ratio (SNR_i) for echo signals, to formulate the performance metric $\text{SNR}_0/\text{SNR}_i$. This quantity characterizes the noise properties, dynamic range, and sensitivity of strain images based on the spatial resolution requirements. The results indicate that low noise, high sensitivity, and limited dynamic range strain images are obtained for high-frequency bandpass signals when the applied strain is small. For large strains, however, one strategy for low-noise strain imaging employs base-band signals to obtain images with large dynamic range but limited peak sensitivity and noise figure. A better strategy includes companding, which eliminates the average strain in the echo signal before cross-correlation to reduce the dynamic range requirement and increase peak sensitivity for strain estimates. © 1997 Acoustical Society of America. [S0001-4966(97)03702-8]

PACS numbers: 43.80.Cs, 43.80.Ev, 43.80.Qf [FD]

INTRODUCTION

Acoustic elastography is a remote-sensing technique for imaging elastic properties of biological tissues, *in vivo*.¹ Compared with existing diagnostic techniques, elastography has great potential for increasing cancer detection rates provided the large difference in stiffness between a tumor and its surrounding tissues can be fully exploited. One particularly promising application of elastography is the detection of malignant breast disease.²

Elastograms display the elastic constants that are measured by a static-compression measurement technique. A compressor generates a stress field that deforms a volume of tissue. Local tissue displacements are tracked through changes in ultrasonic echo signals. Strain images are estimated from the gradient of the displacement field, and, subsequently, elastic modulus images may be obtained by substituting the strain tensor and the stress field into the constitutive equations of continuum mechanics.³⁻⁶ Ultimately, the quality of an elastographic image depends on the accuracy and precision of the strain estimates.

Figure 1 illustrates tissue states at various stages in the strain estimation procedure. The example is a material with three layers [Fig. 1(a)] that is compressed by a force along the z axis and distorted according to the stiffness of each layer [Fig. 1(b)]. The average strain was 5.5%, but the strains are greater in the soft layers than in the hard layer [Fig. 1(d)], so that the rate of change of axial displacement is greatest in the soft layers [Fig. 1(e)]. The relationship between s , the axial component of the strain tensor, and D , the displacement along the z axis, is $s = dD/dz$.

In elastography, axial strain is estimated from the difference formula,

$$\hat{s} = \frac{(\hat{D}_2 - \hat{D}_1)}{\Delta Z}, \quad (1)$$

where \hat{D}_1 and \hat{D}_2 are the displacement estimates measured from acoustic waveforms recorded in two sequential, and often overlapping, observation windows. The two windows have length Z and are separated axially by the distance ΔZ . (For an example, see Fig. 1 in the companion paper.)⁷

An axial displacement is measured for each observation window by cross-correlating two pulse-echo waveform segments, one acquired before compression r_I and one after compression r_{II} . \hat{D} is the correlator lag value τ at the peak of the cross-correlation function $\phi(\tau)$. Specifically,

$$\phi(\hat{D}) = \max_{\tau} \phi(\tau) = \max_{\tau} \int_{-Z/2}^{Z/2} dz r_I(z + \tau) r_{II}(z). \quad (2)$$

(Readers are referred to the glossary in Ref. 7 for a complete summary of terms.) We know from previous analyses where we studied the ensemble cross-correlation at a point,⁸ $E[r_I(z + \tau)r_{II}(z)]$, and the corresponding correlation estimate over an observation window,⁷ $E[\phi(\tau)]/Z$, that the cross-correlation peak amplitude must approximate the auto-correlation peak amplitude, $E[r_I^2(0)]$, in order to minimize displacement errors, i.e., to obtain unbiased \hat{D} and minimize $\text{var}(\hat{D})$. This situation occurs under ideal measurement conditions, where D is constant along z (stationary r_I and r_{II}), the observation window is much larger than the ultrasonic pulse length, and the transducer has a high center frequency

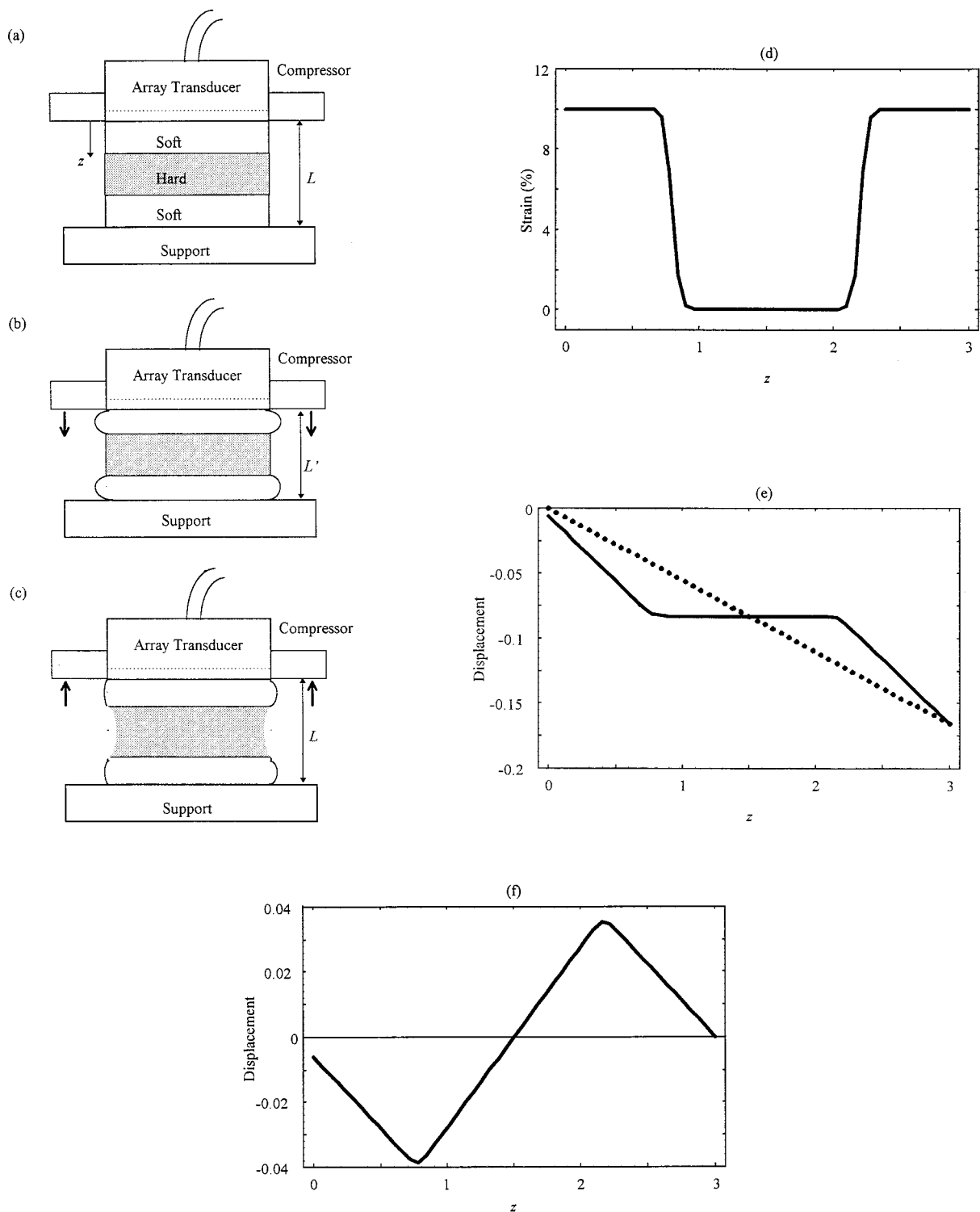


FIG. 1. An illustration of tissue states during an example strain estimation experiment. The layered sample is scanned before (a) and after (b) compression. The sample deforms according to the stiffness of each layer and the boundary conditions. Echo-waveform companding is equivalent to stretching the whole sample according to the average strain (c). The strain profile for the sample is shown as a function of depth z in (d), and the corresponding displacement is indicated by the solid line in (e). The dotted line in (e) indicates how the post-compression echo-waveform is stretched. The residual displacement, after linear companding, is shown in (f).

and large bandwidth. For these ideal conditions, the estimator in Eq. (2) is efficient in the sense that $\text{var}(\hat{D})$ approaches the lower bound for displacement variance as defined by the Cramer–Rao inequality. Unfortunately, the ideal conditions are violated in most practical situations of interest. Such vio-

lations lead to a loss of echo signal coherence and a large strain variance.

Large strains produce large signal and noise amplitudes in elastograms. The strategy for maximizing the output signal-to-noise ratio for strain SNR_0 relative to the input

signal-to-noise ratio for the echo signals SNR_i is to generate the largest strain that can be removed from the echo signals by preprocessing before cross-correlation. Imagine, for example, that a compressional force induces a simple shift in the post-compression waveform, i.e., $r_{\text{II}}(z) = r_{\text{I}}(z + D)$. The analysis begins by shifting r_{II} along z by the amount $-D$ before cross-correlation with r_{I} via Eq. (2). Since the coherence between r_{I} and r_{II} is limited only by the additive noise, the variance of the displacement estimate is minimum. The signal processing goal is to adjust the experimental parameters to give, simultaneously, the largest strain and the maximum correlation between r_{I} and r_{II} . The signal processing challenge is to achieve this goal in heterogeneous media by adaptively adjusting many dependent parameters for a variety of measurement situations. Two common situations produce particularly noisy strain images because of decorrelation between r_{I} and r_{II} .

First, decorrelation errors are produced when the scatterer displacement varies along the z axis within the observation window. These errors are most significant when the strain is larger than a few percent or the stiffness of the medium is inhomogeneous [Fig. 1(a)–(c)]. The simplest deformation model to describe the resulting echo signal is a constant shift plus a linear rate of displacement, $r_{\text{II}}(D + az)$. Increasing a broadens the cross-correlation peak,^{9–12} and consequently $\text{var}(\hat{D})$ is increased. The simplest correction is to shift and stretch r_{II} according to the average strain to realign it with r_{I} before cross-correlation. This process is known as companding, physically *compressing* the tissue [Fig. 1(b)] followed by computationally *expanding* the echo waveform [Fig. 1(c)].^{10,12,13} Expanding the waveform is equivalent to stretching the sample by the average rate of displacement [dotted line in Fig. 1(e)] although the sample itself is not physically stretched as depicted in Fig. 1(c). Linear companding by the average strain is imperfect for inhomogeneous media [Fig. 1(f)], but nevertheless has been shown to greatly reduce elastographic noise.¹⁴ Companding by the average strain is most effective when applied to media containing low-contrast objects, where the linear displacement model is valid and the residual strain is small compared to the noncompanded signal [Fig. 1(f)]. Adaptive linear companding techniques are now being developed for inhomogeneous media to shift and stretch the post-compression waveform locally and realign r_{I} and r_{II} more precisely. Pulse shaping should be used with companding to maximize signal coherence.⁸

Second, decorrelation errors are produced when scatterers move within the resolution cell volume of the ultrasonic pulse.¹⁵ Squeezing an incompressible material, like breast tissue, reorients and possibly deforms the shape of scatterers within the volume occupied by the acoustic pulse at any instant of time. For random media, the average number of scatterers per pulse volume remains unchanged, although some scatterers are lost from the volume, new scatterers are introduced, and the remaining scatterers are repositioned within the pressure field of the pulse. Such movement decorrelates r_{I} and r_{II} because of the phase-sensitive nature of the ultrasound detector and thereby increases $\text{var}(\hat{D})$ and $\text{var}(\hat{s})$. Companding cannot correct this source of error.

Our purpose in this paper is to derive realistic estimates of the strain variance $\text{var}(\hat{s})$ from knowledge of $\text{var}(\hat{D})$ and $\text{cov}(\hat{D}_1, \hat{D}_2)$, and to use that information to design elastographic experiments that maximize $\text{SNR}_0/\text{SNR}_i$. The quantity $\text{SNR}_0/\text{SNR}_i$ characterizes noise properties of strain images. Bounds on strain variance were given recently in terms of the Cramer–Rao lower bound for time-delay estimation.¹⁶ That analysis assumed ideal conditions to gauge the amount of noise reduction possible, and did not account for decorrelation errors. The current paper predicts the strain variance for a single compression under more realistic conditions that include the amount of applied strain and length of the observation window as well as window separation, transducer frequency, and input signal-to-noise ratio.

The paper is organized as follows. Section I describes echo waveform models and the assumptions that lead to the derivations of the mean and variance for the strain estimates given in Sec. II. The performance metric $\text{SNR}_0/\text{SNR}_i$ is defined in Sec. III, and numerical calculations for $\text{var}(\hat{s})$ and $\text{SNR}_0/\text{SNR}_i$ are illustrated for a variety of experimental parameters in Sec. IV. Section V discusses the qualitative features of the results and suggests signal processing strategies for minimizing strain image noise. The paper concludes with a summary in Sec. VI.

I. MODELS AND ASSUMPTIONS

The pre- and post-compression echo waveforms $r_{\text{I}}(z)$ and $r_{\text{II}}(z)$ for the i th observation window are modeled as a linear function of the tissue reflectivity profile $f(z)$ according to the equations

$$\begin{aligned} r_{\text{I}}(z) &= h(z) \otimes f(z) + n_{\text{I}}(z) \\ r_{\text{II}}(z) &= h(z) \otimes f((1 + a_i)z + D_i) + n_{\text{II}}(z) \quad 0 \leq z \leq Z, \end{aligned} \quad (3)$$

where $h(z)$ is the point spread function of a broadband ultrasonic imaging system, $n_{\text{I}}(z)$ and $n_{\text{II}}(z)$ are additive noise processes, and \otimes denotes convolution. Compression of the medium in the i th window is represented as a linear scaling and shifting of the axial reflectivity profile with parameters a_i and D_i , respectively. To apply this model in biological tissues, we make the following simplifying assumptions.

(1) The signal $f(z)$ and noises $n_{\text{I}}(z)$, $n_{\text{II}}(z)$ are weakly stationary, bandlimited, zero mean random processes that are uncorrelated with each other. Also, the power spectra for $f(z)$ and $n(z)$ are $G_f(k)$ and $G_n(k)$, respectively, where, for example, $G_f(k) = \int_{-\infty}^{\infty} d\tau E[f(z)f(z + \tau)] \exp(-j2\pi k\tau)$. Consequently, $r_{\text{I}}(z)$ and $r_{\text{II}}(z)$ are each weakly stationary, although the processes are jointly nonstationary.

(2) The window length Z is large compared to the correlation length of the tissue scattering structure L_f and acoustic pulse length L_h , but small compared to the axial strain variation L_s . More precisely,⁷ $L_f, L_h \ll Z \leq L_s$. Therefore, the observation window provides sufficient time-bandwidth product to assume $\phi(\tau) \cong ZE[f(z)f(z + \tau)]$, and yet is short enough so that the residual displacement of the companded waveform r_{II} can be approximated as a linear function of z .

(3) Furthermore, assume $L_h \ll L_f$ so that $h(z) \approx \delta(z)$ and the echo waveforms of Eq. (3) become $r(z) = f(z) + n(z)$. Hereafter, we set $L = L_f$.

(4) The input signal-to-noise ratio SNR_i , is relatively large to ensure that the magnitudes of the cross-correlation sidelobes are smaller than that of the main lobe.

(5) The linear scaling parameter a is ‘‘small’’ to ensure that $\phi(\tau)$ has a single main lobe, where $a = \bar{s}/1 - \bar{s}$ and \bar{s} is the average strain in the observation window. The strain is ‘‘small’’ when $aZ\sqrt{L^{-2} + k_0^2} \leq \sqrt{20}$.⁷ A similar result was found by Betz¹² who studied time-delay estimation. The linear displacement model is valid in tissues when the strain contrast is small or when the spatial extent of high-contrast objects is small compared to the total size of the compressed medium.

II. MEAN AND VARIANCE OF STRAIN ESTIMATES

The mean and variance of the strain estimated from Eq. (1) are presented in this section. The expression for the mean strain is

$$E[\hat{s}] = \frac{E[\hat{D}_2 - \hat{D}_1]}{\Delta Z}, \quad (4)$$

and for the variance

$$\text{cov}(\tilde{D}_1, \tilde{D}_2) = \frac{[d^2 g(\tilde{\tau}_1, \tilde{\tau}_2, \tilde{D}_1, \tilde{D}_2, \Delta \tilde{Z}, a_1, a_2, W, Y, \text{SNR}_i)]_{\tilde{\tau}_1 = \tilde{D}_1, \tilde{\tau}_2 = \tilde{D}_2}}{[d^2 E[\phi_{1ff}(\tilde{\tau}_1, \tilde{D}_1, a_1, W, Y)]/d^2 \tilde{\tau}_1]_{\tilde{\tau}_1 = \tilde{D}_1} [d^2 E[\phi_{2ff}(\tilde{\tau}_2, \tilde{D}_2, a_2, W, Y)]/d^2 \tilde{\tau}_2]_{\tilde{\tau}_2 = \tilde{D}_2}}. \quad (9)$$

For Gaussian bandpass signal and noise spectra, the function $g(\cdot)$ in the numerator is given by Eqs. (18) and (19), and the $E[\phi_{iff}(\cdot)]$ in the denominator are given by Eq. (20) in Ref.

7. Displacement variances $\text{var}(\tilde{D}_i)$ are obtained from the above covariance expression by setting $i=1=2$ and $\Delta Z=0$. The complexity of the exact expression for $\text{var}(\hat{s})$ makes it too lengthy to give explicitly. However, with the aid of MATHEMATICATM, we have computed the results exactly and present them in Sec. IV. We give approximate forms for $\text{var}(\hat{s})$ that show its general relation to SNR_i , W , and other important experimental parameters.

Two of the dimensionless parameters in Eq. (9), W and Y , require further description. W is the number of uncorrelated samples per observation window, the spatial equivalent of the time-bandwidth product. W , $\Delta \tilde{Z}$, and a are the free parameters to be optimized for each measurement situation. Y is inversely proportional to the fractional bandwidth (FB) of the ultrasonic system response. If FB is the 6-dB fractional bandwidth of the signal spectrum, then the exact relation is $\text{FB} = 2\sqrt{\ln 2}/Y$. It is common to find a system bandwidth of 67%, which corresponds to $Y=2.5$. Analyses of base-band signals, $Y=0$, and bandpass signals, $Y>0$, are discussed below.

III. SIGNAL-TO-NOISE ANALYSIS

The output signal-to-noise ratio SNR_0 for the strain estimator is defined as

$$\text{var}(\hat{s}) = \frac{M}{\Delta Z^2}. \quad (5)$$

The parameter M in the numerator is defined by

$$M = \text{var}(\hat{D}_1) + \text{var}(\hat{D}_2) - 2 \text{cov}(\hat{D}_1, \hat{D}_2), \quad (6)$$

where

$$\text{var}(\hat{D}_1) = E[(\hat{D}_1 - D_1)^2] \quad (7)$$

is the variance of the displacement estimate and

$$\text{cov}(\hat{D}_1, \hat{D}_2) = E[(\hat{D}_1 - D_1)(\hat{D}_2 - D_2)] \quad (8)$$

is the covariance between displacements measured in two observation windows.

Equations (4) and (5) relate the mean and variance of \hat{s} to the mean, variance and covariance of \hat{D}_1 and \hat{D}_2 . Equations (7) and (8) are derived in a companion paper⁷ for Gaussian signal and noise spectra, G_f and G_n . Those results are summarized below using the dimensionless quantities $\tilde{D} = D/Z$, $\tilde{D} = \hat{D}/Z$, $\tilde{\tau} = \tau/Z$, $\Delta \tilde{Z} = \Delta Z/Z$, $Y = k_0 L$, and $W = Z/L$ to express the displacement covariance $\text{cov}(\tilde{D}_1, \tilde{D}_2)$:

$$\text{SNR}_0 = \frac{\bar{a}^2}{\text{var}(\hat{s})}, \quad (10)$$

where $\bar{a} = (a_1 + a_2)/2$ is approximately equal to the average strain $\bar{s} = (s_1 + s_2)/2$ since, for small s , $a_i = \bar{s}_i/(1 - \bar{s}_i) \cong \bar{s}_i$. The numerator of Eq. (10) describes the mean of the true tissue strain, while the denominator describes the variance of the estimated strain. In x-ray imaging and sonography, SNR_0 also describes image noise¹⁷ but is given by simple equations: SNR_0 is proportional to exposure in x-ray imaging and is constant in sonography. Unfortunately, SNR_0 for strain imaging is a complex function of strain as shown below.

The advantages of echo signal companding may be understood from Eq. (10) by noting that the strain variance is minimum when $a=0$. Companding preserves the strain signal while minimizing the strain variance. The curve of $\sqrt{\text{SNR}_0}$ versus a is analogous to the mean-to-standard deviation ratio defined to describe the ‘‘strain filter’’ concept discussed by Varghese and Ophir.¹⁸

The input signal-to-noise ratio SNR_i was defined for Gaussian spectra⁷ as the ratio of the strength of the signal spectrum (which includes speckle) to that of the additive noise spectrum: $\text{SNR}_i = \sigma_f^2/\sigma_n^2$. It is a measure of echo waveform quality and typically exceeds 40 dB. For this work, $\text{SNR}_i > 10$ dB is considered to be large. Studying the asymptotic behavior of the expression for strain variance, it can be shown⁷ that $\text{var}(\hat{s}) \propto 1/\text{SNR}_i$ for large SNR_i and $\text{var}(\hat{s}) \propto 1/\text{SNR}_i^2$ for small SNR_i . For large SNR_i , the ratio of output to input signal-to-noise ratios, $\text{SNR}_0/\text{SNR}_i$, is studied

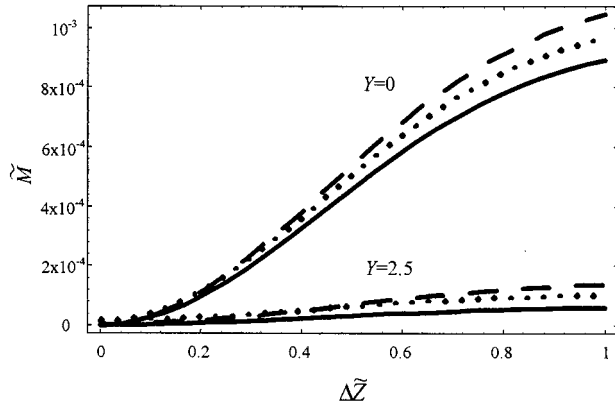


FIG. 2. Shows the variation of $\tilde{M} = \text{var}(\tilde{D}) + \text{var}(\tilde{D}_2) - 2 \text{cov}(\tilde{D}_1, \tilde{D}_2)$ with the window separation $\Delta\tilde{Z}$ for base-band, $Y=0$, and bandpass, $Y=2.5$, echo spectra. Solid lines: $a_1=0, a_2=0$, dotted lines: $a_1=0, a_2=0.1$, broken lines: $a_1=0.1, a_2=0.1$. Other parameters set in Eq. (9) are $\text{SNR}_i=10, W=10, \tilde{D}_1=\tilde{D}_2$, and $\tilde{D}_1=\tilde{D}_2$.

to reduce the number of variables in the results plotted and because this ratio describes an *efficiency* for obtaining precise strain estimates from the information available from the acoustic echo signals. Although high SNR_i conditions are emphasized in this paper, the corresponding efficiency measure at low SNR_i is given by $\text{SNR}_0/\text{SNR}_i^2$.

IV. RESULTS

In this section, we plot calculations of $\text{var}(\hat{s})$ and $\text{SNR}_0/\text{SNR}_i$ to investigate their dependence on the experimental parameters $a, \tilde{D}, \tilde{D}, W, Y$, and $\Delta\tilde{Z}$.

A. Strain variance

Figure 2 shows the dependence of the normalized variance function \tilde{M} defined in Eq. (6), i.e., $\tilde{M} = M/Z^2$. \tilde{M} increases with the window separation $\Delta\tilde{Z}$ for base-band ($Y=0$) and bandpass ($Y=2.5$) signal spectra. In the figure, solid lines are for $a_1=a_2=0$; dotted lines are for $a_1=0, a_2=0.1$, and broken lines are for $a_1=a_2=0.1$. Other fixed parameter values are $\text{SNR}_i=10, W=10, \tilde{D}_1=\tilde{D}_2$, and $\tilde{D}_1=\tilde{D}_2$. $\tilde{M}=0$ where the two windows are completely overlapped ($\Delta\tilde{Z}=0$) because $\text{var}(\tilde{D}_1) = \text{var}(\tilde{D}_2) = \text{cov}(\tilde{D}_1, \tilde{D}_2)$. At the other extreme, $\tilde{M} = \text{var}(\tilde{D}_1) + \text{var}(\tilde{D}_2)$ where the two windows have no overlap ($\Delta\tilde{Z}=1$). The shape of the curve between these points is determined by the Gaussian approximation to the uniform window function.⁷ Base-band signals produce more variance than bandpass signals because the main lobe of the cross-correlation function is broader. Finally, if the strains in the two windows are not equal, i.e., $a_1 \neq a_2$, there is a slight increase in variance.

Figure 3 illustrates the calculation of $\text{var}(\hat{s}) = \tilde{M}/\Delta\tilde{Z}^2$ as a function of $\Delta\tilde{Z}$ for the same parameters specified in Fig. 2. In general, less overlap between windows, larger $\Delta\tilde{Z}$, results in less strain variance. When the strains in the two windows are unequal, $a_1 \neq a_2$, the strain variance becomes very large for $\Delta\tilde{Z} < 0.1$ as illustrated by the dotted lines in Fig. 3. However, this is not a realistic situation because, when $\Delta\tilde{Z}$ is

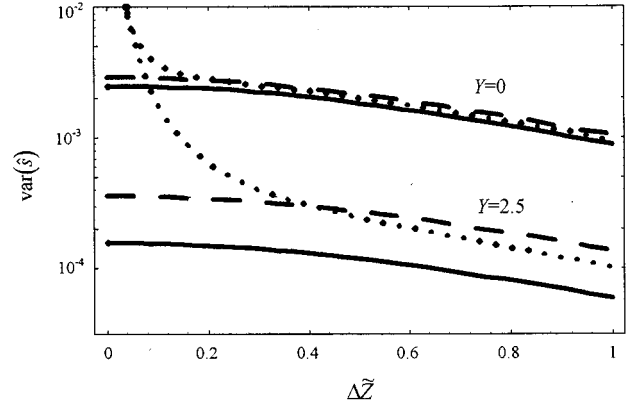


FIG. 3. Shows the variation of strain variance $\text{var}(\hat{s})$ with the window separation $\Delta\tilde{Z}$ for base-band, $Y=0$, and bandpass, $Y=2.5$, echo spectra. Solid lines: $a_1=0, a_2=0$, dotted lines: $a_1=0, a_2=0.1$, broken lines: $a_1=0.1, a_2=0.1$. Other parameters set in Eq. (9) are $\text{SNR}_i=10, W=10, \tilde{D}_1=\tilde{D}_2$, and $\tilde{D}_1=\tilde{D}_2$.

small, the signals in the two windows are very similar, i.e., $a_1 \cong a_2$. For $\Delta\tilde{Z} > 0.1$ and the above parameter values, the strain variance is independent of a_1 and a_2 provided that assumption 5, $a_i W \leq \sqrt{20/(1+Y^2)}$, is satisfied.

Figure 4 describes the effect on the strain variance of unequal displacements in the two observation windows. Since displacement covariance is a function of the actual \tilde{D} and estimated \tilde{D} displacements, the strain variance also depends on these values. In Figs. 2 and 3, we assumed $\tilde{D}_1=\tilde{D}_2$ and $\tilde{D}_1=\tilde{D}_2$. However, Fig. 4 shows that if the displacements in the two windows are unequal, strain variance is increased. The solid lines are for the case where the actual and estimated displacements are equal, i.e., $\tilde{D}_1=\tilde{D}_2$ and $\tilde{D}_1=\tilde{D}_2$, the dotted lines are for $\tilde{D}_2-\tilde{D}_1=0.05$ and $\tilde{D}_1=\tilde{D}_2$, and the broken lines are for $\tilde{D}_1=\tilde{D}_2$ and $\tilde{D}_2-\tilde{D}_1=0.05$. Other parameter values are $\text{SNR}_i=10, W=10$, and $a_1=a_2=0$. The mismatch in displacement significantly increases the strain variance when the windows

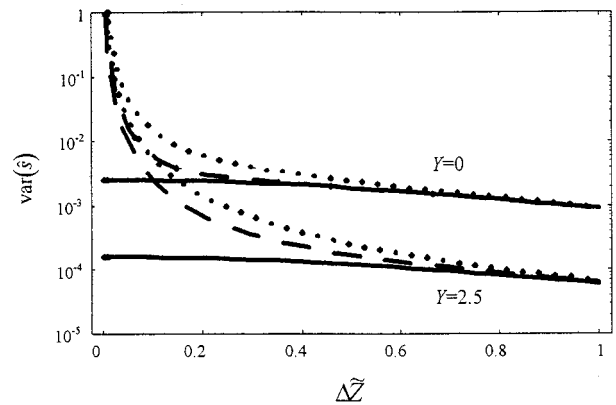


FIG. 4. Shows the variation of strain variance $\text{var}(\hat{s})$ with the window separation $\Delta\tilde{Z}$ for base-band, $Y=0$, and bandpass, $Y=2.5$, echo spectra. Solid lines: $\tilde{D}_1=\tilde{D}_2$ and $\tilde{D}_1=\tilde{D}_2$, dotted lines: $\tilde{D}_2-\tilde{D}_1=0.05$ and $\tilde{D}_1=\tilde{D}_2$, broken lines: $\tilde{D}_1=\tilde{D}_2$ and $\tilde{D}_2-\tilde{D}_1=0.05$. Other parameters are $\text{SNR}_i=10, W=10, a_1=0$, and $a_2=0$.

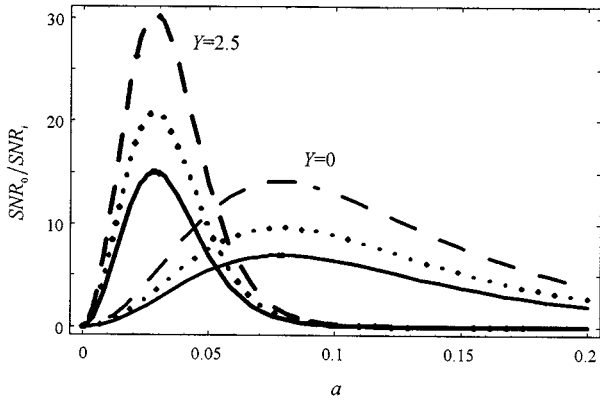


FIG. 5. Shows the variation of output to input signal-to-noise ratio with the strain a for base-band, $Y=0$, and bandpass, $Y=2.5$, echo spectra. Solid lines: $\Delta\tilde{Z}=0.5$, dotted lines: $\Delta\tilde{Z}=0.75$, and broken lines: $\Delta\tilde{Z}=1.0$. Other parameters are $W=40$, $\tilde{D}_1=\tilde{D}_2$, and $\tilde{D}_1=\tilde{D}_2$.

overlap more than 50% ($\Delta\tilde{Z}<0.5$) and the increase is greater for $\tilde{D}_2-\tilde{D}_1>0$ than for $\tilde{D}_2-\tilde{D}_1<0$. For example, strain variance is increased tenfold for bandpass signals ($Y=2.5$) when the estimated displacement difference is 5% of the window length (the dotted line where $\tilde{D}_2-\tilde{D}_1=0.05$) and the two windows overlap 80% ($\Delta\tilde{Z}=0.2$). At larger $\Delta\tilde{Z}$, the strain variance calculations are asymptotically independent of $\tilde{D}_2-\tilde{D}_1$ and $\tilde{D}_2-\tilde{D}_1$.

The strain variance depends strongly on the time-bandwidth parameter W (not shown in the figures). For $a_i W \leq \sqrt{20/(1+Y^2)}$ a good rule of thumb is $\text{var}(\hat{s}) \propto W^{-3}$. However, for experimental situations with larger $a_i W$ product, assumption 5 is violated and the strain variance increases dramatically with W .

B. $\text{SNR}_0/\text{SNR}_i$

The ratio of output to input signal-to-noise ratios, $\text{SNR}_0/\text{SNR}_i$, is proposed to characterize the noise and dynamic range of a strain image. Large $\text{SNR}_0/\text{SNR}_i$ values indicate low noise and broad peaks in the $\text{SNR}_0/\text{SNR}_i$ versus a curve indicate a wide dynamic range in strain. The parameter $a = \bar{s}1 - \bar{s}$ is the linear rate of displacement along z , although we will occasionally refer to a as the strain. Curves of $\text{SNR}_0/\text{SNR}_i$ versus a (strain) are plotted for several experimental parameters in Figs. 5–8. In all cases, $a_1 = a_2 = a$.

Figure 5 shows the variation of $\text{SNR}_0/\text{SNR}_i$ with strain for three values of $\Delta\tilde{Z}$ and for base-band ($Y=0$) and bandpass ($Y=2.5$) signals. Other parameters are set to $W=40$, $\tilde{D}_1=\tilde{D}_2$, and $\tilde{D}_1=\tilde{D}_2$. The solid lines in Fig. 5 represent the calculation for $\Delta\tilde{Z}=0.5$, the dotted lines are for $\Delta\tilde{Z}=0.75$, and the broken lines are for $\Delta\tilde{Z}=1.0$ (0% overlap). The magnitude of the peak increases with $\Delta\tilde{Z}$ because the lowest strain variance is obtained when the windows are fully separated. The peaks in the curves occur at $a = \sqrt{20}/W \sqrt{1+Y^2}$, the same value for which the displacement variance is minimum.⁷

Figure 6 shows the variation of $\text{SNR}_0/\text{SNR}_i$ with strain for three values of $W=Z/L$, the time-bandwidth parameter.

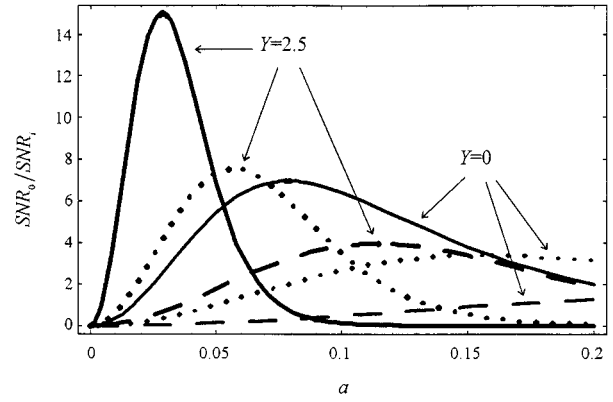


FIG. 6. Shows the variation of output to input signal-to-noise ratio with the strain a for base-band, $Y=0$, and bandpass, $Y=2.5$, echo spectra. Solid lines: $W=40$, dotted lines: $W=20$, and broken lines: $W=10$. Other parameters are $\Delta\tilde{Z}=0.5$, $\tilde{D}_1=\tilde{D}_2$, and $\tilde{D}_1=\tilde{D}_2$.

Curves for base-band, $Y=0$, and bandpass, $Y=2.5$, spectra are presented. The solid lines in the figure are for $W=40$, the dotted lines are for $W=20$, and the broken lines are for $W=10$. The other parameters are $\Delta\tilde{Z}=0.5$, $\tilde{D}_1=\tilde{D}_2$, and $\tilde{D}_1=\tilde{D}_2$. Small W values shift the peak in the $\text{SNR}_0/\text{SNR}_i$ curve to larger strains, broaden the width of the curve (in-

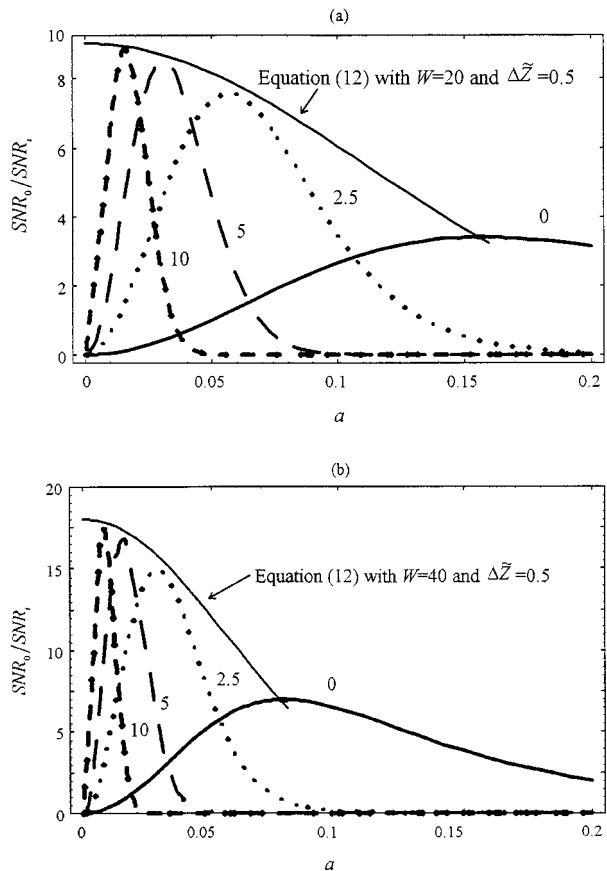


FIG. 7. Shows the variation of output to input signal-to-noise ratio with the strain a for (a) $W=20$ and (b) $W=40$. Solid lines: $Y=0$, dotted lines: $Y=2.5$, broken lines: $Y=5$, and dot-dashed lines: $Y=10$. Other parameters are $\Delta\tilde{Z}=0.5$, $\tilde{D}_1=\tilde{D}_2$, and $\tilde{D}_1=\tilde{D}_2$.

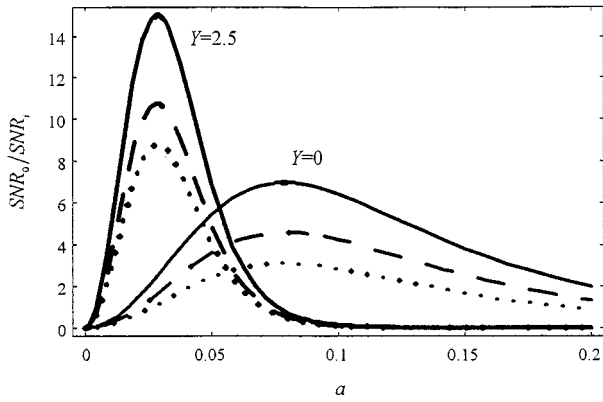


FIG. 8. Shows the variation of output to input signal-to-noise ratio with the strain a for base-band, $Y=0$, and bandpass, $Y=2.5$, echo spectra. Solid lines: $\tilde{D}_1 = \tilde{D}_2$ and $\tilde{D}_1 = \tilde{D}_2$, dotted lines: $\tilde{D}_2 - \tilde{D}_1 = 0.05$ and $\tilde{D}_1 = \tilde{D}_2$, broken lines: $\tilde{D}_1 = \tilde{D}_2$ and $\tilde{D}_2 - \tilde{D}_1 = 0.05$. Other parameters are $\Delta\tilde{Z}=0.5$ and $W=40$.

creasing the dynamic range), and reduce the peak amplitude (increasing noise). Therefore, short-window lengths lead to more noise in a strain image, but also greater sensitivity to large strains and higher spatial resolution.

Figure 7 shows the variation of $\text{SNR}_o/\text{SNR}_i$ with strain for four different values of Y : 0, 2.5, 5, 10. The echo envelope is used to estimate strain when $Y=0$. As Y is increased, the fractional bandwidth of the transmitted ultrasound pulse is decreased until, at $Y=10$, the echo-signal bandwidth is very narrow. $W=20$ in Fig. 7(a) and $W=40$ in Fig. 7(b) and in both figures $\Delta\tilde{Z}=0.5$, $\tilde{D}_1 = \tilde{D}_2$, and $\tilde{D}_1 = \tilde{D}_2$. As before, the peak in the $\text{SNR}_o/\text{SNR}_i$ versus a curves occurs at $a = \sqrt{20}/W\sqrt{1+Y^2}$. The lowest peak amplitude occurs when the echo envelope is used to estimate strain ($Y=0$). However, as Y increases, the peak amplitude increases and shifts to lower values of a . The peaks of the $\text{SNR}_o/\text{SNR}_i$ curves vary according to the expression

$$[\text{SNR}_o/\text{SNR}_i]_{\text{peak}} \cong 0.9\Delta\tilde{Z}W \exp(-a^2W^2/10),$$

provided

$$a^2W^2 = 20/(1+Y^2). \quad (11)$$

The thin solid curves joining the peaks at the top of Fig. 7(a), (b) were calculated using Eq. (11). These curves show that images with the lowest noise (greatest SNR_o) are obtained by applying very little compression to the medium (small a), using narrow-band and high-frequency ultrasound pulses (large Y), long window lengths (large W) and no window overlap ($\Delta\tilde{Z}=1$). However, such images will have essentially no spatial resolution and will be sensitive to only a small range of strains (little dynamic range). Resolution and dynamic range may be improved at the expense of noise, by increasing the fractional bandwidth (decrease Y), reducing the window length, and increasing the amount of window overlap. Given the resolution and dynamic range required for

a specific situation, Eq. (11) predicts how the critical experimental parameters of strain imaging should be adjusted to minimize noise.

The curves in Fig. 7 also provide an approach to adaptive companding. The ideal amount of post-compression echo signal stretching and shifting will vary with location for inhomogeneous media. At first pass, the displacement field is processed by companding using the average strain and the echo envelope (setting $Y=0$) to provide the greatest possible dynamic range for strain estimates. Those strain estimates may then be used to apply another signal companding that varies with position. With each iteration of companding, the dynamic range for strain narrows and the need for higher spatial resolution is reduced. Therefore the fractional bandwidth of the pulse spectrum can be reduced and the window length can be lengthened to increase $\text{SNR}_o/\text{SNR}_i$ and reduce noise in the strain image.

Figure 8 describes changes in $\text{SNR}_o/\text{SNR}_i$ when the displacements in the two observation windows are not the same. Results for base-band, $Y=0$, and bandpass, $Y=2.5$, spectra are shown. The solid lines represent the calculations for $\tilde{D}_1 = \tilde{D}_2$ and $\tilde{D}_1 = \tilde{D}_2$, the broken lines are for $\tilde{D}_1 = \tilde{D}_2$ and $\tilde{D}_2 - \tilde{D}_1 = 0.05$, and the dotted lines are for $\tilde{D}_2 - \tilde{D}_1 = 0.05$ and $\tilde{D}_1 = \tilde{D}_2$. Other parameters are $\Delta\tilde{Z}=0.5$ and $W=40$. The results for Fig. 8 indicate that small differences in \tilde{D}_1 and \tilde{D}_2 produce large increases in strain image noise.

V. DISCUSSION

Analyzed in its entirety, the data in the previous section suggest a strategy for adjusting experimental parameters to minimize the noise in strain images. First, determine the size of the smallest structure to be resolved in the medium and choose Z to be 1/4 of that value. The resolving power of the system is a function of Z , ΔZ , and L , however, the window length is often the greatest of these quantities and hence the limiting parameter for determining spatial resolution. The factor 1/4 was arbitrarily chosen. Second, use the fractional bandwidth of the ultrasound system and the window length to find the amount of compression that minimizes the noise via the expression $a \cong \sqrt{20}/W\sqrt{1+Y^2}$. The dynamic range of strains that will be visible with this system, i.e., the width of the $\text{SNR}_o/\text{SNR}_i$ versus a curve, is $\Delta a \cong \sqrt{20}/W\sqrt{1+Y^2}$. If Δa is too small for the application, it can be expanded by increasing the fractional bandwidth (reducing Y), reducing the window length, or companding r_{II} . The effect of these adjustments on the image noise is predicted by Eq. (11).

The effects of overlapping the observation windows are understood from Eq. (11) by studying the factor $\Delta\tilde{Z}W = \Delta Z/L$, which is the number of echo correlation lengths contained in the shift. Variations in $\Delta\tilde{Z}$ scale the $\text{SNR}_o/\text{SNR}_i$ versus a curves, as shown in Fig. 5, such that the maximum value (the least image noise) occurs when $\Delta\tilde{Z}=1$ (the poorest spatial resolution). Equation (11) describes essential compromises between noise and resolution in a strain image due to the amount of compression, the transducer properties, and the window length and overlap.

This analysis does not yet include all sources of strain error. First, we ignored the loss of signal coherence caused by movement of scatterers within the pulse by setting $L_h \ll L_f$. Second, the displacement error derivation involved a second-order Taylor series expansion of a cross-correlation function⁷ that may not accurately represent the situation when $a > 0.05$ or $W > 10$ and the displacement errors are large. Third, the analysis assumes all scatterers move axially, whereas, in reality, scatterers move in three dimensions. Each of these effects decreases the coherence between $r_1(z)$ and $r_{II}(z)$ and thereby increases $\text{var}(\hat{s})$. Consequently, the predictions of Eqs. (5)–(9) are likely to underestimate measurements of $\text{var}(\hat{s})$ for $a \neq 0$.

The analysis focuses on the noise properties of strain imaging, which is only one aspect of elastographic image quality. For example, to predict the visibility of targets imbedded in a background using strain images, we must compute the contrast-to-noise ratio (or target signal-to-noise ratio),¹⁷ $\text{CNR} = (\Delta \bar{s})^2 / \text{var}(\Delta \hat{s})$, where $\Delta \bar{s} = \bar{s}_t - \bar{s}_b$ and \bar{s}_t is the average strain in a target and \bar{s}_b is the average strain in the surrounding background. Also, in the formulation we assumed the strain is estimated from a single compression of the tissue. The results in this paper can be easily extended to the analysis of multiple-compression techniques.

VI. SUMMARY

Strain variance was estimated from the statistical properties of displacement estimates. The results were used to describe how to optimally adjust experimental parameters to minimize strain image noise. The analysis is based on a physical model that describes changes in the echo signal caused by movement of the ultrasonic scatterers within incompressible and elastic biological media. The functional dependence of the strain variance on important experimental variables was examined.

The important parameters to be adjusted are the amount of tissue compression a , the observation window length Z , the amount of window overlap ΔZ , and the fractional bandwidth Y^{-1} . Strategies for minimizing strain image noise, given the requirements for spatial resolution and dynamic range, predict that large improvements in image quality are possible with the appropriate signal processing.

ACKNOWLEDGMENTS

This work was supported by NIH Grant No. P01 CA64597 (through the University of Texas) and by the Clinical Radiology Foundation at KUMC.

- ¹J. Ophir, I. Cespedes, H. Ponnekanti, Y. Yazdi, and X. Li, "Elastography: a quantitative method for imaging the elasticity of biological tissues," *Ultrasonic Imaging* **13**, 111–134 (1991).
- ²B. S. Garra, I. Cespedes, J. Ophir, R. Zuurbier, C. Magnant, and M. Pennanen, "Analysis of breast lesions using elastography: initial clinical results," *Radiology* (in press).
- ³Y. C. Fung, *A First Course in Continuum Mechanics*, 3rd ed. (Prentice-Hall, Englewood Cliffs, NJ, 1994), 3rd ed.
- ⁴C. Sumi, A. Suzuki, and K. Nakayama, "Estimation of shear modulus distribution in soft tissue from strain distribution," *IEEE Trans. Biomed. Eng.* **42**, 193–202 (1995).
- ⁵F. Kallel and M. Bertrand, "Tissue elasticity reconstruction using linear perturbation method," *IEEE Trans. Med. Imaging* **15**, 299–313 (1996).
- ⁶A. R. Skovoroda, S. Y. Emelianov, and M. O'Donnell, "Tissue elasticity reconstruction based on ultrasonic displacement and strain images," *IEEE Trans. Ultrason. Ferroelectr. Freq. Control* **42**, 747–765 (1995).
- ⁷M. Bilgen and M. F. Insana, "Error analysis in acoustic elastography. I. Displacement estimation," *J. Acoust. Soc. Am.* **101**, 1139–1146 (1997).
- ⁸M. Bilgen and M. F. Insana, "Deformation models and correlation analysis in elastography," *J. Acoust. Soc. Am.* **99**, 3212–3224 (1996).
- ⁹W. R. Remley, "Correlation of signals having a linear delay," *J. Acoust. Soc. Am.* **35**, 65–69 (1963).
- ¹⁰C. H. Knapp and G. C. Carter, "Estimation of time delay in the presence of source or receiver motion," *J. Acoust. Soc. Am.* **70**, 1545–1549 (1977).
- ¹¹W. B. Adams, J. P. Kuhn, and W. P. Whyland, "Correlator compensation requirements for passive time-delay estimation with moving sources or receivers," *IEEE Trans. Acoust. Speech Signal Process.* **28**, 158–168 (1980).
- ¹²J. W. Betz, "Effects of uncompensated relative time companding on a broad-band cross correlator," *IEEE Trans. Acoust. Speech Signal Process.* **33**, 505–510 (1985).
- ¹³J. W. Betz, "Comparison of the deskewed short-time correlator and the maximum likelihood correlator," *IEEE Trans. Acoust. Speech Signal Process.* **32**, 285–294 (1984).
- ¹⁴I. Cespedes and J. Ophir, "Reduction of image noise in elastography," *Ultrason. Imag.* **15**, 89–102 (1993).
- ¹⁵F. Kallel, M. Bertrand, and J. Meunier, "Speckle motion artifact under tissue rotation," *IEEE Trans. Ultrason. Ferroelectr. Freq. Control* **41**, 105–122 (1994).
- ¹⁶I. Cespedes, M. F. Insana, and J. Ophir, "Theoretical bounds on strain estimation in elastography," *IEEE Trans. Ultrason. Ferroelectr. Freq. Control* **42**, 969–972 (1995).
- ¹⁷S. W. Smith, R. F. Wagner, J. M. Sandrick, and H. Lopez, "Low contrast detectability and contrast/detail analysis in medical ultrasound," *IEEE Trans. Sonics Ultrason.* **30**, 164–173 (1983).
- ¹⁸T. Varghese and J. Ophir, "A theoretical framework for performance characterization of elastography: the strain filter," *IEEE Trans. Ultrason. Ferroelectr. Freq. Control* (in press).

Broadband through-transmission signal loss measurements of Alunex[®] suspensions at concentrations approaching *in vivo* doses

Jon N. Marsh and Christopher S. Hall

Laboratory for Ultrasonics, Department of Physics, Washington University, St. Louis, Missouri 63130-4899

Michael S. Hughes

Mallinckrodt Inc., 675 McDonnell Boulevard, Hazelwood, Missouri 63042

Joel Mobley and James G. Miller

Laboratory for Ultrasonics, Department of Physics, Washington University, St. Louis, Missouri 63130-4899

Gary H. Brandenburger

Mallinckrodt Inc., 675 McDonnell Boulevard, Hazelwood, Missouri 63042

(Received 2 January 1996; accepted for publication 29 August 1996)

Broadband normalized signal loss of commercially available Alunex[®], an ultrasonic contrast agent, was measured *in vitro* at concentrations approaching those which may be found *in vivo* for clinical doses. The measurements were made using a novel specimen chamber, careful material handling procedures, and a broadband square wave pulser system. Results were obtained over the full bandwidth of the experimental system (1 to 20 MHz) at concentrations up to 1.9×10^6 microspheres/mL. Further results were obtained over a partial bandwidth of the experimental system at concentrations up to 1.5×10^7 microspheres/mL. The frequency-dependent signal loss exhibited a peak for all concentrations investigated. In the meaningful bandwidth of the system, the signal loss (expressed in dB) was directly proportional to microsphere concentration. The experimental results for normalized signal loss were compared with predictions from a linear single-scattering model for encapsulated bubbles. The experimental data was used to estimate values for the two adjustable parameters in the model: microsphere shell elasticity (4200 ± 1000 dyn/cm) and friction (0.0054 ± 0.0015 dyn s/cm). © 1997 Acoustical Society of America. [S0001-4966(97)04001-0]

PACS numbers: 43.80.Ev, 43.80.Jz, 43.80.Qf, 43.80.Vj [FD]

INTRODUCTION

Models for encapsulated gas-filled bubbles in a liquid¹⁻⁴ predict a peak in ultrasonic scattering intensity and attenuation due to bubble resonance. These models correspond well with observed measurements in dilute concentrations of Alunex[®], a commercially available ultrasonic contrast agent. Alunex (Mallinckrodt Inc., Hazelwood, MO) consists of encapsulated air-filled microspheres suspended in a solution of 5% human serum albumin, the microsphere shells being composed of a thin layer of denatured albumin protein molecules.

Clinical doses of Alunex may yield considerably higher local concentrations in the blood than those used in previously reported through-transmission attenuation measurements. The manufacturer recommends doses of undiluted Alunex of 0.08 to 0.22 mL per kg body mass for left heart echocardiography. One might imagine an injected bolus of Alunex initially having approximately the same size distribution and concentration in the blood as undiluted Alunex has in the vial. However, other factors (such as injection rate, filtering by the lungs, gas balance in the blood, and dilution of the bolus) clearly may act over time to affect both the size distribution and local concentration of microspheres reaching the cardiac chambers or the myocardium itself; the effects of these factors may be difficult to quantify *in vivo*. Our approach in this study has been to perform *in vitro* attenuation

measurements in which we vary only the total microsphere concentration, while attempting to maintain a constant size distribution. This corresponds to an *in vivo* scenario in which the injected Alunex is homogeneously diluted in the blood, while its size distribution remains relatively unaffected. It was thus deemed appropriate to perform measurements at Alunex microsphere concentrations spanning a large range (0.08 to 21.25 mL Alunex/liter, more than 2 orders of magnitude), including fairly high concentrations which may exist *in vivo*.

It is unclear whether present mathematical models will still correspond with observed results for such high concentrations of Alunex, since certain common assumptions may no longer apply. For instance, the average microsphere separation distance may no longer be much greater than the average microsphere size, and independent scattering among the microspheres may no longer apply. Experimental data are difficult to obtain at high microsphere concentrations, since the resonant properties that make bubbles such efficient scatterers also cause them to be very attenuative at certain frequencies when highly concentrated.

Alunex presents other special challenges which must be addressed when performing *in vitro* measurements. For example, measurements must be performed rapidly, since Alunex microspheres tend to deteriorate over time when removed from the vial. It has been our experience that the

TABLE I. Maximum concentrations for selected reported signal loss measurements in Alburnex.

| Investigator | Maximum concentration ($\times 10^6$ microspheres/mL) |
|---------------------------------|--|
| deJong <i>et al.</i> (1992) | 0.23 |
| Bleeker <i>et al.</i> (1990) | 1.4 |
| This study: | 1.9 (full bandwidth)
15.0 (partial bandwidth) |
| Undiluted Alburnex [®] | 700 |

ultrasonic properties of Alburnex diluted in Isoton[®] (a saline solution used as a diluent in the ultrasonic and bubble sizing measurements described below) are stable for only a few minutes. Alburnex microspheres are also highly sensitive to changes in environmental conditions such as temperature, gas balance, and hydrostatic pressure.⁵⁻⁹ The Alburnex suspension must be mixed thoroughly and continuously during measurement to ensure a random, homogeneous spatial distribution of microspheres, and to prevent flotation. Previous *in vitro* work^{1-3,5,6,10} illustrated and addressed many of these issues. In this study, we seek to extend the work already in the literature by measuring *in vitro* broadband through-transmission normalized signal loss of commercially available Alburnex at high concentrations using a novel specimen chamber, careful material handling procedures, and a broadband square wave pulser system.

Table I shows the maximum concentrations for some reported *in vitro* signal loss measurements in Alburnex. In this study, we obtained results over the full bandwidth of the experimental system (1 to 20 MHz) at concentrations up to 1.9×10^6 microspheres/mL. We obtained further results over a partial bandwidth of the experimental system at concentrations up to 1.5×10^7 microspheres/mL. The experimental results were also compared with predictions from a single scattering model (which does not include nonlinear or multiple scattering effects) described in detail in Refs. 1-3, in order to determine the applicability of such a model at high scatterer concentrations.

I. METHODS

A. Specimen chamber

An important element of the measurement system was the specimen chamber that contained the Alburnex during insonification. Simplified drawings of the specimen chamber are shown in Fig. 1. The chamber was composed of two circular Lexan[®] face plates (approx. 6 in. diam, 0.5 in. thick) bolted to each side of a circular Lexan middle section (approx. 6 in. diam, 1 in. thick). Both the face plates and the middle section had a 2-in.-diam hole passing through their centers. Each face plate served to clamp O-rings, a washer, and a Saran Wrap[®] sheet against its side of the middle section, so that the completed chamber had a hollow, circular central section with parallel faces of Saran Wrap serving as acoustic windows. The Alburnex was contained within this part of the chamber during measurements. The distance between the Saran Wrap walls could be varied by using washers of various thicknesses; for this experiment, the wall separation

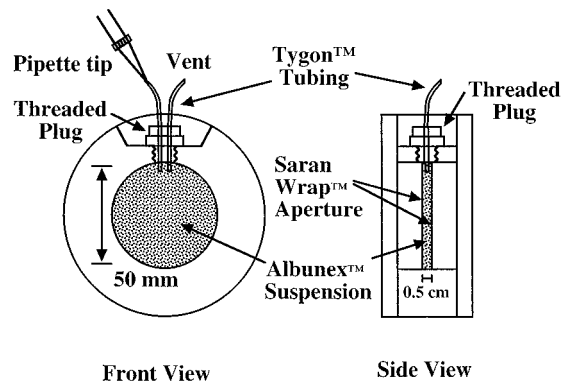


FIG. 1. Simplified diagram of specimen chamber used to contain Alburnex suspension during measurements.

distance was maintained at approximately 5.17 mm. The middle section of the chamber had a large threaded hole drilled radially from its outer edge to its inner edge, such that the hole was open to the central part of the chamber that contained the specimen. The Alburnex suspensions were introduced into the chamber through this port. The chamber was sealed by screwing a threaded Delrin[®] plug into the port. Two Tygon[®] tubes (1 mm inner diameter) passed through the plug and protruded slightly into the chamber. When Alburnex was in the chamber, the ends of the tubes were submerged in the suspension and were used in the mixing of the suspension during measurement (described below).

B. Pipette mixing

During measurement, the suspension was mixed continuously in order to prevent the buoyant Alburnex microspheres from floating to the top of the chamber. The mixing also ensured that the suspension exhibited a different random, homogeneous spatial distribution of the microspheres for each radio-frequency (rf) waveform acquisition (see Sec. I D). The mixing was performed using a micropipette. The micropipette tip was inserted into one of the Tygon tubes projecting from the chamber plug, while the other end of the tube was submerged in the Alburnex suspension. Using the micropipette, $64 \mu\text{L}$ of the suspension was then rapidly and repeatedly drawn and reintroduced into the chamber during the course of the ultrasonic measurement. The other Tygon tube acted as a vent to prevent excess pressure buildup inside the chamber. This type of mixing was found to yield more consistent experimental results than other mixing techniques. These alternative mixing schemes (which were not used in this study) typically involved steady rotation of the entire sealed chamber during measurement, as well as the introduction of a small impeller free to “tumble” inside the chamber itself. The efficacy of the pipette mixing technique was initially confirmed by observation of the rf signal transmitted through the Alburnex suspensions while pipette mixing was performed. Within a few seconds after mixing began, the through-transmitted waveform’s oscilloscope trace would stabilize and remain constant for a minute or more. When mixing ceased, the trace could be observed changing over time in a manner consistent with microsphere flotation and

redistribution. A medical ultrasound imaging system was also used to scan the chamber while pipette mixing was performed. The image of the contrast agent suspension appeared uniform and showed no appreciable temporal variability, indicating homogenous and uniform mixing. Additional measurements performed using a sample chamber filled only with Isoton while undergoing pipette mixing showed no evidence of bubble creation.

At the time these experiments were performed, a Coulter Multisizer® was used to quantitatively measure the size distribution of Albnex straight out of the vial (see Chamber dosing procedure below). Due to the time sensitive nature of the ultrasonic measurements, and the fact that the Multisizer apparatus was located in a laboratory room some distance from the laboratory in which the ultrasonic measurements were performed, it was impractical to measure the microsphere size distributions of samples extracted from within the specimen chamber itself. We have subsequently acquired an optical particle sizer (Accusizer™ 770, Particle Sizing Systems, Inc.) which now enables rapid determination of the Albnex microsphere size distribution which exists within the chamber. This apparatus has been recently used to characterize Albnex suspensions withdrawn directly from the specimen chamber, in order to independently examine the effects of our material handling procedures. It has been found that neither pipette mixing nor insonification (alone or in combination) appears to have any significant effect on the size distributions over the time period needed for a typical measurement run (approximately 30 s; see Chamber dosing procedure below).

C. Chamber dosing procedure

Due to the sensitivity of Albnex to its environment and the manner in which it is handled, a rigorous material handling procedure was developed in order to optimize measurement repeatability. Each experiment consisted of a series of ultrasonic measurements of Albnex suspensions having different concentrations. Before each experiment, an unopened vial of standard, commercial-grade Albnex (lot H9415) was retrieved from refrigerated storage and was allowed to warm to room temperature (approximately 22 °C) while undergoing resuspension (using a roller mixer) consistent with the Albnex package insert. The vial's metal and rubber seals were then carefully removed, and the desired amount of Albnex (ranging from 1 to 255 μL) was withdrawn using a micropipette. The rubber seal was then replaced and the vial was placed back on the roller mixer. The pipetted volume was delivered into the specimen chamber (which, for the experiments described here, was filled with 12 mL of Isoton at approximately 27 °C). The chamber was quickly placed into a temperature-regulated water tank maintained at approximately 27 °C, and the suspension was pipette-agitated during the course of the measurement. The 27 °C operating temperature was chosen primarily to keep the results on an even footing with extensive (unreported) Albnex studies we had previously performed to gain experience and to refine the measurement techniques. The measurement took approximately 20 s to complete, after which the chamber was

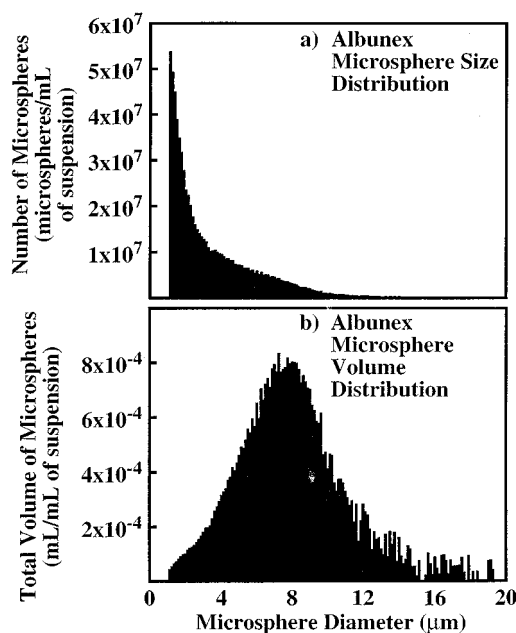


FIG. 2. (a) Microsphere size distribution of undiluted Albnex as determined by Coulter counter. Vertical axis represents total number of microspheres per mL of suspension, and horizontal axis is microsphere diameter in μm . (b) Microsphere volume distribution of undiluted Albnex as determined by Coulter counter. Vertical axis represents total volume in mL of microspheres per mL of suspension, and horizontal axis is microsphere diameter in μm .

rinsed with deionized water and redosed with 27 °C Isoton. This procedure was repeated for each concentration investigated.

Additionally, 20 μL of undiluted Albnex was withdrawn (using a micropipette) from the vial immediately preceding and again immediately following the measurements, diluted in 200 mL of Isoton, and then delivered to a Coulter Multisizer® (Coulter Corporation, Hialeah, FL) particle counter (50- μm orifice diameter, sensitive to a diameter range from 1.0 to 32.0 μm in 0.125- μm steps) to determine the Albnex microsphere size distributions in the vial before and after the experiment. The microsphere size distributions in the vial did not differ significantly over the course of the entire experiment. Figure 2(a) displays the Albnex size distribution for the vial used in the experiment described here; Fig. 2(b) displays the corresponding distribution by volume count. The total particle count for the undiluted agent was 7.3×10^8 microspheres/mL, the mean particle diameter was 3.4 μm , and the gas volume fraction was 4.4%. Measurements of size distribution (as determined by the Multisizer) from other Albnex vials from the same lot yielded similar results, with total microsphere concentration typically ranging between 6×10^8 and 8×10^8 microspheres/mL.

It should be noted that different size distribution results might be obtained if the material handling procedure had included delivery of the agent via hypodermic needle, as would be done, for instance, if a determination of the likely size distribution *in vivo* were sought. The material handling procedure used here was chosen in order to maximize the number of particles delivered into the measurement appara-

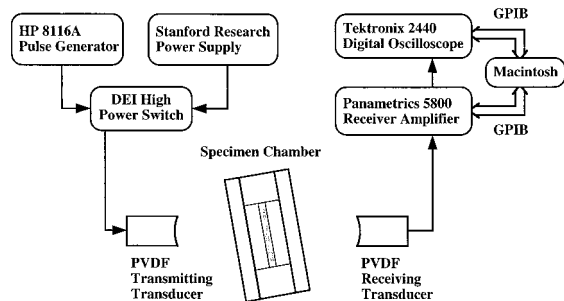


FIG. 3. Diagram of experimental setup used for measurements of signal loss of Alburnex suspensions. Transducers and specimen chamber are immersed in a temperature controlled water bath during measurements.

tus. This was deemed appropriate for our experiments, which were aimed at determination of the scattering properties of highly concentrated Alburnex suspensions.

D. Experimental setup and acquisition

The measurements were performed in a through-transmission setup using a pair of broadband immersion PVDF transducers (0.4 in. diam, 3.25 in. focal length, model ZF3002-SU, Panametrics, Waltham, MA). The transmitting transducer was excited using a dc voltage step. The pulser system was composed of a function generator (model 8116A, Hewlett-Packard, Palo Alto, CA), a high voltage power supply (model PS310, Stanford Research Systems, Inc., Sunnyvale, CA), and a high power switch (model GRX-1.5K-E, Directed Energy, Inc., Ft. Collins, CO). This system produced square pulse trains whose duty cycle and amplitude could be precisely controlled. For the measurements described here, the transmitting transducer was excited on the downward sloping edge of a 200-V amplitude square pulse (256-Hz repetition rate). The subsequent upward sloping edge of the exciting square pulse occurred 200 μ s later, but the results of this transducer excitation were excluded by gating. The amplitude used was well below the 350-V allowable maximum for this transducer type. This yielded a broadband (1 to 20 MHz), approximately unipolar ultrasonic pulse. A calibrated, 1-mm-diam PVDF hydrophone (Force Institute, Copenhagen, Denmark) was used to determine the peak pressure in the focal plane of the transmitting transducer. The peak positive pressure amplitude was 0.30 MPa, and the peak negative pressure amplitude was 0.24 MPa.

A schematic of the experimental setup is shown in Fig. 3. The transducers were placed roughly 6 in. apart, and the sample chamber was positioned midway between them during measurement. The specimen chamber was placed on a tilted platform angled at 10° relative to the axes of the transducers. This was done in order to minimize effects from internal reflections. The transmitted ultrasonic pulse passed through the Alburnex suspension and was intercepted by the receiving transducer. A broadband receiver (Panametrics model 5800) provided software-controlled amplification prior to digitization at 250 megasamples per second by an 8-bit digitizing oscilloscope (model 2440, Tektronix, Beaverton, OR). Total receiver gain varied between 0 and 40 dB, depending on the concentration of Alburnex in the chamber.

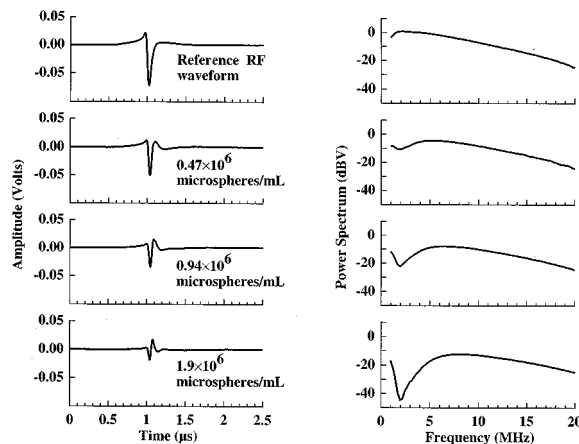


FIG. 4. Four graphs on left show example segments of time-domain-averaged rf traces. Top waveform is reference trace (average of 500 acquisitions); lower three waveforms are through-transmitted signals (averages of 100 acquisitions each) for Alburnex concentrations of 0.47×10^6 , 0.94×10^6 , and 1.9×10^6 microspheres/mL, respectively. Four graphs on right are corresponding power spectra for these time domain waveforms.

500 rf traces (each 1024 points long) were acquired at a rate of approximately 30 traces per second for each concentration of Alburnex in the chamber. A Macintosh computer was used to control acquisition via GPIB, and to store data to disk. 500 reference traces acquired in the same manner using a specimen chamber filled only with Isoton provided a reference for normalization.

E. Analysis

The rf traces for each concentration were averaged together in the time domain in five sets of 100 traces each. All 500 reference rf traces were similarly averaged in the time domain. Time-domain averaging of the through-transmitted waveforms was possible because of the relatively large beam diameter (-6 -dB beam diameter of approximately 2.5 mm at 5 MHz), the small size of the microspheres compared to a wavelength, and the great number of homogeneously dispersed microspheres in theinsonified region (ranging from about 200 to more than 10^5 microspheres, depending on concentration and the size of the frequency-dependent beam volume). The Alburnex suspension effectively presented a nearly uniform attenuating medium to theinsonifying beam. Thus the through-transmitted waveform amplitude and phase remained constant during the course of each measurement, except for effects from random noise. Time-domain averaging of the rf traces effectively averaged away the zero-mean random noise, yielding a clean, bit-dithered signal with enhanced dynamic range (equivalent to using an approximately 11-bit digitizer). The four graphs on the left of Fig. 4 are example segments of time-domain-averaged rf traces for the reference measurement and three specific concentrations of Alburnex in the chamber. The corresponding power spectra of these traces (determined using the fast Fourier transform) are plotted on the right side of Fig. 4. Note the progressive change in frequency content of the through-transmitted waveforms as the microsphere concentration is increased.

Frequency-dependent signal loss was determined for each concentration of Alburnex microspheres in the chamber.

The log spectral power of each of the time-domain-averaged rf traces was subtracted from the log spectral power of the time-domain-averaged reference rf trace to compensate for electromechanical effects, yielding signal loss in dB. These signal loss results were then divided by the sample path length (5.25 mm, which was slightly longer than the chamber thickness due to the chamber's 10° tilt) to yield normalized signal loss in dB/cm. The resulting five normalized signal loss curves were averaged together, and their standard deviations determined. This procedure was repeated for each concentration investigated.

II. THEORY

The theoretical results in this work were generated using the encapsulated bubble model described in detail by de Jong.³ The model is a single-scattering model; i.e., the incident sound wave is assumed to be scattered only once by each microsphere in the field, and subsequent rescatterings of the scattered waves are not considered. Additionally, only terms linear in the applied acoustic pressure are retained. The model includes assumptions that (1) the wavelength of the incident pressure field is much larger than the microsphere diameter, (2) the microspheres are uniformly and homogeneously distributed, (3) the number of microspheres in the sound beam is much greater than one, (4) the average distance between the microspheres is much greater than their size, and (5) forward scattering is negligible. There are two adjustable parameters in the model to account for the effects of the microsphere's solid shell: an elasticity parameter and a friction parameter. Varying these parameters changes the frequency dependence of the bubble's scattering cross section. The total scattering cross section for a group of microspheres is obtained by summing the scattering cross sections of all the individual microspheres. The model predicts several important results. First, the scattering cross section of an individual microsphere exhibits a resonance peak. Second, the signal loss of a suspension of microspheres increases with increasing concentration. Third, the signal loss through a microsphere suspension, measured on a logarithmic basis in dB, is directly proportional to the number of microspheres.

The microsphere size and number density information obtained from the Coulter Multisizer were used in generating theoretical fits to the experimental signal loss data. The contributions to the total extinction cross section from each microsphere size were multiplied by the respective number density of each bubble size; these contributions were then summed to obtain the total extinction cross section for the microsphere distribution. Signal loss for the microsphere distribution was then calculated from the total extinction cross section. Theoretical signal loss curves generated in this manner were fit to the experimental signal loss curves by adjusting the shell elasticity and friction parameters to minimize the square of the difference between the two curves.

III. RESULTS

The results displayed in Figs. 5–7 were determined from measurements using a single vial of Alburnex. The normalized signal loss of specific concentrations of Alburnex is plot-

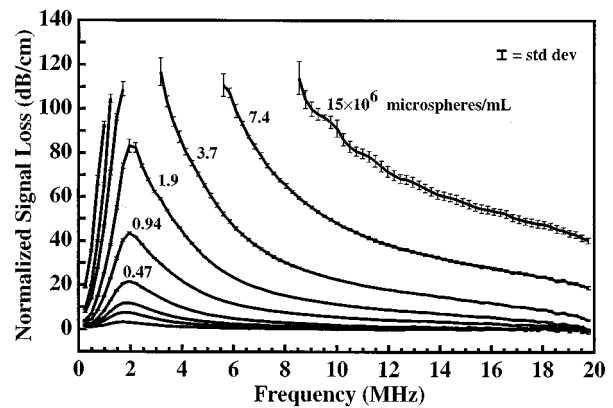


FIG. 5. Normalized signal loss for specific concentrations of Alburnex. Microsphere concentrations corresponding to each curve are given in ($\times 10^6$ microspheres)/mL. The concentrations of the three unlabeled curves are 0.059×10^6 , 0.12×10^6 , and 0.23×10^6 microspheres/mL. Vertical axis represents normalized signal loss in dB/cm, and horizontal axis represents frequency in MHz. Error bars represent standard deviations of the determination of normalized signal loss at each frequency.

ted in Fig. 5. These concentrations were (from lowest to highest): 0.059×10^6 , 0.12×10^6 , 0.23×10^6 , 0.47×10^6 , 0.94×10^6 , 1.9×10^6 , 3.7×10^6 , 7.4×10^6 , and 15×10^6 microspheres/mL of suspension. The vertical axis represents normalized signal loss of the suspension in dB/cm, and the horizontal axis is frequency in MHz. Each curve represents the normalized signal loss data for a specific concentration of Alburnex. Standard deviations at each frequency are plotted over the curves. No data are displayed for the three highest concentrations around the region of peak signal loss because these Alburnex suspensions attenuated the incoming pulse so highly that no meaningful signal could be observed in this frequency range.

Figure 6 displays the signal loss data for the lowest six concentrations, along with theoretical fits to the data obtained using the independent scattering model described by de Jong. For each concentration, the shell parameters were adjusted to minimize the square of the difference between

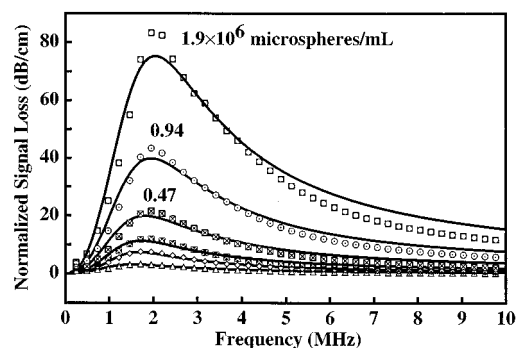


FIG. 6. Theoretical fits to normalized signal loss data at specific Alburnex concentrations. Vertical axis represents normalized signal loss in dB/cm, and horizontal axis represents frequency in MHz. Experimental results from the lowest six concentrations (0.059×10^6 , 0.12×10^6 , 0.23×10^6 , 0.47×10^6 , 0.94×10^6 , 1.9×10^6 microspheres/mL) are displayed as data points, with the theoretical fit corresponding to each curve shown as solid line. The mean value and standard deviation for the elasticity parameter is 4200 dyn/cm (± 1000), and the mean value and standard deviation for the friction parameter is 0.0054 dyn s/cm (± 0.0015).

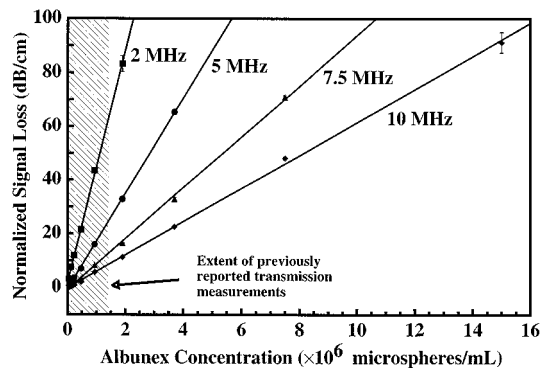


FIG. 7. Normalized signal loss of Alburnex concentration at 2, 5, 7.5, and 10 MHz. Horizontal axis represents Alburnex concentration in ($\times 10^6$ microspheres)/mL. Experimental results are displayed as data points, with linear fit to the data at each frequency shown as solid lines. Error bars represent standard deviations of the determination of normalized signal loss at each frequency. Shaded area on left side represents extent of concentrations used in previously reported through-transmission signal loss measurements of Alburnex.

each of the theoretical curves and the corresponding experimental values. The theoretical fits generated in this way are shown as solid lines overlying the data points. The six pairs of parameter values were then averaged together to obtain a mean value and standard deviation for the elasticity parameter of 4200 dyn/cm (± 1000), and a mean value and standard deviation for the friction parameter of 0.0054 dyn s/cm (± 0.0015).

Figure 7 shows normalized signal loss of specific concentrations of Alburnex at 2, 5, 7.5, and 10 MHz. The vertical axis represents normalized signal loss in dB/cm, and the horizontal axis represents concentration of Alburnex in total number of microspheres/mL. Standard deviation bars are plotted over each data point. A linear fit is plotted through each data series; the r^2 value for each linear fit is greater than 0.999. The shaded area on the left side of the graph indicates the range of concentrations spanned by previously reported broadband through-transmission signal loss measurements.

IV. DISCUSSION

Several significant features should be noted about Figs. 5–7. First, the signal loss increases with increasing concentration, which is an expected result and a prediction of the model. Each signal loss curve also displays a pronounced peak; this is also a model prediction (given this particular microsphere size distribution). A more interesting result is that the signal loss *in* dB is directly proportional to concentration,¹¹ so that a doubling of microsphere concentration doubles the attenuation in dB. This effect is observed (in the meaningful bandwidth) even at the highest concentrations we are currently able to measure. Again, this is a prediction of the single-scattering model, even though it is not clear *a priori* whether the single-scattering approximation is valid for microsphere concentrations this high. Previous work^{12–14} has indicated that it may be necessary to include multiple scattering effects in the mathematical description of sound propagation through a concentrated cloud of strong scatterers. The experimental implications of multiple scatter-

ing effects might include nonproportionality of signal loss measured in dB with concentration of scatterers. Indeed, in a separate preliminary study (data not shown), we were able to observe a low-frequency (lower than 1 MHz) signal propagating through a specimen chamber filled with undiluted Alburnex (approximately 7×10^8 microspheres/mL), whereas the single-scattering model predicted an attenuation so high ($\sim 10^3$ dB/cm at 1 MHz) that no observable signal should have passed through. This evidence suggests that the single-scattering approximation may eventually break down for Alburnex microspheres, but at concentrations higher than we are yet able to measure quantitatively.

The fact that the model parameters used in generating the theoretical fits of Fig. 6 were similar, but not identical, from concentration to concentration gives some idea of the experimental variability in the measurements. If the experiment were ideal, and if there were no multiple scattering, one would expect all the signal loss curves to have exactly the same shape (apart from the multiplicative concentration scaling factor), and thus the model fits would be described by the same elasticity and friction parameters for each curve. The modest differences in the parameter values from concentration to concentration are due to subtle changes in the shape of the curves (e.g., width and position of signal loss peak), and indicate the sensitivity of the model to such changes.

Although the results presented here and those measured by other researchers are qualitatively similar, some differences exist. All published signal loss curves for unfiltered Alburnex have the same general features: the signal loss rises from a minimum at low frequencies to a peak in the low MHz range, and then tails off slowly at higher frequencies. Previous published results exhibit modest differences in the position and width in frequency of the signal loss peak, as well as in overall magnitude. Such differences in measured values can affect the estimation of the shell elasticity and friction parameters, because the model used here is highly sensitive both to changes in these parameters and also to microsphere size distribution. In a study by de Jong and Hoff,² the model fit the data best using a shell elasticity of 8000 dyn/cm and a shell friction of 0.004 dyn s/cm, whereas here we obtained values of 4200 dyn/cm and 0.0054 dyn s/cm, respectively. These differences may be explained by several factors. Size distribution of the microspheres has the largest impact on ultrasonic characteristics of the suspensions. As described above, material handling can affect the size distribution and population of the microspheres, and may thus affect the signal loss measurement. In this study, we have attempted to treat the suspensions as carefully and reproducibly as possible to ensure the stability of the samples. This is also the first study of this type to have used fresh, commercially available Alburnex. Signal loss measurements of Alburnex suspensions using different vials from the same production lot yielded nearly identical results, demonstrating the consistency of both the size distribution of commercially available Alburnex and the measurement system employed here.

Additionally, it is important to consider the potential for nonlinear bubble behavior when interpreting these measurements. In another preliminary study (data not shown), we

observed very modest apparent downward shifts in frequency and increases in magnitude of the signal loss peak of Alburnex suspensions as functions of increasing insonifying power. The mechanism for this behavior is currently unclear, but is suggestive of nonlinear acoustic wave propagation in the microsphere suspensions. If nonlinearity does occur, it may represent another explanation of differences in reported signal loss measurements, since any result would necessarily depend on the particulars of the experiment (e.g., level of insonifying power, type of transducer focusing, and position of the sample in the insonifying field). It should be noted again that in the data reported in this paper, the transmitting transducer was excited with a voltage level that yielded pressure amplitudes in the Alburnex-filled chamber that were comparable to or less than those encountered in clinical echocardiography. Operating at lower insonifying power levels would presumably decrease any nonlinear effects, but at the expense of decreased dynamic range of the measurement system. We intend to investigate this behavior in more detail in future work.

V. SUMMARY AND CONCLUSIONS

The present work extends the range of concentrations and frequency over which the signal loss of Alburnex has been measured. Full-bandwidth through-transmission signal loss was measured at concentrations up to 1.9×10^6 microspheres/mL, and partial bandwidth results were obtained at concentrations up to 1.5×10^7 microspheres/mL. The signal loss exhibits a peak for all concentrations investigated. The notch filtering effect of the microspheres on the through-transmitted ultrasonic signal limits the meaningful bandwidth of the current measurement system at concentrations higher than 1.9×10^6 microspheres/mL. The single-scattering linear model predictions correspond well with experimental data in the meaningful bandwidth. In the

meaningful bandwidth, the signal loss (expressed in dB) of Alburnex suspensions is directly proportional to concentration, suggesting the single-scattering approximation is valid at the highest concentrations investigated here.

- ¹N. de Jong, L. Skotland, and N. Bom, "Absorption and scatter of encapsulated gas filled microspheres: theoretical considerations and some measurements," *Ultrasonics* **30**, 95–103 (1992).
- ²N. de Jong and L. Hoff, "Ultrasound scattering properties of Alburnex microspheres," *Ultrasonics* **31**, 175–181 (1993).
- ³N. de Jong, "Acoustic Properties of Ultrasound Contrast Agents," Ph.D. thesis, Erasmus University, 1993.
- ⁴C. C. Church, "The effects of an elastic solid surface layer on the radial pulsations of gas bubbles," *J. Acoust. Soc. Am.* **97**, 1510–1521 (1995).
- ⁵H. J. Bleeker, K. K. Shung, and J. L. Barnhart, "Ultrasonics characterization of Alburnex®, a new contrast agent," *J. Acoust. Soc. Am.* **87**, 1792–1797 (1990).
- ⁶H. J. Bleeker, K. K. Shung, and J. L. Barnhart, "On the Application of Ultrasonic Contrast Agents for Blood Flowmetry and Assessment of Cardiac Perfusion," *J. Ultrasound Med.* **9**, 461–471 (1990).
- ⁷N. de Jong, F. J. ten Cate, W. B. Vletter, and J. R. T. C. Roelandt, "Quantification of transpulmonary echocontrast effects," *Ultrasound Med. Biol.* **19**, 279–288 (1993).
- ⁸J. G. Wiencek, S. B. Feinstein, R. Walker, and S. Aronson, "Pitfalls in Quantitative Contrast Echocardiography: The Steps to Quantitation of Perfusion," *J. Am. Soc. Echocardiography* **6**, 395–416 (1993).
- ⁹C. Vuille, M. Nidorf, R. L. Morrissey, J. B. Newell, A. E. Weyman, and M. H. Picard, "Effect of Static Pressure on the Disappearance Rate of Specific Echocardiographic Contrast Agents," *J. Am. Soc. Echocardiography* **7**, 347–354 (1994).
- ¹⁰P. H. Chang and K. K. Shung, "Attenuation and backscatter measurements on Alburnex®," *IEEE Ultrason. Symp. Proc.* 913–916 (1993).
- ¹¹S. Holm, M. Myhrum, and L. Hoff, "Modelling of the ultrasound return from Alburnex microspheres," *Ultrasonics* **32**, 123–130 (1994).
- ¹²P. C. Waterman and R. Truell, "Multiple Scattering of Waves," *J. Math. Phys.* **2**, 512–537 (1961).
- ¹³K. W. Commander and A. Prosperetti, "Linear pressure waves in bubbly liquids: Comparison between theory and experiments," *J. Acoust. Soc. Am.* **85**, 732–746 (1989).
- ¹⁴J. L. Leander, "Transient wave propagation through bubbly layers via the Foldy–Twersky integral equation," *J. Acoust. Soc. Am.* **95**, 2378–2386 (1994).

Broadband measurements of the attenuation coefficient and backscatter coefficient for suspensions: A potential calibration tool

Christopher S. Hall and Jon N. Marsh

Laboratory for Ultrasonics, Department of Physics, Washington University, St. Louis, Missouri 63130-4899

Michael S. Hughes

Mallinckrodt Inc., 675 McDonnell Boulevard, Hazelwood, Missouri 63042

Joel Mobley, Kirk D. Wallace, and James G. Miller

Laboratory for Ultrasonics, Department of Physics, Washington University, St. Louis, Missouri 63130-4899

Gary H. Brandenburger

Mallinckrodt Inc., 675 McDonnell Boulevard, Hazelwood, Missouri 63042

(Received 13 August 1996; accepted for publication 20 August 1996)

Tissue characterization would be facilitated by improved methods of calibration with which to make absolute measurements of the backscatter and attenuation of tissue or contrast agents. In this paper, the use of polystyrene microspheres is examined as a potential broadband *in vitro* calibration tool by employing an experimental system designed to characterize ultrasonic contrast agents. The frequency-dependent attenuation coefficient and backscatter coefficient were measured for a series of microsphere size distributions with a broadband ultrasound system using a custom-built specimen chamber and a novel suspension mixing technique. The measurements were used in a broadband reduction method to yield the backscatter coefficient. The range of ka spanned in this study is from $ka=0.5$ to $ka=12$. The broadband nature of the pulses permitted simultaneous measurement of different regimes of scattering of the microspheres (specifically, the transition region from Rayleigh to short-wavelength asymptotic scattering). Experimental results were compared with corresponding theoretical predictions for the attenuation and backscatter of solid elastic spheres in liquid and yielded good quantitative agreement. Discussion of some possible applications of this technique to the fields of tissue characterization and contrast is presented. © 1997 Acoustical Society of America. [S0001-4966(97)04101-5]

PACS numbers: 43.80.Ev, 43.80.Vj, 43.35.Yb [FD]

INTRODUCTION

The use of high-frequency ultrasound for medical applications has been increasing in recent years with the advent of intravascular ultrasound,¹⁻⁴ acoustic microscopy,^{5,6} and second harmonic imaging with ultrasonic contrast agents.^{7,8} Higher frequencies allow new morphologic structures to be examined and open a new area for ultrasonic tissue characterization. In the past, tissue characterization has been hampered by the lack of a standard method of calibration with which to make absolute measurements of the backscatter and attenuation. In this paper we examine a possible calibration technique for use in a frequency range above that which is currently employed in conventional transthoracic ultrasonic medical imaging machines.

The ultrasonic scatter from tissue is often modeled as a collection of scatterers suspended in a water-like medium. The use of calibration standards or "phantoms" that mimic tissue has been of particular interest to the tissue characterization community. A substantial body of work exists that examines phantoms for ultrasound in the frequency range below 5 MHz.⁹⁻¹³ These phantoms have worked well for calibration of conventional imaging modalities in the heart,¹⁴ kidney,¹⁵ liver,¹⁰ etc., and often consist of a collection of scatterers held in an agarose or gelatin-like matrix. The geo-

metrical shape and physical parameters of the scatterers within tissue can be further derived with the use of an appropriate data reduction method.^{11,16} In the higher frequency world of acoustic microscopy and intravascular imaging, it is not clear if the existing phantoms will provide a useful and reproducible method for calibration. An alternative ultrasonic calibration technique was proposed by T. Rhyne.¹⁷ This system consists of microspheres which are constantly stirred by a rotary mixer to allow for reconfiguration of the scatterers in the ultrasonic field. In this study, we explore the feasibility of an extension of this calibration technique by implementing a system that utilizes a continuously agitated suspension of polystyrene spheres in a saline solution (Coulter™ Isoton II) with surfactant.

The scattering of sound from solid spheres has been a topic of many avenues of research in acoustics.^{18,19} The first complete description of scattering from a solid sphere has been attributed to Faran.²⁰ Solid plastic and metallic spheres in a fluid have provided a simple system with which to understand the physics of ultrasonic scattering in a wide variety of experiments. Early research was driven by interest in the effects of scatterers on sonar.²¹ The problem of scattering of sound by spherical inhomogeneities suspended in a fluid has also been of interest in fields such as the prediction of sedi-

mentary transport processes in the marine environment^{22–25} and more recently, ultrasonic contrast agents.^{26–28}

Previous measurements have yielded results for a wide range of ka where k is the wavenumber of insonifying ultrasound and a is the scatterer diameter. One major advantage to using agitated suspensions of elastic spheres, compared to more conventional calibration techniques such as gelatin phantoms, is the inherent ensemble averaging due to the motion and distribution of scatterers within the suspension. Investigations of the attenuation of sound in suspensions²⁹ and resonance scattering in suspensions³⁰ have shown that increased backscatter cross sections of up to five times the geometric cross section can occur at frequencies corresponding to the rigid resonances and modal resonances of the spheres.

This study was designed to validate an experimental system used in the measurement of the physical properties of certain ultrasonic contrast agents. These microbubbles exhibit sharply peaked resonances which lead to scattering and absorption cross sections that can differ from the microbubbles' geometric cross sections by an order of magnitude or more in certain frequency ranges.³¹ The large scattering cross sections of resonating bubbles are useful clinically because of their increased echogenicity relative to blood and most types of tissue, providing enhanced visualization of blood–tissue boundaries, and potentially enabling quantification of tissue perfusion. This system has been used previously to analyze the physical properties of Alunex^{®32} and other contrast agents. In this study, plastic spheres were employed for several reasons: their shape is similar to most solid and gas bubble based contrast agents;³³ the scatterers exhibit resonances, although for different physical reasons than do gaseous, microbubble, contrast agents; the plastic microspheres can be made in a similar size range to the agents; and it is possible to manufacture the suspension in a repeatable manner. All measurements were made with a single matched pair of transducers excited by a broadband pulse to obtain data from 5 to 30 MHz in a single measurement.

Several factors distinguish this work from similar studies already in the literature. Each of the microsphere suspensions used in this study was carefully sized and shown to have a very narrow size distribution. The narrowness of the distributions permitted the “sharp” character of the spheres' acoustic resonances to be more easily observed. Each complete distribution was used then used to directly compare theoretical predictions of the suspensions' attenuation and backscatter to measurements. The narrowness of the distributions and the inherent ensemble averaging resulting from the constant agitation of the microspheres permitted comparison of spectral structure, which has not been published in the tissue characterization community previously. Other previously reported broadband investigations of the scattering properties of solid spheres have used several transducers operating in overlapping frequency ranges, or have employed continuous wave insonification swept over many discrete frequencies in order to span a large bandwidth of interest.^{2,22,30} Such measurements have been used to verify the theoretical solutions^{34–36} to the scattering problem, which predict com-

plex frequency- and angle-dependent behavior for the scattered pressure wave. The use of continuous wave insonification is useful because of the lower instantaneous power in the field compared to that of a broadband pulse. However, in clinical imaging systems and various high-frequency applications, it is necessary to use broadband pulses for increased spatial location and resolution. Thus any potential calibration technique should be based on the use of broadband pulses. In addition, the use in this study of a single broadband-pulsed transducer pair circumvents certain problems arising from multiple transducer and narrow-band setups by permitting simultaneous measurement over a broad continuum of frequencies. Finally, when utilizing a single transducer pair system it is not necessary to “piece together” spectral results obtained from different transducer pairs that may potentially exhibit very different diffraction corrections due to differences in transducer geometry or variations between commercially manufactured transducers.

The study makes use of a simple, first-order, broadband reduction technique previously used by our laboratory.^{16,37,38} This technique makes several simplifying approximations about the transducer's beam diffraction and the effects of time domain gating of the signal. The well-controlled experimental system of a suspension of polystyrene spheres aided in testing the validity of these approximations. The data reduction technique is not computationally intensive and could be used in future *in vivo* tissue characterization applications.

Section I describes briefly the theoretical predictions of a scattering model developed by Faran. Section II describes the experimental setup and the data reduction techniques used in the study. Section III contains the experimental results and comparisons with the theoretical predictions, while Sec. IV discusses the limitations and applications of the presented work.

I. THEORY

The theoretical prediction of the scattering of sound from solid spheres is well known.²⁰ In this section, we will attempt to summarize the relevant parts of the theory applied within this study. The predictions of the elastic scattering of sound from solid spheres can be obtained by solving the wave equation in three dimensions and using the physical boundary conditions at the solid–liquid interface. The three relevant boundary conditions are (i) the pressure in the fluid must be equal to the normal (radial) component of stress in the solid at the interface; (ii) the normal component of the displacement of the fluid must be equal to the normal component of the displacement of the solid; (iii) the tangential components of shearing stress must vanish at the surface of the solid.

Using these boundary conditions and the wave equation, it is possible to derive an exact expression for the scattering from a sphere due to an incident plane wave. The expression for the pressure due to scattering from a sphere is^{30,38,39}

$$p_r = p_0 \sum_{q=0}^{\infty} (2q+1) i^q A_q h_q(k_c r) P_q(\cos \theta) e^{-i\omega t}, \quad (1)$$

where p_0 is the incident wave's amplitude, h_q is the q th spherical Hankel function of the first kind, k_c is the wave number in the surrounding fluid, r is the radial distance from the center of the scatterer, P_q is the q th Legendre polynomial, θ is the scattering angle, and ω is the angular frequency. The boundary conditions at the surface of the sphere determine the coefficients A_q , which are functions of sphere radius a , angular frequency ω , liquid density ρ_l , scatterer density ρ_s , liquid compressional wave velocity c_l , scatterer compressional wave velocity c_s , and scatterer shear wave velocity s_s .

The total cross section for a single sphere (due to scattering only) is then given by^{29,39,40}

$$\sigma_s = \frac{4\pi}{k_c^2} \sum_{q=0}^{\infty} (2q+1) |A_q|^2. \quad (2)$$

If we now define an attenuation coefficient α such that $p = p_0 e^{-\alpha x}$, where p_0 is some incident acoustic pressure, then we can say that for a number density n of identical scatterers, $\alpha = n\sigma_s/2$,⁴⁰ or, for a discrete distribution of scatterers,

$$\alpha = \frac{\sum_m n(a_m) \sigma_s(a_m)}{2}, \quad (3)$$

where $n(a_m)$ is the number density of scatterers of size a_m . The final result is then

$$\alpha = \frac{\sum_m n(a_m) \cdot \left[\left(\frac{4\pi}{k_c^2} \sum_{q=0}^{\infty} (2q+1) |A_q(a_m, \rho_l, \rho_s, c_l, c_s, s_s)|^2 \right) \right]}{2}, \quad (4)$$

where α (in cgs units) is given in nepers/cm. The quantity we measured experimentally was signal loss in dB, which, in terms of the preceding expressions can be written

Signal loss in dB

$$\begin{aligned} &= 20 \log_{10} \left(\frac{p_0}{p} \right) \\ &= 20 \log_{10} (e^{\alpha x}) = 4.343x \left[\sum_m n(a_m) \cdot \left(\frac{4\pi}{k_c^2} \sum_{q=0}^{\infty} (2q+1) |A_q|^2 \right) \right]. \end{aligned} \quad (5)$$

The attenuation coefficient (dB/cm) is obtained by dividing the signal loss by the thickness, x , of the sample.

We assume that the backscatter of many spheres can be calculated from the backscatter due to one sphere if effects due to multiple scattering are ignored.⁴¹ In particular the differential scattering cross section, $d\sigma_{\text{tot}}(f)/d\Omega|_{180^\circ}$, from identical spheres with a number density n , is

$$\frac{d\sigma_{\text{tot}}(f)}{d\Omega} \Big|_{180^\circ} = n \frac{d\sigma_s(a, f)}{d\Omega} \Big|_{180^\circ}, \quad (6)$$

where $d\sigma_s(a, f)/d\Omega|_{180^\circ}$ is the differential scattering cross section due to one sphere of size a . With the introduction of a distribution of sizes, $n(a_m)$, the expression for the total differential scattering cross section becomes

$$\frac{d\sigma_{\text{tot}}(f)}{d\Omega} \Big|_{180^\circ} = \sum_m n(a_m) \frac{d\sigma_s(a_m, f)}{d\Omega} \Big|_{180^\circ}. \quad (7)$$

The backscatter coefficient is the differential scattering cross section per unit volume, i.e., Equation (7) divided the volume of tissue insonified. Equation (7) was used in conjunction with the measured scatterer sizes to compute the theoretical predictions presented later in the paper.

Material parameters obtained both from the manufacturer and the literature were used to compute the backscatter from the suspension. The values for the material parameters are listed in Table I. The values were a particle density of 1.055 g/cm³, density of Isoton of 1.0 g/cm³, a longitudinal speed of sound in Isoton of 1490 m/s, a longitudinal speed of sound in the polystyrene microsphere of 2380 m/s, and a shear velocity of the polystyrene microsphere of 1180 m/s. The value for the shear velocity of polystyrene was adjusted from the previously reported range of 1100 to 1120 m/s in order to provide better agreement between experimental results and theoretical predictions. A more detailed discussion of this adjustment occurs in Sec. V.

II. METHODS

A. Microspheres

All of the microsphere suspensions used in this study were obtained from Duke Scientific Corporation (Palo Alto, CA). These suspensions are manufactured for use in calibrating particle sizing systems. According to the manufacturer, the microspheres were composed of polystyrene and/or polystyrene divinylbenzene, and were suspended in a saline solution (Isoton II[®], Coulter Corp.) having a small amount of dispersant added to prevent microsphere flocculation. The suspensions' compositions were typically about 1% solids by volume, and the microspheres were listed as having a nominal density between 1.00 and 1.05 g/mL. Although size dis-

TABLE I. Listed here are the material parameters used for the calculations of the theoretical predictions of the scattering model.

| | Numerical values of materials properties | | |
|----------------------|--|-----------------------------|----------------------|
| | Density (g/cm ³) | Longitudinal velocity (m/s) | Shear velocity (m/s) |
| Polystyrene | 1.055 | 2380 | 1180 |
| Isoton TM | 1.0 | 1490 | N/A |

TABLE II. Listed here are the measured values of the distributions of polystyrene microspheres made using the optical particle sizer.

| Nominal diameter (μm) | Microsphere distributions | | Number density ($\times 10^4$ particles/mL) |
|------------------------------------|--|--------------------------------------|--|
| | Measured mean diameter (μm) | Standard deviation (μm) | |
| 30 | 29.6 | 1.2 | 29.0 |
| 40 | 40.4 | 4.0 | 14.0 |
| 50 | 50.6 | 6.4 | 13.0 |
| 60 | 59.0 | 6.8 | 7.4 |
| 70 | 69.6 | 7.0 | 6.7 |
| 80 | 83.1 | 7.0 | 2.9 |
| 100 | 101.6 | 8.0 | 1.8 |

tribution information was provided by the manufacturer, an optical particle sizer (described below) was used to obtain independent measurement of the distributions of each suspension employed in the study, concurrent with the ultrasonic measurements. Seven different suspensions were used, having narrow size distributions centered around 30-, 40-, 50-, 60-, 70-, 80-, and 100- μm sphere diameters, respectively. Typical half-widths of the distributions were about 5% of the mean diameter. The measured values for the mean diameter, standard deviation and number density of microspheres is summarized in Table II.

B. Specimen chamber

The specimen chamber used for all the measurements in this study was the same one employed and described in detail in our previous study of the attenuation of suspensions of the ultrasonic contrast agent Alunex[®].³² A simplified diagram of the specimen chamber is shown in Fig. 1. The chamber was composed of two circular Lexan[®] face plates (approx. 6 in. diameter, 0.5 in. thick) bolted to each side of a circular Lexan middle section (approx. 6 in. diameter, 1 in. thick). Both the face plates and the middle section had a 2-in.-diam hole passing through their centers. Each face plate served to clamp O-rings, a washer, and a Saran Wrap[®] sheet against its side of the middle section, so that the completed chamber had a hollow, circular central section with parallel faces of Saran Wrap serving as acoustic windows. The bead suspension was contained within this part of the chamber

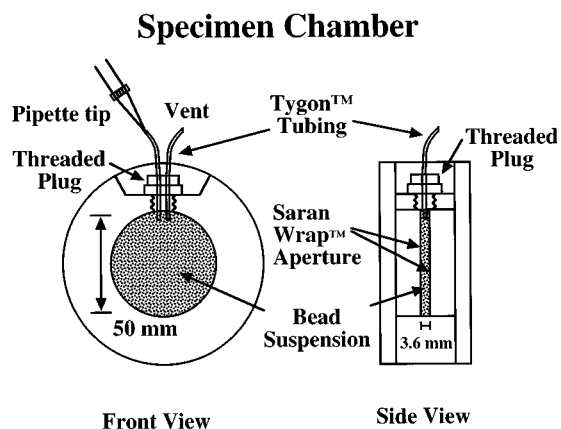


FIG. 1. A diagram of the specimen chamber used to hold and agitate the suspension of polystyrene microspheres during ultrasonic interrogation.

during measurements. The distance between the Saran Wrap walls could be varied by using washers of different thicknesses; for this experiment, the wall separation distance was maintained at approximately 3.6 mm. The middle section of the chamber had a large threaded hole drilled radially from its outer edge to its inner edge, such that the hole was open to the central part of the chamber that contained the specimen. The microsphere suspensions were introduced into the chamber through this port. The chamber was sealed by screwing a threaded Delrin[®] plug into the port. Two Tygon[®] tubes (1 mm diam) passed through the plug and protruded slightly into the chamber. When the microsphere suspension was in the chamber, the ends of the tubes were submerged in the suspension and were used in the mixing of the suspension during measurement (described below).

C. Pipette mixing

The suspension was mixed continuously during measurement in order to prevent the microspheres from settling to the bottom of the chamber, and to ensure that the suspension exhibited a different random, homogeneous spatial distribution of the microspheres for each rf acquisition (see Sec. II E). The mixing was performed using a micropipette. The micropipette tip was inserted into one of the Tygon tubes projecting from the chamber plug, while the other end of the tube was submerged in the microsphere suspension. Using the micropipette, 64 μL of the suspension was then rapidly and repeatedly drawn and reintroduced into the chamber during the course of the ultrasonic measurement. The other Tygon tube acted as a vent to prevent excess pressure buildup inside the chamber. Within a few seconds after mixing began, the through-transmitted waveform's oscilloscope trace would stabilize. When mixing ceased, the trace could be observed changing over time in a manner consistent with microsphere redistribution due to settling.

The mixing rate of the suspension was roughly 1 to 2 times per second. The efficacy of this mixing technique has been validated by both optical inspection and use of a medical imaging array. In addition, we have investigated several other means of mixing, such as the method proposed by Rhyne.¹⁷ We have found that many suffer from one or more of the following defects: failure to adequately mix highly concentrated suspensions; generation of regularly spaced lamina or gradients of scatterer densities (i.e., inhomogeneities in distribution); and destruction of scatterers (for the case of microbubbles).

D. Chamber dosing procedure and particle sizing

A standardized material handling procedure was followed in order to ensure consistency among measurements of different suspensions. First, the suspension to be used was gently agitated in its original container in order to resuspend the particles. At all points during the procedures, care was taken to minimize the introduction of air bubbles into the suspension. After agitation, approximately 8 mL of the suspension was rapidly delivered from the vial into the specimen chamber. The chamber was sealed and placed in a room temperature (22.6 ± 0.5 °C) water tank, and the suspension

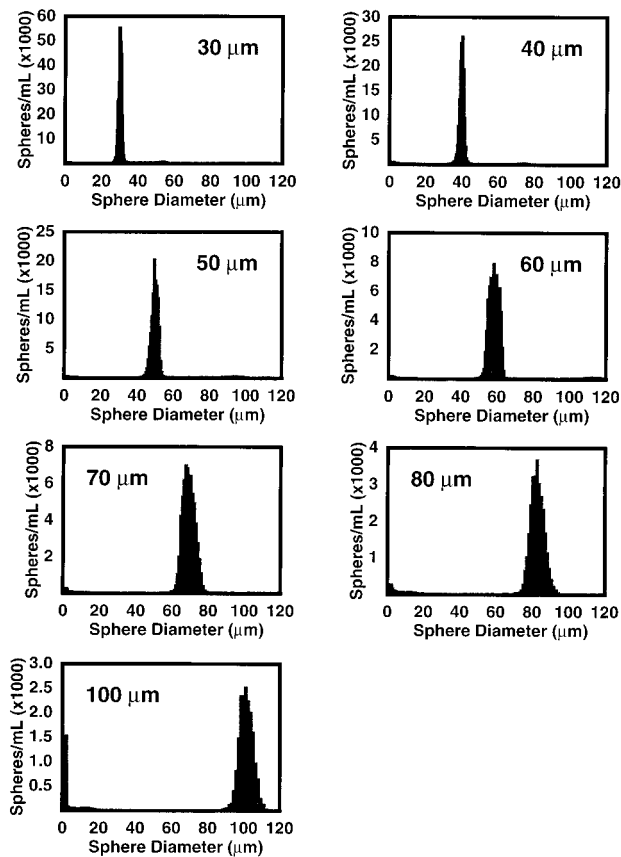


FIG. 2. Typical measured distributions of polystyrene microspheres used in the theoretical predictions of attenuation and backscatter.

was pipette-agitated during the period (approximately 40 s) of the measurement. After the measurement was completed, the chamber was removed from the tank and gently agitated to maintain the suspension, and a syringe having a 20 gauge needle was then used to withdraw 1 mL of the suspension from the center of the chamber before the microspheres had a chance to settle. This 1-mL sample was then injected into an optical particle sizer (Accusizer™ 770 with 512 channels from 1.5 to 400 μm , Particle Sizing Systems, Inc.), which returned the microsphere size distribution. Figure 2 displays the distributions of the suspensions used in this study. The chamber was emptied, disassembled, and thoroughly cleaned in order to remove any microspheres that may have adhered to the chamber surface. Fresh Saran Wrap was then used in the reassembly of the chamber. This procedure was repeated for each suspension used in the study.

E. Experimental setup and data acquisition

The measurements of the attenuation coefficient were performed in a through-transmission setup using a single pair of broadband immersion PVDF transducers (0.4-in.-diam, 3.25-in. focal length Panametrics model ZF3002-SU). The transmitting transducer was excited using a broadband pulser (Panametrics 5800). Connections to the transducers were made with short (less than 24 in.), ultra-low capacitance RG-62/U cables. This system yielded a usable bandwidth of 5 to

30 MHz which was determined by the position at which the signal was 20 dB above the noise floor. The transducers were placed about 6 in. apart. Initially, the sample chamber was placed at the center of the overlapping foci of the two transducers. However, results were measured which suggested a negative signal loss at low frequencies. By positioning the chamber progressively closer to the receiving transducer, the signal loss became positive. This effect may be due to focusing of the beam when passing through a highly dispersive medium such as the microspheres. The sample chamber was positioned close to the receiving transducer to produce the most consistent results. The transmitted ultrasonic pulse passed through the polymer microsphere suspension (which was undergoing pipette mixing) and was intercepted by the receiving transducer. The received signal passed directly into a digital oscilloscope (Tektronix 2440) for digitization (8 bit) at 250 megasamples per second. One thousand rf traces (each 1024 points long) were acquired at a rate of approximately 30 traces per second for each sample of microspheres in the chamber. The total measurement time was approximately 40 s. One thousand reference traces acquired in the same manner using a specimen chamber filled only with Isoton provided a reference for normalization. A Macintosh® computer was used to control acquisition via GPIB, and to store data to disk.

Measurements of the backscatter from the suspensions were made with a similar setup. A pulser/receiver (Panametrics 5800) was used to drive a broadband PVDF transducer (0.4-in.-diam, 3.25-in. focal length, Panametrics ZF3002-SU). The transducer was placed so that the focal region occurred immediately after the echo from the front wall of the specimen chamber. In the focus of a transducer, the insonifying waves are roughly constant in amplitude and phase which allows for several simplifications in the data reduction technique. The backscattered signal was amplified by 40 dB using the Panametrics 5800. One thousand backscattered waveforms were then captured by a digitizing oscilloscope and sent to the computer.

F. Data reduction

A first-order, broadband data reduction method was employed to reduce the measurements of the backscatter and attenuation to the inherent backscatter coefficient of a distribution of spherical scatterers.^{16,38} The raw backscattered signal can be thought of as a convolution of effects due to the electromechanical response of the transducer and accompanying electronics, the effects of the frequency-dependent beam volume, the attenuation due to the suspension, and the inherent scattering of the suspension. In order to compensate for the effects due to the electronics, the backscattered signal was compared to the signal returned from a polished steel reflector. By normalizing the spectra returned from the suspension by the spectrum of the steel plate reflection, the effects of the electromechanical response of the transducer and accompanying electronics can be removed, leaving any effects due to time-domain gating and the diffraction correction for the transducer.

The effect of the frequency-dependent beam volume and attenuation can be removed by making several simplifica-

tions. The first simplification is that the beam volume is defined laterally by the frequency-dependent beamwidth and along the beam axis by the gate duration. The second simplification, that the scatterers are uniformly distributed throughout the scattering volume, was verified with a medical imaging system and by visual inspection. Using both of these approximations, the backscatter coefficient can be expressed as

$$\eta(f) = \frac{\Gamma^2}{4T^4} R^2 F(\alpha, \tau) \frac{1}{V(f)} \langle |S(f)|^2 \rangle, \quad (8)$$

where $\eta(f)$ is the frequency-dependent backscatter coefficient, Γ is the amplitude reflection coefficient of our polished steel reflector, T is the transmission coefficient between the water and the suspension of the polystyrene microspheres, R is the focal length of the transducer, $V(f)$ is the frequency-dependent beam volume, $|S(f)|^2$ is the apparent backscatter transfer function of our suspension, and $F(\alpha, \tau)$ is an attenuation correction factor. $F(\alpha, \tau)$ can be expressed

$$F(\alpha, \tau) = e^{4\alpha(f)x} e^{\alpha(f)c\tau} \frac{2\alpha c \tau}{e^{\alpha c \tau} - e^{-\alpha c \tau}}, \quad (9)$$

where α is the frequency-dependent attenuation of the suspension, c is the speed of sound within the suspension, x is the position of the window after the front wall of the chamber, and τ is the gate duration.

In the above analysis, we have ignored the effect of time-domain gating on the backscattered signal. Others have shown that it is necessary to account for the convolution of the time domain gate with the scattered spectrum.¹¹ In the case of long gate lengths, however, this effect becomes substantially weaker. For the measurements made in this paper, we have employed a 2.56- μ s Hamming windowing function for our time-domain gate. The amount of spectral ‘‘smearing’’ can be estimated to be roughly 400 kHz with this gate, which is on the order of our frequency resolution due to the digitization rate we employed. For this reason, we chose not to compensate for the effect of time-domain gating.

The beam volume, $V(f)$, was calculated by setting the measurements of backscatter coefficient for one distribution equal to theoretical predictions. The calculated beam volume was then used in the calculation of the backscatter coefficient for the other distributions of microspheres. The beam volume was independent of the choice of the particular distribution used to calculate it. The frequency dependence of the beam volume was found to agree well with the well-known f^2 dependence of the diffraction pattern. This data reduction method was used to compare experimental results with theoretical predictions of the scattering due to an ensemble of spherical scatterers.

G. Data analysis

The apparent backscatter transfer function was calculated by applying a 2.56- μ s Hamming window to the trace at a position of 0.4 μ s after the echo from the chamber wall. Other combinations of window position and length yielded similar results when reduced to backscatter coefficient. The

power spectra of the gated traces were calculated, normalized by the power spectrum of a polished stainless-steel plate, and averaged.

The apparent attenuation coefficient was calculated from ten measurements of the through-transmitted signal when the suspension was in the chamber. Each measurement consisted of 100 time domain averages of the waveform made possible because of the stability of the through-transmitted pulse while the microsphere suspension was being constantly agitated. The averaged waveform has an increased signal-to-noise ratio. In addition, the dynamic range was also increased as a result of ‘‘bit dithering.’’⁴² A calibration trace was taken by filling the chamber with Isoton™, a saline-buffered solution, and measuring the through-transmitted pulse. No time-domain gating was necessary for the through-transmitted pulses. The power spectra of the ten averaged suspension-path traces were subtracted from the power spectrum of the saline-path trace to yield signal loss as a function of frequency. The attenuation coefficient was measured by normalizing the signal loss by the chamber thickness which was found using a standard pulse/echo method.^{43,44}

III. RESULTS

Figure 2 shows the distribution of sizes of polystyrene microspheres found by the optical particle sizer for the dif-

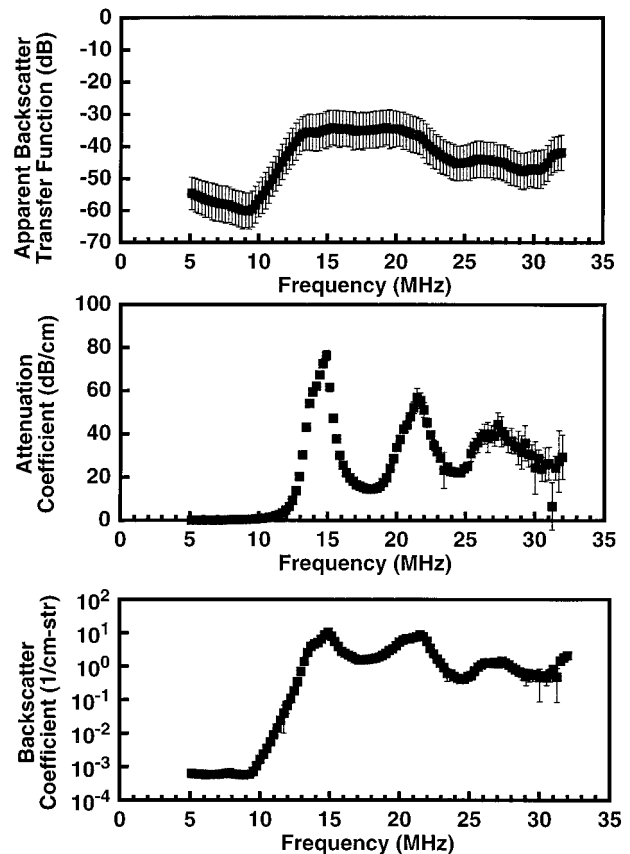


FIG. 3. The top panel shows the usable bandwidth of a typical apparent backscatter transfer function for polystyrene microspheres with a mean diameter of 49.5 μ m. The middle panel shows the corresponding measurement of the attenuation coefficient. The bottom panel is the resulting backscatter coefficient. All error bars represent the standard deviation of the measurements.

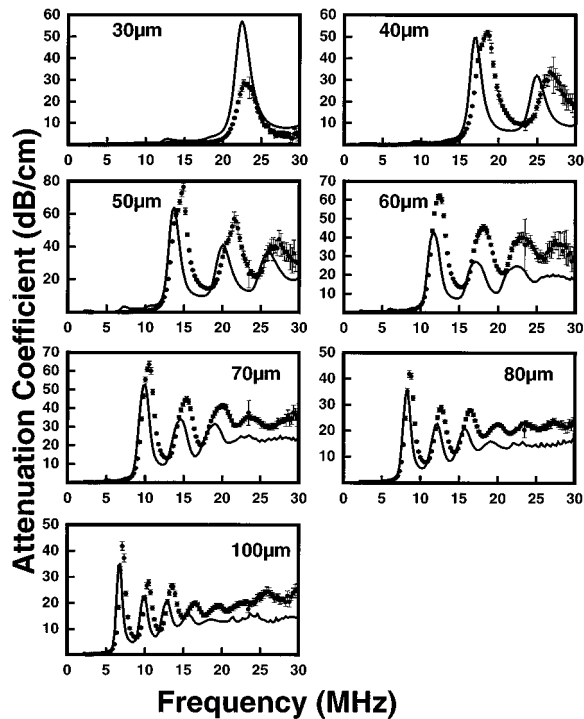


FIG. 4. Comparison of the theoretically predicted values of the attenuation coefficient with the experimental results for a polystyrene shear velocity of 1100 m/s. All error bars represent the standard deviation of the measurements.

ferent suspensions of microspheres used in this study. The larger diameter microsphere suspensions have some particles which are much smaller than the mean diameter. The scattering cross section of these small particles is negligible in comparison to those of the larger particles.

Figure 3 illustrates the measurements needed for the data reduction method described in Sec. II F. The top panel demonstrates the apparent backscatter transfer function for the nominal 50- μm -diam microspheres. The center panel shows the measured attenuation coefficient for the same distribution of microspheres. It is interesting to note that the spectral resonances of the attenuation coefficient are easier to recognize than those of the apparent backscatter transfer function. This effect may be due to the fact that the backscattered signal is attenuated preferentially at the frequencies of high scatter by the overlying material and material within the gated volume. The overall effect is to damp out the frequency variation of the backscattered signal. The effect of compensating the backscatter for the attenuation of the measurement is shown in the bottom panel. The backscatter coefficient demonstrates the same resonances that appear in the measurements of the apparent backscatter transfer function and attenuation coefficient.

Figures 4 and 5 compare the measured attenuation coefficient for the suspension of microspheres along with the theoretical predictions using Eq. (5). Figure 4 illustrates the theoretical attenuation coefficient for a shear velocity of polystyrene of 1100 m/s. Figure 5 shows the results when the shear velocity has been adjusted to 1180 m/s. This single adjustment aligned the position of the theoretically predicted

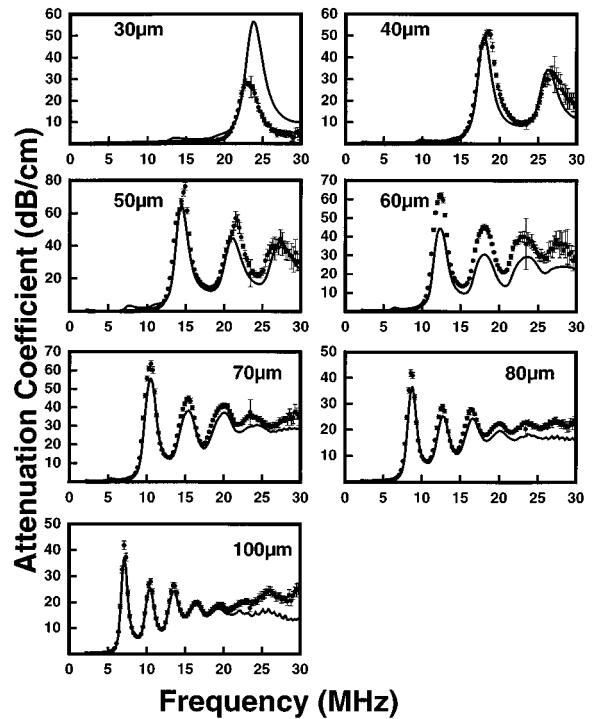


FIG. 5. Comparison of the theoretically predicted values of the attenuation coefficient with the experimental results for a polystyrene shear velocity of 1180 m/s. All error bars represent the standard deviation of the measurements.

spectral peaks to those of the experimentally measured data for all distributions of microspheres. Both experimental results and theoretical predictions agree well for most of the distributions of microspheres with some discrepancies for the 30- and 60- μm mean diam spheres. All error bars represent the standard deviation of the measurements.

Figure 6 shows the measured apparent backscatter transfer function which is the backscatter compensated for the effects of the measurement electronics but not for attenuation or any diffraction corrections. One can see the presence of the resonance regions in the spectra although these features are not as obvious as those in the through-transmitted attenuation.

Figure 7 compares the experimentally measured backscatter coefficient and the theoretical predictions of the scattering model for a variety of suspensions of narrowly distributed microsphere diameters. Agreement between experiment and theory was quite good although there are several discrepancies in the magnitude of the backscatter coefficient near the resonances in the backscatter spectrum.

IV. DISCUSSION

A broadband, single transducer pair experimental system has been developed for measuring the physical properties of ultrasonic contrast agents. The system has been used successfully to measure the attenuation coefficient and backscatter coefficient of suspensions of polystyrene microspheres in the frequency range from 5 to 30 MHz. The use of a single transducer pair for broadband measurements is advantageous for several reasons. It allows quick and reliable investiga-

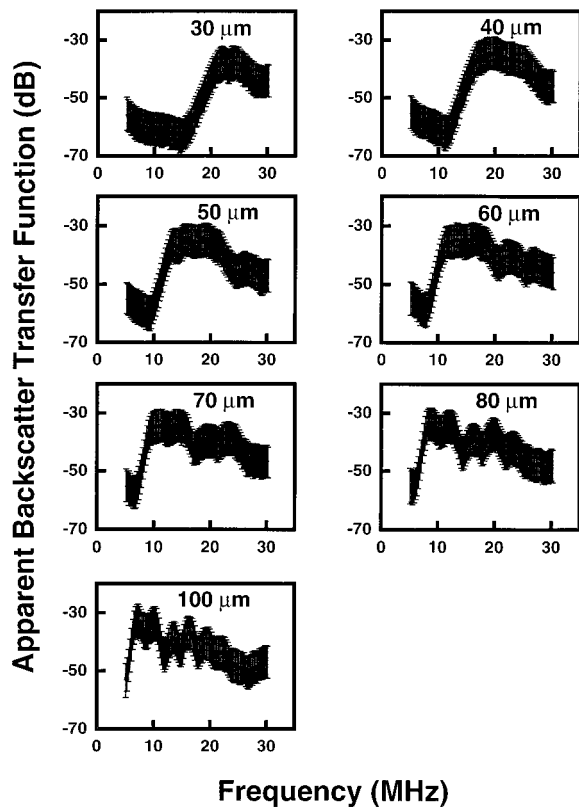


FIG. 6. The apparent backscatter transfer function for a series of polystyrene microsphere distributions. All error bars represent the standard deviation of the measurements.

tions of time-varying substances such as contrast agents. Also, the compensation for the effect of the transducer's diffraction pattern is similar for each set of measurements because knowledge of only one set of transducer characteristics is necessary.

The ability to make reliable measurements of polystyrene microspheres over this broad bandwidth suggests that a preparation of suspended and agitated spheres may be a useful *in vitro* calibration device for high-frequency ultrasound systems. This experimental system may serve as a calibration device for several reasons, some of which have been previously investigated by others in connection with tissue-mimicking phantoms. However, we have introduced a suspension system with a novel mixing technique which leads to improved ensemble averaging of the backscatter in contrast to the spatial averaging required with the use of a conventional phantoms with stationary scatterers. This mixing technique allows the averaging of many more scatterer arrangements in substantially less time than would be required with a conventional gelatin phantom with embedded scatterers. This results in a more stable and convenient calibration technique.

There are several reasons why a suspension of particles might provide a better calibration device than a planar reflector like a polished stainless-steel plate. The backscatter is returned from a volume of the suspension while the backscatter from a planar reflector represents only surface reflection of the insonifying wave. Unlike the extremely high amplitude of the reflection from a polished steel plate, the

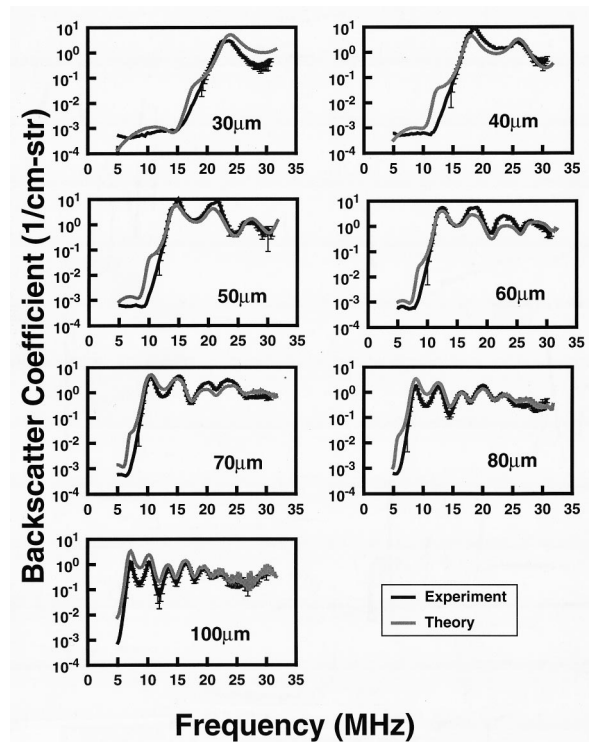


FIG. 7. Comparison of the theoretically predicted values of the backscatter coefficient with the experimental results. The error bars represent propagation of the standard errors for the apparent backscatter transfer function and the attenuation coefficient.

scatter from a suspension of spheres is of the same order of magnitude as the scatter from within a volume of tissue. The use of such microspheres thereby permits calibration of the ultrasound system over the range of amplitudes for which it will be used *in vivo*. This may facilitate calibration of high-frequency scan heads or intravascular ultrasound catheters before each use and allow comparisons between studies conducted at different times or by different investigators or clinicians. Suspensions of solid, elastic spheres may also prove useful in the area of acoustic microscopy. The current standard for calibration is the reflection from a polished stainless-steel plate which is sensitive to alignment of the surface of the plate. Alignment is not as crucial an issue when measuring backscatter for a suspension of spheres because of the symmetry of the fundamental scatterer.

In the area of ultrasound contrast agents, tightly sized polystyrene spheres provide a possible calibration for both future *in vivo* and current *in vitro* measurements of the effects of contrast agents. Suspensions of the spheres could be used in an *in vitro* setting to calibrate the ultrasonic measurement system before injection of the contrast agent. In addition, our techniques may be extendible to the measurement of the properties of specific contrast agents. In fact, the use of contrast agents *in vivo* as a possible calibration tool for the longitudinal study of a patient is an area of interest and may even provide a method to compare acoustic measurements between different patients if effects due to lung filtration and bubble destruction can be taken into account.

The current study has several limitations. We examined the backscatter from a suspension of polystyrene microspheres with diameters ranging from 30 to 100 μm . In the

field of medical ultrasonic contrast agents, sizes below 10 μm are required to pass through the vascular bed of the lungs. However, the agreement between measurements of the backscatter coefficient and theoretical predictions shows the feasibility of making direct measurements of contrast agents with our experimental setup. Multiple scattering effects were also presumed to be minimal, though they may be important at high concentrations and for frequency ranges where the scattering cross section is especially large.^{45,46} It has been shown by other researchers that the scatter from suspensions of solid spheres exhibits temperature dependence.²⁹ We maintained the water bath at a constant temperature during the course of a measurement for each size of microspheres, although the temperature between measurements varied by as much as 1.6 C. For the purpose of using suspended particles as a calibration standard, careful control of the temperature would be necessary. Another possible limitation is the fact that the beamwidth varies with frequency. Even though all the spectral components of the insonifying pulse are exposed to the same instantaneous configuration of scatterers in the suspension, the amount of power delivered to each scatterer differs with frequency. However, the data reduction technique employed in this study attempts to account for the effect of frequency-dependent beamwidth by using a different insonified volume for each frequency. In the case of high frequencies, the relatively small beamwidth may limit the number of scatterers in the insonified volume to a smaller number than for lower frequencies.

In the model, the positions of the resonances in the backscatter coefficient spectrum are very sensitive to the value chosen for the transverse velocity of the material which makes up the scatterers. In the case of polystyrene microspheres, a range of transverse velocities has been reported which varies from 1100 to 1120 m/s.³⁰ In this study, we chose a value of 1180 m/s in order to adjust the "theoretical" resonances to overlap with our measured resonances. Independent of scatterer size, the same transverse velocity of 1180 m/s resulted in theoretical predictions that agreed with experimentally measured resonances. This modified value was chosen by shifting the shear wave velocity in steps of 10 m/s until the root-mean-square deviation between the simulation and the experimental data for the 100- μm bead suspension was minimized. The theory was less sensitive to similar changes in the other physical constants (i.e., compressional wave velocities and densities of the fluid and scatterers). The discrepancy between the values of transverse velocity for polystyrene reported in the previous literature and those measured in this study could be due to the microspheres having a mixed chemical make-up of polystyrene and polystyrene divinylbenzene, a system which has not been well characterized ultrasonically.

The data presented in this study also suggest that the use of a simple, first-order, broadband reduction technique for the backscatter coefficient yields quantitatively good agreement with theoretical predictions. At different frequencies, the depth of field of a focused ultrasonic transducer varies, and has led many researchers to study the use of sophisticated correction techniques for modeling the ultrasonic beam as a function of frequency and space.^{11,47,48} Comparisons be-

tween the simple reduction technique described in this paper and other more sophisticated methods are the subject of ongoing study. The apparent agreement between the measurements presented here and the theoretically calculated values for backscatter suggests that a simpler approach to modeling the beam volume might be adequate for many measurements in this frequency range. However, although consistent in all the measurements made in this study, the adjustment of the diffraction compensation term remains an intriguing problem for future study.

The ability to make reliable measurements of polystyrene microspheres over a broad bandwidth suggests that such a preparation of suspended spheres may prove to be a useful calibration device for high-frequency ultrasound systems.

ACKNOWLEDGMENT

We would like to thank Mallinckrodt Group for its support of this work.

- ¹D. T. Linker, A. Kleven, A. Gronningsaether, P. G. Yock, and A. J. Angelsen, "Tissue-Characterization with Intra-Arterial Ultrasound: Special Promise and Problems," *Int. J. Card. Imag.* **6**, 255–263 (1991).
- ²B. F. Waller, C. A. Pinkerton, and J. D. Slack, "Intravascular Ultrasound: A Histological Study of Vessels During Life," *Circulation* **85**, 2305–2310 (1992).
- ³L. Landini, R. Sarnelli, E. Picano, and M. Salvadori, "Evaluation of the Frequency Dependence of Backscatter Coefficient in Normal and Atherosclerotic Aortic Walls," *Ultrasound Med. Biol.* **12**, 397–340 (1986).
- ⁴D. H. Christy, K. D. Wallace, G. M. Lanza, M. R. Holland, C. S. Hall, M. J. Scott, W. P. Cacheris, P. J. Gaffney, J. G. Miller, and S. A. Wickline, "Quantitative Intravascular Ultrasound Demonstration Using a Novel Site Targeted Acoustic Contrast Agent," *Proc. IEEE Ultrason. Symp.* **95**, CH35844, 1125–1128 (1995).
- ⁵G. R. Lockwood, L. K. Ryan, J. W. Hunt, and F. S. Foster, "Measurement of the Ultrasound Properties of Vascular Tissues and Blood from 35–65 MHz," *Ultrasound Med. Biol.* **17**, 653–666 (1991).
- ⁶A. K. Wong, T. G. Osborn, J. G. Miller, and S. A. Wickline, "Quantification of Ventricular Remodeling in the Tight-Skin Mouse Cardiomyopathy with Acoustic Microscopy," *Ultrasound Med. Biol.* **19**, 365–374 (1993).
- ⁷N. deJong, F. J. Ten Cate, C. T. Lancee, J. R. T. C. Roelandt, and N. Bom, "Principles and recent developments in ultrasound contrast agents," *Ultrasounds* **29**, 324–330 (1991).
- ⁸F. Villanueva and S. Kaul, "Assessment of myocardial perfusion in coronary artery disease using myocardial contrast echocardiography," *Coronary Artery Disease* **6**, 18–28 (1995).
- ⁹J. A. Campbell and R. C. Waag, "Normalization of ultrasonic scattering measurements to obtain average differential scattering cross sections for tissues," *J. Acoust. Soc. Am.* **74**, 393–399 (1983).
- ¹⁰J. A. Campbell and R. C. Waag, "Ultrasonic scattering properties of three random media with implications for tissue characterization," *J. Acoust. Soc. Am.* **75**, 1879 (1984).
- ¹¹M. F. Insana, E. L. Madsen, T. J. Hall, and J. A. Zagzebski, "Tests of the accuracy of a data reduction method for determination of acoustic backscatter coefficients," *J. Acoust. Soc. Am.* **79**, 1230–1236 (1986).
- ¹²M. F. Insana, R. F. Wagner, D. G. Brown, and T. J. Hall, "Describing small-scale structure in random media using pulse ultrasound," *J. Acoust. Soc. Am.* **87**, 179 (1990).
- ¹³F. L. Lizzi, M. Ostromogilsky, E. J. Feleppa, M. Rorke, and M. M. Yaremko, "Relationship of Ultrasonic Spectral Parameters to Features of Tissue Microstructure," *IEEE Trans. Ultrason. Ferroelectr. Freq. Control* **33**, 319–329 (1986).
- ¹⁴J. G. Mottley and J. G. Miller, "Anisotropy of the Ultrasonic Attenuation in Soft Tissues: Measurements *In Vitro*," *J. Acoust. Soc. Am.* **88**, 1203–1210 (1990).
- ¹⁵M. F. Insana, "Modeling acoustic backscatter from kidney microstructure using an anisotropic correlation function," *J. Acoust. Soc. Am.* **97**, 649–655 (1995).
- ¹⁶M. O'Donnell, J. W. Mims, and J. G. Miller, "The Relationship Between

- Collagen and Ultrasonic Backscatter in Myocardial Tissue," J. Acoust. Soc. Am. **69**, 580–588 (1981).
- ¹⁷T. L. Rhyne, K. B. Sagar, S. L. Wann, and G. Hassler, "The Myocardial Signature: Absolute Backscatter, Cyclical Variation, Frequency Variation, and Statistics," *Ultrason. Imag.* **8**, 107–120 (1986).
- ¹⁸G. C. Gaunard and H. Uberall, "RST analysis of monostatic and bistatic acoustic echoes from an elastic sphere," J. Acoust. Soc. Am. **73**, 1–12 (1983).
- ¹⁹W. G. Neubauer, R. H. Vogt, and L. R. Dragonette, "Acoustic selection from elastic spheres. I. Steady-state signals," J. Acoust. Soc. Am. **55**, 1123–1129 (1974).
- ²⁰J. J. Faran, "Sound Scattering by Solid Cylinders and Spheres," J. Acoust. Soc. Am. **23**, 405–418 (1951).
- ²¹R. Hickling, "Analysis of Echoes from a Solid Elastic Sphere in Water," J. Acoust. Soc. Am. **34**, 1582–1592 (1962).
- ²²P. D. Thorne and S. C. Campbell, "Backscattering by a suspension of spheres," J. Acoust. Soc. Am. **92**, 978–986 (1992).
- ²³P. D. Thorne, L. Hayhust, and V. F. Humphrey, "Scattering by non-metallic spheres," *Ultrasonics* **30**, 15–20 (1992).
- ²⁴A. E. Hay and R. W. Burling, "On sound scattering and attenuation in suspensions, with marine applications," J. Acoust. Soc. Am. **72**, 950–959 (1982).
- ²⁵J. Sheng and A. E. Hay, "An examination of the spherical scatterer approximation in aqueous suspensions of sand," J. Acoust. Soc. Am. **83**, 598–610 (1988).
- ²⁶H. J. Bleeker, K. K. Shung, and J. L. Barnhart, "Ultrasonic characterization of Alburnex[®] a new contrast agent," J. Acoust. Soc. Am. **87**, 1792–1797 (1990).
- ²⁷N. deJong and L. Hoff, "Ultrasound scattering properties of Alburnex microspheres," *Ultrasonics* **31**, 175–181 (1993).
- ²⁸C. C. Church, "The effects of an elastic solid surface layer on the radial pulsations of gas bubbles," J. Acoust. Soc. Am. **97**, 1510–1521 (1995).
- ²⁹J. R. Allegra and S. A. Hawley, "Attenuation of Sound in Suspensions and Emulsions: Theory and Experiments," J. Acoust. Soc. Am. **51**, 1545–1564 (1972).
- ³⁰A. E. Hay and A. S. Schaafsma, "Resonance scattering in suspensions," J. Acoust. Soc. Am. **85**, 1124–1138 (1989).
- ³¹N. deJong, L. Hoff, T. Skotland, and N. Bom, "Absorption and scatter of encapsulated gas filled microspheres: theoretical considerations and some measurements," *Ultrasonics* **30**, 95–103 (1992).
- ³²J. N. Marsh, C. S. Hall, M. S. Hughes, J. Mobley, J. G. Miller, and G. Brandenburger, "Broadband through transmission signal loss measurements of Alburnex[®] suspensions at concentrations approaching *in vivo* doses," J. Acoust. Soc. Am. **101**, 1155–1161 (1997).
- ³³B. B. Goldberg, J. B. Liu, and F. Forsberg, "Ultrasound Contrast Agents: A Review," *Ultrasound Med. Biol.* **20**, 319–333 (1994).
- ³⁴D. Brill and G. Gaunard, "Resonance theory of elastic waves ultrasonically scattered from an elastic sphere," J. Acoust. Soc. Am. **81**, 1–21 (1987).
- ³⁵L. Flax and L. R. Dragonette, "Theory of elastic resonance excitation by sound scattering," J. Acoust. Soc. Am. **63**, 723–731 (1978).
- ³⁶R. H. Vogt and W. G. Neubauer, "Relationship between acoustic reflection, and vibrational modes of elastic spheres," J. Acoust. Soc. Am. **60**, 15–22 (1976).
- ³⁷S. L. Bridal, K. D. Wallace, R. L. Trousil, S. A. Wickline, and J. G. Miller, "Frequency Dependence of Acoustic Backscatter from 5 to 65 MHz ($0.06 < ka < 4.0$) of Polystyrene Beads in Agarose," J. Acoust. Soc. Am. **100**, 1841–1848 (1996).
- ³⁸M. O'Donnell and J. G. Miller, "Quantitative Broadband Ultrasonic Backscatterer. An Approach to Non-Destructive Evaluation in Acoustically Inhomogeneous Materials," J. Appl. Phys. **52**, 1056–1065 (1981).
- ³⁹P. M. Morse and K. U. Ingard, *Theoretical Acoustics* (Princeton U.P., Princeton, NJ, 1968).
- ⁴⁰A. E. Hay and D. G. Mercer, "On the theory of sound scattering and viscous absorption in aqueous suspensions at medium and short wavelengths," J. Acoust. Soc. Am. **78**, 1761–1771 (1985).
- ⁴¹E. Merzbacher, J. M. Feafin, and T.-H. Wu, "Superposition of the radiation from N independent sources and the problem of random flights," Am. J. Phys. **45**, 964 (1977).
- ⁴²R. K. Elsley, *Accurate Ultrasonic Measurements with the Biomation 8100 Transient Recorder*, edited by M. Linzer (National Bureau of Standards, Gaithersburg, MD, 1980), pp. 311–317.
- ⁴³B. D. Sollish, "A Device for Measuring Ultrasonic Propagation Velocity in Tissue," in *Ultrasonic Tissue Characterization II*, edited by M. Linzer (National Bureau of Standards, U.S. Government Printing Office, Washington, DC, 1979), Vol. Spec. Publ. 525.
- ⁴⁴D. K. Hsu and M. S. Hughes, "Simultaneous ultrasonic velocity and sample thickness measurement and application in composites," J. Acoust. Soc. Am. **92**, 669–675 (1992).
- ⁴⁵K. W. Commander and A. Prosperetti, "Linear pressure waves in bubbly liquids: Comparison between theory and experiments," J. Acoust. Soc. Am. **85**, 732–746 (1989).
- ⁴⁶P. C. Waterman and R. Truell, "Multiple Scattering of Waves," J. Math. Phys. (N.Y.) **2**, 512–537 (1961).
- ⁴⁷J.-F. Chen, J. A. Zagzebski, and E. L. Madsen, "Tests of Backscatter Coefficient Measurement Using Broadband Pulses," IEEE Trans. Ultrason. Ferroelectr. Freq. Control **40**, 603–607 (1993).
- ⁴⁸K. A. Wear and T. J. Hall, "Measurements of ultrasonic backscatter coefficients in human liver and kidney *in vivo*," J. Acoust. Soc. Am. **98**, 1852–1857 (1995).

Harmonic amplitude distribution in a wideband ultrasonic wavefront after propagation through human abdominal wall and breast specimens

Dong-Lai Liu and Robert C. Waag

Department of Electrical Engineering, University of Rochester, Rochester, New York 14627

(Received 5 February 1996; accepted for publication 21 September 1996)

The amplitude characteristics of ultrasonic wavefront distortion produced by transmission through the abdominal wall and breast is described. Ultrasonic pulses were recorded in a two-dimensional aperture after transmission through specimens of abdominal wall or breast. After the pulse arrival times were corrected for geometric path differences, the pulses were temporally Fourier transformed and two-dimensional maps of harmonic amplitudes in the measurement aperture were computed. The results indicate that, as the temporal frequency increases, the fluctuation in harmonic amplitudes increases but the spatial scale of the fluctuation decreases. The normalized second-order and third-order moments of the amplitude distribution also increase with temporal frequency. The wide range variation of these distribution characteristics could not be covered by the Rayleigh, Rician, or K -distribution because of their limited flexibility. However, the Weibull distribution and especially the generalized K -distribution provide better fits to the data. In the fit of the generalized K -distribution, a decrease of its parameter α with increasing temporal frequency was observed, as predicted by analysis based on a phase screen model. © 1997 Acoustical Society of America. [S0001-4966(97)03402-4]

PACS numbers: 43.80.Vj, 43.80.Ev, 43.80.Qf [FD]

INTRODUCTION

Ultrasonic wavefront distortion produced by propagation through inhomogeneities in tissue is a major obstacle to large-aperture, high-resolution imaging of human body with ultrasound.¹⁻⁵ Early studies of focus compensation have concentrated on the correction of arrival time fluctuation, using either cross correlation⁶ or maximum brightness techniques.⁷ However, later studies⁸ have shown that correction of arrival time fluctuation alone is not sufficient to compensate fully for ultrasonic distortion caused by propagation through an extended thickness of tissue. Measurements⁹⁻¹² indicate that the propagated wavefront contains not only time-shift aberration, but also severe energy level fluctuation and significant waveform changes. Based on these observations, an improved wavefront distortion model that consists of a time-shifting screen placed some unknown distance away from the measurement aperture has been proposed.¹³ The results obtained using this model suggest that a better way to compensate for wavefront distortion is first to backpropagate the wavefront by an appropriate distance, and then to time-shift compensate the wavefront at that distance. To gain further understanding of wavefront distortion, however, a close examination of the statistical distribution of harmonic amplitudes is needed. This paper reports the results of such an examination in which experimentally measured wavefronts that have propagated through specimens of human abdominal wall or breast are analyzed.

A large body of literature exists on the study of wave propagation in a random medium and wave scattering from a random medium. Reference 14 and the literature cited therein provide a good recent review of this subject. The phenomena studied include radio wave propagation through

the atmosphere,¹⁵ sonic wave propagation in the ocean,¹⁶ laser speckle caused by propagation through air^{17,18} or by scattering from a rough surface,¹⁹ and ultrasonic speckle caused by random scattering from soft tissue.²⁰⁻²² Due to the complicated and unknown variations in the medium, quantitative studies are typically based on a statistical model of the medium and results are obtained for the statistical properties of the random wave field.

The consideration of harmonic amplitudes in our current study of an ultrasonic pulse wavefront through tissue is motivated by three reasons. First, the pulse waveforms received in the aperture have complicated and varying shapes. These waveforms cannot be analyzed easily in the time domain. However, once transformed into the frequency domain, each measured waveform at a particular harmonic frequency needs only an amplitude and a phase for description. Second, the propagation of ultrasonic waves in tissue for imaging applications is a linear phenomenon due to the low amplitudes that are involved. Thus, each frequency component can be analyzed independently as no interaction occurs among different frequencies. Third, many statistical models are based on a two-dimensional random walk, and such random walks can be interpreted as the summation of complex numbers. Therefore, these statistical models are directly applicable to the description of single frequency phenomena.

The rest of this paper is divided into four sections: method, results, discussion, and conclusion. In the method section, Sec. I, the flow of processing is described, and five statistical models, i.e., Rayleigh, Rician, Weibull, K -, and generalized K -distributions, are introduced to represent the data in this study. Also, the two-dimensional random walk models on which the probability density functions are based are described, as is the estimation of parameters for each

distribution. Section II presents results that include representative amplitude maps, histograms, fitted probability density functions, and statistics of amplitude fluctuation versus temporal frequency. In Sec. III, discussion, the diffraction integral is analyzed using a zone division to relate distribution parameters to physical propagation conditions. Additionally, the connection between multipath propagation and random walk models is considered. Finally, conclusions are drawn in Sec. IV.

I. METHOD

A. Flow of processing

The measurement technique has been detailed elsewhere,⁹ so only a summary is included here. Pulse waveforms were recorded in a two-dimensional aperture after emission from a pointlike source and propagation through a tissue path. The measurements were made by mechanically translating a one-dimensional, 128-element array through 32 elevations. The pitch of the array elements was 0.72 mm. Their effective dimension in the elevation direction was restricted to 1.44 mm by a reflecting mask. The step of the mechanical translation in the elevation direction was also 1.44 mm. The size of the two-dimensional aperture was thus $92.16 \times 46.08 \text{ mm}^2$. The source–aperture distance was about 180 mm. The received pulse waveforms had a nominal center frequency of 3.75 MHz and -6-dB bandwidth of about 2.2 MHz. The waveforms were sampled over a $11.8\text{-}\mu\text{s}$ interval at a 20-MHz rate that yielded 236 samples. Measurements were made using 14 different specimens of human abdominal wall⁹ and 9 different specimens of human breast¹⁰ obtained during autopsy. For the abdominal wall, the average values of specimen thickness, rms arrival time fluctuation, and energy level fluctuation, were 21.6 mm, 43.0 ns, and 3.30 dB, respectively, as given in Ref. 9 along with other abdominal wall statistics, while the corresponding values for breast tissue were 26.9 mm, 66.8 ns, and 5.03 dB, respectively, as given in Ref. 10 along with other breast statistics.

The measured wavefront was first corrected for geometric delay. This was accomplished by estimating the arrival time surface of the two-dimensional wavefront, fitting a fourth-order polynomial surface to the estimated arrivals, and using the fit for a reference to time-shift the wavefront as described in Refs. 9 and 13. After geometric correction, the wavefront is planar except for small fluctuations caused by the tissue. The signal length was reduced from 236 samples to 40 samples in this process. The rms amplitude of each signal was obtained by taking the square root of the sum of the squares of the signal amplitude over time. Therefore, the square of the rms amplitude is proportional to the total signal energy received by each element. The signals were amplitude compensated for variations in element sensitivity, using sensitivity data determined from water path measurements. The signals were also amplitude compensated for geometric factors through division by $e^{P(x,y)}$, where (x,y) denotes the receive element position and $P(x,y)$ is a fourth-order polynomial fit to the logarithm of the rms amplitude of each signal in the two-dimensional aperture.

The geometrically corrected and amplitude compensated

wavefront was then zero padded to 64 samples and temporally Fourier transformed. Thus, the temporal harmonic frequency corresponding to a harmonic number can be obtained by multiplying that number with 20 MHz (sampling rate) and dividing by 64 (FFT length). The range of harmonic frequencies that have been considered in this study was determined by the bandpass nature of the signal. Based on the existence of significant signal power, this range was set between harmonic 9 and 16 (inclusive), corresponding to frequencies from 2.8 MHz to 5.0 MHz, which is within the nominal -6-dB bandwidth. The nominal center frequency 3.75 MHz of the transducer corresponds to harmonic 12.

At each temporal harmonic frequency, a matrix (with dimensions of 128×32) of complex amplitudes was thus obtained. The harmonic amplitude was computed as the square root of the sum of the squares of the real and imaginary parts of the complex amplitude. A fourth-order polynomial was fit to the logarithm of the amplitudes and the rms value of the fit residual, calculated in dB units, was used to characterize the level of the amplitude fluctuation. The spatial scale of the fluctuation was characterized by the half-maximum, full-width of the spatial autocorrelation function of the amplitude. The calculation of these statistics is detailed in Ref. 9.

The histogram of the amplitude at each harmonic frequency is the main subject of study in this paper. Several statistical models were used to fit to the data and are described below. These models have been considered because of their connections with the two-dimensional random walk model. The advantage of having a model behind a fit is that the parameters of the fit have physical meaning. After a fit was obtained, it was tested using the χ^2 goodness-of-fit.²³ See Appendix A for a summary of this procedure.

B. Statistical models

All the statistical models considered in this paper may be derived from consideration of a two-dimensional random walk that is represented as the summation of complex steps and can be written

$$Ae^{j\theta} = \sum_{i=1}^M a_i e^{j\phi_i},$$

where M is the number of steps and $a_i e^{j\phi_i}$ denotes a single random complex number of amplitude a_i and phase ϕ_i . Thus, $Ae^{j\theta}$ is the summation of M random complex numbers. All the random complex numbers are assumed to be independent and identically distributed, and the number of such terms M may also be randomly distributed. For the amplitude of the sum A , the following is known:

- (1) If ϕ_i are uniformly distributed, a_i are independent and identically distributed, and $M \rightarrow \infty$, then A is Rayleigh distributed.²⁴
- (2) If $a_1 = \text{const}$ is significantly larger than the rest of the a_i 's, while other conditions are the same as in 1, then A is Rician distributed.²⁴
- (3) If A is Rayleigh distributed, then $A_1 = A^{2/\alpha}$ is Weibull distributed.²⁵

TABLE I. Probability density functions of five statistical models and the range of their normalized moments.

| Model | $p(A) (A > 0)$ | $I_2 = \frac{\langle A^4 \rangle}{\langle A^2 \rangle^2}$ | $I_3 = \frac{\langle A^6 \rangle}{\langle A^2 \rangle^3}$ |
|-------------------------------------|---|---|---|
| Rayleigh (σ) | $\frac{A}{\sigma^2} e^{-A^2/2\sigma^2}$ | 2 | 6 |
| Rician (σ, s) | $\frac{A}{\sigma^2} \exp\left(-\frac{A^2+s^2}{2\sigma^2}\right) I_0\left(\frac{sA}{\sigma^2}\right)$ | [1, 2] | [1, 6] |
| Weibull (α, a) | $\frac{\alpha}{a} \left(\frac{A}{a}\right)^{\alpha-1} \exp\left[-\left(\frac{A}{a}\right)^\alpha\right]$ | [1, 6] | [1, 90] |
| K-Dist (α, b) | $\frac{2b}{\Gamma(\alpha)} \left(\frac{bA}{2}\right)^\alpha K_{\alpha-1}(bA)$ | [2, 4] | [6, 36] |
| Gen K-Dist
(α, v, η) | $\frac{2b}{\Gamma(\alpha)} \left(\frac{2\alpha A}{b\eta^2}\right)^\alpha I_0\left(\frac{v}{\eta}A\right) K_{\alpha-1}(bA)$
where $b = \sqrt{4\alpha + v^2}/\eta$ | [1, 6] | [6, 36] |

- (4) If M is also a random variable and is negative binomially distributed with average approaching infinity, while the other conditions are the same as in 1, then A is K -distributed.²⁶
- (5) If, in addition to the conditions in 4, ϕ_i are nonuniformly distributed (biased random walk), then A has a generalized K -distribution.^{27,28}

The probability density function with associated parameters for each of the above statistical models is given explicitly in Table I.

C. Distribution moments and parameter estimation

To prepare for parameter estimation, the following quantities were first computed using a total of N ($N=4096$ in the present study) sample values of harmonic amplitudes a_i that were available.

$$\text{Average: } \mu_A = \frac{1}{N} \sum_{i=1}^N a_i$$

$$\text{Standard deviation: } \sigma_A = \sqrt{\frac{1}{N} \sum_{i=1}^N a_i^2 - \mu_A^2}$$

$$\text{Even-order moments: } M_n = \frac{1}{N} \sum_{i=1}^N a_i^n, \quad n=2,4,6.$$

The normalized intensity moments were also computed using the definitions

$$I_2 = M_4 / M_2^2$$

and

$$I_3 = M_6 / M_2^3.$$

1. Rayleigh distribution (parameter: σ)

The parameter σ is a scale factor and measures the magnitude of the random variable. The relation

$$\sigma^2 = M_2/2$$

was utilized to calculate σ . (Note that σ denotes the parameter of Rayleigh distribution while σ_A denotes the standard deviation of the sample data.)

2. Rician distribution²⁴ (parameters: σ, s)

The parameter s measures the magnitude of the fixed vector while the parameter σ measures the magnitude of the remaining random components. The ratio $k=s/\sigma$ was defined and the following equations were solved for k and σ^2 :

$$M_2 = 2\sigma^2(1 + \frac{1}{2}k^2),$$

$$M_4 = 8\sigma^4(1 + k^2 + \frac{1}{8}k^4).$$

No real solution for k exists if $I_2 = M_4/M_2^2$ is greater than 2. Thus, fitting the Rician model to given data is not possible in general.

3. Weibull distribution²⁹ (parameters: α, a)

The parameter a is a scale factor while the parameter α controls the shape of the probability density function. (A smaller α corresponds to a broader distribution.) The following relations were utilized for parameter estimation:

$$\mu_A = a\Gamma\left(1 + \frac{1}{\alpha}\right),$$

$$\sigma_A = a\left[\Gamma\left(1 + \frac{2}{\alpha}\right) - \Gamma^2\left(1 + \frac{1}{\alpha}\right)\right]^{1/2}.$$

To obtain α and a from these equations, a curve of

$$\frac{\mu_A}{\sigma_A} = \frac{\Gamma(1 + 1/\alpha)}{[\Gamma(1 + 2/\alpha) - \Gamma^2(1 + 1/\alpha)]^{1/2}}$$

was computed as a function of α . This curve is almost linear, and, for α increasing from 1.0 to 20.0, μ_A/σ_A varies monotonically from 1.0 to 16.1. A cubic spline interpolation³⁰ was utilized to solve the above equation for α . Specifically, values of μ_A/σ_A at 200 points of evenly distributed α values between 1.0 and 20.0 were computed. The spline interpolation was performed with μ_A/σ_A being the variable and α

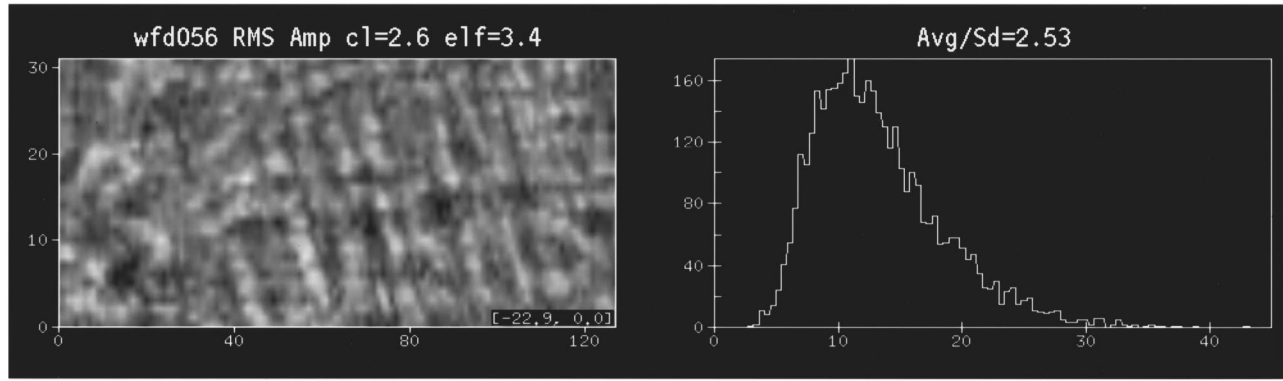


FIG. 1. Representative map of root-mean-square (rms) pulse amplitude (left) and the associated amplitude histogram (right). In the map, the horizontal axis is the array direction and spans 92.16 mm while the vertical axis is the elevation direction and spans 46.08 mm. The rms amplitude is shown on a logarithmic scale, with white corresponding to 0 dB and black corresponding to -22.9 dB. The title bar includes the correlation length (c1) and the rms value of energy level fluctuation (elf). In the histogram, the horizontal axis is the rms amplitude and the vertical axis is the number of occurrences. The ratio of the average amplitude to the standard deviation of the amplitudes is given in the title bar.

being the function. Thus, for a given μ_A/σ_A , the interpolated value gives the desired value of α .

The error of this scheme was investigated. For 2000 values of μ_A/σ_A evenly distributed between 1.0 and 16.1, corresponding α values were determined by this scheme and used to compute new μ_A/σ_A values. The maximum error between the computed and the original μ/σ_A values, occurring in the neighborhood of $\alpha=1$, was less than 0.001%. The maximum error, e.g., for $\alpha>1.2$, was another magnitude smaller.

4. *K*-distribution²⁶ (parameters: α, b)

The parameter b is a scale factor while the parameter α determines the shape of the distribution. These parameters were estimated by utilizing:

$$I_2 = 2 + \frac{2}{\alpha}, \quad M_2 = \left(\frac{2}{b}\right)^2 \alpha.$$

For given input data with $I_2 \leq 2$, the value of α becomes negative or infinite. A *K*-distribution fit to the data, thus, does not exist in this case. Noteworthy is that a given set of data can always be fit by a Rician distribution if it cannot be fit by a *K*-distribution, and *vice versa*.

5. Generalized *K*-distribution²⁷

The parameter η is a scale factor while the parameters α and v control the shape of the distribution. The relations between these parameters and the moments are:

$$\begin{aligned} M_2 &= (1 + \frac{1}{4}g_1(\alpha)v^2)\eta^2, \\ M_4 &= (2g_1(\alpha) + g_2(\alpha)v^2 + \frac{1}{16}g_3(\alpha)v^4)\eta^4, \\ M_6 &= (6g_2(\alpha) + \frac{9}{2}g_3(\alpha)v^2 + \frac{9}{16}g_4(\alpha)v^4 + \frac{1}{64}g_5(\alpha))\eta^6. \end{aligned}$$

In these expressions,

$$g_n(\alpha) = \prod_{i=1}^n \left(1 + \frac{i}{\alpha}\right).$$

The estimation of parameters for the generalized *K*-distribution using given moments M_2 , M_4 , and M_6 is discussed in Appendix B. The generalized *K*-distribution re-

duces to the *K*-distribution with $v=0$, approaches the Rician distribution with $v \neq 0$ and $\alpha \rightarrow \infty$, and approaches the Rayleigh distribution with $v=0$ and $\alpha \rightarrow \infty$.

II. RESULTS

A representative example of the rms amplitude distribution of the two-dimensional wavefront after propagation through an abdominal wall specimen and the associated histogram are shown in Fig. 1. The energy level fluctuation (which has the same value as the amplitude fluctuation when presented in the units of dB) has a standard deviation of 3.4 dB and a correlation length of 2.6 mm. Also, the average-to-standard deviation ratio of the rms amplitude distribution has a value of 2.53.

A representative harmonic amplitude distribution and the associated histogram derived from the same measurement data as Fig. 1 are shown in Fig. 2 for three harmonic numbers, 9, 12, and 15, that correspond to temporal frequencies of 2.81, 3.75, and 4.69 MHz, respectively. The spatial scale of the amplitude fluctuation decreases with temporal frequency. This is characterized by a decreasing correlation length. The magnitude of the fluctuation increases with the temporal frequency. This is reflected in an increase in the standard deviation of energy level fluctuation, as well as in a reduction of the average-to-standard deviation ratio of the amplitude histogram.

Statistics of the normalized moments of the amplitude distribution at all the eight harmonic frequencies are presented in Table II for 14 sets of abdominal wall data and for nine sets of breast data. These moments cover a wide range of values. This implies that distributions with a limited range of moments cannot fit all of the data. In particular, the calculation of Rician and *K*-distribution parameters from moments of the data will not generally be possible as no real solution exists in some cases. Therefore, these distributions are excluded in further comparison studies. For the Rayleigh distribution, which has fixed values of normalized moments ($I_2=2$ and $I_3=6$), the only parameter is a scale factor that can always be calculated from the data. Thus, a fit of the Rayleigh distribution is always obtainable, though the fit will

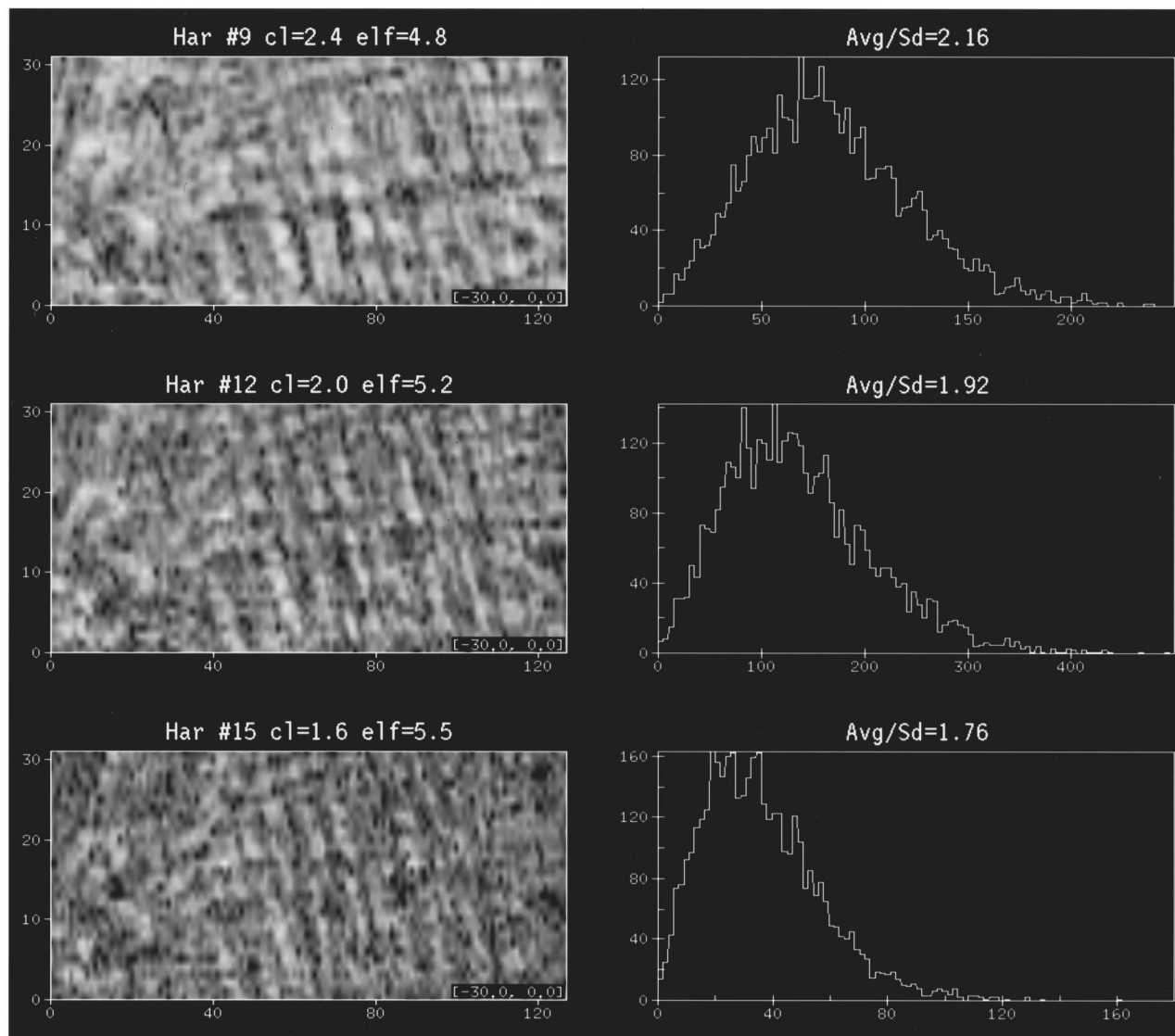


FIG. 2. Representative maps of harmonic amplitude and the associated amplitude histogram. The top, middle, and bottom rows correspond to harmonics 9, 12, and 15, respectively. The format is the same as that of Fig. 1 except that the display dynamic range is truncated at -30 dB.

be poor as the data usually do not have either the fixed values of 2 and 6 for normalized moments I_2 and I_3 , respectively, or the average-to-standard deviation ratio that is $\sqrt{\pi/(4-\pi)} \approx 1.913$ for Rayleigh distribution.

A comparison of the data in Table II shows that the breast data has significantly larger moments than the ab-

TABLE II. Statistics of normalized second-order and third-order intensity moments for eight harmonics measured from 14 abdominal wall specimens and 9 breast specimens. The sample size (number of data points) is 112 for abdominal wall data and 72 for breast data.

| | | Avg | Sd | Min | Max |
|-------|----------|------|------|------|------|
| I_2 | Abd wall | 2.10 | 0.34 | 1.40 | 3.22 |
| | Breast | 3.07 | 0.59 | 2.10 | 4.68 |
| I_3 | Abd wall | 7.60 | 3.67 | 2.60 | 26.0 |
| | Breast | 19.4 | 9.7 | 6.9 | 48.6 |

dominal wall data, which is consistent with the larger energy level fluctuations in the breast data.

The normalized moments are plotted in Figs. 3 and 4 and are overlaid with the moment curves of Weibull distribution and of the generalized K -distribution. The agreement between the normalized moments of the data and of Weibull distribution is good for $I_2 < 2.5$, but some deviation is seen for $I_2 > 2.5$. The family of curves of the generalized K -distribution generally follows moments of the measured data well, but some deviation is noticeable in the region of $3.0 < I_2 < 4.0$.

Illustrative histograms together with probability density functions that are fit to the histograms are shown in Fig. 5. These plots illustrate the variability of the histograms and the goodness-of-fit of the Rayleigh distribution, the Weibull distribution, and the generalized K -distribution to the data.

The average and the standard deviation of various parameters that describe the harmonic amplitude distribution are presented in Fig. 6 for abdominal wall data and corre-

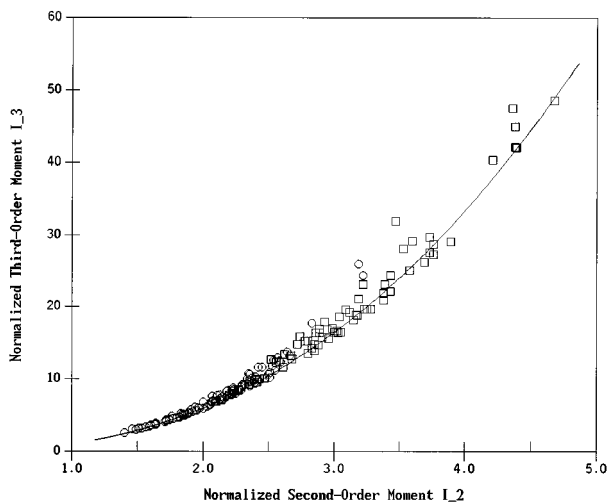


FIG. 3. Normalized second-order and third-order intensity moments of abdominal wall data (circles) and breast data (squares) with the moment curve of the Weibull distribution. The number of abdominal wall points is 112 (8 harmonics for each of 14 specimens) and the number of breast points is 72 (8 harmonics for each of 9 specimens). As the parameter α increases from 1.1 to 5.1, the position on the moment curve of the Weibull distribution moves from right-top to left-bottom.

spondingly in Fig. 7 for breast data. The data show that, with increasing temporal frequency (harmonic number), the energy level fluctuation increases, the correlation length decreases, the μ_A/σ_A ratio decreases, and the normalized moments I_2 and I_3 increase. The curve of $E(A^2)$ has a peak near harmonic 12, which corresponds to the nominal center frequency 3.75 MHz of the signals. Further examination of the variation of correlation length with temporal frequency revealed that the correlation length varies more slowly than the wavelength. In other words, the number of wavelengths con-

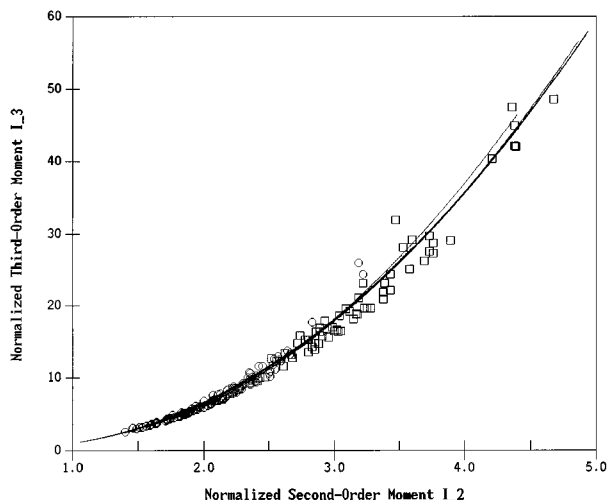


FIG. 4. Normalized second-order and third-order intensity moments of abdominal wall data (circles) and breast data (squares) with moment curves of the generalized K -distribution. The data are the same as in Fig. 3. The moment curves of the generalized K -distribution are calculated with parameter ν varying from zero to 19.0 and α varying from 1.25 to 100. For a given value of ν , increasing α moves position on the curve from right-top to left-bottom; for a larger value of ν , the curve with the same α variation has a higher starting point and a lower ending point.

tained in a correlation length is fewer at lower frequencies than at higher frequencies.

The following parameters are only scale factors of the distributions: σ in Rayleigh distribution, a in Weibull distribution, and η in the generalized K -distribution. The variation of these parameters with harmonic frequency is, therefore, about the same as the variation of $\sqrt{E(A^2)}$. The variation of the parameter α in Weibull distribution is about the same as that of μ_A/σ_A , because of the approximately linear relation between them. For these reasons, statistics for these parameters are not shown.

Statistics for the parameters α and ν in the generalized K -distribution are included in Figs. 6 and 7. For abdominal wall data, both α and ν showed a gradual decrease with increasing temporal frequency. For breast data, α showed a small decrease but ν showed no significant change with frequency.

Statistics of the χ^2 number computed in goodness-of-fit tests are also shown in Figs. 6 and 7. The dashed threshold line corresponds to an acceptance level of 95% (the meaning of which is that, if the fit is the true probability density function, it will be accepted 95% of the time). The results show that the Rayleigh distribution is unable to fit the data most of the time, the Weibull distribution fits most of the abdominal wall data but few of the breast data, and the generalized K -distribution fits almost all of the abdominal wall data and about half of the breast data.

III. DISCUSSION

A noteworthy feature of the pulse amplitude histogram in Fig. 1 is that the curve does not start from the origin. This is not due to nonzero dc components because such components have already been removed from the signals. On the other hand, histograms of harmonic amplitude distribution do start from origin (see Fig. 2). This contrast exists in all the data that have been analyzed here, and indicates that nulls (close-to-zero energy) are unlikely to happen in pulse wavefronts but are likely to happen in harmonic wavefronts. Since pulse energy is the summation of individual harmonic energy, the above observation leads to the conclusion that the nulls of the different harmonics do not coincide in space. This is reasonable because the spatial scales of amplitude fluctuation varies (decreases) with temporal harmonic frequency. Since the statistical models in Table I all have probability density functions starting from origin, the observation also indicates that modeling the rms amplitude of the pulses with those statistical models is inappropriate.

Besides the harmonic amplitude histogram, a scatter diagram of the complex amplitudes at a certain harmonic frequency can also be generated. In such a diagram, the horizontal axis is the real part, the vertical axis is the imaginary part, and each complex amplitude is represented by a point. A speculation about the property of such a scatter diagram is of interest. For an ideal wavefront with all the waveforms being the same, all the complex amplitudes will be clustered at one point. When the ideal wavefront is time shifted, the complex amplitudes will be distributed on a circle because time shifts correspond to phase rotations of the complex am-

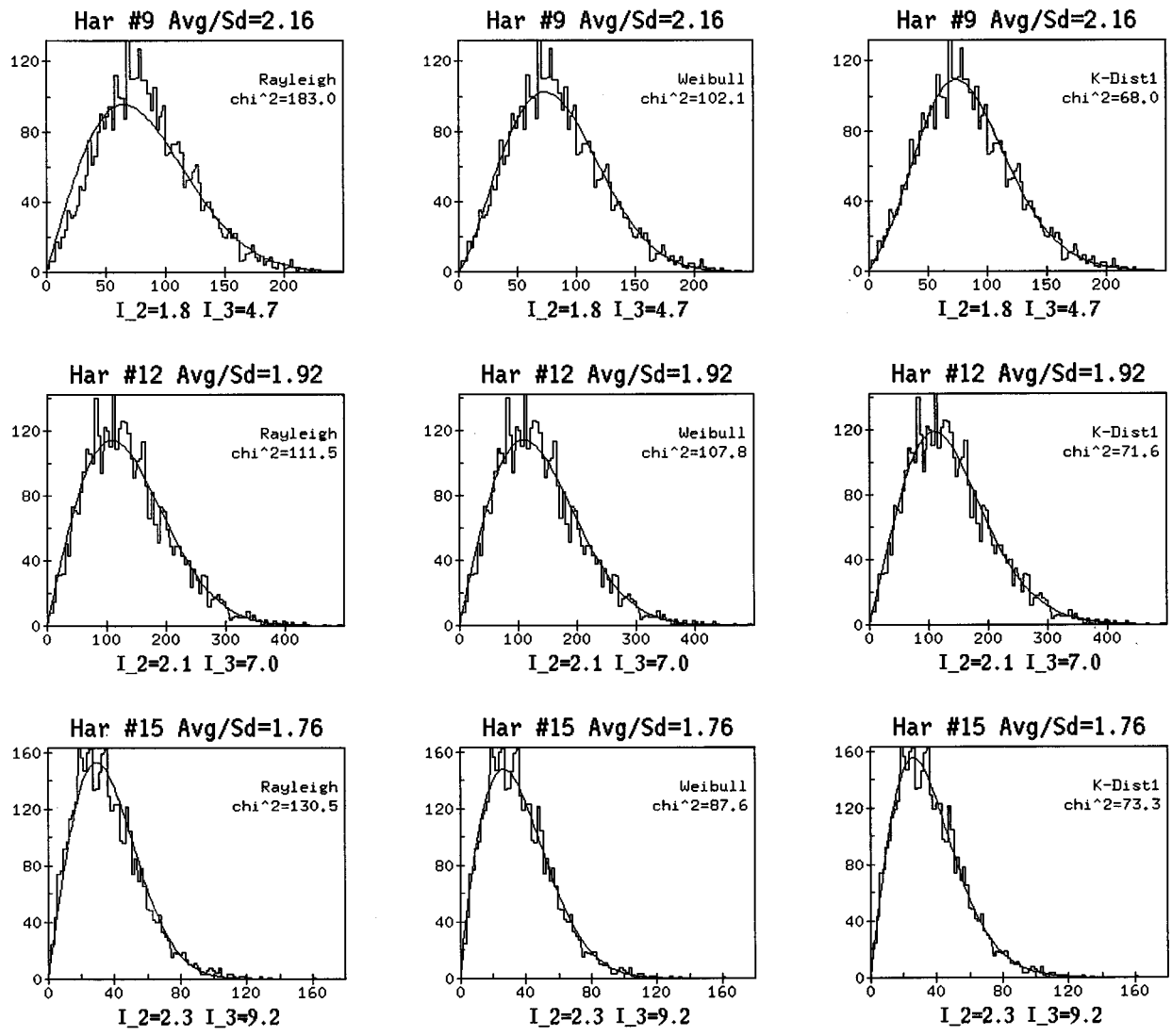


FIG. 5. Representative histograms (fluctuating curves) with different fitted probability density functions (smooth curves). The data are from a representative abdominal wall study (wfd056). The top, middle, and bottom rows correspond to harmonic number 9, 12, and 15, respectively, while the left, center, and right columns correspond to the Rayleigh, Weibull, and generalized K -distributions. In each panel are shown the average-to-standard deviation ratio (Avg/Sd) and the normalized moments I_2 and I_3 , as well as the χ^2 value (chi²) that measures the difference between the fit and the histogram. The upper χ^2 threshold values for 95% acceptance level, determined by sample size and the number of fit parameters, are about 95, 94, and 93, for the Rayleigh, Weibull, and generalized K -distributions, respectively.

plitudes. For measured data that also contain amplitude variations, the scatter diagram will be more complicated. Although such a diagram could be used to study the distributions of the real and the imaginary parts of the complex amplitude, the disadvantage of this kind of study is that, if the wavefront is time shifted, all the points representing the complex amplitudes will be rotated by varying angles, so that the distributions of the real and the imaginary parts could be changed drastically. However, the distribution of the harmonic amplitude is not influenced by such rotations as the harmonic amplitude is the distance from each point to the origin and is not changed by rotation. In this sense, harmonic amplitude distribution is more intrinsic than the distributions of the real and the imaginary parts.

The relevance of random walk models in the analysis of harmonic amplitude distribution may be understood by considering the received signal $s(t, x, y)$ to be a delayed sum of the input signal $g(t)$, i.e.,

$$s(t, x, y) = \sum_{i=1}^M a_i(x, y) g[t - \tau_i(x, y)],$$

where x, y denotes a point in space and t denotes time. This can be viewed as an M -path propagation response in which each path has a gain a_i and a delay τ_i . Fourier transform of the above equation yields

$$S(\omega, x, y) = \sum_{i=1}^M a_i(x, y) e^{-j\omega\tau_i(x, y)} G(\omega).$$

This equation indicates that, for a fixed temporal frequency ω , the response of this linear system formed by multipath propagation can be viewed as the result of an M -step random walk, provided that each path has a random delay and gain that are independent of other paths.

The random walk model described above is appropriate when the signal results from the summation of arrivals over a number of ray paths. The representation has the same form

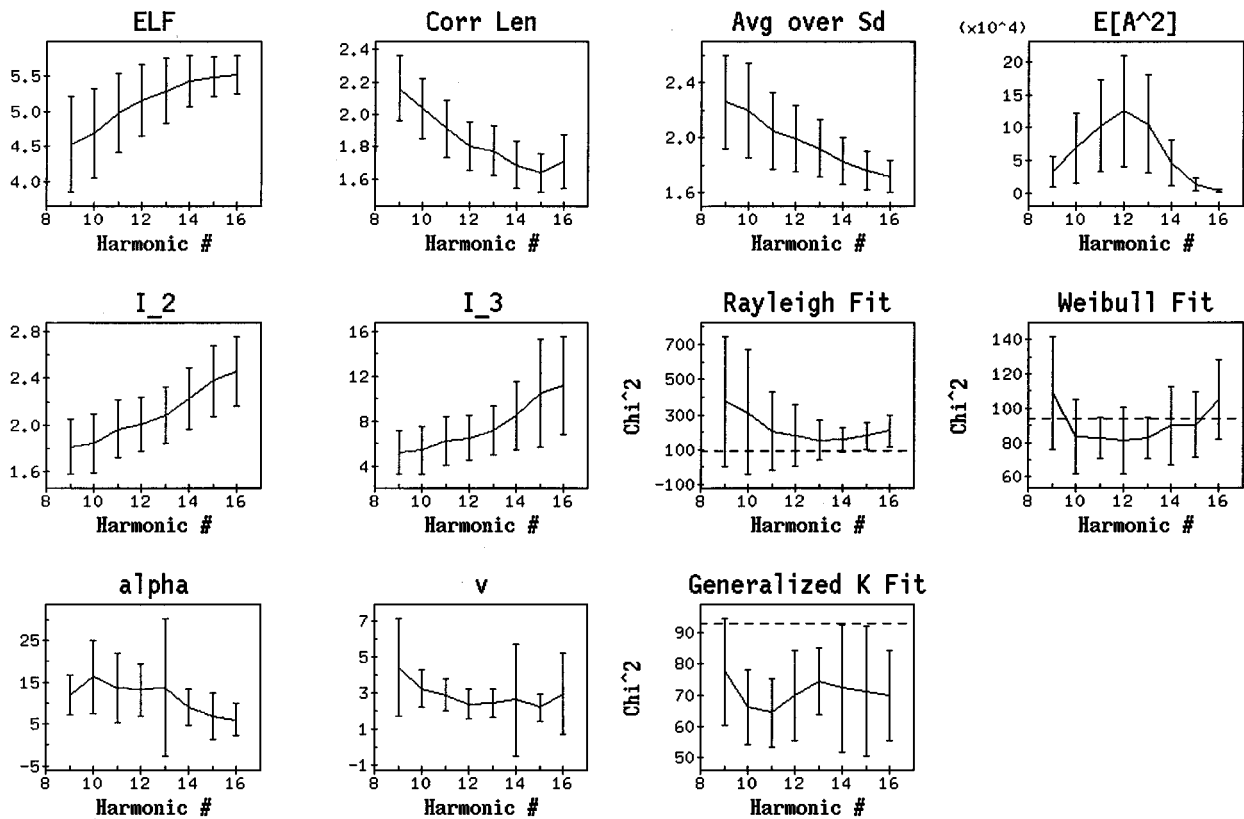


FIG. 6. Statistics of abdominal wall data. In each plot, the horizontal axis is harmonic number and the curve shows the average of 14 different specimens. The bars correspond to plus and minus one standard deviation. The units are dB for energy level fluctuation (ELF) and mm for correlation length (Corr Len). The units of $E[A^2]$ are A/D converter counts (range: -2048 to 2047). The other plots are dimensionless.

as a first-order scattering model in which the received signal is the sum of the signals from a number of scatterers. This additive model is analogous to the result of the Born approximation.

Another model, analogous to the result of the Rytov approximation, employs a multiplicative form to represent the distortion. In this model, expressions for the amplitude and phase are obtained by writing the wave field as an exponential in which the unknowns are the real and imaginary parts of the exponent. These unknowns are each expressed as a summation of contributions from a number of paths, for which a corresponding tapped delay line model can be postulated. If the contributions were large in number and independent, the log of the amplitude would be normally distributed. However, computations showed that the so-called log-normal distribution²⁴ is a poor fit (as measured by the χ^2 test) of the histogram of the harmonic amplitudes so investigation along this line was not pursued.

Additional insight about the relation between the harmonic amplitude distribution and physical propagation conditions is obtained from consideration of the amplitude distribution caused by propagation of a time-shifted wavefront. Assume that a plane wavefront passes through a phase screen at $z=0$ and continues to propagate over a distance $z_0(>0)$. The pressure at point $P_0(x_0, y_0, z_0)$ can be expressed in terms of the Rayleigh-Sommerfeld diffraction integral of the pressure at points $P_1(x, y, 0)$ in the plane $z=0$ as

$$U(P_0) = \frac{1}{j\lambda} \int_{-\infty}^{\infty} \int_{-\infty}^{\infty} dx dy U(P_1) \frac{e^{jkr}}{r} \cos(\mathbf{n}, \mathbf{r}),$$

where \mathbf{r} is the vector from P_0 to P_1 and \mathbf{n} is a unit vector in the $-z$ direction. Without loss of generality consider the point at $x_0=0$ and $y_0=0$. Then $r = \sqrt{x^2 + y^2 + z_0^2}$. Rewriting the above integral in polar coordinates ($x = \rho \cos \theta$ and $y = \rho \sin \theta$) results in

$$U(P_0) = \frac{1}{j\lambda} \int_0^{2\pi} d\theta \int_0^{\infty} \rho d\rho U(P_1) \frac{e^{jkr}}{r} \cos(\mathbf{n}, \mathbf{r}).$$

Next, define a series of circles with $r_n = n\lambda$ in which n is an integer. Since $r^2 = \rho^2 + z_0^2$, the radius of the circle corresponding to r_n is $\rho_n = \sqrt{r_n^2 - z_0^2}$. The smallest circle corresponds to the smallest integer n_0 that satisfies $n_0\lambda \geq z_0$. The diffraction integral can then be written as a summation of integrals in each concentric circular band defined by $\rho_n < \rho < \rho_{n+1}$, and the use of $\rho d\rho = r dr$ yields

$$U(P_0) = \frac{1}{j\lambda} \int_0^{2\pi} d\theta \sum_{n=n_0}^{\infty} \left[\int_{r_n}^{r_{n+1}} U(P_1) e^{jkr} \cos(\mathbf{n}, \mathbf{r}) dr \right].$$

When r goes from r_n to r_{n+1} , e^{jkr} completes a full cycle. The corresponding variation of $U(P_1)$ is found from examining the width of the circular band

$$\Delta\rho_n = \rho_{n+1} - \rho_n = \sqrt{[(n+1)\lambda]^2 - z_0^2} - \sqrt{n^2\lambda^2 - z_0^2}$$

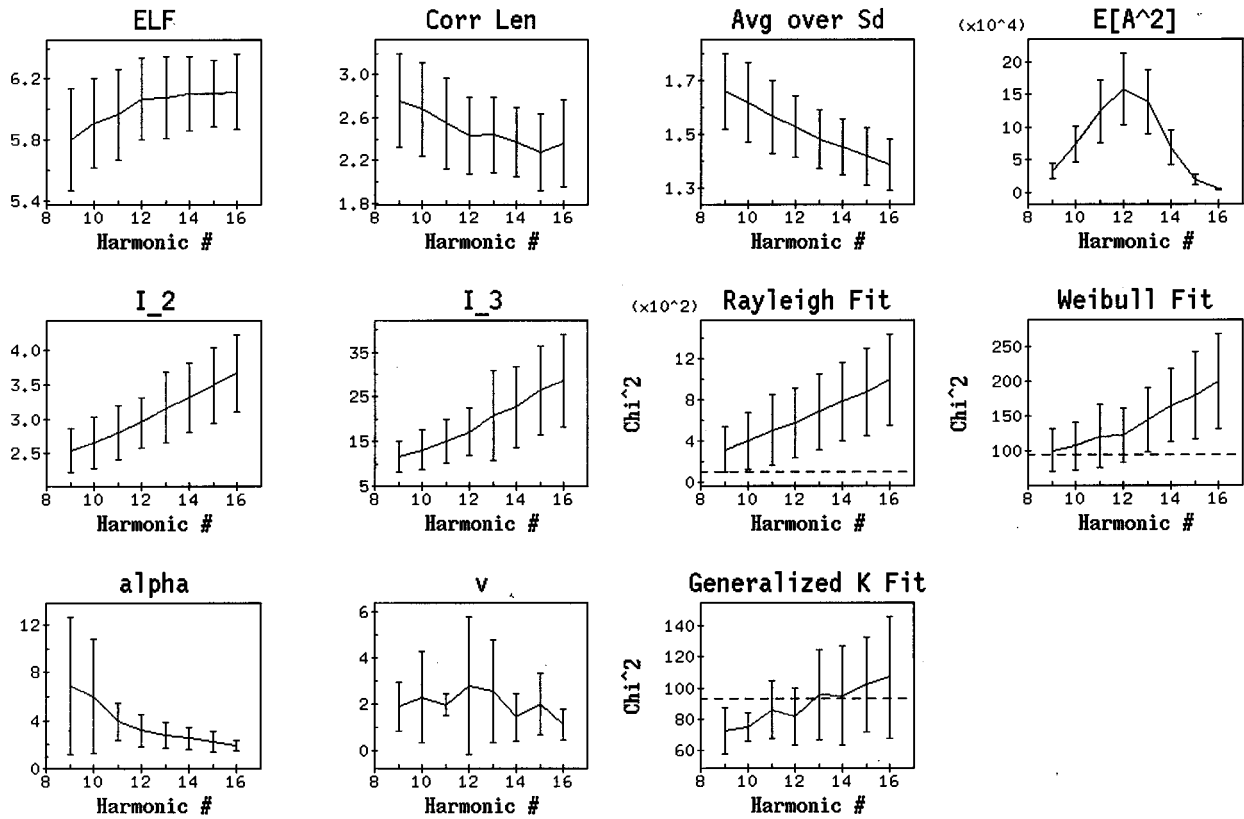


FIG. 7. Statistics of breast data. The format is the same as that of Fig. 6 but the number of specimens is nine.

relative to the correlation length of $U(P_1)$. The maximum of $\Delta\rho_n$ occurs at $n=n_0$, and equals approximately $\sqrt{2z_0\lambda}$, while the minimum occurs when $n\rightarrow\infty$, and equals λ .

Two extreme cases can be identified in a comparison of the widths of these bands and the correlation length of the variation in $U(P_1)$.

(1) If the bands are much wider than the correlation length, i.e., propagation distance z_0 is large or correlation length is small, then the diffraction integral has many small components uniformly contributing, so that the amplitude distribution approaches either the Rayleigh or the Rician distribution. (The former is a special case of the latter.) Furthermore, if $U(P_1) = e^{j\phi(x,y)}$ and $\phi(x,y)$ is assumed to be Gaussian distributed, the expected value of $U(P_1)$ is $\exp(-\sigma_\phi^2/2)$ in which σ_ϕ^2 is the variance of $\phi(x,y)$. This implies that $U(P_0)$ will be Rayleigh distributed if the phase screen is deep [$\exp(-\sigma_\phi^2/2) \ll 1$] because each contributing component has virtually zero average. Otherwise $U(P_0)$ will be Rician distributed because each component has a nonzero average. This agrees with the result obtained in Ref. 31.

(2) If the bands are much narrower than the correlation length, i.e., propagation distance z_0 is small or correlation length is large, then most contributions to the diffraction integral cancel because e^{jkr} varies rapidly, and the major contribution comes from a small number of locations where the spatial variation of $U(P_1)$ happens to have about the same spatial scale as that of e^{jkr} . This is similar to the evaluation of an integral using the stationary phase approximation. In such cases where the contribution could come from a varying, small number of independent factors, the distribution is

known to be better modeled with either the K - or the generalized K -distribution since these models are based on the assumption that the number of steps in the random walk model is negative binomially distributed and can have larger fluctuations.²⁷ Since the K -distribution is based on unbiased random walk while the generalized K -distribution is based on biased random walk, the latter has a wider range of applicability and can be used in the case of a shallow phase screen.

In the case of tissue data analyzed here, the situation is somewhere between the two extremes noted above. For example, the nominal value of correlation length is 7.9 mm for the abdominal wall specimen⁹ and 4.3 mm for the breast specimen.¹⁰ At a frequency 3.75 MHz, the wavelength $\lambda=0.4$ mm, and for a propagation distance $z_0=20-40$ mm, the largest width of the circular band is $\sqrt{2z_0\lambda}=4-5.66$ mm. Thus, the width of the band is comparable to the correlation length at the beginning and gradually gets smaller.

In both K - and generalized K -distribution, α is the parameter that controls the distribution of the number of steps. For α large, the negative binomial distribution approaches Poisson distribution. This represents the limit of a uniformly large number of steps. On the other hand, if α is relatively small, the negative binomial distribution exhibits a long tail and a large variance. In this case, even if the average number of steps is very large, the probability of having a small number of steps in a particular observation is not negligible. The above reasoning indicates that a large propagation distance, a large wavelength, and a small correlation length lead to the

contribution of many factors in the final amplitude, and to a large α .

Using a homodyned K -distribution model,³² the positive correlation between propagation distance and the parameter α has been verified experimentally for laser light diffracted by ground glass. The results in Figs. 6 and 7 show that α decreases with increasing temporal frequency (or decreasing wavelength). Thus, even though a tissue specimen has a significant thickness and differs from a single phase screen, the expected tendency of larger α values corresponding to larger wavelengths has been confirmed.

Lastly, limitations to the study of amplitude distribution using statistical models deserve comment. The presence of large scale features (such as the stripes in Fig. 1) in amplitude distribution indicates the existence of different tissue structures, like muscle or tendon, in certain areas of some specimens. Such specimens cannot be regarded as a statistically uniform medium, and the harmonic amplitude distribution across the whole measurement area is not likely to be governed by a single probability density function. Furthermore, different specimens present different features and the corresponding distorted wavefronts may need to be described by different statistical models. However, in spite of these limitations, the current study showed that the generalized K -distribution is remarkably capable of fitting satisfactorily more than three quarters of the data.

IV. CONCLUSION

Harmonic amplitude distributions of pulse wavefronts after propagation through specimens of human abdominal wall and breast have been analyzed. The results indicate that these distributions show a wide range of variations. As the temporal frequency increases, the fluctuation in harmonic amplitudes increases but the spatial scale of the fluctuation, characterized by the correlation length of the fluctuation, decreases. The normalized second-order and third-order intensity moments also increase with temporal frequency.

Five statistical models based on the random walk have been considered for fitting the data. Two of them, Rician and the K -distribution, cannot fit all of the data because of their limited coverage of the moment space. Fitting results were presented for the other three statistical models. Based on a 95% acceptance level, the Rayleigh distribution fits the data poorly, the Weibull distribution fits most of the abdominal wall data but few of the breast data, and the generalized K -distribution fits all of the abdominal wall data and about half of the breast data.

A phase screen model has been analyzed using the diffraction integral. Insights have been gained about the qualitative relation between physical propagation parameters (such as propagation distance, wavelength, depth, and correlation length of the phase screen), and the parameters α and ν of the generalized K -distribution that can be used to describe the amplitude distribution. The analysis provides an explanation why the generalized K -distribution models the observed amplitude fluctuation in tissue data analyzed here.

ACKNOWLEDGMENTS

Laura M. Hinkelman is thanked for providing the measurements used in the processing reported here. Gratefully acknowledged is support from the University of Rochester Diagnostic Ultrasound Research Laboratory Industrial Associates, NIH Grant Nos. DK45533 and HL150855, and the US Army Medical Research and Development Command Grant No. DAMD17-94-J-43834. The computations in this research were performed at the Cornell National Supercomputing Center, which is supported by the National Science Foundation, New York State, and the IBM Corporation.

APPENDIX A: χ^2 GOODNESS-OF-FIT TEST

Given N realizations of a random variable X and a suggested probability density function (pdf) $p(x)$, the problem is to determine whether $p(x)$ provides a good description of the data. The first step is to divide the x axis into K intervals of equal probability using the given distribution function

$$F(x) = \int_{-\infty}^x p(t) dt.$$

In the current study, the integration is carried out numerically using Simpson's formula, and the number of intervals K is empirically set to $1.2\sqrt{N}$ based on recommendations in Ref. 23. The points that define intervals of equal probability are found using spline interpolation, with $F(x)$ going from zero to 1.0 as the variable, and x being the function. The values interpolated at k/K , $k = 1, 2, \dots, K-1$, define the break points of the intervals. Next, form

$$J = \sum_{k=1}^K \frac{(f_k - F_k)^2}{F_k},$$

where f_k is the number of samples that fall into the k th interval, and $F_k = N/K$. The J so formed obeys approximately the χ^2 distribution, with the number of degrees of freedom n being equal to $K-1$ minus the number of parameters in $p(x)$ that have been estimated from the data.²³ Thus, n equals $K-2$ for the Rayleigh distribution, $K-4$ for the generalized K -distribution, and $K-3$ for the rest of the distributions.

To test whether a fit can be the true pdf of the sample data, a criterion such as $J < \chi_{n;0.95}^2$ can be used as follows: if it is true, then accept the fit as being the true pdf, otherwise reject. The meaning of this acceptance is that, if the fit is the true pdf, then 95% of the time the pdf will be accepted while only 5% of the time it will be rejected. A larger number (say 0.99) means that the pdf is more likely to be accepted.

APPENDIX B: PARAMETER ESTIMATION FOR THE GENERALIZED K -DISTRIBUTION

To estimate parameters for the generalized K -distribution using given moments M_2 , M_4 , and M_6 , first note that η is a scale factor, and once α and ν have been obtained, η can be computed using

$$\eta = \sqrt{M_2 / (1 + \frac{1}{4}g_1(\alpha)\nu^2)}.$$

Next, from the relations between moments and parameters of the generalized K -distribution, expressions for normalized moments I_2 and I_3 are obtained as

$$I_2 = \frac{2g_1(\alpha) + g_2(\alpha)v^2 + \frac{1}{16}g_3(\alpha)v^4}{(1 + \frac{1}{4}g_1(\alpha)v^2)^2},$$

$$I_3 = \frac{6g_2(\alpha) + \frac{9}{2}g_3(\alpha)v^2 + \frac{9}{16}g_4(\alpha)v^4 + \frac{1}{64}g_5(\alpha)}{(1 + \frac{1}{4}g_1(\alpha)v^2)^3}.$$

Using these expressions, a family of curves of I_3 vs I_2 , with v and α as parameters, can be plotted. See Fig. 4 as well as Ref. 27.

In the plot, the given moment pair (I_{20}, I_{30}) is represented by a point, and because the calculation employs a finite number of samples, random error is always present and causes the point (I_{20}, I_{30}) to not fall exactly on any one of the curves. Thus, an exact solution to the above moment equations may not always exist, and, even if it exists, it is not more meaningful than an approximate solution. Also noteworthy is that many curves lie close to each other, so that many pairs of (α, v) exist that will result in similar distances between computed and given normalized moments. So the problem of finding (α, v) using given (I_{20}, I_{30}) is ill-posed. In our study, we first search for pairs of (α, v) that produce points close to the given (I_{20}, I_{30}) , and then for each pair of (α, v) , we compute the corresponding probability density function and use the χ^2 criterion as described in Appendix A to pick the best pair.

Based on the known variations of I_2 and I_3 vs α and v ,²⁷ the range of search for α is set between 1.0 and 200.0 and spanned by 200 numbers that form a geometric series. The range of search for v is set between 0.1 and 15.0 and spanned by 400 numbers that form again a geometric series. Then, define the distance measure to be

$$d(\alpha, v) = \sqrt{[I_2(\alpha, v) - I_{20}]^2 + [I_3(\alpha, v) - I_{30}]^2}.$$

For each fixed value of v , $d(\alpha, v)$ is a function of α , and α is searched to locate the minimum position $\alpha_{\min}(v)$. This is relatively easy because $d(\alpha, v)$ as a function of α contains only one minimum either at the ends of the α interval, or within the interval. The search is made using a one-dimensional cubic spline interpolation. The next step is to eliminate the pairs of (α_{\min}, v) in which α_{\min} is at the ends of the α interval (i.e., close to 1.0 or 200). These pairs correspond to I_3 vs I_2 curves that are too short and do not cover the input data point. (See Fig. 4.) All the remaining pairs of parameters result in similar normalized moments, and further comparison is made using the χ^2 goodness-of-fit test described in Appendix A, and the pair with the lowest J value is chosen.

¹M. Moshfeghi and R. C. Waag, "In-vivo and in-vitro ultrasound beam distortion measurements of a large aperture and a conventional aperture focussed transducer," *Ultrason Med. Biol.* **14**, 415–428 (1988).

²S. W. Flax and M. O'Donnell, "Phase-aberration correction using signals from point reflectors and diffuse scatterers: Measurements," *IEEE Trans. Ultrason. Ferroelectr. Freq. Control* **35**, 768–774 (1988).

³G. E. Trahey, P. D. Freiburger, L. F. Nock, and D. C. Sullivan, "In-vivo

measurements of ultrasonic beam distortion in the breast," *Ultrason. Imag.* **13**, 71–90 (1991).

⁴Y. Sumino and R. C. Waag, "Measurements of ultrasonic pulse arrival time differences produced by abdominal wall specimens," *J. Acoust. Soc. Am.* **90**, 2924–2930 (1991).

⁵Q. Zhu and B. D. Steinberg, "Large-transducer measurements of wavefront distortion in the female breast," *Ultrason. Imag.* **14**, 276–299 (1992).

⁶S. W. Flax and M. O'Donnell, "Phase-aberration correction using signals from point reflectors and diffuse scatterers: Basic principles," *IEEE Trans. Ultrason. Ferroelectr. Freq. Control* **35**, 758–767 (1988).

⁷L. Nock, G. E. Trahey, and S. W. Smith, "Phase aberration correction in medical ultrasound using speckle brightness as a quality factor," *J. Acoust. Soc. Am.* **85**, 1819–1833 (1989).

⁸D.-L. Liu and R. C. Waag, "Time-shift compensation of ultrasonic pulse focus degradation using least mean square error estimates of time delay," *J. Acoust. Soc. Am.* **95**, 542–555 (1994).

⁹L. M. Hinkelman, D.-L. Liu, L. A. Metlay, and R. C. Waag, "Measurements of ultrasonic pulse arrival time and energy level variations produced by propagation through abdominal wall," *J. Acoust. Soc. Am.* **95**, 530–541 (1993).

¹⁰L. M. Hinkelman, D.-L. Liu, R. C. Waag, Q. Zhu, and B. D. Steinberg, "Measurements and correction of ultrasonic pulse distortion produced by human breast," *J. Acoust. Soc. Am.* **97**, 1958–1969 (1995).

¹¹G. E. Trahey, P. D. Freiburger, L. F. Nock, and D. C. Sullivan, "In-vivo measurements of ultrasonic beam distortion in the breast," *Ultrason. Imag.* **13**, 71–90 (1991).

¹²Q. Zhu and B. D. Steinberg, "Wavefront amplitude distribution in the female breast," *J. Acoust. Soc. Am.* **96**, 1–9 (1994).

¹³D.-L. Liu and R. C. Waag, "Correction of ultrasonic wavefront distortion using backpropagation and a reference waveform method for time-shift compensation," *J. Acoust. Soc. Am.* **96**, 649–659 (1994).

¹⁴A. Ishimaru, "Wave propagation and scattering in random media and rough surfaces," *Proc. IEEE* **79**, 1359–1366 (1991).

¹⁵H. G. Booker and J.-W. Tao, "A scintillation theory of the fading of HF waves returned from the F-region: Receiver near transmitter," *J. Atmos. Terr. Phys.* **49**, 915–938 (1987).

¹⁶S. M. Flatté, "Wave propagation through random media: Contributions from ocean acoustics," *Proc. IEEE* **71**, 1267–1294 (1983).

¹⁷H. G. Booker and H. O. Vats, "Application of refractive scintillation theory to laser transmission through the atmosphere near ground level," *Radio Sci.* **20**, 833–841 (1985).

¹⁸L. C. Andrews and R. L. Phillips, "I-K distribution as a universal propagation model of laser beams in atmospheric turbulence," *J. Opt. Soc. Am. A* **2**, 160–163 (1985).

¹⁹C. Jung, D. Kim, and S. Y. Kim, "Surface roughness dependence of the first-order probability density function for integrated speckle," *Opt. Commun.* **100**, 508–517 (1993).

²⁰L. Weng, J. M. Reid, P. M. Shankar, and K. Soetanto, "Ultrasound speckle analysis based on the K distribution," *J. Acoust. Soc. Am.* **89**, 2992–2995 (1991).

²¹P. M. Shankar, J. M. Reid, H. Ortega, C. W. Piccoli, and B. B. Goldberg, "Use of non-Rayleigh statistics for the identification of tumors in ultrasonic B-scan of the breast," *IEEE Trans. Med. Imaging* **12**, 687–692 (1993).

²²J.-F. Chen, J. A. Zagzebski, and E. L. Madsen, "Non-Gaussian versus non-Rayleigh statistical properties of ultrasound echo signals," *IEEE Trans. Ultrason. Ferroelectr. Freq. Control* **41**, 435–440 (1994).

²³J. S. Bendat and A. G. Piersol, *Random Data: Analysis and Measurement Procedures* (Wiley, New York, 1971), Chap. 4.

²⁴J. W. Goodman, *Statistical Optics* (Wiley, New York, 1985), Chaps. 2 and 8.

²⁵R. S. Raghavan, "A method for estimating parameters of K-distributed clutter," *IEEE Trans. Aero. Electr. Sys.* **27**, 238–246 (1991).

²⁶E. Jakeman and P. N. Pusey, "A method for non-Rayleigh sea echo," *IEEE Trans. Antennas Propag.* **24**, 806–814 (1976).

²⁷R. Barakat, "Weak-scatterer generalization of the K-density function with application to laser scattering in atmospheric turbulence," *J. Opt. Soc. Am. A* **3**, 401–409 (1986).

²⁸E. Jakeman and R. J. A. Tough, "Generalized K-distribution: A statistical model for weak scattering," *J. Opt. Soc. Am. A* **4**, 1764–1772 (1987).

²⁹F. T. Ulby and M. C. Dobson, *Handbook of Radar Scattering Statistics for Terrain* (Artech House, Boston, 1989), Chap. 3.

³⁰S. D. Conte and C. Boor, *Elementary Numerical Analysis (An Algorithmic Approach)* (McGraw-Hill, Singapore, 1981), Chap. 6.

³¹R. P. Mercier, "Diffraction by a screen causing large random phase fluctuations," *Proc. Camb. Philos. Soc.* **58**, 382–400 (1962).

³²E. Jakeman, "On the statistics of K -distributed noise," *J. Phys. A* **13**, 31–48 (1980).

LETTERS TO THE EDITOR

This Letters section is for publishing (a) brief acoustical research or applied acoustical reports, (b) comments on articles or letters previously published in this Journal, and (c) a reply by the article author to criticism by the Letter author in (b). Extensive reports should be submitted as articles, not in a letter series. Letters are peer-reviewed on the same basis as articles, but usually require less review time before acceptance. Letters cannot exceed four printed pages (approximately 3000–4000 words) including figures, tables, references, and a required abstract of about 100 words.

On the Mie potential and the acoustic nonlinear parameter B/A

B. Frank and J. D. N. Cheeke

Department of Physics, Concordia University, 1455 Blvd de Maisonneuve W., Montreal, Quebec H3G 1M8, Canada

(Received 10 July 1996; accepted for publication 25 September 1996)

The set of two coupled equations of Hartmann connecting the acoustical nonlinear parameter B/A with the reciprocal sound velocity $1/c$, for liquids, through the parameters of the Mie potential, is replaced by a simple empirical equation linear and near quadratic in linear combinations of B/A and $1/c$. The latter equation contains an exponent μ which is a function of the Mie exponents m and n . It is shown that this empirical relation closely approximates the pair solution over a significantly wider range of variables than the purely linear equation posited by Hartmann to explain the empirical Ballou's rule. © 1997 Acoustical Society of America. [S0001-4966(97)01502-6]

PACS numbers: 43.25.Ba [MAB]

INTRODUCTION

The nonlinear acoustic properties of liquids is a subject that is becoming of increasing importance in a number of areas, particularly in medical imaging,¹ cavitation,² and shock wave lithotripsy.³ The high acoustic power densities associated with focused acoustic beams lead to strong harmonic generation, and this can be of concern for aspects such as tissue damage, image contrast, and medical diagnostics.

The subject was formalized by Beyer⁴ who defined the nonlinear parameter from the adiabatic equation of state:

$$\frac{B}{A} = 2\rho c \left(\frac{\partial c}{\partial p} \right)_T + \left(\frac{2\alpha c T}{C_p} \right) \left(\frac{\partial c}{\partial T} \right)_p. \quad (1)$$

For liquids, B/A is known as *the* nonlinear acoustic parameter.

There have been many measurements of B/A in liquids, ranging from early measurements of p and T derivatives of the sound velocity by Beyer and co-workers to more recent methods such as finite amplitude,⁵ constant entropy,⁶ and optical methods.⁷ B/A generally lies in the range 5–12, with extreme variations 2 and 13 being reported. An early observation was made by Ballou⁸ regarding the approximate linear variation of B/A with $1/c$. Further experimental work by Madigosky *et al.*⁹ showed, for a wide range of liquids, that although B/A generally does increase with $1/c$, the scatter is so large that there does not seem to be *any* universal curve that would truly fit the existing data; a straight line would describe the behavior only very roughly.

In order to understand the B/A vs $1/c$ data, therefore, the best that one can do is divide the acoustic materials into

families, and attempt to provide a theoretical treatment for each family separately. A pioneering effort in this direction was made by Hartmann¹⁰ who considered families of liquids with characteristic intermolecular Mie potentials, each with its own set of Mie parameters. Starting with a pair of coupled equations incorporating neglect of a small thermal pressure term, Hartmann, (inspired by Ballou's rule) assumed linearity for each family, and showed how to calculate the slopes and intercepts, carrying this out explicitly for a specific potential. The B/A data then, on this model, would be represented by a set of straight lines, one for each family.

The need for a more complete theory has long been recognized (see, e.g., the thermodynamic approach of Sharma¹¹), but no effort has heretofore been made to extend the calculations in the direction laid out by Hartmann. To this end, it is here proposed to take the next step in the analysis of Hartmann's molecular approach, namely, to investigate the shape of the B/A vs $1/c$ curves flowing from the coupled equations when the linearity assumption is not made. It will be shown in this paper that the coupled equations lead numerically to substantial nonlinear behavior. As well, for the specific potential chosen by Hartmann, a simple empirical nonlinear equation is found that represents this behavior over a wide range of the variables.

I. THEORY

Hartmann's molecular approach was based on the theoretical framework developed by Moelwyn-Hughes¹² (MH). In this framework, an intermolecular Mie potential in the form

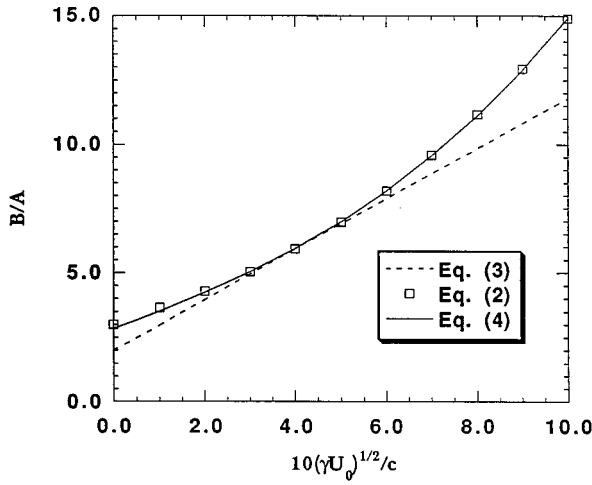


FIG. 1. Dimensionless graph of B/A vs $10(\gamma U_0)^{1/2}/c$. Equation (3) is represented by symbols at selected points, rather than by a continuous curve, in order to render it visually distinguishable from Eq. (4).

$$U/U_0 = (n-m)^{-1} [m(V/V_0)^{-n/3} - n(V/V_0)^{-m/3}]$$

is assumed, where $-U_0$ is the minimum value of the potential, and V_0 corresponds to the molecular separation at which U is at a minimum. Hartmann uses the equation

$$c^2 = \frac{U_0 \gamma m n}{9(n-m)} \left[(n+3) \left(\frac{V}{V_0} \right)^{-n/3} - (m+3) \left(\frac{V}{V_0} \right)^{-m/3} \right], \quad (2a)$$

where near $V=V_0$ he has neglected a term $\gamma RT(n+m+1)/2M$ as contributing less than 10% to c^2 at room temperature. This term, arising from the thermal pressure, appears on the right-hand side of the corresponding equation of MH.

With the assumptions (i) that γ is a constant; (ii) that the intermolecular potential is a central force potential that depends only on the distance r between two molecules; and (iii) that the thermal pressure can be neglected, Hartmann notes that B/A can be expressed as $B/A = -2(d \ln c / d \ln V)$. The differentiation is carried out using the V dependence of c in (2a) to give

$$B/A = [m(m+3) - n(n+3)(V/V_0)^{-(n-m)/3}] / 3[(m+3) - (n+3)(V/V_0)^{-(n-m)/3}]. \quad (2b)$$

Elimination of V/V_0 from Eqs. (2a) and (2b) could in principle yield B/A as a function of c . However, at this point Hartmann, effectively assuming B/A to be linear in $1/c$, proceeds to calculate the slope and intercept of this linear relationship, using zero temperature and pressure (i.e., $V=V_0$) as the reference point. For $m=9$ and $n=6$, he arrives at the following linear equation:

$$B/A = 2 + (96\gamma U_0)^{1/2}/c. \quad (3)$$

For different m , n , and γU_0 , the numbers 2 and 96 in the above equation would be appropriately replaced and the resulting equation would then describe a different family of materials. (Provided that these replacements do not substantially alter the slope and intercept, and to the extent that γU_0 is approximately the same for all liquids, this equation may be said to have the general form of Ballou's rule.)

TABLE I. B/A vs $10(\gamma U_0)^{1/2}/c$ from Eqs. (2), (3), and (4).

| $10(\gamma U_0)^{1/2}/c$ | B/A [Eq. (4)] | B/A [Eq. (2)] | B/A [Eq. (3)] |
|--------------------------|-----------------|-----------------|-----------------|
| 0 | 2.849 | 3.000 | 2.000 |
| 1 | 3.511 | 3.651 | 2.979 |
| 2 | 4.233 | 4.283 | 3.959 |
| 3 | 5.028 | 5.030 | 4.939 |
| 4 | 5.920 | 5.920 | 5.919 |
| 5 | 6.975 | 6.968 | 6.899 |
| 6 | 8.816 | 8.186 | 7.879 |
| 7 | 9.557 | 9.583 | 8.859 |
| 8 | 11.110 | 11.165 | 9.839 |
| 9 | 12.877 | 12.935 | 10.819 |
| 10 | 14.907 | 14.898 | 11.799 |

We now ask how closely linearity serves to describe the full curve of Eqs. (2). It is observed that one need not make any assumption about the linearity or otherwise of B/A as a function of $1/c$, as it is a simple matter to compute the graph of B/A vs $(\gamma U_0)^{1/2}/c$, for a given family of potentials m , n . This is most easily done by replacing the variable V/V_0 in the equations by the variable η given by

$$\eta = (V/V_0)^{-(n-m)/3},$$

and using, e.g., the two-variable Newton-Raphson procedure. We have computed Eqs. (2) for the choice $m=9$, $n=6$ in order to compare with Hartmann's linear ($m=6$, $n=9$) result. The resulting graph is shown in Fig. 1, where the exact solution of Eqs. (2) used by Hartmann is superimposed on Hartmann's linear solution equation (3). It is seen that in the range $5 < B/A < 7$, the curve of (2) is indeed almost linear. However, outside this range, deviations from linearity are evident.

A simple nonlinear fit to Eq. (2) may be devised by examining Fig. 1. There, if we set up a new, rotated coordinate frame with origin at the reference point $(B/A)_0=6$, $(96\gamma U_0)^{1/2}/c_0=4$ and abscissa x' along the linear curve (3), then the curve of Fig. 1 would to good accuracy be symmetrical about the new ordinate y' . It would look, in fact, roughly quadratic, prompting a trial function of the form $y' = \text{const}(x')^\mu$ with $\mu \approx 2$. Transforming back to the original coordinate frame, ensuring that the trial curve passes through the point [which satisfies Eqs. (2)] $B/A=8.186$, $1/c=0.0006 \text{ s m}^{-1}$, and experimenting with different values of μ , we find that the following curve gives a very accurate representation of Fig. 1:

$$y - x = 0.0246(y+x)^{1.8}, \quad (4a)$$

where

$$y = B/A - 6, \quad x = (96\gamma U_0)^{1/2}/c - 4. \quad (4b)$$

Table I compares the values obtained from Eqs. (2), (3), and (4).

Higher accuracy can no doubt be obtained by doing a least-squares fit, to selected points on curve (2), of

$$y - x = c'(y+x)^{\mu'}$$

with parameters c' and μ' to be determined. However, at this stage in the comparison with experiment, this would not be of special interest.

II. CONCLUDING REMARKS

We have in this paper taken the next logical step in the solution of the coupled equations of the molecular model, realizing that it is not necessary to make, as does Hartmann, an assumption of linearity (or of any other functional dependence) in order to find the solution. A numerical treatment of these equations has yielded an exact set of solution points for a wide range of values of $1/c$. A comparison of the results of Hartmann's linear model with our exact set shows that the former is indeed accurate, but only over a relatively very small energy range. We have also found a simple expression, resulting from a two-parameter trial function, which closely represents the exact solution for the choice $m=9$, $n=6$. It does so over almost the full range of $1/c$; i.e., wherever $B/A > 3$.

ACKNOWLEDGMENTS

This work was supported by the Natural Sciences and Engineering Research Council (NSERC) of Canada. The authors thank Dr. N. W. Eddy for technical help with Fig. 1.

¹C. A. Cain, "Ultrasonic reflection mode imaging of the nonlinear parameter B/A : I. A theoretical basis," *J. Acoust. Soc. Am.* **80**, 28–32 (1986).

- ²E. A. Neppiras, "Acoustic cavitation," *Phys. Rep.* **61**, 160–251 (1980).
- ³L. A. Crum, C. C. Church, and D. T. Blackstock, "Extracorporeal shock wave lithotripsy," *Phys. Today* **42**(1), S.4 (January 1989).
- ⁴R. T. Beyer, "Parameter of nonlinearity in fluids," *J. Acoust. Soc. Am.* **32**, 719–721 (1960).
- ⁵W. N. Cobb, "Finite amplitude method for the determination of the acoustic nonlinearity parameter B/A ," *J. Acoust. Soc. Am.* **73**, 1525–1531 (1983).
- ⁶C. M. Sehgal, R. C. Bahn, and J. F. Greenleaf, "Measurement of the acoustic nonlinearity parameter B/A in human tissues by a thermodynamic method," *J. Acoust. Soc. Am.* **76**, 1023–1029 (1984).
- ⁷H. A. Kashkooli, P. J. Dolan, and C. H. Smith, "Measurement of the acoustic nonlinearity parameter in water, methanol, liquid nitrogen, and liquid helium-II by two different methods: A comparison," *J. Acoust. Soc. Am.* **82**, 2086–2089 (1987).
- ⁸A. B. Coppens, R. T. Beyer, and J. Ballou, "Parameter of nonlinearity in fluids. III. Values of sound velocity in liquid metals," *J. Acoust. Soc. Am.* **41**, 1443–1448 (1966).
- ⁹W. M. Madigosky, I. Rosenbaum, and R. Lucas, "Sound velocities and B/A in fluorocarbon fluids and in several low density solids," *J. Acoust. Soc. Am.* **69**, 1639–1643 (1981).
- ¹⁰B. Hartmann, "Potential energy effects on the sound speed in liquids," *J. Acoust. Soc. Am.* **65**, 1392–1396 (1979).
- ¹¹B. K. Sharma, "Nonlinearity acoustical parameter and its relation with Rao's acoustical parameter of liquid state," *J. Acoust. Soc. Am.* **73**, 106–109 (1983).
- ¹²E. A. Moelwyn-Hughes, *Physical Chemistry*, 2nd ed. (Pergamon, Oxford, 1961).

Understanding the periodic driving pressure in the Rayleigh–Plesset equation

William C. Moss^{a)}

Lawrence Livermore National Laboratory, P.O. Box 808, Livermore, California 94550

(Received 6 November 1995; revised 24 June 1996; accepted 30 September 1996)

The Rayleigh–Plesset equation is the basis of most theoretical analyses of bubble dynamics. Surprisingly, experiment and theory do not agree on the spatial location and the value of the periodic driving pressure. In the experiment the driving pressure is located near the bubble, whereas, the theory assumes that the driving pressure is far from the bubble. The paradox is resolved by deriving a modified equation that is valid for compressible flows in a finite spherical geometry. The modified equation is identical to the incompressible Rayleigh–Plesset equation with the driving pressure at infinity replaced by the actual driving pressure, which is located within 25 bubble radii of the bubble. We show that a hydrophone at the center of the flask measures this driving pressure, which is why the theory and experiment agree when an incompressible Rayleigh–Plesset equation is used to describe compressible flows. © 1997 Acoustical Society of America. [S0001-4966(97)03002-6]

PACS numbers: 43.25.Yw [MAB]

The Rayleigh–Plesset equation (RPE) describes the radial growth and collapse of a gas bubble in a periodically driven incompressible liquid. It was formalized in 1950, based on the work of Rayleigh,¹ Plesset,² and Noltingk and Neppiras.³ Although the RPE and its subsequent modifications^{4–8} remain the basis of almost all theoretical analyses of bubble dynamics, there is some confusion among experimentalists and theorists about the location and magnitude of the pressure that actually drives the motion of the bubble. Experimentalists place a hydrophone at the location of a bubble (thus destroying the bubble) and use the measured pressure as the driving pressure in the RPE. There usually is good agreement between the resulting solution of the RPE and the experimental data. Theoretical derivations of the RPE (and its modifications),^{3–8} with the exception of Plesset,² define the driving pressure as the liquid pressure far from the bubble. The theoretical and experimental locations of the driving pressure are not the same, which creates a paradox. This paradox was recognized by Moss *et al.*,⁹ who analyzed the growth and collapse of a sonoluminescing bubble, by solving numerically the full hydrodynamic equations, including nonlinearly compressible liquids and gases. These numerical solutions required much smaller driving pressures than the RPE solutions to obtain the same maximum bubble radii. The difference was attributed to the compressibility of the liquid and/or spherical convergence, but was not discussed by the authors. This letter shows that the paradox arises primarily from the assumption that the far-field pressure is the same as the effective pressure that drives the motion of the bubble. Although this assumption is correct for an incompressible fluid, it is not correct for a compressible fluid. We review first the standard derivation of the RPE in an incompressible flow, then we show that the RPE can be modified to account for the pressure that actually drives the radial motion of a bubble in a compressible flow. This theo-

retical approach resolves the paradox and yields results that are consistent with experimental practice.

The RPE may be derived³ by considering a bubble of radius R in an incompressible liquid of density ρ and uniform hydrostatic pressure P_0 . A time-dependent pressure, $P_\infty(t) \equiv -P_A \sin 2\pi vt$, is applied at $t=0$. Although $P_\infty(t)$ is applied *infinitely* far from the bubble, the assumption of incompressibility allows the bubble to respond immediately to $P_\infty(t)$. The RPE is obtained by equating the $P dV$ work at the boundaries of the liquid to the kinetic energy acquired by the liquid. The internal energy of the liquid is ignored. The kinetic energy acquired by the liquid is

$$\text{KE}_{\text{tot}} = \frac{\rho}{2} \int_R^\infty \dot{r}^2 4\pi r^2 dr = 2\pi\rho R^3 \dot{R}^2, \quad (1)$$

where incompressibility requires $r^2 \dot{r} = R^2 \dot{R}$.

We assume the gas in the bubble is ideal, has a constant specific heat ratio γ , and compresses isentropically and uniformly. Consequently, the gas pressure P_g is only a function of R :

$$P_g(R) = P_0(R_0/R)^{3\gamma}. \quad (2)$$

The change in the size of the bubble is the only volume change that can occur, so the $P dV$ work done to the liquid as the radius of the bubble changes from an initial value R_0 to R is done by the net pressure $P_g(R) - (P_0 + P_\infty(t))$. We ignore surface tension and viscosity and write

$$\text{IE} = \int_{R_0}^R (P_g(R) - P_0 - P_\infty(t)) 4\pi R^2 dR. \quad (3)$$

The RPE is obtained by equating the internal and kinetic energies [Eqs. (1) and (3)] and differentiating with respect to R :

$$\frac{P_0(R_0/R)^{3\gamma} - P_0 - P_\infty(t)}{\rho} = \frac{3\dot{R}^2}{2} + R\ddot{R}, \quad (4)$$

where $d\dot{R}/dR = \ddot{R}/\dot{R}$.

^{a)}Electronic mail: wmoss@llnl.gov

Equation (4) is solved for $R(t)$ by numerical integration with initial conditions $R(0)=R_0$ and $\dot{R}(0)=0$. It is important to note that the derivation of Eq. (4) assumes that all the $P dV$ work is converted to kinetic energy. There is no internal energy stored in the liquid, because it is incompressible.

The RPE [Eq. (4)] is valid for a globally incompressible flow in an infinite medium. Unfortunately, real liquids are compressible and real experiments have boundaries. Even modified RPE that have first-order corrections for compressibility⁵⁻⁸ do not account for the actual pressure that drives the bubble, or finite boundaries. These modified equations are derived by considering only the differences of thermodynamic quantities at the bubble wall and infinity. The pressure that drives the bubble in a compressible flow is not located at infinity.

We rederive the RPE in the following paragraphs, for a compressible flow in a finite spherical geometry. We describe the kinetic energy using *locally incompressible* flow, and we replace $P_\infty(t)$ with a linear elastic standing wave solution that accounts for the spherical geometry and the finite boundaries.

The radius of the bubble changes in response to pressure waves in the liquid. The bubble can respond *only* to waves that reach it. During an increment δt , the bubble motion is influenced by the pressure field $P(r,t)$ in a shell of liquid of thickness $c \delta t = (\alpha - 1)R$ that surrounds the bubble, where α is a number greater than one. We consider the $P dV$ work done to the bubble by the net pressure $P_g(R) - (P_0 + P(\alpha R, t))$ at the boundaries of the region that can influence the bubble during the time δt . We may equate the total $P dV$ work to the kinetic energy acquired by the liquid, by analogy to the derivation of Eq. (4), if $P(\alpha R, t)$ and R do not change appreciably during δt , that is, if the liquid is *locally incompressible*.

The two main time scales for the dynamics are set by the drive frequency ($1/\nu_{\text{drive}} \approx 40 \mu\text{s}$) and the Minnaert resonance frequency¹⁰ for bubble oscillations ($1/\nu_{\text{Minnaert}} \approx 1-30 \mu\text{s}$). Consequently, the Minnaert frequency sets the time scale δt and the distance scale α . Estimates for δt and α can be obtained by equating δt to a small fraction β of the natural period of a freely oscillating bubble, i.e., the reciprocal of the Minnaert resonance frequency. We write

$$\delta t = \frac{(\alpha - 1)R}{c} = \frac{\beta}{\nu_M} = \beta 2 \pi R \sqrt{\frac{\rho_L}{3 \gamma P_0}}, \quad (5)$$

where ρ_L is the liquid density, and $\alpha - 1$ is the thickness of the liquid shell in units of the bubble radius. We must compromise between a δt that is small enough to ensure incompressibility and an α that is large enough to account for most of the kinetic energy in the flow. The latter requirement is necessary for our theoretical analysis to be consistent with experimental practice.

We relate α to the total kinetic energy by replacing the upper limit in the integral in Eq. (1) with αR , which yields¹¹

$$\text{KE}(\alpha) = \frac{\rho}{2} \int_R^{\alpha R} r^2 4 \pi r^2 dr = \text{KE}_{\text{tot}} \left(1 - \frac{1}{\alpha} \right). \quad (6)$$

Equation (6) shows that most of the kinetic energy in the liquid is located near the bubble, e.g., 96% of the kinetic energy is contained within a shell that is $25R$ thick ($\alpha=26$); when $R=100 \mu\text{m}$, $26R=2.6 \text{ mm}$. Equation (5) shows that $\beta=0.05$, when $\alpha=26$ ($P_0=1 \text{ bar}$, $\rho=1 \text{ g/cc}$, and $\gamma=1.4$). A small value of β , that is, a time that is a small fraction of the natural oscillation period, ensures the pressure has sufficient time to reach the bubble before significant incremental motion occurs. Consequently, the driving pressure is located within 25 bubble radii from the bubble when $\alpha=26$. Fully compressible hydrodynamic numerical simulations confirm this result.¹²

We substitute Eq. (6) for Eq. (1) and replace $P_\infty(t)$ in Eq. (3), with the as yet unknown pressure $P(\alpha R, t)$. The same procedure that was used to obtain Eq. (4) from Eqs. (1)–(3) yields a modified RPE that accounts for the finite sound speed in the liquid. The condition of local incompressibility allows the relevant part of the globally compressible flow to be modeled using an RP energy analysis. We write

$$\frac{P_0(R_0/R)^{3\gamma} - P_0 - P(\alpha R, t)}{\rho} = \left(\frac{3\dot{R}^2}{2} + R\ddot{R} \right) \left(1 - \frac{1}{\alpha} \right), \quad (7)$$

where $P(\alpha R, t)$ remains to be determined. The factor in Eq. (7) that contains α may be neglected, when $\alpha=26$, so that the modified RPE [Eq. (7)] differs from the RPE [Eq. (4)] only in the value of the time-dependent driving pressure $P(\alpha R, t)$.

We use Euler's equation¹³

$$\rho \left(\frac{\partial \mathbf{v}}{\partial t} + \mathbf{v} \cdot \nabla \mathbf{v} \right) + \nabla P = 0, \quad (8)$$

to obtain an approximate linear elastic standing wave solution for $P(\alpha R, t)$, by superposing two solutions that give the desired boundary conditions. The first piece is the lowest-order term of an incompressible solution of Eq. (8) with the boundary conditions $P(R, t) = P_g(R) - P_0$ and $P(R_L, t) = 0$, where R_L is the radius of the liquid that surrounds the bubble. We assume for convenience that a flask having the same impedance as the liquid and infinitesimal thickness surrounds the liquid. The second piece is a linearized solution¹⁴⁻¹⁶ of Eq. (8) with the boundary conditions $P(R, t) = 0$ and $P(R_L, t) = -P_A \sin 2\pi \nu t$. We obtain

$$P(r, t) = \frac{R P_0 ((R_0/R)^{3\gamma} - 1)}{r} - \frac{P_A R_L}{r} \frac{-\cos kr + \cot kR \sin kr}{-\cos kR_L + \cot kR \sin kR_L} \sin 2\pi \nu t, \quad (9)$$

where $k = 2\pi \nu / c$. The first term is always small for the values of r ($r > 10R$) we are considering, so we neglect it in the subsequent discussion. The second term in Eq. (9) differs from the RPE driving pressure $P_\infty(t)$ only by a time independent multiplicative factor. Figure 1 (lines) shows the amplification factor $P(r, t) / (P_A \sin 2\pi \nu t)$ as a function of r , for constant bubble radii of 4, 40, and 100 μm . Spherical convergence amplifies the pressure that is applied at the flask boundary. The peak pressure is located within a few mm of

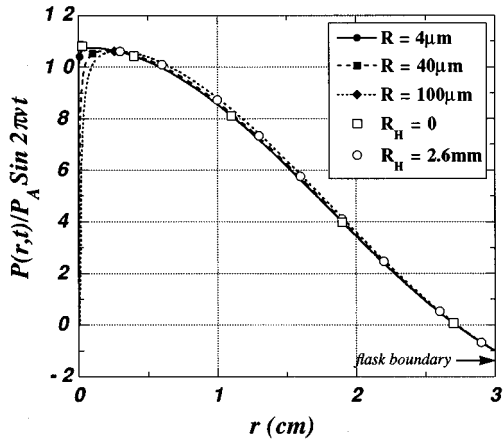


FIG. 1. Radial dependence of the (analytic) standing wave amplification factor, for constant bubble radii of 4, 40, and 100 μm . The solid symbols show the values of the amplification factor at $r=26R$ for each bubble. The driving pressure (solid symbols) is insensitive to the radius of the bubble. The open symbols show the radial dependence of the analytic standing wave amplification factor, for hydrophone radii of 0 (open squares) and 2.6 mm (open circles). Either hydrophone measures the correct driving pressure.

the center of the flask. The solid symbols in the figure show the amplification factors at $r=26R$, which is the location of the driving pressure. These values are relatively insensitive to the bubble radius, which helps validate our use of a locally incompressible RP analysis.

Although Eq. (9) and Fig. 1 show the standing wave solution in the presence of a bubble, there is no bubble present when a hydrophone is used to measure the driving amplitude. The pressure near the hydrophone and the bubble will differ, because the boundary conditions for a standing wave solution in the presence of a bubble differ from those for a hydrophone. We obtain a linear elastic standing wave solution for the pressure in the presence of a hydrophone, by linearizing¹⁴ and solving^{15,16} Eq. (8). The boundary conditions are $\mathbf{v}(R,t)=0$ and $P(R_L,t)=-P_A \sin 2\pi vt$. We write

$$P(r,t) = -\frac{P_A R_L}{r} \times \frac{kR_H \cos k(r-R_H) + \sin k(r-R_H)}{kR_H \cos k(R_H-R_L) - \sin k(R_H-R_L)} \times \sin 2\pi vt, \quad (10)$$

where R_H is the radius of the hydrophone. The open symbols in Fig. 1 show the radial dependence of the amplification factor $P(r,t)/(P_A \sin 2\pi vt)$ for the hydrophone solution [Eq. (10)]. Solutions for hydrophones having radii of 0 (open squares) and 2.6 mm (open circles) are shown. The calculated pressure at either hydrophone (open symbols at $r=0$ and $r=2.6$ mm) is nearly the same as the pressure at $r=26R$ with the bubble present, for the three different bubble radii. We conclude that a hydrophone measures the correct driving pressure.

Equations (9) and (10) can be simplified, because we are concerned only with the value measured by the hydrophone

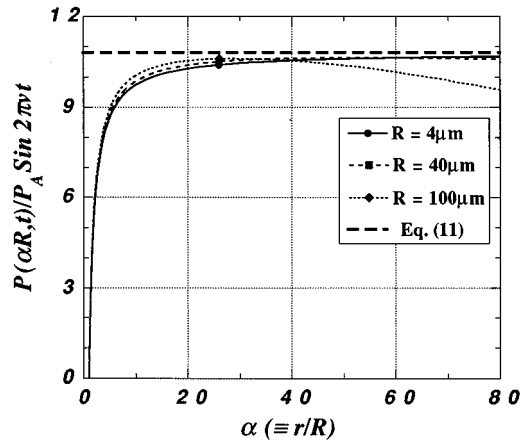


FIG. 2. Same as Fig. 1. Curves are shown as a function of $\alpha(\equiv r/R)$. The thick dashed line is the amplification factor from Eq. (11) [$kr \ll 1$, $kR \ll 1$, $r > 10R$, and $R_H=0$].

near the center of the flask. *Both* equations reduce to the same form, when kr and $kR \ll 1$, $r > 10R$, and $R_H=0$. We obtain

$$P(r,t) \approx [-kR_L \csc kR_L][P_A \sin 2\pi vt], \quad (11)$$

where the amplification factor is $-kR_L \csc kR_L$. Equation (11) is exact to $O[R_H^2]$. The amplification results from spherical convergence and depends only on the driving frequency, the sound speed in the liquid, and the radius of the flask (liquid). This approximate but simple expression shows the relationship between the boundary pressure and the pressure near the bubble, which drives the radial motion. Figure 2 replots the graphs in Fig. 1, as a function of $\alpha(\equiv r/R)$. The thick dashed line shows the amplification factor from Eq. (11), which is a constant. A hydrophone that is placed near the center of the flask measures the entire r.h.s. of Eq. (11), whereas, the second bracketed term is the pressure applied to the flask. Equation (11) and the RPE become identical (the amplification factor equals 1) as $kR_L \rightarrow 0$, which occurs in the limit of large sound speeds, small flask radii, or small frequencies. Substituting Eq. (11) for $P(\alpha R,t)$ in Eq. (7), and setting $\alpha=26$, we obtain a modified RPE that is valid for a compressible flow in a finite spherical geometry. This modified RPE is identical to the incompressible RPE [Eq. (4)] with $P_\infty(t)$ replaced by the pressure that is measured by a hydrophone at the center of the flask. Thus, we have derived theoretically the equation for the radial motion of a bubble that experimentalists use routinely to analyze their data.

Our results show that the Rayleigh–Plesset equation, which has been used for nearly 50 years to describe bubble dynamics, has been misinterpreted by theorists in its application to liquids under typical experimental conditions, i.e., compressible liquids in a finite geometry. We have shown that the periodic driving pressure P_A , which is assumed by theorists to be (i) applied at an infinitely distant boundary and (ii) responsible for driving the bubble motion, is *only* the pressure that is applied at the boundary of the system. P_A is amplified near the bubble by spherical convergence, and it is the amplified pressure within 25 radii of the bubble that

drives the radial motion of the bubble. This resolves the paradox of the location and the magnitude of the pressure that drives the motion of the bubble.

We derived a modified RPE [Eq. (7)] for a compressible liquid in a finite spherical geometry, using “local incompressibility” and the actual driving pressure near the bubble. The modified RPE is identical to the incompressible RPE [Eq. (4)] with the far-field pressure $P_\infty(t)$ replaced by the amplified pressure near the bubble. We showed that a hydrophone measures this amplified pressure, so that our modified RPE is completely consistent with the experimental practice of using hydrophone measurements of the driving pressure in the incompressible RPE [Eq. (4)] to describe the motion of bubbles in compressible liquids with finite geometries. Our analysis unites theory and experimental practice.

It is important to note that the inconsistencies in the interpretation of the RPE would have remained hidden without the compressible hydrodynamic numerical simulations, which illuminates the intrinsic strengths and value of hydrodynamic numerical simulations.

ACKNOWLEDGMENTS

The author thanks R. Keolian for motivating this paper, particularly Eq. (6), and R. Roy, A. J. C. Ladd, and D. B.

Clarke for insightful comments. J. Levatin’s computational assistance is appreciated greatly. This work was performed under the auspices of the U.S. Department of Energy by Lawrence Livermore National Laboratory under Contract No. W-7405-Eng-48.

¹Lord Rayleigh, *Philos. Mag.* **34**, 94–98 (1917).

²M. Plesset, *J. Appl. Mech.* **16**, 277–282 (1949).

³B. E. Noltingk and E. A. Neppiras, *Proc. Phys. Soc. London, Sec. B* **63**, 674–685 (1950).

⁴T. G. Leighton, *The Acoustic Bubble* (Academic, San Diego, CA, 1994), Chap. 4, pp. 306–308.

⁵H. G. Flynn, “Physics of Acoustic Cavitation in Liquids,” in *Physical Acoustics*, edited by W. P. Mason (Academic, New York, 1964), Chap. 9, pp. 72–78.

⁶C. Herring, OSRD Report No. 236 (1941).

⁷J. G. Kirkwood and H. A. Bethe, OSRD Report No. 588 (1942).

⁸F. R. Gilmore, Report No. 26-4, Hydrodynamics Laboratory, California Institute of Technology (1952).

⁹W. C. Moss, D. B. Clarke, J. W. White, and D. A. Young, *Phys. Fluids A* **6**, 2979–2985 (1994).

¹⁰Reference 4, p. 139.

¹¹R. Keolian (private communication).

¹²W. C. Moss (unpublished).

¹³Reference 4, Chap. 2, pp. 96–101.

¹⁴Reference 4, Chap. 2, pp. 101–103; $|\mathbf{v} \cdot \nabla \mathbf{v}| \ll |\dot{\mathbf{v}}|$ and $\delta \rho \ll \rho_0$.

¹⁵A. C. Eringen, *Mechanics of Continua* (Krieger, Huntington, NY, 1980), Chap. 6.

¹⁶*Mathematica* (Wolfram Research, Inc., Champaign, IL, 1993), Vol. 2.2.

An empirical relation to predict ultrasonic velocity in electrolytic solutions

S. Sivaramakrishna Iyer^{a)} and M. Abdulkhadar^{b)}

School of Pure and Applied Physics, Mahatma Gandhi University, Kottayam 686560, Kerala, India

(Received 8 March 1996; accepted for publication 20 August 1996)

An empirical relation to predict ultrasonic velocity in an electrolytic solution in terms of the surface tension and density of and ultrasonic velocity in water and surface tension, density and a function $f(\alpha)$ of degree of dissociation of the solution is suggested. The relation may be used to predict ultrasonic velocity at any concentration of the solution, provided the ultrasonic velocities at two other concentrations are known. The agreement between the predicted and observed values is good.

© 1997 Acoustical Society of America. [S0001-4966(97)00701-7]

PACS numbers: 43.35.Bf [HEB]

INTRODUCTION

Ultrasonic studies in electrolytic solutions provide us with information regarding their structure as well as physical and chemical processes taking place in them. Extensive studies are available on the dependence of quantities like ultrasonic velocity, adiabatic compressibility, molar sound velocity and hydration number of electrolytic solutions on their concentrations.¹⁻³ Many empirical as well as theoretical relations based on Debye-Huckel theory¹ are used in the study of parameters like Bachem's constants, Molar compressibility and Rao's constant to cite a few.⁴ But there is no relation available for the satisfactory prediction of ultrasonic velocity in electrolytic solutions.

Many theories, like collision factor theory of Schaaffs,^{5,6} statistical theory of Flory⁷ combined with Auerbach's empirical relation,⁸ and free length theory of Jacobson⁹ are available for the prediction of ultrasonic velocity in pure liquids and their mixtures.¹⁰⁻¹³ But none of these theories are successful in the prediction of ultrasonic velocities in electrolytic solutions.^{1,2} It seems that any expression for the ultrasonic velocity in electrolytic solutions must take into account the number of ions partaking in the transfer of acoustic energy and hence should involve some function of the degree of dissociation. Debye-Huckel theory, which takes into account the number of ions per unit volume of the ionic atmosphere, has been found successful in the determination of acoustic parameters like apparent molar compressibility and apparent molar volume of low as well as high concentrations.^{1,2}

Prompted by Auerbach's relation,⁸ and making use of Debye-Huckel theory, an attempt has been made here to obtain an empirical relation for the ultrasonic velocity in electrolytic solutions.

I. THEORY AND METHOD

According to Oka's relation¹⁴ based on Debye-Huckel theory, the surface tension (σ_c) of an electrolytic solution at a temperature t , and concentration c is given by

$$\sigma_c = \sigma_w + (Ne^2 Z^2 c / 4000D),$$

where c = concentration of the electrolytic solution in moles per liter, σ_c = surface tension in cgs units at temperature t and concentration c , σ_w = surface tension of water in cgs units at temperature t , D = dielectric constant of water at temperature t , $Z^2 = Z_+ Z_-$, where Z_+ = valency of the positive ion, Z_- = valency of the negative ion, e = electronic charge in esu, and N = Avogadro's number.

For various electrolytic solutions, σ_c is calculated using Oka's relation for different values of c for which the values of ultrasonic velocity v_c and density ρ_c are available from the literature.^{15,16} σ_w and D along with v_w , the ultrasonic velocity in water and ρ_w , the density of water at temperature t are taken from international critical tables. Then

$$(\sigma_w \rho_w / v_w) / (\sigma_c \rho_c / v_c) = \gamma \quad (1)$$

is calculated. Temperature remaining constant, γ is found to decrease at different rates for different electrolytes from a value of approximately unity as c increases (Table I). γ and c are found to have an approximate inverse linear relation between them (Fig. 1).

For the present calculations, we assume an exact inverse linear relationship between γ and c . Using calculated values of γ for two extreme concentrations for which v_c and ρ_c are available from the literature, values of γ for other intermediate values of c are graphically interpolated. The mean square deviations of the interpolated values of γ from those calculated using relation (1) are found to be extremely small in all the systems studied (Table II), justifying the assumption of an inverse linear relationship between γ and c . From the interpolated values of γ , v_c is calculated using relation (1).

II. RESULTS AND DISCUSSION

Auerbach⁸ observed that the addition of a salt increases both the surface tension of and ultrasonic velocity in water in the same sequence. But his relation⁸ yielded a value which is only 50% of the observed value for the surface tension of water when he used measured values of density and ultrasonic velocity. The relation failed in the case of aqueous solutions of electrolytes also. Auerbach's relation⁸ has been

^{a)}Department of Physics, University College, Thiruvananthapuram 695034, India.

^{b)}To whom correspondence should be addressed.

TABLE I. Calculation of γ and α' .

| Electrolyte | c
mol/liter | v_c
obs m s ⁻¹ | ρ_c
g/cc | σ_c
cgs units | γ | $\frac{\Lambda}{\text{ohm}^{-1} \text{m}^2}$
$\times 10^{-4}$ | $\frac{\Lambda_0}{\text{ohm}^{-1} \text{m}^2}$
$\times 10^{-4}$ | α' |
|---|------------------|--------------------------------|------------------|-------------------------|----------|--|--|-----------|
| NaCl | 0 | 1483.0 | 0.9982 | 72.92 | | | | |
| $M=58.44$ (20 °C) | 1.0690 | 1554.5 | 1.0413 | 73.38 | 0.9986 | 76.5 | 113.9 | 0.6716 |
| | 1.8308 | 1600.5 | 1.0707 | 73.71 | 0.9953 | 68.5 | | 0.6014 |
| | 3.0572 | 1673.0 | 1.1162 | 74.24 | 0.9909 | 58.0 | | 0.5092 |
| | 3.9248 | 1772.5 | 1.1478 | 74.62 | 0.9872 | 52.5 | | 0.4609 |
| | 4.8461 | 1771.5 | 1.1804 | 75.01 | 0.9820 | 47.0 | | 0.4126 |
| KBr | 0.0830 | 1486.5 | 1.0054 | 72.96 | 0.9945 | 114.5 | 136.5 | 0.8388 |
| $M=119.0$ (20 °C) | 0.5271 | 1495.0 | 1.0426 | 73.15 | 0.9622 | 109.0 | | 0.7985 |
| | 0.9002 | 1502.5 | 1.0740 | 73.31 | 0.9367 | 106.0 | | 0.7766 |
| | 1.9464 | 1521.5 | 1.1601 | 73.76 | 0.8727 | 100.0 | | 0.7326 |
| | 3.1730 | 1545.5 | 1.2593 | 74.29 | 0.8108 | 95.0 | | 0.6960 |
| | 4.6173 | 1573.0 | 1.3746 | 74.91 | 0.7498 | 90.5 | | 0.6630 |
| NaI | 0.4180 | 1483.0 | 1.0463 | 73.10 | 0.9517 | 89.5 | 109.4 | 0.8180 |
| $M=149.9$ (20 °C) | 0.7220 | 1483.0 | 1.0808 | 73.23 | 0.9196 | 85.0 | | 0.7769 |
| | 1.5669 | 1486.5 | 1.1769 | 73.60 | 0.8423 | 76.5 | | 0.6992 |
| | 2.5794 | 1494.0 | 1.2907 | 74.03 | 0.7673 | 68.5 | | 0.6261 |
| | 3.8083 | 1509.0 | 1.4271 | 74.57 | 0.6960 | 61.0 | | 0.5575 |
| | 4.5201 | 1524.0 | 1.5062 | 74.87 | 0.6633 | 57.0 | | 0.5210 |
| KNO ₃ | 0.2500 | 1516.0 | 1.0179 | 71.35 | 0.9791 | 123.0 | 125.8 | 0.9777 |
| $M=101.1$ (30 °C) | 0.5000 | 1524.0 | 1.0287 | 71.47 | 0.9724 | 114.0 | | 0.9062 |
| | 1.0000 | 1539.0 | 1.0613 | 71.70 | 0.9489 | 102.5 | | 0.8148 |
| | 2.0000 | 1569.0 | 1.1112 | 72.15 | 0.9180 | 86.0 | | 0.6836 |
| | 2.5000 | 1584.0 | 1.1309 | 72.38 | 0.9077 | 79.0 | | 0.6280 |
| | 3.5000 | 1598.0 | 1.1806 | 72.84 | 0.8718 | 67.0 | | 0.5326 |
| Ca(NO ₃) ₂ ·4H ₂ O: | 0.2640 | 1524.0 | 1.0311 | 71.48 | 0.9700 | 95.5 | 112.6 | 0.8481 |
| $M=236.2$ (30 °C) | 0.5280 | 1541.0 | 1.0612 | 71.72 | 0.9498 | 85.0 | | 0.7549 |
| | 0.8000 | 1552.0 | 1.0867 | 71.97 | 0.9309 | 78.0 | | 0.6927 |
| | 1.0600 | 1568.0 | 1.1166 | 72.21 | 0.9123 | 72.5 | | 0.6439 |
| | 1.6000 | 1600.0 | 1.1812 | 72.70 | 0.8740 | 63.0 | | 0.5695 |
| | 2.0000 | 1618.0 | 1.2207 | 73.07 | 0.8509 | 56.0 | | 0.4973 |
| Pb(NO ₃) ₂ | 0.1210 | 1510.0 | 1.0332 | 71.35 | 0.9609 | 92.0 | 122.6 | 0.7504 |
| $M=331.2$ (30 °C) | 0.2500 | 1501.0 | 1.0731 | 71.47 | 0.9180 | 84.5 | | 0.6892 |
| | 0.5000 | 1491.0 | 1.1392 | 71.70 | 0.8563 | 74.0 | | 0.6036 |
| | 1.0000 | 1469.0 | 1.2687 | 72.15 | 0.7528 | 60.0 | | 0.4894 |
| | 1.5380 | 1459.0 | 1.4038 | 72.65 | 0.6711 | 48.0 | | 0.3915 |

applied successfully in the case of liquids¹⁰ and their mixtures,¹¹⁻¹⁵ the surface tension being calculated on the basis of Flory's statistical theory.^{7,10}

In the empirical relation (1) for v_c, σ_c has been calculated using Oka's relation which is based on Debye-Huckel theory. So the relation has a direct dependance on Debye-Huckel theory. A detailed analysis using literature values of σ_w, ρ_w, ρ_c , and v_c and calculated value of σ_c shows that at a temperature t , the ratio $(\sigma_w \rho_w / v_w) / (\sigma_c \rho_c / v_c) = \gamma$, decreases approximately from a value of 1 as c increases. The calculated values of σ_c , literature values of σ_w, ρ_w, ρ_c , and v_c and the calculated values of γ are given in Table I. It may be noted that σ_w, ρ_w , and v_w are the values for water at t °C and not at 0 °C or any other temperature, since the modification of ultrasonic velocity at t °C due to the addition of an electrolyte in water is to be accounted for. The relation (1) is found to hold good for twelve 1-1 and 2-1 electrolytic solutions in a wide range of concentration of about 0.1 to 5 mole/liter, the molecular weights of the salts used ranging from about 58 in the case of NaCl to 331 in the case of Pb(NO₃)₂ (Table I). To save space data of only six systems are included in Tables I and II.

It is but logical to argue that any modification of the ultrasonic velocity in water due to the addition of an electrolyte must depend on the molecular weight of the electrolyte, concentration of the solution and the number of ions in the

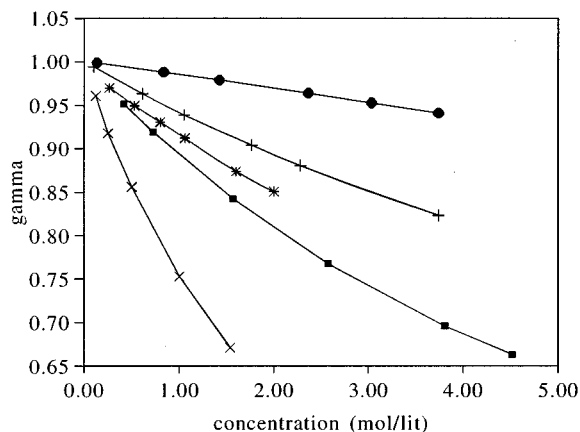


FIG. 1. Variation of gamma with concentration. ● KCl, + NaBr, * calcium nitrate, ■ NaI, × lead nitrate.

TABLE II. Mean square deviation of γ and calculated values of v_c .

| Electrolyte | c
mol/liter | v_c
(obs)
m s ⁻¹ | γ
(graphically
interpolated) | Mean square
deviation of
γ | v_c
(cal)
m s ⁻¹ |
|---|------------------|-------------------------------------|---|---|-------------------------------------|
| NaCl: $M=58.44$ (20 °C) | 1.8308 | 1600.5 | 0.9953 | 8.11×10^{-7} | 1600.5 |
| | 3.0572 | 1673.0 | 0.9899 | | 1671.3 |
| | 3.9248 | 1722.5 | 0.9860 | | 1720.7 |
| KBr: $M=119.0$ (20 °C) | 0.5271 | 1495.0 | 0.9700 | 2.53×10^{-4} | 1507.0 |
| | 0.9002 | 1502.5 | 0.9500 | | 1524.0 |
| | 1.9464 | 1521.5 | 0.8950 | | 1560.0 |
| | 3.1730 | 1545.5 | 0.8275 | | 1577.0 |
| NaI: $M=149.9$ (20 °C) | 0.7220 | 1483.0 | 0.9325 | 5.69×10^{-4} | 1504.0 |
| | 1.5669 | 1486.5 | 0.8700 | | 1535.0 |
| | 2.5794 | 1494.0 | 0.8000 | | 1557.0 |
| | 3.8083 | 1509.0 | 0.7125 | | 1545.0 |
| KNO ₃ : $M=101.1$ (30 °C) | 0.5000 | 1524.0 | 0.9705 | 1.22×10^{-5} | 1521.0 |
| | 1.0000 | 1539.0 | 0.9540 | | 1548.0 |
| | 2.0000 | 1569.0 | 0.9210 | | 1574.0 |
| | 2.5000 | 1584.0 | 0.9045 | | 1578.0 |
| Ca(NO ₃) ₂ ·4H ₂ O: $M=236.2$ (30 °C) | 0.5280 | 1541.0 | 0.9510 | 7.29×10^{-6} | 1543.0 |
| | 0.8000 | 1552.0 | 0.9330 | | 1556.0 |
| | 1.0600 | 1568.0 | 0.9150 | | 1573.0 |
| | 1.6000 | 1600.0 | 0.8780 | | 1607.0 |
| Pb(NO ₃) ₂ : $M=331.2$ (30 °C) | 0.2500 | 1501.0 | 0.9325 | 5.45×10^{-4} | 1525.0 |
| | 0.5000 | 1491.0 | 0.8825 | | 1537.0 |
| | 1.0000 | 1469.0 | 0.7800 | | 1522.0 |

solution. Tracing a physical meaning for γ , we see that the degree of dissociation of an electrolyte decreases with increase of concentration. $\alpha' = \Lambda/\Lambda_0$ (Table I) is calculated where Λ and Λ_0 are, respectively, the equivalent conductances of aqueous electrolytic solutions at concentration c and at infinite dilution, at temperature t (available from international critical tables). α' gives the approximate value of the degree of dissociation α . Although the numerical value of α' is slightly less than γ , it has the same decreasing tendency as that of γ , with increase of c . This prompts us to conclude that γ must be a function, $f(\alpha)$, of the degree of dissociation, the exact nature of which is presently not known. Once this functional relation is found out, the ultrasonic velocity in electrolytic solutions may be predicted by the relation

$$v_c = \sigma_c \rho_c f(\alpha) / (\sigma \rho_w / v_w).$$

In this work, using γ in the place of $f(\alpha)$, it is shown that this relation is valid for a number of systems for which ultrasonic velocity has been reported in the literature.

The values of v_c calculated using the interpolated values of γ for intermediate concentrations agree fairly well with observed values (Table II). It may be noted that the use of Debye–Huckel theory for the calculation of σ_c even at high concentrations does not cause a great deviation in the calculated values of v_c from the observed values. The literature values of v_c for KI show first a decreasing and then an increasing tendency with increase of c . In the case of Pb(NO₃)₂ there is a decreasing tendency for v_c as c increases. Even though such tendencies cannot be predicted using relation

(1), the calculated values of v_c in these cases have only small deviations from the literature values.

The use of the expression (1) for v_c demands an exact knowledge of $f(\alpha)$ which is presently not available. γ should be effectively obtained from α' directly or through combinations involving the molecular weight M of the electrolyte, c , ρ_c , and ionic radius. Our attempt to find an exact expression for γ in terms of α' continues. In spite of the above shortcomings, the present relation for v_c is attractive partly due to the absence of a similar expression to predict ultrasonic velocity in electrolytic solutions and partly in view of the fact that, given the ultrasonic velocity at two concentrations, the ultrasonic velocity at any other concentration can fairly accurately be predicted.

III. SUMMARY

A new parameter γ is defined in terms of surface tension and density of and ultrasonic velocity in water, and surface tension and density of and ultrasonic velocity in an electrolytic solution at concentration c . An almost inverse linear relationship is found to exist between γ and c . Knowing the value of γ at two concentrations and assuming an exact inverse linear relationship between γ and c , γ value corresponding to any other c can be obtained by interpolation. Then the ultrasonic velocity in an electrolytic solution at any concentration can be calculated. The calculated values of velocity are found to agree closely with measured values for the 12 systems studied. The essence of this method is the assumption of an inverse linear γ - c relation, to testify the validity of which more systems are to be studied.

- ¹H. S. Harned and B. B. Owen, *The Physical Chemistry of Electrolytic Solutions* (Reinhold, New York, 1958), 3rd ed.
- ²J. Stuehr and E. Yeager, "The propagation of ultrasonic waves in electrolytic solutions," in *Physical Acoustics, Principles and Methods*, edited by W. P. Mason (Academic, New York, 1964), Chap. 6, Vol. IIA.
- ³S. P. Tandon and S. Gambhir, *J. Acoust. Soc. Am.* **88**, 1837–1841 (1990).
- ⁴A. K. Das and B. L. Jha, *J. Pure Appl. Ultrason.* **11**, 67–72 (1989).
- ⁵W. Schaaffs, *Molecular Akustik* (Springer-Verlag, Berlin, 1963), Chaps. XI and XII.
- ⁶S. Parthasarathy and N. N. Bakshi, *J. Sci. Ind. Res.* **12A**, 448–453 (1953).
- ⁷P. J. Flory, *J. Am. Chem. Soc.* **87**, 1833–1838 (1965).
- ⁸R. Auerbach, *Experientia* **IV**, 473–474 (1948).
- ⁹B. Jacobson, *Acta Chem. Scand.* **6**, 1485–1497 (1952).
- ¹⁰J. D. Pandey, *J. Chem. Soc. Faraday Trans. I* **75**, 2160–2124 (1979).
- ¹¹M. S. Khanwalkar, J. S. Murty, and D. D. Deshpande, *Acoust. Lett.* **13**, 121–126 (1990).
- ¹²M. S. Khanwalkar, *Acoust. Lett.* **14**, 229–234 (1991).
- ¹³A. N. Kannappan and V. Rajendran, *Acustica* **75**, 192–195 (1991).
- ¹⁴J. R. Partington, "The properties of liquids," in *An Advanced Treatise on Physical Chemistry* (Longmans, London, 1962), Vol. II (3rd imp.), p. 198.
- ¹⁵E. B. Freyer, *J. Am. Chem. Soc.* **53**, 1313–1320 (1931).
- ¹⁶S. V. Subrahmanyam and J. Bhimsenachar, *J. Acoust. Soc. Am.* **32**, 835–838 (1960).

The frequency response of the ER-2 speaker at the eardrum

M. L. Whitehead, I. Simons, B. B. Stagner, and G. K. Martin

University of Miami Ear Institute, Miami, Florida 33101

(Received 27 March 1995; revised 10 May 1996; accepted 30 September 1996)

Distortion-product otoacoustic emissions are often measured using ER-2 speakers and the ER-10B microphone probe (Etymotic Research). The frequency response at the eardrum of the ER-2 speaker used in this configuration has not been described. An indirect estimate of the average eardrum frequency response of the ER-2 speaker used with the ER-10B probe has been obtained. The average eardrum frequency response varies less than ± 5 dB from 0.3 to 10 kHz. © 1997 Acoustical Society of America. [S0001-4966(97)05002-9]

PACS numbers: 43.64.Jb, 43.64.Yp, 43.66.Yw, 43.80.Vj [RDF]

INTRODUCTION

Measurements of distortion-product otoacoustic emissions (DPOAEs) are often made using ER-2 speakers (Etymotic Research) with an ER-10 or ER-10B microphone probe. The frequency response of the ER-2 speaker in a Zwislocki coupler is flat up to 10 kHz, when used with a 292-mm length of 1.35-mm-i.d. sound-delivery tubing and an EAR foam eartip, i.e., conditions similar to those with the ER-10 probe (see Etymotic Research literature). To a first approximation, the flat response in a Zwislocki coupler suggests a flat response at the eardrum in an average human ear canal. However, the Zwislocki coupler does not (and was not designed to) accurately simulate the average human ear canal above 4 kHz.

The ER-10B probe is more commonly used for DPOAE measurements than the ER-10. When used with the ER-10B, the ER-2 speaker is coupled to the ear canal via 228 mm of tubing, consisting of 76-mm lengths of 1.35-mm, 0.86-mm, (ER-10B-3), and 0.5-mm (ER7-14C) i.d. tubing. Relative to the tubing used with the ER-10, the tubing used with the ER-10B attenuates stimulus sound-pressure levels (SPLs) in the ear canal, and alters the frequency response of the ER-2 within the stimulus-frequency range of DPOAE studies (0.5–10 kHz). The purpose of this study was to estimate the average frequency response of the ER-2 at the eardrum, in real ears, when used with the ER-10B.

I. ESTIMATION OF EARDRUM SPL

The procedure consists of two steps, which are summarized in this paragraph, and described in more detail below. Step A determines the average SPL at the eardrum at hearing threshold in a group of subjects. Thus, the average hearing threshold curve was measured by conventional swept-frequency audiometry, using TDH-49 headphones. This average threshold curve was compared to Killion's (1978) minimum audible pressure at the eardrum curve, to determine the average SPL at the subjects' eardrums at hearing threshold. Step B determines the average voltage level at the ER-2 speaker at hearing threshold. Thus, swept-frequency audiometry was repeated using an ER-2 speaker instead of a TDH-49 headphone, and the average voltage at the ER-2 speaker (not the SPL) at hearing threshold was measured. This mean voltage is the input to the ER-2 required to pro-

duce the average SPL at threshold at the subjects' eardrums, which is known from step A. Thus, subtracting the dB voltage values from the eardrum dB SPL values of step A yields the SPL frequency response of the ER-2 at the average eardrum.

A. The average SPL at our subjects' eardrums at hearing threshold

Data were obtained from 23 ears of 8 male and 5 female adults (mean ± 1 s.d., age 25.1 ± 3.9 years) with normal middle-ear function, as assessed by standard tympanometry and acoustic-reflex testing, and hearing thresholds of < 20 dB HL, as determined by standard clinical audiometry (0.25–8 kHz), and Bekesy swept-frequency audiometry (0.25–10 kHz). All data were obtained in a soundproofed booth. For swept-frequency audiometry (TDH-49 headphone, Demlar model 120 audiometer, calibrated as ANSI-1969), the frequency-sweep rate was 1.3 oct/min, and the attenuation rate was 2.5 dB/s. Thresholds were read from the audiometer plots by measuring the midpoint of the trace excursions at frequencies of threshold maxima and minima, and at frequencies at which threshold deviated from an otherwise constant value, and extrapolating between these points in 100-Hz steps over regions of constant threshold, or of uniformly increasing or decreasing threshold. Figure 1(a) shows the mean (± 1 s.d.) dB HL thresholds obtained in this manner for the 23 ears.

The minimum audible pressure (MAP) curve of Killion (1978, his Fig. 1) describes the average stimulus SPL at the eardrum at hearing threshold in normal human ears, derived from the data of several studies that employed free-field or headphone stimulation. It is emphasized that this MAP curve is distinct from the "minimum audible pressure in a coupler" curve, which is the basis of the audiometer calibration. Adding the mean dB HL values of Fig. 1(a) to the MAP curve of Killion (1978) produces a "group-specific MAP" curve (not shown), which was assumed to give the average SPL at the eardrum at hearing threshold in the 23 ears tested.

B. The average voltage at the ER-2 speaker at hearing threshold

Swept-frequency audiometry was repeated, in the same manner as with the TDH-49 headphone, but using an ER-2

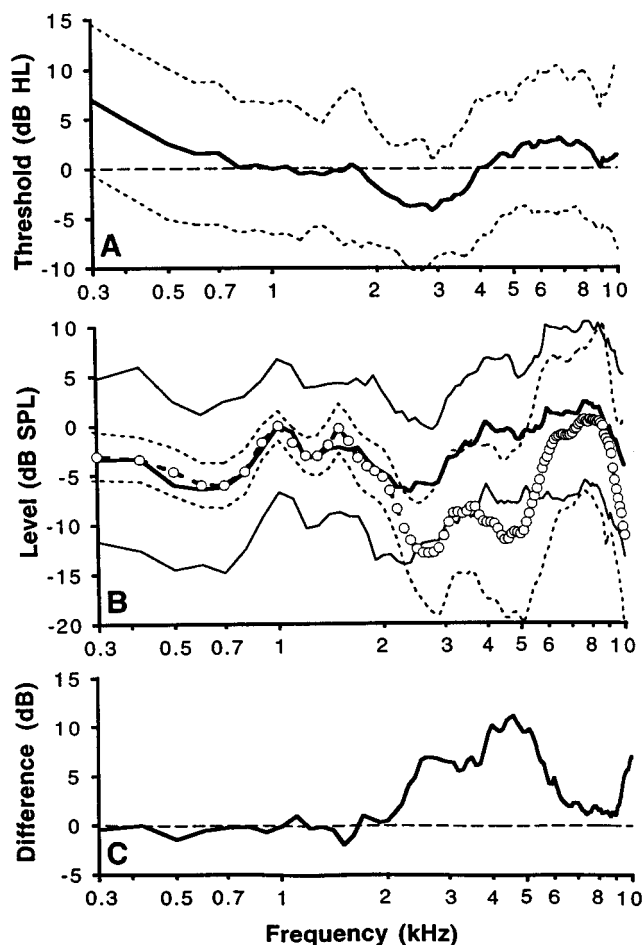


FIG. 1. (a) Mean ± 1 s.d. ($n=23$ ears) behavioral hearing threshold (dB HL) measured by swept-frequency Bekesy-tracking audiometry using a TDH-49 headphone. (b) Bold \pm standard continuous lines; mean ± 1 s.d. stimulus SPL at the eardrum upon iso-voltage input to the ER-2 speaker, derived as described in the text. Note that the data have been normalized to 0 dB SPL at 1 kHz. Open circles \pm dashed lines; mean ± 1 s.d. stimulus SPL measured by the ER-10B upon iso-voltage input to the ER-2 speaker, in 100-Hz steps, in the same 23 ears. The ER-2 was coupled to the ear canal by the three-stage sound-delivery tubing used with an ER-10B probe. The speaker command-voltage level was that which produced 65 dB SPL at 1 kHz at the ER-10B microphone, but the data have been normalized to 0 dB SPL at 1 kHz to facilitate comparison with the estimate of eardrum SPL. (c) The ratio of the mean stimulus SPL estimated at the eardrum to that directly measured at the ER-10B, i.e., the difference of the two mean curves in (b).

speaker to deliver the stimuli. An ER-10B probe was coupled to the ear canal using a standard rubber immittance eartip, in a fashion identical to its use for DPOAE testing. The ER-2 sound-delivery tubing passed through the ER-10B, and extended 5 mm beyond the probe tip, as recommended by the manufacturer. The ER-2 threshold-dB values were read from the Bekesy tracing, as described above, and averaged. In this case, however, the mean voltage (dB *re*: 1 V) delivered by the audiometer to the ER-2 speaker at threshold was determined, *not* the mean SPL at threshold. The resulting mean voltage curve (not shown) gives the voltage input to the ER-2 required to produce the mean SPL at the eardrum at hearing threshold, i.e., the SPL values of the group-specific MAP curve.

C. The frequency response of the ER-2 at the average eardrum

The voltage dB values measured in Sec I. B are the mean input to the ER-2 required to produce the SPL values of the group-specific MAP curve. Thus, subtracting these voltage dB values from the group-specific MAP dB SPL values yields the mean SPL frequency response of the ER-2 at the eardrum for an iso-voltage input. This curve is plotted as a bold line in Fig. 1(b), normalized to 0 dB SPL at 1 kHz. The average eardrum SPL frequency response is relatively flat, in that it varies by a maximum of ± 4.6 dB over the 0.3–10 kHz range. There is a pronounced SPL maximum at 1 kHz, broad minima around 0.7 and 2.7 kHz, a gradual increase from 2.7 to 8 kHz, and a rapid decline above 8.5 kHz. The standard deviations of these mean SPLs are equal to those of the mean Bekesy-tracking hearing thresholds obtained using the ER-2 speaker, and were approximately 6.5 dB between 0.8 and 6 kHz, increasing to around 8.5 dB below 0.8 kHz and above 6 kHz.

II. DISCUSSION

A. Comparison of SPL at the eardrum and probe

The mean (± 1 s.d.) stimulus SPL measured at the ER-10B microphone upon iso-voltage stimulation of the ER-2 is also shown in Fig. 1(b) (open circles \pm dotted lines). These data were obtained from the 23 ears during the same fit of the probe as the Bekesy-tracking threshold measurements. The speaker command-voltage level was that which produced 65 dB SPL at 1 kHz at the ER-10B microphone, but the data have been normalized to 0 dB SPL at 1 kHz to facilitate comparison with the estimate of eardrum SPL. Below 2 kHz the fine structure of the estimated mean stimulus SPL at the eardrum (bold line) was very similar to that directly measured by the ER-10B. At these low frequencies, where standing waves in the ear canal have little influence, stimulus SPLs are expected to be similar at both ends of the ear canal. Thus, the similarity of the average SPLs at the eardrum and the ER-10B in this frequency region suggests that the indirect measurement of average eardrum SPL is quite accurate.

Above 2 kHz, two major factors cause SPLs at the ER-10B to deviate from those at the eardrum. The first factor is standing-wave effects. Between 2 and 6 kHz, stimulus waves reflected from the eardrum partially cancel in-going pressure waves, resulting in standing-wave minima at the emission probe, but not at the eardrum (Siegel, 1994; Siegel and Hirohata, 1994; Whitehead *et al.*, 1995). When averaged across ears, the minima result in a broad reduction between 2 and 6 kHz of the mean SPL at the probe below that at the eardrum, which is clear in Fig. 1(b). Figure 1(c) shows the dB difference of mean stimulus SPL between the eardrum and the ER-10B. The difference, reaching 11 dB around 4.5 kHz, is consistent with previous descriptions of the effects of standing-wave minima (Siegel, 1994; Siegel and Hirohata, 1994; Whitehead *et al.*, 1995). In the 6–9 kHz region, standing-wave maxima occur. In Fig. 1(b) it is difficult to assess the contribution of the standing-wave maxima, as they tend to be “smoothed out” by averaging across ears, and are partially superimposed on the steep decline of stimulus SPL

above 8.5 kHz. From acoustical theory, and measurements in cylindrical cavities, stimulus SPLs are expected to be of similar magnitude at both ends of the occluded ear canal in the region of standing-wave maxima (Siegel, 1994). The similarity of the mean SPLs in the 6–9 kHz region [Fig. 1(b) and (c)] is consistent with this expectation.

The second factor causing stimulus SPLs at the ER-10B to deviate from those at the eardrum is that the microphone elements of the ER-10B probe directly pick-up some of the stimulus energy from the ER7-14C sound-delivery tubes that pass through the probe. As noted by Siegel (1994, his footnote 1) this direct pick-up can be of similar amplitude to the ear-canal stimulus levels above 4 kHz. Thus, the SPLs measured at the ER-10B microphone above 4 kHz are determined by the complex interaction between the SPLs in the ear canal at the microphone port (which are influenced by ear-canal standing-wave effects) and the direct pick-up of stimulus energy from the sound-delivery tubes. This factor may reduce the apparent depth of the standing-wave minima at the ER-10B (particularly in those ears in which the minima occur at higher frequencies), and complicates interpretation of stimulus levels measured by the ER-10B at high frequencies.

The pronounced fine structure of stimulus SPL below 3 kHz, that is apparent both at the eardrum and at the ER-10B in Fig. 1(b), consists primarily of a peak at 1 kHz, and broad minima around 0.7 and 2.7 kHz. Measurements (not shown) in a hard-walled, 9-mm i.d., cylindrical plastic cavity, using an ER-7C probe microphone at the “eardrum” position, suggest that this fine structure is associated with the three-stage sound-delivery tubing used with the ER-10B probe. This fine structure is not present in the cavity or in real ears when the ER-2 speaker is used with the 292-mm length of 1.35-mm-i.d. sound-delivery tubing used with the ER-10 probe.

B. Stimulus levels during DPOAE measurements

Two stimulus-presentation strategies have been used for DPOAE measurements (see Whitehead *et al.*, 1995, for review). In the “iso-voltage” strategy, the voltage presented to the speakers is held constant across frequency, on the basis of the assumption that the frequency response of the speakers is approximately flat at the average human eardrum. The bold line of Fig. 1(b) gives an estimate of the *average* eardrum stimulus frequency response for the iso-voltage stimulus-presentation strategy, used with an ER-2 speaker and ER-10B probe. In individual ears there will be idiosyncratic variations of the eardrum frequency response, particularly at high frequencies, because of across-ear variations of eardrum impedance (Stinson, 1990; Keefe *et al.*, 1993; Voss and Allen, 1994; Siegel and Hirohata, 1994).

In the more commonly used “in-the-ear adjustment” strategy, the voltage command to the speakers is adjusted to maintain a constant stimulus SPL across frequency at the DPOAE-measurement microphone. Figure 1(c) shows the dB difference of mean stimulus SPL between the eardrum and the ER-10B. Because the in-the-ear adjustment strategy holds the SPL at the emissions probe constant, the curve of Fig. 1(c) is an estimate of the *average* eardrum stimulus frequency response for the in-the-ear adjustment strategy,

used with an ER-2 speaker and ER-10B probe. Across individual ears, there will be large variations of the eardrum frequency response above about 2.5 kHz, depending on standing-wave effects in the ear canal, and on the interaction at the microphone of ear-canal sound pressure with direct pick-up of stimulus energy from the sound-delivery tubes.

It is clear that the average eardrum stimulus frequency response differs between the two stimulus-presentation strategies. Because the differences are primarily determined by ear-canal standing waves, and to a lesser extent by direct pick-up of stimulus energy from sound-delivery tubes, they will vary greatly across individual ears and also across probe designs (Siegel, 1994; Siegel and Hirohata, 1994; Whitehead *et al.*, 1995).

C. The estimate of eardrum SPL

The method used to measure eardrum SPL in the present study is indirect, and inaccuracies could arise from several sources. The MAP function is an estimate that may contain errors of up to 4–6 dB at 500 Hz and around 4–6 kHz, although it is thought to be accurate to within ± 1 dB at intermediate frequencies (Killion, 1978). Moreover, some inaccuracy is inherent in Bekesy swept-frequency audiometry, even at the relatively slow frequency sweep and attenuation rates used in the present study. Most of the subjects in this study were inexperienced at swept-frequency audiometry. However, the criteria the subjects used to judge threshold were presumably the same for both the TDH-49 headphone and the ER-2 speaker. Thus, for present purposes, any effects of these criteria should have effectively canceled. The excellent agreement of the mean SPL curves at the eardrum and the ER-10B below 2 kHz [Fig. 1(b)] suggests that the indirect estimate of average eardrum SPL is quite accurate.

It is emphasized that the present study estimated *average* eardrum SPLs. This technique cannot be applied to individual ears. The eardrum frequency response of the ER-2 will differ across ears, particularly at high frequencies, because of variations of ear-canal geometry and eardrum impedance (Stinson, 1990; Keefe *et al.*, 1993; Voss and Allen, 1994). Siegel and Hirohata (1994, their Fig. 5) used a probe-tube microphone near the eardrum to measure the output of an ER-1 speaker in five ears. The ER-1 was coupled to the ear canal via a 1-mm o.d. sound-delivery tube passed through a hole drilled in the immittance eartip used to seal the ER-10B probe to the ear canal. The frequency response was highly repeatable across ears up to 5 kHz, but quite variable at higher frequencies. At low frequencies, direct measurement of SPL near the eardrum is expected to be more accurate than the technique used in the present study. However, because the eardrum is positioned at an angle to the plane of the ear canal, at frequencies above 6-kHz stimulus SPLs may vary across the eardrum, and the pattern of variation across the eardrum will be frequency dependent. Stimulus SPLs measured near the eardrum at high frequencies can vary substantially as the probe-tube tip position varies by a couple of millimeters across the surface of the eardrum, or away from the eardrum parallel to the axis of the ear canal (Stinson *et al.*, 1982; Chan and Geisler, 1990; Siegel and Dreisbach, 1995). Thus, at high frequencies, SPLs

measured by a probe tube near the eardrum may not accurately indicate the SPLs effectively “seen” by the eardrum.

ACKNOWLEDGMENTS

This work was supported by funds from the Public Health Service (DC00613, DC01668, ES03500).

ANSI (1969). S3.6-1969, “American National Standard Specifications for audiometers” (American National Standards Institution, New York).

Chan, J. C. K., and Geisler, C. D. (1990). “Estimation of eardrum acoustic pressure and of ear canal length from remote points in the canal,” *J. Acoust. Soc. Am.* **87**, 1237–1247.

Keefe, D. H., Bulen, J. C., Arehart, K. H., and Burns, E. M. (1993). “Ear-canal impedance and reflection coefficient in human infants and adults,” *J. Acoust. Soc. Am.* **94**, 2617–2638.

Killion, M. C. (1978). “Revised estimate of minimum audible pressure: Where is the ‘missing 6 dB’?” *J. Acoust. Soc. Am.* **63**, 1501–1508.

Siegel, J. H. (1994). “Ear-canal standing waves and high-frequency sound

calibration using otoacoustic emission probes,” *J. Acoust. Soc. Am.* **95**, 2589–2597.

Siegel, J. H., and Hirohata, E. T. (1994). “Sound calibration and distortion product otoacoustic emissions at high frequencies,” *Hear Res.* **80**, 146–152.

Siegel, J. H., and Dreisbach, L. E. (1995). “Optical placement of a probe tube in the occluded human ear canal,” *Abst. Assoc. Res. Otolaryngol.* **18**, 119.

Stinson, M. R. (1990). “Revision of estimates of acoustic energy reflectance at the human eardrum,” *J. Acoust. Soc. Am.* **88**, 1773–1778.

Stinson, M. R., Shaw, E. A. G., and Lawton, B. W. (1982). “Estimation of acoustical energy reflectance at the eardrum from measurements of pressure distribution in the ear canal,” *J. Acoust. Soc. Am.* **72**, 766–773.

Voss, S. E., and Allen, J. B. (1994). “Measurement of acoustic impedance and reflectance in the human ear canal,” *J. Acoust. Soc. Am.* **95**, 372–384.

Whitehead, M. L., Stagner, B. B., Lonsbury-Martin, B. L., and Martin, G. K. (1995). “Effects of ear-canal standing waves on measurements of distortion-product otoacoustic emissions,” *J. Acoust. Soc. Am.* **98**, 3200–3214.

TECHNICAL NOTES AND RESEARCH BRIEFS

Paul B. Ostergaard

10 Glenwood Way, West Caldwell, New Jersey 07006

Editor's Note: Original contributions to the Technical Notes and Research Briefs section are always welcome. Manuscripts should be double-spaced, and ordinarily not longer than about 1500 words. There are no publication charges, and consequently, no free reprints; however, reprints may be purchased at the usual prices.

A demonstration apparatus of the cochlea

[43.10.Sv, 43.64.Kc]

Robert M. Keolian

Department of Physics, Naval Postgraduate School, Code PH/Kn, Monterey, California 93943-5117

The passive tonotopic traveling wave seen by von Békésy in his experiments on the cochlea is demonstrated with a hydrodynamic analog. The model apparatus consists of an 85-cm-long, 1.6-cm-i.d. horizontal tube representing the scala, closed at one end and driven by a diaphragm at the other. Projecting above this are about 120 closely spaced transparent vertical channels representing the cochlear partition, whose length varies exponentially from 21 cm near the diaphragm to 84 cm near the closed end. Water poured into the apparatus fills the horizontal tube and rises up the vertical channels to a height of 20 cm. The tops of the channels are then sealed, and the air trapped above the water surface acts like a place-dependent spring. By driving the diaphragm at various frequencies, a wave on the free surface can be seen traveling towards the channel that is resonantly excited, where most of the energy will be deposited. A derivation of the wave is presented. © 1997 Acoustical Society of America. [S0001-4966(97)04702-4]

INTRODUCTION

Part of the mystery of the mammalian cochlea is how it distinguishes different frequencies from one another so well. Even though it is small, filled with fluid, and made from tissue, its frequency selectivity corresponds to a quality factor Q which can be quite high—on the order of 100. The answer partially lies with an unusual traveling wave, first seen by von Békésy,¹ that passively deposits the energy of different frequencies at different positions along the basilar membrane. Starting with Zwislocki,² there have been numerous mathematical models of this wave throughout the years.³ This paper describes a lecture demonstration, shown in Fig. 1, which pedagogically displays the essential physics of the wave and many of the properties of the models.

I. APPARATUS

Several theoretical models of the cochlea include a basilar membrane that has a uniform mass but has a stiffness that decreases exponentially with distance from the oval window. A membrane of this type is represented by a vertical 6.0-mm-thick LEXAN THERMOCLEAR sheet.⁴ Usually used for architectural glazing, it is a hollow polycarbonate structure in the form of two thin sheets held apart by thin parallel ribs. In effect, it comprises many parallel rectangular channels, each of area $3.2 \times 10^{-5} \text{ m}^2$ and spaced apart by 6.5 mm. The sheet is cut with the channels oriented vertically into a piece 76 cm across, with a height h that varies exponentially with the horizontal distance x given by the formula $h = h_0 + H10^{x/D}$, where $h_0 = 20 \text{ cm}$, $H = 0.63 \text{ cm}$, and $D = 38 \text{ cm}$. The overall size is limited by the desire for portability. The mass of the basilar membrane is represented by water which fills the channels up to a height of h_0 . The channels of the vertical sheet are sealed at the top by a metal strip that has a small hole drilled in it above each channel. After filling, these holes are covered with vinyl electric tape to form a seal. The air trapped above the water columns, varying in length by a factor of 100, represents the stiffness of the basilar membrane.

The vertical sheet is glued into a slot cut along the length of a 85-cm-long horizontal plastic tube representing the scalas of the cochlea. Water flows freely between the horizontal tube and the vertical channels of the

vertical sheet. The inside diameter of the tube is 16 mm, but smaller may be better (see below). A single vertical 0.95-cm-i.d. tube, about 40 cm long and open at the top, branches from the horizontal tube past the sheet to represent the helicotrema. A cap at the end of the horizontal scala tube allows for draining the fluid and cleaning. An aluminum frame supports the plastic pieces and protects the joint between the vertical sheet and the horizontal tube.

In the ear, the fluid in the scala is oscillated by the stapes pressing on the oval window. This function is represented by a 7-cm-diam 1.6-mm-thick rubber diaphragm driven in its center by a small plate. A connecting rod attached to the plate joins with an eccentric, flywheel, gearbox, and hand crank mechanism through a spring. The spring gives a little compliance to the coupling, so that approximately a frequency-independent reciprocating force, rather than displacement, is applied to the rubber diaphragm.⁵ A small electromechanical shaker has been used to drive the diaphragm as well. It allows more control over the force, plus various waveforms can be applied, but with its electronics it is not nearly as portable.

Water mixed with food coloring and about 1/2 cc of Kodak Photo-Flo 200 solution⁶ per liter is poured into the apparatus through the helicotrema tube while the seals at the top of the vertical sheet are open. Too much Photo-Flo and the water foams up; too little and the water does not slide freely and the Q is poor. After air is worked out of the drive mechanism, the level is topped off and the top of the vertical sheet is sealed with tape,

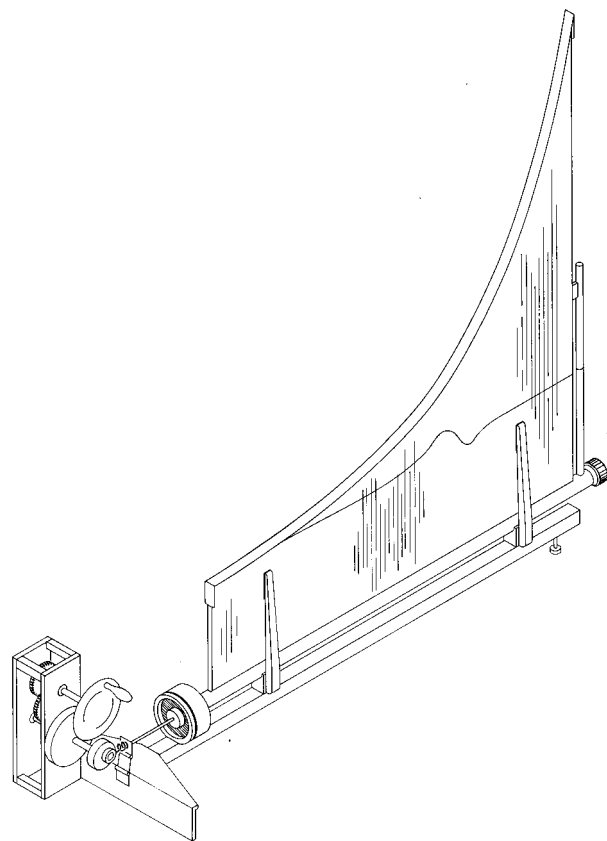


FIG. 1. The demonstration apparatus, driven by a hand crank, shows the cochlear wave on the surface of colored water contained within a hollow, ribbed plastic sheet.

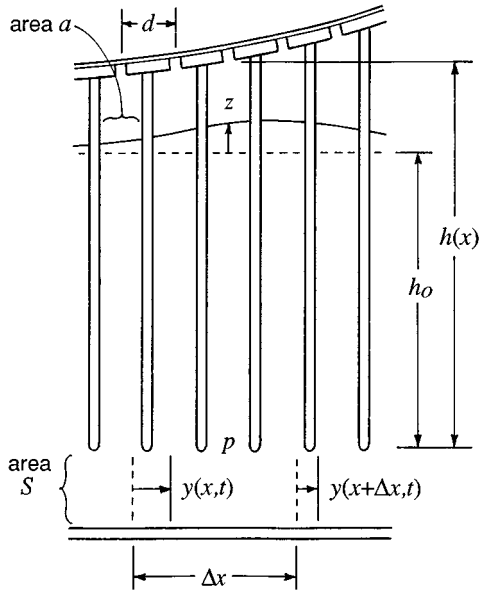


FIG. 2. Schematic detail of the vertical sheet and horizontal tube. Equilibrium positions of the liquid are shown with a dotted line; displaced positions with a solid line.

trapping air in the vertical columns. With a turn of the crank a traveling wave appears on the water surface similar to the numerical results described below.

II. WAVE EQUATION WITH VARYING MODULUS

The derivation of the wave equation for the demonstration apparatus can proceed similarly to the derivation for sound in an ordinary fluid. Assuming harmonic time variations, let $y(x,t) = Y(x)e^{j\omega t}$ be the horizontal displacement of the fluid from equilibrium in the horizontal tube, $z(x,t) = Z(x)e^{j\omega t}$ be the vertical displacement of the fluid in the THERMOCLEAR sheet, and $p(x,t) = P(x)e^{j\omega t}$ be the excess oscillatory pressure at the base of the THERMOCLEAR sheet, as shown in Fig. 2. Neglecting dissipation in the horizontal tube,⁷ Newton's force equation can be written

$$\frac{\partial p}{\partial x} + \rho \frac{\partial^2 y}{\partial t^2} = 0, \quad (1)$$

where ρ is the density of water.

The equation of continuity would normally relate the divergence of the horizontal flow to a compression of the fluid. But here, as in the cochlea, the fluid is essentially incompressible and is allowed instead to move up the THERMOCLEAR sheet—the sheet acting as a yielding side wall to the horizontal tube. If we let Δx be a short length of horizontal tube such that $d \leq \Delta x \ll \lambda$, d being the distance between vertical channels in the THERMOCLEAR sheet (we are imagining that the channels in the sheet are close enough that they can be treated as a continuum) and λ being the local wavelength, then the volume of fluid entering the short section at x is $Sy(x,t)$, the volume leaving at $x + \Delta x$ is $Sy(x,t) + S\Delta x \partial y(x,t)/\partial x$, and volume leaving through the top is $z(x,t)\Delta xa/d$, where S is the area of the horizontal tube and a is the area of each vertical channel. The continuity equation then becomes a statement that the net volume change is zero, or

$$S \frac{\partial y}{\partial x} + \frac{za}{d} = 0. \quad (2)$$

Third in the derivation for sound, an equation of state for the medium is used to relate the pressure fluctuations to the density fluctuations. Here, the mechanical properties of the vertical sheet performs this function, as does the basilar membrane in the cochlea. The pressure at the base of the vertical channels is given by the force per channel area needed to move the water column in the channel and compress the gas, given by

$$p = (K(x) + j\omega R - \omega^2 M)z/a, \quad (3)$$

where $K(x)$ is the position dependent spring constant of the gas spring, R is

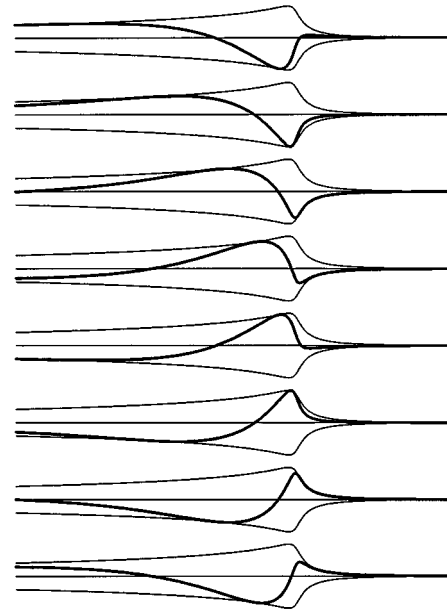


FIG. 3. Numerical results for the surface wave height z (heavy line) and its envelope (thin line) at progressive eighth cycles of the wave, from $x=0$ to 0.76 m, using, in mks units, $\omega=20\pi$, $S=1.98 \times 10^{-4}$, $a=3.16 \times 10^{-5}$, $d=6.45 \times 10^{-3}$, $h_0=0.203$, $H=6.35 \times 10^{-3}$, $D=0.381$, $R=0.0257$, $\rho=1000$, and $P_0=1.01 \times 10^5$.

the mechanical resistance of the column, and $M = \rho ah_0$ is the water mass in the column. If isothermal compressions of the gas are assumed for simplicity, a little manipulation of the ideal gas law gives $K(x) = P_0 a / h(x)$, where P_0 is the ambient atmospheric pressure. The lengths $h(x)$ and h_0 are picked to make the local side wall resonant frequency $f = (2\pi)^{-1}(K(x)/M)^{1/2}$ reasonably low. With the lengths given above, f is calculated⁸ to range from about 45 to 4.5 Hz. The damping term R can be estimated⁹ by considering the effect of the dynamic viscosity η on the water oscillating in the vertical channels. Because the viscous penetration depth $\delta_\eta = (2\eta/\rho\omega)^{1/2}$ is small compared to the size of the channel— δ_η is 0.15 mm for $f=14$ Hz, the resonant frequency at the center of the apparatus—the resistive force per channel wall area is given¹⁰ approximately by η/δ_η , so that $R = h_0 \Pi (\eta\rho\omega/2)^{1/2}$, where Π is the inside perimeter of the channel cross section.

We now have three differential equations, Eqs. (1)–(3), for the three unknowns, y , z , and p . Taking the derivative of Eq. (3) with respect to x and substituting into Eq. (1), we obtain

$$\frac{1}{a} \frac{\partial z}{\partial x} (K(x) + j\omega R - \omega^2 M) + \frac{z}{a} \frac{\partial}{\partial x} (K(x) + j\omega R - \omega^2 M) + \rho \frac{\partial^2 y}{\partial t^2} = 0. \quad (4)$$

For gradual enough variations in $K(x)$, the second term is negligible compared to the first and can be neglected. We do not want the variations to be too gradual, though, or the apparatus will be unnecessarily long. On the other hand, if the variations in K are too quick, a substantial amount of energy would be reflected back to the drive, which would not be so bad here, but in the ear it would mean that the cochlea was not absorbing all the energy that it could. So we will be guided by the ‘‘cochlear compromise’’ condition,¹¹ which is essentially the limit of validity of the WKB approximation, which states¹²

$$N \delta^{1/2} = D(4 \ln_e 10)^{-1} (R/\omega h_0^2 \rho S d)^{1/2} > 1/4, \quad (5)$$

where N is approximately the total number of cycles of the wave, and $\delta = R/\omega M = 1/Q$ is the damping function. This condition helps determine S in the design of the apparatus.

Continuing, by taking the derivative of Eq. (2) with respect to x and substituting into Eq. (4) with its second term dropped, we obtain

$$-(K(x) + j\omega R - \omega^2 M)S d a^{-2} \frac{\partial^2 y}{\partial x^2} + \rho \frac{\partial^2 y}{\partial t^2} = 0, \quad (6)$$

or if rewritten in the form

$$\frac{\partial^2 Y}{\partial x^2} + \frac{\omega^2}{c^2(x)} Y = 0, \quad (7)$$

a position-dependent complex wave speed $c(x)$ and effective bulk modulus $B(x)$ can be identified, given by

$$c^2(x) = \rho^{-1} B(x) = \rho^{-1} [K(x) + j\omega R - \omega^2 M] S d a^{-2}. \quad (8)$$

Thus it can be seen that the essential difference between the passive classical cochlear wave in this model and ordinary sound is the varying wave speed, in this case due to the apparent bulk modulus given by the side wall. Other parameters such as the membrane mass or the scala area could be varied as well.

Equation (7) was solved numerically using parameters from the apparatus, and the surface height z was obtained from this solution with Eq. (2) and plotted at eight phases of the wave in Fig. 3. Near the driven end, the effective modulus B is spring-like, as in the case for ordinary sound, and a traveling wave is seen going from left to right. But as $K(x)$ gets softer the wave slows down and grows in amplitude because of the increased compliance and the compression of energy—much like ocean waves approaching a beach. At some point the mass inertia cancels the stiffness, leaving only the dissipative part, and the wave deposits its energy at this resonant position.¹³ Further down, B is negative, c is imaginary, and the wave becomes evanescent, giving the cochlea an enhanced frequency selectivity because of the exponentially rapid falloff. The rapid falloff and the phase shifts from the traveling wave depend on the narrowness of the horizontal scala tube. The tube area chosen above for the apparatus is already somewhat large compared to the value $S = 4.2 \times 10^{-5} \text{ m}^2$ (a 7-mm-i.d. tube) given by the cochlear compromise condition, Eq. (5), at 10 Hz. Had the scala tube been much wider, all parts of the side wall would have been driven with the same pressure resulting in much larger displacements at the farther end. A smaller tube would give more cycles N of the traveling wave before reaching the resonant point, making for a better demonstration of the physics of the wave, although at the cost of increased dissipation in the horizontal tube.

III. CONCLUSIONS

The apparatus described here demonstrates von Békésy's classical passive wave, which still forms the foundation for understanding the mammalian cochlea. With additional machining of the horizontal tube, the apparatus could be modified to include the effects of variable basilar membrane mass or scala cross-sectional area. But the classical wave does not possess suffi-

cient frequency selectivity to account for the tuning found in the healthy living ear. It remains a challenge to incorporate into the apparatus the active processes¹⁴ included in more modern theories of the cochlea.

¹G. v. Békésy, *Experiments in Hearing* (McGraw-Hill, New York, 1960; republished by the Acoustical Society of America, New York, 1989).

²J. Zwislocki, "Theorie der Schneckenmechanik," *Acta Otolaryngol.* (Stockholm) Suppl. **72** (1948).

³For reviews, see: E. R. Lewis, E. L. Leverenz, and W. S. Bialek, *The Vertebrate Inner Ear* (CRC, Boca Raton, FL, 1985); or C. D. Geisler, "Mathematical Models of the Mechanics of the Inner Ear," in *Handbook of Sensory Physiology*, Vol. V/3: Auditory System, edited by W. D. Keidel and W. D. Neff (Springer-Verlag, Berlin, 1976).

⁴General Electric Company, One Plastics Avenue, Pittsfield, MA 01201.

⁵At high enough frequencies, the accelerations of the vertical water columns are large enough that surface waves are parametrically excited at the water-air interface, foaming the water [M. Faraday, "On the Forms and States assumed by Fluids in contact with vibrating elastic surfaces," *Philos. Trans. R. Soc. London*, 319–340 (1831)]. The spring helps with this problem.

⁶Eastman Kodak Company, Rochester, NY 14650, USA.

⁷Dissipation can be included with another term in Eq. (1), or by letting ρ here be complex.

⁸Slight deviations of f from these values occur because the gas compressions are actually somewhat in between being isothermal and adiabatic, which also adds some dissipation. Contributions due to gravity are negligible. A larger apparatus and lower frequencies would make a more impressive demonstration.

⁹This calculation neglects several other effects, such as turbulence generated by the sharp turn at the bottom and the slip-stick friction of the water-air interface which is being decreased by the Photo-Flo.

¹⁰L. D. Landau and E. M. Lifshitz, *Fluid Mechanics* (Pergamon, Oxford, 1959), p. 90, Eq. 24.6.

¹¹G. Zweig, R. Lipes, and J. R. Pierce, "The cochlear compromise," *J. Acoust. Soc. Am.* **59**, 975–982 (1976)

¹²To make connection to Zweig *et al.*'s Eq. (21), let their $\delta = R/2\omega M$, their $d = D/\ln_e 10$, their $L_1 = \rho/S$, and their $L = Md/a^2$.

¹³Numerical results with R about doubled give better agreement with the apparatus. The peak in the envelope is rounded a bit.

¹⁴T. Gold, "Hearing II. The physical basis of the cochlea," *Proc. Phys. Soc. London, Ser. B* **135**, 492–498 (1948).

Advanced-degree dissertations in acoustics

Editor's note: Abstracts of Doctoral and Master's theses will be welcomed at all times. Please note that they must be double spaced, limited to 200 words, must include the appropriate PACS classification numbers, and formatted as shown below (don't make the editor retype them, please!). The address for obtaining a copy of the thesis is helpful. Please submit two copies.

Characterization of cylindrical objects placed in a plane-stratified acoustic waveguide for shallow water applications [43.30.Pc, 43.20.Fn, 43.60.Pt]—Christophe Rozier, *Laboratoire des Signaux et Systemes (CNRS-SUPELEC), Plateau de Moulon, 91192 Gif-sur-Yvette Cedex, 16 October 1996 (French doctorate, University Denis Diderot, Paris)*. The inversion of closed cylindrical objects of smooth cross-sectional contours in a planar acoustic waveguide is investigated. Time-harmonic contour integral formulations of the pressure are derived for both vibrating bodies and passive-penetrable or -impenetrable obstacles immersed in a homogeneous water layer of finite depth above a hard or penetrable bottom, which models a shallow water configuration. Pressure values follow by the Nystrom method, the Green's function being calculated via a hybrid ray-mode representation. At one given frequency, two inversion problems are attacked from the resulting synthetic data: (i) the normal velocity distribution on the contour of a vibrating body is retrieved by SVD with a Tikhonov filter whose regularization parameter is found by the L curve; (ii) the contour of a convex or concave obstacle illuminated by line sources at a large range in water is constructed iteratively by a complete family approach where the scattered pressure is represented as a sum of Green's functions whose source locations evolve with the retrieved contour. The mathematical basis and the numerical machinery of the solution methods are detailed. Simulations are carried out for several objects from low- and high-frequency exact and noisy data, in near-field and far-field measurement configurations, and with partial or full coverage of water column.

Thesis advisor: Dominique Lesselier.

Frequency specificity of the auditory brainstem (ABR) and the middle latency (MLR) responses [43.64.Qh, 43.64.Ri]—Margaret A. Oates, *Doctoral Program in Speech and Hearing Sciences, Graduate Center, City University of New York, New York, NY 10036, February 1996 (Ph.D.)*. Three issues concerning the frequency specificity of the ABR and MLR to tonal stimuli were examined: (1) recording the ABR to high-intensity low-frequency stimuli; (2) the suggestion that the MLR provides a more frequency-specific response to low-frequency tones compared to the ABR; and (3) the use of nonlinear- versus linear-gated stimuli to improve the frequency specificity of these responses. The frequency specificity of these evoked potentials was investigated (12 normal subjects) using the

high-pass noise (HPN) masking/derived response (DR) technique. Stimuli were 500- and 2000-Hz exact-Blackman and linear-gated tones presented at 80 dB peak-to-peak equivalent SPL. Cochlear contributions to ABR $V-V'$ and MLR $Na-Pa$ were assessed by: (1) effects of HPN masking on ABR/MLR amplitudes and latencies; and (2) response amplitude profiles as a function of derived-band center frequency. The HPN and DR results indicate good frequency specificity for both the ABR and MLR. Maxima in the amplitude profiles occurred in the 500- and 707-Hz derived bands for responses to the 500-Hz tones and in the 1410- and 2000-Hz derived bands in response to the 2000-Hz stimuli. No significant differences were found in the frequency specificity of: (1) ABR versus MLR; (2) responses to 500- vs 2000-Hz tones; and (3) responses to exact-Blackman versus linear-gated tones.

Thesis advisor: Dr. David R. Stapells.

Thesis may be obtained from University Microfilms International, 300 North Zeeb Road, Ann Arbor, MI 48106-1346. Publication number: 9618088 in Dissertation Abstracts International Vol. (57), issue 2B, p. 973.

Critical and uncritical low-frequency relaxation processes in mixtures near the critical point of stratification [43.35.Bf] (in English and Russian)—Sirojiddin Mirzaev, *Heat Physics Department Academy of Sciences Republic of Uzbekistan, Chilonzor "C," Katarial 28, 700135, Tashkent, Uzbekistan, 16 May 1996 (Ph.D.)*. The aim of this thesis is the experimental study of critical and uncritical low-frequency relaxation processes in mixtures with small values of critical sound absorptions. In the first chapter of the thesis a review of experimental and theoretical works on investigation of acoustical properties of liquids having critical point stratification (CPS) was made. Works which study chemical reaction kinetics near CPS are analyzed separately. The influence of closeness to critical points on the rate of a molecular reaction, is discussed. In the second chapter a brief description of the experimental technique is given. A description of the experimental installation aimed to study liquid-liquid phase diagrams near the boiling temperature of solutions having CPS is presented. The results of this investigation, consisting of two main parts is dealt with in chapters three and four. The third chapter describes the basic results of investigation by means of acoustical spectroscopy of mixtures, methanol-heptan, methanol-cyclohexane, and methanol-benzene-water in a wide region of temperatures near the critical one. A description of the analysis of acoustical absorption spectra is also presented. The critical attenuation is analyzed in terms of the dynamic scaling theory of Ferrell-Bhattachardjee. In the fourth chapter the results of investigation of the kinetics of mono- and bimolecular reactions near CPS of three-component mixtures: cyclohexanol-water-methanol and acetic acid-heptane-water are given. Kinetic parameters characterizing mono- and bimolecular reactions were established not to depend on the closeness to the critical point.

Thesis advisor: Academician, Prof. P. Khabibullaev.